C 55.2:C 61/2/988

Proceedings of the Thirteenth Annual Climate Diagnostics Workshop

Atmospheric and Environmental
Research Inc.
Cambridge, Massachusetts

October 31-November 4, 1988

PENNSYLVANIA STATE UNIVERSITY
APR 26 1989
DOCUMENTS COLLECTION

U.S. Depository Copy

U.S. DEPARTMENT OF COMMERCE
National Oceanic and Atmospheric Administration
National Weather Service
Climate Analysis Center / NMC

Publications listed below are available in both hard copy and microfiche form from the National Technical Information Service, U.S. Department of Commerce, Sills Building, 5285 Port Royal Road, Springfield, VA 22161. Prices on request. Order by accession number (given in parentheses). When articles in any of the Workshops are referenced, please include the appropriate number at the end of the reference. This allows various journals to accept these references more readily.

Proceedings of the First Climate Diagnostics Workshop	(PB264993)
Proceedings of the Second Climate Diagnostics Workshop	(PB282151)
Proceedings of the Third Climate Diagnostics Workshop	(PB298355)
Proceedings of the Fourth Climate Diagnostics Workshop	(PB80-201130)
Proceedings of the Fifth Climate Diagnostics Workshop	(PB81-222200)
Proceedings of the Sixth Climate Diagnostics Workshop	(PB82-219486)
Proceedings of the Seventh Climate Diagnostics Workshop	(PB83-208033)
Proceedings of the Eighth Climate Diagnostics Workshop	(PB84-192418)
Proceedings of the Ninth Climate Diagnostics Workshop	(PB85-183911)
Proceedings of the Tenth Climate Diagnostics Workshop	*
Proceedings of the Eleventh Climate Diagnostics Workshop	(PB87-175741)
Proceedings of the Twelfth Climate Diagnostics Workshop	(PB88-191747)

* Proceedings of the Tenth Climate Diagnostics Workshop was combined with the First WMO Workshop on the Diagnosis and Prediction of Monthly and Seasonal Variations over the Globe. Reference is WMO/Long-Range Forecasting Research Report Series No. 6, Volumes I and II, WMO/TD-No. 87, January 1986.

Proceedings of the Thirteenth Annual Climate Diagnostics Workshop

Held at the

Atmospheric and Environmental
Research Inc.
Cambridge, Massachusetts

October 31-November 4, 1988

March 1989

U.S. DEPARTMENT OF COMMERCE
C. William Verity, Secretary

National Oceanic and Atmospheric Administration
William E. Evans, Under Secretary

National Weather Service
Dr. Elbert W. Friday, Jr., Assistant Administrator

Thirteenth Annual
Climate Diagnostics Workshop
Cambridge, Massachusetts
October 31-November 4, 1988

PREFACE

The Thirteenth Annual Climate Diagnostics Workshop was hosted by the Atmospheric and Environmental Research, Inc. (AER) in Cambridge, MA. The success of the Workshop was enhanced by the work of Rick Rosen, David Salstein, David Gutzler and the AER organizing committee, who with the Climate Analysis Center jointly planned and organized the Workshop. Session Chairmen: Rick Rosen, Phillip Arkin, Chester Ropelewski, John Janowiak, Dave Gutzler, Ants Leetmaa, Vern Kousky, Wei-Chyung Wang, Dale Lowry, Robert Livezey and Donald Gilman are commended for their effective and enthusiastic management of the sessions. The excellent facilities, local arrangements, and hospitality provided by the AER staff made the Workshop a pleasant and intellectually stimulating experience for all participants.

Thanks also go to Professor Michael B. McElroy, Harvard College, who gave his viewpoints on "The Challenge of Global Change" at the evening dinner for the Workshop participants.

At the Climate Analysis Center, Chester Ropelewski served as Chairman of the organizing committee. Gail Lucas and Elaine Michaelides provided secretarial services. Finally, Luke Mannello served as Editor of the final volume of manuscripts and was responsible for the timely publication of these Proceedings.

These Proceedings provide a published record of the presentations made at the Workshop. This Workshop, the largest of this series of 13, had sessions on the following topics: Analysis of Recent Climate Anomalies, Large-Scale Diagnostics, Interannual Variability, Climate Trends, Regional Climate Studies, Large-Scale Model Diagnostics, Coupled Ocean-Atmosphere Models, Intraseasonal Oscillations, Climate Data Sets, and Medium and Extended Range Forecasting (Experimental Forecast Center Related Activities, Errors and Predictability, and Empirical Studies).

I would like to thank all participants for their contributions and participation in another successful Workshop.

David R. Rodenhuis, Director
Climate Analysis Center
February 1989

Thirteenth Annual Climate Diagnostics Workshop
Cambridge, Massachusetts
October 31 - November 4, 1988

List of Participants

John Anderson	University of Wisconsin
Phillip A. Arkin	NOAA/NWS/CAC
Klaus Arpe	European Centre for Medium Range Weather Forecasting
Timothy Barnett	Scripps Institution of Oceanography, Univ. of Calif.
Tony Barnston	NOAA/NWS/CAC
Lennart Bengtsson	European Centre for Medium Range Weather Forecasting
Uma S. Bhatt	University of Wisconsin
George J. Boer	Canadian Climate Center
William Bolhofer	National Climate Program Office
Grant Branstator	NCAR
Garrett Campbell	Colorado State University
Mark A. Cane	Lamont/Doherty Geological Observatory/Columbia Univ.
Peter Caplan	NOAA/NMC
Dan Cayan	Scripps Institution of Oceanography, Univ. of Calif.
Fung C. Chang	NASA/GLA
Mike T.-C. Chen	Iowa State University
Shyh-Chin Chen	Scripps Institution of Oceanography, Univ. of Calif.
Wilbur Chen	NOAA/NWS/CAC
John Christy	University of Alabama
Ulrich Cubasch	Max Planck Institute
Clara Deser	University of Washington
Henry F. Diaz	NOAA/ERL
Randall Dole	Massachusetts Institute of Technology
Stephen Doty	NOAA/NESDIS
Arthur V. Douglas	Creighton University
Richard Eilbert	Entropy Limited
Jan Eischeid	CIRES
Ron Englebertson	SAIC
Edward S. Epstein	NOAA/NWS/CAC
Chris Folland	NOAA/NWS/CAC
Francis Fujioka	US Forest Service, USDA
Oswaldo Garcia	NOAA/ERL
Joyce Gavin	Lamont/Doherty Geological Observatory/Columbia Univ.
Donald L. Gilman	NOAA/NWS/CAC
Nick Graham	Scripps Institution of Oceanography, Univ. of Calif.
Gary Greenhut	NOAA/ERL
Arnold Gruber	NOAA/NESDIS
G. V. Gruza	USSR Department of Climate Monitoring/HYDROMET
David S. Gutzler	Atmospheric and Environmental Research, Inc.
Stefan Hastenrath	University of Wisconsin
Wayne Higgins	NASA/GLA
David Howarth	University of Louisville
John Janowiak	NOAA/NWS/CAC
Roy Jenne	NCAR
C.-Y. Jim Kao	Los Alamos National Laboratory
Thomas R. Karl	NOAA/NESDIS
David Karoly	Princeton University/AOS Program

Siri J. S. Khalsa	CIRES
George Kiladis	CIRES
William H. Klein	University of Maryland
John L. Knox	Canadian Climate Center
Vernon Kousky	NOAA/NWS/CAC
T. N. Krishnamurti	Florida State University
Kenichi Kuma	Florida State University
Yochanan Kushnir	Princeton University/AOS Program
Peter J. Lamb	Illinois State Water Survey
K.M. Lau	NASA/GLA
Ants Leetmaa	NOAA/NWS/CAC
Kerang Li	Atmospheric and Environmental Research, Inc.
Brant Liebmann	CIRES
Richard Lindzen	Massachusetts Institute of Technology
Robert E. Livezey	NOAA/NWS/CAC
Dale A. Lowry	National Climate Program Office
John McAfee	NOAA/ERL
Morris McCutchan	US Forest Service, USDA
Michael McElroy	Harvard University
Gerald Meehl	NCAR
Arthur J. Miller	Scripps Institution of Oceanography, Univ. of Calif.
Kingtse Mo	NOAA/NWS/CAC
Mark L. Morrissey	University of Hawaii
Steven Mullen	Universtiy of Michigan
Tom Murphree	University of Calif., Davis
Paul Mutschlecner	Los Alamos National Laboratory
Jerome Namias	Scripps Institution of Oceanography, Univ. of Calif.
Peter Nelson	Atmospheric and Environmental Research, Inc.
Reginald E. Newell	Massachusetts Institute of Technology
Sumant Nigam	Universtiy of Maryland
Julia Nogues-Paegle	University of Utah
Edward O'Lenic	NOAA/NWS/CAC
Jerry G. Olsen	NCAR
Jan Paegle	University of Utah
Chung-Kyu Park	NASA/GLA
David Portman	Atmospheric and Environmental Research, Inc.
John Prohaska	Marblehead, MA
V.T. Radiuhin	USSR World Data Center, Obninsk
Eugene Rasmusson	University of Maryland
V.N. Razuvaev	USSR World Data Center, Obninsk
Robert Reeves	NOAA/R/CAR
George C. Reid	NOAA/ERL
Richard W. Reynolds	NOAA/NWS/CAC
Michael B. Richman	Illinois State Water Survey
John O. Roads	Scripps Institution of Oceanography, Univ. of Calif.
Alan D. Robock	University of Maryland
David Rodenhuis	NOAA/NWS/CAC
Jeffrey C. Rogers	Ohio State University
Baruch Ronberg	US Forest Service, USDA
Chester Ropelewski	NOAA/NWS/CAC
Richard D. Rosen	Atmospheric and Environmental Research, Inc.
David A. Salstein	Atmospheric and Environmental Research, Inc.
Edward S. Sarachik	University of Washington
Crystal Schaaf	Air Force Geophysics Laboratory

Jae Schemm	NASA/GLA
Peter Scholefield	Canadian Climate Center
Siegfried Schubert	NASA/GLA
Amir Shabbar	Canadian Climate Center
Ellen Steiner	University of Colorado
Paul Tattelman	Air Force Geophysics Laboratory
James W. Telford	Desert Research Institute
Robert A. Tomas	NOAA/NOS
Zoltan Toth	University of Maryland
M. Stephen Tracton	NOAA/NWS/CAC
Huug van den Dool	University of Maryland
A. James Wagner	NOAA/NWS/CAC
Wei-Chyung Wang	Atmospheric and Environmental Research, Inc.
Michael N. Ward	United Kingdom Meteorological Office
Klaus W. Weickmann	NOAA/ERL
Tom Wigley	Universtiy of East Anglia
Klaus Wolter	NOAA/NWS/CAC
Tamara M. Wood	Atmospheric and Environmental Research, Inc.
Stanley F. Woronko	Canadian Climate Center
Chien-Hsiung Yang	Air Force Geophysics Laboratory
John Zapotocny	Creighton University
Stephen Zebiak	Lamont/Doherty Geological Observatory, Columbia Univ.
Francis W. Zwiers	Canadian Climate Center

Program for the 13th Annual
Climate Diagnostics Workshop
Cambridge, Massachusetts
October 31 - November 4, 1988

Session I. Analysis of Recent Climate Anomalies
Chair: D. R. Rodenhuis

	Page
Ocean/Atmosphere variability during 1985-1988. . . V. E. Kousky and A. Leetmaa	1
Interannual variability in the tropical Pacific Ocean during 1985 -1988 . . . . . A. Leetmaa and M. Ji	9
The severe drought of 1988: Possible response to persistent El Niño conditions . . . . . A. V. Douglas	12
The 1988 drought in Canada . . . . . P. Scholefield, T. Guezen and R. Raddatz	19
Large scale patterns of tropical convection during 1986-1988 . . . . . O. Garcia and P. S. Naegele	24

Session II. Large Scale Diagnostics
Chair: R. Rosen

Low frequency variations of the Southern Hemisphere circulation . . D. Karoly	29
Cloud-radiative forcing obtained from NOAA OLR data . . . . . A. Gruber and A. Thomasell	34
Temporal variations in the relationships between analyzed upper tropospheric divergence and inferred convection in the tropics. . . . . P. A. Arkin, K. C. Mo, F. Sornatale and A. Vernekar	41
An analysis of Pacific Ocean jet streams during 1986-87 Winter . . . . . K. M. Weickmann and G. M. Kiladis	*
Global scale diabatic heating distributions and atmospheric mass anomalies . . . . . J. Christy	46
Observed large-scale spatial relationships between sea surface temperature and atmospheric circulation across the tropical Pacific. . . . . D. S. Gutzler and T. M. Wood	52
Climatological aspects of the tropical annual cycle. . . . . C. F. Ropelewski, M. S. Halpert and E. M. Rasmusson	57
The response of tropical troposphere and lower stratosphere to variations in Pacific sea-surface temperature . . G. C. Reid, K. S. Gage, and J. R. McAfee	61

* Presentation was made at the Workshop, but paper was not submitted.

Page

Planetary scale waves: stationary, persistent, and transient . . . . . .R. S. Lindzen, S. Nigam, and A. Da Silva *

A composite study of intraseasonal oscillations in atmospheric angular momentum and outgoing long-wave radiation during Northern Hemisphere winter . . . . . S. J. S. Khalsa and K. M. Weickmann 66

Relationships among observed sea level pressure, sea-surface temperature and surface wind over the tropical Pacific during warm and cold years. . . . . .C. Deser and J. M. Wallace 73

A global re-analyses; Data input and methods. . . . . R. Jenne 79

Standard meteorological observations set for the U.S.S.R. area and its application to regional climate research. . . . . T. A. Belokrylova, N. V. Mamontov, B. A. Martuganov and V. N. Razuvayev 85

Session III. Interannual Variability
Chair: P. Arkin

The response of mid-latitude cyclones to interannual and intra-annual changes in the tropical circulation . . . . . J. R. Anderson and J. Gyakum *

Interannual variability of intra-seasonal oscillations . . . . . K. Kuma 90

A solar-ocean relation: Fact or fiction?. . . . . T. P. Barnett 96

An evaluation of an association between the 11-year solar cycle, the QBO, and the atmosphere . . . . . A. G. Barnston and R. E. Livezey 102

Annual and interannual variation of global water vapor transport . . T-C. Chen 109

Variability of surface wind stress over the ocean. . . . . J. G. Olson and K. E. Trenberth 118

Climatology of west wind bursts in the equatorial western Pacific and their relationship to El Niño . . . . . M. L. Morrissey and M. A. Lander 127

The interannual variability of growing season precipitation over central North America . . . . . M. B. Richman and P. J. Lamb 133

Relationships between seasonal circulation modes of the tropics and the Northern Hemispheric extratropics . . . . . K. Wolter and R. Livezey 143

Recent temperature trends in the N. Hemisphere . . . . . D. Karoly 147

Location periods with linear trends in climatic data series. . . . . V. T. Radiuhin and B. L. Shilenko 153

* Presentation was made at the Workshop, but paper was not submitted.

Page

Session IV. Climate Trends
Chair: C. F. Ropelewski

Comparison of corrected sea surface and air temperature for the globe and the hemispheres, 1856 - 1988 . . . . . C. K. Folland and D. E. Parker 160

Statistical significance of global warming . . . . T. M. L. Wigley, P. D. Jones, P. M. Kelly, and S. C. B.Raper A-1#

Annual cycle and long-term trends of large-scale features of the tropical climate system . . . . . K. Wolter and S. Hastenrath 166

Seasonal temperature variability over the North Atlantic Arctic...J. C. Rogers 170

Session V. Regional Climate Studies
Chair: J. Janowiak

Regional analysis of the secular variation of Northern Hemisphere 50-kPA heights . . . . . A. Shabbar, K. Higuchi and J. L. Knox 176

Relationships between sea surface temperatures and seasonal rainfall in the Sahel and N.E. Brazil . . . . . M. N. Ward 184

Experimental indices for monitoring global drought conditions. . . . . K. H. Bergman, P. Sabol, and D. Miskus 190

Circulation regimes of drought in the eastern versus the western part of the Subsaharan Africa . . . . . U. S. Bhatt 198

Specifying surface temperature, dew point, wind speed and precipitation frequency for monthly fire-weather outlooks . . . W. H. Klein and B. T. Whistler 204

Monthly precipitation and temperature relations, the United States, 1931-1987 . . . . . H. M. van den Dool 210

Precipitation fluctuation over semi-arid region in northern China and the relationship with El Niño/Southern Oscillation . . . . . K. Li and W-C. Wang 214

Session VI. Large Scale Model Diagnostics
Chair: D. Gutzler

The April-June 1988 North American Drought as a tropically forced phenomenon . . . . . G. Branstator, K. Trenberth, and P. Arkin 220

Blocking and GCMs: An overview . . . . . S. L. Mullen 224

Climate experiments with the NMC model . . .M. Kanamitsu, E. Kalnay, and K. Mo 231

Tropical-extratropical interactions in a model atmosphere . . . . . T. Murphree and B. Weare 235

Manuscript arrived late; see Appendix.

Page

Linear predictability . . . . . J. O. Roads 241

GCM observational comparison: regional and local climate. . . . . T. R. Karl, W-C. Wang, D. A. Portman and M. E. Scheslinger 251

Regional climate characteristics: A comparison between observations and general circulation model statistics. . D. A. Portman, W-C. Wang, and T. R. Karl 256

Multiple recurrence analysis . . . . . F. W. Zwiers and H. von Storch 261

Vorticity budget of the upper tropical troposphere as evaluated from NMC analyses . . . . . E. M. Rasmusson and K. Mo 265

A comparison of poleward momentum transports from GCM simulations to observations . . . . . .R. W. Higgins, C. K. Park and D. M. Straus 269

Session VII. Coupled Ocean-Atmosphere Models
Chair: A. Leetmaa

Dynamical forecasts of the 1986-1987 ENSO with a coupled model . . . . . M. A. Cane and S. E. Zebiak 278

Diagnostic studies of a coupled model's climate variability. . . . . S. E. Zebiak and M. A. Cane 283

Southern Oscillation phenomena in a coupled ocean-atmosphere GCM . . G. Meehl 289

A coupled global atmosphere-ocean model. . . . . U. Cubasch 292

Large scale surface heat flux variations over the North Pacific and North Atlantic during winter . . . . . D. Cayan 298

Session VIII: Intraseasonal Oscillations
Chair: V. Kousky

Easterly waves along the equator . . . . . B. Liebmann and H. Hendon 303

Intraseasonal oscillations in the global atmosphere . . . M. Ghil and K. Mo 307

An observational study of the relationship between high latitude blocking onset and the 30-60 day oscillation in the near-equatorial convection during Northern Hemisphere winter . . . . . J. V. Zapotocny 309

Dynamics of multi-scale atmosphere-ocean interactions over the tropical western Pacific . . . . . K-M. Lau 315

Intercomparison of intraseasonal (30-60 day) oscillations in three general circulation models . . . . . C-K. Park, D. M. Straus, K-M. Lau 320

Frequency dependence of teleconnection patterns . . . . . Y. Kushnir and J. M. Wallace 324

Page

Session IX. Climate Data Sets
Chair: W.-C Wang

A comparison of tropical surface winds from buoys and operational analysis . . . . . R. W. Reynolds 329

A precipitation climatology of five-day sequences: National patterns of frequencies and amounts . . . . . A. G. Barnston and E. S. Epstein 335

A precipitation climatology of five-day periods . . . . . E. S. Epstein and A. G. Barnston 339

The Global Precipitation Climatology Project: Description, goals and progress . . . . . J. Janowiak and P. A. Arkin 343

Higher moment statistics from a 40-year sample of 15-day mean 700 mb heights . . . . . A. J. Wagner and T. N. Maisel 347

Session X. Medium and Extended Range Forecasting: Experimental Forecast Center Related Activities
Chair: D. Lowry

Development of a simplified NMC spectral model with empirically-determined forcings . . . . . S-C. Chen and J. O. Roads 356

A reduced version of the NMC DERF II dataset and a preliminary error growth analysis . . . . . F-C. Chang, S. Schubert, K-M. Lau, and R. Kistler 362

Slowly evolving features in the winter Northern Hemisphere 500 mb field and their influence on medium-range forecasts . . . . . N. Graham 371

Forecasts of zonal wind and global momentum from the NMC MRF model . . . . . R. D. Rosen and D. A. Salstein 377

Preditability and its relationship to cyclone/planetary scale interactions . . . . . M. S. Tracton 383

Session XI. Medium and Extended Range Forecasting: Errors and Predictability.
Chair: R. E. Livezey

Systematic errors in medium-range prediction and possible consequences for climate studies . . . . . L. Bengtsson *

Comparison of surface stresses and latent heat fluxes, over oceans in short-range forecasts by the ECMWF, UKMO, and NMC. . . . . K. Arpe, D. Burridge, and A. Gilchrist 389

A dynamical extended range forecasting experiment with the CCC GCM..G. J. Boer 398

* Presentation was made at the Workshop, but paper was not submitted.

Page

Extended-range predictability estimates from a simple coupled model of the mid-latitude circulation . . . . . A. J. Miller and J. O. Roads 403

The effect of tropical Atlantic heating anomalies upon GCM forecasts over the Americas . . . . . J. Buchman, J. Paegle, L. Buja and R. E. Dickinson 408

Predictability of time averages in a simple GCM. . . . . S. Schubert, M. Suarez, and J.Schemm 413

Effects of recent changes in NMC models upon global analyses and medium-range forecasts . . . . . P. Caplan, G. White and B. Ballish 416

Predictability of low frequency modes . . . . . T. N. Krishnamurti 422

Normal mode structure of the transient response of a General Circulation Model to tropical heading . . . . . J. Nogues-Paegle and W. Zhong 427

Estimates of dynamical predictability from NMC DERF experiments. . . W-Y. Chen 433

Session XII. Medium and Extended Range Forecasting: Empirical Studies
Chair: D. L. Gilman

Anomalous climatological background for some explosive storms (Bombs) . . . . . J. Namias 437

On tropical climate prediction: A progress report 1985-88 . . . S. Hastenrath 443

Amplitude-persistence-transitions of low frequency modes . . . . . E. O'Lenic, R. E. Livezey and L. W. Hinkelman 448

Further case studies of tropical Atlantic surface circulation patterns associated with Subsaharan drought . . . . . P. J. Lamb and R. A. Peppler 454

Mixed analog/persistence prediction of U.S. seasonal temperatures . . . . . R. E. Livezey, A. G. Barnston, and B.K. Neumeister 461

Verification of Canadian monthly temperature anomaly forecasts . . A. Shabbar 468

Specification of monthly and seasonal precipitation in California and Arizona River Basins . . . . . W. H. Klein and H. J. Bloom 475

Specification of winter precipitation over Canada from the surrounding 50-kPa height field . . . . . A. Shabbar 481

The relationship between Canadian Prairie dry and wet months, and circulation anomalies in the mid-troposphere . . . . . J. L. Knox and R. G. Lawford 488

Dependency of long-range temperature predictability in Hungary on circulation weather type and forecast category . . . . . Z. Toth 497

Author Index
Thirteenth Climate Diagnostics Workshop

Author	Page
Arkin, P. A.	41, 220, 343
Arpe, K.	389
Ballish, B.	416
Barnett, T. P.	96
Barnston, A. G.	102, 335, 339, 461
Belokrylova, T. A.	85
Bergman, K. H.	190
Bhatt, U. S.	198
Bloom, H. J.	475
Boer, G. J.	398
Branstator, G.	220
Buchman, J.	408
Buja, L.	408
Burridge, D.	389
Cane, M. A.	278, 283
Caplan, P.	416
Cayan, D.	298
Chang, F-C.	362
Chen, S-C.	356
Chen, T-C.	109
Chen, W-Y.	433
Christy, J.	46
Cubash, U.	292
Deser, C.	73
Dickinson, R. E.	408
Douglas, A. V.	12
Epstein, E. S.	335, 339
Folland, C.	160
Gage, K. S.	61
Garcia, O.	24
Ghil, M.	307
Gilchrist, A.	389
Graham, N.	371
Gruber, A.	34
Guezen, T.	19
Gutzler, D. S.	52
Halpert, M. S.	57
Hastenrath, S.	166, 443
Hendon, H.	303
Higgens, R. W.	269
Higuchi, K.	176
Hinkelman, L. W.	448
Janowiak, J.	343
Jenne, R.	79
Ji, M.	9
Jones, P. D.	A-1
Kalnay, E.	231
Kanamitsu, M.	231
Karl, T. R.	251, 256
Karoly, D.	29, 147
Kelly, P. M.	A-1
Khalsa, S. J.	66
Kistler, R.	362
Klein, W. H.	204, 475
Knox, J. L.	176, 488
Kousky, V.	1
Krishnamurti, T. N.	422
Kuma, K.	90
Kushnir, Y.	324
Lamb, P. J.	133, 454
Lander, M. A.	127
Lau, K-M	315, 320, 362
Lawford, R. G.	488
Leetmaa, A.	1, 9
Li, K.	214
Liebmann, B.	303
Livezey, R. E.	102, 143, 448, 461
Maisel, T. N.	347
Mamontov, N. V.	85
Martuganov, B. A.	85
McAfee, J.	61
Meehl, G.	289
Miller, A. J.	403
Miskus, D.	190
Mo, K. C.	41, 231, 265, 307
Morrissey, M. L.	127
Mullen, S. L.	224
Murphree, T.	235
Naegele, P. S.	24
Namias, J.	437
Neumeister, B. K.	461
Nogues-Paegle, J.	427
O'Lenic, E.	448
Olson, J. G.	118
Paegle, J.	408
Park, C. K.	269, 320
Parker, D. E.	160
Peppler, R. A.	454
Portman, D.	251, 256
Raddatz, R.	19
Radiuhin, V. T.	153
Raper, S. C. B.	A-1
Rasmusson, E. M.	57, 265
Razuvayev, V. N.	85
Reid, G. C.	61
Reynolds, R. W.	329
Richman, M. B.	133
Roads, J. O.	241, 356, 403

Author	Page
Rogers, J. C.	170
Ropelewski, C. F.	57
Rosen, R. D.	377
Sabol, P.	190
Salstein, D. A.	377
Schemm, J.	413
Scheslinger, M. E.	251
Scholefield, P.	19
Schubert, S.	362, 413
Shabbar, A.	176, 468, 481
Shilenko, B. L.	153
Sornatale, F.	41
Straus, D. M.	269, 320
Suarez, M.	413
Thomasell, A.	34
Toth, Z.	497
Tracton, M. S.	383
Trenberth, K. E.	118, 220
van den Dool, H.	210
Vernekar, A.	41
von Storch, H.	261
Wagner, A. J.	347
Wallace, J. M.	73, 324
Wang, W-C.	214, 251, 256
Ward, M. N.	184
Weare, B.	235
Weickmann, K. M.	66
Whistler, B. T.	204
White, G.	416
Wigley, T. M. L.	A-1
Wolter, K.	143, 166
Wood, T. M.	52
Zapotocny, J.	309
Zebiak, S.	278, 283
Zhong, W.	427
Zwiers, F. W.	261

Ocean/Atmosphere Variability During 1985-1988

Vernon E. Kousky and Ants Leetmaa
Climate Analysis Center, National Meteorological Center
Washington, D.C. 20233

Tropical Pacific atmospheric circulation and oceanic anomaly patterns began to clearly show warm (El Niño/Southern Oscillation [ENSO]) episode characteristics during mid-1986. This followed a period of more than two years during which sea surface temperatures (SSTs) were colder than normal, lower tropospheric easterlies were stronger than normal, and the central and eastern equatorial Pacific were drier than normal. This paper examines the evolution of some of the oceanic and atmospheric anomaly fields from the period immediately following the 1982-83 ENSO episode until the end of the 1986-87 ENSO. A comparison is made between this latter episode and other warm episodes that have occurred during the last 20 years. Recently, a capability for producing model-based analyses of the oceanographic fields in the tropical Pacific has been developed at the Climate Analysis Center. Some of these analyses will be used to describe the evolution of major features from 1985 to 1988.

Following the 1982-83 ENSO episode, negative 850 mb zonal wind anomalies (enhanced easterlies) prevailed throughout the equatorial Pacific east of 160^{o}E until early 1986. However, the easterlies that were present throughout most of 1983 and 1984 to the west of 160^{o}E were already replaced by anomalous westerlies in late 1985. Westerly wind anomalies increased in the central Pacific (160^{o}E-160^{o}W) (Fig. 1a) in mid-1986 and continued into the fall (October-November) of 1986. The SST anomalies in the western and central equatorial Pacific, on the other hand, gradually increased from 1984 through early 1986 (Fig. 1c). From early 1986 through mid-1986, the highest equatorial SSTs (as high as 30^{o}C) shifted to near the date line (Fig. 1b), and positive anomalies spread throughout all except the extreme eastern equatorial Pacific (Fig. 1c). During the September-November period, enhanced convection--indicated by negative outgoing longwave radiation (OLR) anomalies--spread into the central equatorial Pacific (Fig. 1d) near the region of warmest equatorial water. At the same time, the atmospheric pressure changes normally associated with the warm phase of the Southern Oscillation became evident. Sea level pressure rose to above normal at Darwin, Australia, and fell to below normal at Tahiti, resulting in a drop in the Southern Oscillation Index (SOI). By November, all the major indices used in monitoring the Southern Oscillation indicated that a warm episode was under way. However, classical El Niño conditions, characterized by anomalously warm SSTs along the west coast of South America, did not appear until early 1987.

During March-May, SST anomalies throughout the central and eastern Pacific were generally between +1^{o} and +2^{o}C. At this time the SOI reached its lowest values for the 1986-87 warm episode. During the last 20 years, only the 1982-83 ENSO episode featured lower values of the SOI. Persistent enhanced atmospheric convection continued to dominate the central equatorial Pacific in the vicinity of the date line, accompanied by an upper tropospheric anticyclonic anomaly couplet and surface westerly wind anomalies.

Positive SST anomalies of between 1^{o} and 3^{o}C prevailed throughout the central and eastern equatorial Pacific during the July-September period, except for the immediate coastal areas of South America where anomalies were between 0 and 1^{o}C. Enhanced equatorial convection continued near the date line during July and August, but this activity decreased substantially in September (Fig. 1d).

The SOI continued to be less than -1.5 through August, but rose steadily between August and December. Equatorial low-level easterlies gradually strengthened during this period, and the convective activity near the date line weakened (Figs. 1a and 1d, respectively). However, convective activity remained weaker than normal over northern and eastern Australia, New Guinea and the Philippines and stronger than normal along the equator near the date line. During the period November 1987-March 1988 positive SST anomalies decreased (Fig. 1c) throughout the equatorial Pacific as most tropical Pacific indices indicated a return towards normal conditions. By March 1988, the equatorial easterlies were once again stronger than normal, the SOI was near zero and equatorial convection in the central Pacific was near normal.

An ocean general circulation model, into which thermal data is assimilated monthly, is in routine operation at the Climate Analysis Center. The model is run in a hindcast mode. It is forced with monthly mean climatological heat fluxes and a monthly mean surface wind stress field. For January 1985 through September 1987 the stress was derived from a subjective analysis of wind information that is available on the Global Telecommunications System (GTS). As of October 1987 the stress field used is estimated from the lowest sigma level winds obtained from the NMC's global medium range forecast model. Monthly corrections are made to the hindcasts through the assimilation of surface and subsurface thermal information.

To illustrate the subsurface thermal variability in the near-equatorial zone, the depth of the 20^{o}C isotherm along the equator is shown in Fig. 2. This isotherm lies in the middle of the thermocline, and its variability is closely related to the changes in the upper ocean heat content. Deepest (shallowest) values of the thermocline are found in the western (eastern) Pacific. This is the dynamical response of the ocean to the prevailing easterlies. As these weaken the thermocline deepens in the east and shoals (gets shallower) in the west. From mid-1985 through 1986 this isotherm slowly deepened in the eastern Pacific, i.e., suggesting a gradual weakening of the easterlies. Superimposed on this were more rapid eastward propagating excursions that occurred in late 1985, during the northern spring of 1986, and after August 1986. These eastward movements are manifestations of intraseasonal relaxations of the easterlies (or westerly anomalies). The more rapid changes of the winds excite well-defined Kelvin wave pulses, which propagate eastward and cause a deepening of the thermocline. These are not well-resolved here because of the monthly mean forcing and the assimilation procedure that was used.

Largest westerly wind anomalies close to the equator occurred in late 1986. Shortly after that, in early 1987, the zonal asymmetry along the equator became most pronounced. In the western Pacific this isotherm rapidly rose to its shallowest values, and in the eastern Pacific it reached its greatest depths. The anomalously shallow depths in the central and western Pacific persisted through 1987. Only in mid-1988 did conditions become more normal.

In the eastern Pacific, near normal depths for this isotherm reappeared in mid-1987. However, positive SST anomalies persisted in this region until late 1987.

Although the oceanic and atmospheric anomaly fields observed during the 1986-87 ENSO episode were weaker than those observed during 1982-83 (the event of the century), they were quite comparable to and in some aspects stronger than the composite of several ENSO episodes. Sea surface temperature anomalies were as large as $+2^{o}C$ in the central Pacific, a region which, because of its relatively warm water, cannot achieve anomalies much greater than that. Sea surface temperature anomalies for March exceeded $+2^{o}C$ in the eastern equatorial Pacific and locally, e.g., at Paita, Peru, were close to $+5^{o}C$. The occurrence of large positive SST anomalies at the time of year when the SSTs are normally at the peak of their seasonal cycle greatly contributed to the enhanced convective cloud development evident throughout the equatorial eastern Pacific during February-April (Fig. 1d).

The most notable differences between the 1986-87 ENSO episode and the composite ENSO of Rasmusson and Carpenter (1982), MWR, pp. 354-384, were the timing of the peak in the mid-Pacific warming, the timing of El Niño in relation to the mid-Pacific warming, and the duration of the warming. The central Pacific warming lasted approximately 18 months, which is about six months longer than shown in the composite. A weak warming along the South American coast was observed early in 1986. However, the strongest warming lagged the onset of the mid-Pacific warming rather than leading it, and the peak in the mid-Pacific SST anomalies occurred during the August-October period rather than during December-February.

The temporal evolution of selected oceanic and atmospheric parameters, presented in Figs. 1b, 1c, and 2, show seasonally modulated, low-frequency trends. Interestingly, the SOI signal does not appear to have this feature (see Janowiak, 1988, MWR, p. 1022, Fig. 3). Surface temperature anomalies increased almost linearly with time in the central equatorial Pacific from negative values in 1984 to large positive values in late 1986 (Fig. 1c). In this same region, except for intraseasonal variability, the depth of the $20^{o}C$ isotherm increased in a similar fashion (Fig. 2). Similar low-frequency variability was evident in the SST for most of the previous ENSO episodes during the past 20 years, with the exception of the 1982-83 event. The trends are less obvious in atmospheric fields such as anomalous OLR and 850 mb wind. Both fields are strongly modulated seasonally.

Empirically these trends, by themselves, do not appear to be very useful for forecast purposes (especially in real-time). For example, the OLR and 850 mb wind anomalies extended about as far eastward in early 1986 as in early 1985. However, if by July westerly anomalies persist at the date line, the recent record indicates that further development is likely. This still provides a lead time of almost a season for predicting the more event-like strong anomalies that occur during the northern winter season. The different forecast models, as one would hope, appear to provide an additional lead time of several months (Barnett et al., 1988, Science, 241, pp. 192-196).

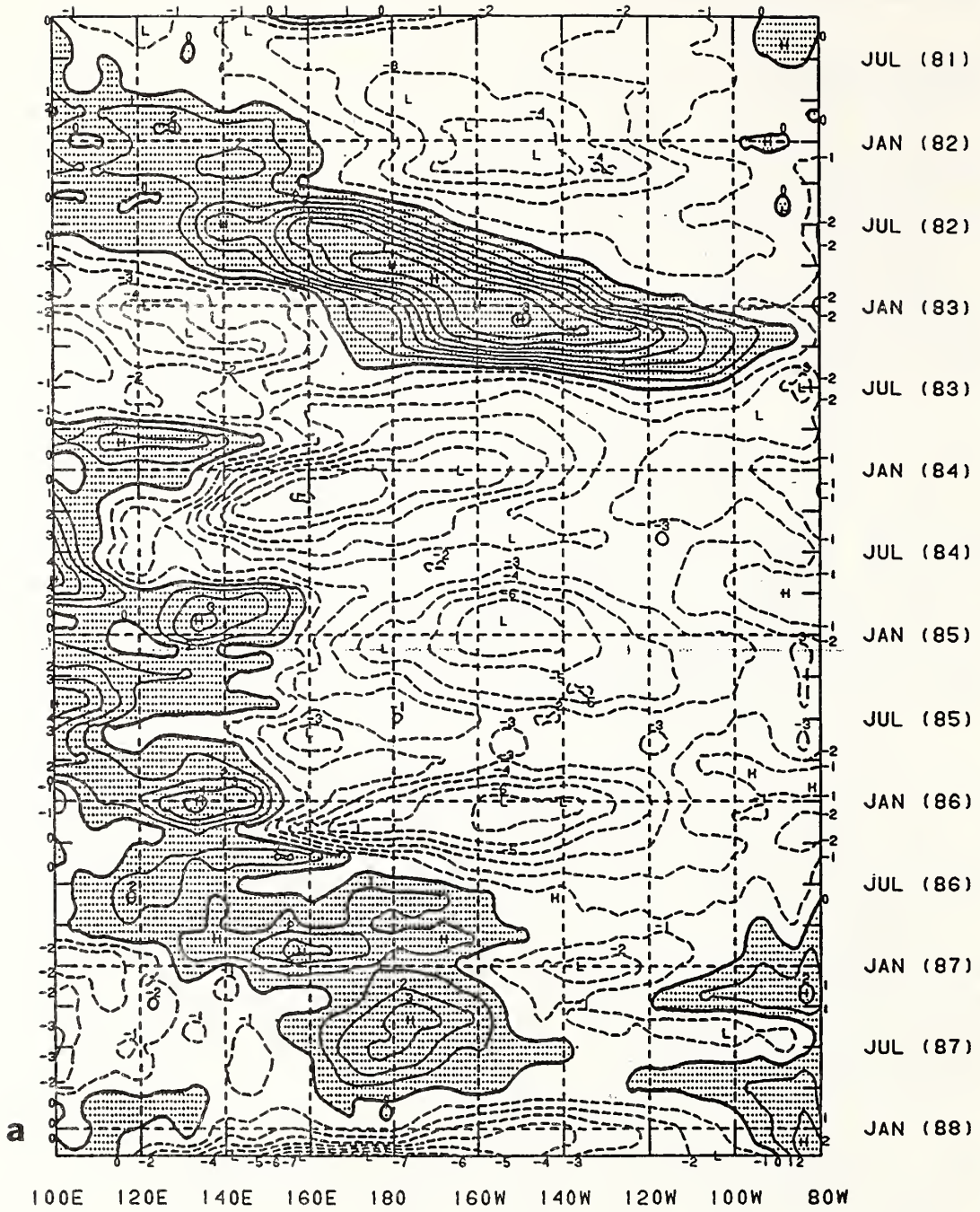

Figure 1 Time-longitude sections of a) 850 mb anomalous zonal wind, b) sea surface temperature, c) anomalous sea surface temperature and d) anomalous outgoing longwave radiation. Dashed contours indicate negative anomalies. Shaded regions indicate positive anomalies in a), SST greater than 28^{o}C in b), anomalies less than -0.5^{o}C in c) and negative anomalies in d). Contour intervals are 1 ms^{-1} for a), 1^{o}C for b), 0.5^{o}C for c) and 10 Watts m^{-2} for d). Zonal wind anomalies in a) are computed with respect to the March 1980 - February 1984 base period. SST anomalies are with respect to the 1950-1979 period. OLR anomalies are computed from the 1974-1983 base period means.

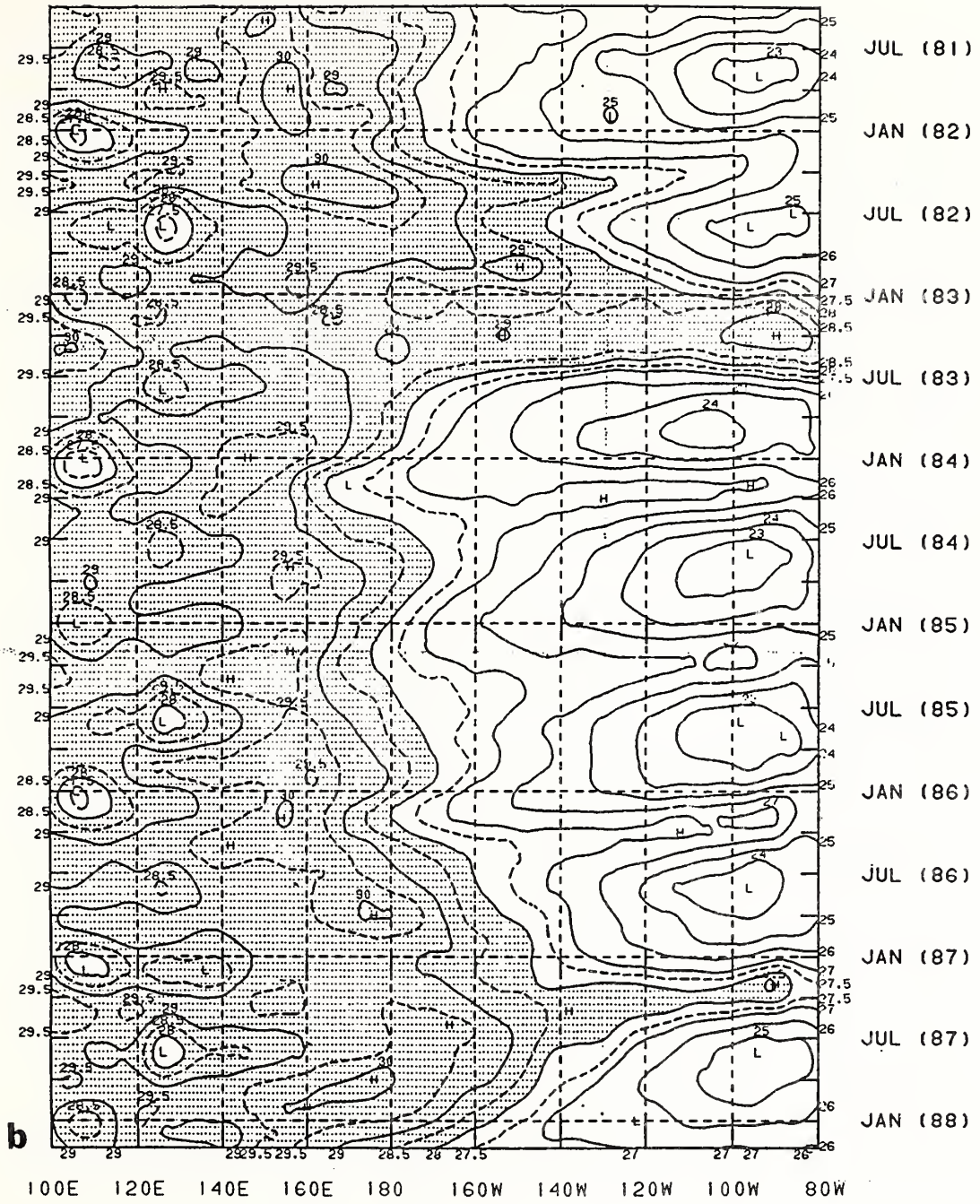
JUL (81)
JAN (82)
JUL (82)
JAN (83)
JUL (83)
JAN (84)
JUL (84)
JAN (85)
JUL (85)
JAN (86)
JUL (86)
JAN (87)
JUL (87)
JAN (88)
b
100E
120E
140E
160E
180
160W
140W
120W
100W
80W

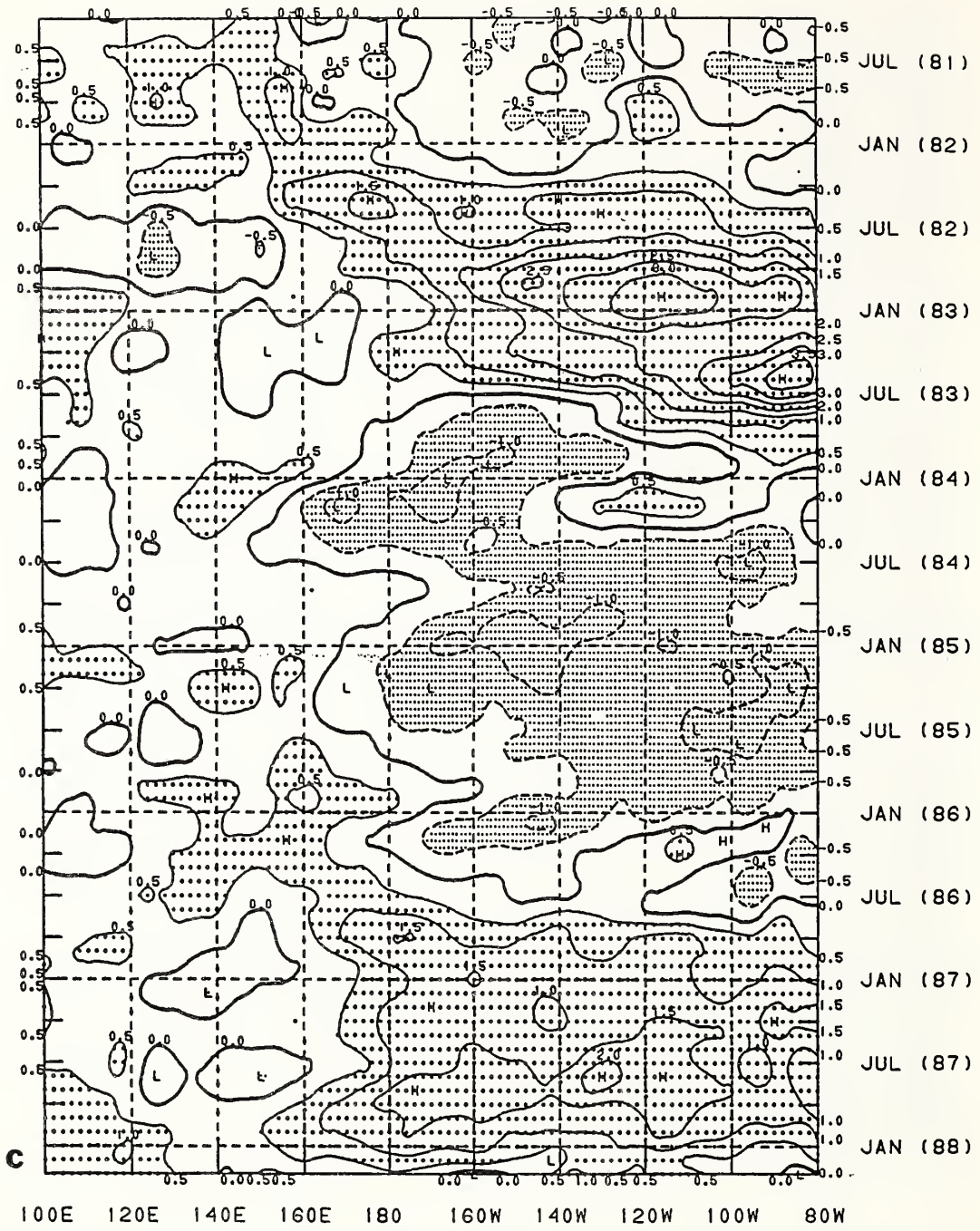
JUL (81)
JAN (82)
JUL (82)
JAN (83)
JUL (83)
JAN (84)
JUL (84)
JAN (85)
JUL (85)
JAN (86)
JUL (86)
JAN (87)
JUL (87)
JAN (88)
c
100E 120E 140E 160E 180 160W 140W 120W 100W 80W

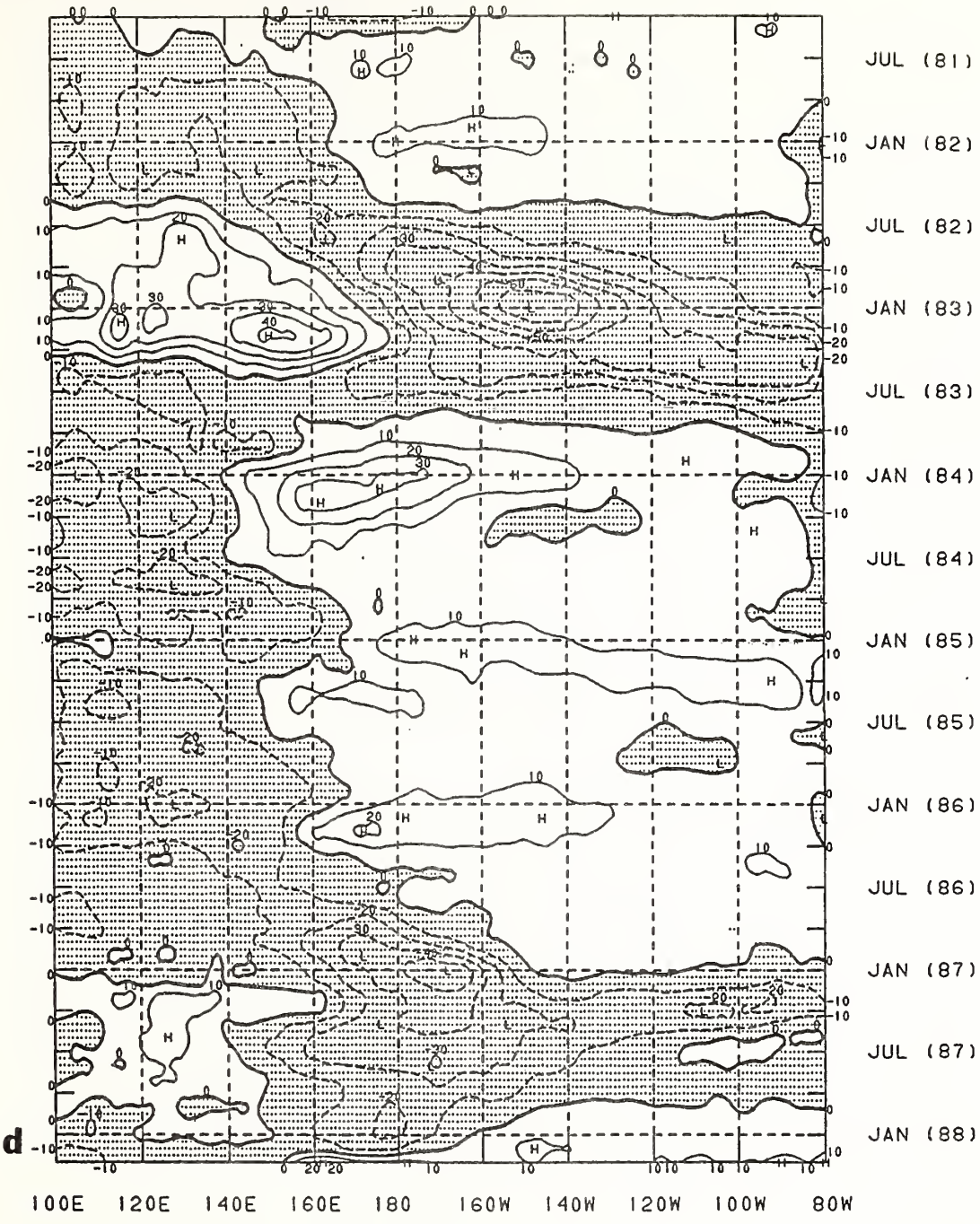
JUL (81)
JAN (82)
JUL (82)
JAN (83)
JUL (83)
JAN (84)
JUL (84)
JAN (85)
JUL (85)
JAN (86)
JUL (86)
JAN (87)
JUL (87)
JAN (88)
d
100E 120E 140E 160E 180 160W 140W 120W 100W 80W

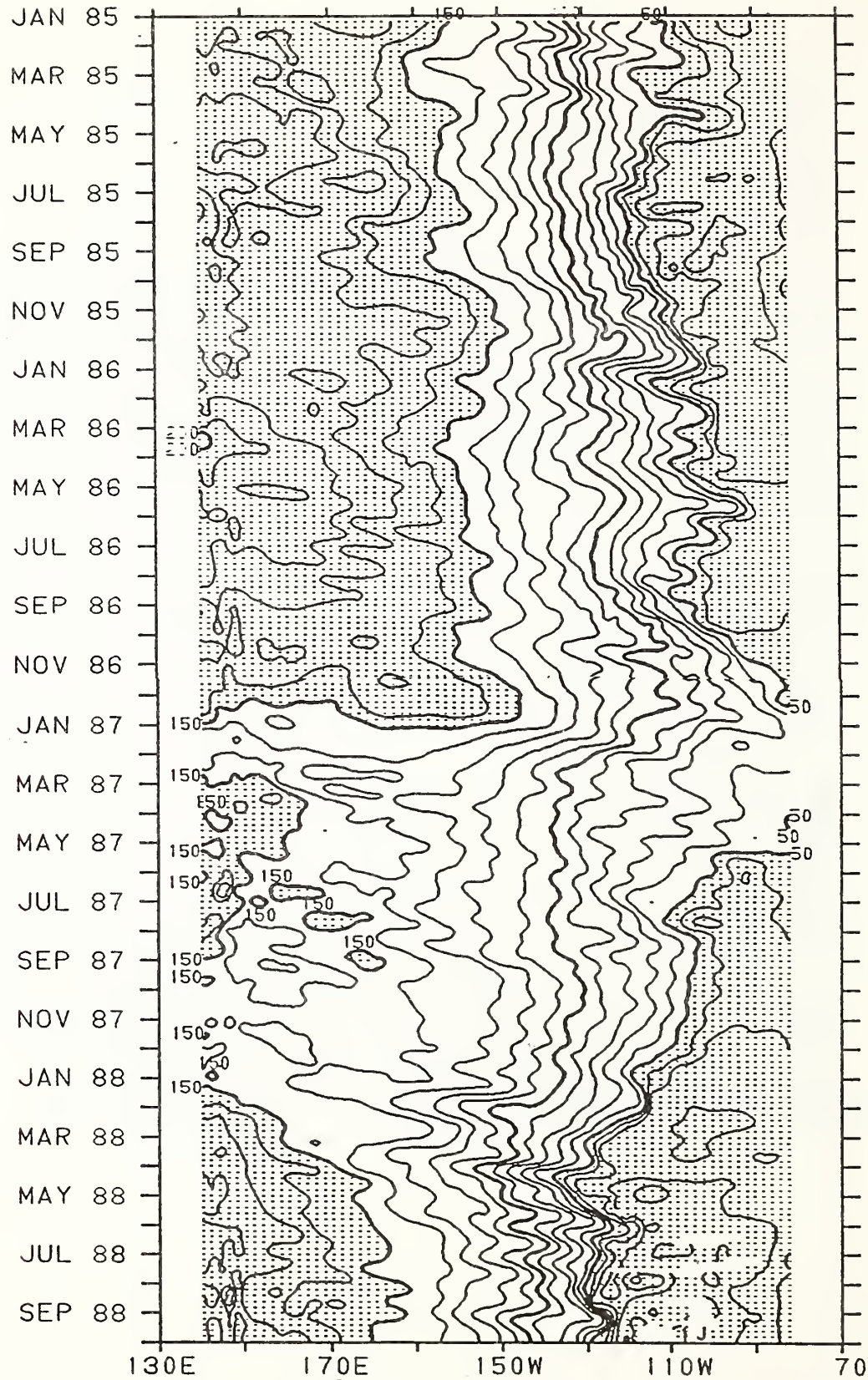

Figure 2 - Depth of the 20°C isotherm along the equator in the Pacific Ocean. The contour interval is 10 m with shading for values less than 50 m and also for values greater than 150 m.

INTERANNUAL VARIABILITY IN THE TROPICAL PACIFIC DURING 1985-1988

Ants Leetmaa and Ming Ji
Climate Analysis Center,NMC/NWS/NOAA
Washington, DC 20233

INTRODUCTION

Monthly hindcasts from a primative equation ocean model into which thermal data is assimilated are used to examine the climatic variability of the tropical Pacific for the period January 1985 to October 1988. The ocean model is described in Philander and Seigel (1985). The model is forced with monthly mean fields for wind stress and net heat flux. The former were derived from surface marine observations until September 1987 and from the output of NMC's global forecast model since then. The latter are monthly climatological values of Esbensen and Kushnir (1981). Subsurface thermal data from XBTs and surface thermal data are assimilated monthly to reduce the error resulting from inaccurate forcing fields and model biases. The quantity which will be discussed is the surface dynamic height relative to the ocean bottom. This in the tropics is almost equivalent to sea level and proportional to the vertically integrated heat content. Comparisons to sea level information from the various island stations show that the r.m.s. error of the model analyses is of the order of 4 to 6 dynamic centimeters. A fuller discussion of the model-based analysis system is given in Leetmaa and Ji (1988).

DISCUSSION

Representative time series from the model-based analyses are shown in Figure 1. Shown are the time-longitude sections of surface dynamic height relative to 4150 db along the equator in the left panel and along 5 S in the right panel from January 1985 to the present. Note that the longitude scale has been reversed for the 5 S section, ie, east is on the left handside of the panel. The annual variability has been removed so that these fields represent interannual variability. During 1985 no longterm coherent pattern of anomalies was present along the equator. Off the equator, there is a suggestion of westward propagatio of a band of positive anomalies which reaches the western boundary between August 1985 and February 1986. It is during this time interval that persistent positive anomalies start to appear along the equator. These are clearly evident by July; largest anomalies occur late in 1986 when strong anomalous westerlies were present in the western Pacific. The slope of the the stronger positive anomaly patterns is close to that which would be associated with the eastward propagation speed of the first vertical mode Kelvin wave, i.e. about 300 cm/sec. Almost coincident with the development of positive anomalies along the equator early in 1986 positive anomalies start to move westward from the eastward boundary along 5S (and 5N). These are quite prominent by mid-1986. By late 1986 a clear east-west asymmetry has developed both on and off the equator.

The negative anomalies that appeared first in the western Pacific slowly spread westward so that by late 1987 the whole equatorial zone shows negative anomalies. These persist to the present. The

westward movement of the off-equatorial positive anomalies is obscured by the development of strong negative anomalies in the western Pacific in late 1986 and early 1987. Presumably these are locally produced.

First of all this figure illustrates the link between the enhanced positive Kelvin wave activity along the equator and the development of the off-equatorial zonal asymmetry. Secondly there is the suggestion that there might have been anomalous positive Rossby wave activity which reached the western boundary late in 1985 and possibly contributed to the subsequent development of positive anomalies along the equator. Development of similar anomaly patterns has been shown in some coupled-model simulations of ENSO (Schopf and Suarez, 1988). Because of the relatively large uncertainty associated with the values in these figures, quantitative intercomparisons between individual theories and observations await improved analyses.

Sea surface temperature anomalies in the equatorial zone similarly showed a slow evolution from negative anomalies in the central and eastern Pacific during 1985 to near average conditions in early 1986. Positive anomalies starting in mid-1986 and continued until late 1987. The slow evolution of these ocean fields supports the idea that ENSO represents a low-frequency coupling between the ocean/atmosphere system.

REFERENCES

Esbensen, S.K., Y.Kushnir, 1981. The heat budget of the global ocean: An atlas based on estimates from surface marine observations. Climate Research Institute, Report No. 69, Oregon State University, Corvallis.

Leetmaa, A., Ming Ji, 1988. Operational Hindcasting of the Tropical Pacific. in press, Dynamics of Atmospheres and Oceans.

Philander, S.G., A.D. Seigel, 1985. Simulation of El Nino of 1982-83. In Hydrodynamics of the Equatorial Ocean, ed. J.C.J.Nihoul, pp. 517-42, New York ,Elsevier.

Schopf, P.S., M.J.Suarez, 1988. Vacillations in a Coupled Ocean-Atmosphere Model. J.Atmos.Sci. Vol.45, No.3,pp 549-566.

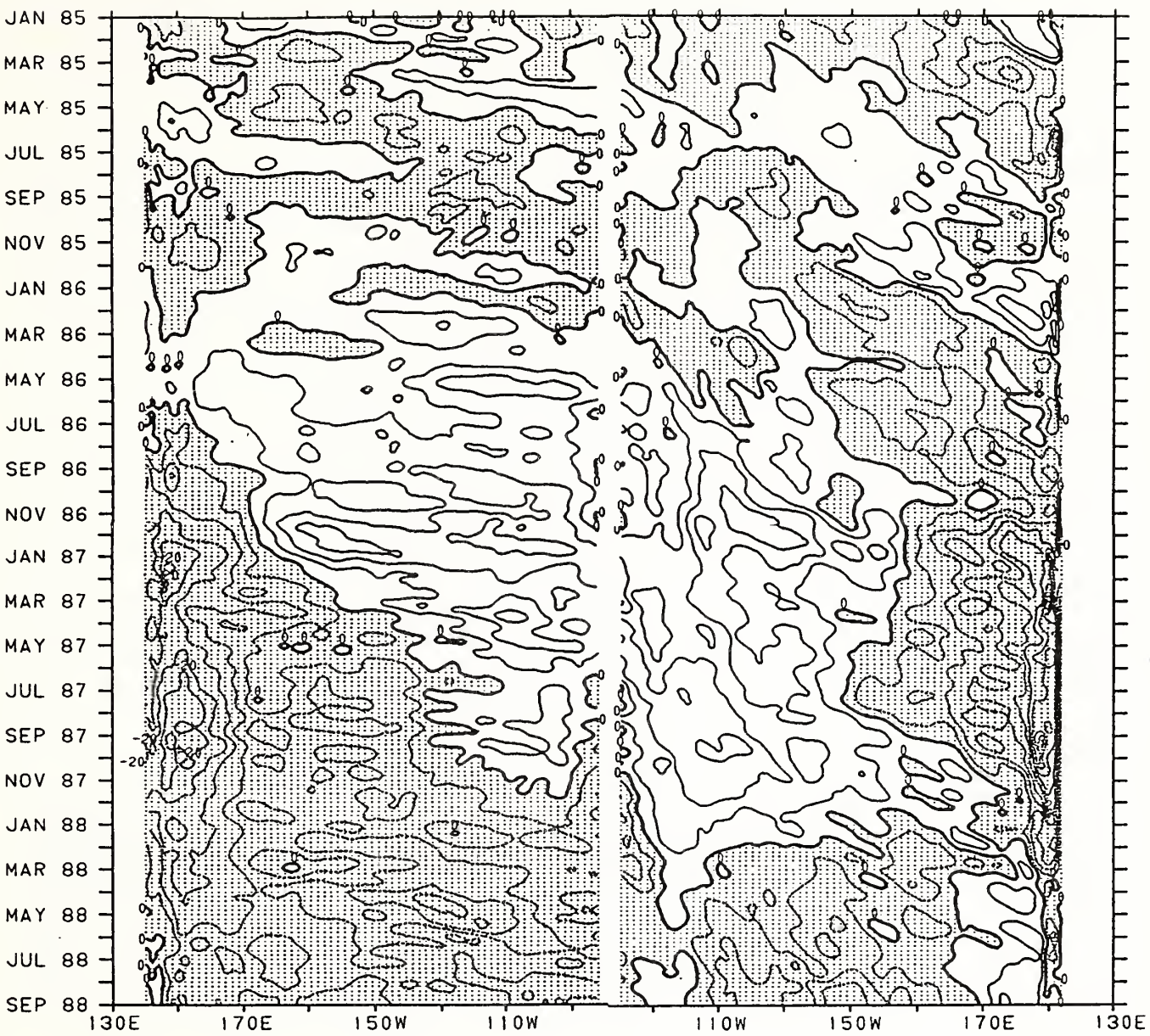

Figure 1. Interannual variability of surface dynamic height along the equator and 5 S. The contour interval is 4 dyn.cms..

The Severe Drought of 1988:
Possible response to persistent El Nino conditions

Arthur V. Douglas
Department of Atmospheric Sciences, Creighton University
Omaha, Nebraska 68178

A severe drought affected northern and western sections of the United States in 1988. In the spring drought conditions were most prevalent across the Pacific Northwest and the Tennessee Valley (Figure 1A). By midsummer drought conditions in these two regions intensified and spread into the North Central Plains, thus creating one of the worst droughts since the 1930s (Figure 1B). This paper focuses on possible causes of the two droughts and the factors which led to their eventual "link up" in the midsection of the country.

Subnormal precipitation typified much of the West during the winters of 1985-86, 1986-87, and 1987-88. The lack of precipitation during these three winters can be attributed to anomalous ridging across western North America (Figure 2). The observed height anomalies for these winters resembled the well-known PNA pattern which is frequently associated with El Nino. Persistent El Nino conditions from the fall of 1986 to early winter 1987 may have encouraged the development of the drought producing ridge in the United States for the winters of 1986-87 and 1987-88.

Dry conditions in the Tennessee Valley began in the spring of 1985, and much of this region experienced dry springs in 1985, 1986, 1987, and 1988. These four anomalously dry springs were the result of split flow conditions across North America (Figure 3). During Spring, positive height anomalies in the Plains reflect frequent, low amplitude ridging inside a mean zonal westerly flow. In the past four springs the westerlies were charcterized by a strong branch across central Canada and a secondary branch across the Gulf of Mexico. This flow pattern precluded the normal northward flow of moisture into the continent. Developing storms tended to track across central Canada--far north of their preferred track into the Ohio Valley. Springtime blocking across central North America is apparently a common feature during the spring of an El Nino year (Figure 4). Large displacements in key centers of action are evident in the point correlation map (Figure 4) and the height anomaly map for the springs of 1985-88 (Figures 3). However, the preference for positive heights in North America in Spring following an El Nino is evident in Figure 4 and very suggestive of the split flow pattern observed in the past four springs.

During the spring and early summer of 1988, severe drought conditions spread rapidly into the northern plains in response to an intense buildup of a closed anticyclone over the central United States. This anticyclone may have been forced by conditions in the North Pacific. When troughing is present in the North Pacific (Figure 5), downstream ridging in North America is common. Point correlations between the equatorial index and 700mb height anomalies indicate troughing is expected in the North Pacific following an El Nino (Figure 4). Note that in June 1988 (Figure 6) the negative height anomalies were shifted about 20^{o} east of the "preferred" teleconnection center indicated in the point correlation map of Figure 4. Summer teleconnections (Figure 5) indicate that a 20^{o} eastward shift in the negative center results in a corresponding

eastward shift in positive heights across North America--in fact to a position very close to that observed in June 1988.

Across the Northern Plains, temperature anomalies peaked in June, while extreme precipitation deficits continued into July. The last section of this paper deals with the relationship between the end of an El Nino and the June heat wave and severely dry conditions of July. The S.O.I. underwent a rapid rise from January to June with an extreme peak (positive) value in June 1988. This change in the S.O.I. might suggest a tropical forcing for the severe drought. Two questions can be asked: (1) Are droughts or heat waves likely during periods of rapid cooling in the equatorial Pacific (large increases in the S.O.I.), and (2) Are droughts and heat waves likely when the equatorial Pacific is anomalously cold (high values of the S.O.I.). The time coefficients for the eigenvectors of continental air temperature were examined for a consistent signal during years with either a rapid rise or a high value of the S.O.I. (as observed in Spring to Summer 1988). Tables 1 and 2 indicate that there is apparently no preference toward anomalous heat during these two phases of the S.O.I. (Period of analysis 1907-1978). Likewise an analysis of July precipitation frequency (1951-80) indicates little preference for a given drought regimes in either the western or central United States during rapid rises or peaks in the S.O.I. The average time coefficients for all factors is close to zero--indicating no preference for a given climate anomaly in these select years.

The severe drought of 1988 was a result of the merging and intensification of droughts from the Pacific Northwest and Tennessee Valley. Three excessively dry winters in the West and four dry springs in the Tennessee Valley preceded the summer drought of 1988. The circulation patterns of the three winters and springs resembled those expected during various phases of El Nino. The severe heat and dryness in the summer do not appear to be a preferred condition during anti-El Nino summers, since many cool, wet summers have also occurred in the past during cold phases of the Southern Oscillation Index.

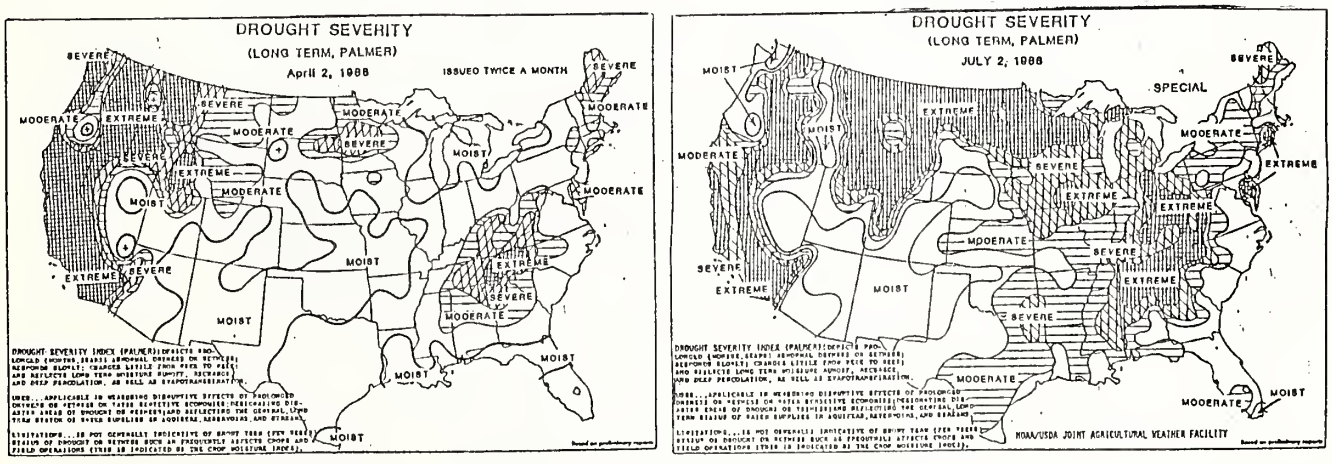

Figure 1. Palmer Drought Index for April and July, 1988. Note expansion of drought into the northern plains by July.

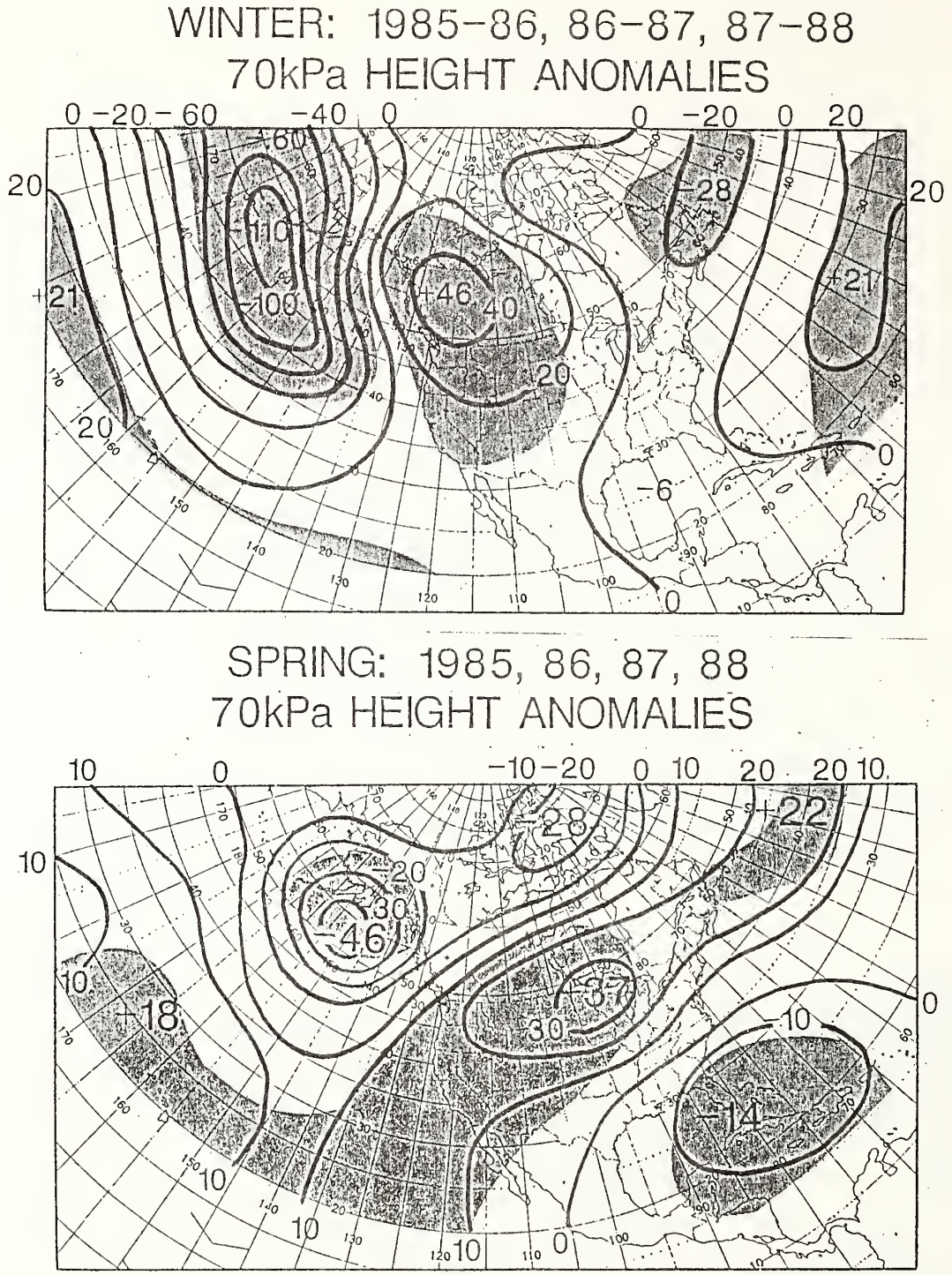

Figures 2 (upper) and 3 (lower). The observed 700mb height anomalies for the winters of 1985-86 to 1987-88 (upper) and springs of 1985 to 1988. Note the PNA-type pattern in the winter and split flow regime of spring with negative heights in Canada and the Southeast. Shaded areas kept the same anomaly sign in the three winters and four springs.

CORRELATION BETWEEN JANUARY EQUATORIAL INDEX AND JUNE 70kPa HEIGHT ANOMALIES

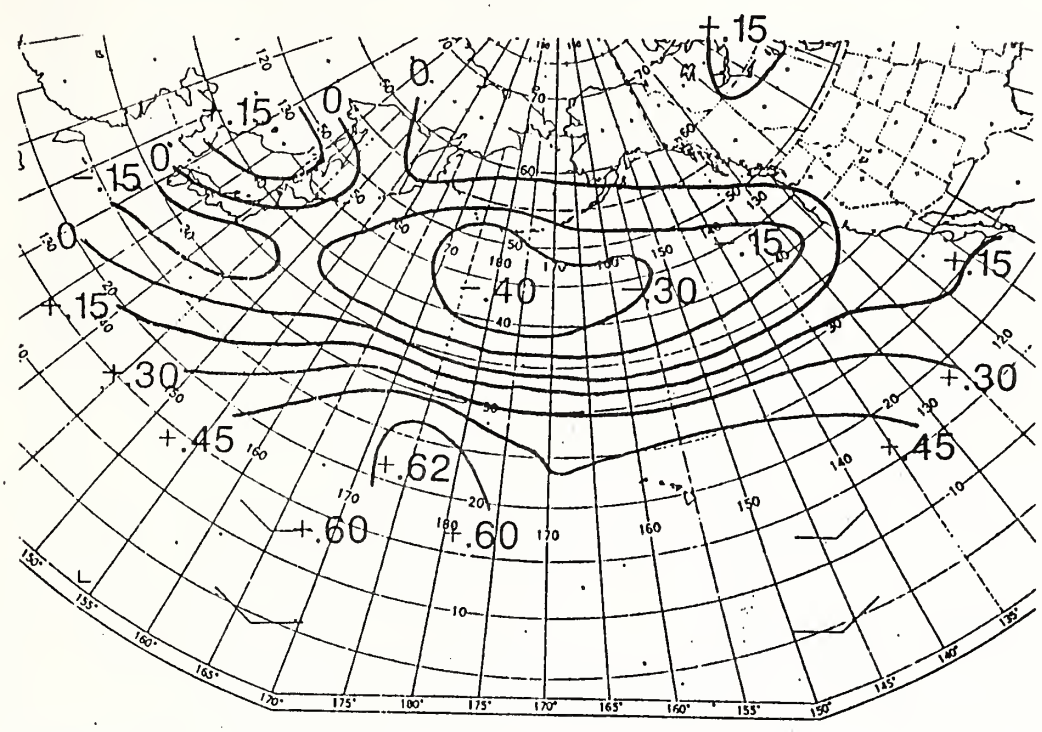

Figure 4. Correlation between the equatorial index of January and the subsequent 700mb height anomalies of June. High index values (El Nino) are followed by below normal heights in June across the North Pacific.

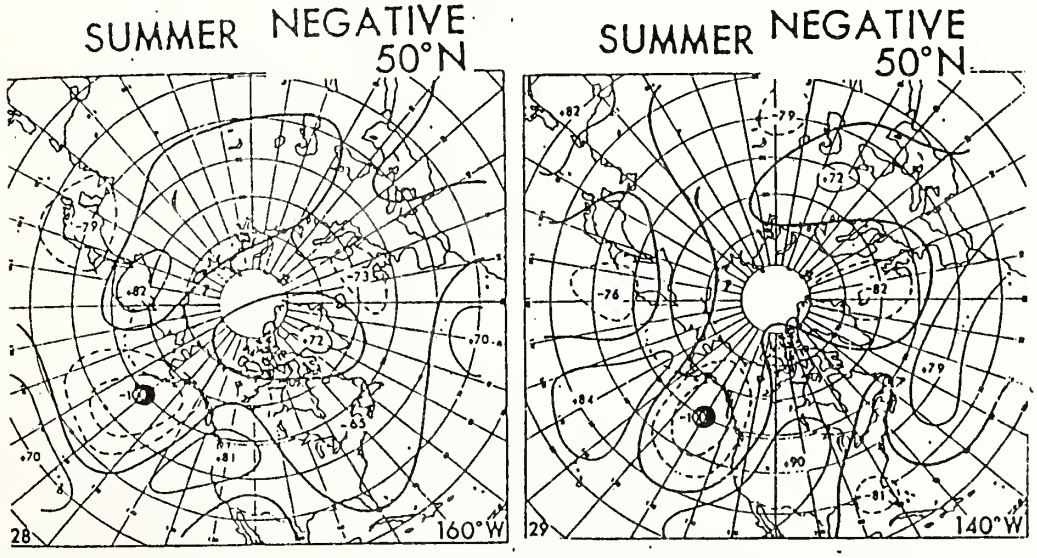

Figure 5. Summer teleconnection charts showing the relationship between negative heights in the North Pacific and ridging in North America. Compare Figures 5 and 6.

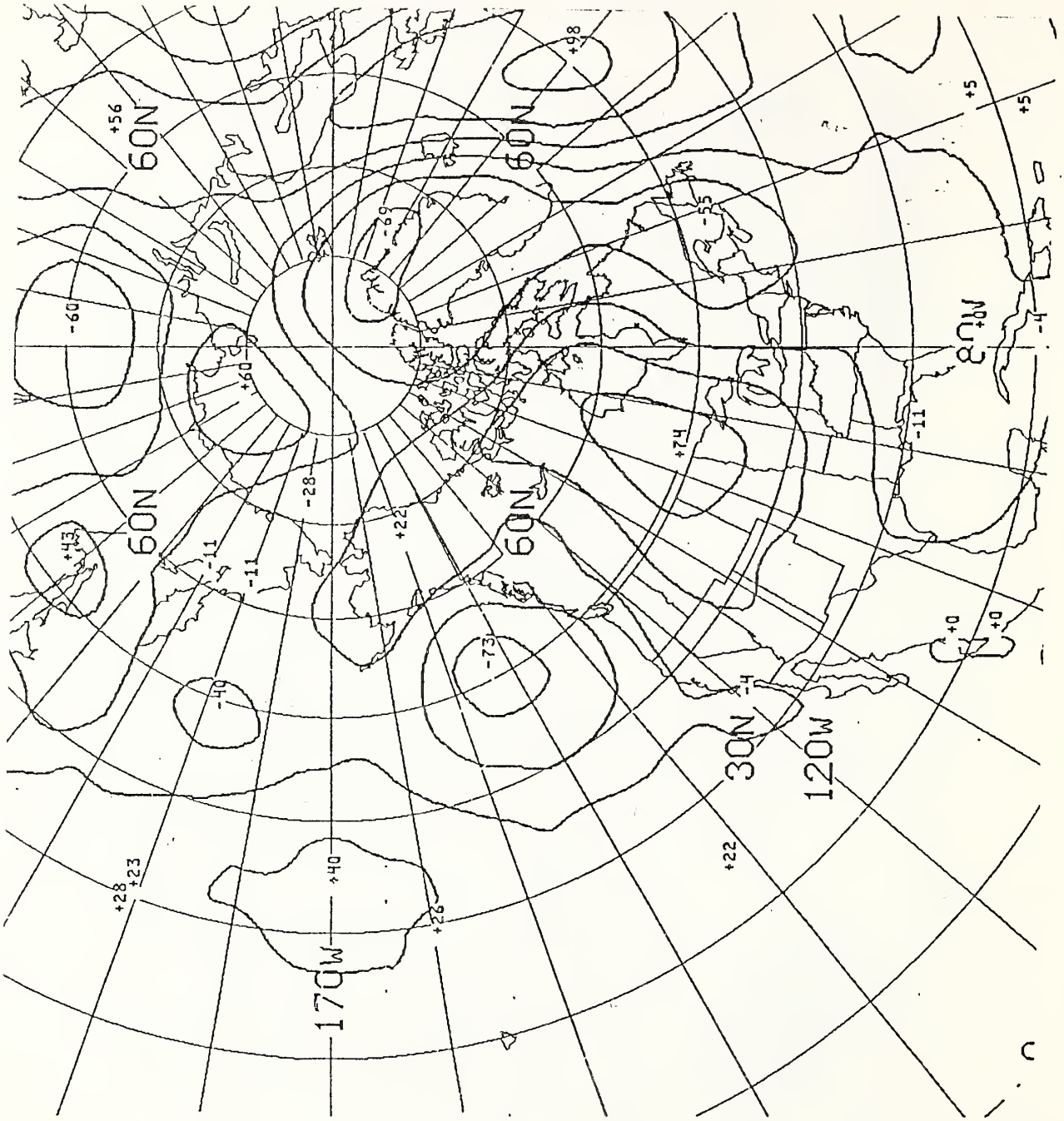

Figure 6. The observed 700mb height anomalies for June 1988. Note the strong ridges in the central North Pacific, North America and the central North America. The troughing in the central Gulf of Alaska was in a key position to favor the downstream ridging in North America (as noted in Figure 5).

TABLE 1. TIME COEFFICIENTS FOR FACTORS OF JUNE TEMPERATURE DURING RAPID RISES IN THE S.O.I. FROM WINTER TO SUMMER.

YEAR	F-1 WARM CENTRAL	F-2 WARM WEST	F-3 COOL NORTH
1915	-1.75	-1.27	0.83
1920	-0.52	-0.00	-1.24
1924	0.01	-0.34	1.99
1926	-0.81	1.22	1.44
1942	-0.22	-1.14	0.32
1958	-0.80	0.04	2.27
1964	0.01	-0.87	-0.88
1970	-0.22	1.04	-0.41
1973	0.37	0.61	-0.31
$\bar{X}$	-0.44	-0.08	+0.44
EXTREMES FOR THE ENTIRE 72 YEARS			
HIGHEST	+2.48	+2.89	+2.33
LOWEST	-1.99	-2.01	-2.00

ANALYSIS 1907 - 1978

TABLE 2. TIME COEFFICIENTS FOR FACTORS OF JUNE TEMPERATURE DURING ANTI-EL NINO SUMMERS (HIGH S.O.I., GREATER THAN 1 STANDARD DEVIATION).

YEAR	F-1 WARM CENTRAL	F-2 WARM WEST	F-3 COOL NORTH
1909	0.16	-0.03	-0.51
1916	-1.66	-0.64	0.46
1917	-1.15	-0.49	0.23
1938	-0.04	0.63	-0.10
1950	-0.40	-0.55	-0.50
1955	-1.44	0.43	-1.24
1956	1.07	0.92	-0.47
1960	0.15	0.76	1.33
1962	-0.40	0.31	-0.85
1970	-0.22	1.04	-0.41
1971	1.19	-0.43	-0.94
1973	0.37	0.61	-0.31
1975	-0.33	-0.58	-0.55
$\bar{X}$	-0.21	+0.15	-0.22
EXTREMES FOR THE ENTIRE 72 YEARS			
HIGHEST	+2.48	+2.89	+2.33
LOWEST	-1.99	-2.01	-2.00

ANALYSIS 1907 - 1978

TABLE 3. TIME COEFFICIENTS FOR FACTORS OF JULY PRECIPITATION DURING RAPID RISES IN THE S.O.I. FROM WINTER TO SUMMER.

YEAR	F-1 WET MIDWEST	F-2 DRY N. PLAINS	F-3 WET N.W. AND S.E.
1958	2.81	-0.63	0.13
1964	-0.31	0.62	1.84
1970	-0.64	-0.21	-0.49
1973	0.62	0.30	-1.72
$\bar{X}$	+0.62	-0.02	-0.01
EXTREMES FOR THE ENTIRE 30 YEARS			
HIGHEST	+1.89	+3.00	+3.08
LOWEST	-2.05	-1.41	-1.70

ANALYSIS 1951 - 1980

TABLE 4. TIME COEFFICIENTS FOR FACTORS OF JULY PRECIPITATION DURING ANTI-EL NINO SUMMERS (HIGH S.O.I., 1 STANDARD DEVIATION).

YEAR	F-1 WET MIDWEST	F-2 DRY N. PLAINS	F-3 WET N.W. AND S.E.
1955	-0.06	-0.01	0.01
1956	-0.38	-1.28	-0.58
1960	0.86	-0.64	0.37
1962	1.89	0.40	0.08
1970	-0.26	0.15	0.77
1971	-0.27	0.10	-1.69
1973	0.76	-0.88	0.36
1975	0.77	0.76	-1.55
$\bar{X}$	+0.43	-0.20	-0.28
EXTREMES FOR THE ENTIRE 30 YEARS			
HIGHEST	+1.89	+3.00	+3.08
LOWEST	-2.05	-1.41	-1.70

ANALYSIS 1951 - 1980

Tables 1-4. An examination of the time coefficients of June temperature and July precipitation in years following an El Nino. Tables 1 and 3 consider periods of a rapid rise in the SOI following the termination of an El Nino, while Tables 2 and 4 consider periods of a high SOI value following an El Nino. The factor analysis maps are shown in Figure 7. The average time coefficients for the two types of index are very close to zero, indicating a given sign of the factor is not preferred following and El Nino. Cool-wet summers were observed following El Ninos in 1915,1924,1926 and 1958.

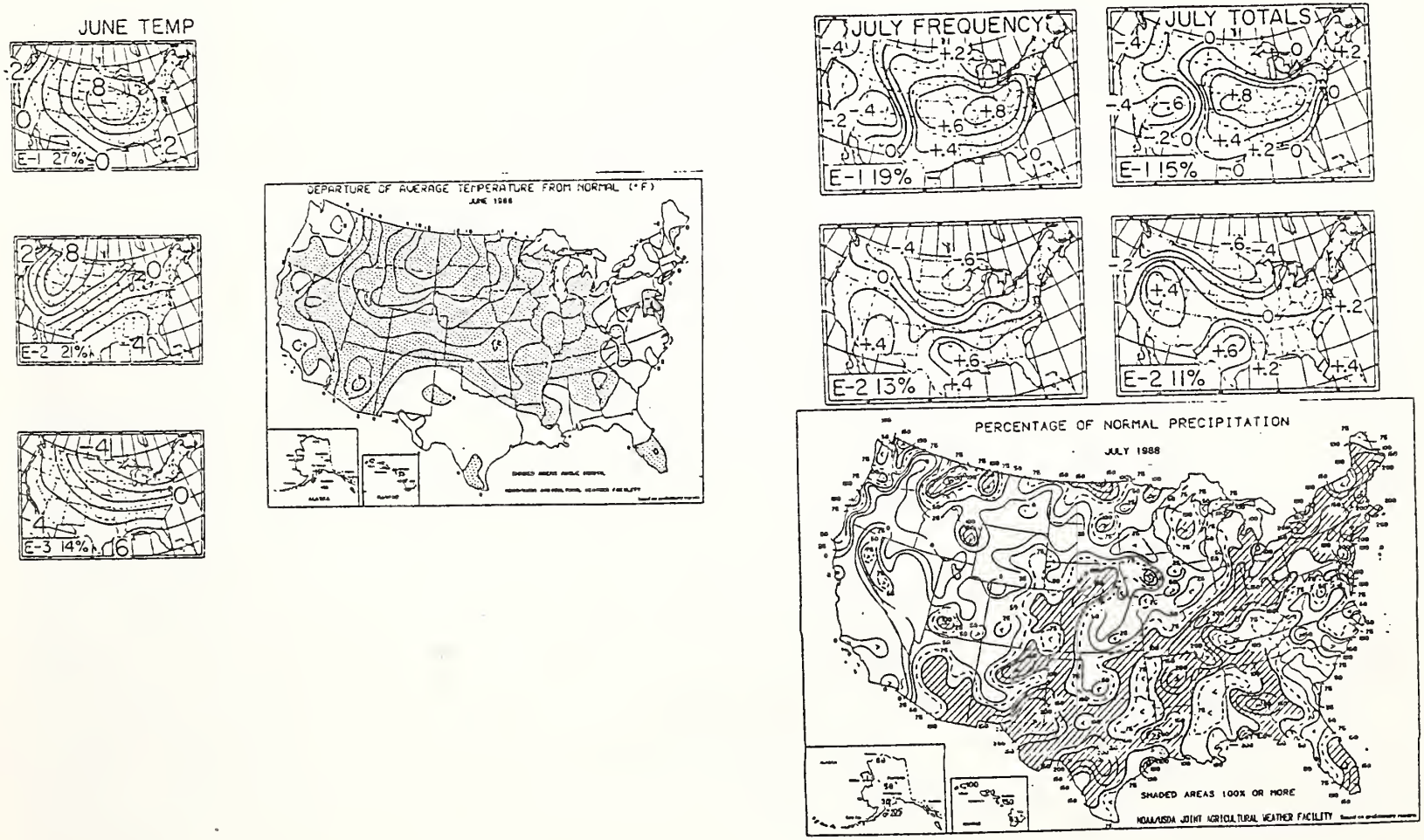

Figure 7. The observed June temperatures and July precipitation for 1988 and the corresponding factors of June temperature and July precipitation. Temperatures in June 1988 closely resembled those of Factor 2, while July precipitation closely resembled precipitation Factor 2. Temperature factor analysis for 1907-78 and July precipitation (frequency and totals) for 1951-80. Tables 2 and 4 utilize time coefficients for July precipitation frequency (days with precipitation 0.10" and greater).

THE 1988 DROUGHT IN CANADA

P. Scholefield, Canadian Climate Centre, Toronto
T. Guezen & R. Raddatz, Atmospheric Environment Service, Winnipeg

Introduction

This paper will describe the severe drought situation that developed across western and central Canada during 1988 which actually evolved from, and was exacerbated by, a dry year in 1987. The evolution of the drought will be traced by relating surface meteorological conditions to the upper atmospheric circulation patterns with particular reference to the geopotential height anomalies at the 50-kPa level. The paper will finish with a comparison of the 1988 Prairie drought with some previous major drought years.

1987

The year 1987 will, no doubt, be best remembered for its record mean annual temperatures which engulfed a huge portion of the country, extending from the Great Lakes basin westward well into the western cordillera of British Columbia (B.C.) and the southern parts of the Northwest Territories. It was also a drier than normal year, with central and western Canada receiving 80-90% of their normal annual precipitation. Drought concerns arose on the Prairies in June following a very dry winter and spring which seemed related to a persistent negative 50-kPa height anomaly in the North Pacific Ocean and associated pronounced ridging over western Canada. The breakdown of this pattern in July and August lead to ample rainfalls across most parts of central and western Canada, although it was very dry in southern B.C. during August. September was the start of a very dry fall for most of southern Canada west of the Great Lakes, as strong upper-level ridging predominated. The situation in B.C. became critical as farmers and ranchers in the southern interior had to truck water due to dangerously low levels of water in their reservoirs.

Winter 1987/88

As was the case in 1987, the extended dry spell of the 1987/88 winter appears to have been related to a strong negative 50-kPa height anomaly that, in response to the ENSO (El Nino-Southern Oscillation) warming of the eastern tropical Pacific Ocean, became established over the North Pacific late in the fall and persisted into the winter. During November, a positive 50-kPa height anomaly over the eastern Prairies slowly shifted westward and by the end December, became firmly established over B.C. The persistent upper ridge over western Canada restricted the approach of moisture-bearing storms from the Pacific, deflecting them either northward into the Yukon and Northwest Territories or southward through the U.S.A., which kept the interior of B.C. and the western Prairie Provinces drier than normal.

Spring 1988

Finally, a break-down of the persistent winter circulation pattern late in March permitted some Pacific weather sytems to penetrate inland. The western upper ridge became re-established in April but in a position further to the east which permitted the influx of moist Pacific air masses into B.C., bringing drought relief to the southern interior valleys. The southern Prairies, however, remained very dry with some locations receiving only 10-20% of their normal April precipitation. A collapse of the upper ridge in western Canada at the end of April resulted in continued drought relief in southern B.C. through the first two weeks of May. On the Prairies, a couple of active weather systems moved into the southeastern Prairies and stalled near Lake Winnipegosis, dumping copious quantities of rain in the area. This resulted in a remarkable contrast in that widespread flooding occurred in this region, while regions a few hundred kilometres south and west were beset by severe drought conditions.

Summer 1988

Summer came early to the Prairies this year as a pronounced upper ridge began building over the central and eastern Prairies during the latter part of May, producing a heat wave in southern Saskatchewan and Manitoba. This situation persisted through the month of June, resulting in all-time record mean monthly temperatues across the southern Prairies which, along with continued lack of rain, aggravated the drought conditions. June was also a very dry month in southern Ontario. The position of the upper ridge near the Saskatchewan-Manitoba border permitted the penetration of moist Pacific air into Alberta, particulary the northern half, where heavy rains brought a quick end to the drought conditions in this area, but not in the south. A major change in the upper atmospheric circulation occurred in early July when the upper ridge and associated positive 50-kPa height anomaly shifted eastward over the Great Lakes. This significant change in circulation brought some drought relief as cool, moist, unstable air invaded the Prairies. **Figure 1** shows the extent of drought conditions in North America and how the region of drought expanded eastwards over the Great lakes with the changing circulation pattern. This shift in the drought from the Prairies to southern Ontario is shown in the water budget time series for Saskatoon and Toronto (**figure 2**).

The positive 50-kPa height anomaly continued its slow eastward progression across the Great Lakes during July, resulting in the hottest July since 1955 in southern Ontario. At Toronto, it had been the second driest May-June period since records began in 1840 (the driest was in 1949). By mid July, the drought worsened as cumulative rainfalls since May 1st were less than 40% of normal in southwestern Ontario. After the upper-level height anomaly moved east of the Great Lakes in mid July, the trajectory of the upper level flow into southern Ontario shifted from the parched regions of the American mid and southwest to the more humid areas of the Gulf Coast. This influx of humid air effectively brought an end to

the drought conditions in southern Ontario by the end of July. By mid August, the changed 50-kPa ciculation pattern had alleviated most of the summer drought concerns in Canada. The mean 50-kPa flow pattern returned to near normal over Canada in August and substantial rainfalls fell in regions that had previously suffered under drought conditions.

The 1988 Prairie Drought in Historical Perspective

T. Guezen and R. Raddatz did some comparative studies to see how the drought years of the 1980's compared with those of the 1930's. They produced the comparative statistics shown in **table 1.** and included the year 1961 which had been a memorable drought year between the decades of the thirties and the eighties. Using historical data from 9 selected stations across the Prairie provinces, they listed the precipitation shortfall as the percentage of the 1951-80 normal amount that would have been needed to bring the total up to normal over the period from September of the preceding year up to the end of August of the listed year. For example, the most severe shortfall this past year occurred at Lethbridge, where the total was 45% short of the normal total or, in other words, the total precipitation was 55% of the normal. The averages listed at the bottom of the table were calculated using only those locations with negative shortfalls for that year. It can be seen that 1988 was certainly a major drought event comparable to, but not any worse than previous major drought years. Overall, 1961 was most severe and the hardship in the thirties was in part due to the fact that there were two consecutive dry years.

Summary

The upper atmospheric circulation patterns that lead to two consecutively dry winters across central and western Canada appear to have been related to the ENSO event of 1987/88 and were instrumental in setting the stage for the severe moisture shortages during the spring and summer of 1988. The development and dissipation of the drought events followed a chronological progression which began in B.C. in the spring and ended up in southern Ontario in July. These drought events were clearly related to a similar eastward progression of positive 50-kPa height anomalies. A return to more normal precipitation regimes progressed eastward across the country so that surface drought conditions had dissipated by August at most locations, but there remained isolated pockets of moisture shortages, mostly in the southern Prairies. Except for southern B.C., there remained a deficit in soil moisture reserves at the end of September across the southern parts of central and western Canada. This problem was aggravated by a dry September over the southern Prairies. Drought concerns could rise again in 1989 if soil moisture reserves are not recharged this coming winter.

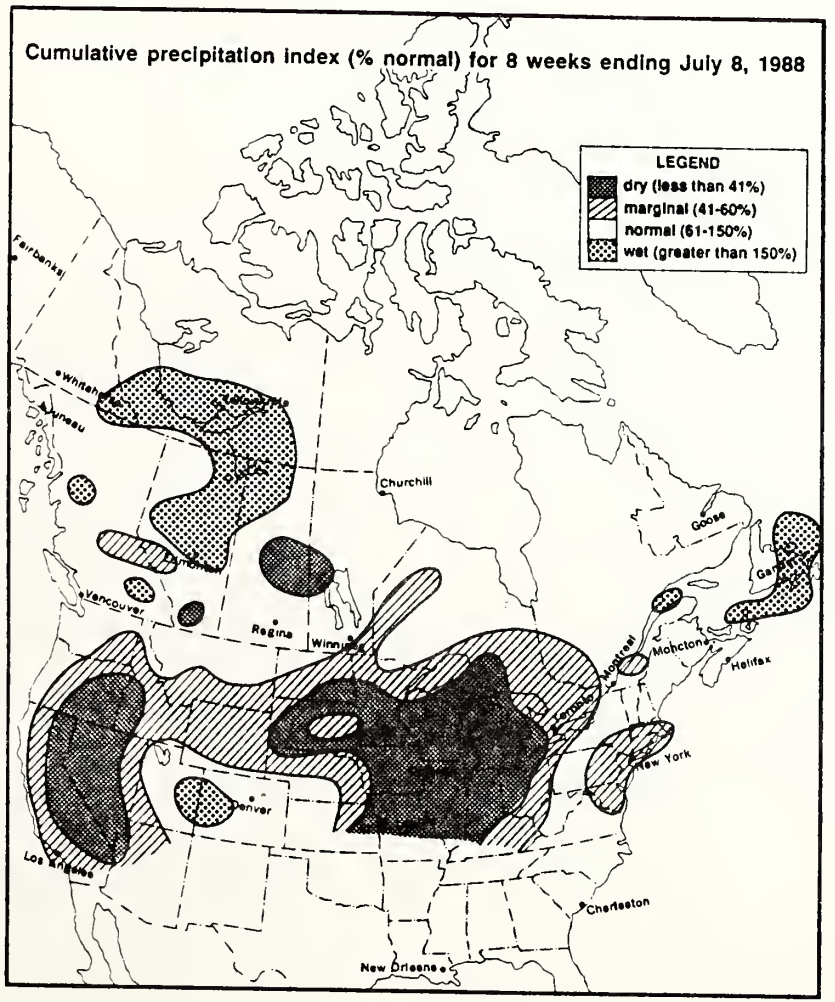

Figure 1

DROUGHT INTENSITY IN THE PRAIRIES

PRECIPITATION SHORTFALL
SEPTEMBRER-AUGUST

STATION	1936	1937	1961	1984	1988
WINNIPEG	-0.26	-0.06	-0.42	-0.06	-0.38
BRANDON	-0.31	+0.35	-0.43	-0.06	-0.22
SASKATOON	-0.05	-0.19	-0.19	-0.24	-0.21
REGINA	-0.16	-0.53	-0.57	-0.34	-0.27
SWIFT CURRENT	-0.20	-0.50	-0.35	-0.39	-0.25
PRINCE ALBERT	-0.33	-0.13	-0.23	+0.34	+0.03
LETHBRIDGE	-0.30	0.00	-0.31	-0.33	-0.45
CALGARY	-0.37	+0.01	-0.12	-0.32	-0.10
EDMONTON	+0.05	+0.01	-0.20	-0.32	+0.18
AVERAGE	-0.25	-0.28	-0.31	-0.26	-0.27

Table 1

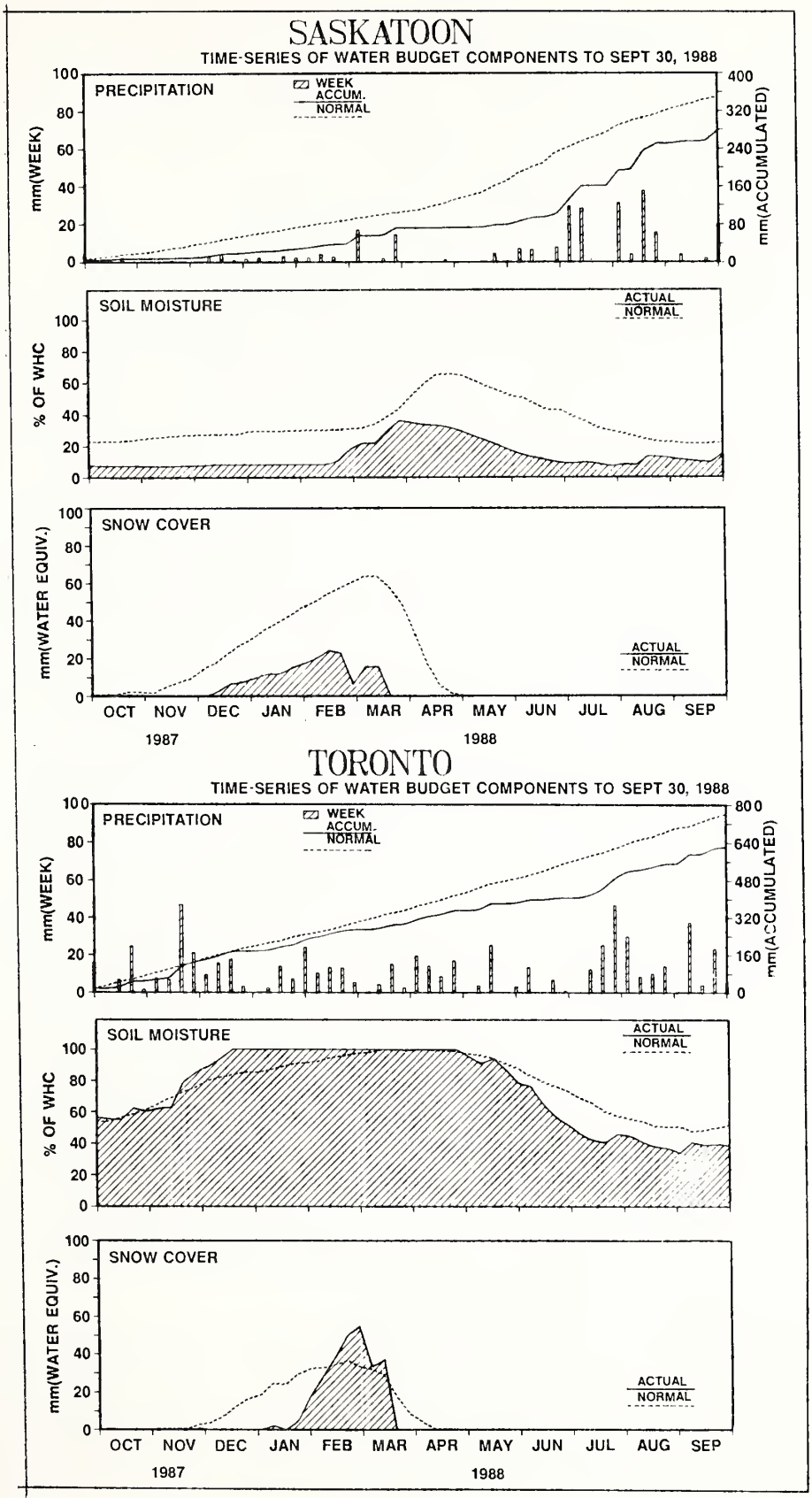
SASKATOON
TIME-SERIES OF WATER BUDGET COMPONENTS TO SEPT 30, 1988
PRECIPITATION
WEEK
ACCUM.
NORMAL
mm(WEEK)
mm(ACCUMULATED)
SOIL MOISTURE
ACTUAL
NORMAL
% OF WHC
SNOW COVER
mm(WATER EQUIV.)
OCT NOV DEC JAN FEB MAR APR MAY JUN JUL AUG SEP
1987
1988
TORONTO
TIME-SERIES OF WATER BUDGET COMPONENTS TO SEPT 30, 1988
PRECIPITATION
WEEK
ACCUM.
NORMAL
mm(WEEK)
mm(ACCUMULATED)
SOIL MOISTURE
ACTUAL
NORMAL
% OF WHC
SNOW COVER
mm(WATER EQUIV.)
OCT NOV DEC JAN FEB MAR APR MAY JUN JUL AUG SEP
1987
1988

Figure 2

Large Scale Patterns of Tropical Convection during 1986-1988

Oswaldo Garcia
NOAA/Environmental Research Labs.
Boulder, Colorado 80303
and
P. Stuart Naegele
CIRES/University of Colorado
Boulder, Colorado 80309

The tropics recently experienced a strong El Niño/Southern Oscillation event (ENSO) that began in late 1986 and ended in early 1988. Based on the Southern Oscillation index or SOI, a commonly used measure of ENSO events, 1987 was comparable to 1972-1973 in magnitude, although the most recent event began a few months earlier than other ENSOs. By late 1988, conditions in the tropics had reverted to a strong anti-ENSO regime, characterized by large positive SOI values, negative sea surface temperature anomalies and enhanced easterly winds in the equatorial Pacific. In addition, unusually heavy rains were reported in the Malay Peninsula and other areas in the eastern Indian Ocean. This dramatic shift from ENSO to anti-ENSO conditions had not occurred since 1972-1973. By contrast, the period from 1976 to 1986, which included the 1976-1977 ENSO and the extremely strong 1982-1983 event, did not have any sustained positive SOI anomalies.

In this paper we discuss the evolution of large-scale patterns of tropical convection for the period 1986-1988 in comparison to the long term mean values of the Highly Reflective Cloud (HRC) data set. The HRC data set is an 18 year (1971-1988) daily record of areas of organized convection around the global tropics. The location and extent of convective areas are identified subjectively in satellite picture mosaics covering the global tropics obtained from polar orbiting satellites. Over a month's time, the HRC data set shows the distribution of the number of days that highly reflective clouds were noted in the area between 25N and 25S. The distribution of HRC days can then be related to the monthly rainfall amounts recorded at hundreds of stations throughout the tropics by means of a linear regression equation. That way, a rough estimate of rainfall can be obtained in areas, such as the oceans, where no rainfall measurements are available. The resulting "HRC rainfall index" can be used to compare and contrast changes in large scale patterns of convective rainfall that occur throughout the tropics as a result of seasonal cycles and climate anomalies such as ENSO events. An advantage of these data is that they provide a record of the 1972-1973 ENSO, which occurred before the commonly used Outgoing Longwave Radiation (OLR) data set became available. Thus, it is possible to compare the evolution of the convective rainfall morphologies in the 1986-1988 period with those of 1972-1973, as well as with the long term means of the HRC rainfall index.

Figure 1 shows the 17 year means (1971-1987) of the HRC rainfall index for the mid-season months of January, April, July and October. Areas with monthly index values over 100 mm are shown with vertical hatching. Major features of the annual cycle appear prominently in this figure, such as the meridional excursion of convective rainfall in the Asian monsoon region and African continent. Over the Pacific, the southwest Pacific convergence zone

experiences a maximum of convective rainfall in the southern summer, while convective areas north of the equator in the central and eastern Pacific have relatively small changes in latitude throughout the year. Near the equator, areas with mean index values over 100 mm are only found in the far western Pacific throughout most of the year, except during the northern winter, when convection moves eastward toward the dateline. This eastward movement is more pronounced and persistent during ENSO events and much weaker when anti-ENSO conditions are present.

To better understand the evolution of tropical convective rainfall during 1986-1988, it is instructive to follow the development of the 1972-1973 event, which was of similar magnitude as described by the SOI. Figure 2 shows the areas with HRC rainfall index values exceeding 100 mm for 1972 in horizontal hatching together with the 17 year means in vertical hatching. While January 1972 was relatively close to the 17 year mean, negative anomalies began appearing in the Indonesia area in April. By July, this negative anomaly area had expanded considerably, while strong positive anomalies had developed in the central equatorial Pacific. This anomaly pattern, the distinctive signature of an ENSO event, persisted until January of 1973 (Figure 3). Another noteworthy feature was the southward displacement of tropical convective rainfall during January 1973.

By April 1973, convective cloudiness along the equatorial strip moved sharply westward beyond its average position, a change which was accompanied by a shift in the SOI values from negative to positive. The pattern for the rest of 1973 was marked by positive anomalies of the HRC rainfall index in the Indian Ocean and negative anomalies in the central and western equatorial Pacific, the typical pattern of anti-ENSO conditions. The 1972-1973 pattern, therefore, illustrates what occurs when an strong ENSO event is immediately followed by the onset of anti-ENSO conditions. The ENSO events of 1976-1977 and 1982-1983 did not evolve in this fashion, but rather were followed by SOI values averaging near zero.

The HRC rainfall index maps for 1986 are shown in Figure 4. Early in the year the distribution of convective rainfall was very close to the 17 year average, except for an area of positive anomalies in the western Indian ocean in April. By October, an area of positive index anomalies had begun to appear in the equatorial Pacific west of the dateline. In contrast to 1972, the first indications of positive anomalies on the equator near the dateline did not appear until October. By January 1987 (Figure 5) the positive anomalies in this area became very strong and persisted for the rest of the year into January 1988 (Figure 6). Negative HRC index anomalies began appearing in the central equatorial Pacific in April 1988 with positive anomalies in the western Indian Ocean and eastern Africa. By October of 1988, positive anomalies were found over Indonesia and negative anomalies persisted in the equatorial Pacific.

In summary, it is clear that the ENSO-type anomalies for 1986-1988 lasted over a much longer period than in 1972-1973 and occurred during a different time in the annual cycle. The transition from ENSO to anti-ENSO conditions was also more gradual in 1988 than 1983. These facts point to the large variety of conditions that can be encountered when examining the convective rainfall characteristics of ENSO events.

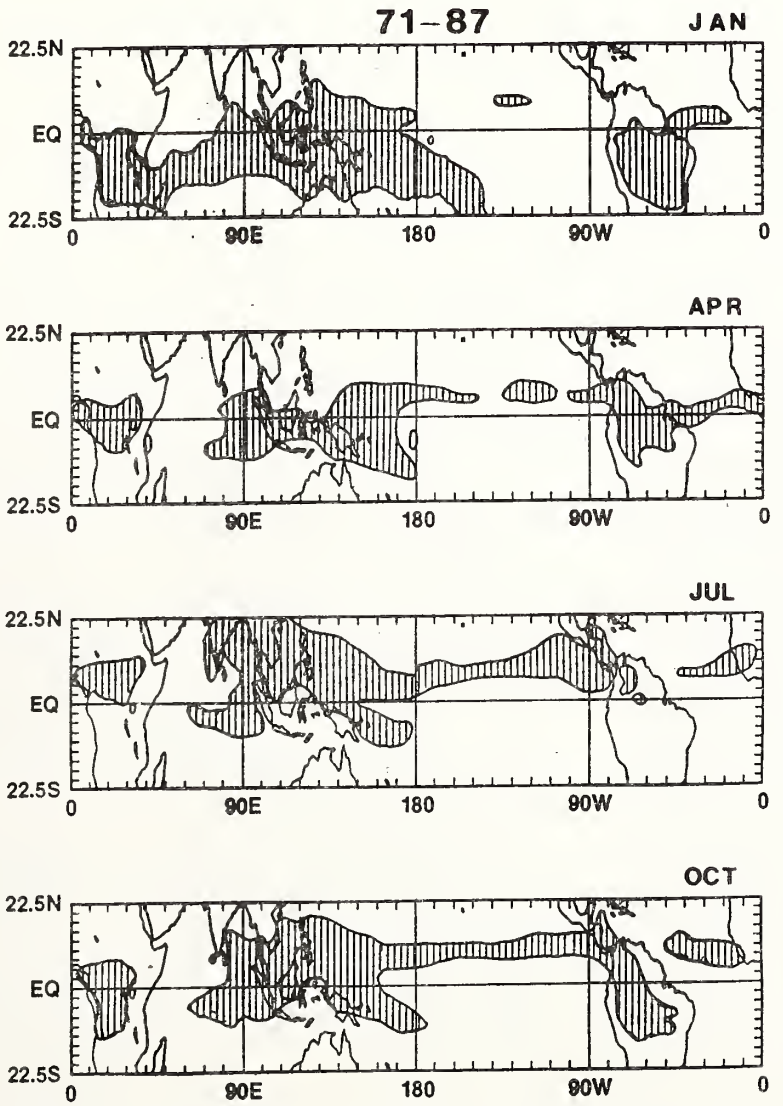

Figure 1. Vertical hatching: Areas where the 17 year (1971-1987) mean value of the HRC rainfall index exceeds 100 mm for the month of January, April, July and October.

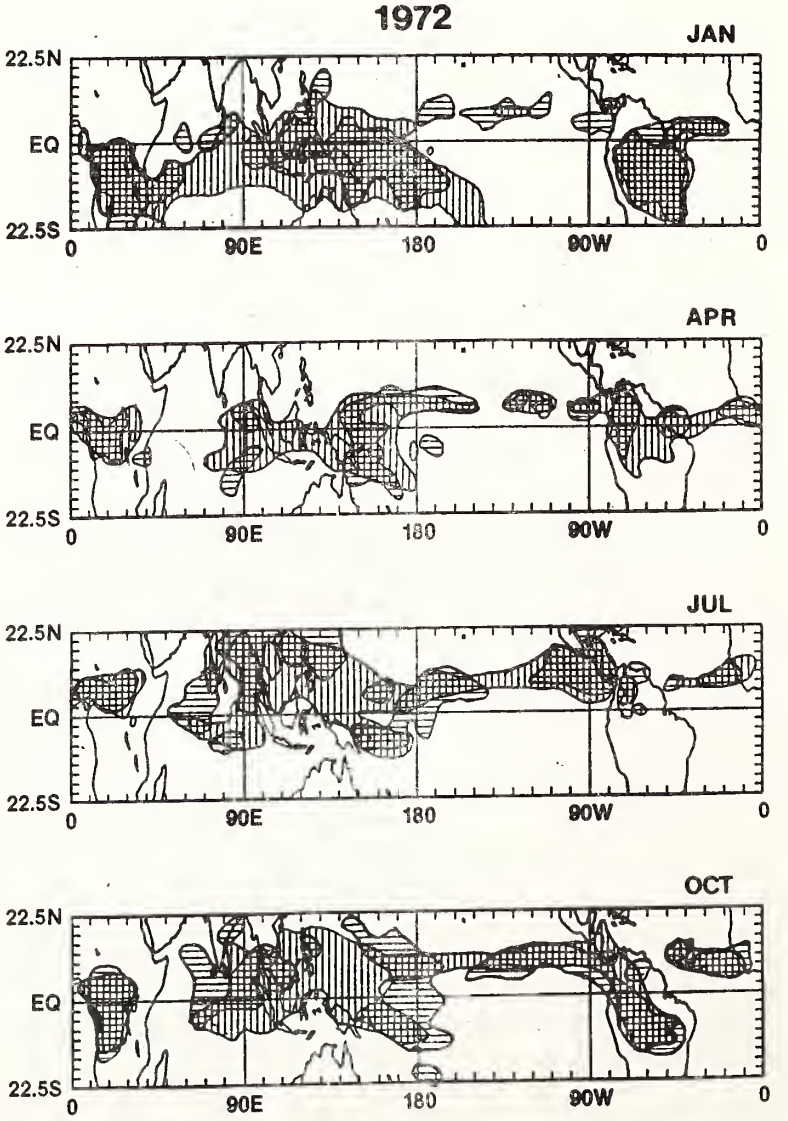

Figure 2. Vertical hatching: As in Figure 1. Horizontal hatching: Areas where the HRC rainfall index exceeds 100 mm for the months of January, April, July and September 1972.

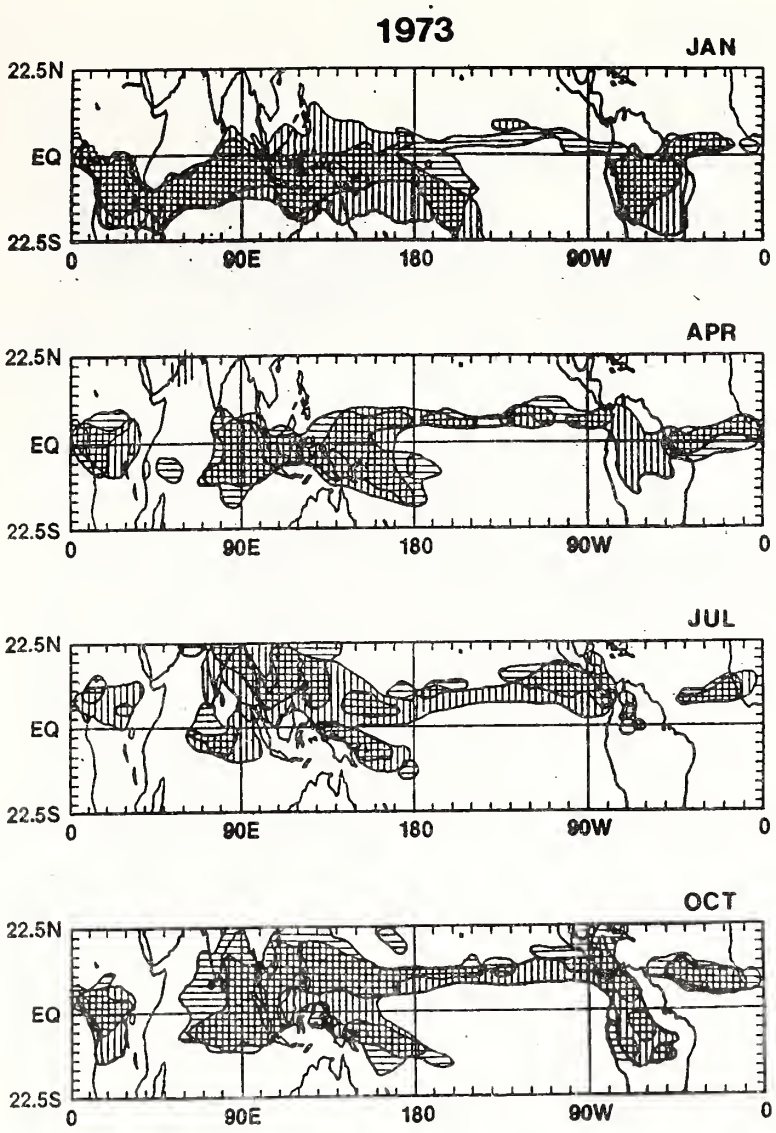

Figure 3. As in Figure 2, for 1973.

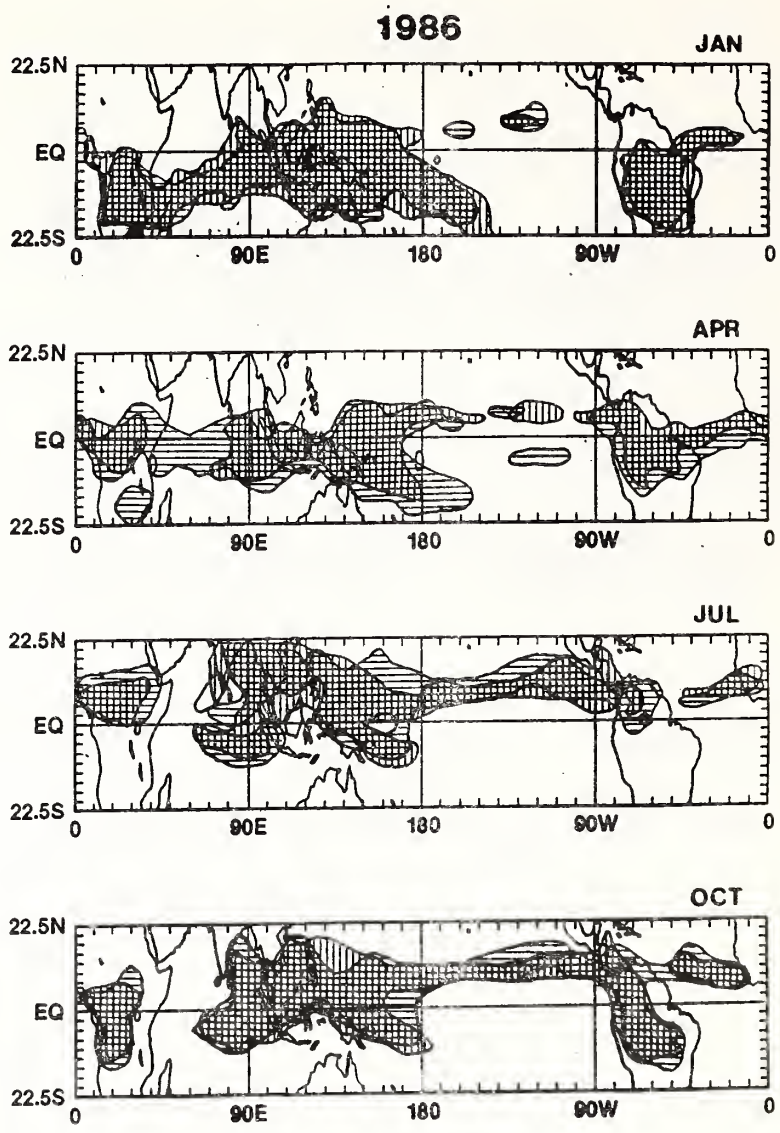

Figure 4. As in Figure 2, for 1986.

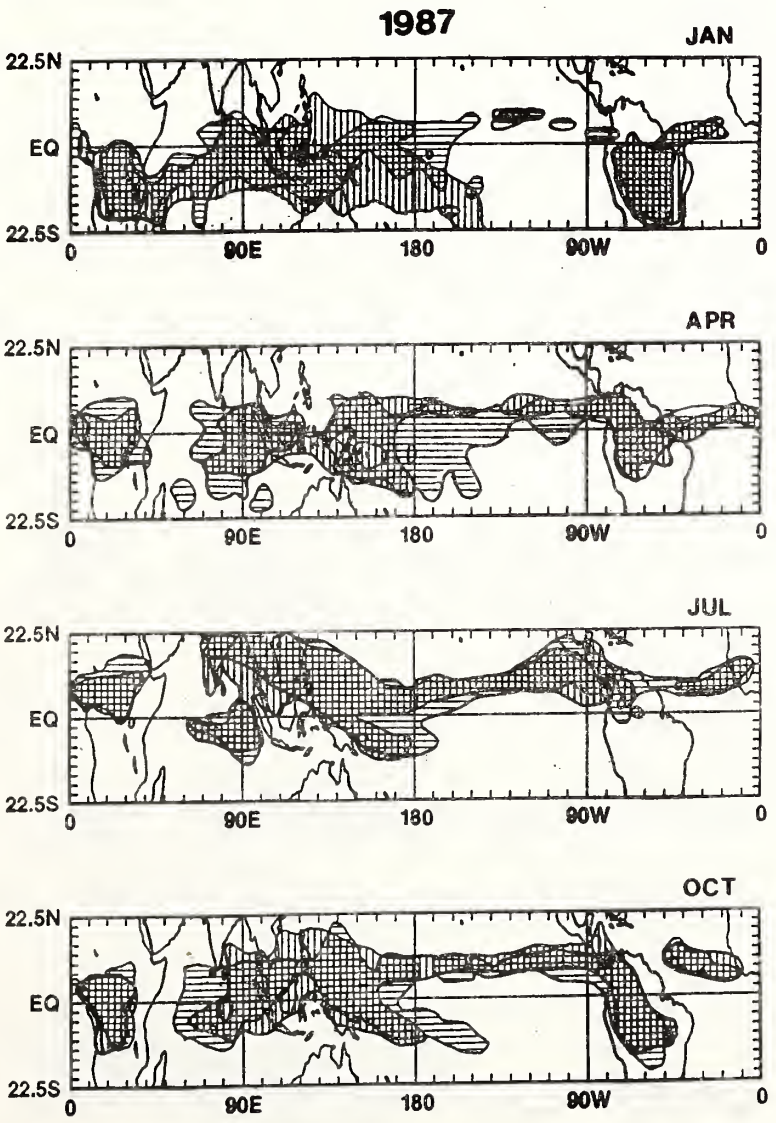

Figure 5. As in Figure 2, for 1987.

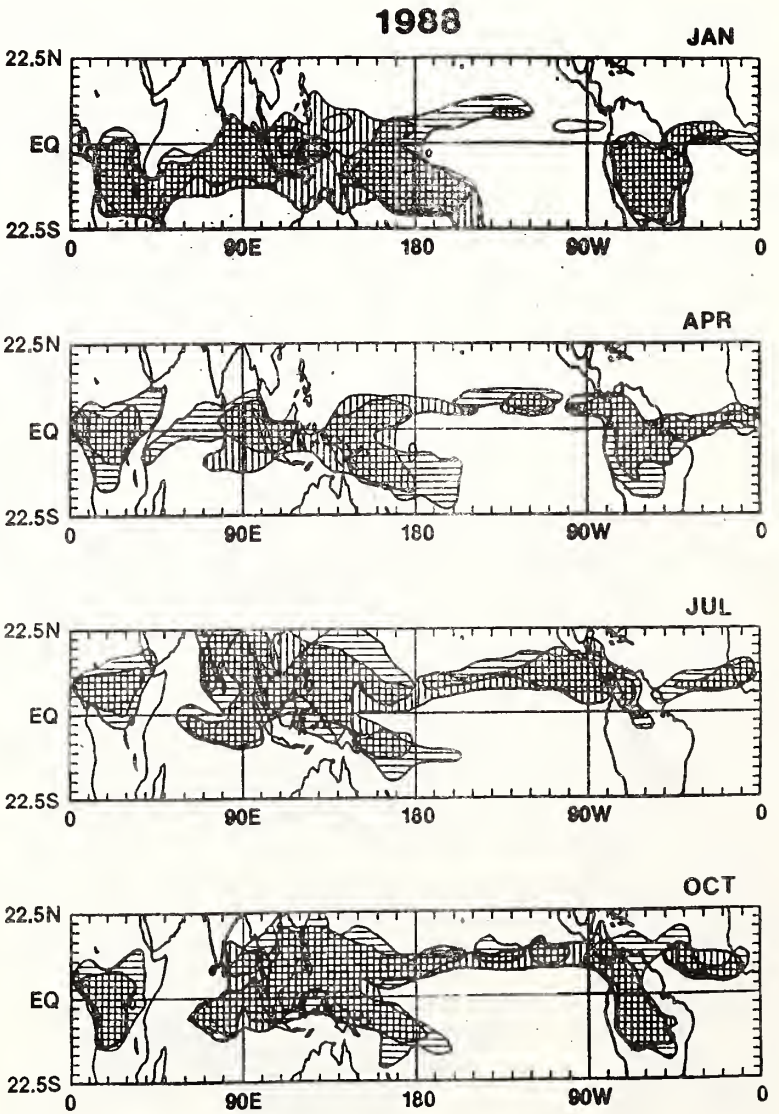

Figure 6. As in Figure 2, for 1988.

LOW FREQUENCY VARIATIONS OF THE SOUTHERN HEMISPHERE CIRCULATION

David J. Karoly *
AOS Program, Princeton University
PO Box 308, Princeton, NJ 08542

Over the past decade, there have been many studies of the low frequency variations of the Northern Hemisphere (NH) circulation, which have documented the typical modes of variation of monthly mean and seasonal mean NH geopotential height. Relatively less attention has been paid to the low frequency variations of the Southern Hemisphere (SH) circulation. Several studies have examined the low frequency variations of the zonal mean SH circulation (Trenberth, 1979; Mo and White, 1985; Kidson, 1988) but they have not tried to assess the relative importance of zonally-symmetric and zonally-asymmetric variations. Mo and White (1985) also examined one-point teleconnection patterns in the SH using 8 years of monthly mean SH analyses. They found that zonally-symmetric and zonal wavenumber 3 patterns were the leading structures in the SH winter. Using monthly mean station data, Szeredi and Karoly (1987) found that the leading modes of intermonthly variability in the SH are zonally-symmetric. In that study, the sparse and irregular station network in the SH may have meant that only the largest scale modes could be identified. The following results, describing the leading modes of low frequency variations of the SH circulation, have been taken from the graduate study of Imre Szeredi at Monash University and are presented in more detail in Szeredi (1987).

Monthly mean numerical analyses for the SH from the Australian Bureau of Meteorology for the period June, 1972 to March, 1987 have been used. Monthly anomalies were prepared for four month winter (JJAS) and summer (DJFM) seasons over the 15 years, giving 60 monthly anomalies for each season. The data were available on a 5° latitude × 10° longitude grid poleward of 10°S, giving 577 gridpoints. The results were obtained using a reduced grid of 103 points, approximately equally-spaced with half the resolution of the full grid. The primary analysis was perfomed on the 300mb height field but other variables were also considered. A rotated principal factor analysis was performed on the correlation matrix on the reduced grid to identify the different modes of variation. The results were compared using principal components and obliquely-rotated and orthogonally-rotated principal factors with variable numbers of factors rotated. The leading modes were stable, having very similar structure using all the different methods. The factors were verified using composite anomalies and one-point teleconnection maps.

To save space, only the results for 300mb height variations in winter are presented. The results are displayed using maps of the correlation between the time series of the scores for the factors on the reduced grid and the time series of the monthly anomalies of 300mb height on the full grid. Three different types of pattern have been identified; zonally-symmetric, zonal wavetrain and meridional wavetrain modes.

The two leading modes are primarily zonally-symmetric, representing out-of-phase variations of height between middle and high latitudes in one

---

* On leave from Dept. of Mathematics, Monash University, Victoria, Australia

case (high latitude mode) and between the tropics and middle latitudes in the other (tropical mode). The structure of the two leading rotated factors is shown in Fig.1. The two factors explain similar amounts of variance and together explain 23% of the variance of monthly mean 300mb height in the SH. They are also the leading modes of intermonthly variability of SH station data found by Szeredi and Karoly (1987). Both modes have an equivalent barotropic vertical structure in the extratropics.

The second most important structure in terms of variance explained is a zonal wavenumber three wavetrain with large amplitude at high latitudes, shown in Fig. 2. There are two factors with this wavenumber three structure, shifted by one-quarter wavelength and with similar amounts of variance. Hence there is no preferred phase for this pattern, since linear combinations of these 2 factors would give a wavenumber three pattern at any longitude. These two factors together explain 12% of the variance.This wavenumber three structure has also been found by Mo and White (1985).

The third type of structure is more of a meridional wavetrain and, again, there are two factors, as shown in Fig. 3. The third winter height factor was not stable under the different methods, apart from over the central Pacific. There it is associated with a dipole structure straddling the SH winter subtropical jet exit region. This factor had significant correlation with the Southern Oscillation Index, consistent with an enhanced height gradient and stronger westerlies over the subtropical Pacific during ENSO events. The fifth factor was stable and associated with a clearer wavetrain extending from Australia over the South Pacific to South America. This factor had negligible correlation with the SOI.

References

Kidson, J. W., 1988. Indices of the Southern Hemisphere zonal wind. J. Climate, 1, 183-194.

Mo, K. C., and White, G., 1985. Teleconnections in the Southern Hemisphere. Mon. Wea. Rev., 113, 22-37.

Szeredi, I., 1987. The structure of monthly fluctuations of the Southern Hemisphere troposphere. Ph.D. thesis, Monash University, Australia.

Szeredi, I., and Karoly, D. J., 1987. The horizontal structure of monthly fluctuations of the Southern Hemisphere troposphere from station data. Aust. Met. Mag., 35, 119-129.

Trenberth, K. E., 1979. Interannual variability of the 500mb zonal flow in the Southern Hemisphere. Mon. Wea. Rev., 107, 1515-1524.

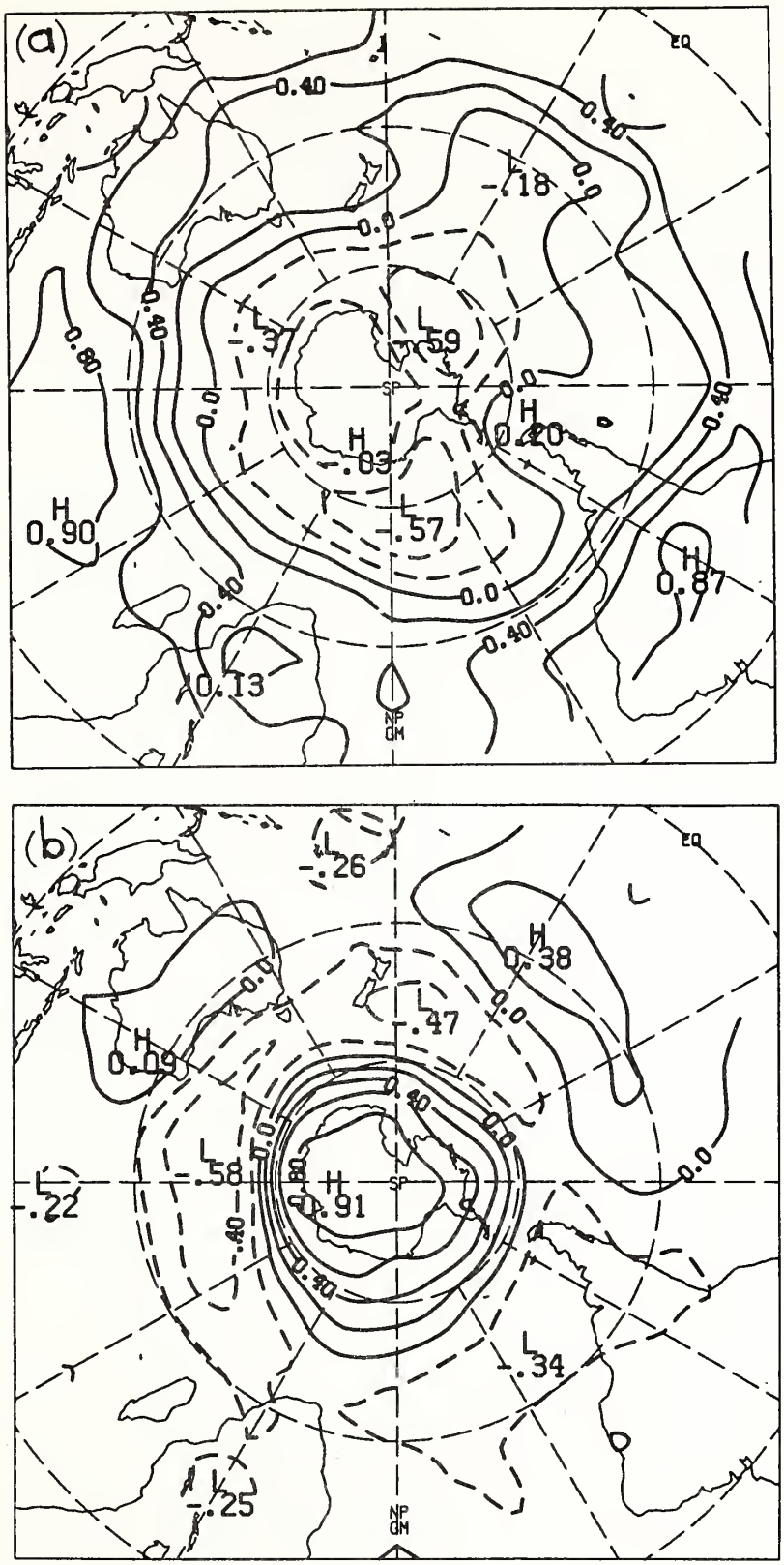

Figure 1. Zonally-symmetric modes:
(a) tropical mode, factor 1, 12.8% variance explained
(b) high latitude mode, factor 2, 10.3% variance.
Correlation of the time series of factor scores and monthly anomalies of 300mb height in winter.

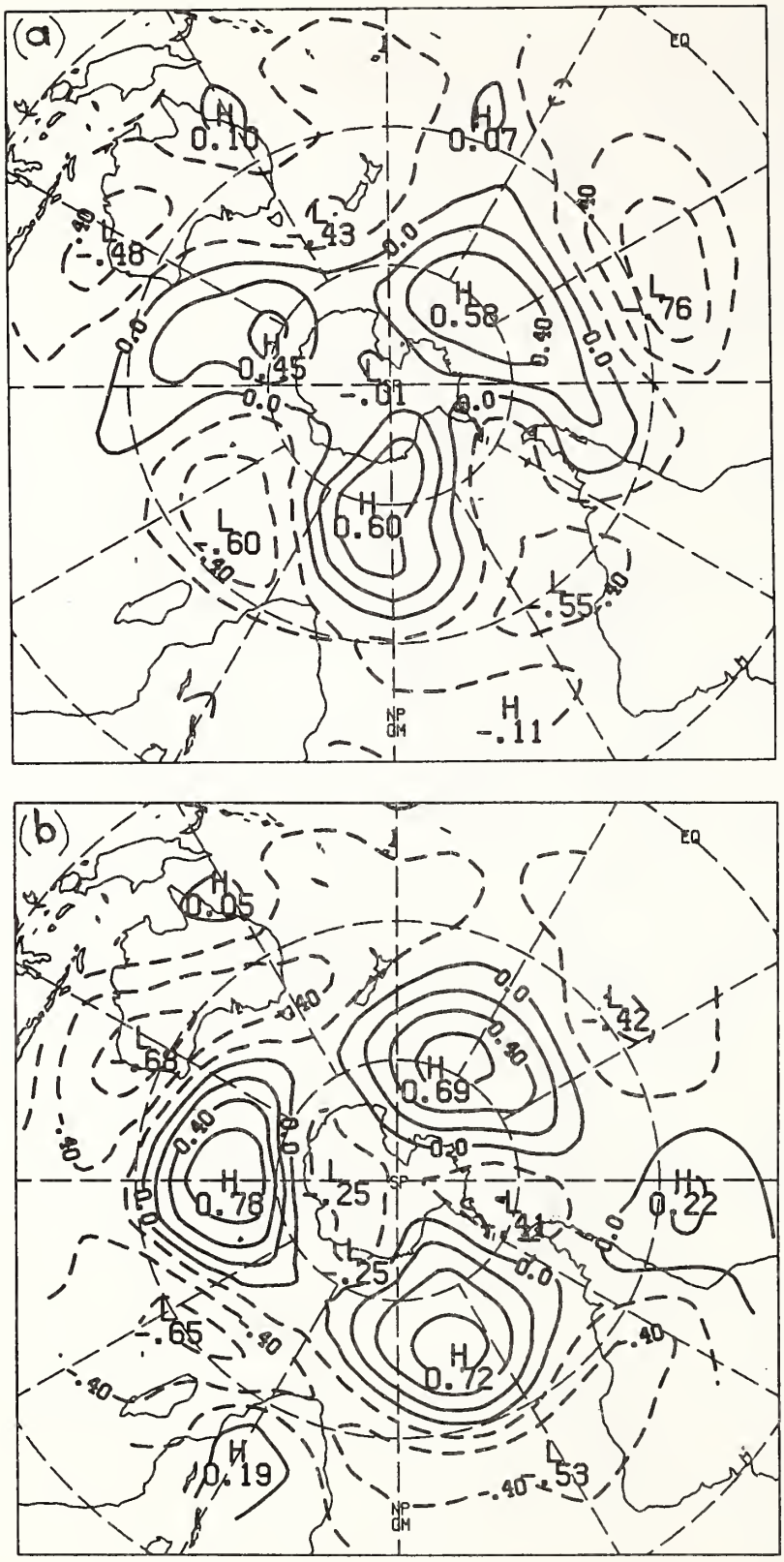

Figure 2. Zonal wavenumber three modes:
(a) factor 4, 6.9% variance, and (b) factor 8, 5.3% variance.

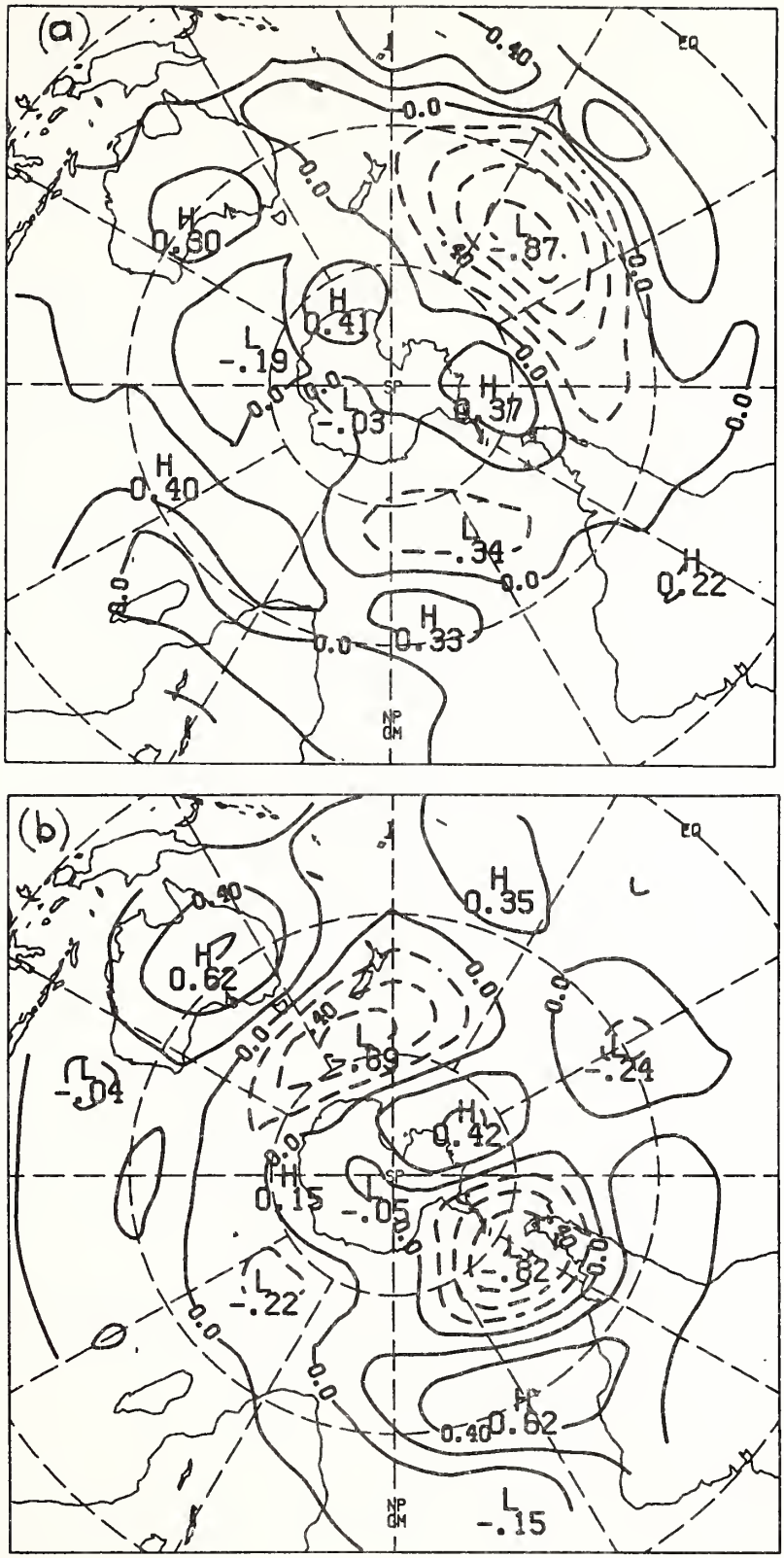

Figure 3. Meridional wavetrain modes:
(a) ENSO mode, factor 3, 8.0% variance and (b) factor 5, 5.9% variance.

Cloud - Radiative Forcing Obtained from NOAA OLR Data

Arnold Gruber and Albert Thomasell

Satellite Research Laboratory, NESDIS*

I. Introduction

Estimates of planetary outgoing longwave radiation, commonly known as OLR, are available beginning in June 1974 and is continuing. These data have been used in numerous studies to diagnose and analyse the climate.

Mostly, these data have been used as an index for clouds or precipitation rather than for its inherent energetic quantity. What we would like to do is suggest another way of utilizing these data that incorporates the effects of clouds as well as temperature changes on the OLR and ultimately provides a measure of the diabatic heating of the atmosphere. This comes about through the concept of cloud forcing (Ramanathan 1987). The cloud forcing as given as

$$CF = F_{CLR} - F_{CLD}$$

where F_{CLR} is the cloud free OLR and F_{CLD} is the cloudy (clear plus overcast OLR). This physically represents the effect of clouds on the radiative losses to space. Since the longwave radiative heating mainly affects the atmosphere, the cloud forcing provides a direct measure of atmosphere diabatic heating due to clouds.

For diagnostic and modeling purposes it is important to know the anomalous cloud forcing. This is expressed as

$$CF' = CF - \overline{CF}$$

$$CF' = F_{CLR} - F_{CLD} - \bar{F}'_{CLR} + \bar{F}_{CLD} = F'_{CLR} - F'_{CLD}$$

*Presented at 13th Annual Climate Diagnostics Workshop - Cambridge, Mass. Oct. 31 - Nov. 4, 1988.

where $\overline{(\quad)}$ is the time average and $(\quad)'$ is the departure from the average.

An example of the calculations will be shown for Feb. 1983. Thus, the anomalous cloud/forcing is equal to the anomaly in the clear flux minus the anomaly in the average flux. The average flux anomaly is easily obtained from NOAA OLR data (Gruber et al., 1986) and so the problem reduces to obtaining estimates of the clear flux anomaly. Since the NOAA OLR data is for average cloud conditions only it is not possible to reliably obtain the clear flux anomaly from the OLR data. However, it is reasonable to assume that the clear flux anomaly is related to the surface temperature anomaly. Thus, the clear flux anomaly is given by

$$F'_{CLR} = T'_{SFC} \times \frac{\partial F}{\partial T_{SFC}}$$

where $\partial F/\partial T$ represents the change in OLR for a given change in surface temperature. This study presents preliminary calculation of cloud forcing anomalies and discusses some of its characteristics. An example of cloud forcing anomalies will be shown for February 1983 a time when the El Nino was well developed.

Data Sources

Surface temperature anomalies were taken from Jones et al, (1986) for land surfaces and Reynolds (1986) for sea surfaces and a value of $\partial F/\partial T$ of 2 Wm^{-2}/C was taken from Ohring and Gruber (1983) who summarized a variety of studies that investigated this relationship. The anomalies in OLR were taken from Gruber et al, (1986). All data were analysed to a common 2° latitude/longitude grid, between 60N and 30S. Also, land surface temperature anomalies for this initial study were only for the Northern Hemisphere. The base periods used for the anomalies were as follows; sea surface temperature 1950-1979, land temperature 1951-1970 and OLR 1974-1983.

Results

Figure 1 a,b show the estimates of OLR anomaly and clear flux anomaly respectively. Note the large anomalies in the tropical pacific ocean associated with the El Niño. There is a positive clear flux anomaly in excess of 6 Wm^{-2} associated with higher sea surface temperatures and a large negative OLR anomaly, in excess of 70 Wm^{-2} associated with increased cloudiness. There is also a sizeable positive anomaly in OLR in the western pacific, associated with a decrease in cloudiness, but only very small anomalies in the clear flux. Note, also, that in the tropics the OLR anomaly is about an order of magnitude larger than the clear flux anomaly, indicating the dominant effect of high clouds associated with convection, underlain by warm surfaces. In the mid-latitudes the clear and OLR anomalies are of the same order of magnitude, particularly over the land areas. It is also interesting that over central Asia and central U.S.A. the clear and cloudy OLR anomalies are of the same sign. This of course, results in cloud forcing anomalies that are small or zero. Figure 2 shows the cloud forcing anomaly. As was anticipated from Figures 1a, b, the tropical and sub-tropical CF anomaly has a spatial distribution and magnitude much like the OLR anomaly and over the N.H. land surfaces the cloud forcing anomaly is small or zero. Converting the cloud forcing to a heating rate by assuming that the anomaly goes into heating the atmosphere yields a heating rate associated with the El Niño of about 0.8° c/day. This is about 1/3 of the anomalous latent heating estimated for the El Niño (Arkin, personal communication). Zonal average of clear flux, cloudy flux and cloudy forcing anomalies are shown in Fig. 3. One clearly sees the influence of the El Niño in the 10N - 10S zone and the increased contribution of the clear flux to the cloud forcing anomaly outside the tropics. The associated zonal heating rates are shown in Figure 4.

Conclusions

The cloud forcing anomaly represents a source of anomalous heating to the atmosphere. This heating acts in addition to any latent heating that may be present. In the tropics the cloud forcing anomaly is mostly determined by the cloudy flux anomaly because of the high clouds associated with convective activity underlain by warm surfaces. During the El Niño, the longwave heating due to cloud forcing was estimated to be about 1/3 of the estimate latent heating; clearly a significant amount that should be accounted for in climate models.

There are some aspects of the anomalous cloud forcing that needs further study. It is important to establish the vertical distribution of the heating related to the cloud forcing. This will depend to a large extent on the vertical distribution of cloudiness, and the anomalous cloud forcing needs to be examined for other months and years. Also, we have been able to examine only the longwave component of the anomalous cloud forcing. A complete understanding of the effects of the anomalous radiational heating on the atmospheric circulation will come when we can obtain the shortwave component of the cloud forcing.

References

Gruber, A., M. Varnadore, P.A. Arkin, J.S. Winston, 1986: Monthly and seasonal mean outgoing longwave radiation and anomalies. NOAA Tech. Rpt. NESDIS 26.

Jones, P.D., S.L.B. Roper, R.S. Bradley, H.F. Diaz, P.M. Kelly and T.M.L. Wigley, 1986: Northern hemisphere surface air temperature variations: 1851-1984.

Ohring, G. and A. Gruber, 1983: Satellite radiation observations and climate theory. Advances in Geophysics 25, 237-304.

Ramanathan, V., 1987: The role of Earth radiation budget studies in climate and general circulation research. J. Geophys. Res., 92, 4075-4095.

Reynolds, R.W., 1988: A real time global sea surface temperature analysis. J. Clim., 1, 75-86.

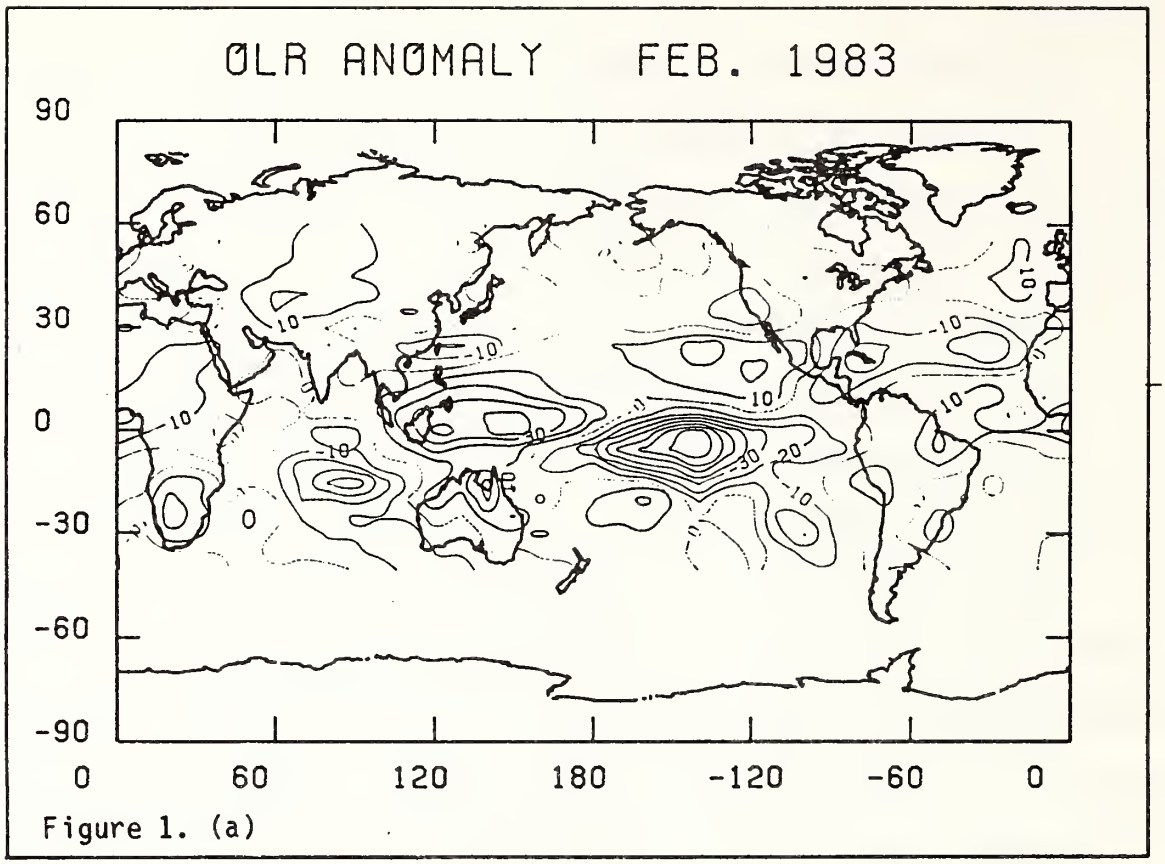

Figure 1. (a)

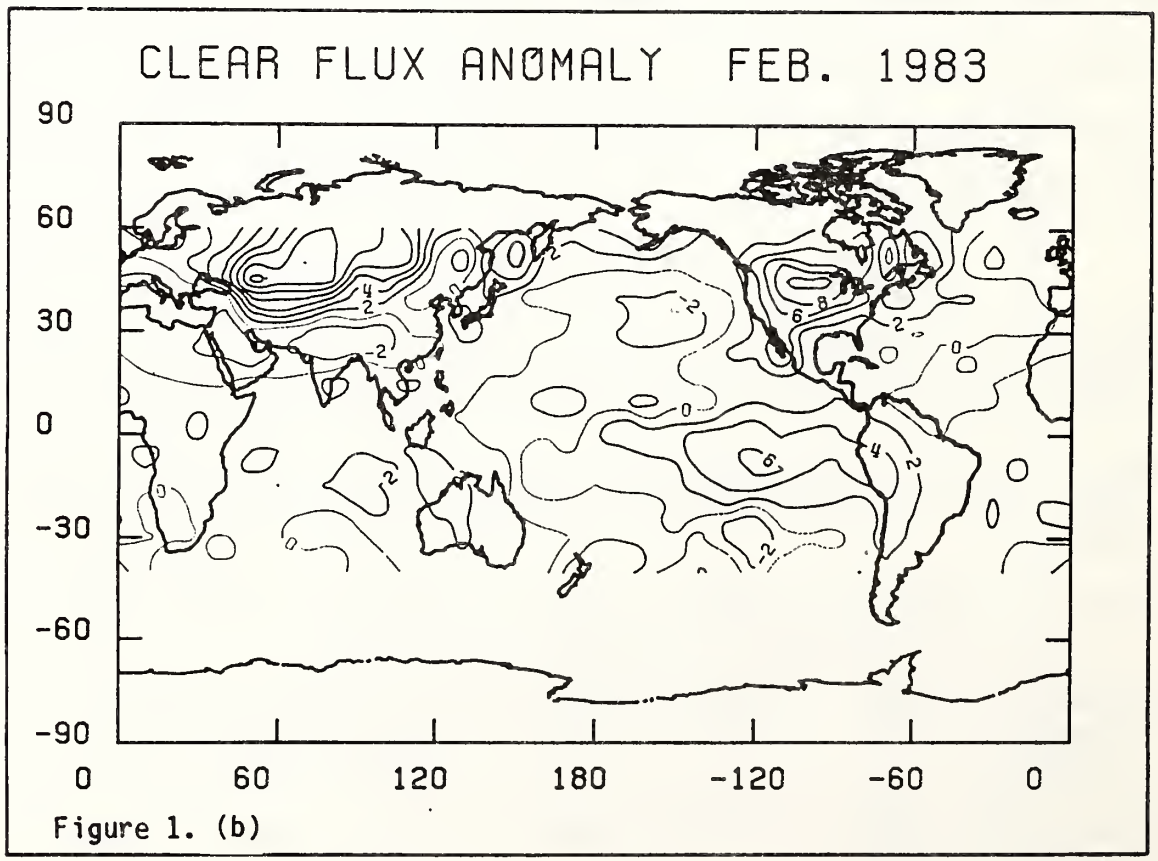

Figure 1. (b)

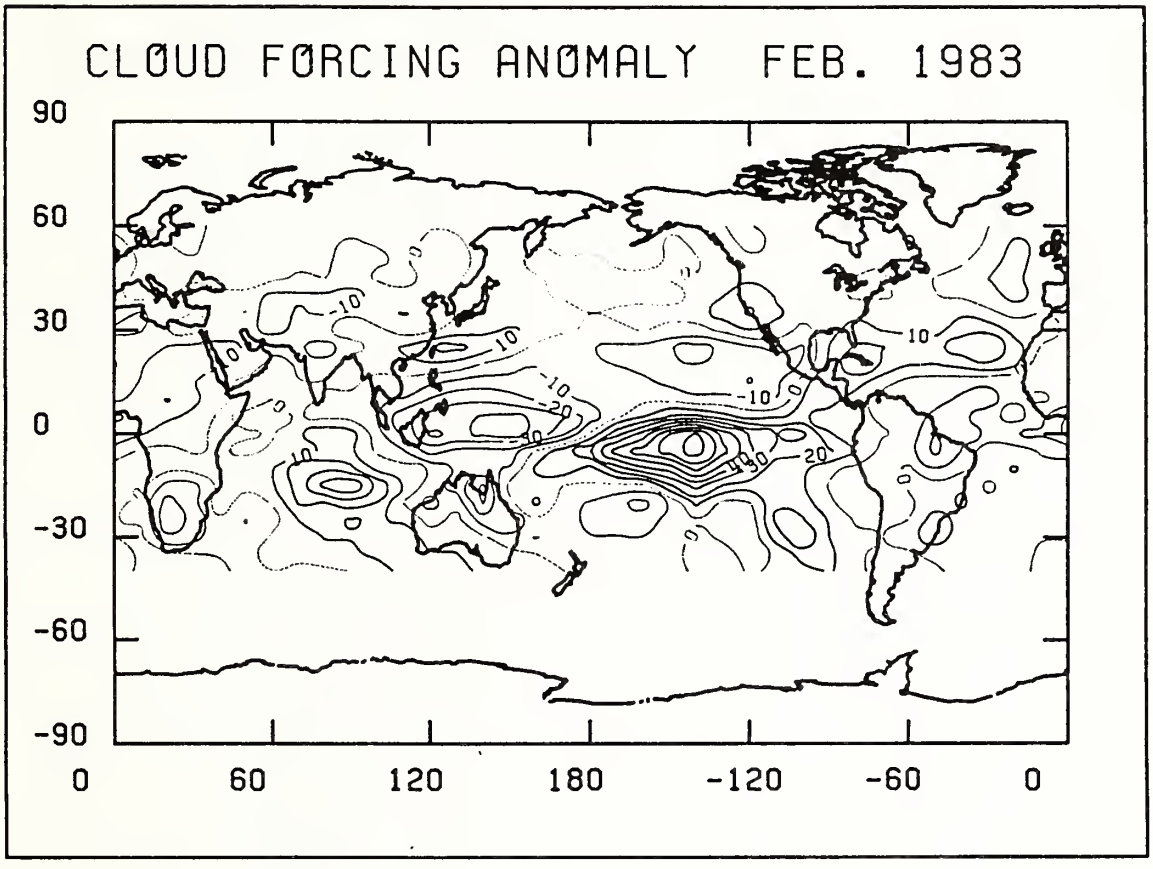
CLØUD FØRCING ANØMALY FEB. 1983
90
60
30
0
-30
-60
-90
0
60
120
180
-120
-60
0

Figure 2.

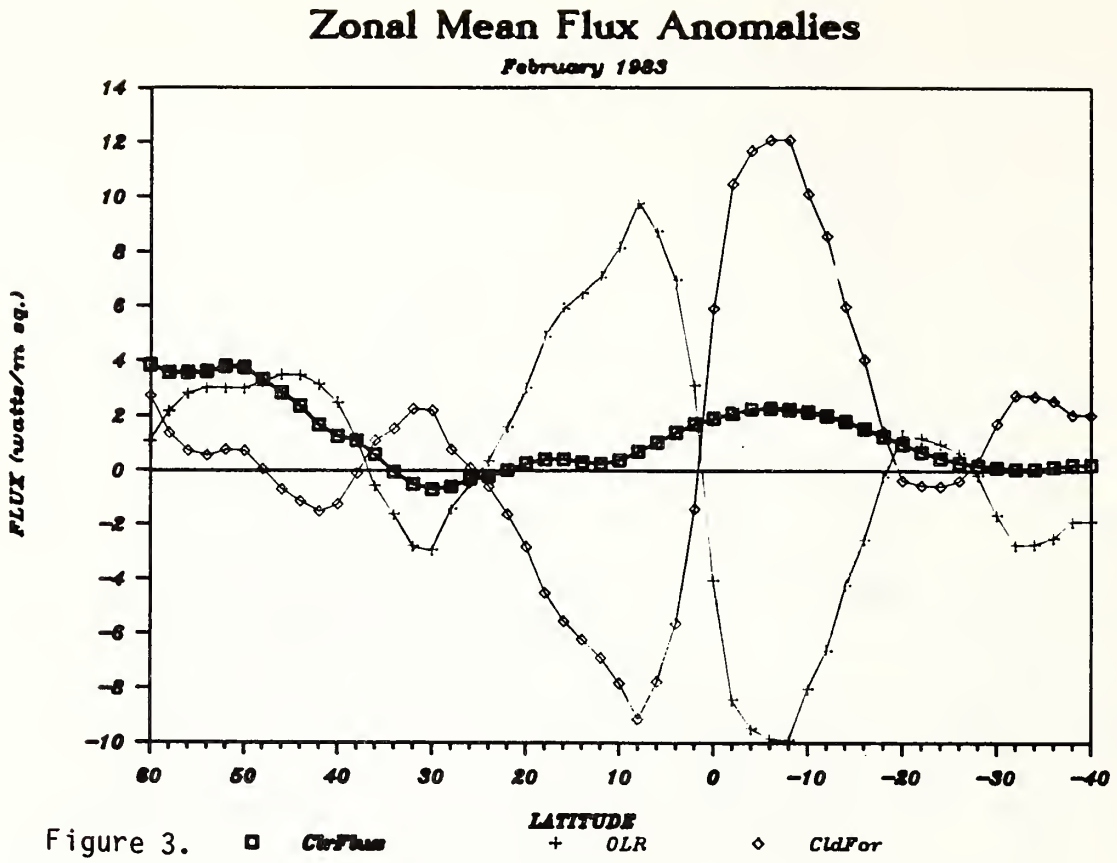

Figure 3.

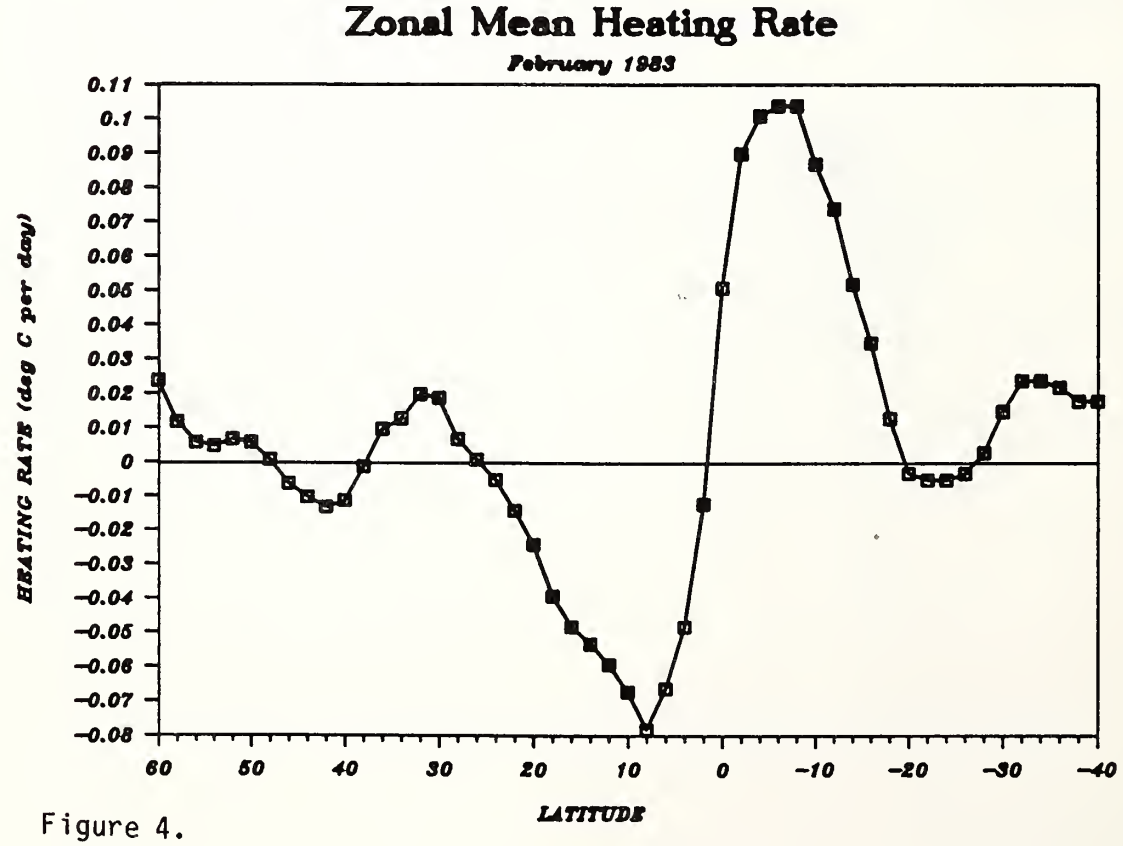

Figure 4.

Temporal Variations in the Relationship between Analyzed Upper Tropospheric Divergence and Inferred Convection in the Tropics

Phillip A. Arkin and Kingtse C. Mo
Climate Analysis Center, NOAA
Washington, DC 20233

Frank Sornatale
1st Weather Wing/DNC
Hickam AFB, HI 96853-5000

Anandu Vernekar
Meteorology Department, University of Maryland
College Park, MD 20742

Accurate diagnoses of the divergent component of the large-scale circulation of the troposphere are important in a number of different ways to studies of the global climate. Recent studies appear to indicate that annual and interannual changes in the divergent flow both within the tropics and into higher latitudes are critical in determining the global distribution of climate anomalies associated with the El Niño/Southern Oscillation (ENSO) phenomenon. Seasonal anomalies in divergent flow at 200 mb during the winter of 1986-87 appeared to have been forced by anomalies in tropical convection centered near the dateline and the equator, and seem to have played some role in the anomalous cyclonic circulation in the North Pacific. In this case, accurate measurements of divergent flow could be used to diagnose the momentum and vorticity budgets, and thus to better understand the physics involved. In the summer of 1987, the Indian summer monsoon was exceptionally poor; the worst in over 100 years by some accounts. During the same season, convective activity in the equatorial Pacific was highly anomalous. Diagnoses based on the divergent flow might serve to establish the physical mechanisms responsible for this coincidence of events, which has been observed in many ENSO warm episodes in the past. A third example is provided by a model simulation of the U.S. drought of the April-June 1988 period. In the simulation, latent heating anomalies associated with convection in the eastern Pacific between the equator and 20^{o}N caused a wave train of geopotential height anomalies extending across North America. A strong anticyclonic center in the upper Midwest led to the dryer than normal conditions. While the simulated circulation anomalies resembled those observed outside the tropics, accurate measurements of the divergent circulation are necessary to provide a more rigorous test of the hypothesuized connection.

In this paper, we compare two of the principal methods used to diagnose the pattern and intensity of these divergent circulation: analyses of 200 mb circulation from the National Meteorological Center's Global Data Assimilation System and maps of outgoing longwave radiation (OLR) derived from NOAA polar orbiting satellite data. Our analysis will cover the period from January 1979 to April 1988 and will use monthly mean data. Annual and interannual variability in both divergent wind and tropical convection as inferred from OLR during this period have been described in other publications, and space will not permit extensive reproduction of those results here. We will focus upon the associations between areas of strong

divergent/convergent flow and extensive cloudy/clear regions. Our objective is to establish the degree to which the NMC analysis of upper tropospheric divergence represents the real atmosphere. We shall begin with two assumptions. These are, first, that OLR is well correlated with convection (and, therefore, with upper tropospheric divergence) in the tropics, and, second, that the relationship between convection and OLR is approximately stable with time.

Scatter plots of divergence and OLR for several individual months show that a large negative correlation exists in the tropics. The pattern correlation over the region 20^{o}N-20^{o}s between mean OLR and divergence has been calculated for each month and is shown in Fig. 1. There appear to be several regimes during this period. Before 1982, the correlation averaged about 0.4 (all values have been multiplied by -1), with considerably lower values from early 1982 until mid-1984. From mid-1984 until mid-1986, values were somewhat higher than during the earliest several years, while since mid-1986 correlations have averaged near 0.6. Two of the transitions can be identified with changes to the NMC analysis system: during September 1984, the analysis of tropical divergence was changed (and apparently improved) through the incorporation of a diabatic non-linear normal mode initialization; and in May 1986, much more sophisticated physical parameterizations began to be used in the NMC forecast model. These changes appear to have improved the analysis of tropical divergent flow. The reason for the decrease in correlations around 1982 is not clear. It appears that the OLR is quite good at distinguishing areas of convergence and divergence at 200 mb in the tropics. Its skill at specifying variations within regions of divergent flow is also substantial, and has been increasing (fig. 2). However, within areas of convergent flow the correlation between divergence and OLR is smaller (fig. 3).

These results indicate that the skill of NMC analyses in reproducing the divergent component of the tropical circulation has improved in recent years. The improvement has occurred both in regions of divergent and convergent (at 200 mb) flow, and has been associated with specific changes in the analysis system. At the present time, close to half the spatial variability in tropical divergence can be specified from OLR. Since the correlation between OLR and convection is not perfect, it may be difficult to identify further improvements in the analysis system. One implication of the present study is that diagnostic studies of the large-scale tropical circulation, to the extent that they rely on NMC analyses, should probably concentrate on the period since May 1986. It also seems quite desirable to perform a similar study using ECMWF analyses.

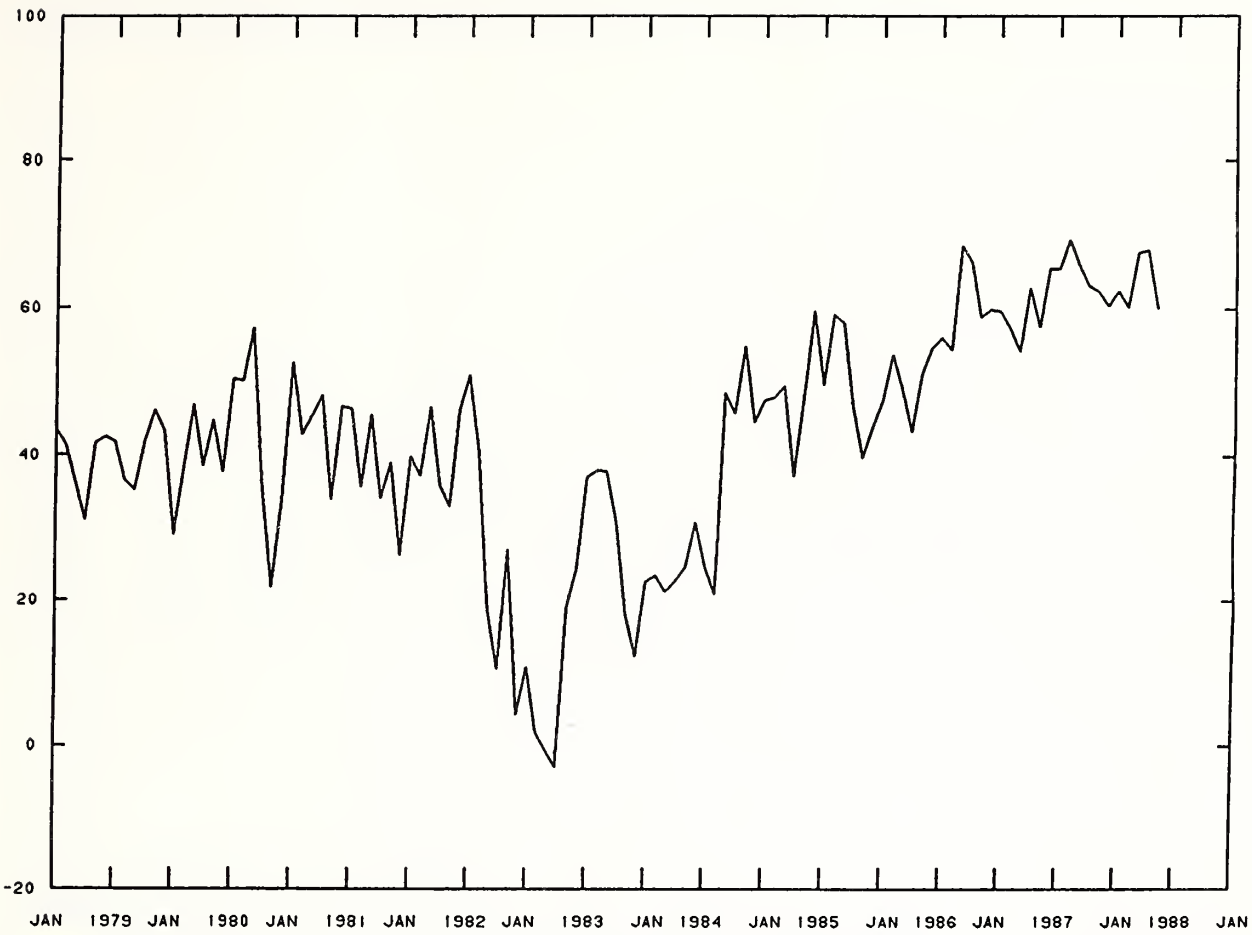

Figure 1. Pattern correlation (multiplied by -100) between monthly mean OLR and divergence at 200 mb for each month from January 1979-April 1988 for 2.5^{o} latitude/longitude areas in the region 20^{o}N-20^{o}S.

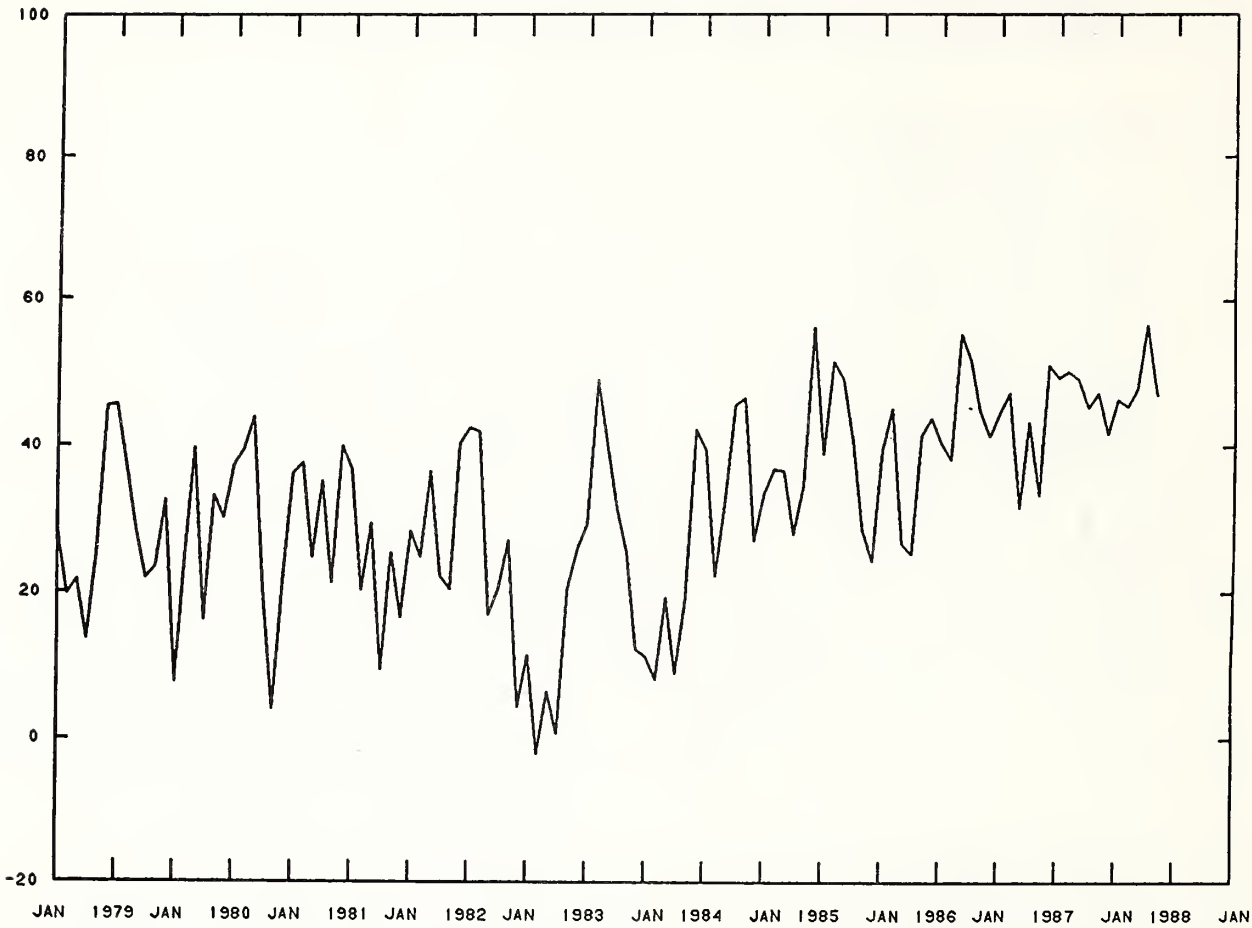

Figure 2. As in fig. 1 except the correlation is computed using only grid points where the 200 mb flow is divergent.

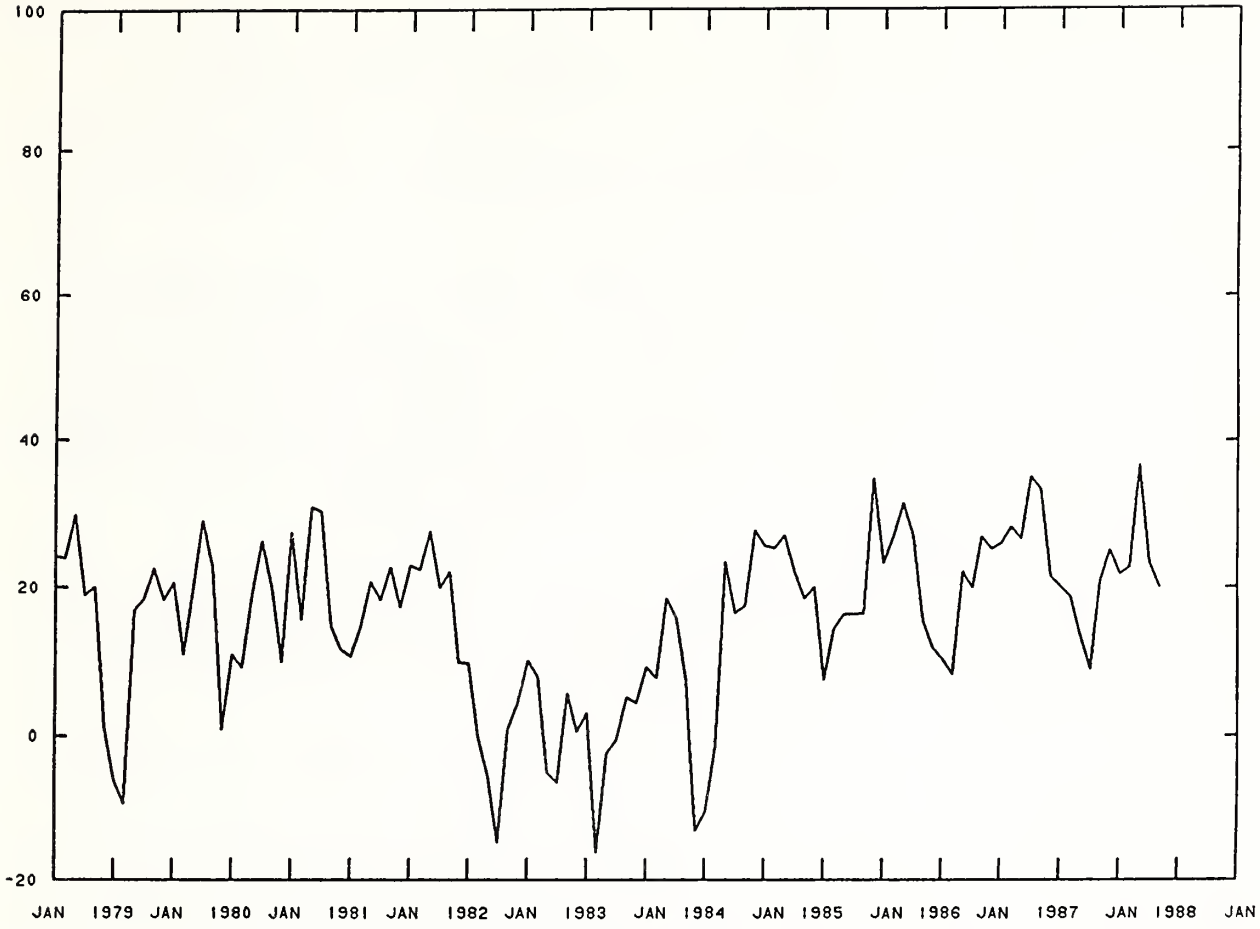

Figure 3. As in fig. 1 except the correlation is computed using only grid points where the 200 mb flow is convergent.

Global Scale Diabatic Heating Rate Distribution and Atmospheric Mass Anomalies

John R. Christy
University of Alabama in Huntsville

Global data sets with sufficient consistency through time to monitor the climate system accurately would be of tremendous value. However, because of operational changes in the production of analyses at the major forecast centers, global analyses are in many ways unsuitable for climate studies. One variable, surface pressure (P_s), derived from the European Centre for Medium-Range Weather Forecasts (ECMWF) geopotential fields does appear to offer time-consistency since 1979.

The utility of P_s as a climate monitor is the subject of the following research. P_s will be compared with precipitable water (P_w), diabatic heating rates (Q), and outgoing longwave radiation (OLR). Our expectations are as follows. Gridpoint values of P_w should represent in some sense the low-level convergence/divergence of moisture, and therefore of mass. Low P_s is associated with surface convergence, therefore P_s and P_w will show negative correlations. For the global mean values of P_w and P_s however, a positive correlation is expected because the dry atmosphere is assumed to be constant in time, so that variability global mean P_s and P_w would be identical. Because of the strong relation between tropospheric temperature and P_w, one would expect to be able to track global warming and cooling from accurate values of P_s and/or P_w.

The expected relation between Q and P_s reflects the mass circulation associated with heating. Column integrated divergence (low P_s) would be negatively correlated with heating (positive Q). For OLR, we expect cold values to correspond with deep convection which in turn indicates low P_s (*i.e.* positive correlation). This relationship would be much weaker in latitudes which have considerable high cloudiness not associated with precipitation.

The data from which P_w and Q are derived are the ECMWF 12 hourly, 7 level (1000, 850, 700, 500, 300, 200, 100 hPa) global grids for 1 May 1985 - 29 Dec. 1986 for P_w and 1 Jan 1985 - 29 Dec. 1986 for Q. The gridpoint vertically integrated values are determined over four-day periods. Time (4-day) and spatial (vertical integral) averaging reduces random errors yet has enough time resolution to define slow tropical motions. All data are on a 2.5° regular grid. The OLR data are the daily mean values of the day and nighttime crossings of the observed (not interpolated) data.

Any calculation of Q is notoriously suspect since it relies heavily on the value of the vertical motion of the atmosphere. We use the residual of the vertically integrated dry thermodynamic equation to estimate Q (Q_e).

$$Q_e = Q + \text{error} = \frac{\partial \bar{T}}{\partial t} + \nabla \cdot \overline{V'T'} + \bar{V} \cdot \nabla \bar{T} + \left(\frac{P}{P_0}\right)^{\kappa} \left[\bar{\omega} \frac{\partial \bar{\theta}}{\partial p} + \frac{\partial \overline{\omega'\theta'}}{\partial p} \right]$$

Figure 1 displays the 4-day values of P_w and Q_e for the globe, NH and SH. Though there is a positive global bias in Q_e (+0.05 K/day) note that the greatest heating occurs in NH spring and summer prior to the attained maximum global temperature in late NH summer. The smoothed annual cycle amplitude is about 0.03 K/day which upon time integration (neglecting the 0.05 k/day bias) implies a global temperature range of 3.5 K per year. Q_e shows greater extrema in 1986 than in 1985 due to changes in the analysis production. Figure 2 gives the global distribution of Q_e for 1985-1986.

The correlations for global and hemispheric mean values of P_s versus P_w, Q_e and OLR are given in the table below (unfiltered: U). There are 182 4-day periods for the Q_e and OLR correlations and 152 periods for P_w. Filtered correlations (F) are also shown for periods in the interseasonal time frame (24-74 day band).

Correlations between P_s and the following:

	Global mean		NH mean		SH mean	
	U	F	U	F	U	F
P_w	0.81	0.06	-0.35	-0.02	-0.43	-0.07
Q_e	0.01	-0.05	-0.50	-0.62	-0.59	-0.07
OLR	0.75	0.09	-0.43	-0.01	-0.08	-0.10

The correlations of zonal mean quantities are shown in Fig. 3, again with unfiltered (dots) and filtered (solid line) values. In Fig. 4, the gridpoint correlations for the filtered values are given. Values with magnitude greater than 0.25 are considered significant at the 2% level, however, only values which exceed a magnitude of 0.4 are shown. This threshhold is closer to satisfying our goal of *utility* rather than significance.

The results show that for much of the tropics, filtered P_s and P_w are negatively correlated. In midlatitudes there are positive correlations. For P_s and Q_e, the midlatitude oceanic regions and the area east of African offer the most significant correlations (negative). Correlations between filtered P_s and OLR are generally positive, being most significant over Europe, North Indian Ocean and the SH circumpolar trough.

To interpret these results one must incorporate a host of physical processes. For example, the positive correlation at midlatitudes for P_s vs. P_w relates to the fact the large scale P_w field is out of phase with the surface pressure. However, in the tropics, systems are more vertically aligned and a strong negative correlation is seen (Fig. 4a). Over all, the expected associations mentioned at the beginning are verified for the tropical regions east of Africa to the western Pacific for the 24-74 day band. Because this is the tropical region of greatest diabatic heating, one may infer that variabiltiy in P_s is at least a rough proxy for the variability in heating rates in the 24-74 day band. For the zonal mean correlation of P_s and Q, latitude bands around 30° show the most significant values ($\approx$ -0.6).

When the total variance for all periods resolved by the 4-day time unit is taken into account (*i.e.* unfiltered), zonal correlations prove the expected associations in those tropical regions which experience the poleward extent of the ITCZ. Correlations in these regions north and south of the 0°-10°N band often exceed $\pm$ 0.9. For these latitudes, the interannual variability of the P_s field could provide a means of estimating the interannual variability of the zonal mean diabatic forcing and precipitable water there.

We also note that low correlations for the 24-74 day band are the rule from South America eastward through Africa. Continents in general have significant correlations only in the gridpoint unfiltered (*i.e.* annual cycle included) maps (not shown). In the great majority of these just mentioned areas, the amount of variance explained by the 24-74 day filter is less than 20%.

The correlations shown in this research indicate that one may *infer* variability in diabatic heating and precipitable water for the band-pass values of P_s in certain key areas (*e.g.* Maritime Continent). However, the associations are not solid, rarely explaining over 50% of the band-pass variances. The correlations show that the physical processes of the atmosphere are sufficiently complex that for much of the globe, knowledge of the surface pressure alone provides only limited information as to the colocated diabatic forcing and precipitable water. In any case, because of the correlations in key areas, P_s does have utility as a climate variable for the past 10 years.

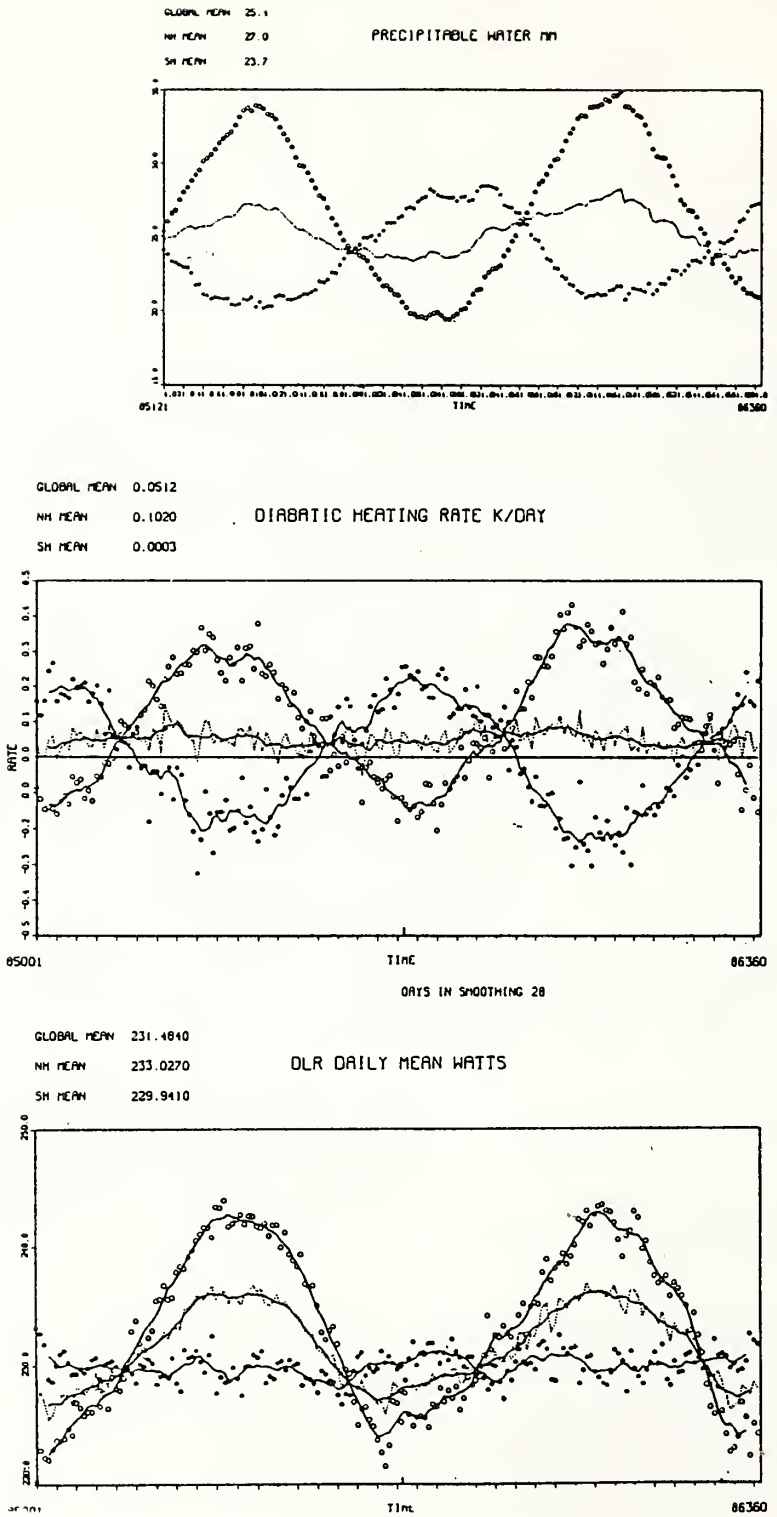

Fig. 1 Time series of 4-day values of P_w (top), Q_e (middle) and OLR (bottom). The lower two begin on 1 Jan 1985, while P_w begins on 1 May 1985. All end on 29 Dec 1986. Open circles represent NH values, filled circles - SH and dashed lines - global mean values. The solid lines in the lower two are 28 day running means.

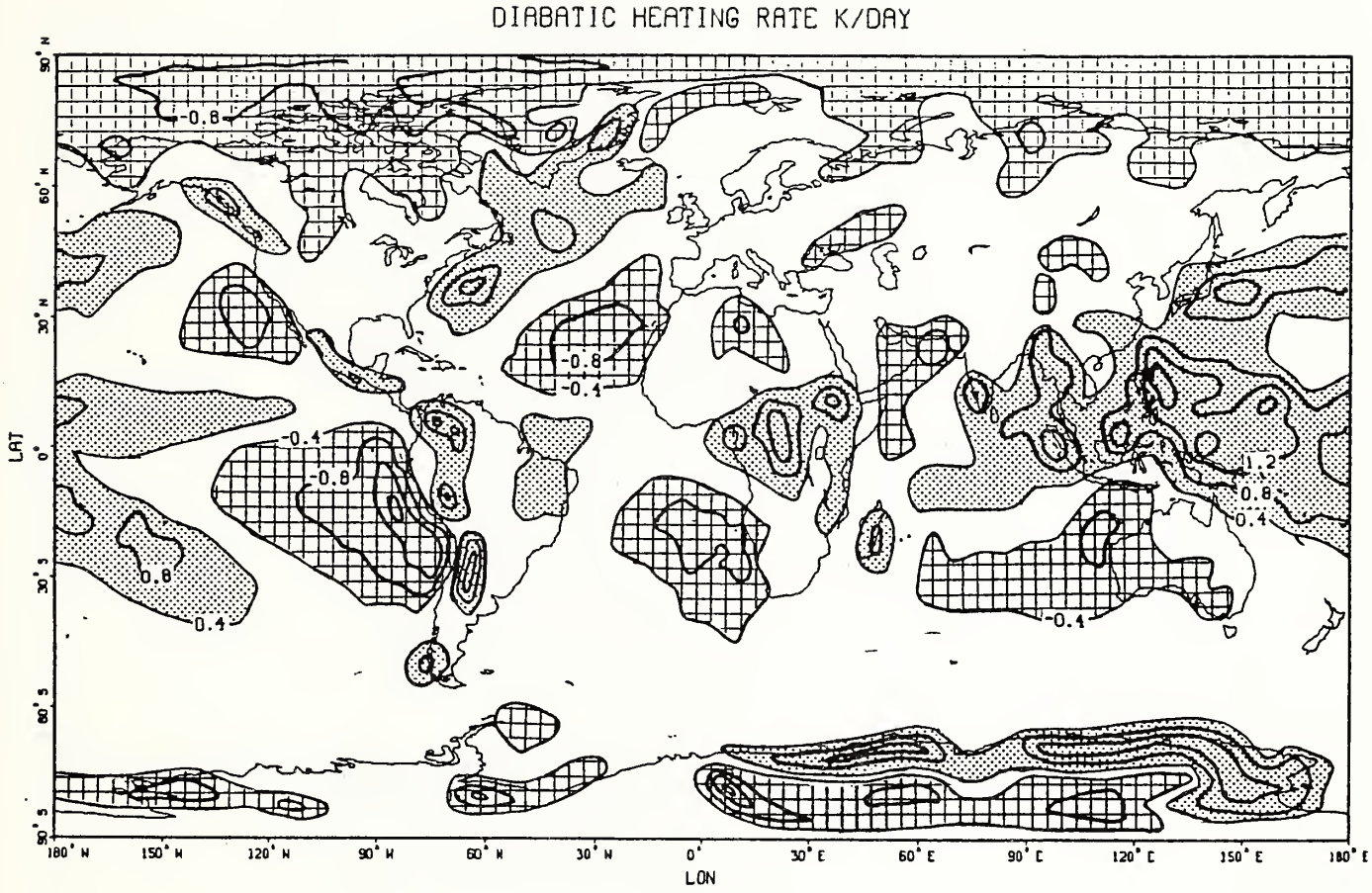

Fig. 2 Vertically integrated Q_e (1985-1986) with contours of 0.4 K/day omitting the 0.0 contour. Positive areas are stippled, negative areas are hatched.

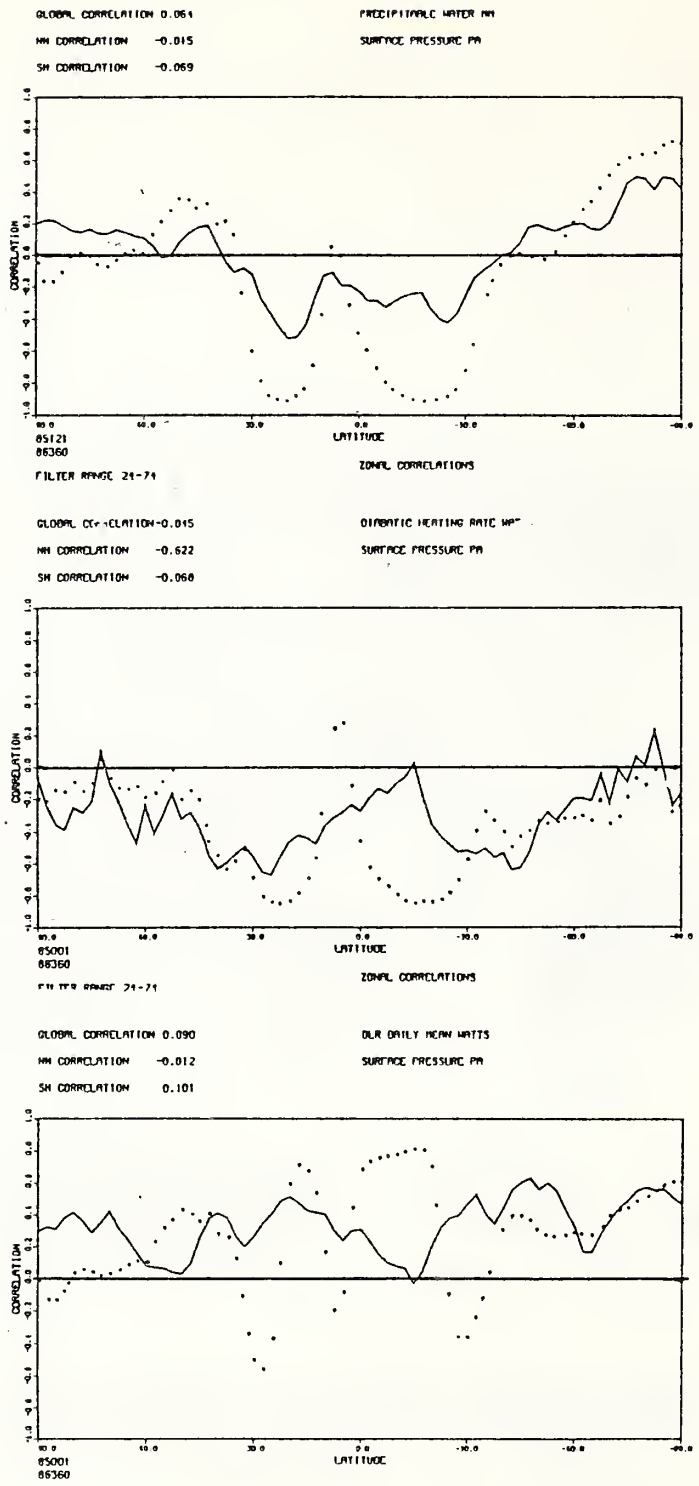

Fig. 3 Correlations with $[P_s]$ of zonal mean values of (top to bottom) $[P_w]$, $[Q_e]$, and [OLR]. Dots represent unfiltered 4-day correlations and solid lines, filtered (24-74 day band).

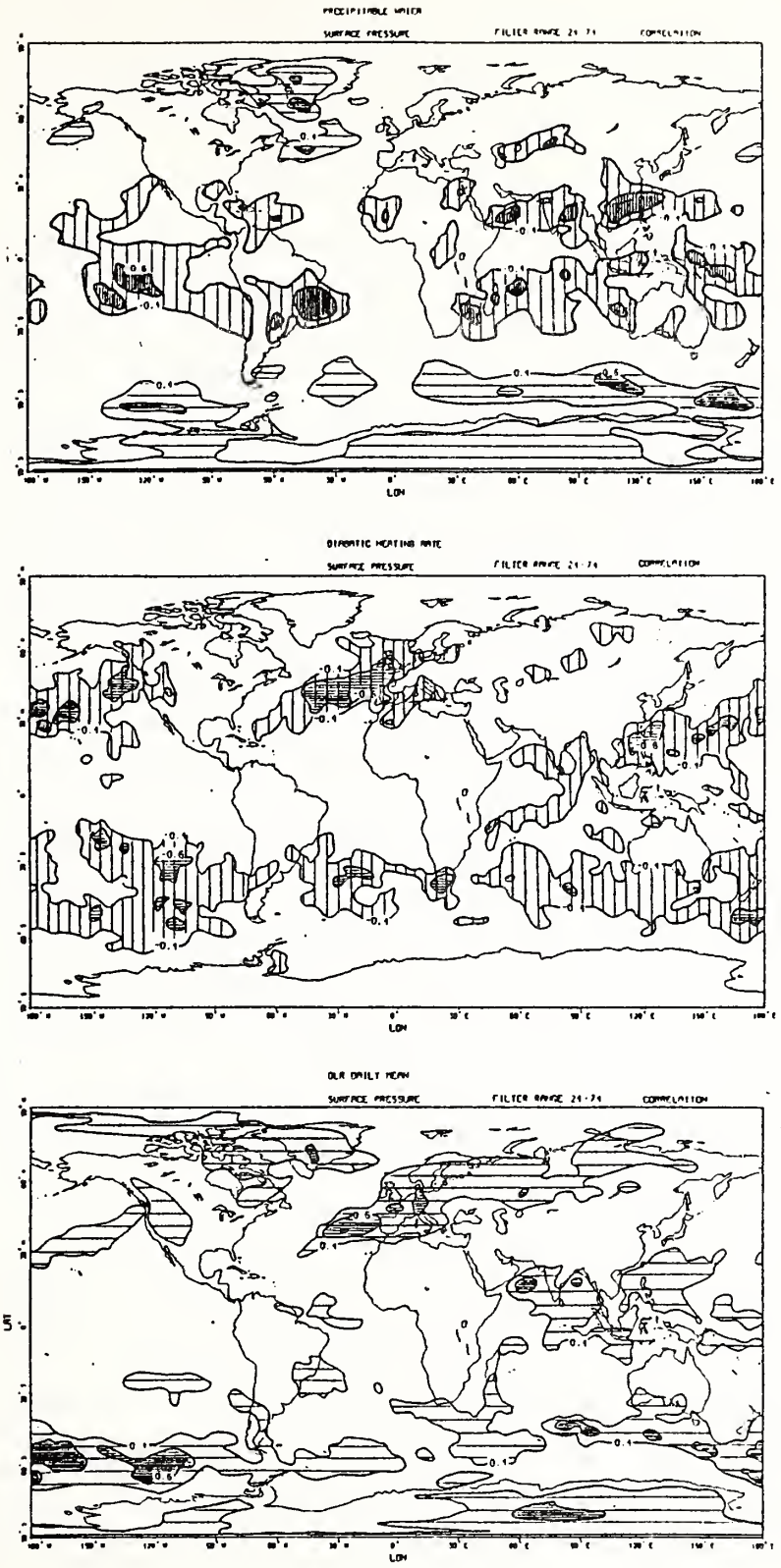

Fig. 4 Gridpoint correlations of filtered (24-74 day band) P_s and (top to bottom) P_w, Q_e and OLR. Lined areas represent correlations with magnitudes above 0.4.

OBSERVED LARGE-SCALE SPATIAL RELATIONSHIPS BETWEEN SEA SURFACE TEMPERATURE AND ATMOSPHERIC CIRCULATION ACROSS THE TROPICAL PACIFIC

David S. Gutzler and Tamara M. Wood
Atmospheric and Environmental Research, Inc.
840 Memorial Dr.
Cambridge, MA 02139

An uncertain component of current efforts to simulate coupled ocean-atmosphere anomalies in the tropics is the mechanism by which variations in near-equatorial sea surface temperature (SST) force perturbations in the overlying atmosphere. Several different forcing mechanisms have been proposed. Gill (*QJRMS*, 1980, pg. 447) developed a simple model in which the low-level atmospheric circulation is driven by deep convection. Zebiak (*MWR*, 1986, pg. 1263) adapted and extended this model by parameterizing the link between SST anomalies and convection anomalies in terms of anomalous latent heat flux from the ocean surface over warm SST regions and including the effects of the mean atmospheric circulation via a convergence feedback. An entirely different ocean-atmosphere coupling mechanism was explored by Lindzen and Nigam (*JAS*, 1987, pg. 2418), who proposed that the atmospheric boundary layer could be approximated by a homogenous slab and SST gradients are dynamically equivalent to surface pressure gradients, which then drive the low-level circulation directly. The important distinction between these two mechanisms is that deep convection forces the circulation in the Gill/Zebiak scheme whereas convection is a dynamically passive byproduct of pressure gradient-driven low-level convergence in the Lindzen/Nigam scheme.

In this study we use observations to diagnose the extent to which each of these two forcing mechanisms are operative. Since simple models driven by these different mechanisms have each achieved quite reasonable simulations of the low-level wind field, it is likely that both mechanisms are effective in nature. If anomalies of SST, deep convection, and convergence throughout the boundary layer were mutually well-correlated then it would not be possible to separate the effects of the two mechanisms. On the other hand, if "low-level" convergence is not vertically homogeneous then it seems plausible to hypothesize that surface gradients might be relatively more effective at forcing the surface wind field and interior heating might be relatively more effective at forcing winds in the free atmosphere near the top of the boundary layer. We therefore base our study on a comparison of convergence statistics at the surface and at 850 mb.

We use monthly mean fields of SST, outgoing longwave radiation (OLR; a proxy for deep convection), NMC-analyzed 850 mb winds, and surface winds analyzed subjectively from ship reports, for the 9-year period January 1979-Decenber 1987 (108 months). The surface wind data were derived from wind stress analyses produced at Florida State University and the other fields were provided by the NMC Climate Analysis Center. All data have been interpolated to a common $2.5^\circ \times 2.5^\circ$ latitude-longitude (ϕ,λ) grid extending from 30°N to 30°S across the Indian and Pacific Oceans (Indian Ocean surface wind analyses were available only through December 1986). Climatological monthly means were calculated at each gridpoint by averaging over the nine-year period, and monthly anomalies were then formed by subtracting the monthly climatological value from each gridpoint. Wind divergence fields were derived from the centered difference calculation

$$\nabla \cdot \underset{\sim}{v} = (1/a\cos\phi)\partial u/\partial\lambda + (1/a\cos\phi)\partial(v\cos\phi)/\partial\phi$$

(where a is the radius of the earth) without additional smoothing. Emphasis is placed on variance and correlation statistics derived from the time series of monthly anomalies across the Pacific.

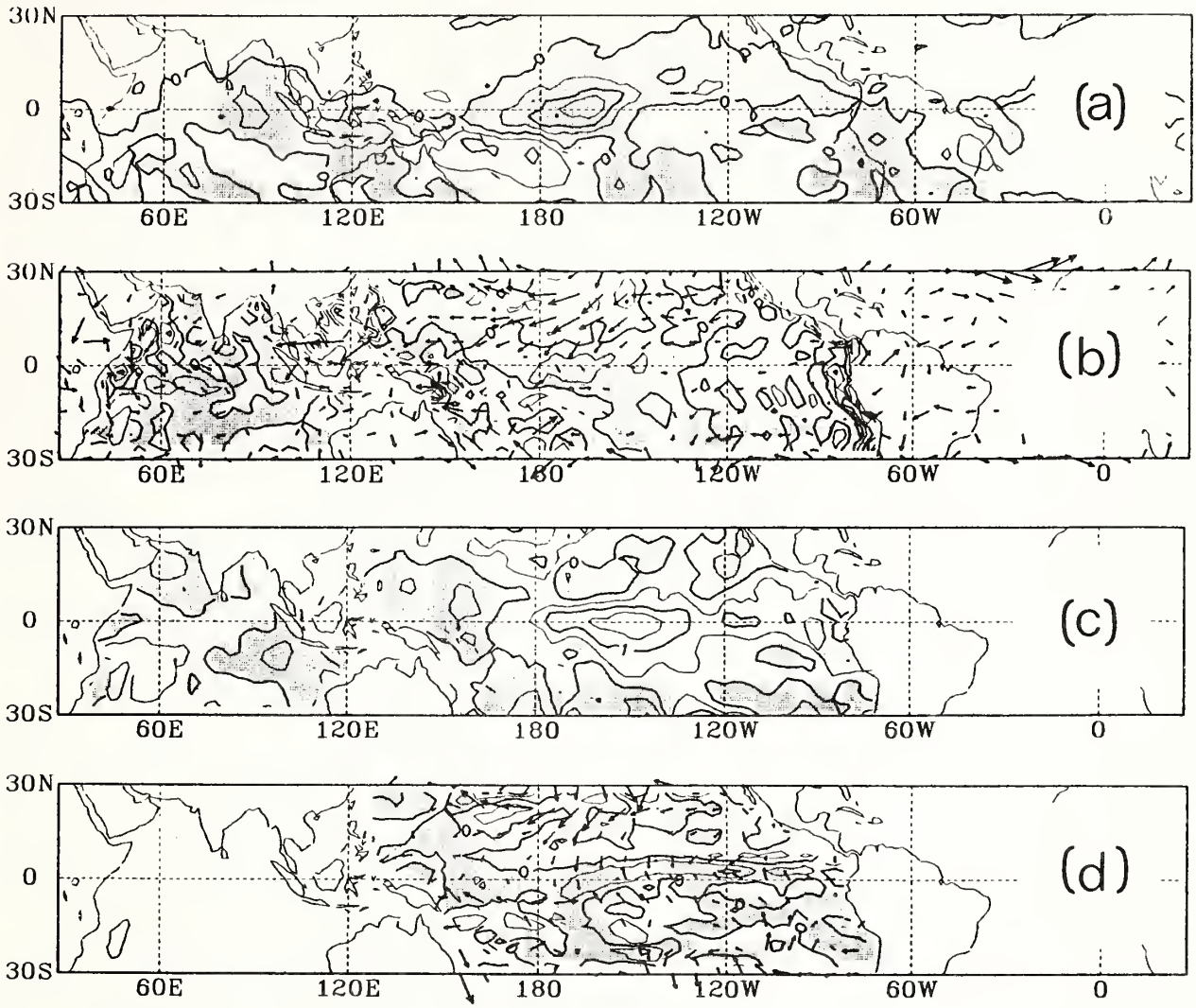

FIGURE 1: Monthly mean anomalies for January 1987, defined relative to the January average at each gridpoint for years 1979-1987 (negative values shaded).
(a) OLR (b) $\underset{\sim}{v}_{850}$ and $\nabla \cdot \underset{\sim}{v}_{850}$ (c) SST (d) $\underset{\sim}{v}_s$ and $\nabla \cdot \underset{\sim}{v}_s$

Anomalies of OLR, SST, and the surface and 850 mb wind and divergence fields for January 1987 (during the mature phase of the 1986-87 ENSO warm event) serve as an illustrative example of the results (Fig. 1). The upper two panels show the OLR and $\underset{\sim}{v}_{850}$ anomaly fields. The largest negative OLR anomaly (indicative of enhanced convection) is centered on the equator between 160°E and 150°W, coincident with a large 850 mb convergence anomaly. The warm SST and $\nabla \cdot \underset{\sim}{v}_s$ anomalies, in the lower two panels, are also coincident but they extend between the date line and the South American coast, distinctly to the east of the OLR and $\nabla \cdot \underset{\sim}{v}_{850}$ anomalies.

Fig. 2 shows plots of the local variance of anomalies of OLR, SST, $\nabla\cdot\underset{\sim}{v}_{850}$ and $\nabla\cdot\underset{\sim}{v}_s$ in the 108-month time series. Variance maxima in OLR and 850 mb divergence are nearly coincident across the near-equatorial Pacific to the west of about 120°W. SST and $\nabla\cdot\underset{\sim}{v}_s$ variance maxima are located east of the dateline extending to the South American coast. We crudely divide the near-equatorial Pacific into three longitudinal zones based on these anomaly variance calculations: in the west (the maritime continent to the dateline) OLR and $\nabla\cdot\underset{\sim}{v}_{850}$ variances are large and SST and $\nabla\cdot\underset{\sim}{v}_s$ variances are small; in the east (120°W to South America) OLR and $\nabla\cdot\underset{\sim}{v}_{850}$ variance are small and SST and $\nabla\cdot\underset{\sim}{v}_s$ variances are large; in the mid-Pacific (between the dateline and 120°W) the variances of all these fields are large.

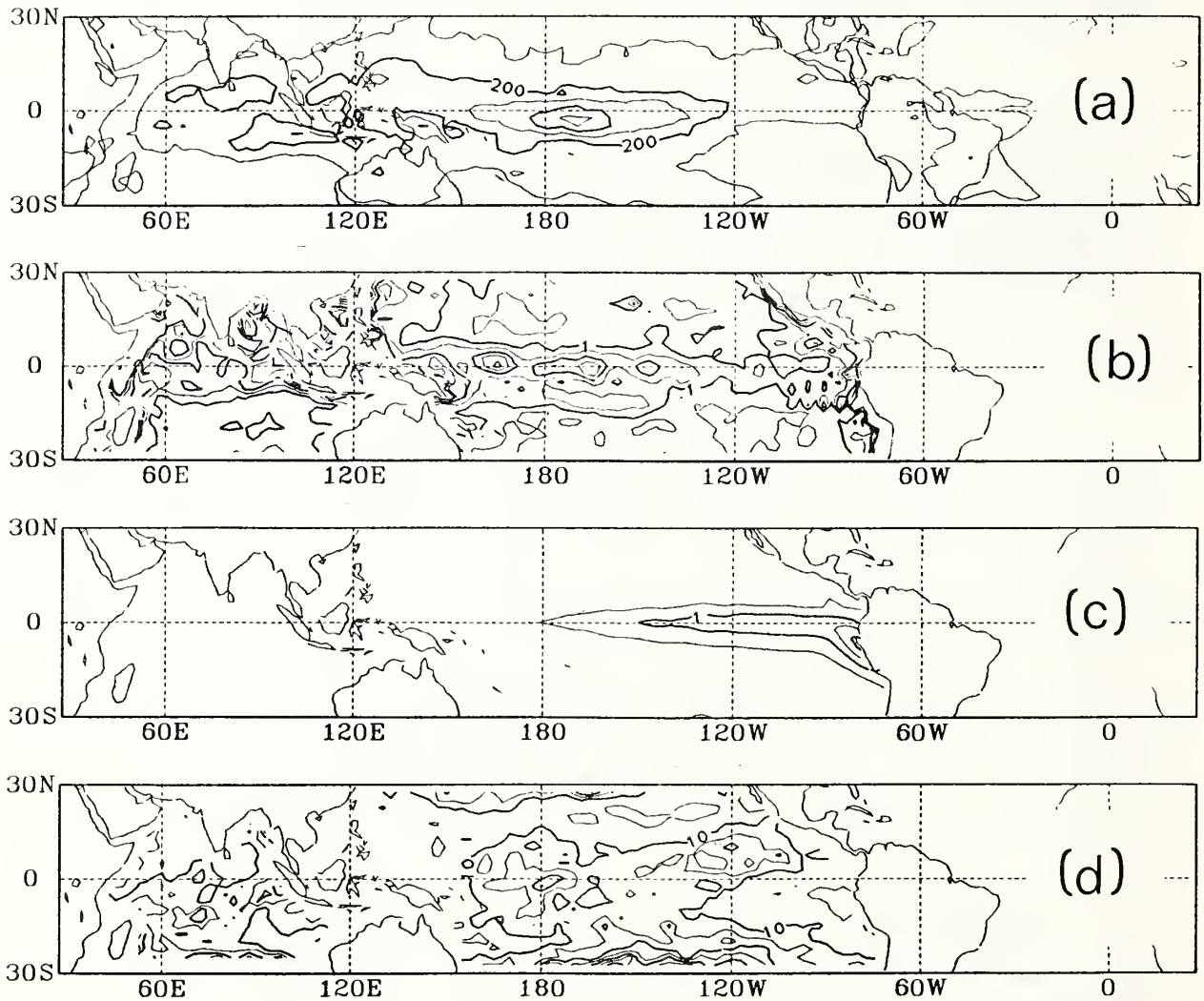

FIGURE 2: Variance of monthly anomalies for the period Jan. 1979 - Dec. 1987. (a) OLR (b) $\nabla\cdot\underset{\sim}{v}_{850}$ (c) SST (d) $\nabla\cdot\underset{\sim}{v}_s$

Geographical variations of pointwise correlations between monthly anomalies of OLR and $\nabla\cdot\underset{\sim}{v}_{850}$ or $\nabla\cdot\underset{\sim}{v}_s$ (Fig. 3) underscore the distinctions implied by the January 1987 example and by the geographical distributions of variance in the previous two figures. The OLR-$\nabla\cdot\underset{\sim}{v}_{850}$ correlation exceeds 0.4

(considerably above the 95% significance level) in a band across the western and central Pacific as far east as about 120°W. In contrast, significant OLR-$\nabla \cdot \underset{\sim}{v}_s$ correlations are located along the equator from the South American coast westward only to the dateline. Hence surface convergence and OLR anomalies are highly correlated over the eastern Pacific despite the low variance of OLR anomalies there.

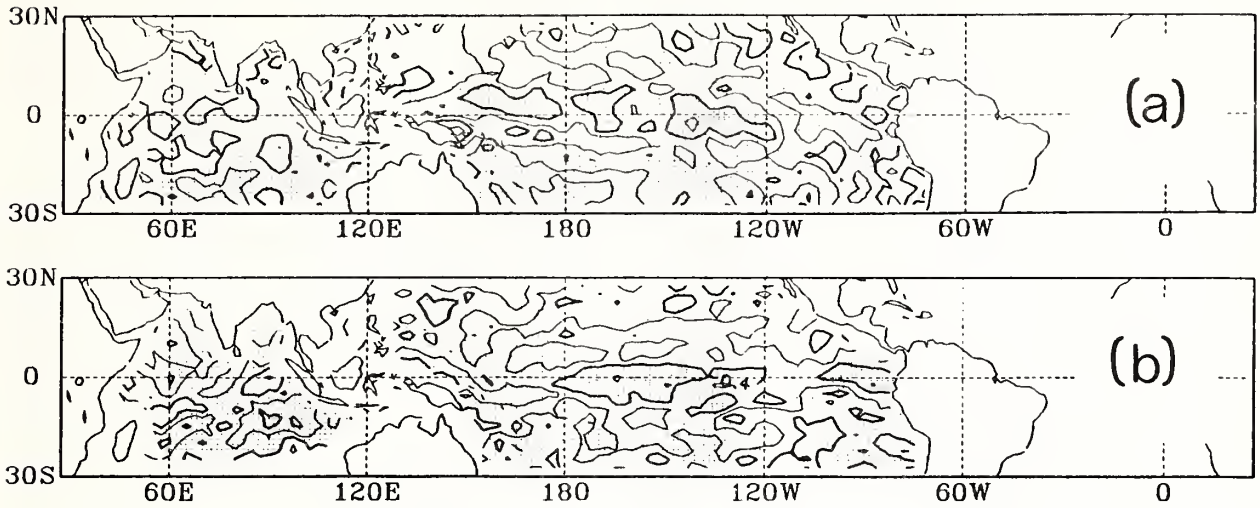

FIGURE 3: Pointwise correlation between monthly anomalies of OLR and monthly anomalies of (a) $\nabla \cdot \underset{\sim}{v}_{850}$ (b) $\nabla \cdot \underset{\sim}{v}_s$. Negative values are unshaded; values between 0.0 and 0.4 are lightly shaded; values greater than 0.4 are heavily shaded.

Our results and interpretation are summarized in Fig. 4 by a schematic depiction of longitudinal variations in the relationships among monthly anomalies of SST, convection and low-level wind convergence across the near-equatorial Pacific.

- *West of the dateline*, where the mean SST field features warm temperatures and small temperature gradients and the mean low-level atmospheric circulation is convergent, monthly anomalies of SST and $\nabla \cdot \underset{\sim}{v}_s$ are small and anomalies of OLR and $\nabla \cdot \underset{\sim}{v}_{850}$ are large (as determined by the variances of the anomaly time series). OLR anomalies are better correlated with $\nabla \cdot \underset{\sim}{v}_{850}$ anomalies than with $\nabla \cdot \underset{\sim}{v}_s$ anomalies.

- *From 120°W eastward to the South American coast*, in contrast, the mean SST field is cold with large temperature gradients and the mean low-level atmospheric circulation is divergent. Monthly anomalies of SST and $\nabla \cdot \underset{\sim}{v}_s$ are large and anomalies of OLR and $\nabla \cdot \underset{\sim}{v}_{850}$ are small. OLR anomalies are better correlated with $\nabla \cdot \underset{\sim}{v}_s$ anomalies than with $\nabla \cdot \underset{\sim}{v}_{850}$ anomalies.

- *In the central Pacific between the dateline and 120°W*, anomaly variances of all these quantities are relatively large and well-correlated.

Taken together these results support the conclusion that forcing of the low-level wind field (particularly at 850 mb) by *interior heating* is highly effective over the *western* Pacific, whereas forcing by *surface gradients* is highly effective (particularly right at the surface) over the *eastern* Pacific. It seems likely that the central Pacific is a regime in which both forcing mechanisms are effective.

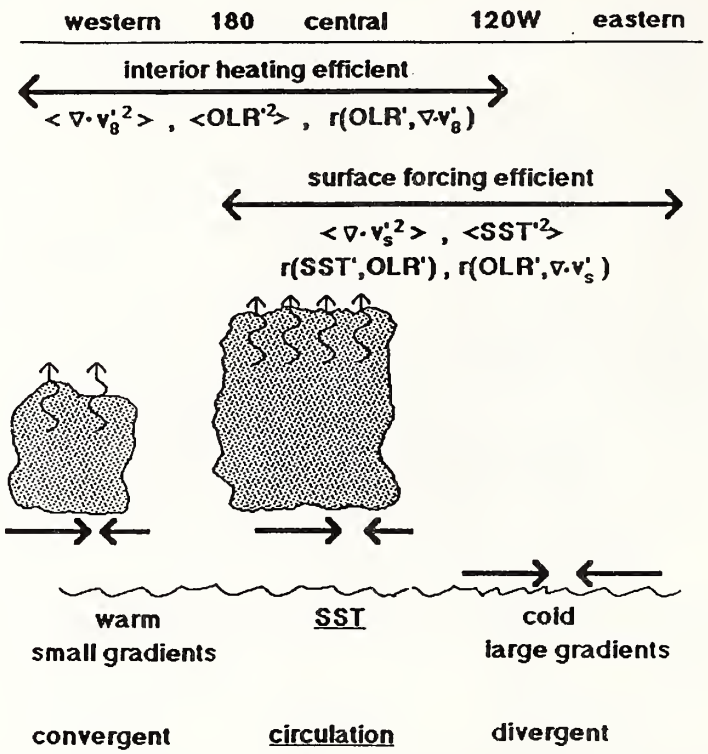

FIGURE 4: Schematic depiction of longitudinal variations of SST-OLR-wind relationships across the near-equatorial Pacific.

Several additional conclusions follow from the results. First, it must be emphasized that the convergence of the surface wind field is significantly different from the convergence at 850 mb, reinforcing the results of a previous comparison of *u* and *v* winds derived from individual station data (Harrison and Gutzler, *MWR*, 1986, pg. 285). Winds from these two levels should therefore not be used interchangeably, particularly for purposes of vertically extrapolating the horizontal wind convergence. Second, our results imply that *neither* of the two forcing mechanisms considered can individually provide a satisfactory parameterization of large-scale ocean-atmosphere coupling. Furthermore it appears that "simple" coupled models must include a boundary layer with vertical structure to simulate correctly the low-level convergence field.

Of course, forcing of atmospheric circulation anomalies by the ocean is but one-half of the coupled ocean-atmosphere forcing problem. Our study does not address the question of *why* the variance of SST anomalies is large in the eastern Pacific and small in the western Pacific, for which consideration of ocean dynamics and atmospheric forcing of the ocean are required.

CLIMATOLOGICAL ASPECTS OF THE TROPICAL ANNUAL CYCLE

Chester F. Ropelewski and Michael S. Halpert
Climate Analysis Center, NMC/NWS/NOAA, Washington, DC 20233
and
Eugene M. Rasmusson
Dept. of Meteorology, U. of Maryland, College Park, MD 20742

INTRODUCTION

Analyses of temporal variability in the global tropics have suggested that the annual cycle plays a central role in virtually all of the recognized principal modes of large scale climate variability. Intraseasonal oscillations appear to be modulated by the annual cycle (Knutson and Weickmann, 1987), El Niño/Southern Oscillation (ENSO) episodes are often phase locked to the annual cycle (Rasmusson and Carpenter, 1983) and recent studies (Ropelewski et al., 1988a, 1988b) have indicated that tropospheric biennial variability also has a tendency to be tied to the annual cycle. The pervasiveness of variability at periods of the annual cycle is evident in the relatively large annual coherence between central Pacific and eastern Pacific sea surface temperature (SST) even with the mean annual cycle removed (Fig. 1), indicating an annual cycle in interannual variability. Previous research, e.g., Horel, 1982, has shown that the annual cycle is a particularly rich and complex phenomenon in the tropical Pacific. Here, we describe the re-examination of the tropical annual cycle, including the Indian and Atlantic Ocean basins, in the context of the interactions among the other principal temporal modes of variability.

ANALYSIS

The tropical annual cycle is described through an analysis of monthly SST and surface wind data derived from the Comprehensive Ocean-Atmosphere Data Set (COADS) of Woodruff et al., 1987. Conventional mean monthly charts (not shown) indicate that poleward of 20^0 latitude in both hemispheres the SST tends to reach a maximum towards the end of the respective summer seasons, while the surface winds tend to reach their maximum strength during the winter. In equatorial regions, however, the annual SST cycle becomes more complex with maxima tending to occur during the northern spring along the eastern boundaries of both the Atlantic and Pacific Ocean basins. The magnitude of the equatorial SST annual cycle tends to diminish westward across both ocean basins and drops to near zero in the central Pacific and remains small through most of the equatorial Indian Ocean.

The tropical surface winds tend to show summer maxima associated with the Asian and Australasian monsoons, while winter maxima prevail at higher latitudes. Transition season wind maxima are evident in near equatorial regions of the eastern Pacific and in the equatorial Atlantic. These features are enhanced if we examine the mean transition-season wind fields by forming monthly mean differences from the annual means (Fig. 2). Of particular interest are the strong suggestion of monsoon-like circulation features in the eastern Pacific and equatorial Atlantic in the absence of the classic ocean-continent thermal contrasts to drive the monsoon. The strong temperature

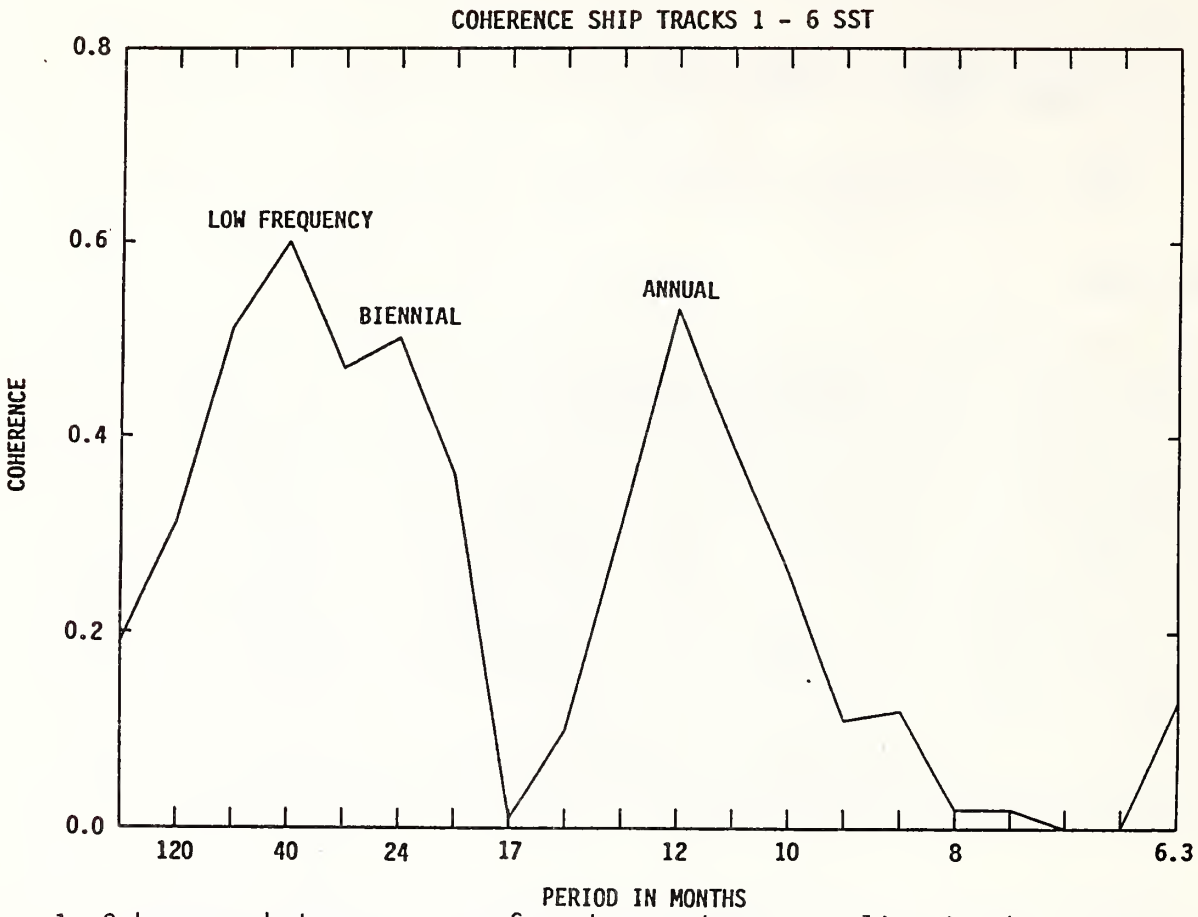

Fig. 1 Coherence between sea surface temperature anomalies in the central Pacific and east Pacific (1949 - 1986 data).

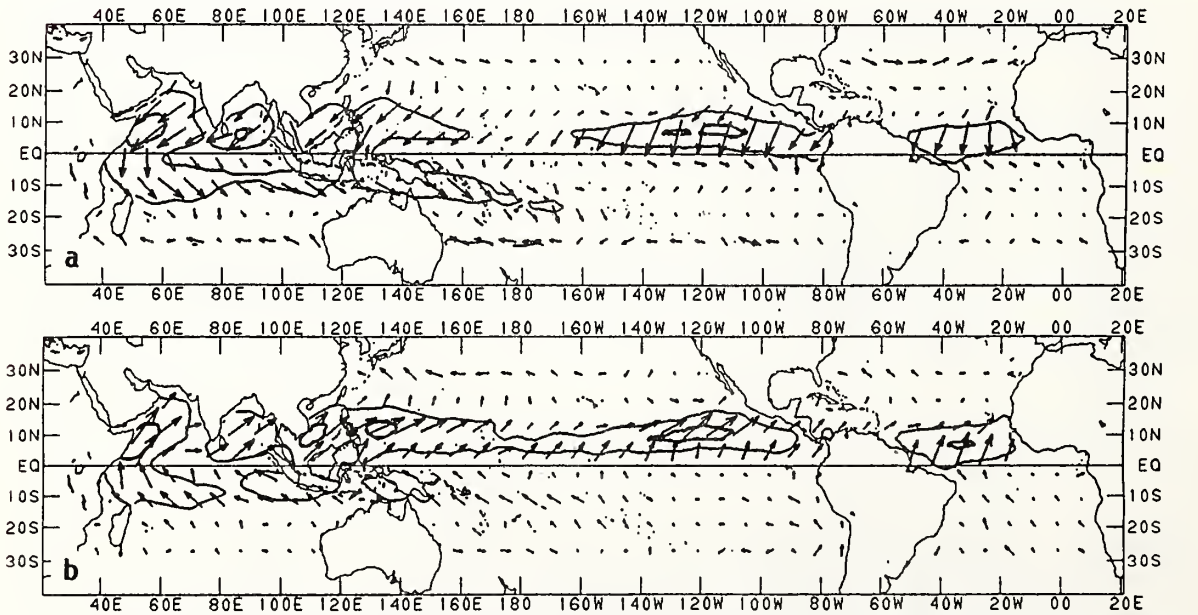

Fig. 2 Mean vector wind expressed as the difference from the annual mean vector wind for a) March, b) September. Based on 1950-1979 COADS data.

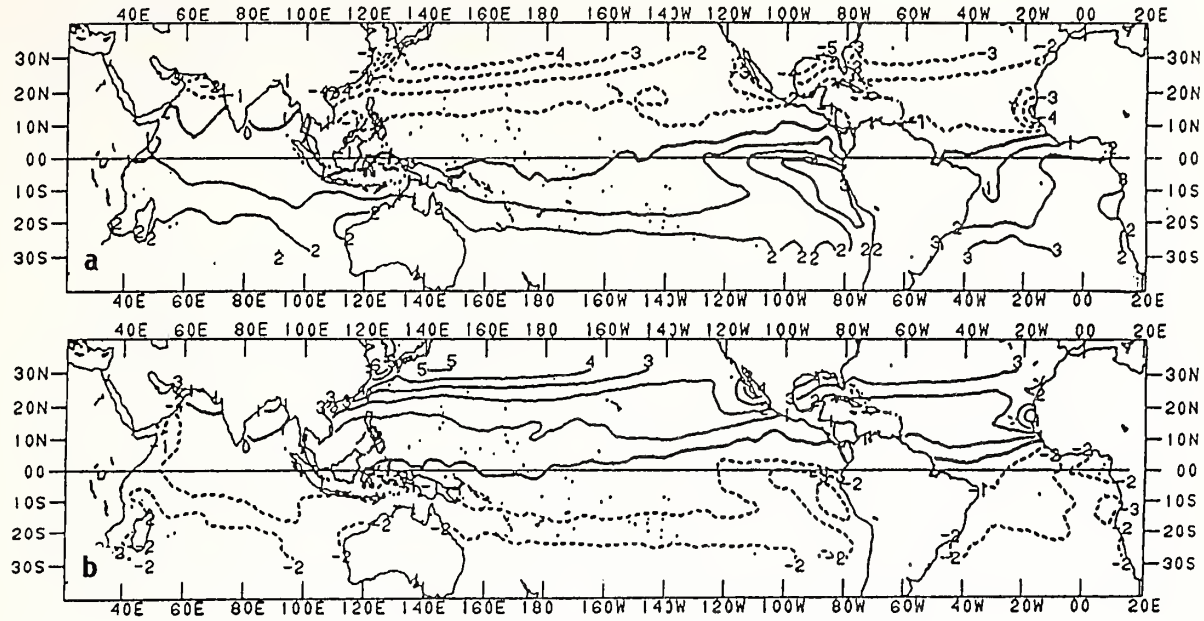

Fig. 3 Same as Fig. 2, except for sea surface temperature.

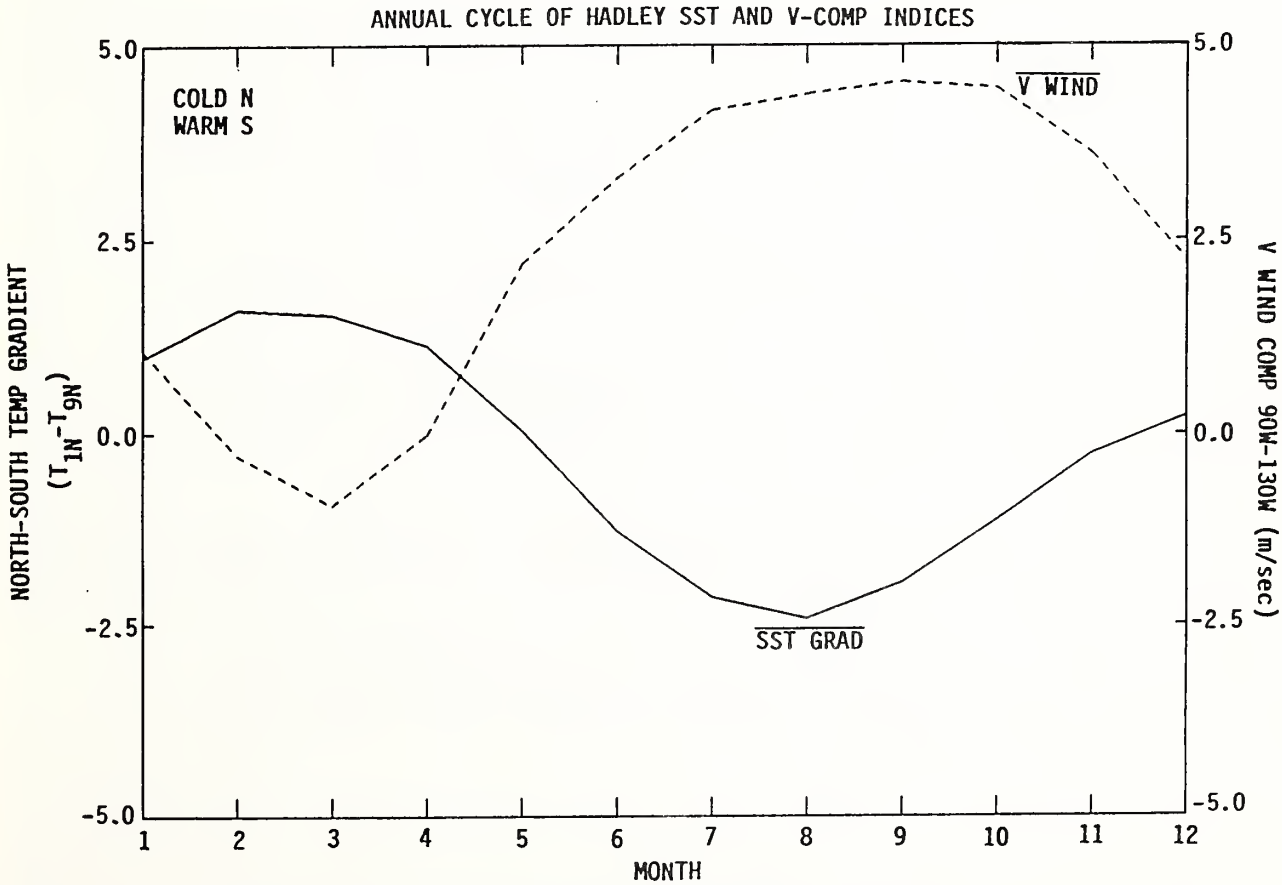

Fig. 4 The mean annual cycle of the eastern Pacific mean temperature gradient (solid) and meridional wind component (dashed).

gradients apparent in the monthly mean SST analysis, also presented as anomalies from the annual mean (Fig. 3), strongly suggest that the monsoon-like character of these oceanic winds may be interpreted in terms of thermally driven circulations. The annual cycle of these oceanic surface winds can also be viewed as modulations of the Hadley circulation.

DISCUSSION

This preliminary look at the annual cycle of the winds and SST in the eastern Pacific and equatorial Atlantic suggest the formation of indices to monitor these monsoon-like circulation patterns. One such pair of indices is the mean temperature gradient between 1^{0}N and 9^{0}N and the mean meridional wind component in the eastern Pacific (Fig. 4). Other temperature gradient-wind index pairs suggested by this analysis are also being studied.

Our previous preliminary investigations of the principal temporal scales in the global tropics have focused on biennial time scale and longer periods. This more recent work emphasizes the importance of the annual cycle itself and sets the stage for a more comprehensive investigation of temporal variability in the tropics.

REFERENCES

Horel J. D., 1982: On the annual cycle of the Tropical Pacific atmosphere and ocean. Mon. Wea. Rev., 110, 1863-1878.

Knutson T. R., and K. M. Weickmann, 1987: 30-60 day atmospheric oscillations: Composite life cycles of convection and circulation anomalies. Mon. Wea. Rev,. 115, 1407-1436.

Rasmusson E. M., and T. H. Carpenter, 1982: Variations in tropical sea surface temperature and surface wind fields associated with the Southern Oscillation. Mon. Wea. Rev., 111, 517-528.

Ropelewski C. F., M. S. Halpert, and E. M. Rasmusson, 1988a: Interannual variability in the tropical belt. Proc. 7th Conf. on Ocean-Atmosphere Interaction, Jan 31 - Feb 5, 1988, Anaheim CA.

_____, _____, and _____, 1988b: Tropospheric biennial variability and its relationship to the Southern Oscillation. Proc. of the 12th Annual Climate Diagnostics Workshop, Oct 12-16, Salt Lake City, UT.

Woodruff S. D., R. J. Slutz, R. L. Jenne, and P. M. Steurer, 1987: A comprehensive ocean-atmosphere data set. Bull. Amer. Meteor. Soc., 68, 1239-1250.

THE RESPONSE OF THE TROPICAL TROPOSPHERE AND LOWER STRATOSPHERE TO VARIATIONS IN PACIFIC SEA-SURFACE TEMPERATURE

G.C. Reid, K.S. Gage, and J.R. McAfee

Aeronomy Laboratory
NOAA/ERL
Boulder, Colorado

The objective of this work was to investigate the thermal response of the tropical atmosphere at all available levels to ENSO-related variations in Pacific SST. The approach differs from earlier studies by using archived radiosonde temperature data rather than geopotential heights, and emphasizing the responses at individual stations instead of looking at averages over large areas, in an attempt to gain some insight into the mechanisms at work.

The basic data used were the monthly values of the ENI index of Pacific SST anomalies (B. C. Weare, *Mon. Wea. Rev.*, **114**, 644-647 [1986]), and radiosonde temperatures measured at four stations in the tropical Pacific basin (Yap [10N, 138E], Wake Island [19N, 167E], Majuro [7N, 171E], and Pago Pago [14S, 171W]), and one in the Caribbean (Curacao [12N, 69W]). The time period covered was 1966-82, and a total of 30 pressure levels were used at each station, ranging from 1000 mb to 15 mb. Monthly mean temperatures were found for each level, and monthly anomalies formed by subtracting the 17-year mean for each calendar month. The resultant time series all showed significant trends, which will be discussed later. For correlation purposes, they were removed by fitting a least-squares straight line and subtracting it from the individual monthly values. A weak positive trend was also removed from the SST time series.

Figure 1 shows a portion of the Fourier-transform power spectra of the SST time series (a), and the temperature anomaly time series from Majuro at the 600-mb level (b), and at the 15-mb level (c). Note the strong similarity between (a) and (b), with the main peak at a period of about 3.5 years, the quasi-period of the ENSO cycle. The influence of the ENSO cycle has disappeared at 15 mb, where the principal peak is at the QBO period of about 27 months.

Figures 2 and 3 are examples of the correlation plots, for Yap and Majuro respectively. The contours show cross-correlation coefficients between the SST time series and the temperature anomaly time series for lags ranging from +30 months to -30 months (SST anomalies lead for positive lag). They show features that are common to all five such plots, the major one being the apparent division of the atmosphere into four distinct regimes. In the main troposphere (850 - 150 mb) the correlation is positive, with a lag of 3 - 4 months, and the same lag is seen in the lower stratosphere (100 - 40 mb), but with reversed sign. Different responses are seen in the surface layer (1000 - 850 mb) and in the upper troposphere (150 - 100 mb), which again show similar lag characteristics to each other, again with reversed signs for the correlation. At Yap the surface layer has negative correlation and the upper troposphere positive correlation, both with near zero lag, while at Majuro the surface layer has positive correlation and the upper troposphere negative correlation, both with a negative lag of 3 months.

These responses are consistent with a picture in which increases in SST lead to intensified tropical convection and an enhancement in the gentle subsidence of the tropical troposphere outside the regions of active convection, with a corresponding gentle upwelling in the lower stratosphere. The lag may be explained as an "inertial" time needed to develop these motions on a planetary scale. The surface layer and the upper tropospheric layer, on the other hand, are more directly involved in the enhanced convection, since they form respectively the convergent inflow and divergent outflow regions. For this reason, the fact that they show responses that are similar to each other but different from the responses of the other regions, is perhaps not surprising. This aspect of the work will be pursued further using both tropical and extratropical radiosonde data.

Figure 4 shows the slopes of the linear trends in atmospheric temperature anomalies over the 1966-82 time period. Broad similarities among the individual stations are apparent, but the trends do not unequivocally show the characteristics that have been predicted for "greenhouse" warming of the atmosphere. In fact, the altitude profiles have some resemblance to those of the correlation plots, suggesting that the trends may be the dynamical result of an overall warming of the Pacific Ocean rather than a radiative effect due to composition changes within the atmosphere itself.

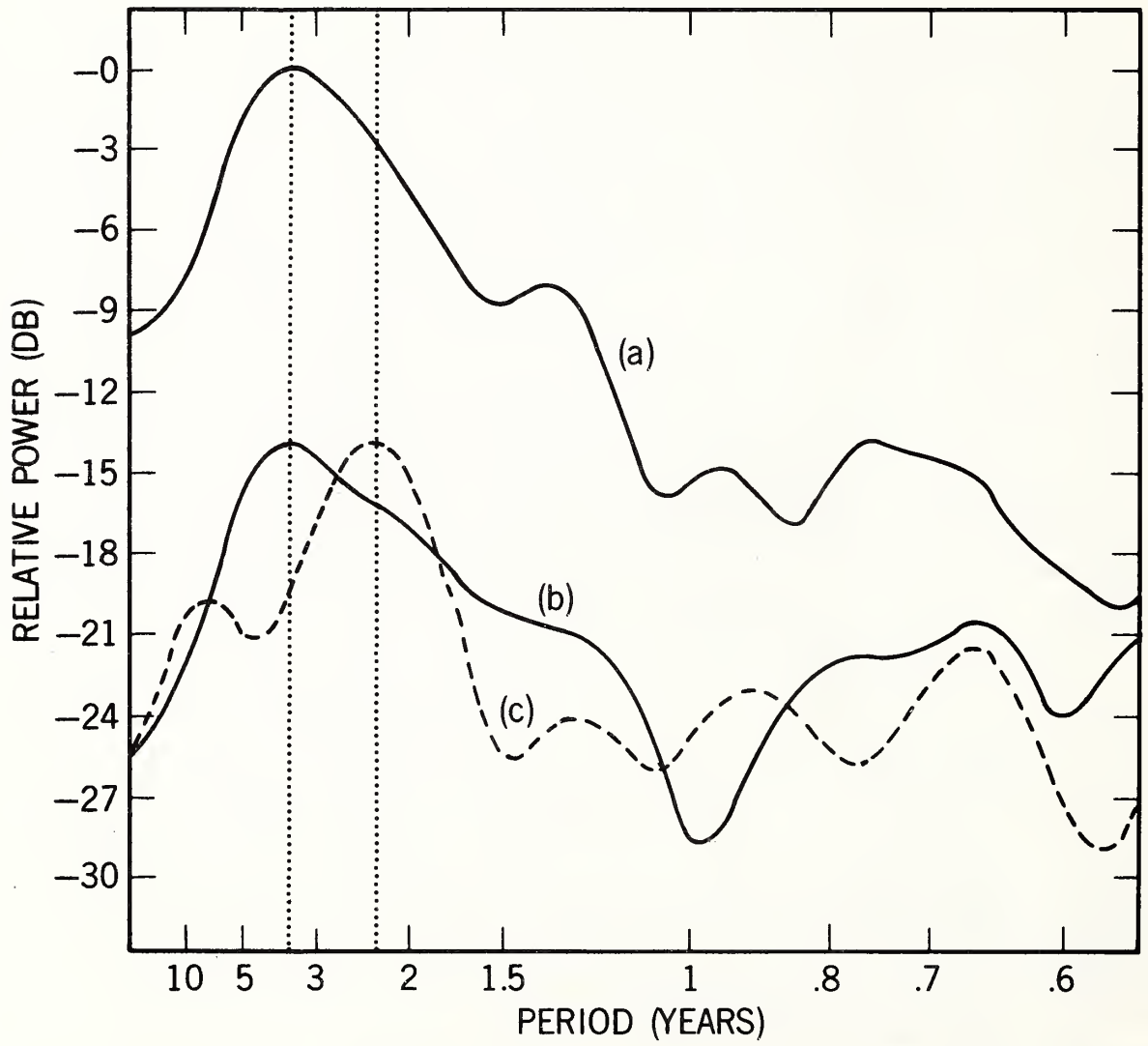

Fig. 1. Fourier-transform power spectra. (a) SST time series, (b) 600 mb temperature anomaly time series at Majuro, (c) 15 mb temperature anomaly time series at Majuro.

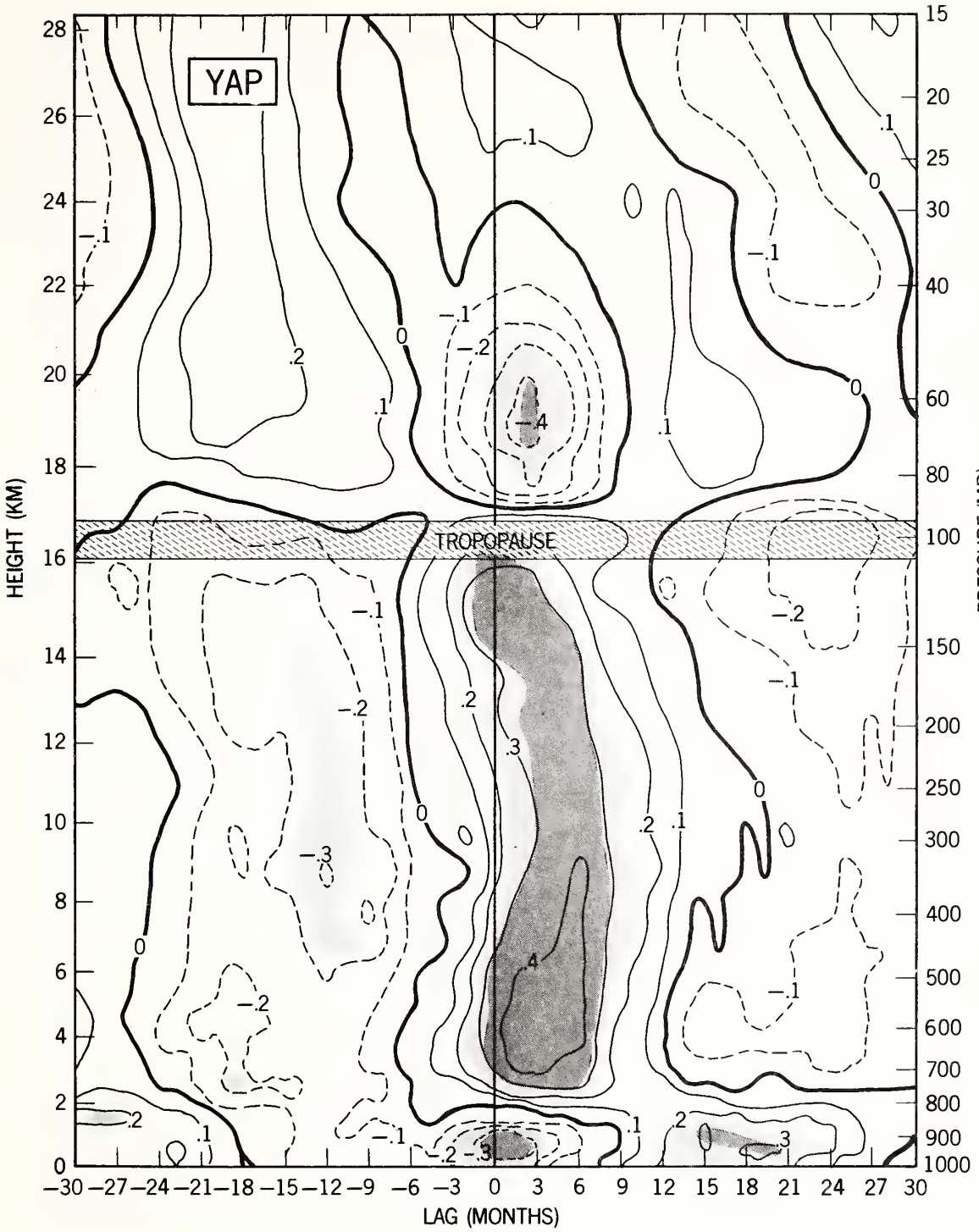

Fig. 2. Cross correlation between SST and temperature anomalies at Yap. Shading indicates correlation significant at greater than the 99% confidence level.

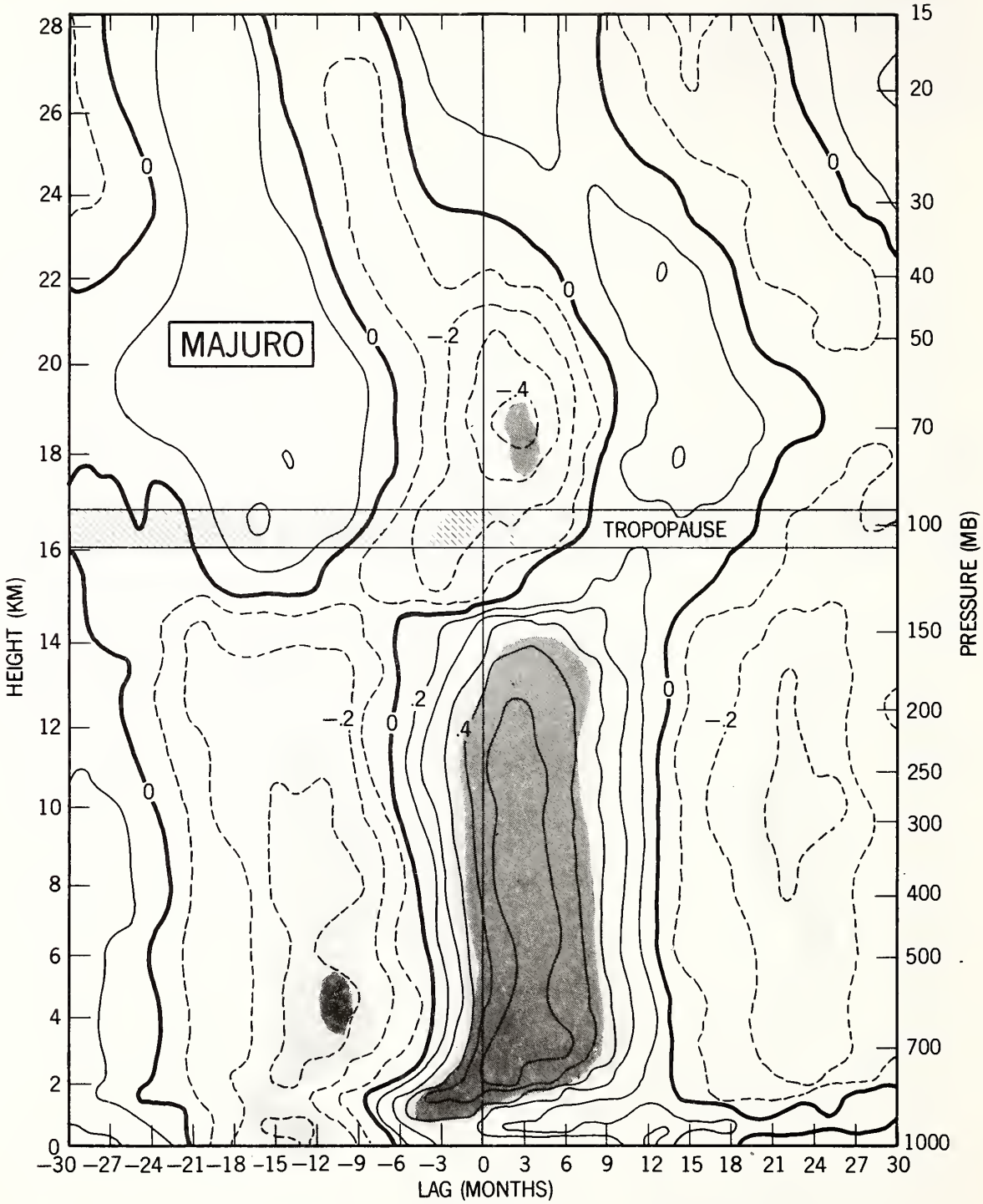

Fig. 3. Cross correlation between SST and temperature anomalies at Majuro. Shading indicates correlation significant at greater than the 99% confidence level.

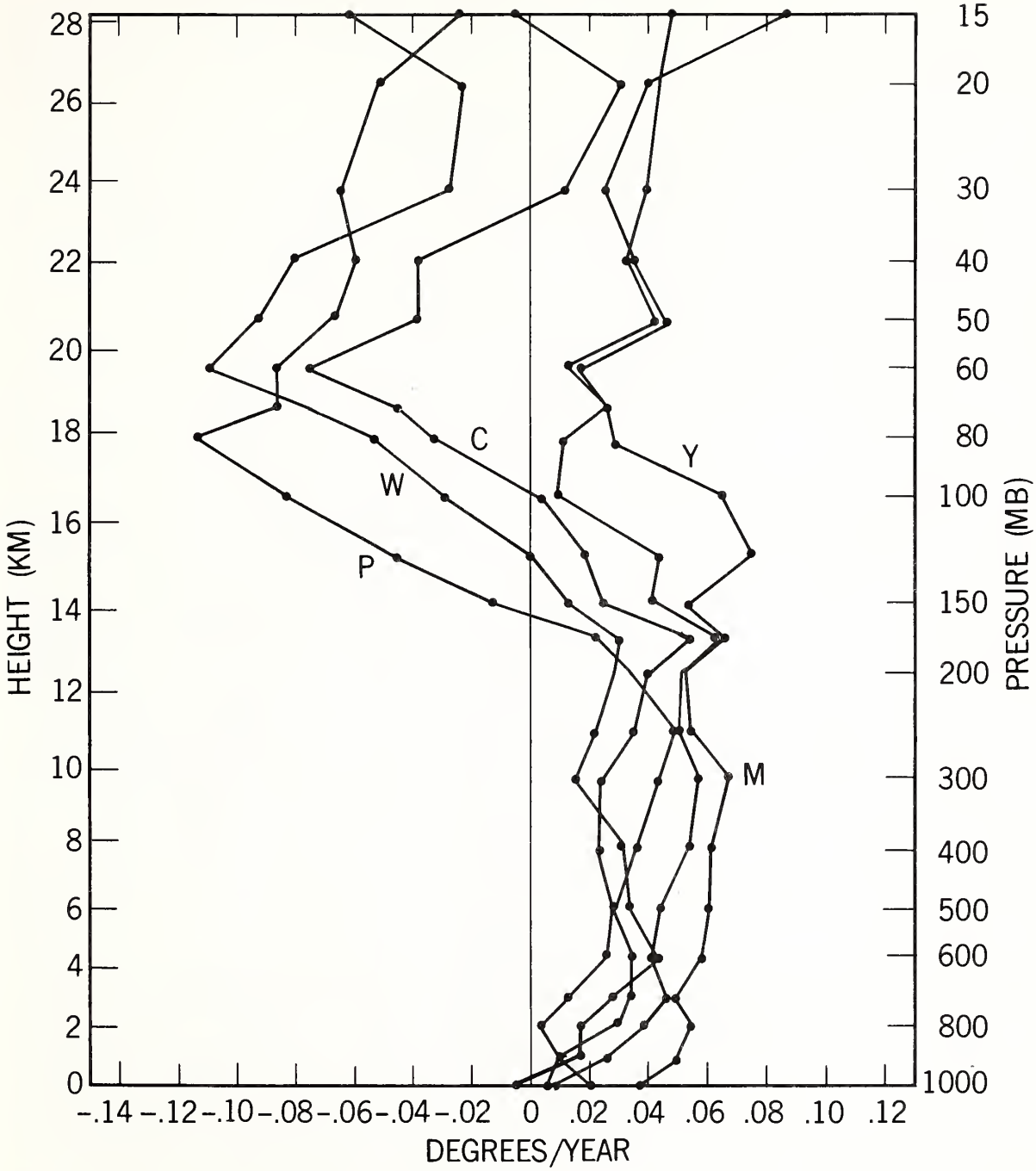

Fig. 4. Slope of linear temperature trends during 1966-82 at Yap (Y), Majuro (M), Pago Pago (P), Wake Island (W), and Curacao (C).

A COMPOSITE STUDY OF INTRASEASONAL OSCILLATIONS IN ATMOSPHERIC ANGULAR MOMENTUM AND OUTGOING LONGWAVE RADIATION DURING NORTHERN HEMISPHERE WINTER

Siri Jodha S. Khalsa
Cooperative Institute for Research
in Environmental Sciences
University of Colorado
Boulder, CO 80309-0449

and

Klaus M. Weickmann
Climate Research Division
NOAA/ERL, R/E/AR6
325 Broadway
Boulder, CO 80303

I. INTRODUCTION

We investigate the relationship between intraseasonal oscillations of outgoing longwave radiation (OLR) in the tropics and oscillations in the zonally symmetric component of the atmospheric circulation as manifest in the total atmospheric angular momentum (AAM). The NMC 850 mb winds and sea level pressure are used to infer fluctuations in tropical frictional torques and mountain pressure torques. Our work is motivated in part by modeling studies that suggest a linkage between the zonally symmetric oscillation, viewed as oscillations in the Hadley circulation, and the tropical 30-60 oscillation, viewed primarily as an eastward propagating wavenumber 1 phenomenon.

II. METHODOLOGY

Composites are formed based on a time series of northern hemispheric AAM during the November to March season for the years 79-80, 81-82, 84-85, and 85-86. Pentads corresponding to four phases, maximum, descending, minimum, and ascending, were identified in each season making 7 to 10 pentads in each phase. Before compositing, pentad anomalies relative to the seasonal cycle were formed by subtracting the ensemble mean pentad from the individual pentads. Because the years chosen reflect anti-ENSO conditions, the fields for each phase also had the mean over all 4 phases removed to show variations from the interannual base state. We will discuss our results by phase of the AAM cycle.

III. RESULTS

At the minimum phase of Northern Hemisphere (NH) AAM (Fig. 1a), a chain of

upper level anticyclones extends from Saudi Arabia northeast to the central Pacific with a separate anticyclone over the mid-latitude Atlantic Ocean. The easterly anomalies to the south of these anticyclones contribute to the low AAM during this phase. In the tropics, widespread negative OLR anomalies occur over the western Pacific and Indonesian signifying a maximum in tropical convection over the oceanic warm pool. Zonally symmetric 850 mb easterlies cover the northern subtropics (Fig. 2b) and have a regional focus as enhanced trades over the subtropical North Pacific (not shown). The stronger trades flow toward the enhanced convection over the western Pacific and represent an anomalous frictional torque that transfers angular momentum from the earth to the atmosphere. Fig. 3b) and c) show that the zonally symmetric 200-300mb temperature is warm and low level moisture is low, both of which contribute to higher zonally symmetric static stability. (The numbers, however, are small.) This result suggests conditions for tropical convection are becoming less favorable on the largest spatial scales.

In the ascending phase of NH AAM (Fig. 1b), the anticyclonic structures over Asia and the North Pacific have broken into individual vortices and zonally symmetric westerlies appear over the equator (Fig. 2a and arrows on Fig. 1b). A northwest-southeast low/high couplet has developed over Asia and is linked to sea level pressure (SLP) fluctuations around the periphery of the Tibetan Plateau which could give rise to pressure torques. The pressure anomalies, however, are not very large over the sloping terrain. Tropical convection has shifted east to the southern Philippines and to the region of the SPCZ (Fig. 1b). At 850 mb, westerly wind anomalies extend to the dateline while easterly anomalies are confined to the eastern Pacific (not shown). As a result, the zonally averaged 850 mb wind (and implied frictional torque) is near zero (Fig. 2b).

During the maximum phase of NH AAM (Fig. 1c), the circulation anomalies observed during minimum AAM (Fig. 1a) have reversed as a chain of upper level cyclones stretches from Saudi Arabia to the central North Pacific. The resulting westerlies in the northern subtropics contribute to the high AAM and may partially reflect a northward shift of the 250 mb westerly anomalies from the previous phase (Anderson and Rosen, 1983). Widespread positive OLR anomalies occur over the Indonesian region and signify a period of suppressed convection over the oceanic warm pool. Convection is now enhanced over South America and Africa suggesting either continued eastward propagation of OLR or excitation of a standing east-west oscillation between the oceanic warm pool and the equatorial continents. At low levels, planetary scale zonal outflow from the Indonesian region of suppressed convection gives rise to westerly anomalies over the Pacific and Atlantic Oceans and easterly anomalies over the Indian Ocean (not shown). The resulting zonally averaged westerly anomalies (Fig. 2b) suggest an anomalous transfer of angular momentum from the atmosphere to the earth through frictional torques.

During the descending phase of NH AAM, an easterly anomaly in the zonally symmetric 250 mb flow (Fig. 1d and 2a) appears over the equator and leads the pending decrease of NH AAM. The upper troposphere is cool relative to the northern subtropics (Fig. 3b) suggesting the zonally averaged easterly anomalies have broader meridional extent at higher levels. The zonally oriented circulation centers that were present during maximum AAM have become vortices and a high-low circulation couplet has organized over Asia. The suppressed convection over the oceanic warm pool has shifted east and

convection is increasing over the Indian Ocean. The next regime of minimum NH AAM and enhanced tropical convection tends to occur in about 13 days +/- 6 days.

IV. DISCUSSION

Our results indicate that the frictional torques associated with tropical convection tend to be in phase with the NH AAM variations during the composite AAM cycle. For example, large easterly anomalies occur at 850 mb during the minimum phase of NH AAM and are approximately zero during the increasing phase. Madden (1987), on the other hand, obtains good agreement between the cycle of global AAM calculated from tropical frictional torques and the observed cycle of AAM during an annual mean 30-60 day oscillation. Some reasons for the apparent discrepancy between our inferred frictional torques and the AAM changes include: 1) the presence of other compensating torques (e.g., pressure torque), 2) a net cross-equatorial transport of momentum between hemispheres or 3) smaller time lags between the torques and the momentum changes than can be resolved by a four category composite analysis. We have computed sea level pressure anomalies for each of our phases and compared the results with the earth's orography. Our subjective conclusion is that pressure torques are of secondary importance in the AAM cycle. Finally, a consistent feature in our results that requires further investigation is the zonally averaged easterly (westerly) wind anomaly that appears over the equator during the descending (ascending) phase of AAM.

V. SUMMARY

Intraseasonal oscillations in NH AAM during four northern winters with cool eastern Pacific SSTs include both convective fluctuations over Indonesia and well-defined 250 mb circulation patterns especially over subtropical Asia and the North Pacific. Differences in vertical structure between high and low latitudes result in surface patterns distinct from the upper level patterns. As a result, meridionally extensive zonal wind anomalies are observed at 850 mb over the Pacific Ocean. The relative importance of friction versus pressure torques in the AAM oscillations is not resolved in our composite results and an angular momentum budget study may be required. Preliminary indications from NMC SLP indicate that the anomalies in vicinity of the orography are relatively small. In the tropics, the AAM cycle includes an eastward propagating component in OLR as well as a wavenumber 1 standing oscillation between the western Pacific and the South America-Africa region.

VI. REFERENCES

Anderson, J. R., and R. D. Rosen, 1983: The latitude-height structure of 40-50 day variations in atmospheric angular momentum. J. Atmos. Sci., 40, 1584-1591.

Madden, R. A., 1987: Relationships between changes in the length of day and the 40- to 50- day oscillation in the tropics. J. Geophys. Res., 92, 8391-8399.

VII. FIGURE CAPTIONS

Figure 1. a) 250 mb wind anomalies and OLR anomalies exceeding 10 W/m^2 for the four phases of northern hemisphere angular momentum. Each phase is a composite of pentad anomalies from the 1979-80, 1981-82, 1984-85, and 1985-86 northern hemisphere winter seasons. The mean over all four phases has been removed.

Figure 2. a) zonally averaged 250 mb zonal wind anomalies for the four phases as described in Fig. 1, b) same for 850 mb zonal winds.

Figure 3. a) Zonally averaged outgoing longwave anomaly, b) Zonally averaged 200 - 300 mb temperature anomaly from TOVS, c) Zonally averaged precipitable water anomaly in the 1000-700mb layer. All data derived from composite means as described in Fig. 1.

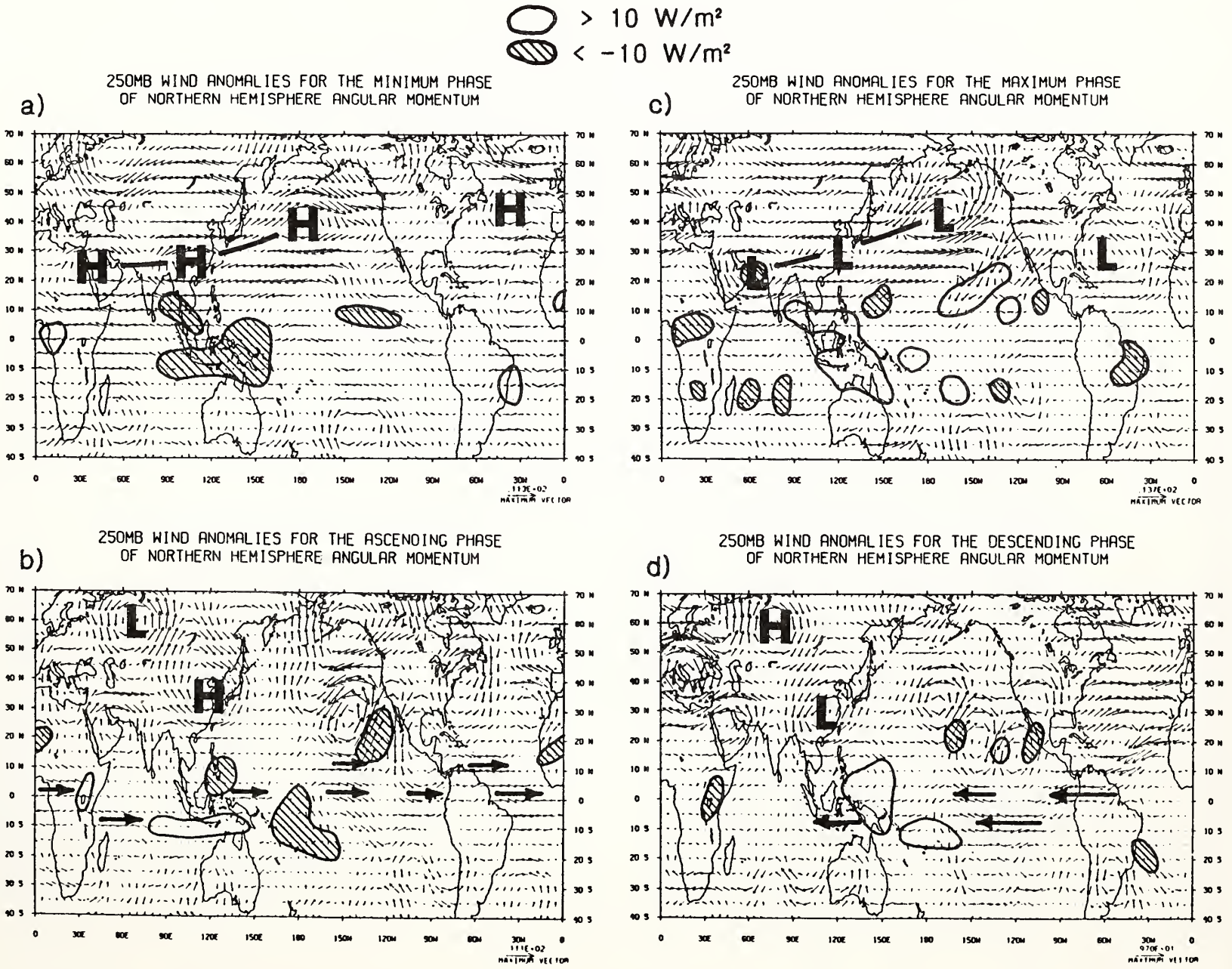
> 10 W/m²
< -10 W/m²
a)
250MB WIND ANOMALIES FOR THE MINIMUM PHASE
OF NORTHERN HEMISPHERE ANGULAR MOMENTUM
H
H
H
H
c)
250MB WIND ANOMALIES FOR THE MAXIMUM PHASE
OF NORTHERN HEMISPHERE ANGULAR MOMENTUM
L
L
L
L
b)
250MB WIND ANOMALIES FOR THE ASCENDING PHASE
OF NORTHERN HEMISPHERE ANGULAR MOMENTUM
L
H
d)
250MB WIND ANOMALIES FOR THE DESCENDING PHASE
OF NORTHERN HEMISPHERE ANGULAR MOMENTUM
H
L

Figure 1.

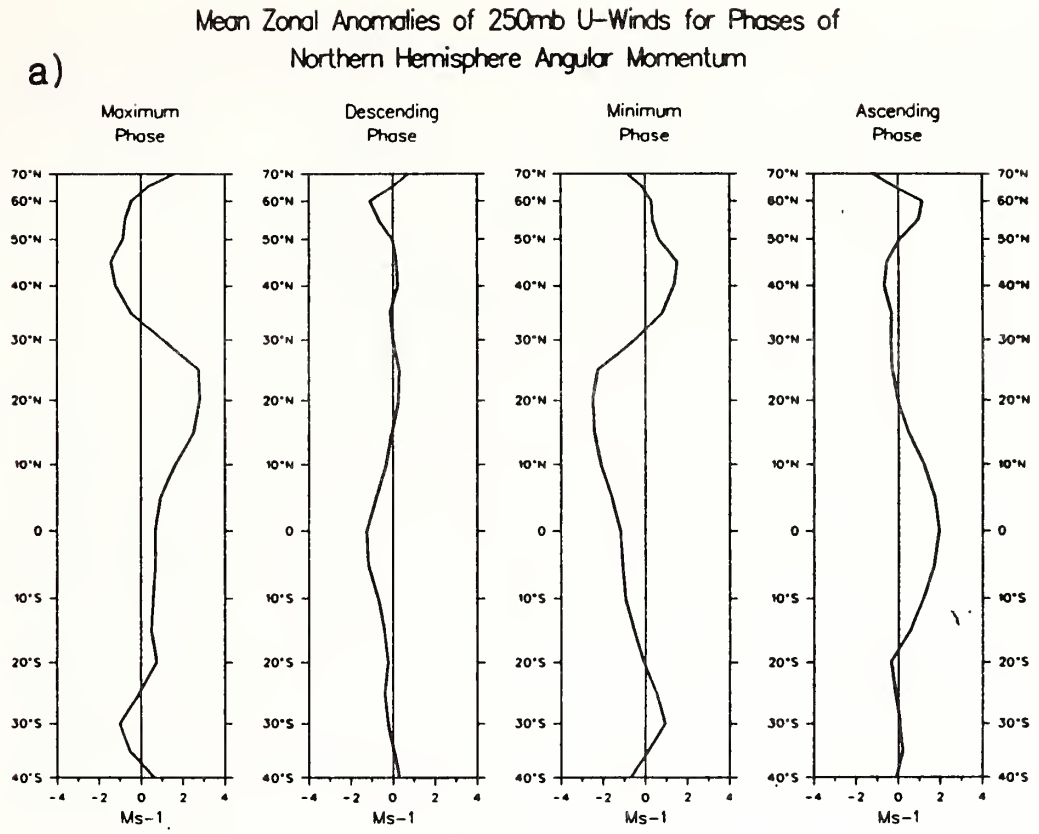
a)
Mean Zonal Anomalies of 250mb U-Winds for Phases of
Northern Hemisphere Angular Momentum
Maximum Phase
Descending Phase
Minimum Phase
Ascending Phase
70°N
60°N
50°N
40°N
30°N
20°N
10°N
0
10°S
20°S
30°S
40°S
-4 -2 0 2 4
Ms-1

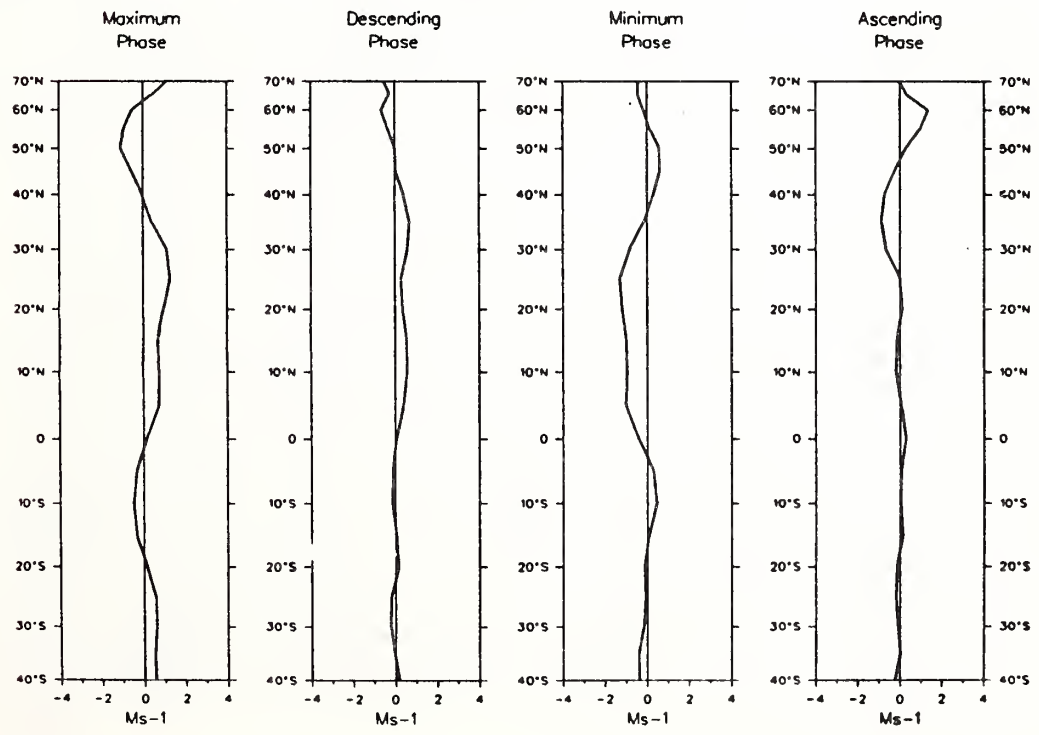
b)
Mean Zonal Anomalies of 850mb U-Winds for Phases of
Northern Hemisphere Angular Momentum
Maximum Phase
Descending Phase
Minimum Phase
Ascending Phase
70°N
60°N
50°N
40°N
30°N
20°N
10°N
0
10°S
20°S
30°S
40°S
-4 -2 0 2 4
Ms-1

Figure 2.

a) OLR

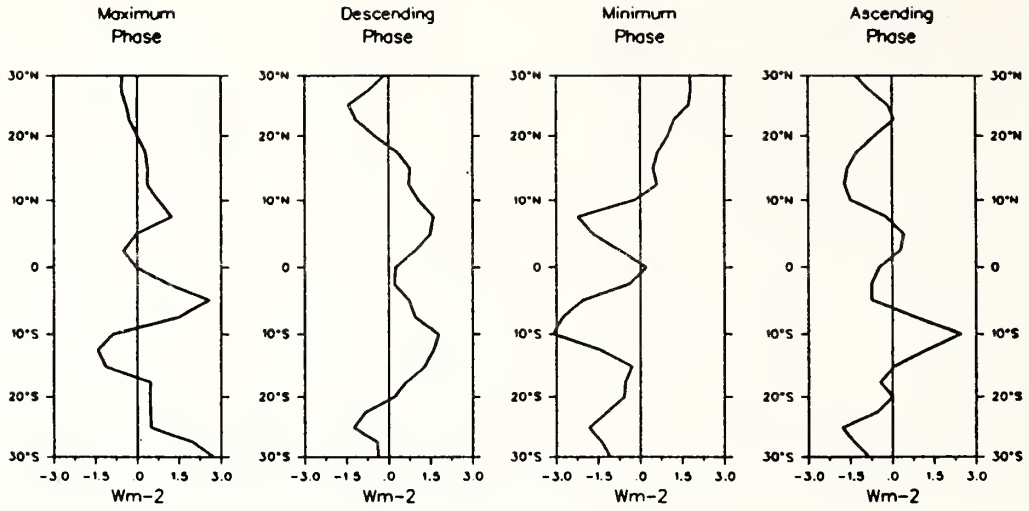

b) $T_{200-300\ mb}$(°C)

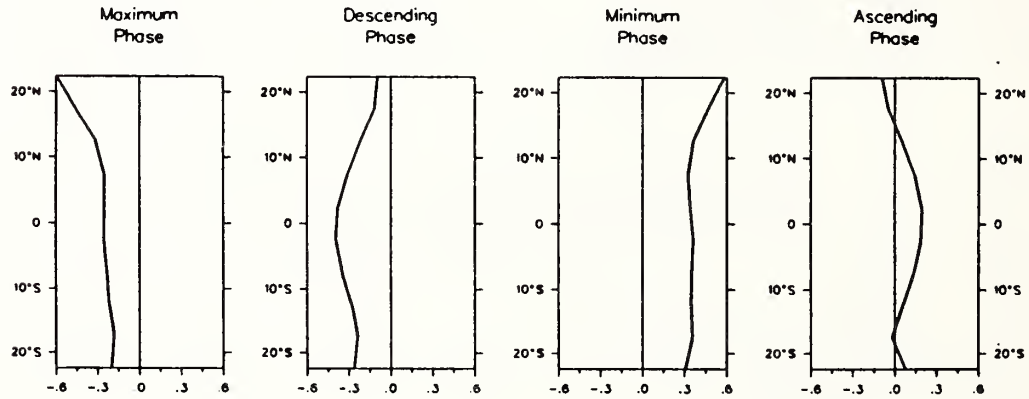

c) $PW_{1000-700mb}$

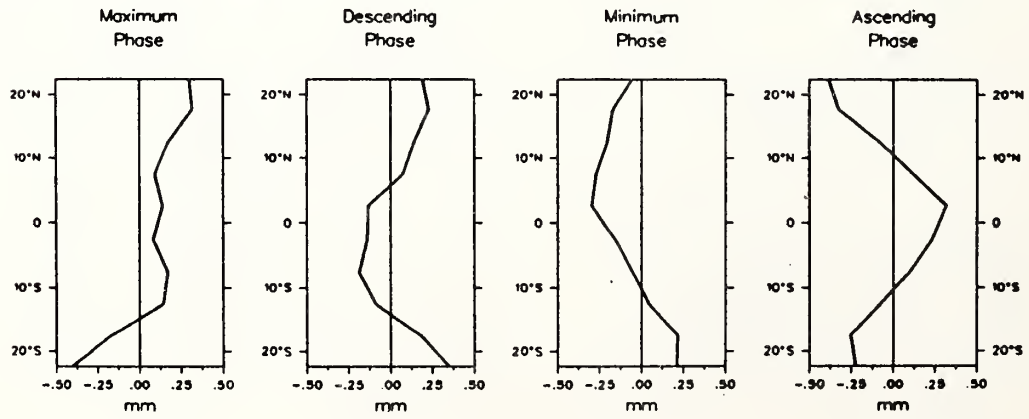

Figure 3.

RELATIONSHIPS AMONG OBSERVED SEA LEVEL PRESSURE, SEA SURFACE TEMPERATURE AND SURFACE WIND OVER THE TROPICAL PACIFIC DURING WARM AND COLD YEARS

Clara Deser and John M. Wallace
Department of Atmospheric Sciences, AK-40
University of Washington
Seattle, WA 98195

In this brief report, we document the relationships among sea level pressure, sea surface temperature (SST) and surface wind variations over the tropical Pacific Ocean associated with the El Niño/Southern Oscillation phenomenon using ship observations from the Comprehensive Ocean-Atmosphere Data Set for the period 1946-85. Our results are based on averages for the July-November season when relations among the variables are strongest.

Fig. 1 shows the changes in July-November sea level pressure associated with warm events. This field was constructed by regressing July-November average pressure in each 2° square upon an SST index (defined as July-November SST averaged from 6°N-6°S, 180°-80°W). Regressions are based on the period 1946-85. The regression coefficients (shown in Fig. 1) are expressed in mb per °C of the SST index. The SST index averaged 1.4°C above normal for the 5 warmest years and 0.8°C below normal for the 5 coldest years during the period 1946-85. Thus, multiplying the regression coefficients shown in Fig. 1 by 1.4 (–0.8) gives typical magnitudes for the pressure variations associated with strong warm events (cold events).

The dominant pattern in Fig. 1 is the Southern Oscillation, defined by a center of negative pressure anomalies in the Southeast Pacific and a region of positive pressure anomalies over Australia and Indonesia. The new feature that emerges from this analysis is the narrow band of negative pressure anomalies along the equator in the eastern Pacific. This equatorial pressure signal is separated from the subtropical pressure changes by an area of relatively weak anomalies. The largest absolute changes in pressure along the equator occur in the east.

Fig. 2 shows the sea level pressure variations in relation to the July-November SST changes. The SST field is based on linear regressions between SST in each 2° square and the SST index. It can be seen that the equatorial band of negative pressure anomalies in the eastern Pacific roughly coincides with the region of large positive SST anomalies. The correlation coefficient between July-November pressure and SST averaged over the region of large anomalies (6°N-6°S, 130°W-84°W) is –0.90 based on the period 1946-85. The corresponding regression coefficient indicates that on average a 1°C increase in SST is accompanied by a 0.65 mb fall in pressure in this region. Following the ideas of Lindzen and Nigam (*JAS*, 1987), we propose that the strong coupling observed between pressure and SST in this region is a result of changes in temperature (and hence density) of the air in the planetary boundary layer induced by SST variations. In particular, if a SST anomaly of

1°C were uniformly mixed through a boundary layer 1.5 km deep, then by the hydrostatic relation surface pressure would fall by 0.7 mb. The magnitude of the pressure change predicted by this simple model is in good agreement with the observed regression coefficient. Rawinsonde data (50 mb vertical resolution) for Guayaquil (3°S) on the Peru coast indicate that temperature changes during July-November 1957 (a warm year) relative to July-November 1960 (a cold year) are confined to the lowest 150 mb (not shown). We cannot verify this result for other warm years as the Guayaquil record is limited to the period 1957-60.

Cold SSTs and strong low-level divergence help to maintain a highly stable planetary boundary layer over the eastern equatorial Pacific during July-November. This strong boundary layer stability serves to prevent the SST anomalies from reaching the free atmosphere above. It may be noted that the eastern equatorial Pacific (east of 130°W) during July-November remains free of deep convection even during warm years. Thus, the pressure anomalies in the eastern equatorial Pacific during July-November are not locally forced by deep convection.

Finally, it is worth noting from Fig. 2 that the pressure variations over the equatorial Pacific are not a simple linear function of the SST changes. In particular, in the eastern equatorial Pacific the meridional scale is larger for pressure than for SST. In addition, the relationship between interannual variations in sea level pressure and SST is weak over the western equatorial Pacific (not shown).

Fig. 3 shows the sea level pressure variations in relation to the July-November surface wind changes. The wind field is based on linear regressions between the zonal and meridional wind components in each 2° square and the SST index. Winds are plotted only where the magnitude of the correlation coefficient for either component exceeds 0.3. Simple dynamical balances between the large-scale wind and pressure fields are seen in Fig. 3: along the equator, westerly wind anomalies flow down the anomalous pressure gradient; northerly wind anomalies near 6°N and southerly wind anomalies near 2°S in the eastern Pacific are directed towards anomalously low pressure. However, the detailed structure of the wind field near the equator cannot be inferred from a simple balance between frictional and pressure gradient forces. As an example, we note that in the eastern equatorial Pacific southerly anomalies occur where the anomalous meridional pressure gradient is zero. It can also be seen that the zonal wind anomalies in the western equatorial Pacific are twice as large as the northerly wind anomalies in the eastern Pacific, yet the anomalous pressure gradients are larger in the east than in the west. It appears that realistic boundary layer physics are needed to account for the observed relationships between surface wind and pressure in the equatorial Pacific.

Another way of looking at the variability associated with the El Niño/Southern Oscillation phenomenon is in terms of the total (as opposed to anomalous) fields for warm and cold years. We reconstructed the actual conditions for a warm (cold) July-November by adding the regressions times 1.4 (–0.8) to climatology. Fig. 4a shows the July-November conditions for a cold year: the top panel contains pressure and surface wind and the bottom panel shows SST and surface wind. As can be seen from Fig. 4a, the strong Southeast Pacific Subtropical High extends westward into the central South Pacific and northward across the equator. Along the equator, pressure decreases westward by nearly 5 mb between 120°W and 160°E. This strong zonal pressure gradient drives surface

easterly winds across the central equatorial Pacific to beyond 160°E. Southerly winds dominate the eastern equatorial Pacific. The Southeast Trades extend northward to around 9°N where they converge with the Northeast Trades. The flow is strongly divergent along the equator east of 170°E. The far western Pacific is a region of surface convergence.

The SST field exhibits a well developed equatorial "cold tongue" that extends from the coast of South America to 160°E. This feature is associated with easterly wind stress along the equator. A sharp temperature gradient between the equator and 5°N is found in the far eastern Pacific. This baroclinic zone is reflected in the sea level pressure field as a tightening of the pressure gradient near 4°N. Wind speeds in the eastern Pacific reach a minimum over the cold tongue and attain maximum strength at the northern edge of the baroclinic zone. The warmest water (>29°C) is found in the far western Pacific, north of New Guinea. The Inter-Tropical Convergence zone (ITCZ) coincides with the band of warm water near 10°N. The South Pacific Convergence Zone (SPCZ) lies just south of the axis of warmest water.

Fig. 4b shows the July-November conditions for a warm year: the top panel contains pressure and surface wind and the bottom panel shows SST and surface wind. Compared to the cold July-November conditions, the following changes are noted:

The Southeast Pacific Subtropical High has weakened by several mb. Its western and northern margins have receded eastward and southward, respectively. Pressures over Australia and Indonesia have increased. A trough has developed in the central South Pacific, in agreement with the strengthened southerly flow. The east-west pressure difference along the equator is much weaker. The lowest pressure in the equatorial zone is found near the dateline. Consistent with this pressure pattern, the equatorial easterlies have weakened and extend only as far as the dateline; weak westerlies are found west of the dateline, centered at 3°N. Southerly flow has developed between New Guinea and Borneo, in agreement with the enhanced meridional pressure gradient. The flow east of New Guinea also exhibits a stronger southerly component. In the eastern Pacific, the southerly flow just north of the equator has weakened, consistent with the reduced meridional pressure gradient. The southerlies just south of the equator in the eastern Pacific have strengthened slightly. The divergence along the equator has weakened; convergence is found west of 160°W. However, the equatorial Pacific east of 160°W remains an area of divergence. The ITCZ has shifted southward by about 2° and has broadened in meridional extent; however, the ITCZ remains north of the equator.

The warmest water (>29°C) has shifted eastward and is now centered near the dateline. The surface waters in the eastern equatorial Pacific and along the coasts of Ecuador and Peru have warmed by several degrees. The east-west temperature gradient has weakened. Both the warmest water and lowest pressure are found in the central equatorial Pacific. The equatorial cold tongue has weakened and extends only as far as 150°W. The cold tongue remains an area of divergence. The meridional temperature gradient between 5°N and the equator in the far eastern Pacific is substantially reduced. The ITCZ is still found over the band of warmest water, now located near 7°N in the central Pacific. SSTs have cooled slightly east of New Guinea in the area of enhanced southerlies.

We are currently completing a more comprehensive set of reconstructed fields (including convergence, cloudiness, relative humidity and air-sea temperature difference) for several seasons.

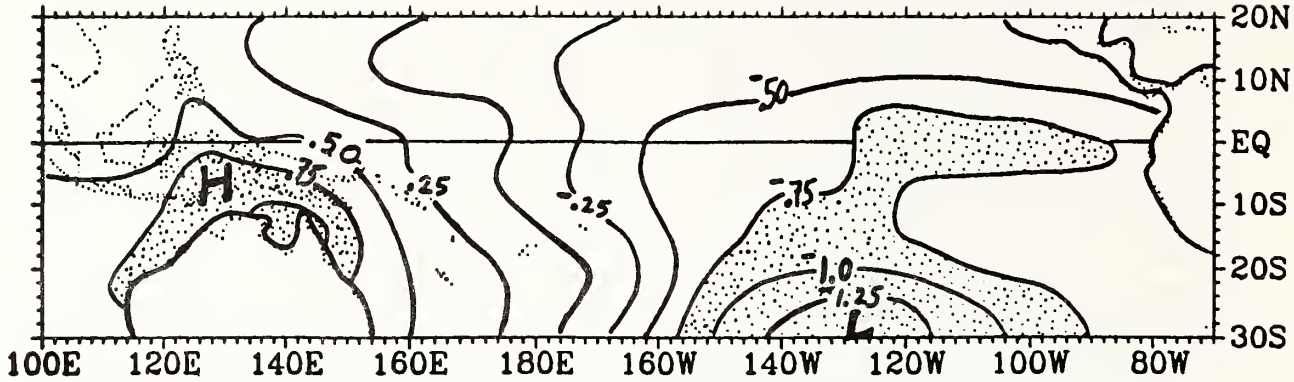

Fig. 1 Sea level pressure anomalies (mb) during July-November associated with warm events. See text for definition of warm events.

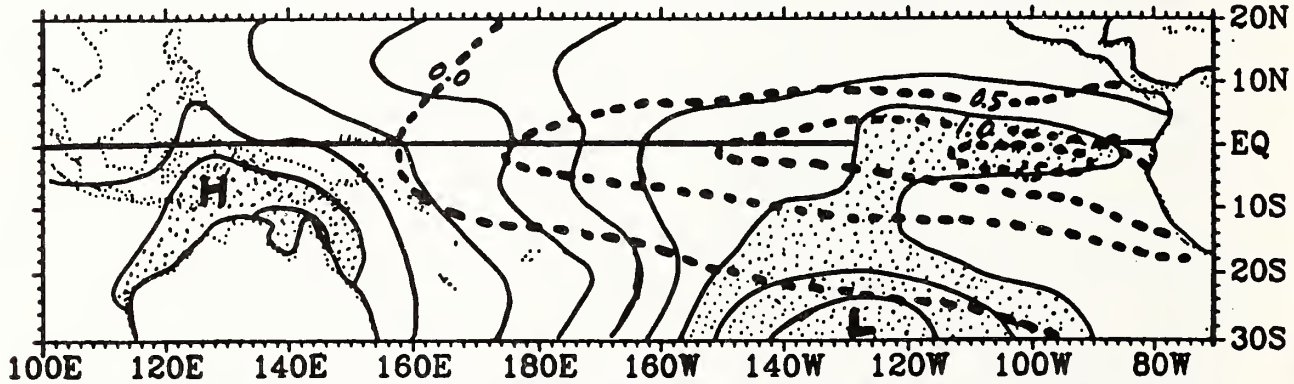

Fig. 2 Sea level pressure (mb; solid lines) and sea surface temperature (°C; dashed lines) anomalies during July-November associated with warm events.

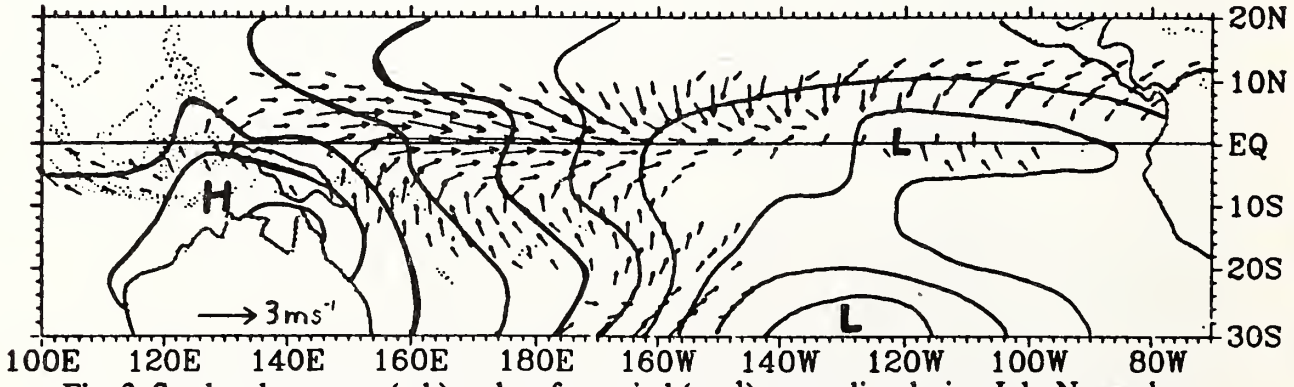

Fig. 3 Sea level pressure (mb) and surface wind (ms^{-1}) anomalies during July-November associated with warm events. See text for plotting convention for winds.

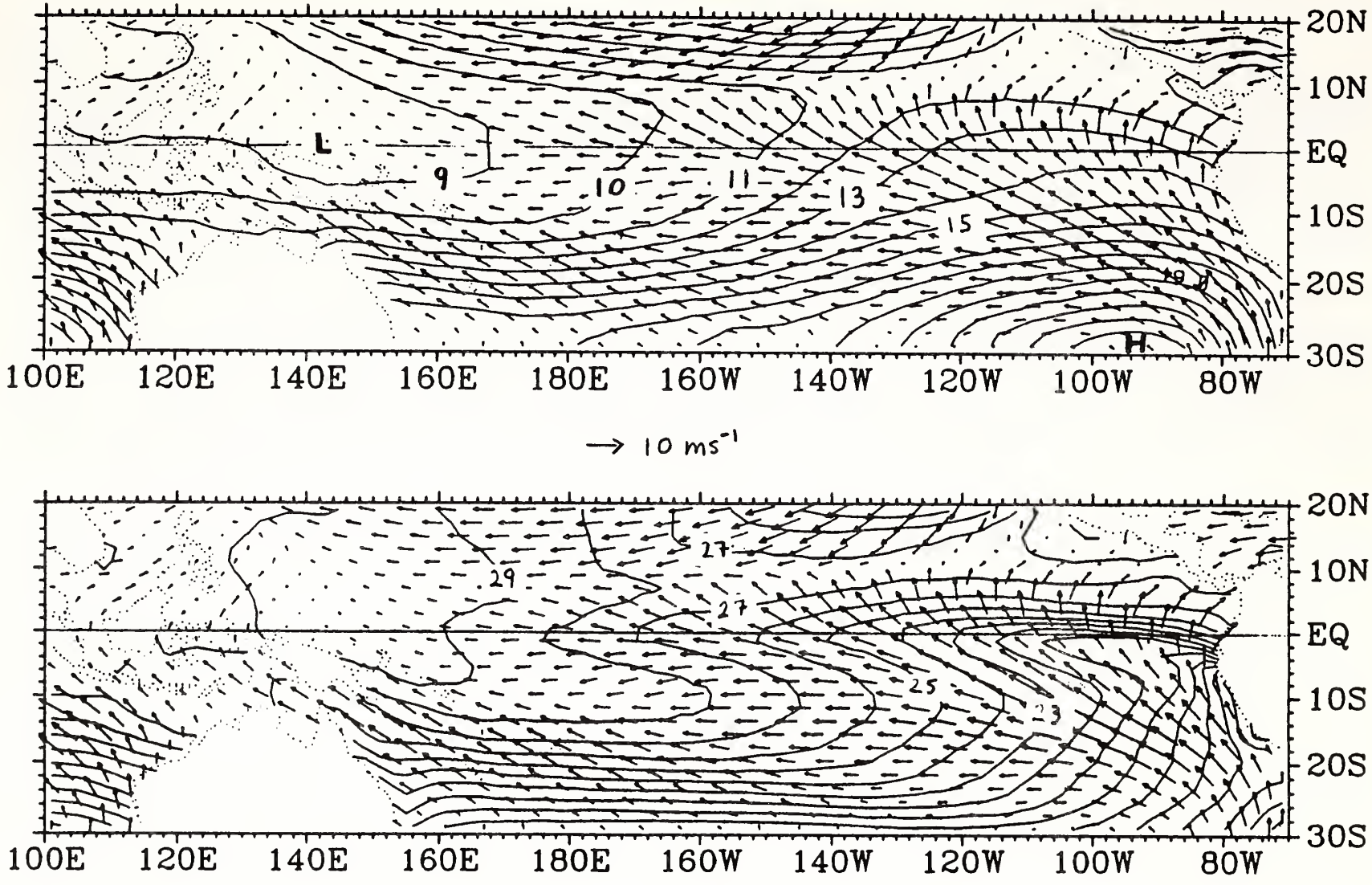

Fig. 4a Top panel: July-November sea level pressure (mb-1000) and surface wind (ms^{-1}) during cold years. Bottom panel: July-November sea surface temperature (°C) and surface wind (ms^{-1}) during cold years. See text for definition of cold years.

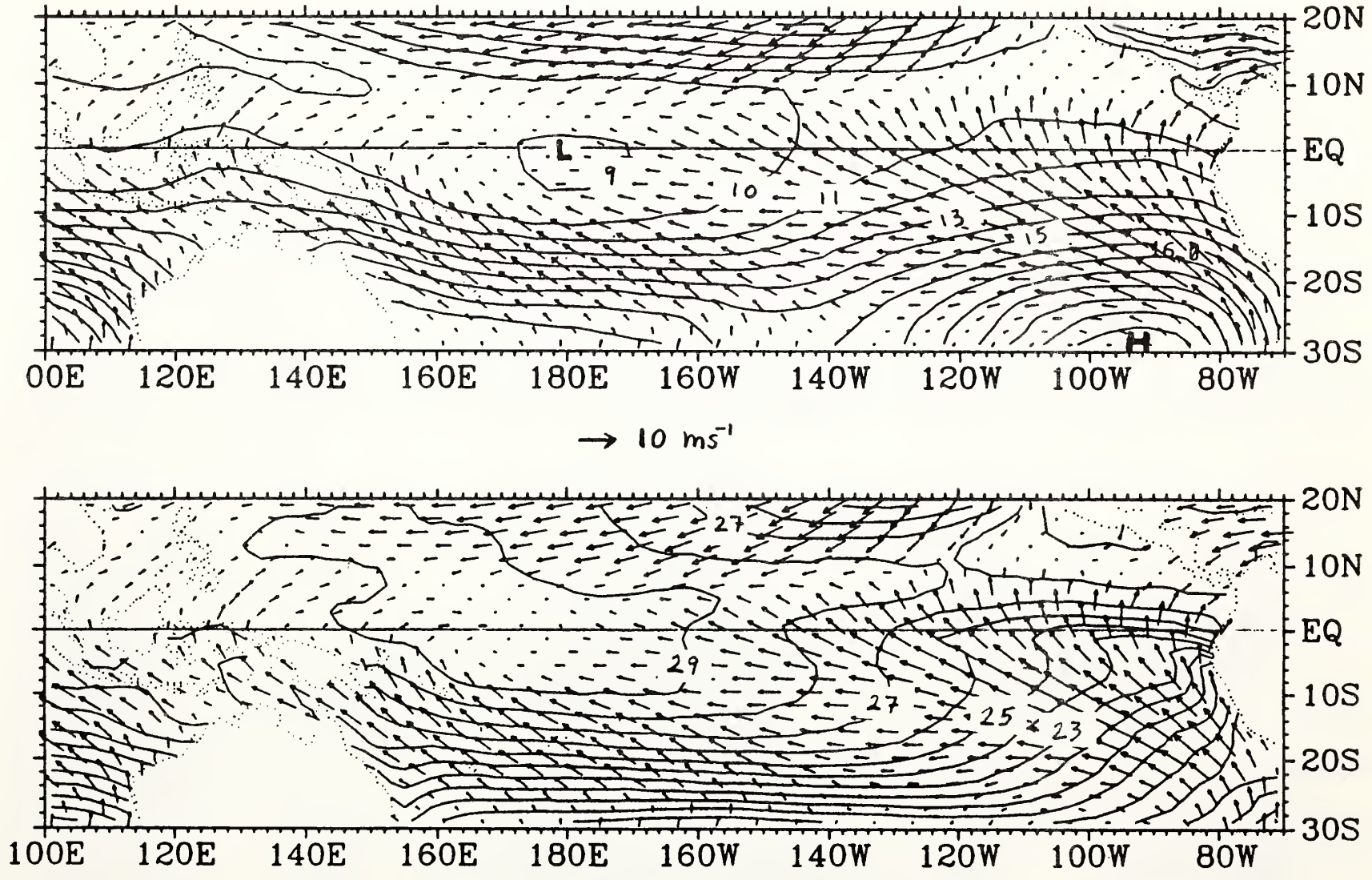

Fig. 4b As in Fig. 4a but for warm years.

A GLOBAL REANALYSIS; DATA INPUTS AND METHODS

Roy L. Jenne/NCAR*

Some of the problems and opportunities of making a reanalysis of global meteorological data will be considered. A delay of a few years from real time provides time to gather significantly more data, and to clean out errors. Analysis methods in use today are much better than those used operationally on FGGE data in 1979, or for the delayed FGGE analyses made in 1980–82. A reanalysis of the last 10 years (or more) of data would greatly increase the quality of available analyses, and the method used would be uniform with time.

Considering the data inputs, we should put a reasonable amount of effort into improving the data inputs before making a reanalysis. It is possible to consider a set of extra inputs that would greatly improve the datasets and still not cause extended delays for the new analysis projects. A discussion of selected types of data follows:

1. Availability of Upper-Air Data

There are archives of NMC upper-air decoded data starting in March 1962. These became global in June 1966. There are not very many missing time periods. NCAR had to go through over 1000 tapes to extract data for the first 10 years. Data for the whole time period is now relatively easy to use. That is, these tapes could be used as is and the data input would be as good as NMC originally had. After April 1979, the satellite sounding data are in a separate archive. Now we will separately consider a few of the types of data.

a. Rawinsondes and Pibals

There are basic rawinsonde archives for 1957–62 from Starr's general circulation project at MIT. Then the NMC archives start, but there is no data from the S. Hemisphere until June 1966. Regional data inputs could be used to improve the dataset. This would include data from US (starting 1946), Canada, Antarctica, China, Australia. Data from at least Argentina, S. Africa, and Zimbabwe also should be included, if possible. Note that the inclusion of the national archive usually gives cleaner, more complete data, and often provides data for earlier years.

b. Aircraft Data (Sadler, 1975)

Sadler (U. of Hawaii) collected reports from many remote aircraft routes for 1960–73, (Sadler, 1975). There are 13 years of data for the Pacific and 10 for the Atlantic. These should be included in a combined aircraft dataset. Data from the NMC and USAF decodes would be used together with data from New Zealand in recent years. J. Kidson has told me that only half of the reports available for ocean areas near New Zealand get onto GTS in recent years. NCAR has plans to start a project to take aircraft data from various sources and make a combined set with data 1960–on. Competing projects have delayed this effort for the last two years.

c. Satellite Cloud Drift Winds

Cloud drift winds from stationary satellites have been on the NMC tapes stored at NCAR starting in June 1969. Starting in about 1978, winds from the Japanese and European satellites have also been on the tapes. The stationary satellites see a disk over 100° latitude by 100° longitude.

Separate national archives of cloud winds started in the US (1974), in Japan (March 1981), and in Europe. Cloud winds have a bias toward lower speeds, especially at high wind speeds.

In April 1976, NESS produced 5000 to 6000 cloud winds a day from the two satellites. About 60% to 70% of these were from low-level clouds; most of the rest were high clouds, plus a few middle-cloud winds.

---

* The National Center for Atmospheric Research is Operated under sponsorship of the National Science Foundation.

d. Satellite Soundings

There are good archives of all basic satellite sounder data for the periods:

SIRS April 1969–April 1971
NOAA VTPR Nov 1972–28 Feb 1979 (48 Gbits)
NASA HIRS 17 Aug 1975–4 Mar 1976
NOAA TOVS 29 Oct 1978–Present (2075 Gbits to Apr 85)
(one Gbit equals 125 MB equals 1 tape, 6250 BPI)

The basic data could be used to recompute the soundings, or the previously inverted soundings could be used. For TOVS, there is a series of tapes that have basic radiances each 250 Km and a retrieved sounding. This has a much lower volume than the basic data. There were some bad retrievals in the early years of TOVS that can be removed by removing cases of heavy rainfall as determined by the microwave channels. The day-by-day archive of basic sounding data has only a few gaps. NCAR has a compact inventory that shows the number of orbits of data each day.

A few experts should meet to document what is known about the satellite sounder data. This would include information about how certain channels have become noisy or gone bad, or how the calibration has changed with time. Retrieval methods use raobs for calibration to avoid problems due to drifting calibrations. Retrieval methods based on regression push the solutions toward the averages.

2. Drifting Balloons

EOLE balloons: Period 21 August 1971 – 23 December 1972. NCAR has several tapes with the data.

TWERLE: Period July 1975 – 10 August 1976. On 17 August 1975, 95 balloons were working, 29 balloons on 9 August 1976, 16 on 1 December 1976. They flew near 150 mb. The data includes wind, temperature, pressure, and geometric height. Thus, it gives the height of a pressure surface near 150 mb over the ocean, like one level in a raob.

FGGE ARGOS tropical balloons: January – July 1979. About 330 balloons were launched near 135 mb. The data includes temperature and wind.

3. Surface Data

Good global archives of ship data start well before 1950. Land synoptic data from GTS is only available from 1967. In several years, an archive back to at least 1950 could be developed using national archives and other sources.

a. Land Synoptic

Data from the NMC surface decode starts in July 1976. However, data from the Navy and Air Force decodes start about 1967. The volume can be high; 12.5 years from NMC amount to about 223 Gbits, but the binary Navy decode with somewhat fewer stations has about 56 Gbits for 22 years. A binary version of the best of the data needs to be made.

b. Ship Synoptic

In the COADS project, ship data from the NMC decode and from delayed ship logs are combined into one dataset. All data from 1854–1979 (72 million reports) are on 40 tapes (40 Gbits of data). The data coverage is shown in Woodruff, et al. 1987. An update through 1987 will be available about Jan 1989. The NMC decode has 100,000 ship reports per month. Ship reports from the US Merchant Marine ship logs are

available three months after the fact (30,000 reports/month). NCDC, Asheville, also receives ship log data from other countries. After some years, there are about 85,000 reports per month of these foreign data. About 90% of these are usually available by two years after data time.

Several percent of the ship reports received over GTS have location problems. This is certainly not an acceptable level of error. Part of the problem is that the code form for location is complicated and probably invites errors from a human factors standpoint. Some ships also have barometers with bias errors. The bias should be corrected in reanalyses, when possible. Note that ship track checks (for location) and checks for pressure bias require that ship name be present.

c. Drifting Buoys

The drifting buoys are such an important source of data from isolated areas that they deserve separate consideration. They are critical for good S. Hemisphere analyses. There was a good network during 1979-80, then few buoys for awhile. A reasonably good network of buoys was reestablished in the S. Hemisphere by late 1984. The buoy data still have various types of errors, including location problems. Arctic ice buoys are available from 1979. The delayed archive is much more complete and has fewer errors than the real time data collection.

4. Special Project for Remote Areas

Before a new analysis is done, efforts are needed to ensure that surface and upper air data are gathered from remote locations (such as islands, Antarctica, etc.), where the real time receipt has been poor. Some of this work has already been done.

5. Tropical Storm Centers

Tapes are available from NCDC and the Hurricane Center that have the location and intensity of tropical storms. It is necessary to decide how one wants these storms to be handled in the analyses. Probably the decisions are a function of the resolution of the analysis system. They should be drawn for, but perhaps as a weaker system than is real.

6. Advantages of a Delayed Reanalyses

There are advantages to waiting several years after real time before making a new analysis. First, significantly more data can be included after 2 or 3 years. Second, the analysis methods now are much better than a few years ago. A striking example of this is a comparison of analyses of the Presidents' day storm, 1980 (Figure 1). Also, the delayed analyses of several years of data will be made using only one procedure.

7. The Analysis/Forecast System

The major analysis methods use a forecast to define a first guess. The guess gives a way to detect and eliminate bad data. It also defines the analysis where there is no data. Observations are needed because the forecasts are not perfect. The scheme permits some difference between the guess and the data. This difference permits some bad data to slip through, but not data that are really wild. Some methods permit data to "vote"; if several nearby observations agree with each other, they might be accepted by the analysis, even if they are slightly outside of limits.

There have been two basic approaches to the analyses problem. In one method, there is a 6 or 12 hour forecast. Then all data within about 3 hours of basic analysis time is used for the analysis. In the other case, the data is assimilated directly into the forecast model as it runs. GFDL tried this method in its pure form, and found that it produces analyses that are too ragged. Let us consider an example to see how GFDL used the

improved version of this method to prepare FGGE analyses. Suppose that we have just finished analyzing 00Z data. Consider the next raob at 12Z. They found that the raob needed to have some effect before its observation time or else the perturbation compared to the forecast would be too large. For FGGE they used 12 hour persistence to decide whether to accept the raob. Then they linearly interpolated for raob values at 2, 4, 6, 8, 10Z based on the 00Z assimilation and the 12Z raob. Data observed at 09Z would only give interpolated data for 2, 4, 6, and 8Z. These data values were analyzed with an OI scheme each two hours and the OI analyses were then used for insertion into the assimilation forecast each time step.

After FGGE, GFDL changed the method because 12 hours is too long a time for linear change. First GFDL changed to a six-hour persistence and now (Oct 86) use a six-hour forecast. The advantage of the six-hour forecast rather than persistence is that one can make a better judgment as to whether the raob (or other observed data) at the future time should be believed. Some of the FGGE analyses have been redone using these new methods and they are better now.

8. Staff Requirements to Reanalyze Years of Data

During operational analyses in forecast centers, many people are available to keep monitoring the new analyses. If this level of staffing were necessary for reanalyses, it would be difficult to afford to do it. The GFDL experience is encouraging in this regard. When GFDL did their official analysis of FGGE in 1982, they first did about 30 days of analyses per month. Later, this became about 90 days per month. Let us review the level of analysis effort at GFDL. Then the ECMWF estimate of needed resources will be given.

GFDL started on OI methods and related programming for making analyses in 1968. For two years it was quite a simple analysis system. During 1971–76 Ron Lusen worked on aspects of the problem. Over the years about 15 different people have been involved in developing different aspects of the analysis system, only two to five people at any one time.

- In 1974–75 GFDL analyzed GATE data (summer 1974) using a rather simple scheme.
- During the period 1973–77, there were usually two or three people working on the GFDL analyses systems.
- Spectral model: This was developed, then adapted to FGGE reanalysis by two people.
- GFDL had about four people working on data analysis problems for about three years prior to the FGGE reanalysis; the latter effort started about 1977.
  - — Adapted the analysis programs to what was needed. An OI analysis scheme had been developed at GFDL earlier.
  - — Prepared the data inputs.
  - — Used DST (Data Systems Test) data. (This Aug 1975 data was analyzed several times in the 1977-79 period.) It was last analyzed about 1979; four people worked on that, and later worked on FGGE data (1 Dec 1978–30 Nov 1979).
  - — Gate (Summer 1974 data) was analyzed for the third time in 1979.
- In 1980 GFDL started the preliminary analysis of FGGE data. These analyses were too ragged. GFDL redid all of FGGE during Feb through Sept 1982.
- FGGE Reanalysis operations (four people), during Jan-Sept 1982.
  - — Two people ran the system at GFDL; there were two others to help.
- This history of the analysis effort at GFDL is from a talk with Jeff Ploshay, Oct 1986.

In Oct 1988, ECMWF estimated the resources that would be needed to make new analyses, not counting work to improve data inputs. The estimates are for running analyses at state-of-the-art resolution, which is now 106 Fourier waves (T-106) on the XMP-48. They would need 2.3 years of a dedicated XMP-48 to do 10 years of

analyses. The calendar time needed would be 6 months for 1 year, 15 months for 5 years, and 27 months for 10 years of analyses. About three people would be busy just running the reanalyses, and two or more would be needed to help look at output and carry out associated research.

9. Computer Timing

The GFDL FGGE analyses were done on a Gausian grid 3.75° lon by 2.25° lat. By 1986, GFDL used 2.85° by 1.71°. For the latter grid, the total assimilation took about 6 hours of CDC-205 CPU time (about 12 hours wall clock) for a 24-hour cycle of analyses. The 42-wave, 18-level sigma level forecast model (sigma) takes 53 minutes (included in the 6 hours of CPU time) for a 24-hour forecast. For this timing they did not optimize the vectors. The 205 timing is probably comparable to a CRAY-1A or somewhat slower.

10. The UK Forecast/Analysis System

The UK forecast model will be briefly discussed, followed by a brief description of how the analysis/forecast system works.

The UK Meteorological Office used a 10-level PE model starting in 1972. A global 15-level model has been used since 1982 when it was introduced on the Cyber 205 computer. It includes precipitation, clouds, a diurnal cycle, and surface exchanges. It is a sigma-level model that uses a grid point system (not spectral), 1.875° longitude by 1.5° latitude. The four lowest sigma levels are at 0.997, 0.975, 0.935, and 0.870.

The analyses are done on the same sigma coordinates as the forecast model, and on the same grid except that the number of points are reduced near the pole. The analyses are made for temperature, wind components, relative humidity and surface pressure.

How are the analyses made? Suppose that an analysis for 06Z has been made. A first guess forecast for 12Z is made. Observations at 12Z are rejected if they are too far from the guess, except that they may still be retained if supported by other observations.

An analysis of the increments from the first guess at 12Z is made, using data from 09 to 15Z. From this analysis, increments are calculated for each model time step between 6 and 12Z. Then the forecast model is rerun from 6 to 12Z assimilating data (the increments) at each time step.

Using this procedure, the Met. Office does not have to make any initialization during analyses or assimilation. Without the assimilation at each time step, the changes are so large by the six-hour time that they shock the model too much, producing a noisy forecast, and, more seriously, they dissipate much of the information from the observations. See Atkins and Woodage, 1985 for a description of the analysis procedure.

In earlier years, analyses at forecast centers were typically made in a 12-hour cycle, 0Z and 12Z. That is, a 12-hour forecast was made to be used as a first guess. Then observed data valid at that time was used to make an analysis. People were aware that a considerable amount of data was also available at 6 and 18Z, which was not being used. In fact, large parts of the earth often had no satellite sounder data, if only the data near 0 and 12Z were used. Therefore, the centers gradually went to a 6-hour cycle rather than 12-hours. When this was done in a center, the forecasters were often unsure whether the result was slightly better or slightly worse. This was a surprise since an improvement was expected. Perhaps the problem is that if only a few observations are inserted, they tend to produce local anomalies rather than a whole atmospheric structure that is internally consistent.

11. Conclusions

Data inputs are available to accomplish reanalyses starting 1979 or earlier. New analysis projects should at least take advantage of several datasets that give considerable improvements over the operational data. The reanalyses take considerable computer and human resources, but still at a practical level. The benefits would be large. I believe that it will be done, perhaps starting within a few years.

12. References

Atkins, Margaret J., and Margaret J. Woodage, 1985: "Observations and data assimilation." *Met. Mag., UK*, Vol 114, Aug, 227-233.

Bengtsson, L., and J. Shukla, 1988: "Integration of Space and In-situ Observations to Study Global Climate Change." *Bul AMS*, Vol 69, 1130-1143.

Sadler, James C., 1975: "The Upper Tropospheric Circulation over the Global Tropics." UHMET 75-05, Univ of Hawaii, 35 p. Monthly maps and aircraft data density.

Woodruff, S.D., R.J. Slutz, R.L. Jenne, and P.M. Steurer, 1987: "A Comprehensive Ocean-Atmosphere Dataset." *Bul AMS*, Vol 68, No. 10, 1239-1250.

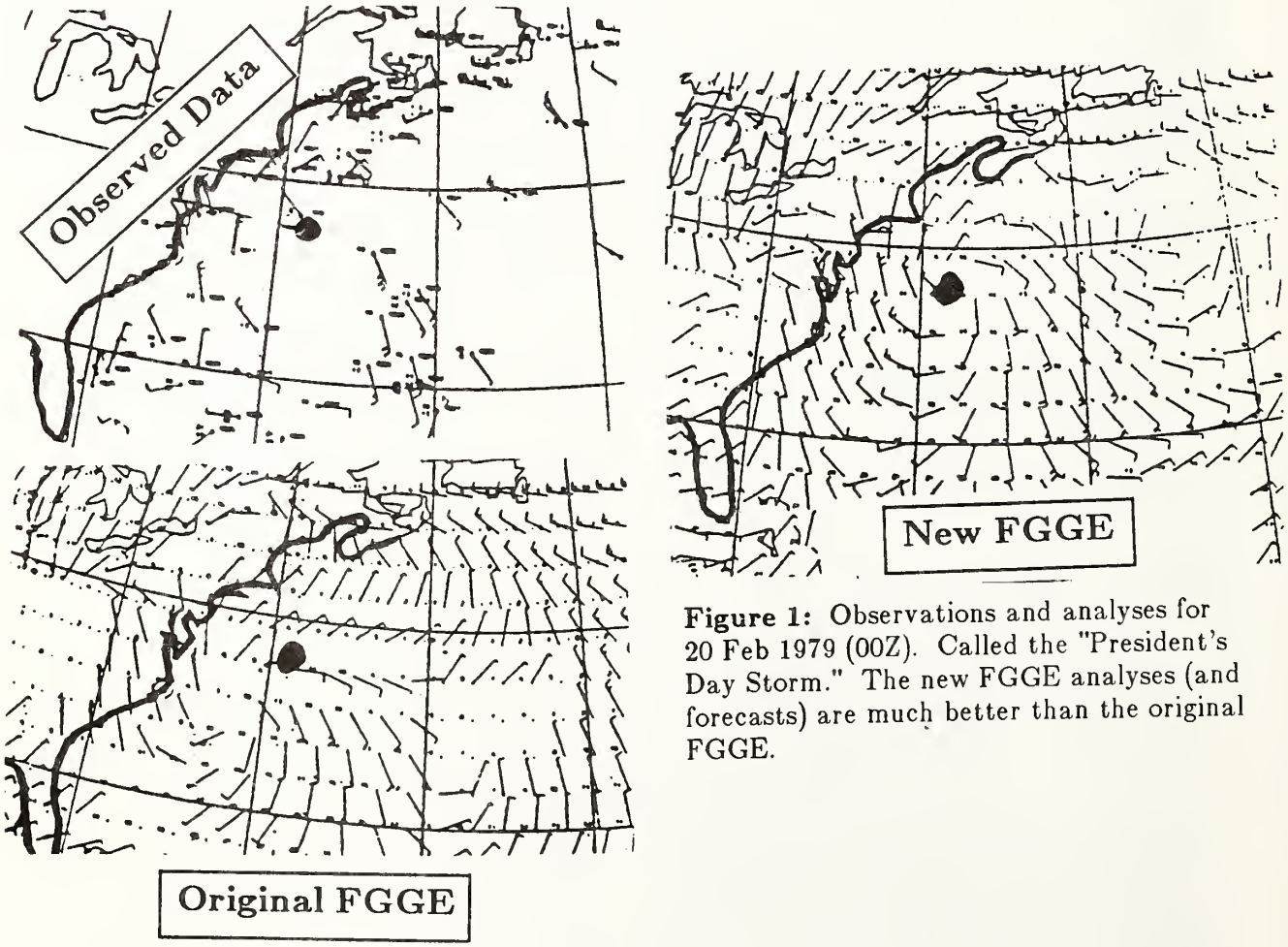

Figure 1: Observations and analyses for 20 Feb 1979 (00Z). Called the "President's Day Storm." The new FGGE analyses (and forecasts) are much better than the original FGGE.

STANDARD METEOROLOGICAL OBSERVATION SET FOR THE USSR AREA AND ITS APPLICATION TO REGIONAL CLIMATE RESEARCH

T.A. Belokrylova, N.V. Mamontov,
B.A. Martuganov, V.N. Razuvayev
All-Union Research Institute of Hydrometeorological Information - World Data Centre
USSR

1. INTRODUCTION

The first portion of a 3-hourly meteorological data set for the USSR area has been prepared. The main characteristics of the data set are described with examples of its application to climate research.

The data set contains data for 3-hourly meteorological observations for 223 stations of the USSR for the period 1966 to 1980. The stations are somewhat more densely spaced on the European portion of the USSR. The average density of the network is about one station per 10^5 km^2. 1966 is taken as the starting date since beginning on 1 January, 1966 3-hourly observations at standard synoptic hours (00, 03, 06, ... GMT) were started at the USSR meteorological stations. In the years 1936-1965 there were 6-hourly observations at 01, 07, 13 and 19 local time. The whole of the set is recorded on 40 magnetic tapes with a recording density 1600 bpi in EBCDIC. The records are blocked into 360 byte blocks.

2. DESCRIPTION OF 3-HOURLY OBSERVATION DATA SET

The structure of the record for one observation hour is given in Fig. 1. The observation site is identified by the coordinate number which is the coordinate value rounded to the nearest tenth of a degree and given in the file mark. Information on the main meteorological parameters, (air temperature, precipitation, air pressure, humidity, wind, clouds, soil surface temperature) atmospheric phenomena, and weather at the observation hour and between the hours are given in the set.

Since the instruments recording wind speed and direction were substituted during the period 1966-80, the wind record is nonhomogeneous. Also, the height of the barometer was changed at a number of stations which affected the pressure data series. In each case the nonhomogeneity was examined; however, corrections were not introduced because information on the dates of wind instrument substitution and the change of the barometer heights are given as a separate file to be used for data recover. In the future, other information on the station history and

changes in the mode of observations will be introduced in the reference file.

All the parameters with the exception of precipitation have been quality controlled. Mean values and variances as well as elements of meteorological control, based on the use of known relationships between the values of some parameters (i.e., air pressure at station and sea levels; pressure tendency and air temperature), were used to detect inconsistent values. Suspect values were checked and replaced by the correct ones. If the correct value could not be recovered, the value was replaced by 99999 and the assigned quality flag "9".

3. EXAMPLES OF THE DATA SET APPLICATION TO CLIMATE STUDY

i) Air temperature and soil temperature difference.

Mean values of the soil and air temperature difference for 1966-80 for four months for night (first line) and day (lower line) at two stations in the north and south of the USSR are given in Table 1. Note that the temperature difference in the south in Summer amounts to 28.1°C in the day time, while in the north this effect is much weaker. At night, the air temperature is higher than the soil surface temperature over the whole of the USSR though the differences between the values are not high and generally do not exceed 2°C.

ii) Wind

Wind speed monthly means were determined at individual synoptic hours for 223 stations in the USSR. The wind speed annual variations for stations located in different latitudinal zones in the USSR are shown in Fig. 2. Most stations exhibit two maxima in the annual variation curve for the day time. Generally, the Spring maximum is greater than the Autumn maximum (Fig. 2a). Wind strengthening in transition periods is caused by sharper thermal contrasts and intensified cyclonic activity. Note, that the time of maximum wind speeds is different for different zones of the USSR. In southern and western regions the first maximum is observed in March or even in February, the second one - in November (Fig. 2a). For stations in moderate latitudes, Spring and Autumn maxima are observed in April - May, September-October (Fig. 2b). Only one Summer maximum in the annual variation of the day time wind speeds is observed at the northern stations of the Asian portion of the USSR (Fig.2b). The character of wind speed distribution in the annual variation for night hours (dotted line in Fig. 2) is different from the day hours.

Wind speed decreases during 1966-76 at a number of the USSR meteorological stations cannot be accounted for either by the

urbanization effect or by changes in the observation methods (1). Running 3-year departures of the average mean annual wind speed values from the long-term values are shown in Fig. 3 for two USSR stations for 1936-1986. The wind conditions of each of the stations involved in the analysis exhibit some specific regional characteristics. Note, however, that mean annual wind speed values for 1966-80 for most of the stations were smaller than for 1935-66.

The occurrence of different direction winds in the calendar seasons for the station Genichesk located in the European portion of the USSR is compared in Fig. 4. The dotted line corresponds to the wind occurrence in 1931-65, the solid line to 1966-80. A weakening of westerlies was observed in 1966-80 while the occurrence of easterlies and southerlies increased. This agrees with the data available on the variability of the occurrence of the atmospheric circulation patterns for the period 1936-80; i.e., an increase in the occurrence of stationary large-amplitude waves (eastern circulation pattern) and a decrease of small-amplitude waves quickly moving from west to east (western circulation pattern [2]. A similar conclusion was made [3] during a study of the relationship between the wind speed and the atmospheric circulation pattern over Great Britain.

4. CONCLUSIONS

A 3-hourly meteorological data set for 223 stations in the USSR for 1966-80 has been prepared as a result of the first stage of an effort aimed at creating high-quality climatic data sets for the USSR. The next stage is expected to extend the set to cover the period through 1990 using more stations. Examples of climate study using the 3-hourly meteorological observation data set show some interesting wind and temperature variation between the northern and southern USSR latitudes.

Acknowledgements

The original English version of the paper was prepared by L.B. Ravina. The edited version for the Climate Diagnostics Workshop Proceedings was prepared by W.C. Bolhofer, NOAA/NCPO.

References

1. Baidal M.Kh., Khanzhina D.G. Long-term variability of climate macrocirculation factor, M., Gidrometeoizdat, 1986, 104 pp.

2. Palutikof J.P., Kelly P.M., Davis T.D. Windspeed variations and climatic change. Wind Engineering, vol. 10, N°4, 1986, pp. 182-189.

3. Shkolar L.F. On wind speed decrease during the last decade. WGO Proceedings, 1980, issue 435, pp. 96 - 98.

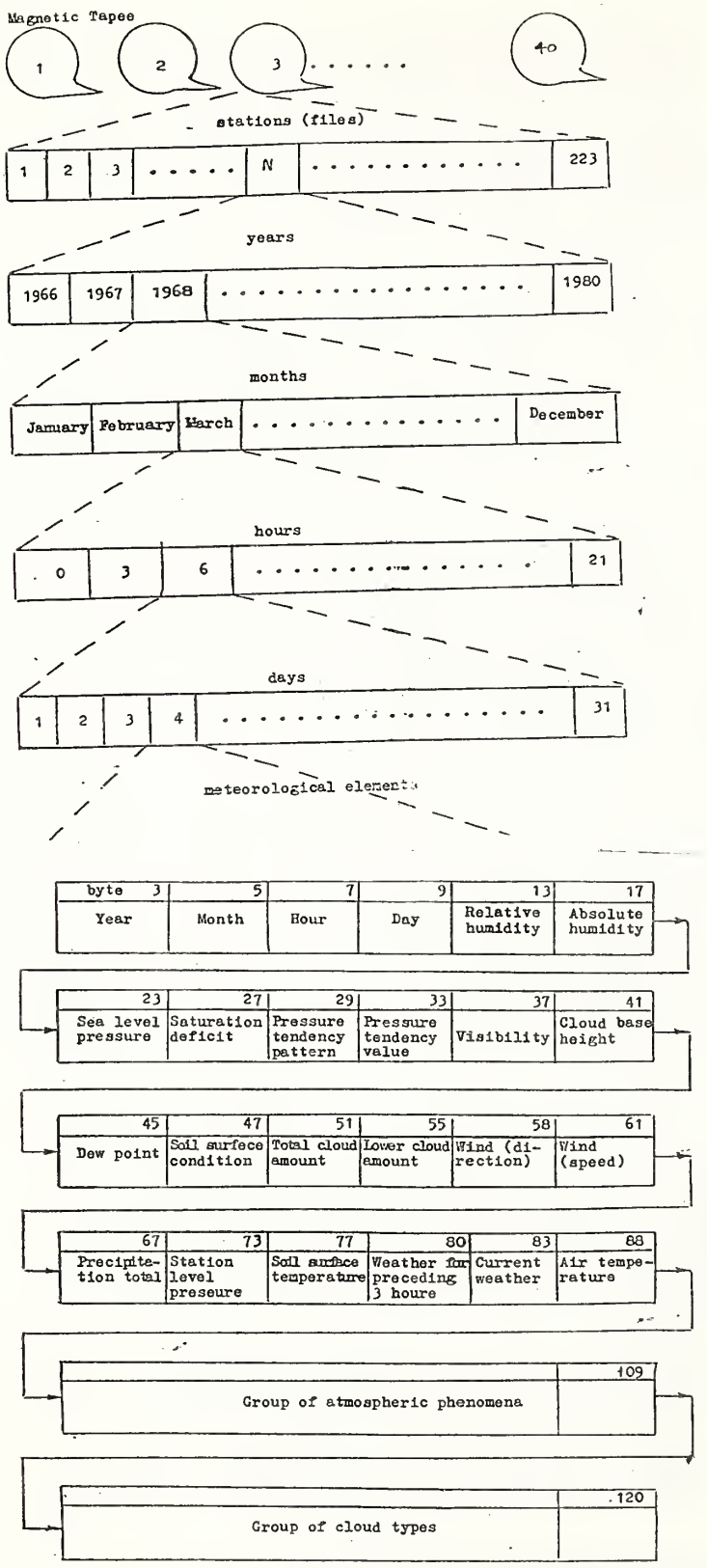

Fig. 1 Archive structure and record format.

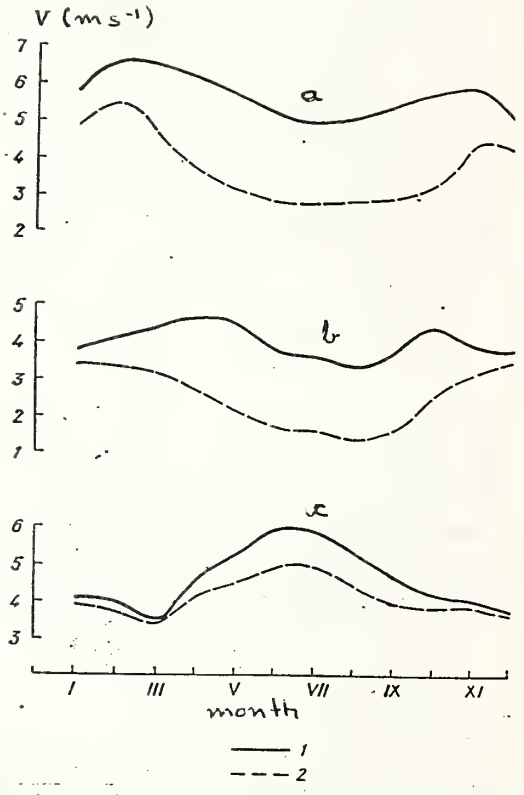

Fig. 2 Annual variations of mean wind speed during the day (1) and at night (2) at stations Askania Nova (a) = 46°N, Veronezh (b) = 52°N, and, Chekurdah (c) = 70°N.

Monthly means of the difference between soil surface temperature and air temperature in the night (first line) and day (second line) hours, °C

Table 1

Stations	Months			
	January	April	July	October
Berezovo /North/	-1.5	-2.2	-1.5	-0.8
	-1.3	+0.1	8.9	0.2
Bajram-Ali /South/	-1.2	-2.6	-4.4	-3.5
	5.7	17.3	28.1	16.6

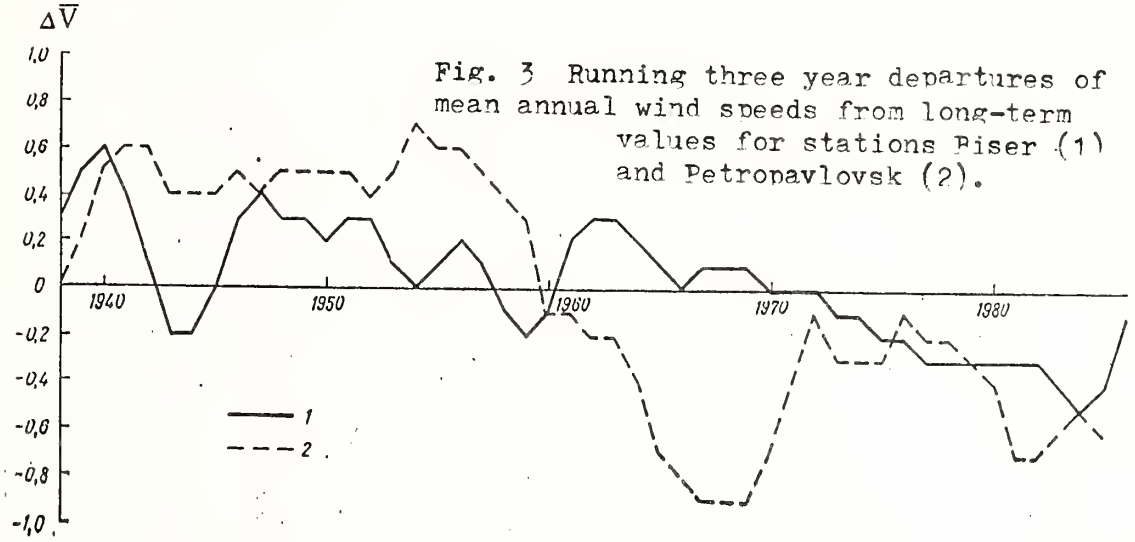

Fig. 3 Running three year departures of mean annual wind speeds from long-term values for stations Piser (1) and Petropavlovsk (2).

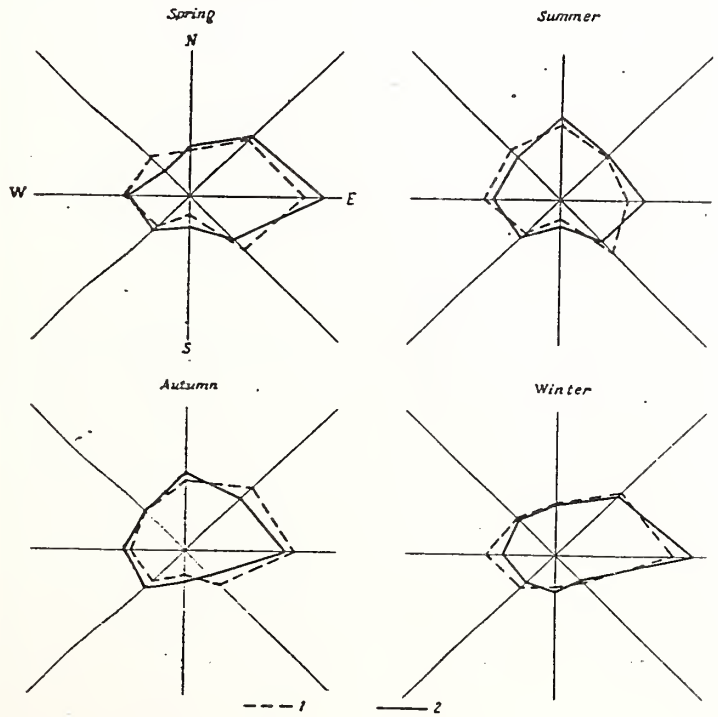

Fig. 4 Occurences of different direction winds for station Genichesk for periods 1936 - 1965 (1) and 1966 - 1980 (2).

Interannual Variability of Intra-Seasonal Oscillation

Ken-ichi Kuma

Department of Meteorology,
Florida State University
Tallahassee, FL 32306.

In this short report, we present the temporal variability of Intra-Seasonal Oscillation (hereafter called ISO). For the long term analysis of ISO, we have used the radiosonde observation at Singapore, located near the equator (1°N, 104°E). This data set, which is available from NCAR, covers the period 1960 to 1985.

First, at each standard level we have linearly interpolated the time series to missing data points. Then, we have applied a time filter for the whole period to remove the high frequency (larger than $^1/_{3\mathfrak{C}}$ (^{1}/day)) and the low frequency (smaller than $^1/_{90}$ (^{1}/day)) phenomena. To see the temporal changes in the spectrum, we divided the whole period into 101 subperiods, each of which includes 90 days of data. Since the seasonal variation of ISO is one of our targets, subperiods begin at Sep.1, Dec.1, Mar.1, and Jun.1. These four categories represent Fall, Winter, Spring, and Summer, respectively. Since the 30-60 day period is comparable to the 90 day subperiod, we are forced to use the Maximum Entropy Method (MEM) instead of the FFT or B-T method.

Fig.1 shows the averaged power spectrum of the zonal wind at 150 mb. for each season. Although the peak between 30 and 60 days is evident for any season, it is the strongest in the winter and the weakest in the summer. Our results regarding the annual variation of ISO are consistent with recent studies by Madden (1986) and Hartmann and Gross (1988).

To see the interannual variability of ISO, we should extract the ISO from the power spectrum analysis. For this purpose, we have computed the following value for each subperiod.

$$\mathrm{Var} = \int_{\nu_1}^{\nu_2} P(\nu)\,d\nu \qquad (1)$$

where $P(\nu)$ is the power spectrum of the zonal wind at 150mb, $\nu_1 = {}^1/60$ (^{1}/day), and $\nu_2 = {}^1/30$ (^{1}/day). We have assumed that the temporal changes of Var should represent that of ISO. This parameter compares favorably with the filtered time sequence with 30-60 day mode.

Fig. 2 shows the time sequence of ISO from the fall of 1960 to the fall of 1985. We note the two to three year oscillation as well as the annual variation. A similar two to three year oscillation in the intensity of the ISO has been reported by T. Murakami et. al. (1986). They found the same cycle using EOF analysis of OLR data. They speculated that this cycle should be the results of the modulation by two modes which have similar frequencies.

Spectral analysis of the ISO intensity (Fig. 3) shows two characteristic time scales. As previously noted, one is the annual cycle and the other is the Quasi Biennial Oscillation (QBO). Since we have now confirmed the existence of the QBO in the data set, we can apply a band pass time filter from which we will obtain the phenomena with periods between 2 years and 5 years. Fig. 4 shows the QBO mode of ISO intensity along with the traditional QBO mode of the zonal wind at 70mb. The QBO and the QBO mode of the ISO are clearly evident and generally oscillate out of phase.

Before we discuss the QBO mode of ISO in detail, it is worth examining in what situation ISO becomes strong. For this purpose, we will show a composite analysis for winter. We have computed the mean intensity of ISO for 25 winters. If the intensity of ISO is stronger (weaker) than the mean intensity, we call this winter a 'strong (weak) ISO winter'. The vertical structure of the zonal wind for each composite is shown in Fig. 5. In the weak ISO winter, we have westerlies at 70mb and stronger easterlies in the upper troposphere. In other words, we have stronger westerly shear near the tropopause. By thermal wind considerations, this implies relatively warmer air near the tropopause for the case of weak ISO. Thus, we can expect a difference in the static stability between the two categories in the upper troposphere near the tropopause.

Using the global wind and OLR analyses from NMC, we have made horizontal structure maps for the two composites. These figures (not shown) reveal that we have stronger Hadley and weaker Walker circulations in strong ISO winters than in weak ISO winters.

From these results, ISO at 150mb seems well related with u at 70mb, u at 150mb, and static stability N^2 between 100mb and 150mb. Fig. 6 shows the relationships with the identification of the season. Easterly wind at 70mb seems to be more favorable than westerly wind for the strong ISO, even though the strongest ISO in the winter of 1969-1970 occurs with the westerly wind. As for the zonal wind at 150mb, the larger easterly we have, the ISO appears. In the same way, weaker static stability corresponds with stronger ISO. These relations seem to be valid not only for the seasonal variation but also for the interannual variation.

In order to confirm this point of view, a cross spectrum analysis has been made for every pair of four parameters ———— u at

70mb, u at 150mb, N^2 between 100mb and 150mb, and the intensity of ISO at 150mb. Fig. 7 shows the coherence square and phase difference of cross spectrum. As you can see, there are two characteristic time scales. For the annual cycle, it is easy to explain the existence, because there is a strong forcing on this mode. On the other hand, it seems to be difficult to explain the QBO mode. From Fig. 7, we have made the schematic diagram of Fig. 8 which shows the connections among four parameters with two time scales.

As may be expected, the annual cycle of ISO is not related with u at 70mb. This cycle should be purely a tropospheric phenomenon. We should examine here how these three tropospheric parameters are related to one another. The link between u at 150mb and N^2 is easily understood by the thermal wind relations, although we cannot tell which is the cause and which is the result.

Since weak static stability decrease the phase speed of Kelvin wave, the change of N^2 can influence the intensity of ISO. Further, the easterly at 150mb can affect the ISO through Doppler shifts and wave responses. It is not easy to understand why we have weak ISO when the easterly at 150mb is very strong. There has been a lot of theoretical work devoted to understanding the slow phase speed of ISO. For the slow eastward phase speed, the strong easterly seems to be favoured. From another point of view, the equatorial circulation is more stationary for weak ISO. That can be the reason why we have stronger easterly at 150mb of Singapore. It should be noted here that the zonal mean of u at 150mb around the equator does not differ between stronger and weaker ISO winters.

Closer examination of the cross spectra reveals that the strong ISO precedes the small N^2 by the phase lag of $\pi/3$ for QBO mode. Further u at 70mb is nearly in phase with N^2. When we have a strong ISO, the easterly at 70mb is increasing and the heat is transported from the equator to higher latitude near the tropopause. By the traditional QBO theory, these features are realized through the activity of Yanai wave. It may not be feasible that the strong ISO generates strong Yanai wave. It is more acceptable that the stratospheric QBO affects the tropospheric QBO. Since the stratospheric QBO is the zonal mean phenomena, the heat transport from the equator to higher latitudes will occur over any equatorial region. By the zonal cooling near the tropopause, ISO will be somehow intensified. We need more works for the physical explanation of this mechanism. These works also lead to the better understanding of ISO itself.

Figure. 1. Averaged power spectrum of the zonal wind at 150 mb. Solid line shows the power spectrum while dashed line indicates the 95% significance level. Each figure indicates fall, winter, spring, and summer from the top to the bottom. Units are (m^2/s^2) day

Figure. 2. Time sequence of the power of 30-60 day mode. Each bar indicates the power for each sub period. Units are (m^2/s^2)

Figure. 3. Spectrum of the ISO intensity. Units are $((m^2/s^2)^2)$ year.

Figure. 4. Time filtered ISO intensity. (solid line) and time filtered zonal wind at 70 mb (dashed line). Units are (m^2/s^2) for solid line and (m/s) for dashed line.

Figure. 5. Vertical zonal wind profile during winter for strong ISO composite (solid) and weak ISO composite (dashed). Units are (m/s)

Figure. 6. a) Scatter diagram for the relation between u 70 mb and ISO

b) Same as (a) but for U 150 mb and ISO

c) Same as (a) but for N^2 and ISO

W, S, U, F indicate winter, spring, summer, and fall, respectively.

Figure. 7. Coherence square (SOLID) and phase difference (DASHED) from the cross spectrum.

a) ISO and U at 70 mb
b) ISO and U at 150 mb
c) ISO and N^2 between 100 mb and 150 mb
d) U at 70 mb and U at 150 mb
e) U at 70 mb and N^2 between 100 mb and 150 mb
f) U at 150 mb and N^2 between 100 mb and 150 mb

The positive phase lag means that the latter precedes the former parameter.

Figure. 8. Schematic diagram which shows the correlations among four parameters.

Figure. 1.

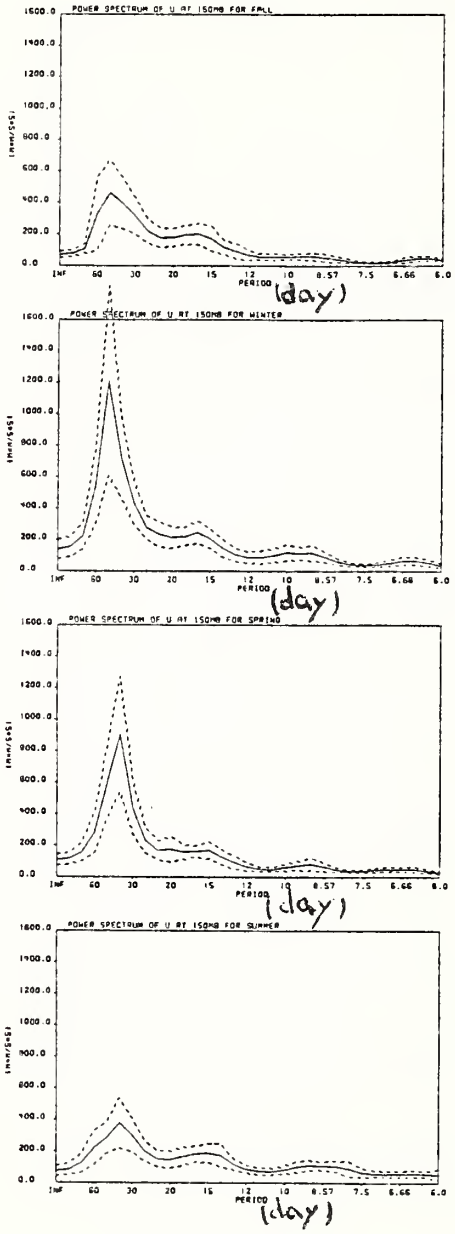
POWER SPECTRUM OF U AT 150MB FOR FALL
POWER SPECTRUM OF U AT 150MB FOR WINTER
POWER SPECTRUM OF U AT 150MB FOR SPRING
POWER SPECTRUM OF U AT 150MB FOR SUMMER
PERIOD (day)

Figure. 2.

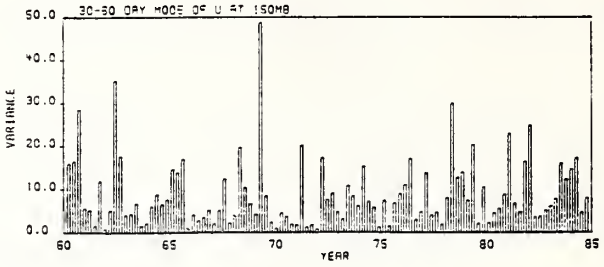

Figure. 3.

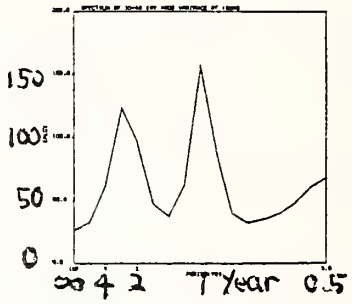

Figure. 4.

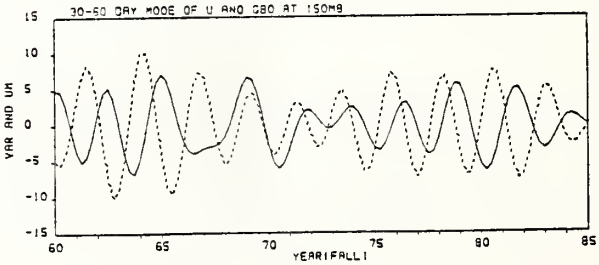

Figure. 5.

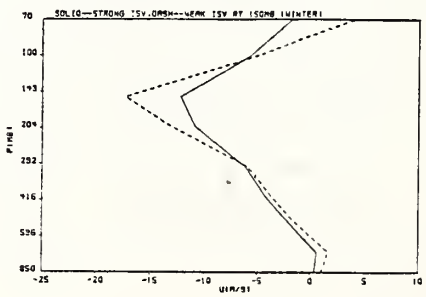

Figure. 6.

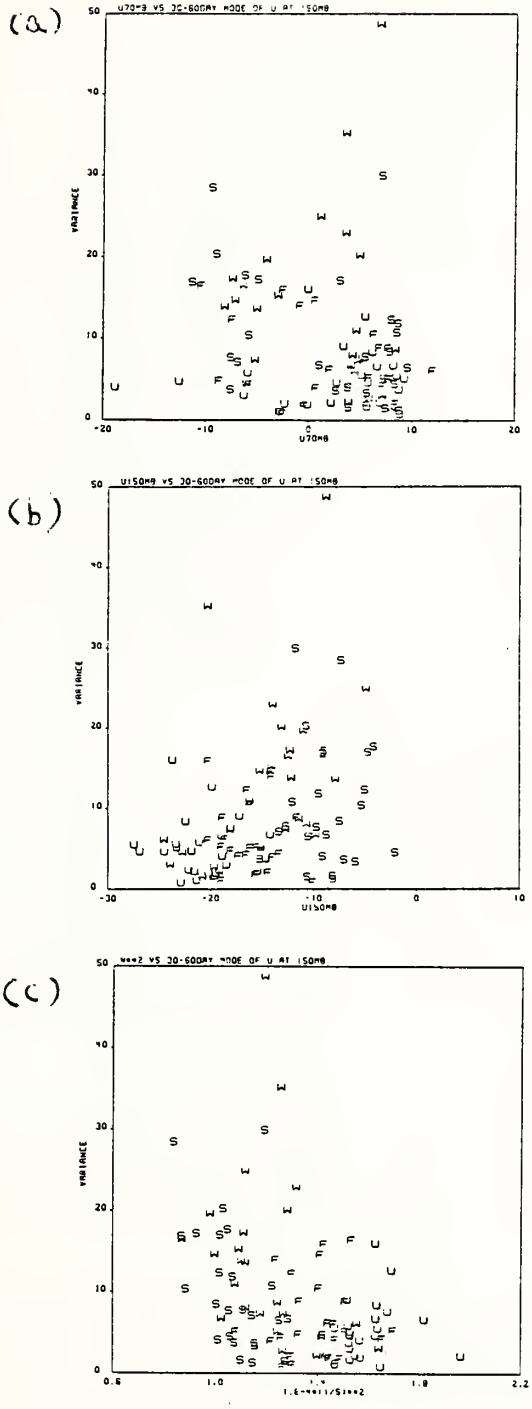

Figure. 7.

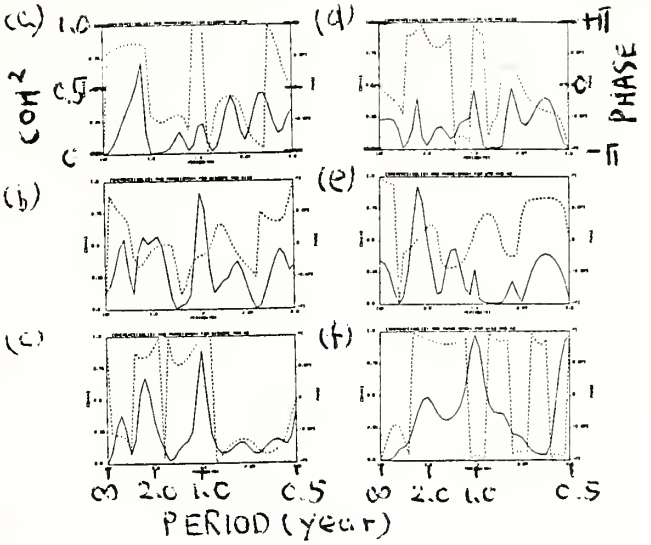

Figure. 8.

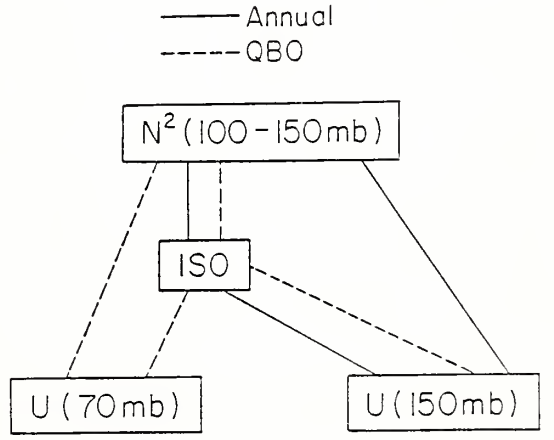

A SOLAR-OCEAN RELATION: FACT OR FICTION?

Tim P. Barnett
Scripps Institution of Oceanography
La Jolla, CA 92093

November 29, 1988

Abstract

In the course of studying Quasi-biennial (QB) variations in the global sea surface temperature (SST) field, an apparent solar signal was detected. Specifically, the amplitude of variations in the QB frequency band appear to be modulated at the 11 year solar cycle (Fig. 1) at least over the last four cycles. The sense of the relation is that high solar activity goes with low amplitude variations in the QB frequency band. In a series of recent papers, van Loon and Labitzke (1) (hereafter vLL) have found in the same frequency band a similar amplitude modulation in atmospheric fields of both Hemispheres also over the last four solar cycles. A hypothesis to explain the observed relation in the tropics is proposed. In an effort to study the apparent relation over more solar cycles, the analysis of the time series of SST was extended back to 1884. The solar-SST relation shown in Fig. 1 was found to hold back to about 1925 (Fig. 6). Before that time, remnants of the SST signal can still be observed but the relation to the solar cycle becomes more confused. This lack of consistency through the 10 solar cycles examined here may be due to the fact that the apparent relationships are fictitious. They may also be partially due to poor SST data before 1920; the major failure in the solar-SST relation occurring in the data sparse 1915-1920 period. It may also be that the weak solar variability at the turn of the century could not force an observable response in the SST field.

Global sea surface temperature data for the period 1950-1986 were band pass filtered to retain information in the 20-30 month period band in order to study the Quasi-biennial Oscillation (QBO) in the ocean. The filtered data were decomposed into a set of complex empirical orthogonal functions (2) (CEOFs) as a means of succinctly studying the variability of the SST field in this QBO frequency band. As a by-product of this analysis, an estimate is made of the amplitude modulation, if any, of the basic QBO signal. This modulation for the period 1950-86 is shown in Fig. 1 along with the solar flux in the 10.7 cm band (scale inverted). The agreement appears remarkable. The interpretation is that higher levels of solar activity go with lower variability of SST in the QB band. Note this relation is opposite that proposed by some researchers (3) but in qualitative accord with the results of others (4).

The physical meaning of the CEOF amplitude modulation function is made clear by reconstructing the QBO signal at a somewhat arbitrary location in the equatorial Pacific (Fig. 2). The basic QBO "waves" clearly undergo amplitude modulation. The envelope of the QBO amplitude is what is measured by the CEOF amplitude modulation function. The simple reconstruction shows the modulation envelope to have an approximate 11 year period over the nearly 4 solar cycles considered.

The relation between the above results and those of vLL is close since they essentially performed an analysis comparable to that described above. They stratified atmospheric data from both Hemispheres by the west/east phase of the stratospheric QBO and then correlated that sub-sampled data set with the solar flux time series. Their stratification procedure, shown schematically in Fig. 3, is basically a rectification of the original signal. The rectified signal in the hypothetical example represents the amplitude envelope of the QBO; exactly the quantity in the SST field that was related to the solar flux. Thus they have correlated the amplitude modulation signal of various atmospheric fields with the solar cycle...and found highly significant results over four solar cycles.

The above results suggest that there may be something to the solar-SST relation. If so, how might this result be rationalized physically? One possible scenario is shown in Fig. 4. It draws partially on ideas presented by Staley (5) and Newell (6) as they attempted to explain the QBO itself. Here we consider a very different time scale and add some ocean physics. In the following, we assume the existence of a well-documented QB cycle (6) and seek only to explain how it might be more (less) vigorous at solar minima (maxima). Thus, we discuss the modulation of the QB cycle; not the cycle itself.

(a) The stratosphere is in radiative balance with the heating being provided principally by the absorption of ultra-violet (UV) energy in the 200-300 nm range (7). Direct measurements suggest the UV experiences a roughly 3-9% fluctuation near 200 nm between solar maximum and minimum (8) and virtually no change at 300 nm and above. Forcing a radiative convective model (9) of the stratosphere with a 5% change in the UV in the 200 nm range produced a 2°C change in the temperature of the stratosphere between solar extrema. In this one dimensional model, the associated temperature change in the lower troposphere is negligible for reasons given below.

(b) The decreased (increased) stability associated with the stratospheric temperature change will lead to more (less) heat flux from the underlying troposphere, i.e., a modulation of the Hadley Cell (6). Since it is an observational fact that the interannual temperature anomalies in the stratosphere are 180° out of phase with those in the troposphere the interaction proposed seems quite probable (1, 6, 10). Further, the one dimensional model used in (a) cannot simulate the processes needed to reproduce this effect. It would take a full 3D model to capture the Hadley Cell modulation.

(c) A stronger (weaker) Hadley Cell will be characterized by stronger (weaker) tropical surface winds, particularly the meridional component. This signal will in turn give colder (warmer) SST due to latent heat flux perturbations and/or more importantly, to modulation of upwelling if the surface solar-induced signal in the windfield is strong near the equator. The fact that the CEOF analysis showed the modulation of the QB SST field to be strongest near the equator, suggests the dominance of the upwelling mechanism.

We used ship observed winds for the period 1960-1986 in a CEOF analysis for the region $\pm$ 15° of the equator to investigate the possible modulation of the Hadley Cell at the sea surface. The principal Hadley Cell variance in the QB band was indeed located on the equator in the central Pacific just where the SST signal was strongest and in the sense required, e.g. stronger winds (divergence) going with colder SST. The amplitude modulation of the surface Hadley Cell agreed very well with the SST/solar curves (Fig. 1) over the last three solar cycles, the limit of adequate wind data set. While this result is encouraging we would have more or less expected it, given the nature of air/sea interactions in the tropics regardless of solar activity. In summary, virtually all aspects of the hypothesis shown on Fig. 4 seem observable.

The major weaknesses in the hypotheses of Fig. 4 are the estimation of UV variability over a solar cycle and the modeling of its effects on stratospheric temperature. It is suspected that our estimates of this latter effect are probably low due to the "global" characteristics of the model we used. In any event, the subsequent connection to the Hadley Cell is only inferred. We need a simulation of the complete set of atmospheric physics with a full GCM driven only by the observed radiation fluctuations described by, say, reference (8) to fully investigate the hypothesis.

Prior to any such simulation a critical question must be answered: Does the relationship show in Fig. 1 hold for more solar cycles? vLL could not investigate this possibility since the upper air data needed to perform their data stratification does not exist. The SST data, however, allows us to answer the question but the answer is only partially satisfying.

The CEOF analysis of the 1950-86 SST data showed that by far the largest QBO signal in the SST occurs along the equator; particularly in the central and eastern Pacific (63% of the total signal variance). Regional averages of SST in all three equatorial oceans were formed using the historical ship observations. The regions are shown in Fig. 5 and were defined from the CEOF analysis of the 37 year global, gridded SST set and the existence of adequate data. Suffice-it-to-say, the series in these areas could be extended back to 1884 with few data gaps (except for the period 1915-1919 when coverage was poor to nonexistent in the Pacific.) The CEOF analysis was repeated on the extended regional data sets and the resulting amplitude function was compared with sunspot number (Fig. 6). The results of the CEOF analysis were verified, using

only lightly processed SST data. In this case, actual data from the two SST regions off South America (P4 and P5), accounting for 42% of the tropical QBO signal were averaged together and passed through the QBO filter. The resulting time series were then simply squared (rectified) and the resulting envelope function compared with the (inverted) solar data (Fig. 7).

Both sets of analyses give similar results. The agreement between the modulation function which now can be thought of as representation of the entire equatorial strip, and (inverted) solar cycle is apparently good through 6 solar cycles back to the mid 1920's with minimum SST variability going with maximum solar activity as before (Fig. 6). The raw data analysis (Fig. 7) shows that locally in the eastern Pacific, at least, the minimum SST variability occurs after the solar maxima as the cycle itself decreases in strength. However, the phase relation in both cases is not perfect as ± 2 year shifts in the stated relationship can be found in a particular solar cycle.

Before 1925 the relation is not nearly as clear. It is still true that minima in SST variability are associated with the solar maxima in 1894 and 1906. The 1917 solar maximum is associated with a broad period of minimum SST variability (Fig. 6). But the character of the solar-SST relation before, say, 1925 is clearly different than the post-1925 epoch (see particularly Fig. 7) where the 'B' arrows seem to define a new phase relation; at least over 4 solar cycles up to 1930).

The above results raise more questions than they answer. Are all the results simply statistical flukes? It seems unlikely, given that they appear in numerous climatic fields (using vLL results plus those presented here) for 4-6 solar cycles. But then all of the fields alluded to are highly interdependent so this is not as strong an argument as one might think. However, the self similarity of the pre-1920 results will be encouraging to those who believe in solar-weather relations. But why should there be an apparent change in the relations in the 1920's? H. van Loon suggests it may be associated with a basic change in atmospheric state that occurred in at last some parts of the Northern Hemisphere at that time (11). Perhaps it is due to the low levels of solar variation that generally characterized the earlier period. In this case, any potential solar forcing of the stratosphere would be reduced and the SST variability could be due to other physics. Perhaps the SST data, which becomes relatively sparse before 1920, is the culprit. The data may be so meager that they cannot be used in a study such as this. Indeed the data density plot for Pacific regions P3, P4, and P5 suggest this might be the case; especially for the period 1915-1920 when the solar-SST relation is in greatest disarray. Finally, there is the disturbing fact that we could not detect the same amplitude modulation in frequency bands above or below the QB band. Perhaps the modulation of the annual signal, if it is present, is too small compared to the seasonal range to be seen. At lower frequencies, aliasing becomes a problem. But these are only modest rationalizations and not necessarily good answers to the questions raised.

One thing is clear. The apparent change in the relationship between the SST amplitude modulation and the solar cycle around 1925 will, if real, have to be satisfactorily explained before one can accept the solar-ocean relation as real. In the meantime, the results presented here are probably best described as provocative, hardly conclusive, and perhaps (unintentionally) misleading. But there seems enough strength in the current results to encourage additional research in this area. That has been the main purpose of this note.

References and Footnotes

1. Labitzke, K. and H. van Loon, *J. Atmos. and Terrest. Physics*, in press, (1988).

van Loon, H. and K. Labitzke, *J. Clim.*, **1**, 905, (1988).

van Loon, H. and K. Labitzke, *J. Clim.*, **2**, in press, (1988).

2. Barnett, T.P., *Mon. Wea. Rev.*, **111**, 756, (1983).

The CEOF analysis can be thought of as a coordination transformation that maximizes the amount of variance represented by a minimum of dimensions. It is just an expanded version of Principal Component Analysis.

3. Gage, K. and G. Reid, *Geophys. Res. Letters*, **8(2)**, 187, (1981).

4. Reid, G. and K. Gage, *Secular, Solar, and Geomagnetic Variations in the Last 10,000 Years*, Kluwer Academic Publishers, 225, (1988).

5. Staley, D.O., *J. Atmos. Sci.*, **20**, 506, (1963).

6. Newell, R., J. Kidson, and D. Vincent, *Nature*, **222**, 76, (1969).

7. Davies, K., *Ionospheric Radio Propagation*, Dover Publications, (1966), pp. 470.

8. Lean, J., *J. Geophys. Res.*, **92(D1)**, 839, 1987.

9. The author is indebted to Sam Iacobellis for making these calculations. The model he used is described in Somerville, R. and S. Iacobellis, Collection of Papers Presented at the WMO/IUGG NWP Symposium, Tokyo, August, 177, 1986.

10. Reid, G., K. Gage, J. McAfee, *J. Geophys. Res.*, in press, (1988).

11. van Loon, H. and J.C. Rogers, *Mon. Wea. Rev.*, **106**, 296, (1978).

Figures

Fig. 1: Amplitude modulation function for the Quasi-biennial oscillation of global sea surface temperature (solid line) obtained from CEOF analysis. Also shown is the solar flux at 10.7 cm wavelength (dashed line). Note the solar flux series has been inverted for easier comparison.

Fig. 2: A reconstruction of the QBO signal in the SST field at 2 S 158 W in the Central Equatorial Pacific. Note the amplitude envelope corresponds to the solar cycle shown in Fig. 1. It is the envelope function shown in this figure that is represented by the amplitude modulation in the CEOF analysis.

Fig. 3: A schematic of the calculations carried out by van Loon and Labitzke (1). The upper panel shows a hypothetical QBO oscillation that experiences its "west" phase at the crest of each cycle and "east" phase at the trough of each cycle. Subsampling according to, say, west phase, as did vLL, would produce the signal shown in the lower panel of the diagram, i.e., the envelope of the original QB fluctuations. Shown for comparison is a typical solar cycle. Clearly the two curves in the lower panel will be highly correlated.

Fig. 4: The schematic hypothesis of how the solar connection might work. Many features of the diagram represent known relationships. A numerical model result suggests the UV-stratopheric temperature connection may produce the realistic temperature changes in the stratosphere over a solar cycle.

Fig. 5: Location map showing the areas for which regional average SSTs were developed back to 1884. The numbers in each box show the percent of signal variance associated with each region in a subsequent CEOF analysis. The central and eastern equatorial Pacific account for the majority (62%) of signal. These regions are labeled P3-P5.

Fig. 6: Same as Fig. 1 except now the period of analysis is between 1884 and 1986. The SST signal is given by the dashed curve. The solar variability (solid line) is measured by sunspot number (time series inverted). The dashed vertical lines are located at sunspot maxima.

Fig. 7: Relation between SST variability off the coast of central and South America (regions P4 and P5) and sunspot number (solid line, scale inverted). In this case, the SST time series (dashed line) was passed through a QBO filter and the resulting anomaly time series and squared for display. The 'A' arrows represent a set of fairly consistent SST-solar relations that occur in 8 out of 9 cycles. The 'B' arrows indicate an additional relationship that holds prior to 1925.

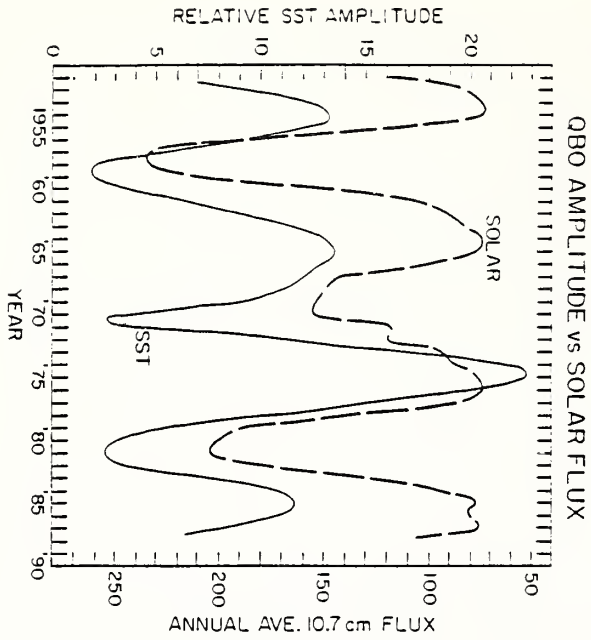

Fig. 1

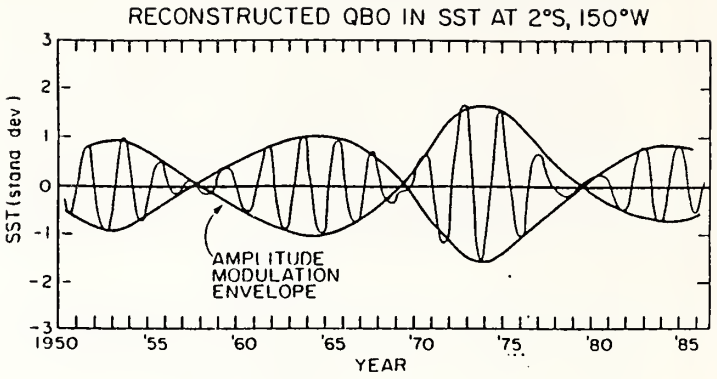

Fig. 2

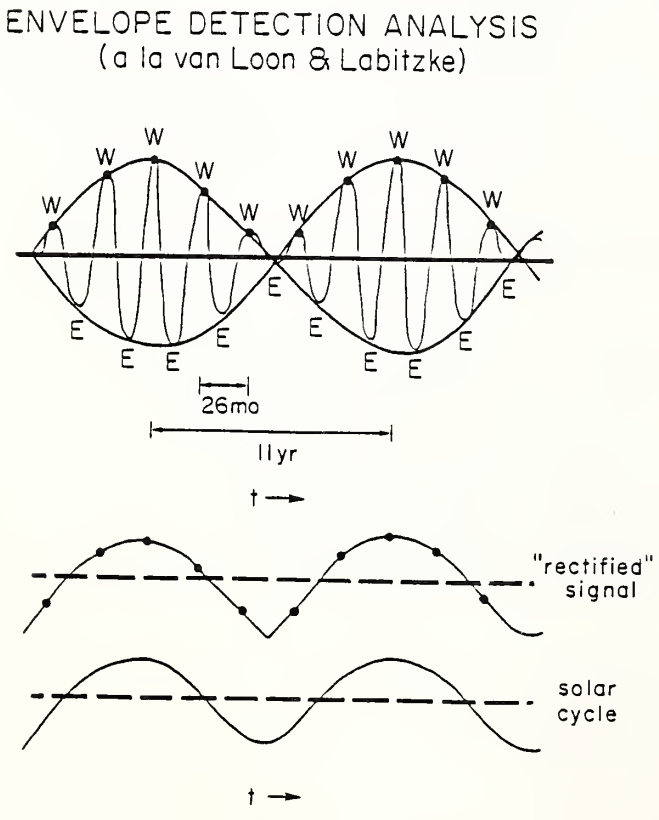

Fig. 3

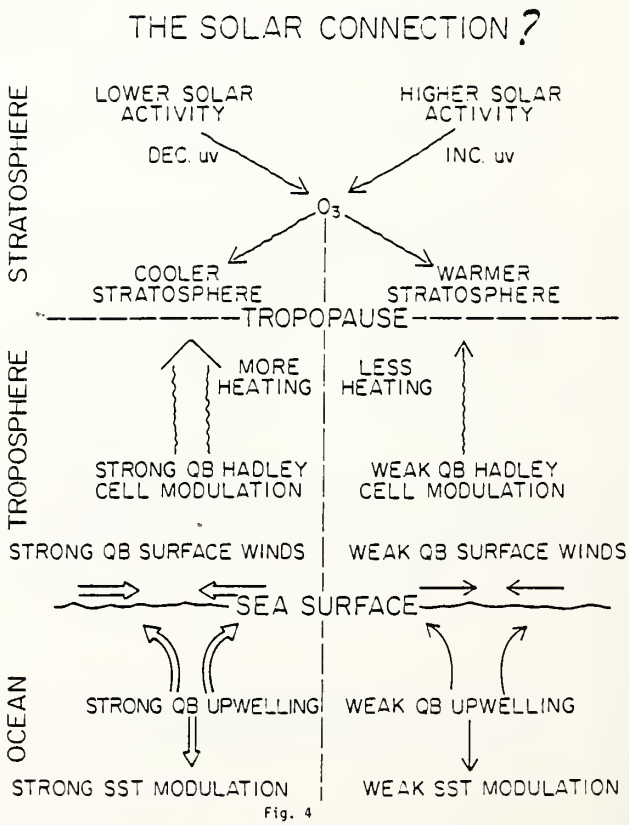

Fig. 4

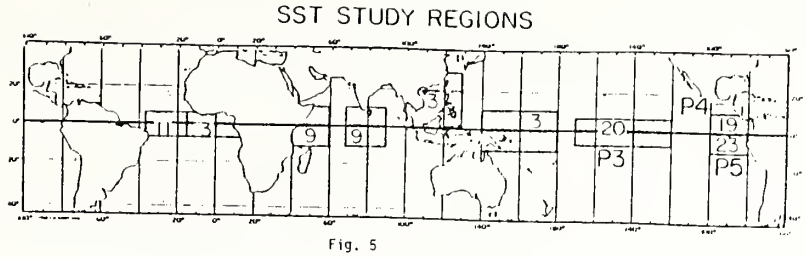

Fig. 5

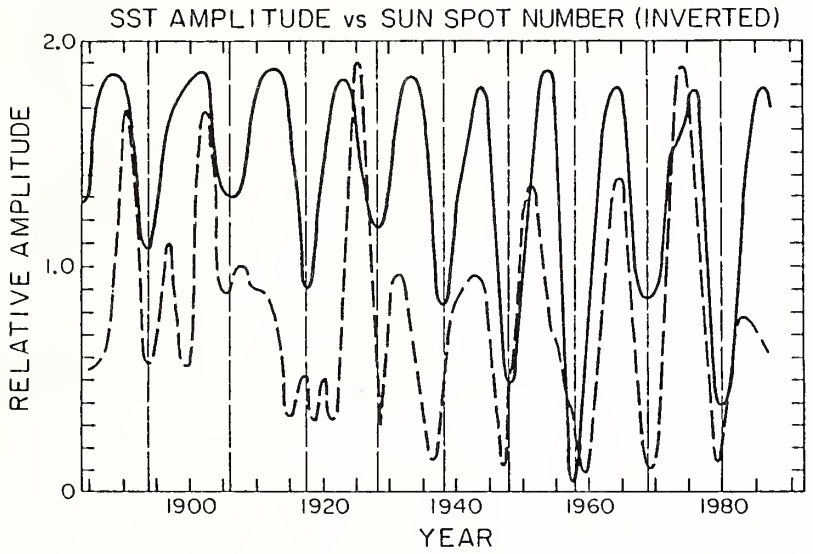

Fig. 6

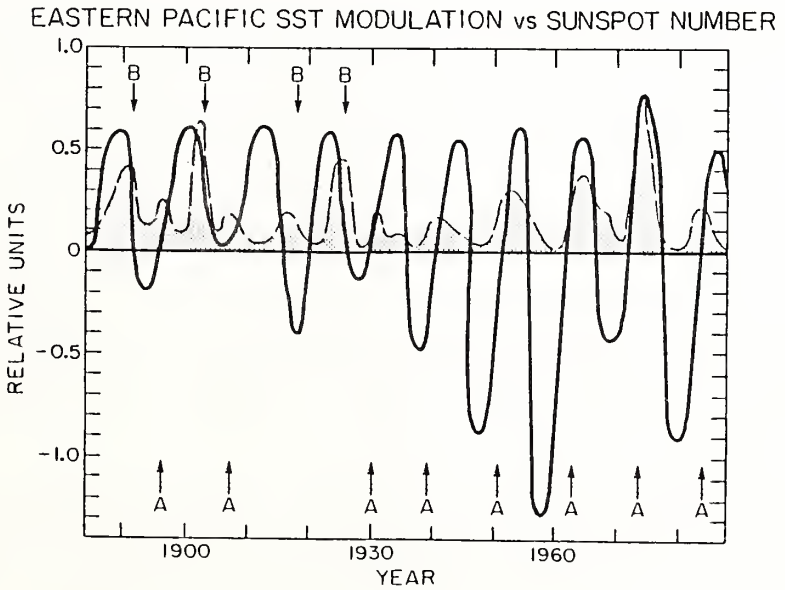

Fig. 7

An evaluation of an association between the 11-year solar cycle, the QBO, and the atmosphere

A. G. Barnston and R. E. Livezey

NWS/NMC/Climate Analysis Center
Washington, D. C. 20233

This study examines further a recently discovered association between the 11-year solar cycle and the atmosphere that is most easily detectable when the two phases of the Quasi-Biennial Oscillation (QBO) are considered individually rather than pooled.

Documentation of a solar cycle-QBO-atmosphere relationship in Northern Hemisphere winter began for the stratosphere near the North Pole (Labitzke, 1987) and was subsequently extended throughout the extratropical Northern Hemisphere for the lower stratosphere and middle troposphere (Labitzke and van Loon, 1988), and finally for the lower troposphere and the surface (van Loon and Labitzke, 1988). The latter paper reported highly statistically significant QBO-stratified solar cycle-atmosphere relationships at a number of locations; these involved surface air temperature, sea level pressure and geopotential height. The present study examines the global statistical significance of the overall spatial pattern of the solar-atmosphere relationship for the extratropical Northern Hemispheric 700 mb height and for U.S. surface temperature. Only the January-February 2-month mean relationships are considered here.

The data used in this study include the QBO phase (east or west) as determined by the average of the 50 and 40 mb average equatorial zonal wind (Naujokat, 1986), the 10.7 cm solar flux, U.S. surface temperature, and 700 mb geopotential height from 20^{o}N northward. January-February 2-month means were derived. The period of record is limited to 1952-88 because QBO data are unavailable before 1952. The QBO goes through one cycle in slightly longer than two years; the solar flux does so in about 11 years, resulting in an availability of somewhat more than 3 solar cycles for the study. Stratification by the QBO phase yields sample sizes of 20 and 17 years of Jan-Feb data for the west and east phases, respectively.

The first step in our study was to reproduce the findings of van Loon and Labitzke (1988) regarding the correlation between the solar flux and both the 700 mb height and the U.S. surface temperature for the west and east QBO phases. Figs. 1 and 2 give the correlations with 700 mb height, while Figs. 3 and 4 do likewise for U.S. surface temperature. All four figures represent a satisfactory reproduction of the van Loon and Labitzke results, although the relationships here are slightly weaker, perhaps because 1988 data are included or because the data sources are not identical. The correlations for the unstratified, 37-year data sets are considerably weaker than the stratified ones, but more will be said about the 37-year flux-height correlation map below. The west phase flux-height correlation map (Fig. 1) has several strong centers, and is reminiscent of the Tropical/Northern Hemisphere and the North Atlantic Oscillation patterns of low frequency variability as depicted using rotated principal components in Barnston and Livezey (1987). The statistical significance of this resemblance will be discussed below. The east phase flux-height correlation map (Fig. 2) also has noticeably strong centers and resembles certain documented modes of low frequency variability.

The map of correlation between flux and U.S. surface temperature for the west QBO phase (Fig. 3) shows moderately strong negative correlations in much of the eastern, southern midwestern and southern central sectors of the country. The east phase map (Fig. 4) reveals a weaker relationship pattern with a small area of moderately strong positive correlations in the Southern Rockies.

The method of testing of the global (or field) significance of the flux-height and flux-temperature correlation maps is now described. A t-statistic is calculated at each of the 358 grid points of Northern Hemisphere flux-height correlation coefficient (r) and at each of the 92 grid points of U.S. flux-temperature correlation coefficient. These local t values are calculated as $t=[r^2(N-2)/(1-r^2)]^{1/2}$, where N is the number of independent time points. Because the solar flux is strongly autocorrelated and the temperature and height are moderately correlated with the flux at some grid points, the number of independent time points at such points is less than the number of years in the sample. The effective time between independent samplings is estimated using a modified version of a formula used in Davis (1976):

$$N=NY/(1 + 2 \sum_{l=1}^{N-3} w\ CFF_l CXX_l)$$

where NY is the unreduced temporal sample size (i.e., 20 years for west QBO phase), l is the lag in years, CFF_l and CXX_l the autocorrelations of the flux and of variable X (e.g., height or temperature) at lag l, and w is a weighting factor that damps results as a linear function of l to reduce the effects of sampling errors at large l where fewer pairs of data are available to autocorrelate. The denominator is called the integral time scale, which exceeds 1 when the variables tend to have like-signed autocorrelations over the range of l. For the 37 years of flux vs. height data, the integral time scale is near 1 year over about two-thirds of the map, but peaks at approximately 4 years in three locations: (1) eastern Alaska/north-central Canada, where west phase correlations are quite high, (2) western Atlantic near 30°N, where west phase correlations are quite strongly negative, and (3) eastern Pacific, where west phase correlations are moderately negative. The integral time scale for flux vs. U.S. surface temperature is somewhat comparable, with an area in the eastern U.S. having peak values close to 4, corresponding to the strongest negative correlations of west phase flux vs. temperature.

The occurrence of the longest integral time scales in regions of strongest flux-height (or flux-temperature) correlations appropriately diminishes values of t in those regions. Because east and west phase analyses already contain data from essentially every two years, only locations with integral time scales of greater than 2 are of concern. As an approximation to a more exact but unknown adjustment (since the above formula provides only rough estimates), locations with integral time scales of 3 or more were sampled only once for every two possible time points, resulting in one data point every 4 years and a 50% reduced N.

The field significance test statistic is simply the average of the t values over all grid points of the map. Before averaging, however, the t value at each grid point was converted to a z value (i.e., the t value for an infinitely large sample) having equivalent significance. (For example, a t value of 2.306 for a correlation derived from 10 time points, or 8 degrees of freedom, would be converted to 1.960.) This was done so that equal t's would represent equal significances, given that N is only half as large at certain grid points as at most others. This average t field significance test statistic differs from that discussed in Livezey and Chen (1983) in that it represents an integrated significance level using the local t values themselves rather than a count of how many of them exceed a given local significance threshold such as 0.05. The latter (Livezey and Chen) procedure is perfectly suitable when the distribution of local significances is reasonably smooth. The average t, however, includes more information about the local significance levels (e.g., "near misses" or extremely high significances) and thus can more accurately evaluate irregularly shaped distributions of local significance. Since our data have considerable spatial dependence, Monte Carlo simulations rather than the binomial are required to define the random or "no effect" distribution. The integrated t test

statistic as well as a local significance count were employed; the former was chosen as the primary evaluation method.

Monte Carlo simulations were carried out in which the QBO phase assignments were randomly shuffled with respect to year. 2000 iterations were run: 1000 for "odd" time points at locations having high integral time scales, and 1000 for "even" time points. (At the other locations, all time points were used in all cases.) The result using actual data was ranked among the random runs, and the fraction of random runs not exceeded (i.e., the field significance) was found. Results are shown in Table 1.

Table 1

P-values for correlation maps, with respect to QBO phase assignment

QBO Phase	N. Hemisphere 700 mb height	U.S. surface temperature
west	.002	.057
east	.016	.397
joint (E,W)	.004	.023

Note that results for 700 mb height vs. solar flux are highly significant for both QBO phases. The joint result (for getting both east and west phase results as observed) has only about one chance in 250 of occurring by chance. For the U.S. surface temperature correlation pattern the east phase shows no effect while the west phase barely misses the customary 0.05 significance level. The joint result is significant, however, which lends more credence to the west phase result. When the field significance test statistic was a count of the number of local significances at the 0.05 level (Livezey and Chen, 1983), generally stronger field significances resulted, including a 0.037 significance for west phase temperature.

Another approach to the field significance tests was used, in which the correlation coefficients at all grid points were simply squared and summed for comparison with Monte Carlo simulations with random QBO phase assignments. This method was not complicated by explicit autocorrelational considerations. Again, results were generally stronger than those in Table 1, including a 0.029 p-value for west phase temperature.

Monte Carlo tests using the integrated t statistic were also carried out where instead of shuffling the QBO phase assignment to create the "no effect" distribution, the solar cycle phase was randomly assigned without destroying the general shape and autocorrelational properties of the cycle. Thousands of cycles containing realistic amplitudes, periods and shapes were simulated. Resulting field significances are given in Table 2. Note that now the all-years condition could be tested.

Table 2

P-values for correlation maps, with respect to solar cycle phase and shape

QBO Phase	N. Hemisphere 700 mb height	U.S. surface temperature
west	.068	.011
east	.024	.073
joint (E,W)	.001	.014
all (no stratif)	.521	.245

The all-years condition fails the field significance test for height and temperature, which agrees with the van Loon and Labitzke (1988) assertion that a relationship is only detectable for QBO phase-stratified data. For the stratified samples the p-values are highly significant for joint results, and either significant or nearly significant for the results for the individual QBO phases. One should be aware that these individual phase results might become stronger if a relatively small lead or lag were introduced into the observed data (which has not yet been looked into), and also that the power of this significance test is less than that for the QBO phase shuffle test because the latter has more diverse permutations than the flux phase and shape shuffle test. The results of these latter tests, then, generally corroborate those of the QBO phase assignment Monte Carlo significance tests.

To help define the morphology of the flux-atmosphere correlation pattern for the two QBO phases, additional significance tests were carried out for the correlation between the solar flux and the amplitude of the 10 leading January-February rotated principal component loading patterns. Table 3 lists these correlations and also shows significant p-values for Monte Carlo significance tests where either the QBO phase assignment is shuffled (no asterisk) or the phase and shape of the solar flux is shuffled (has asterisk).

Table 3

Correlation between solar flux and 700 mb rotated principal component mode
(p-value follows if <0.05)

Mode		Percent Variance	West QBO Phase	East QBO Phase	No Stratification
1	PNA	11.8	-.10	.38	.13
2	NAO	10.3	.35 (.03)	-.28	.05
3	WPO	10.0	.06	-.00	.03
4	TNH	9.1	.48 (.02)	-.06	.23
5	---	7.7	.02	.56 (.05)	.26
6	EA	7.5	.26	-.02	.09
7	EU1	7.0	.28 (.04)	-.33 (.04)	.03
8	NA	6.0	.04	.03	.03
9	EU2	6.0	-.04	-.24	-.15
10	EP	5.9	-.48	-.68 (.02)*	-.59 (.03)*

Several noteworthy results are found. For the west QBO phase the Tropical/Northern Hemisphere (TNH) pattern principal component is correlated 0.48 with the flux (explaining 23% of the variance), significant at the 0.02 level; for the North Atlantic Oscillation (NAO) the corresponding figures are 0.35 (12%) and 0.03. The Eurasian Pattern No. 1 (EU1; Barnston and Livezey, 1987) has a significant but low correlation. For the east QBO phase the principal component of an unclassified pattern involving the Pole and parts of Eurasia correlates 0.56 with the flux (explaining 31% of variance), and the EU1 pattern shows a systematic relationship--this time in the opposite direction to that of the west QBO phase.

An interesting finding arises regarding the East Pacific (EP) pattern. Note that with all other patterns the correlation values are either of opposite sign for the west vs. east QBO phase, or are of like sign with one of them close to zero. The East Pacific pattern, by contrast, has a moderately strong correlation of the same (negative) sign for both QBO phases. In this case the QBO phase assignment shuffle Monte Carlo test does not produce significant results because the east and west

phases do not differ from one another sufficiently. When the flux phase (and shape) is shuffled, though, the observed case stands out significantly against the large set of random phase settings for both the east QBO phase and, uniquely, for the no stratification condition. This last finding suggests that the solar flux may impart a signal, as detected by the rotated principal component analysis filter, to the Northern Hemisphere extratropical atmosphere that is not modulated by the QBO phase. The no stratification flux-height correlation map is shown in Fig. 5.

In conclusion, the 11-year solar cycle appears to be one of the factors governing the Northern Hemisphere January-February climate. The QBO phase, when dichotomously defined (east vs. west), strongly modulates the relationship, producing separate solar flux vs. 700 mb height correlation patterns possessing globally highly significant strength. For the flux vs. U.S. surface temperature correlation pattern this field significance is limited to the west QBO phase and is close to the 0.05 level. More highly significant flux-temperature relationships undoubtedly exist in other parts of the Hemisphere, especially for the east QBO phase. Without stratification by the QBO phase, none of these overall significant results occur. The flux vs. Northern Hemisphere height correlation pattern for the west QBO phase has the strongest statistically significant resemblance to the Tropical/Northern Hemisphere (TNH) and secondarily to the North Atlantic Oscillation (NAO) rotated principal component patterns (Barnston and Livezey, 1987); for the east QBO phase the resemblance is mostly to certain Eurasian patterns. Without QBO phase stratification, although the overall flux vs. height correlation pattern is not significant, there is a highly significant relationship to the East Pacific (EP) pattern, suggesting the possibility of an overall extratropical manifestation of the solar-atmosphere relation.

Work is underway to extend these findings to other seasons, other averaging periods and to lagged relationships.

References

Barnston, A. G., and R. E. Livezey, 1987: Classification, seasonality and persistence of low-frequency atmospheric circulation patterns. Mon. Wea Rev., 115, 1083-1126.

Davis, R. E., 1976: Predictability of sea surface temperature and sea level pressure anomalies over the North Pacific Ocean. J. Phys. Oceanogr., 6, 249-266.

Labitzke, K., 1987: Sunspots, the QBO, and the stratospheric temperature in the north polar region. Geophys. Res. Lett., 14, 535-537.

_____ and H. van Loon, 1988: Association between the 11-year solar cycle, the QBO, and the atmosphere. Part I: The troposphere and stratosphere on the Northern Hemisphere in winter. J. Atmos. Terres. Phys., 50, 197-206.

Livezey, R. E. and W. Y. Chen, 1983: Statistical field significance and its determination by Monte Carlo techniques. Mon. Wea. Rev., 111, 46-59, 1983.

Naujokat, B., 1986: An update of the observed Quasi-Biennial Oscillation of the stratospheric winds over the tropics. J. Atmos. Sci., 43, 1873-1877.

van Loon, H. and K. Labitzke, 1988: Association between the 11-year solar cycle, the QBO, and the atmosphere. Part II: Surface and 700 mb in the Northern Hemisphere in winter. J. Climate, 1, 905-920.

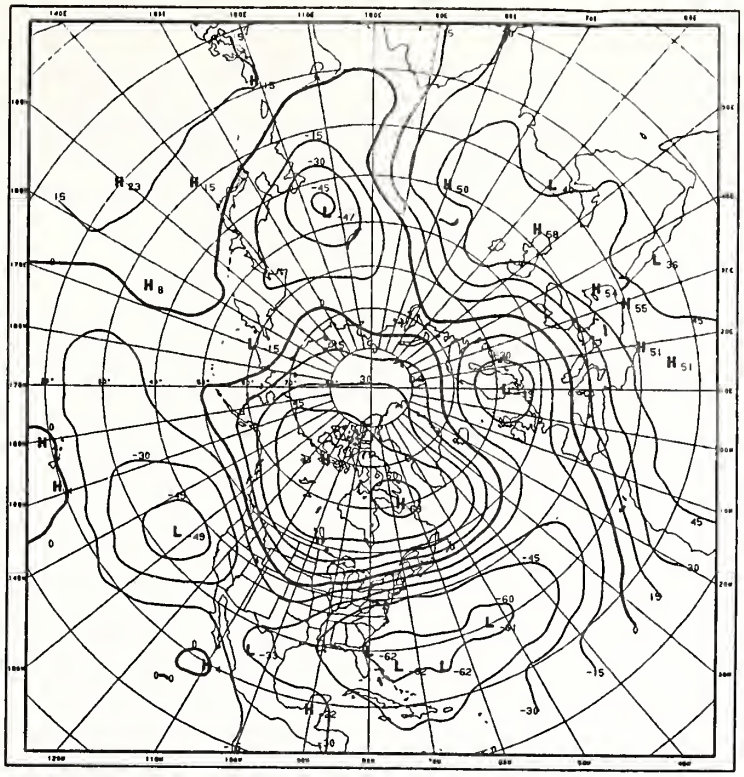

Fig. 1. Jan-Feb correlation between solar flux and 700 mb height for the west QBO phase (20 years).

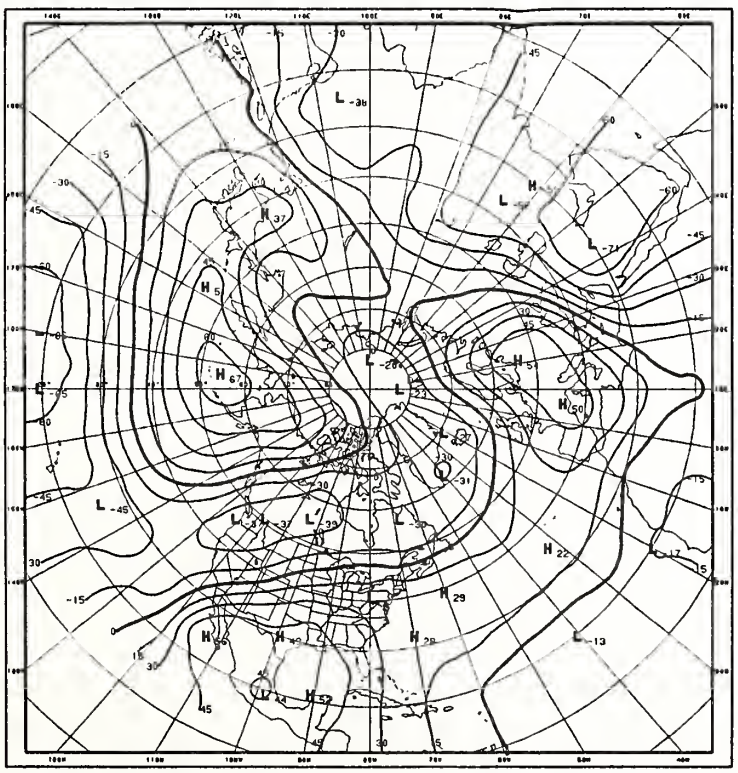

Fig. 2. As in Fig. 1 except for east QBO phase (17 years).

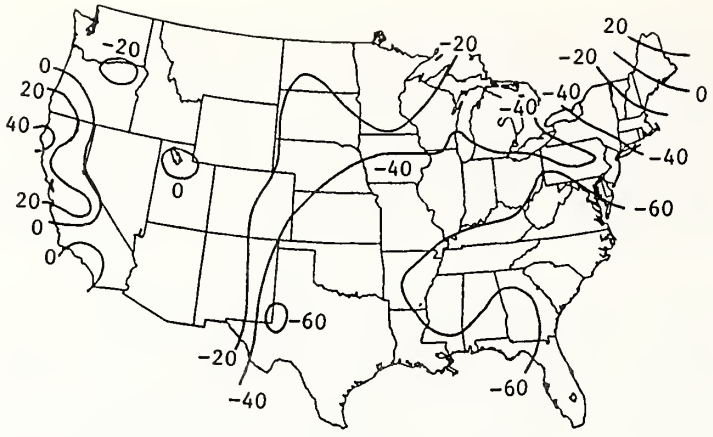

Fig. 3. Jan-Feb correlation between solar flux and surface temperature for the west QBO phase (20 years).

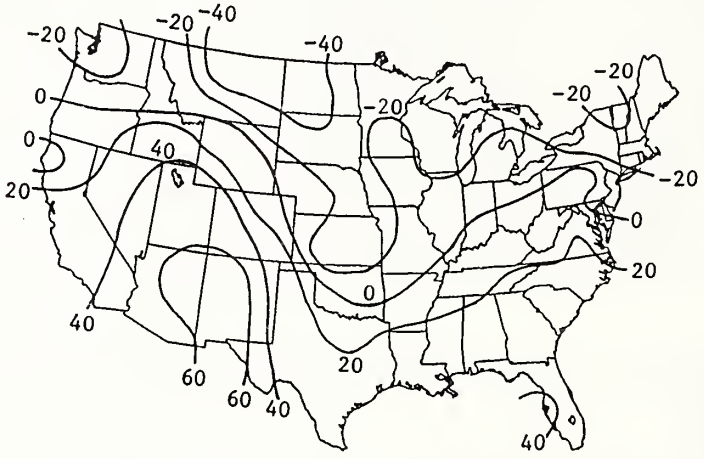

Fig. 4. As in Fig. 3 except for east QBO phase (17 years).

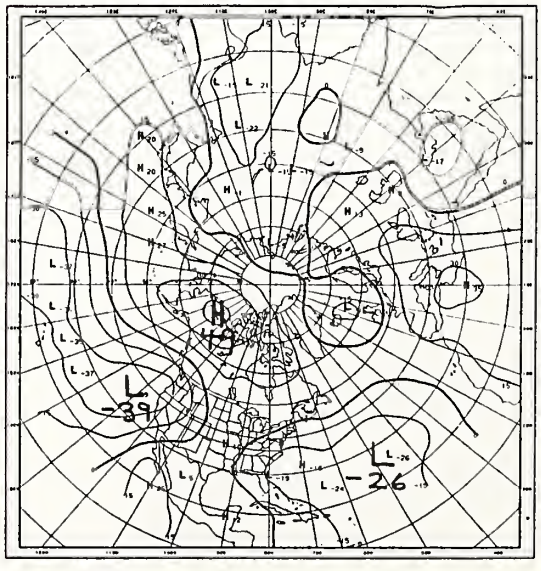

Fig. 5. As in Figs. 1 and 2 except for both QBO phases (37 years).

ANNUAL AND INTERANNUAL VARIATION OF WATER VAPOR TRANSPORT

Tsing-Chang Chen/Department of Geological and
Atmospheric Sciences, Iowa State University Ames, IA 50011

1. INTRODUCTION

The latent heat released by tropical cumulus convection is a major agent in driving low-latitude circulations, in supplying energy to balance the radiative cooling, and to support circulations of middle and high latitudes. However, the cumulus convection is maintained by the water-vapor supply. For this reason, the global water-vapor budget analysis becomes an indispensable step in understanding the atmospheric climate. As for the climate change, the tropics are important because responses of the atmosphere to changes of sea-surface temperature near the equator can have a significant influence on the atmosphere extending to latitudes far from the tropics. The most pronounced short-term climate problem of this sort is the El Nino-Southern Oscillation (ENSO) phenomenon which is an interannual variation of atmospheric circulation responding to the anomalous warm surface water over the central and/or eastern Pacific. However, before attempting to probe the interannual variability of the atmospheric climate system, an understanding of the climatological mean annual cycle is necessary. If we can determine the average annual cycle, we can more confidently describe the year-to-year variations from the mean. Therefore, an effort of investigating the annual and interannual variation of global water-vapor transport and their relationship with cumulus convection is needed. To accomplish this goal, the operational data of the National Meteorological Center (NMC) from January 1979 to December 1986 are used.

2. Data and Computations

The data used in this study are derived from the NMC global data produced by the Global Data Assimilation System (GDAS). The specific humidity was computed in terms of temperature and relative humidity with the scheme described in Chen et al. (1985). The horizontal resolution of both the NMC and OLR data are 2.5^{0} (lat.) x 2.5^{0} (long.). Since this study deals with the annual and interannual variations of global water-vapor transport, only the month-by-mean data are used. Note that the water-vapor transport is computed daily.

The precipitable water, W, and water vapor transport, Q, were computed and integrated from 1000 to 500 mb. According to Chen (1985), the water-vapor transport can be separated into rotational (Q_R) and divergent (Q_D) components,

$$Q = Q_R + Q_D \quad . \tag{1}$$

Moreover, these two water-vapor transport components can be expressed in terms of the streamfunction, ψ_Q, and potential function, χ_Q,

$$Q = \hat{k} \times \nabla\psi_Q + \nabla\chi_Q \quad . \tag{2}$$

Note that only the divergent component of the water-vapor transport contributes to the water balance equation, i.e.,

$$\frac{\partial w}{\partial t} + \nabla \cdot Q_D = E - P \,. \qquad (3)$$

The empirical orthogonal function (EOF) analysis was applied to the χ_Q and ψ_Q departure from their 8-year averages to extract out the annual variation mode of χ_Q and ψ_Q fields. Their annual variation anomalies were constructed with the eigenvector and eigencoefficient time series which exhibit pronounced annual variation. The vectors of Q_R and Q_D anomaly fields were obtained from horizontal gradients of the ψ_Q and χ_Q anomaly fields as indicated by Eq. (2). On the other hand, the interannual variations of ψ_Q and χ_Q fields were obtained first by removing the multi-year average, and the annual and semiannual components at each grid point by the simple harmonic analysis of ψ_Q and χ_Q in time. Then, the EOF analysis was applied to the residual ψ_Q and χ_Q fields. To express the interannual variation of global atmospheric water-vapor budget, the same procedures used in the annual variation analysis was adopted.

3. Annual Variation

The variance explained by the first three principal eigenmodes of various physical variables are displayed in Table 1. The first principal eigenmodes of W and χ_Q are exclusively dominant ones. As indicated by their fractional variances, which are larger than 90%, the first principal eigenmodes of these variables are annual variation component. The first principal eigenmode of ψ_Q which explains 38.8% of total variance (Table 1) is not the only annual variation component. The second and third principal eigenmodes of ψ_Q, which explain 26.8% and 7.6% of total variance (Table 1), respectively, should also be included as the annual cycle component.

We shall superimpose the seasonal-mean W anomalies of the annual variation mode on the divergent water-vapor transport of this mode to illustrate how the former is supported by the latter. To accomplish this goal, we constructed the annual variation mode of these variables in the physical domain by multiplying eigencoefficients of the annual variation mode with the corresponding eigenvector. In order to demonstrate the seasonal shift of annual variation component, the 8-year averages of OLR and W superimposed on the divergent water-vapor transport are displayed, respectively, in the bottom panel of Fig. 1.

The large precipitable water appears in the tropics, especially over three tropical continents where deep cumulus convection exists. As suggested by Chen (1985), Fig. 1c shows that the precipitable water is converged toward tropics, particularly three tropical continents by planetary-scale divergent circulation, e.g., east-west Walker and local Hadley circulations.

Shown in Fig. 1 are three maxima and minima of W annual variation

components on each side of the equator. Compared to 8-year mean fields with these maximum and minimum centers, it is revealed that there are major seasonal shifts of global W over the maxima and minima of their annual cycle. To maintain these centers, the water vapor is diverged out from the minimum centers of W in the winter hemisphere by the annual variation mode of divergent water-vapor transport. Chen et al. (1988) showed that the annual variation mode of the planetary-scale divergent circulations converge air mass in the lower troposphere from the winter to summer hemisphere and then return in the upper troposphere in the opposite sense, particularly over three tropical continents. Based upon Chen's (1985) suggestion and the annual cycle mode of the planetary-scale divergent circulations portrayed by Chen et al. (1988), it is conceivable that the annual variation mode of planetary-scale divergent circulations are responsible for the water-vapor transport maintaining centers of large precipitable water and cumulus convection.

Since the rotational component of water-vapor transport does not contribute to the maintenance of W centers [see Eq. (3)], we shall only highlight its interesting features. Let us first deal with the 8-year mean fields displayed in Fig. 2c:

- Three anticyclonic gyres of water-vapor transport are associated with oceanic anticyclones.

- In the tropics, centers of the minimum OLR (Fig. 5c) and maximum W (Fig. 6c) are located in the downstream sides of trades where they encounter tropical continents. The only exception is over the Indian Ocean. The center of maximum W located at the region from eastern Indian Ocean adjacent to the Malaysia Peninsula is in the downstream side of the Indian oceanic gyre.

The winter and summer averages of Q_R annual variation component can be depicted as follows:

- The Q_R annual variation component is anticyclonic in the summer hemisphere, but cyclonic in the winter hemisphere. By combining the 8-year mean and annual variation component, we can see that the water-vapor transport by oceanic anticyclones of the summer hemisphere is intensified, while that of the winter hemisphere is weakened.

- As inferred from the Q_R annual variation component, the annual variation of water-vapor transport in the Northern Hemisphere is much more significant, especially over the monsoon region.

- In the summer hemisphere, W maxima of the annual variation component usually exist over tropical continents where anticyclonic gyres of the Q_R annual variation component

meet them. Conversely, W minima and of this component appear over continents where cyclonic gyres of the Q_R annual variation component exit.

4. Interannual Variation of Water-Vapor Transport

According to Quiroz (1983) and Kousky (1987), two ENSO episodes occurred in this decade: 1982-83 and 1986-87. Based upon the sea-surface temperature (SST) anomaly over the eastern equatorial Pacific (EEP), the 1982/83 ENSO event, whose seasonal EEP SST anomaly reached about 4°C, was the strongest warm event up to the present time. Our pursuit of the interannual variation of water-vapor budget focused on the time period between 1981 and 1986.

Heddinghaus and Krueger (1981) used the EOF analysis to investigate the interannual variation of the outgoing longwave radiation. Following the same approach, we adopt three criteria to determine the interannual variation component of water vapor transport in the EOF analysis:

1. The eigencoefficient time series of any eigenmode selected should closely follow the SOI of Climate Analysis Center (CAC) of the National Meteorological Center.
2. The eigencoefficient values of a given eigenmode should be significant during the Negative Southern Oscillation Phase, i.e., warm event of ENSO, in addition to significant variance explained by this eigenmode.
3. The structure of the anomaly eigenvector (or eigenvectors) should resemble that of the anomaly field itself.

Based upon these criteria, the eigenmodes of various variables selected to show the interannual variation of global water vapor transport are exhibited in Table 2. To obtain a physical picture of how the nonseasonal W anomaly associated with the 1982/83 ENSO is maintained in terms of the water vapor budget analysis, we shall map the interannual variation modes of W on those of χ_Q and ψ_Q in the physical domain.

Recall that during the normal northern winter the upward branch of the east-west Walker circulation of the Asian monsoon is located over the maritime continent. Lau and Chan (1983) suggested that this upward branch is shifted eastward with the anomalous warm water to the eastern Pacific and the direction of east-west Walker circulation is reversed. The downward branch becomes situated in the western Pacific. Of course, this anomalous circulation would cause the anomalous convergence (divergence) of large-scale water-vapor transport over the eastern (western) Pacific during the ENSO event. This expectation is consistent with Rasmusson and Carpenter's (1982) argument that the enhancement of large-scale water vapor convergence occurs over the eastern Pacific where the enhanced convection exists.

The superimposition of W (Fig. 3a) anomalies on (χ_Q,Q_D) anomalies clearly reveals that the low-level divergent circulation anomalies during the 1982-83 ENSO event diverges water vapor out of the western Pacific and converges it toward the eastern Pacific, as observed by Rasmusson and Carpenter for several

ENSO events. Thus, the anomalous divergence of water vapor flux makes the western Pacific drier, while the anomalous convergence of water vapor flux makes the eastern Pacific wetter. In turn, the cumulus convection is suppressed over the former region, but enhanced over the latter region. Note that the nonseasonal W anomalies extend from the eastern Indian Ocean, across the Africa continent, to the west coast of this continent as the OLR anomalies depicted by Quiroz (1983). A convergence anomaly of water vapor flux, shown in Fig. 3, maintains the large W anomalies.

The nonseasonal (ψ_Q,Q_R) anomalies shown in Fig. 3b for the 1982-83 northern winter exhibit patterns similar to low-level circulation anomalies (Quiroz, 1983). Q_R is responsible for the major water-vapor transport but not for the balance of the water-vapor sink (P) or source (E). However, Fig. 3b reveals that the water vapor is transported from the western Pacific, where it becomes drier, to the eastern Pacific by the westerly anomalies and to the Indian Ocean and equatorial Africa by the easterly anomalies. The positive nonseasonal W anomalies appear in the downstream sides of both the westerly and easterly anomalies, which originate from the western Pacific and radiate to both oceans, respectively.

Acknowledgments

This study was partly supported by the NSF Grant ATM-8611476 and NOAA Grant NA87AA-D-AC044. Thanks go to Ms. Reatha Diedrichs for her typing. The computations for this study were performed on the CRAY-1 and XMP supercomputer of the National Center for Atmospheric Research, which is sponsored by the National Science Foundation.

References

Chen, T.-C., 1985: Global water vapor flux and maintenance during FGGE. Mon. Wea. Rev., 113, 1801-1819.

_____, C.-B. Chang, and D. J. Perkey, 1985: Synoptic study of a medium-scale oceanic cyclone during AMTEX'75. Mon. Wea. Rev., 113, 349-361.

_____, R.-Y. Tzeng, and M.-C. Yen, 1988: Development and life cycle of the Indian monsoon: Effect of the 30-50 day oscillation. Mon. Wea. Rev., 116, 2183-2199.

Heddinghaus, T. R., and A. Krueger, 1981: Annual and interannual variations in outgoing longwave radiation over the tropics. Mon. Wea. Rev., 109, 1208-1218.

Kousky, V. E., 1987: The global climate for December 1986-February 1987: El Niño returns to the tropical Pacific. Mon. Wea. Rev., 115, 2822-2838.

Lau, K.-M., and P. H. Chan, 1983: Short-term climate variability and atmospheric teleconnections from satellite observed outgoing longwave radiation. Part I: Simultaneous relationships. J. Atmos. Sci., 40, 2735-2750.

Quiroz, R. S., 1983: The climate of the "El Niño" winter of 1982-83 - A season of extraordinary climatic anomalies. Mon. Wea. Rev., 111, 1685-1706.

Table 1. Variance (VE) explained by the first three eigenmodes of W, χ_Q, and ψ_Q, and fractional variance (FV) explained by annual (12-month) and semiannual (6-month) harmonics of these first three eigenmodes. VE and FV are expressed in terms of percentages (%). The maximum phases of significant components are denoted by (month/day), i.e., parenthesized numbers following FV.

			FV %	
Variable	Eigenvector	VE(%)	12-mo.(phase)	6-mo.(phase)
	1	62.6	97.9 (7/21)	0.4
W(40°S-40°N)	2	12.8	1.4	5.2
	3	3.8	29.1	10.6
	1	72.1	91.4 (7/4)	0.8
χ_Q(50°S-50°N)	2	9.1	9.7	9.2
	3	7.6	0.6	35.7
	1	38.8	39.3 (7/1)	20.9
ψ_Q(60°S-65°N)	2	26.8	55.8 (7/5)	2.2
	3	7.6	69.9 (3/27)	9.0

Table 2. Variance explained by significant nonseasonal eigenmodes of W, χ_Q, and ψ_Q nomalies, in which multiyear mean, annual, and semiannual variation components were removed, and which have significant values of eigencoefficients during 1982-83 winter.

Variable	Eigenvector	Variance (%)
W (40°S-40°N)	1	26.3
	2	12.4
χ_Q (50°S-50°N)	1	39.5
	5	6.0
ψ_Q (60°S-65°N)	2	7.4

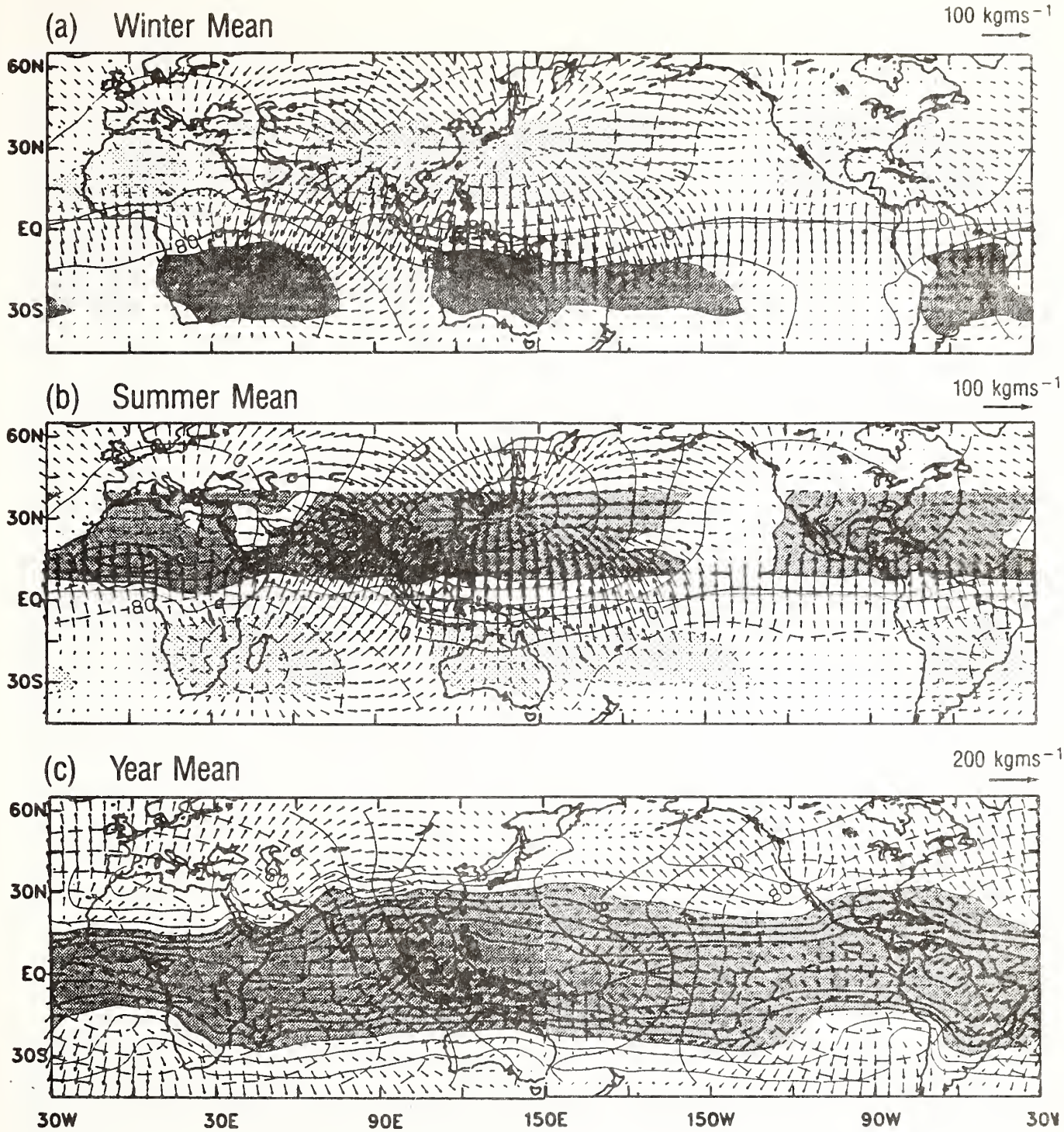

Fig. 1. Same as Fig. 3, except the OLR field itself and its anomalies are replaced by the W field itself and its anomalies. They are contoured with intervals of 5 kg m^{-2}. The areas with W anomaly $\geq$5 kg m^{-2} are lightly shaded, while those with W anomaly $\geq$5 kg m^{-2} are heavily shaded. The 8-year averaged W is contoured by thin solid lines with intervals of 5 kg m^{-2}. The areas with W$\geq$30 kg m^{-2} are heavily shaded.

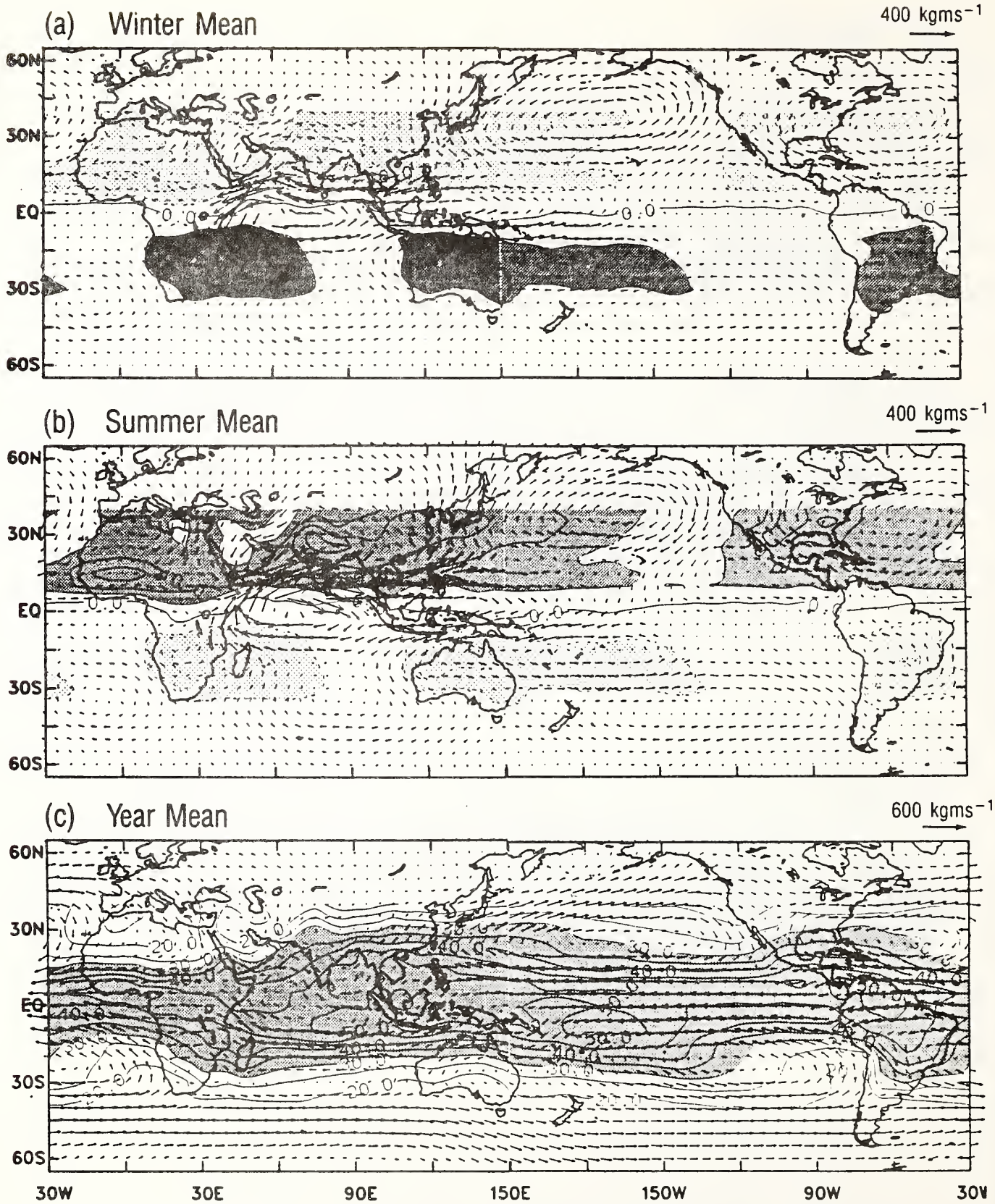

Fig. 2. Same as Fig. 4, except (χ_Q,Q_D) are replaced by Q_R.

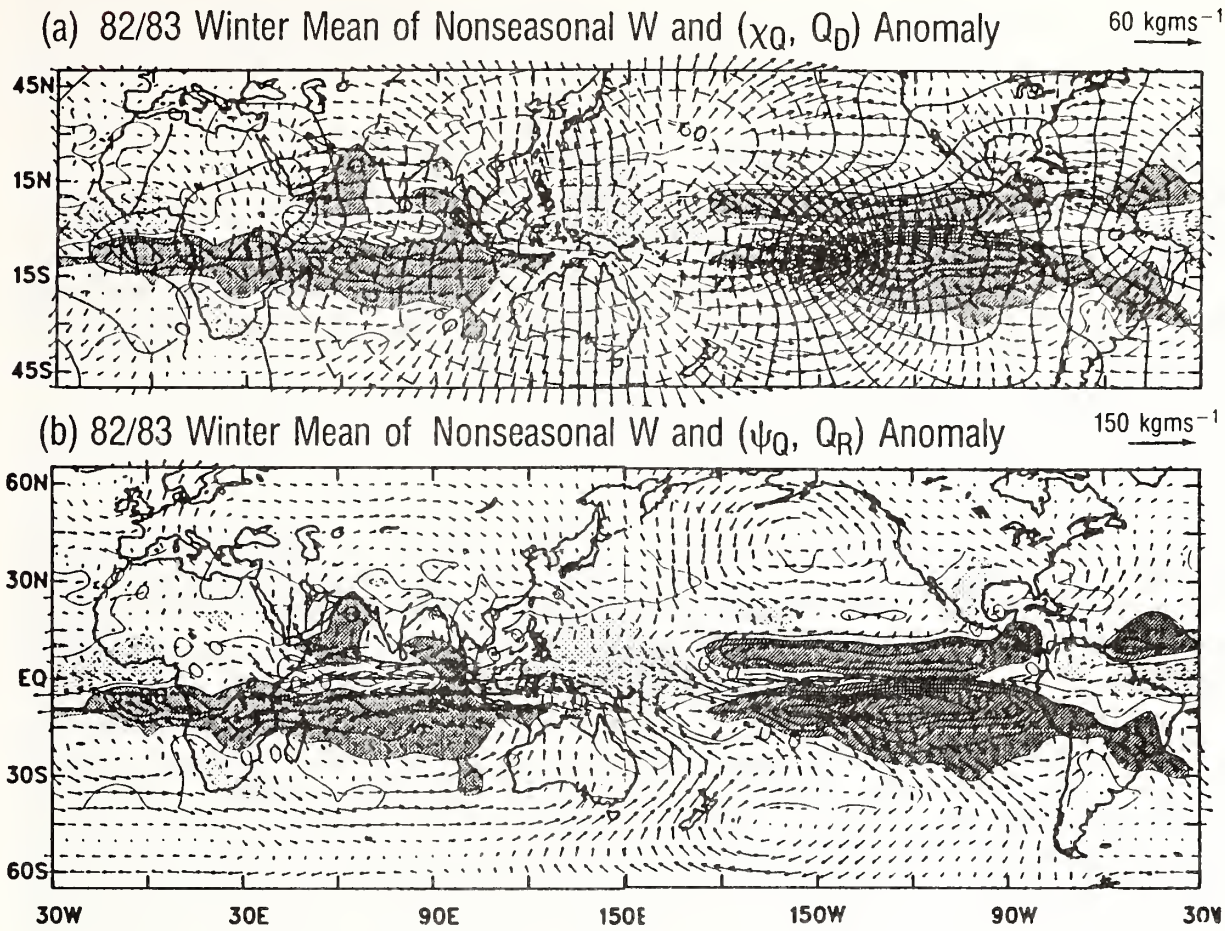

Fig. 3. (a) The constructed W and (χ_Q,Q_D) anomaly fields of the interannual variation component with eigenmodes 1 and 5 of the nonseasonal χ_Q anomaly and eigenmodes 1 and 2 of the nonseasonal W anomaly. The χ_Q anomaly field is contoured by thick solid (positive-value) and dashed (negative-value) lines with intervals of 15×10^6 kg ms^{-1}. The W anomaly field is contoured by thin solid (positive-value) and dashed (negative-value) lines with intervals of 2.5 kg ms^{-1}. The areas with W anomaly $\leq$-2.5 kg ms^{-1} are lightly shaded, while those with the OLR anomaly $\geq$2.5 kg^{-2} ms^{-1} are heavily shaded. (b) The constructed W and (ψ_Q,Q_R) anomaly fields of the interannual variation component with eigenmode 5 of ψ_Q.

Variability of Surface Wind Stress Over the Oceans

J. G. Olson and K. E. Trenberth
National Center for Atmospheric Research*
Boulder, Colorado 80307

An accurate knowledge of sea surface wind stresses is important for both observational and modeling studies of the ocean since wind stress is a primary driver of the world's ocean currents. Likewise, an accurate assessment of atmospheric momentum loss through sea surface wind stresses aids in a better understanding of the atmospheric momentum budget and its evolution. However, "measurements" of wind stress over the global oceans are inherently difficult because 1) stress is not a directly measurable quantity by conventional means; it must be derived from other meteorological parameters and 2) spatial and temporal data coverage is not good, particularly over the SH oceans.

Seven years (1980–1986) of monthly mean wind stresses have been computed on a 2.5° × 2.5° grid based upon the twice-daily 1000 mb wind analyses from the European Centre for Medium Range Weather Forecasts (ECMWF). Despite uncertainties of up to 5 m s^{-1} in the wind speed over portions of the NH oceans and much of the SH oceans south of 30°S (Trenberth and Olson, 1988) these analyses provide much better coverage and possibly more accurate estimates of the true wind speeds over the oceans than in previous studies of wind stress. Although 1000 mb is not a "surface" (10 m) level, prior to 9 September 1986, ECMWF routinely analyzed surface ship observations at the 1000 mb level with essentially no corrections for height and the analyzed 1000 mb wind was, in fact, a better surface wind than the nominal 10 m wind. However, after September 1986 due to modifications in the analysis procedure, the 1000 mb winds were no longer a valid proxy for the surface winds. Therefore in this study, computations of wind stress climatologies such as the annual and seasonal means and the annual cycle are based upon results from January 1980–August 1986. The wind stress calculations were adjusted for stability based upon monthly air-sea surface temperature difference climatologies and surface relative humidity climatologies derived from an analysis of 80 years (1900–1979) of COADS observations.

Stresses were computed based upon the bulk aerodynamic method such that:

$$\tau_x = \rho C D |\vec{V}| u \,, \qquad \tau_y = \rho C D |\vec{V}| v$$

where τ_x and τ_y are the stresses in the zonal and meridional directions, respectively, ρ is the air density, CD is the nondimensional drag coefficient, $|\vec{V}|$ is the 10 m wind speed and u and v are the east-west and north-south components of the wind, respectively. From Monin-Obukhov similarity theory, CD is an elaborate function of wind speed, lapse rate, and vertical moisture differences and was determined for each point based on formulae from Large and Pond (1981, 1982). Figure 1 depicts several examples of CD versus wind speed for various lapse rates (moisture considerations not included). As stability, measured

* The National Center for Atmospheric Research is sponsored by the National Science Foundation

by $\Delta T = T_s - T_a$, increases (ΔT becomes more negative), the drag coefficient decreases (light solid lines). Conversely, as stability decreases the drag coefficient increases (light dashed lines). The enhanced buoyancy effects that accompany decreased stability result in greater communication between the sea surface and 10 m level of the atmosphere, thereby enhancing wind stress. However, at high wind speeds, as turbulent mixing begins to dominate, stability plays a less important role and all of the CD profiles in Fig. 1 converge to that of the neutral stability profile (ΔT = 0). The values we have used for C_D are noticeably lower than those of Hellerman and Rosenstein (1983).

Based upon our results, CD has significant spatial and temporal variability. Figure 2 shows a measure of the time mean drag coefficient known as the effective drag coefficient which is a ratio of the time mean magnitudes of the stress and "pseudo-stress":

$$\rho_0 \ CD_{EFF} = \frac{\overline{\rho CD|\vec{V}|^2}}{\overline{|\vec{V}|^2}}$$

where $\rho_0 = 1.2$ kg m^{-3}. Figures 2a and 2b depict CD_{EFF} for NH winter and SH winter, respectively. Goldenberg and O'Brien (1981) suggest a drag coefficient of 1.5×10^{-3} when converting their pseudo-stress results to stress. However, a globally averaged value would appear to be closer to $1.3 - 1.4 \times 10^{-3}$. The tropics and subtropics have typical values of 1.1×10^{-3} to 1.3×10^{-3} while the extratropics can have values as high as 1.8×10^{-3}. A very distinct annual cycle is also evident in the extratropics—especially in the Northern Hemisphere. This is due largely to the dependence of CD on the wind speed which also exhibits an annual cycle. There is very little interannual variability in CD_{EFF}, however. The standard deviation (not shown) of the monthly means about the climatological mean is not much more than 5% of the value of CD in the extratropics and less so in the tropics and subtropics.

A map of the annual averaged stresses (Fig. 3) shows a typical distribution of the wind stress associated with global ocean currents. The circulation around the Icelandic and Aleutian lows generate stresses of 1–2 dynes cm^{-2} while stresses in the tropics are typically 0.2–0.5 dynes cm^{-2}. Stress magnitudes in the region of the Antarctic circumpolar current are roughly twice as large as those exhibited in the NH extratropics with values between 2.0 and 3.5 dynes cm^{-2}. Problems with the stress field which may reflect wind analysis defects are the excessive convergence off the coast of Peru and other details in the tropics.

The curl of the stress field provides insight into various aspects of the internal ocean dynamics, not just surface currents. If the equation of motion (including pressure gradient forces) is integrated over the depth of the ocean with some simplifying assumptions we obtain the Sverdrup relation between surface stresses and the north-south mass transport over the depth of the ocean:

$$M_y \beta = \text{curl}\,(\vec{\tau}),$$

where

$$M_y \equiv \int_{-h}^{0} \rho \, v dz$$

and ρ = density of water, v is the north-south velocity of the ocean current, β is the gradient of the Coriolis parameter with latitude, and h is the depth of the ocean. Furthermore, we can define a horizontal streamfunction based upon this mass transport such that:

$$M_y = \frac{\partial \psi_s}{\partial x}$$

therefore

$$\psi_s(x) = -\int_{x_E}^{x} \frac{\mathrm{curl}(\vec{\tau})}{\beta} dx$$

with the boundary condition that $\psi_s = 0$ on the eastern boundary of ocean basins. Figure 4 depicts the mass transport derived from Fig. 3. Mass transport is parallel to contours of the streamfunction. The circulation inferred from the ψ_s-field in the NH subtropics gives rise to the Kuroshio (Pacific) and Gulf Stream (Atlantic) boundary currents. Results are in general agreement with Harrison (1988) and Hellerman and Rosenstein (1983), although, as expected from the different drag coefficients, the values are slightly less than the latter. The maximum circulation is 50 Sverdrups (1 Sverdrup = 1×10^{12} g s^{-1}) in the subtropical North Pacific and 25 Sverdrups in the corresponding North Atlantic. However, the maximum for the Greenland-Iceland region is about 1/2 of the maxima found in the above-mentioned studies.

The annual cycle of the stresses exhibit several interesting characteristics. Figure 5 depicts time-latitude cross-sections of the zonal component of the stress, zonally averaged across a) all ocean basins, b) the Pacific Ocean, and c) the Atlantic Ocean. The NH exhibits a strong wave 1 in the annual cycle while the SH has a distinct semiannual cycle. The zonal component of the stress is also stronger in the SH (a maximum of 2 dynes cm^{-2}) than in the NH (1.35 dynes cm^{-2}). A comparison of the Pacific (Fig. 5b) and Atlantic (Fig. 5c) basins reveals that the maxima in the Atlantic (both NH and SH) lead those of the Pacific by approximately one month. Similar depictions (Fig. 6) of the zonal average of the stress magnitudes show that the zonally averaged maximum in the NH annual cycle is of comparable strength to that of the SH. However, the amplitude of the NH annual cycle is much stronger. The NH Atlantic basin has a stronger maximum (4 dynes cm^{-2}) than the Pacific (3 dynes cm^{-2}). Note also that the maximum stress in the tropical regions of all ocean basins (Fig. 6a) is approximately 0.3 dynes cm^{-2}. Conventional wisdom holds to a value closer to 0.5 dynes cm^{-2}.

Time series of the monthly mean zonally averaged x-component of the stress are shown in Fig. 7. Particularly evident are the maxima associated with the El Niño events of 1982–1983 and 1986–1987 (Fig. 7a). Zonal averages over the Pacific basin (Fig. 7b) more clearly distinguish these phenomena. Note the reversal of the tropical Pacific easterlies during the 1982–1983 El Niño event.

The wind stress statistics over the southern oceans are believed to be the most reliable available and there are quantitative differences from previous results elsewhere. The main shortcomings with the current results appear to be in the tropics. All the results, including long term and individual monthly means, are archived and available at NCAR.

REFERENCES

Goldenberg, S. B., and J. J. O'Brien, 1981: Time and space variability of tropical Pacific wind stress. *Mon. Wea. Rev.*, **109**, 1190-1207.

Harrison, D. E., 1988: On climatological monthly mean wind stress and wind stress curl fields over the world ocean. *J. Climate*, (to be submitted).

Hellerman, S., and M. Rosenstein, 1983: Normal monthly windstress over the world ocean with error estimates. *J. Phys. Oceanogr.*, **13**, 1093-1104.

Large, W. G., and S. Pond, 1981: Open ocean momentum flux measurements in moderate to strong winds. *J. Phys. Oceanogr.*, **11**, 324-336.

Large, W. G., and S. Pond, 1982: Sensible and latent heat flux measurements over the ocean. *J. Phys. Oceanogr.*, **12**, 464-482.

Trenberth, K. E., and J. G. Olson, 1988: An evaluation and intercomparison of global analyses from the National Meteorological Center and the European Centre for Medium Range Weather Forecasts. *Bull. Amer. Meteor. Soc.*, **69**, 1047-1057.

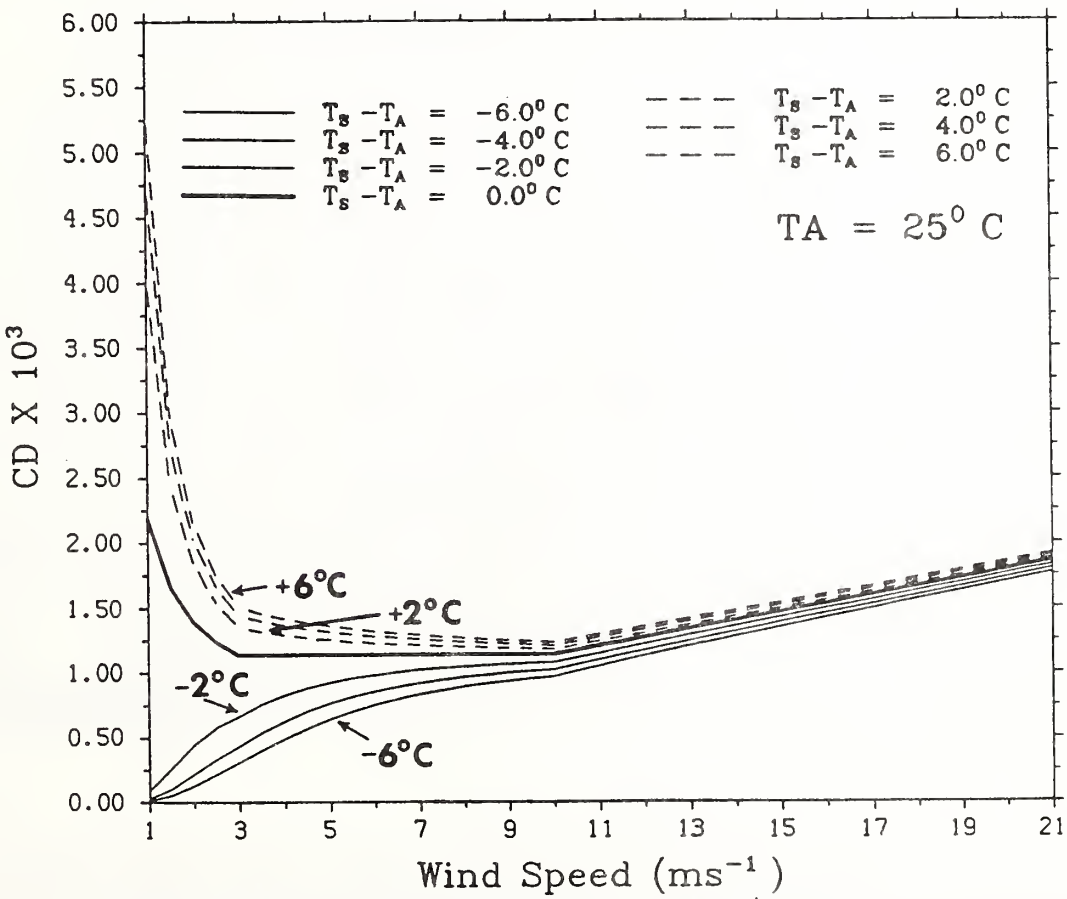

Fig. 1. Drag coefficient ($\times 10^3$) as a function of wind speed (m s^{-1}) for various air–sea surface temperature differences. Light solid lines, $\Delta T < 0$; dark solid line, $\Delta T = 0$; dashed lines, $\Delta T > 0$.

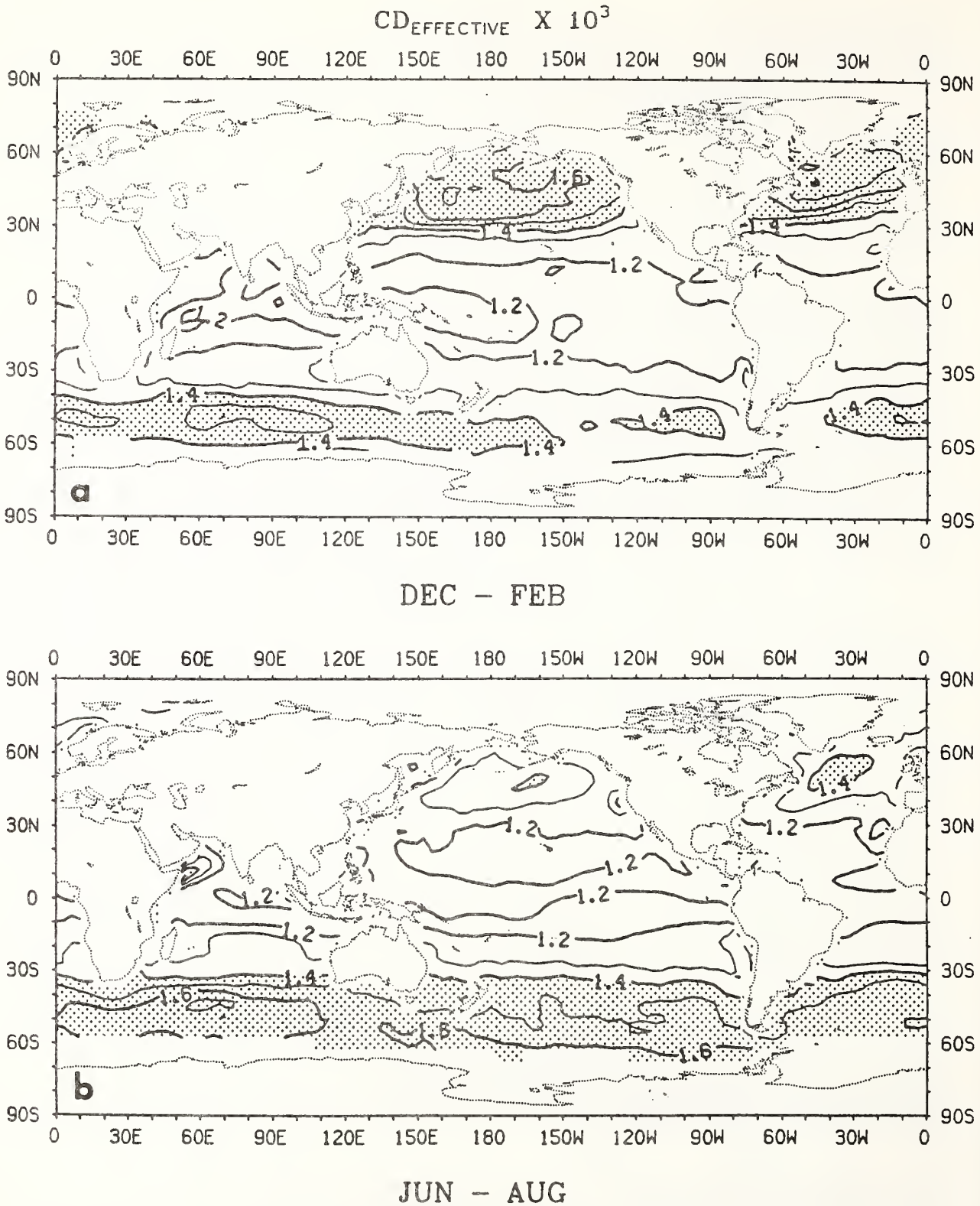

Fig. 2. Effective drag coefficient ($\times 10^3$) for a) December–February and b) June–August climatologies. The contour interval is 0.1×10^{-3}. Regions greater than 1.4×10^{-3} are stippled.

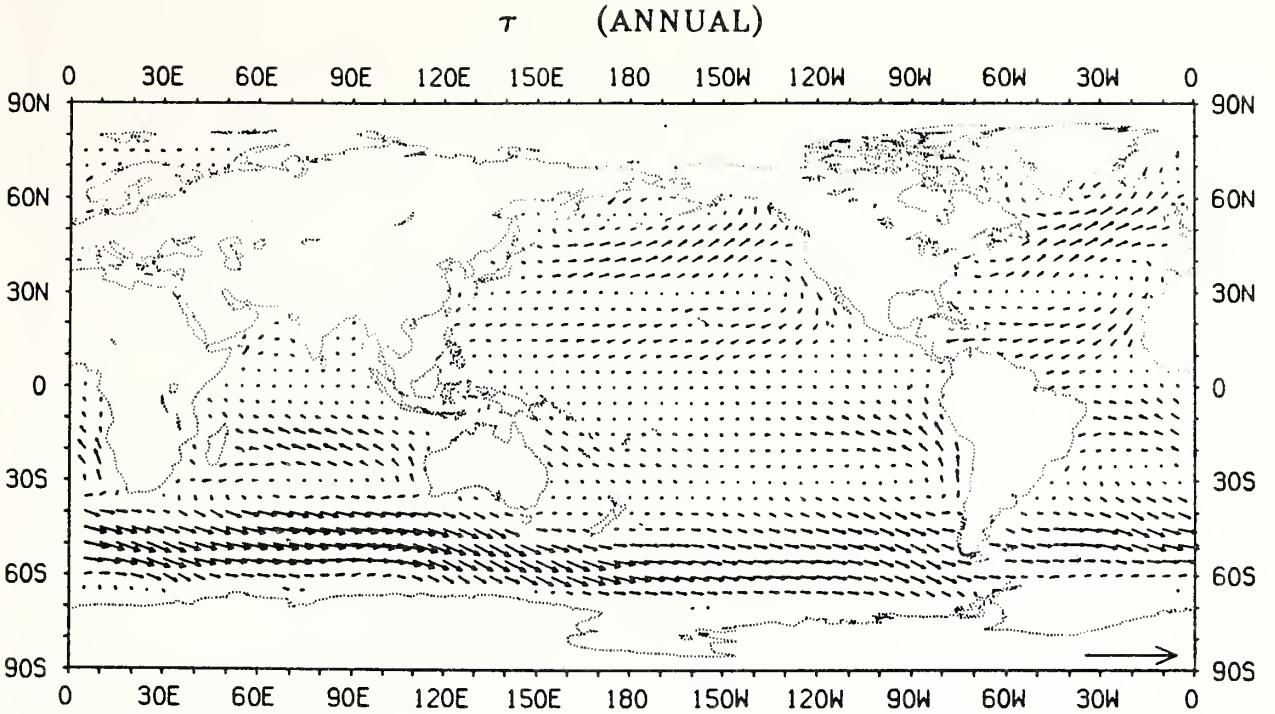

Fig. 3. Annual averaged surface stress vectors (for the period 1980–1986) over the oceans. Vector length is proportional to stress magnitude; reference vector (lower right corner) = 10 dynes cm^{-2}.

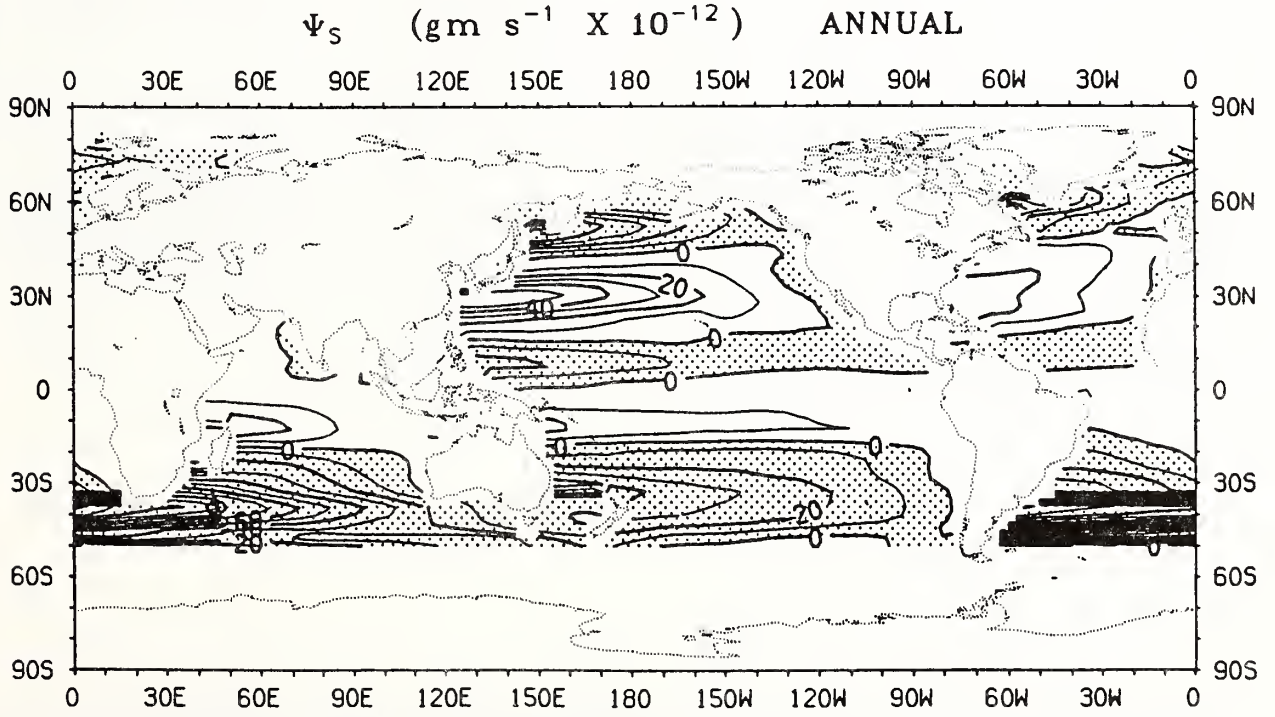

Fig. 4. Annual averaged Sverdrup transport streamfunction. The contour interval is 10 Sverdrups; negative regions are stippled.

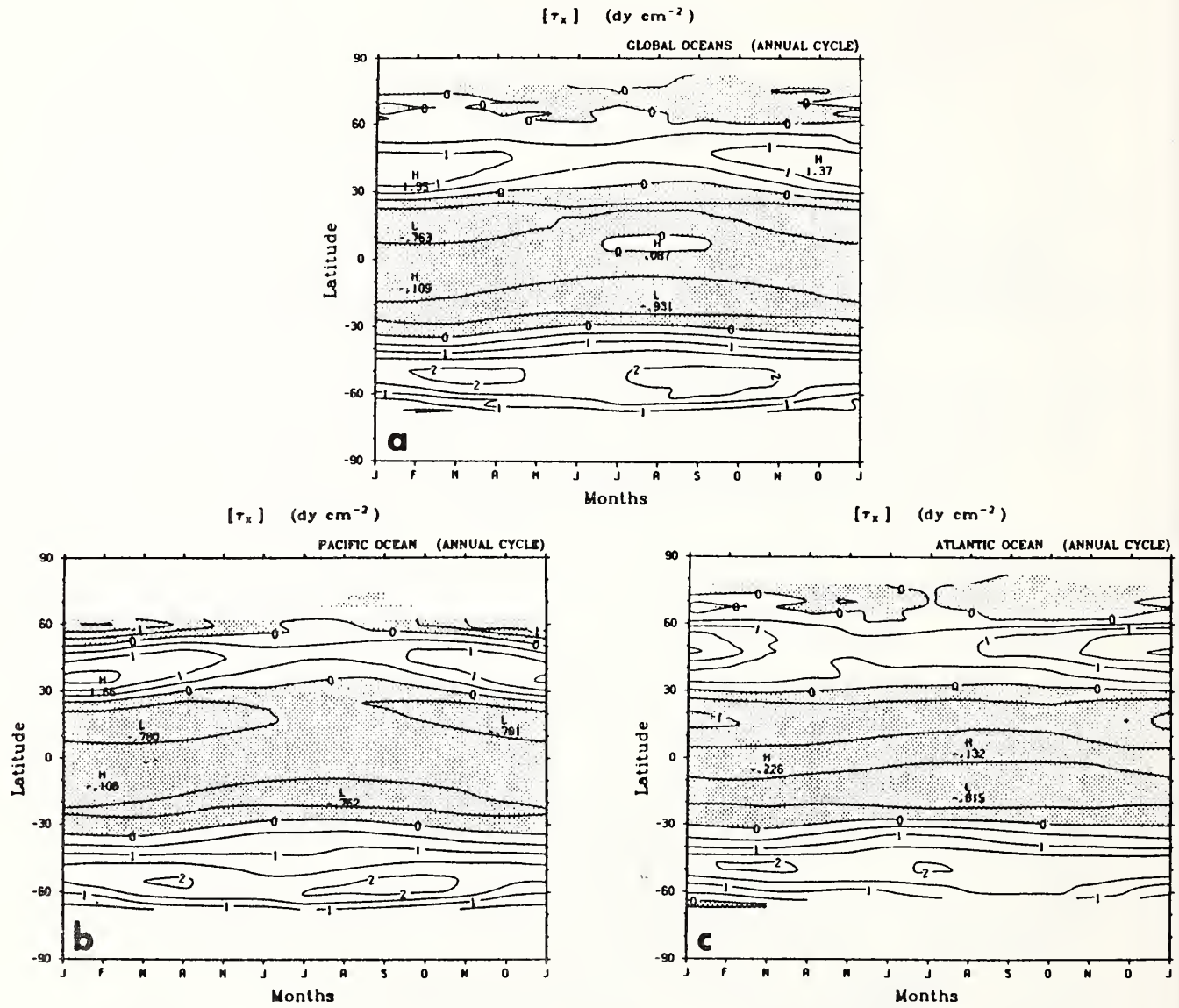

Fig. 5. Annual cycle of the zonally averaged zonal component of the stress as a function of month and latitude for a) global oceans, b) Pacific Ocean and c) Atlantic Ocean. Smoothed using 3-month running mean. The contour interval is 0.5 dynes cm^{-2}; easterlies are stippled.

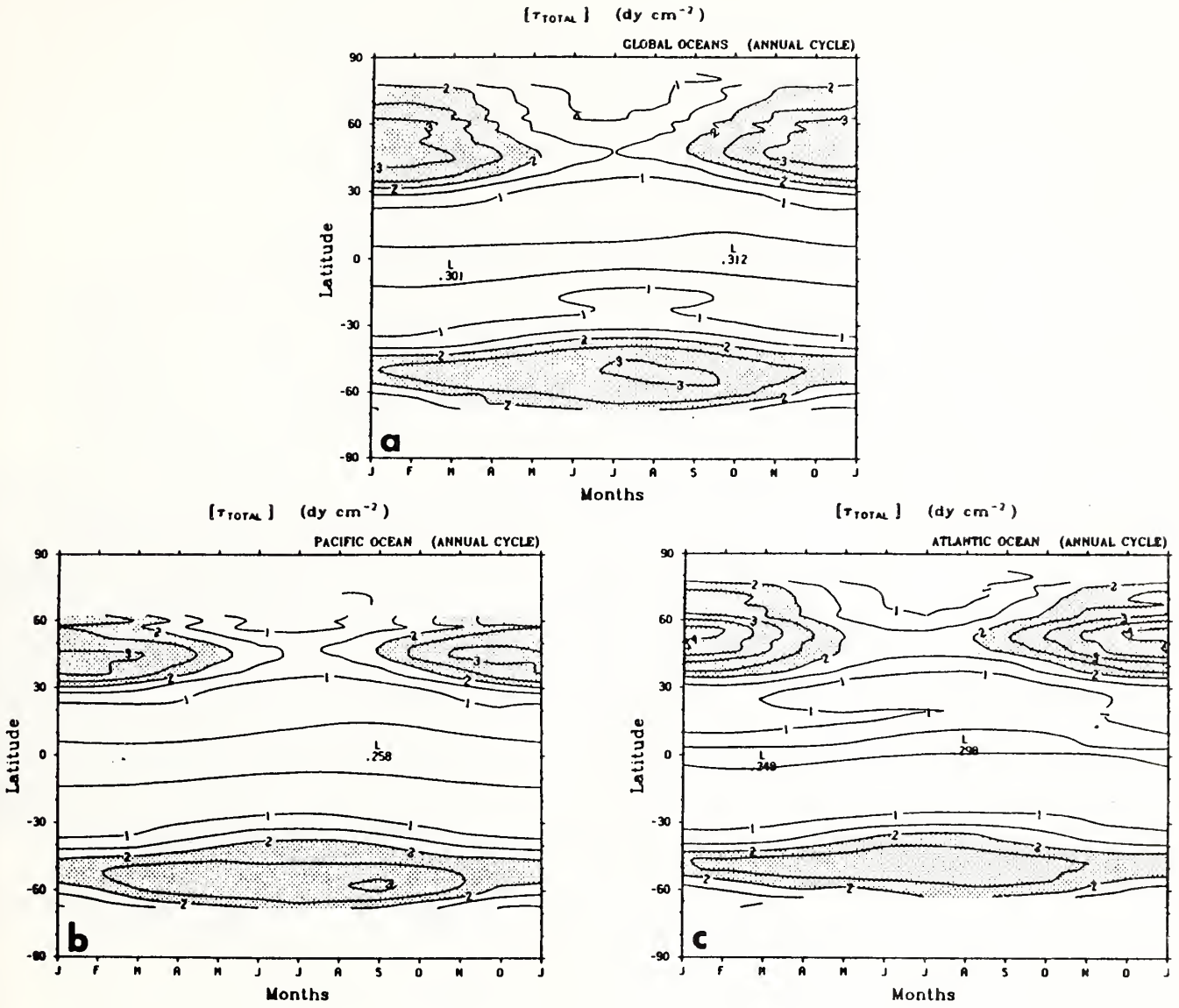

Fig. 6. Same as Fig. 5 except for the magnitude of the stress. Values greater than 2 dynes cm^{-2} are stippled.

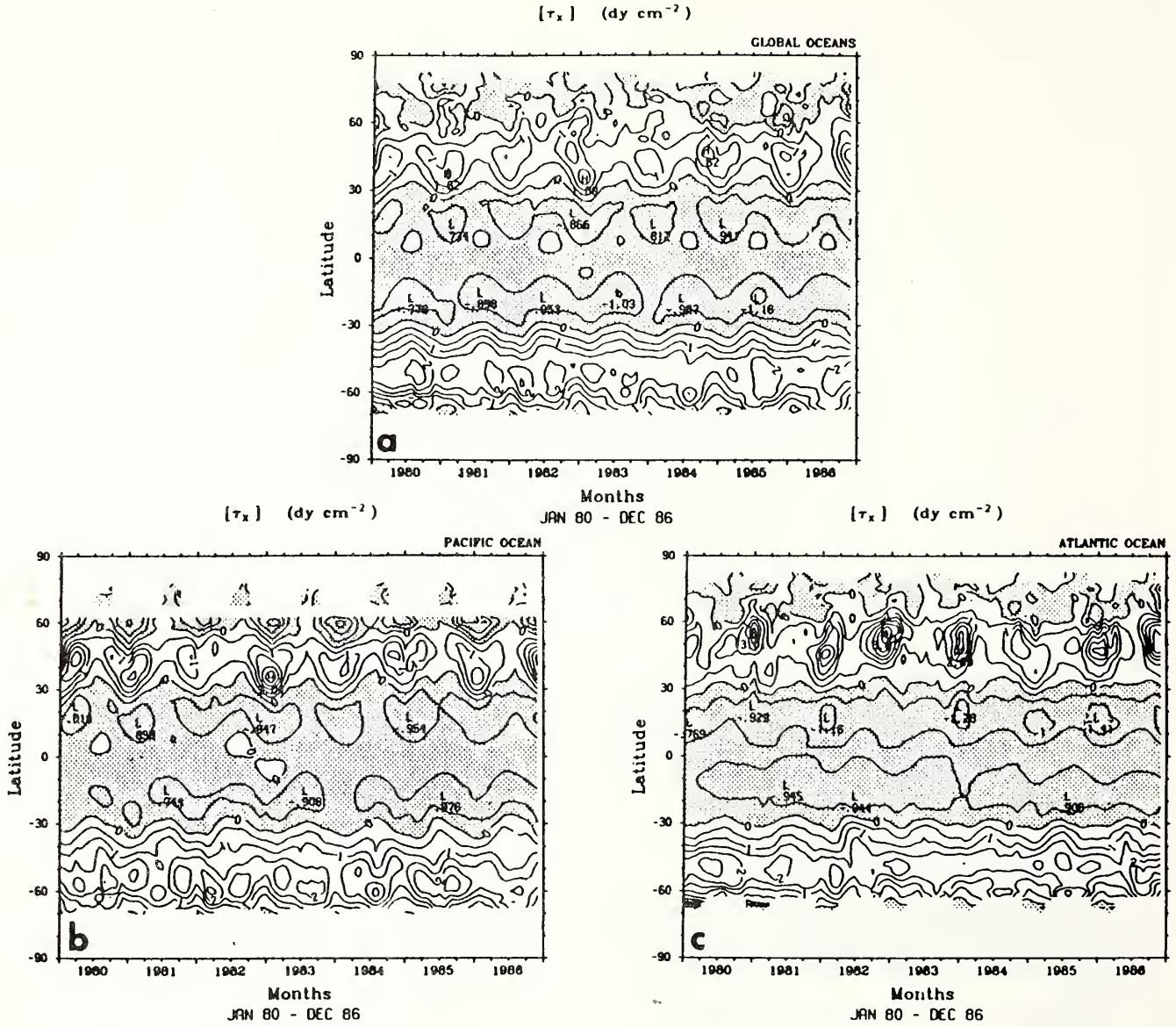

Fig. 7. Time series of the monthly mean zonally averaged zonal component of the stress as a function of time and latitude for a) global oceans, b) Pacific Ocean and c) Atlantic Ocean. Smoothed using 3-month running mean. The contour interval is 0.5 dynes cm^{-2}; easterlies are stippled.

Climatology of west wind bursts in the equatorial western Pacific and their relationship to El Nino

Mark L.Morrissey
Mark A. Lander

Department of Meteorology
University of Hawaii
2525 Correa Rd.
Honolulu, HI 96822

It is well recognized that the El Nino is a complex air-sea interaction process. In a generally favored hypothesis, strong synoptic-scale (one to two week) westerly wind bursts generate large amplitude oceanic Kelvin waves in the Equatorial Western Pacific (EWP). These waves act to advect warm water eastward along the equator and suppress the thermocline, thus, directly and indirectly producing anomalously high sea surface temperature (SST) in the central and eastern Pacific.

The effect of equatorial west wind bursts on low-frequency SST variations in the central and eastern Pacific has been described theoretically. It has been speculated that these bursts occur prior to El Nino onset and thus, may be responsible for its initiation. However, the existence of precursor signals in the EWP have yet to be firmly established.

The time and space structure of the surface wind in the EWP has only recently been investigated. Unfortunately, island reporting stations in the EWP with adequately long records are relatively sparse (Fig. 1). Ship observations which could be utilized to supplement island reports are scant except within a north-south swath of concentrated ship traffic along 155^{o}E (hereafter referred to as the EWP ship track). Many problems have been attributed to ship data. In a recent study, however, we have concluded that ship-observed winds along 155^{o}E, when suitably averaged, are as good or better a measure of the synoptic-scale surface wind flow than are measurements made from the island transect. Standard error estimates indicate that spatially averaged zonal and meridional wind along the ship track can resolve monthly fluctuations greater than 2.5 and 1.5 m s^{-1}, and 3-day fluctuations of 4 m s^{-1} and 2.5 m s^{-1}, respectively.

If anomalous equatorial westerlies act to initiate EL Nino they must occur at least 1-3 months prior to the onset of the anomalous sea surface warming off the west coast of South America. This lag is consistent with the trans-Pacific travel time of first or second baroclinic mode Kelvin waves. The existence of such precursors should be detectable with ship wind along 155^{o}E. We present the initial results of an investigation utilizing monthly and 3-day averaged data along the EWP ship track from 1959 through 1985.

Anomalous monthly mean equatorial westerlies are frequently observed along the EWP ship track throughout the period of record (Fig. 1). However, the consistent pattern of strong and persistent westerly and southerly anomalies during the boreal spring and summer, as shown in the composite of 4 major El Nino events (Fig. 2), signal the occurrence of major El Nino events. This pattern can be described as anomalous double trough conditions during April(0) and May(0), and the subsequent anomalous eastward extension of the Northern Hemisphere monsoon trough through September(0). The consistency of this pattern suggests that the character of EWP surface wind be used to diagnose major El Nino conditions.

With the exception of 1983-82 El Nino, anomalous monthly mean westerlies along 155^{o}E were not found to precede anomalous eastern Pacific sea surface warming. Positive anomalies of 3-day averaged zonal wind occur quasi-randomly throughout the period of record (Fig. 3), as do positive anomalies of the 3-day change in the zonal wind (Fig. 4). This, together with Harrison's (1987) results using EWP island wind along 175^{o}E, suggests that there are no identifiable precursor signals in the EWP surface wind.

The probable absence of precursor signals in the EWP leads one to again question the cause of El Nino. Perhaps the gradual buildup of the heat content of the upper layers of the ocean reaches a threshold value where, after several years, it can be released in the form of oceanic Kelvin waves triggered by bursts of equatorial westerlies which normally occur in the EWP during November and December. Or perhaps the onset of El Nino is the result of large-scale changes involving the Southern Oscillation where equatorial westerlies act to maintain the event.

Whatever the onset mechanism, it is clear from observational and modelling studies that variations in the EWP surface wind play an important role in the air-sea interaction processes associated with El Nino. Thus, these variations should be further detailed so that they may be better incorporated into conceptual models.

Reference

Harrison, D.E., 1987: Monthly mean island surface winds in the central tropical Pacific and El Nino events, Mon. Wea. Rev., 115, 3133-3145.

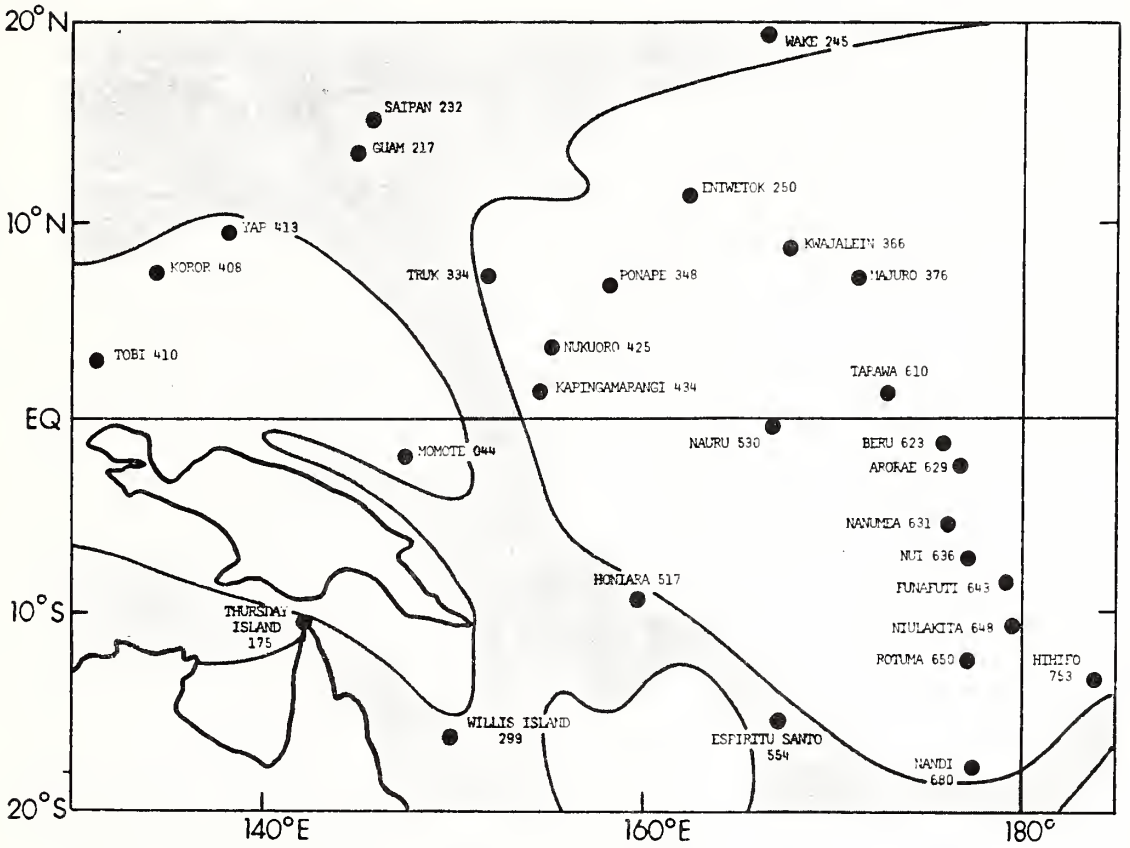

Fig. 1. Distribution of COADS ships and locations of island stations in the western Pacific. Shading indicates ship density greater than ten per month per 2° x 2° boxes after 1945.

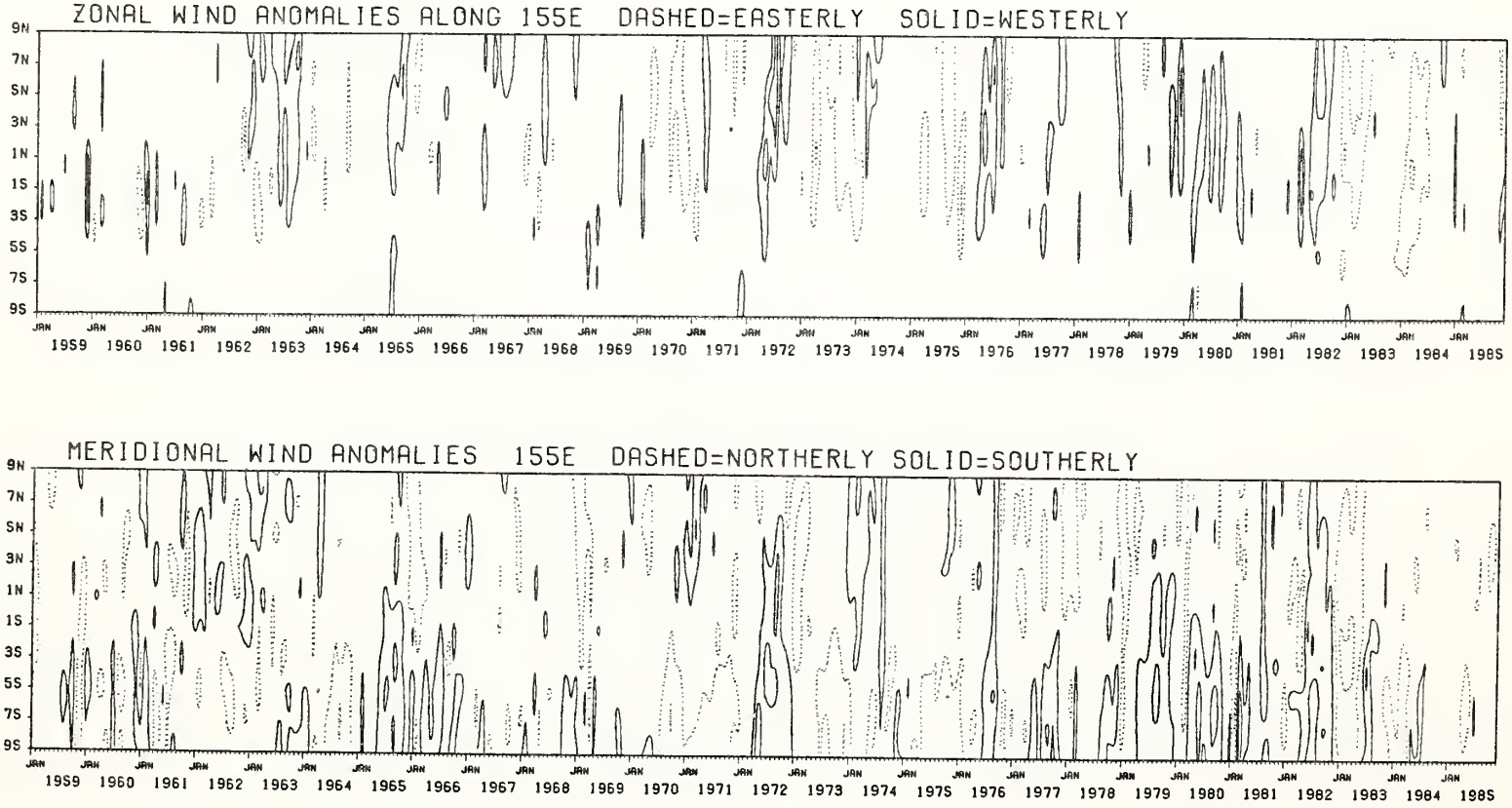

Fig. 2. Time-latitude depeiction of the anomalies of the zonal (top) and meridional (bottom) components of the monthly mean surface wind along 155^{o}E. Contour intervals are: 2 ms^{-1} beginning with $\pm$ 2 ms^{-1} (top) and 2 ms^{-1} beginning with $\pm$ 1 ms^{-1} (bottom). The zero wind-speed line has been omitted for clarity.

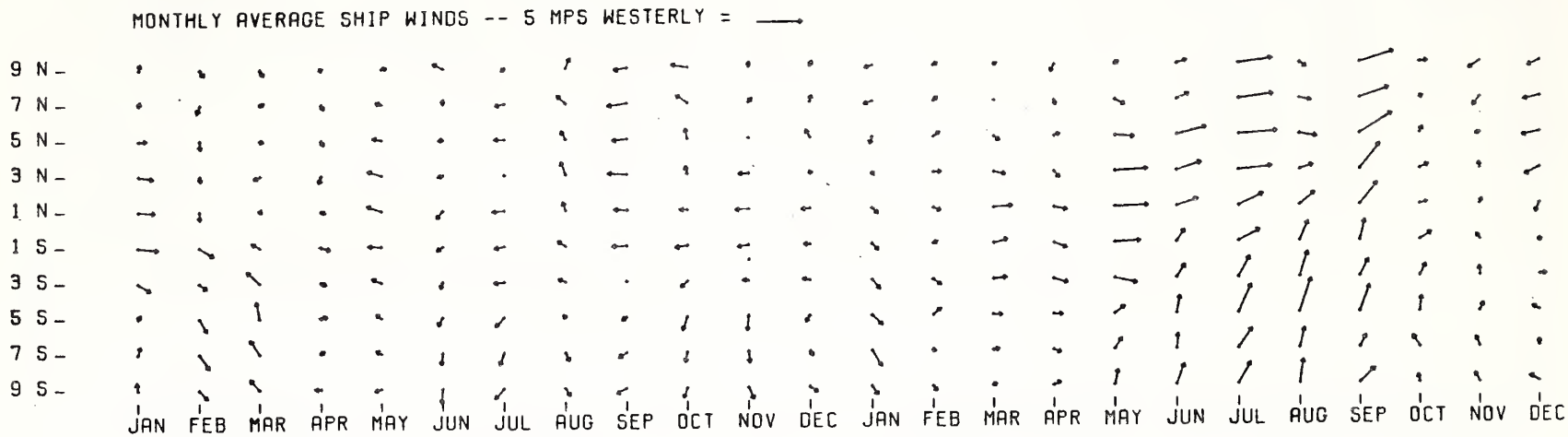
MONTHLY AVERAGE SHIP WINDS -- 5 MPS WESTERLY = ——→
9 N
7 N
5 N
3 N
1 N
1 S
3 S
5 S
7 S
9 S
JAN FEB MAR APR MAY JUN JUL AUG SEP OCT NOV DEC JAN FEB MAR APR MAY JUN JUL AUG SEP OCT NOV DEC

COMPOSITE: 1964-65, 1971-72, 1975-76 and 1981-82

Fig. 3. Time-latitude depiction of the anomaly of the monthly mean surface wind along 155°E for a composite of the following El Ninos: 1964-65, 1972-73, 1976-77 and 1982-83.

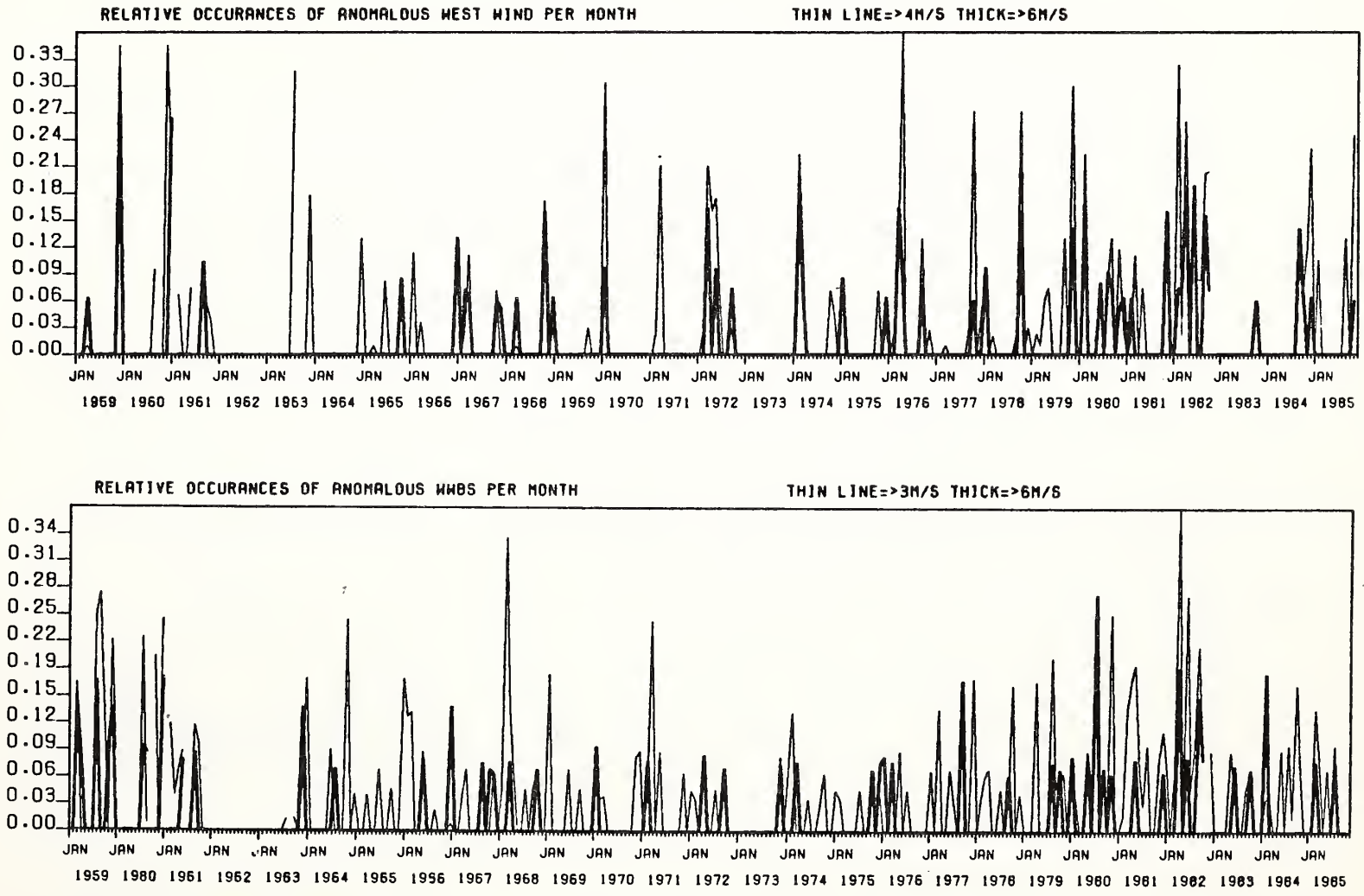

Fig. 4. Monthly anomalies of the relative number of positive 3-day averages of zonal wind per month (top) and positive changes in 3-day averaged zonal per month (bottom).

ON THE INTERANNUAL VARIABILITY OF GROWING SEASON PRECIPITATION IN CENTRAL NORTH AMERICA

Michael B. Richman and Peter J. Lamb[1]

Climate and Meteorology Section
Illinois State Water Survey
Champaign, IL 61820

1. INTRODUCTION

Our previous work has characterized the spatial patterns of rainfall variation over central North America for the 1949-80 period as a whole (Richman and Lamb, 1985, 1987). We extend that effort here by investigating the interannual variability that underlies those basic patterns. This is accomplished through the detailed consideration of key areas and time periods identified from the earlier research. We investigate the representativeness of the patterns obtained for the full 1949-80 period by matching them against those for individual years during 1970-80. This inquiry is designed to identify spatial variations in the potential predictability of the rainfall. Finally, we use some previous results (Richman and Lamb, 1988) as a framework for addressing the question of how short-term rainfall patterns (i.e., those derived from 3-day totals) evolve into the longer-term climate patterns (i.e., 30-, 41- or 61-day totals). This last goal is pursued through the use of a newly introduced multivariate technique to facilitate the matching. Our overall concern here is thus with the issue of how weather integrates to climate or, in other words, with the "building blocks" of climate.

2. DATA AND ANALYSIS TECHNIQUES

The data set used has been described in detail elsewhere (Richman and Lamb, 1985, 1987); therefore, only a brief description will be provided here. The study domain extends from the Gulf of Mexico north into populated areas of southern Canada and from the Rocky Mountains eastward to the Appalachians. The motivation for studying this region was its high national and international agricultural importance. The data set is built from NCDCs cooperative network of daily climate stations; it contains daily rainfall totals for 557 quality controlled stations in a near 1^{o} x 1^{o} grid-like network for the May-August periods of 1949-80 (Fig. 1). Approximately 2.2 million daily observations are involved, and there is no missing data.

In our previous work, regionalizations of the domain into compact sets of coherent basis functions were produced for various time scales through Varimax

---

[1] Also affiliated with Department of Atmospheric Sciences, The University of Illinois.

Rotated Principal Component (VRPC) analyses of interstation correlation matrices (Richman and Lamb, 1988). The immediate regionalization tool was the plotting of the 0.4 loading isopleths for each VRPC on the same map (Fig. 2). A second analysis technique, Procrustes Target Analysis (PTA), can build upon PC analysis by linearly transforming two sets of vectors to a least-squares optimized match (Richman and Easterling, 1988) as:

$$\underline{B} = \underline{A}\underline{T} + \underline{E}$$

where the matrix $\underline{B}$ is the pattern one wishes to attempt to match (known as the "target"), $\underline{A}$ is the matrix of unrotated PC loadings, $\underline{T}$ is the transformation matrix which optimally matches $\underline{A}$ to $\underline{B}$, and $\underline{E}$ is the matrix of residuals. In this paper, one methodological goal is to match the 3-day rainfall patterns (Fig. 2) to a target of the 30-day patterns (Fig. 2) using the PTA methodology summarized in Fig. 3.

3. RESULTS

a. Interannual Spatial Variability

Here we seek to examine the stability and representativeness of our long term (1949-1980) 3-day regionalization by comparing Fig. 2a to separate VRPC 3-day analyses for each individual year during 1970-80. The basic scientific questions posed are: (a) Are certain coherent regions more stable than others? and (b) Which years best match the full regionalization? The 1970-1980 results appear in Fig. 4. They indicate that there is a wide range of matches to the climatological patterns (compare each panel of Fig. 4 to Fig. 2a). The most stable areas, in terms of best overall pattern correlation matches (Fig. 5), were Fig. 2a's VRPC 2, 4 and 9 (Canada) and, to a lesser extent, VRPC 5 and 10 (eastern part of central U. S.). The coherent Canadian regions presumably appear more consistently because they receive more of their precipitation from large-scale synoptic systems. Fig. 5 also implies that the "Corn Belt" VRPC 5 of Fig. 2a exhibits the lowest interannual variability and has the highest correlation match of any U. S. region, thereby suggesting the potential for higher growing season rainfall predictability in this part of the domain. To facilitate discriminating whether certain years had better matches with the 1949-80 pattern, we have considered all regions together for each year in Fig. 6. The findings were surprising in that they exhibited little range in the mean, yet the variances exhibit approximately a 2:1 range (i.e., 1971<<1976 matches). This suggests that one needs to subdivide the domain prior to making meaningful statements about the interannual variability of growing-season rainfall patterns.

b. How Do Short-Period Rainfall Patterns Evolve Into Longer-Term Climate Patterns?

In order to begin addressing this question, we use PTA to try to mimic the 30-day patterns in Fig. 2 with 3-day data. Two issues arise: (a) Can the 3-day data be transformed to look like 30-day patterns? (b) If this is the case, how do we gauge the degree-of-fit? The former question is answered by examining the least-square fit matrix ($\underline{A}\underline{T}$) of spatial patterns for 3-day

rainfall based on a 30-day target (Fig. 7). Visual comparison of Fig. 7 to Fig. 2d indicates a good fit across 14 of the 15 regions. A quantitative comparison using the RMS of the discrepancies, and correlation (to measure pattern overlap) and congruence (to measure both pattern and magnitude) pattern matches, is shown in Table 1. Of particular interest are the low RMS discrepancies of the first 14 roots. We may therefore confidently accept the first 14 VRPCs (and the 15th with less assurance) generated from the 3-day data using PTA as a good proxy for the 30-day patterns to answer question (b) above. The major advantage is that these new PTA spatial patterns have a corresponding time series with a densely packed 3-day time interval (see Fig. 3) allowing us to investigate how synoptic high-frequency events contribute to climate patterns. This would hitherto have been impossible without PTA.

A example of the utility of this approach is shown in Table 2, which lists the number of extreme-events by year and month (defined as PC scores in excess of $|2\sigma|$) to illustrate how the overall patterns are "shocked" and shaped by various short-period events. The results of Table 2 indicate a large amount of interannual variability. For example, 1951, 1960, 1961, 1962, 1964, 1970 and 1974 all indicate means (across all 15 regions) of >3.0 extreme events per year whereas 1956, 1969 and 1977 contribute <1.0 events. Furthermore, May dominates by contributing over one-third of the total extremes. However, certain regions (i.e., 1 and 8) are built most by June precipitation anomalies. More specific climate insight is gained when the PTA scores (time series) are decomposed into positive (wet) and negative (dry) extremes in Tables 3 and 4, respectively. Table 3 shows that the years having the most synoptic wet events were 1962, 1964 and 1974. Similarly, Table 4 supplies information on the number of 3-day extreme dry periods per year, isolating 1951, 1960, 1961, 1964, 1974 and 1979. Interestingly, 1964 and 1974 stand out for both their extreme wetness and dryness in shaping the overall 30-day patterns. A spatial examination of which patterns were shocked by different extremes revealed that patterns 1, 5 and 8 (Fig. 7; all in the northwest portion of the domain) were largely built by wet events whereas most other regions had a more uniform distribution between wet and dry events. This type of unique information provides us with a quantitative documentation of how 3-day patterns build into 30-day patterns. Further case study analyses of specific synoptic events are now being undertaken.

4. SUMMARY

We have quantitatively documented both the spatial and temporal interannual variability of central North American growing season rainfall. Spatial analyses indicate that the Canadian patterns for individual years are more consistently similar to the full 1949-80 patterns than most of the U. S. patterns. The most stable U. S. region was the "Corn Belt". These findings are important for a number of uses such as climate predictability, crop modeling, and even the siting of field projects.

Procrustes Target Analysis was successfully applied to help answer the question: how does weather integrate into climate? Since the 30-day rainfall patterns shown in Fig. 2d could be mimicked using 3-day data, this provides evidence that the previously delineated 3-day patterns (Fig 2a) constitute the

basic building blocks for longer-term patterns. The evolution of 3- to 30-day patterns can be documented by examining the PTA scores or time series. This match between two temporal scales is vital to our understanding of climate processes, sheds light on the potential for 30-day rainfall prediction, and continues along the line of applying multivariate statistics to enhance physical interpretation of growing season rainfall.

ACKNOWLEDGMENTS

This research was supported by NSF Grant ATM 85-20877. The technical assistance of Linda Riggin, Rebecca Runge, and Phyllis Stone is greatly appreciated.

REFERENCES

Richman, M. B. and W. E. Easterling, 1988: Procrustes target analysis: A multivariate tool for identification of climate fluctuations. J. Geophys. Res. (Atmospheres), 93, 10989-11003.

Richman, M. B. and P. J. Lamb, 1985: Climatic pattern analysis of three- and seven-day summer rainfall in the central United States: Some methodological considerations and a regionalization. J. Clim. Appl. Meteor., 24, 1325-1343.

Richman, M. B. and P. J. Lamb, 1987: Pattern analysis of growing season precipitation in southern Canada. Atmosphere-Ocean, 25, 137-158.

Richman, M. B. and P. J. Lamb, 1988: On the modes of growing-season precipitation over central North America. Proc. Twelfth Annual Climate Diagnotics Workshop, U. S. Dept. of Commerce, Washington, DC, 284-291.

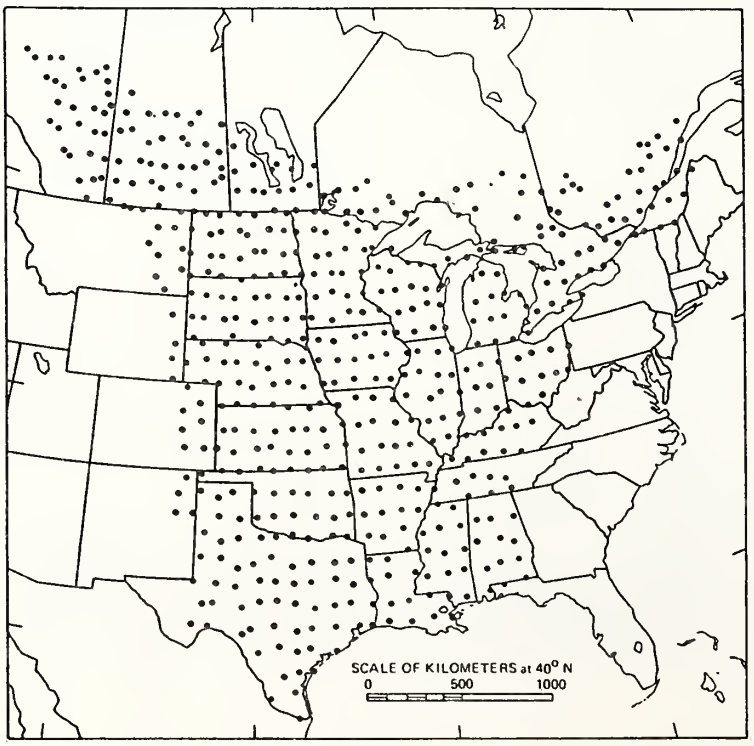

Fig. 1

Table 1. Quantitative matches between matched vectors in the matrices B and (AT) (Fig. 2d and 7, respectively) using RMS discrepancies, correlations and congruence coefficients.

PC #	RMS Discrepancy	Correlation Match	Congruence Match
1	.064	.959	.969
2	.076	.934	.951
3	.070	.935	.945
4	.074	.923	.940
5	.067	.942	.946
6	.080	.902	.910
7	.097	.868	.895
8	.082	.884	.905
9	.087	.896	.901
10	.093	.842	.881
11	.085	.848	.855
12	.080	.860	.866
13	.090	.793	.801
14	.082	.818	.820
15	.125	.638	.647
$\bar{X}$ =	.083	.869	.882
σ =	.015	.080	.081

Table 2. PTA time series extreme events by year and month for all PC scores exceeding $|2\sigma|$. PC numbers refer to the regions in Fig. 7.

Year	PC 1	PC 2	PC 3	PC 4	PC 5	PC 6	PC 7	PC 8	PC 9	PC 10	PC 11	PC 12	PC 13	PC 14	PC 15	$\bar{X}$
1949	2	3	2	2	2	2	2	3	2	1	3	2	2	2	2	2.133
1950	2	2	3	2	1	2	2	2	2	2	2	2	2	1	2	1.933
1951	2	4	4	4	4	4	4	1	4	4	4	4	4	4	4	3.667
1952	1	1	1	1	1	2	1	1	1	1	1	1	1	2	1	1.133
1953	3	2	2	2	2	2	2	2	2	2	2	2	1	1	2	1.933
1954	4	2	2	2	3	1	2	2	2	2	3	3	2	3	3	2.400
1955	0	3	3	3	5	2	3	0	3	3	3	3	3	3	3	2.667
1956	2	0	0	0	0	0	0	1	0	1	0	0	0	0	0	0.267
1957	0	2	2	2	2	2	2	2	3	2	2	2	3	2	2	2.000
1958	1	2	2	2	1	3	3	3	2	2	3	1	1	0	1	1.800
1959	0	1	1	1	1	1	1	1	2	2	1	1	1	1	1	1.067
1960	0	3	4	3	4	3	4	1	4	2	4	4	3	3	3	3.000
1961	1	4	3	3	5	4	3	1	3	3	4	3	3	4	4	3.200
1962	4	3	3	3	6	3	4	6	3	4	3	3	3	5	3	3.733
1963	4	2	1	2	1	2	2	2	1	1	2	1	2	2	1	1.733
1964	6	4	4	4	3	4	4	3	3	4	3	4	3	5	4	3.867
1965	4	2	2	2	4	2	2	1	2	2	2	2	2	2	2	2.200
1966	1	1	1	1	1	1	1	3	1	1	1	1	1	2	1	1.200
1967	1	1	1	2	0	1	0	3	2	1	1	1	2	0	0	1.067
1968	2	3	3	3	3	3	3	4	3	2	3	3	3	2	2	2.800
1969	3	0	0	0	0	0	1	4	0	1	0	0	0	0	0	0.600
1970	2	3	3	3	2	3	3	3	4	3	3	3	3	5	3	3.067
1971	2	2	1	1	2	1	1	1	1	1	1	1	1	3	1	1.333
1972	3	3	2	3	2	3	3	4	3	3	3	3	3	2	3	2.867
1973	2	1	2	3	3	1	3	2	3	3	1	2	2	4	2	2.267
1974	3	6	5	5	1	4	5	1	4	3	4	5	4	5	5	4.000
1975	1	2	2	3	2	2	3	3	2	3	2	3	2	1	2	2.200
1976	2	1	1	1	1	1	1	3	1	1	1	1	1	1	1	1.200
1977	0	1	1	1	1	1	0	2	1	1	1	1	0	1	1	0.867
1978	2	4	3	3	3	3	3	3	3	3	3	3	3	2	3	2.933
1979	1	3	3	3	4	3	3	1	3	5	3	3	3	3	3	2.933
1980	1	3	1	3	1	2	3	1	2	0	2	2	3	2	2	1.867
Σ	63	74	68	73	71	68	74	70	72	69	71	70	67	73	68	70.067
May's	19	29	31	28	23	27	28	14	29	24	29	27	26	24	28	25.733
Jun's	28	17	13	15	18	15	17	27	13	18	17	12	15	20	12	17.133
Jul's	7	12	10	14	15	11	14	15	14	12	13	14	12	11	12	12.400
Aug's	9	16	14	16	15	15	15	14	16	15	12	17	14	18	16	14.800

Table 3. PTA time series extreme events by year and month for wet events exceeding $+2\sigma$. PC numbers refer to the regions in Fig. 7.

Year	PC 1	PC 2	PC 3	PC 4	PC 5	PC 6	PC 7	PC 8	PC 9	PC 10	PC 11	PC 12	PC 13	PC 14	PC 15	$\bar{X}$
1949	1	1	1	1	1	1	1	3	1	0	1	2	1	1	1	1.133
1950	2	2	3	0	1	0	2	2	0	2	2	0	0	0	0	1.067
1951	2	3	3	1	3	1	3	1	1	3	3	1	1	1	1	1.867
1952	1	0	0	1	0	1	0	1	1	0	0	1	1	1	1	0.600
1953	2	1	1	1	1	1	1	2	1	0	1	1	1	1	1	1.067
1954	4	2	2	0	3	0	2	1	0	2	2	0	0	1	0	1.267
1955	0	1	1	2	3	2	1	0	2	1	1	2	2	2	2	1.467
1956	2	0	0	0	0	0	0	0	0	1	0	0	0	0	0	0.200
1957	0	1	1	1	1	1	1	2	2	1	1	1	2	1	1	1.133
1958	1	1	1	1	0	2	1	3	1	1	1	0	1	0	0	0.933
1959	0	0	0	1	0	1	0	1	1	0	0	1	1	1	1	0.533
1960	0	3	4	0	4	0	4	1	0	2	4	0	0	0	0	1.467
1961	0	2	2	1	4	2	2	1	1	2	2	1	1	1	2	1.600
1962	3	1	1	2	4	2	2	5	2	2	1	2	2	3	2	2.267
1963	4	1	1	1	1	1	1	2	0	1	1	0	1	1	0	1.067
1964	6	4	4	0	3	0	4	2	0	4	3	0	0	0	0	2.000
1965	4	0	0	2	2	2	0	0	2	0	0	2	2	2	2	1.333
1966	1	0	0	1	0	1	0	2	1	0	0	1	1	2	1	0.933
1967	0	0	0	2	0	1	0	2	2	0	0	1	2	0	0	0.667
1968	2	2	2	1	1	1	2	3	1	2	2	1	1	1	1	1.533
1969	3	0	0	0	0	0	1	3	0	1	0	0	0	0	0	0.533
1970	2	2	2	1	1	1	2	2	2	2	2	1	1	2	1	1.600
1971	1	1	0	1	1	1	0	1	1	0	0	1	1	2	1	0.800
1972	2	2	1	1	1	1	2	3	1	2	2	1	1	1	1	1.469
1973	1	1	1	1	2	0	2	1	1	2	1	1	1	1	1	1.133
1974	2	3	3	3	0	2	2	1	3	1	2	3	2	3	3	2.200
1975	1	1	1	2	1	1	1	2	1	1	1	2	1	0	1	1.133
1976	2	0	1	1	1	1	0	2	1	1	0	1	1	1	1	0.932
1977	0	1	1	0	1	0	0	2	0	1	1	0	0	0	0	0.467
1978	1	1	1	2	1	2	1	2	2	1	1	2	2	1	2	1.467
1979	0	1	1	2	2	2	1	1	2	1	1	2	2	1	2	1.400
1980	0	0	0	3	0	2	0	1	2	0	0	2	3	2	2	1.133
Σ	50	38	39	36	43	33	39	55	35	37	36	33	35	33	31	38.200
May's	14	17	20	12	12	13	16	12	12	12	16	11	12	11	12	13.467
Jun's	27	7	7	8	13	9	9	18	7	10	7	6	9	8	6	10.067
Jul's	5	8	6	6	11	3	8	11	6	7	8	6	5	4	4	6.533
Aug's	4	6	6	10	7	8	6	14	10	8	5	10	9	10	9	8.133

Table 4. PTA time series extreme events by year and month for dry events exceeding -2σ. PC numbers refer to the regions in Fig. 7.

Year	PC 1	PC 2	PC 3	PC 4	PC 5	PC 6	PC 7	PC 8	PC 9	PC 10	PC 11	PC 12	PC 13	PC 14	PC 15	$\bar{X}$
1949	1	2	1	1	1	1	1	0	1	1	2	0	1	1	1	1.000
1950	0	0	0	2	0	2	0	0	2	0	0	2	2	1	2	0.867
1951	0	1	1	3	1	3	1	0	3	1	1	3	3	3	3	1.800
1952	0	1	1	0	1	1	1	0	0	1	1	0	0	1	0	0.533
1953	1	1	1	1	1	1	1	0	1	2	1	1	0	0	1	0.867
1954	0	0	0	2	0	1	0	1	2	0	1	3	2	2	3	1.133
1955	0	2	2	1	2	0	2	0	1	2	2	1	1	1	1	1.200
1956	0	0	0	0	0	0	0	1	0	0	0	0	0	0	0	0.067
1957	0	1	1	1	1	1	1	0	1	1	1	1	1	1	1	0.867
1958	0	1	1	1	1	1	2	0	1	1	2	1	0	0	1	0.867
1959	0	1	1	0	1	0	1	0	1	2	1	0	0	0	0	0.533
1960	0	0	0	3	0	3	0	0	4	0	0	4	3	3	3	1.533
1961	1	2	1	2	1	2	1	0	2	1	2	2	2	3	2	1.600
1962	1	2	2	1	2	1	2	1	1	2	2	1	1	2	1	1.467
1963	0	1	0	1	0	1	1	0	1	0	1	1	1	1	1	0.667
1964	0	0	0	4	0	4	0	1	3	0	0	4	3	5	4	1.867
1965	0	2	2	0	2	0	2	1	0	2	2	0	0	0	0	0.867
1966	0	1	1	0	1	0	1	1	0	1	1	0	0	0	0	0.467
1967	1	1	1	0	0	0	0	1	0	1	1	0	0	0	0	0.400
1968	1	1	1	2	2	2	1	1	2	0	1	2	2	1	2	1.400
1969	0	0	0	0	0	0	0	1	0	0	0	0	0	0	0	0.067
1970	0	1	1	2	1	2	1	1	2	1	1	2	2	3	2	1.467
1971	1	1	1	0	1	0	1	0	0	1	1	0	0	1	0	0.533
1972	1	1	1	2	1	2	1	1	2	1	1	2	2	1	2	1.400
1973	1	0	1	2	1	1	1	1	2	1	0	1	1	3	1	1.133
1974	1	3	2	2	1	2	3	0	1	2	2	2	2	2	2	1.800
1975	0	1	1	1	1	1	2	1	1	2	1	1	1	1	1	1.067
1976	0	1	0	0	0	0	1	1	0	0	1	0	0	0	0	0.267
1977	0	0	0	1	0	1	0	0	1	0	0	1	0	1	1	0.400
1978	1	3	2	1	2	1	2	1	1	2	2	1	1	1	1	1.467
1979	1	2	2	1	2	1	2	0	1	4	2	1	1	2	1	1.533
1980	1	3	1	0	1	0	3	0	0	0	2	0	0	0	0	0.733
Σ	13	36	29	37	28	35	35	15	37	32	35	37	32	40	37	31.867
May's	5	12	11	16	11	14	12	2	17	12	13	16	14	13	16	12.267
Jun's	1	10	6	7	5	6	8	9	6	8	10	6	6	12	6	7.067
Jul's	2	4	4	8	4	8	6	4	8	5	5	8	7	7	8	5.867
Aug's	5	10	8	6	8	7	9	0	6	7	7	7	5	8	7	6.667

FIGURE CAPTIONS

Fig. 1. Station network (557) for central North American daily precipitation data set for May-August periods of 1949-1980.

Fig. 2. Regionalization of central North America based on the +0.4 loading isopleths of Varimax Rotated Principal Component (VRPC) patterns for (a) 3-day rainfall totals, (b) 7-day rainfall totals, (c) 15-day rainfall totals, (d) 30-day rainfall totals, (e) 41-day rainfall totals, and (f) 61-day rainfall totals. Note that the totals in (a) -(d) were square-root transformed. From Richman and Lamb (1988).

Fig. 3. Flow diagram of Procrustes Target Analysis (PTA) used in this research design.

Fig. 4. Regionalization of central North America based on the +0.4 loading isopleths of Varimax Rotated Principal Component patterns for 3-day square-root transformed rainfall totals for (a) 1970, (b) 1971, (c) 1972, (d) 1973, (e) 1974, (f) 1975, (g) 1976, (h) 1977, (i) 1978, (j) 1979, (k) 1980.

Fig. 4. Continued.

Fig. 5. Box and whisker plots of the correlation between each individual 3-day region in Fig. 2a and its closest matching spatial counterpart in Fig. 4. PC root number corresponds to regions shown in Fig. 2a. Upper and lower edges of each box represent the standard deviation whereas whiskers represent best and worst yearly match.

Fig. 6. Box and whisker plots of the pattern correlation between each individual year (over all regions) in each panel of Fig. 4 compared to the full regionalization in Fig. 2a. Upper and lower edges of each box represent the standard deviation whereas whiskers represent best and worst region's match.

Fig. 7. Procrustes Target Analysis least-squares fit (matrix AT from Fig. 3 flow chart) of three-day data to thirty-day target (Fig. 2d). The +0.4 PTA loadings are isoplethed to yield a regionalization of 3-day rainfall optimally matching the 30-day regionalization.

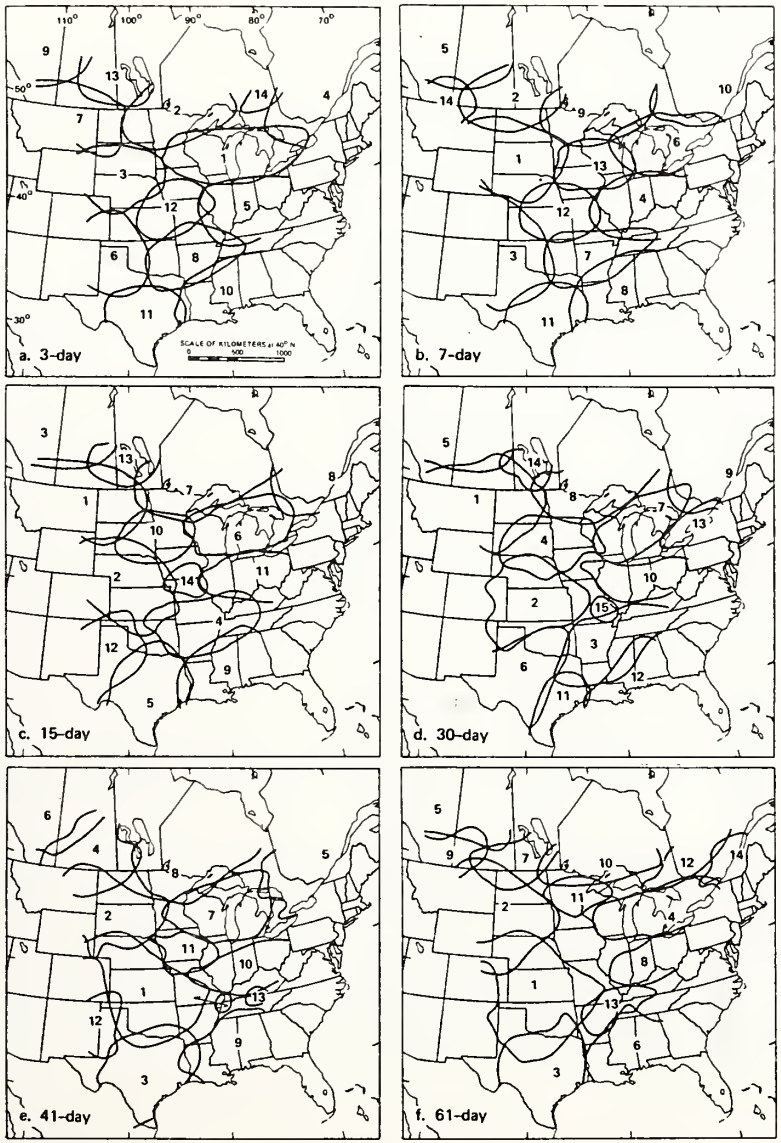
a. 3-day
b. 7-day
c. 15-day
d. 30-day
e. 41-day
f. 61-day

Fig. 2

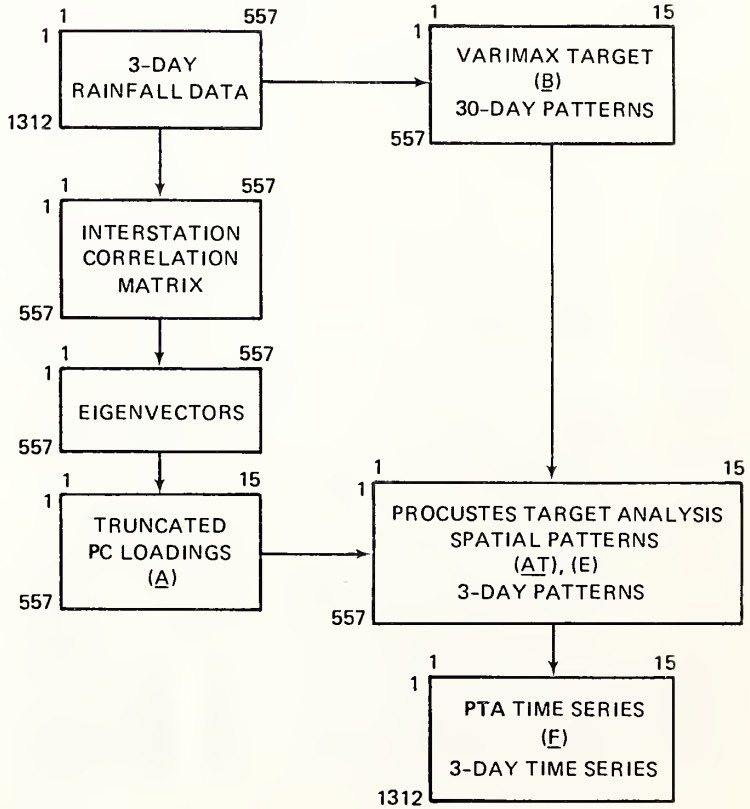
3-DAY RAINFALL DATA
1312
557
VARIMAX TARGET (B) 30-DAY PATTERNS
15
INTERSTATION CORRELATION MATRIX
EIGENVECTORS
TRUNCATED PC LOADINGS (A)
PROCUSTES TARGET ANALYSIS SPATIAL PATTERNS (AT), (E) 3-DAY PATTERNS
PTA TIME SERIES (F) 3-DAY TIME SERIES

Fig. 3

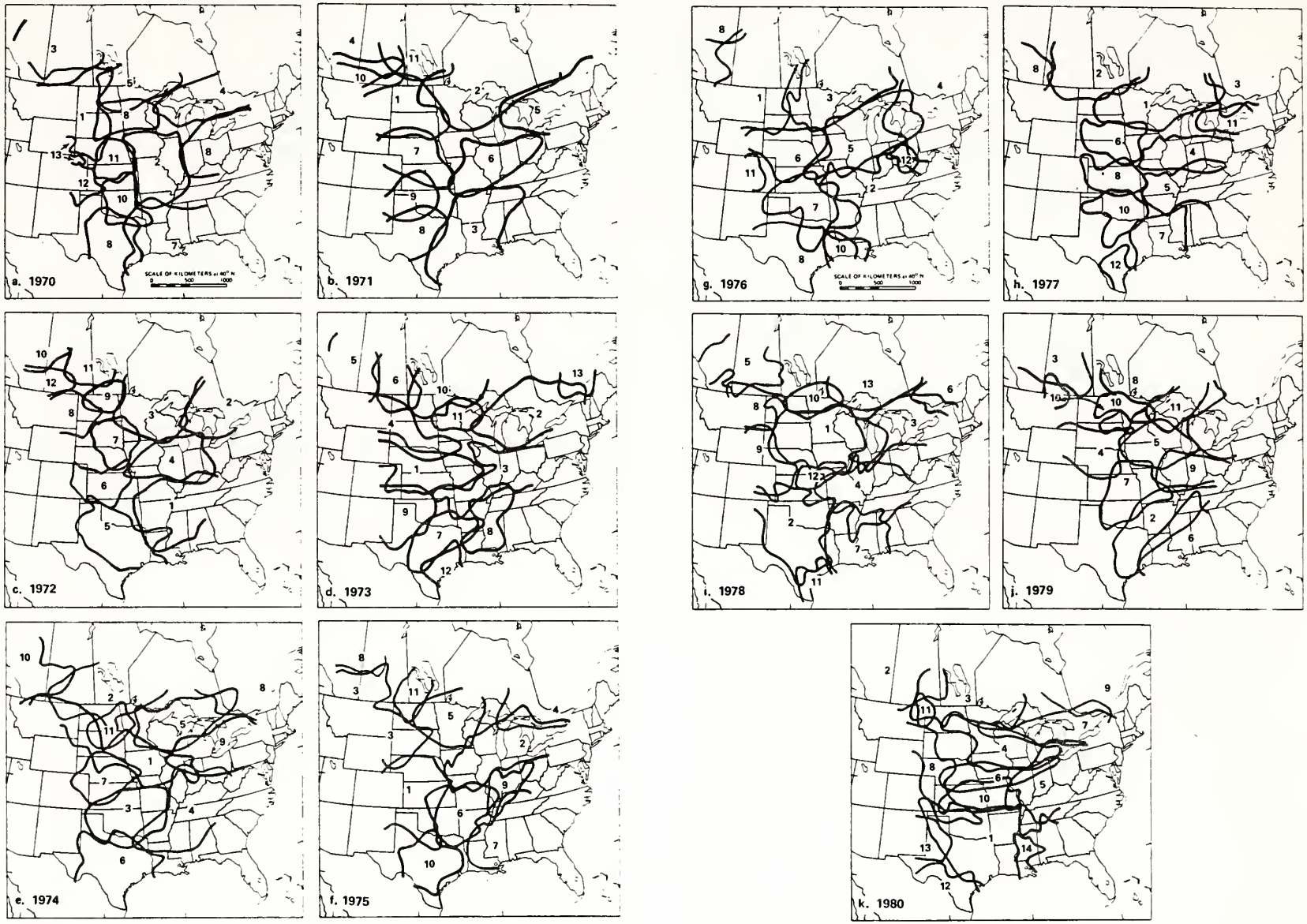
a. 1970
b. 1971
c. 1972
d. 1973
e. 1974
f. 1975
g. 1976
h. 1977
i. 1978
j. 1979
k. 1980

Fig. 4

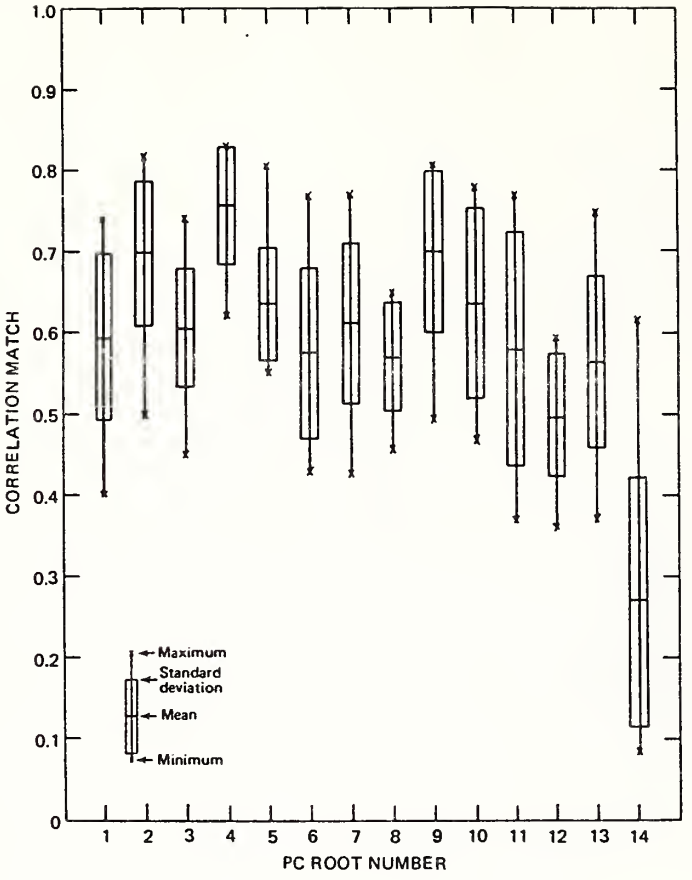

Fig. 5

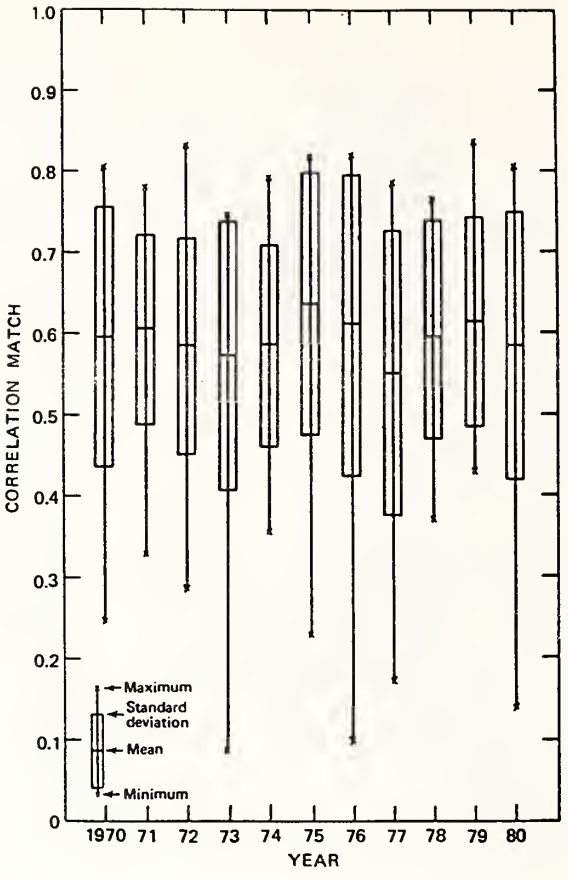

Fig. 6

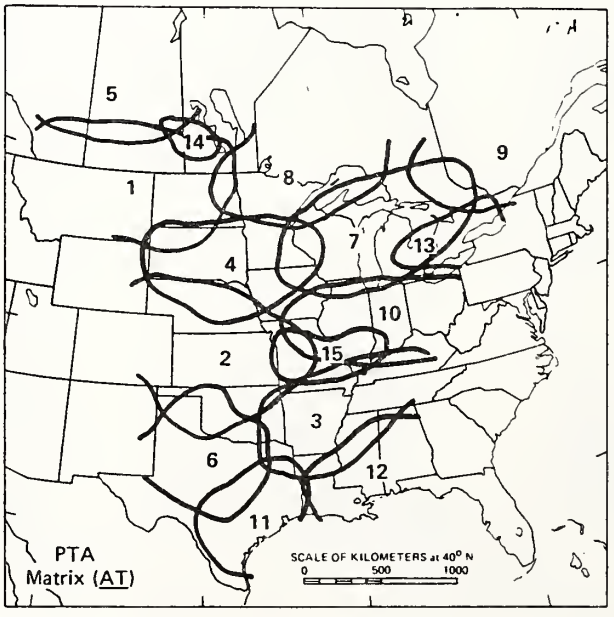

Fig. 7

Relationships between seasonal circulation modes of the tropics and the northern hemispheric extratropics

Klaus Wolter* and Robert E. Livezey
Climate Analysis Center W/NMC51, NMC/NWS/NOAA, Washington, DC 20233

Teleconnections between the tropics and extratropics continue to receive a lot of attention, prompted largely by recent ENSO events. They are understood here as linear correlations between extratropical and tropical planetary circulation patterns, predefined through rotated principal component analyses for Northern hemispheric extratropical 700 mb geopotential heights (Barnston and Livezey, 1987), and for tropical ship data (Wolter, 1989). Such a streamlining of both data sets expedites the search for teleconnections between them. In addition, if a principal component (PC) of one domain correlates highly with a PC of the other domain, we know *a priori* that this teleconnection contributes substantially to the variance of both fields.

The 700 mb modes were based on monthly, bi-monthly, and three-monthly PC analyses from 1950 to 1987 with respect to all twelve months of the year (Barnston and Livezey, 1987). The ship data (SLP, wind speed, cloudiness, and SST) were analyzed for 1948-83 January/February and July/August for SST and all four elements combined within the tropical Atlantic, Eastern Pacific, and Indian Oceans (Wolter, 1989).

Correlations were computed among time series of all ten rotated 700 mb modes for each season or month and of all five (four) rotated tropical all-element (SST) modes for boreal winter and summer, up to one and a half years lead/lag. The strongest relationships account for about 40% of the variance of the involved time series. Table 1 shows the number of concurrent correlations with all-element modes to exceed the 95% (99%) significance level. Six (two) and more significant correlations for a given month or season exceed the number of such correlations to be expected by chance in 5% (1%) of the cases, based on the fact that PC's are temporally uncorrelated. Correlations are more often significant in boreal winter than in boreal summer (Table 1). Several of these relate a single extratropical mode with two or more tropical modes (Table 1a). Such extratropical modes usually feature loading centers over North America and the Pacific, i.e., where the longitudinal overlap between tropical and extratropical domain is smallest. Among the tropical modes (Table 1b) the most active ones are Southern Oscillation modes (#1,2 in boreal winter, and #1 in boreal summer), and North Atlantic modes (#5 in boreal winter, and #2,4 in boreal summer), while the Atlantic ENSO mode (#5 in boreal summer) shows little engagement in northern hemispheric affairs (Table 1b). Similar results are found with respect to tropical SST modes (not shown here). A detailed description of the tropical modes is given in Wolter (1989).

With respect to lagged relationships we find cross-correlations up to a significance level of 99.99% (5 for all-element modes, 3 for SST), with a slight preference for July/August modes of the tropics to lead the northern extratropics, while January/February modes of the tropics tend to lag after the extratropics. Links between winter circulation features of the northern extratropics and tropical anomalies of boreal summer are most significant. Four-element PC's of the tropics have more significant teleconnections with extratropical 700 mb modes than tropical SST PC's. However, this difference in significance is mainly due to the more prominent persistence and associated reduction in the temporal degrees of freedom that is typical of SST modes.

Two examples of such lagged interaction between tropics and extratropics are illustrated in Figs. 1 - 4. The first case (Figs. 1,2) links the tropical "Global Sahel mode" (Fig. 1; ref. Wolter, 1989) of boreal summer with the subsequent November-January extratropical "Eurasian pattern type 1" (Fig. 2; ref. Barnston and Livezey, 1987) at a correlation of - 0.64 (99.99% significance).

---

* presently at CIRES, University of Colorado at Boulder, Boulder, CO 80309-0216

In its positive phase, it features anomalously low pressure in the North Atlantic sector (Fig. 1a), possibly related to anomalous diabatic heating over West Africa, which in turn may entail a Rossby wave train propagating into Eurasia (Fig. 2). Both PC time series have strong linear trends, the extratropical one upward, the tropical one downward. Hence, the correlation drops to -0.47 if both trends are removed from the analysis. Winter weather in Europe is strongly affected by the behavior of this mode (the loading center over Scandinavia in Fig. 2 reaches - 0.91).

The second example relates the extratropical mode #1 of late winter (Fig. 3), also known as the North Atlantic Oscillation (NAO; ref. Barnston and Livezey, 1987) to the subsequent "Atlantic Sahel mode" of boreal summer (Fig. 4; ref. Wolter, 1989). The correlation is the most extreme of this study: - 0.67 (99.99% significance), and is not tied to long-term trends (it stays at - 0.65 for detrended time series). Summer monsoonal rainfall in the Western Sahel (based on Lamb, 1985) is strongly associated with this mode - its correlation during 1948-83 is + 0.53. Further work to cross-validate these and other relationships is under way.

Acknowledgments:
We thank Anthony Barnston at the Climate Analysis Center for providing us with the updated 700 mb principal component time series and loading patterns. KW acknowledges postdoctoral support from the University Corporation for Atmospheric Research (UCAR).

References:

Barnston, A. G., Livezey, R. E., 1987: Classification, seasonality and persistence of low-frequency atmospheric circulation patterns. *Mon. Wea. Rev.*, **115**, 1086 - 1126.

Lamb, P. J., 1985: Rainfall in Subsaharan West Africa during 1941 - 1983. *Zeitschrift für Gletscherkunde und Glazialgeologie,* **21**, 131 - 139.

Wolter, K., 1989: Modes of tropical circulation, Southern Oscillation, and Sahel rainfall anomalies. *J. Climate*, **2**, in press

Table 1: Number of significant correlation coefficients at the 95% (99%) level between extratropical 700 mb geopotential height PC's (ref. Barnston and Livezey, 1987) and tropical surface circulation PC's (ref. Wolter, 1989). Statistical significance of a month's or season's results at the 95% (99%) level is indicated by an asterisk. Simultaneous correlations are shown in (a) for the extratropical modes, and (b) for the tropical modes.

a) Near simultaneous teleconnections with respect to extratropical modes

PC	1	2	3	4	5	6	7	8	9	10	Total (of 50)
JAN	1(1)	2(1)	2(1)	-	-	1(0)	-	-	1(0)	1(0)	8*(3*)
FEB	2(0)	-	1(0)	-	-	1(1)	-	-	-	-	4 (1)
JUL	1(0)	-	-	1(0)	-	1(1)	-	1(0)	-	-	4 (1)
AUG	-	1(1)	1(0)	1(0)	-	1(0)	-	-	1(1)	1(1)	6*(3*)
J/F	-	1(1)	3(0)	1(1)	1(0)	1(0)	1(0)	1(0)	-	-	9*(2*)
J/A	-	2(0)	1(0)	-	-	1(1)	-	-	1(0)	-	5 (1)
D-F	1(1)	2(0)	2(0)	1(0)	-	1(0)	1(1)	-	1(0)	-	9*(2*)
J-M	-	2(1)	-	2(1)	-	1(1)	-	-	-	1(0)	6*(3*)
J-A	-	1(1)	-	1(0)	1(1)	-	-	-	-	-	3 (2*)
J-S	-	1(0)	-	1(0)	-	1(1)	-	-	-	1(1)	4 (2*)

b) Near simultaneous teleconnections with respect to tropical four-element modes

PC	1	2	3	4	5	Total (of 250)
J/F	8(3)	10(2)	3(1)	6(1)	9(4)	36*(11*)
J/A	9(3)	7(3)	-	6(3)	-	22 (9*)

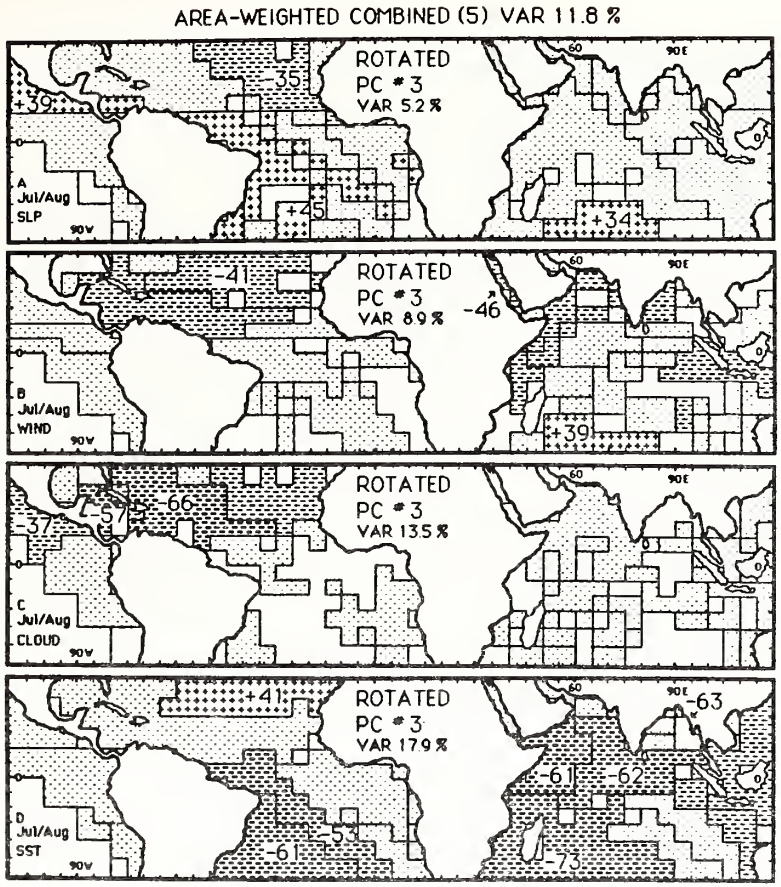

Fig. 1: Loading patterns (in hundredths) of the third of five rotated principal components for combined elements of time-averaged July-August during 1948-83, with (a) SLP, (b) wind speed, (c) cloudiness, and (d) SST. The total explained variance of the combined PC is given on top of the first panel. Variance explained by the individual element PC portion is given under "VAR". Enhanced symbols represent loadings of at least 0.50, while dot raster indicates loadings under 0.30. This PC is also referred to as Global Sahel mode (Wolter, 1989).

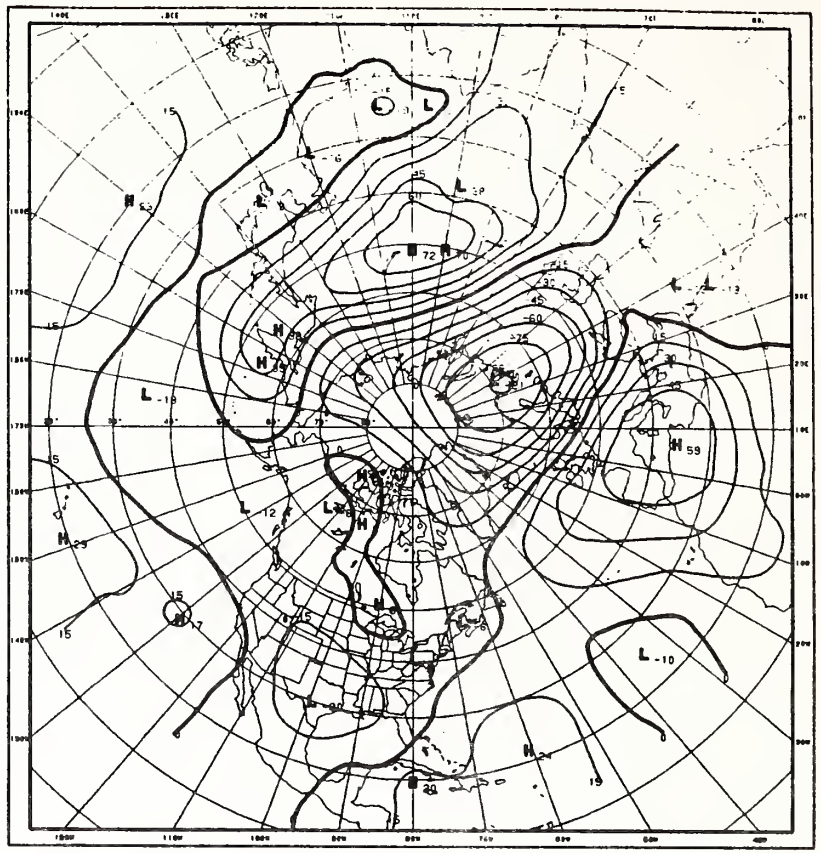

Fig. 2: Loading patterns (in hundredths) of the fourth of ten rotated principal components for time-averaged November-January 700 mb geopotential heights during 1950-87 (courtesy of A. G. Barnston). This PC is referred to as Eurasian pattern type 1 (Barnston and Livezey, 1987) and explains 9.3 % of the variance during that season.

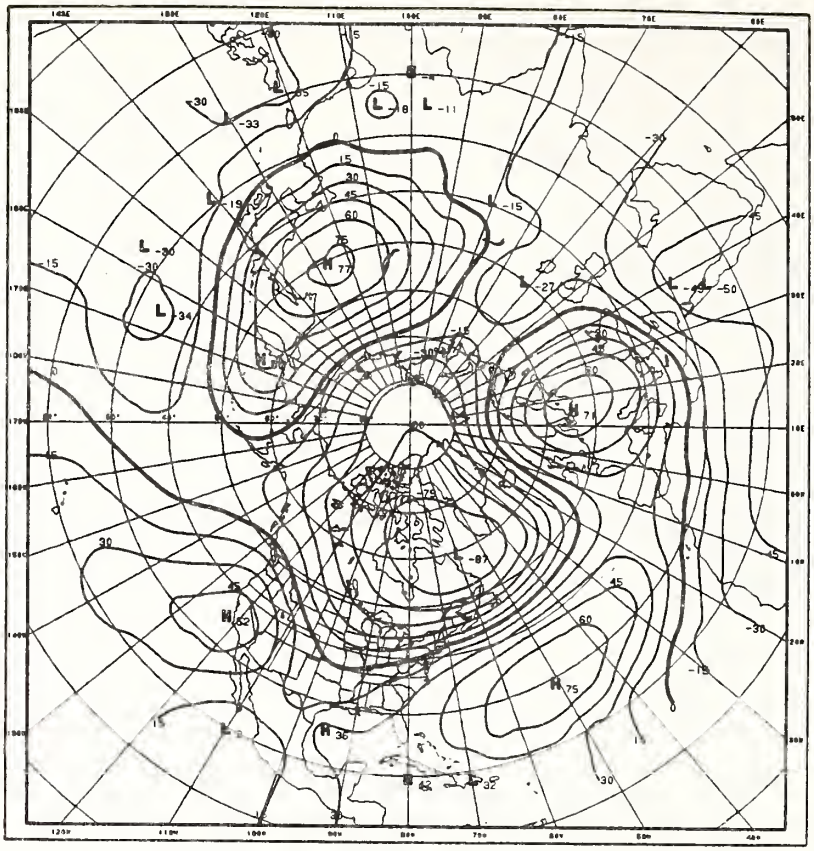

Fig. 3: As in Fig. 2, except for the first of ten rotated PC's for time-averaged January-March (Courtesy of A. G. Barnston). This PC is also referred to as North Atlantic Oscillation (Barnston and Livezey, 1987) and explains 15.3 % variance during that season.

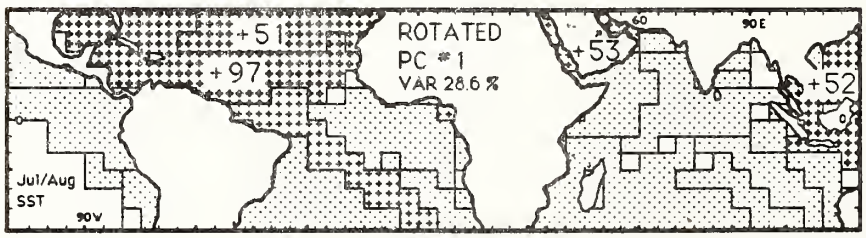

Fig. 4: As in Fig. 1, except for the first of four rotated PC's for SST only, in July-August. This PC is also referred to as Atlantic Sahel mode (compare to combined element PC #2 during that season in Wolter, 1989).

RECENT TEMPERATURE TRENDS IN THE NORTHERN HEMISPHERE

David J. Karoly *
AOS Program, Princeton University,
PO Box 308, Princeton, NJ 08542

1. Introduction

Experiments on the effects of increased concentrations of carbon dioxide using atmospheric general circulation models show warming in the troposphere and cooling in the lower stratosphere. Recently, Karoly (1987) developed an index to identify this difference in temperature change and applied it to radiosonde data from 19 stations in the Southern Hemisphere for the period 1964-85. This index had a positive trend at all the stations, consistent with the greenhouse effect, and the trends were significant at most of the stations. In this study, the index defined by Karoly (1987) is applied to Northern Hemisphere radiosonde station data. The horizontal variation of the temperature trends is considered.

2. Data and Analysis Procedure

Monthly mean temperature observations from all available radiosonde stations in the NH for the period 1950-85 were obtained on magnetic tape from NCAR. Data at pressure levels of 850, 700, 500, 300, 100, 50 and 30hPa (approximate altitudes of 1, 3, 5, 9, 16, 20 and 24km) were used. Data were available at the 50 and 30hPa levels from 1964 only so the analysis was limited to the 22 year period from 1964 to 1985. Stations with more than 10% of the monthly data missing at 50hPa were rejected. The data were checked for extreme anomalies or discontinuities in the time series at all levels and stations. After this data checking, 147 stations were retained.

From this stage, the analysis was similar to that described by Karoly (1987) for SH station temperatures, with one important difference. To allow for the large number of stations and variations in station density over the NH, the stations were grouped into 10° latitude by 20° longitude grid boxes. It was assumed that the inter-decadal variations of temperature would be coherent on horizontal scales larger than these boxes. For each station at each level, time series of monthly anomalies were computed by subtracting the long-term means for each calendar month from the individual monthly means. The monthly anomalies for all stations in each grid box were averaged to give time series of monthly temperature anomalies on a regular grid. Only 61 out of the possible 162 grid boxes in the NH contained at least one station. The number of stations in each of the grid boxes is shown in Fig. 1. The station selection criterion of less than 10% of monthly data missing at 50hPa has meant that there have been very few stations from Africa, eastern Europe and Asia included in the analysis. Time series of seasonal anomalies were computed by averaging the monthly anomalies over the 3-month calendar seasons (DJF, MAM, JJA and SON). To allow for missing monthly data, a seasonal anomaly was computed only if at least two monthly anomalies were available. Time series of annual anomalies were computed by averaging the 4 seasons in each year. An annual anomaly was computed only if at least three seasonal anomalies were available in that year.

---

* On leave from Dept. of Mathematics, Monash University, Victoria, Australia

A least-squares straight line was fitted to the time series of annual temperature anomalies at each level for all the grid boxes. In addition, the normalized annual temperature index, defined by Karoly (1987),

$$z = \frac{1}{\sigma} \left(\frac{T_{850}}{\sigma_{850}} + \frac{T_{700}}{\sigma_{700}} + \frac{T_{500}}{\sigma_{500}} - \frac{T_{100}}{\sigma_{100}} - \frac{T_{50}}{\sigma_{50}} - \frac{T_{30}}{\sigma_{30}} \right) , \qquad (1)$$

was computed. This is the sum of the annual temperature anomalies at the three levels in the lower troposphere, normalized by their standard deviations, minus the normalized temperature anomalies at the three levels in the lower stratosphere. The index has been normalized by dividing by its standard deviation. The presence of a trend in the time series was tested using a non-parametric rank test [Kendall, 1970].

3. Results

The annual temperature trends for the stations in each of the grid boxes over the period 1964-85 at 700hPa and at 50hPa are shown in Fig. 2. The magnitudes of the trends are plotted in the centre of each box in degrees/century, rounded to the nearest integer to simplify the diagram. At 700hPa, in the lower troposphere, there is a warming trend for the large majority of the stations (50 out of 61 grid boxes), typically between 1° and 4°C/century. There are marked geographical variations in the trends, with the largest warming over the subtropical Pacific and cooling over the north Atlantic and north-west Pacific. The average trend at 700hPa of 0.17°C/decade is smaller than found in the SH [Karoly, 1987] but similar to the NH 850-300hPa average annual trend of 0.13°C/decade from Angell (1986). Using the non-parametric rank test, the warming trend is statistically significant at the 97.5% level (95% level using a two-sided test) in 13 of the grid boxes. None of the regions of cooling has significant trend.

At 50hPa, in the lower stratosphere, there is a cooling trend for the large majority of the stations (50 out of the 61 grid boxes), typically between -2° to -5°C/century. The geographical variations in the lower stratosphere are similar to those in the lower troposphere, with largest cooling over the subtropical Pacific and warming or weak cooling over the north Atlantic and north-west Pacific. The average trend at 50hPa of -0.27°C/decade is larger than the NH 100-50hPa average annual temperature trend of -0.02°C/decade from Angell (1986) but similar to the NH average 30hPa trend of -0.24°C/decade for the 1966-80 period of Labitzke et al. (1986). The cooling trend is significant in 7 of the boxes using the rank test.

The trends of the normalized temperature index, defined by (1), are shown in Fig. 3, in units of standard deviations/century. The vast majority of the stations have a positive trend in the index (only 7 out of the 61 boxes have negative trend), indicating warming in the lower troposphere and cooling in the lower stratosphere. There is a strong spatial coherence in the trends, with anomalous negative or weak positive trends over the north Atlantic and north-west Pacific. The trend in the normalized index is statistically significant at the 97.5% level in 13 out of the 61 boxes (21%), which suggests that it is highly significant overall. The fraction of stations in the NH with significant trend in the index is much smaller than was found in the SH.

The non-parametric rank test has been applied to the annual temperature anomaly time series for the individual grid boxes to determine whether the

trends are significant. In essence, the test is used to reject or accept the null hypothesis that there is no temperature trend, with a specified confidence. Although this test has been applied to the individual grid boxes, it can be used to provide an estimate of the significance of the trends for all the stations used. The rank statistic is normally distributed with mean zero and unit standard deviation [Kendall, 1970]. If the null hypothesis is valid then the average of the rank statistics for all the grid boxes should be normally distributed, with zero mean and standard deviation dependent on the number of degrees of freedom between the grid box time series (the horizontal coherence of the time series). The number of degrees of freedom (d.o.f.) for the grid box time series has been estimated from a principal component analysis of the correlation matrix between the detrended time series. The number of degrees of freedom was assumed to be the number of independent principal components according to the Kaiser-Guttman criterion (eigenvalues greater than 1.0). The average rank statistic, number of d.o.f. and the significance level are given in Table 1 for the temperatures at 700hPa and at 50hPa and for the normalized index. The results show that the null hypothesis of no trend for all the grid boxes may be rejected for temperature at 700hPa and at 50hPa and for the normalized index, with the highest confidence level for the normalized index, 99.99%.

4. Discussion

This analysis of NH radiosonde temperature data has shown that, for the period 1964-85, there has been a warming trend in the lower troposphere and a cooling trend in the lower stratosphere at most stations. These trends are consistent with the effects of increasing concentrations of greenhouse gases in the atmosphere. There is strong horizontal coherence of the trends, with anomalous regions of weaker or opposite trends over the north Atlantic and north-west Pacific.

The analysis has been simplistic in that no attempt has been made to take account of different instrument types, observing times, radiation corrections etc. prior to averaging the individual station monthly temperature anomalies within the grid boxes. The horizontal coherence of the results supports their validity. There are other possible problems which must be considered. The radiosonde station data was available for a short period only and with uneven coverage over the NH. The results may be biased by the uneven sampling over the hemisphere. No account has been made of shorter period climate fluctuations such as the effects of volcanic eruptions or El Niño-Southern Oscillation events in the temperature time series. There are other possible causes of the observed temperature trends, including increases in sea surface temperatures over this period or decreases in ozone in the stratosphere. The pattern of lower tropospheric temperature trends over the Pacific and Atlantic Oceans is consistent with the changes in NH sea surface temperatures over this period, with warming in the subtropical Pacific and cooling in the north Atlantic and north Pacific [C. Folland, personal communication].

References

Angell, J.K., 1986, Annual and seasonal global temperature changes in the troposphere and low stratosphere, 1960-85. Mon. Wea. Rev., 114, 1922-1930.

Karoly, D.J., 1987, Southern Hemisphere temperature trends: a possible greenhouse gas effect? Geophys. Res. Lett., 14, 1139-1141.

Kendall, M.G., 1970, Rank Correlation Methods, 4th Ed., Griffin, London.

Labitzke, K., G. Brasseur, B. Naujokat and A. DeRudder, 1986, Long-term temperature trends in the stratosphere: possible influence of anthropogenic gases. Geophys. Res. Lett., 13, 52-55.

TABLE 1. Hemispheric Rank Test

Variable	Average Rank Statistic	Deg. of Freedom	Significance
700 hPa Temp.	0.98	12	99.96%
50 hPa Temp.	-0.81	9	99.07%
Normalized Index	1.09	12	99.99%

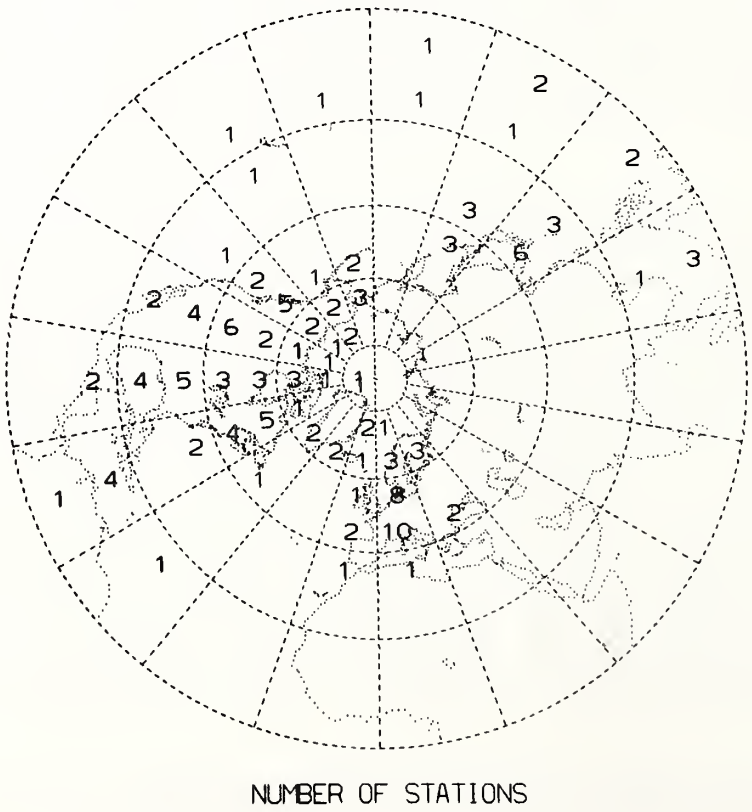

Fig. 1. Number of stations used in the analysis in each 10° latitude by 20° longitude grid box.

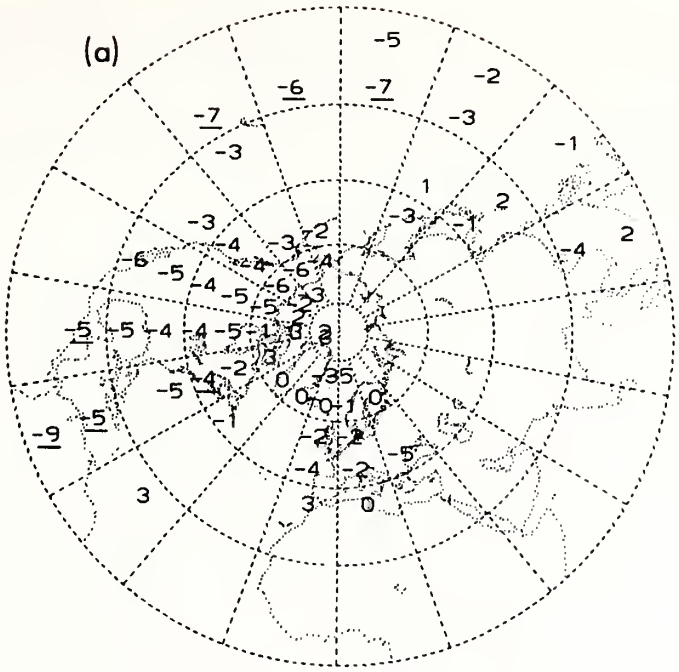

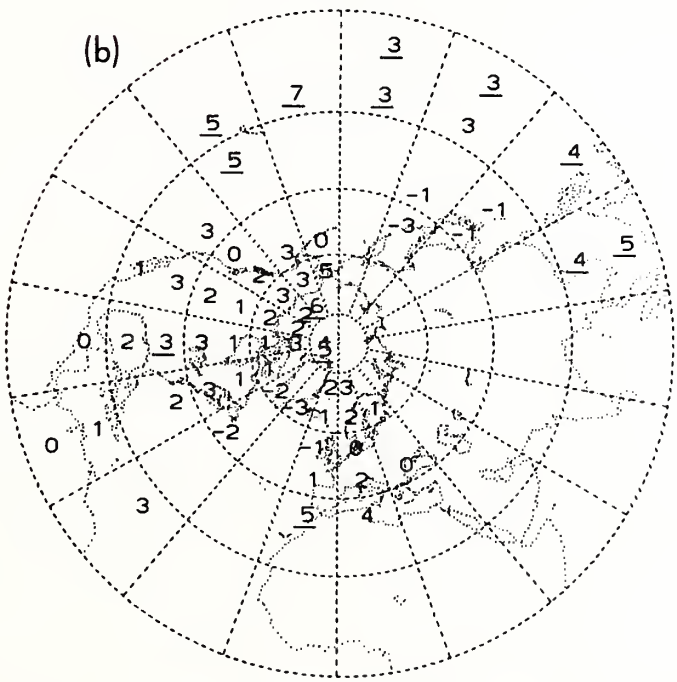

Fig. 2. Plotted at the centre of each grid box is the trend (in °C/century) of the least-squares straight line fitted to the time series of annual temperatue anomalies at (a) 50hPa and (b) 700hPa. The trend is underlined if it is significantly different from zero at the 97.5% level using a one-sided rank test.

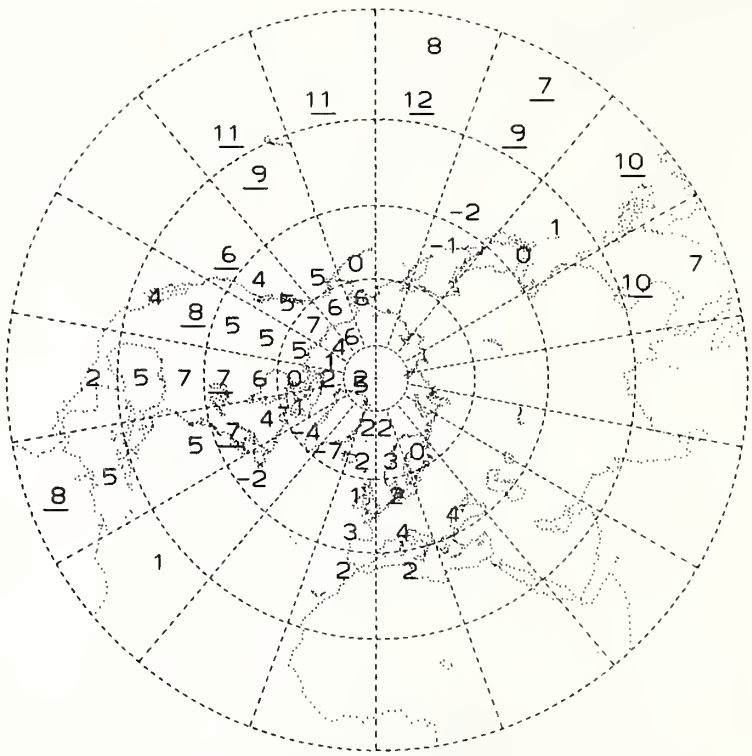

Fig. 3. Plotted at the centre of each grid box is the trend (in std. devn/century) of the least-squares straight line fitted to the time series of the normalized annual temperature index (1). The trend is underlined if it is significantly different from zero at the 97.5% level using a one-sided rank test.

Vladimir T. Radiuhin, Boris L. Shilenko
All-Union Research Institute of Hydrometeorological Information - World Data Centre
Obninsk, USSR

LOCATION PERIODS WITH LINEAR TRENDS IN CLIMATIC DATA SERIES

1. INTRODUCTION

One of the most important characteristics of the climatic signal is the moment of its occurence in the climate system parameter time series, and detecting such moments as well as further assessment of the signal and noise characteristics are important both historically (from the archived observation series available) and on the basis of the current data used for monitoring the climate system state.

Detecting the changes in the climate system state and estimating the statistical signal and noise characteristics can be looked upon as the problem of searching for change points in the time series characteristics by means of the failure detection theory (Nikiforov,1983).

In (Radiuhin and Mikhlin, 1986) the authors have examined the statistical properties of several randomness tests often used in climate change analysis, and concluded that among the tests considered the one based on the number of inversions in the time series is most efficient in detecting the monotonic variations in the time series means. In (Kleschenko and Radiuhin, 1987; Radiuhin and Mikhlin, 1986) this test was used to estimate the probability of monotonic trends in the gridded Northern Hemisphere series of mean monthly temperatures at sea level and the 500-1000 mb thickness. It is evident that if the signal occurs but only in the part of the series analysed, it is easier to detect it with a statistical method if one applies the test employed to the part with a trend (at least, the detection is more confident the less is the relative series part without a trend).

Below is described an algorithm based on computing the inversion test statistic from the moving parts of the series analysed, to detect the parts with a monotonic trend in the means and assess the signal-to-noise (S/N) ratio within this part. As in (Kleschenko and Radiuhin, 1987; Radiuhin and Mikhlin. 1986), here the signal-to-noise ratio is understood as the relation of the determined change of the time series mean for the section to the standard of deviations from the trend, which obscure the signal.

2. THE ALGORITHM FOR DETECTING PARTS WITH LINEAR TRENDS

Note, that the inversion test statistic t is computed by the formula $t=1-4Q/n(n-1)$, where n is the length of the time series part for which the statistic is computed and Q - the number of inversions in this part of the time series. When analysing a time series of length N, computing the inversion test statistic t from the moving parts of length n, with the moving step K, generates a series of the statistic values of length $L=\left[\frac{N-n}{K}\right]+1$ ($[\ ]$ denotes the operation of taking the integer part of the number). The values of t for the part of the series under consideration without a trend fluctuate about the zero mean level with a distribution according to the null hypothesis of a trend absence (Kendall and

Stuart, 1973; Radiuhin and Mikhlin, 1986). When a moving part covers the part with a trend the statistics distribution shifts from the centre of the segment, [-1,1] - the range of values of the statistic t, to its ends (to the right in case of a positive trend, and to the left in case of a negative one). The extent of shift in the statistic series mean depends on the level of the S/n ratio in the initial time series. Table 1 gives estimates of the first two moments of the statistic distribution for various values of n and S/n, obtained from the simulated time series. If the monotonic signal disappears from the series analysed, the original distribution of the series of values of the inversion test statistic is recovered.

Table 1. Estimates of the inversion test statistics distribution moments

S/n	n					
	25	30	35	40	45	50
	0.0	0.0	0.0	0.0	0.0	0.0
0.0	0.1430	0.1290	0.1180	0.1100	0.1030	0.0976
	0.1007	0.0969	0.1024	0.0952	0.0981	0.0989
0.5	0.1429	0.1243	0.1154	0.1099	0.0998	0.0952
	0.1936	0.1980	0.1858	0.1915	0.1893	0.1907
1.0	0.1365	0.1202	0.1145	0.1007	0.0963	0.0921
	0.2858	0.2852	0.2762	0.2771	0.2732	0.2745
1.5	0.1281	0.1173	0.1063	0.0952	0.0894	0.0858
	0.3722	0.3619	0.3579	0.3586	0.3548	0.3575
2.0	0.1177	0.1069	0.0982	0.0893	0.0869	0.0776
	0.4360	0.4341	0.4261	0.4241	0.4233	0.4224
2.5	0.1015	0.0962	0.0885	0.0797	0.0753	0.0761
	0.5003	0.4923	0.4906	0.4889	0.4900	0.4847
3.0	0.0927	0.0830	0.0786	0.0730	0.0685	0.0649

Figure 1 shows a series obtained from averaging over 1000 realizations of the inversion test statistic series, generated by computing the statistic t from the moving parts of the simulated series containing parts with a linear trend. Each realization of the time series is a determined component, of the type:

$$x_i = \begin{cases} 0, & i \leqslant 50, \\ Mi, & 50 < i \leqslant 150, \\ 0, & i > 150 \end{cases} \qquad i=0,200$$

which is obscured at each i-th point by random noise with a normal distribution of the zero mean and the unity standard deviation. For the case shown in Figure 1, n=25, k=1 and the parameter M is so chosen that the signal-to-noise ratio for the moving part is equal to 1.25. Thus, there occur some changes in the mean value of the statistic series in certain moments (to be more exact, during some intervals) and one can try to detect these changes.

To implement the algorithm for detecting parts of the timeseries with a monotonic trend, the quantiles of the statistic extreme ($max(t)$ and $min(t)$) distrubitions for various lengths n of the moving parts and values of S/n were first estimated using the statistical simulation method.

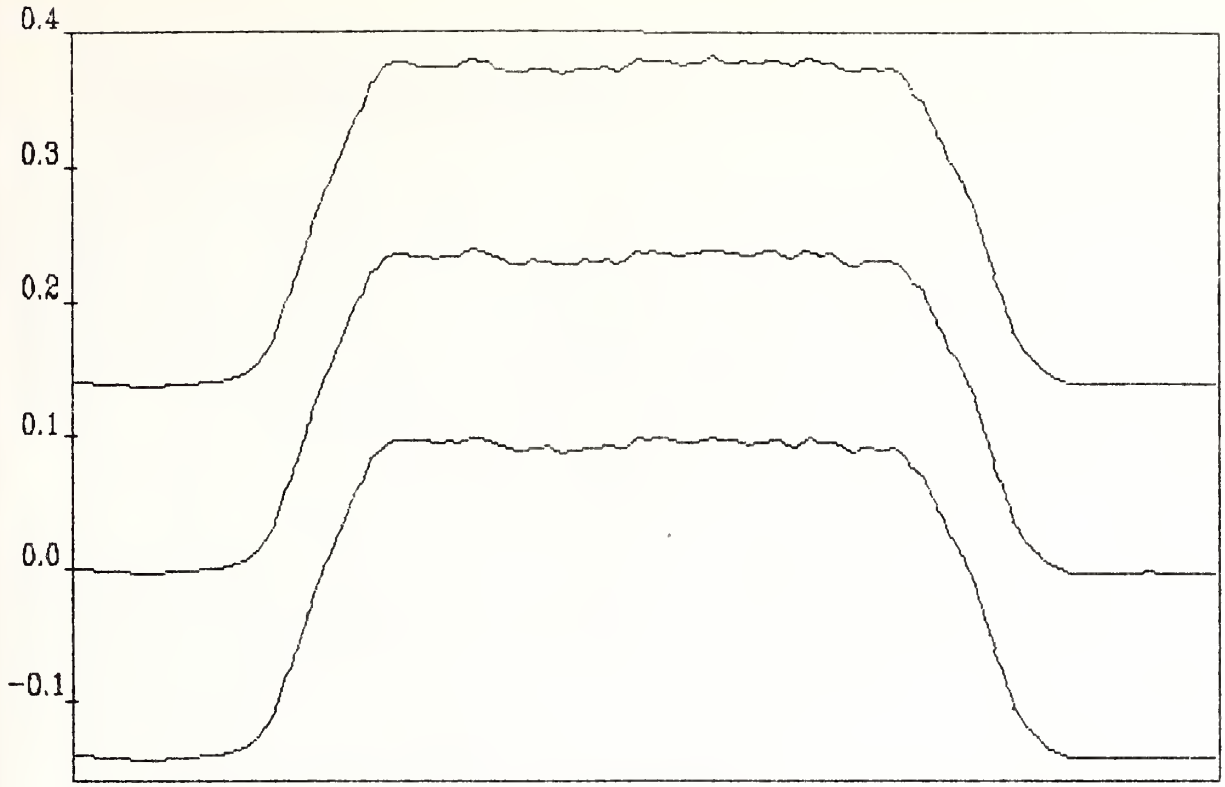

Fig.1 Mean variation of the inversion statistic values (for 1000 realizations). S/n=1.25, n=25.

The algorithm for detecting the start and end moments of a monotonic trend in the time series mean comprises the following major steps:

(i) Using the initial data series of the climate system characteristic analysed, a series of the inversion test statistic values is computed from the moving parts of length n.

(ii) Maximum and minimum values are determined among the ones of the series t.

(iii) Using the above values as well as the $max(t)$ and $min(t)$ distribution quantiles for a zero signal-to-noise ratio and a corresponding n, the hypothesis H_0 of the absence of a monotonic signal at any significance level is tested.

(iv) If H_0 is not rejected, no further analysis is performed. If H_0 is rejected, the alternative hypothesis H_1^l of the presence of a monotonic signal with the S/n_l ratio is defined using the $max(t)$ (or $min(t)$) value. As an alternative to the null hypothesis H_1^l is assumed with a corresponding signal-to-noise ratio, if $t_\alpha^{l-1} < max(t) \leqslant t_\alpha^l$ ($-t_\alpha^l \leqslant min(t) < -t^{l-1}$), where t_α^l is the α % quantile of the $max(t)$ or $min(t)$ distribution when there is a signal in the series with the S/n_l ratio.

(v) The change points in the mean of the series of the statistic t are detected by the cumulative sum algorithm (Nikiforov, 1983), i.e. a series of the cumulative sum (CS) values is computed:

$$\rho_k = \sum_{i=1}^{k} \left[\ln \omega(t_i/\theta_0,\sigma_0) - \ln \omega(t_i/\theta_1,\sigma_1) \right], \quad k=\overline{1,L}$$

where $\omega(t/\theta,\sigma)$ is assumed to be the density of normal distribution, θ_1,σ_1 correspond to the alternative hypothesis assumed at the previous step. Within the series part where the hypothesis of the signal absence is more probable the CS increases, while within the part where the alternative hypothesis is more probable the CS decreases. Thus, the part with a trend is the one where the CS decreases.

3. VERFICATION OF THE ALGORITHM AND EXAMPLES OF ITS USAGE

The algorithm has been tested using simulated time series and accuracy characteristics for defining the signal-to-noise ratio and trend start and end moments have been obtained (Radiuhin and Shilenko,1988). Conclusion was drawn fromthis that using the algorithm described one can define parts with a linear trend in the mean even at modest signal levels with a varying degree of uncertainty. The algorithm was implemented on the basis of four secular time series of the annual mean surface air temperatures averaged over the Northern Hemisphere: a series by K.Ya.Vinnikov, G.V.Gruza et al. published in (Vinnikov et al.,1980) and updated in (Vinnikov, 1985) (S1), a series by P.D. Jones et al. published in (Jones et al., 1982) (S2), ascertained series by P.D.Jones et al. (Jones et al., 1986) (S3) and a series obtained in the SHI[1] from 301 long-record stations by the statistically optimal averaging techniques (Vinnikov et al., 1987) (S4).

Table 2. Periods with linear trends detected in the series of annual mean surface air temperature averaged over the Northern Hemisphere

Series	n	Warming period	S/n	Cooling period	S/n
S1	25	1909 - 1936	2.0	1941 - 1969	-0.0
	50	1905 - 1936	3.0	1943 - 1958	-1.0
S2	25	1910 - 1936	2.0	1941 - 1969	-0.0
	50	1905 - 1937	3.0	------	
S3	25	1886 - 1904	0.5	1870 - 1886	-0.0
		1912 - 1937	1.5	1941 - 1967	-0.0
	50	1898 - 1939	2.5	1943 - 1959	-0.0
S4	25	1854 - 1871	0.0	1871 - 1885	-0.5
		1886 - 1906	0.0	------	
		1912 - 1933	2.5	1937 - 1967	-0.0
	50	1900 - 1938		1865 - 1880	-0.0
				1944 - 1960	-1.0

[1]The State Hydrological Institute

Table 2 gives the estimates of global warming and cooling periods as well as the signal-to-noise ratios for these parts of the time series for two lengths of the moving parts (n=25 and n=50).

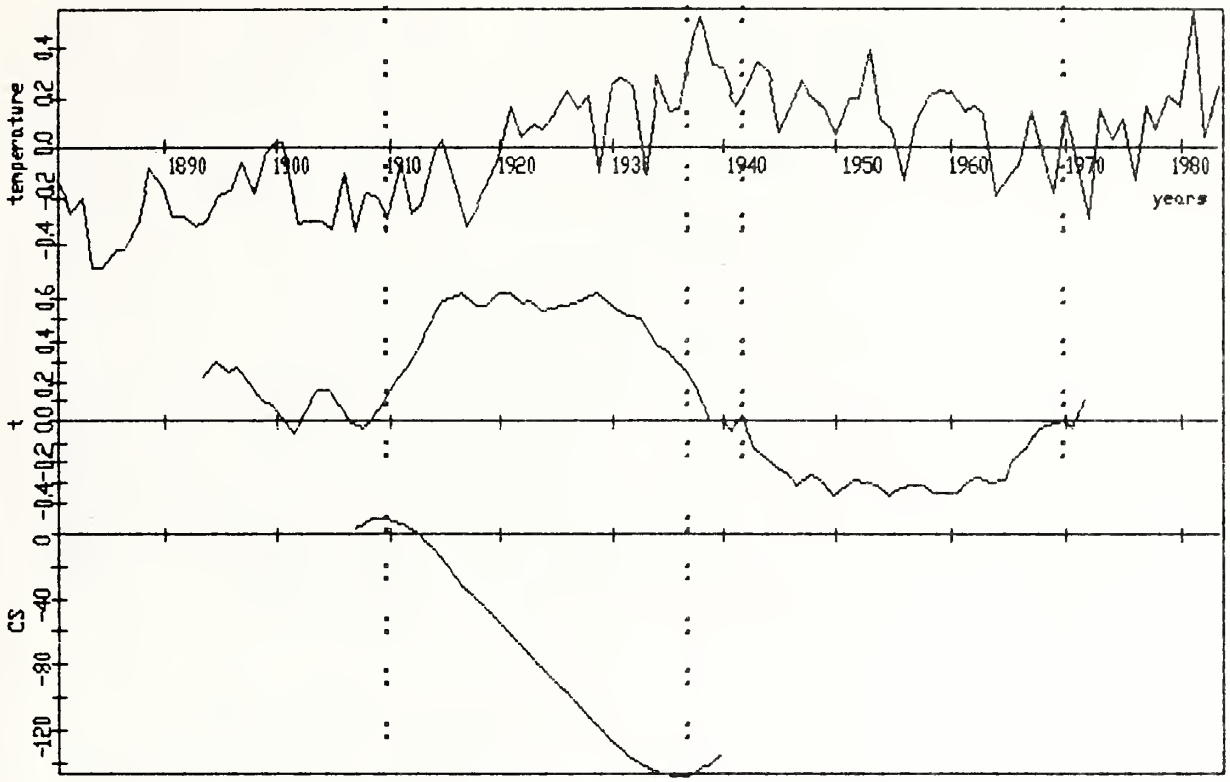

Fig.2 An example of using the algorithm for detecting periods with trends in S1 (a=0.1, n=25).

The zero values of the signal-to-noise ratio given in the table (and the corresponding time segments) denote that the null hypothesis is not rejected at the third step of the algorithm used; however, there are periods in the statistics series when it constantly has nonzero values. Dashes in some squares of the table denote that for the respective series there are not even insignificant (in the above sense) arguments in favour of rejecting the hypothesis of no trend. When analysing Table 2 rather a good agreement could be noted of the results obtained from the Northern Hemisphere mean annual temperatures which could have been expected due to the high correlation of the series (e.g., the correlation coefficient between *S1* and *S2* is 0.955, between *S1* and *S3* - 0.933, between *S1* and *S4* - 0.940, between *S2* and *S3* - 0.973, between *S3* and *S4* - 0.940 (Jones et al., 1986;Vinnikov, 1985)). Portions with insignificant or weakly significant cooling in the second half of the last century are found in series *S3* and *S4* which agrees with the conclusions of(Jones et al., 1986).Fig.2 which illustrates the application of the above algorithm to the first of the time series considered, shows the series, *S1*, itself, the series of the inversion test statistic obtained for the moving part length n=25, as well as the parts of the cumulative sum value series with warming and cooling periods detected.

4. CONCLUSION

The results from the algorithm for detecting in the time series parts with linear trends applied both to the simulated series with given characteristics and the real climatic time series which are well-known and well-studied, tell in favour of the suggested method which enables estimating with a varying degree of uncertainty start and end moments of the linear signal obscured by noise. There is evidence (Radiuhin and Mikhlin, 1986) to believe that this is also true of a monotonic signal which is not greatly different from the linear one. The algorithm enables objectivizing the process of seaching for new empirical facts of the climatic signals on the basis of many time series, which is next to impossible for subjective visual approach.

In conclusion it should be mentioned that quantiles necessary for realizing the algorithm, as well as the estimates of algorithm accuracy characteristics were obtained for the case of the deviations from the trend being mutually independent and the persistence within a series might be mistaken for a signal even in its absence. When enlarging the sphere of application of the algorithm suggested, it is useful to consider the effect of the series element interdependence.

REFERENCES

Goossens Ch., and A.Berger, 1983: Evaluation of the statistical significance of climatic changes. *Preprints Second International Conf. on Stat Clim.*, Lisbon, Portugal, 14.6.1-14.6.8

Jones P.D., T.M.L.Wigley and P.M.Kelly, 1982: Variations in surface air temperatures: Part 1. Northern Hemisphere, 1881-1980. *Mon.Wea.Rew.*, **110**, 59-72.

Jones P.D., S.C.B.Raper, R.S.Bradley, H.F.Diaz, P.M.Kelly and T.M.L.Wigley, 1986: Northern Hemisphere surface air temperature variations: 1851-1984. *J.Clim. Appl. Meteor.*, **25**, 161-179.

Kendall M. and A.Stuart, 1973: *Statistical inferences and relationships*, Nauka, Moscow, 900 pp. (in Russian).

Kleschenko L.K., and V.T.Radiuhin, 1988: Monotonic trends in the series of the Northern Hemisphere surface and lower troposphere air temperatures. *Proc. of VNIIGMI-WDC*, **143**, 31-44 (in Russian).

Leith C.E., 1973: The standart error of time-average estimates of climatic means. *J.Appl. Meteor.*, **12**, 1066-1069.

Nikiforov I.V.,1983: *Consecutive detection of changes in the time series properties*, Nauka, Moscow, 199 pp. (in Russian)

Radiuhin V.T., and Ya.E.Mikhlin, 1986: Comparing the efficiences of some nonparametric tests used in climate change analysis. *Proc. of VNIIGMI-WDC*, **129**, 17-26 (in Russian).

Radiuhin V.T., and Ya.E.Mikhlin, 1987: Using nonparametric randomness tests for climate change analysis. *Preprints Third International Conf. on Stat. Clim.*, Vienna, Austria, 256-264.

Radiuhin V.T., and B.L.shilenko, 1988: Algorithm for locating periods with linear trends in the mean value of time series. *Proc. of VNIIGMI-WDC*, **143**, 3-9 (in Russian).

Vinnikov K. Ya., 1985: Contemporary variations of the global climate. A review. *Seria Meteorologiia*, Obninsk, VNIIGMI-WDC, **8**, 52pp. (in Russian).

Vinnikov K.Ya., P.Ya.Groysman, K.M.Lugina and A.A.Golubev, 1987: Change in mean air temperature of the Northern Hemisphere for the period 1841-1985. *Meteor.Gidrol.*, **1**,45-55 (in Russian).

Vinnikov K.Ya., G.V.Gruza, V.E.Zakharov, N.P.Kirillov, N.V.Kovyneva and E.Ya.Rankova, 1980: Contemporary variations of the Northern Hemisphere climate. *Meteor. Gidrol.*, **6**, 5-17 (in Russian).

COMPARISON OF CORRECTED SEA SURFACE AND AIR TEMPERATURE FOR THE GLOBE AND THE HEMISPHERES, 1856-1988

C K FOLLAND[1] and D E PARKER

Meteorological Office, Bracknell, Berkshire, England RG12 2SZ

Introduction. There is considerable interest in variations of climate during the instrumental period. Studies of these variations can cast light on the natural variability of climate, and on climatic mechanisms including those of the greenhouse effect, and are needed for empirical long-range forecasting research. Sea surface temperature (SST) is particularly important. Unfortunately historical SST data are not only incomplete but suffer from seriously changing biases. There are also substantial disagreements between the global and hemispheric bias estimates of Jones et al (1986) and Folland et al (1984) for SST data before 1905. We summarise recent research into these biases and provide a new set of corrections. An earlier version of this approach has been used in Bottomley et al (1989).

Results. Fig. 1 shows uncorrected seasonal SST and corrected night marine air temperature (NMAT) anomalies averaged over the globe for 1856 to (July-Sept) 1988. The reference period is 1951-80. The corrections that have been applied to the NMAT data are to compensate for changes in deck elevation and for changed observing practices in World War II (see Figure caption), but are slightly different from those described in Folland et al (1984). A sudden change in the difference between the uncorrected SST and corrected NMAT anomalies can be seen in Fig. 1 around 1942, much as shown in Barnett (1984) and Folland et al (1984).

Fig. 2 shows a spectral analysis of uncorrected SST anomalies for 1901-1941 for the whole N Atlantic. A large spectral peak can be seen at periods near one year, i.e. there appears to be a strong annual cycle relative to the 1951-80 reference period. Correspondingly, we find that many series of extratropical SST anomalies that have been band-pass filtered to pass periods centred on one year show enhanced variance until around 1942 (e.g. Fig. 3, top curve). Only in areas of little real annual cycle near the equator is this behaviour absent. The change around 1942 is abrupt in the extratropical N. Hemisphere. We attribute the changes in the annual cycle to a worldwide change in the instrumentation used to measure SST. It is known that the predominant instrument used before the second World War was the uninsulated or partially insulated sea bucket. It is thought that around 1941-2 engine intake measurements became predominant because of the exigencies of war. These will show a reduced annual cycle of SST relative to those derived from uninsulated buckets because the seasonally varying effects of evaporation and sensible heat transfer from the bucket walls have no counterpart in engine intake measurements. Documentation suggests that after 1945 engine intake techniques retained their prominence or shared it with insulated buckets, though it is known that some uninsulated buckets were used for many years e.g. by the UK.

The top curve of Fig. 3 shows, for 1858-1984 for the latitude band 30°N-40°N, a 15 year running ratio of the variance of uncorrected SST anomalies near the one year time scale to the total variance. The data for before about 1880 are less complete so the ratio is less reliable then. A large reduction in the ratio can be seen centred around 1942. A correction

---

[1] currently at Climate analysis Center, National Meteorological Center, Washington, D C, 20233

technique has been devised which takes advantage of this behaviour. It combines an a priori component, i.e. a physical model of the heat exchange from uninsulated buckets, and an a posteriori component, i.e. a statistical requirement that the above variance ratio for the period before 1942 should be as similar as possible to its value in 1951-80. Thus the correction procedure attempts to correct the SST data relative to the data mix in 1951-80. It does not, in principle, supply absolute corrections.

The model was used to calculate corrections for uninsulated bucket SST on 5° latitude x longitude and monthly resolution for many latitude zones away from the equator. The corrections varied according to the assumed exposure time as well as the size of the uninsulated bucket and the assumptions about atmospheric conditions on a ship's deck relative to those in standard 1951-80 climatologies. Climatological data for each calendar month and 5° x 5° area were used in the derivation of the boundary conditions for the model. Fig. 3 includes the results of applying test-corrections to pre-1942 data in the zone 30°N-40°N. As the modelled exposure time of the bucket was increased, all other parameters being held fixed, the variance ratio first decreased to a minimum (at about 1.5 minutes exposure time for this case) and then increased as exposure time increased further. The latter behaviour indicates that the data have been overcorrected because the assumed exposure time was too long. The exposure time yielding minimum variance ratio was taken as optimal. Estimation of the optimal exposure time must be carried out for entire zonal belts because real interannual and interdecadal climatic variations in the annual cycle of SST are most likely to occur in local zones of longitude. Reasons for this include changes in the phase or intensity of atmospheric long waves and in regional oceanic processes. Nevertheless, the corresponding corrections can be retrieved on a 5° x 5° space scale. Inspection of Fig. 3 and similar diagrams for other latitude zones away from the equator shows that the enhanced annual-cycle variance observed in the uncorrected data is consistently and strongly reduced throughout the record before 1942 using optimal exposure times provided by this technique.

For each latitude belt, the optimal exposure time was estimated separately for 1861-90, 1881-1910, 1901-30 and 1911-40 for a variety of model assumptions (on e.g. bucket size) by minimising the variance ratio as described above. Using analysis of variance tests, it was found that, for a given set of model assumptions, the same exposure time could be used for all available latitude zones of the global ocean that show an appreciable annual cycle. It was then assumed that the same exposure time could be used everywhere for a given set of model assumptions, including in equatorial regions. Although this universal optimal exposure time depended substantially on the model assumptions e.g. being longer for a larger bucket which cools (or occasionally warms) more slowly, the consequent optimal corrections produced by the model were quite similar in a given 5° x 5° region and calendar month. The variations that did occur were mostly considerably less than a typical mean annual correction of 0.25-0.5°C. However, the universal optimal exposure time for a given set of model assumptions tended to increase between the 19th and 20th Century portion of the record. This was assumed to be mostly because the later ships moved more quickly, strengthening the effective wind, so that in the model the bucket needed to cool for a little longer for a given ship's speed if the amplified annual cycle of heat loss was to be reproduced. If an appropriate sequence of estimated ship speeds was used in the model the same optimal exposure time could be applied throughout the record, and the optimal corrections up to 1890 were then typically one third smaller than those after 1910. The final corrections for a given location and calendar

month were computed by averaging the optimal corrections for a range of reasonable assumptions about bucket size and degree of shelter on deck, but with slow (4 m/sec) and fast (7 m/sec) ships' speed for 1856-90 and 1911-41 respectively. This change in mean ships' speed is only a first estimate of the effects of the transition from sail to steam. The corrections for a given calendar month were interpolated linearly in time to yield corrections for 1891-1910. Although the new corrections are much more complex, their globally averaged value in the late nineteenth century, about 0.26°C, is only slightly less than the constant value of 0.3°C used in Folland et al (1984).

Fig. 4 shows the corrections calculated for December 1856-1890. The corrections are quite large near the equator because differences between saturation vapour pressures at the SST and atmospheric vapour pressures allow substantial rates of evaporation from the bucket. As expected, the corrections there are similar there throughout the year. The mean annual magnitude of the corrections is broadly consistent with the results of an extensive worldwide comparison of bucket (believed to be mostly uninsulated) and engine intake data performed by Walden (1966). The comparison is best equatorwards of 40°N or S.

Fig. 5 compares decadal running differences between air temperature anomalies observed on islands distributed worldwide and nearby corrected SST anomalies. The reference period is 1951-80. The number of islands varies from about 10 in 1870 to about 55 in recent decades. The air temperature data have been kindly provided by Dr P Jones (Climatic Research Unit, Univ. of E. Anglia, Norwich, UK). The differences are statistically insignificant in both hemispheres in the late nineteenth century while between 1900 and 1940 the land air temperature anomalies are between 0.1°C and 0.2°C higher than the SST anomalies. When the SST and NMAT data are compared in similar regions surrounding the above islands, their differences are found to be statistically insignificant in all decades.

Fig. 6 shows time series of corrected, smoothed, seasonal SST and NMAT anomalies, relative to 1951-80, for the two hemispheres for 1856 to (July-Sept) 1988. The agreement between SST and NMAT was not forced by the correction procedures and is therefore powerful evidence for their validity. Work is underway to test the sensitivity of these results to a similar correction procedure that uses models of partially insulated (wooden, leather etc) buckets.

REFERENCES

Barnett, T P (1984) Mon Weath Rev, 112, 303-312
Bottomley, M et al (1989) Global Ocean Surface Temperature Atlas (GOSTA). (Joint Met Office/MIT project), MIT Press (in press)
Folland C K, Parker D E, and Kates F E (1984) Nature, 310, 670-673
Jones P D, Wigley T M L, and Wright P B (1986) Nature, 322, 430-434
Walden H, (1966) Deutsche Hyd., Zeits., 19, 1, 21-28

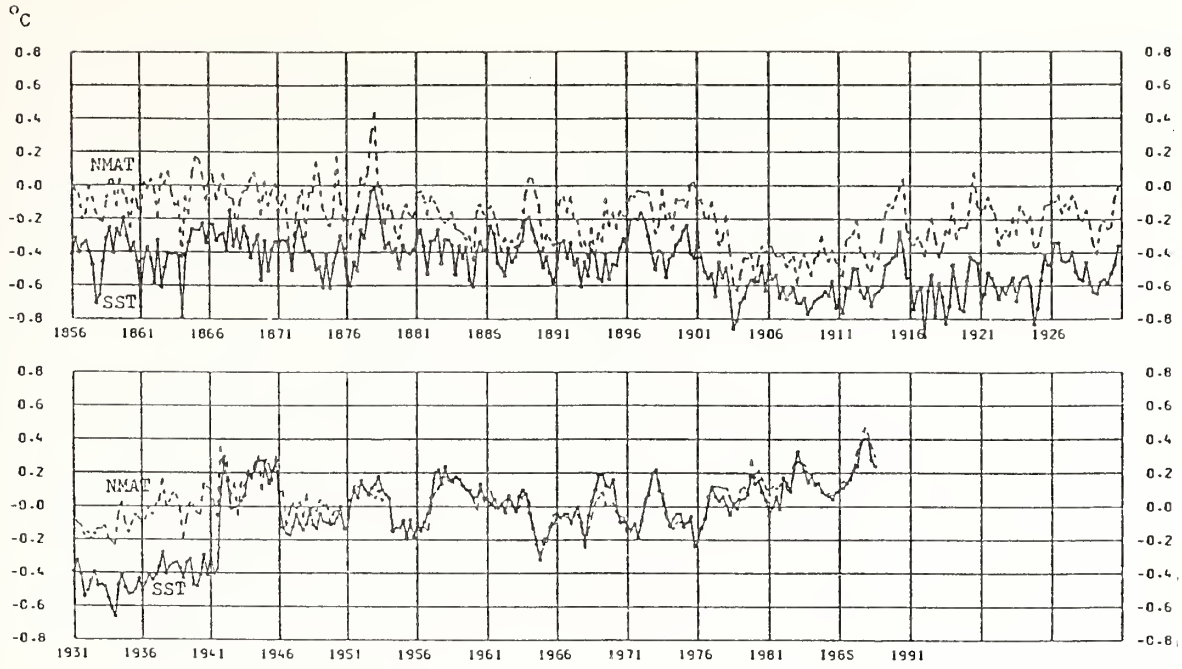

Figure 1. Global seasonal anomalies of uncorrected SST and corrected* night marine air temperature, 1856 to (July-Sept)1988.

* INSTRUMENTAL CORRECTIONS APPLIED TO NMAT:-0.15 <1891:LINEAR RISE TO 1911 THEN NIL TO MAR40:-0.1 TO DEC41: NIL FROM OCT 1945 ALSO -0.5 1942-SEP45 BUT -0.6 IN ATL>20N.-0.9 IN PAC>25N420-25N.W OF 165W.1942-SEP45 BAD MAT ANOMALIES 1876-93 IN MEDITERRANEAN & N.INDIAN OCEAN REPLACED BY SST ANOMALIES

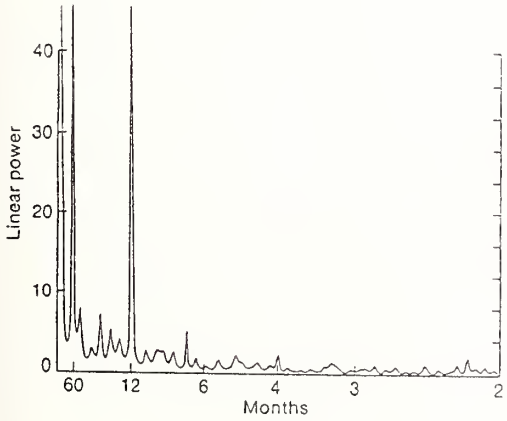

Figure 2.
Spectral analysis of uncorrected SST anomalies for N.Atlantic, 1901-1941.

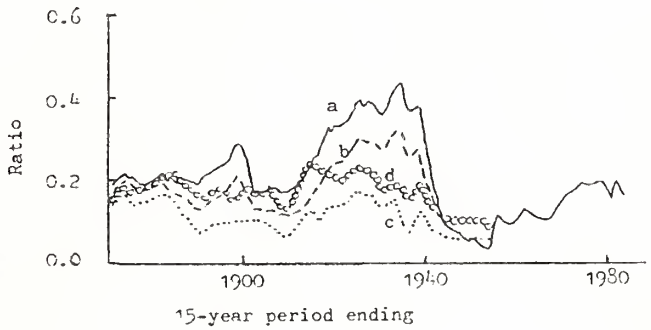

Figure 3.
15-year running ratio of annual-cycle variance to total variance of monthly SST anomalies (w.r.t.1951-80 climatology) for the belt 30°N to 40°N, 1858-72 to 1970-84.

a. Uncorrected.
b. Corrected up to 1941 assuming ½ minute exposure time.
c. As b. but 1½ minutes' exposure time
d. As b. but 3 minutes' exposure time.

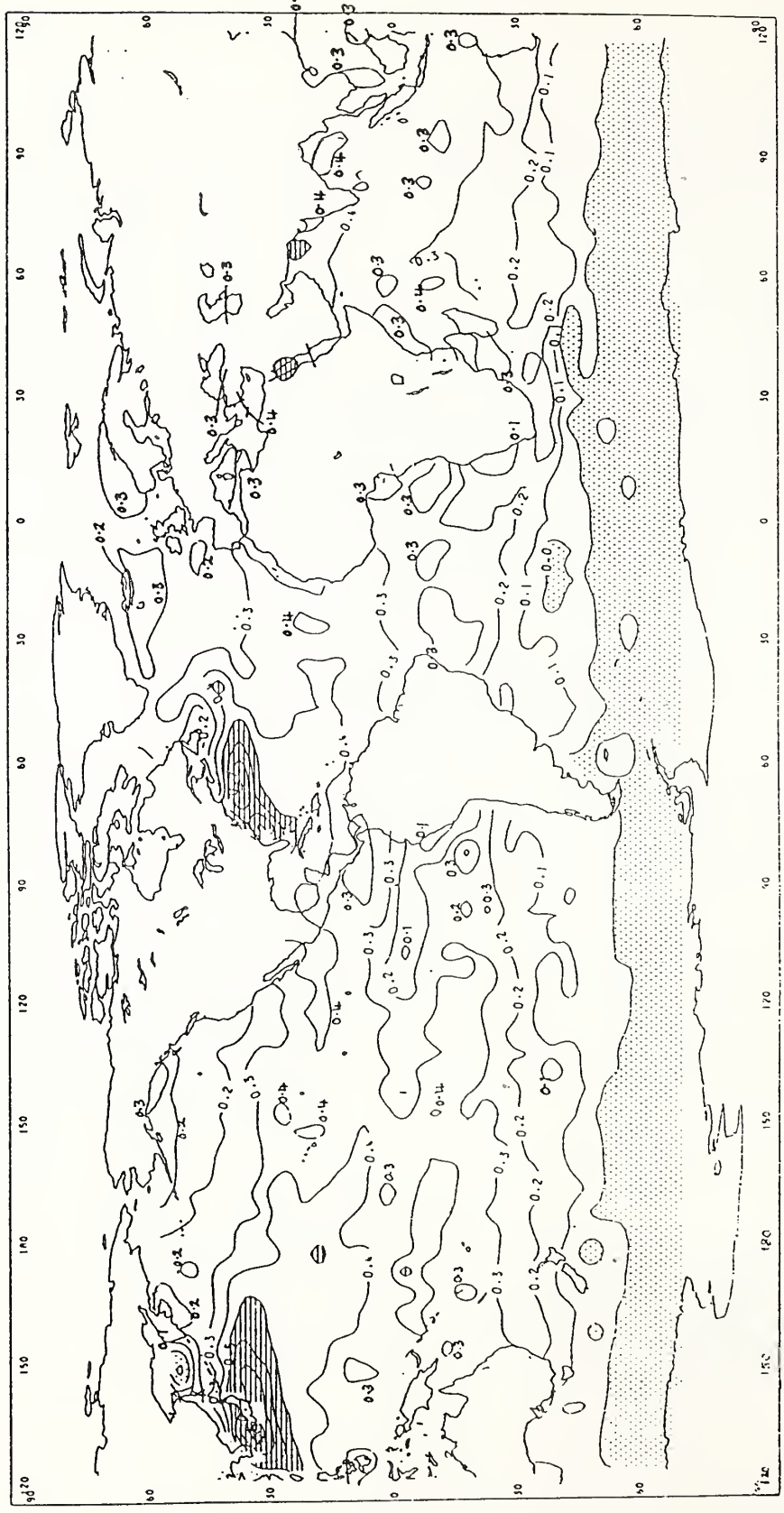

Figure 4. Corrections (°C) applied to worldwide SST anomalies in December, 1856-1890.

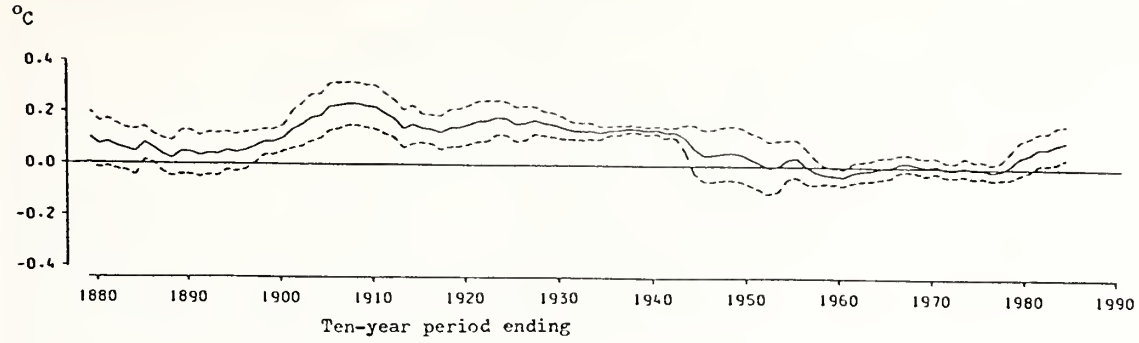

Figure 5. Worldwide average differences between decadally-averaged anomalies of island air temperature and of nearby corrected SST, 1870-79 to 1975-84. Estimates of +/- 2 standard errors are shown by the dotted lines.

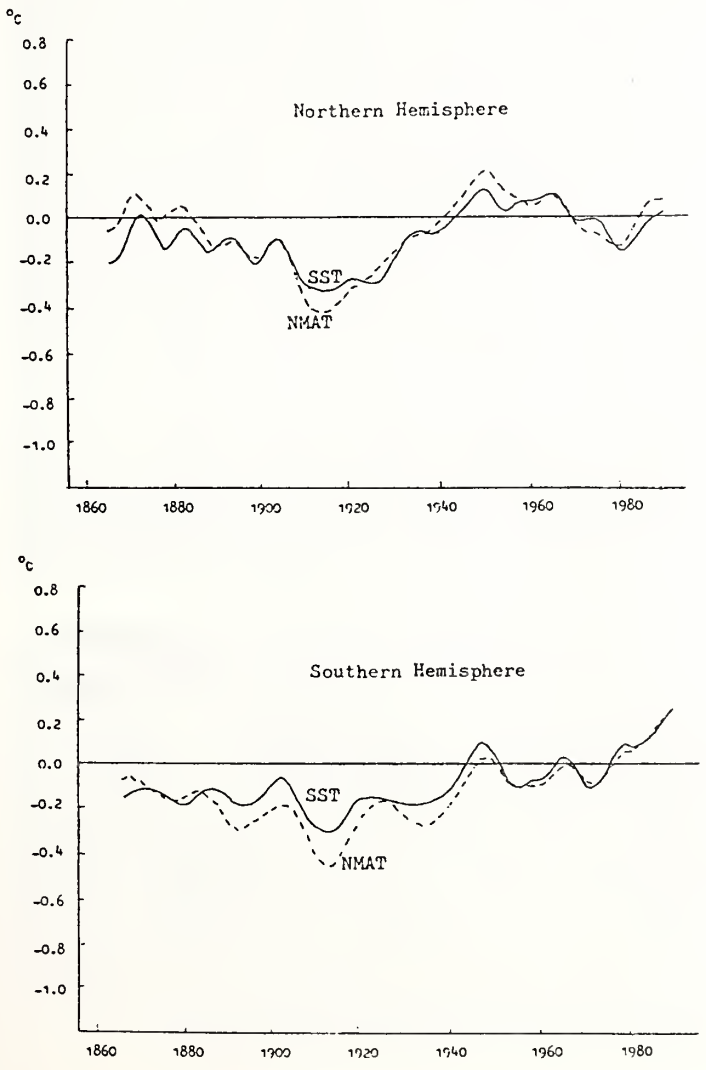

Figure 6.

Smoothed corrected SST and NMAT anomalies for the Northern and Southern Hemispheres, 1856 to (July-Sept)1988. Triangular smoothing eliminates fluctuations with periods less than about 5 years. Values are plotted against the end-date of the smoothing interval.

Annual cycle and long-term trends of large-scale features of the tropical climate system

Klaus Wolter* and Stefan Hastenrath
Department of Meteorology, University of Wisconsin
Madison, Wisconsin 53706

The tropical oceans are now widely recognized as a particularly active component of the climate system. Long-term ship observations have become a standard data source for investigations into the mechanisms of interannual climate variability. Distributed as they are irregularly in time and space, a compaction of the data is desirable. To this end, Wolter (1987) introduced clustering techniques, thus reducing the data volume while preserving the large-scale signal of the most coherent regions. The present study subjects the clustered data to an extensive trimming procedure which serves as a final filter and cluster classification check. Detailed results on the variability of circulation and climate and its areal coherence with respect to the annual cycle will be presented elsewhere (Wolter and Hastenrath, 1988). Here we will focus on trends in the large-scale circulation setting and seasonal characteristics of interannual climate variability.

We base our study on long-term ship observations in the tropical oceans obtained from the National Climate Center at Asheville, North Carolina, for individual months and with a one degree square spatial solution. These served as a source for a series of climatic atlases (e.g., Hastenrath and Lamb, 1977), and were later extended to 1983 and compiled into five-degree square areas. Elements used in the present study are sea level pressure (SLP), zonal (u) and meridional (v) components of wind, sea surface temperature (SST), and total cloudiness (CLOUD). These were compiled into the bi-monthly seasons January/February through November/December for 1948-83. On the whole, observations are densest along the major shipping lanes and scarcest in the Southern tropical oceans (Fig. 1a). In order to corroborate trends from ship data, records for selected tropical island and coastal stations were examined. Surface air temperature and sea level or station pressure based on World Weather Records were available on magnetic tape (Roy Jenne, NCAR, pers. comm., "World Monthly Surface Station Data"). Cloudiness observations for Florida were obtained from the National Climate Data Center in Asheville, North Carolina. All but about one fifth of the temperature and pressure records thus compiled were eliminated because of excessive gaps and obvious errors. Fig. 1, parts a,b, shows the locations of the remaining stations utilized here.

Cluster analysis captures such features as the westward shift of the North Atlantic subtropical high from boreal winter to summer, seasonal latitude displacements of the near-equatorial trough over the Eastern Pacific, wintertime cold-air invasions across the Central American Isthmus, the cross-equatorial flow of the Indian summer monsoon, and the evolution of the cold-water tongue to the South of the Atlantic Equator in boreal summer (ref. Wolter and Hastenrath, 1988).

Each cluster time series C_{it} is examined for its linear trend in time t using the least-squares fit equation:

$$C_{it} = s_i * t + b_i \qquad (1)$$

with s_i being the slope of the time series i with time (i.e., its trend), and b_i being its interception point with the ordinate. The formula reflects a least squares fit of the original time series with respect to time. Statistical significance is assessed by comparing the trend against the possibility of arriving at the same trend by chance if the real trend were equal to zero (Spiegel, 1975, p. 289). Similar statistical tests are used to check station-based versus ship-based trends where applicable. Note that differences in trend size are more important for this comparison than actual trend values.

---

* presently at CIRES, University of Colorado at Boulder, Boulder, CO 80309-0216

Long-term trends are shown in Figs. 2 and 3. Most prominent are the following evolutions over the 1948-83 period: (i) a tendency towards increasing prevalence of the negative Southern Oscillation mode (characterized by anomalously low/high pressure at Tahiti/Darwin) accompanying the increase of El Niño occurrences (ref. Figs. 2 and 3, parts a and d); (ii) in boreal summer a southward shift of the Atlantic near-equatorial low-pressure trough and embedded confluence zone and warming/cooling of surface waters to the South/North of the Equator (Fig. 3, parts a - d), paralleling the progressive aggravation of drought in Subsaharan Africa; (iii) likewise in boreal summer a more easterly position of both the North and South Atlantic highs (Fig. 3a) which together with (ii) connotes a reduced annual cycle of circulation in the tropical Atlantic sector, commensurate with the increasing prevalence (i) of the negative SO mode; (iv) increased cloudiness over the North Atlantic Ocean throughout the year (Figs. 2e and 3e); and (v) warming in the Indian Ocean (Figs. 2d and 3d). Note that the station-based trends essentially corroborate the ship-based cluster trends (Figs. 2 and 3, parts a,d, and e), best for cloudiness, less so for pressure, and least for temperature. Spurious trends are assumed to be prevalent in the wind data, since the match with the SLP fields is rather poor, especially in the Southern hemisphere (Figs. 2 and 3, parts a-c).

Acknowledgments:

This study was supported through U.S. National Science Foundation Grant ATM-8722410. We thank Chester Ropelewski and Michael Halpert at the Climate Analysis Center for surface station data, and the Climate Prediction Branch for purchasing the utilized cloudiness data from the National Climate Data Center in Asheville, North Carolina. KW acknowledges postdoctoral support from the University Corporation for Atmospheric Research.

References:

Hastenrath, S., Lamb, P., 1977: *Climatic atlas of the tropical Atlantic and Eastern Pacific Oceans.* University of Wisconsin Press, Madison, 113 pp.

Spiegel, M. R., 1975: *Probability and statistics.* Schaum's Outline Series, McGraw-Hill, 372 pp.

Wolter, K., 1987: The Southern Oscillation in surface circulation and climate over the tropical Atlantic, Eastern Pacific, and Indian Oceans, as captured by cluster analysis. *J. Climate Appl. Meteor.*, **26**, 540 - 558.

Wolter, K., Hastenrath, S., 1988: Annual cycle and long-term trends of interannual circulation and climate variability over the tropical oceans. Submitted to *J. Climate*

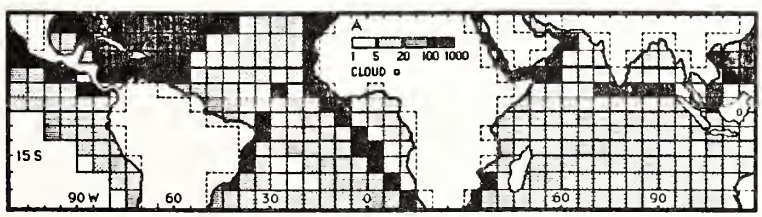

Fig. 1: Orientation maps.
(a) Ship data domain and density of ship observations by five degree square areas. Numbers indicate calendar monthly averages (total number of observations during the period 1948 - 83 divided by 432 = 36 times 12). Cloudiness stations are indicated by squares. Located in Florida, they are (North to South): Apalachicola, Daytona Beach, Fort Myers, Miami, and Key West.

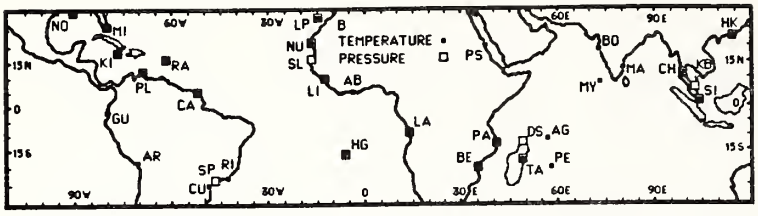

Fig. 1: Orientation maps continued.
(b) Stations with temperature (dots) and pressure (squares) observations. Going from North to South, they are in the Americas: NO New Orleans, MI Miami, KI Kingston, RA Raizet, PL Plesman, CA Cayenne, GU Guyaquil, AR Arica, RI Rio de Janeiro, SP Sao Paulo, and CU Curitiba; along the West African seaboard: LP Las Palmas, NU Nouadhibou, SL Saint-Louis, LI Lungi, AB Abidjan, LA Luanda, HG Hutt's Gate; along the East African seaboard: PS Port Sudan, AG Agalega, DS Diego-Suarez, PA Porto Amelia, TA Tamatave, BE Beira, PE Plaisance; in the Australasian sector: HK Hong Kong, BO Bombay, MA Madras, CH Chumphon, MY Minicoy, KB Kota Bharu, and SI Singapore.

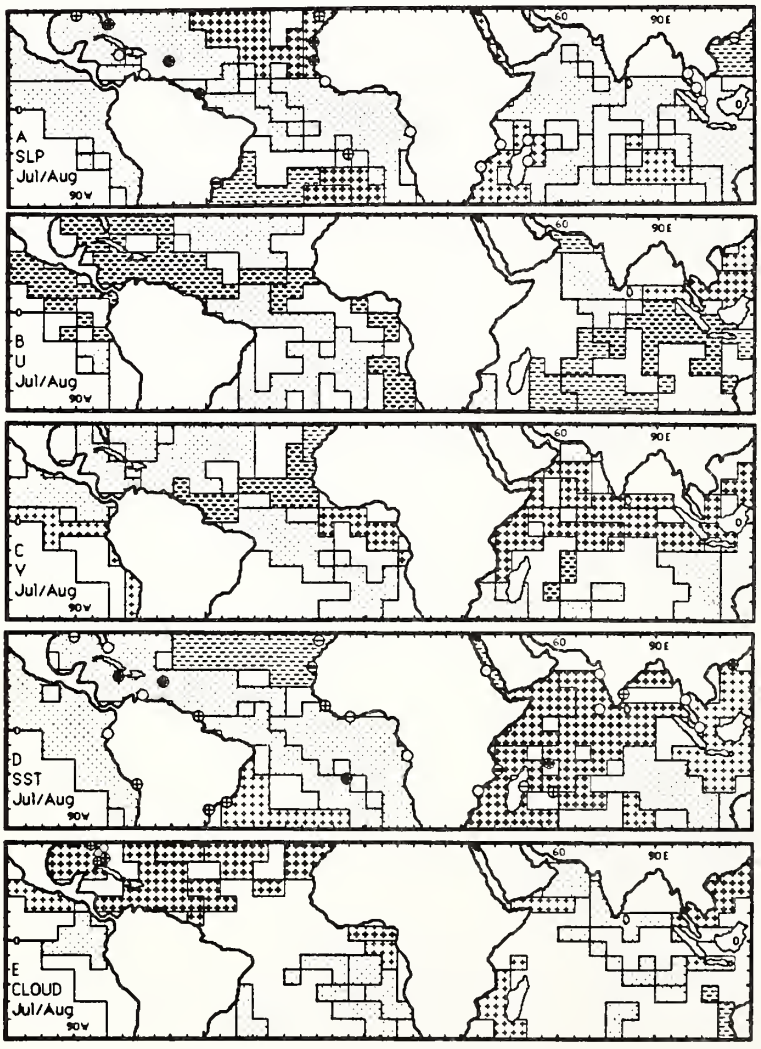

Fig. 3: As in Fig. 2, except for July/August.

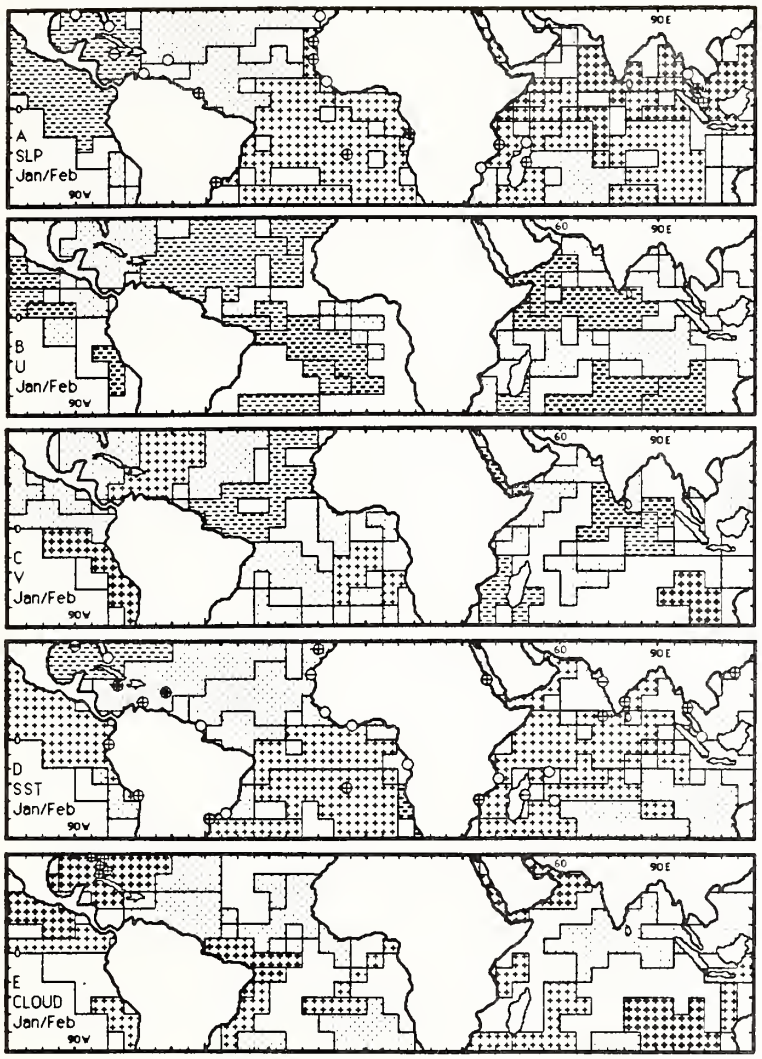

Fig. 2: Linear trends in 1948 - 83, mapped for January/February clusters and stations of (a) SLP, (b) u - wind component, (c) v - wind component, (d) SST, (e) cloudiness. Stations are denoted by circles. Enhanced symbols represent 95 percent significance levels. Dot raster indicates absolute trends below the following threshold values: 1.6 mb, 1.5 ms^{-1}, 0.8 °C, and one tenth per hundred years for pressure, wind speed, temperature, and total cloudiness, respectively. Discarded five degree squares are left unmarked.

Seasonal Temperature Variability over the North Atlantic Arctic

Jeffrey C. Rogers
Department of Geography, The Ohio State University
Columbus, Ohio 43210-1361

This study is an attempt to evaluate the existence and significance of seasonal mean temperature variability in the North Atlantic Arctic. Other papers at this workshop have drawn attention to the fact that the region is currently unusually cold and is not partaking in the apparent warming occurring in other parts of the hemisphere. Recent temperature variability is described in this paper as is the association between long-term changes in pressure and geostrophic wind linked to the temperature variations. Twenty-four Atlantic Arctic stations are used (Fig. 1) to examine regional climatic fluctuations. Pressure data are the 5x5° latitude/longitude gridded values based on the Historical Weather Maps, available since 1899.

The Cramer t statistic is calculated for five year subperiods of the 107 year (1881-1987) record of Atlantic Arctic seasonal mean temperatures. The Cramer t statistic is useful in evaluating the constancy of the mean of a time series by determining if differences in subperiod means are no larger than would be compatible with a null hypothesis of randomness. The t statistic for a subperiod is:

$$t = \left[\frac{n(N-2)}{N - n(1+\tau_s^2)}\right]^{1/2} \tau_s$$

where n=5 and N=107 and where

$$\tau_s = \left(\frac{\bar{T}_s - \bar{\bar{T}}}{S}\right)$$

where $\bar{T}_s$ and $\bar{\bar{T}}$ are the subperiod and long-term means and S the long-term standard deviation. Ordinarily the test is performed on subperiods of specific interest but in this cases it is done for all possible N-4 subperiods, meaning that the subperiods overlap each other. The statistic t is distributed as Student's t, usually with N-2 degrees of freedom (d.o.f.). Due to the overlapping subperiods, the number of d.o.f. used here is arbitrarily chosen as 10, about one-tenth of N-2.

The field significance of the N-4 Cramer t values is further evaluated by comparing the results to those for 1000 similar time series (same record length and standard deviation) of white noise random numbers. Fig. 2 shows that of 1000 randomly generated time series it is not uncommon that none of the t values are significant with 95% confidence tested with 10 d.o.f. However, 5% of the time series have 7 or more significant t values. It is assumed that the time series shown in this paper are significantly non-random if 7 or more significant t values are calculated.

The time series of North Atlantic Arctic seasonal mean temperature (Fig. 3) have several interesting features. Significantly high temperatures occur in many subperiods in all seasons of the 1920s and 1930s. Significant subperiods do not occur after the 1940s except in autumn in the late 1950s. A steady decline in temperature takes place in all seasons from the 1930s to the present. Arctic mean temperature is now over 2°C lower than in the 1930s and it is over 1°C lower in the other seasons.

The winters and springs of the late 1960s are very cold. The ice in the North Atlantic pushed southward and encroached on Iceland in this period, especially in spring. Fig. 4 shows composites of pressure/height differences obtained by subtracting the mean values in warm springs (1964, 1972, 1973, 1974, 1976) from those of the cold springs (1965 through 1970). Anomalous northerly geostrophic flow is noted around Iceland.

Composites of sea level pressure differences between the periods of highest North Atlantic Arctic temperatures (generally the years of the 1920s and 1930s) and lowest temperatures (1960s through 1980s) are also calculated. The largest pressure differences (Fig. 5) in the composites take place across a region extending from southern Greenland to Baffin Island. In all seasons, the highest levels of statistically significant pressure differences occur in the region 60-65°N, 55-70°W, an area encompassing the Davis Strait. Fig. 6 shows the time series of seasonal mean pressure for this area in each season. Each pressure time series is characterized by lower pressure in the early decades and higher pressure in more recent times. The five-year subperiods of pressure in Fig. 6 are tested using the Cramer t test. Several subperiods have significantly high pressure in recent decades in winter and autumn. In lieu of more detailed analysis of the pressure-temperature relationships, one can only point out that the correspondence between Figs. 3 and 6 seems fairly reasonable, especially at lower frequencies. This is especially true in summer and autumn when the periods of lowest pressure correspond very closely to those of highest temperature. One also notes a three-regime structure in summer and autumns in Figs 3 and 6, with regimes in the 1930s, 1940-1960 and 1965-1985.

The inverse relationship between mean pressure and mean temperature in the North Atlantic Arctic suggests that periods of more intense cyclonic activity around southern Greenland and Baffin Island are associated with higher numerical values in the regional mean temperature while higher pressure is associated with lower mean temperature. The region around southern Greenland is along several of the major storm tracks. The cold Atlantic arctic is potentially poised for another rapid warming, such as occurred in the mid-1920s (Fig. 3). If a warming of 1-3°C takes place in the North Atlantic Arctic, explanations as to its cause cannot exclude pressure/advective changes from consideration as long as the warming is accompanied by increasingly intense cyclonic activity and decreases in mean pressure.

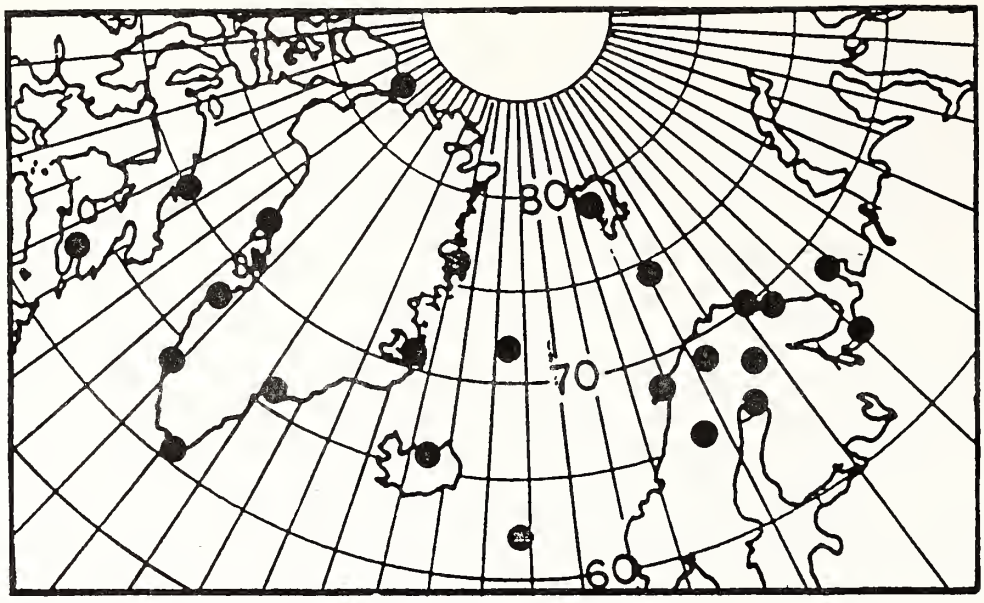

Fig. 1 The 24 Atlantic Arctic Stations.

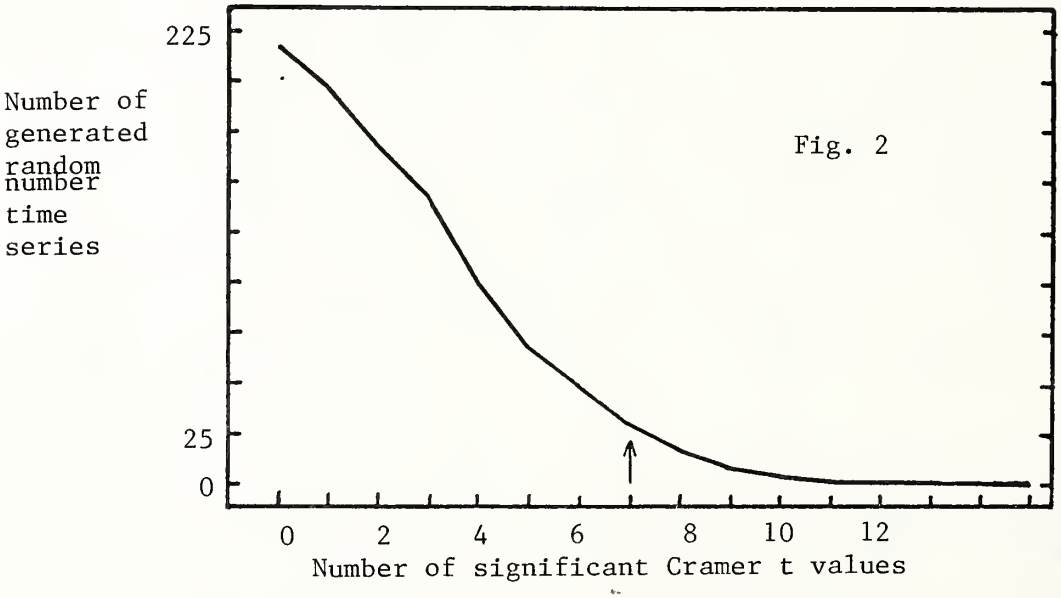

Fig. 2

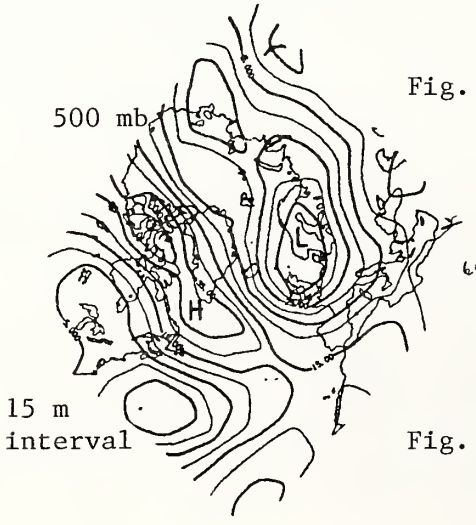

Fig. 4

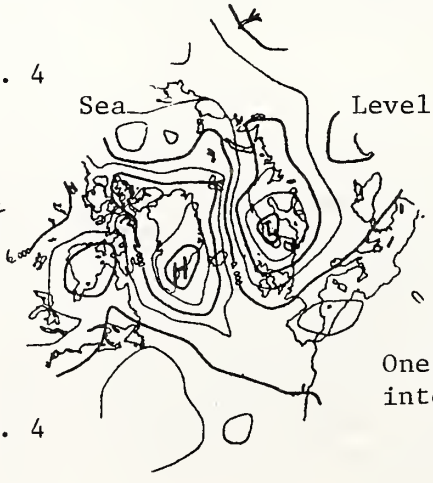

Fig. 4

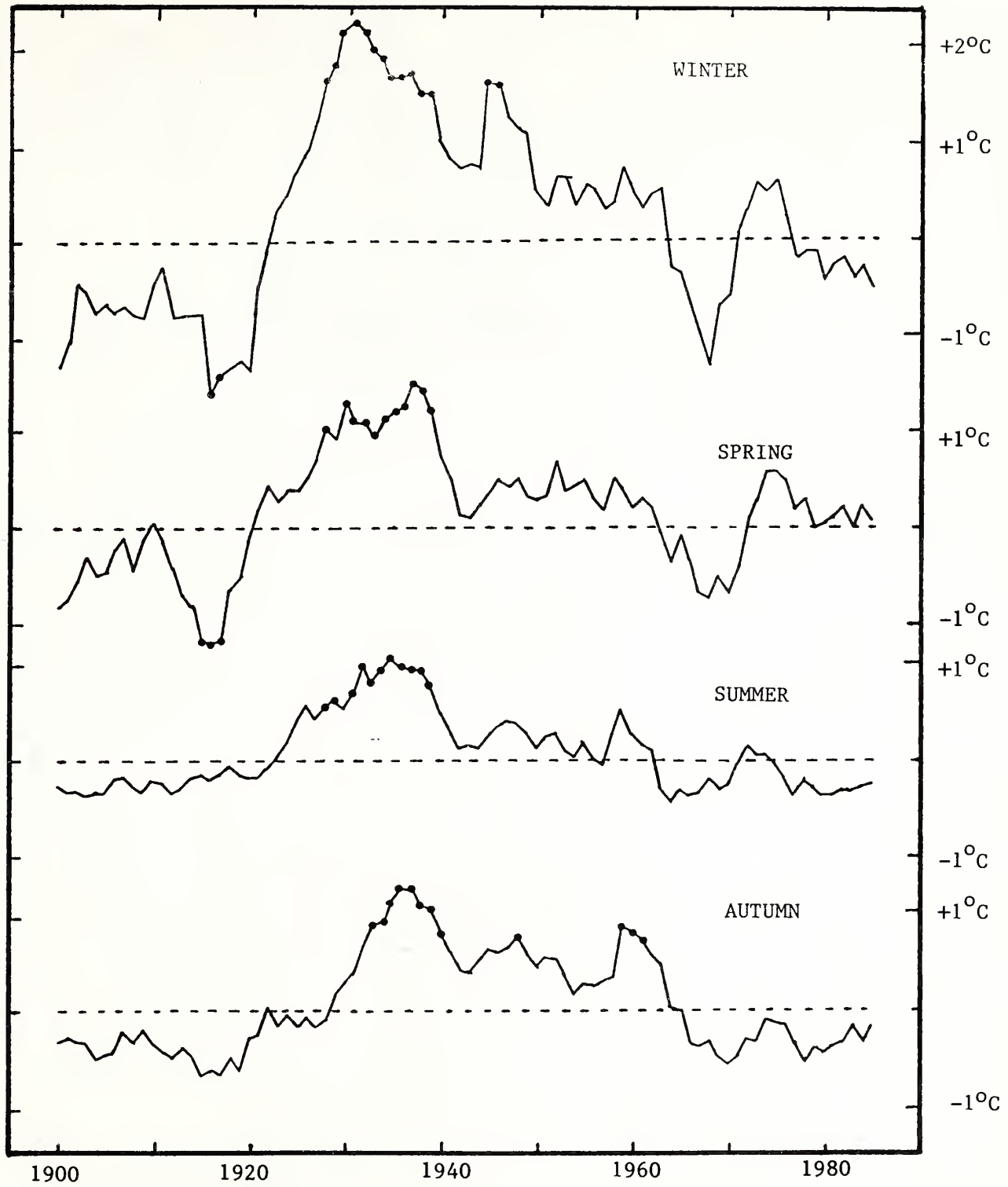

Fig. 3 Five-year averages of seasonal temperature anomalies over the Atlantic Arctic since 1900. Dots indicate five-year means temperature anomalies which are signifcantly above or below the 1881-1987 mean using the Cramer t-test. Temperatures are plotted on the middle year of the five-year means.

Fig. 5 The seasonal differences in sea level pressure obtained when the mean pressure during more recent (colder) years is subtracted from the mean pressure in warmer years of the 1920s and 1930s.

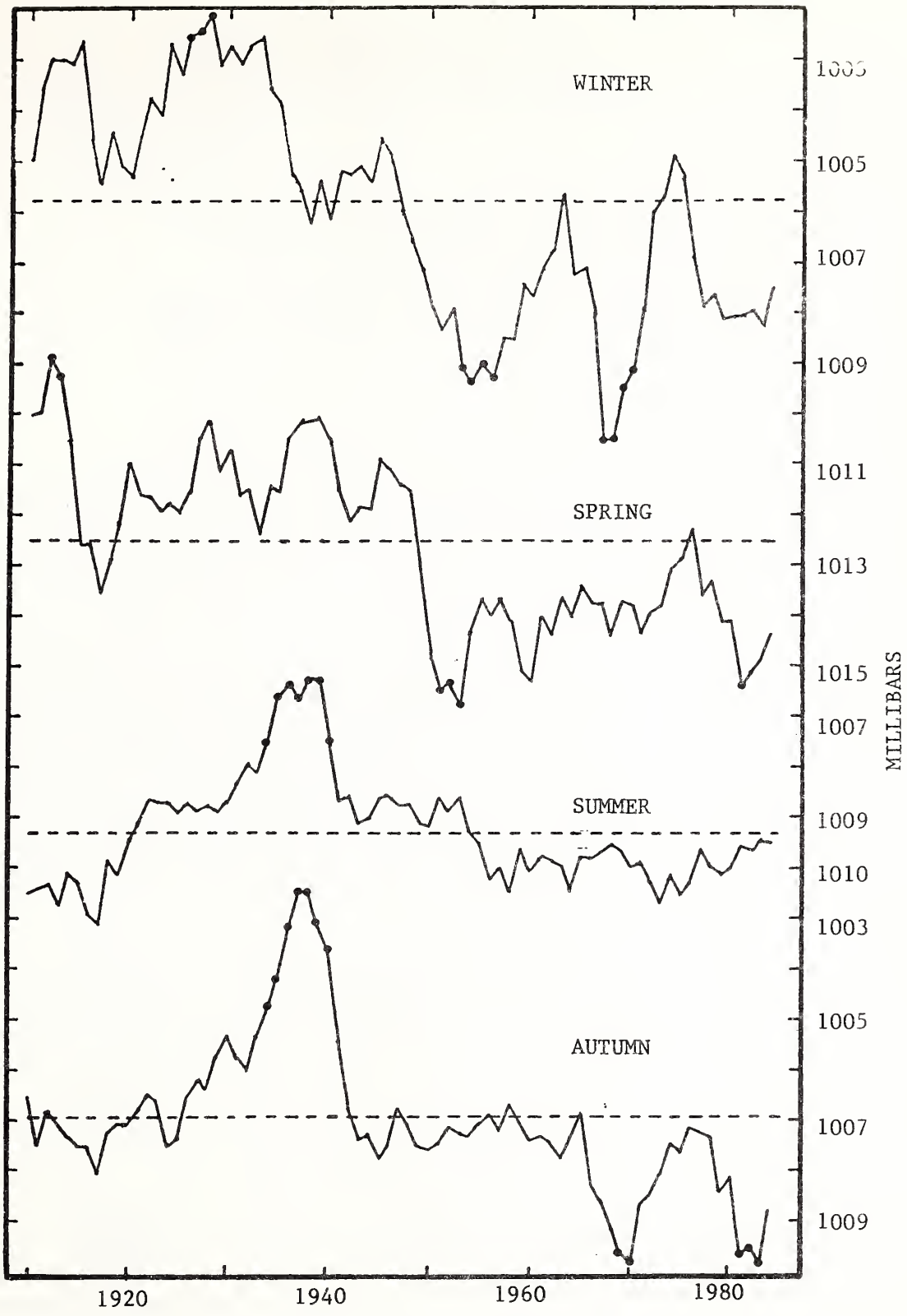

Fig. 6 Five-year averages of seasonal sea level pressure since 1910 in the region 60-65°N, 55-70°W. Dots indicate five-year mean pressure anomalies which are significantly above or below the 1899-1986 mean using the Cramer t-test. The pressure values are plotted on the central year in the means.

Regional Analysis of the Secular Variation of Northern Hemisphere 50-kPa Heights

A. Shabbar, K. Higuchi and J. L. Knox
Climate Diagnostic Research Group
Atmospheric Environment Service
4905 Dufferin Street, Downsview, Ont., Canada

Summary

Our investigation of the 50-kPa height data from 30°N to the pole and for the period 1946-85 (40 years) strongly supports the existence of two short-term climate regimes. The transition from one to the other was fairly abrupt and seemed to occur about 1962-63. A preliminary survey indicates that for all seasons there is a preponderance of above-normal heights for the first 10-15 years and below-normal heights for the balance of the record. The characteristics of the two climates were different with regards to means, trends, distribution and the nature of the variability (Tables 1 and 2). The predominantly low frequency mode during the early years gives way to a high frequency mode over the second half of the period (Fig.1). In order to avoid prejudging the point where the two climate regimes were contiguous, we divided the data record into two sliding-scale periods and calculated the difference between the means via the *t-statistics*. Figs. 2,3 and 4 indicate the likelihood that the transition did indeed take place in the early 1960s.

Regional analysis of the two regimes reveals significant lowering of 50-kPa heights over the subtropical North Pacific and the mid-Atlantic oceans in the second regime during the winter season (Fig. 5). The 50-kPa heights have risen during the same period over western North America and the north Atlantic ocean. Close examination of the trend in the 1980s (Fig. 6) shows dramatic drop in heights, relative to 1950-80 period, over northeastern Pacific and north Atlantic oceans. In contrast, heights are higher than the 30-yr normal over northwestern North America and eastern U.S.S.R. The corresponding (50-100)kPa thickness trend, as depicted in Fig. 7, is not only consistent with the trend at 50 kPa but also indicates significant cooling (0.6°C) over Scandinavia 1981-1987. The same magnitude of cooling is also indicated for the summer season (Fig. 8).

Table 1. Comparison, between the two regimes, of the seasonal and annual means and linear trends of the 50 kPa height anomaly (30°-80°N). Anomalies are calculated from the 40-yr mean (1946-1985).

Season	1946-62	1963-85
	Means (dams)	
Summer	0.64	-0.47
Winter	0.75	-0.52
Annual	0.66	-0.49
	Trend (dams/y)	
Summer	-0.08	0.05
Winter	-0.11	0.02
Annual	-0.10	0.03

Table 2. Comparison, between the two regimes, of the distributions of the 50 kPa height anomaly (30°-80°N) as characterized by the standard deviation and the coefficients of skewness and kurtosis. (Anomalies linearly detrended).

Season	1946-62	1963-85	Level of sig. of difference
	Standard deviation (dams)		
Summer	0.62	0.35	
Winter	0.41	0.41	
Annual	0.37	0.33	
	Skewness coefficient		
Summer	0.70	-0.32	93.6
Winter	0.39	-1.51	99.6
Annual	0.17	-0.81	92.6
	Kurtosis coefficient		
Summer	2.40	2.63	48.0
Winter	2.32	5.26	97.9
Annual	2.01	3.82	90.4

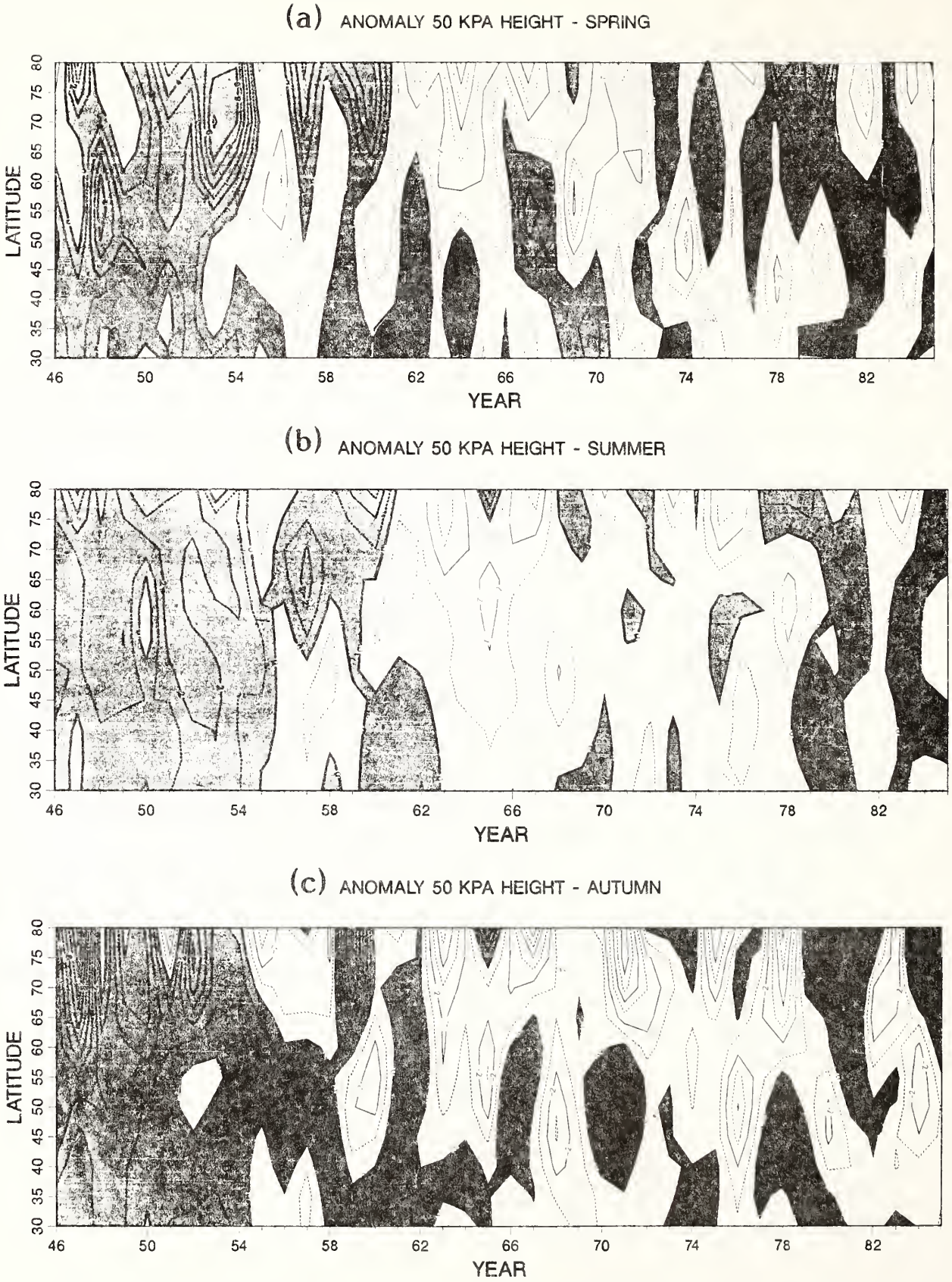

Fig. 1. (a) Variation by year and latitude of the spring season zonally averaged 50 kPa height anomaly. Spring is defined as April and May. (b) As in (a) except for summer (June, July, August and September). (c) As in (a), except for autumn (October, November). (d) As in (a) except for winter (December, January, February and March).

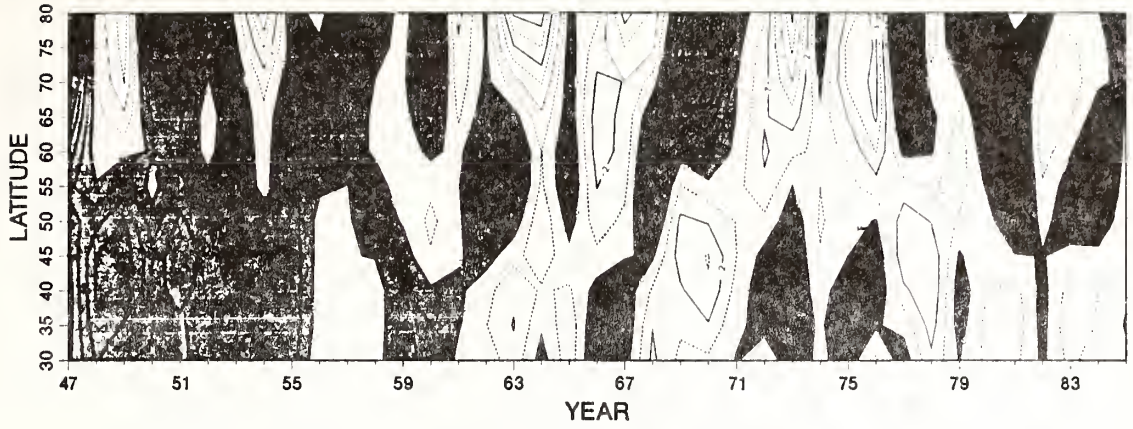

Fig. 1. (Continued)

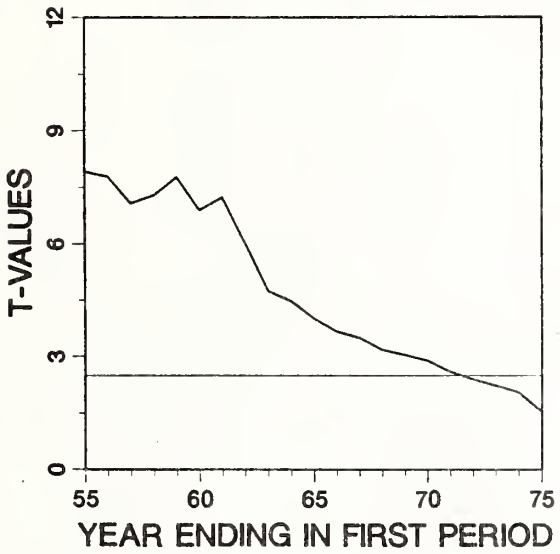

Fig. 2. Time series for winter of the t-statistic for the difference between the first and second period means of 50 kPa height anomalies for the 30°-80°N domain (Northern Hemisphere). Horizontal line is the 99% significance threshold. YEAR designates the last year of the first period. For further details see text.

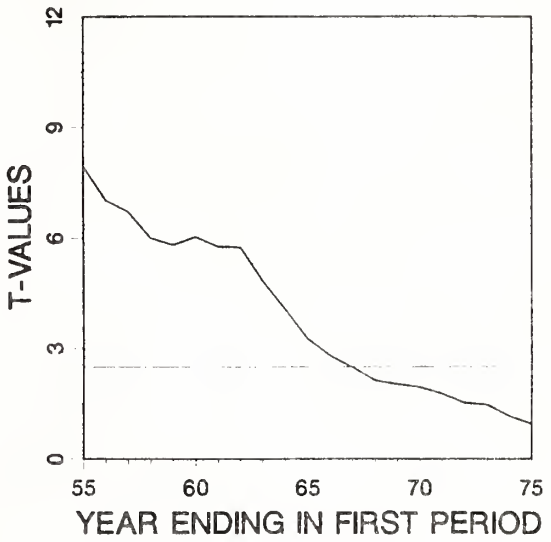

Fig. 3. As in Fig. 2, except for summer.

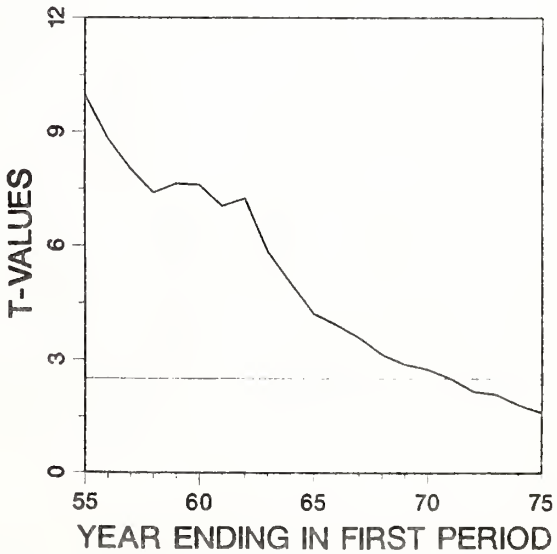

Fig. 4. As in Fig. 2, except for the entire year.

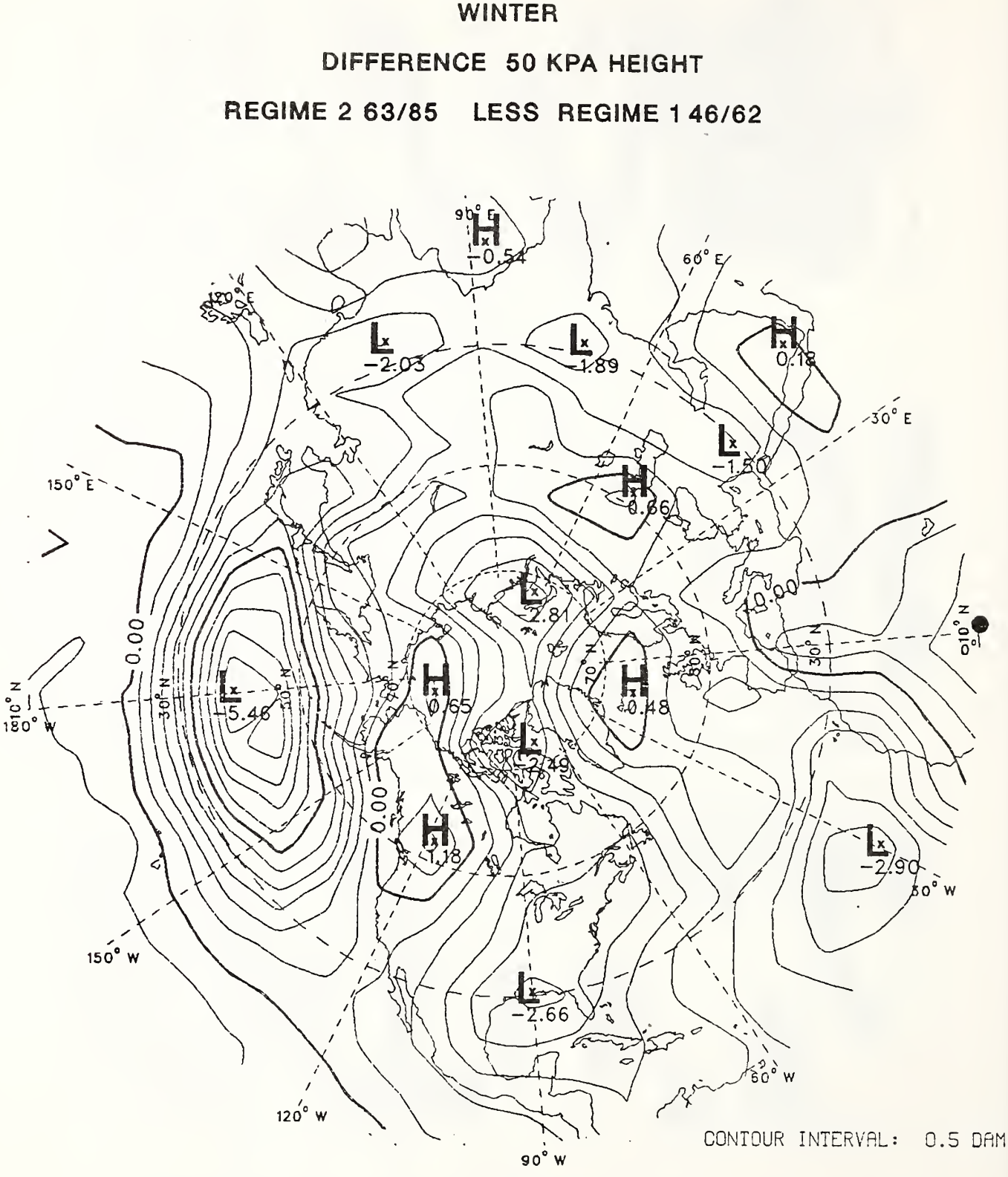

Fig. 5. Spatial distribution of the difference in 50 kPa heights between regime 2 (1946-1962) and regime 1 (1963-1985) for the winter season (December, January, February and March).

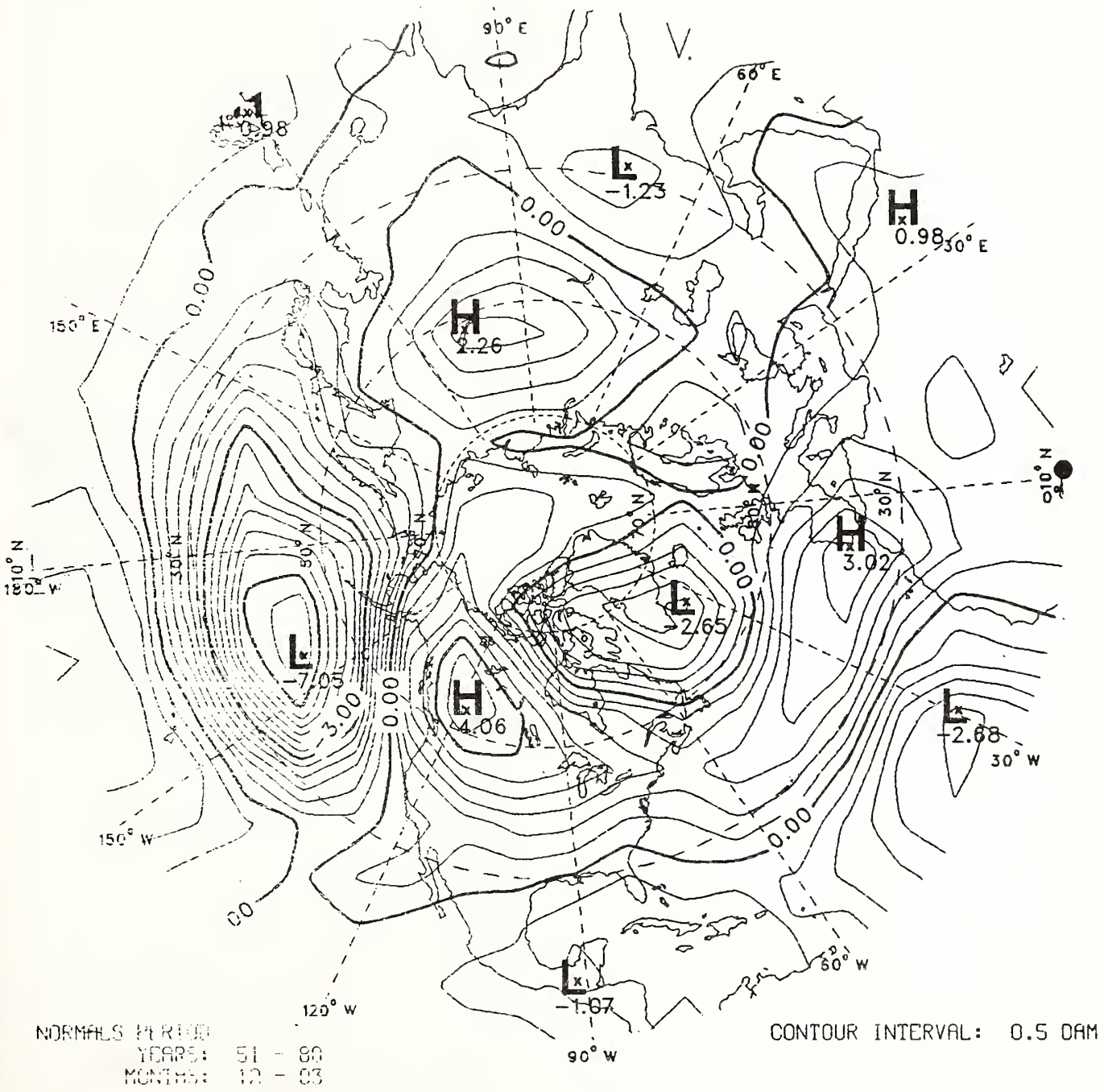

Fig. 6. Departure of 50-kPa heights (1981-1987) from 1951-1980 for the winter season.

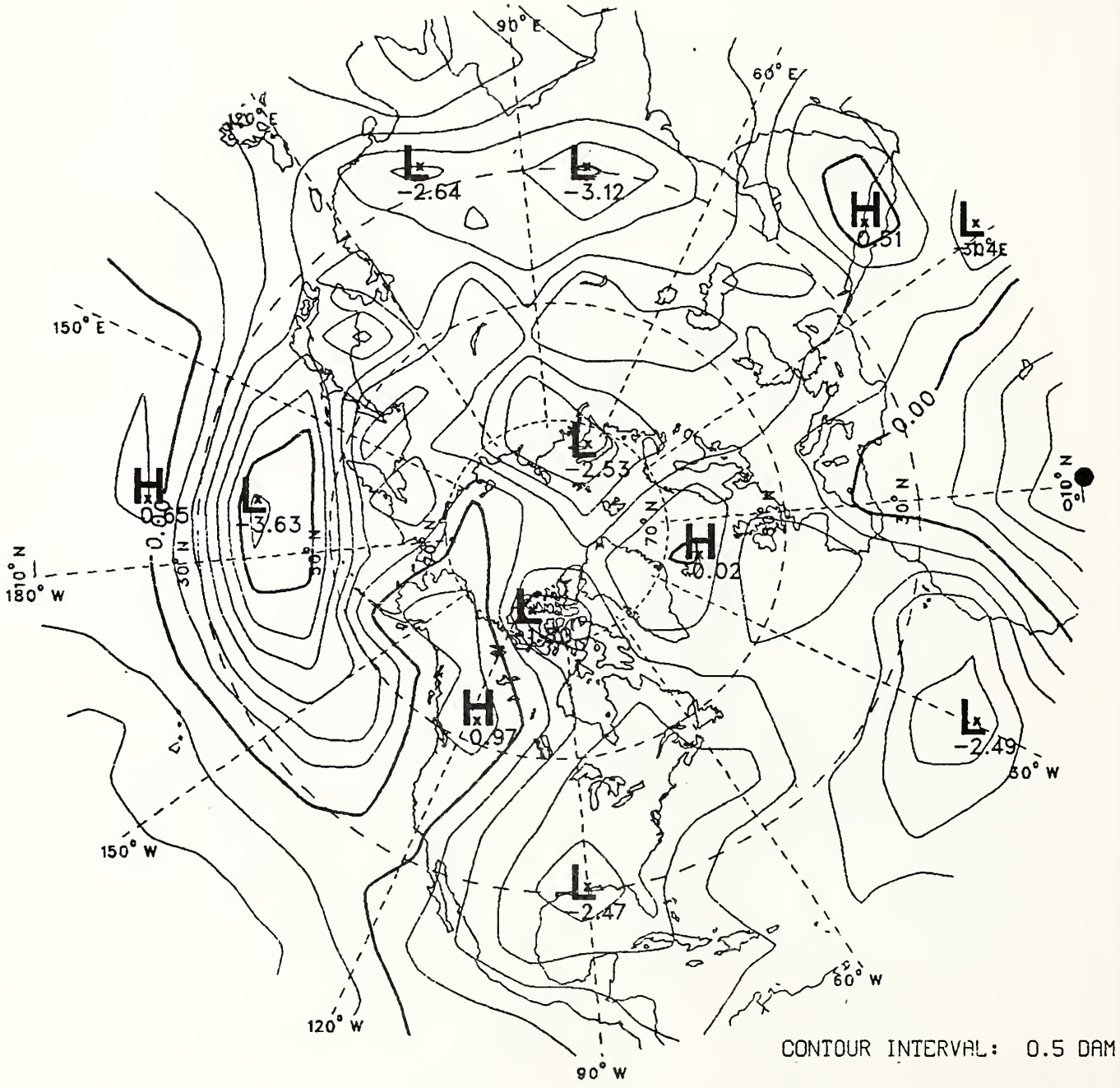

Fig. 7. Departure of (50-100)kPa thickness (191-1987) from 1951-1980 for the winter season.

SUMMER

DIFFERENCE (50 - 100)KPA THICKNESS

REGIME 2 63/85 LESS REGIME 1 46/62

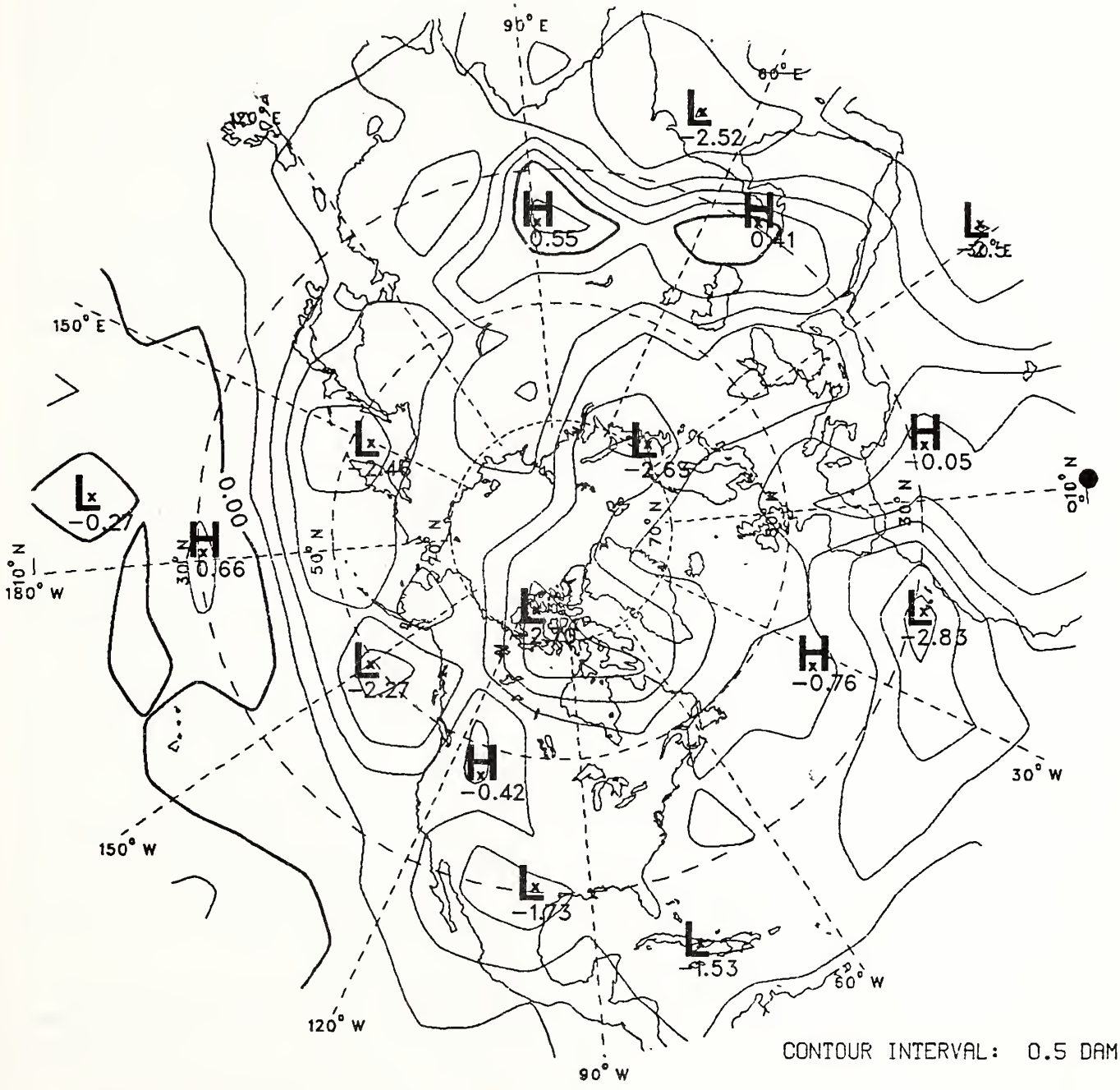

Fig. 8. Same as Fig. 7. except for the summer season.

Relationships between sea surface temperatures and seasonal rainfall in the Sahel and NE Brazil

M N Ward
Meteorological Office, Bracknell, Berks, U.K., RG12 2SZ

Introduction This paper presents relationships between sea surface temperature anomalies (SSTAs) and seasonal rainfall in the Sahel and N Nordeste, Brazil. The relationships are used to produce seasonal rainfall forecasts which have skill that compares favourably with other promising attempts at predicting seasonal tropical rainfall from pre-season observations of various climatic elements such as MSL pressure, zonal and meridional wind components, and SSTAs (review in Hastenrath, this volume). The improved performance in this study of SSTAs alone is attributed to (a) careful quality controlling and correcting of the Meteorological Office historical SST dataset (MOHSST, see Folland and Parker, this volume); (b) use of a global SSTA dataset (important for the Sahel where most previous work had concentrated on pre-season conditions in just the tropical Atlantic (see Lamb, this volume)); and (c) use of patterns in the SSTA field as indicators of rainfall.

Data SST data are taken from the corrected MOHSST dataset and formed into 10deg x 10deg monthly and seasonal anomalies relative to a climatology which varies according to the annual cycle. Spatial and temporal interpolations are applied to the seasonal dataset but not to the monthly dataset. Nicholson's Sahel rainfall series for 1901-84 is used with updates to 1987 from available data. The series is annual, but mainly represents the July-Sept rainfall season. For N Nordeste (in NE Brazil), work reported here uses Nobre's Feb-May series.

Correlation fields Figs 1 and 2 show fields of correlations between SSTA time series and rainfall in the N Nordeste and Sahel. Both fields have significant correlations in the tropics and extratropics, suggesting tropical-extratropical interactions are involved. According to the field significance tests of Livezey and Chen (1983), the results for the whole analysis area are statistically significant at much greater than the 95% level.

SSTA eigenvectors and Sahel rainfall The covariance eigenvectors of the seasonal SSTA dataset have been calculated. The first eigenvector (E1) has loadings of the same sign over the whole globe and much of the variance in the E1 time series (T1) can be attributed to global warming. T1 is not related to Sahel rainfall.

E2 (Fig 3) has loadings which resemble the SSTAs observed during an El Nino event. July-Sept values of the E2 time series (T2) are, over 1901-87, very weakly linked to Sahel rainfall (r=-.26, but see discussion of Table 2 below).

E3 is a largely bi-polar pattern (Fig 4) which probably has a physical basis since composite SSTA patterns suggest that out-of-phase warming and cooling in the two hemispheres is a real mode of climatic variability. The E3 time series (T3) values in July-Sept and Sahel rainfall (plotted together in Fig 5) are linked during the latter part of this century, when there was high interannual persistence in Sahel rainfall, and during the early part of the century when Sahel rainfall had near zero year to year persistence. To assess the relative importance of tropical and extratropical SSTAs for this link, further time series (T3T and T3E) were formed by projecting (a) tropical SSTA fields onto the tropical part of E3 (b) extratropical fields onto the extratropical part of E3. Table 1 shows that, as an indicator of Sahel rainfall, T3E out-performs T3T in both halves of the historical period whether the time series have zero or one season lead time on the rainfall season. The marginally best results are nonetheless with the original T3 series, which seems to offer the best single predictor of seasonal Sahel rainfall yet discovered.

Other factors will account for further variability of seasonal Sahel rainfall. Indeed Lough (1986) found a tropical Atlantic SSTA pattern that at times was linked to Sahel rainfall. A similar pattern to Lough's appears as the second rotated eigenvector (RE2, see Fig 6) when E4 to E13 of the original analysis are rotated according to the VARIMAX criterion. Before rotation, patterns E4 onwards were generally incoherent and difficult to interpret. Like Lough's pattern, RE2's link with Sahel rainfall is strongest in recent decades (Table 1).

Table 2 categorises years according to extremes in Sahel rainfall and July-Sept values of T3 and T2. It suggests that strong La Nina and El Nino events can modulate the strength of the relationship between Sahel rainfall and T3.

SSTA Eigenvectors and N Nordeste rainfall Fig 7 shows the third covariance eigenvector of seasonal SSTAs in the Atlantic Ocean (A3). Its time series (TA3) is linked to N Nordeste rainfall when leading by zero and one season. However the extratropical signal of A3 is not linked to N Nordeste rainfall when leading by one season. Thus the tropical signal of A3 (TA3T) has been used in forecast experiments. In addition the strength of El Nino is needed as a predictor since ENSO has a complex interaction with both N Nordeste rainfall and the tropical Atlantic signal of A3 (see Fig 8).

Forecasts Tests have used half the historical data period to establish statistical forecast models and the remaining half to produce and verify forecasts. For the Sahel, the pre-rainfall season values of the E3 and RE2 time series are used as predictors. N Nordeste forecasts use the pre-rainfall season value of the A3T time series along with an El Nino eigenvector time series derived using data for the Pacific Ocean. Two statistical techniques have been employed; multiple regression predicts the values of the rainfall series from the values of the predictors, discriminant analysis is used to estimate the probability of five climatologically equiprobable rainfall ranges (quints) from the values of the predictors. Table 3 summarises the skill of the multiple regression tests.

Three Sahel and two N Nordeste rainfall seasons have now been forecast in real time. The dry 1987 and wet 1988 N Nordeste rainfall seasons were anticipated correctly. The decline in rainfall in the Sahel from 1985 to 1986 and from 1986 to 1987 (probably the fourth driest year this century) was also well forecast. For 1988, another very dry year was expected on the basis of SSTAs in March to mid-May. However 1988 has probably been the wettest year in the Sahel since 1967, though still only slightly above the 1951-80 normal. By July-August the value of T3 had risen from its March-May value to a less extreme level. In addition, the strongest La Nina since 1975 had developed rapidly in the tropical Pacific. Prior knowledge of these two changes in the SSTA field would have yielded a better forecast from the empirical relationships discussed in this paper.

Future work The 1988 Sahel forecast has highlighted the vulnerabilty of the current forecast system to abrupt large scale SSTA changes. The possibility of making and using SSTA forecasts is being explored. Methods of forecasting tropical rainfall using Atmospheric GCMs forced with observed SSTAs are being tested. Existing and future GCM experiments will be used to study the physical basis of links between SSTAs and rainfall in the Sahel and other tropical regions. Empirical study of the SSTA dataset, using eg various forms of eigenvector analysis will continue. The introduction of predictors other than SST into the forecast models will be considered.

References

Hastenrath, S. 1987. 'On the prediction of India monsoon rainfall anomalies', J.Clim.Appl.Met. 26, 847-857.
Livezey, R.E. and Chen, W.Y. 1983. 'Statistical field significance and its determination by Monte Carlo techniques', MWR 111, 46-59.
Lough, J.M. 1986. 'Tropical Atlantic sea surface temperatures and rainfall variations in sub-Saharan Africa', MWR 114, 561-570.

Table 1. Correlations between Sahel rainfall and time series of SSTA eigenvector patterns.

	SSTA fields projected onto eigenvector pattern							
	July-Sept				April-May			
Time series formed	T3	T3T	T3E	TR2	T3	T3T	T3E	TR2
correlation with) 1901-45	-.52	-.26	-.51	-.24	-.45	-.32	-.42	-.26
Sahel rainfall) 1946-87	-.69	-.52	-.68	-.70	-.63	-.44	-.61	-.50

T3: time series of eigenvector 3 (E3, see Fig 4)
T3T: as above, but projecting only tropical SSTA data onto the tropical part (30S-30N) of the E3 pattern
T3E: projecting only extratropical data onto the extratropical part of the E3 pattern
TR2: second of the solutions after rotating E4 to E13 (see Fig. 6).

Table 2. Contingency table classifying years 1901-87 according to Sahel rainfall and the June-August values of eigenvector time series 2 and 3.

		Sahel rainfall		
T3	T2	low	mod	high
low	low	0	0	2
	mod	0	7	3
	high	0	1	1
moderate	low	1	4	3
	mod	4	25	10
	high	1	7	2
high	low	1	2	0
	mod	5	5	0
	high	3	0	0

T3 = SSTA eigenvector 3 time series (high = S Hemisphere anomalies >> N Hemisphere anomalies)
T2 = SSTA eigenvector 2 time series (high = strong El Nino, low = strong La Nina)

Notice that in La Nina entries (cells) the observed frequency of wet years is generally more than that expected from the T3-Sahel rainfall relationship alone (or, in high T3, the observed frequency of moderate Sahel years is raised with probably 1988 to add further to this cell). An opposite effect is found in El Nino entries. A chi-square test (using log-linear models) does not assess the T2 effect to be statistically significant, but the presence of the effect in most of the table warrants further investigation.

Table 3. Statistical forecast experiments for Sahel and N Nordeste seasonal rainfall.

			Forecast verification statistics					
rainfal series	training period	testing period	r(f,o)	ABSE	RMS	BIAS	S.D. fcst	S.D. obs
Sahel	1901-45	1946-86	.72	36	44	+1	40	64
	1946-86	1901-45	.54	29	37	-2	29	44
N. Nordeste	1913-45	1946-81	.73	37	45	+14	53	63
	1946-81	1913-45	.76	41	52	-11	53	79

Sahel forecasts use March-April values of eigenvector 3 and rotated eigenvector 2 time series. N Nordeste forecasts use Dec-Feb values of Atlantic eigenvector 3 (tropical signal) and Pacific eigenvector 1 time series. Diagnostics given for the forecasts made in the testing period (see eg Hastenrath, 1987) are (i) correlation between forecast and observed (ii) mean absolute error (iii) root mean square error (iv) overall forecast bias (v) standard deviation of forecast (vi) standard deviation of observed. Diagnostics (ii) to (v) are, like the rainfall series used, in standardized units x 100.

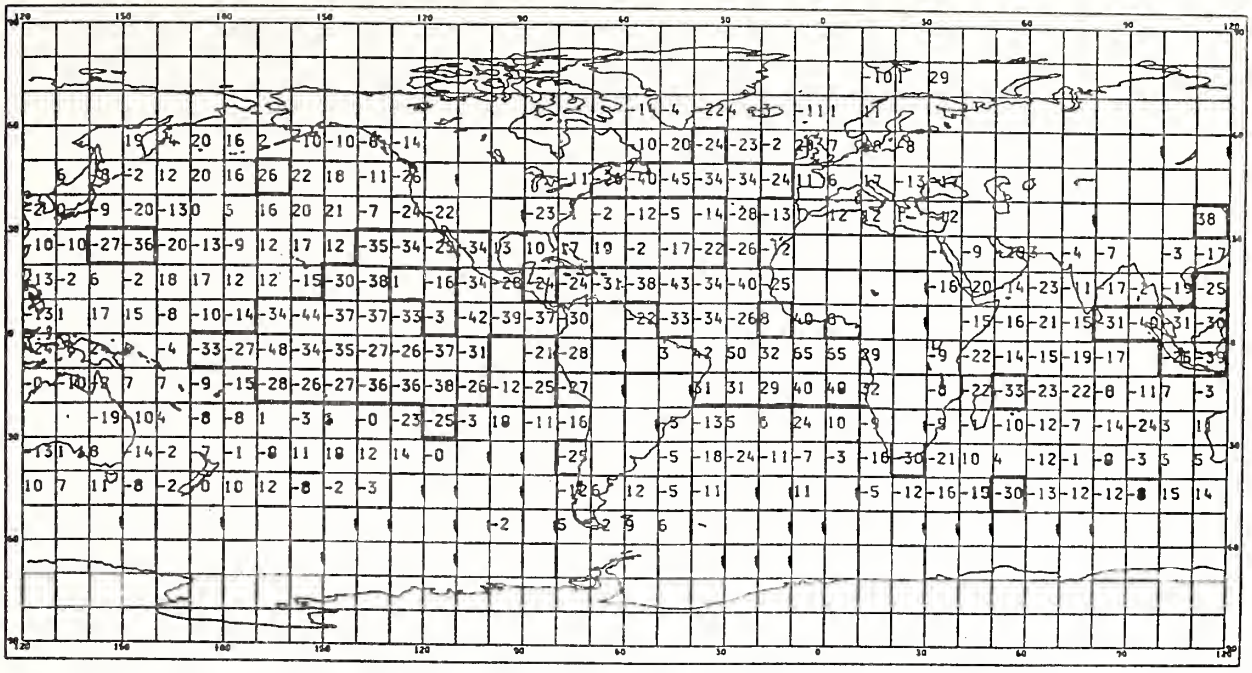

Fig 1. Correlations (in hundredths) between SSTA in March-May and N Nordeste rainfall 1913-81. No interpolated SSTA data are used. Correlations significant at the 95% level are boxed. The percentage of analysis area covered with significant correlations is 29% for the globe, 40% for the Atlantic, 27% for the Pacific.

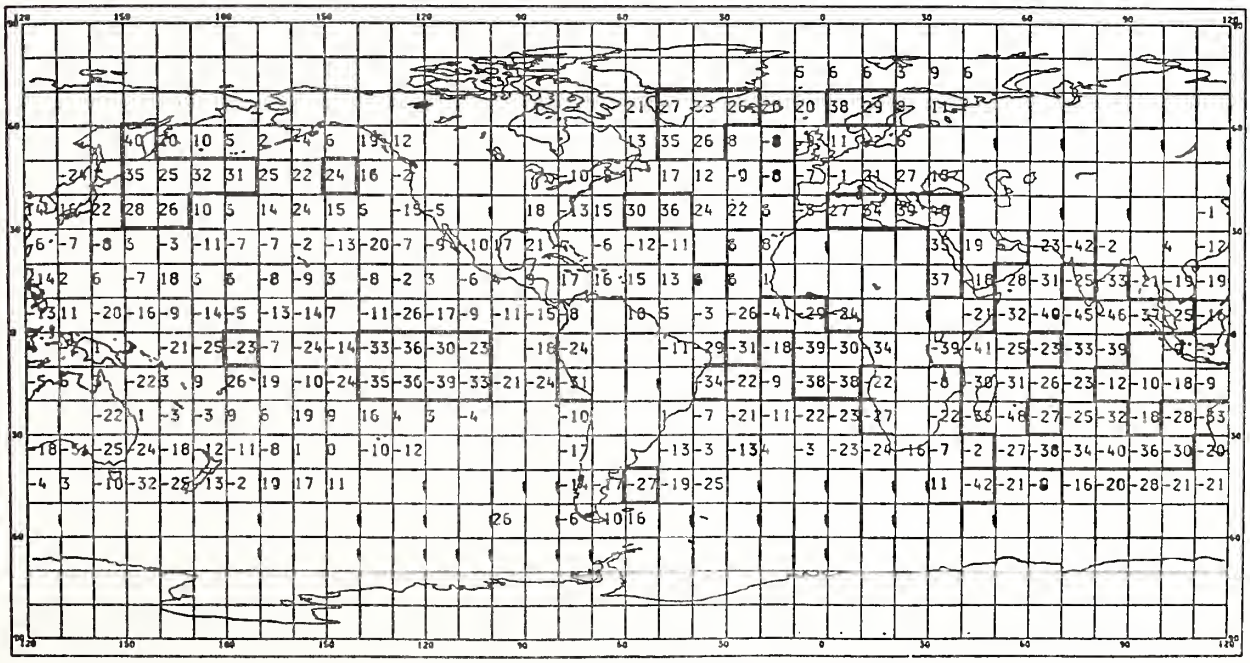

Fig 2. Correlations (in hundredths) between SSTA in July-Sept and Sahel rainfall 1901-86. Correlations significant at the 95% level are boxed. (Degrees of freedom in each correlation estimated as $(N/(1+2\Sigma r_i s_i))-1$, where N is the number of years in the analysis and $r_i s_i$ is the product of the serial correlations in the two series at lag i). The percentage of analysis area covered with significant correlations is 24% for the globe, 26% for the tropics, 21% for the extratropics.

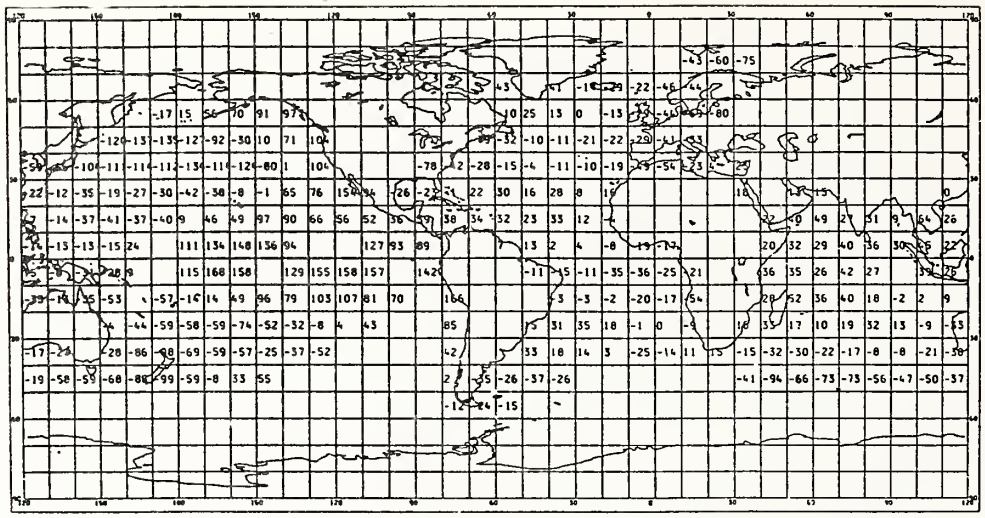

Fig 3. Second covariance eigenvector of seasonal SSTA, 1901-80. Loadings shown are x1000. The time series of this eigenvector traces the history of El Nino and La Nina events this century.

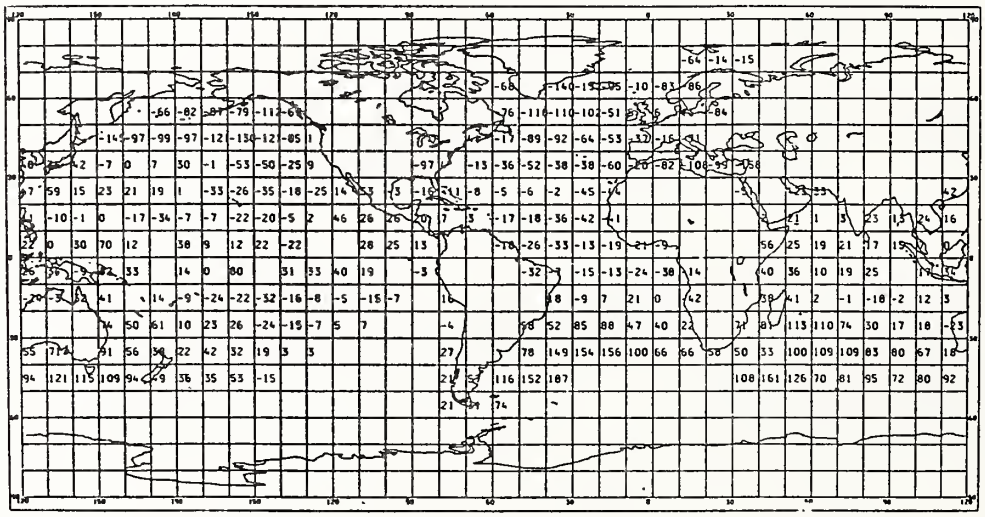

Fig 4. Third covariance eigenvector of seasonal SSTA, 1901-80. Mainly a bi-polar pattern contrasting the N Atlantic + N Pacific with the S Atlantic + Indian Ocean.

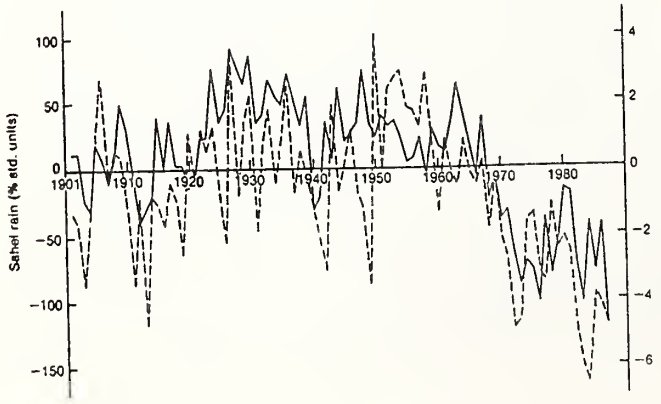

Fig 5. Sahel rainfall 1901-87 (dashed line) along with July-Sept values of the eigenvector three time series (solid line). The sign of the pattern in Fig 4 has been reversed for this plot. A July-Sept value for the time series is calculated by projecting the monthly July, Aug, and Sept SSTAs separately onto eigenvector three to give a value for each month and then averaging.

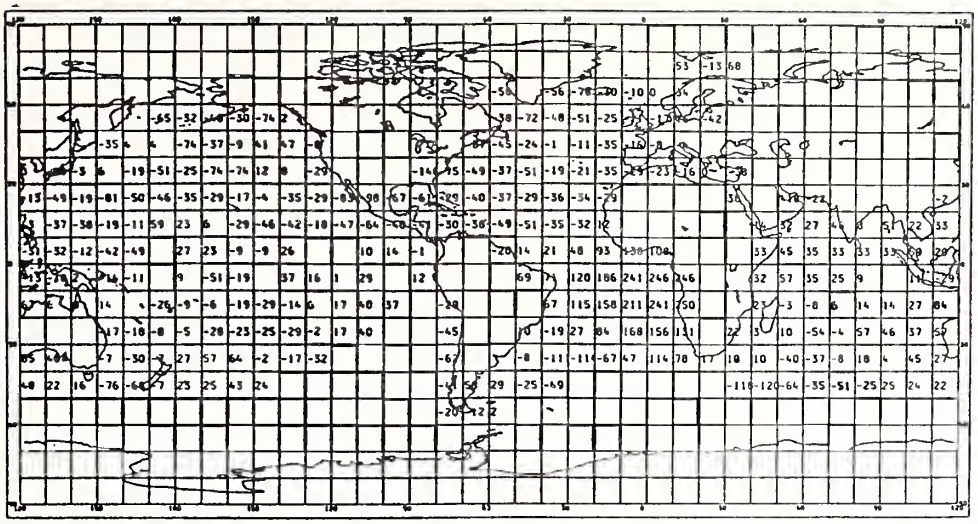

Fig 6. Second eigenvector after VARIMAX rotation of seasonal SSTA eigenvectors 4 to 13. Mainly a S tropical Atlantic pattern.

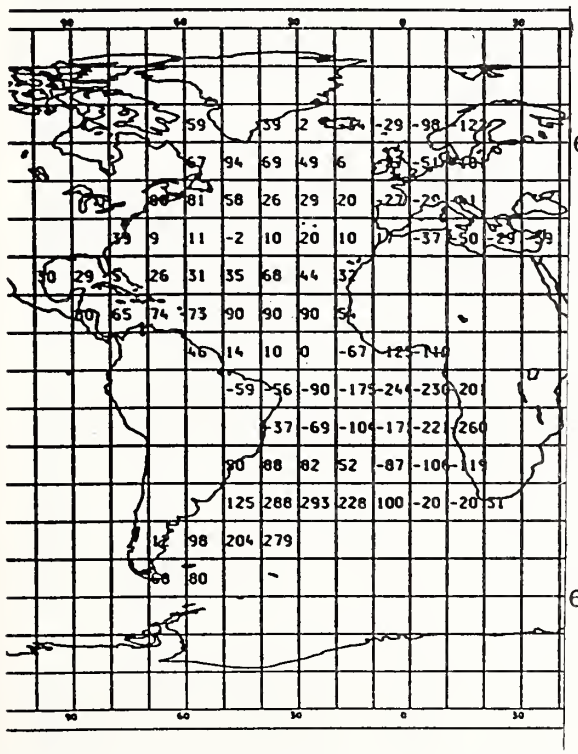

Fig 7. Third covariance eigenvector of seasonal Atlantic SSTA 1901-80

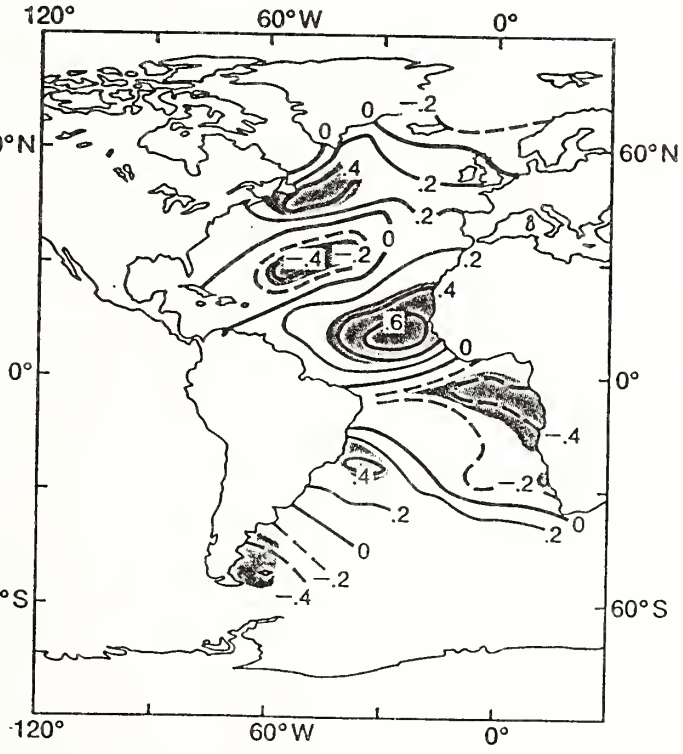

Fig 8. Correlation between the value of the Pacific El Nino eigenvector time series in January (very positive = El Nino) and the change in SSTA from Jan to May. Stippled areas are significant at the 95% level, assuming a conservative estimate of 30 degrees of freedom. The suggestion is that in El Nino years, SSTA's tend to rise in the N tropical Atlantic and fall in the S tropical Atlantic during boreal winter and spring.

EXPERIMENTAL INDICES FOR MONITORING GLOBAL DROUGHT CONDITIONS

K.H. Bergman*, P. Sabol, and D. Miskus
Climate Analysis Center, NWS/NOAA
W/NMC5, Washington, DC 20233

1. Description of the Indices:

Two related moisture, or drought, indices have been developed:

1. Cumulative Moisture Anomaly Index (CMAI). This index reflects the amount of excess runoff that has accumulated in time compared to the amount of unsatisfied moisture demand imposed by cumulative excess potential evapotranspiration, compared to normal conditions. It is intended to be a measure of moisture conditions as they affect reservoirs, large streams, deep well water, etc.

2. Soil Moisture Anomaly Index (SMAI). This index reflects the degree of saturation or dryness of the soil, compared to normal conditions, and is intended to be a measure that is useful in evaluating the effect of recent moisture conditions on agricultural crops.

Both of these indices are based on the precipitation vs. potential evapotranspiration moisture accounting approach of C.W. Thornthwaite (1948 and later years). The indices are both cumulative in the sense that a set of moisture parameters for the preceding week (or month) is updated to reflect precipitation vs. evapotranspiration conditions for the current week (month). The computations and the resulting indices evaluate anomalous moisture conditions, that is, the normal precipitation and potential evapotranspiration are subtracted from the currently observed or computed values of these quantities in doing the calculations.

For precipitation, normal weekly (monthly) values are subtracted from reported values for the current week (month). Potential evapotranspiration (PET) is computed from a formula that is a function of mean weekly (monthly) temperature, latitude, and calendar day of the year. This formula closely approximates Thornthwaite's more complicated formulae. Since anomalous values of PET are computed, approximations in the PET formulation tend to cancel out. However, the approximation used here, like the Thornthwaite formulation, neglects the effects of varying cloudiness, humidity, and wind speed on evapotranspiration. (An alternate, more comprehensive expression for PET could be

* (Current affiliation: Board on Atmospheric Sciences and Climate, National Research Council/National Academy of Sciences, 2101 Constitution Ave. (HA 594), Washington, DC 20418.)

substituted provided current and normal measurements of these additional variables are available.)

Another factor that enters into the computations is the soil moisture capacity. Following W.C. Palmer (1965) and K.J. Johnstone and P.Y.T. Louie (1984), a soil reservoir for moisture consisting of two layers, "topsoil" and "deepsoil", is assumed to exist at each station. In the experimental version, the soil is assumed to be capable of holding a total of 180 mm of moisture (the average value for the US that is used in the Palmer Drought Severity Index) at every station, but individual values could be assigned on the basis of soil type. Since Johnstone and Louie have extensively studied the relative roles of topsoil and deepsoil in soil moisture capacity, their ratio of two parts of topsoil to three parts of deepsoil is used here, i.e, topsoil moisture capacity = 72mm and deepsoil moisture capacity = 108mm.

In doing the soil moisture computations, when precipitation exceeds PET, the excess moisture is added first to the topsoil, until it is saturated, and any additional excess is treated in the following way: The amount of moisture already present in the deepsoil is noted, the difference between that and full deepsoil capacity is determined, and the percent saturation of the deepsoil is computed. Subtracting this from 100 percent gives the percent of the total deepsoil that is not saturated. Only this percentage of the excess left over after the topsoil is filled is added to the moisture already present in the deepsoil. This procedure is similar to that of Johnstone and Louie, and its purpose is to reflect the increasing difficulty of adding additional moisture to deepsoil that is approaching saturation. The excess precipitation that is not added to the soil is denoted as "runoff."

When PET exceeds precipitation, the process works as follows: Moisture is first withdrawn from the topsoil layer to satisfy the PET demands until it is completely dry. Then, moisture is withdrawn from the deepsoil to partially satisfy any additional PET demand, but only in proportion to the percentage of moisture, compared to saturation, that remains in the deepsoil. Once again, the purpose is to reflect the increasing difficulty of removing moisture from the deepsoil as it becomes increasingly dry.

The above soil moisture calculations are done for both the current week (month) and the "normal" week (month), and anomalies computed. These anomalies form the basis for the calculation of the CMAI and SMAI. After the soil moisture needs and changes have been computed, the anomalous precipitation excess (anomalous runoff), or the anomalous precipitation deficiency (anomalous unsatified water need), represents the week's (month's) contribution to the CMAI. The weekly (monthly) anomaly is added to (excess) or subtracted from (deficiency) the CMAI for the preceding week (month) to get the new CMAI value. For interstation comparison purposes, the CMAI is normalized by the annual precipitation of the station. The SMAI is obtained from

the amount of moisture present in both layers of soil, compared to normal conditions. All of the indicated computations are done each week (or month) in order to obtain continuing updates of the CMAI and SMAI.

2. Some Preliminary Results

Experimental runs for both the CMAI and the SMAI have been made, using both weekly and monthly updates. The runs were started from January 1987 data, with the assumption that both layers of soil were saturated at the beginning of January and that this was the normal climatological condition (near-saturation is to be expected at most humid temperate stations in midwinter). The expectation was that, after a year had elapsed, the system would be "spun up" enough to reflect actual moisture conditions. These experimental runs continue at this writing (January 1989).

Space does not permit listing the relatively straightforward moisture budget bookkeeping equations upon which the index values are based. For easy recognition on maps, categories of dryness or wetness were defined (see lower left-hand corners of Figs. 1 and 2). These categories were arbitrarily chosen but appear to be useful in delineating areas with significant moisture anomaly.

Figs. 1 and 2 show the categorical distribution of the CMAI and the SMAI respectively for the U.S. at the end of June 1988. Note that stations indicated by commas have an annual precipitation of less than 250 mm; most of these are located in the West. Computations were not done for these relatively dry stations.

Figs. 3 and 4 show analyzed categorical maps for the PDSI and CMI as of July 2, 1988 (from the Weekly Weather and Crop Bulletin) for comparison. The severe drought conditions that developed over large parts of the nation during the spring and early summer were near their worst at this time. It should be noted that the PDSI and CMI maps are based on climate division data, whereas the experimental CMAI and SMAI maps show individual station values.

Both the CMAI and the SMAI maps show widespread anomalous dryness over large parts of the nation, consistent in general with the PDSI and CMI and with the widespread reports of severe drought conditions. The most noteworthy differences between the CMAI and SMAI depiction are in the zone from the western Great Lakes region eastward to northern New England, where the CMAI reflects the unusually wet conditions of 1987, and along parts of the West Coast, where 1987 was unusually dry. Because the CMAI continues to "remember" past moisture anomalies until they have been countered by equal anomalies of the opposite sign, the CMAI has in effect a very long memory. This feature is appropriate for an index that is intended to be a measure of slowly changing factors such as reservoir levels and major streamflow.

The SMAI tends to change more rapidly with changing soil moisture conditions, but the pattern of dryness is, perhaps fortuitously,

similar to that of the CMAI on June 30. The differences can be traced to comparatively recent anomalous events that have not lasted long enough to significantly change the cumulative index. In general, the SMAI chart shows moderate to severe anomalous soil dryness extending from the northern Great Plains eastward into the Great Lakes and Ohio Valley and southward into parts of the Southeast. These are all areas that reported severe agricultural drought conditions by the end of June 1988. By way of contrast, the western Texas - eastern New Mexico area, which has seen well above normal rainfall during most of the last three years, shows up as an unusually wet region according to both the CMAI and SMAI.

The general agreement of the CMAI and SMAI with the indications of the PDSI and CMI is heartening, although, as mentioned above, a direct comparison cannot be made. Furthermore, the new indices are not attempts to duplicate the PDSI and CMI exactly; see the next section for more discussion of this point. In many respects, the SMAI map looks more like the PDSI map than the rapidly changing CMI map. Although more test runs are needed, our results to date suggest that the SMAI changes somewhat more rapidly in time than the PDSI but not as rapidly as the CMI.

At present, the CMAI and SMAI are being computed and updated every week as well as once a month for over 1000 stations worldwide. The indications of severe anomalous dryness lingering in parts of the Great Plains and prevailing in northern Argentina and adjacent areas of South America, in southwestern Europe, and in much of eastern China in late December 1988 (Fig. 5) accords well with other information about drought conditions in these areas.

3. Discussion

One may ask the question: Why develop another set of indices when we already have the Palmer Drought Severity Index (PDSI) and the Crop Moisture Index (CMI)? Three responses to this question are:

1. The PDSI and CMI, although based on considerations of precipitation *vs.* evapotranspiration similar to those used for the CMAI and SMAI, involve more complex reasoning and more calculations than the relatively straightforward "bookkeeping" procedure described above. As a result, the PDSI and CMI are indices that may have utility in describing moisture conditions but that are not easily related to the physical processes involved.

2. The PDSI and CMI contain several arbitray assumptions that condition the resulting index values. The CMAI and SMAI also contain arbitrary assumptions, at least in the experimental versions described here, but generally it is easier to see how modifications to the CMAI and SMAI methodologies might be made to remove the arbitrary features than it is for the PDSI and the CMI.

3. The PDSI and CMI were developed originally for a restricted region, namely the central United States; as a result, these indices were "tuned" in order to be meaningful in that region. Their applicability to other regions is therefore questionable; even in the rest of the United States their use has been criticised. The CMAI and SMAI, on the other hand, have been designed for global climate monitoring purposes, and the more basic and (hopefully) less arbitrary nature of their calculation should befit them better for global use.

There are several ways in which the CMAI and SMAI formulations might be improved. Probably the most severe limitation of the current formulations is the use of a universal value of 180mm for the total soil moisture capacity. Studies by Johnstone and Louie (1984) for Canadian stations show that soil moisture capacities for individual locations range from around 100 mm to more than 300 mm, depending on the type of soil. For the PDSI calculations in the U.S., each climate division is assigned a soil moisture capacity. These average about 180 mm but also show a wide range. Clearly, the first priority in improving the system should be to estimate the soil moisture capacity for each location or region using a global soil map or similar information.

Other items that might be included if the data are available in real time are inclusion of clouds, wind, relative humidity, and sunshine in the potential evapotranspiration computations; inclusion of the delayed moisture effects of snowcover (see Johnstone and Louie for a scheme to do this) in the moisture budget computations; and improved partitioning of the amount of moisture added to the soil vs. amount of runoff, based on streamflow measurements.

In summary, two new related indices for monitoring moisture conditions on a global basis have been described and some early experimental results shown. We have argued that their relative simplicity of computation from basic moisture budget considerations may make them more universally useful and interpretable than the well known PDSI and CMI, but acknowledge that much work still needs to be done, especially with regard to variable soil moisture capacity, in order to make the new indices truly useful for the monitoring of global drought conditions.

References

Johnstone, K.J., and P.Y.T. Louie, 1984: An Operational Water Budget for Climate Monitoring. Canadian Climate Centre, Report No. 84-3, Atmospheric Environment Service, Downsview, Ont., 45pp.

Palmer, W.C., 1965: Meteorological Drought. U.S. Dept. of Commerce, Weather Bureau Research Paper No. 45, Washington, DC, 58pp.

Thornthwaite, C.W., 1948: An Approach Toward a Rational Classification of Climate, Geographical Review, v. 38, pp 55-94.

72268 ROSWELL, NM UNITED STATES 3330 10453 270.9 0.5000

DATE	P	PN	E	EN	M	MN	M*	M*N	SIB	SIBN	SIB	SIBN	Q	I	J	NO	CHARS
870131	6.4	10.1	7.0	6.3	-0.6	3.8	0.0	0.0	71.4	72.0	108.0	108.0	0.0	0.0	-0.01	31.0	. *** . ***
870228	51.3	11.8	16.9	14.4	34.4	-2.6	0.0	0.0	72.0	69.4	108.0	108.0	0.0	0.0	0.04	28.0	. *** . ***
870331	5.2	10.1	28.3	32.7	-23.1	-22.6	0.0	0.0	48.9	46.8	108.0	108.0	0.0	0.0	0.04	31.0	. *** . ***
870430	5.8	10.3	57.3	66.4	-51.5	-56.1	0.0	0.0	0.0	0.0	105.4	98.7	0.0	0.0	0.19	30.0	. *** . ***
870531	33.1	18.0	102.7	109.6	-63.6	-91.6	-10.9	-42.3	0.0	0.0	52.7	49.3	31.4	11.6	0.19	31.0	+ *** . ***
870630	93.8	24.9	146.0	157.6	-52.2	-132.7	-26.7	-108.0	0.0	0.0	27.2	24.7	112.6	41.6	0.29	30.0	W WET . ***
870731	10.2	43.2	165.8	168.3	-155.6	-125.1	-142.0	-112.8	0.0	0.0	13.6	12.3	83.5	30.8	0.29	31.0	W WET . ***
870831	121.5	53.2	148.4	146.6	-26.9	-93.4	-23.5	-87.2	0.0	0.0	10.2	6.2	147.1	54.3	1.46	31.0	W WET + +++
870930	19.9	44.2	101.1	102.7	-81.2	-58.5	-76.1	-55.5	0.0	0.0	5.1	3.1	126.5	46.7	1.46	30.0	W WET + +++
871031	7.2	26.6	67.1	56.8	-59.9	-28.2	-57.3	-27.4	0.0	0.0	2.6	2.3	96.5	35.6	0.33	31.0	W WET . ***
871130	10.9	8.7	23.8	19.6	-12.9	-10.9	-12.5	-10.7	0.0	0.0	2.3	2.0	94.6	34.9	0.27	30.0	W WET . ***
871231	35.2	9.8	6.0	7.5	29.2	2.3	0.0	0.0	29.2	2.3	2.3	2.0	94.6	34.9	5.73	31.0	W WET W WET
880131	5.6	10.1	4.6	6.3	1.0	3.8	0.0	0.0	30.2	6.1	2.3	2.0	94.6	34.9	3.99	31.0	W WET W WET
880229	37.5	11.8	15.6	14.5	21.9	-2.7	0.0	0.0	52.1	3.4	2.3	2.0	94.6	34.9	6.62	29.0	W WET W WET
880331	0.7	10.1	13.5	32.8	-32.8	-22.7	0.0	-18.9	19.4	0.0	2.3	1.7	113.6	41.9	7.37	31.0	W WET W WET
880430	6.9	10.3	65.5	66.6	-58.6	-56.3	-38.5	-55.4	0.0	0.0	1.4	0.8	130.6	48.2	1.54	30.0	W WET M MST
880531	86.8	18.0	106.2	103.8	-19.4	-91.8	-19.1	-91.4	0.0	0.0	1.2	0.4	202.9	74.9	2.97	31.0	W WET M MST
880630	32.2	24.9	154.5	157.6	-122.3	-132.7	-121.7	-132.5	0.0	0.0	0.6	0.2	213.7	78.9	2.97	30.0	W WET M MST

72312 GREENVILLE, SC UNITED STATES 3490 8222 1293.9 0.5000

DATE	P	PN	E	EN	M	MN	M*	M*N	SIB	SIBN	SIB	SIBN	Q	I	J	NO	CHARS
870131	117.7	107.4	6.6	8.9	111.5	98.9	0.0	0.0	72.0	72.0	108.0	108.0	0.0	0.0	0.00	31.0	. *** . ***
870228	186.0	111.1	12.7	13.7	173.3	97.4	0.0	0.0	72.0	72.0	108.0	108.0	0.0	0.0	0.00	28.0	. *** . ***
870331	127.5	152.6	31.7	33.1	95.8	119.5	0.0	0.0	72.0	72.0	108.0	108.0	0.0	0.0	0.00	31.0	. *** . ***
870430	58.1	109.4	60.4	60.2	-2.3	49.2	0.0	0.0	69.7	72.0	108.0	108.0	0.0	0.0	-0.04	30.0	. *** . ***
870531	33.7	99.0	119.3	109.7	-85.6	-9.7	0.0	0.0	0.0	62.3	92.1	108.0	0.0	0.0	-1.77	31.0	. *** 0 ORY
870630	15.4	113.4	153.6	144.1	19.2	-33.3	0.0	0.0	19.2	28.9	92.1	108.0	0.0	0.0	-0.60	30.0	. *** - ---
870731	41.0	114.2	168.6	159.3	-77.6	-45.1	-12.4	0.0	0.0	0.0	66.0	91.8	-12.6	-1.0	-1.99	31.0	. *** 0 ORY
870831	70.9	102.0	154.2	146.7	-83.3	-42.7	-60.3	-6.4	0.0	0.0	23.0	55.5	-66.3	-5.1	-2.54	31.0	- --- 0 ORY
870930	82.0	117.9	103.6	106.6	-21.5	11.5	-17.0	0.0	0.0	11.5	18.4	55.5	-83.3	-6.4	-3.72	30.0	- --- S SVR
871031	7.4	46.8	61.6	57.7	-32.0	29.1	-26.5	0.0	0.0	40.5	13.0	55.5	-109.8	-8.5	-5.78	31.0	- --- S SVR
871130	71.4	79.3	31.6	28.0	39.8	51.3	0.0	10.2	39.8	72.0	13.0	65.2	-120.0	-9.3	-2.75	30.0	- --- 0 ORY
871231	117.3	102.7	14.8	12.2	102.5	90.5	22.8	89.1	72.0	72.0	60.5	86.6	-166.3	-12.9	-0.52	31.0	- --- - ---
880131	91.3	107.4	2.5	8.9	88.8	98.9	73.0	88.2	72.0	72.0	86.2	97.3	-181.5	-14.0	-0.23	31.0	- --- . ***
880229	65.5	111.1	11.2	13.7	54.3	97.4	26.7	92.0	72.0	72.0	91.8	102.6	-246.8	-19.1	-0.19	29.0	0 DRY . ***
880331	93.2	152.6	34.2	33.1	59.0	119.5	50.9	116.4	72.0	72.0	99.9	105.3	-312.3	-24.1	-0.09	31.0	0 DRY . ***
880430	86.6	109.4	64.3	60.2	22.3	40.5	20.7	39.5	72.0	72.0	101.6	106.3	-331.2	-25.6	-0.08	30.0	0 DRY . ***
880531	49.8	99.0	102.6	109.3	-52.8	-10.0	0.0	0.0	19.2	62.0	101.6	106.3	-331.2	-25.6	-0.96	31.0	D DRY - ---
880630	43.0	110.8	145.1	144.2	-62.1	-33.4	-2.6	0.0	0.0	28.7	61.2	106.3	-333.7	-25.8	-2.28	30.0	0 DRY 0 ORY

72405 WASHINGTON/NATIONAL, D UNITED STATES 3885 7703 984.9 0.5000

DATE	P	PN	E	EN	M	MN	M*	M*N	SIB	SIBN	SIB	SIBN	Q	I	J	NO	CHARS
870131	124.4	59.7	1.2	1.8	123.2	67.9	0.0	0.0	72.0	72.0	108.0	108.0	0.0	0.0	0.00	31.0	. *** . ***
870228	54.2	65.1	3.9	4.5	50.3	61.6	0.0	0.0	72.0	72.0	108.0	108.0	0.0	0.0	0.00	28.0	. *** . ***
870331	34.7	47.6	25.0	20.5	13.7	66.9	0.0	0.0	72.0	72.0	108.0	108.0	0.0	0.0	0.00	31.0	. *** . ***
870430	57.8	73.9	44.5	55.2	9.3	13.7	0.0	0.0	72.0	72.0	108.0	108.0	0.0	0.0	0.00	30.0	. *** . ***
870531	64.5	87.8	103.1	98.5	-38.6	-10.7	0.0	0.0	33.4	61.3	108.0	108.0	0.0	0.0	-0.52	31.0	. *** - ---
870630	99.2	44.5	152.0	143.2	-52.8	-53.7	0.0	0.0	0.0	2.7	88.6	108.0	0.0	0.0	-0.64	30.0	. *** - ---
870731	66.2	98.3	183.2	165.0	-117.3	-64.7	-72.7	-8.1	0.0	0.0	44.3	54.0	-64.6	-6.6	-0.57	31.0	- --- - ---
870831	52.7	111.3	150.6	145.6	-97.9	-34.3	-75.8	-17.2	0.0	0.0	22.2	36.8	-121.2	-12.5	-1.47	31.0	- --- - ---
870930	129.7	81.2	109.7	103.1	22.0	-22.0	0.0	-14.5	22.0	0.0	22.2	29.3	-104.7	-11.0	1.18	30.0	- --- + +++
871031	94.3	73.3	33.6	52.4	25.7	20.9	0.0	0.0	47.7	20.9	22.2	29.3	-108.7	-11.0	0.95	31.0	- --- + +++
871130	116.0	71.2	24.3	22.1	89.7	49.1	22.4	0.0	72.0	70.0	65.1	29.3	-86.3	-8.8	0.93	30.0	- --- + +++
871231	65.3	40.3	8.9	5.6	56.4	34.7	34.9	33.3	72.0	72.0	86.5	68.7	-84.7	-8.6	0.35	31.0	- --- . ***
880131	77.8	69.7	0.0	1.8	77.8	67.9	69.1	68.2	72.0	72.0	97.3	88.1	-63.8	-6.5	0.16	31.0	- --- . ***
880229	66.1	66.1	4.1	4.6	60.0	61.5	54.6	51.7	72.0	72.0	102.6	98.2	-60.9	-6.2	0.07	29.0	- --- . ***
880331	67.7	47.6	23.6	20.6	44.1	66.8	32.6	61.9	72.0	72.0	104.3	103.1	-90.3	-9.2	0.02	31.0	- --- . ***
880430	50.8	73.9	47.8	55.5	3.0	18.4	2.9	17.6	72.0	72.0	104.6	103.9	-104.9	-10.7	0.01	30.0	- --- . ***
880531	114.3	87.8	97.9	98.7	16.4	-10.9	15.9	0.0	72.0	61.1	105.0	103.9	-89.1	-9.0	0.20	31.0	- --- . ***
880630	24.0	84.5	143.2	143.2	-119.2	-58.7	-1.3	0.0	0.0	2.6	59.1	103.9	-90.6	-9.2	-1.70	30.0	- --- D ORY

72530 CHICAGO/O'HARE, IL UNITED STATES 4198 0790 867.0 0.5000

DATE	P	PN	E	EN	M	MN	M*	M*N	SIB	SIBN	SIB	SIBN	Q	I	J	NO	CHARS
870131	42.7	41.0	0.0	0.0	42.7	41.0	0.0	0.0	72.0	72.0	108.0	108.0	0.0	0.0	0.00	31.0	. *** . ***
870228	25.1	24.9	0.0	0.0	24.2	28.9	0.0	0.0	72.0	72.0	108.0	108.0	0.0	0.0	0.00	28.0	. *** . ***
870331	33.9	66.8	10.7	4.0	23.2	64.8	0.0	0.0	72.0	72.0	108.0	108.0	0.0	0.0	0.00	31.0	. *** . ***
870430	59.6	97.8	36.9	33.6	22.7	67.2	0.0	0.0	72.0	72.0	108.0	108.0	0.0	0.0	0.00	30.0	. *** . ***
870531	55.6	79.6	88.3	70.4	-32.7	9.2	0.0	0.0	39.3	72.0	108.0	108.0	0.0	0.0	-0.58	31.0	. *** - ---
870630	55.8	104.9	134.3	114.9	-74.7	-6.0	0.0	0.0	0.0	66.0	68.6	108.0	0.0	0.0	-2.69	30.0	. *** 0 DRY
870731	107.4	83.8	153.8	134.7	-65.4	-50.9	-17.0	0.0	0.0	15.1	39.1	108.0	-17.0	-2.0	-3.31	31.0	. *** S SVR
870831	436.4	90.1	120.2	119.1	316.2	-29.0	207.7	0.0	72.0	0.0	73.5	94.0	190.8	22.0	1.26	31.0	M MST + +++
870930	23.9	104.0	80.0	78.1	-56.1	25.9	0.0	0.0	15.9	25.9	73.5	94.0	190.8	22.0	-0.85	30.0	M MST - ---
871031	40.0	50.3	21.7	36.0	18.3	14.3	0.0	0.0	34.1	40.2	73.5	94.0	190.8	22.0	-0.64	31.0	M MST - ---
871130	70.4	54.2	13.0	7.5	57.4	46.6	13.3	12.9	72.0	72.0	79.8	96.0	191.2	22.0	-0.29	30.0	M MST . ***
871231	95.4	53.6	0.0	0.0	95.4	59.6	81.7	53.6	72.0	72.0	93.9	102.0	219.2	25.3	-0.14	31.0	M MST . ***
880131	47.8	41.0	0.0	0.0	47.8	41.0	41.0	38.7	72.0	72.0	100.1	104.3	222.1	25.6	-0.07	31.0	M MST . ***
880229	32.8	28.9	0.0	0.0	32.4	28.9	30.4	27.9	72.0	72.0	102.5	105.3	224.6	25.9	-0.04	29.0	M MST . ***
880331	54.6	66.8	0.0	4.0	49.6	64.8	46.1	63.4	72.0	72.0	105.0	106.6	207.3	23.9	-0.03	31.0	M MST . ***
880430	52.8	97.8	29.7	33.7	23.1	67.1	22.6	66.6	72.0	72.0	105.6	107.3	163.3	18.8	-0.03	30.0	M MST . ***
880531	30.3	79.6	78.5	70.6	-49.2	9.0	0.0	9.0	23.9	72.0	105.6	107.4	154.4	17.8	-0.94	31.0	M MST - ---
880630	27.0	104.9	131.6	115.0	-104.6	-6.1	-27.9	0.0	0.0	65.9	52.8	107.4	126.4	14.6	-3.43	30.0	+ +++ S SVR

Table 1

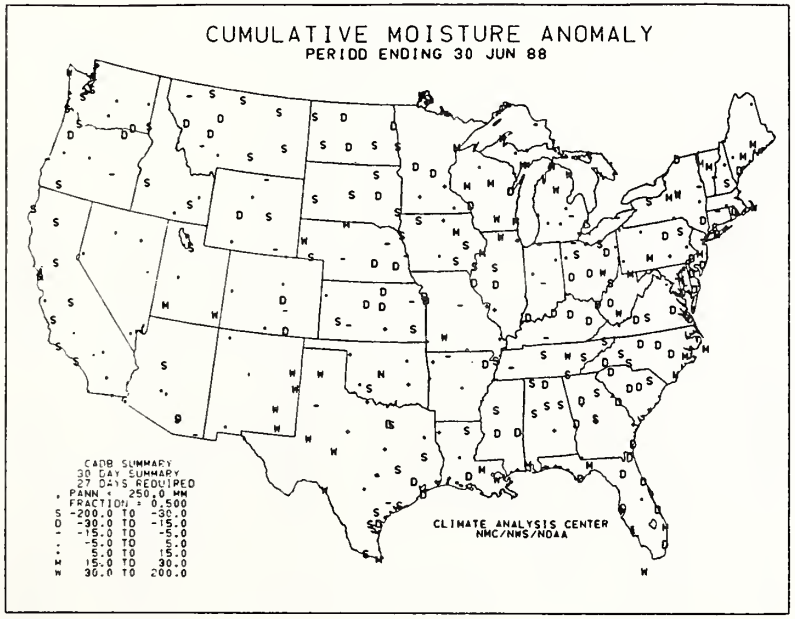

Fig. 1

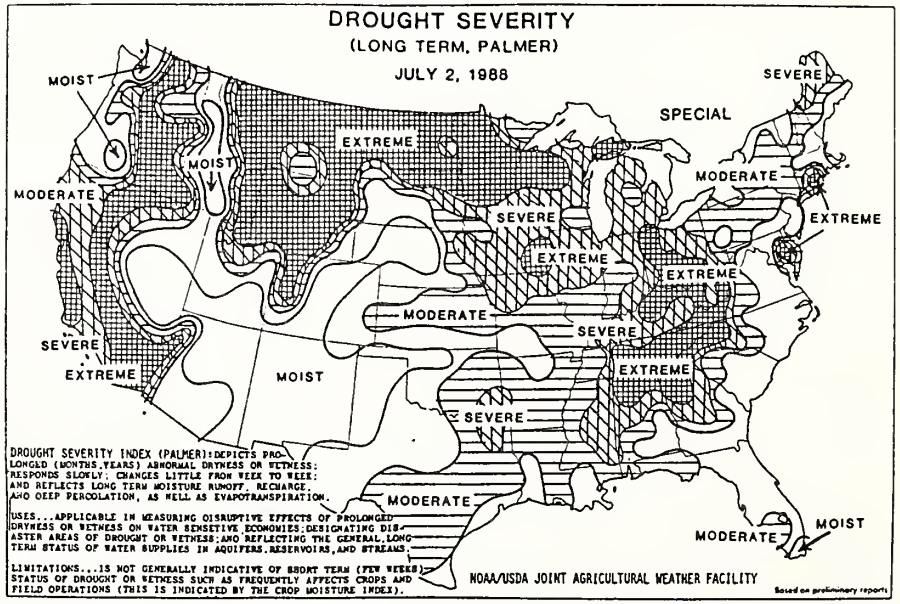
DROUGHT SEVERITY
(LONG TERM, PALMER)
JULY 2, 1988
MOIST
MODERATE
SEVERE
EXTREME
SPECIAL
DROUGHT SEVERITY INDEX (PALMER):DEPICTS PROLONGED (MONTHS,YEARS) ABNORMAL DRYNESS OR WETNESS; RESPONDS SLOWLY; CHANGES LITTLE FROM WEEK TO WEEK; AND REFLECTS LONG TERM MOISTURE RUNOFF, RECHARGE AND DEEP PERCOLATION, AS WELL AS EVAPOTRANSPIRATION.
USES...APPLICABLE IN MEASURING DISRUPTIVE EFFECTS OF PROLONGED DRYNESS OR WETNESS ON WATER SENSITIVE ECONOMIES;DESIGNATING DISASTER AREAS OF DROUGHT OR WETNESS;AND REFLECTING THE GENERAL,LONG TERM STATUS OF WATER SUPPLIES IN AQUIFERS,RESERVOIRS,AND STREAMS.
LIMITATIONS...IS NOT GENERALLY INDICATIVE OF SHORT TERM (FEW WEEKS) STATUS OF DROUGHT OR WETNESS SUCH AS FREQUENTLY AFFECTS CROPS AND FIELD OPERATIONS (THIS IS INDICATED BY THE CROP MOISTURE INDEX).
NOAA/USDA JOINT AGRICULTURAL WEATHER FACILITY
Based on preliminary reports

Fig. 3

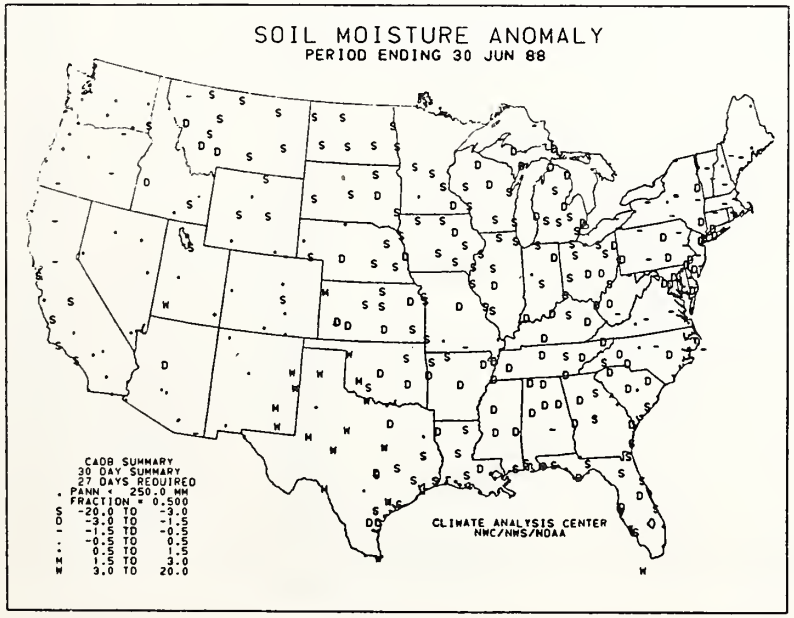

Fig. 2

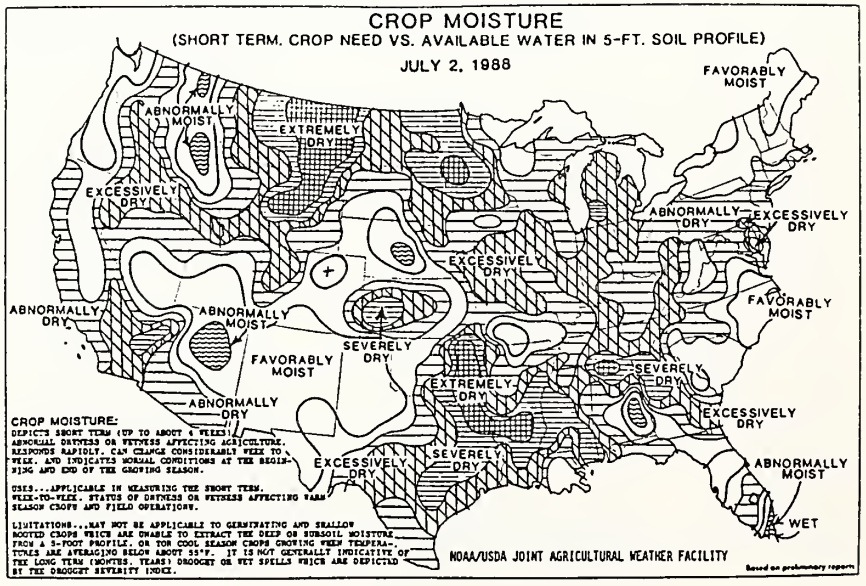
CROP MOISTURE
(SHORT TERM, CROP NEED VS. AVAILABLE WATER IN 5-FT. SOIL PROFILE)
JULY 2, 1988
FAVORABLY MOIST
ABNORMALLY MOIST
EXTREMELY DRY
EXCESSIVELY DRY
ABNORMALLY DRY
SEVERELY DRY
CROP MOISTURE:
DEPICTS SHORT TERM (UP TO ABOUT 4 WEEKS) ABNORMAL DRYNESS OR WETNESS AFFECTING AGRICULTURE. RESPONDS RAPIDLY, CAN CHANGE CONSIDERABLY WEEK TO WEEK, AND INDICATES NORMAL CONDITIONS AT THE BEGINNING AND END OF THE GROWING SEASON.
USES...APPLICABLE IN MEASURING THE SHORT TERM, WEEK-TO-WEEK, STATUS OF DRYNESS OR WETNESS AFFECTING WARM SEASON CROPS AND FIELD OPERATIONS.
LIMITATIONS...MAY NOT BE APPLICABLE TO GERMINATING AND SHALLOW ROOTED CROPS WHICH ARE UNABLE TO EXTRACT THE DEEP OR SUBSOIL MOISTURE FROM A 5-FOOT PROFILE, OR FOR COOL SEASON CROPS GROWING WHEN TEMPERATURES ARE AVERAGING BELOW ABOUT 55°F. IT IS NOT GENERALLY INDICATIVE OF THE LONG TERM (MONTHS, YEARS) DROUGHT OR WET SPELLS WHICH ARE DEPICTED BY THE DROUGHT SEVERITY INDEX.
NOAA/USDA JOINT AGRICULTURAL WEATHER FACILITY
Based on preliminary reports
WET

Fig. 4

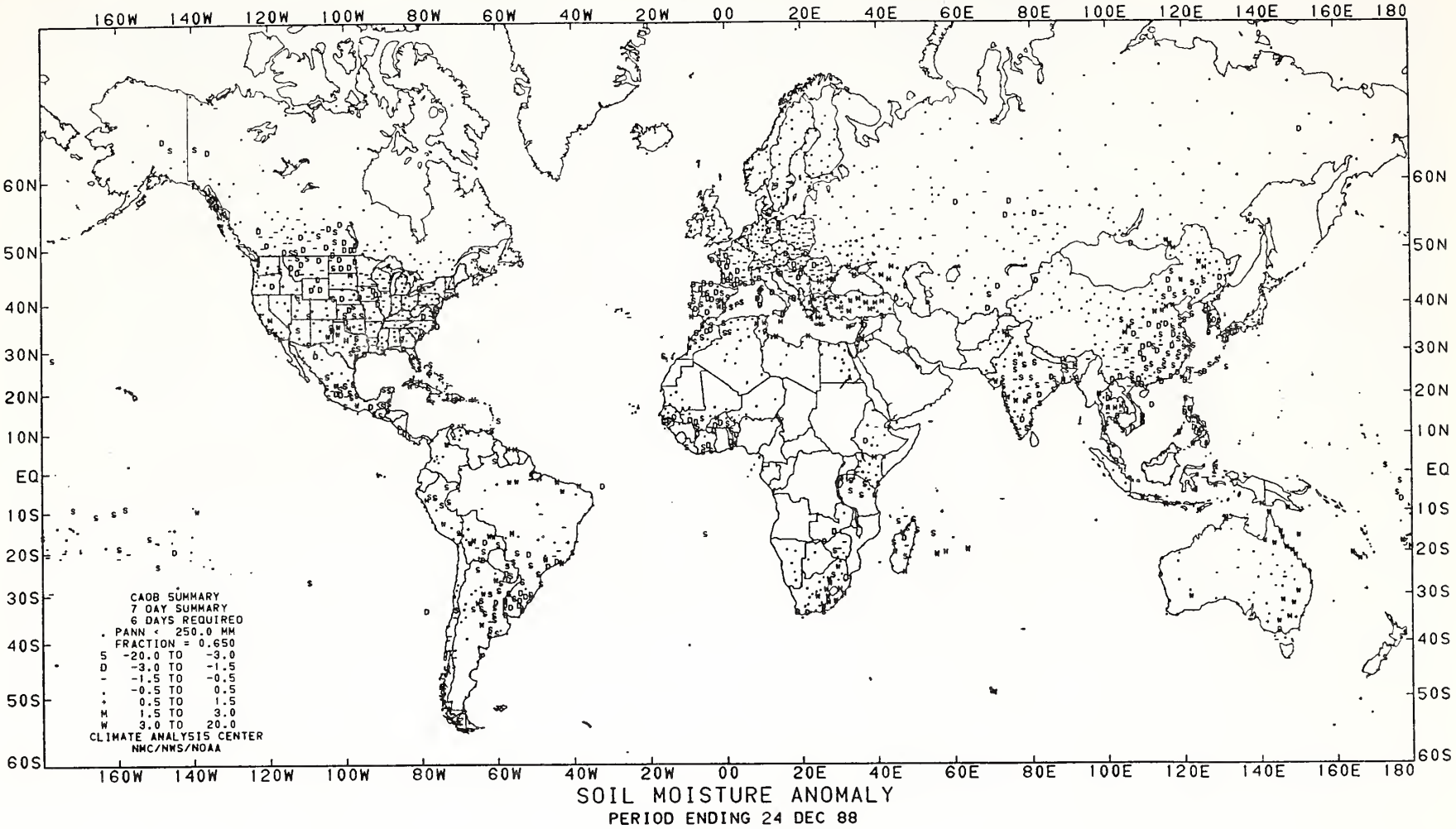
160W 140W 120W 100W 80W 60W 40W 20W 00 20E 40E 60E 80E 100E 120E 140E 160E 180
60N 50N 40N 30N 20N 10N EQ 10S 20S 30S 40S 50S 60S
CAOB SUMMARY
7 DAY SUMMARY
6 DAYS REQUIRED
PANN < 250.0 MM
FRACTION = 0.650
5 -20.0 TO -3.0
D -3.0 TO -1.5
- -1.5 TO -0.5
. -0.5 TO 0.5
+ 0.5 TO 1.5
M 1.5 TO 3.0
W 3.0 TO 20.0
CLIMATE ANALYSIS CENTER
NMC/NWS/NOAA

SOIL MOISTURE ANOMALY
PERIOD ENDING 24 DEC 88

Fig. 5

Circulation regimes of drought in the eastern versus the western part of Subsaharan Africa

Uma Bhatt
Department of Meteorology
University of Wisconsin
Madison, Wisconsin, 53706

The droughts of Subsaharan Africa represent an especially challenging climate problem in terms of the general circulation mechanisms involved and in relation to their severe human impact. The purpose of the present empirical study is to explore the spatial differentiation of climate anomalies and underlying circulation mechanisms across the African-South Asian monsoon belt. While seasonal evolutions warrant attention in further work, the present study concentrates on conditions at the height of the boreal summer, when the large-scale circulation reaches an extremum in the annual cycle and when the rainfall activity across the monsoon belt is concentrated.

Surface ship observations during 1948-83 in the tropical Atlantic, Eastern Pacific, and Indian Oceans between 30 °N and 30 °S were obtained from the National Climatic Center at Asheville, North Carolina for individual months and compiled into five-degree square areas. Elements used here are sea level pressure (SLP), zonal (u) and meridional (v) components of wind, sea surface temperature (SST), and total cloudiness (CLOUD). Data were combined into bi-monthly values for July-August over the period 1948-83, when coverage is most satisfactory. In addition various index series (Fig. 1, Table 1) were used to capture the interannual variability of hydrometeorological conditions across the African-South Asian monsoon belt. Three of these were compiled from the river discharge of large catchments: monthly values for the Senegal river over the period 1948-83 were combined into twelve-monthly values with seasonalization from May to April (SENEGAL), while index series for the Blue Nile at Roseires (ROSEIRES) and the River Atbara (ATBARA) were obtained by seasonalizing from April to March and over the period 1948-72, in accordance with the respective annual cycles of river discharge. Further used were Lamb's (1985) index series compiled from April-October precipitation at 20 stations across Subsaharan West Africa (SAHEL) over the period 1941-83 and Mooley and Parthasarathy's (1984) all-India index of summer monsoon rainfall (NIR) derived from the June-September totals at 306 stations during 1948-83. Finally, the pressure difference Tahiti minus Darwin in 1948-83 was used as an index SOI of the Southern Oscillation (SO).

Correlation coefficients were calculated between the aforementioned hydrometeorological and circulation indices and the July-August atmospheric and oceanic fields. Also constructed were the fields of regression coefficients for SLP, which together with the SLP correlation patterns permit to ascertain the spatial distribution of pressure gradients. The *local* significance was assessed using the Student's t-test at the 5 percent level and accounting for the reduction of effective degrees of freedom due to persistence using the methods described by Quenouille (1952, p. 168). The *field* significance of correlation patterns was ascertained by Monte Carlo simulations similar to those described by Livezey and Chen (1983). This field significance testing procedure was applied to the combined Atlantic and Eastern Pacific and separately to the Indian Ocean.

Table 1 indicates a strong association between SENEGAL and SAHEL, a decrease from either of these domains eastward to the Nile catchment (ROSEIRES, ATBARA), and a further decrease to India (NIR). Conversely, correlations are remarkably high between the water discharge of the Nile basin (ROSEIRES and ATBARA), and even more so with India rainfall (NIR). It is further noteworthy that SOI is correlated positively with the hydrometeorological conditions throughout the monsoon belt, but most strongly in the East (NIR), and least in the West (SENEGAL).

Fig. 2 presents the maps of correlation with SENEGAL. Negative values in the SLP correlation map in the North Atlantic, together with the pressure regression coefficients (not shown), also largest in this region, indicate for abundant Senegal River discharge a more poleward position of the near-equatorial trough. Consistent with this, the positive u and v correlations indicate reduced Northeast trades and enhanced southerly cross-equatorial flow in the Atlantic sector. In the Western Indian Ocean, the SST and v correlation maps both display strong negative values. In sum, abundant Senegal River discharge is, in the Atlantic sector characterized by a poleward displaced near-equatorial trough, weakened Northeast trades, and enhanced southerly flow, while in the Western Indian Ocean surface waters are anomalously cold and the southwesterly monsoon flow weak. Patterns of correlation with SAHEL are similar to those with SENEGAL.

Fig. 3 presents maps of correlation with ROSEIRES. Most prominent are the positive SLP and negative SST correlations in the Eastern Pacific. Correlation patterns in the Atlantic are similar to those for SENEGAL. In the Western Indian Ocean correlations are negative for SLP and SST, and positive for u, v, and CLOUD, and pressure regression coefficients (not shown here) are prevailingly negative. In synthesis, abundant Blue Nile discharge at Roseires is associated in the Eastern Pacific with anomalously high pressure and cold surface waters; in the Atlantic with a poleward displaced near-equatorial trough, weakened Northeast trades and enhanced southerly cross-equatorial flow, and warm surface waters to the North of the Equator; and in the Western Indian Ocean by anomalously low pressure, enhanced Southwest monsoon flow, cold surface waters, and abundant cloudiness. Patterns of correlation with ATBARA are similar to ROSEIRES.

In the maps of correlation (not shown) with NIR significance is reached only in the Indian Ocean for SLP and CLOUD. In the Eastern Pacific the SLP correlation map contains positive values and the SST correlation map strong negative values. The patterns in the Atlantic are indistinct. In the Western Indian Ocean, correlations are predominantly negative with SLP and SST, and positive with u, v, and CLOUD. In summary, copious India rainfall is characterized by anomalously high pressure and cool surface waters in the Eastern Pacific and by low pressure, increased southwesterly cross-equatorial flow, cool surface waters, and abundant cloudiness in the Western Indian Ocean.

In the maps of correlation (not shown) with SOI significance is reached for all fields in the Pacific-Atlantic domain and for SLP, v, SST, and CLOUD in the Indian Ocean. In the Eastern Pacific there are positive values in the SLP and negative values in the SST correlation maps. The patterns in the Atlantic are indistinct. In the Indian Ocean sector SLP and SST correlation maps show negative values and CLOUD and v maps contain positive values. In summary, the positive phase of the Southern Oscillation (anomalously high/low pressure at Tahiti/Darwin) is characterized by anomalously high pressure overlying cool surface waters in the Eastern Pacific and by anomalously low pressure, enhanced southerly flow, cool surface waters, and abundant cloudiness in the Indian Ocean.

Revealed in this study is not only a coherence but also a remarkable difference between the hydrometeorological anomalies in the eastern versus the western parts of Subsaharan Africa. The western Sahel shows strongest associations with circulation departures in the Atlantic. Thus, abundant rainfall in the western Sahel is characterized by anomalously low pressure in the North Atlantic, decreased northeast trades, enhanced southerly flow, and a more northerly position of the near-equatorial trough. Despite receiving the majority of its moisture from the

Atlantic, eastern Subsaharan Africa indicates strongest associations with the anomalies of India rainfall and circulation patterns in the Indian Ocean sector. Abundant rainfall in eastern Subsaharan Africa is characterized by low pressure, increased southerly flow, cool surface waters, and cloudiness in the Indian Ocean.

Both empirical upper-air case studies and numerical modeling experiments are in order to further explore the general circulation mechanisms for the coherence and diversity of rainfall anomalies across the monsoon belt.

Acknowledgements:

This work was supported by NSF Grant ATM-8722410 and NOAA Grant NA86AA-D-AC064.

REFERENCES

Lamb, P. J., 1985: Rainfall in Subsaharan West Africa during 1941-83.
Zeitschrift für Gletscherkunde und Glazialgeologie, **21**, 131-139.

Livezey, R. E., Chen, W. Y., 1983: Statistical field significance and its determination by Monte Carlo techniques.
Mon. Wea. Rev., **111**, 46-59.

Mooley, D. A., Parthasarathy, B., 1984: Fluctuations in all-India summer monsoon rainfall during 1871-1978.
Climatic Change, **6**, 287-301.

Quenouille, M. H., 1952: Associated measurements .
Butterworths, London. 242 pp.

Table 1 Correlation coefficients in hundredths between hydrometeorological indices (Fig. 1) for 1948-72. One and two asterisks indicate significance at the 5 and 1 percent levels, respectively. In the significance testing of correlation coefficients QUENOUILLE'S (1952, p. 168) method was used to account for the reduction of the effective number of degrees of freedom due to persistence.

	SENEGAL	SAHEL	ROSEIRES	ATBARA	NIR	SOI
SENEGAL		+77**	+49*	+47*	+23	+35
SAHEL			+31	+48*	+14	+27
ROSEIRES				+77**	+84**	+50*
ATBARA					+69**	+37
NIR						+51**
SOI						

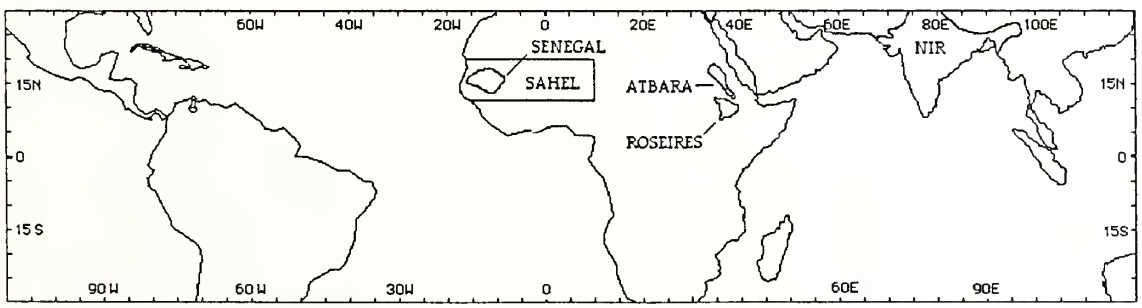

Fig 1. Domains of hydrometeorological index series: Senegal River basin, SENEGAL; Subsaharan West Africa, SAHEL; Blue Nile at Roseires, ROSEIRES; Atbara river basin, ATBARA; all-India rainfall index, NIR.

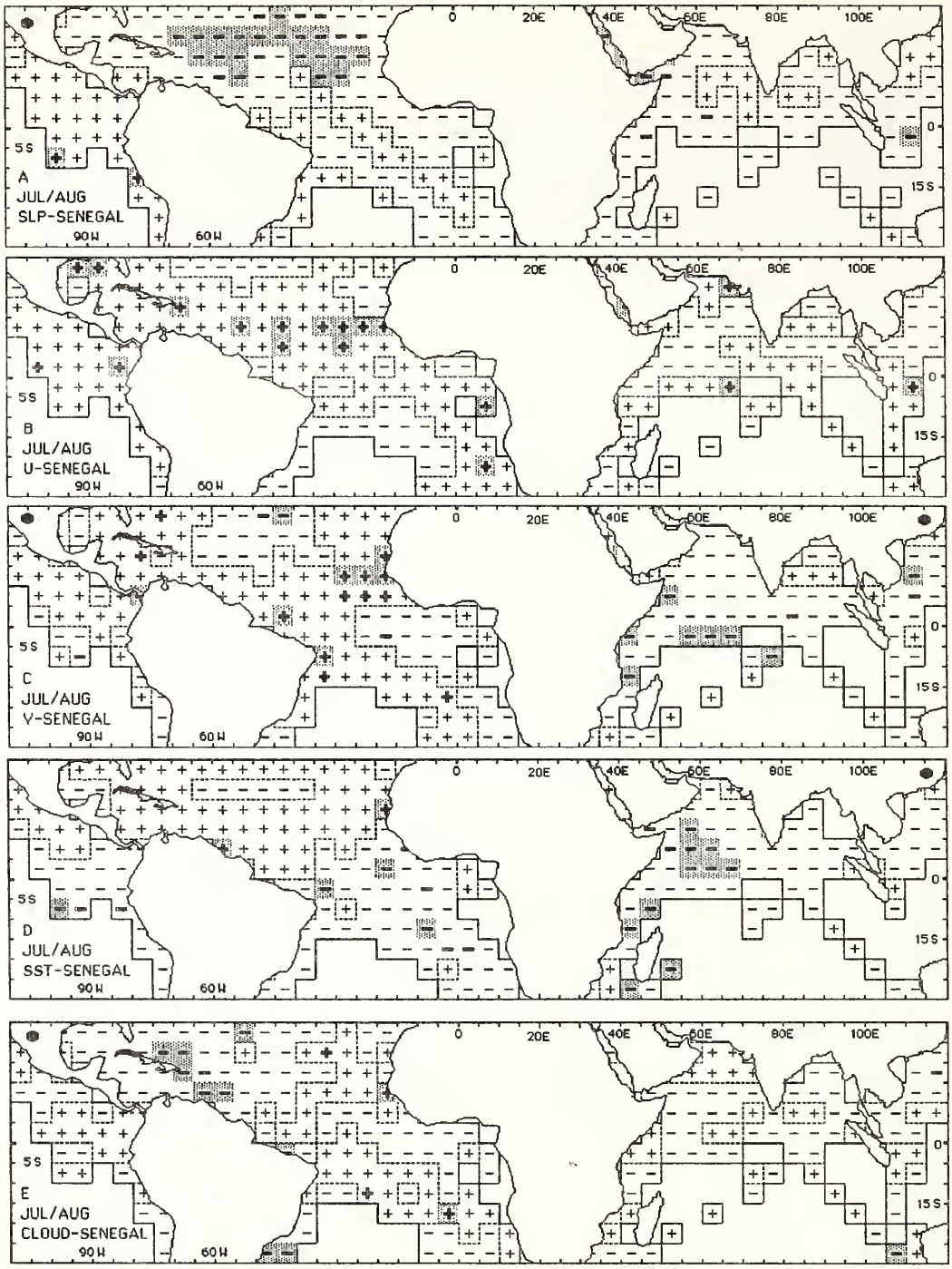

Fig 2. Patterns of correlation between an index of Senegal River discharge (SENEGAL) and July/Aug values of indicated elements during 1948-83. (a) sea level pressure SLP, (b) zonal u, and (c) meridional wind component v, (d) sea surface temperature SST, and (e) cloudiness CLOUD. Plus and minus signs denote the sign of the correlation, shading absolute values greater than 0.4, and bold signs indicate local significance at the 5 percent level. Quenouille's (1952, p.168) formulation was used to account for the reduction of the effective temporal degrees of freedom due to persistence. Blank areas indicate blocks with less than 29 years of data. Field significance at the 5 percent level, as determined by Monte Carlo experiments, is indicated by dots, in the northwestern corner of the map for the Pacific-Atlantic domain, and in the northeastern corner for the Indian Ocean.

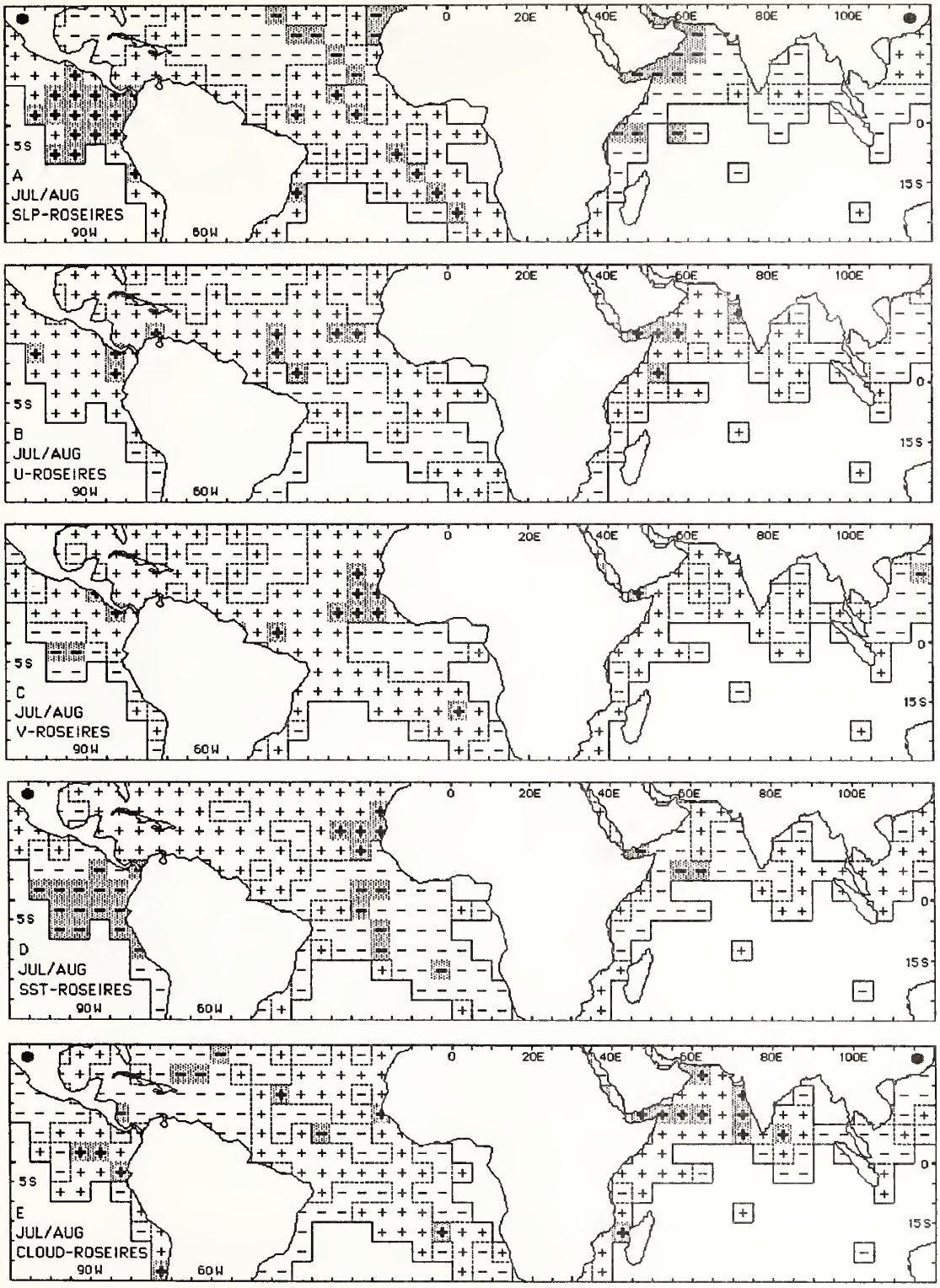

Fig 3. As in Fig. 2 except for ROSEIRES, period 1948-72. Blank areas indicate blocks with less than 20 years of data.

Specifying Surface Temperature, Dewpoint, Wind Speed and Precipitation Frequency for Monthly Fire-Weather Outlooks

William H. Klein and Bruce T. Whistler
Department of Meteorology
University of Maryland
College Park, MD 20742

Specification of monthly mean surface weather elements from concurrent fields of 700 mb height anomaly (HA) can help the U.S. Forest Service evaluate the potential for wildland fires in the United States. We have therefore derived multiple regression equations for anomalies of monthly precipitation frequency (PF), midday temperature (T), dewpoint (D or Td), relative humidity (RH) and wind speed (V) by forward selection (screening) of potential HA predictors. Although computed from a long period of observed data, these equations will be applied to monthly mean values of HA forecast routinely in the Climate Analysis Center (CAC).

We first derived specification equations for PF (the number of days with precipitation ≥0.10 inches) at each of 60 climate divisions across the United States from 30 years of data (1951-1980) by pooling each month with its two immediately adjacent months and screening the simultaneous HA at a network of 79 grid points in North America and vicinity. Figure 1 shows the annual cycle of the average reduction of variance (RV) (multiple correlation squared) for PF (dashed) and PA (precipitation amounts at the same 60 divisions for the same period of record). Note that PF outperforms PA each month, with greatest difference in the summer when precipitation is difficult to specify because of localized convective activity.

We next obtained a set of 3-hourly surface observations at 116 stations plotted in Fig. 2 for the 20-year period: 1964-1983. After computing monthly mean values of T, D, RH and V observed at approximately 1300, local standard time, we selected a representative subset of 58 stations for experimentation with 3-month seasons centered on Feb., May, Aug. and Nov. For each of the above weather elements, we screened HA at a field of 121 grid points (Fig. 3). The results (Fig. 4) show that the RV, averaged over all months and stations, had the following rank: T (best), D, PF, RH and V (worst). We were able to increase the RV by about 4%, on the average, by including the previous month's value of the predictand (dependent variable) as an additional potential predictor (local persistence). However, previous values of other local elements (such as D to predict T) or of the same element at the entire network of 58 stations (such as one station's D to predict another's D) did not produce meaningful improvement. Also we could not increase the RV of V by screening the field of 700 mb geostrophic wind speeds and components instead of heights. In view of the above results, we decided to omit RH from further consideration and to derive final specification equations for T, D and V from HA and local persistence only.

Fig. 5 shows the annual cycle of persistence in terms of the one-month lag autocorrelation coefficient, averaged over all 116 stations of Fig. 2, separately for D, T and V. All three elements exhibit maxima in month-to-month persistence in late summer and late winter and minima in late spring and late fall. Annual average values (upper right hand corner) are slightly higher for D (.23) than for T (.20), perhaps because of persistence of soil moisture. However, the unexpectedly high average autocorrelation for V (.30) cannot be readily explained.

In the results described thus far, we used a cut-off criterion of approximately 99% on the classical F-test as an estimate of the true 95% significance level for terminating selection

of variables in the specification equations. To establish a more exact criterion, we performed a series of Monte Carlo simulations summarized in Fig. 6. It shows that the 95th percentile of F-values obtained by screening 1200 randomly shuffled samples of our data (critical F) increases as the number of potential predictors increases from 1 (classical) to 79 (for PF) to 121 (for T, D and V). Since the critical F also varies slightly with month and element, we made separate Monte Carlo runs for each of these factors and used the results as our primary tool in selecting the final specification equations.

The statistics involved in selecting a sample equation are illustrated in Table 1 for D during summer months at Scottsbluff, NE (BFF). The first predictor selected is the HA at 50°N, 100°W., just northeast of BFF, with an RV of 20% and F of 14.6. The second variable is the previous month's dewpoint, which adds 15% to the total RV. The third predictor is the HA at 30°N, 120°W, well southwest of BFF, which adds 11% to the RV. The negative sign of its regression coefficient, in conjunction with the positive sign for the first variable, indicates that high (low) dewpoints are favored by anomalous flow of moist (dry) air from the southeast (northwest). The selection process was stopped at this point, with a standard error of 2.5°F and 46% of the variance explained by only three terms, because no other predictor made good synoptic sense or produced an F in excess of the critical value.

Specification equations similar to those in Table 1 have been selected for each station, month and weather element. The annual cycle of RV for D and T is plotted in Fig. 7, where each point represents the mean over all 116 stations of Fig. 2. Although T exhibits higher values than D each month, the difference in RV is very small in January, when both elements are well specified by the large-scale 700 mb circulation. However, the difference is very large in July, when D is apparently very sensitive to boundary layer phenomena and small-scale factors (e.g., evaporation of soil moisture) which are not well represented by the large scale 700 mb pattern.

On an overall basis, for all stations and all months, our final specification equations explain approximately 67.7% of the temperature variance by means of 3.5 variables. The corresponding statistics for dewpoint are 56.5% and 3.1 terms, for precipitation frequency 41.4% and 2.8 terms, and for wind speed 37.1% and 2.4 terms. Since large geographical and temporal variations are evident in these and other climatological statistics, we are analyzing, for each element and each month, maps of the explained variance, autocorrelation, mean and standard deviation. These maps should help forecasters interpret the final specification equations and the Forest Service prepare monthly fire-weather outlooks.

ACKNOWLEDGMENTS

This research was supported by the U.S. Department of Agriculture, Forest Service, under Cooperative Agreement No PSW-87-0023CA. Surface data was obtained from the Forest Service in East Lansing, MI; climate division data from Creighton University, NE; and 700 mb heights from the CAC in Camp Springs, MD. We thank Francis Fujioka, Morris McCutchan and Bill Main of the Forest Service; Art Douglas and Phil Englehart of Creighton University; Don Gilman of CAC and Ferd Baer, Hal Bloom and Runhua Yang of the University of Maryland for help in various aspects of this project.

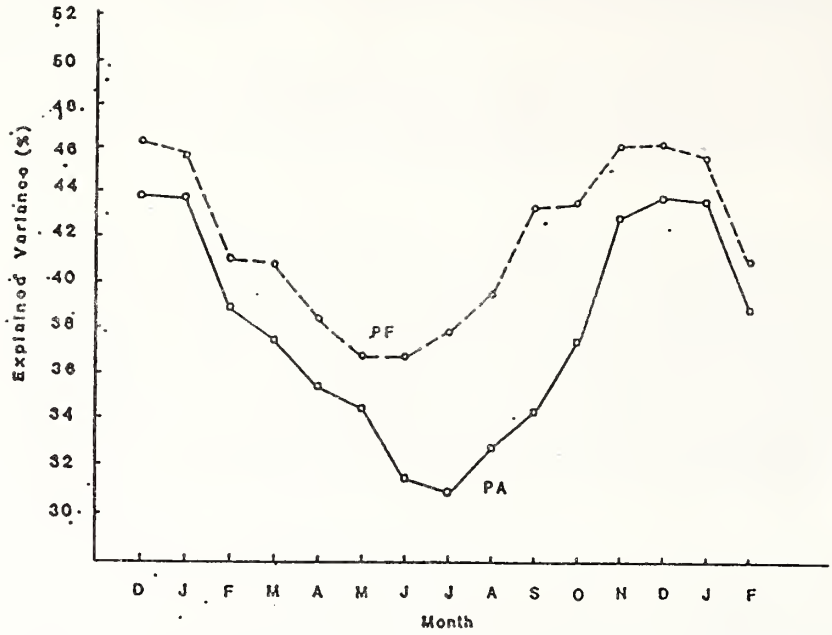

Fig. 1. Percent of variance explained by monthly precipitation specification equations, averaged over 60 climate divisions, as a function of concurrent 700 mb mean height anomalies at 79 grid points for frequency (PF) and amounts (PA) during 1951-1980.

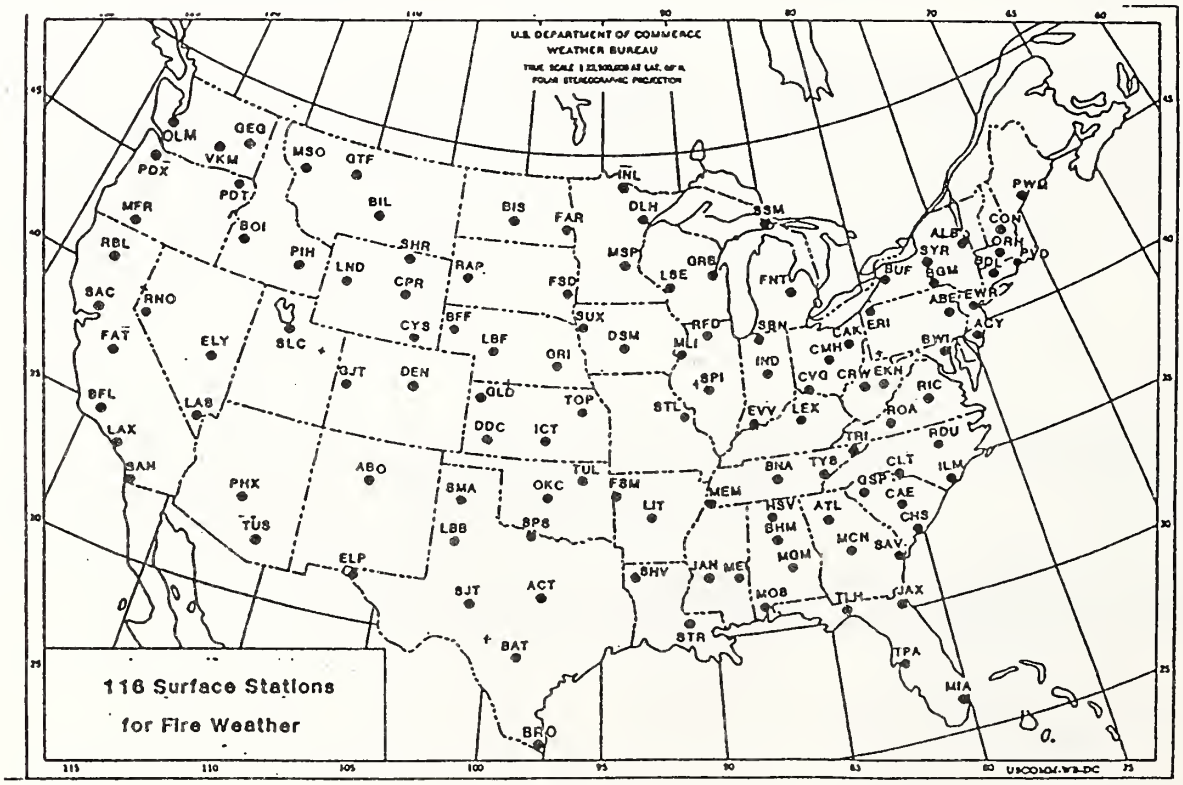

Fig. 2. Locations and call letters of 116 surface stations used in this study.

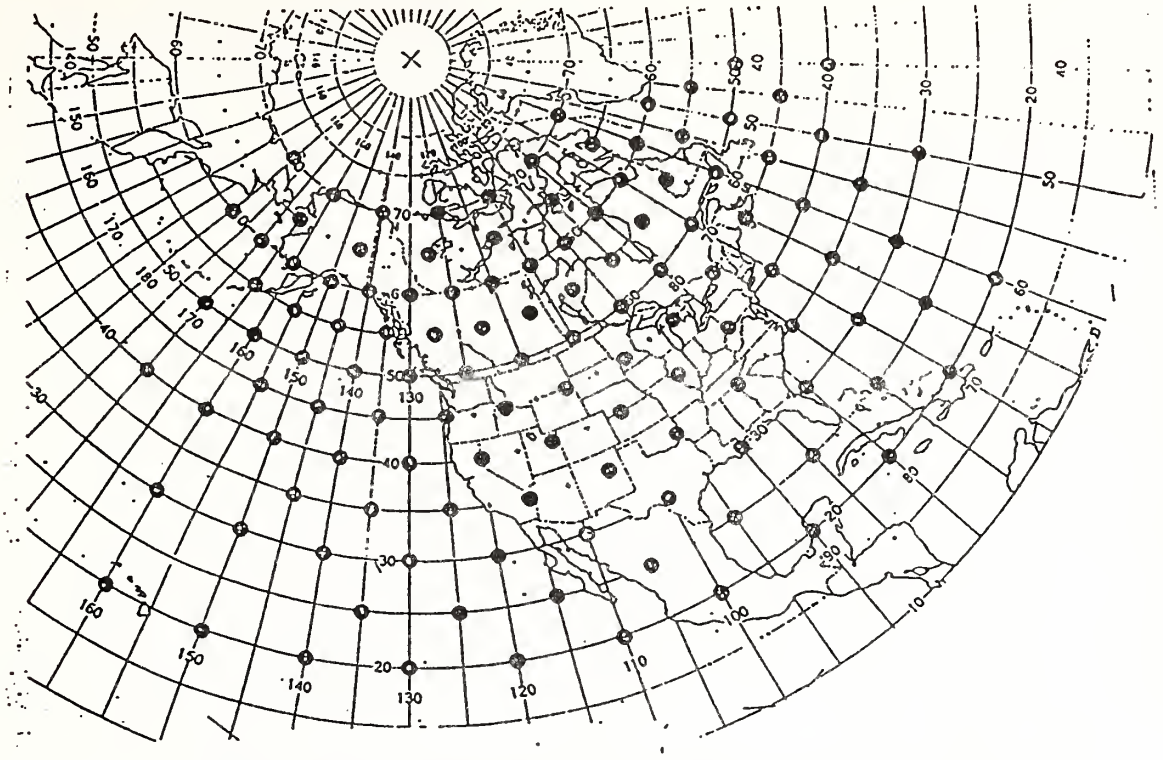

Fig. 3. Network of 121 grid points used to delineate the field of 700 mb height.

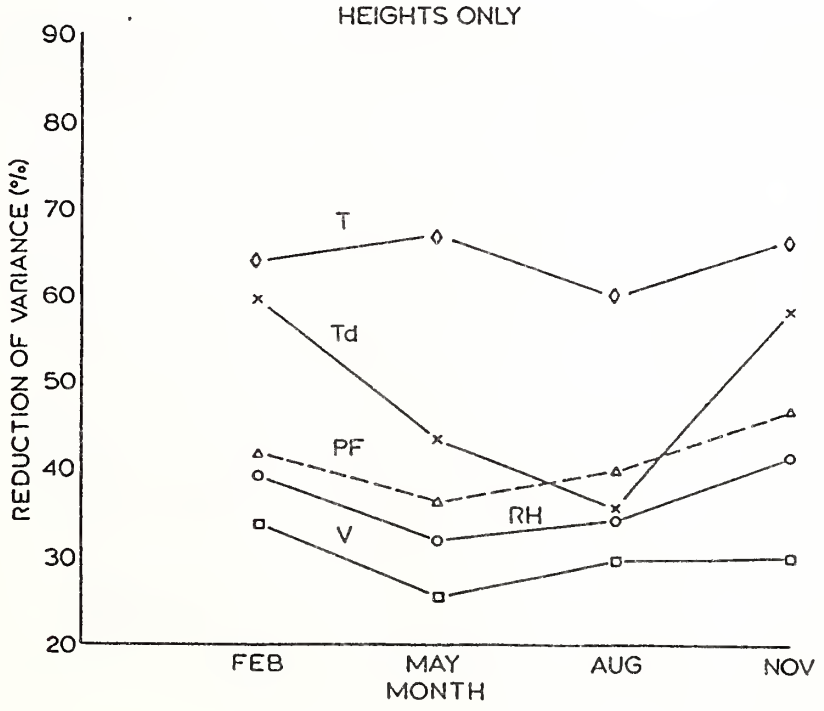

Fig. 4. Average reductions of variance for 58 stations during Feb., May, Aug. and Nov. obtained by specifying temperature, dewpoint, relative humidity and wind speed (solid) over a 20-year period from the height field of Fig. 3. Comparable statistics for precipitation frequency at 60 climate divisions over 30 years are dashed.

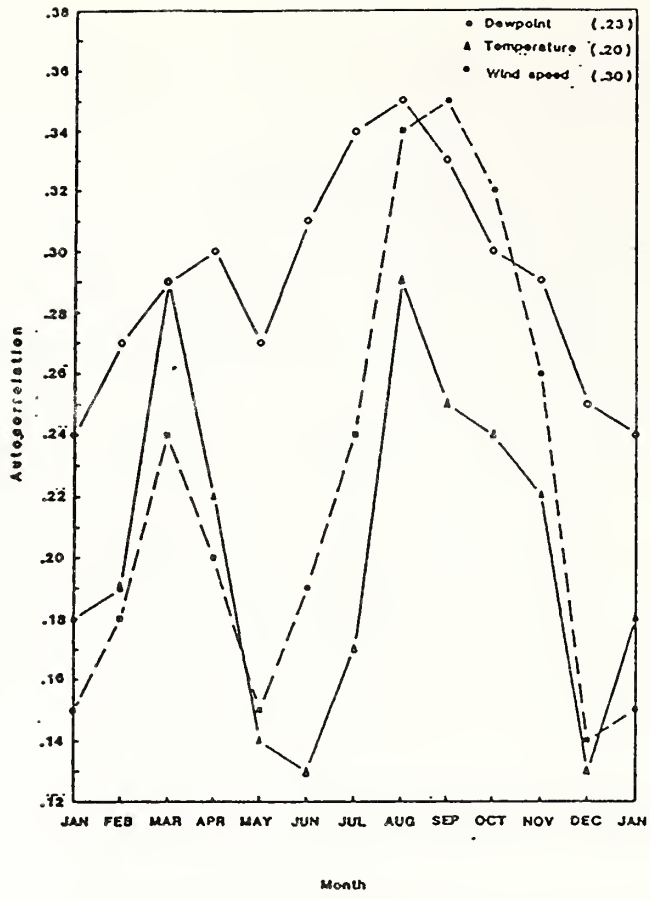

Fig. 5. Month-to-month variations of the one-month lag autocorrelation for surface dewpoint, temperature and wind speed, averaged over 116 stations of Fig. 2. Annual average values of each element are given in the upper right hand corner.

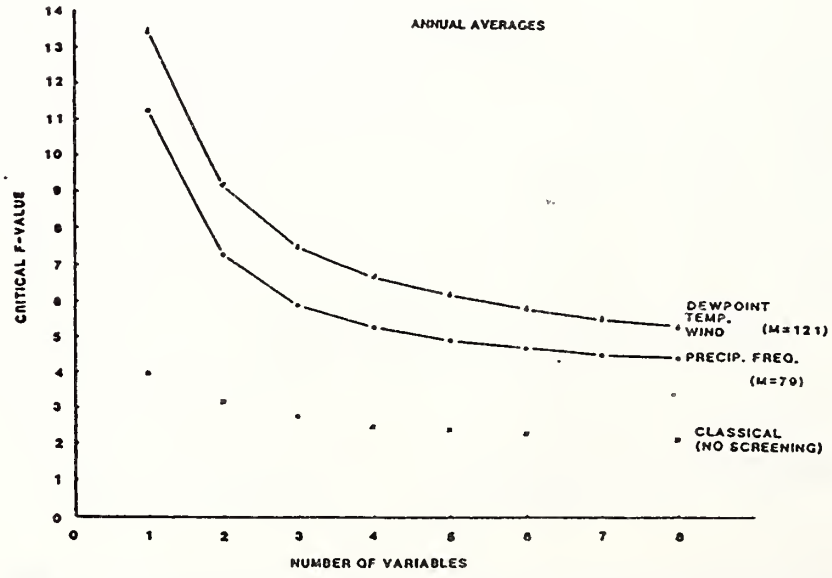

Fig. 6. Mean annual values of the critical F statistic as a function of number of terms in multiple regression equation and number of potential predictors (M). The critical values represent the 95th percentile of all F's obtained by screening randomly shuffled data for 121 predictors (mean of curves for D, T and V) and for 79 predictors (PF). Crosses denote classical F values without screening.

Table 1. Summary of the stepwise regression statistics obtained by screening monthly mean surface dewpoint at Scottsbluff, NE (42°N, 103°W) during June, July and August, 1964-1983, as a function of the concurrent field of 700 mb height anomalies. The critical F-values were determined by a Monte Carlo procedure. The final equation selected for use in specification is starred.

Step	Grid point for height	Reg. coeff. on entry	Added RV(%)	Total RV(%)	Computed F-value	Prob. level(%)	Critical F-value	SE (°F)
1	50°N,100°W	+0.073	20.1	20.1	14.6	99.9	13.7	3.0
2	PREV.DEWP.	+0.396	15.1	35.2	13.3	99.9	10.0	2.7
3*	30°N,120°W	-0.105	10.8	46.0	11.2	99.8	8.8	2.5
4	60°N,70°W	+0.023	4.0	50.0	4.4	95.8	7.2	2.4
5	60°N,100°W	-0.045	3.8	53.8	4.5	96.1	6.6	2.3

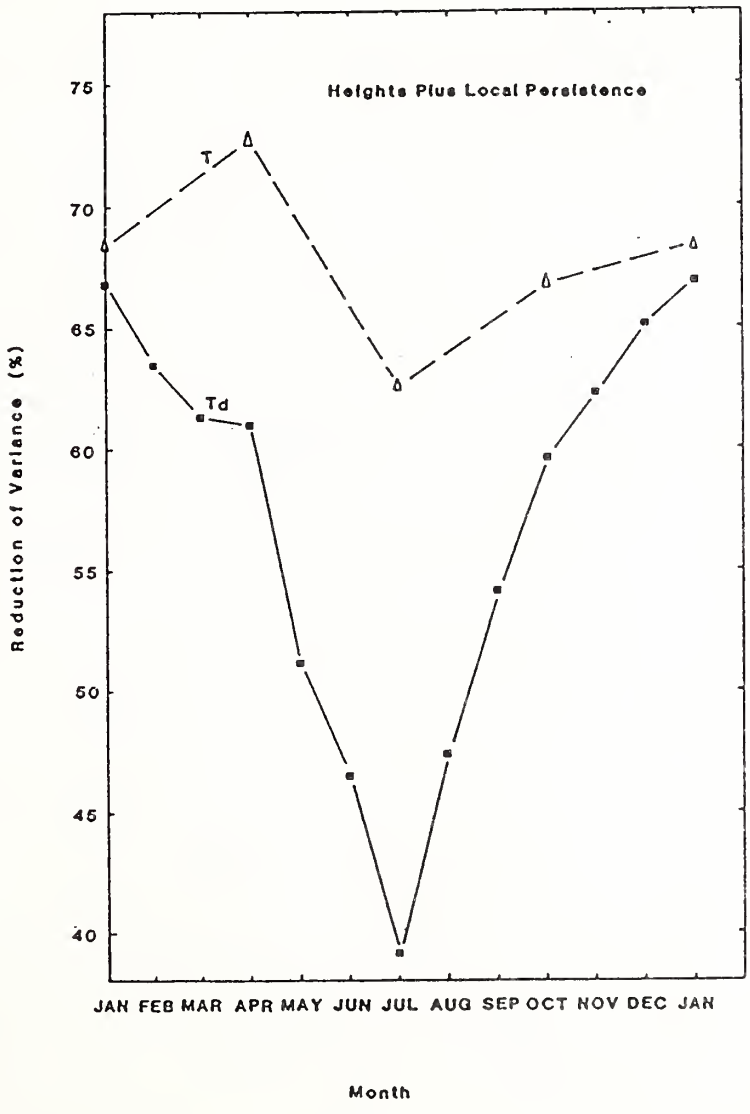

Fig. 7. Month-to-month variations in the reduction of variance of specification equations for surface dewpoint and temperature, averaged over 116 stations of Fig. 2.

Monthly Precipitation-Temperature Relations, the United States, 1931-1987.

H. M. van den Dool
Cooperative Institute for Climate Studies
University of Maryland
College Park, MD 20742

1. Introduction

Recently an atlas has been put together (Van den Dool 1988) containing 32 maps that display the relationship between time-mean precipitation (P) and temperature (T) anomalies over the United States. The first twelve maps show the linear correlation between synchronous colocated monthly P and T, and the second set describes the relationship when monthly P leads T by one month. (The remaining 8 are for seasonal means). This atlas was meant primarily to aid operational monthly and seasonal forecasting at the Climate Analysis Center.

The data used here consist of 57 years of monthly T and P at 344 United States Climate Divisions (CD). The period is 1931-1987; adjacent data for 1988 has been used where needed.

The assumption/philosophy is that P has an impact on soil moisture, and therefore an impact on near-surface T, particularly by changing the Bowen ratio. This impact, which is at least local but perhaps on a large scale, has a look-ahead aspect! Even though rainfall itself has little or no persistence, the effects of rainfall on the earth's surface (soil moisture, roughness, color, albedo, aerosol) do. We know that drought (and its opposite: flood) is a complicated beast with numerous hypothesized feedbacks and causes and therefore we choose to focus on a little portion of the whole problem: temperature effects lagging excess/deficiency in P.

Because of the expected decrease (increase) in sensible heat transfer following positive (negative) rainfall anomalies we test the null-hypothesis that P and T are not negatively correlated. The hypothesis will be rejected if the correlation is more negative than -0.22 (a one-sided t-test, 57 pairs).

2. Results of correlating simultaneous P and T.

There are at least 3 'regimes' in the 12 simultaneous P,T correlation maps (see Atlas) :

A) Negative correlation in the Northern Central States in winter months.
B) Positive correlation in the Eastern one third of the country in winter months.
C) Negative correlations in a broad band covering the area over and just east of the Rocky Mountains in summer.

Of these 3 regimes only C qualifies, in our opinion, to be of a somewhat local nature. In the absence of strong advection, 'hot and dry' or 'cold and rainy' is the rule just about everywhere in the 48 contiguous states in summer. Fig.1 serves as a good example of regime C. In August the negative correlations cover a band from Texas and Arkansas up to Montana i.e. in a largely land-locked area. Positive correlations are virtually absent. Amazing gradients can be seen: while the correlation is highly negative in, say, Nebraska, insignificant correlations are found on either side in Iowa and Colorado. The pattern in Fig.1 exists more or less from May through September.

3. Some results of lagged P,T relation.

Fig.2 is as Fig.1 except that P is one month earlier (i.e. in July) and at one CD only. This CD is in Northern Oklahoma, indicated in Fig.2 by the asterisk. A considerable area of moderately useful negative correlation is seen over Oklahoma and neighboring states. This indicates that a dry/wet July in Oklahoma tends to be followed by a warm/cold August, not only strictly locally but at some modest distance too. Fig.2 is very similar to the colocated P,T time-lagged correlation for July/Aug (shown in the Atlas), implying that P-anomalies have non-zero spatial correlation.

Showing the lagged-space-time correlation is a natural intermediate step to constructing composites. Let us define dry/wet as departures (from normal) of one standard deviation or more in P. Applying this definition to CD#237 in Oklahoma yields about 10 dry and 10 wet Julys. Figs. 3 and 4 show composite T anomaly distributions in August over the United States following wet and dry 'events' in Oklahoma respectively. A peculiar asymmetry, not evident in Fig.2 is unearthed now. Note first of all the extraordinary magnitude of the T anomalies following dry months in Oklahoma: up to one standard deviation positive departure. Comparison of Figs 3 and 4 yields the following asymmetries: i) The spatial scale of positive T anomalies following dry months in Oklahoma is much larger than that for the negative T anomalies following wet months. This seems to imply that drought operates on larger scales than flood; the latter could be a single shower. ii) Although bigger in scale and larger in amplitude the T aftermath of drought is local in the sense that teleconnected anomalies of opposite sign are almost absent. Note that local and large-scale are not mutually exclusive.

In judging these maps, note also the following. i) The July-to-August correlation in P is negligible. Nevertheless the composite P anomalies following dry Julys in Oklahoma (not shown) are somewhat supportive (i.e. they are negative) in explaining the large hot area in Fig.4. Hence Fig.4 features more than just a local T aftermath of previous drought. In contrast composite P anomalies following wet Julys do not show organized wetness in August near Oklahoma. ii) There is no correlation between T in July and P in August. iii) There is persistence in T from July to August and we speculate that this is caused, to a large extent, by a local soil moisture feedback. The latter is consistent with the finding by Van den Dool, Klein and Walsh(1986) that persistence in circulation anomalies is not the cause of persistence in monthly T over the central United States in summer.

Time mean data could obscure the true time scale of the delay of T behind P. Could it be that an actual e-folding of a few days has been smeared out to an artificial 'monthly' effect by using monthly meaned data? Preliminary exercises with daily data at just Oklahoma City indicate that in the cases used in the composite in Figs 3 and 4 an effect in daily maximum temperature is present out to 6 weeks or so. This may be an extreme example, but if it holds up we would have some evidence of legitimate extended, if not long, range predictability using empirical means. We intend to calculate e-folding constants for the T-effect lagging P 'events' from daily data for many sites in the land-locked areas of the United States.

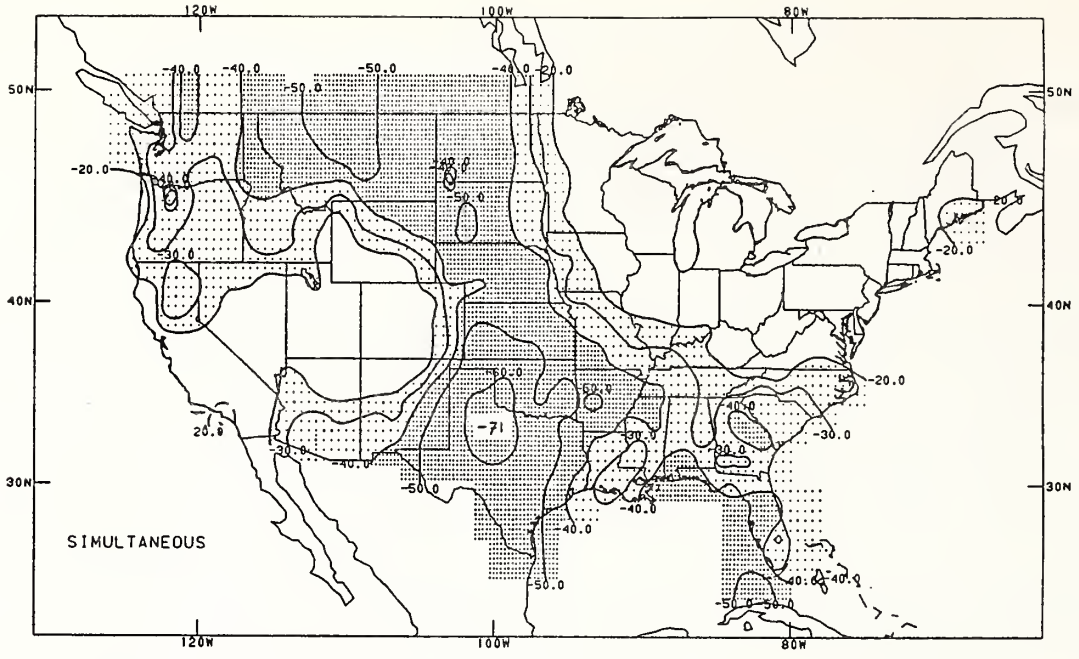

PP,TT LOCAL TEMPORAL CORRELATION AUG 1931-87

Fig.1 The synchronous P,T temporal correlation in August over the United States. Zero ,+10% and -10% contours are omitted. Negative contours are in full, positive dashed. Light (heavy) stippling is applied in areas with correlation less than -20%(-40%).

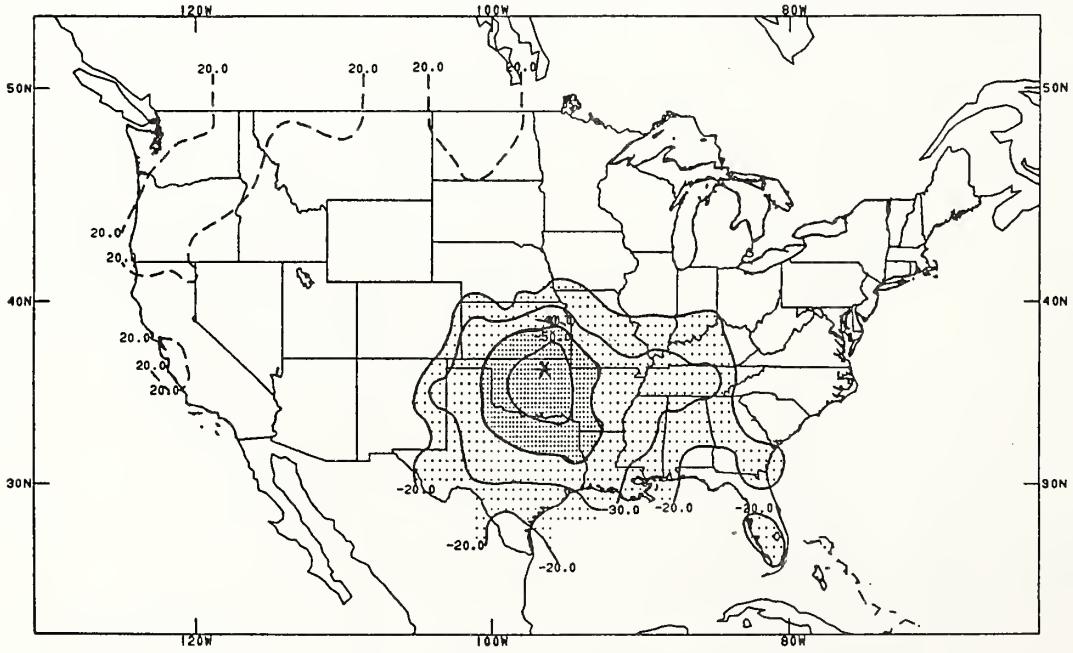

PP,TT TEMPORAL CORRELATION JLAU 1931-87

Fig.2 As Fig.1 except for P(July) leading T(August) by a month. Moreover, instead of spatially colocated P,T data, a single P time series at CD#237 in Oklahoma has been correlated with T elsewhere.

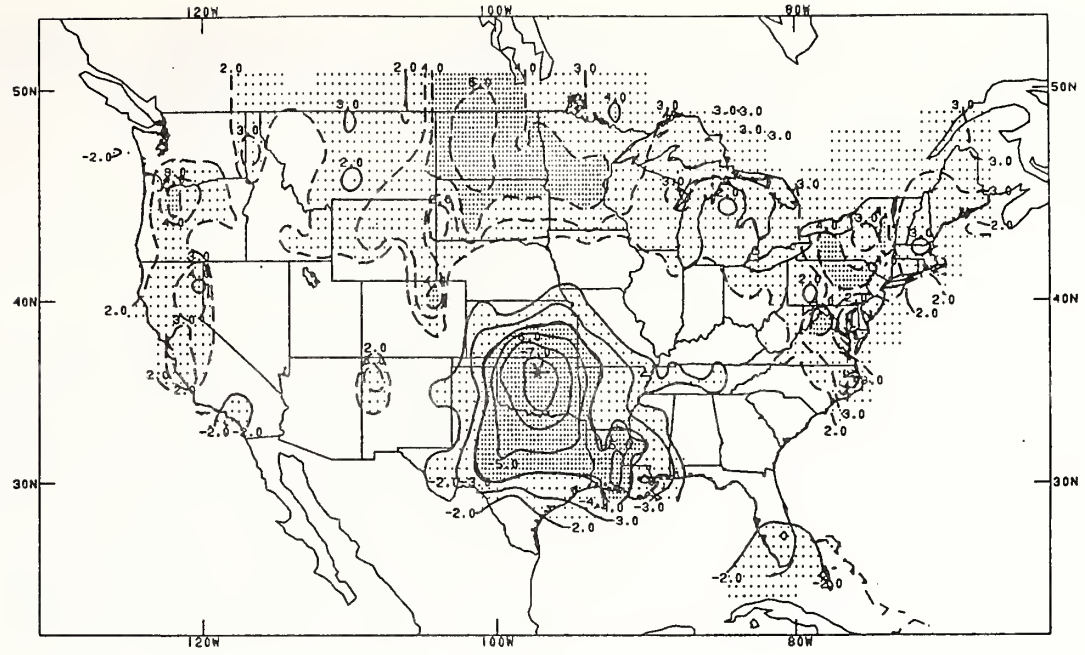

TT COMPOS AU 1931-87 AFTER WET JL IN OKLA

Fig.3 Ensemble mean temperature anomalies over the United States in August following a wet July in CD#237 in Oklahoma. Units are standard deviation/10. Positive(negative) contours stippled(full). Light(heavy) stippling is applied for values in excess of + and - 0.2(0.4) standard deviation.

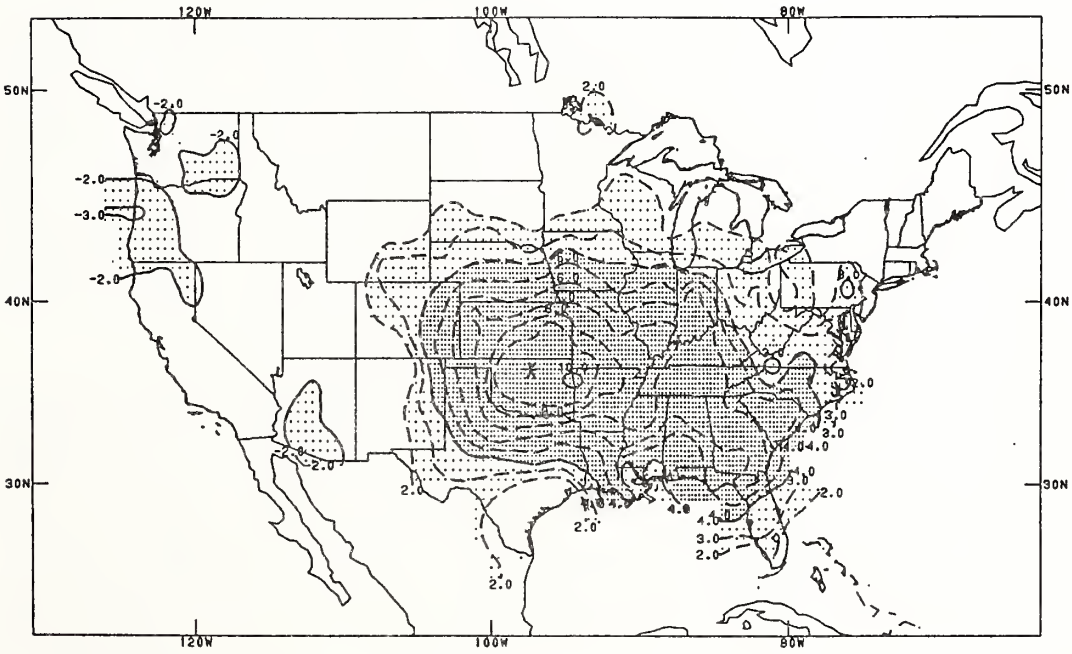

TT COMPOS AU 1931-87 AFTER DRY JL IN OKLA

Fig.4 As Fig.3 but following a dry July. See text for definition of wet/dry.

Precipitation Fluctuation Over Semiarid Region in Northern China and the Relationship with El Niño/Southern Oscillation

Kerang Li† and Wei-Chyung Wang
Atmospheric and Environmental Research, Inc.
840 Memorial Drive
Cambridge, MA 02139

Summary In recent years the semiarid region in northern China (Fig. 1), which has total annual precipitation between 200 and 500 mm, has shown signs of severe desertification (Zu and Liu, 1983). We used the 1951-1986 monthly precipitation measurements of seventeen stations (Table 1) in this region to study their fluctuations and relationship with the El Niño (EN)/Southern Oscillation (SO). Three main features are identified: (1) a 2-3 year quasi-periodic fluctuation, (2) a significant correlation between the precipitation fluctuation in the middle and southern part of this region and ENSO with the former lagging the latter by 2-5 months, and (3) a tendency for rainfall deficiency for the whole region during ENSO years. These statistics are demonstrated here for Hohhot.

Analysis Figure 2 shows the time series of precipitation anomaly. After eliminating the short-term fluctuations with a six-month running mean filter, the precipitation anomalies, especially the precipitation shortage, seem to persist for many years. The power spectrum at Hohhot (Fig. 3) shows peaks at 32, 8.7, 5.1 and 2.1 months, all significant at 95% confidence level.

For cross-correlation spectra between the SO index and precipitation the results shown in Fig. 4 indicate that the maximum coherence in the low frequency is 0.423, at a corresponding period of 33 months with 0.001 level of significance. Note that peaks also occur at high frequency bands of 2 to 8 months. Co-spectrum analysis shows that cross-correlation of these two series at the same phase have positive contribution in the low frequency of 11-33 months. The phase spectrum, shown on the upper panel of the figure, indicate that variation of the SO in the low frequency band with periods of 18.9-44 months generally precedes the precipitation variation by 2-5 months; for example, the lag time for period 33 months is 2.9 months. These results imply that about 3 months after the anomaly of SO changes from positive to negative, the precipitation changes from positive to negative.

The cross-correlation analysis between the precipitation and the EN (SST index) is shown in Fig. 5. The pronounced peaks of coherence are found at periods 25-66 months, all at 95% confidence level. The peaks of coherence in the low frequency are 0.451 at period 33 months and 0.481 at period 18.9 months, both with 0.001 significance level. However, the co-spectrum analysis shows that the cross-correlation of these two series have negative contribution in the low frequency bands 15-44 months. The phase-spectrum indicates that the variation of EN in the low frequency generally precedes the precipitation variation by 2-5 months; for example, the lag time corresponding to 33 months is 2.9 months.

---

†On leave from the Institute of Geography, Chinese Academy of Sciences, Beijing. Visiting scholar under the United States' Department of Energy and the People's Republic of China's Chinese Academy of Sciences Joint Research on the Greenhouse Effect.

Discussion It is known that the summer rainfall belt of west-east orientation in eastern China has seasonal variations in latitudes (see Fig. 6). From late spring to late summer, there exist two jumps and three stable periods of the latitudinal movement of the rainfall belt. After the middle of May, for a month the rainfall belt moves between 23-30°N over southern China. Then, within about 10 days it advances rapidly northward 6 to 7 degrees of latitude and, by the end of June, reaches the middle and lower Changjiang (Yangtze River) valley. For the next few weeks, the rainfall belt stays between 30-35°N. In the middle of July, it jumps northward again and reaches its extreme northern latitudes in early August. Shortly after, the rainfall belt starts to move southward.

It is also known that the western Pacific subtropical high has a dominant influence on the summer monsoon and rainfall belt. The latter lies about 8-9 degrees of latitude to the north of the subtropical high ridge. The subtropical high moves northwest and strengthens from winter to summer, and vice versa. It also possesses two sudden jumps and three stable periods, which coincide with the timings of the latitudinal variations in the rainfall belt. Therefore, the location of the major rainfall belt and distribution of rainfall are directly related to the variation in the western Pacific subtropical high.

On the other hand, studies have shown that there is a close relationship between the intensity and location of the western Pacific subtropical high and the SST in the equatorial ocean (Fu and Li, 1978). Both the subtropical high and the SST have a quasi period of 3 years oscillation with the variation of the former lagging the latter by 6 months.

Ye (1987) has reviewed the studies of the correlations between the SST anomalies in eastern equatorial Pacific and the surface pressure anomaly. His analysis indicates that the variation in intensity of the subtropical high in the eastern Pacific leads that of SST and the variation of SST leads that of the variation of the intensity of subtropical high in western Pacific. They all have a quasi period of 3 years. Consequently, it is not surprising that in our study the precipitation over the semiarid region in northern China which has 2-3 years dominant period, is closely associated with the ENSO.

References

Fu, C., and K.R. Li, 1978: The effects of tropical ocean on the western Pacific subtropical high. *Ocean Selections*, No. 2, 16-21, Ocean Press, Beijing.

Xu, G., M. Li, and Z. Zhang, 1983: Seasonal variation of the rain-belts in China. *Scientia Atmospherica Sinica*, 7, No. 3. (in Chinese).

Ye, D., 1987: Some aspects of low-frequency phenomena of the air-sea interaction - A review of the recent advances. *The climate of China and Global Climate*, 154-156. Ocean Press, Beijing.

Zhu, Z., and S. Liu, 1983: *Combatting desertification in arid and semiarid zones in China*. Institute of Desert Research, Academia Sinica, Lanzhou China. 69 pp.

Acknowledgements The work was supported by a grant from the Carbon Dioxide Research Division of the Department of Energy (DE-FG02-86-ER60422).

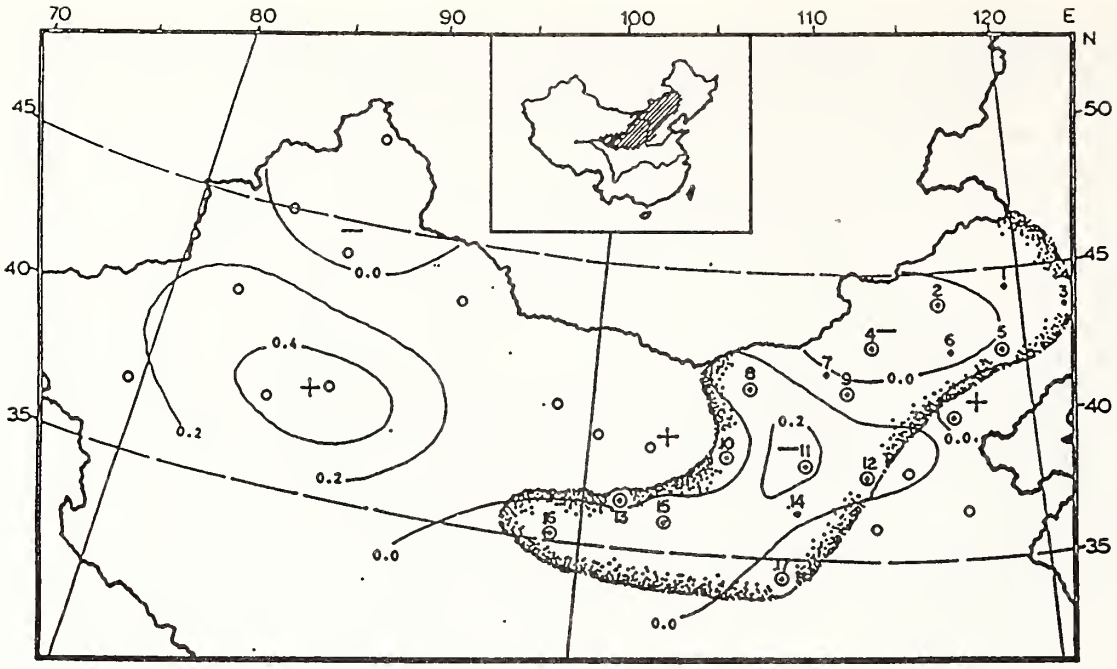

Figure 1. The first eigenvector of the empirical orthogonal function of 1954-1986 annual precipitation anomaly for arid/semiarid region in northern China. Twenty-seven stations, denoted by circles, are used. The stippled-circled region is the semiarid region where the numbered stations (with black dots) are those which monthly precipitation measurements are used to analyze the precipitation fluctuations.

Table 1. Stations used in the present study of precipitation fluctuations† (see Fig. 1 for station network). The lag time (months)* corresponding to period 33 months between ENSO and precipitation.

No.	WMO No.	Station	Latitude (°,'N)	Longitude (°, 'E)	Height (m)	SO	EN
1	54027	Lindong	44,00	119,12	483	10.9	10.6
2	54102	Xilinhot	43,57	116,04	990	2.6	2.1
3	54135	Tongliao	43,36	122,16	179	8.2	0.9
4	53276	Ondor Sum	42,24	113,00	1150	0.9	0.9
5	54218	Chifeng	42,16	118,58	571	-4.4	0.1
6	54208	Duolun	42,11	116,28	1245	-2.9	-4.2
7	53352	Bailingmiao	41,42	110,26	1376	-1.3	-2.4
8	53513	Shamba	40,54	107,06	1039	-5.0	-5.0
9	53463	Hohhot	40,49	111,41	1063	-2.9	-2.9
10	53614	Yinchuan	38,29	106,13	1112	-2.0	-2.4
11	53646	Yulin	38,14	109,42	1050	-3.0	-2.7
12	53772	Taiyuan	37,47	112,33	778	-0.5	-4.5
13	52866	Xining	36,37	101,46	2261	-2.3	-2.3
14	53845	Yan'an	36,36	109,30	958	-3.1	-3.6
15	52889	Lanzhou	36,03	103,55	1517	-2.7	-2.3
16	56033	Madoi	34,55	98,13	4272	-2.0	-1.1
17	57036	Xian	34,18	108,56	397	-2.1	-2.3

†All stations have 1951-1986 monthly precipitation measurements except Xining and Lindong where no data were taken at 1951-1953 and 1951-1952 respectively.
*Positive/negative values mean that the variation of SO (or EN) succeeds/precedes the variation of precipitation.

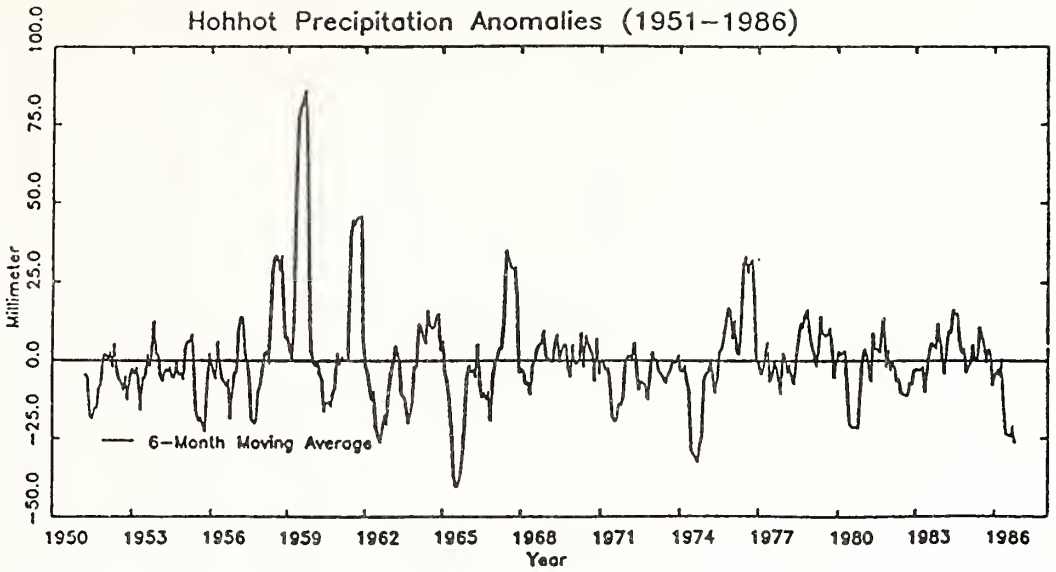

Figure 2. 1951-1986 monthly precipitation anomaly (mm) at Hohhot.

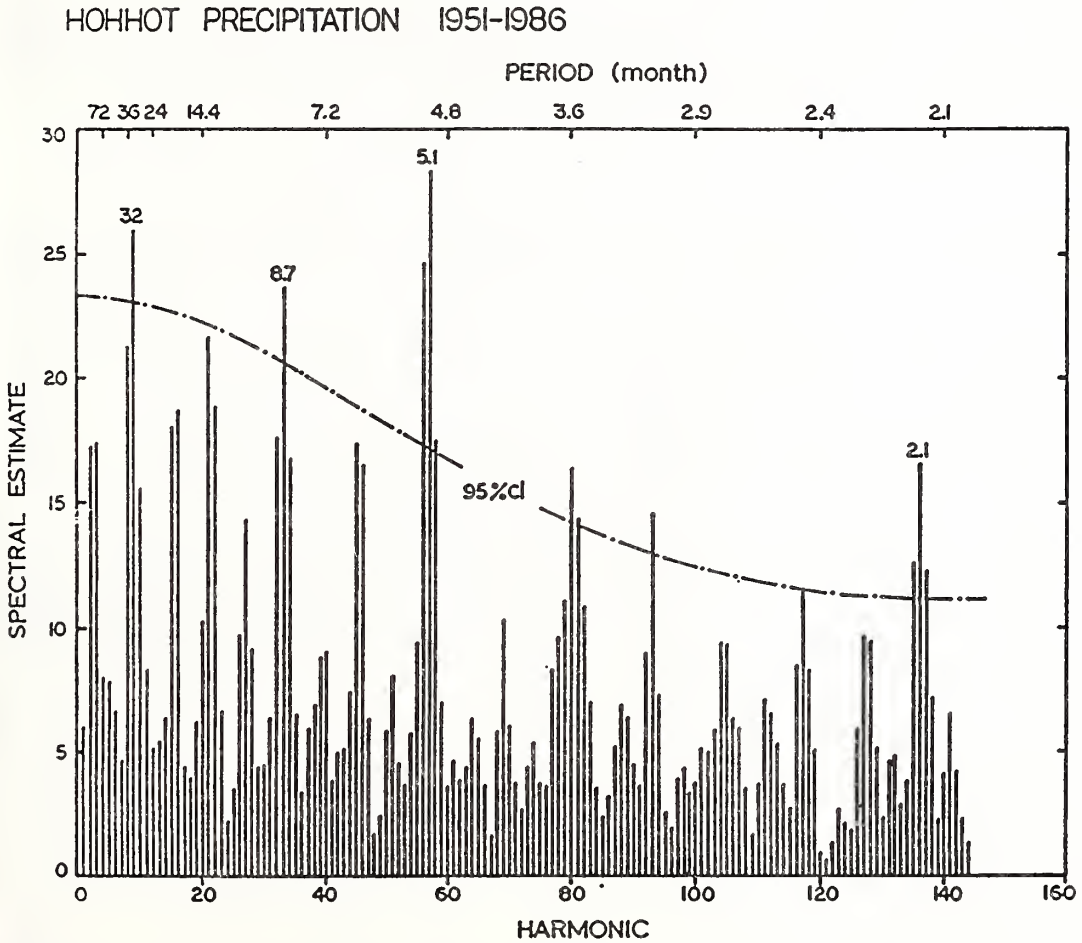

Figure 3. Power spectrum of 1951-1986 precipitation anomaly at Hohhot. Broken line is 95% confidence level and maximum lag is 144 months.

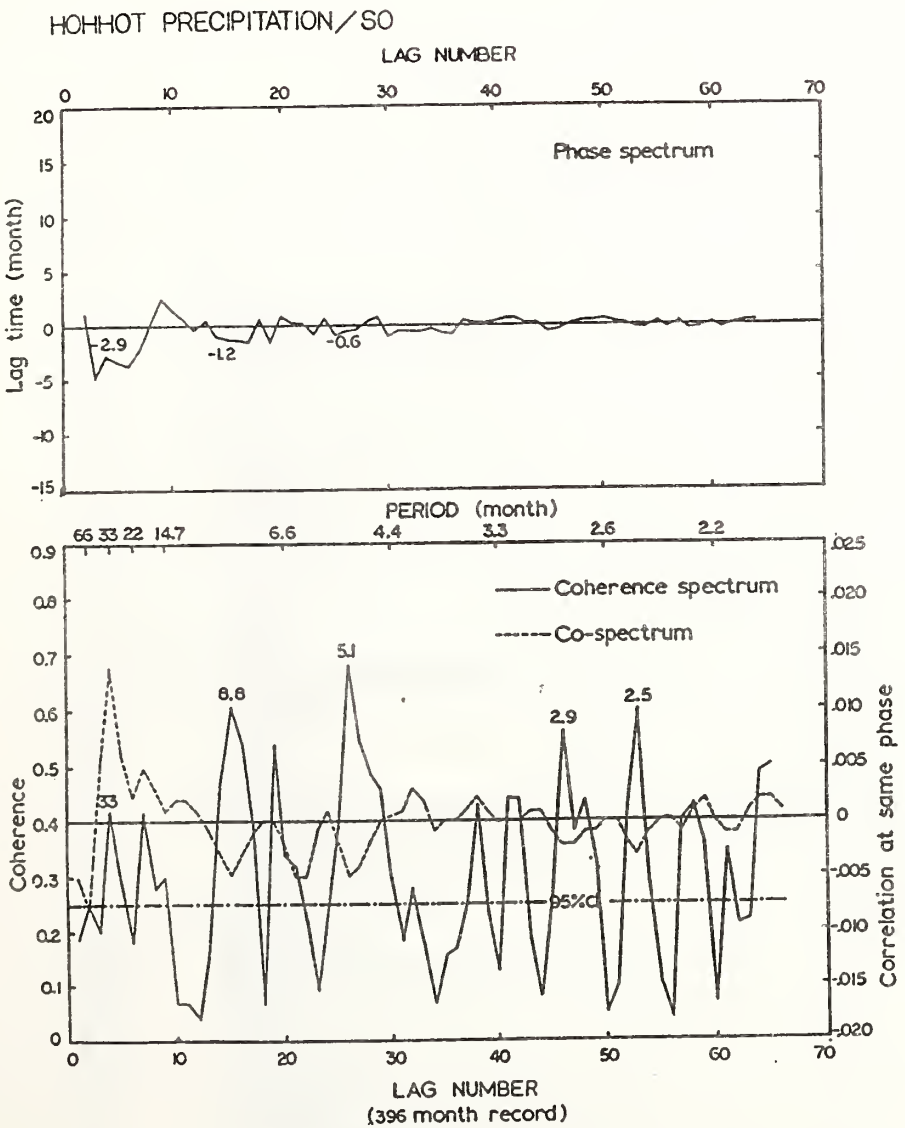

Figure 4. The cross-spectrum analysis between the Southern Oscillation (SO) Index and precipitation at Hohhot for 1951-1983. Broken line is 95% confidence level and maximum lag is 66 months.

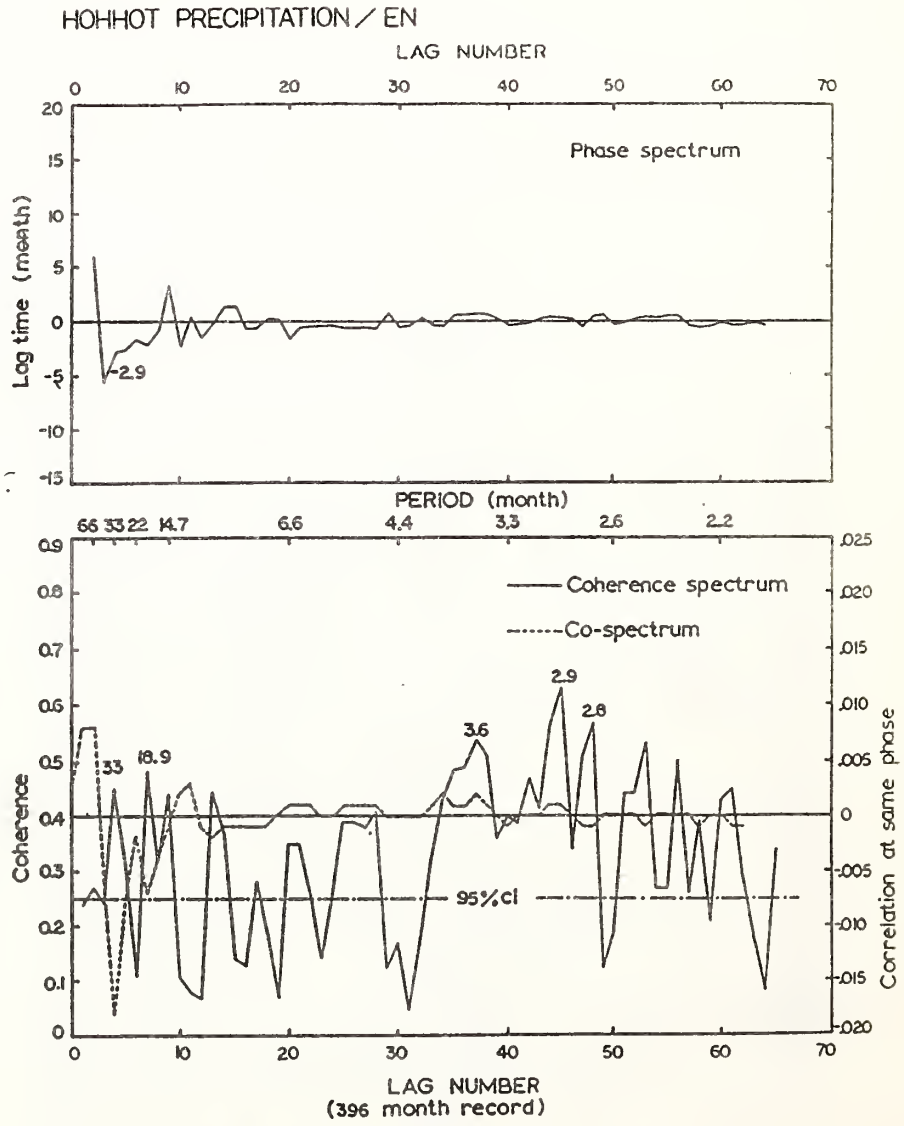

Figure 5. Same as in Figure 4 except between sea surface temperature (SST) index and precipitation.

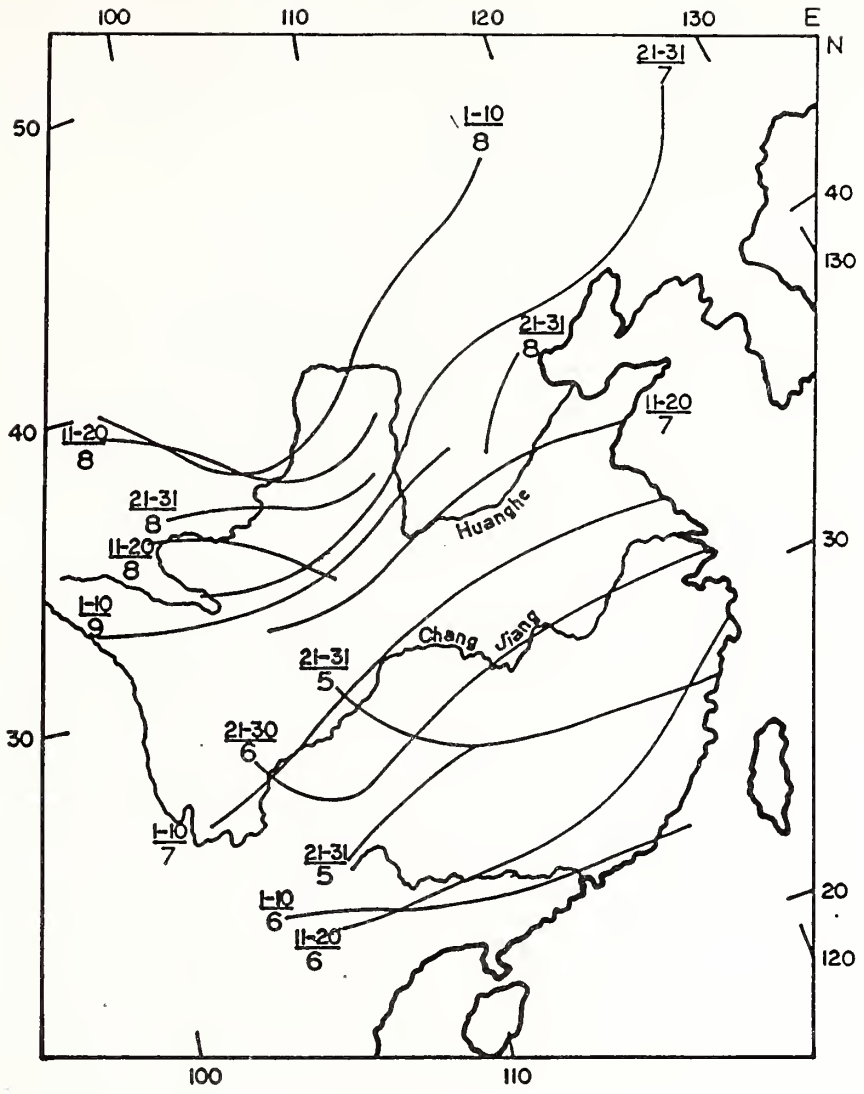

Figure 6. The latitudinal variation of the rainfall belt in eastern China. The denominator is the month and the numerator the date (after Xu, et al., 1983). The starting and ending dates of the two jumps are (11-20/6, 21-30/6) and (11-20/7, 1-10/8).

The April–June 1988 North American Drought as a Tropically Forced Phenomenon

GRANT BRANSTATOR AND KEVIN TRENBERTH
*National Center for Atmospheric Research**, *Boulder, Colorado, 80307*

PHILLIP ARKIN
Climate Analysis Center, Washington, DC 20233

The drought that occurred in the central United States and Canada during April, May and June 1988 was one of the most severe droughts of this century. Many districts in Wisconsin, Illinois, Indiana, Ohio, Iowa, Missouri and Michigan experienced a drier April–June than any previously recorded since 1895. The *Weekly Weather and Crop Bulletin* reports that by July 23, 43% of the area of the contiguous United States was in the severe or extreme drought category, a value that has been exceeded in only four previous years: 1934, 1936, 1954 and 1956.

These dry conditions were almost certainly linked to mean tropospheric flow anomalies that were present during this period. As Figure 1 indicates, there was a pronounced anomalous high in the 300 mb geopotential field over the center of the continent. This feature would have steered rain-bearing storms away from the drought region. This high was part of a larger pattern made up of highs and lows configured in an arching pattern. As we know from studies of Rossby wave dispersion on the sphere (Hoskins *et al.*, 1977) such a wavetrain is often the signature of energy propagating away from a local source. Given the orientation of the flow anomalies in Figure 1, we speculate that an energy source in the eastern tropical Pacific could have been responsible for the observed wavetrain.

The plot of OLR anomalies for May–June 1988 (Figure 2) indicates that indeed there were heating and cooling anomalies in the requisite position during the drought. In particular there was an elongated OLR negative anomaly from about 8N to 20N centered at 130W and a very long band of positive OLR anomalies to the south of this feature. These were probably a result of the strong anti-El Niño cooling that was occurring along the equator at this time and a patch of warm water centered at 15N and 130W, as shown in Figure 3.

Tropical heating is usually considered to be a source of midlatitude anomalies in only the winter hemisphere because low-frequency Rossby waves cannot penetrate easterlies. To test whether this fact precludes the eastern tropical Pacific heating anomalies implicit in Figure 2 from forcing the pattern of Figure 1, we use a steady linear baroclinic primitive equation model. This model is based on the same equations and discretization as the NCAR Community Climate Model. It employs five evenly spaced vertical levels and 16 meridional spherical harmonics for each zonal wavenumber up to wavenumber 6.

* The National Center of Atmospheric Research is sponsored by the National Science Foundation.

Lacking detailed information from observations, we assume that a heating/ cooling profile with a value of 2.5°C/day in the two upper tropospheric levels and minus half that value in the top level is a reasonable approximation to the profile associated with the OLR anomalies. The tropospheric value is attained from regression calculations that relate OLR and precipitation anomalies. To represent the negative OLR anomalies an elongated area of forcing with midtropospheric heating is centered at 15N in the position indicated in Figure 4 and to represent the positive OLR anomalies a region of forcing with midtropospheric cooling is centered at 5N.

The steady response at 300 mb to such a forcing, when the model is linearized about zonal mean June climatological conditions, is shown in Figure 4. The midlatitude component of the response is very weak. Furthermore, its structure bears little resemblance to the drought pattern of Figure 1. Apparently in this configuration the model does not represent the processes which caused the drought.

As depicted in Figure 5, if the model is linearized about the combined zonal mean and zonally asymmetric June climatological state, then the midlatitude response is much stronger and the three main circulation features of the drought wavetrain are reproduced. Use of the asymmetric basic state has allowed more energy out of the tropics because the westerlies extend farther south in the east Pacific than they do in the zonal mean. Furthermore, zonal gradients in the background can refract and focus the perturbations (Branstator, 1983) and serve as internal energy sources (Simmons *et al.*, 1983). Both of these effects may be contributing to the pattern produced by the linear model.

A final experiment with the linear model suggests that the subtropical heating anomaly may have been far more instrumental in producing the wavetrain over North America than the equatorial cooling was. If the model is forced by only the region of cooling, then (Figure 6) the midlatitude response is very weak and loses most of the features which were reminiscent of the drought.

We conclude that subtropical heating anomalies that were associated with a northward shift of the ITCZ during April–June 1988 could have stimulated a wavetrain that reached across North America and caused drought conditions. Once established, other factors may have helped maintain and strengthen the pattern. For example, Figure 2 indicates diabatic processes over North America may have had this effect.

References

Branstator, G., 1983: Horizontal energy propagation in a barotropic atmosphere with meridional and zonal structure. *J. Atmos. Sci.*, **40**, 1689–1708.

Hoskins, B.J., A. J. Simmons and D.C. Andrews, 1977: Energy dispersion in a barotropic atmosphere. *Quart. J. Roy. Meteor. Soc.*, **103**, 553–567.

Simmons, A.J., J. M. Wallace and G. W. Branstator, 1983: Barotropic wave propagation and instability, and atmospheric teleconnection patterns, *J. Atmos. Sci.*, **40**, 1363–1392.

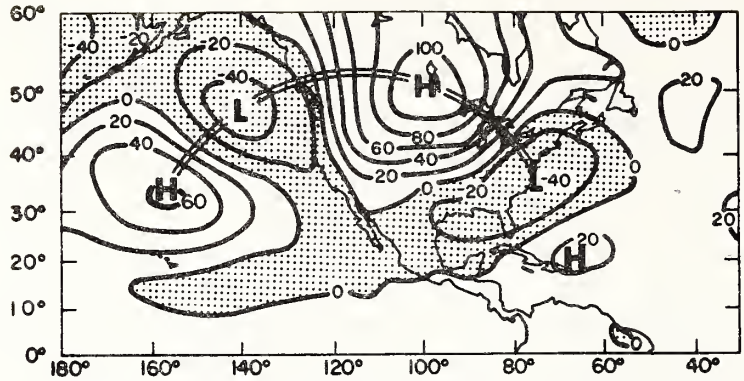

Figure 1 Average geopotential height anomalies at 300 mb for April–June 1988.

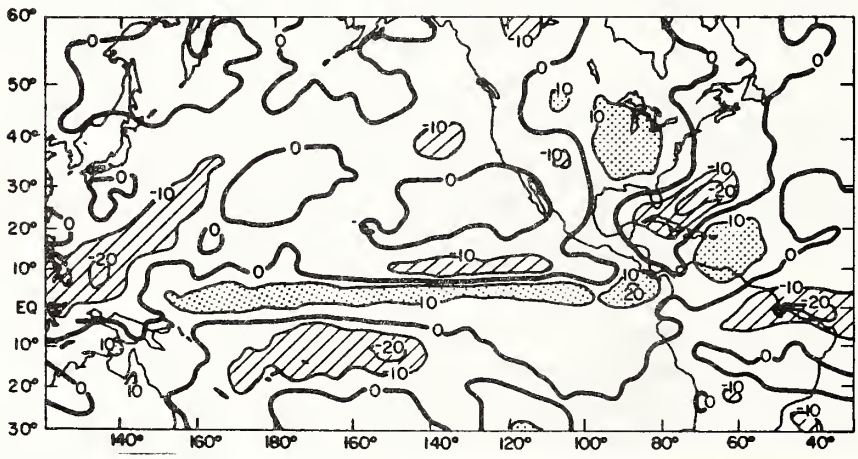

Figure 2 Average May–June 1988 OLR anomalies. Values exceeding ± 10W m^{-2} are shaded.

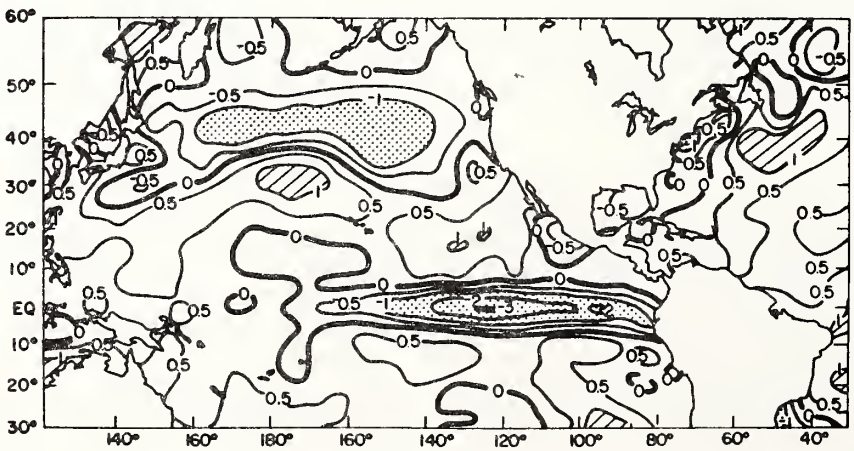

Figure 3 Average May–June 1988 SST anomalies. Values exceeding ±1°C are shaded.

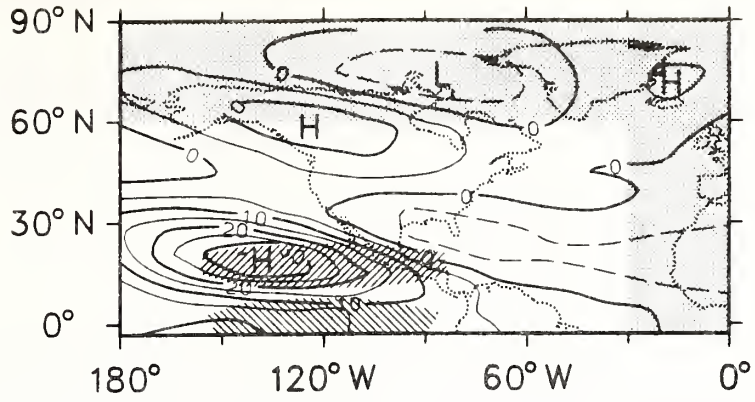

Figure 4 Geopotential height anomalies at about 300 mb resulting from midtropospheric heating in the hatched region centered at 15N and cooling in the hatched region centered at 5N. The result is from a model linearized about zonal mean climatological June conditions. Contour interval is 5 m.

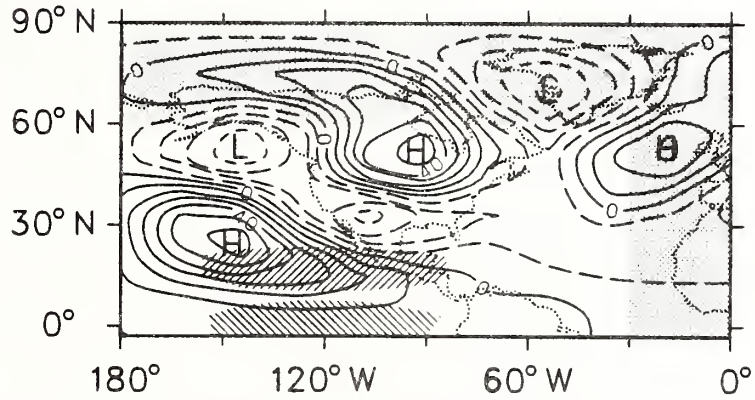

Figure 5 Like Fig. 4 except the model is linearized about both the zonal mean and zonally asymmetric component of climatological June flow. Contour interval is 10 m.

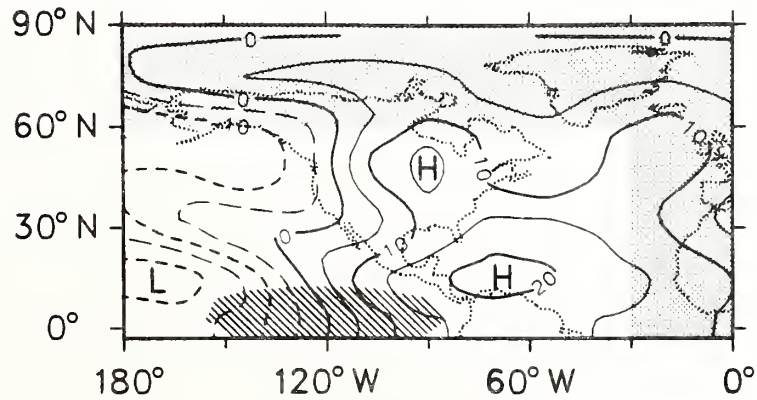

Figure 6 Like Fig. 5 except only the region of equatorial midtropospheric cooling forces the model. Contour interval is 5 m.

BLOCKING AND GCM'S: AN OVERVIEW

Steven L. Mullen
Department of Atmospheric, Oceanic and Space Sciences
The University of Michigan
Ann Arbor, MI 48109-2143

INTRODUCTION

There are clear advantages with using GCM's to diagnose blocking instead of only relying upon observational data sets. A few of these advantages are:

- The possibility for a much larger sample size exists with a GCM. The only limiting factor is the amount of computer time. With the cost of computer time continuing to decrease in the future, this limitation becomes even less of a problem.
- A GCM (or any model for that matter) produces dynamically consistent fields. Such quantities as vertical velocity, diabatic heating, moisture, etc., are output by models. With observational data, these key quantities are very difficult, if not impossible, to measure directly and must be estimated as residuals from balance requirements.
- Sensitivity experiments can be conducted with a GCM. For example, such things as the impact of different SST distributions on blocking or of initial condition uncertainity on the predictability of blocking can be tested with a GCM.

Past research by the author utilized a low resolution, perpetual January version of the NCAR Community Climate Model (CCM) to study blocking. Current research utilizes a higher resolution, seasonal-cycle version of the NCAR CCM. The purpose of this paper is (1) to document improvements in the blocking characteristics of the higher resolution, seasonal-cycle version of the CCM and (2) to report preliminary results on the predictability of blocking based on forecast experiments with the higher resolution model.

MODEL IMPROVEMENTS

The author's previous work was based on version 0A of the CCM (CCM0A). CCM0A has a rhomboidal 15 (R15) truncation and nine vertical levels. The current work involves a new version of the model (CCM1) that has a triangular 31 (T31) truncation with 12 vertical levels. The new version also incorporates refinements in the physical parameterizations (Williamson et al., 1987).

The climatology, structure and synoptic behavior of blocking in CCM0A was documented by Blackmon et al. (1986). In general, there was good agreement between the model and observations in blocking characteristics over the North Pacific Ocean and North Atlantic Ocean. Blocking was totally absent over Siberia, however, the third observed location of enhanced activity. Other GCM's also

seem to exhibit similar simulation errors in blocking frequency over Siberia (e.g. Dugas and Derome, 1988).

One major improvement with T31 CCM1 is the existence of the third observed center of enhanced low-frequency variability (LFV) over Siberia. This center is clearly evident in Fig. 1, which shows the root-mean-square of 500 mb height based on unfiltered daily data for the 10 boreal winters of the T31 simulation. It is interesting to note that this third region of enhanced LFV *does not* exist in the R15 seasonal cycle version of CCM1 (fig. II.C.12 of Williamson and Williamson, 1987). Apparently the Siberian center in T31 CCM1 is due the increase in horizontal resolution and not the refinements in physical parameterizations.

This increase in LFV is also reflected in the CCM1's persistent anomalies (Dole and Gordon, 1983), which should include many model blocking events. Figure 2 shows the distribution of the total number of days that satisfy a +100 m, +10 day criterion. A third center of action over Siberia is simulated by the T31 CCM1 but it is weaker than the observed one. This result indicates that model blocking exists in the region, although less frequently than observed.

Another apparent improvement in the T31 version concerns the interaction of the cyclone-scale transient eddies (TE) with the blocking pattern. The TE forcing in R15 CCM0A seemed slightly weaker than observed (Mullen, 1985). Early results with the T31 CCM1 suggest that the TE forcing may be somewhat stronger than that for CCM0A. Figure 3 shows, for five composite Pacific blocking events, the distribution of 500 mb height (fig. 3a) and the convergence of TE vorticity flux at sigma level .335 for synoptic-scale transients (fig. 3b). The observed phase relationship between the TE forcing and the blocking pattern, with the anticyclonic eddy forcing shifted somewhat upstream of the blocking ridge (Mullen, 1987; Holopainen and Fortelius, 1987), is still maintained in T31 CCM1, but the upstream maximum in anticyclonic forcing is appoximately 50% greater than in CCM0A (cf. fig. 4d of Mullen 1986). The increase in eddy forcing is likely related to the anisotrophy characteristics of the synoptic transients as they impinge against they the west side of the block. Observations indicate that the synoptic eddies elongate meridionally and lose their kinetic energy as they approach the blocking pattern. This deformation of the eddies cascades energy to larger scales and produces anticyclonic forcing just upstream of the block (Shutts, 1983). Observations indicate that the eddies are not elongated enough in R15 CCM0A (Mullen, 1987). In T31 CCM1, however, the anisotrophy characteristics are much closer to those observed (results not shown). These early results suggest that the interactions between the cyclone-scale transients and the larger-scale blocking pattern are much improved with just a moderate increase in the horizontal resolution of the model.

PREDICTABILITY OF BLOCKING: PRELIMINARY RESULTS

Recent studies at the operational forecast centers indicate that the performance of medium-range (5 to 10 days) forecasts is generally poorer whenever a blocking pattern either forms, persists or breaksdown during the forecast period (Tibaldi

and Molteni, 1987). It appears that blocking, for whatever reasons, is more unpredictable in operational forecast models than the "typical" atmospheric state. This situation leads to the following questions:

- Given a "perfect" model, are forecasts of blocking more sensitive to initial condition error than for other flow situations?
- Given "perfect" initial conditions, are forecasts of blocking more sensitive to model error?
- Are blocking situations more sensitive, in some nonlinear sense, to the combination of initial condition uncertainity and model error?

Since operational forecasts will always contain both data error and model error, these questions cannot be addressed in a straightforward manner using historical output from the operational models. This problem does suggest a useful application of GCM's, however, to address the above issues. Since the CCM1 has exact restart capability, the model's blocking events can be used for predictability studies that test the forecast sensitivity to just initial condition error, just model error, or the combination of both.

This strategy is being used in an attempt to address the first question above. The predictability of the CCM1's blocking flows is compared to that for its persistent "high-index" flows. A comparison was made among 15-day forecasts beginning -8 days, -4 days and 0 days prior to the initiation of a block and beginning 0 days prior to the start of persistent high-index flow situation. For each forecast time, a series of five Monte Carlo forecasts was made. The size and spatial characteristics of the perturbations used to represent random data error in the Monte Carlo experiments were based on estimates of global analysis error (Daley and Mayer, 1986). Thus, in a globally-averaged statistical sense, the initial perturbations used in the Monte Carlo simulations were realistic.

Only forecasts for two cases of blocking and two cases of high-index flow have been completed to date, so meaningful conclusions are not possible at this time. The results for these two cases are summarized in Table 1. The table shows the forecast day that the 500 mb anomaly correlation coefficient first drops below the value of 0.6, a commonly-accepted lower bound of useful skill (Hollingsworth, 1980). The period of of useful skill is clearly much shorter for the -8 day blocking forecasts than for the other forecasts, especially compared to the high-index situations.

Although the small sample size precludes meaningful conclusions, the results provide a working hypothesis that can be tested under the scrutiny of a larger sample size. Future research using more cases is planned to test the following hypothesis:

- Forecasts of blocking, especially those beginning a week prior to its onset, are more sensitive to initial error, and hence are inherently more unpredictable, than forecasts of high-index flow.

Research is also planned to test the sensitivity to a "typical" level of model error (e.g. a 5X decrease in the coefficient of horizontal diffusion) and to the combination of initial error and model error.

Table 1

Average forecast day in which the anomaly correlation coefficient ρ for 500 mb height first drops below 0.6. The first row gives the average value for all five Monte Carlo forecasts (Average ρ) and the second row gives the value for the average of all five Monte Carlo forecasts (ρ Average). The anomaly coefficient was calculated over the Northern Hemispheric region from approximately 70°N to 30°N for forecasts that were spatially smoothed by retaining only zonal wavenumbers 0-5.

Flow Type: Forecast Start:	BLOCKING -8 days	BLOCKING -4 days	BLOCKING 0 days	HIGH-INDEX 0 days
Average ρ	7.5	11.0	10.0	12.0
ρ Average	9.5	12.5	11.0	13.5

REFERENCES

Blackmon, M.L., S.L. Mullen and G.T. Bates, 1986: The climatology of blocking events in a spectral general circulation model. *J. Atmos. Sci.*, **43**, 1379-1405.

Daley, R. and T. Mayer, 1986: Estimates of global analysis error from the global weather experiment observational network. *Mon. Wea. Rev.*, **114**, 1642–1653.

Dole, R.M. and N.D. Gordon, 1983: Persistent anomalies of the extratropcial Northern Hemisphere wintertime circulation: geographical distribution and regional persistence characteristics. *Mon. Wea. Rev.*, **111**, 1567–1586.

Dugas, B. and J. Derome, 1988: A comparative study of atmospheric circulation statistics as found in observations and in a general circulation model. *Preprints Volume: Palmen Memorial Symposium on Extratropical Cyclones, Helsinki, Finland, 29 August–2 September 1988*, 46–49. Available from American Meteorological Society, 45 Beacon St., Boston MA 02108.

Hollingsworth, A., K. Arpe, M. Tiedtke, M. Capaldo and H. Savijarvi, 1980: The performance of a medium-range forecast model in winter–impact of physical parameterizations. *Mon. Wea. Rev.*, **108**, 1736–1773.

Holopainen, E.O. and C. Fortelius, 1987: High-frequency transient eddies and blocking. *J. Atmos. Sci.*, **40**, 1632–1645.

Mullen, S.L., 1987: Transient eddy forcing of blocking flows. *J. Atmos. Sci.*, **44**, 3–22.

Mullen, S.L., 1986: The local balances of vorticity and heat for blocking anticyclones in a spectral general circulation model. *J. Atmos. Sci.*, **43**, 1406–1441.

Mullen, S.L., 1985: *On the Maintenace of Blocking Anticyclones in a General Circulation Model*, NCAR Cooperative Thesis No. 86, 260pp. Available from NCAR, P.O. Box 3000, Boulder CO 80307-3000.

Shutts, G.J., 1983: The propagation of eddies in diffluent jet streams: eddy vorticity forcing of blocking flow fields. *Quart. J. Roy. Meteor. Soc.*, **109**, 737-761.

Tibaldi, S. and F. Molteni, 1987: On the operational predictability of blocking. *ECMWF Seminar Proceedings: The nature and prediction of extra-tropical weather systems, 7-11 September 1987, Volume II*, 329–371. Available from European Centre for Medium-Range Weather Forecasts, Shinfield Park, Reading RG2 9AX, U.K.

Williamson, D.L., J.T. Kiehl, V. Ramanathan, R.E. Dickinson and J.J. Hack, 1987: *Description of NCAR Community Climate Model (CCM1)*. NCAR Technical Note NCAR/TN-285+STR. Available from NCAR, P.O. Box 3000, Boulder CO 80307-3000.

Williamson, D.L. and G.S. Williamson, 1987: *Circulation Statistics from the NCAR Community Climate Model (CCM1):R15*. NCAR Technical Note NCAR/TN-302+STR. Available from NCAR, P.O. Box 3000, Boulder CO 80307-3000.

FIGURE CAPTIONS

Fig 1. Distribution of root-mean-square 500 mb height field for the 10 boreal winters (December, January, February) of the T31 CCM1 simulation. Contours are every 10 m with values greater than 120 m stippled.

Fig 2. Distribution of the total number of days in 10 boreal winters of the T31 CCM1 simulation which satisfy Dole and Gordon's (1983) +100 m, +10 day persistent anomaly criterion. Contours are every 20 days with values between 60 and 100 days stippled.

Fig 3. Distribution of (a) 500 mb height (contours every 60 m) and (b) the convergence of eddy vorticity flux at $\sigma = .335$ mb for highpass filtered eddies (contours every $0.5 \times 10^{-10} s^{-2}$ with negative contours dashed; stippling denotes values greater than $1.0 \times 10^{-10} s^{-2}$ and cross hatching denotes values less than $-1.0 \times 10^{-10} s^{-2}$) for a composite of five Pacific blocking events from the T31 CCM1 simulation.

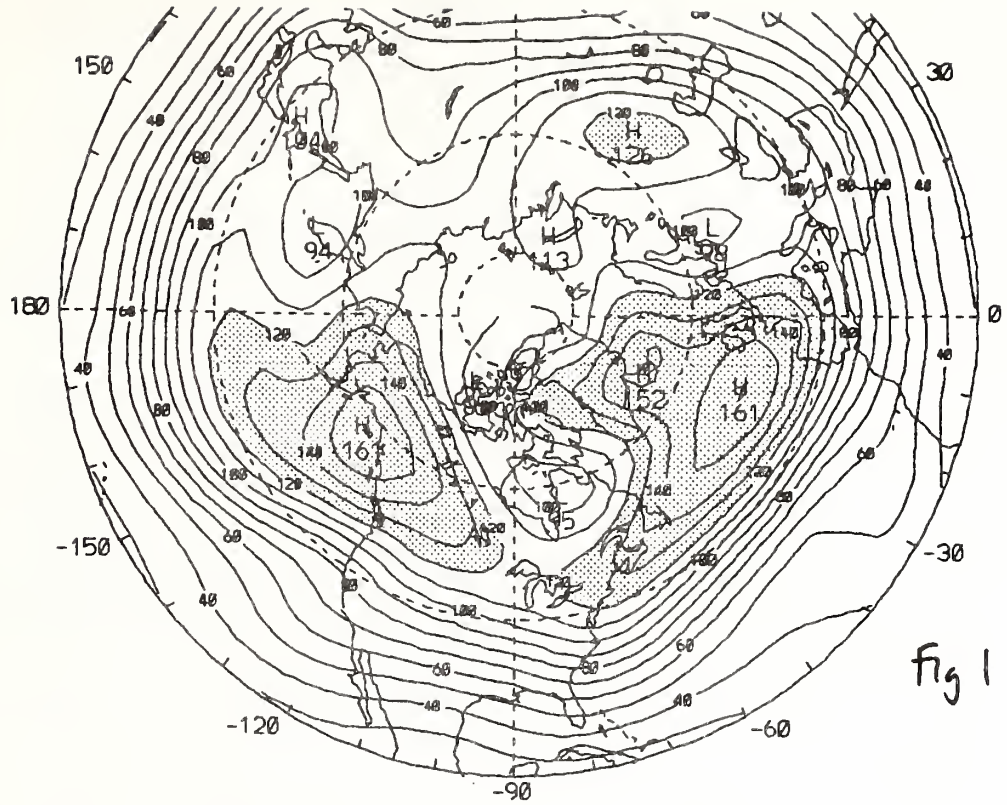
150
30
180
0
-150
-30
-120
-60
-90
H
126
H
94
H
13
L
98
H
152
H
161
H
161
H
95

Fig 1

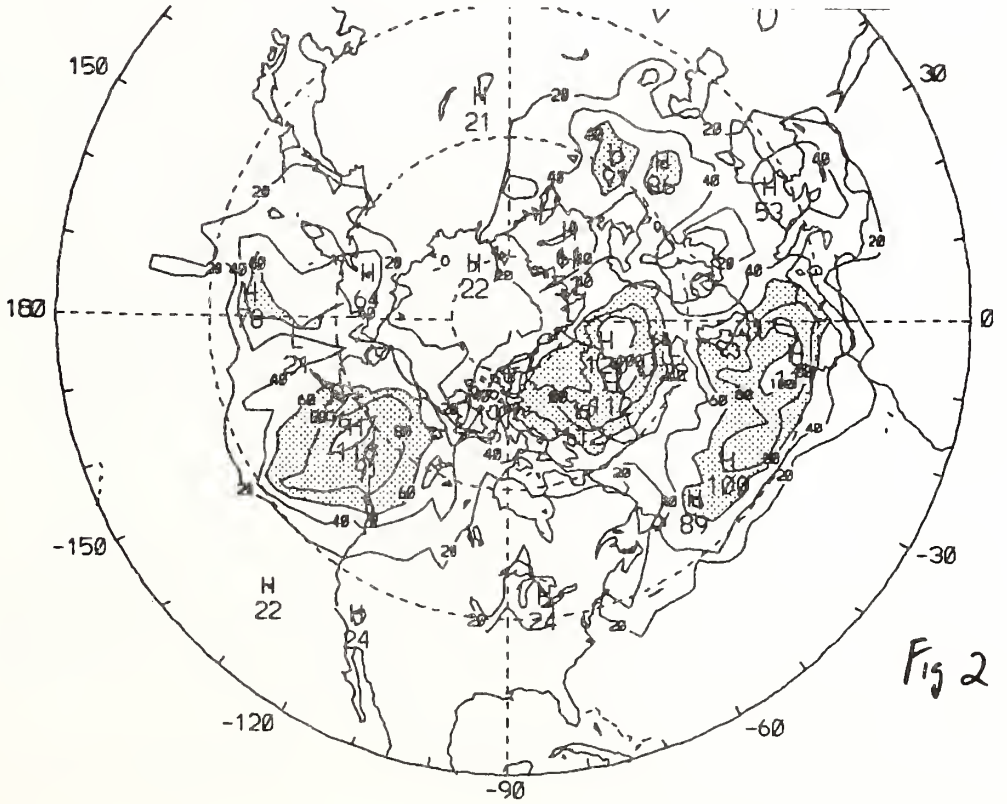
150
30
180
0
-150
-30
-120
-60
-90
H
21
H
22
H
93
H
94
H
78
H
100
H
89
H
22
H
24

Fig 2

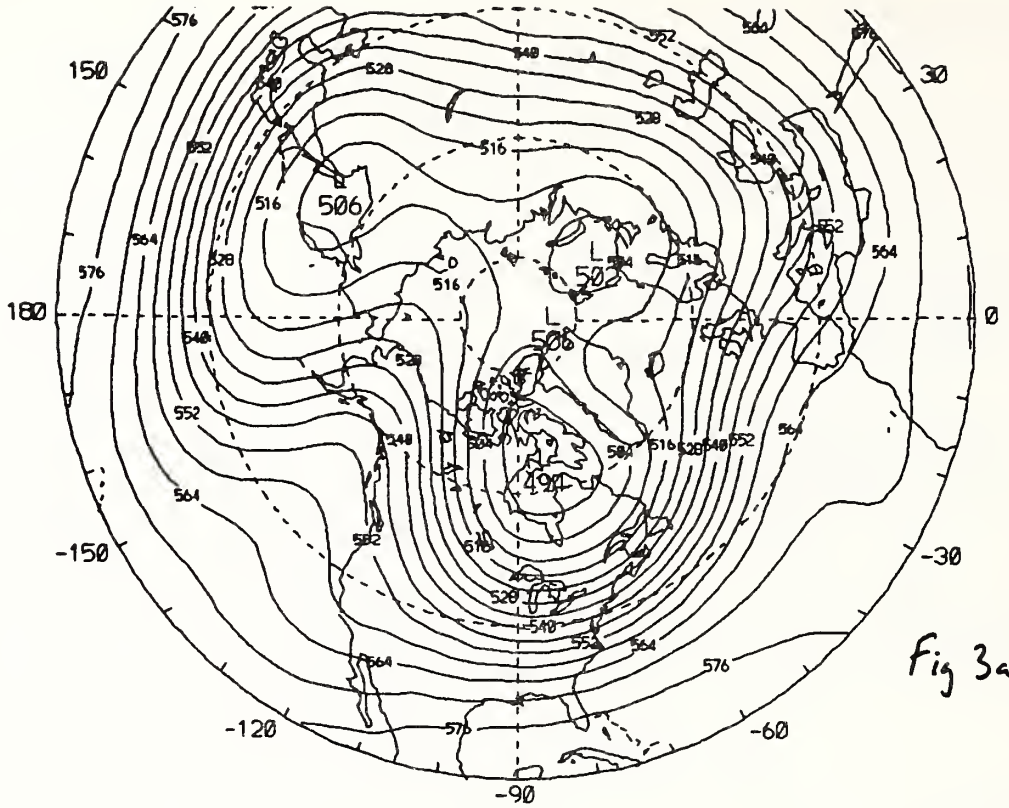
150
30
180
0
-150
-30
-120
-60
-90
506
504
506
492

Fig 3a

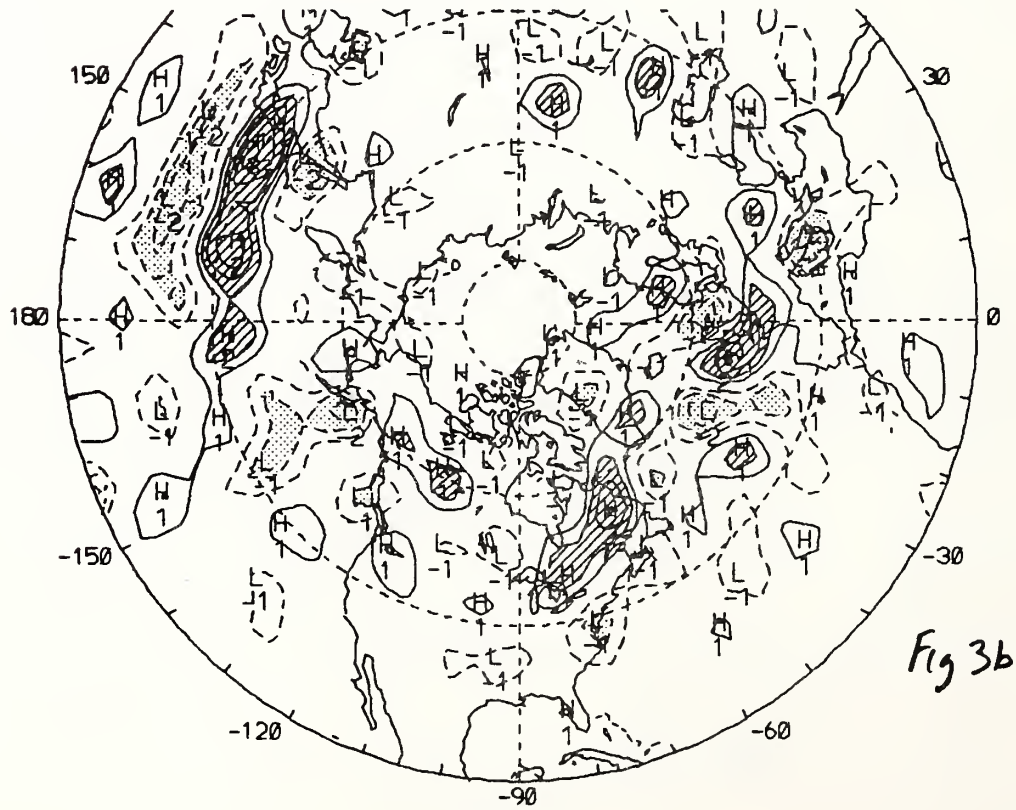
150
30
180
0
-150
-30
-120
-60
-90

Fig 3b

CLIMATE EXPERIMENTS WITH THE NMC MODEL

Masao Kanamitsu
Eugenia Kalnay
Development Division/NMC/NWS/NOAA
Washington, D. C. 20233

and

Kingtse Mo
Climate Analysis Center/NMC/NWS/NOAA
Washington, D. C. 20233

I. Introduction

For the first time, we have made 150-day summer simulations with the NMC Medium Range Forecast (MRF) model for the purpose of studying the long-term model climatology. The model is very similar to the current operational model (December 1988). It is also similar to the model used in the Dynamic Extended Range Forecast experiment (DERF) of the winter of 1986-1987, except that it includes a number of improvements (gravity wave drag, cloud-radiation interaction, a better formulation of surface fluxes and others).

We performed two simulations starting from initial conditions corresponding to 15 May 1988 and used climatological SSTs. The difference between the two runs is their horizontal resolution (T40 and R16). The vertical resolution (18 levels) is the same in both runs. In the present note, we compare monthly mean or seasonal mean (JJA) fields with the CAC climatology for the period 1978-1987.

II. Results

Generally speaking, both simulations are quite successful for the Northern Hemisphere (NH), but the R16 is much poorer than the T40 in the Southern Hemisphere (SH). In Fig. 1, we present the July 500 mb standing waves simulated with the T40 (Fig. 1a), R16 (Fig. 1b) and observed from climatology (Fig. 1c). The Northern Hemisphere simulation is quite good in both runs, especially for the wave train that dominates the Pacific-North American sector. In the SH, the T40 simulation is also excellent, with a very good reproduction of the strength and phase of the wave 1 pattern. The R16 simulation of the SH standing waves is considerably worse and is dominated by shorter wavelengths. Comparisons with sea level pressure and tropospheric temperatures give similar results.

A comparison of the wind fields (not shown) indicates that both models simulate the SH subtropical jet well. The T40 model reproduces the double jet in the SH (Fig. 2a), but the R16 model fails to do so (Fig. 2b). Over the eastern Pacific the R16 has a westerly bias, whereas the T40 has an easterly bias. This agrees with the tendency of some models to increase tropical upper level easterly bias with resolution.

In Fig. 3, we compare the upper-level divergence of the models averaged over the three summer months. Although the field is somewhat noisy, the T40

simulation (Fig. 3a) agrees well with the OLR fields (not shown), especially in regions of tropical convection. On the other hand, the R16 simulation is once again dominated by small scale features and does not show the proper zonal structure in the convective regions of Central America and Africa.

Finally, we present the rainfall maps for July--the T40 is once again far superior in reproducing the sharp zonal structure of the precipitation in the ITCZ, central America and central Africa, as well as the monsoonal rainfall over Asia and Indonesia. The South Pacific and South Atlantic convergence zones are also more realistic in the T40 simulation.

III. Summary

Both the T40 and R16 NMC model simulations of the NH summer season are quite successful. In the tropics and SH, however, the R16 is much worse than the T40, with less well defined stationary waves, precipitation patterns, and, surprisingly, more dominant small scale waves. The T40 simulation is very good overall; but, as with other higher resolution models, it also shows a tendency toward easterly bias in the tropics.

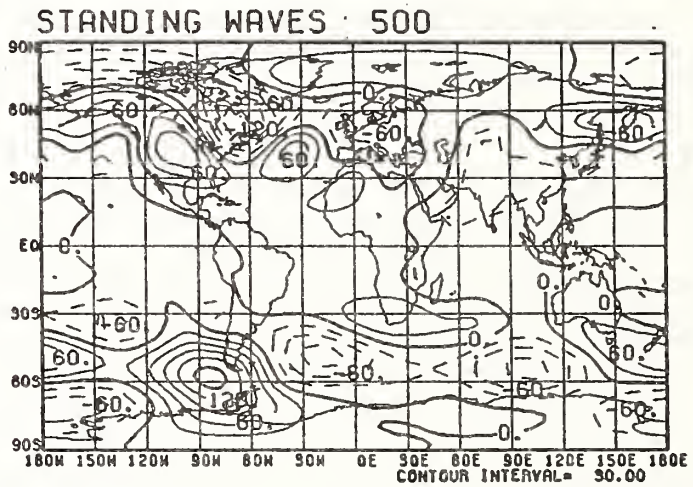

Fig. 1a July 500 mb standing waves simulated with the T40 model, contour interval is 30 m.

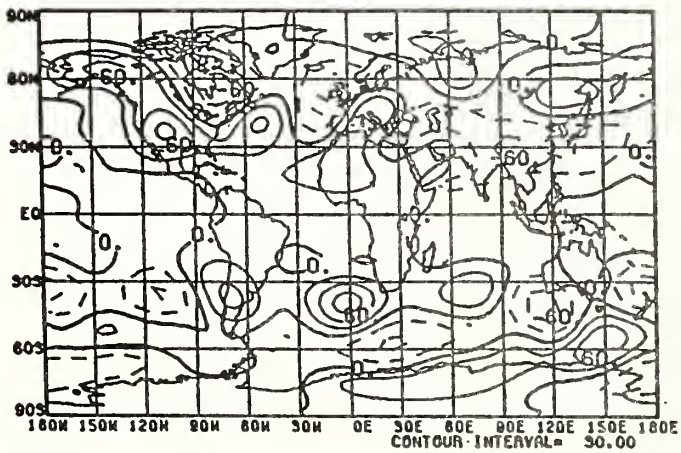

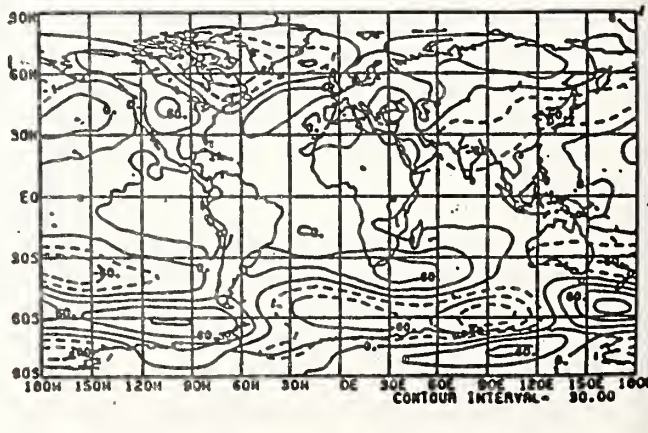

Fig. 1b Same as Fig. 1a, except for the R16 model

Fig. 1c Same as Fig. 1a, except for climatology

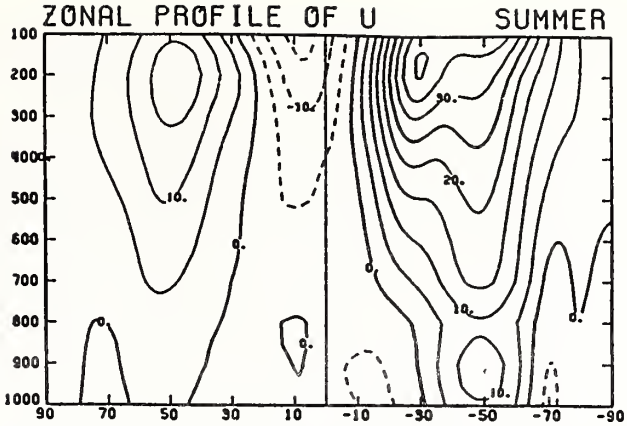

Fig. 2a Pressure-latitude cross section for the zonal wind averaged over summer (JJA) of the T40 simulation, contour interval is 5m/s.

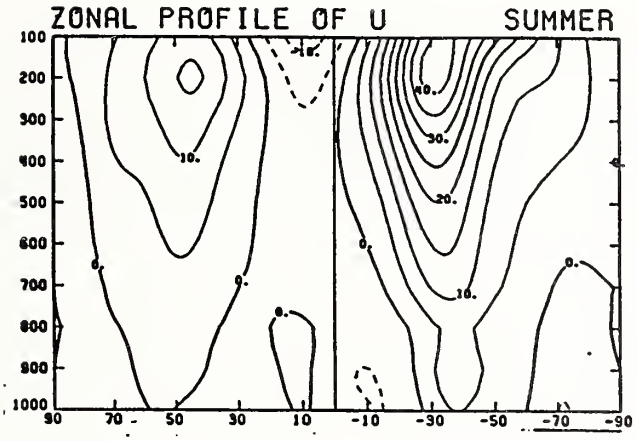

Fig. 2b Same as Fig. 2a, except for the R16 model

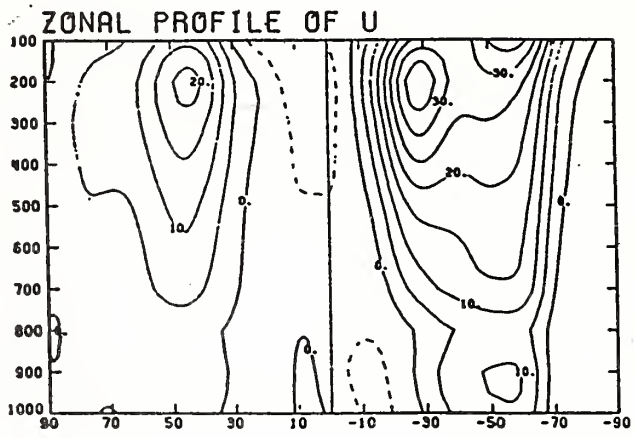

Fig. 2c Same as Fig. 2a, except for climatology

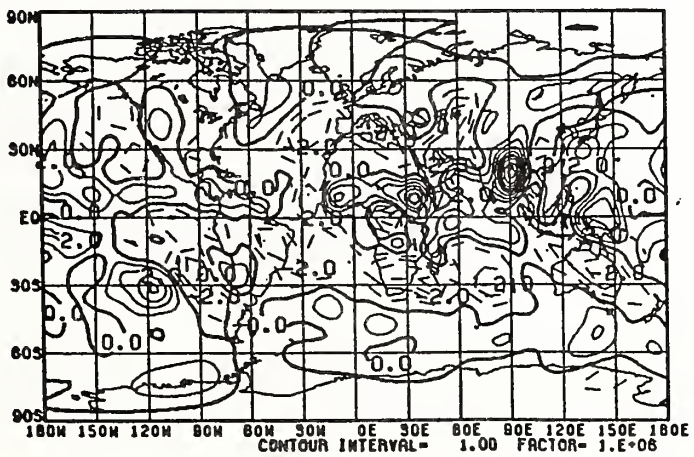

Fig. 3a 200 mb divergence averaged over summer of the T40 simulation, contour interval 1.E-06/s.

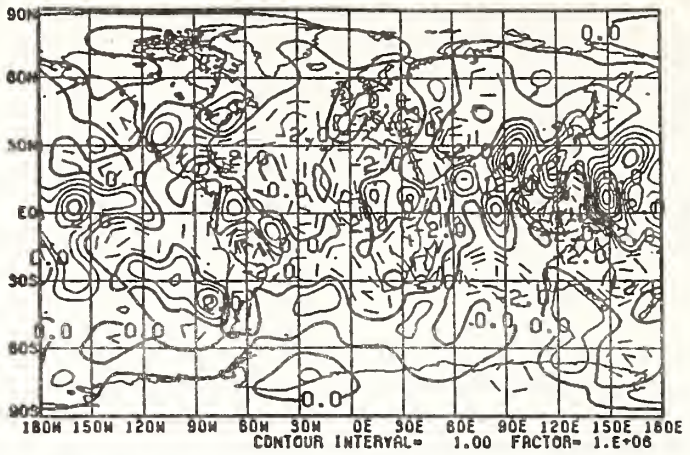

Fig. 3b Same as Fig. 3b, except for the R16 model.

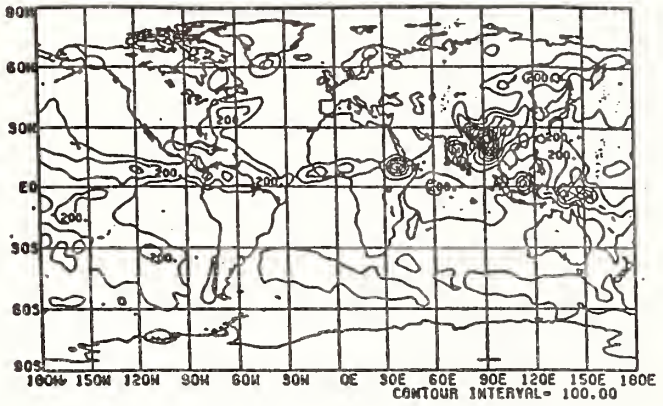

4a

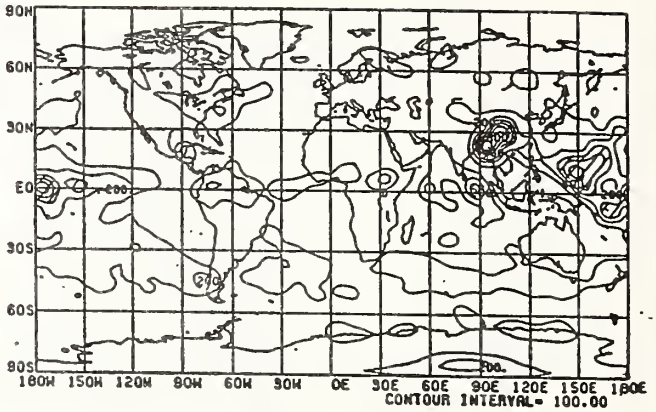

4b

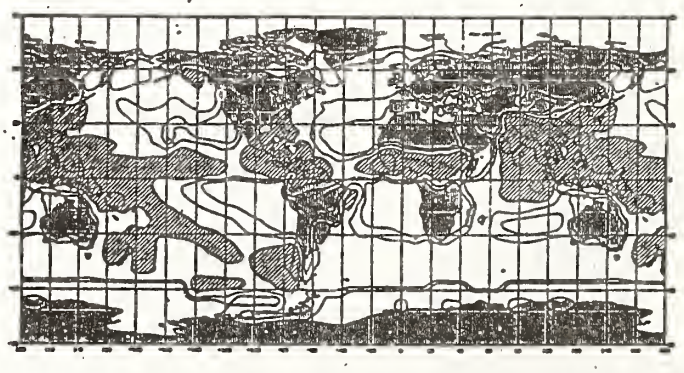

4c

Fig. 4a Total rainfall averaged over July of the T40 simulation, contour interval is 100 mm.

Fig. 4b Same as Fig. 4b, except for the R16 simulation.

Fig. 4c Observed July rainfall by Jaeger, contour interval is 1,2,4 and 8 mm/day.

TROPICAL-EXTRATROPICAL INTERACTIONS IN A MODEL ATMOSPHERE

Tom Murphree and Bryan Weare
Atmospheric Sciences Group
Department of Land, Air, and Water Resources
University of California
Davis, CA 95616

The interaction of various regions of the atmosphere via planetary wave propagation has been an intriguing subject for almost 50 years. In recent years, the wave dynamics of tropical-extratropical interaction has received particular attention. This interest has been promoted by observational studies showing teleconnection patterns resembling the wave trains derived from simple models of the planetary wave response to localized tropical forcings. These modeling studies have helped develop the basic theory for planetary wave propagation on a sphere through various mean fields. As the theory has grown, increasingly realistic mean fields have been used, giving new insights into propagation dynamics while also confirming many of the preceeding theoretical conclusions. In this study, we continue this process using a relatively simple nonlinear model with realistic basic states.

We focus on the role of the subtropical basic state in controlling the location and amplitude of the global response to tropical forcing. We expect from simple linear theory that in areas of realistically strong (weak) upper tropospheric subtropical westerlies, meridional propagation should be inhibited (favored). Basic theory also suggests that the subtropical jets may be, in response to tropical forcing, areas of strong relative vorticity generation and barotropic instability. Thus the jets are potential major energy sources for the response wave field. For realistic basic states, these subtropical factors might well overwhelm other factors, such as the longtitude of the tropical forcing, in determining the structure of the global response.

The basic state fields are the Dec.-Feb. 1985-86 means of the 200mb ECMWF analyses of streamfunction, velocity potential and geopotential. The zonal wind and heights for this state are shown in Fig. 1. Note the zonal asymmetry (symmetry) in the northern (southern) hemisphere and the strong (weak) subtropical winds flanking tropical easterlies (westerlies). The basic state tropical outflow (not shown) is strongest in the longtitude bands with strong jets and tropical easterlies. These jets and easterlies should sharply inhibit meridional propagation in the model. However, the strong outflow along the high subtropical ambient vorticity gradients in these bands should favor planetary wave formation along the jets.

The model is based on the shallow water equations on a global spherical domain. The equivalent depth is 2000m. A constant basic forcing that maintains the basic state, in the absence of any other forcing, is prescribed. Our model dissipation choices (relaxation damping at 1/15 day rate, del-4th diffusion with 10^{17} constant) give steady solutions. The model is in spectral form with R25 truncation. In model runs with perturbation forcing, a steady tropical forcing, representing heating in a long-lived tropical convection anomaly, is applied to the geopotential equation. The model response to this forcing is calculated as the steady solution

with such forcing minus that without.

To interpret the model response with a fully wavy basic state, it is helpful to first examine the response with four simpler basic states. The first case is the wavy state's zonal mean. This state has westerlies everywhere, except in an equatorial strip of weak easterlies. The westerly maxima are at 30N (40m/s) and 45S (25m/s). The tropical forcing and the eddy part of the height response for this state are shown in Fig. 2. (The eddy picture is given here in order to emphasize the wavetrains in a relatively weak overall response.) Two patterns in Fig. 2 stand out: (a) belts of high and low heights trending west-northwest out of the tropics (e.g., the belt of undulating highs extending from southeast Asia across the Mediterranean and Atlantic into Canada), and (b) alternating highs and lows extending out of the tropics along eastward and poleward arching paths (e.g., the high-low-high pattern extending from southeast Asia over the Pacific to northern Canada). Pattern (a) is formed by the wave trains arising from westward and poleward group propagation of zonally long waves. Pattern (b) is the more familiar great circle pattern arising from shorter wave propagation. Note that (a) and (b) intersect over much of the globe, indicating that interference of the long- and shorter-wave trains may be important in producing some features of the response (e.g., those over North America, the north Atlantic, and Europe).

Case two is a zonal mean basic state having westerlies everywhere. This state (based on the east Pacific band of the wavy basic state) has weak jets (25m/s) at 30N and 50S, and peak tropical westerlies of 10m/s. The response (Fig. 3) is similar to that in the previous case, but with a more developed arching train (including equatorward extensions out of the high latitudes) and about twice the high latitude amplitudes. In this case, the siting of the forcing within westerlies and the weaker northern jet permit more high latitude propagation of shorter wave energy.

Our third case is a basic state with a banded structure (Fig. 4a). For this state, the winds in the east Pacific-Atlantic band are the same westerlies as in case two. The Asia-west Pacific band (based on the Indonesian band of Fig. 1) has a strong jet (65m/s) at 30N and peak equatorial easterlies of -10m/s. The response for this state (Fig. 4b,c) resembles the preceeding ones, but with some interesting differences: (1) the eastward and poleward trains arching out of the Pacific are shifted east, with the northern train passing through the subtropics in the weak westerlies band; (2) the westward long-wave train over Asia is meridionally confined along the jet, with poleward propagation limited to the weak westerlies band; (3) the amplitudes are much larger. Differences 1 and 2 show the constraints on meridional propagation imposed by the strong northern jet. Difference 3 indicates that the jet is a major energy source for the response. The streamfunction response in the tropical east Pacific (not shown) reveals southward energy propagation from the north Pacific jet exit, suggesting a feedback from the jet source to the tropics and southern hemisphere.

The fourth simple state is like the third, except that North and South American jets (40m/s at 40N and 30m/s at 45S) are added to give the banded height field in Fig. 5a. The response with this state (Fig. 5b) resembles the previous response (Fig. 4c), except for additional arching trains associated with the additional jets and weak subtropical westerlies in the Atlantic band.

Finally, the results when the fully wavy basic state of Fig. 1 is used are shown in Fig. 7. From the preceeding results, most of the features of this complex response can be identified; in particular, the westward and poleward long-wave trains, and the eastward and poleward shorter-wave trains. A new feature in this response is the wave train along the Asian jet. We tentatively identify this as shorter waves preferentially trapped and amplified at the jet. Their marked appearance here, compared to Figs. 4c or 5b, is due to the use of a weaker basic state jet over Asia. This weaker jet permits a greater poleward propagation of long waves while still being strong enough to confine shorter waves, thus giving a wavelength dependent filtering effect.

There are observations which suggest that these wave patterns and their associations with subtropical flow may occur in the real atmosphere. For example, the Climate Analysis Center's Climate Diagnostics Bulletin shows, for a number of monthly analyses of 200 mb streanfunction anomalies, wave trains along the Asian jet resembling those in Fig. 7. In addition, the response in Fig. 7 shows several features similar to observed teleconnection patterns (e.g., the Pacific - North American and East Atlantic patterns). The model patterns also appear in ECMWF analyses. For example, the eddy heights for Dec.-Feb. 1985-86 (Fig. 6) show an arching wave train over North America, a zonal wave train along the north African - Asian jet, and westward and poleward long-wave trains.

The results shown here represent the primary responses found when using a number of different basic states (different times, averaging periods, levels). In all cases with realistic basic states, the westward and poleward long-wave, and the eastward and poleward shorter-wave trains are seen, although their strengths may vary greatly. Studies with wavy basic states in which the tropical forcing longtitude is shifted around the globe show no qualitative change in the response, except regionally within the tropics, suggesting that the subtropical effects discussed here may dominate the global response. Unlike some recent modeling studies, our results show that equatorial regions of strongly negative zonal gradients of the zonal wind are not preferred emanation sites for tropical - extratropical wave trains.

We conclude with a summary of our main points. A nonlinear model with realistic basic states gives a complex pattern of tropical - extratropical interaction in response to localized tropical forcing. Two main patterns of interaction are found: (a) westward and poleward long-wave trains; (b) eastward and poleward shorter - wave trains. Meridional energy propagation within these trains is greatest in regions of relatively weak subtropical westerlies and is very limited at strong jets. The jets appear to be important energy sources for the planetary wave response, with the jet exits being potential sites for feedbacks from the subtropics to the tropics. (This may help explain the maxima in perturbation kinetic energy observed in regions of persistent upper level equatorial westerlies, since these regions tend to be flanked by jet exits.) Thus, the subtropical flow structure plays a large role in mediating tropical-extratropical communication by controlling the propagation patterns and amplitudes of the planetary wave field. This of course makes the modeling of the intricacies of this communication a highly interactive problem, since, to a large extent, subtropical flow is a product of tropical-extratropical interaction.

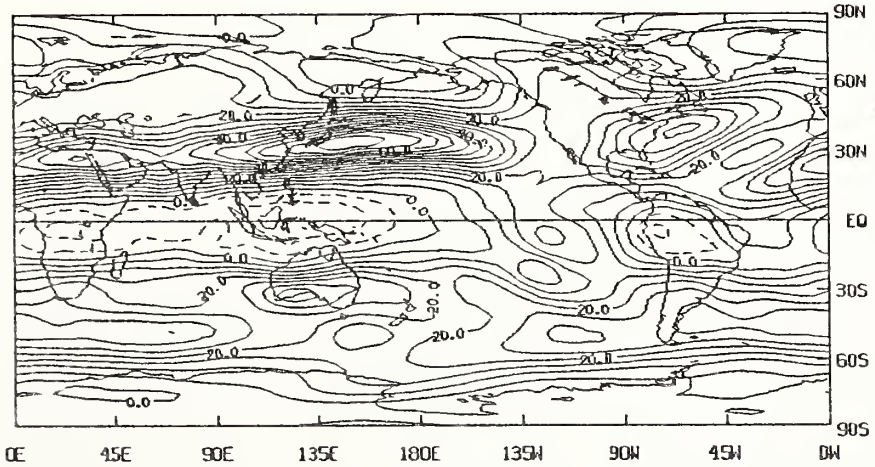

Fig.1a. ECMWF DJF 85-86 200 mb u wind. Interval = 5m/s. Note: (1) tropical easterlies flanked by N. hemisphere jets; (2) relatively weak subtropical westerlies over E. Pacific and Atlantic areas; (3) max. westerlies = 75 m/s over W. Pacific; (4) max. easterlies = -14 m/s over Indonesia.

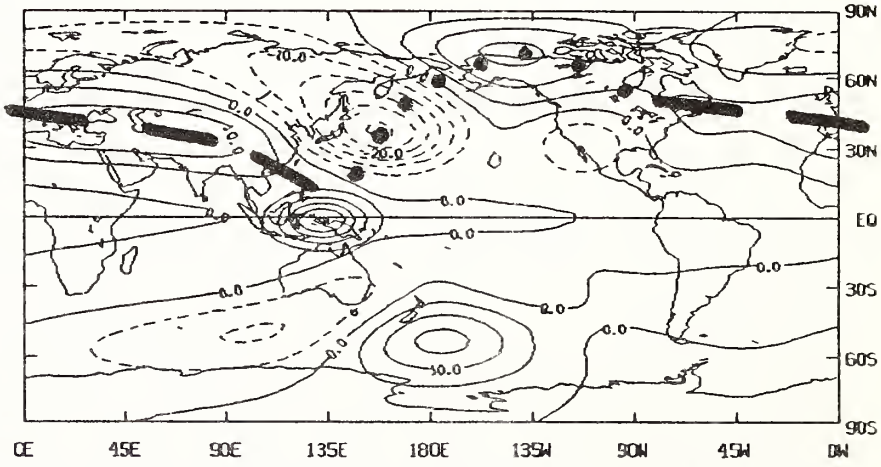

Fig.2. Case 1 eddy height response to tropical W. Pacific forcing (oval area), for zonal mean basic state with 40 (25) m/s jet at 30N (45S) and weak equatorial easterlies. Intervals =5m, 1K/day. Note westward and poleward long-wave trains, plus arching eastward and poleward shorter-wave trains. Example trains are dashed and dotted, respectively. Peak central forcing corresponds to 5K/day heating rate.

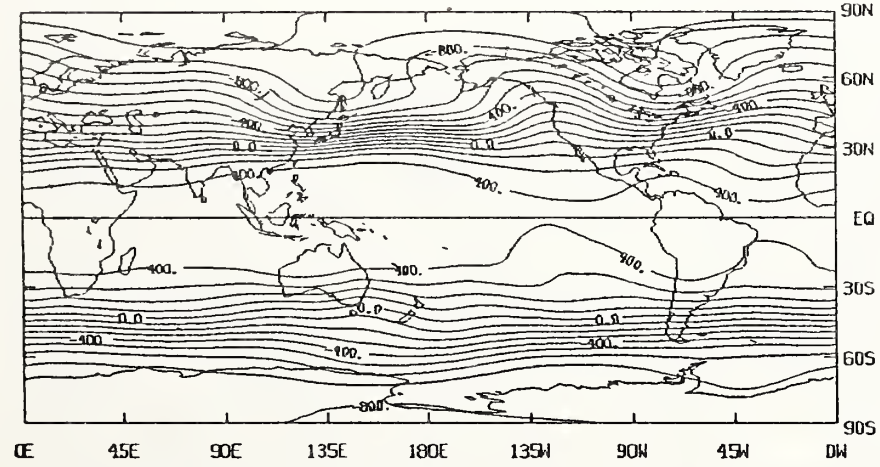

Fig.1b. ECMWF DJF 85-86 200mb heights, minus global mean. Interval = 100m. Note strong (weak) meridional gradients in subtropics associated with strong jets (weak westerlies). This field used as part of the fully wavy basic state model runs.

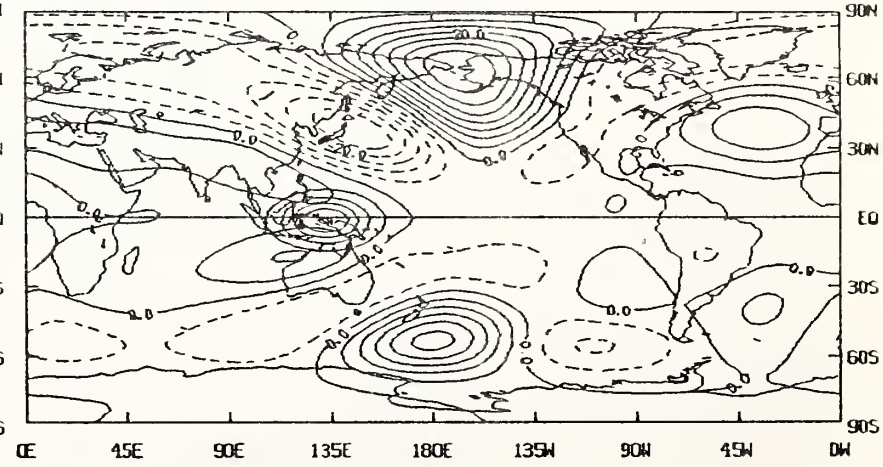

Fig.3. Case 2 eddy height response and forcing. As in Fig. 2, but for zonal mean basic state with 25 m/s jets at 30N and 50S,and equatorial easterlies (< 10m/s). Note resemblance to Fig. 2 but larger high latitude response.

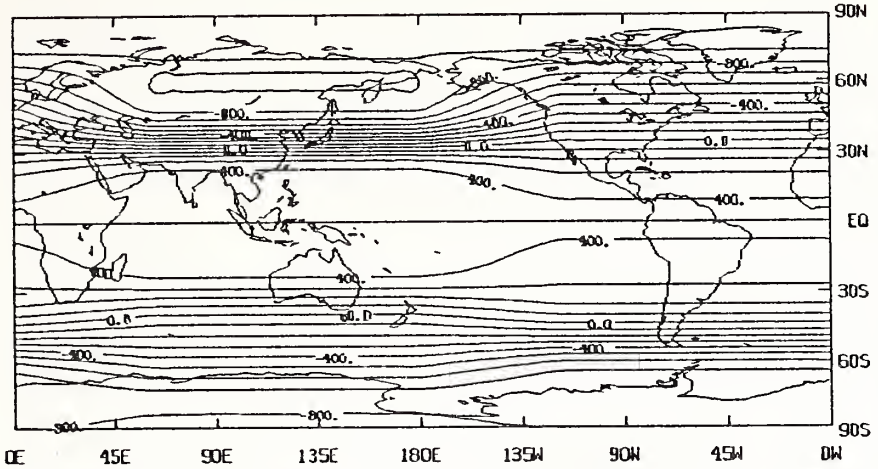

Fig.4a. Case 3 basic state heights, minus global mean. Interval =100m. Corresponding winds: (1) strong jet (65 m/s) in Asian-W.Pacific area; (2) weak subtropical westerlies in E. Pacific - Atlantic area; (3) equatorial easterlies (westerlies) in Indian - W. Pacific (E. Pacific - Atlantic) areas. Cf. Fig. 1b.

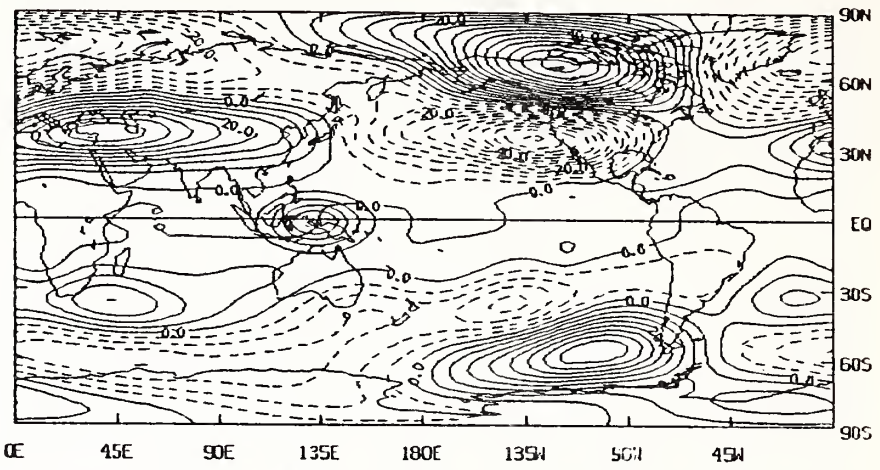

Fig.4b. Case 3 eddy height response and forcing, as in Figs. 2 & 3, but for basic state represented in Fig. 4a. Note: (1) meridional confinement of long-wave train along Asian jet; (2) strong meridional propagation in eastward and poleward wave trains through weak subtropical westerlies in E. Pacific.

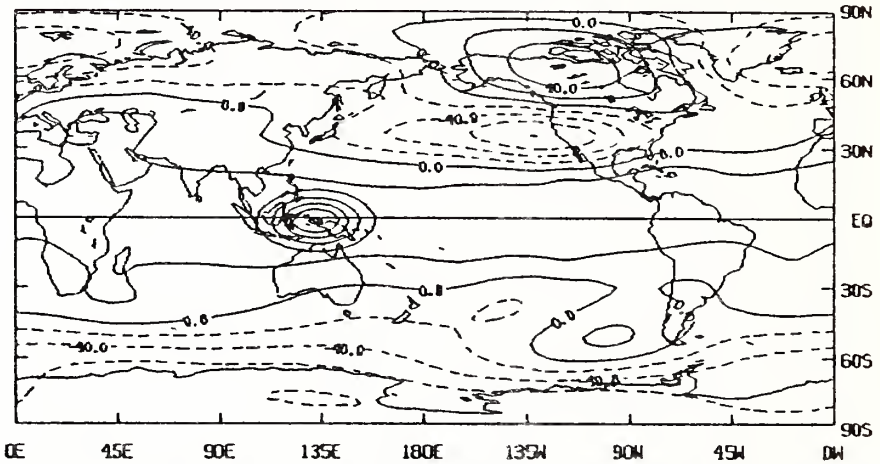

Fig.4c. Case 3 height response and forcing. Intervals = 20m, 5K/day. This is the total response corresponding to Fig. 4b. It is shown here for comparison with subsequent cases with large total responses.

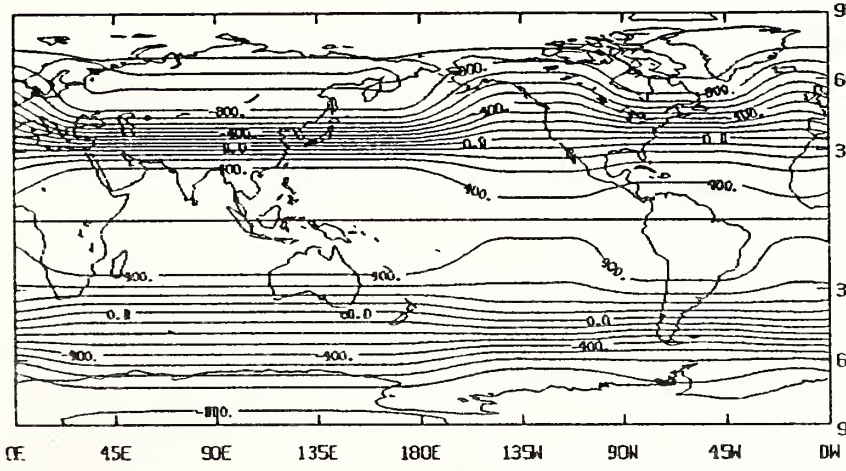

Fig.5a. Case 4 basic state heights. Similar to heights in Fig. 4a, except in the N. American-Atlantic area where the height changes correspond to the addition of a 40 m/s jet at 40N. Note the two regions of weak westerlies in the northern subtropics over the E. Pacific and E. Atlantic. Cf. Fig. 1b.

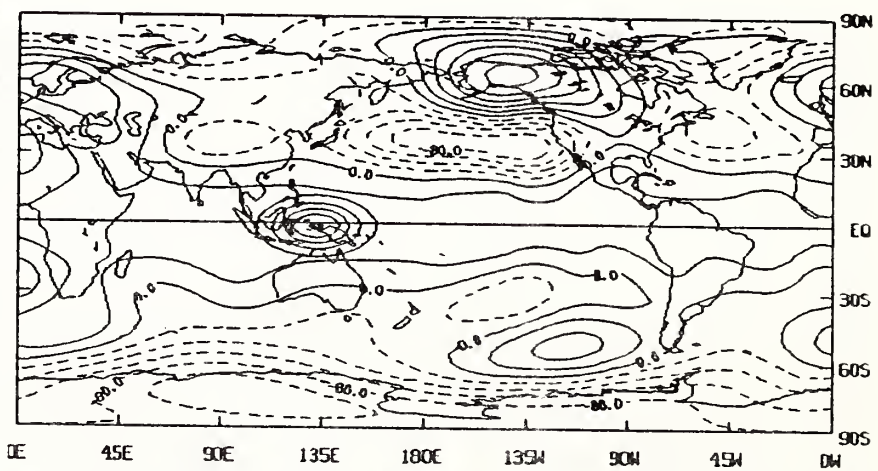

Fig.5b. Case 4 height response and forcing for basic state represented in Fig. 5a. Intervals = 20m, 5k/day. Note similarity to Fig. 4c, but with additional eastward and poleward wave train through E. Atlantic region of weak subtropical westerlies.

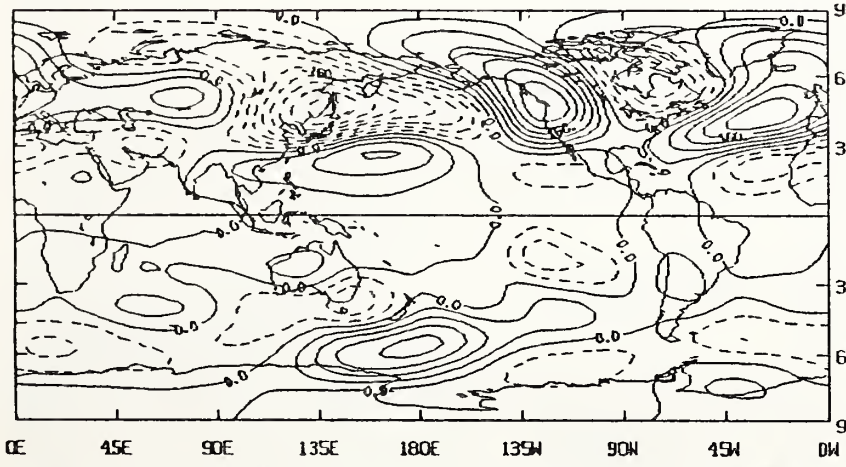

Fig.6. ECMWF DJF 85-86 200mb eddy heights. Interval = 40m. Note: (1) eastward and poleward arching wave train over N. America; (2) zonal wave train along N. African-Asian jet; (3) westward and poleward long-wave trains, especially in S. hemisphere.

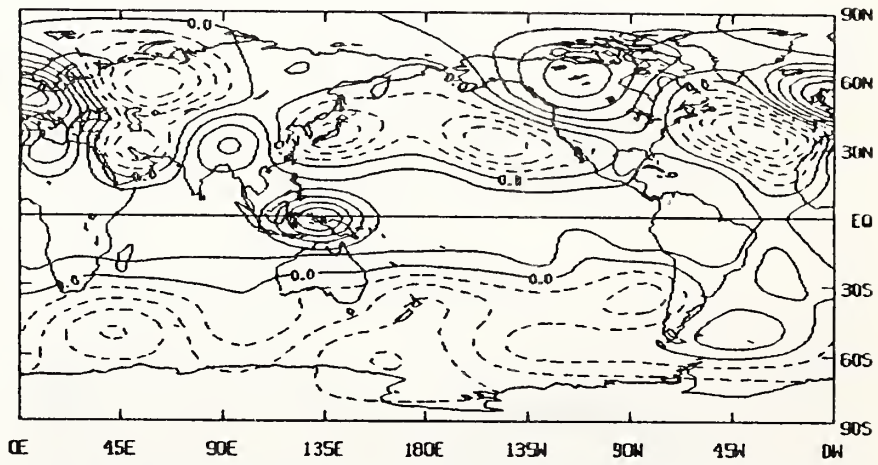

Fig.7. Height response and forcing for fully wavy basic state represented in Fig.1. Intervals = 20m, 5K/day. Note: (1) similarity to responses for simple basic states shown in Figs. 4c, 5b; (2) short-wave train along Aaian jet.

LINEAR PREDICTABILITY

John O. Roads
Scripps Experimental Climate Forecast Center
UCSD, A-024
La Jolla, CA 92093

1. Introduction

Recently Palmer (1987) described temporal variations in forecast skill with the ECMWF model, related these variations to variations in the PNA pattern and suggested that barotropic instability was the key feature for describing loss of predictability. Another theory which may be related to Palmer's observation is what may be referred to as neutral mode excitation. This theory developed from work by Branstator (1985) who described a barotropic eigenanalysis of the NCAR CCM. The original reason that Branstator had looked at this problem was that previous modeling studies with the NCAR CCM (Geisler et al., 1985) had suggested that some of the anomalous responses were independent of location of forcing. Since linear responses are supposed to be strongly dependent upon the location of the heating through downstream responses a quasi-normal mode response was suggested which essentially means that the geographical characteristics of the forcing are not as essential as the basic background state which can influence near-resonant solutions. Branstator's paper was also important because it described the importance of all the linear eigenvectors and eigenvalues to any solution since any solution could be expanded as a linear combination of eigenvectors. This type of analysis may therefore be important for explaining climatic variations as well as for explaining predictability variations.

Therefore a linear barotropic analysis of a 5 year perpetual January run with the two-level nonlinear quasi-geostrophic model described by Roads (1988) is described here. As is shown, since the eigenvalues of the linear system are distinct, all variables can be easily described by a linear combination of the associated eigenmodes. Short term (weather) variations require a large set of eigenmodes to describe solutions but long term (climate) variations require a smaller set of eigenmodes to describe the solutions. Basically, time averaging effectively eliminates the fast eigenmodes resulting in slow (almost neutral) modes dominating the variances of long term averages. Furthermore, the slow modes are most persistent and predictable by the linear model. This allows some advance knowledge of when predictions by linear models and perhaps numerical weather prediction models are likely to be good or bad. If the initial state is dominated by slow modes the linear prediction is likely to be good and if the initial state is dominated by fast modes the linear prediction is likely to be bad.

2. Theory

Let us write the proto-typical anomaly model as

$$\frac{\partial \psi}{\partial t} + L\psi = F,$$

where L denotes a linear operator and F denotes everything else not included in L. F is sometimes related to the ocean surface temperature anomalies although it is not clear yet that forcings like the transient eddies can be omitted from consideration. The linearization is taken here to be the linearization around a three dimensional climatology. This equation is solved by the methods of normal modes. That is, the homogeneous equation is first used to find the eigenvalues and eigenvectors or normal modes. For the equation

$$\frac{\partial \psi}{\partial t} + L\psi = 0,$$

assume $\psi = Ee^{\sigma t}$ and, simplifying, obtain the eigenvalue problem

$$-LE = \sigma E.$$

If we now find the eigenvalues and eigenvectors of the (N x N) matrix $(-L)$, and they are distinct, we can find the solution for any nonhomogeneous equation since any vector can be represented as a sum of normal modes. That is,

$$\psi = \sum_{j=1}^{N} \psi_j E_j$$

where ψ_j is the eigenvector weight and E_j is the eigenvector. The importance of this expansion is that any climatic state or anomaly can be expanded in a natural basis system that takes into account the idiosyncracies of a particular climatic state. This expansion thus provides a natural framework in which to look at climatic anomalies.

Substituting this expression in the anomaly model above yields

$$\frac{\partial \psi_j}{\partial t} - \sigma \psi_j = F_j$$

which has the asymptotic solutions

$$\psi_j \sim \psi_j(0) e^{\sigma_j t} \qquad t \sim 0$$

$$\hat{\psi}_j \sim \frac{-\hat{F}_j}{\sigma} \qquad T \sim \infty$$

where

$$\hat{\psi}_j = \frac{1}{T} \int_o^T \psi_j \, dt$$

and the intermediate solution

$$\hat{\psi}_j \sim \frac{-\psi_j(0)}{\sigma_j T} - \frac{\hat{F}_j}{\sigma_j} \qquad 0 << T << \infty$$

The major point about these asymptotic solutions is that long term climate variations are inversely related to the eigenvalues and directly related to the forcing which becomes more important than the initial state for sufficiently long time periods. Thus, for sufficiently long time averages the modes with the smallest eigenvalues, i.e. the near-neutral modes, should have the largest responses. Similarly, the most persistent and predictable modes should be

the same near-neutral modes. The major caveat to this theory is that it is assumed here that all σ_j are < 0. If any $\sigma_j > 0$ i.e. instability, then we must expect that the unstable modes will dominate the total solution. Assuming that this is not the case -and for the models examined here which include friction it was not the case- then this possible problem can be ignored for now. Thus, this theory assumes that the near-neutral modes are preferentially excited and preferentially predicted at long time scales. For example, the PNA pattern is thought to be such a mode.

3. Models

The basic nonlinear time-dependent model to be used for the test of the above theory is a two-level quasi-geostrophic model with a surface mixed layer forced with stationary forcings designed to yield a model climatology close to the observed. (See Roads, 1988.) The model has moderate truncation of T21 which is comparable to most climate models, the major differences being that the quasi-geostrophic equations rather than the primitive equations are the basis set, only two vertical levels are used, and the model is run as a hemispheric model. As shown in Figure 1, the model does a credible job of simulating the observed climatology at least in middle latitudes. For a 5 year perpetual January run, the model barotropic streamfunction was close to the observed; the confluent region off the coast of Asia and North America as well as the location and magnitude of the subtropical highs were well simulated. The thermal streamfunction was also well represented as was the surface temperature. The major model defect is that over the west coast the high seems to be overly emphasized. Another defect is that due to the hemispheric nature of the model, all variables are expanded in antisymmetric harmonics which results in unrealistic surface temperatures near the equator. However, only the antisymmetric part of the temperature is dynamically significant in a hemispheric quasi-geostrophic model.

A linear model linearized about this climatology which included all viscous terms was developed. Figure 2 shows the eigenvalues for a linear barotropic model. Both the real and imaginary parts of the eigenvalues as well as the modulus of the total eigenvalue are shown. These eigenvalues are sorted in terms of modulus of increasing amplitude. The real part describes the exponential decay of each mode and the imaginary part describes the propogating part. If the real part is much greater than the imaginary part then the mode is basically stationary. If the imaginary part is much greater than the real part then the mode is basically propagating. As may be seen, the smallest eigenvalues tend to be dominated by low frequency stationary modes and the largest eigenvalues are dominated by high frequency propagating modes. In no case was an exponentially growing solution found. Ostensibly this might seem to be due to using a barotropic model and heavy damping but even for a linear baroclinic model the modes were damped, albeit less so. For example, in a baroclinic version of the linear model, the first mode had an e-folding time scale of 80 days compared to the 13 day time scale for the first barotropic mode. Only when the model was linearized around a state far away from the climate were unstable modes found. Of course, the climatological state is not a steady state solution since the transient eddies play an important role. If the climatology is assumed as an initial state then the model moves away from the climatology until such time that the transient eddies play an important role and then over long time averages the climatological solution is obtained. The point of all this discussion is that instability is not playing the primary role in this model for explaining climate anomaly variations. The most important modes are the slow near-neutral modes because they have slow time scales whereas the fast time scales will tend to be filtered out of long term averages.

4.0 Linear Predictability

Figure 3 shows predictions based upon the initial state. The upper curves show forecasts

of time averages, the lower curves show forecasts of instantaneous states. As shown, the linear model is slightly better for forecasts of 90 day averages and slightly better than persistence out to day 20. The forecasts are substantially better if only the first 5 modes are forecast and observed. At 90 days the correlation is .35 for persistence and .4 for the linear wave model if only the first 5 eigenmodes are used, in contrast to .19 and .27 for the total solution. Forecasts of the slow modes are substantially better than the fast modes and total solutions.

Figure 4 shows a stratification in terms of a priori and a posteriori determined forecast skill(correlation) for forecasts of time averages. From these curves we see that there is a distinct difference between the most and least skillful forecasts and that we can probably predict this variation. The rule for predicting this variation is shown in Figure 5 which shows the average variance for the most skillful and least skillful seasonal forecasts and the average variance of the initial state for the most skillful and least skillful seasonal forecasts. The major thing to note here is that the variance is largest in the slowest modes both for the predicted and final states and moreover the variance is largest for the slowest modes in the initial state even though the total variance is slightly smaller for the most predictable solutions. Thus, the skill of these seasonal predictions seems to be tied to the variations of the slowest modes.

Finally, Figure 6 shows the smoothed variation of the slowest mode in contrast to the correlation of the seasonal linear prediction. Overall, there seems to be a good correspondence between the variations in predictability with the variations of this slowest mode. When this mode is large, predictability is high and when this mode is small, predictability is low. Thus if the initial state projects strongly onto the slowest modes the linear model and presumably persistence as well as nonlinear models, should have greater forecast skill.

Acknowledgements

This work was supported by NSF and CAC Grant ATM85-20540, NOAA Grant NA86AA-D-CP104, and Calspace. The figures were drafted by M. Schultz.

References

Branstator, G., 1985: Analysis of general circulation model sea-surface temperature anomaly simulations using a linear model. Part II: Eigenanalysis. *J. Atmos. Sci.*, **42**, 2242-2254.

Geisler, J.E., M.E. Blackmon, G.T. Gates, and S. Munoz, 1985: Sensivity of January climate response to the magnitude and position of equatorial Pacific sea surface temperature anomalies, *J. Atmos. Sci.*, **42**, 1037-1049.

Palmer, T.N. 1988: Medium and extended range predictability and stability of the Pacific/North American mode, *Q. J. R. Meteorol. Soc.*, **114**, 691-713.

Roads, J.O., 1988: Linear and nonlinear responses to middle latitude surface temperature anomalies, *J. Clim.*, submitted.

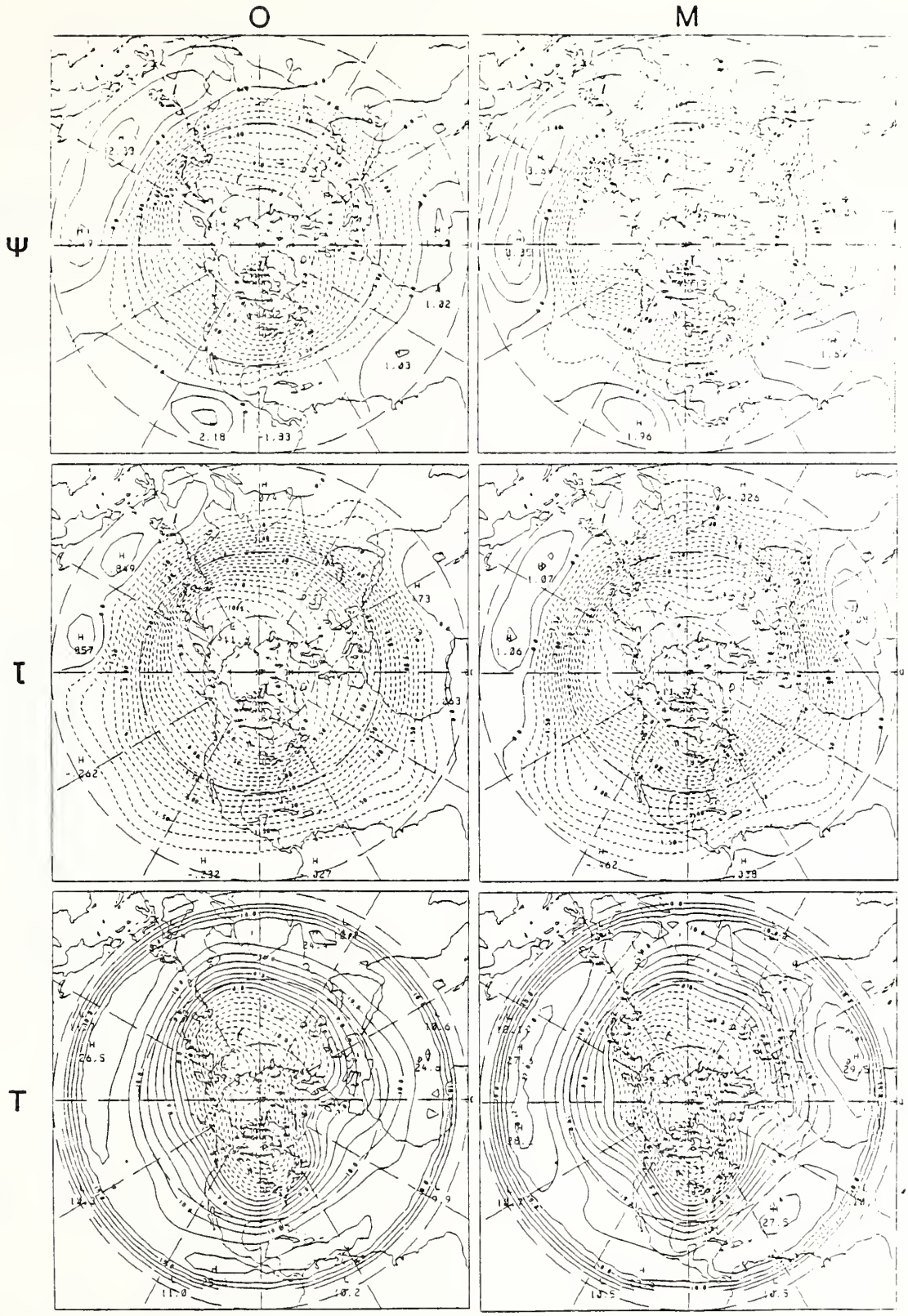

Fig. 1: Climatology for observed, O, January climate (10 Januaries) and model climatology, M, for a 5 year perpetual January control run. The barotropic streamfunction, ψ, thermal streamfunction, τ, are in nondimensional units and surface temperature, T, is in °C.

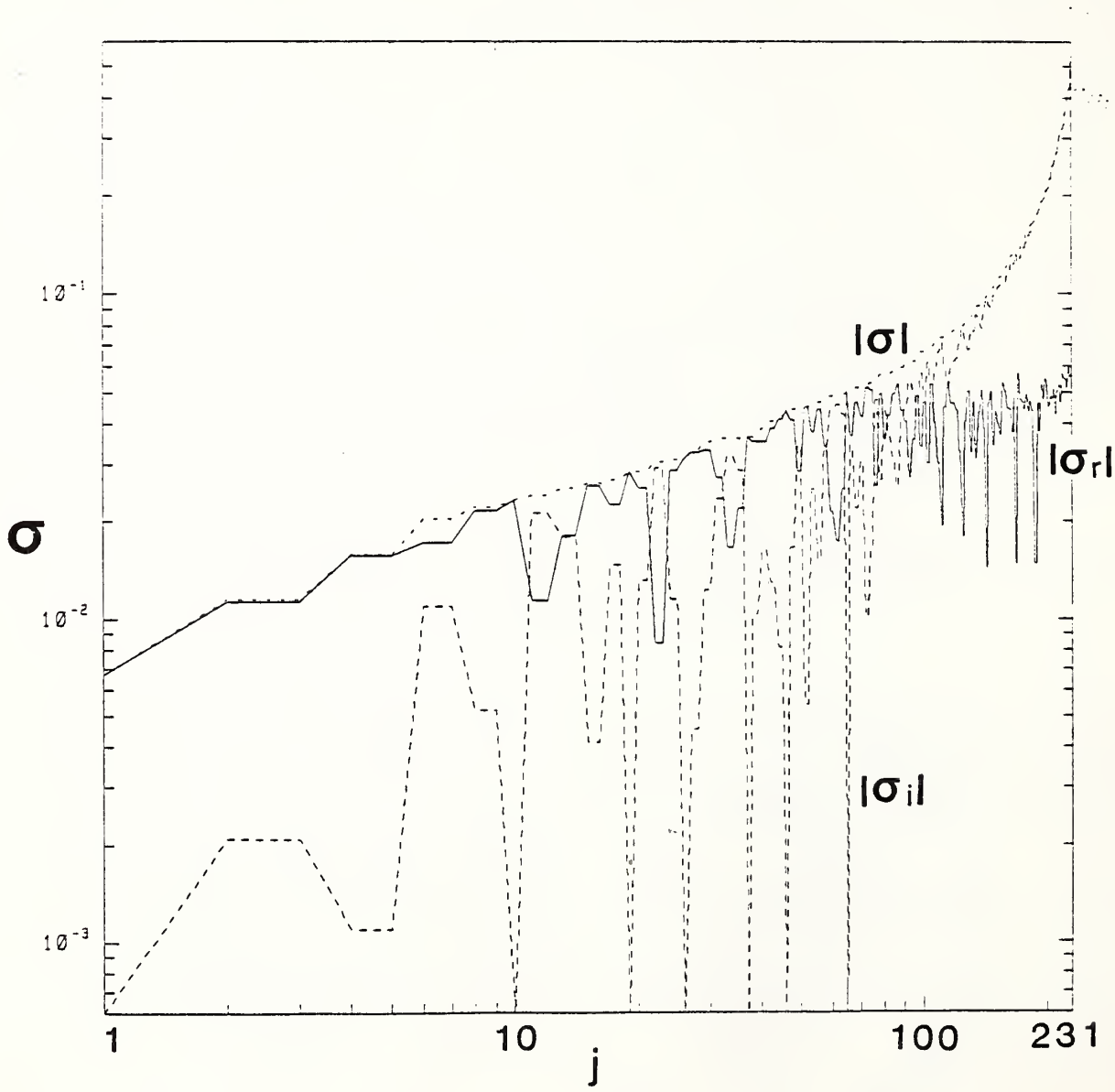

Fig. 2: Eigenvalues for linear barotropic model. The linear model assumes $\psi = \psi(0)e^{\sigma_r t}e^{i\sigma_i t}$. Only absolute values are shown but all σ_r are less than zero. The σ are shown in nondimensional units. Dimensional values can be found by multiplying by (2 x .7292 x 10^{-4} s^{-1})

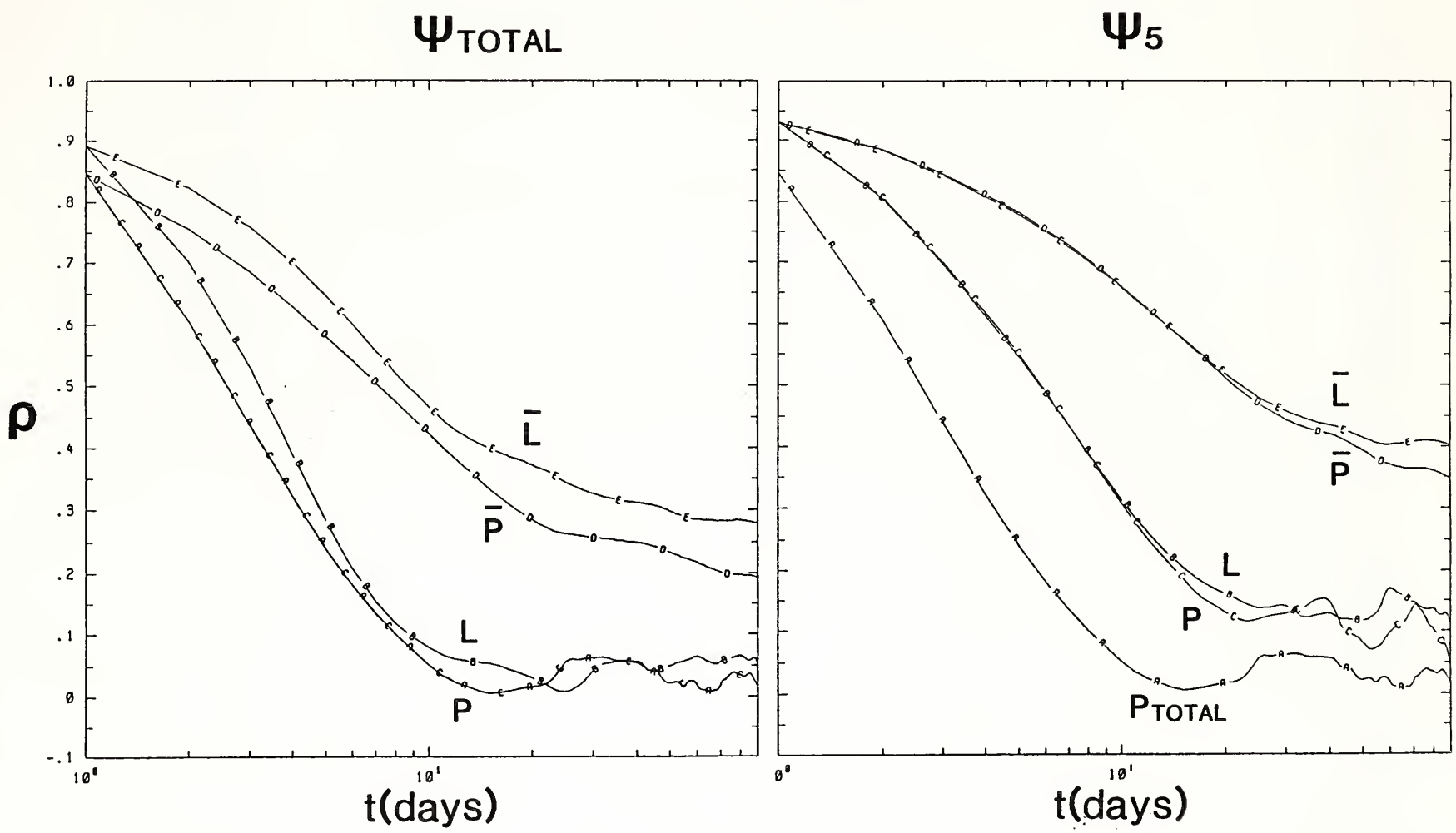

Fig. 3: Linear predictions, L, versus persistence predictions, P, for daily and time averages, $\overline{L}$ and $\overline{P}$, as measured by the correlation, ρ. ψ_{TOTAL} refers to predictions and observations using all eigenvectors or total solution. ψ_5 refers to predictions and observations using the first 5 eigenvectors only. 1-90 day predictions are shown.

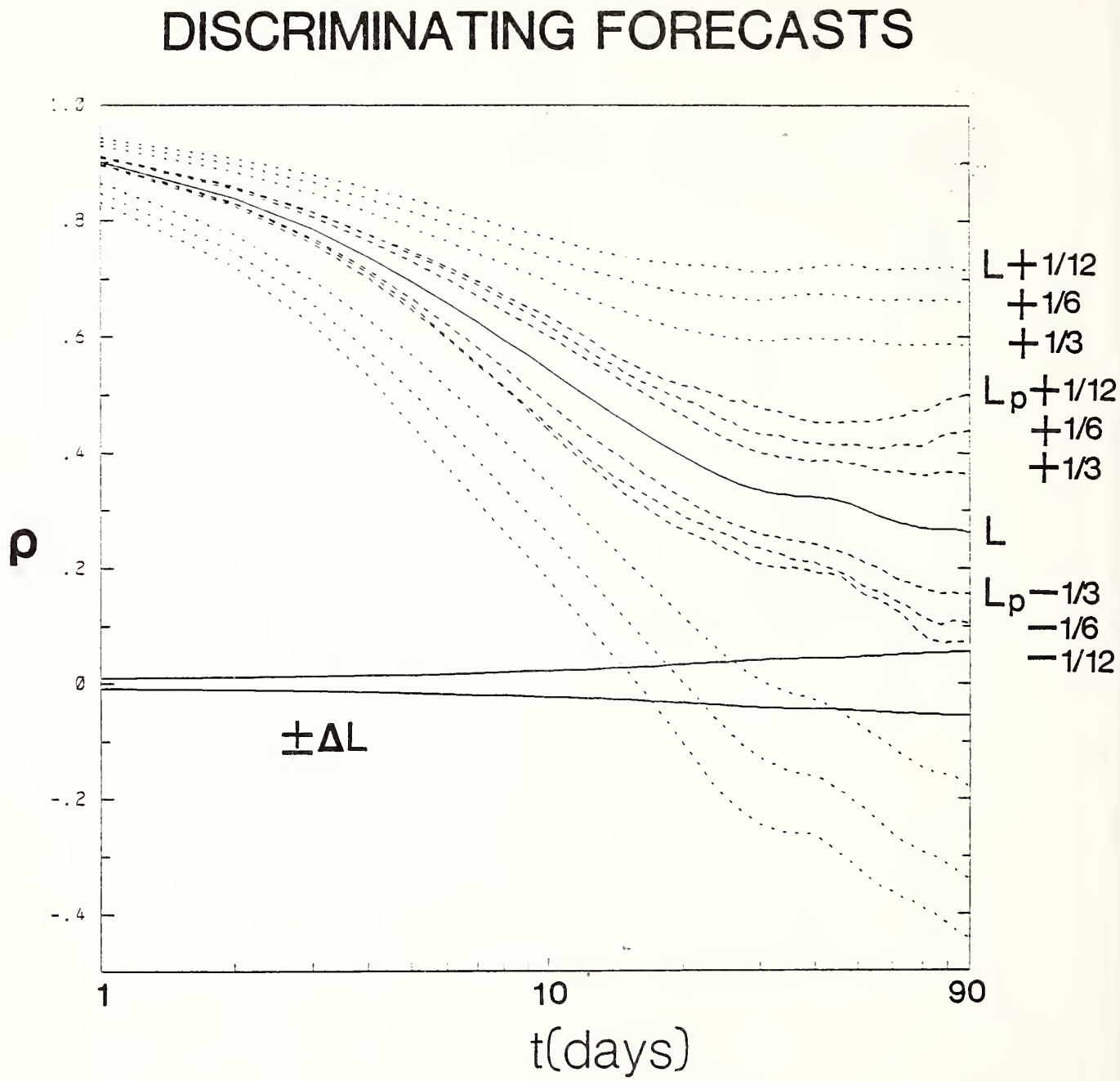

Fig. 4: Discriminating forecasts as measured by the correlation, ρ, for forecasts of 1-90 days. $L + 1/12, 1/6, 1/3$ refers to the average correlation of the $1/12, 1/6$, and $1/3$ best forecasts. Similarly, $L - 1/12, -1/6, -1/3$ refers to the average of the $1/12, 1/6, 1/3$ worst forecasts. L_p refers to the average of the a priori predicted best and worst forecasts. L refers to the average of all forecasts and ΔL is the estimated noise level in the average forecast skill ($\pm$ 1 standard deviation).

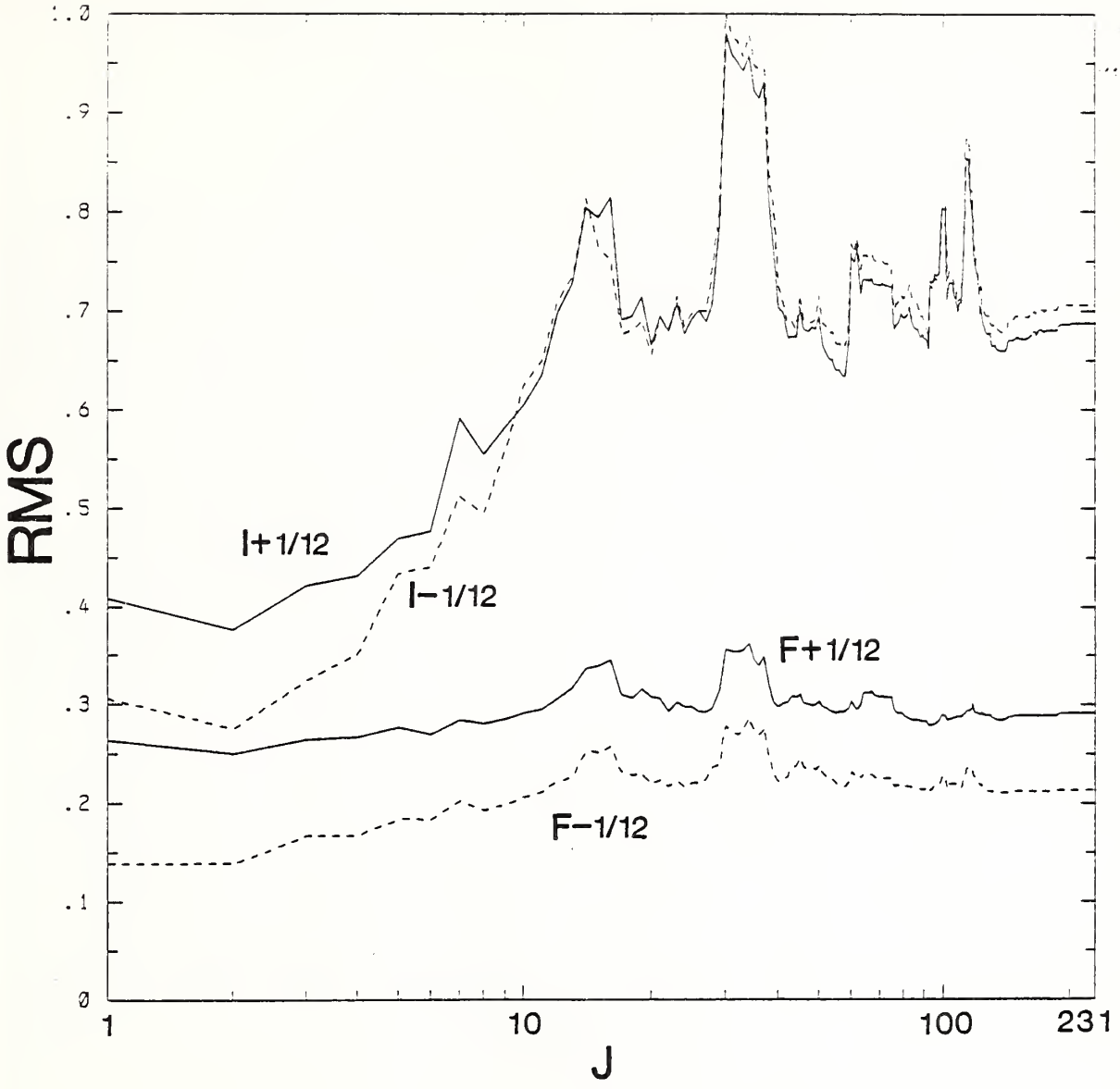

Fig. 5: The initial I, and the final states, F, for the 1/12 best and worst forecasts of the seasonal average are shown here in terms of the RMS of the continuous sum of areally weighted eigenvectors: RMS= $< (\sum_{j=1}^{J} \psi_j E_j)^2 >^{\frac{1}{2}}$.

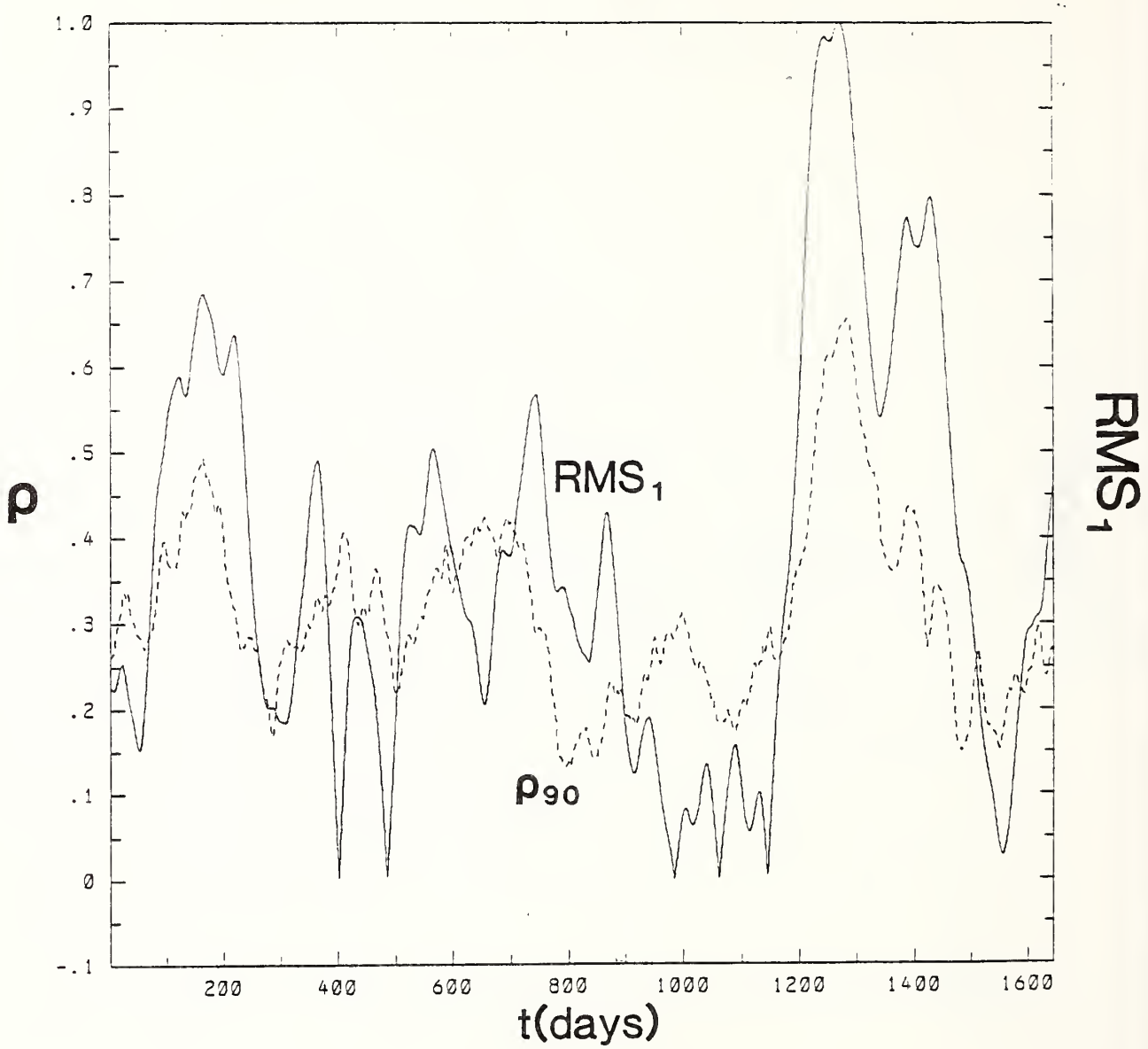

Fig. 6: Temporal variations in skill (correlation) of linear forecasts of seasonal averages, ρ_{90}, and the RMS of the first (and slowest) eigenmode. The correlations and RMS amplitude are smoothed by a running 90 day average.

GCM/OBSERVATIONAL COMPARISON: REGIONAL AND LOCAL CLIMATE

Thomas R. Karl
National Climatic Data Center/NESDIS/NOAA

Wei Chyung Wang and David Portman
Atmospheric Environmental Research, Inc.

Michael E. Schlesinger
Oregon State University

Direct comparisons of climate observations at the surface with GCM model output is difficult to assess due to the mismatch of space-scales and boundary conditions between the model-world and the real-world. Surface observations are of particular interest because of their long records, and because of their bio-physical and socio-economic impacts. A method has been developed which allows for indirect comparison of the surface climate with the model generated surface climate influence. Relationships are developed between free-atmosphere variables and surface variables of interest in the observed data. These relationships are then applied to the model projections of these free-atmosphere variables to obtain climatological predictions of the surface variables of interest for a specific location. Since the space scale of free-atmosphere variables is much more homogeneous than those at the surface the problems associated with inhomogeneous boundaries and large model grid scales are greatly mitigated. In this regard a more realistic assessment of the model's performance is possible.

The method uses several standard multivariate statistical procedures, but is conceptually similar to the approach used in numerical weather prediction specification equations, i.e. Model Output Statistics (MOS) and the Perfect Prog (PP) technique. There are three reasons why the MOS and PP technique were not used in this application. Our goals were to develop a method which ensures that the simultaneous prediction of each of a number variables is consistent among themselves. When multiple regression equations are developed using different independent variables this cannot be assumed to be true. Second, we wanted a method that would lend itself to classification of daily weather at any given location. Finally in the MOS and PP approaches the interest lies in minimizing the mean square error between observations on a specific day and predictions. For GCM validation the interest focusses on the ability of the model to reproduce the statistical properties of the distribution of the daily weather or "climate".

Rotated Principal Components are used to reduce the redundancy in a list of free-atmosphere potential predictors of the daily surface maximum and minimum temperature (MAX & MIN) as well as the total daily precipitation (PCP) and the average cloud ceiling (CIG) height (the criteria variables). Subsequent to this reduction canonical correlation is used to identify the simultaneous relationship between the predictors and the criteria variables. Canonical correlation can be regarded as a more general form of the

traditional multivariate regression equations in that there is more that one dependent variable. Next, a procedure called inflated regression is used to relate the important canonical variates as defined in the previous step to each of the four criteria variable, MAX, MIN, PCP, and CIG. The concept of inflation prevents the predictions from clustering about the line of best fit and preserves the variance of the original observations.

This method has been applied to the daily output from a 10-year simulation of the two-layer OSU GCM with prescribed sea-surface temperatures and a diurnal cycle for five stations across North America (Fairbanks, AK; Spokane, WA; Bismarck, ND; Topeka, KS, and Charleston, SC). Results indicate that the model predictions of the surface climate compare much more favorably to the observed local climate than would otherwise be indicated by direct comparisons of surface climates. Furthermore, the technique lends itself to classification of climate types. Using these classifications the day-to-day changes of climate types at each of the five stations was assessed. The overall ability of this model to simulate day-to-day changes of climate is very good after the model data is internally standardized using the model means and variances to define anomalies. The model simulates day-to-day changes better during winter compared to summer. It tends to be less dynamic with respect to changes compared to the observations.

It is not realistic to expect model output to compare favorably with observed data given the following:

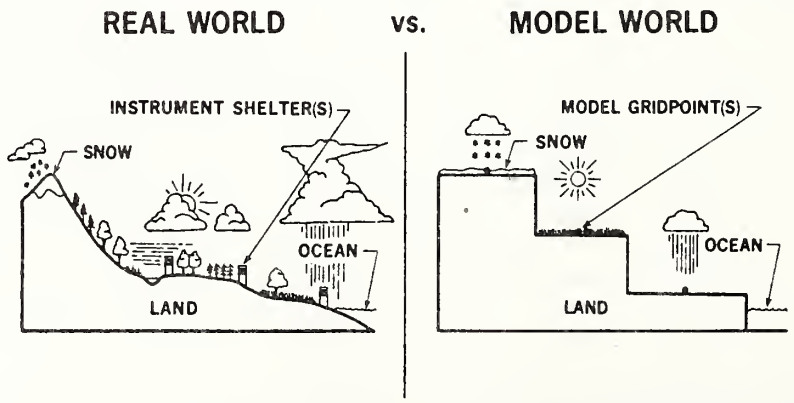

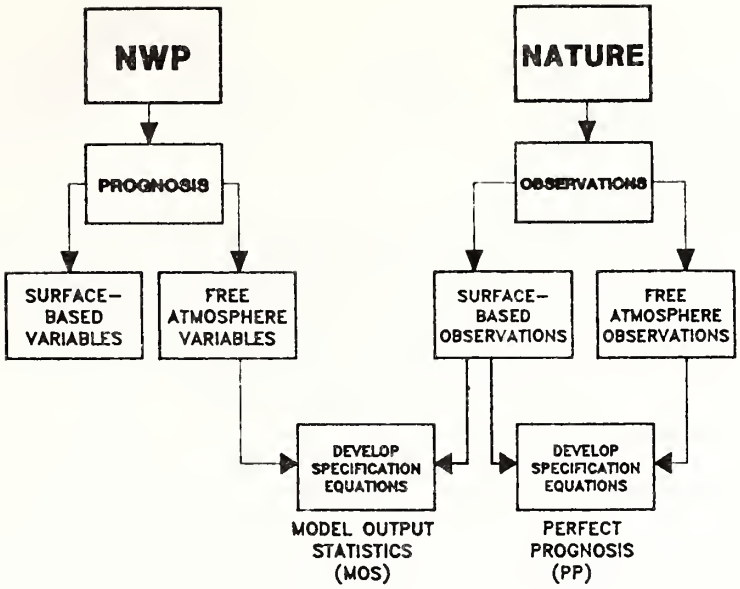

Daily forecasts from Numerical Weather Prediction (NWP) models has traditionally been enhanced by the use of MOS and PP.

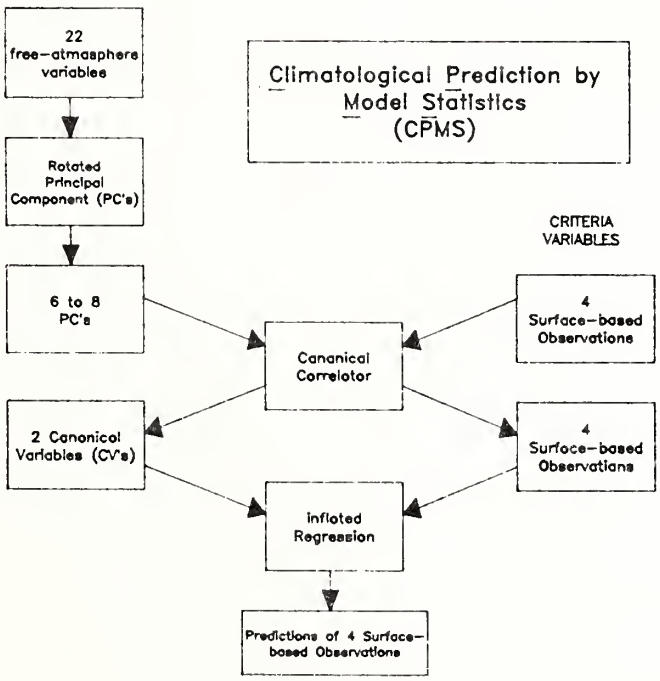

We begin our analyses with 22 free-atmosphere variables. These variables are not independent and were subjectively selected so a PC analysis is used to reduce the dimensionality. In our analysis 6 to 8 PCs were retained. Subsequently, canonical correlation was used to develop relationships between the criteria variables (max and min temp., total precipitation, and cloud ceiling) and the PCs (the predictors) This reduced the problem to the simultaneous relationship between to canonical vectors and the four criteria variables. Inflated regression was used to inflate the variance of the predictions.

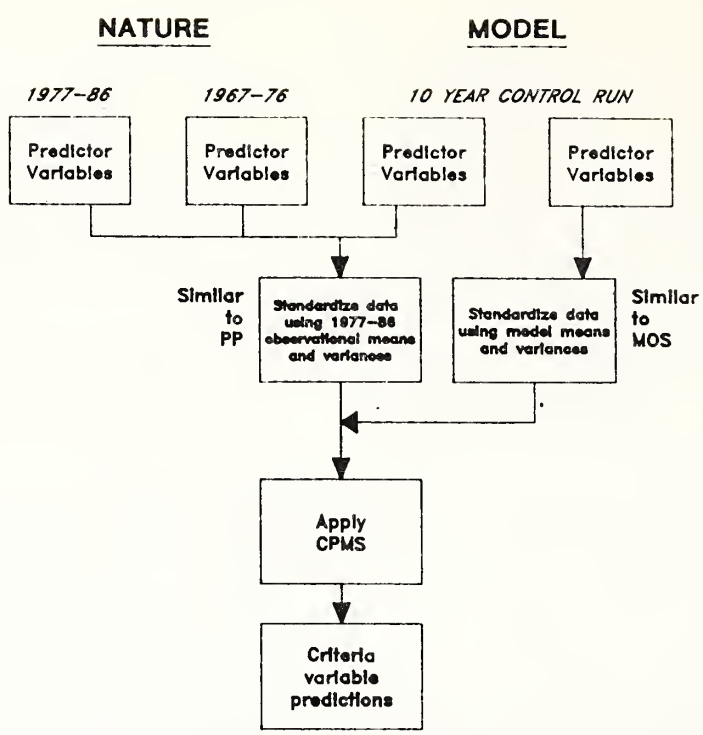

The flow chart depicts the research design strategy of our method.

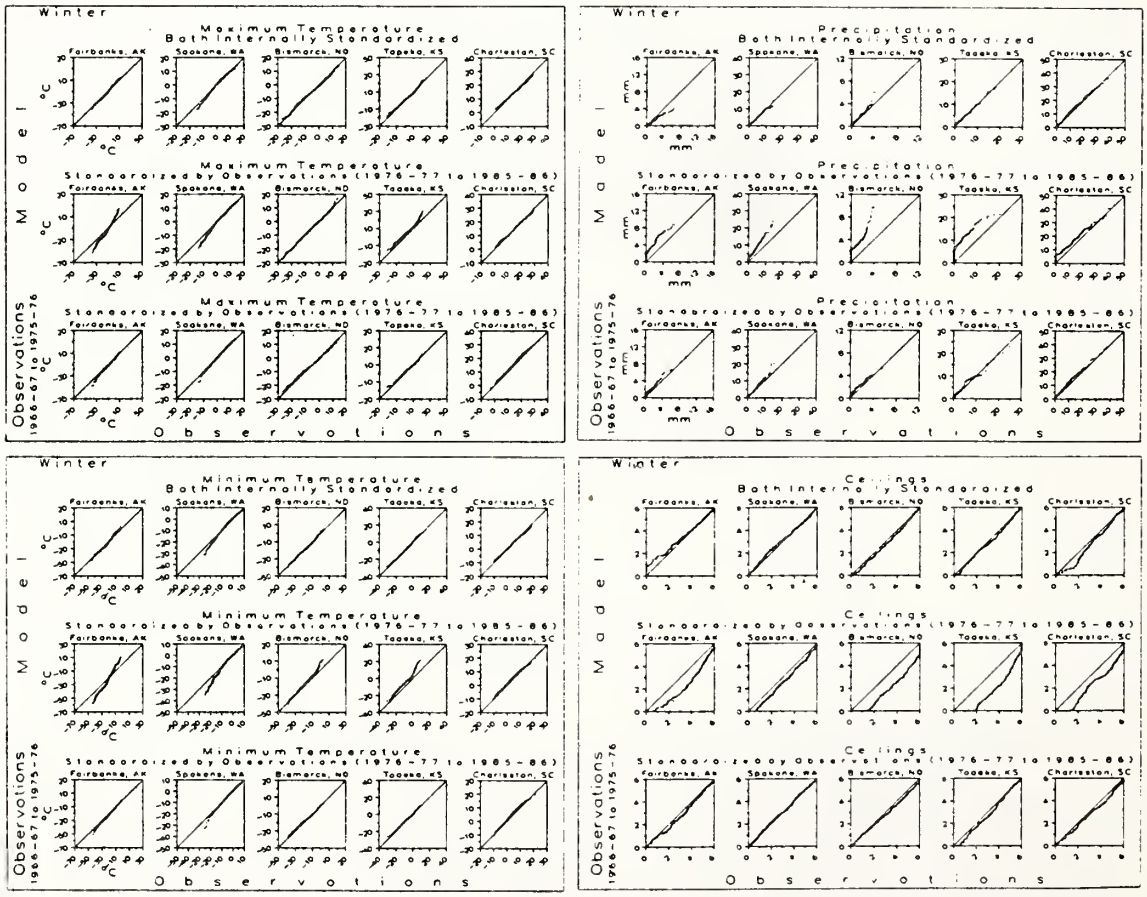

Quantile-quantile plots of the inflated regression predictions from the OSU model output and the observational data during winter.

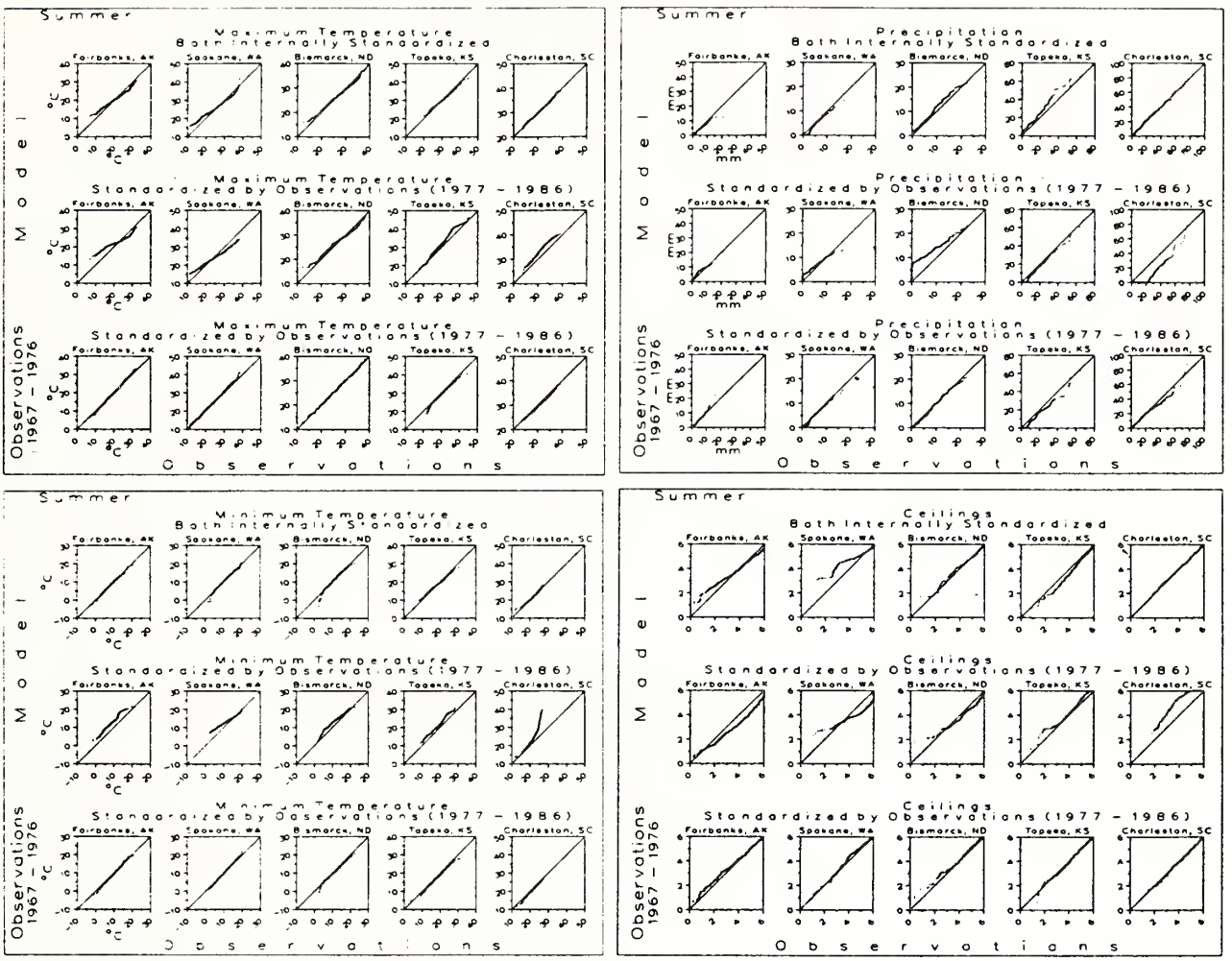

Quantile-quantile plots of the inflated regression predictions from the OSU model output and the observational data during summer.

Regional Climate Characteristics: A Comparison Between Observations and General Circulation Model Statistics

David A. Portman and Wei-Chyung Wang
Atmospheric and Environmental Research, Inc.
840 Memorial Drive
Cambridge, MA 02139

Thomas R. Karl
National Climatic Data Center
NESDIS/NOAA
Ashville, NC 28801

General circulation models (GCM's) have been used to examine the response of the earth's climate to increasing atmospheric CO_2. Understanding how well models reproduce the current climate on a regional basis increases our confidence in using the GCM for predicting CO_2-induced future regional climate change. Although many studies comparing GCM simulations with observations have focused on average statistics for large-scale domains of time (e.g. annual, seasonal and monthly means) and space (e.g. global, hemispheric and zonal means), much of the interest in GCM simulations of current climate and in their predictions for double CO_2 climate is in the shorter-term daily and weekly fluctuations on local and regional spatial scales.

Here we explore means of comparing model with observations by focusing on day-to-day fluctuations of upper air temperature at individual GCM gridpoints and observational stations. Comparing upper air data is more straightforward than comparing surface data since the upper atmosphere is relatively free from the influences of surface topography. We compare 10 years of temperatures simulated by the NCAR Community Climate Model (CCM1) for three U.S. gridpoints with 30 years of observations at nearby stations. Names and locations of stations and gridpoints are indicated in Table 1 and their relative positions are shown in Fig. 1. Stations located within the same gridbox have similar surface climatologies with respect to summer and winter mean surface temperature and precipitation.

We have computed winter (December-January-February) and summer (June-July-August) temperature statistics for three levels of the atmosphere by averaging values calculated independently for the three decades 1957-66, 1967-76 and 1977-86. Some typical values of the mean and variance of daily temperature are shown, respectively, in Figs. 2 and 3 for the eastern-most station in each gridbox (station A in Fig. 1). Differences in mean and variance between station A and the second station in each gridbox (B in Fig. 1) are shown in Figs. 4 and 5. We find that mean temperatures for the two stations in each gridbox typically differ by as much as 4°C at the lower levels of the atmosphere and by smaller amounts higher up. Variance (standard deviation) of daily temperature at single stations is usually less than 10°C and, with few exceptions, wintertime variance is greater than summertime variance. Station-to-station differences in variance are typically less than 10% of the variance at any one station.

To directly compare the observations with the model, we averaged together means and variances of the observed temperatures for the two stations in each gridbox. We then computed similar statistics for the model using 10 years of CCM1 temperatures at each gridpoint and subtracted them from the corresponding observed values. Results are shown for mean daily temperature in Fig. 6 and for variance of daily temperature in Fig. 7. CCM1 temperatures are consistently cooler than the observations, although agreement improves with height. CCM1 variance is less than the observed variance during winter, but is typically greater than the observed variance during summer. These discrepancies between model and observed statistics indicate important differences in their seasonal temperature cycles.

In order to more closely examine the CCM1 and observed seasonal temperature cycles, we have composited daily temperatures for each day of summer and winter. This technique suppresses the high frequency day-to-day noise while enhancing longer term monthly and seasonal fluctuations inherent in the data. Resulting composite curves are shown in Fig. 8 for 300 mb temperatures over the Midwest U.S. Clearly, the most obvious differences between the model and observations occur during summertime. Since the phase of the model seasonal cycle lags that of the observations by between 20 - 30 days and since the model remains several degrees cooler than the observations for over half the season, it follows that the model's seasonal mean temperature is cooler than the observed seasonal mean. Furthermore, the larger range of the CCM1 temperature about it's mean implies that the seasonal variance of temperature in the model is greater than the observed seasonal variance.

We have presented a comparison of daily NCAR CCM1 temperatures at single gridpoints with observations at individual stations. We have found that the model is consistently cooler than observations. Closest agreement occurs at the higher levels of the atmosphere above 500 mb. We have also found some differences between the CCM1 and observed seasonal temperature cycles. Compositing temperatures on a daily basis reveals that a phase lag between their respective seasonal cycles is one source of these inconsistencies. This finding demonstrates the importance of using daily data to compare GCM's with observations.

Acknowledgment

This work was supported by a grant from the Carbon Dioxide Research Division of the Department of Energy (DE-FG02-86-ER60422).

Table 1. NCAR CCM1 gridboxes and observational stations. For each gridbox, positions and elevations of the central gridpoint and nearby stations are indicated. Surface climatological data are averages for 1951-1980 taken from Monthly Climatic Data for the World.

NAME	NORTH LATITUDE	WEST LONGITUDE	HEIGHT (m)	TEMP (°C) DJF	TEMP (°C) JJA	PREC (mm) DJF	PREC (mm) JJA
NORTHWEST	46°40′	120°00′	941				
Spokane WA	47°40′	117°25′	721	-1.7	19.1	167	64
Portland/Salem OR	44°57′	123°01′	61	5.5	19.3	461	80
MIDWEST	37°48′	97°30′	556				
Topeka KS	39°02′	95°41′	270	-0.7	24.7	80	333
Dodge City KS	37°45′	100°02′	790	0.7	25.3	36	224
SOUTHEAST	33°20′	82°30′	116				
Charleston SC	32°48′	79°58′	13	9.6	26.3	250	517
Atlanta GA	33°45′	84°23′	312	6.0	24.9	355	306

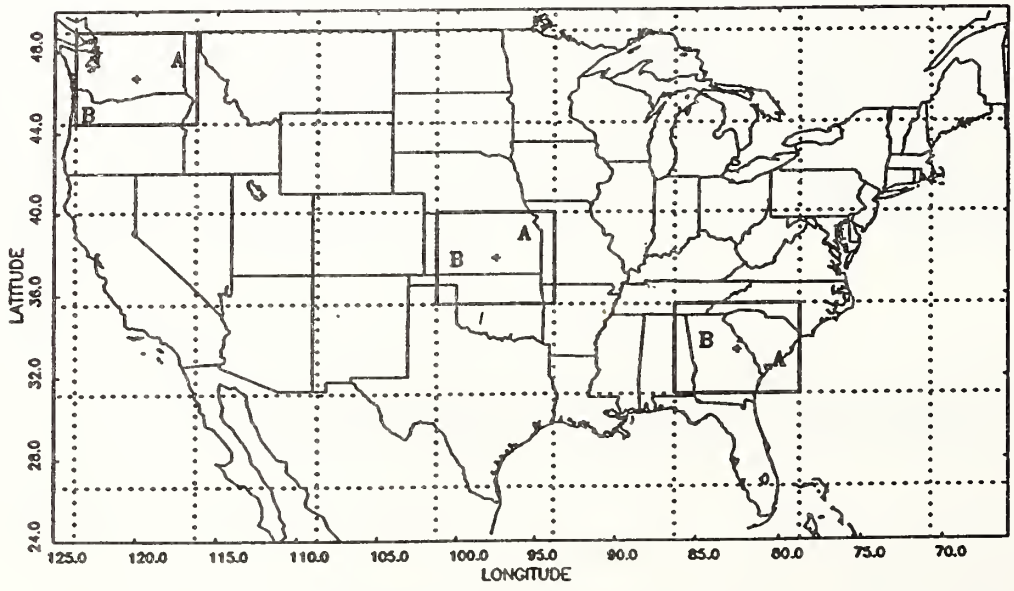

Fig 1. U.S. map showing locations of CCM1 gridboxes and observational stations. Upper air rawinsonde stations (labeled A and B) lie east and west of the central gridpoint in each gridbox. Latitudes, longitudes and surface elevations of gridpoints and stations are summarized in Table 1.

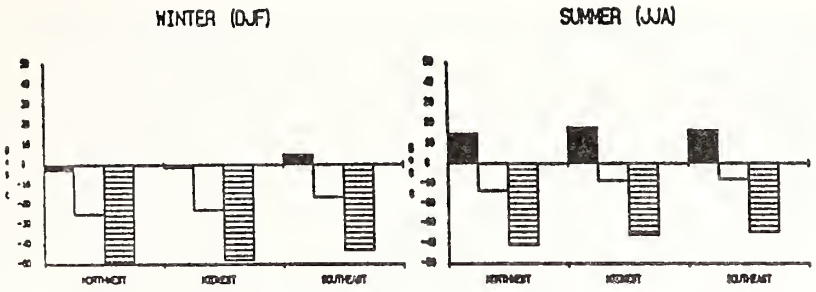

Fig. 2. Observations of daily mean temperature at station A in each gridbox averaged over 30 years (1957-1986) for 850 mb (▮), 500 mb (▯), and 300 mb (▯): (a.) winter and (b.) summer. See Table 1 and Fig. 1 for locations of stations and gridboxes.

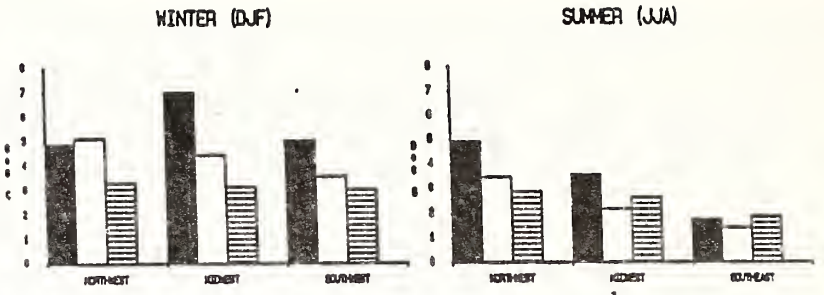

Fig. 3. Variance (standard deviation) of daily temperature at station A in each gridbox based on 30 years of observations (1957-1986) for 850 mb (▮), 500 mb (▯), and 300 mb (▯): (a.) winter and (b.) summer.

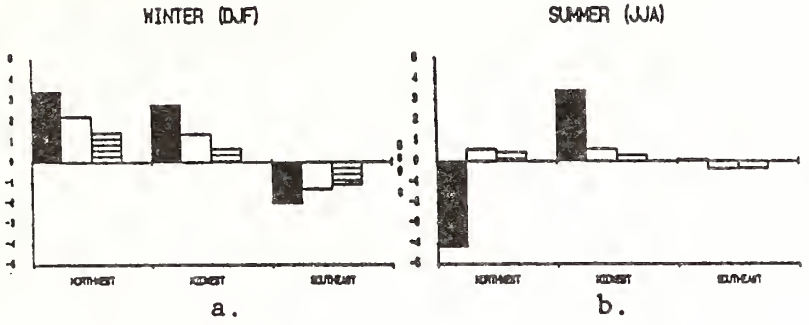

Fig. 4. Difference in 30-year averages of daily mean temperature at the two stations in each gridbox (station B minus station A) computed for 850 mb (▮), 500 mb (▯) and 300 mb (▯): (a.) winter and (b.) summer.

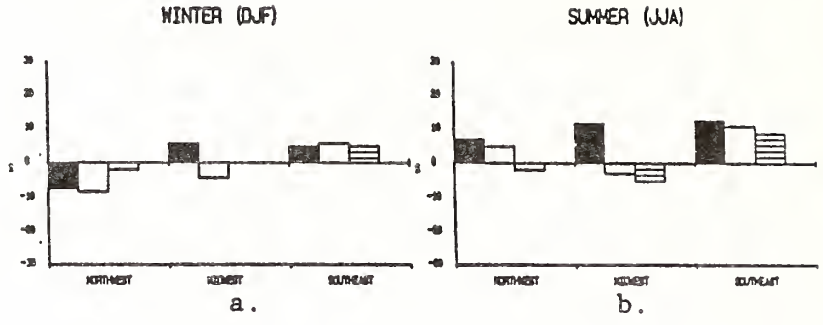

Fig. 5. Difference in 30-year variance of daily temperature at the two stations in each gridbox (station B minus station A) expressed as a percentage of the variance at station A for 850 mb (▮), 500 mb (▯),and 300 mb (▯): (a.) winter and (b.) summer.

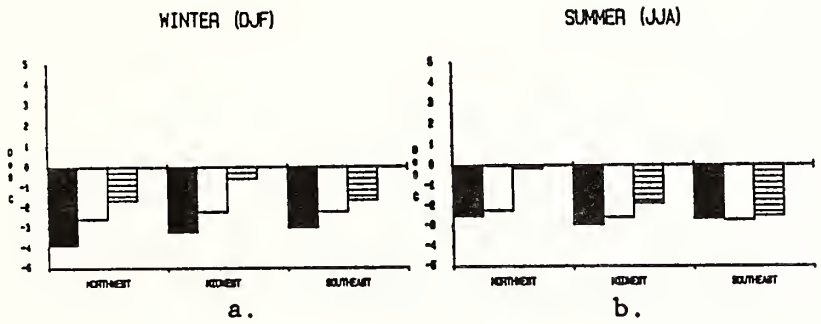

Fig. 6. 10-year averages of daily mean temperature at single CCM1 gridpoints minus 30-year averages of observed temperatures in each gridbox for 850 mb (▮), 500 mb (▯), and 300 mb (▯): (a.) winter and (b.) summer. See Fig. 1 for location of CCM1 gridboxes.

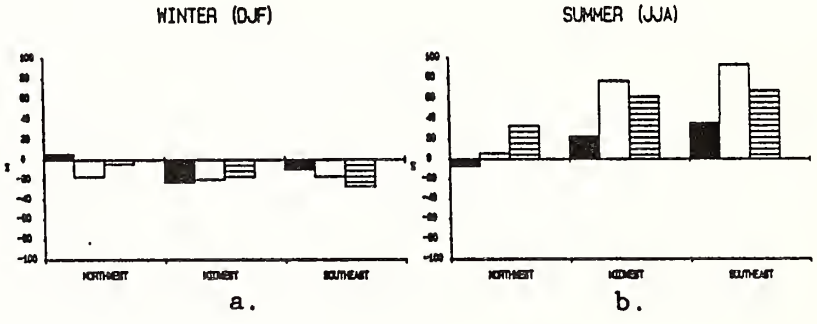

Fig. 7. Variance of daily temperature at single CCM1 gridpoints minus variance of the observed temperatures expressed as a percentage of the observed variance in each gridbox for 850 mb (▮), 500 mb (▯), and 300 mb (▯): (a.) winter and (b.) summer.

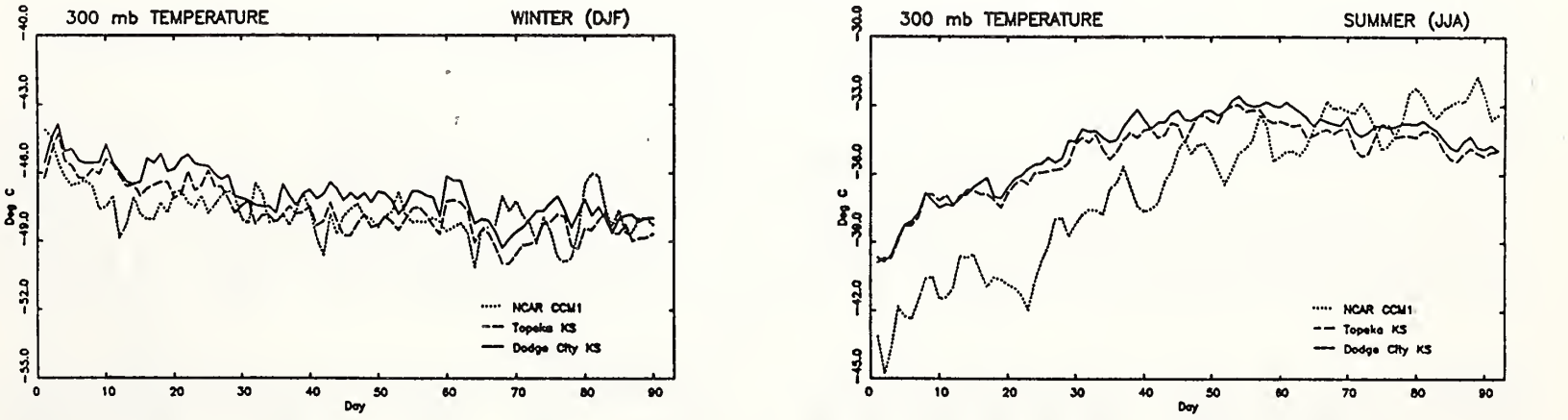

Fig. 8. Composite daily 300 mb temperatures in the MIDWEST gridbox for (a.) winter and (b.) summer. Daily CCM1 data (dotted line) are averaged over 10 years for the gridpoint located at 37°48'N latitude, 97°30'W longitude. Observations are averaged over the period 1957-1986 for stations Topeka, KS (dashed line) and Dodge City, KS (solid Line).

Multiple Recurrence Analysis

Francis W. Zwiers
Canadian Climate Centre
Downsview, Ontario, Canada M3H 5T4

Hans von Storch
Max Planck Institut für Meteorology
Hamburg, F.R. Germany

1. Introduction

Ordinary statistical procedures for the comparison of two climates are generally based on point and interval estimates of the difference of means and corresponding tests of significance. While such objective procedures are a useful part of any analysis comparing a simulated climate with observations or another simulated climate, they do not paint a complete picture of the differences and may in fact obscure important information about the strength of the difference between two climates.

In particular, estimates of the difference between two mean states do not reveal, in an objective way, whether the observed pattern of differences can be recognized as a characteristic of individual realizations of the "experimental" climate. (Our discussion will be in terms of a climate experiment in which there is a "control" simulation and an "experimental" simulation which, for example, may have been forced by anomalous sea surface temperatures (SSTs) or may have an atmosphere of a different composition as in a CO_2 experiment). Tests of the significance of the difference of means also fail to address this question. Such tests are particularly difficult to interpret because the size of difference which can be perceived to be significant by testing procedures depends upon sample size. Even small, physically insignificant differences will be declared to be significant given large enough samples.

The correct interpretation of the word "significant" (from a statistical point of view) is that the observed difference is "unusual"; (i) relative to the null hypothesis that the means are equal, and (ii) relative to the statistical model which is implicit in the testing procedure. The fact the a difference is determined to be "significant" is only a flag that the difference is measurable in some statistical sense, and that it may bear further investigation. We propose that such further investigation should include statistical procedures which are addressed to the question "Are there characteristics of the experimental climate which can be recognized in every realization of the experimental climate?". In many experiments, such as El-Niño sensitivity experiments, it is such differences which provide the important clues to our understanding of the response mechanism.

We have developed procedures for estimating how "recurrent" an estimated response is, and for testing hypotheses about the degree of recurrence. We say that a response is P-recurrent if the probability that an unknown climate realization either either the control climate or the experimental climate is correctly classified is P. A complete description of the techniques and their derivation may be found in Zwiers and Storch (1988; hereafter referred to as ZS).

2. Recurrence Estimation and Testing Techniques

The recurrence estimators which we have developed are based on Multiple Discriminant Analysis (MDA) methodology. The MDA literature is replete with descriptions of many "misclassification error rate estimators" which can be exploited as recurrence estimators. We give a very brief overview of some of the relevant ideas. In the Gaussian setting, a difference between two climates is P-recurrent if the control and experimental climate means, say μ_c and μ_e are separated by Mahalanobis distance $\Delta^2 = (\mu_e-\mu_c)^t\Sigma^{-1}(\mu_e-\mu_c)$ where Σ is the common variance- covariance matrix and where Δ is related to P through the relation $P=\Phi(\Delta/2)$. Here $\Phi(\cdot)$ represents the Gaussian cumulative distribution function. Thus P can be estimated by estimating Δ. A very efficient, and nearly unbiased estimate of Δ^2 can be had by replacing μ_e, μ_c and Σ^{-1} with their respective unbiased estimators. The result is the so-called DS estimate of Δ^2 which is given by $DS = [(n_e+n_c-k-1)/(n_e+n_c-2)]\cdot(\bar{x}_e-\bar{x}_c)^tS^{-1}(\bar{x}_e-\bar{x}_c)$ where n_e and n_c are the control and experimental climate sample sizes respectively, $\bar{x}_e$ and $\bar{x}_c$ are the corresponding sample means, k is the dimension of the observed climate state vectors and S is the usual pooled estimate of the variance-covariance matrix of the observed state vectors. Other "parametric" estimators of Δ^2 which we have studied include the "D-method" (which is optimistically biased) and the "M- and OS-methods" which are both based on asymptotic expansions. The latter two are computationally more complex than DS but have about the same statistical properties.

"Non-parametric" estimators can also be constructed through the application of the "linear discrimination function" (see ZS). The so called "R-method" estimator is constructed by estimating a discrimination rule and using it to classify the observations in both samples. As one might expect, this estimator is optimistically biased. This problem is effectively cured with the "U-method" estimator. Here a single observation is deleted from one of the two samples. Then all remaining observations are used to specify a discrimination rule which is then used to classify the withheld observation. This process is repeated for all observations in the two samples, and the proportion correctly classified is used as the estimate of P. The literature also contains descriptions of several estimators which are based on the bootstrap procedure. The nonparametric estimators are generally more robust than their parametric counterparts, but they are somewhat less efficient and their estimates of P are somewhat more variable.

Parametric and non-parametric tests of a priori specified values of P can also be constructed. The parametric approach is a modification of the usual Hotelling T^2 test for equality of means, the difference being that the observed value of the test statistic is compared to the critical values of a <u>non-central</u> (rather than central) F distribution. The non-centrality parameter, and consequently the critical values, increase with the value of P specified in the null hypothesis <u>and</u> the sample sizes. The result is that much stronger evidence is required to conclude that an experimental response is significantly greater than P-recurrent than is needed to conclude that the response is significant in an ensemble mean sense.

3. An Application

In ZS we describe an application of recurrence analysis to a sequence of El-Niño sensitivity experiments conducted with the Canadian Climate Centre General Circulation Model. Details of the results of the experiment may be found in Boer (1985) and Storch and Zwiers (1988). The experiment consists of three sets of five climate simulations with anomalous SST distributions. Specifically, the observed 1982/83 December/January/February (DJF) SST distribution and two simulated SST distributions with anomalies corresponding to +2 and -2 times the standard Rasmuessen and Carpenter (RC) SST anomaly were imposed. Samples of five DJF 500 mb height fields were obtained from each experiment and compared with a sample of 76 DJF 500 mb height fields obtained from 3 extended climate simulations with prescribed annually varying climatological SSTs.

Comparisons between control and experimental climates were made in two latitude bands ($30^{\circ}S$ - $30^{\circ}N$ and $60^{\circ}S$ - $60^{\circ}N$) using two EOF truncations (EOFS 1-5 and EOFS 1-10 of the 76 control climate realizations). The severe reduction of dimensionality is required because the techniques described above are "multivariate". An additional side benefit of a recurrence analysis in this case is that discrimination rules are produced which may be used to test the fidelity of the model's response to the experimental SST conditions. We tested these rules by applying them to a set of observed DJF mean NH 500mb height anomalies. The general findings of the analysis are:

- in the $30^{\circ}S$ - $30^{\circ}N$ band the response is significant, and also significantly greater than 84%-recurrent. In fact, estimates of P ranged from 98% to almost 100%. "Sun dial" plots of the response indicate that the +2xRC and 82/83 SST anomaly responses have somewhat different structure (the signal is not projected onto the same set of EOFs) although they are of comparable magnitude as measured by P or the T^2 statistic. Such plots also show that the broad structure of the response to the cold SST anomaly is opposite to that of the response to the 82/83 anomalies. In all cases it is possible to characterize the response in such a way that individual realizations can be easily identified.

- in the $60^{\circ}S$ - $60^{\circ}N$ band the response is also significant but not significantly greater than 84% recurrent. Estimates of P ranged between 83% and 93%. In this large region, the first 10 EOFs characterize primarily temperate, northern hemisphere features of the control climate. It is thus not surprising that the response is not found to be strongly recurrent.

- discrimination rules based on the model's response in a $20^{\circ}N$ - $30^{\circ}N$ latitude band were remarkably successful at distinguishing between warm and non-warm years (using the +2xRC experiment) and cold and non-cold years (using the -2xRC experiment) when the rules were used to classify observed DJF NH 500mb height anomalies derived from (mostly) NMC analyses made between 1955 and 1984. Classifications were somewhat less successful with the discrimination rules derived from the 82/83 experiment. This is perhaps due to the difference in structure between the model's responses to the +2xRC and 82/83 SST anomalies. The success of these rules is a strong indication of the fidelity of the model's response to anomalous SST's.

4. Summary

We have shown that recurrence analysis is a powerful tool with which to extract more information from climate comparison studies. Not only do we learn about the significance of a response, but we also obtain information about the relevance to the response to individual climate realizations. In some climate experiments it may also be possible to use discrimination rules that arise from a recurrence analysis to test the fidelity of the model's response to anomalous conditions by applying the rules to archives of climate data. The use of recurrence analysis has been illustrated by applying it to a set of El-Niño sensitivity experiments conducted with the Canadian Climate Centre General Circulation Model.

5. References

Boer, G.J., 1985: Modeling the Atmospheric Response to the 1982/83 El Niño. **Coupled Ocean-Atmosphere Models**, J.C.J.Nihoul, editor, Elsevier, Amsterdam, 7-17.

Storch, H. von and F.W. Zwiers, 1988: Recurrence Analysis of climate sensitivity experiments. **J. Climate, 1,** 151-171.

Zwiers, F.W., and H. von Storch, 1988: **Multiple Recurrence Analysis.** Report No. 17, Max Planck Institut für Meteorologie, Bundesstraße 55, D 2000 Hamburg 13, F.R. Germany. 49pp.

VORTICITY BUDGET OF THE UPPER TROPICAL TROPOSPHERE AS EVALUATED FROM NMC ANALYSES

E. M. Rasmusson
Cooperative Institute for Climate Studies
University of Maryland
College Park, Maryland 20742

and

K. Mo
Climate Analysis Center
NMC/NWS/NOAA
Washington, D. C. 20233

1. Introduction

Both observational and model studies provide persuasive evidence that the tropical regions of large-scale convection are associated with low-latitude sources of Rossby waves, which result in global standing wave patterns, i.e. teleconnections. These sources arise as a result of non-linear interactions between the upper-tropospheric divergent and rotational components of flow. This preliminary study had as its main objective the evaluation of the usefulness and limitations of current NMC analysis products for diagnosing low frequency variability forced from the tropics.

We followed the diagnostic approach of P. D. Sardeshmukh and B. J. Hoskins (Q. J. Roy. Met. Soc., 111, 261-278 (1985); 113, 339-360 [1987]). Using ECMWF analyses, they showed that for seasonal averages at 150 mb, (1) the vertical advection, twisting, and frictional terms, as well as the time derivative, are small enough to be neglected, and (2) the contribution of the transient correlation terms is small, but not totally negligible. Consequently, the time averaged vorticity balance at the level of cumulus outflow in the tropics (150-200 mb) is closely approximated by:

$$\overline{\underset{\sim}{V_\psi} \cdot \nabla(\zeta + f)} = \bar{S} \qquad (1)$$

where:

$$\bar{S} = -\overline{\nabla \cdot (\underset{\sim}{V_\chi}(\zeta + f))} = -\overline{(\zeta + f)\nabla \cdot \underset{\sim}{V_\chi}} - \overline{\underset{\sim}{V_\chi} \cdot \nabla(\zeta + f)} \qquad (2)$$

$\bar{S}$ is the vorticity source term, $\underset{\sim}{V_\psi}$ is the rotational component of flow, $\underset{\sim}{V_\chi}$ is the divergent component of flow, $\zeta + f$ is the vertical component of absolute vorticity, and $\overline{\ }$ indicates a time mean.

For non-divergent flow, the advection of absolute vorticity by the rotational component of flow is balanced by the local time derivative, which is near zero when averaged over a season. Thus, a non-zero value on the left side of Equation 1 implies a non-zero source term on the right side. This source term can be separated into two parts (Equation 2): the vortex stretching term and the advection of absolute vorticity by the divergent component of flow. Both sides of Equation 1 can be evaluated from accurate analyses of the

rotational and divergent components of flow. The degree of imbalance between the right and left sides is a measure of the inconsistency between the rotational and divergent component analyses.

2. Results and Conclusions

We evaluated 3-month mean values of both sides of Equation 1 from NMC 200 mb analyses for the periods January-March and July-September 1987 and 1988. Only results for Jan.-Mar. 1988 are shown and discussed to illustrate the general findings. The following conclusions are in agreement with the conclusions of Sardeshmukh and Hoskins from ECMWF analyses.

a. The advection of absolute vorticity by the divergent component of flow (Figure 1) makes a significant contribution to the source term, and must be evaluated along with the stretching term in order to accurately describe the nature of the tropical Rossby wave source.

b. The Rossby wave source $\bar{S}$ (Figure 2b) extends over much larger areas than does the convective heating (tropical divergent regions of Figure 3). The source is most pronounced not over the convective regions of the deep tropics, where the magnitude and gradients of absolute vorticity are small, but rather on the equatorward flanks of the subtropical westerlies, in the vicinity of the downward branches of the regional Hadley circulations, where both the magnitude and gradient of absolute vorticity is much larger.

c. Over large portions of the tropics, relative vorticity anomalies produce only slight modifications of the climatological field of absolute vorticity, i.e., in the vicinity of the East Asian Jet. Consequently, the position of an anomalous vorticity source is determined, to a significant degree, by the climatological contribution to the non-linear terms of Equation 1, and can be relatively insensitive to the longitudinal position of the heating and upper troposphere divergence anomalies. The predicted source anomaly and atmospheric response can be significantly in error if the climatology of the rotational component of flow is misrepresented.

Using the χ problem procedure described by Sardeshmukh and Hoskins (1987), we expressed the imbalance between the two sides of Equation 1 as the difference in the time-averaged divergence needed to bring them into balance. Sardeshmukh and Hoskins found this difference to be relatively small for ECMWF 150 mb analyses, indicating good consistency between the analyzed rotational and divergent wind fields. The differences for the current NMC analyses are much larger. During the northern winter, the analyzed divergence field shows stronger regional Hadley circulations than that implied by the time-averaged rotational flow, particularly over Brazil and the tropical Atlantic. The divergent wind field also shows a weaker Walker circulation over the tropical Pacific. The question of the source of this inconsistency, whether it is due primarily to errors in the analyzed divergent or rotational component of flow must be determined from other evidence. For the ECMWF analyses, Sardeshmukh and Hoskins concluded that at least some of the features of the derived divergence field had a "more believable structure" than those obtained directly from the analyzed divergent wind field.

While our emphasis is on the tropical belt 30^{o}N-30^{o}S, it should be noted that the source term field exhibits many unrealistic features over the extratropics (Figure 2b). The similar extratropical patterns of Figures 2a and 2b suggest that the extratropical errors result primarily from small errors in the time averaged divergence, which contribute large errors to the vortex stretching term due to the weighting of divergence by the large values of absolute vorticity in the extratropics.

3. Future Work

The current NMC analyses provide important qualitative information on the general nature of the tropical upper tropospheric vorticity balance, but large differences between the computed and implied values of the vorticity source term leave quantitative values in doubt at this time. Thus, the large imbalance in Equation 1 makes it difficult to define the pattern of interannual anomalies, whose amplitude is generally smaller that the equation imbalance. High priority is, therefore, being given to diagnosing the primary source of this imbalance. OLR data can be of considerable value in this analysis, and in a more general way, its use offers the possibility of reconstructing the tropical upper tropospheric divergence field during the 1980s.

Even more demanding is the question of whether the source term can be evaluated accurately enough to diagnose the nature of Rossby wave propagation from the tropics for an observed or hypothesized pattern of heating (divergence) anomalies. This diagnostic problem is the inverse of the χ problem, and is described by Sardeshmukh and Hoskins (J Atmos. Sci., 45, 1228-1251 (1988). Results, thus far, strongly suggest that if such diagnostic or "what if" computations are to be realistic, the vorticity source region must include the downward as well as upward branches of the regional Hadley circulations.

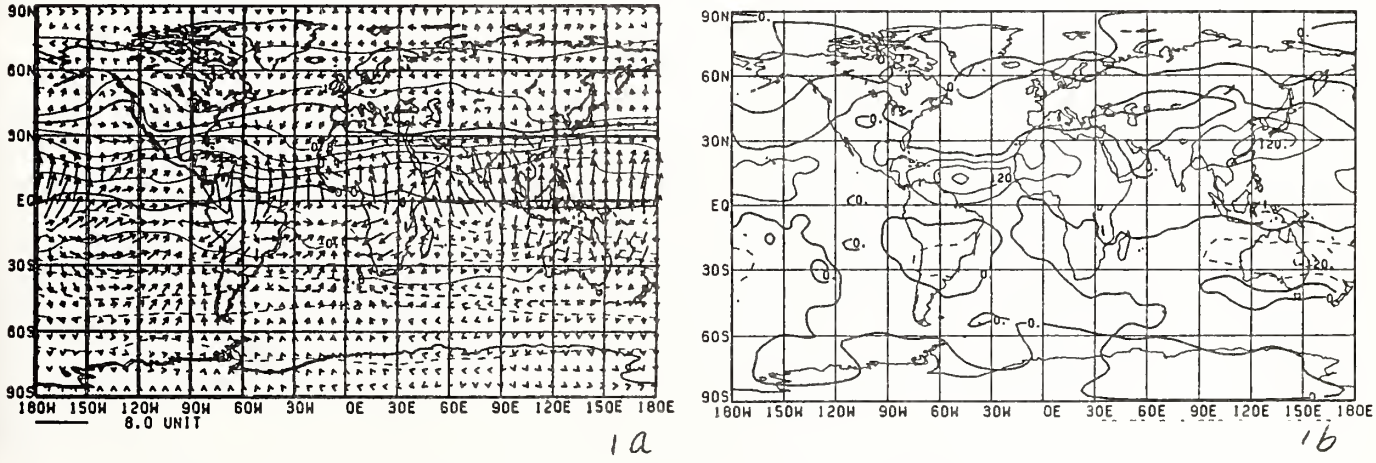

Figure 1. (a) Divergent flow vectors ($\vec{V}_{\chi}$) superimposed on absolute vorticity isolines to illustrate the pattern of vorticity advection by the divergent wind component. Fields are computed directly from the NMC 200 mb analyses for the period January-March 1988. Vorticity contour interval: 10^{-5} sec.$^{-1}$. (b) Directly computed contribution to the vorticity source term by the advection of absolute vorticity by the divergent component of flow ($V_{\chi} \cdot \nabla(\zeta+f)$). Contour interval: 6×10^{-11} sec.$^{-2}$.

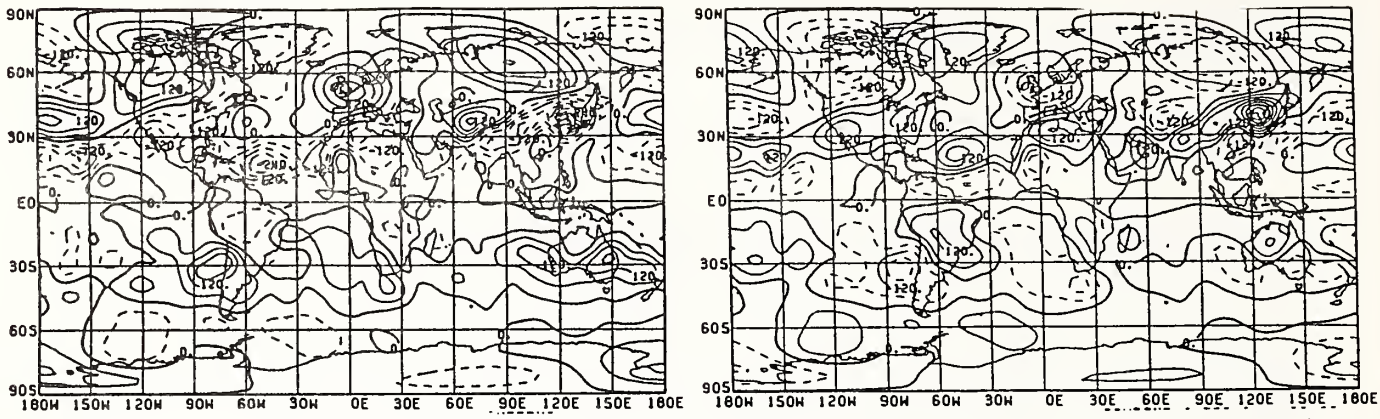

Figure 2. (a) Directly computed contribution to the vorticity source term by the vortex stretching term $(\beta+f)D$. Contour interval: 6×10^{-11} sec^{-2}. Focus should be on the tropical belt 30°N-30°S. Values at higher latitudes do not appear to be reliable (see text).

(b) Computed total vorticity source ($\bar{S}$). Contour interval: 6×10^{-11} sec^{-2}. Focus should be on the tropical belt 30°N-30°S. Values at higher latitudes do not appear to be reliable (see text).

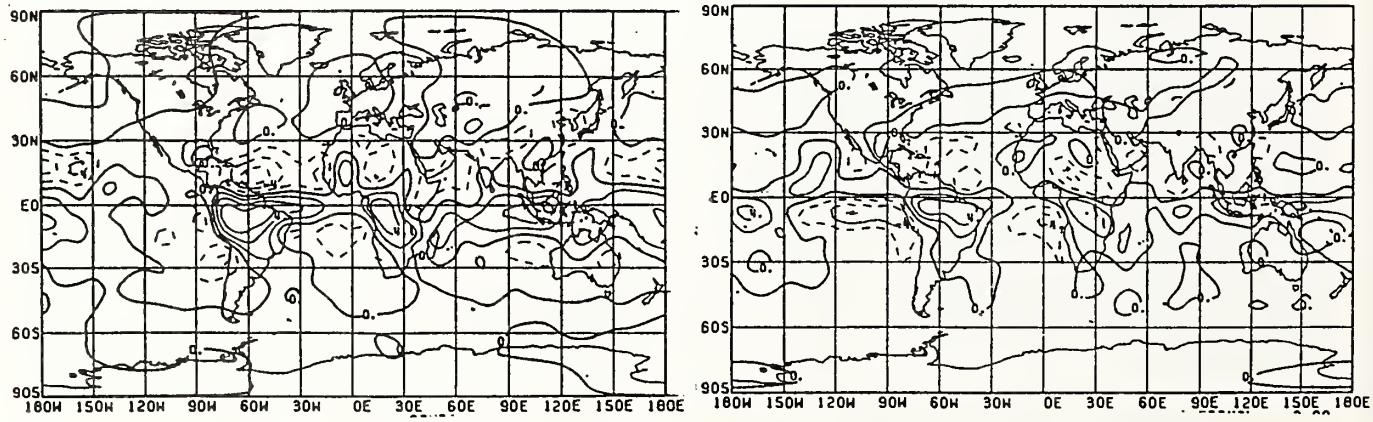

Figure 3. Mean 200 mb divergence field for Jan.-Mar. 1988 as (a)computed directly from NMC analyses, and (b) implied by the left side of Equation 2. Contour interval: 2×10^{-6} sec^{-1}.

A Comparison of Poleward Momentum Transports from GCM Simulations to Observations

R.W Higgins*, C.K Park**
NASA/Goddard Laboratory for Atmospheres
Greenbelt, MD 20771

and

D.M. Straus***
Dept. of Meteorology, University of Maryland
College Park, MD 20742

A diagnostic intercomparison of the poleward transports of momentum in three GCM seasonal cycle simulations and the ECMWF analysis is presented. Using the ECMWF analysis as a verification, we identify several systematic biases in the transports of momentum in these simulations. Moreover, the role of eddies (both stationary and transient) in the total transports in both hemispheres for DJF and JJA is examined.

The role of eddies in maintaining the westerlies in the ECMWF analysis for the years 1979-1982 was first examined by Trenberth (1987). In this study we mimic his Eulerian approach by partitioning the total poleward momentum flux into contributions from the mean circulation, the standing eddies and the transient eddies, so that

$$\overline{[U\ V]} = \overline{[U]}\,\overline{[V]} + \overline{[U^*\ V^*]} + \overline{[U'\ V']} \qquad (1)$$

in which $\overline{\ }$ is a time mean, $'$ is a time departure, $[\ ]$ is a zonal mean, and $*$ is a zonal departure.

As mentioned above, the observational data set we choose is the ECMWF global analysis for 1984-1986. The GCM simulation data sets are the D221 (old GLAS/UMd) two year seasonal cycle run, the UCLA three year seasonal cycle run, and the FLRD (GLA) two year seasonal cycle run. Detailed information on the physics and hydrodynamics in the D221, UCLA, and FLRD (GLA) models may be found in Randall (1982), Randall et al. (1985), and Kalnay et al. (1983) respectively. However, it is important to note that each model is grid point and low resolution (4° latitude by

---

* National Research Council Fellow
** Centel Federal Services Corporation
*** Center for Ocean-Land-Atmosphere Interactions

5° longitude). The D221 and FLRD models have basically the same physics but different finite difference schemes; the UCLA model has both different physics and finite differences from the other two models.

Two sets of time averages were used: four seasonal means and twelve monthly means. Here, seasonal means for December, January, and February (DJF), and June, July, and August (JJA), are shown. Time averages were computed over equivalent periods for each GCM simulation and the analysis.

In Figure 1 we show the combined seasonal zonal wind for DJF and JJA; this quantity has been zonally averaged and vertically integrated. A comparison of the analysis and simulations reveals that the jets are in general too strong in midlatitudes in the simulations, especially in local winter (simulated shear above jet level is opposite to observed), and that there is a westerly bias in the tropics (we note that an easterly bias in the tropics seems to be common in higher resolution models, especially in the upper troposphere). In addition, there is a poleward bias in the northern hemisphere (NH) and an equatorward bias in the southern hemisphere (SH) of the latitude of maximum wind. The simulations capture the interhemispheric asymmetry, which is small in DJF, but quite large in JJA.

In Figure 2 we show the partitioned, combined seasonal poleward momentum flux in DJF; we note that this quantity has been zonally averaged and vertically integrated. In the ECMWF analysis, transient eddies dominate the total transport in the SH; each of the GCM simulations agrees qualitatively with the analysis in the SH. In the analysis in the NH, both transient and standing eddies contribute about equally to the total flux. The partitioning in D221 and FLRD in the NH agrees quite well with the analysis although there are some minor differences in amplitude. However, the partitioning in the UCLA simulation emphasizes the standing eddies too much relative to the transient eddies. We note that the zonal jets in Figure 1, which are quite similar in each of the GCM simulations, gave no indication that there would be a large standing eddy bias in the UCLA simulation.

In Figure 3, we illustrate the spatial nature of the standing eddy bias in the UCLA simulation by comparing the standing eddy in the height field and the standing eddy momentum transport in the ECMWF analysis and the UCLA simulation. A comparison of Figures 3a and 3b reveals that the UCLA simulation captures the locations of the maximum and minimum values of $\overline{Z}^*$ quite well, but the amplitudes are in general too large, especially in the NH. Recall that if the standing eddy $\overline{Z}^*$ is large, then we expect more standing eddy momentum transport $\overline{U}^*\overline{V}^*$ (specifically in the regions where the gradients between maxima and minima are strong), but it is difficult to determine which region in Figure 3b contributes most to the bias. However, Figures 3c and 3d reveal, upon comparison, that much of the bias in the NH in midlatitudes is originating in the tropospheric jet East of the Himalayas.

The partitioned, combined seasonal poleward momentum transport in JJA is shown in Figure 4. In the ECMWF analysis, transient eddies dominate the total transport in both the SH and

the midlatitudes of the NH, in qualitative agreement with the results in Trenberth (1987). In the SH, each of the GCM simulations agrees qualitatively with the analysis. However, in the NH, where the magnitudes are small, the simulations have roughly the right amount of total flux but they tend to have too much standing eddy flux relative to transient eddy flux.

Trenberth (1987) noticed in the ECMWF analysis (JJA, 1979-1982) that the midlatitude westerlies in both hemispheres were maintained mainly by the convergence of westerly momentum by the transient eddies (Eulerian view); this result is also true in the analysis for the years 1984-1986. In JJA, the simulations and the analysis agree qualitatively in the SH. In the NH the FLRD and D221 simulations partition the total convergence rather well, but the UCLA simulation again emphasizes the standing eddy convergence too much (not shown). In Figure 5 we extend this analysis to DJF. As expected, the transient eddy convergence dominates the total convergence in the SH in both the analysis and the models but in the NH there are a number of major differences. Thus in the SH the midlatitude westerlies in both DJF and JJA are maintained by the convergence of westerly momentum by transient eddies in both the analysis and the simulations. However, the midlatitude westerlies in the NH are maintained by a combination of both standing and transient eddies.

In the future, we will focus on the space/time structure of the biases identified here; for example we will apply time filters to the data to determine at which temporal scales these biases occur. In addition, we will assess their sensitivity to model formulation (i.e. physics, hydrodynamics), and develop suitable strategies for their reduction. In this way, we may help to guide model development and at the same time broaden our understanding of intraseasonal atmospheric variability.

REFERENCES:

Kalnay,E.,R. Balgovind, W. Chao, D.Edelmann, J. Pfaendtner, L. Takacs, and K. Takano, 1983: Documentation of the GLAS fourth order general circulation model. NASA Technical Memorandum 86064.

Randall, D.A., 1982: Monthly and seasonal simulations with the GLAS climate model. Proc. Workshop on Intercomparison of Large-Scale Models Used for Extended Range Forecasts, Reading, ECMWF, pp. 107-166.

Randall, D.A., J.A. Abeles, and T.G. Corsetti, 1985: Seasonal simulations of the planetary boundary layer and boundary-layer stratocumulus clouds with a general circulation model. J. Atmos. Sci., 42, 641-676.

Trenberth, K.E., 1987: The role of eddies in maintaining the westerlies in the Southern Hemisphere. J. Atmos. Sci.,44, 1498-1508.

Figure Legends

Figure 1 The combined seasonal zonal wind for a) DJF and b) JJA from the ECMWF analysis and from the UCLA, D221, and FLRD simulations. The winds, which have units of m s^{-1}, have been zonally-averaged and vertically integrated.

Figure 2 The combined seasonal angular momentum flux for DJF from the a) ECMWF analysis; b) UCLA simulation; c) D221 simulation; and d) Flrd simulation. The angular momentum flux, which has units of kg m^2 s^{-2}, has been zonally-averaged and vertically integrated.

Figure 3 The combined seasonal 200 mb standing eddy $\overline{Z^*}$ in DJF in the a) ECMWF analysis and the b) UCLA simulation and the corresponding standing eddy momentum transport $\overline{U^*V^*}$ in the c) ECMWF analysis and the d) UCLA simulation. In (a) and (b) the contour interval is 30 m; the dashed lines indicate negative values and the solid lines indicate nonnegative values. In (c) and (d) the contour interval is 20 m^2 s^{-2}; the dashed lines indicate negative values and the solid lines indicate nonnegative values.

Figure 4 Same as Figure 2, except for JJA.

Figure 5 The combined seasonal convergence of momentum flux for DJF from a) ECMWF analysis; b) UCLA simulation; c) D221 simulation; and d) Flrd simulation. The convergence of momentum flux, which has units of kg m^{-1} s^{-2}, has been zonally averaged and vertically integrated.

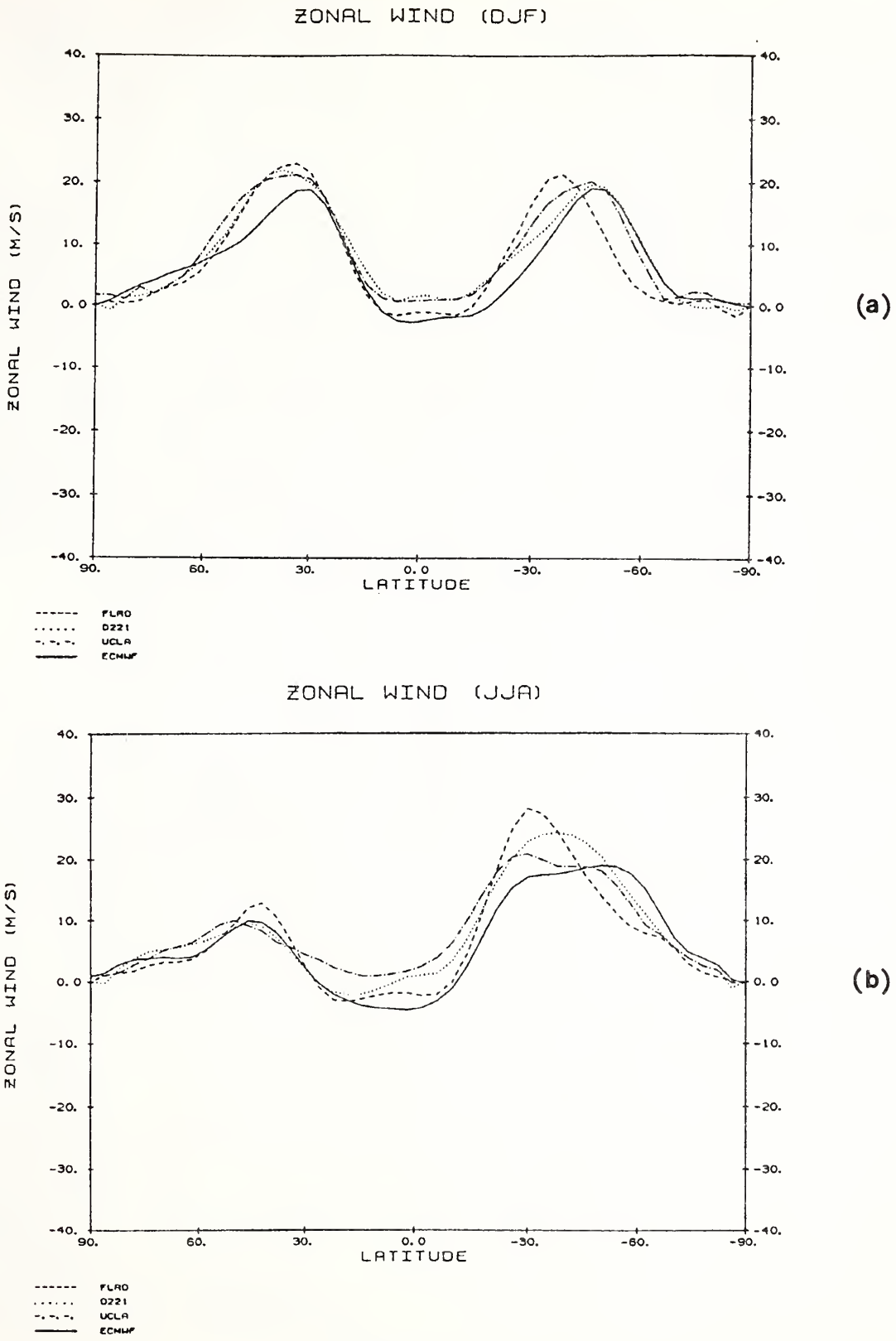
ZONAL WIND (DJF)
ZONAL WIND (M/S)
40.
30.
20.
10.
0.0
-10.
-20.
-30.
-40.
90.
60.
30.
0.0
-30.
-60.
-90.
LATITUDE
FLAO
0221
UCLA
ECMWF
(a)
ZONAL WIND (JJA)
ZONAL WIND (M/S)
LATITUDE
FLAO
0221
UCLA
ECMWF
(b)

Figure 1

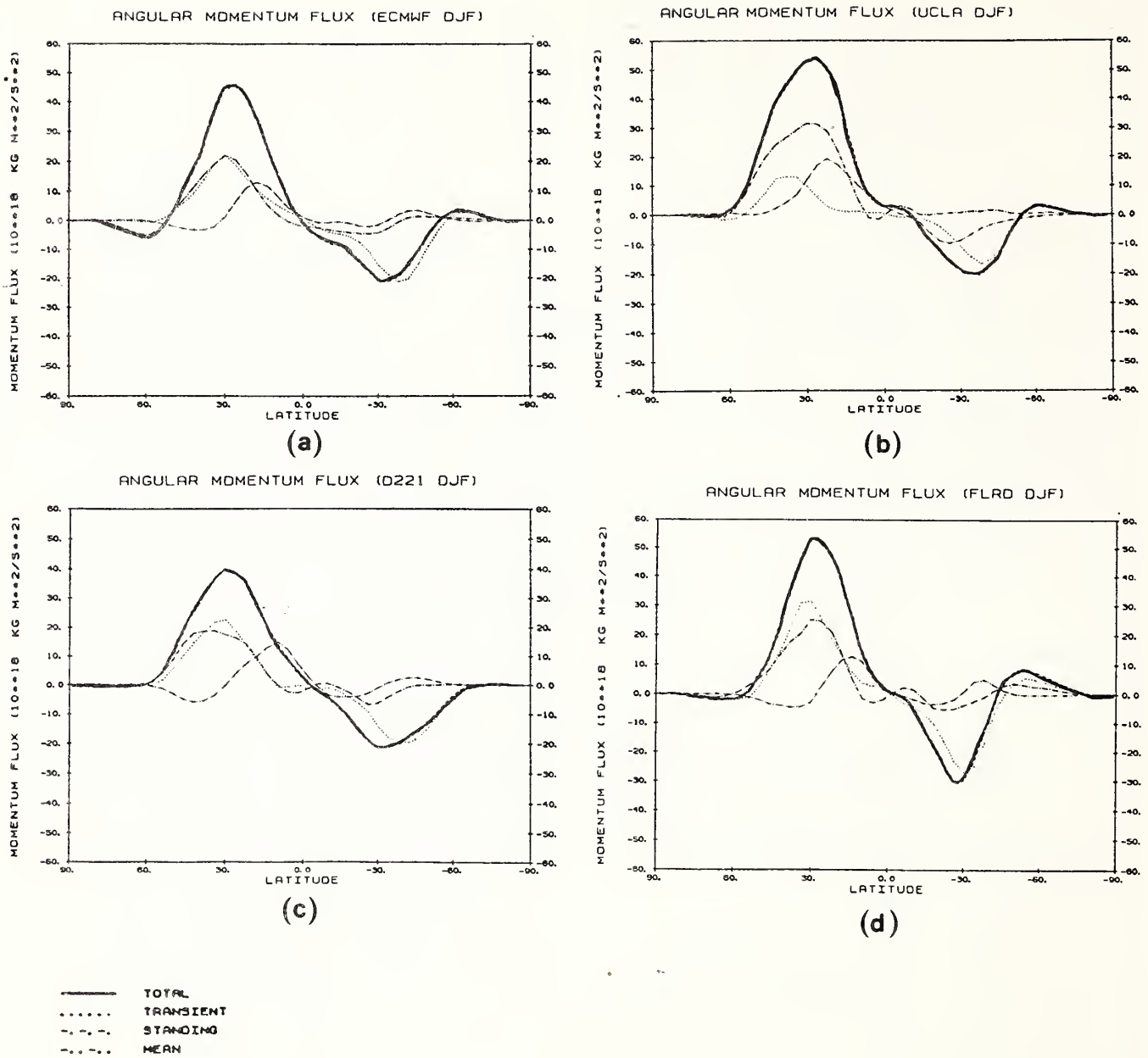
ANGULAR MOMENTUM FLUX (ECMWF DJF)
MOMENTUM FLUX (10**18 KG M**2/S**2)
LATITUDE
(a)
ANGULAR MOMENTUM FLUX (UCLA DJF)
MOMENTUM FLUX (10**18 KG M**2/S**2)
LATITUDE
(b)
ANGULAR MOMENTUM FLUX (D221 DJF)
MOMENTUM FLUX (10**18 KG M**2/S**2)
LATITUDE
(c)
ANGULAR MOMENTUM FLUX (FLRD DJF)
MOMENTUM FLUX (10**18 KG M**2/S**2)
LATITUDE
(d)
TOTAL
TRANSIENT
STANDING
MEAN

Figure 2

200 MB $\overline{Z^*}$ (M)

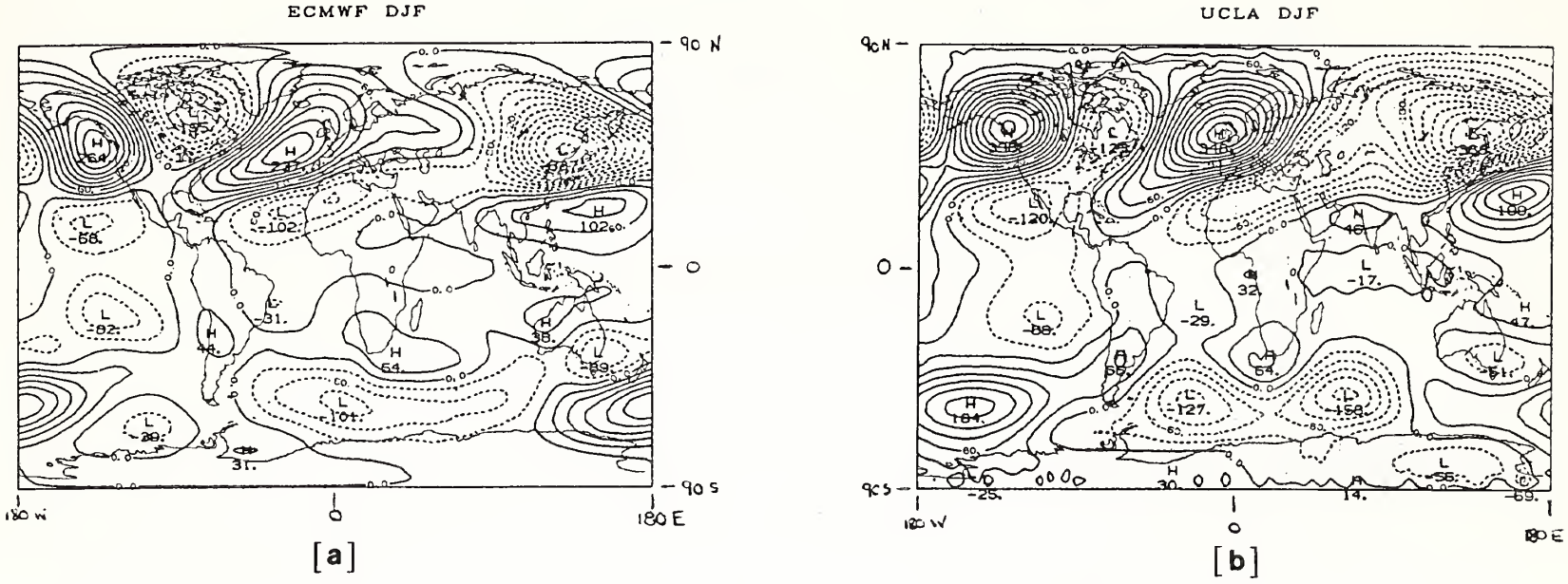

200 MB $\overline{U^*}\,\overline{V^*}$ ($m^2 s^{-2}$)

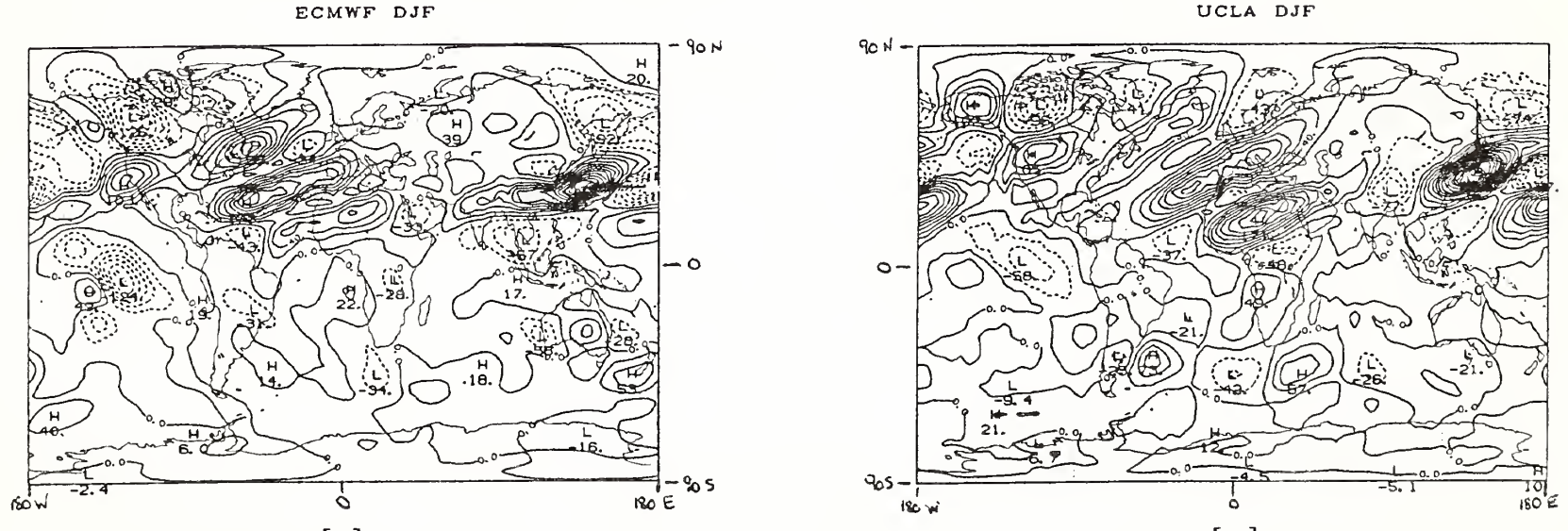

Figure 3

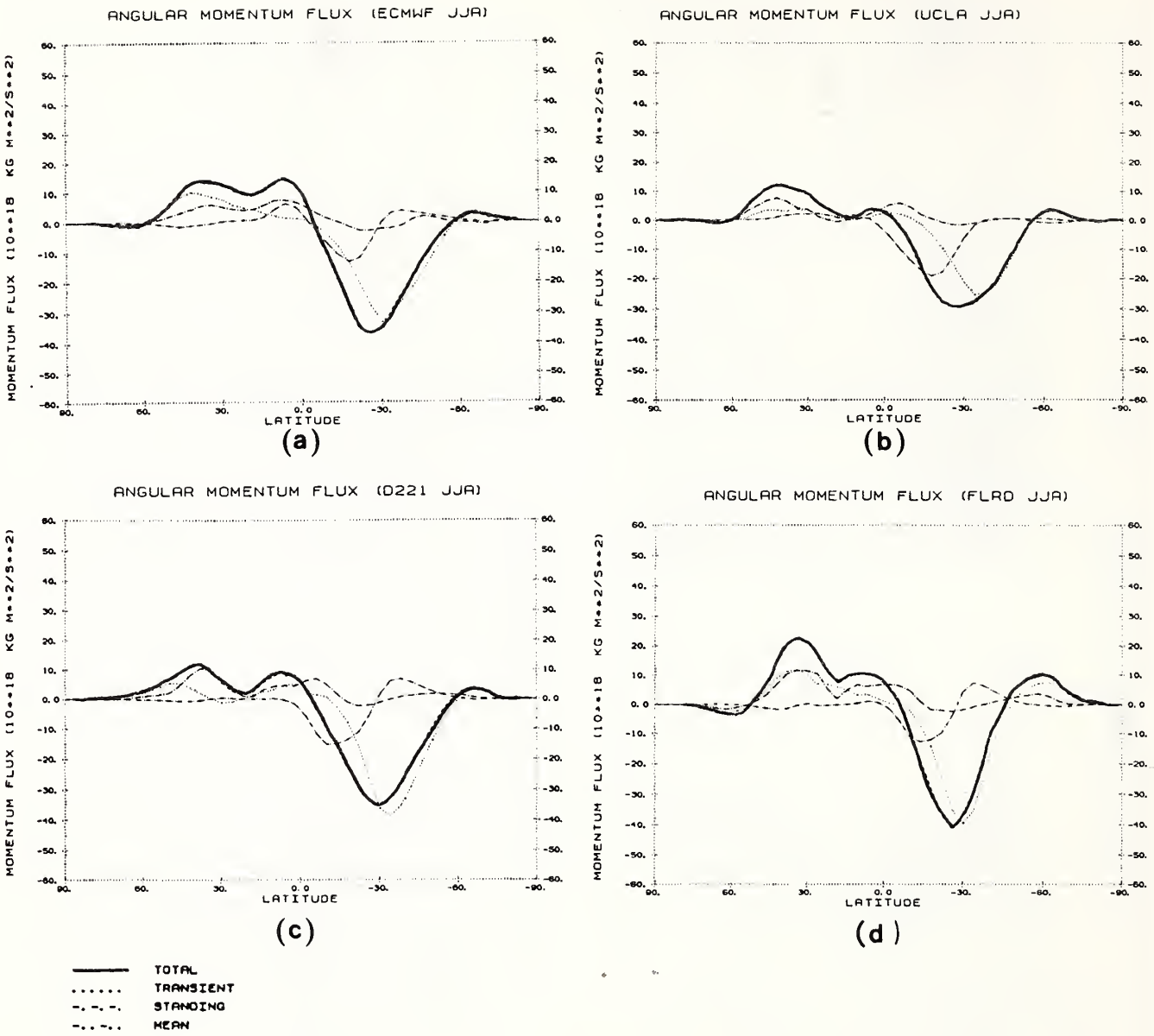
ANGULAR MOMENTUM FLUX (ECMWF JJA)
ANGULAR MOMENTUM FLUX (UCLA JJA)
ANGULAR MOMENTUM FLUX (D221 JJA)
ANGULAR MOMENTUM FLUX (FLRD JJA)
MOMENTUM FLUX (10**18 KG M**2/S**2)
LATITUDE
(a)
(b)
(c)
(d)
TOTAL
TRANSIENT
STANDING
MEAN

Figure 4

CONVERGENCE OF MOMENTUM FLUX

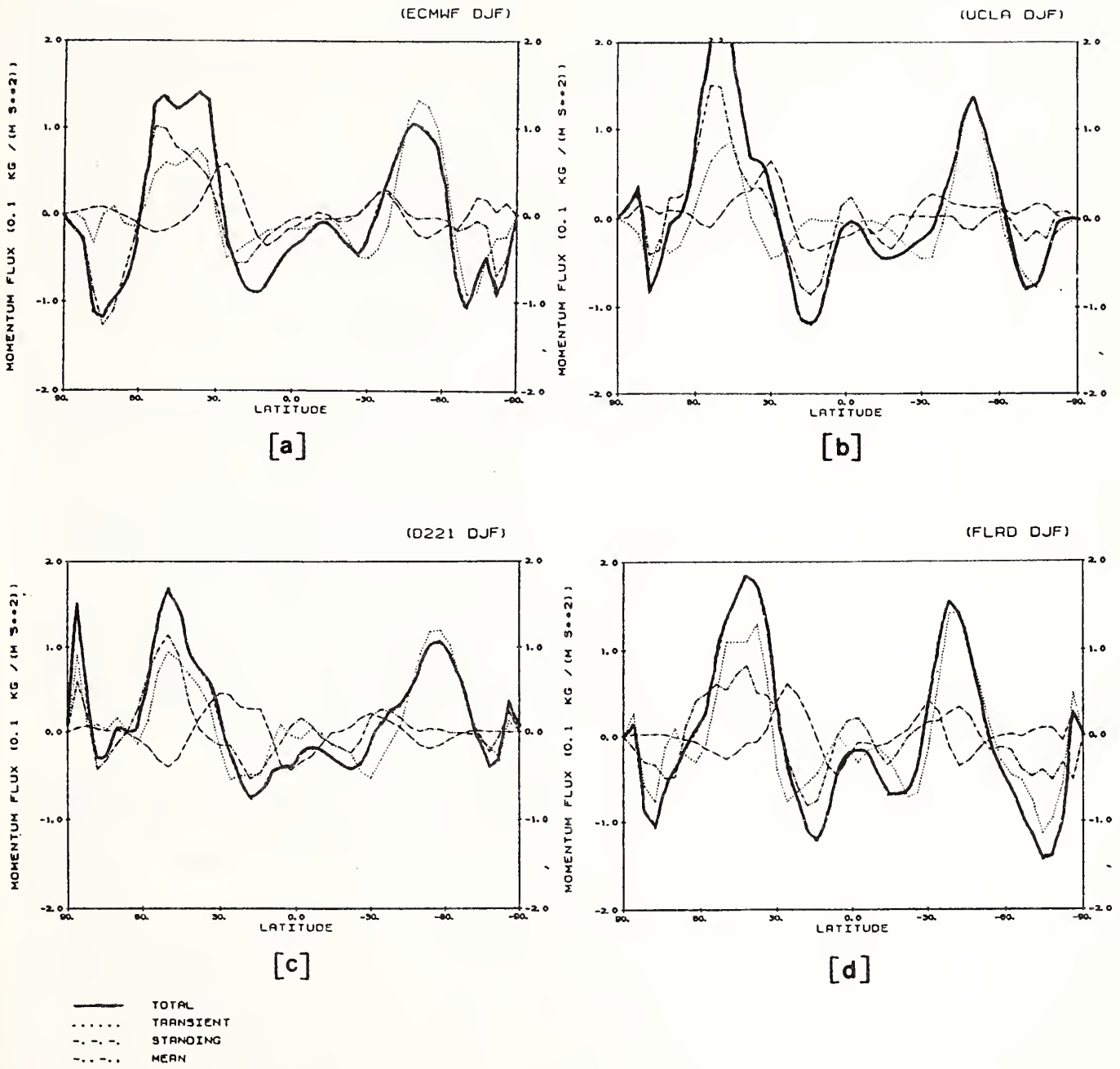

Figure 5

Dynamical Forecasts of the 1986-1987 ENSO with a Coupled Model

Mark A. Cane and Stephen E. Zebiak
Lamont-Doherty Geological Observatory of Columbia University
Palisades, NY 10964

We present a post-mortem of experimental forecasts of the tropical Pacific for the period 1986-1988. Some of the forecasts, which are carried out with a simulation model of the tropical Pacific coupled ocean - atmosphere system, were previously reported in Cane, Zebiak, and Dolan (1986; henceforth CZD) and in Barnett et al (1988).

Details of the model structure and the forecast procedure are given in Zebiak and Cane (1987) and CZD. Our approach to prediction is influenced by our concept of the nature of the ENSO cycle (eg, as discussed in those two papers). In our view, the tropical Pacific is the genesis region for ENSO; it follows that data from this region alone may be sufficient for initializing forecasts. *Inter alia,* success of forecasts which rely on data from this region only is evidence in support of this view. ENSO is a *cycle* of the coupled system; since it is a deterministic process it may be predictable. On the other hand, since it is clearly aperiodic its predictability is limited in principle. Nonetheless, prediction may still be possible for a limited period -- perhaps as long as several years.

Even if possible in principle, prediction may be impossible in practice: the model is highly simplified, and the necessary data is sparse and low quality. Miller and Cane (1988) estimate that the error in a sea level simulation attributable to wind stress errors is 1/2 to 2/3 the observed total sea level variance. According to the theory, the field of anomalies in the heat content (equivalently, sea level or theromocline depth) of the tropical Pacific is the most essential initial condition for the future evolution. Since direct observations of the ocean are inadequate to specify this field, we do so indirectly by forcing the ocean component of the coupled model with observed winds as analyzed at Florida State University. By doing so for a period of time preceding a time t initial conditions at time t are obtained. The only data which goes into the initialization is these FSU winds and, as we shall see, this very minimal data assimilation *cum* initialization procedure can yield very poor initial states. Our forecasting practice is to average the forecasts initiated in 6 consecutive months; thus the forecasts presented below which nominally begin in, say, December, are actually the average of the 6 individual forecasts from December, November, October, September, August, and July.

Fig. 1 compares the observed tropical Pacific sea surface temperature (SST) in January 1987 with the forecast based on data through January 1986, 1 year earlier. This is the same forecast published by CZD some months in advance of the verification period. In general the model does best in the (boreal) winter period. This is discussed further below; (also, viz Fig. 2 of CZD, which shows a 2 year forecast for winter 1982-83).

Fig. 2 shows the forecasts of SST anomalies for the NINO3 region in the eastern Pacific at various lead times. The 9 month lead forecast starts the warming too soon, is correct for the winter of 1986-87, and then cools in the spring while the ocean remains warm. By summer time it recovers, capturing the highly unusual second warming of 1987. Its good performance continues until summer 1988, when it underestimates the cooling event. The 6 month forecast is generally similar, but the 3 month one is markedly worse: it misses the 1987 warming, indicating instead a spring-summer cooling. Significantly, this behavior is shared by the 0 month lead, which is essentially the initial conditions (recall that no SST data is used in the initialization). Thus the ocean model in hindcast mode is trying to cool while the world warms. This behavior appears to be shared by more elaborate ocean models (ie GCMs), and a case study of summer 1987 might help to identify serious flaws in the models or wind forcing data.

It may seem puzzling that the model forecasts can actually improve at longer lead time. One clue to this behavior is suggested in the preceding paragraph: our initialization may be so poor that the model benefits from having a longer lead time to recover (this is similar to the "initialization shock" phenomenon of NWP). Implicit in this is the idea that the essential ENSO signal is low frequency (cf Barnett et al 1988).

A related clue is provided by Fig. 3, which shows that there is a strong seasonal dependence to the forecasting skill. Forecasts for the winter period tend to be more skillful, and forecasts inititiated in winter also tend to be best, especially at long leads. We believe these results may be understood in terms of the seasonally varying stability of the coupled ocean atmosphere in the tropical Pacific. The system is most unstable in the summer and is stable in winter, a pattern evidenced in the fact that ENSO anomalies tend to grow rapidly in summer and early fall, and are nearly stationary in the winter (ie when the typical El Nino anomaly is a maximum). All our initial conditions have considerable noise. For forecasts initiated in summer this noise is amplified by the unstable conditions, often leading to a busted forecast. With a start in winter when the atmosphere-ocean coupling is weakest, noise is readily dispersed by wave motions in the ocean, thus allowing the lower frequency ENSO signal to assume control during the upcoming summer growth season.

The success of our forecasts suggest that aspects of the ENSO cycle are predictable as much as several years ahead. It appears that by providing a stable period each year the seasonal cycle extends predictability: since high frequency "noise" has only a short growing season, the low frequency large scale ENSO mode dominates. Results here are from a relatively simple model using a small amount of low quality data and primitive data assimilation techniques. Avenues for improvement are obvious.

Acknowledgements. Sean Dolan made indispensible contributions to the development of the forecast system. Help in manuscript preparation from Larry Carroll and Virginia DiBlasi is gratefully acknowledged. This work is supported by grant No. NA-87-AA-D-AC081 from the US TOGA Project Office of NOAA.

References

Barnett, T., N. Graham, M.A. Cane, S.E. Zebiak, S. Dolan, J. O'Brien, and D.Legler 1988: Prediction of the El Niño of 1986-1987. *Science,* **241**, 192-196.

Cane, M.A., S.E. Zebiak, and S. Dolan 1986: Experimental forecasts of El Niño. Nature, **321**, 827-832.

Miller, R.N., and M.A. Cane 1988: A Kalman Filter Analysis of Sea Level Height in the Tropical Pacific. *J. Phys. Oceanogr.* accepted.

Zebiak, S.E., and M.A. Cane 1987: A model El Niño Southern Oscillation. *Mon. Wea Rev.* **115**, 2262-2278.

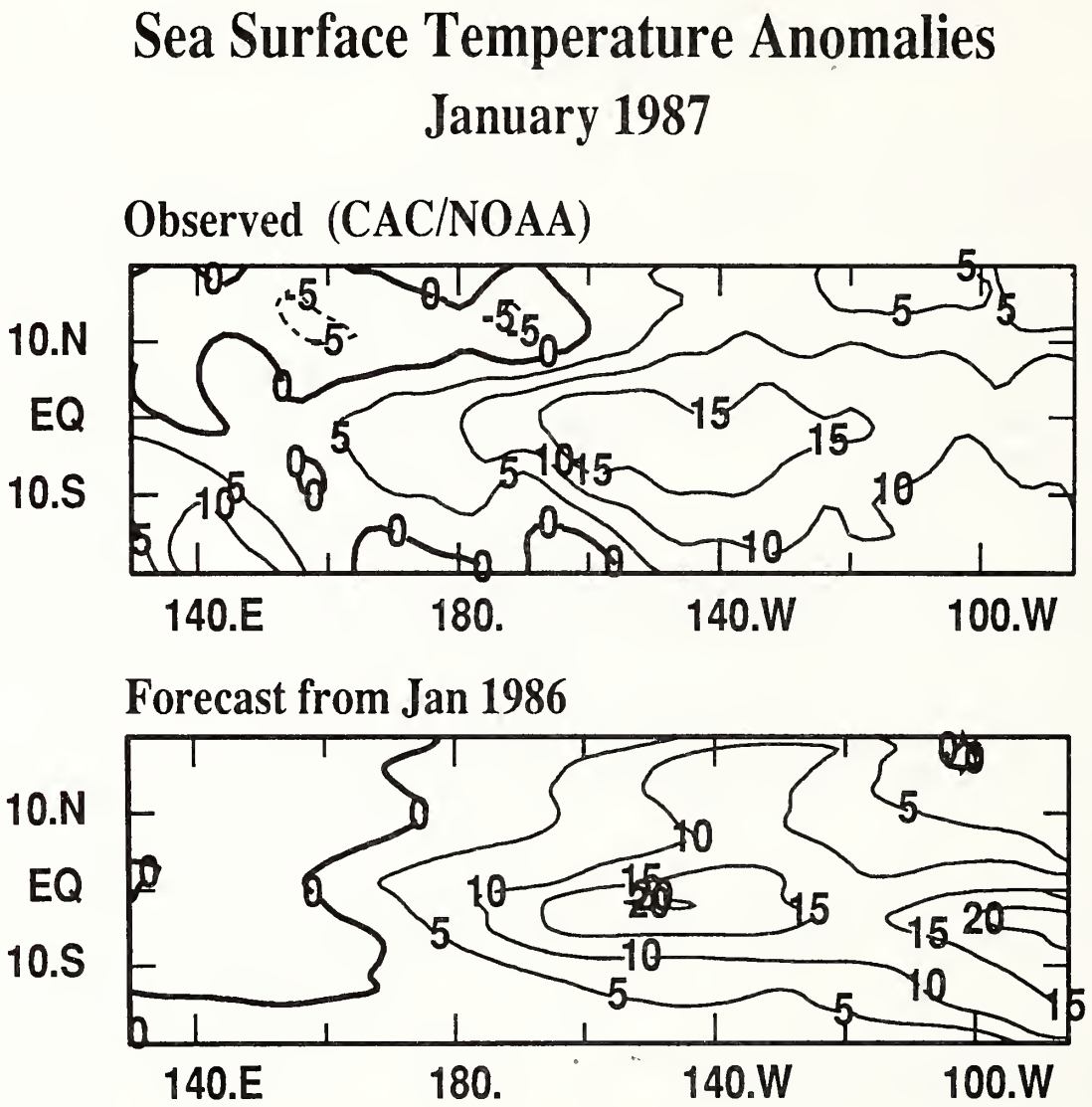

Figure 1. Sea surface temperature anomalies in January 1987 as observed (top) and as forecast from January 1986 (bottom). The observed field is actually the product produced by the Climate Analysis Center (CAC)/ NOAA.

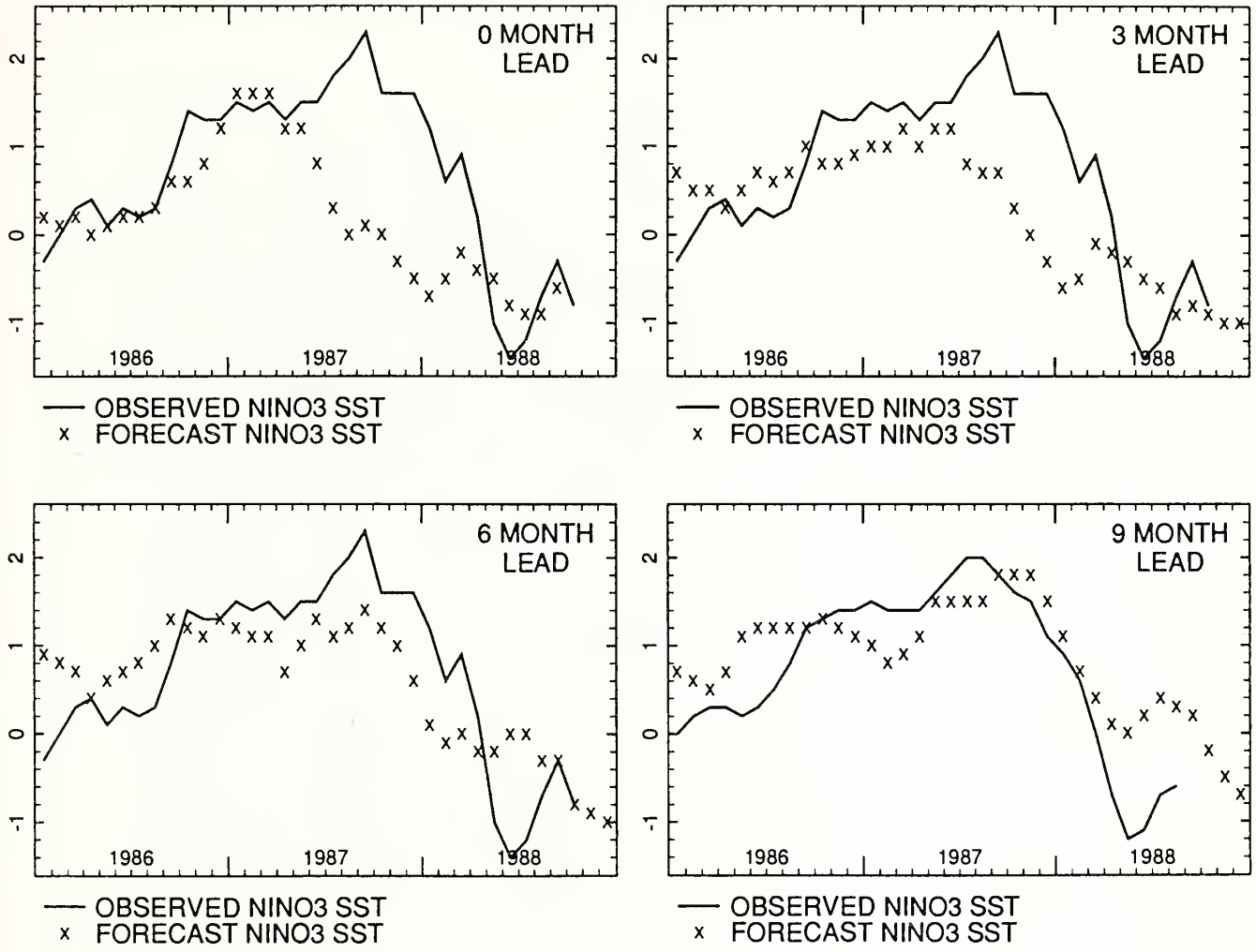

Figure 2. SST anomalies in the NINO3 region (90W-150W, 5N-5S) from the CAC analysis product (solid lines) compared with the forecasts at lead times of 0, 3, 6, and 9 months (x's). For the 9 month lead each point represents the 3-month average. Each forecast value is first normalized by the model mean and standard deviation for the period 1970-1985 (as in Barnett et al, 1988) and then multiplied by the observed standard deviation for the same period.

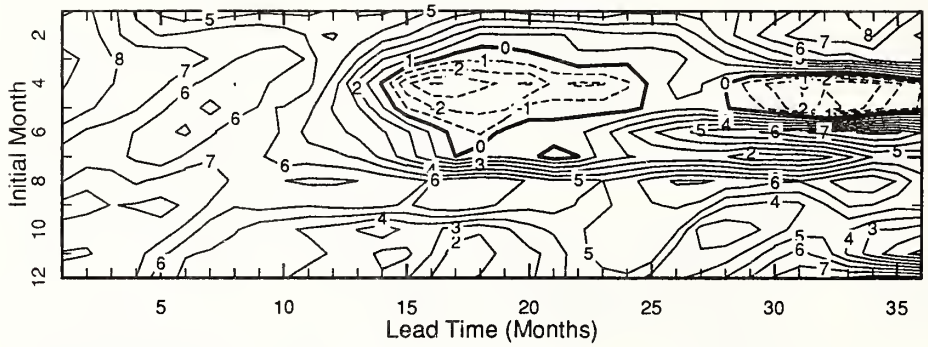

Correlation of Individual Forecasts with Observed NINO3
1970 - 1985

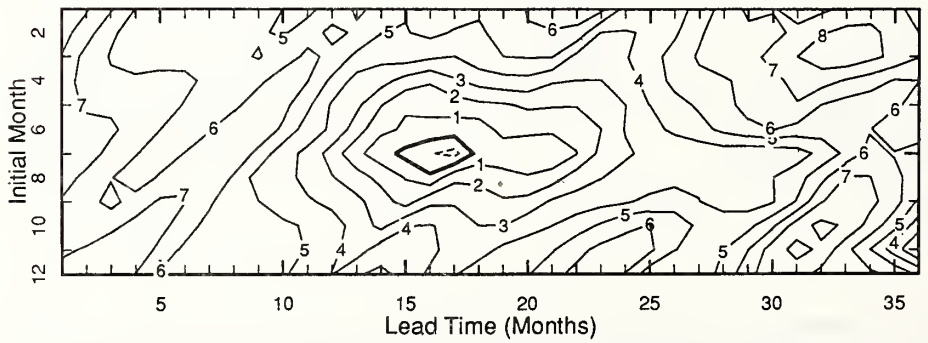

Correlation of Latest 6 Forecasts Averaged with Observed NINO3
1970 - 1985

Figure 3. Correlation coefficients of the model forecast NINO3 index with observed values, 1970-1985. The ordinate gives the calendar month of forecast initiation, with January at the top and December at the bottom. The abscissa is the lead time in months.

Diagnostic Studies of a Coupled Model's Climate Variability

Stephen E. Zebiak and Mark A. Cane

Lamont-Doherty Geological Observatory, Palisades, NY 10964

1. Introduction

In a previous paper, (Zebiak and Cane 1987, MWR, p.2262) we presented an idealized coupled model that produces aperiodic interannual oscillations similar to ENSO in the tropical Pacific. The model behavior was described using a series of simulations ranging from 30 to 90 years in length, and the dominant spatial patterns were identified by examining the evolution of an individual warm event. Parameter sensitivities were indicated by several runs with significant changes in one or more of the model parameters. Here we will augment these earlier results with a rather extensive set of model simulations and analyses that give a more comprehensive description of the model's natural variability and its dependence on specific external factors. One question that arises from the previous results is whether the full range of behavior is sampled in a given simulation of a few decades. There is no assurance that it is, given the apparently chaotic nature of the variability. Only longer simulations and/or multiple realizations can provide this information. Results of both types are presented below. We have defined quantitative measures to describe the results so that, where possible, comparisons with observations are possible.

2. Variability within a multi-century model simulation

Fig. 1 shows a time series of NINO3 (averaged SST anomaly 90°*W* - 150°*W*, 5°*N* - 5°*S*), from a 1024-year run of the model. Inspection of this time series reveals a wide range of behavior: there are well-marked periods of large-amplitude, rather regular oscillations, and other periods of more chaotic, smaller-amplitude variability. Also of note are the period of nearly twenty years with negligible anomalies (near year 450), and periods of similar length with anomalies of only one sign. The other indices of Fig. 1 describe these properties quantitatively, and were devised as follows. The 1024-year (monthly) time series was divided into 51 segments of 24 years length (overlapping each other by 4 years). Within each segment, the mean, standard deviation, and power spectrum were computed. (A Welch window was applied prior to FFT calculation.) The spectral band with largest power was determined, as well as the fraction of total (interannual) variance contained in that band. Shown are the standard deviation, dominant frequency, and fraction-of-variance indices. The latter is a crude measure of the degree of regularity, as nearly periodic oscillations result in large variance accompanying the dominant frequency, and chaotic variations result in variance spread among many or all bands. Two regimes are apparent, one with large variance, high regularity, and a dominant 4 year period, and the other with lower variance, mixed periods, and low regularity. Thus, the indices provide a quantitative measure of the behavior patterns conspicuous in the original time series.

The distributions of the indices (among the 51 realizatons) are shown in Fig. 2. The standard deviation and fraction-of-variance distributions are notably broad, reflecting the distinct regimes. The favored frequency band centers on 4 years, but adjacent bands are also represented (3-6 years). For purposes of comparison, these same indices were computed from the single 18 year realization of observed SST anomalies between 1970 and 1987 (CAC analysis), and are indicated on the distribution plots. The observed values fall well within the range of the model-derived distributions, showing that, at least for this period, the temporal characteristics of observed interannual variability are consistent with those of the model.

To examine the spatial structures, we computed EOF's of model fields based on monthly values from the 1024-year simulation. Fig. 3 shows the first four EOF's of SST anomalies. The first EOF, with 83% of the total variance, is clearly the mature El Niño signal. The others represent various phases of the life cycle of model warm and cold episodes. Corresponding EOF's derived from observed SST anomalies (1970-1987) are shown in Fig. 4. Though there is correspondence between the patterns, two biases of the model are apparent: the underestimation of variability in the South American coastal region and in the vicinity of the dateline at the equator. Also, whereas the first 4 EOF's of the model fields contain 93% of the total variance, only 68% of the variance is accounted for in the observed fields. Partly this reflects the absence of "noise" in the model fields, but in addition, the model anomaly patterns are more consistent from event to event than in the nature.

Figs. 5 and 6 show the corresponding EOF's of model wind stress and thermocline depth anomalies. In both cases, the first EOF again represents a mature warm event configuration. The model wind stress is realistic with respect to the westerly anomalies along the equator, but unrealistic in having off-equatorial easterlies in the eastern Pacific. Compared to other fields, the variance distribution of the thermocline field is broad, reflecting the fact that this field is characterized by features propagating at various speeds depending on location.

3. Parameter-dependence of model variability

Five parameters of the model were chosen for a detailed parameter study. They reflect the oceanic equivalent depth (Par1), the sharpness (Par2) and the amplitude (Par3) of the mean thermocline, the strength of atmospheric heating associated with SST anomalies (Par4), and the atmospheric friction (Par5). A detailed treatment of these parameters can be found in Zebiak and Cane(1987). For this study, each of the five parameters was allowed to assume three values, including the standard one, a 5% decrease, and a 5% increase, in all possible combinations. This amounts to 3^5 or 243 simulations, each of which was run for 100 years (starting with the same initial conditions). The purpose of this study was to determine whether rather modest parameter changes could significantly change the model behavior, and if so, in what sense. Because of the large number of simulations, it is possible to assign statistical significance to the results, avoiding the uncertainties inherent in comparisons of individual realizations. After breaking each 100-year simulation into four segments, the characteristics were evaluated using the four indices defined above. To examine the individual effects of each parameter, the total set of results were grouped into three subsets corresponding to the three values of that parameter. Each of the subsets then contained 324 realizations. The cumulative distributions of each of the four indices were computed for each of the three subsets, and then compared (Fig. 7). In this form, the significance of differences in the distributions can be assessed using the Kolmogorov-Smirnov statistic. The 99% confidence interval derived in this manner is displayed in each distribution plot; there is only a 1% probability that two distributions (of size 324) differing by more than this amount represent the same process.

All five of the parameters produce significant changes in at least one of the indices, and the net effect of each parameter is unique. In the case of Par1, increasing values produce smaller mean and standard deviation, and a tendency toward higher frequencies. Increasing Par2 results only in decreasing the standard deviation on the high end (that is, decreasing the amplitude of the largest warm/cold events). Increasing Par3 acts to increase the mean (marginally) and the standard deviation, while giving a more dominant 4 year period. For Par4, the result is larger mean and standard deviation, and smaller fraction-of-variance (more chaotic). Finally, increasing Par5 leads to much reduced mean and standard deviation, a greater likelihood of dominant periods less than 4 years, and more regular oscillations. All of these effects are consistent and identifiable amid the background of natural variability, showing a genuine sensitivity to externally determined factors making up the background climate state.

4. Conclusions

The important results from this study are: (1) the natural variability in the model is large, and is manifested as transitions between identifiable regimes persisting from a few years to more than a century; (2) the temporal and spatial characteristics of the model's interannual variability are similar in many respects to the observed variability in recent decades, but also show certain model biases; (3) the model behavior is sensitive to various externally imposed parameters, beyond the range of natural variability. It is worth noting that if other coupled models have the properties of ours, then it may be necessary to carry out very lengthy integrations, and/or multiple realizations in order to assess reliably the model's behavior. The parameter sensitivity results can be viewed from two perspectives. On the one hand, the individual sensitivities imply that the model could be tuned, assuming we knew what to tune against. Given the degree of natural variability in the model, and presumably in nature, this does not seem justified or meaningful. On the other hand, the sensitivities suggest that the characteristics of interannual variability may be expected to change in response to externally imposed variations in climate. As ours is a perturbation model, most formal parameter changes can be interpreted in terms of changes in the background climate state. Processes that could change the climate state (external to ENSO) are numerous, including, for example, the oceanic thermohaline circulation and atmospheric trace gas composition. From various proxy data we can infer changes in interannual variability over the past several centuries; whether such changes can be understood in terms of externally induced climate change remains to be seen.

Acknowledgements. This work was supported by NSF grant ATM-8612570 and NOAA grants NA84-AA-D-00031 and NA87-AA-D-AC081. Computations were carried out at the John Von Neumann National Supercomputer Center under award NAC 401.

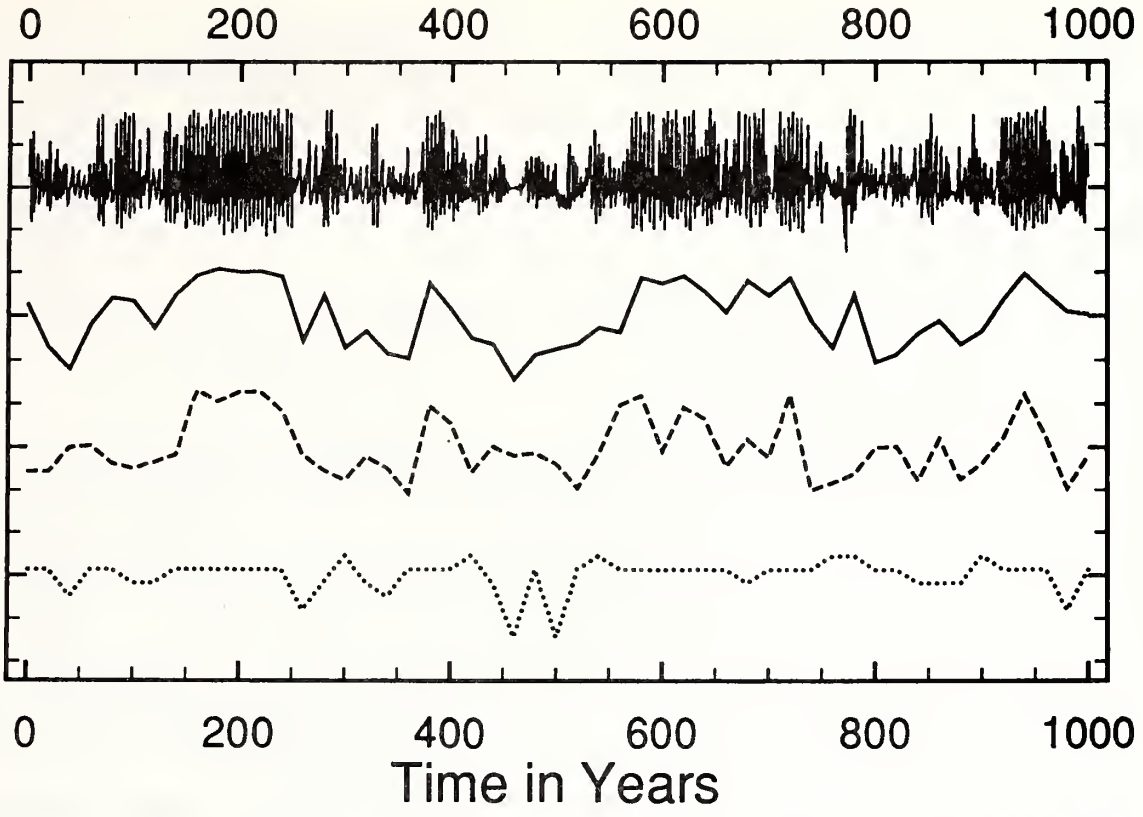

FIG. 1 Time series of NINO3 from a 1024-year coupled model simulation (top). Below are the three indices representing variance (heavy solid line), fraction-of-variance (dashed line) and dominant frequency (dotted line) for successive 24-year segments. See text for definition of indices.

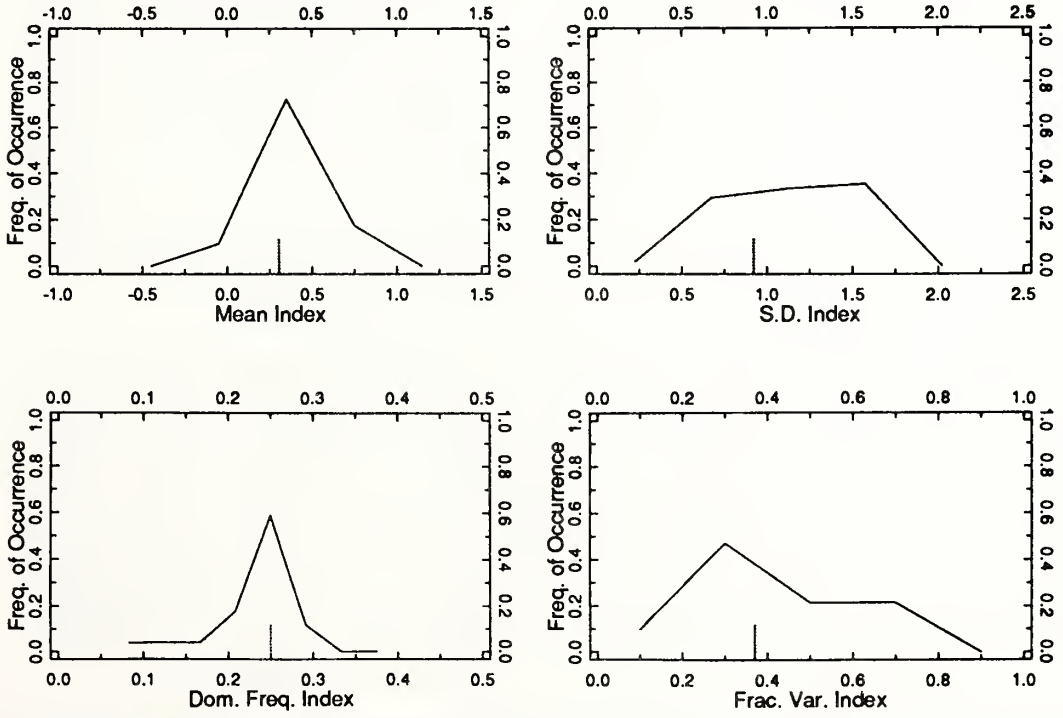

FIG. 2 Distributions of mean (°C), standard deviation (°C), dominant frequency (*years*$^{-1}$), and fraction-of-variance indices from the 1024-year simulation.

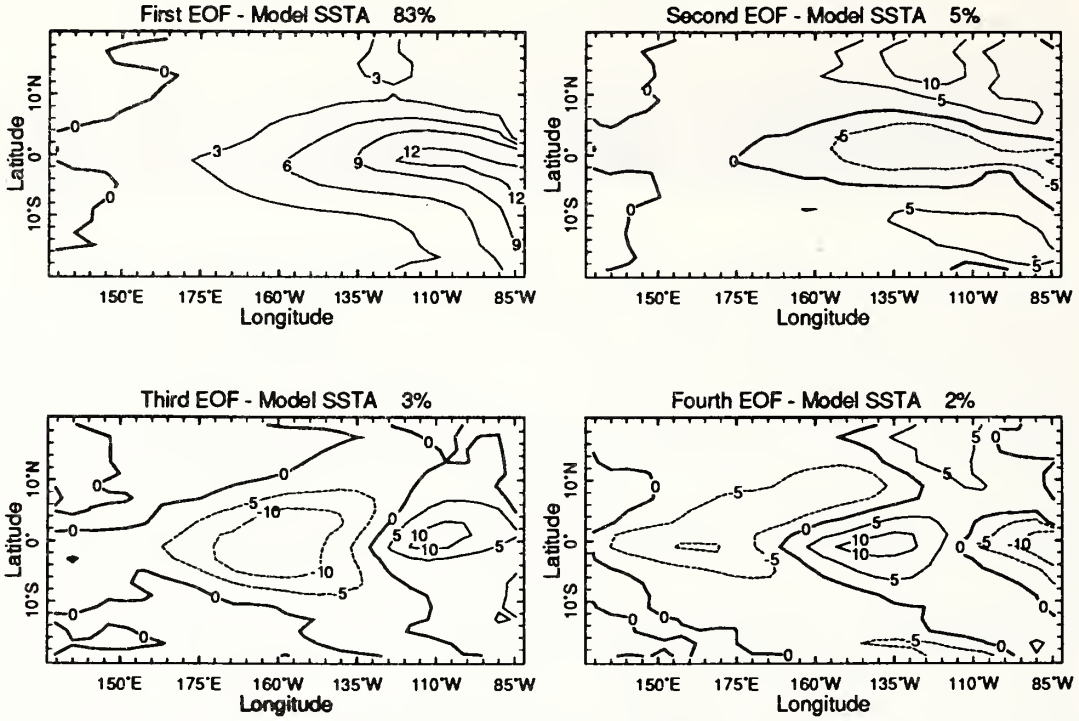

FIG. 3 First four EOF's of the model SST anomalies, calculated from monthly values of the 1024-year simulation.

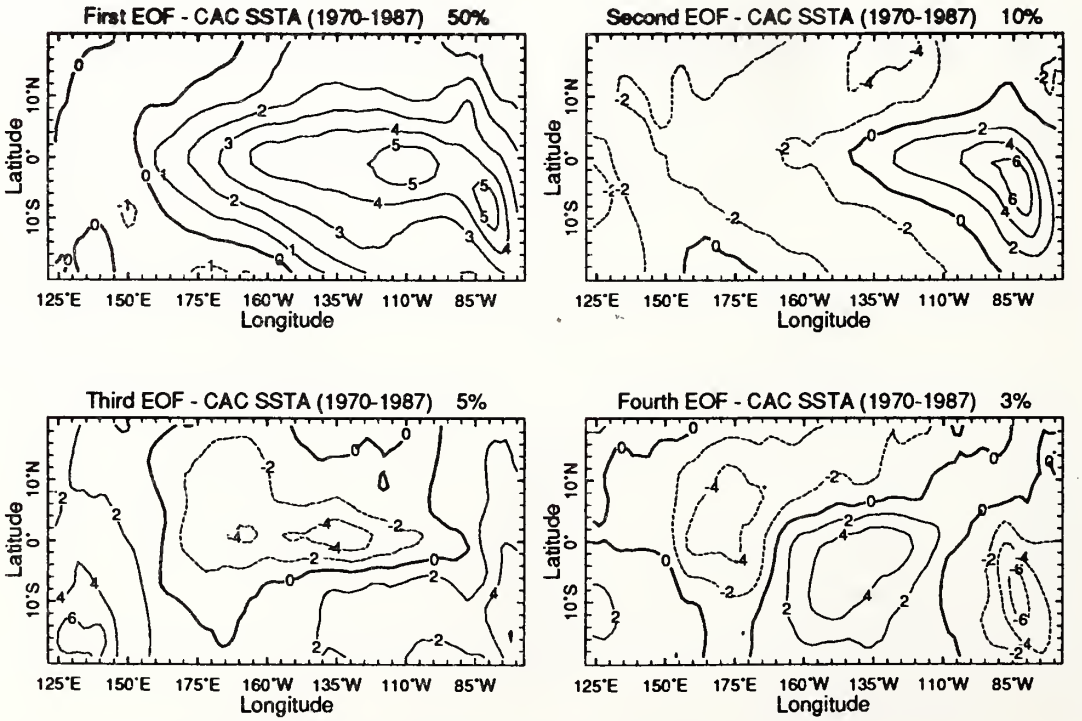

FIG. 4 First four EOF's of observed SST anomalies, calculated from monthly values between the years 1970 and 1987, inclusive (CAC analysis).

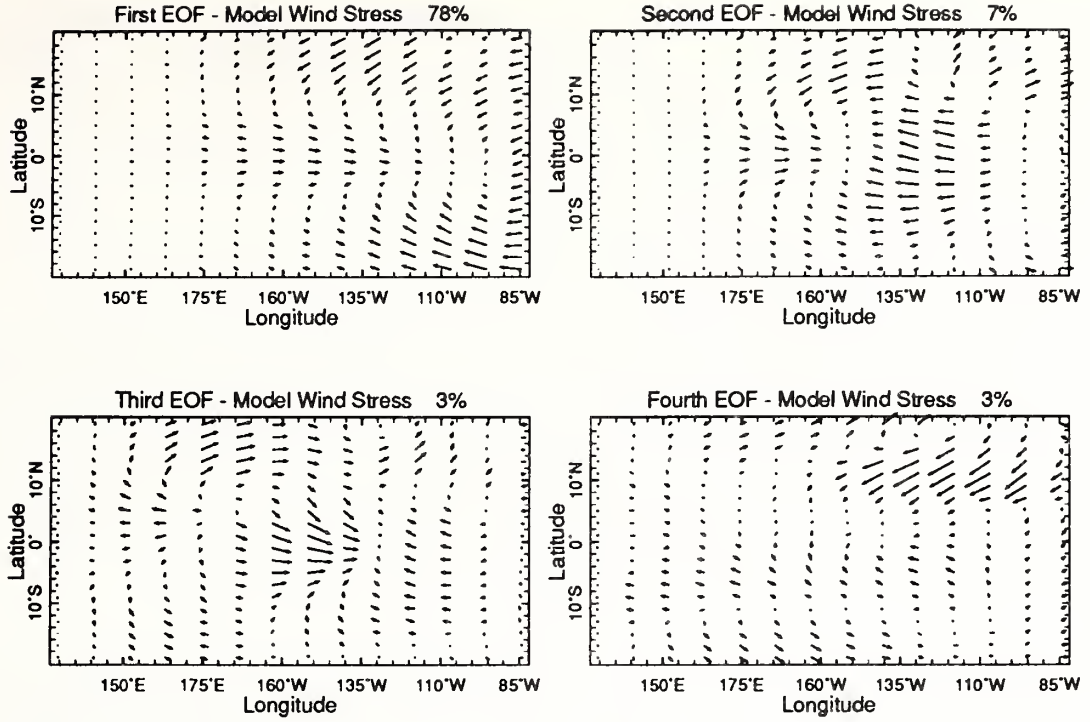

FIG. 5 As in FIG. 3, except for model wind stress anomalies.

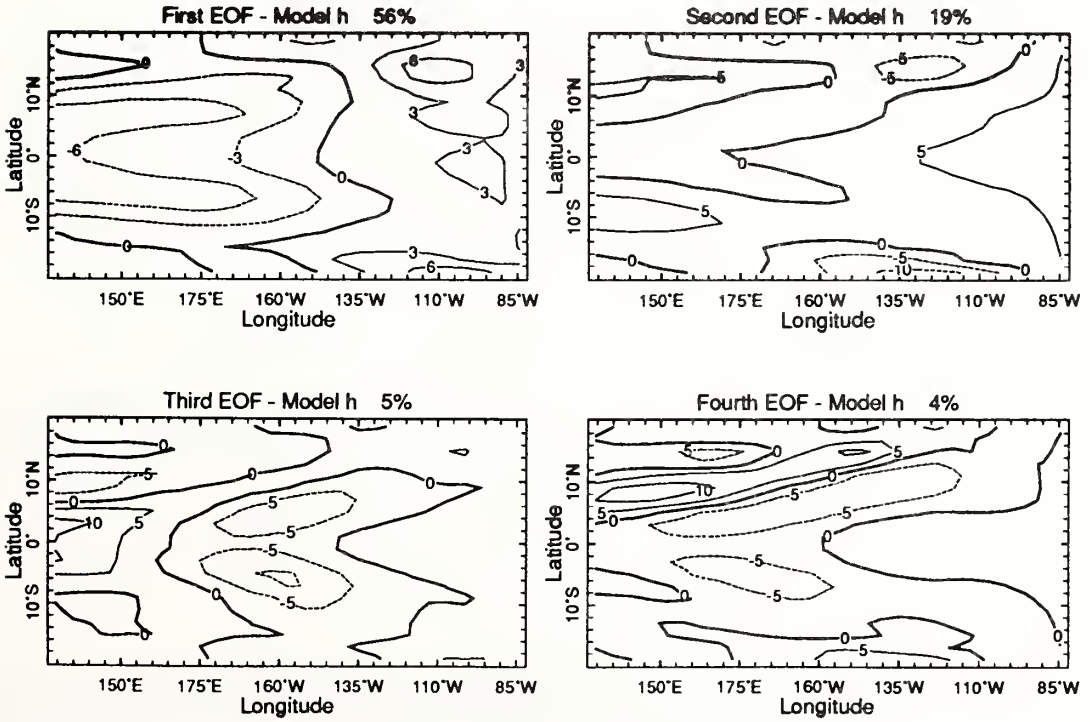

FIG. 6 As in FIG. 3, except for model thermocline depth anomalies.

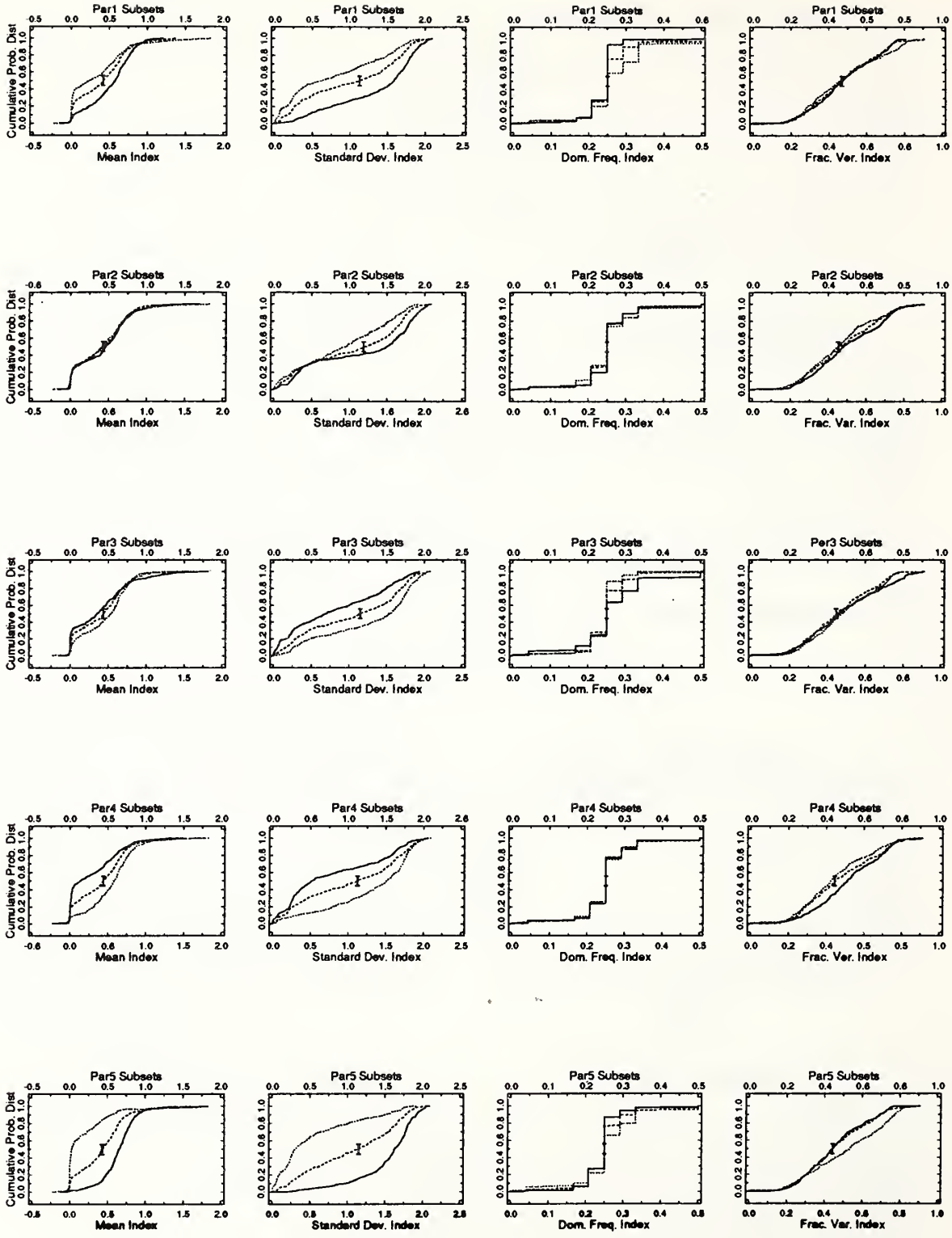

FIG. 7 Cumulative distributions of mean, standard deviation, dominant frequency and fraction-of-variance indices from the set of 243 simulations with variations in five model parameters. Across each row, the total set of results in each plot have been stratified according the the three distinct values of the indicated parameter. The heavy solid line represents the distribution for the subset with 5% reduction of the parameter; the dashed line represents the subset with the standard value, and the dotted line the subset with 5% increase. Also indicated in each plot (vertical bar) is the separation interval beyond which any pair of distributions may be considered distinct at the 99% level.

Southern Oscillation Phenomena in a Coupled Ocean-Atmosphere GCM

Gerald A. Meehl
National Center for Atmospheric Research *
Post Office Box 3000
Boulder, Colorado 80307-3000

Results from a coupled ocean-atmosphere general circulation model (GCM) (R15 version of NCAR Community Climate Model, 5° × 5°, four-layer ocean GCM) show that, in spite of inherent limitations of the coarse model grid, Southern Oscillation-type interannual variability of the ocean-atmosphere system is an inherent aspect of the model. Such variability in the tropical Pacific is part of a global-scale pattern of associated anomalies in both atmosphere and ocean. There is a linkage to the regional-scale sea-level pressure (SLP) patterns associated with the annual cycle of solar forcing and the contrast of land and sea in the eastern Pacific. Transitions between warm and cold events in the eastern Pacific in the model depend on the evolution of seasonally low SLP over South America during northern winter and its movement with the solar cycle to the northwestward during northern spring. Pressure gradients in the eastern Pacific set up by the transition of the seasonal cycle initiate coupled processes of the ocean-atmosphere system that depend on the state of the ocean from the previous seasonal cycle.

For the transition to be made from a cold event to a warm event, the cool water in the equatorial Pacific from the previous seasonal cycle is associated with relatively higher SLP. As the area of seasonally low pressure over South America begins its transition from southern to northern hemisphere, a pressure gradient is set up in the far eastern Pacific that produces westerly wind stress anomalies (Fig. 1a). This suppresses ocean upwelling, the surface layer warms, and the coupled anomalies move to the west (Fig. 1b). By northern summer, relatively warm water is established nearly all the way out to the Dateline (Fig. 1c).

For the transition to be made from a warm to a cold event, the reverse set of processes occurs. The warm water in the equatorial Pacific from the previous annual cycle is associated with relatively low SLP. As the seasonal transition occurs in northern spring, SLP over the water is relatively lower than the seasonally low SLP in transit from South America northwestward. A pressure gradient is set up in the far eastern equatorial Pacific that is associated with easterly wind stresses. These stronger easterly winds intensify upwelling, water cools, and this coupled set of anomalies moves westward. By northern summer, relatively cool water is established almost out to the Dateline.

It is important to note that processes in the Indian Ocean and model western Pacific, thought to be important in transitions from cold to warm events [including the eastward movement of SLP, precipitation, and wind anomalies coincident with the annual cycle there as discussed by Gill and Rasmusson (1983), Meehl (1987), van Loon and Shea (1987) and Gutzler and Harrison (1987)], are not present in the coupled model. Some of these processes are depicted schematically in Fig. 1d-f. The lack of a western Pacific warm pool and absence of the South Pacific Convergence Zone in the model critically affect the simulation of these features (Washington and Meehl, 1988). In effect, the eastern Pacific regime in the model extends all the way to the Indian Ocean. Yet the model is able to make transitions from cold to warm phase and back again in the eastern Pacific with seasonal timing dependent on modulations of the annual cycle similar to the observations. It is possible that

* The National Center for Atmospheric Research is sponsored by the National Science Foundation.

the observed ocean-atmosphere system can make transitions based on remote forcing and coupled interaction in the Indian Ocean and western Pacific, as well as via local mechanisms in the eastern Pacific noted in the coupled model. This could help explain the different character of the onset of El Niños, some of which seem to originate in the east, some in the west (Rasmusson and Wallace, 1983; Fu *et al.*, 1986).

Since a transition from warm to cold phase or back again in the model depends only on the precondition of the SSTs in the tropical Pacific and the passage of the forcing from the annual cycle in northern spring, the system should have an inherent biennial tendency as is observed (Meehl, 1987; Kiladis and van Loon, 1988). That is, if there is relatively cool water in the equatorial Pacific in northern spring, the system should make a transition to warm water there, and vice versa if the system starts out with warm sea-surface temperatures in the tropical Pacific. Yet as in the real ocean-atmosphere system, there are multiyear events that disrupt the biennial cycle. The reason for these multiyear events is currently under investigation and appears to involve heat storage in the upper ocean.

REFERENCES

Fu, C., H.F. Diaz, and J.D. Fletcher, 1986: *Mon. Wea. Rev.* **114**, 1716-1738.

Gill, A.E., and E.M. Rasmusson, 1983: *Nature,* **306**, 229-234.

Gutzler, D.S., and D.E. Harrison, 1987: *Mon. Wea. Rev.* **115**, 169-192.

Kiladis, G.N. and H. van Loon, 1988: *Mon. Wea. Rev.*, **116**, 120-136.

Meehl, G.A., 1987: *Mon. Wea. Rev.*, **115**, 27-50.

Rasmusson, E.M. and J.M. Wallace, 1983: *Science* **222**, 1195-1202.

van Loon, H., and D.J. Shea, 1987: *Mon. Wea. Rev.*, **115**, 370-381.

Washington, W.M., and G.A. Meehl, 1988: *Clim. Dyn.*, accepted for publication.

FIGURE CAPTION

Fig. 1 Schematic diagram of transition from a cold event to a warm event in the equatorial Pacific during that part of the seasonal cycle from northern winter to northern summer. Parts a-c depict transition in coupled ocean-atmosphere GCM. Parts d-f show probable transition processes in the observed system. Ribbon arrows denote large-scale rising motion (associated with lower SLP and increased convection and precipitation over warmer water) and sinking motion (associated with higher SLP and cool water). Large arrows on the surface indicate direction of wind stress anomalies. Note that, for the model, the transition takes place based only on processes in the eastern Pacific. The observed system displays the same seasonal timing, but utilizes not only processes in the eastern Pacific (similar to the coupled model) but mechanisms in the western Pacific involved with the passage of the seasonal cycle there.

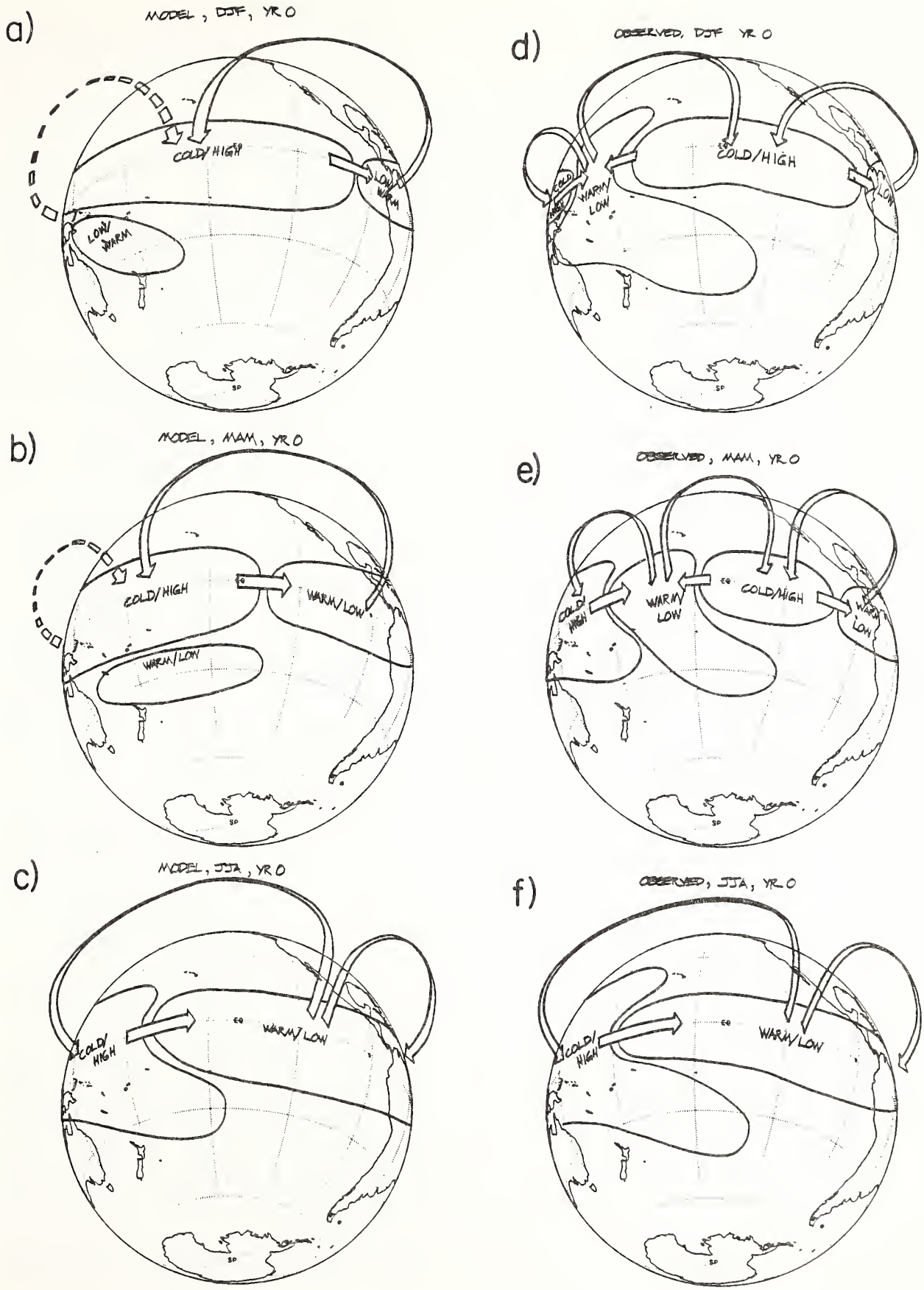
a)
MODEL, DJF, YR 0
COLD/HIGH
LOW/WARM
LOW/WARM
SP
b)
MODEL, MAM, YR 0
COLD/HIGH
WARM/LOW
WARM/LOW
SP
c)
MODEL, JJA, YR 0
COLD/HIGH
EQ
WARM/LOW
SP
d)
OBSERVED, DJF YR 0
COLD/HIGH
COLD/HIGH
WARM/LOW
LOW
SP
e)
OBSERVED, MAM, YR 0
COLD/HIGH
WARM/LOW
EQ
COLD/HIGH
WARM/LOW
SP
f)
OBSERVED, JJA, YR 0
COLD/HIGH
EQ
WARM/LOW
SP

A Coupled Global Atmosphere-Ocean Model

Ulrich Cubasch
MPI fur Meteorologie
Bundesstr.55
D-2000 Hamurg 13
FR Germany

1. Introduction

In order to estimate the greenhouse effect caused by CO_2 or other gases as well as for paleoclimatological studies a global coupled ocean atmosphere model is needed. In this paper the development of such a comprehensive global coupled atmosphere-ocean model from a 'state of the art' atmosphere and ocean models has been described.

2. The Coupled Model

The atmosphere model has been developed as a medium range forecasting model at ECMWF (Louis, 1986). For climate studies its resolution has been decreased to a spectral resolution of T21 and 16 vertical levels. Additionally to the operational ECMWF model the temperature over sea ice is calculated via a balance equation, and the deep soil temperature and deep soil wetness are prescribed by their climatological value every fourth day.

The ocean model has been developed by Maier-Reimer et. al., 1982. Its fully implicit formulation allows a timestep of 30 days and makes it very suitable for climate experiments. In the coupled version it runs with a horizontal resolution of approximately 4° x 4° degrees and 10 levels in the vertical. It includes a thermodynamic ice-model.

The ocean model provides to the atmosphere model the sea-surface temperature and the ice thickness, the atmosphere model in turn calculates the total heat flux (i.e. latent, sensible, short and long wave radiative heat fluxes), the wind stress and the fresh water flux for the ocean model (Fig. 1). Since in the ECMWF model the continental runoff is estimated as a global mean only, it has not yet been incorporated in the calculation of the freshwater flux. As each of the models, even when driven by realistic boundary forcing, tends to generate its own climate, which is different from observation, a coupling creates a nonlinear feedback, which forces some coupled models to drift far from the observed state (Han et al, 1984). Sausen et al, 1988 propose a flux correction to compensate for the individual model errors and which should stabilize the coupled model. This method will be tested in one of the experiments.

The initial data for the atmospheric part of the coupled model have been taken after integrating the atmosphere model alone (i.e. with climatological sea-surface temperature after Alexander and Mobley, 1976) for one year to let it find its own climate. From that date onwards it has been continued for another five years as a control experiment. This uncoupled run has been used to establish the flux correction fields. The coupled runs start at the same date as the control experiment at a January condition.

The initial data for the ocean model have been derived from a 10,000 year integration with the ocean model (Maier Reimer et al, 1982). The ocean model in its uncoupled mode has been driven by a Newtonian coupling to the windstress, salinity and the temperature. The ocean surface temperature has been forced by the "equivalent" temperature and a variable coupling coefficient as defined by Oberhuber (1988). Fig. 2 displayes the temperature field as observed, as simulated by the ocean model and the difference between both for January. The largest differences appear in the Gulf stream and Kuroshio region, where the gradient of the sea surface temperature is not strong enough. This is possibly connected with the too coarse resolution of the ocean model. Large temperature differences also appear on the ice limits:

the observed temperature field contains also temperatures over ice, which can be quite low, while the ocean model never simulates temperatures lower than -1.9^0C, a threshold at which it forms ice. In the tropical Pacific the temperatur is about 2^0C colder than observed. In this region the equatorial upwelling is overestimated.

It is possible to estimate from the Newtonian coupling the heatflux, which would have been necessary to maintain the simulated circulation. The atmosphere model simulates a heatflux comparable to observation (Esbensen and Kushnir, 1981), while the amplitude of the ocean model's heat flux is about 30% larger in the Kuroshio and Gulf stream regions and about twice as large in the oceans of the southern hemisphere. The heatflux simulated by the atmosphere model has a constant negative bias of about 7.3 W/m^2, which means it extractes heat from the ocean, which in an uncorrected run will cool the ocean, if not any compensating feedbacks occur.

The windstress has been taken from a publication by Hellermann und Rosenstein (1983). Since the observed windstress is stronger than the one simulated by the atmosphere model, particulary in the southern hemisphere and in the tropics, the coupling of this quantity creates some problems. There exist two possiblities to counteract these problems: a) to introduce a bias correction, which will be added to the atmosphere model wind stress field to make it look in strength like the observed wind field or, b) to drive the ocean model with the atmosphere wind stress field derived from the control experiment until it reaches stationarity and to couple the models then directly.

The fresh water flux can be derived from the Newtonian coupling to the salinity as observed by Levitus, 1982. The global water budget is balanced in the ocean model with a loss of 24 mm/year, in the atmosphere model with a loss of 46 mm/year, which in the latter accounts at least partially for the continental runoff, which has not been included into this calculation. The largest differences between the ocean model and the atmosphere model fresh water flux appear in the Gulf stream region, where the pattern of maximum evaporation is closely linked to Gulf stream, which, as mentioned before is displaced in the ocean simulation, in the tropics, where the cumulus convection is underestimated in the atmosphere simulation, and along the antarctic coast, where the melting and freezing of ice is not treated properly in the ocean model.

3. The Experiments

Following experiments have been run:

1. coupled without flux correction, ocean start data generated by an ocean model driven by observed winds;
2. coupled with flux correction, ocean start data generated by an ocean model driven by observed winds;
3. coupled without flux correction, ocean start data generated by an ocean model driven by winds generated from the control run with the atmosphere model.

4. Results

The first experiment has been run for 12 month. After that it became clear that the ocean surface currents became more and more unrealistic. The equatorial easterly current had reversed and created an strong El-Nino. In the midlatitudes the currents stayed realistically and the temperature field did not give reasons to be of any concern. But because the equatorial currents were so unrealistically, this experiment had been abandoned in favour of the third experiment, where the ocean currents have been created in an ocean model run forced by the windstress calculated in the atmosphere model. It was hoped that this avoides the backlash of the equatorial current in the coupled model and makes the flux correction redundant.

The second experiment uses the fluxcorrection method and has been integrated

for 4 years so far. In this run a number of problems emerged. Since it was difficult to decide, if they were caused by a straight foreward programming bug when introducing the flux correction or by a dynamical feedback mechanism, which was at least partially concealed by the flux correction, the third experiment had been launched without flux correction. It has been integrated for three years so far.

The sea surface temperature (Fig. 3) in the the coupled runs with and without flux correction cooles in the equatorial Pacific and warms in the midlatitudes. The upper two layers cool in the global mean, while the lower layers become slowly warmer, indicating, that the temperture drift at the surface is not only caused by the heat deficit noticed in the uncoupled run, but also by too strong vertical mixing.

5. Summary

The coupled model has been integrated with or without flux correction for several years. During this period none of the experiments has reached a stationary state, but they all show a distinct trend towards a lower atmospheric temperature and a too cold equatorial ocean. The run with flux correction does not improve on the run without flux correction. This can be either caused by a coding error or by problems in connection with the assumptions going into the flux correction (linearity, small corrections against the mean), which are not in all points fulfilled. Additionally inconsistencies with the flux correction appear at the ice limits, which have not been tested in previous studies with simplified models. The short integration times do not give any indication whether the models will eventually obtain stationarity.

6. Aknowledgements

The author wishes to express thanks to Dr. Maier Reimer for the provision of the ocean model, M. Böttiger and C. Rath for the support with the graphics and M. Lautenschlager for the atmospheric control experiment.

6. References

Alexander, R. C. and R. L. Mobley, 1976: Monthly Average Sea-Surface Temperatures and Ice-Pack Limits on a 1 deg. Global Grid; Mon. Wea. Rev., 104, 143-148.

Bryan, K. and M. J. Spelman, 1985: The Ocean's response to CO2 induced warming; J. Geophys. Res., 90, 11,679-11,688.

Esbensen, S. K. and Y. Kushnir, 1981: The Heat Budget of the Global Ocean: An Atlas based on Estimates from Surface Marine Observations. Climatic Research Institute, Oregon State University, Report No. 26.

Han, Y. J., M. E. Schlesinger and W. L. Gates, 1984: An Analysis of the Air-Sea-Interaction simulated by the OSU coupled Atmosphere Ocean General Circulation Model; in "coupled amtosphere-ocean models", ed. C.J.Nihoul, Elsevier Oceanography Series, 40, 767 pp.

Hellermann, S. and M. Rosenstein, 1983: Normal Monthly Wind Stress Over the World Ocean with Error Estimates; J. Phys. Ocean., 13, 1093-1104.

Levitus, S., 1982: Climatological Atlas of the World Ocean; NOAA Professional Paper 13, Environmental Research Laboratories, GFDL, Princeton, N. J., USA.

Louis, J.F. (ed.), 1986: ECMWF Forecast Model; Meteorological Bulletin, ECMWF, Shinfield Rark, Reading, UK.

Maier Reimer, E., K. Hasselmann, D. Olbers and J. Willebrand, 1982: An Ocean Circulation Model for Climate Studies;. Techn. Rep., MPI fur Meteorologie, Hamburg.

Oberhuber, J., 1988: An Atlas Based on the COADS Data Set: The Budgets of Heat, Buoyancy and Turbulent Kinetic Energy at the Surface of the Global Ocean; Techn. Rep. No. 15, MPI fur Meteorologie, Hamburg.

Sausen, R., K. Barthels and K. Hasselmann, 1988: Coupled Ocean-Atmosphere Models with Flux Correction; Climate Dynamics 2, 154-163.

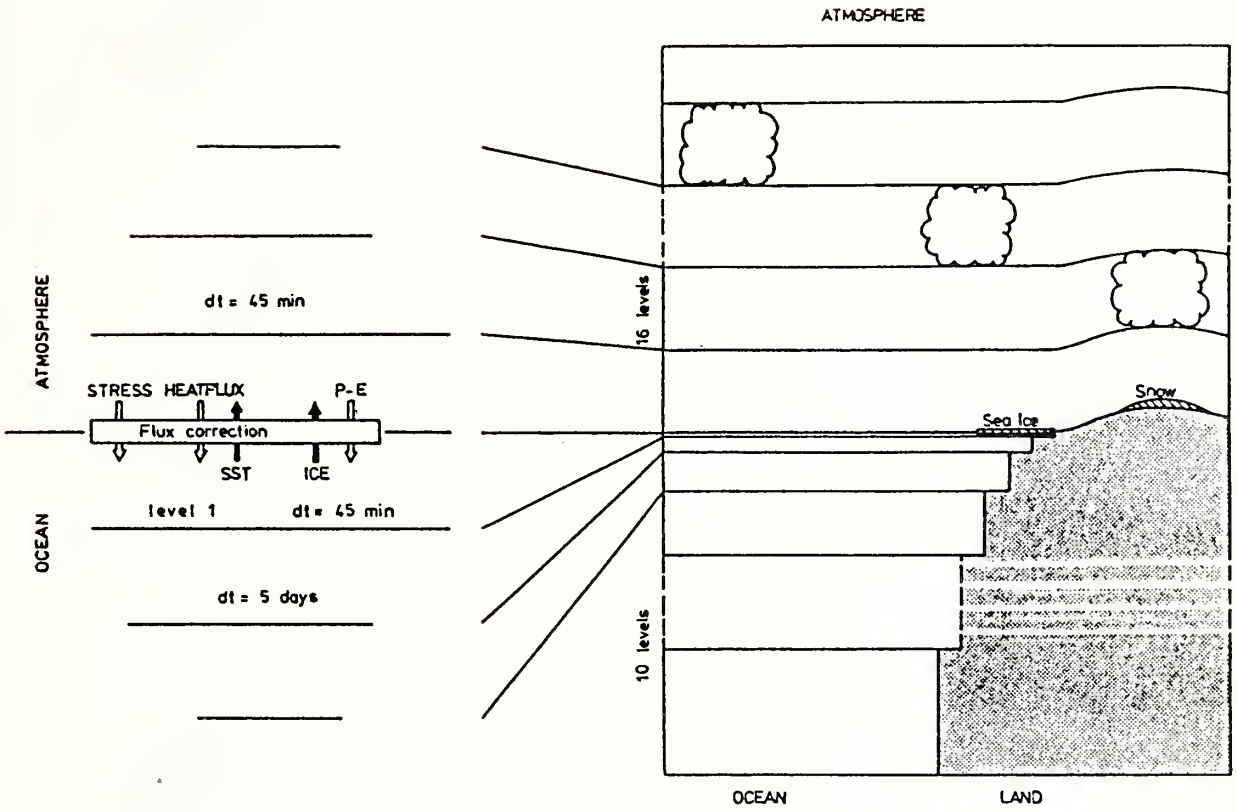

Fig. 1: The coupled models

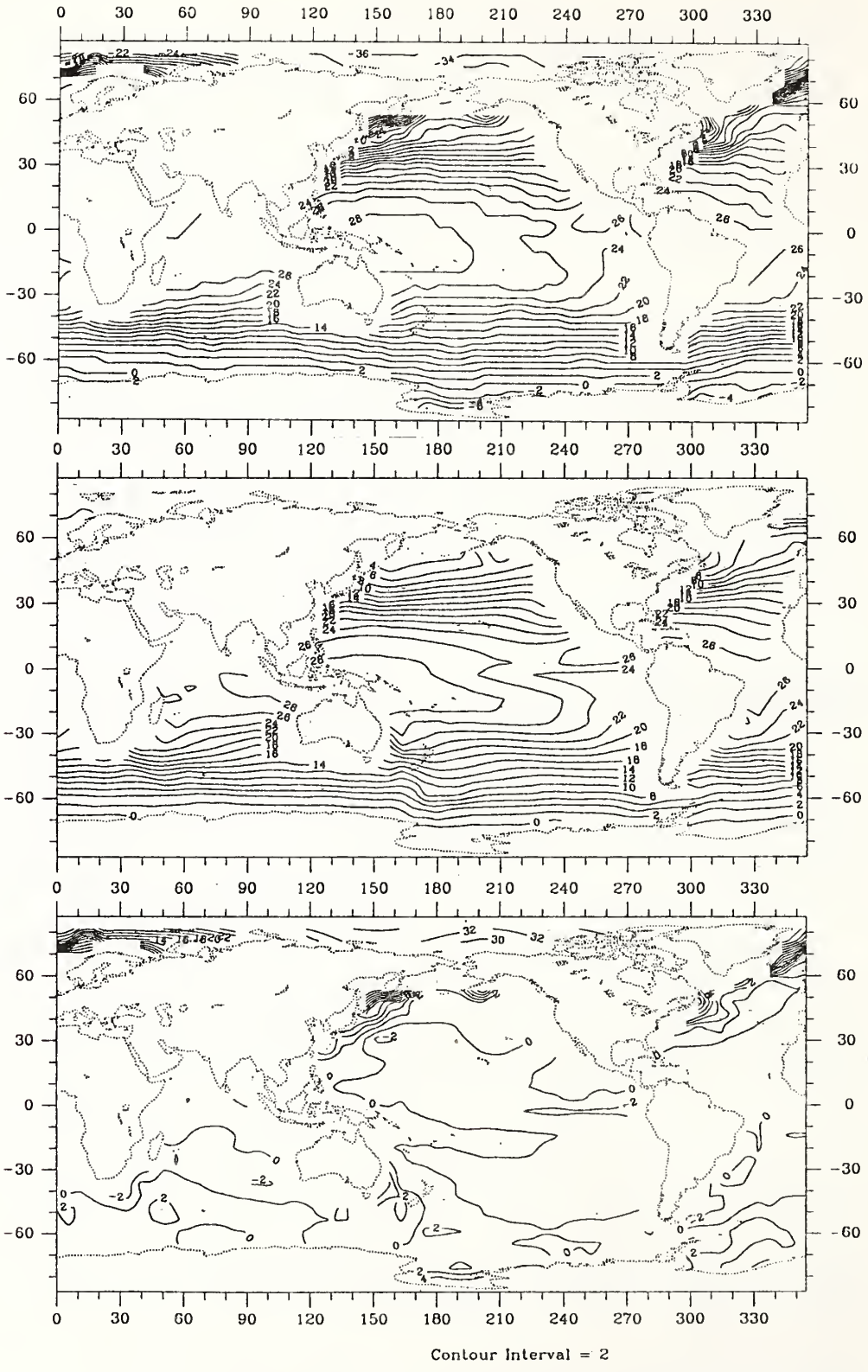

Fig. 2: The sea surface temperature for January. Top: observed (after Alexander and Mobley, 1976), middle: ocean model simulation, bottom: difference between model simulation and observation

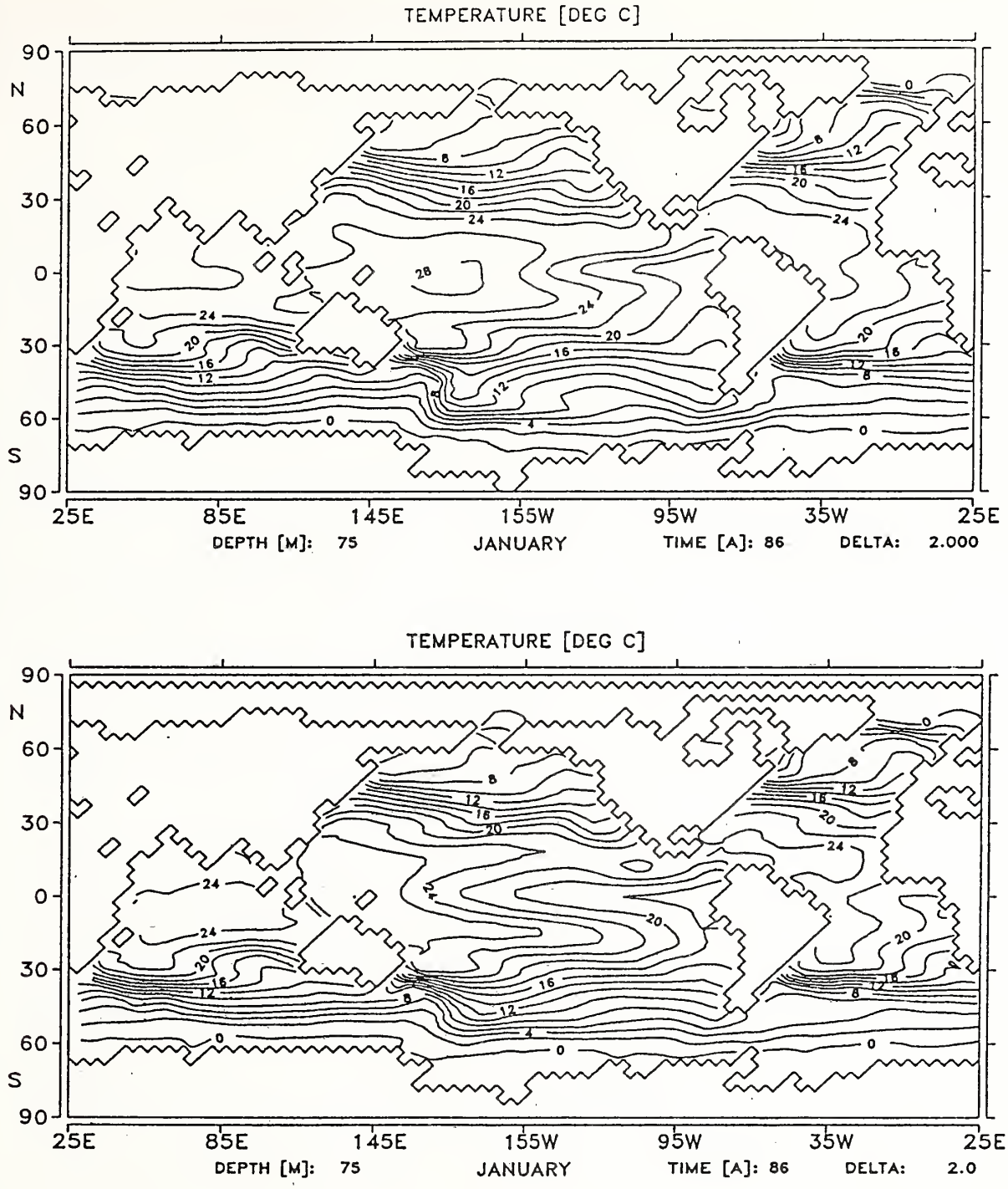

Fig. 3: The ocean surface temperature after three years of integration time for January for the coupled experiment without flux correction (top) and with flux correction (bottom)

Large scale surface heat flux variations over the North Pacific and North Atlantic during winter

Dan Cayan
Scripps Institution of Oceanography, A-024
University of California, San Diego
La Jolla, CA 92093

Four recent decades (1946-1986) of bulk formula parameterized heat fluxes from COADS ship observations are used to describe the anomalous variability of latent and sensible heat fluxes during winter months over the North Atlantic and the North Pacific. Latent and sensible fluxes are estimated from monthly means of individual sample cross products of the scalar wind and a) the sea surface saturation - observation level specific humidity and b) the sea surface temperature - observation level air temperature (AT) differences, respectively. Exchange coefficients for the latent and sensible bulk formulae are assumed to be equal and dependent on the monnthly mean scalar wind and vertical stability, as given by Isemer and Hasse (1987). The climatological mean of these heat fluxes is quite similar to fields derived and explained by others (e.g. Esbensen and Kushnir (1981), and Hsiung (1986)), and will not be discussed here. Instead, we focus on *anomalous* variability of the flux components, a topic that has attracted previous investigators (e.g. Bunker, 1980), but has not been thorougly investigated, probably owing to uncertainties in the accuracy of bulk formulations. Here, we use large statistical samples to inquire how well latent and sensible flux variations are related to the time mean atmospheric circulation and to the sea surface temperature (SST) field.

The monthly latent and sensible flux anomalies are highly correlated, so that they can be dealt with as a sum rather than independently. Although the *mean* heat flux is dominated by the latent component over the subtropics and tropics, the maximum monthly *variance* is shifted to the extratropics, and especially in higher latitudes, the sensible flux also plays a strong role. The anomalous variability peaks during northern winter when extratropical storms are at their peak. Standard deviations of the fluxes are shown in Fig. 1. Patterns of covariability of the fluxes are illustrated in Fig. 2 by the first three empirical orthogonal functions (EOFs) of the North Atlantic latent+sensible fluxes computed for all months. Both oceans exhibit covarying patterns weighted toward the western and central part of the basin. Large scale (thousand km scale) monthly latent+sensible flux anomalies often exceed 50 watts/m^2, which is greater than typical error estimates (Taylor, 1984, Weare, 1988) of the bulk formula flux components.

Cross correlation analyses between the monthly mean sea level pressure (SLP) anomaly field and the flux anomalies can be used to determine if the monthly fluxes are related to the monthly mean atmospheric flow. It is not obvious that the fluxes should be strongly related to the monthly mean flow pattern, since the fluxes are a nonlinear product of short period variables which are essentially observed independently from SLP. In fact, data from both oceans indicate that there is a fair degree of organization by the monthly mean circulation. This is illustrated in Fig. 3 by the field of correlation of time-varying amplitudes of the first two EOFs of SLP with the latent+sensible flux anomalies during winter. In these maps, the heavy solid contours outline the SLP EOFs and the stippling and hatching denotes positive and negative correlations. For the North Atlantic, both EOFs, the North Atlantic Oscillation (top of Fig. 3a) and the East Atlantic Pattern (bottom of Fig. 3a) exhibit correlations such that positive flux anomalies are favored by (a) strong anomalous SLP gradients that reinforce the mean wind or (b) SLP gradients that produce winds with a northerly or continental source. A comprehensive description of these monthly atmospheric EOF modes is presented by Barnston and Livezey, (1987). Similar correlation patterns issue from the same analysis applied to the North Pacific (Fig. 3b.). Although the monthly mean structures are somewhat larger, the patterns here are similar to those produced by synoptic scale winter cyclones, which exhibit high ocean-to-atmosphere vapor and heat fluxes in post-frontal regions and low fluxes in pre-frontal regions (Simpson, (1969); Bond and Fleagle (1988)). Viewed in aggregate, winters with persistently recurrent anomalous circulation modes display altered latitudinal distributions of surface heating in the lower atmosphere. These changes are demonstrated by composite profiles of zonal mean heat flux anomalies across the North Atlantic basin (Fig. 4), showing that the heat extracted by the atmosphere is shifted to higher latitudes during months of strong Icelandic Low phase of the North Atlantic Oscillation and vice-versa during months of the opposite phase. Positive and negative anomaly profiles for these two modes are quite symmetrical, as seen from the nearly mirror image form of the two, and include a broad band of latitude that extends southward to the tropics. A

similar type of profile appears for the strong positive and negative composites for the East Atlantic pattern, except that latitudes of maximum anomalies, of course, differ. The magnitude of the maximum composite anomalies is between 20 and 30 watts/m^2, which approaches one standard deviation (hatches) for individual months, a highly significant result for averages of 20 to more than 30 cases.

A question of interest to oceanographers is to what degree the anomalous fluxes are related to changes in the ocean surface temperature. Scaling arguments by Gill and Niiler (1973) and model experiments by Haney (1980) and Frankignoul and Reynolds (1983) suggest that diabatic heating is a primary source of thermal anomalies in the upper ocean. Note that the equation governing the conservation of heat in the mixed layer predicts that the fluxes should be related to the *time rate of change* of temperature, not the temperature itself. The relationship between the fluxes and this rate of change constitutes another test of the voracity of the fluxes since the bulk formulation is independent of the rate of change of the temperature. Also, the results should be nearly free of fortuitous low frequency influences because the differencing (centered differencing of the monthly SST') used to construct the time derivative results in a high pass version of the SST field. Contemporaneous $\frac{\delta SST'}{\delta t}$ in relation to the fluxes are brought out here by linear correlation analyses (see Graham et. al., 1987 for discussion of canonical correlation and cross-validation techniques). The relationship that emerges is the obvious one that has negative $\frac{\delta SST'}{\delta t}$ changes forced by positive sea-air flux anomalies. This linkage is borne out over both ocean basins, particularly during winter months in the extratropics when latent and sensible fluxes are large and the solar radiation component is relatively small, shown by the local grid point correlations in Fig. 5. Canonical correlation analyses confirm the local relationship between the two fields, as the canonical flux predictor-$\frac{\delta SST'}{\delta t}$ predictand spatial patterns are nearly coincident. In both basins, a cross-validation scheme applied to the canonical regressions yields a winter skill pattern remarkably consistent with the simple correlations shown in Fig. 5, Averaged over the basins, the flux anomalies account for about 10-15% of the $\frac{\delta SST'}{\delta t}$ variance, with the greatest fraction of SST' variance accounted for in low mid-latitudes at about 30-40%.

References

Barnston, A. G., and R. E. Livezey, 1987: Classification, seasonality, and persistence of low-frequency atmospheric circulation patterns. *Mon. Wea. Rev.,* **115**, 1083-1126.

Bond, N. A., and R. G. Fleagle, 1988: Prefrontal and postfrontal boundary layer processes over the ocean. *Mon. Wea. Rev.,* **116**, 1257-1273.

Bunker, A. F., 1980: Trends of variablies and energy fluxes over the Atlantic Ocean from 1948 to 1972. *Mon. Wea. Rev.,* **108**, 720-732.

Frankignoul, C., and R. W. Reynolds, 1983: Testing a dynamical model for mid-latitude sea surface temperature anomalies. *J. Physical Oceanogr.,* **13**, 1131-1145.

Graham, N. E., Michaelsen, J., and T. P. Barnett, 1987: An investigation of the El Niño-Southern Oscillation cycle with statistical models: 1. Predictor field characteristics. *J. Geophys. Res.,* **92**, 14251-14270.

Haney, R. L., 1980: A numerical case study of the development of large scale thermal anomalies in the central North Pacific Ocean. *J. Physical Oceanogr.,* **10**, 541-556.

Isemer, H., and L. Hasse, 1987: **The Bunker Climate Atlas of the North Atlantic Ocean.** Springer-Verkag, Berlin.

Simpson, J., 1969: On some aspects of sea-air interaction in middle latitudes. *Deep-Sea Res., Supp to vol.* **16**, 231-261.

Taylor, P. K., 1984: The determination of surface fluxes of heat and water by satelite microwave radiometry and in situ measurments. In **Large-Scale Oceanographic Experiments and Satellites**, Gautier and Fieux, eds., pp. 223-246.

Weare, B. C., 1988: Uncertainties in estimates of surface heat fluxes derived from marine reports ovet the tropical and subtropical oceans. Unpublished manuscript.

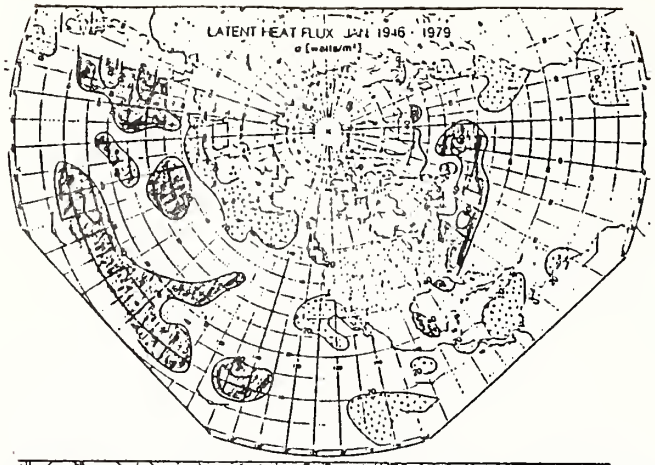
LATENT HEAT FLUX JAN 1946 - 1979

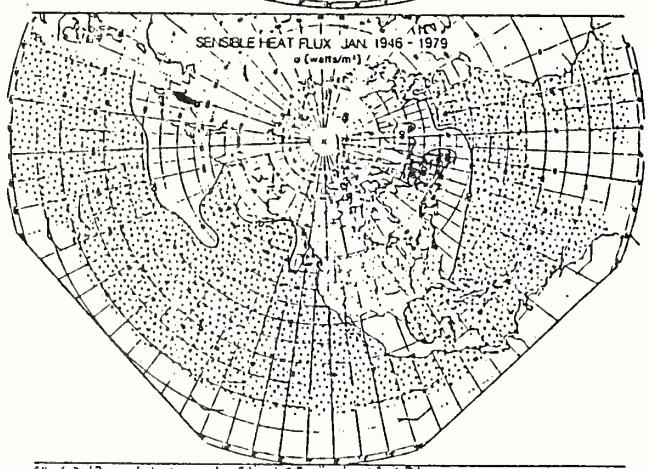
SENSIBLE HEAT FLUX JAN 1946 - 1979

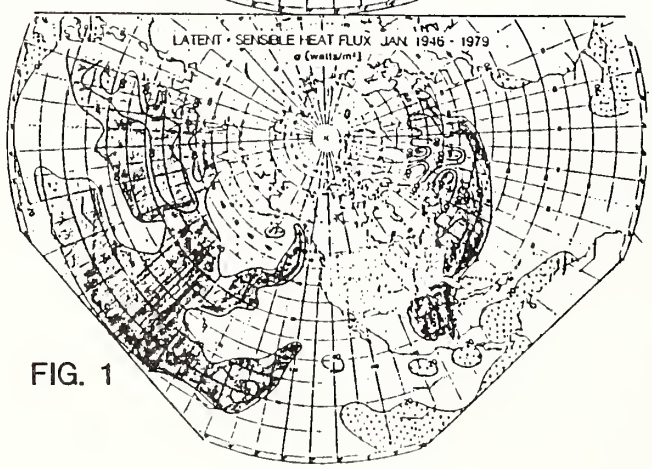
LATENT + SENSIBLE HEAT FLUX JAN 1946 - 1979

FIG. 1

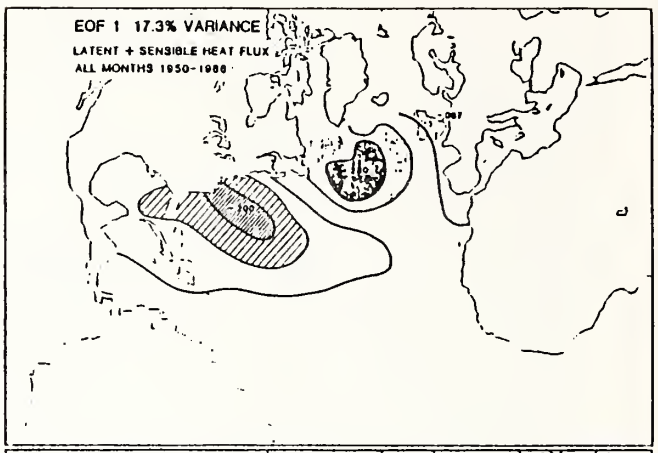
EOF 1 17.3% VARIANCE
LATENT + SENSIBLE HEAT FLUX
ALL MONTHS 1950-1988

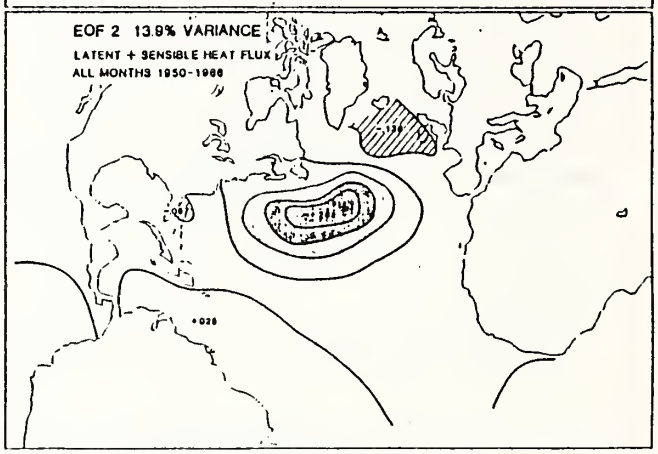
EOF 2 13.9% VARIANCE
LATENT + SENSIBLE HEAT FLUX
ALL MONTHS 1950-1988

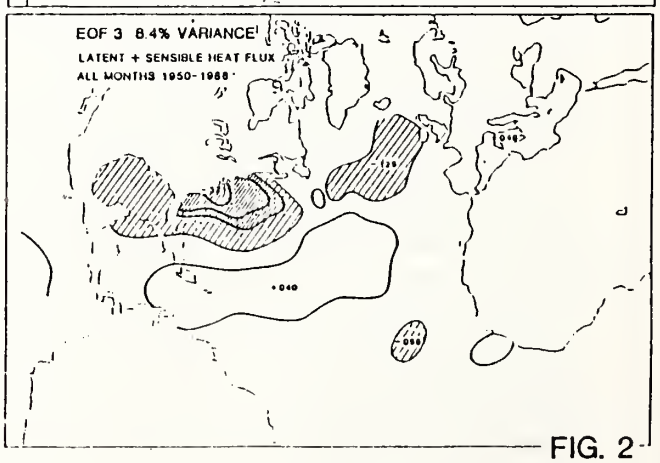
EOF 3 8.4% VARIANCE
LATENT + SENSIBLE HEAT FLUX
ALL MONTHS 1950-1988

FIG. 2

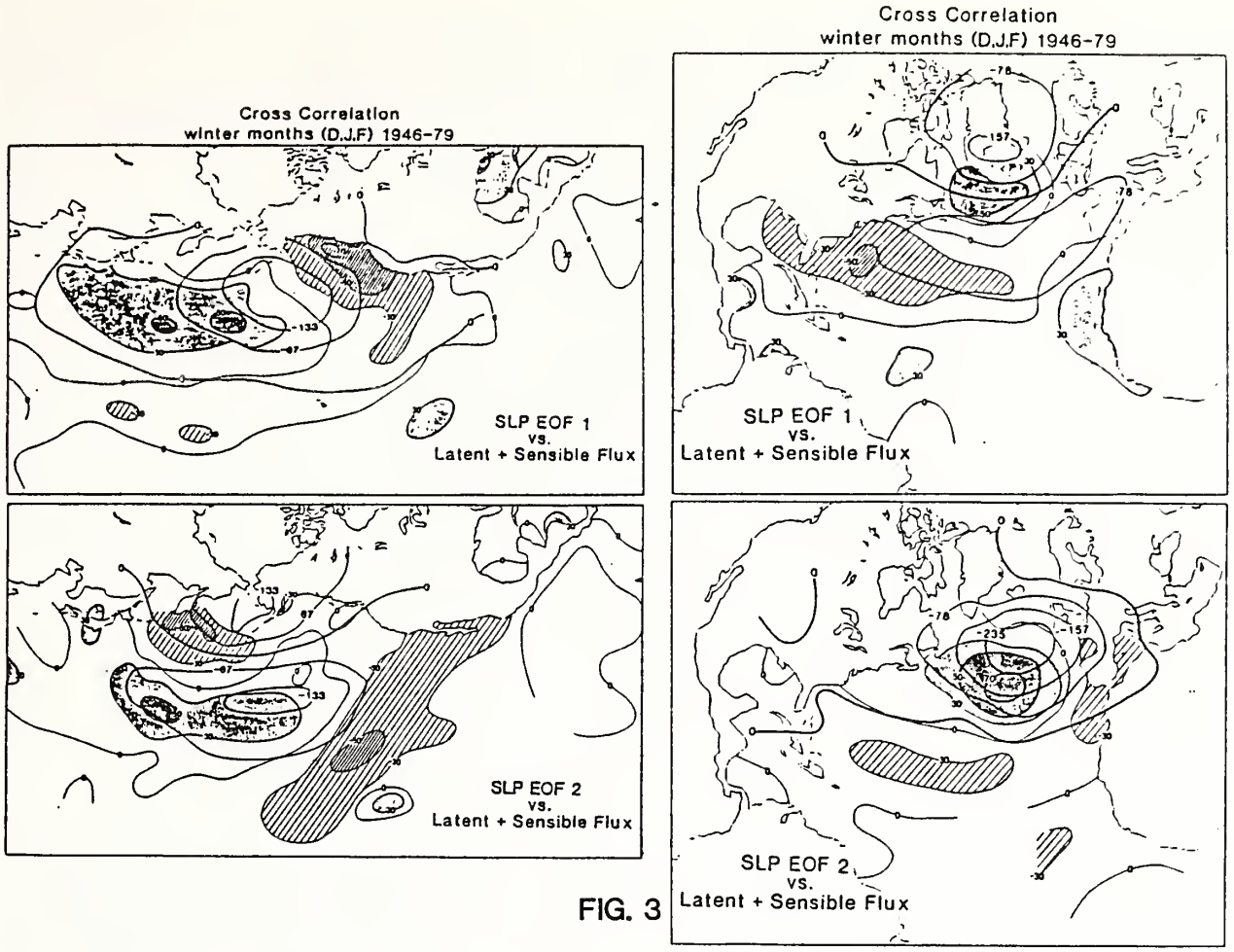
Cross Correlation
winter months (D.J.F) 1946-79
SLP EOF 1
vs.
Latent + Sensible Flux
Cross Correlation
winter months (D.J.F) 1946-79
SLP EOF 1
vs.
Latent + Sensible Flux
SLP EOF 2
vs.
Latent + Sensible Flux
SLP EOF 2
vs.
Latent + Sensible Flux

FIG. 3

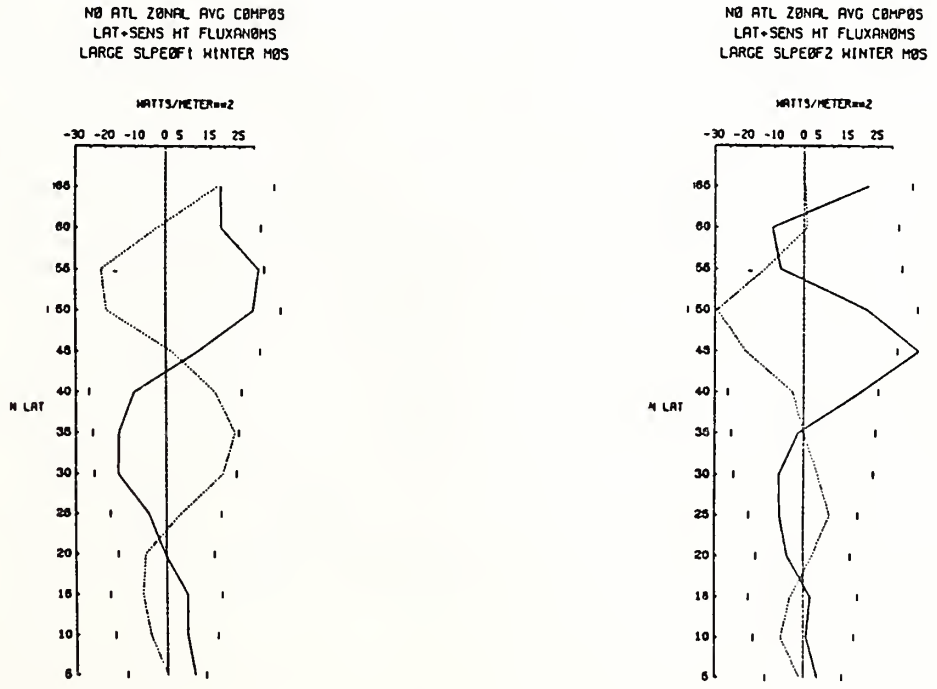
NØ ATL ZØNAL AVG CØMPØS
LAT+SENS HT FLUXANØMS
LARGE SLPEØF1 WINTER MØS
WATTS/METER**2
-30 -20 -10 0 5 15 25
N LAT
NØ ATL ZØNAL AVG CØMPØS
LAT+SENS HT FLUXANØMS
LARGE SLPEØF2 WINTER MØS
WATTS/METER**2
-30 -20 -10 0 5 15 25
N LAT

FIG. 4

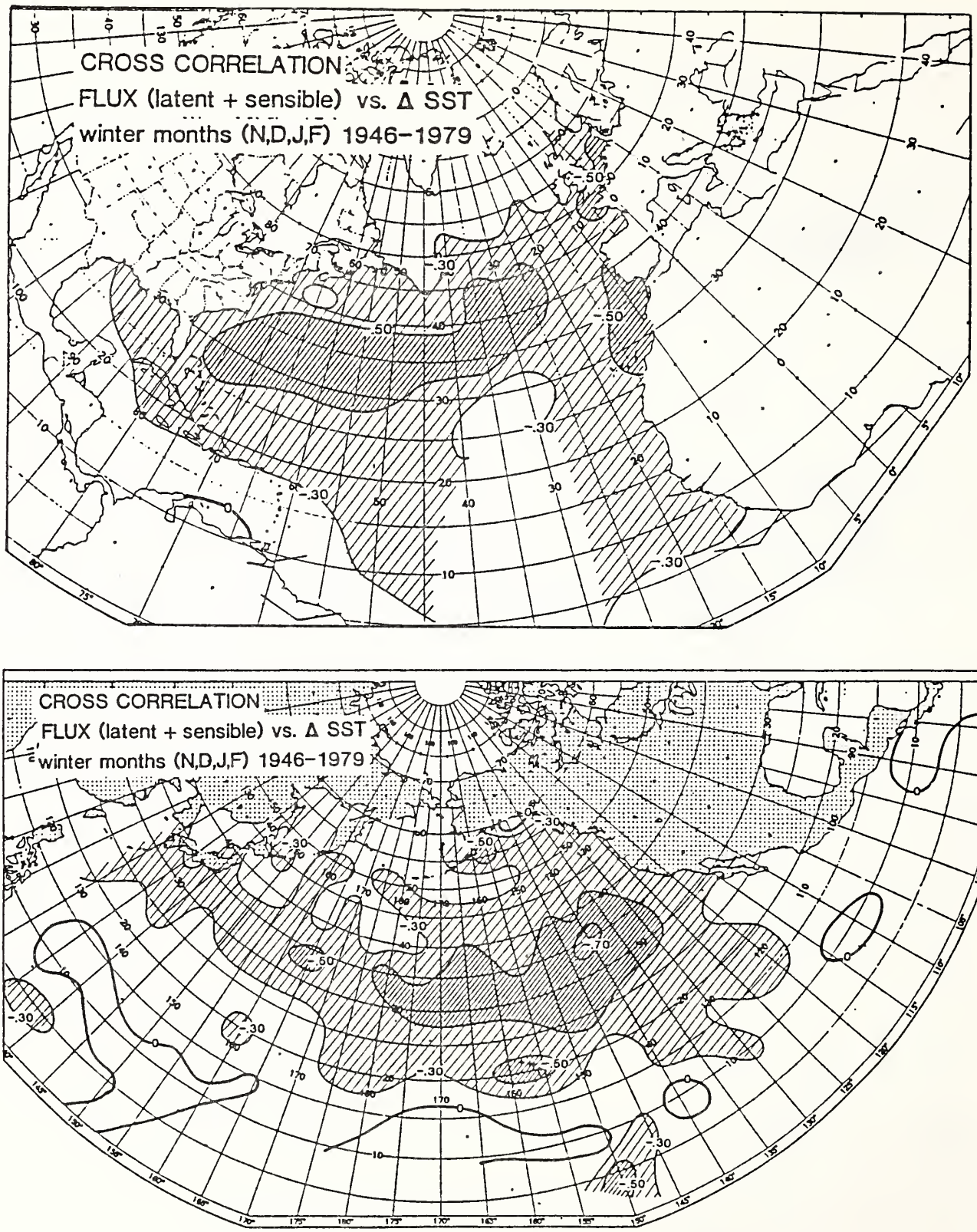
CROSS CORRELATION
FLUX (latent + sensible) vs. Δ SST
winter months (N,D,J,F) 1946–1979
CROSS CORRELATION
FLUX (latent + sensible) vs. Δ SST
winter months (N,D,J,F) 1946–1979

FIG. 5

EASTERLY WAVES ALONG THE EQUATOR

Brant Liebmann
Cooperative Institute for Research in Environmental Sciences
University of Colorado

Harry Hendon
Center for Atmospheric Theory and Analysis
University of Colorado

The power spectrum of the 850 mb meridional (v) component of wind at the equator reveals significant power in a band from seven to three days at almost every longitude (Fig. 1). Other fields exhibit a much more red spectrum. To study this range of periods, a high-pass filter was applied that passes periods shorter than seven days. The subsequent results were obtained using that filter. The data are the ECMWF analyses from September to December, 1980-1986. The results are similar for other seasons.

Figure 2 is a sequence of one-point correlation maps between 850 mb v at 180, Eq. and the entire 850 mb v field which leads by two days, is simultaneous with, and lags behind the point by two days. Westward phase and eastward group velocity are apparent.

The simultaneous correlation between 850 mb v at 180, Eq. and the zonal (u) field at 850 mb is shown in Fig. 3. Lag correlations show that the zonal wind anomalies propagate westward.

One-point correlation maps between 850 mb v at 180, Eq. and the outgoing longwave radiation (OLR) field for OLR leading by one day, simultaneous with, and lagging behind v by one day are shown in Fig. 4. The correlations are larger than if the meridional wind is taken at 200 mb. Again, westward phase and eastward group velocity are apparent. The OLR and u fields associated with v at the equator are both consistent with the expected structure of a mixed Rossby-gravity wave.

When u at the equator is correlated with v everywhere the resultant pattern bears resemblance to the expected structure of a Rossby wave, but the correlations are weak, there is no evidence of propagation with time, and when u is correlated with OLR there are no anomalies evident in the OLR field. The Rossby and mixed Rossby-gravity modes appear to be temporally uncorrelated. Since the evidence of a Rossby wave is weaker than of the mixed mode, the latter will be subsequently emphasized.

From the correlation between 850 mb v at 180, Eq. and itself as a function of height and time (not shown), it appears that although the correlations are rather small at the upper levels, the anomalies seem to tilt eastward with height at this longitude such that they exhibit a first-mode baroclinic structure in the troposphere. At some longitudes, however, there is a westward tilt. The small correlations between upper and lower levels are believed to result from the time-varying shear, resulting in a different tilt for each wave, thus weakening the ensemble correlation. The anomalies appear to originate at upper levels and then propagate downward.

The frequency of the mixed Rossby-gravity mode with respect to the ground is fixed at four days at almost every longitude. An estimate of the wavenumber (k) and intrinsic frequency (w), however, reveals that the characteristics vary dramatically as a function of longitude. Over the central and eastern Pacific they exhibit low w

and small k. Over the Atlantic they exhibit medium k and low w, while over the western Pacific they have large k and high w. Thus, the wavenumber and intrinsic frequency apparently adjust to maintain a constant absolute frequency in the presence of a zonally varying mean zonal wind.

As determined from a one-point correlation map, the structure at longitudes from about 70E-150E appears as a wave train propagating toward the equator from higher latitudes. Closer inspection, however, reveals that the pattern seems to originate at around 10N rather than in midlatitudes. The evidence of equatorward propagation is actually strongest during Northern Hemisphere summer and is not evident during that hemisphere's winter, suggesting that the source of the waves at these longitudes is the convection which is north of the equator during Northern Hemisphere summer.

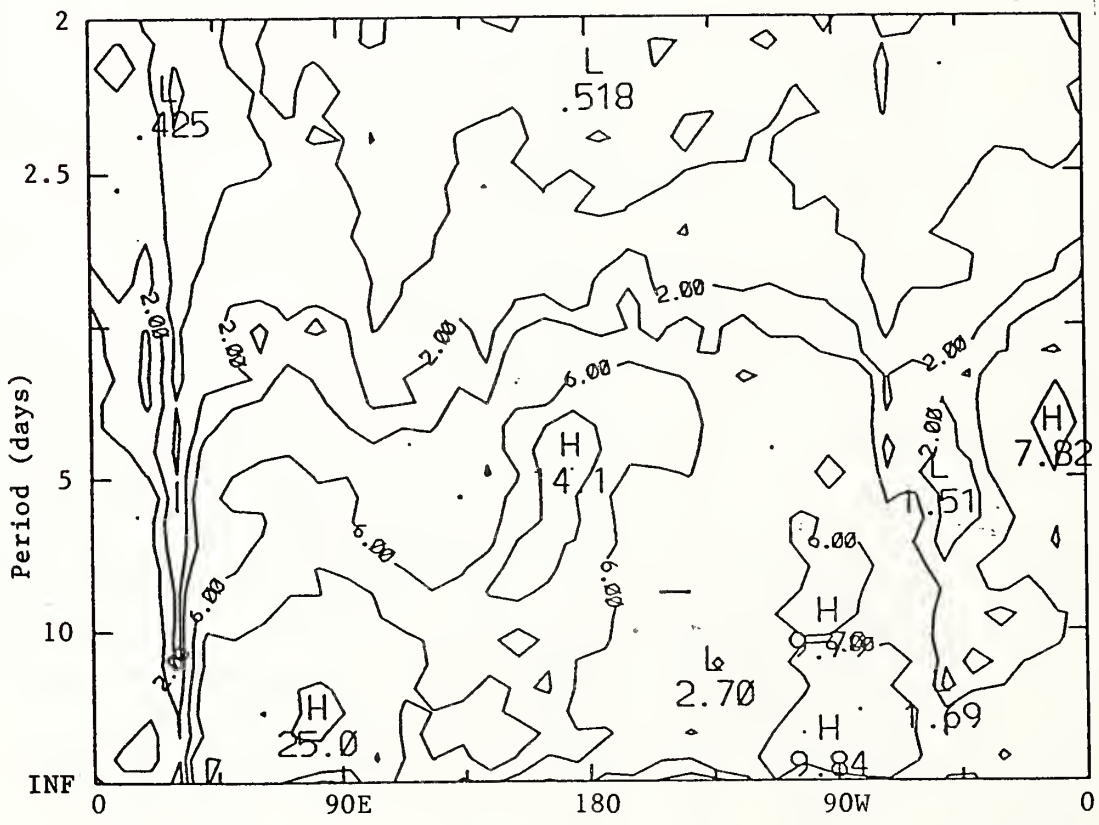

FIGURE 1. The power spectrum of the 850 mb meridional component of wind at the equator as a function of longitude for the September-December season. Contours are plotted at levels of 1, 2, 3, 6, 10, and 20 $m^2s^{-1}day^{-1}$. The data are the ECMWF analyses from 1980-86.

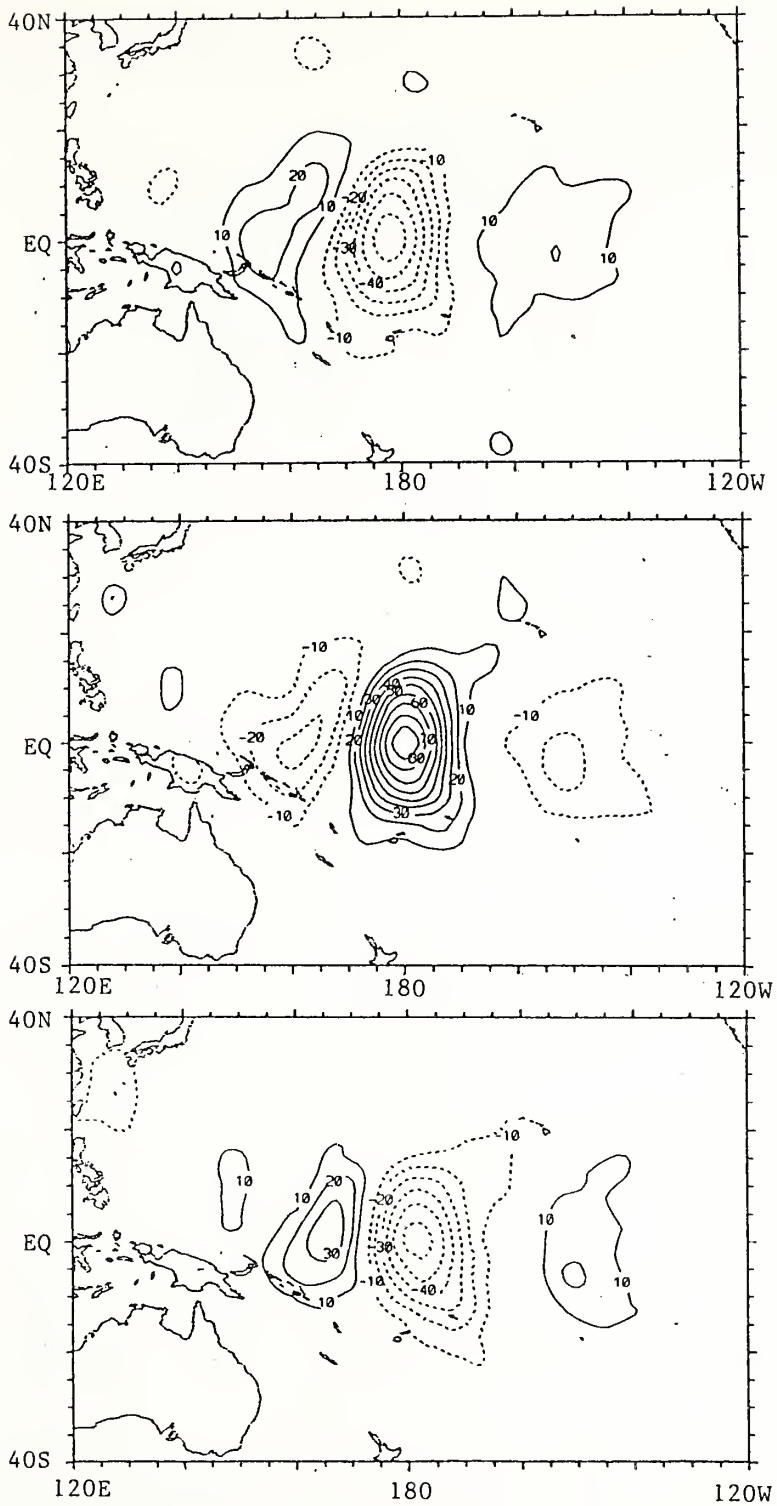

FIGURE 2. One-point correlation map between the 850 mb meridional wind at 180, Eq. and the 850 mb meridional wind field for the field leading by two days, simultaneous with the point, and lagging behind the point by two days. The data have been high-pass filtered with a filter that retains 80% of the power at seven days and 50 percent at ten days. The contours start at 0.1 with an interval of 0.1. Positive contours are solid and negative contours dashed.

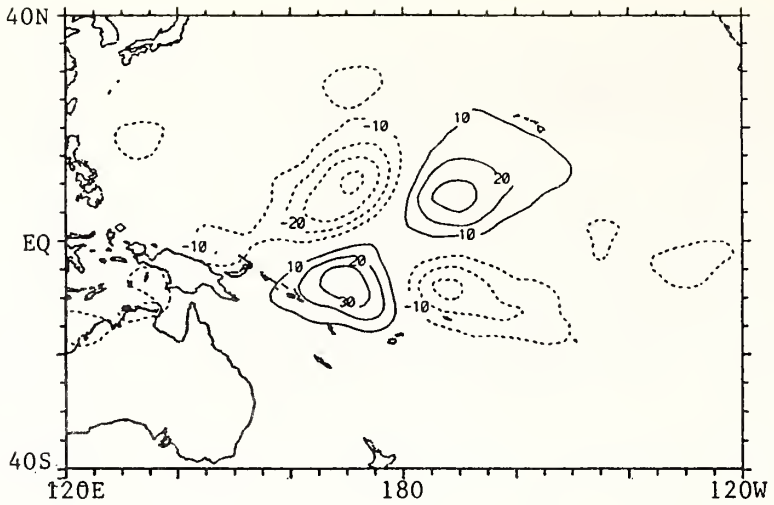

FIGURE 3. The simultaneous correlation between the 850 mb meridional wind at 180, Eq. and the zonal wind field. The filter and the contour interval are the same as in Figure 1.

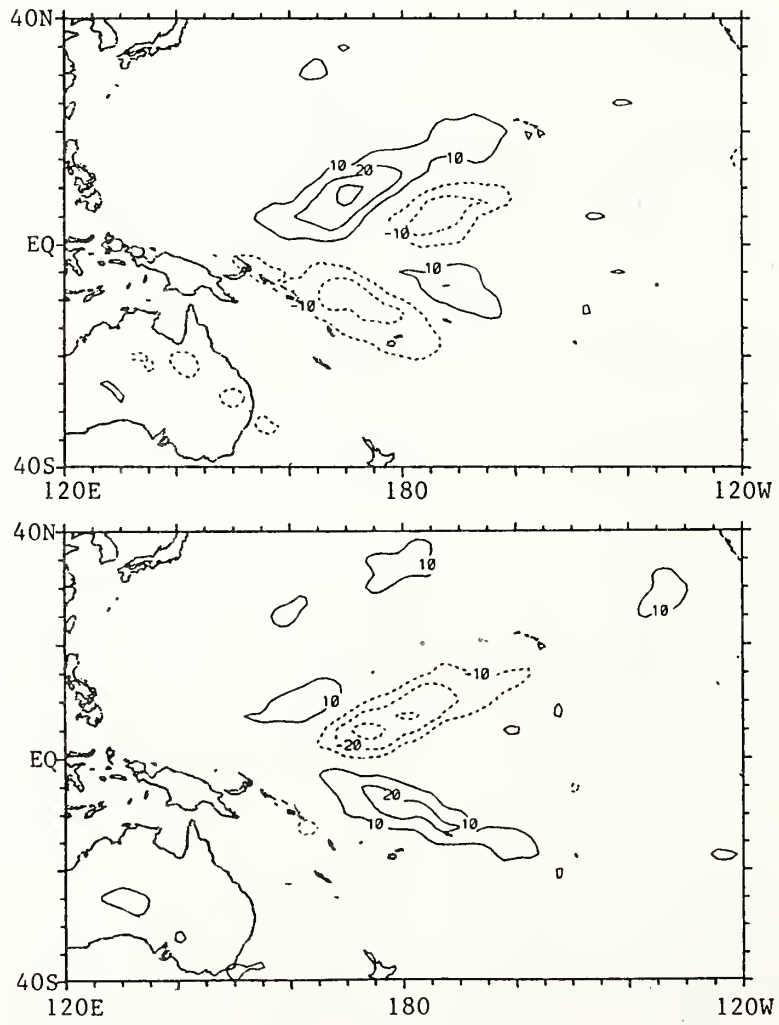

FIGURE 4. One-point correlation map between the 850 meridional wind at 180, Eq. and the outgoing longwave radiation field for the radiation field leading the point by one day and simultaneous with the point. The filter and the contour interval are the same as in Figure 1.

INTRASEASONAL OSCILLATIONS IN THE GLOBAL ATMOSPHERE

Michael Ghil
Department of Atmospheric Science
University of California-Los Angeles
Los Angeles, CA 90024
and
Kingtse Mo
Climate Analysis Center/NMC/NWS/NOAA
Washington, DC 20233

Oscillations on the intraseasonal time scale exist in both the tropics and extratropics. A 30- to 60-day oscillation of zonal wind and cloudiness in the tropics, as well as of mid-tropospheric height fields and upper-tropospheric streamfunction fields in the extratropics, has been studied by many authors. Branstator (1987) discovered a westward traveling wave with a period of 23 to 25 days, which was particularly strong in the Northern Hemisphere during the 79/80 winter.

We have examined systematically oscillatory modes in both hemispheres and in the tropics. In the Northern Hemisphere, 700 mb heights were used to analyze extratropical oscillations; 500 mb heights were used in the Southern Hemisphere. Outgoing long wave radiation data were used to represent tropical convection. All data sets were filtered to focus on the IS band of 10 to 90 days.

Leading spatial patterns of variability were obtained by applying EOF analysis to IS filtered data. The leading principal components (PCs) were subjected to singular spectrum analysis (SSA). SSA is a statistical technique related to EOF analysis, but in the time domain, rather than in the spatial domain (Vautard and Ghil 1988). It helps to isolate the standing and traveling components of the oscillation in a time series.

In the Northern Hemisphere, two EOF patterns are related to 30- to 60-day oscillation. They are EOF 1 (Fig.1) and EOF 4 (Fig.2) in the Northern Hemisphere winter. SSA indicates that both patterns have modes of oscillation with periods near 36, 25, and 17 days, respectively. The 36-day mode is the most dominant one, which consists of 40% of the total variances. Composites show that EOF 1 is a westward traveling pattern. In the winter of 79/80, 25-day mode is the strongest, but in general, 36-day mode is more prominent. EOF 4 has both standing and eastward traveling components.

In the Southern Hemisphere, the 25-day mode dominates, comprising the second and third EOFs in the IS band. This mode (Fig.3) has a zonal wave number 4 structure and is traveling eastward. The next two modes are 36-day mode and 18-day mode. Both are weak.

In the tropics, 36-day mode dominates the Indian and Pacific Oceans from 60E to the date line. This is the 30- to 60 day-wave documented by Madden and Julian (1971, 1972). From 150W to 90W, 25-day wave is the strongest.

Our findings suggest that the tropical and extratropical oscillations have very complex relationships with each other. The extratropical modes are often independent of and sometimes lead the tropical modes. Nonlinear dynamics may play a role in the extratropical oscillations and in the interaction among these modes.

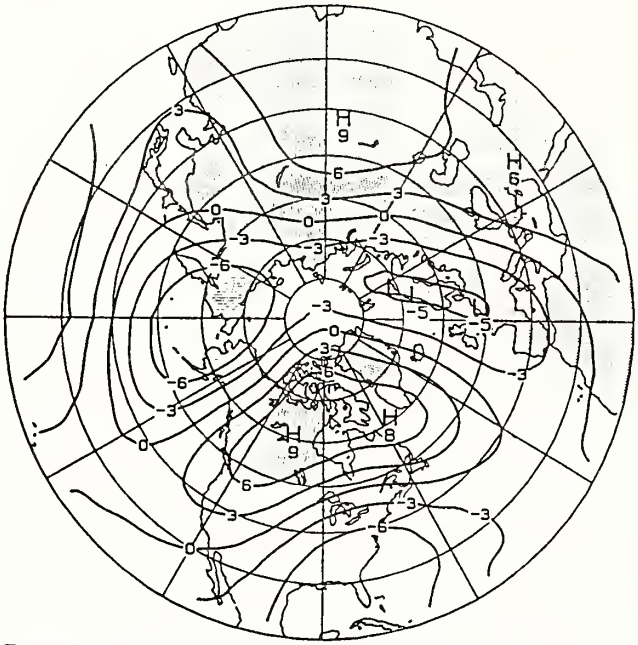

Fig. 1 Spatial EOF 1 pattern in the intra-seasonal band for the NH winter. EOF is normalized to unit vector length x 100, contour interval is 3.

Fig. 2 Same as Fig. 1 but for EOF 4.

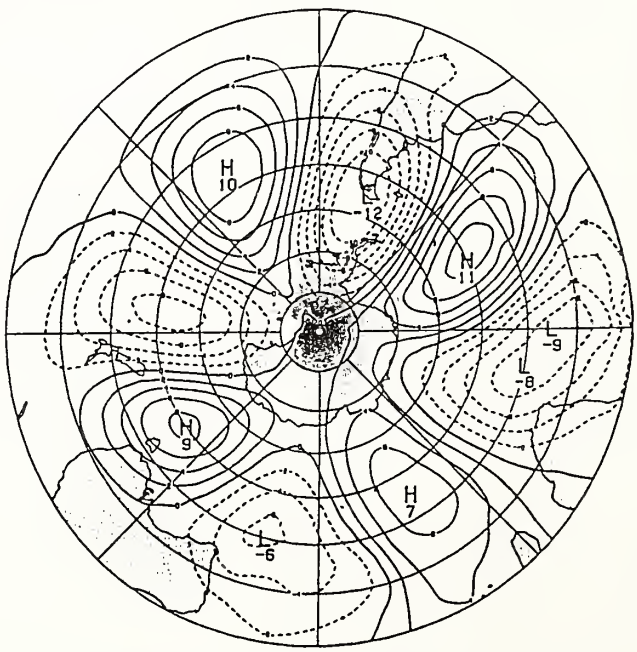

Fig. 3 Same as Fig. 1 but for EOF 2 for the SH winter.

An Observational Study of the Relationship Between High Latitude Blocking Onset and the 30-60 Day Oscillation in Near Equatorial Convection During Northern Hemisphere Winter

John V. Zapotocny
Department of Atmospheric Sciences, Creighton University
Omaha, Nebraska 68178

Seasonal and geographical distributions of northern hemisphere blocking have been examined in numerous studies, as have the dynamical and thermodynamical forcings responsible for the establishment and maintenance of blocks. To date, however, the question of whether a systematic relationship exists between high latitude blocking onset and remote forcings associated with the 30-60 day oscillation in the tropics has not been widely addressed. Although such a relationship has been suggested in various global modeling studies it has not been clearly verified using observational data. This report summarizes preliminary results of a diagnostic investigation into this aspect of the blocking problem.

Blocking data for the study were derived from daily 500mb geopotential heights on a 5° x 5° latitude longitude grid obtained from the National Meteorological Center's operational analyses for the winter seasons (1978/79 - 1987/88). The daily fields were composited into five-day mean height distributions for the 18 pentads comprising the winter season (2 December - 1 March). The study was confined to those regions of the northern hemisphere shown in Figure 1, encompassing the high latitude North Atlantic and North Pacific Oceans, where wintertime blocking has been shown to be most prevalent (Shukla and Mo, 1983; Dole and Gordon, 1983).

A circulation index was used to evaluate the anomalous character of the 500mb flow within the study regions. This index is schematically defined in Figure 2. In essence, the value of the index indicates the large-scale anomalous vorticity within the regions. Positive values are associated with anomalous cyclonic flow while negative values are associated with anomalous anticyclonic flow. It must be remembered that in both study regions the mean wintertime flow tends to be cyclonic so that an anticyclonic deviation from the mean does not necessarily imply an actual flow that is anticyclonic.

Time series of the circulation index for each study region during the 10 winters are shown in Figure 3. A 3-pentad running mean filter was used to remove the highest frequencies. At least some indication of a systematic oscillation is evident during each of the 10 winters in both regions. By simple visual inspection, the period of this oscillation ranges from about five pentads (20-25 days) up to nine pentads (40-45 days). The oscillations are particularly well-defined during certain winters; namely, 1980/81 and 1984/85 in the NA region and 1978/79, 1979/80 and 1983/84 in the NP region, but ill-defined during other winters; 1979/80 and 1985/86 in the NA region and 1980/81 and 1987/88 in the NP region. Longer period oscillations would be difficult to discern given the 18-pentad record for each winter. Data for November and March of each year are presently being added (which will expand each record to 30 pentads). After the addition of these pentads, a spectral analysis will be performed to determine the predominant cycles.

Blocking episodes were defined using the criteria developed by Knox alnd Hay (1984) which considers the magnitude of the 500mb height anomaly as well as the latitude of the anomaly center and the time of year. The criteria for the winter season can be expressed mathematically as: $(A_K - 15)(\phi_K - 49) > 16$. where A_K is the magnitude of the 500mb height anomaly in decameters during the Kth pentad and ϕ_K is the latitude of the anomaly in degrees. If the inequality is satisfied for three consecutive days during a pentad a block is considered to exist during that pentad. The principle advantage to using this definition, as pointed out by Knox and Hay (1984), is that it has the effect of screening out those positive anomalies near 50°N that are attributable to the amplification of the subtropical anticyclone, but will include those relatively short-lived episodoes at higher latitudes that are of synoptic-scale importance. The blocking events are indicated by the shading in Figure 4. A total of 23 blocks were catalogued in both the NA and NP regions during the 10 winters examined. In general, the blocking events correspond to periods when the circulation index is negative or at least a relative minima. The index then, would appear to be an acceptable quantifier for blocking episodes in these regions.

A closer examination of the blocking distributions in Figure 4 reveals that blocking in the high latitude North Atlantic tends to precede blocking in the North Pacific by approximately two to four pentads (10-20 days), implying a retrograde character. This finding is consistent with the results of global modeling studies and may be indicative of the so-called "Branstator wave," a slowly retrogressive mode of mid-tropospheric circulation shown to exist at high latitudes (Branstator, 1987). Linear correlation coefficients between the NA CIRC and NP CIRC time series for each of the ten winter seasons are listed in Table 1. The straight correlations are mostly negative but with values generally near zero. If a three-pentad lag is introduced with NA CIRC leading NP CIRC, the correlations are all positive with values between .29 and .93. Correlation values at or exceeding the 95% confidence threshold of .47 were observed during 8 of the 10 winters, suggesting a retrogression of high latitude circulation anomalies from the North Atlantic to North Pacific regions. Not surprisingly, the winters of 81/82, 86/87 and 87/88 showed the poorest lagged correlations. Each of these winters was characterized by well developed, persistent anomalous circulation patterns in the NA and NP portion of the hemisphere.

Coefficient time series for the first two eigenvectors of outgoing longwave radiation (OLR), as determined by Weickmann (1983), were used for comparing the temporal evolution of blocking patterns to the 30-60 day oscillation. Time series of these coefficients for the six winters from 1978/79 through 1983/84 are depicted in Figure 5. Eastward propagating areas of enhanced tropical cloudiness associated with the 30-60 day wave are represented by the out-of-phase variations in the radiation eigenvector (REV) time series. A complete cycle in the oscillation would consist of positive REV 1 coefficients when the anomalously negative OLR (cloudiness maximum) associated with the 30-60 day wave is centered over Indonesia followed by positive values for REV 2 as the cloudiness propagates to 140-160°, then negative REV 1 coefficients when the anomalous cloudiness is near the dateline and finally negative REV 2 coefficient values as the cloudiness jumps to South America, Africa and re-emerges over the Indian Ocean. It should be pointed out that while Weickmann's analysis was based on data for November-March, only the 18 winter pentads for December-February have been used thus far in this study and are included in Figure 5.

A detailed comparative analysis of the OLR and circulation parameters is not planned until the November and March data have been added to the blocking data base and additional REV data has been obtained for winters subsequent to 83/84; however, results of a simple preliminary analysis are depicted in Figure 6. The suggestion is that blocking in the NA region tends to develop when the REV 1 coefficient time series are at or near a relative minimum. Of the 10 blocking onsets observed in the NA region during this 6 winter period, 7 of them corresponded to negative values of the REV 1 time series (enhanced cloudiness near the dateline). Similarly, blocking onset in the NP region appears to be favored when the REV 1 coefficients are near a relative maximum (enhanced cloudiness near Indonesia), with 11 of 13 blocking onsets during the 6-winter period falling into that category. The relationship, if any, between the REV 2 time series and blocking is not nearly as clear. There appears to be a weak tendency for blocking in the NA region when REV 2 has a negative coefficient. No preference is displayed for NP blocking onset. These early results are in good agreement with those of Weickmann et al. (1985). Their study, however, considered the more general relationship between the evolution of extratropical circulation anomalies and the 30-60 day oscillation without focusing specifically on high latitude blocking.

Clearly, considerable work remains before a thorough understanding emerges of how blocking at high latitudes may be related to the 30-60 day oscillation. The present study has raised some intriguing points for further investigation and future research, following the addition of November and March height data and inclusion of the REV time series for the full ten winters, will hopefully lend some additional insight into this aspect of the blocking problem.

References

Branstator, G., 1987: A striking example of the atmosphere's leading traveling pattern. J. Atmos. Sci., 44, 2310-2323.

Dole, R.M. and N.D. Gordon, 1983: Persistent anomalies of the extratropical northern hemisphere wintertime circulation: Geographical distribution and regional persistence characteristics. Mon. Wea. Rev., 111, 1567-1586.

Knox, J.L. and J.E. Hay, 1984: Blocking signatures in the northern hemisphere: Rationale and identification. Atmosphere-Ocean, 22, 36-47.

Shukla, J. and K.C. Mo, 1983: Seasonal and geographical variation of blocking. Mon. Wea. Rev., 111, 388-402.

Weickmann, K.M., 1983: Intraseasonal circulation and outgoing longwave radiation modes during northern hemisphere winter. Mon. Wea. Rev., 111, 1838-1858.

Weickmann, K.M., G.R. Lussky and J.E. Kutzbach, 1985: Intraseasonal (30-60 day) fluctuations of outgoing longwave radiation and 250mb streamfunction during northern winter. Mon. Wea. Rev., 113, 941-961.

Table 1. Linear correlations between NA CIRC and NP CIRC. Lagged correlations are for NA CIRC leading NP CIRC by three pentads.

YEAR	STRAIGHT CORRELATION	LAGGED CORRELATION
78/79	-.13	.93
79/80	.16	.63
80/81	.21	.20
81/82	-.47	.35
82/83	-.19	.58
83/84	-.12	.51
84/85	-.22	.71
85/86	.09	.54
86/87	-.33	.47
87/88	-.56	.29

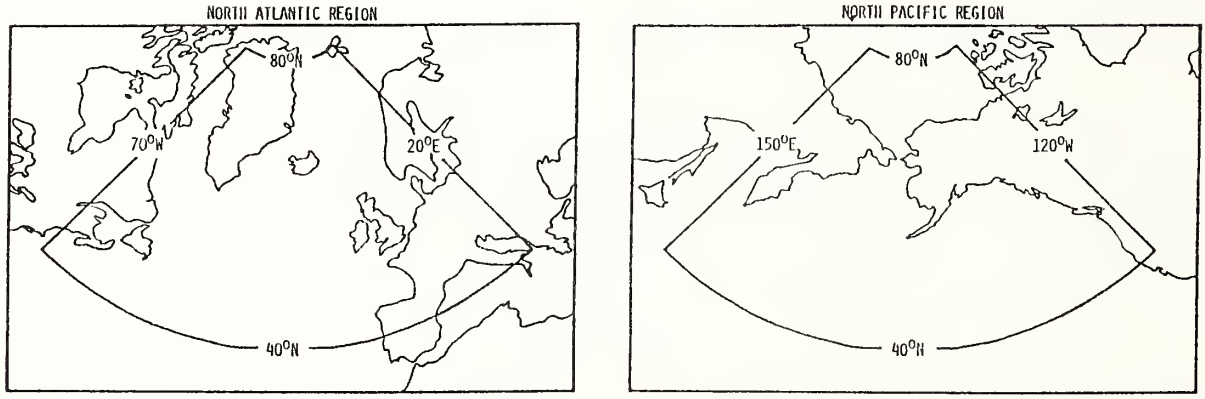

Figure 1. Regions of the northern hemisphere used in this study. The North Atlantic region (NA) and the North Pacific region (NP).

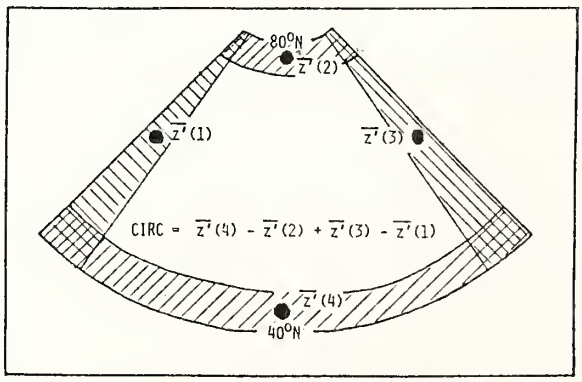

Figure 2. Schematic depicting the circulation index used. The $\overline{Z'}$ values refer to mean 500mb height anomalies in five degree wide meridional sections for $\overline{Z'}$ (1) and $\overline{Z'}$ (3) and five degree zonal belts for $\overline{Z'}$ (2) and $\overline{Z'}$ (4). The index is indicative of the large-scale anomalous vorticity within the region.

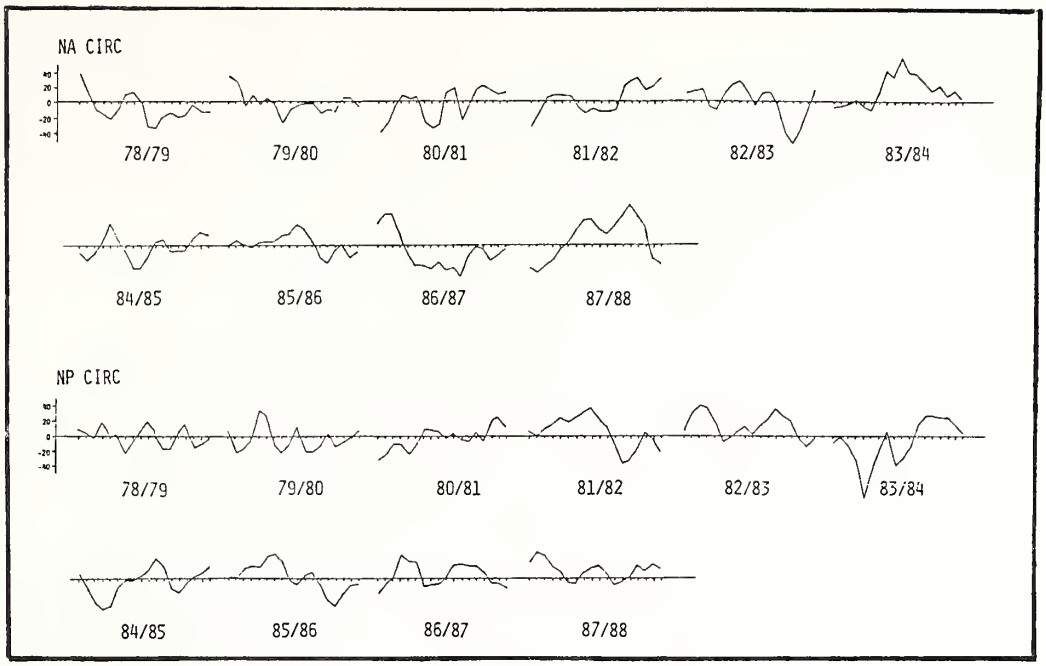

Figure 3. Time series of the circulation index (decameters) for the winters of 1978/79 through 1987/88 in the NA and NP regions.

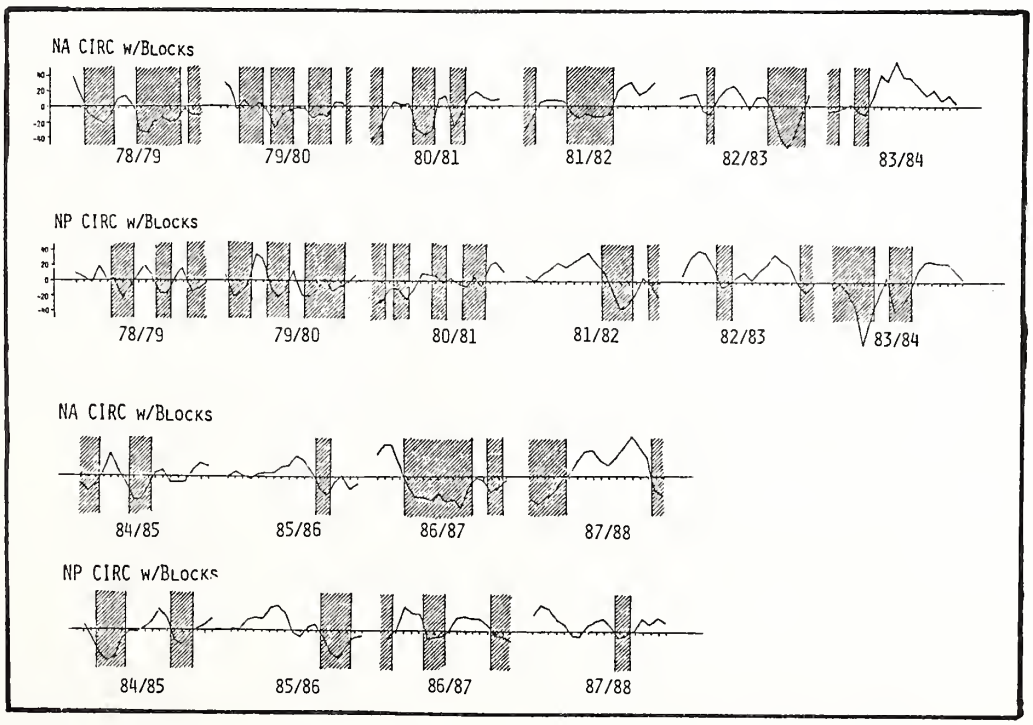

Figure 4. Same as Fig. 3, but with blocking events in the NA and NP regions as defined by the Knox and Hay (1984) criteria (indicated by shading) superimposed.

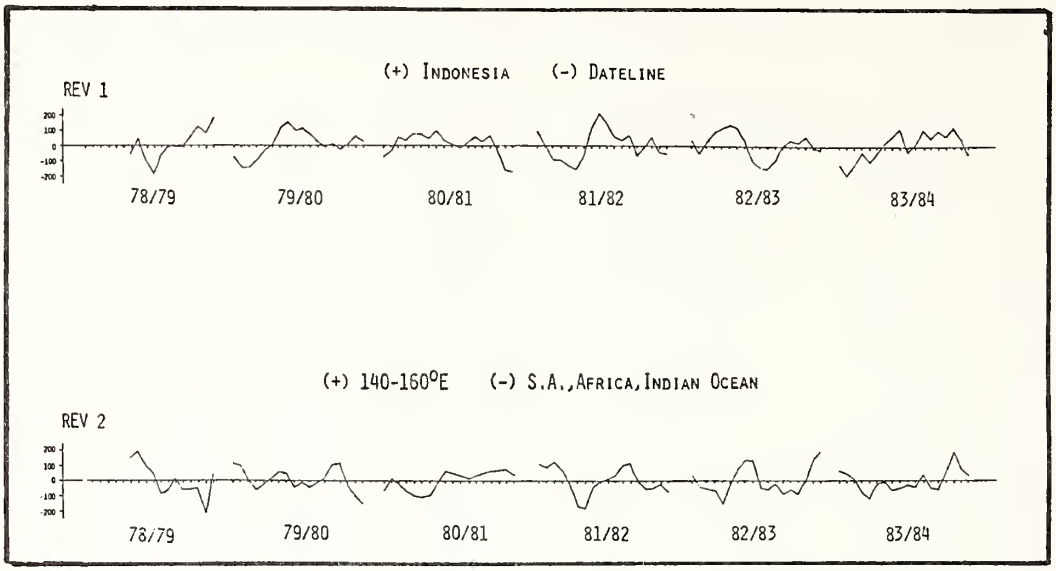

Figure 5. Coefficient time series for radiation eigenvector 1 (REV1) and radiation eigenvector 2 (REV2) for the six winters of 1978/79 through 1983/84 (10-180 day variance retained). These time series quantify the 30-60 oscillation in near-equatorial convection. Obtained from Weickmann (personal communication, 1988).

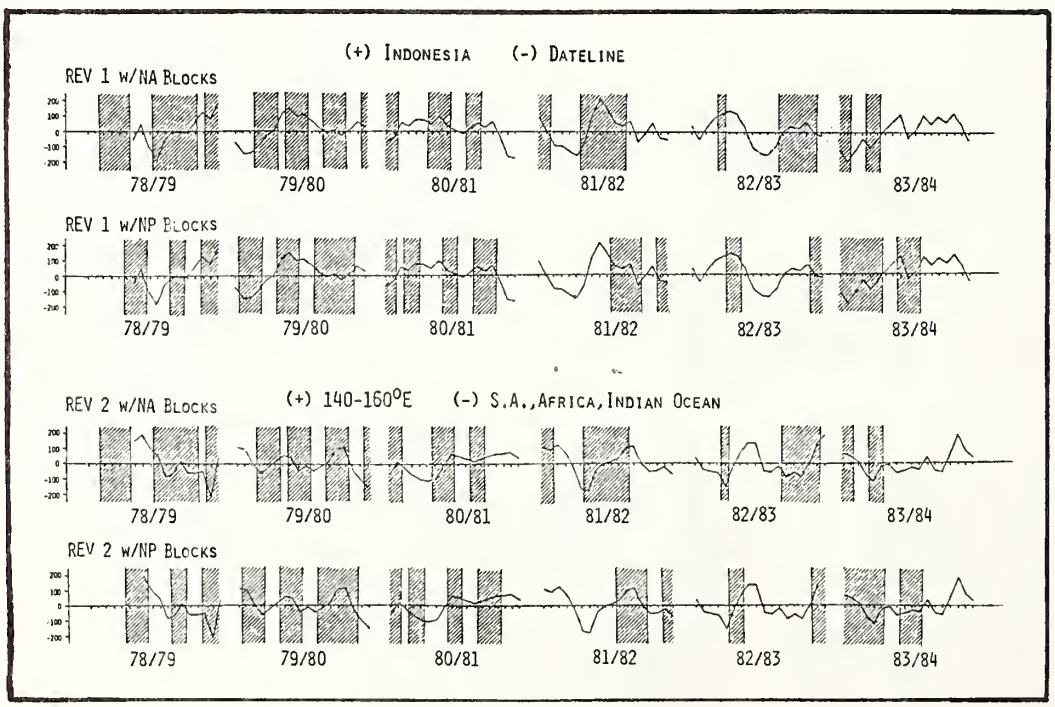

Figure 6. Same as Fig. 5, but with blocking events (indicated by shading) superimposed.

DYNAMICS OF MULTI-SCALE ATMOSPHERE-OCEAN INTERACTIONS OVER THE TROPICAL WESTERN PACIFIC

(Proceedings of the 13th Climate Diagnostic Workshop, November, 1988, Cambridge, MA)

K. M. Lau
Laboratory for Atmospheres, NASA/Goddard Space Flight Center
Greenbelt, MD 20771

In this paper we present results of several numerical experiments to study the mechanism of the observed variabilities in wind and convection associated with super cloud clusters (SCC), westerly wind bursts and 30-60 day oscillations in the western Pacific region (Fig. 1). Using the Lau and Peng (1987) model, we show that the generation of a 30-60 day eastward propagating Kelvin wave-group can be identified as a SCC. This wave-group is accompanied by convective cells moving in opposite direction to that of the SCC itself (Fig.2). The results suggest that these westward propagating cloud cells are Rossby waves produced at the formative stage of the 30-60 day disturbance due to mutual adjustment of the large scale flow and heating.

Model results further suggest that intraseasonal oscillation in the tropical atmosphere is a multi-scale process. Three basic spatial scales are identified, i.e., synoptic scale motion associated with cloud clusters (2000-4000 km), size of the SCC (2000 km) and planetary scale circulation (wavenumber 1 and 2). The first is associated with westerly wind burst , double cyclone formation and high-frequency fluctuations of the order of several days. The second and third are associated with slow eastward propagation of the 30-60 day oscillation. The detailed evolution of the low level flow associated with the splitting of the Rossby and Kelvin waves obtained from the above experiments are shown schematically in Fig. 3. It appears that the westerly wind burst at the surface is produced by the high-frequency (2-3 days) "shedding" of Rossby waves from the developing supercluster. As a result of the separation of the waves, the region of low level westerly expanded abruptly. In addition, the east-west asymmetry of the wind response to convection may be the basic reason for the observation that there is no corresponding "easterly wind burst" at the surface.

The relationship between SCC and westerly wind burst is studied by examining the detailed spatial and temporal variation of the model SCCs as they propagate over zonally varying sea surface temperature. It is found that that wave-CISK heating in the lower troposphere as well as surface heating are crucial in leading to the strongly asymmetric low level westerly wind bursts similar to those observed in the real atmosphere. The present results suggest that the western Pacific (perhaps also the Indian Ocean) is a unique region where multi-scale interactions between atmosphere and ocean are most important.

A scenario of multi-scale interaction involving westerly wind burst, 30-60 day oscillation leading to a possible trigger for the onset of ENSO is shown schematically in Fig. 4.

Reference

Lau, K. M and L. Peng, 1987: Origin of low-frequency (intraseasonal) oscillation in the tropical atmosphere. Part I: the basic theory. J. Atmos. Sci., 44, 950-972.

Lau, K. M. and L. Peng, 1988: An updated theory of the 30-60 day oscillation. Proceeding of the Workshop on Model inter-comparison. ECMWF, Reading, UK.

Lau, K. M., L. Peng, C. H. Sui and T. Nakazawa, 1989: Dynamics of super cloud clusters, westerly wind bursts, 30-60 day oscillations and ENSO : an unified view. J. Meteor. Soc. Japan. (submitted).

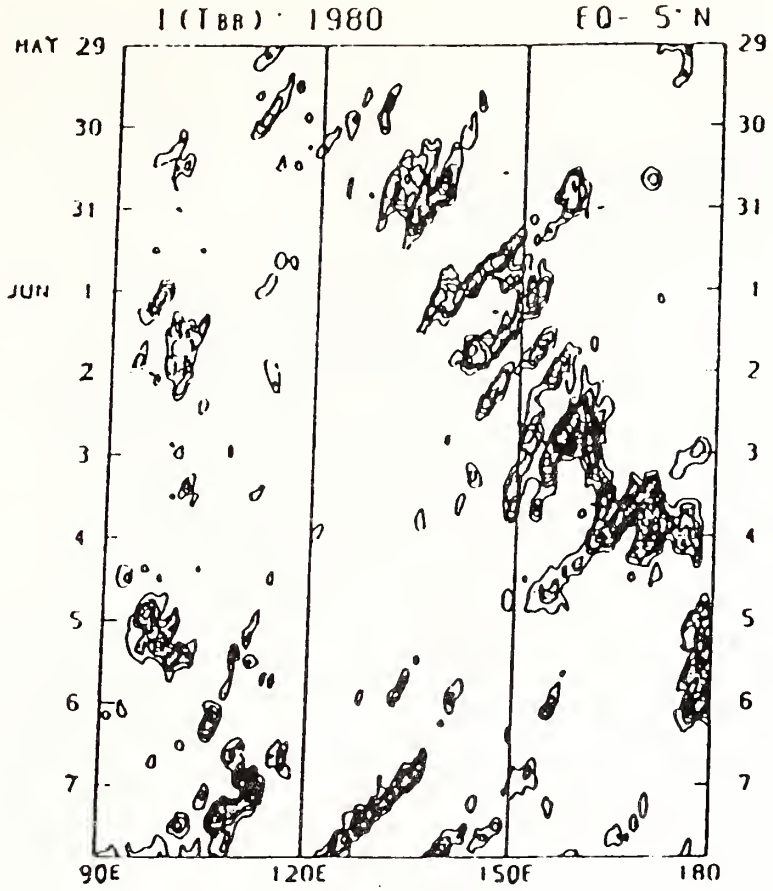

Fig. 1. Time-longitude section of index of deep convection between the equator and 5°N obtained from 3-hourly Japanese Geostationary Meteorological satellite infrared data from 29 May 00Z to 10 June 21 Z, 1980 (Adopted from Nakazawa, 1988)

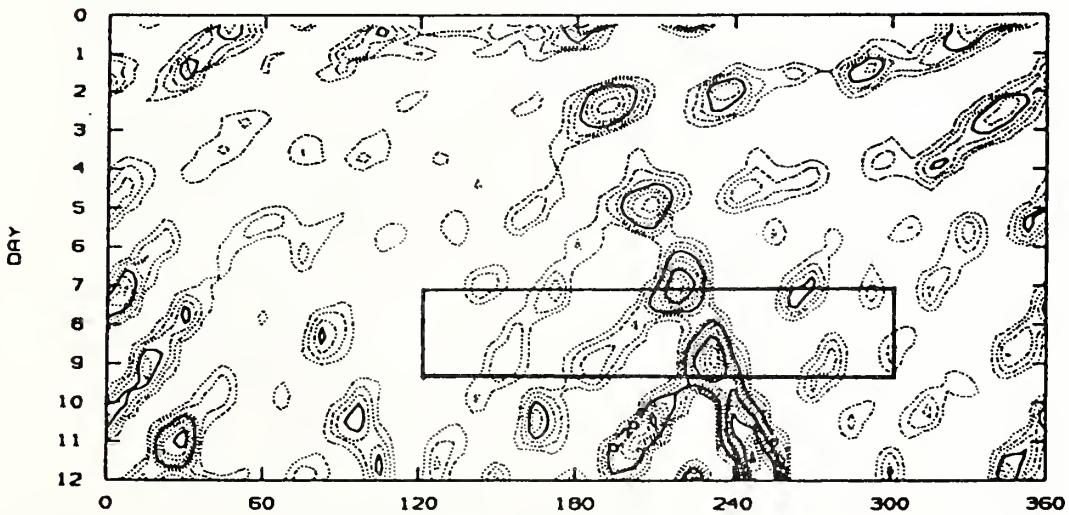

Fig. 2. Time-longitude section of simulated rainfall pattern at the equator using the Lau and Peng model. Contour intervals in 5 mm/day.

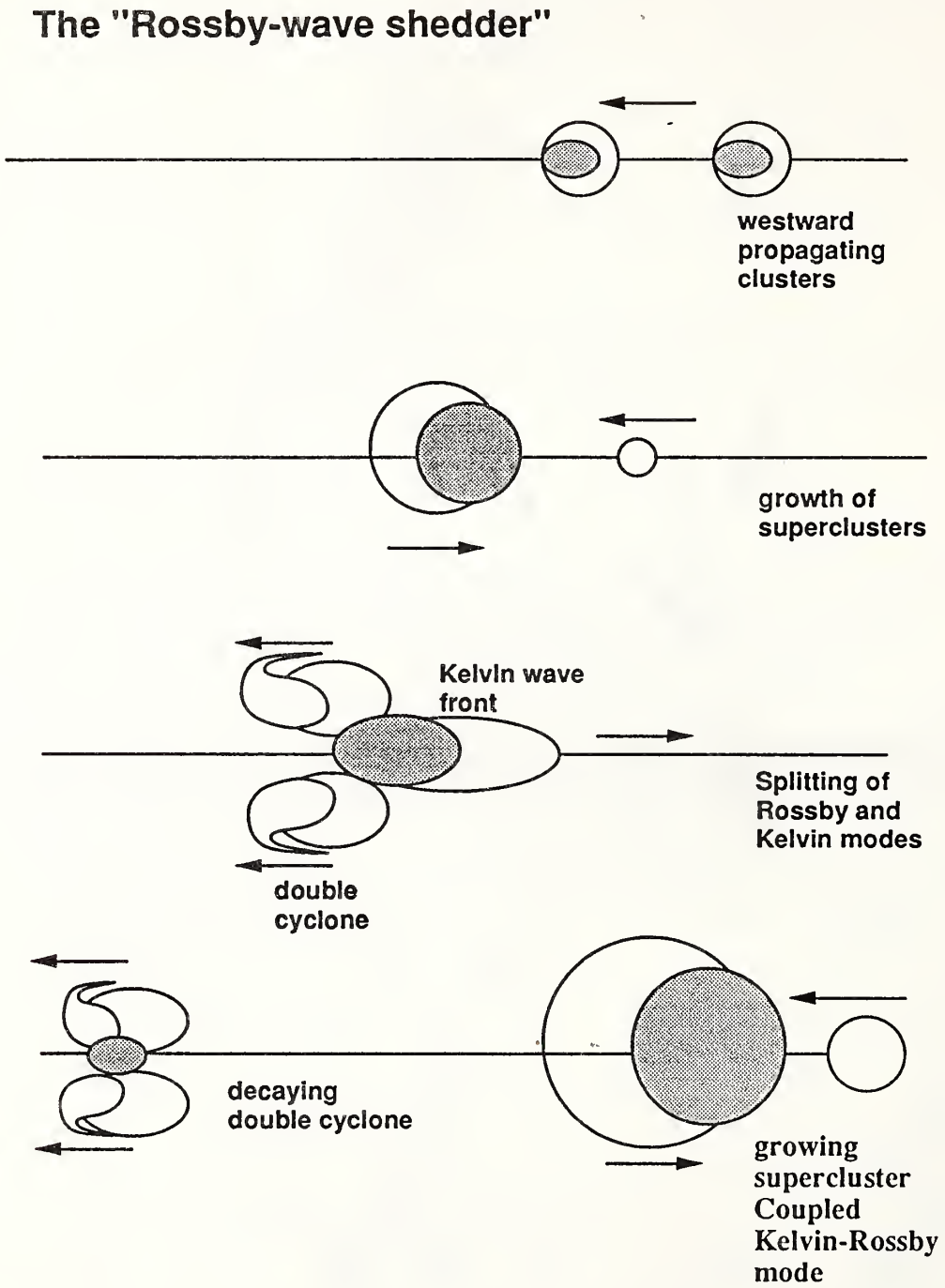

Fig.3 Cartoon showing cloud and circulation patterns associated with the separation of Kelvin and Rossby waves along the equator due to mutual adjustment of heating and circulation.

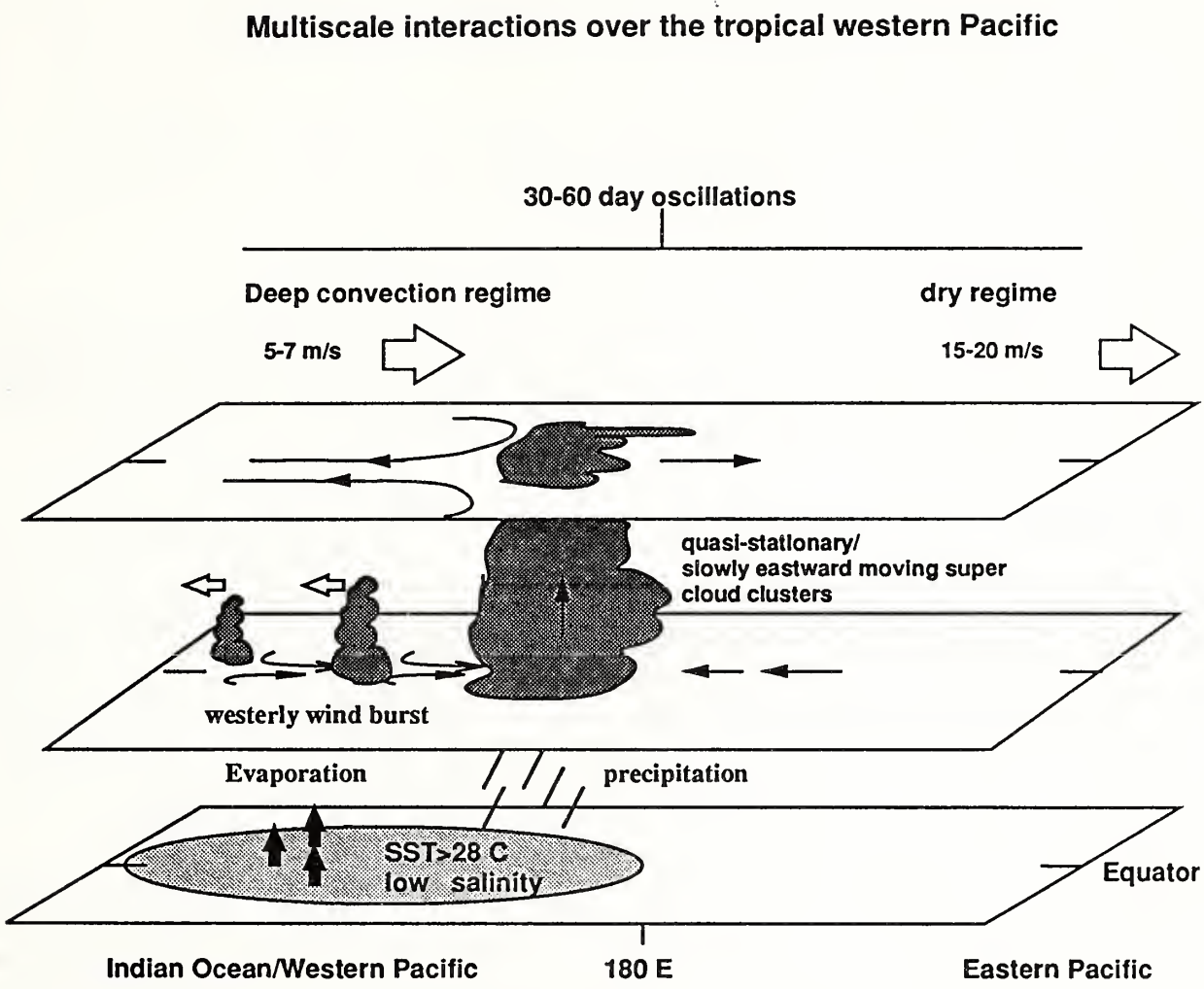

Fig.4 Schematic showing multi-scale interactions among westerly wind bursts, intraseasonal oscillations, superclusters. During onset phase of ENSO, the entire system amplifies and slowly shift eastward due to unstable coupled ocean-atmosphere interaction

INTERCOMPARISON OF INTRASEASONAL (30-60 DAY) OSCILLATIONS IN THREE GENERAL CIRCULATION MODELS

CHUNG-KYU PARK
Centel Federal Services Corporation, NASA/Goddard Space Flight Center
Greenbelt, Maryland 20771

DAVID M. STRAUS
Center for Ocean-Land-Atmosphere Interactions
Department of Meteorology, University of Maryland
College Park, Maryland 20742

KA-MING LAU
Goddard Laboratory for Atmosphere, NASA/Goddard Space Flight Center
Greenbelt, Maryland 20771

1. INTRODUCTION

We compare the structure of the 30-60 day oscillation appearing in annual cycle integrations of three GCMs which have been in use in the Global Modeling and Simulation Branch. These are the GLAS GCM, the UCLA GCM and the GLA GCM. We also present results from the global ECMWF analyses of 1984-1986.

2. GCMS

All the models were integrated for at least two years (three years for the UCLA GCM), and they are all grid point models with 4x5 degree latitude/longitude resolution with nine layers in the vertical. The GLAS GCM uses a staggered grid (so-called B grid), and the second order finite-difference scheme. The cumulus parameterization scheme is that of Arakawa (1972). The GLA GCM is identical to the GLAS GCM in terms of physical parameterizations. However, the GLA GCM uses an unstaggered grid (so-called A grid) with a quadratic energy conserving scheme of fourth order accuracy. The UCLA GCM uses a cumulus parameterization due to Arakawa and Schubert (1974). In this GCM the planetary boundary layer top is prognostic variable and acts as a coordinate surface. The horizontal differencing scheme uses a staggered grid (so-called C grid).

3. RESULTS

The nature of traveling waves is examined with the use of wavenumber-frequency spectra of the 200mb velocity potential at the equator. We find in Figure 1 that the eastward moving waves in the ECMWF analyses are associated with 30-60 day oscillations and a dominant zonal wavenumber of one. The GLAS GCM shows a similar distribution of power to that of the ECMWF analyses, although the magnitudes are considerably weaker in the GLAS GCM. The weakness of the 30-60 day oscillation in the UCLA GCM is apparent, although eastward traveling waves with period near 15 days are evident. For the GLA GCM, the eastward moving waves have a peak around 20-30 days and a second peak at 13 days.

The vertical structure of the 30-60 day oscillation is described by a composite procedure. Figure 2 shows the longitude-pressure sections of zonal-component of wind composite in the tropics for the 30-60 day mode. In the composite process, the 200mb velocity potential [filtered to retain the 30-60 day period] averaged in the tropics (10°S-10°N) was used as an index to define the 30-60 day mode. The band-pass filtered zonal wind fields were composited by translating the longitude of the maximum velocity potential to align with the reference longitude, while the amplitude of velocity potential is used as weighting coefficients. We composited only for the cases in which

the maximum velocity potential is located between 60°E and dateline so that we can isolate the structure of oscillation in the Indian Ocean-west Pacific convective region. Same procedure was repeated for the minimum cases. The composite patterns in Figure 2 are the difference between the composites for the maximum case and minimum case, which illustrates the vertical structure of tropical atmosphere following the center of oscillation.

The ECMWF analyses show a circulation cell along the zonal equatorial plane which has the maximum inflow toward the center of oscillation around 600mb level and the maximum outflow near 200mb level, with a slight westward tilt of phase with height. The low-level westerlies penetrate the center of oscillation. The models generally depict a similar structure of zonal circulation cell along the equatorial plane. The westward tilt of phase with height is more clear in the GLAS GCM and UCLA GCM. The westward tilt of phase with height indicated both in the analyses and the GCMs supports that the wave-CISK mechanism is important for maintaining the eastward propagating waves in the tropics, although it is not clearly indicated in the GLAS GCM.

Figure 3 shows the longitude-pressure sections of specific humidity composite in the tropics. The ECMWF analyses illustrate the wet condition to the east and the dry condition to the west of the oscillation center. The vertical structure of moisture appears to be closely coupled with the zonal circulation cell on the equatorial plane. The zonal circulation supplies the moisture to the east of the oscillation center in the convergence zone and leave the dry zone behind the low-level westerlies. This indicates that the evaporation-wind feedback may also be an important mechanism for the eastward propagation of the 30-60 day oscillation.

In the GLA GCM, the zonal circulation cell confined to the upper troposphere indicates that the internal dynamics associated with deep convective heating is dominant in the free atmosphere, and that the boundary layer process has a weak effect on the zonal circulation cell. The dry conditions near the center of oscillation in the bottom layer of the GLAS GCM and GLA GCM are possibly related to the insufficient wind-effect on the moisture supply near the surface. The inconsistency of the wind and moisture in the UCLA GCM may be explained either by incorrect signal picked up in the composite procedure or complications in the boundary layer process.

4. DISCUSSION

We find that the UCLA GCM has a very weak 30-60 day oscillation, but it appears to support a 15-day eastward propagating wave. It is suggested that nearly uniform heating profile in the model troposphere (not shown) is at least partially responsible. This is confirmed by simple numerical experiments by Lau and Peng (1987) and Sui and Lau (1988).

The GLAS GCM and the GLA GCM simulate a realistic vertical structurte of the 30-60 day oscillation in the tropics. The results indicate that the improvement in the boundary layer process is important for better simulation of the 30-60 day oscillation in the GCMs.

5. REFERENCES

Arakawa,A.,1972: Design of UCLA general circulation model. Numerical simulation of weather and climate. Technical report No.7, Department of Meteorology, UCLA.

Arakawa,A.,and W.M.Schubert,1974: The interaction of a cumulus cloud ensemble with the large-scale environment, Part I. J. Atmos. Sci., 31, 674-701.

Lau,K.-M.,and L.Peng,1987: Origin of low-frequency (intraseasonal) oscillations in the tropical atmosphere. Part I: Basic theory. J. Atmos. Sci., 44, 950-972.

Sui,C.-H., and K.-M. Lau, 1988: Origin of low frequency (intraseasonal) oscillations in the tropical atmosphere. Part II: Effect of improved treatment of moist processes. J. Atmos. Sci.,To be published.

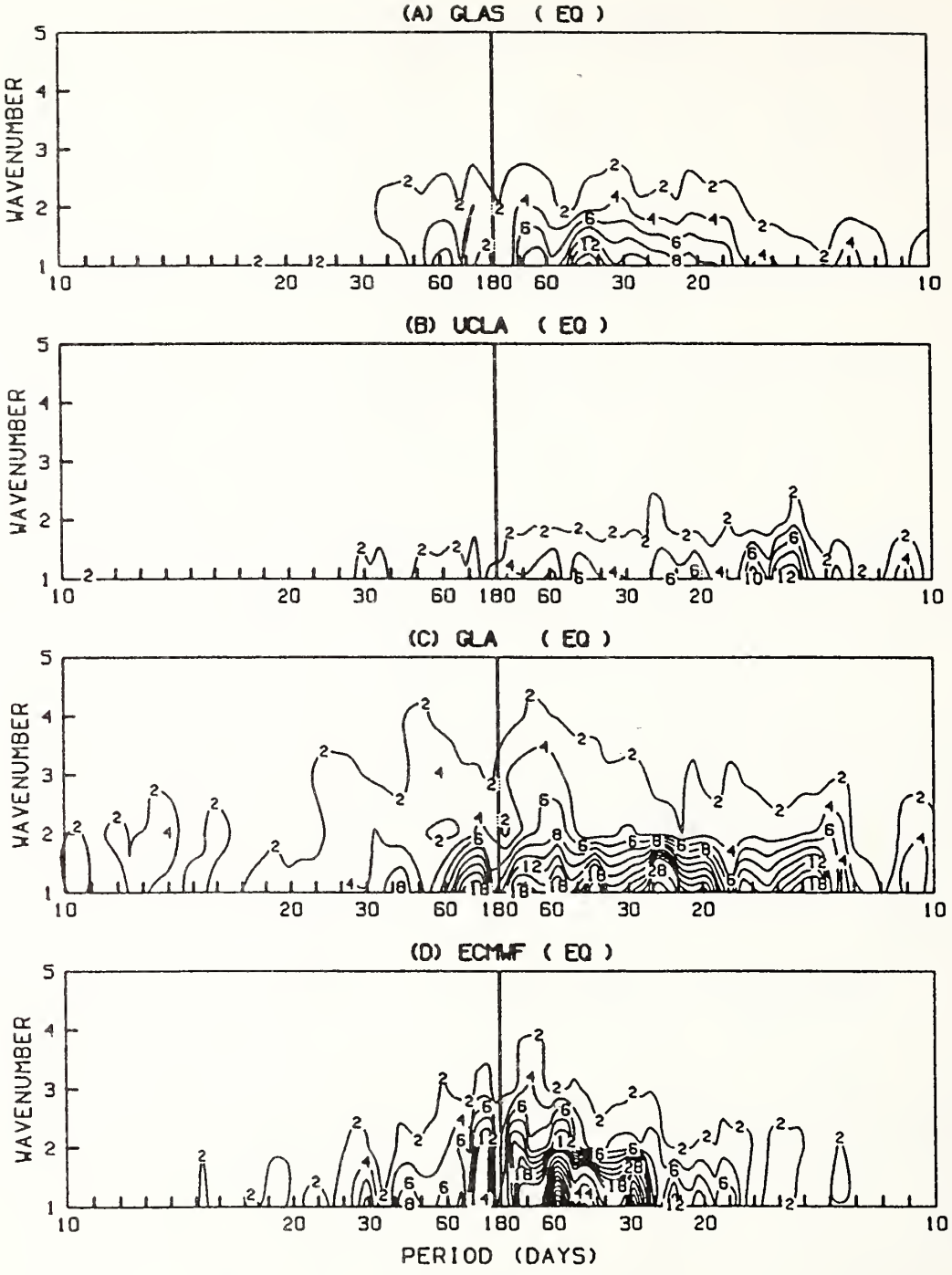

Figure 1 - Wavenumber-frequency spectra of 200 mb velocity potential at the equator for (a) GLAS GCM, (b) UCLA GCM, (c) GLA GCM and (d) ECMWF analyses. Left (right) hand panels correspond to westward (eastward) propagating waves. Contour interval is 2.0 x 10^{11} m^4 S^{-2} day. For values greater than 2.0 x 10^{12} m^4 S^{-2} day, contour interval is 8.0 x 10^{11} m^4 S^{-2} day.

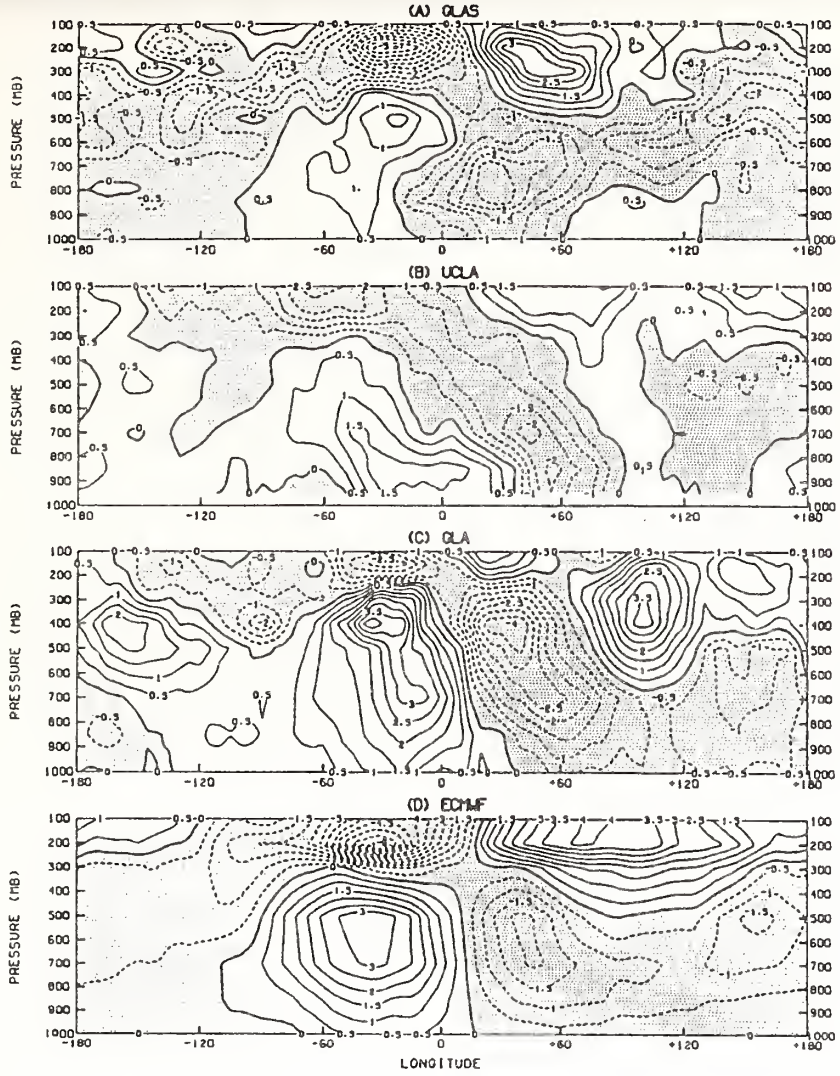

Figure 2 - Longitude-pressure sections of composite for the band-pass filtered zonal-component of wind in the tropics from (a) GLAS GCM, (b) UCLA GCM, (c) GLA GCM and (d) ECMWF analyses. Contour interval is 0.5 m s^{-1} Negative region is shaded.

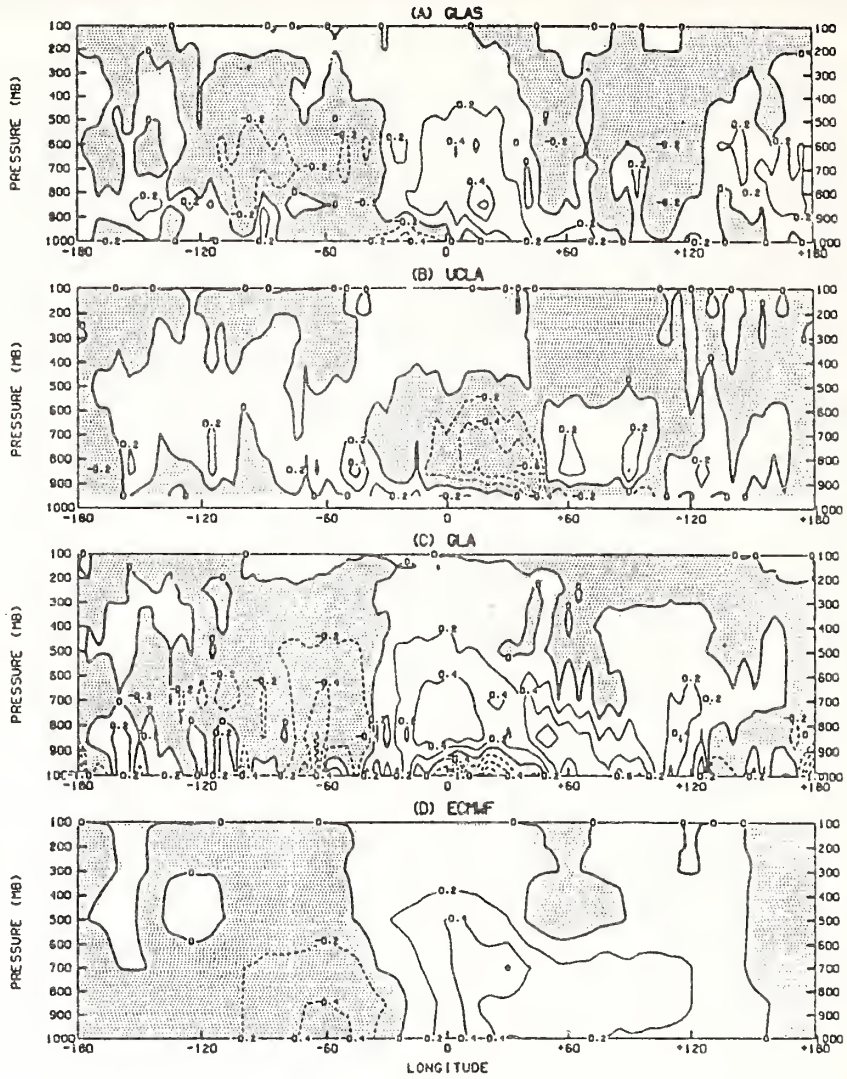

Figure 3 - Same as Figure 2, but for the band-pass filtered specific humidity composite. Contour interval is 0.2 g/g.

FREQUENCY DEPENDENCE OF TELECONNECTION PATTERNS

Yochanan Kushnir[1] and John M. Wallace
Department of Atmospheric Sciences, University of Washington, Seattle, WA 98195

We examine the frequency dependence of the variability with periods longer than 10 days, in the Northern Hemisphere 500 mb geopotential height field during the cold season (November through April). The data is derived from a 39-year record of NMC analyses, time filtered to partition the fluctuations into frequency bands corresponding to periods of 10-60 days, 60-180 days and >180 days. In this way we distinguish between the variability with periods of several weeks or several months within individual winter seasons on one hand and the year-to-year variability in the wintertime circulation on the other. Variance, teleconnectivity and anisotropy fields, as well as the loading vectors of a rotated principal component analysis (RPCA) of the temporal correlation matrix of the height field, are calculated to determine the geographical distribution and characteristic structure of the dominant patters of variability in each frequency band.

Fig. 1 shows the teleconnectivity fields (following the definition by Wallace and Gutzler, 1981) corresponding to fluctuations in the three frequency bands. The 10-60 day band [Panel (a)] is relatively 'flat' and lacks the strong local features that appear in the other two fields, in particular the one corresponding to *interannual* variability [Panel (c)].

Fig. 2 shows the anisotropy of the height perturbations as derived from the local, temporal covariance matrix of the geostrophic wind field (following the method of Hoskins et al., 1983). The line segments in this figure are oriented along the major axis of the local eddy anisotropy and their length is proportional to the amount of anisotropy (eccentricity). The contours represent the zonal (east/west) component of the anisotropy and indicate whether most of the variance in the wind field is in the zonal component (large positive numbers), in the meridional component (large negative numbers), or equally distributed between the two (numbers close to 0). As is the case with the teleconnectivity fields we find that the 10-60 day field [Panel (a)] is relatively flat compared to its lower frequency counterparts. In the *interannual* frequency band [Panel (c)] there is a good correspondence between the regions of minima in the teleconnectivity field and the regions of strong anisotropy (east/west or north/south).

When the patterns emerging from the RPCA in the three frequency bands are compared it is found that the normalized *intraseasonal* variance, in particular that with periods of 10-60 days, is almost equally distributed between the different loading vectors. Moreover, the loading vectors occur in pairs, in which the two patterns are in spatial quadrature with one another, i.e., the centers of action of one, overlap the nodal lines of the other. This relationship can be seen, for example, in Figs. 3 and 4 for the 10-60 day variability over North America and for the 60-180 day variability over the Pacific, respectively[2]. These results are insensitive to the method of rotation (orthogonal or oblique), leading us to

[1] Present affiliation: AOS program, Princeton University, P.O. Box 308, Princeton, NJ. 08542

[2] For a more complete set of patterns the reader is referred to Kushnir and Wallace, 1988.

suggest that they indicate a genuine lack of geographical phase preference in the underlying height perturbations. The loading patterns should thus be interpreted as basis functions which can be linearly combined to form a continuum of anisotropic structures. The featureless teleconnectivity field of 10-60 day variability (Fig. 1a) is consistent with this notion, as was also demonstrated by Blackmon et al. (1984) using 1-point correlation maps. Although we do not find the teleconnectivity field in the 60-180 day band equally featureless, we are forced to conclude, based on the results of the RPCA, that the patterns of variability in this band also exhibit a lack of phase preference, with the exception that the variability over the western ocean basin is more coherent then that over other regions of the hemisphere. Thus, in a statistical sense, *intraseasonal* variability is associated with a continuum of anisotropic perturbations, which are not geographically discrete.

Convincing evidence of the existence of geographically discrete 'modal structures' is found only in the *interannual* band, where the quadrature relationship between patterns is less pronounced (particularly in the oblique rotation) and two patterns stand out clearly above others: The Pacific / North American (PNA) pattern and the North Atlantic Oscillation, shown in Fig. 5. The fact that the centers of action of these patterns coincide with the maxima of the teleconnectivity field (Fig. 1c) and their nodal lines overlap the extrema and are parallel to the line segments in the anisotropy field (Fig. 2c) is indicative of phase fixed perturbations.

Our analysis also shows that geopotential height perturbation in all frequency bands exhibits a substantial amount of anisotropy. Zonally (east/west) elongated dipole-like features (e.g., Figs. 4, 5) prevail over the oceanic regions of the hemisphere and meridionally (north/south) elongated features arranged along zonally oriented wavetrains (e.g., Fig. 3) prevail over the continents. The amount of anisotropy appears to increase as the period of fluctuations increases, particularly over the oceanic regions of the hemisphere.

REFERENCES:

Blackmon, M.L., Y.-H. Lee, and J.M. Wallace, 1984: Horizontal structure of 500 mb height fluctuations with long, intermediate and short time scales. *J. Atmos. Sci.*, **41**, 961-979.

Hoskins, B.J., I.N. James, and G.H. White, 1983: The shape, propagation and mean-flow interaction of large-scale weather systems. *J. Atmos. Sci.*, **40**, 1595-1612.

Wallace, J.M., and D.S. Gutzler, 1981: Teleconnections in the geopotential height field during Northern Hemisphere winter. *Mon. Wea. Rev.*, **109**, 784-812.

Kushnir, Y., and J.M. Wallace, 1988: Low-frequency variability in the Northern Hemisphere winter: Geographical distribution, structure and time-scale dependence. Submitted to *J. Atmos. Sci.*

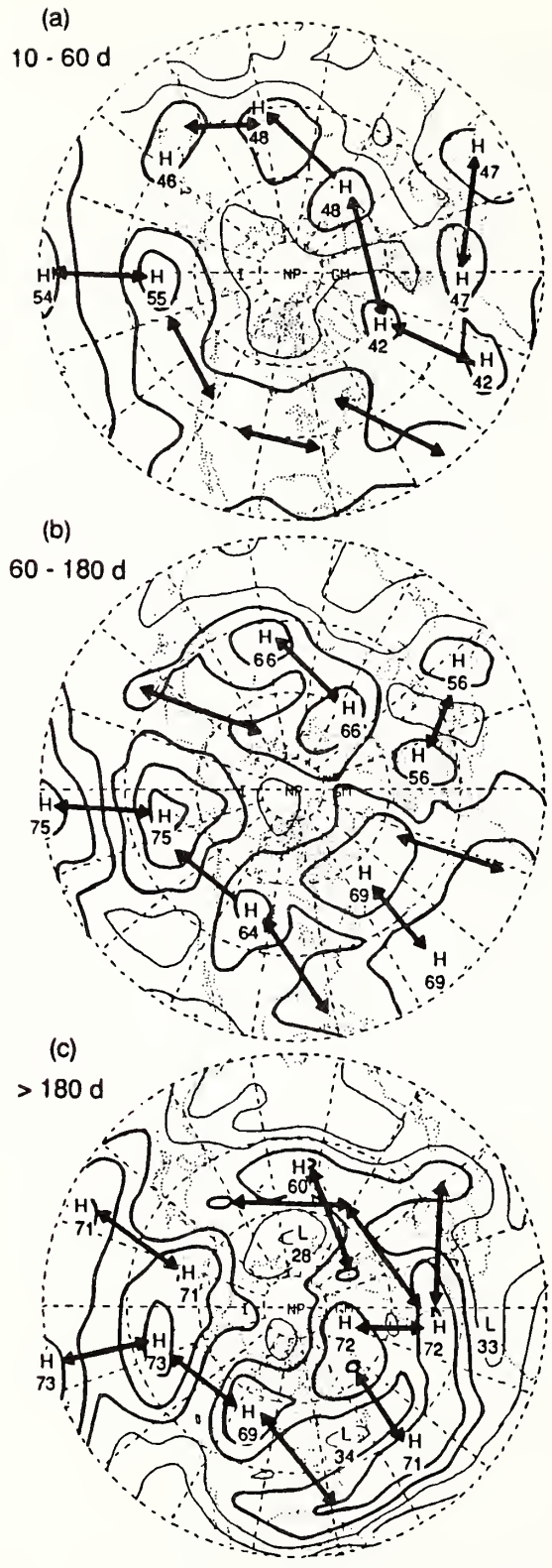

Fig. 1: Teleconnectivity of wintertime 500 mb height fluctuations with a period of (a) 10-60 days, (b) 60-180 days, (c) longer than 180 days. Contour interval 0.1; bold contours indicate values larger than 0.4 in Panel (a) and larger than 0.5 in Panels (b), (c). Decimal points are omitted on labels for extrema.

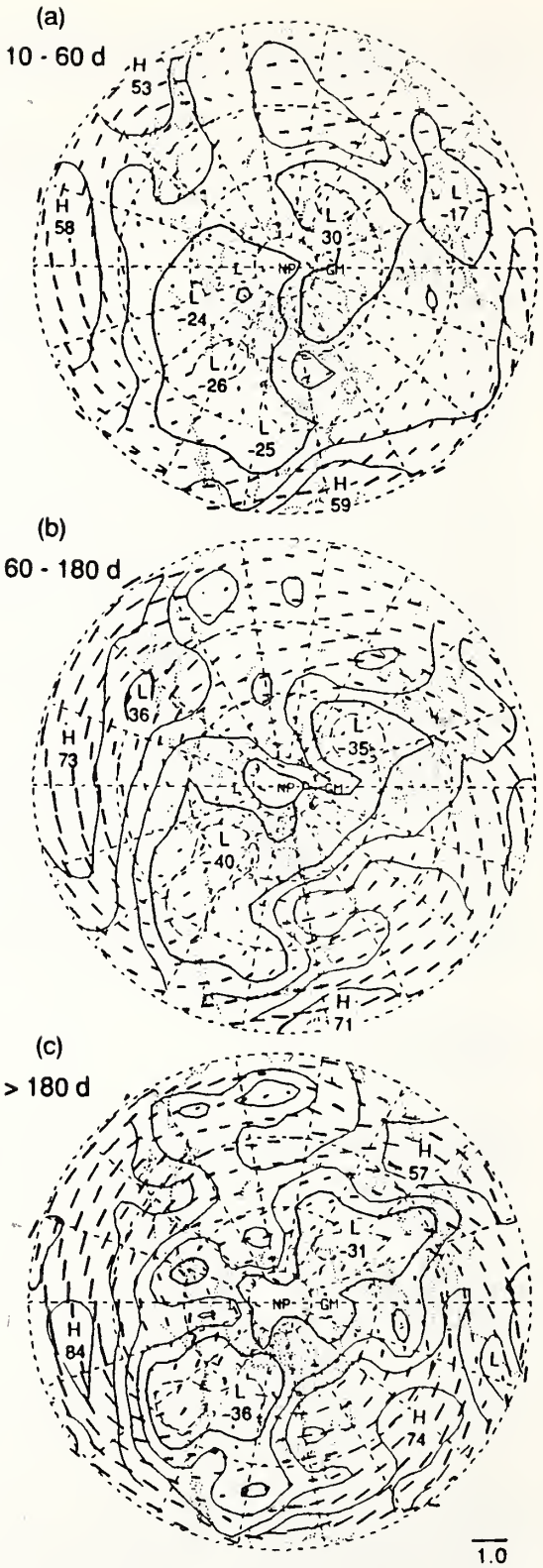

Fig. 2: Anisotropy of 500 mb geopotential height perturbations for (a) the 10-60 day band, (b) the 60-180 day band, (c) the >180 day band. The contoured field is of the zonal component of the anisotropy, contour interval is 0.1; decimal points are omitted in labels for extrema.

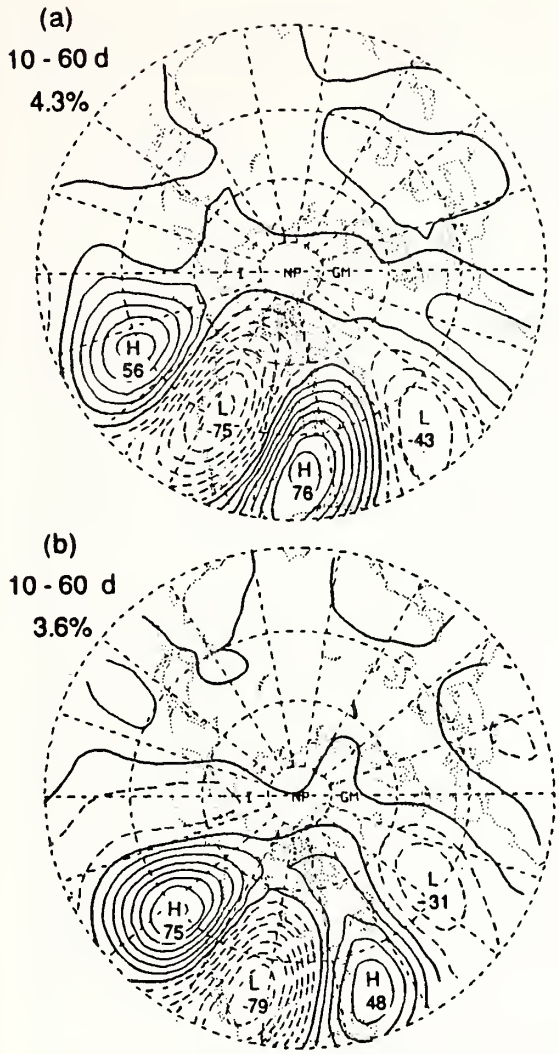

Fig. 3: Loading vectors of the 10-60 day band dominating the variance field over North America. Contour interval 0.1; negative contours are dashed. Decimal points are omitted on labels for the extrema. The percent value at the upper left corner of each Panel denotes the fraction of the normalized hemispheric variance in this band, explained by the respective loading vector.

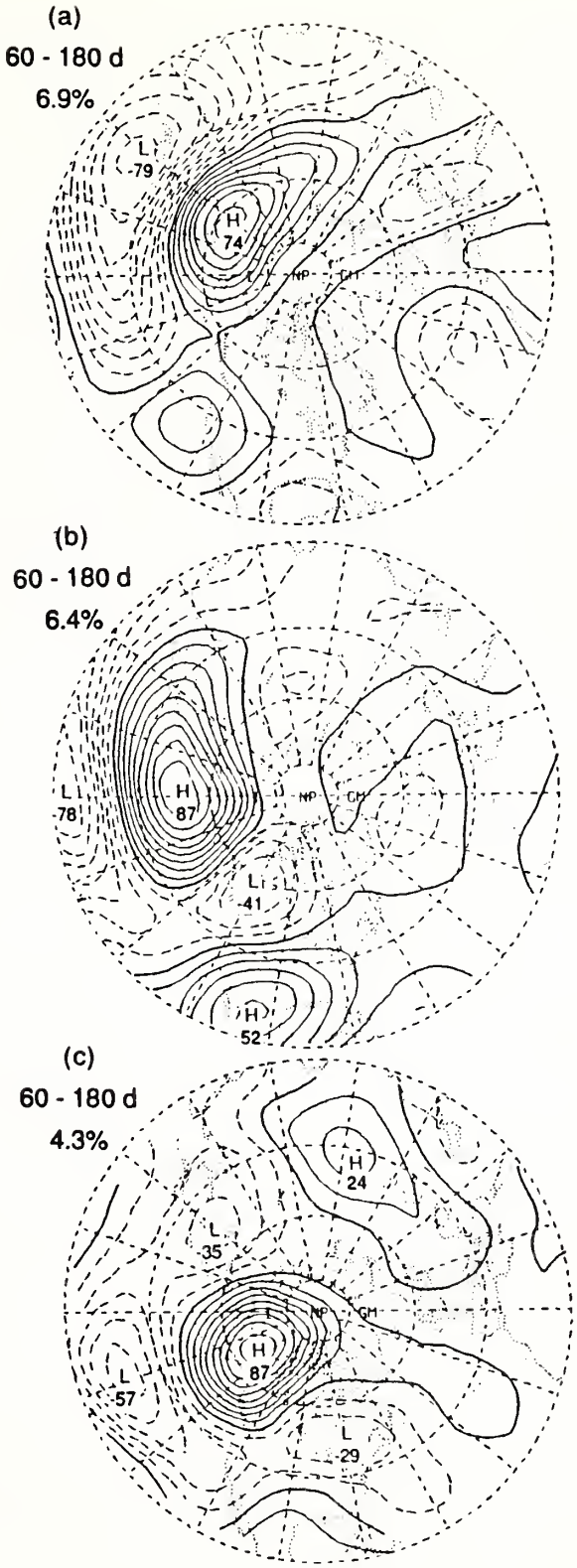

Fig. 4: As in Fig. 3 but for the 60-180 day variability over the Pacific Ocean.

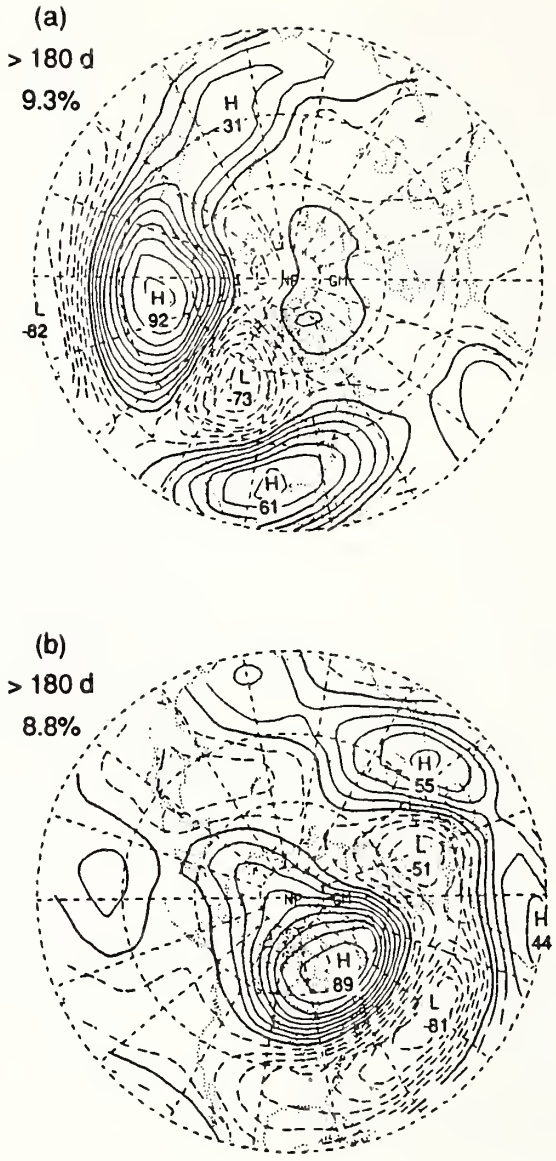

Fig. 5: As in Fig. 3 but for the leading vectors of the variability with periods longer than 180 days.

A Comparison of Tropical Surface Winds From Buoys and Operational Analysis

Richard W. Reynolds
Climate Analysis Center/NMC/NWS/NOAA
Washington, DC 20233

To determine the accuracy of different surface wind analyses, a cooperative program was begun to compare the winds from three operational analysis systems (National Meteorological Center [NMC], U. K. Meteorological Office [UKMO], and European Centre for Medium Range Weather Forecasts [ECMWF]) with independent wind observations from six Pacific Marine Environmental Laboratory (PMEL) buoys. All buoys were located within 8^{o} of the equator in the Pacific; the comparison period was 6-months (February 1 through July 31, 1987). Since the buoy data were not available on the Global Telecommunication System (GTS), they could not be used by any of the data analysis systems.

Daily time series at the six buoy locations were computed from the analysis fields and from the buoy data. For the given data period, means (including monthly means) and correlation statistics were computed. Figure 1 shows the long-term mean wind vectors from the three analysis systems and the buoys at the six locations. The results show large differences between the wind products. At most locations the analyses agree with each other better than with the buoy data. (This is especially evident at 8^{o}S, 110^{o}W and 2^{o}S, 140^{o}W.) Except at 2^{o}S, 165^{o}E, the agreement between the buoy and the analysis systems is better for the zonal, u, component than for the meridional, v, component. At 2^{o}S, 165^{o}E the differences are caused by the higher variability there. These results demonstrate that none of the analysis systems (NMC, UKMO, ECMWF) were decidedly superior in the tropical Pacific. (Further details are described by Reynolds et al., 1989.)

The surface wind comparisons are being continued. For this study only the NMC surface wind analysis will be compared to the buoy winds. The comparison is limited to NMC for the following reasons: a) none of the analysis systems from the earlier study (ECMWF, UKMO and NMC) were superior; b) interactions with scientists at NMC are simple since the Climate Analysis Center (CAC) is part of NMC; c) the NMC fields are available and are now being used to force the CAC tropical ocean model; d) the UKMO and ECMWF fields are no longer as accessible since Reynolds is no longer on detail in the UK. Because NMC implemented a higher resolution forecast model in August 1987, the starting date of this comparison was selected to be September 1, 1987.

Preliminary results of this new comparison have been completed for daily winds for a one year period (September 1, 1987 to August 31, 1988) using 8 PMEL buoys. The long-term mean winds for the period are shown in Fig. 2. The results show that the zonal NMC and PMEL wind components agree to within 1.1 m/s, except at 5^{o}N, 110^{o}W. However, the agreement in the meridional component is generally worse, especially at 5^{o}N, 110^{o}W. These results are similar to the results from the 6-month comparison.

Cross-correlation statistics were computed between pairs of the daily wind time series at the same location. The length of the correlated series at each buoy was defined by the length of the shortest time series. All time series

were detrended by removal of the annual and the semiannual frequencies before the correlations were computed. The correlations were done separately for the u and v components. Thus no correlations are presented between u and v. To determine if the correlations are significantly different from zero, the technique of Sciremammano (1979) was used. In this method the product of the autocorrelations of the two time series is used to compute the effective number of degrees of freedom.

The results of the correlations are presented in Fig. 3. The boxed area shows the region in which the correlations cannot be distinguished from zero at the 95% significance level. All the correlations are significant except the v correlation at $5^{o}S$, $110^{o}W$. The correlations can be seen to vary from 0.15 to almost 0.7. The angle of the correlation vector shows that the u correlations are superior to the v correlations at all locations.

Fig. 4 shows the time series of the PMEL and NMC v components for the one year period (366 days) at $5^{o}N$, $110^{o}W$. (The time series have been smoothed by a five-point binomial filter for visual clarity; the annual and semiannual frequencies have not been removed.) This comparison shows why the v correlations and v means agreed so poorly. The two time series are similar during the first 30 days. After this period, a strong bias (over 5 m/s) develops which persists until approximately day 120. This bias corresponds to the seasonal shift of the Intertropical Convergence Zone (ITCZ). During the period of high bias, the ITCZ shifted close to the position of the buoy. This suggests that the NMC analysis may tend to underestimate tropical divergent and convergent areas.

These surface wind comparisons will be continued. They will be of special interest during the next year when more PMEL buoys become operational and when the PMEL data are made available on the GTS. Because of the present deficiency of low-level wind observations in the tropical Pacific, the addition of the PMEL wind data to the GTS should significantly improve the quality of the assimilated surface wind analyses. This assumption will be tested as soon as possible.

REFERENCES

Reynolds, R. W., K. Arpe, C. Gordon, S. P. Hayes, A. Leetmaa, and M. McPhaden, 1989: A comparison of tropical Pacific surface wind analyses, J. Climate, 2, (in press).

Sciremammano, F., 1979: A suggestion for the presentation of correlations and their significance levels. J. Phys. Oceanog., 9, 1273-1276.

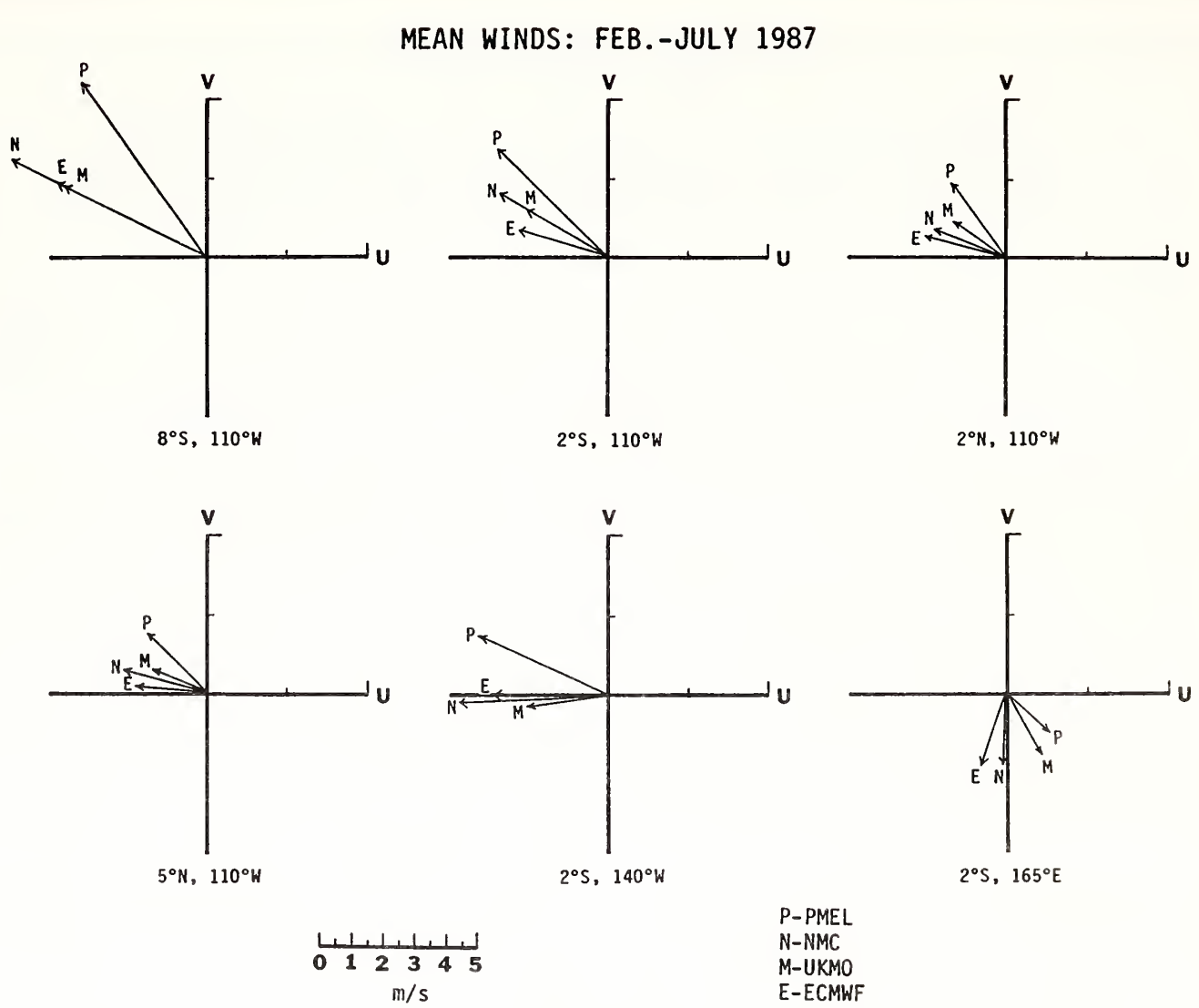

Figure 1. The long-term mean (February 1 - July 31, 1987) surface wind vectors at the 6 buoy locations in the tropical Pacific. The vectors were from PMEL buoys (labeled P) and three operational analyses: NMC (labeled N), UKMO (labeled M), and ECMWF (labeled E).

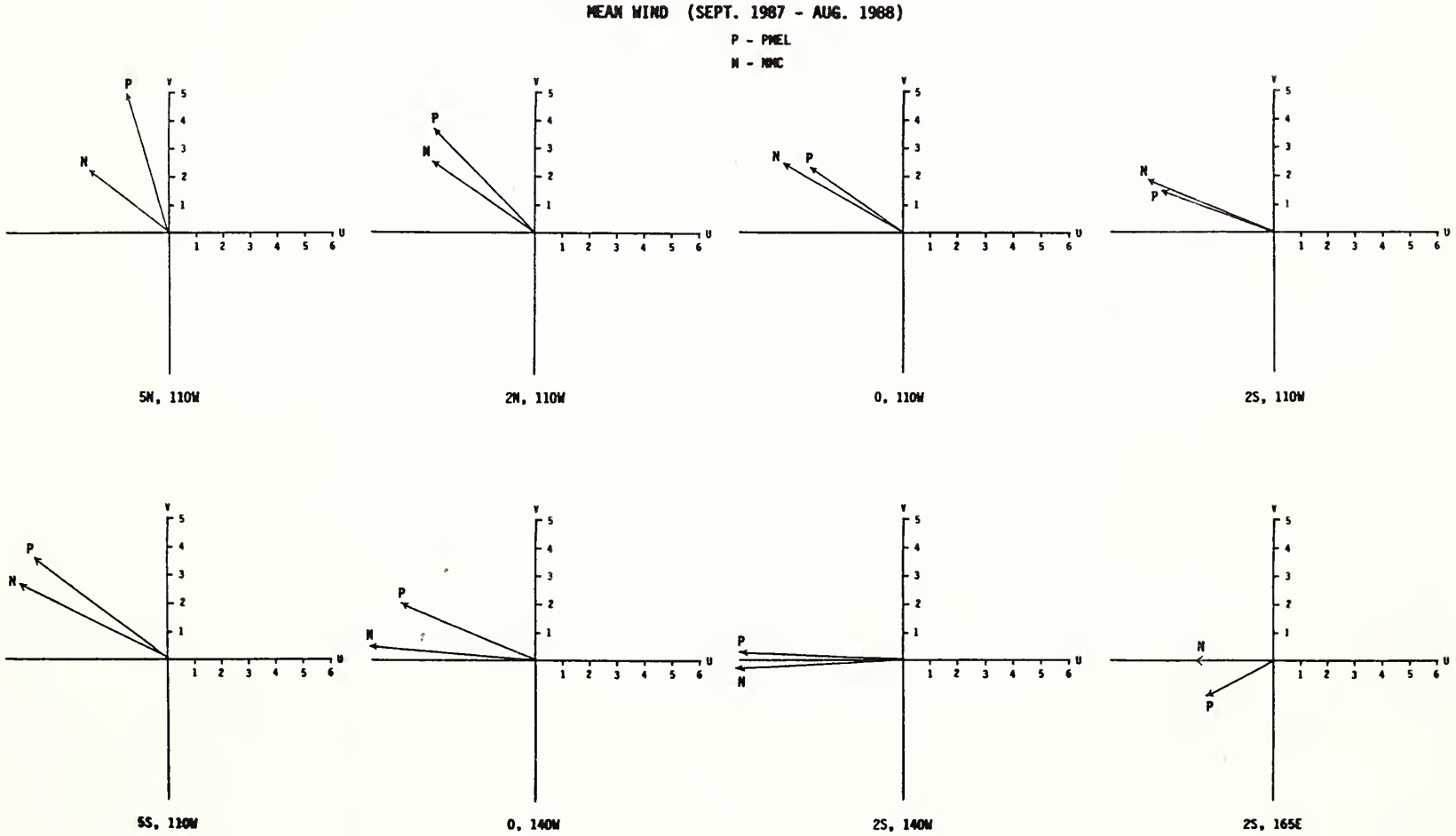

Figure 2. The long-term mean (September 1, 1987 - August 31, 1988) surface wind vectors at the 8 buoy locations in the tropical Pacific. The vectors were from PMEL buoys (labeled P) and the NMC operational analysis (labeled N).

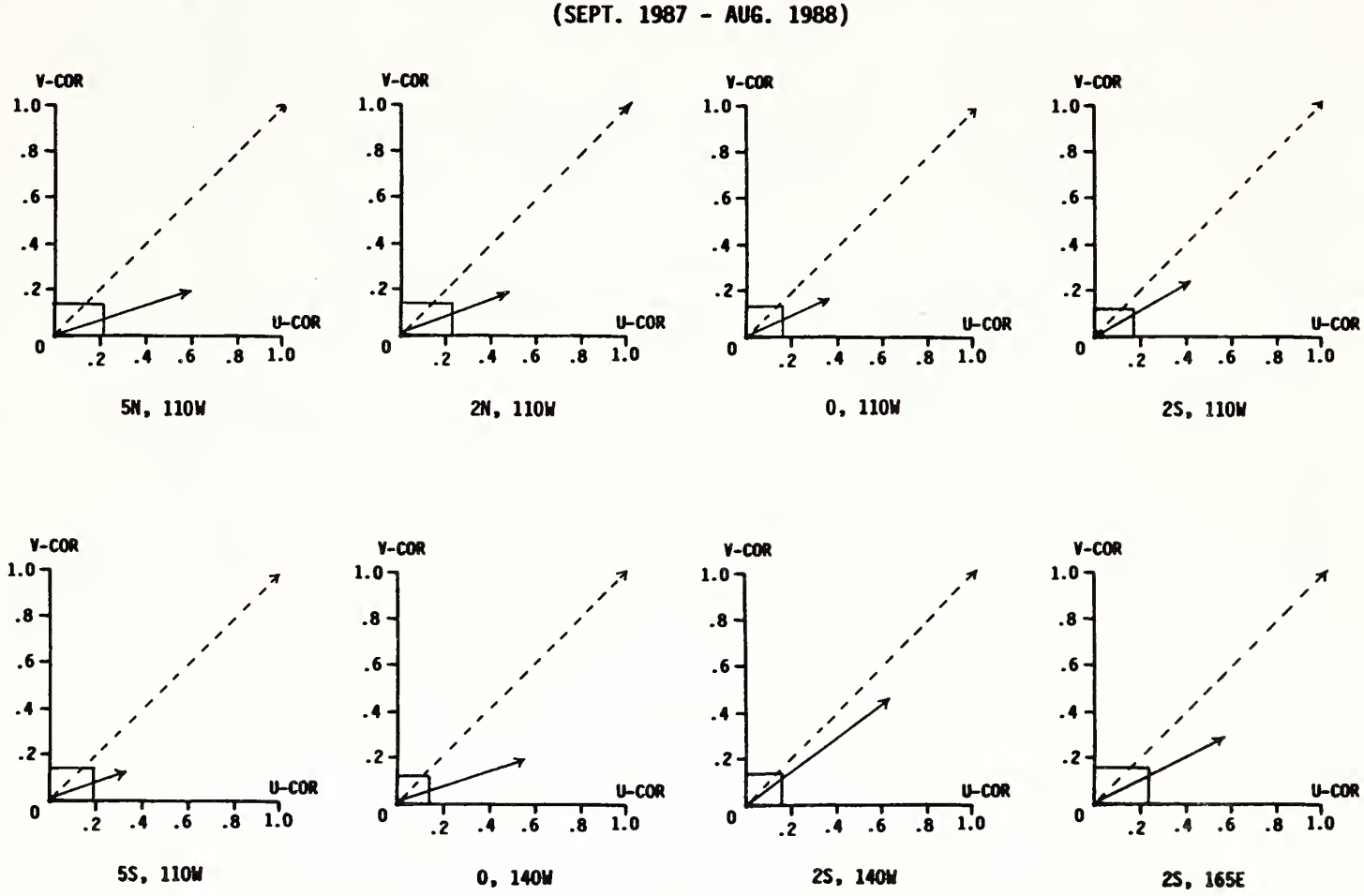

Figure 3. Cross-correlations between the PMEL daily buoy winds and the NMC daily analyzed surface winds for the periods and locations of Fig. 2. The vector shows the zonal and meridional components of the correlation. A perfect correlation (1,1) is shown by the dashed vector. The annual and semiannual frequencies were removed from the time series before the correlations were computed. Correlations not significantly different from zero at the 95% level lie within the boxed areas.

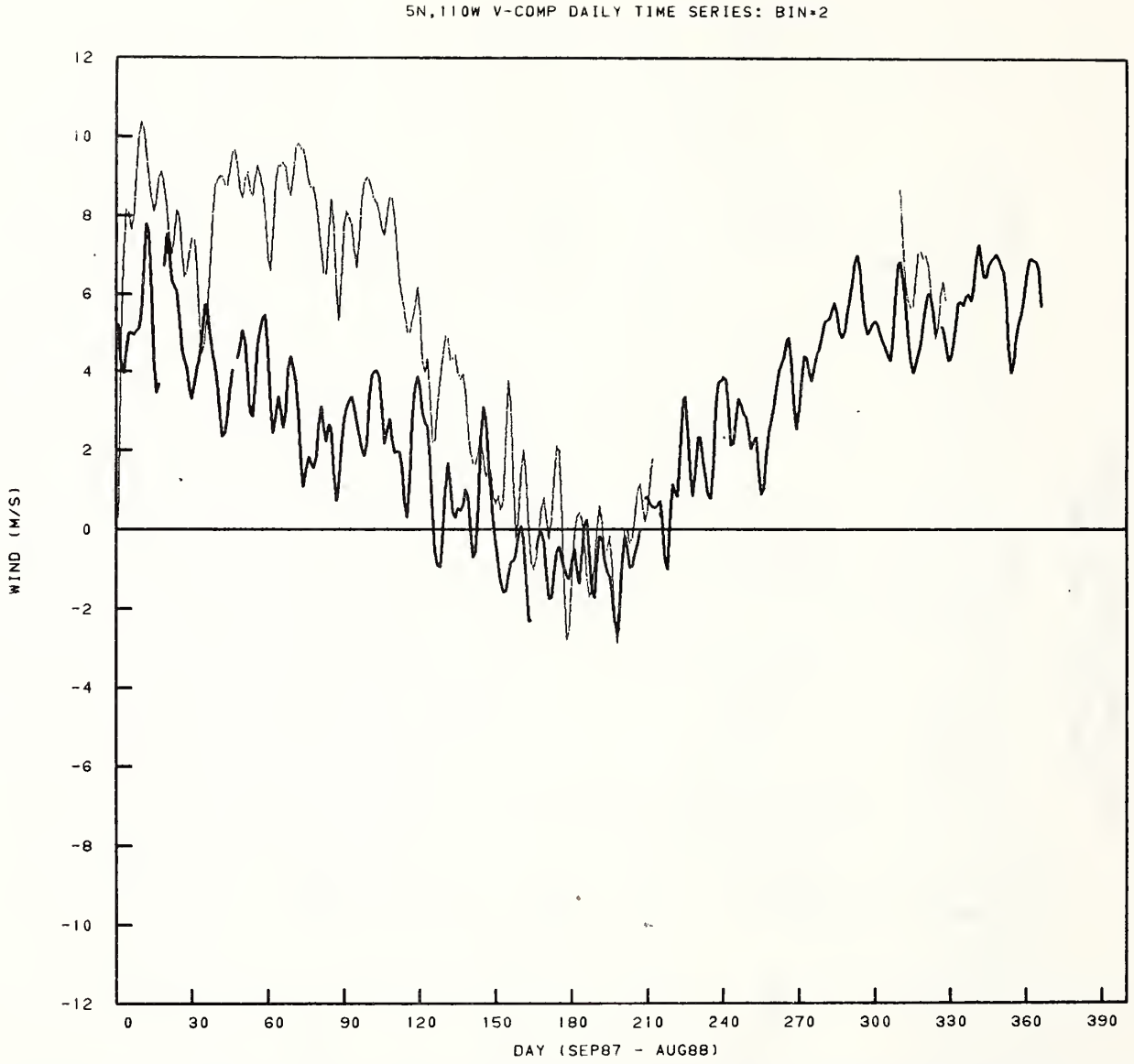

Figure 4. Daily time series of the meridional wind components of PMEL (light line) and NMC (heavy line) at $5^{O}N$, $110^{O}W$. The time series have been smoothed by a five-point binomial filter.

A Precipitation Climatology of Five-day Sequences: National Patterns of Frequency and Amounts

A. G. Barnston and E. S. Epstein

NWS/NMC/Climate Analysis Center
Washington, D. C. 20233

A precipitation climatology has been developed for the relative frequencies of zero, one, or two or more days with measurable precipitation within 5-day periods. The purpose of the climatology is to provide background for the development and introduction of extended-range (6-10 day forecast period) precipitation forecasts in terms of the anomalies of the probabilities of the three frequency categories. In addition, the distribution of precipitation amounts is given, conditional on there being one wet day and two or more wet days in five.

The climatology is based on 36 years (1948-1983) of daily precipitation data at 146 stations in the contiguous United States. For each day of the year, for each station, calculations were made of the percentage of the 36 years in which 0, 1, or 2+ days with precipitation occurred in the five days centered on the day in question. These overlapping daily percentages were smoothed by constructing 9-day running percentages; the results, still very noisy, were then subjected to harmonic analysis.

Roldan and Woolhiser (1982), in a similar context, found that the mean and first harmonic were usually sufficient to represent their data. Our period of record, however, is longer and we preserve more of the time resolution in the data. We decided that three harmonics would adequately represent the real climatic variations of the annual cycle but would not overfit for random undulations in the data that were of questionable climatic reality.

Distributions of precipitation amount, conditional on there being either 1 or 2+ wet days in five, were described by their medians (50 percentile) and 10 percentile and 90 percentile for all days of the year at all locations. A somewhat similar exercise was performed by Jorgensen et al. (1969). The amounts were analyzed similarly to the percentage frequencies, except that at least 15 occurrences (not necessarily separate events) of the frequency category in question were required. If this was not satisfied, the 9-day pooling window was extended to 11, 13, ... days until 15 occurrences were obtained. Only in certain seasonally arid climates in the Southwest was this window enlargement necessary. The other difference in procedure from that for the percentage frequencies is the use of two harmonics rather than three, because the amounts tended to be noisier than the frequencies.

Fig. 1 shows the mean annual frequencies over the U.S. of 5-day periods having 2+ wet days. The highest annual frequencies (>65%) occur in the lower Great Lakes and northern New England, followed closely by the extreme Northwest which may have had more dramatic results if one or two of the wetter extreme coastal stations had been included in the study. The lowest annual frequency (<10%), not surprisingly, lies in the desert Southwest.

The frequency of 1 wet day in five (not shown) is relatively constant, falling between 20 and 30% over all of the country except the West, where it is below 20%. The frequency of dry 5-day periods is roughly the complement of that for 2+ days in five.

The frequency maps vary noticeably by month of the year. For example, for 2+ wet days in five in January, the highs in the Northeast, Great Lakes and Northwest are stronger than for the annual mean; lows appear in the Southwest (extending eastward to the Texas Panhandle) and in southern Florida. In July the Northwest high disappears,

the Northeast and Great Lakes highs are equal to or slightly weaker than in the annual mean, a strong high (near 80%) appears in central Florida, and lows are found in southwest Texas (<20%) and most of coastal California (<5%).

The precipitation amounts conditional on the two frequency categories tell a somewhat different story. The annual means of the median precipitation amounts, given exactly one wet day in five (not shown), features less than 3 mm over most of the western half of the country. An area centered along the central Gulf between the Florida Panhandle and eastern Texas, extending northward to southern Illinois, receives more than 5 mm.

Fig. 2 presents conditional annual means of median amounts, given 2+ wet days in five. The amounts are greater than those for 1 day both because of the greater number of wet days and the greater amounts per day under this condition. As with the 1 day amounts, the maximum appears along the central Gulf coast and exceeds 25 mm. Another relative peak occurs along the West Coast northward from San Francisco. Median amounts are least over the northern high plains, the Rocky Mountains and Great Basin. In the vicinity of the Great Lakes, where the mean annual frequency of wet 5-day periods is greatest, the annual mean of the median amounts per wet 5-day period are modest. On the other hand, the Gulf Coast's impressive median amounts do not coincide with a maximum in the annual frequency of wet 5-day periods.

The annual cycle of frequencies and conditional amounts was examined both with maps at seasonal or monthly intervals, and with maps of harmonic dials of the first and second harmonics. An example of the latter is given in Fig. 3 for the first harmonic of frequencies of dry 5-day periods. The arrows represent the phases and amplitudes of the annual first harmonic, where the arrows point to the time of year (see inset; arrows pointing straight up correspond to July 1) when the frequencies are maximum. The lengths of the arrows are proportional to the amplitudes (in percent) of the annual cycle (i.e., the first harmonic), scaled as indicated by the numerical value in the inset.

There appear to be five regimes. In the West, the annual cycle of dry periods is quite strong, with a maximum (of dryness) in middle to late summer. In Arizona and New Mexico primarily, the annual cycle is quite weak. Over much of the high plains, and extending eastward, the frequency of dry periods is maximum in late fall or early winter. Over most of the eastern half of the country the amplitudes are small, but the phases consistently indicate autumn maxima of dry periods (and corresponding spring minima). The final region is the Florida peninsula, where maximum frequencies of dry periods occur in late winter.

The map of second harmonics for dry 5-day period frequencies (not shown) also shows regional structure--one that varies in terms of its interaction with the first harmonic. For example, in the Pacific Northwest the two harmonic arrows are parallel (the second harmonic "arrows" pointing both forward and backward for two maxima per year), indicating that the summer maximum of dryness is relatively strong and brief while the winter minimum is shallow but long-lasting. Analogous reasoning can be used when the first and second harmonics are orthogonal. In some locations (e.g., Arizona) the second harmonic carries much greater amplitude than the first, indicating a bimodal distribution of precipitation frequency.

The seasonal cycle of the frequency of two or more wet days in five is for the most part the complement of that for no days with precipitation. In terms of harmonic dials this means the first harmonics are 180^{0} out of phase and the second harmonics are orthogonal. The major exception to this rule is in the vicinity of the Great

Lakes where the winter maximum of frequency of wet periods largely is at the expense of periods with one wet day in five rather than the relatively rare completely dry periods.

The harmonic dial map for median precipitation amount given 2+ wet days in five shows a relatively simple pattern: very small amplitudes over most of the Southeast and the region between the high plains and the Cascades; an annual cycle with maximum in summer over most of the central plains and north of the Ohio Valley and also in the Florida peninsula; and a cycle with a minimum in summer and a maximum in winter at stations on the Pacific coast. The map of second harmonics is more complex, and indicates a marked semiannual cycle in Texas and over much of the plains and Rocky Mountains from Colorado north. Over much of this area the two distinct maxima occur in April or May, and in October or November. In the southwest, where the semiannual cycle of precipitation frequency is prominent, there is little evidence of a comparable semiannual cycle in conditional amounts.

The purpose of this study has been to provide a climatological background for five-day periods against which operational forecasts of probability anomalies of the occurrence of 0, 1, or 2+ precipitation days in five could be made. We have discovered, along the way, that the climatology of precipitation frequencies offers a novel and informative perspective on the description of climate.

References

Jorgensen, D. L., W. L. Klein and C. F. Roberts, 1969: Conditional probabilities of precipitation amounts in the conterminous United States. ESSA Tech. Mem., WBTM TDL 18, 89 pp.

Roldan, J. and D. A. Woolhiser, 1982: Stochastic daily precipitaton models I. A comparison of occurrence processes. Water Resources Research, 18, 1451-1459.

ANN FREQ (%) FOR 2+ DAYS IN 5 PRECIP

FIG 1

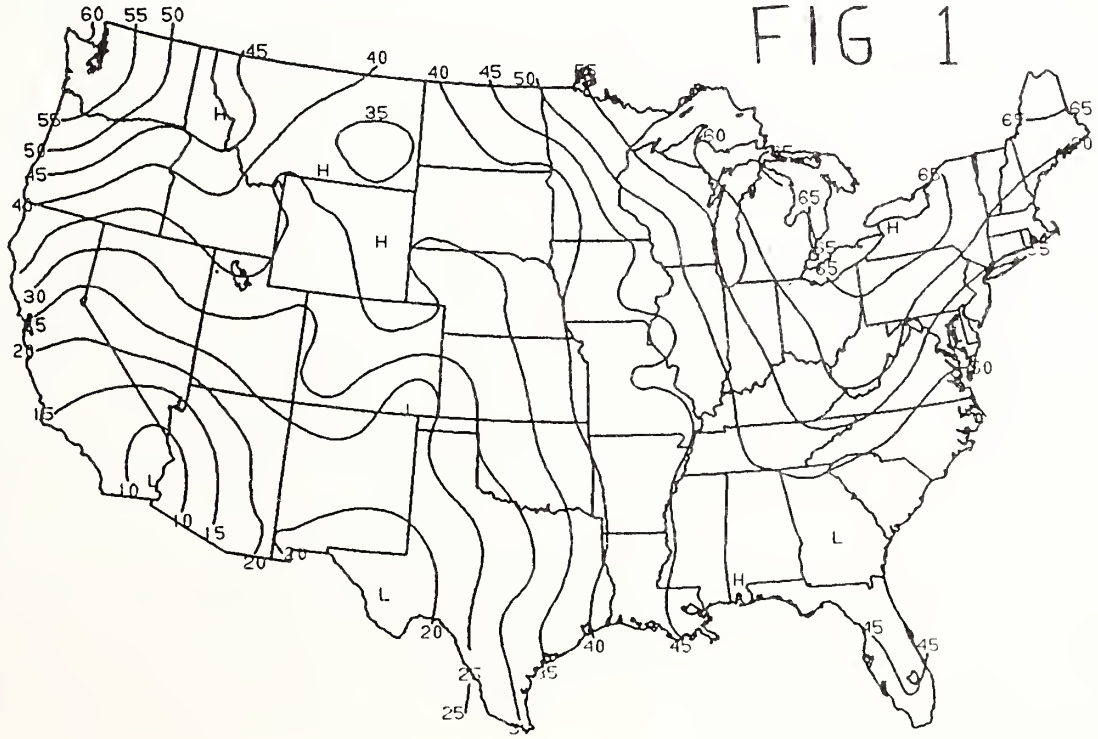

ANN AMT (MM) 2+ DAYS IN 5, 50%ILE

FIG 2

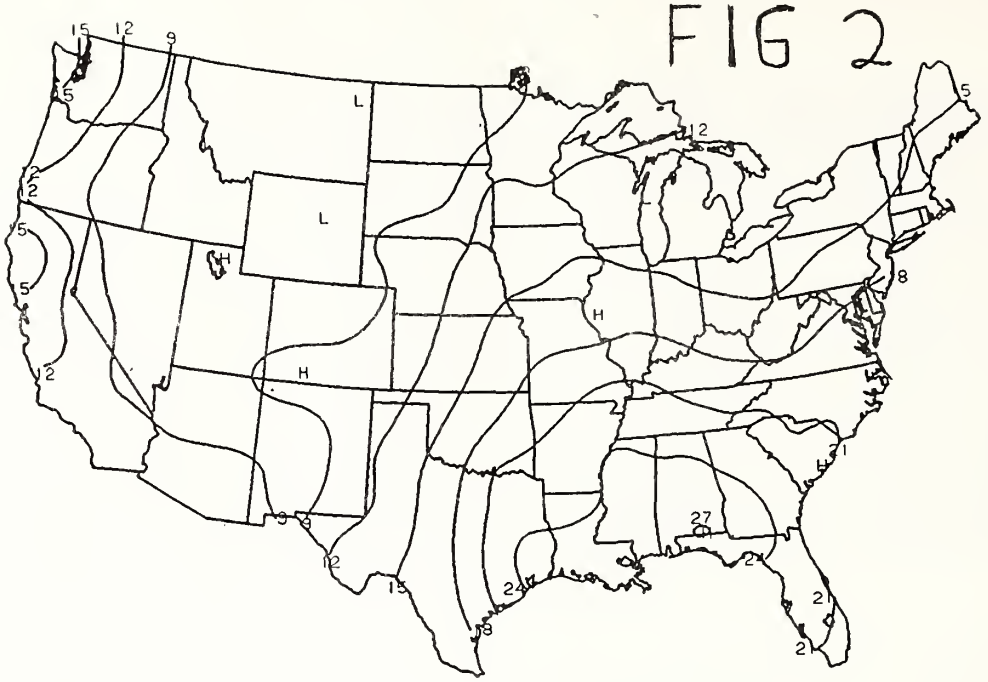

FIG 3

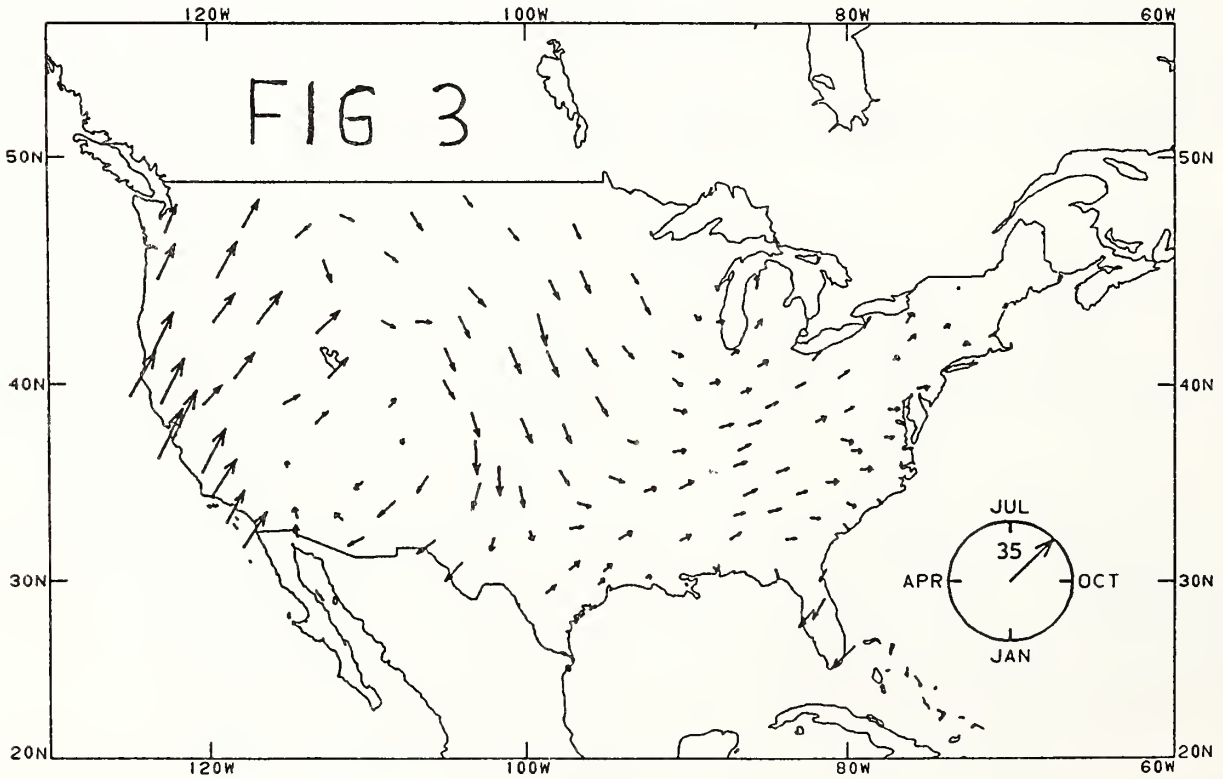

1ST HARMONIC OF PRECIP: FREQ OF 0 DAYS IN 5

A PRECIPITATION CLIMATOLOGY OF FIVE-DAY PERIODS

E. S. Epstein and A. G. Barnston
NWS/NMC/Climate Analysis Center
Washington, D. C. 20233

In this paper, a direct sequel to the previous presentation (Barnston and Epstein, 1988) we look at the precipitation climates of individual stations. Diagrams have been developed to display the seasonal patterns of frequency and amount for individual stations. The frequency diagram is a nomogram based on a first-order Markov chain model for precipitation occurrences. It can be used to infer, from the frequencies of 0 and of 1 wet days in 5, the single-day climatological precipitation probabilities and the probabilities of wet days conditional on precipitation falling on the previous day (or, conversely, to infer, from the daily climatology and knowledge of the persistence, the probability of the three categories of 5-day period). These diagrams are intended to aid the forecaster in making and interpreting probability forecasts of precipitation frequency for the 6-10 day period, where day-by-day forecasts are unfeasible. They are also useful, as will be demonstrated by example, for describing and comparing precipitation climatologies.

The basic diagram is a graph in which p', the relative frequency of entirely dry 5-day periods, is plotted as the abscissa against pa, the relative frequency of 5-day periods in which just one day has measurable precipitation, as the ordinate. Since both p' and pa must be positive and their sum cannot exceed 1.0, only the triangle shown in Fig. 1 is of any interest. The diagonals are isopleths of 1-p'-pa, which is necessarily the probability of two or more wet days in five, or pb, and are so labeled.

If occurrences of precipitation were independent from day to day then the probability of m wet days in five would be dependent only on p_c, the climatological daily probability of precipitation (POP) and given by a binomial distribution. Only combinations of values of p' and pa falling on the curved solid line in Fig. 2 would occur. In fact, independence rarely is the case with respect to daily precipitation. In general precipitation is persistent, and paa, the conditional probability of measurable precipitation on a day preceded by a day with precipitation, is greater than the unconditional POP. Just as p_c alone determines both p' and pa through the binomial distribution for the case of independence, the combination of p_c and paa are sufficient to determine p' and pa in the case of a simple Markov chain model for the day-to-day dependence of precipitation. This functional relationship is represented by the curved dashed lines in Fig. 2. Along each dashed curve the climatological POP is constant, with the value indicated by the small number at the lower end. The dashed lines are all terminated on the solid curve, representing independence, which means that p_c=paa at those termini. As one moves down or to the right along the dashed curves, each marker represents an increment of 0.05 in the value of paa (while of course p_c remains fixed). The the entire region of the graph below the solid curve represents combinations of p' and pa indicating persistence: the further from the solid curve the greater the persistence. The region of the graph above the curved line represents negative persistence, which is rarely, if ever, encountered. Because it is not used, we have found it convenient to omit the upper part of the triangle (pa>0.5) when plotting observed relative frequencies.

Transferring the harmonically smoothed relative frequencies, determined as in Barnston and Epstein (1988), to the plotting diagram (Fig. 2), one obtains, using Los Angeles as an example, a trace that characterizes the station's precipitation frequency climatology, as in Fig. 3. We annotate the trace with numbers corresponding to the mid-point of each month. In Los Angeles, we see, February is the month with the most frequent rain, with January and March not far behind. At the other extreme, June, July and August are very dry; the midsummer probability of two or more wet days in five is less than 1%. The inferred climatological daily POP in the midwinter "wet" period is only slightly in excess of 0.20. However there is strong day-to-day dependence in precipitation (the points are quite far below the solid curve representing independence). The probability of rain today given rain yesterday, in mid-winter, inferred from the diagram, is approximately 0.20+8(0.05)=0.60, because the points in question lie 8 "steps" down the dashed curve labeled 0.20.

When it rains the expected amounts of precipitation also undergo large seasonal changes. Fig. 4 is a depiction of the conditional distributions of precipitation amount for Los Angeles given one wet day in five (upper graph) or two or more wet days in five (lower graph). The vertical lines extend from the 10th percentile to the 90th percentile; the dots on the lines give the median conditional amounts. Conditional amounts, on the rare occasions when it does rain in May and June, are quite small, but because the sample is so small that part of the diagram is subject to large estimation errors.

Climatological precipitation frequencies at Boston (Fig. 5) are essentially constant from December through April, with an inferred climatological daily POP of 0.40. The fewest wet days occur from mid-August through mid-October. The probabilities of 0, 1, and of more than 1 day with precipitation during the five days of the Climate Diagnostic Workshop are, respectively, 0.20, 0.28 and 0.52. The implied values of p_c and paa are 0.33 and 0.49. If there are at least two wet days during the Workshop there is one chance in ten of getting more than 58 mm (2.3 in) of rain. Given one wet day in the five the median amount of precipitation is only 4.3 mm (0.17 in).

We have calculated and plotted frequency and conditional amount diagrams for over 100 stations. Each one has a story to tell. Some of these stories, and tables of bimonthly frequencies and conditional amounts for 146 stations can be found in a NOAA Technical Report (Epstein and Barnston, 1988).

REFERENCES

Barnston, A. G. and E. S. Epstein, 1988: A precipitation climatology of five-day sequences: National patterns of frequency and amounts. Proceedings of the Thirteenth Annual Climate Diagnostics Workshop, Cambridge, MA, Oct. 31, Nov. 4, 1988.

Epstein, E. S. and A. G. Barnston, 1988: A precipitation climatology of five-day periods. **NOAA Technical Report** (in press).

Figure 1.

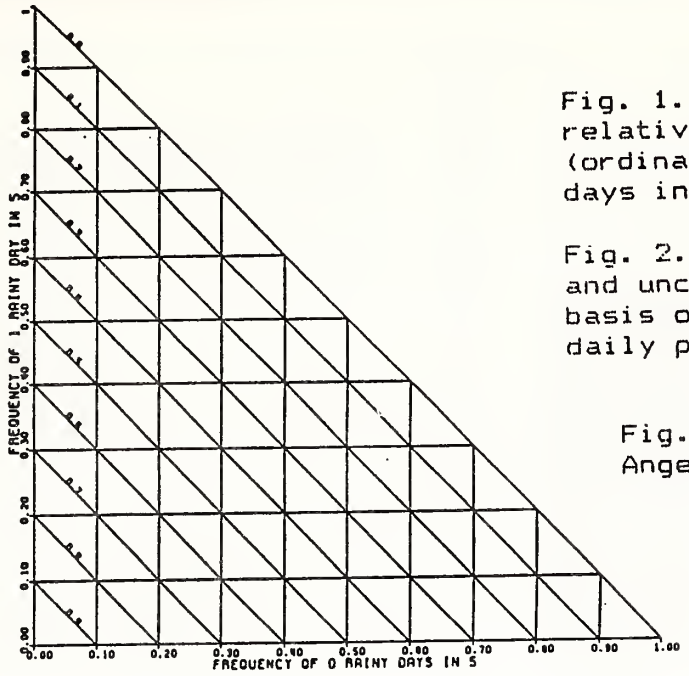

Fig. 1. Basic grid for plotting climatological relative frequencies of zero (abscissa), one (ordinate), and more than one (diagonals) wet days in five.

Fig. 2. Nomogram relating various conditional and unconditional relative frequencies on the basis of a first-order Markov model for daily precipitation. See text for details.

Fig. 3. Climatic frequency diagram for Los Angeles, CA.

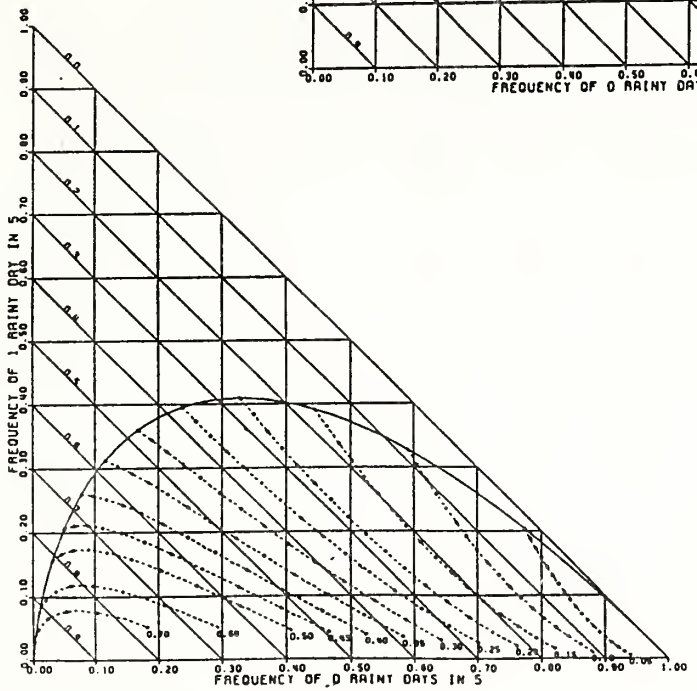

Figure 2.

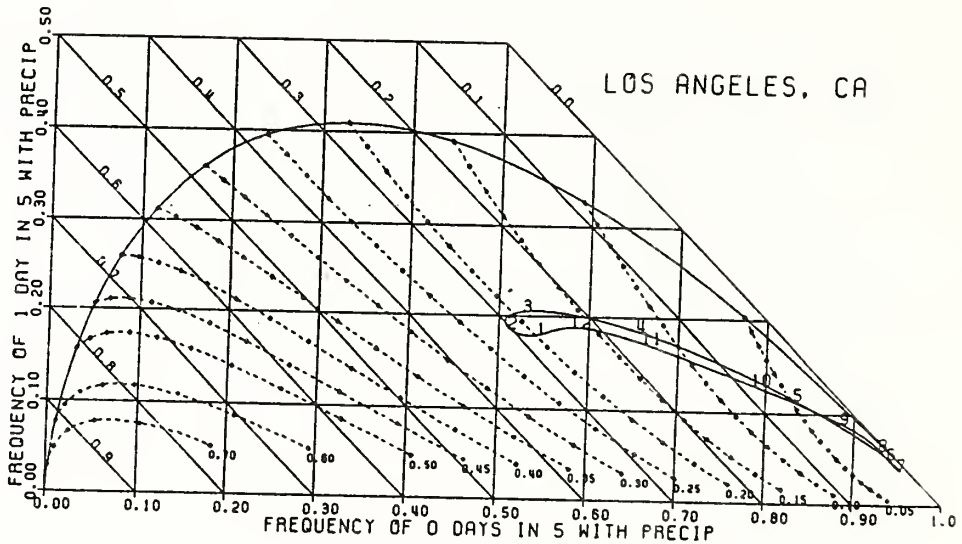

Figure 3.

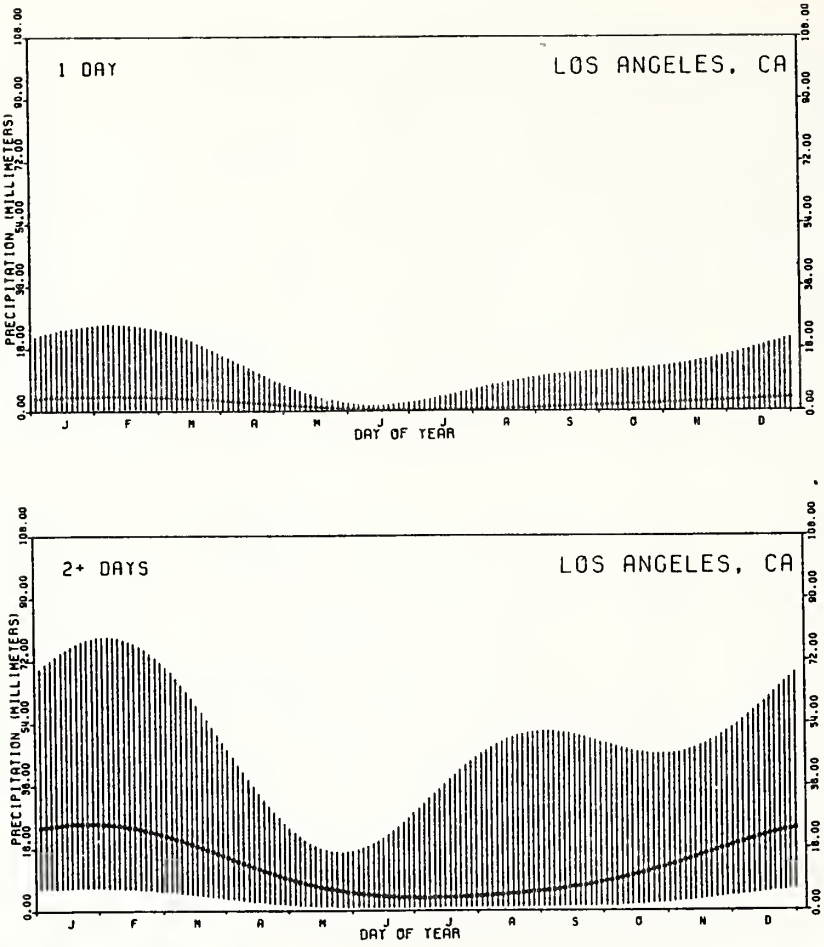

Fig. 4. Climatic conditional 5-day precipitation amounts given one wet day in five (upper chart) and two or more wet days in five (lower chart) for Los Angeles, CA.

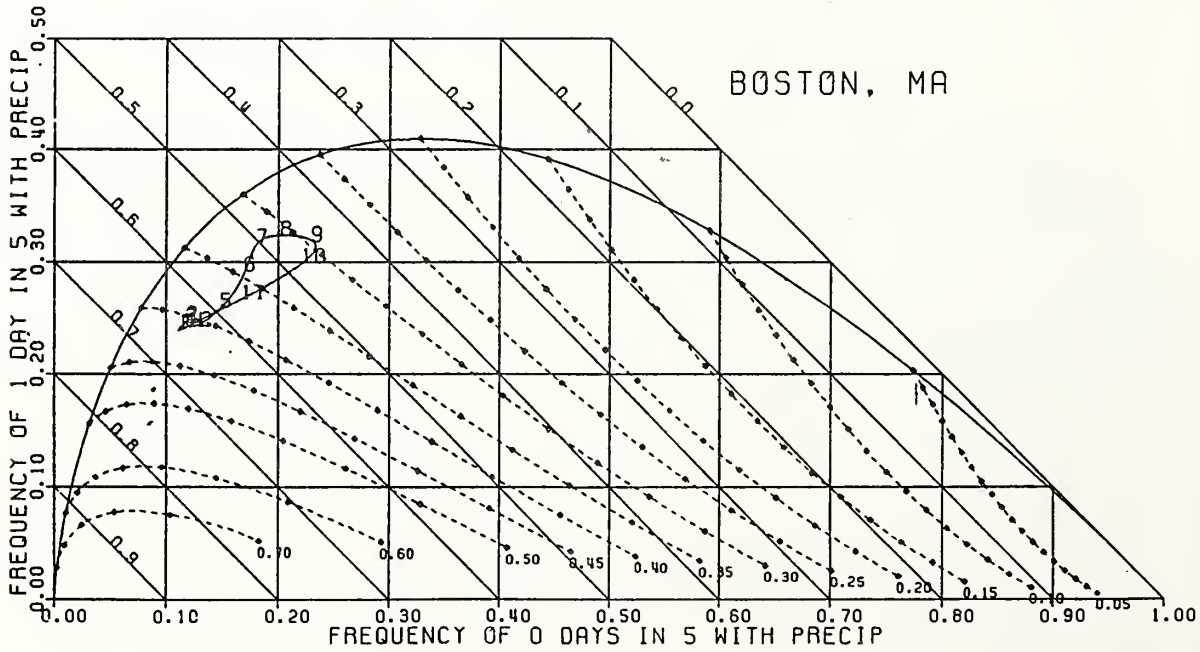

Fig. 5. Climatic frequency diagram for Boston, MA.

The Global Precipitation Climatology Project: Description, Goals and Progress

John E. Janowiak
Phillip A. Arkin
Climate Analysis Center, NMC, NWS, NOAA
Washington, D.C. 20233

1. INTRODUCTION

The Global Procipitation Climatology Project (GPCP) is an international effort with the goal of producing a monthly, 10-year climatology of precipitation, averaged for each 2.5^{o} latitude/logitude box on earth. This 10-year time span encompasses the years 1986 through 1995. To achieve this goal, estimates of monthly accumulated precipitation must be obtained in vast areas of the tropics and polar regions where conventional surface observations are scarce. The precipitation estimates will be inferred from microwave and infrared data that are obtained from polar orbiting and geostationary satellites. The precipitation estimates are to be merged with surface observations to produce monthly, global precipitation data sets. To aid in the calibration and validation of the precipitation estimates, high density precipitation surface observations at selected areas around the world will be employed as ground truth data.

2. Project Organization

The GPCP is composed of several components (Fig. 1) whose responsibilities vary among data collection, precipitation estimation, and data assimilation. The data collection tasks are further sub-divided between the Geostationary Satellite Data Processing Centers, which are responsible for collecting histograms of IR brightness temperatures from the various geostationary satellites, and the Surface Reference Data Center that is responsible for the collection of surface observations of precipitation. The data collected by the former centers are to be primarily used by the Geostationary Satellite Precipitation Data Center for precipitation estimation, while that of the latter are intended for the calibration and validation of these estimates. Similar functions are to be performed by the polar satellite centers, except that microwave data will be used. The surface data and precipitation estimates will be forwarded to the Global Precipitation Climatology Center whose task is to merge these data into an homogenous monthly climatology. The final repositories of these data will be the World Data Centers for Meteorology located in the U.S. and the Soviet Union.

3. Precipitation Estimates

In the tropics, where the annual cycle in temperature is small and the rainfall is primarily convective, rainfall estimates will be computed based on work by Arkin (1979) and Richards and Arkin (1981). The method uses the results of a linear regression between cloud top temperature as inferred from geostationary satellite IR imagery and observed rainfall on the ground to compute monthly accumulated rainfall from satellite data only. In regions for which geostationary data are missing, it is anticipated that estimates based on outgoing longwave radiation (OLR) fron NOAA polar orbiting satellites will be used. An example of estimated rainfall using this technique is shown in Figure 2.

In polar regions and mid-latitudes, precipitation estimates based on microwave data will be used. Presently, the special sensor microwave/imager (SSM/I) is operating aboard a Defense Mapping Satellite Program (DMSP) spacecraft and data are being collected. Although the SSM/I has 4 channels (19.35, 22.235, 37.0, and 85.5 GHz) a precipitation estimation algorithm has been developed only for the 19.35 GHz channel as of this writing.

REFERENCES

Arkin,P.A., 1979: The relationship between fractional coverage of high cloud and rainfall accumulations during GATE over the B-scale array. Mon. Wea. Rev., 107, 1382-1387.

Arkin,P.A. and F. Richards, 1981: On the relationship between satellite-observed cloud cover and precipitation. Mon. Wea. Rev., 109, 1081-1093.

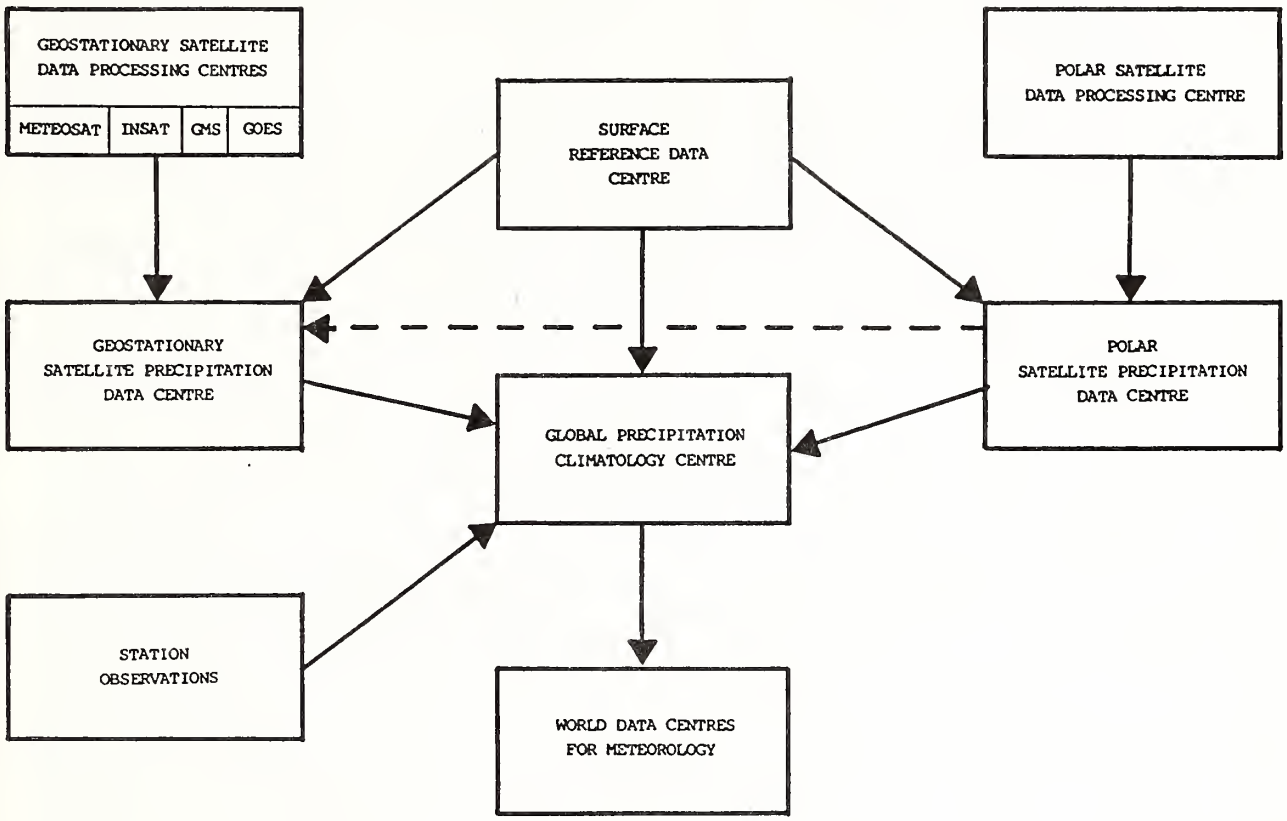

Figure 1. Organization of the Global Climatology Precipitation Project.

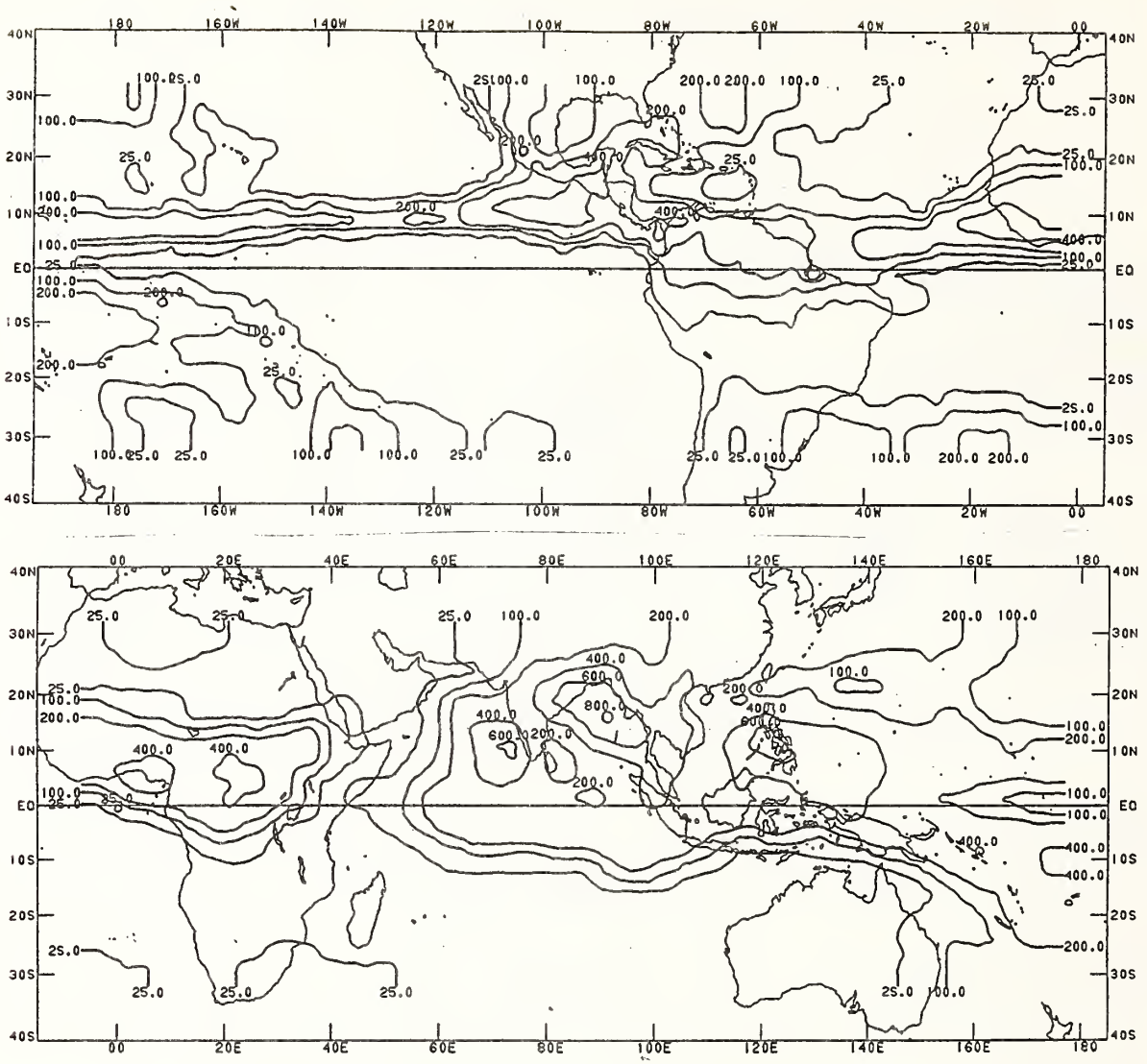

Figure 2. Accumulated rainfall estimates (mm) for the period 31 May - 29 June, 1988 based on IR data from METEOSAT, GOES-EAST, GOES-WEST and the NOAA polar orbiters (NOAA-9 & NOAA10).

HIGHER MOMENT STATISTICS FROM A 40-YEAR SAMPLE OF 15-DAY MEAN 700 MB HEIGHTS

A. James Wagner and T. Norman Maisel

NWS/NMC/Climate Analysis Center
Washington, D. C. 20233

Although the mean and standard deviation are commonly computed for geophysical time series, measures of the third and fourth moments (skewness and kurtosis) are generally not calculated. This neglect may be due to a combination of such factors as difficulty in demonstrating significant departure from normality and lack of utility or interest in such statistics. After all, we are generally interested in knowing the mean and standard deviation (variability) of, for example, temperature at a location where we would consider living, but of what practical use would the skewness and kurtosis be? As we shall see, when carefully interpreted, the skewness and kurtosis can tell us a number of interesting things about the data and the meteorological variable they represent.

Moffitt and Ratcliffe (1972) computed higher moments from a series of 500 mb heights and 1000-500 mb thicknesses covering the period 1951-1966, and more recently White (1980) did similar calculations, using a later data base consisting of twice-daily 500 mb height data from the period 1965-1977, grouped into 4-month winter and summer "seasons." They found significant, but not large departures from normality in several areas of the Northern Hemisphere during both their cold and warm seasonal groupings.

It was decided to see whether the half-month mean 700 mb heights used by Wagner and Maisel (1987) to compute teleconnections displayed significant departures from normality, and whether the patterns (when comparable) were similar to White's. From examination of the relative frequency with which consecutive half-month means were selected to calculate the teleconnection patterns (Wagner and Maisel, 1987) it was concluded that on the average about 2/3 of the half-month means of 700 mb height were independent. For the 40 years of data (1947-1986) in our sample, and recalling that four consecutive half-month periods from each year are used to compile each "month's" statistics, there are 160 half-month means going into each map. If about 2/3 of these are truly independent, a conservative estimate would be about 100 independent 15-day means going into each calculation.

White (1980), in quoting Brooks and Carruthers (1953), listed a value of at least ± 0.49 as the threshold for a significant departure of the coefficient of skewness from normality, and values of more than 4.06 or less than 2.27 as indicating a significant departure of the coefficient of kurtosis from normality. An exactly normal, or Gaussian, distribution has a skewness coefficient of 0.0 and a kurtosis coefficient of 3.0. Further details of how these coefficients are derived from the higher moments can be found either in the paper of White (1980) or the useful statistical text of Spiegel (1975).

It would, however, be useful to display graphically some typical examples of highly skewed (Fig. 1, top) or strongly kurtotic (Fig. 1, bottom) distributions, in order to see how they look compared with the normal distribution (solid lines in Fig. 1). Meteorologists are already

familiar with the tendency for all but monthly and seasonal averages of rainfall in fairly moist climates to display a positively skewed behavior--a characteristic for most values to be less than the mean and for a few outliers representing extreme heavy rainfall events to be on the right--in other words, a long tail along the positive x-axis. A little thought should quickly disclose that sea level pressure in a meteorologically relative quiet area--such as the tropics or subtropics--where on rare occasions extremely low values can be observed in tropical storms, would have a negatively skewed distribution, with most values slightly above the mean and a long tail to the left along the negative x-axis.

The interpretation of distributions with large values of kurtosis (sometimes called leptokurtotic, where the prefix means slim or narrow) is less obvious, as an excessive clustering of values near the mean or in either tail can contribute to this sort of departure from normality. A distribution with low kurtosis is less peaked in the middle than normal and is sometimes called platikurtotic, where the prefix means flat or broad. An extreme example of low kurtosis is afforded by a bimodal distribution, which is often the result of two normal populations with different means being combined together. As White (1980) points out, an area where there was a tendency for two distinct atmospheric regimes to occur (such as fast zonal westerlies and strong "blocking") might be expected to have a platikurtotic distribution of middle tropospheric height.

Maps of the coefficients of skewness and kurtosis of Northern Hemisphere 700 mb height are displayed in Figures 2 through 5 for selected months of the year. The "January" (Dec. 16-Feb. 14) map shows generally positive values of skewness north of the climatological position of the 700 mb wind maximum and negative values to the south (Fig. 2, left) similar to the patterns found by White at 500 mb for "winter" (Nov. 15 - Mar. 15) from a more limited number of years comprising a little over one-fourth of our data time frame. Only limited areas reach local significance, with the greatest departures from normality being downstream from the strongest wind maximum over the North Pacific. A similar, but less strong, pattern is found in the North Atlantic near the regions at maximum blocking frequency. These patterns of skewness could be explained by occasional values of rather low height, such as cut-off lows or sharp troughs interrupting generally high values in the subtropical ridge areas. The reverse is true to the north of the wind maximum--occasionally abnormally high heights (blocking) will interrupt the generally low values in the domains of the Aleutian and Icelandic Lows.

The pattern of kurtosis (Fig. 2, right) shows a generally low coefficient of kurtosis, indicating a platikurtotic distribution of 700 mb height, at middle and high latitudes over the central and eastern oceans. This pattern is again similar to that found by White, and he attributed it to a tendency for the atmosphere to have a bimodal behavior in those areas--either fast zonal westerlies or blocking, each with its own "normal" distribution. Apparently these aspects of mid-tropospheric behavior show up similarly for daily values or 15-day means of 700 mb height.

Fig. 3, which shows the higher moment patterns for "March" (Feb. 15-Apr. 15) has many characteristics similar to Fig. 2. Particularly noteworthy are the even stronger (than in January) areas of positive and negative skewness over the Bering Sea and the subtropical ridge area

directly south, respectively. Each area is accompanied by a corresponding area of locally significantly high kurtosis. Taken together, these maps indicate that the tendency for relatively rare values of unusually high height over the Bering Sea and very low values north of Hawaii is reflected in large values of kurtosis due to the excess (over the normal distribution) of extreme values in the tails. The tendency for bimodality is stronger over North America and the Atlantic than over the Pacific.

It is believed that the general overall consistency of our results with these of White, notwithstanding the partial overlap in data, and the similarity of the gross features from one "month" to another centered two months later (no data overlap) suggests that these departures from normality are real, although generally small. Although it has not been calculated, the overall significance of the whole map fields would probably not be very high (Livezey and Chen, 1983).

The maps for "July" (June 16-Aug. 15) again show the separation of mostly positive skewness to the north and negative skewness to the south of the axes of 700 mb wind maxima. The values of negative skewness are highly significant locally over the western Pacific in the western lobe of the subtropical ridge which is, however, occasionally disrupted by regimes reflecting frequent or recurrent typhoon activity that are persistent enough to show up in half-monthly means. Note the correspondingly high values of kurtosis in the same area.

A similar, but not as strong, combination of skewness and kurtosis appears over the central Great Plains in the United States. It is possible that the normal tendency for a warm, continental midsummer ridge is occasionally disrupted by a cool, troughy regime in this area.

The coincidence of unusually high values of both skewness and kurtosis centered at one grid point (15N^{o}, 135^{o}W) is a fairly reliable signature of a time series with one or more pieces of bad data in it. Because the departure from the mean is raised to the third and fourth powers in order to calculate skewness and kurtosis, respectively, erroneous data shows up here even though the standard derivation may not be noticeably affected. Brooks and Carruthers (1953) also pointed out that higher moments were useful for detecting erroneous data.

The maps for "September" (Aug. 16-Oct. 15) again show similar areas of locally significant departures from normality vis-a-vis the 700 mb wind maxima, the subtropical ridge axes, and climatological tropical storm paths. Note also the areas of marked negative kurtosis near the British Isles on both the July and September maps, British meteorologists have frequently noted a tendency for lengthy periods of middle or late summer to be either predominantly cyclonic or anticyclonic in character, suggesting a tendency for two distinctly different weather regimes in that area (Lamb, 1972).

Thus, like White, who dealt with a more limited (in time) data set of twice daily 500 mb heights, we may tentatively say that there are consistent tendencies for half-monthly mean 700 mb heights to display small but locally significant departures from a normal distribution. These features can be given meteorologically reasonable interpretations with regard to climatologically favored areas for 700 mb wind maxima, the axes of the subtropical ridges, tropical cyclone paths, and strongly contrasting

circulation regimes that tend to be predominantly cyclonic or anticyclonic in character. Unusually high values of skewness and kurtosis, especially when appearing centered at a single grid point near the boundary and not amenable to a reasonable meteorological interpretation, are probably good indicators of one or more bad values in the data time series at that location.

REFERENCES

Brooks, C.E.P., and N. Carruthers, 1953: Handbook of Statistical Methods in Meteorology. Her Majesty's Stationery Office.

Lamb, H.H., 1972: British Isles weather types and a register of the daily sequence of circulation patterns 1861-1971. Geophys. Mem., 16, No. 116.

Livezey, R.E. and W.Y. Chen, 1983: Statistical field significance and its determination by Monte Carlo techniques. Mon.Wea. Rev., 111, 46-59.

Moffitt, B.J., and R.A.S. Ratcliffe, 1972: Northern Hemisphere monthly mean 500 mb and 1000-500 mb thickness charts and some derived statistics (1951-66). Geophys. Mem., 16, No. 117.

Spiegel, M.R., 1975: Probability and Statistics, Schaum's outline series in mathematics, McGraw-Hill Book Co., New York, NY. Chapter 3, 76-107.

Wagner, A.J. and T.N. Maisel, 1988: Northern Hemisphere 700-mb teleconnections based on half-monthly mean anomaly data stratified by season and by sign. Proceedings of the Twelfth Annual Climate Diagnostics Workshop, Salt Lake City, UT, October 12-16, 1987, U.S. Department of Commerce, pp. 228-237. Available from: Climate Analysis Center, W/NMC5, 5200 Auth Road, Washington, DC 20233.

White, G.H., 1980: Skewness, kurtosis and extreme values of Northern Hemisphere geopotential heights. Mon. Wea. Rev. 108, 1446-1455.

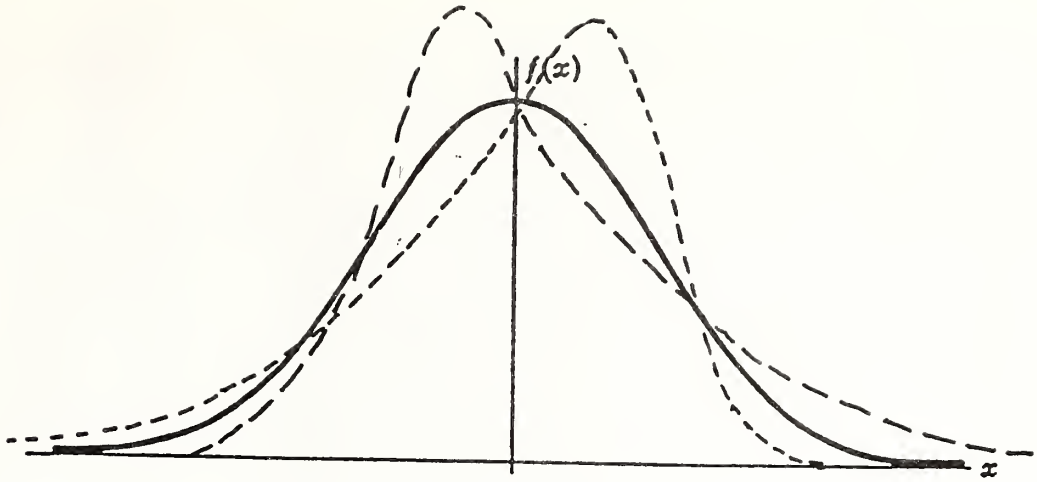

--- Positive Skewness (>0)
or Skewed to the Right

----- Negative Skewness (<0)
or Skewed to the Left

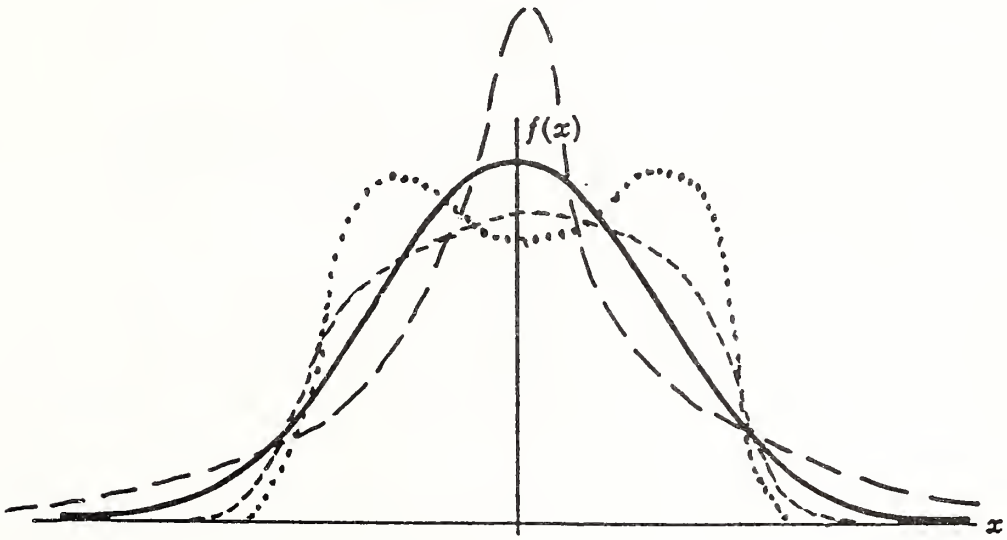

--- High Kurtosis (>3.0)

------ Low Kurtosis (<3.0)

..... Bimodal Distribution (Very Low Kurtosis)

Fig. 1 (top) Comparison of positively and negatively skewed distributions with the normal or Gaussian distribution (solid line).
(bottom) Comparison of distributions with high and low kurtosis and a bimodal distribution with the normal or Gaussian distribution (solid line).

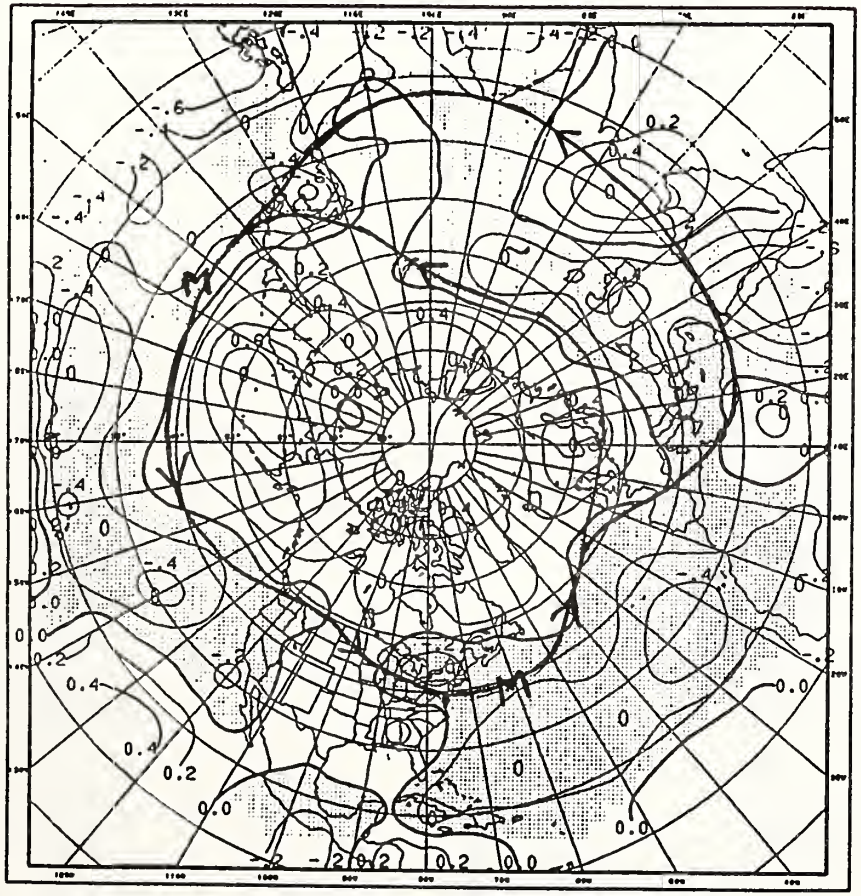

THIRD MOMENT SKEWNESS FOR JAN
CONTOUR INTERVAL = 0.2

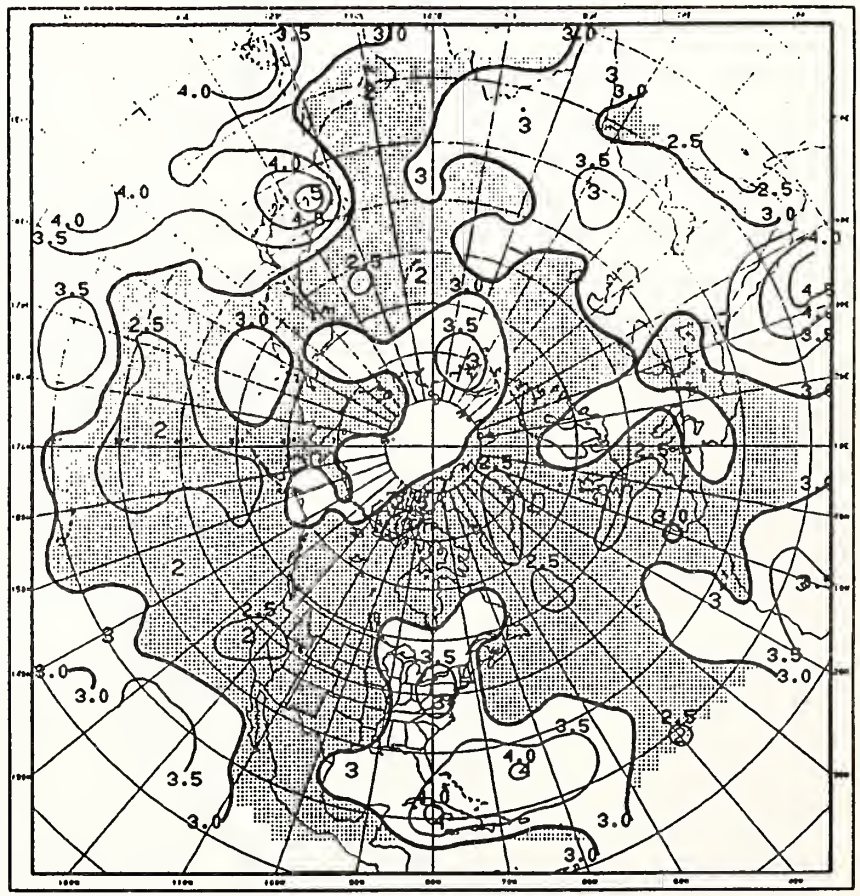

FOURTH MOMENT KURTOSIS FOR JAN
CONTOUR INTERVAL = 0.5

Fig. 2. Third and Fourth Moments of 15-day mean 700 mb heights over the Northern Hemisphere for January. Superimposed heavy solid lines with arrows show axes of normal 700 mb wind maxima. Locations of peak wind speed given by M.

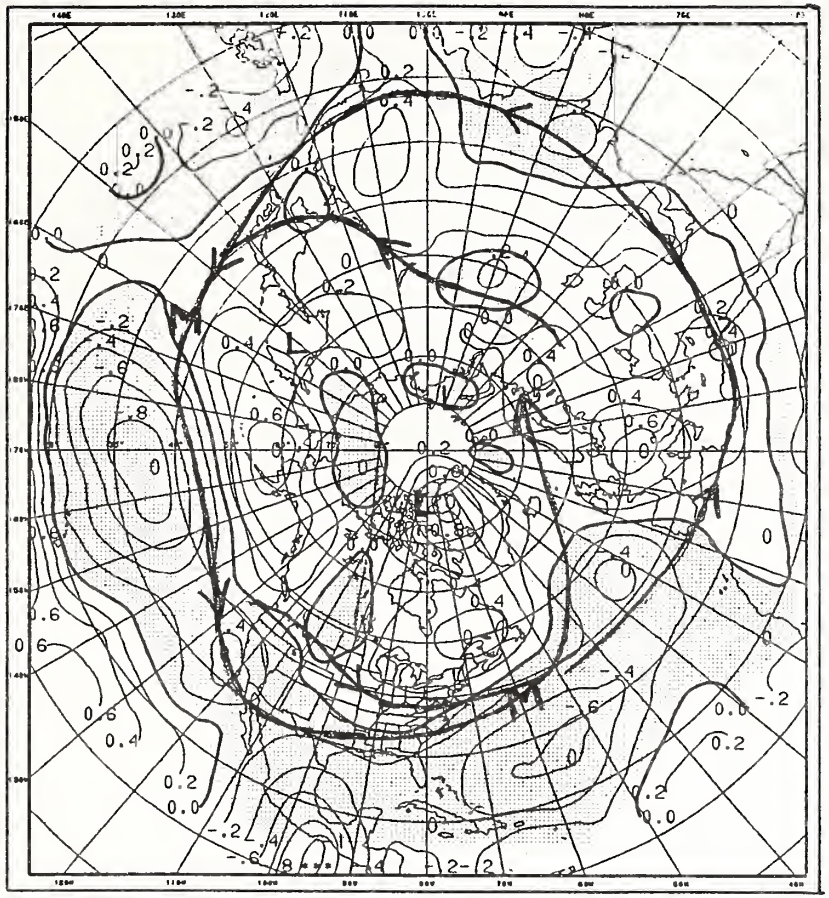

THIRD MOMENT SKEWNESS FOR MAR
CONTOUR INTERVAL = 0.2

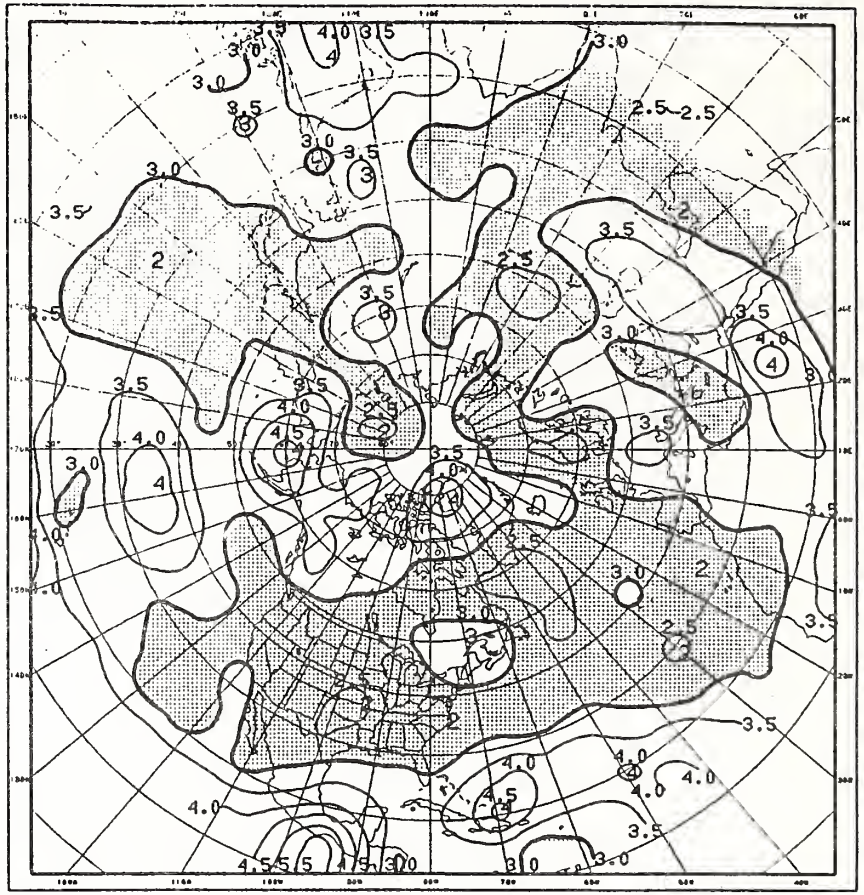

FOURTH MOMENT KURTOSIS FOR MAR
CONTOUR INTERVAL = 0.5

Fig. 3. As in Fig. 2 for March.

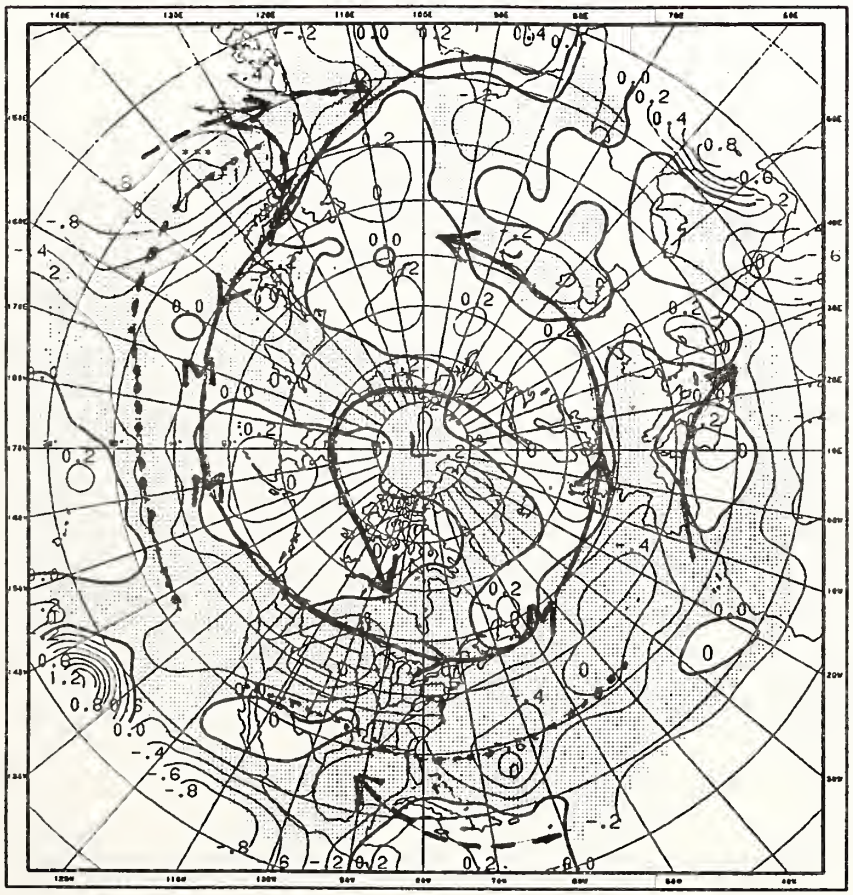

THIRD MOMENT SKEWNESS FOR JUL
CONTOUR INTERVAL = 0.2

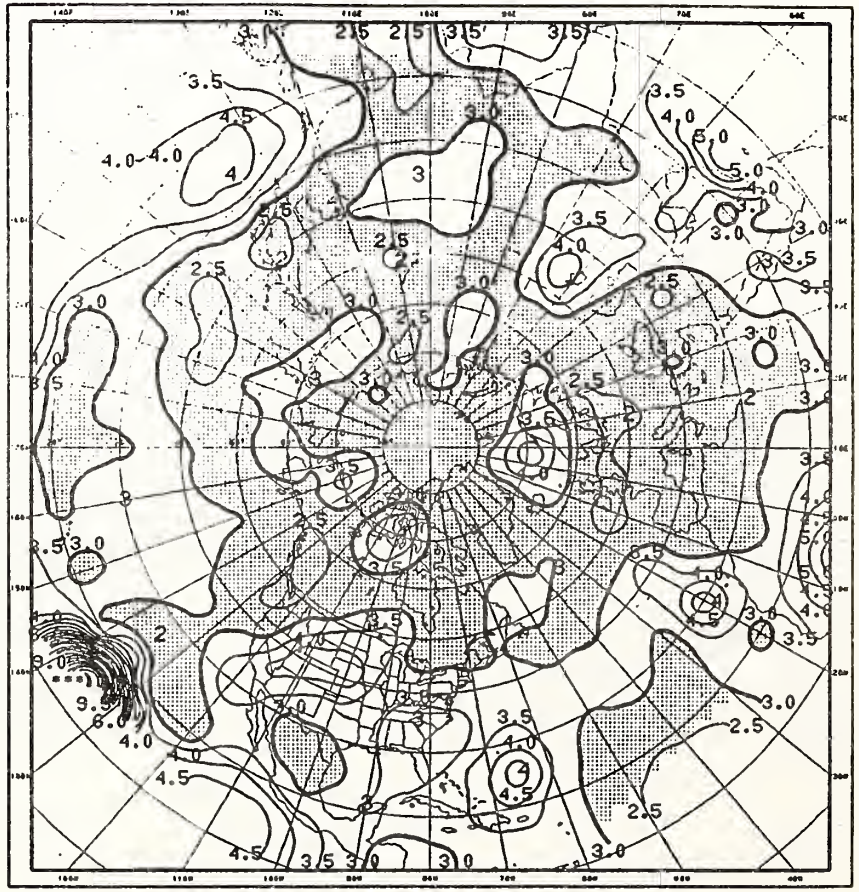

FOURTH MOMENT KURTOSIS FOR JUL
CONTOUR INTERVAL = 0.5

Fig.4. As in Fig. 2 for July, with climatological tropical storm tracks shown by heavy dashed lines with arrows. Heavy dotted line shows axis of 700 mb subtropical ridge.

THIRD MOMENT SKEWNESS FOR SEP
CONTOUR INTERVAL = 0.2

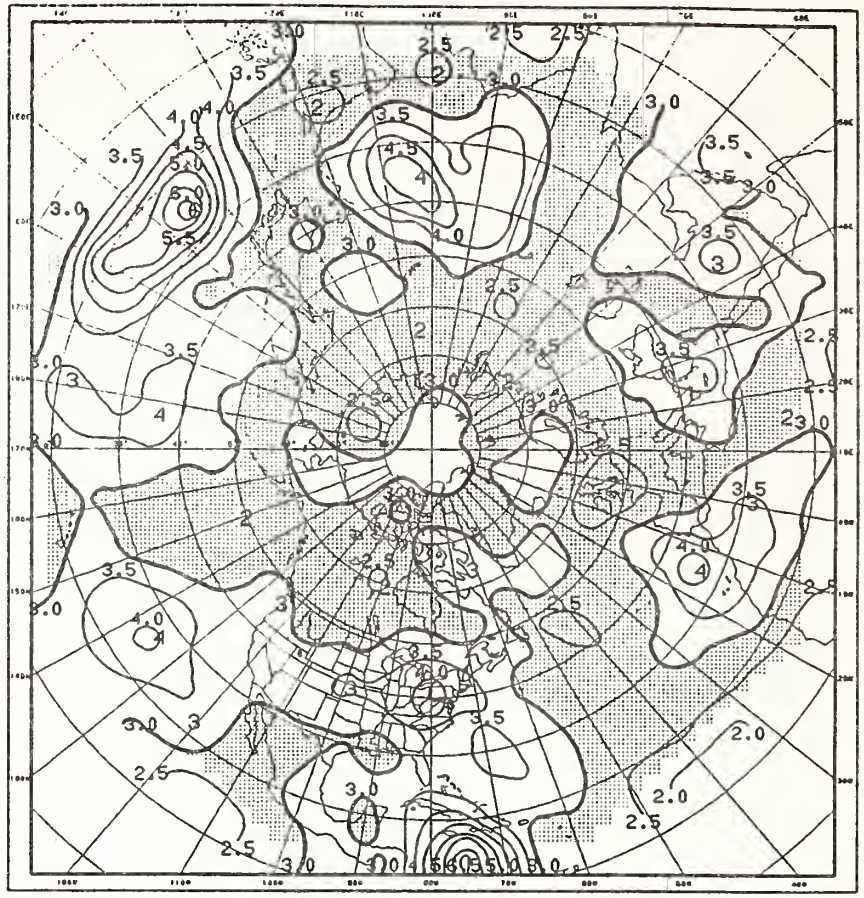

FOURTH MOMENT KURTOSIS FOR SEP
CONTOUR INTERVAL = 0.5

Fig. 5. As in Fig. 4 for September.

DEVELOPMENT OF A SIMPLIFIED NMC SPECTRAL MODEL WITH EMPIRICALLY-DETERMINED FORCINGS

Shyh-Chin Chen and John O. Roads
Scripps Experimental Climate Forecast Center
UCSD, A-024
La Jolla, CA 92093

In order to perform large ensembles of predictability experiments with a realistic model, we are developing a simplified GCM with an empirically-determined forcing. The model is a lower resolution version of the operating NMC spectral global primitive-equation model (Sela, 1980) with only 4-sigma layers and a spectral truncation of rhomboidal 20 (R20). A moisture cycle consisting of large-scale condensation processes and Kuo's convective parameterization is also included. Through the processes of evaporation and sensible heating transfer, the model interacts with the underlying ocean, and the monthly climatological sea surface temperature fields are specified.

When the model is integrated for a period longer than a few days, as demonstrated in Fig. 1a, the global temperature tendency (heavy line) indicates an unrealistic warming trend of the model. This tendency is mainly contributed by the release of latent heat (thin line). Due to the trend, the mean temperature increases from -21 °C to 50 °C in 110 days. We have not continued the integration after 110 days, although presumably the positive tendency will decrease to a small value as the atmosphere becomes too warm to retrieve any vapor from a relatively colder ocean surface. Therefore, either a sophisticated radiation parameterization or some form of forcing in the model is needed to offset the trend. The prescribed forcing is also used to compensate the bias of the model, and also to mimic processes that are excluded in the model but are responsible for the observed climatology.

To illustrate this idea of the empirical-determined forcing, let us consider the thermodynamic equation

$$\frac{\partial T}{\partial t} = -ADV + L + F, \tag{1}$$

where T is the temperature, ADV is the nonlinear advection, L is the release of latent heat and surface sensible heat transfer, and F represents other diabatic processes. For long time averages, the time rate of changes should be relatively insignificant and a balance is, therefore, achieved between $\overline{ADV}$, $\overline{L}$ and $\overline{F}$, where the overbar stands for ensemble average. The $\overline{F}$ can be found empirically by performing series short term forecast, noted by an"$*$", so that

$$\overline{\frac{\partial T^*}{\partial t}} = -\overline{ADV^*} + \overline{L^*}. \tag{2}$$

Assuming $\overline{ADV} \approx \overline{ADV^*}$ and $\overline{L} \approx \overline{L^*}$, we then obtain the forcing by ensemble averaging all the short-term weather forecasts, ie.,

$$\overline{F} = -\overline{\frac{\partial T^*}{\partial t}}. \tag{3}$$

Having determined the forcing, the model can then be reintegrated for an extensive period by replacing F in (1) by a time independent $\overline{F}$. A similar method has been applied to a 2-level quasi-geostrophic hemispheric model without a hydrological cycle (e.g., Roads 1987; 1988). The inclusion of the precipitation process in the current model complicates the procedure since we have to integrate the model from each given observed intial state for a finite interval ($\sim$ 3 days). To calculate the forcing we use January ECMWF daily analyses for 1983, 84, 86 (available through NCAR) as initial fields.

The global mean F has a value of about -0.2 °C/day when (3) is evaluated with the ensemble mean temperature tendency for a 6 hour forecast. The magnitude of the forcing increases with the integration time, and reaches -1.84 °C/day at day 2.75. Apparently the model requires a spin-up time for precipitation to develop. Several experiments have been done by using forcings evaluated at different hour, and we believe that the forcing at day 2.25 is probably most desirable for producing a realistic clmatology. Fig. 2 shows the forcing in physical space. At the lower levels, the forcing is quite noisy but overall it is negative except for a few areas off the coast. The forcing becomes organized into large scale features at higher levels with significant cooling and warming rates in the tropical oceans, Amazon, central Pacific, and over Asia and North America continents. Note also the sign reversal taking place over these areas at levels 3 and 4.

A 160-day integration has been made with the forcing in Fig. 2 included. In Fig. 1b, the forced model initially shows large negative and positive tendency for the global mean temperature and then relaxes toward a zero value. When the model reaches a steady state, the latent heat is about 0.2 °C/day smaller in magnitude than the forcing indicating some sensible heat flux from ocean surface into the atmosphere. After an initial 40 days cooling period, the model comes to equilibrium at a model climatology which is about 3 °C too cold compared to that from the ECMWF analyses for January 1979-1986. The precipitation rate is almost twice as large as the rate when the empirical forcings are absent (see Fig. 1). This is probably because the forced-model produces a climatology which is too cold and as a result too much water vapor evaporates into the atmosphere from the ocean.

The model not only produces a steady global climatology, it also generates realistic NH

January geopotential height fields. Fig. 3a gives the 500 mb height taken from the ECMWF analyses. Further details are shown by removing the zonal mean in order to emphasize the stationary eddy field (Fig. 3b). The model counterparts are given in Figs. 3c and 3d, respectively. Comparing Figs. 3a and 3c, the model does seem to reproduce the observed features well in the NH. The major model defect is that the tropics are too shallow mainly due to the model cold temperature bias. The other major defect is that the jet is too weak in the SH. The stationary eddy fields are, however, fairly well represented, especially in the NH. Note the similarity in planetary wave pattern and magnitude of each center in the observations and the model results. Even in the SH, the amplitude and phase of the weak eddies are appropriate.

We are encouraged that the empirical forcing seems to stabilize the unforced model although it is not clear at present what exact processes are associated with the forcing, and why the signs of major forcing centers at levels 3 and 4 are reversed. We can only speculate that the intense cooling centers over tropics at level 3 might represent radiational cooling which offsets latent heat release of the deep convection. Level 4 corrections may also be due more to a model bias.

Finally we think the global cold bias is due to the global cooling forcing being too large. By including more short term weather forecasts to compute the forcing, we suspect the resulting global forcing will be smaller in amplitude which should reduce the cold bias of the model.

References

Roads, J. O., 1987: Predictability in the extended range. *J. Atmos. Sci.*, **44**, 3495-3527.

Roads, J. O., 1988: Lagged average predictions in a predictability experiment, *J. Atmos. Sci.*, in press.

Sela, J. G., 1980: Spectral modeling at the National Meteorological Center. *Mon. Wea. Rev.*, **108**, 1279-1292.

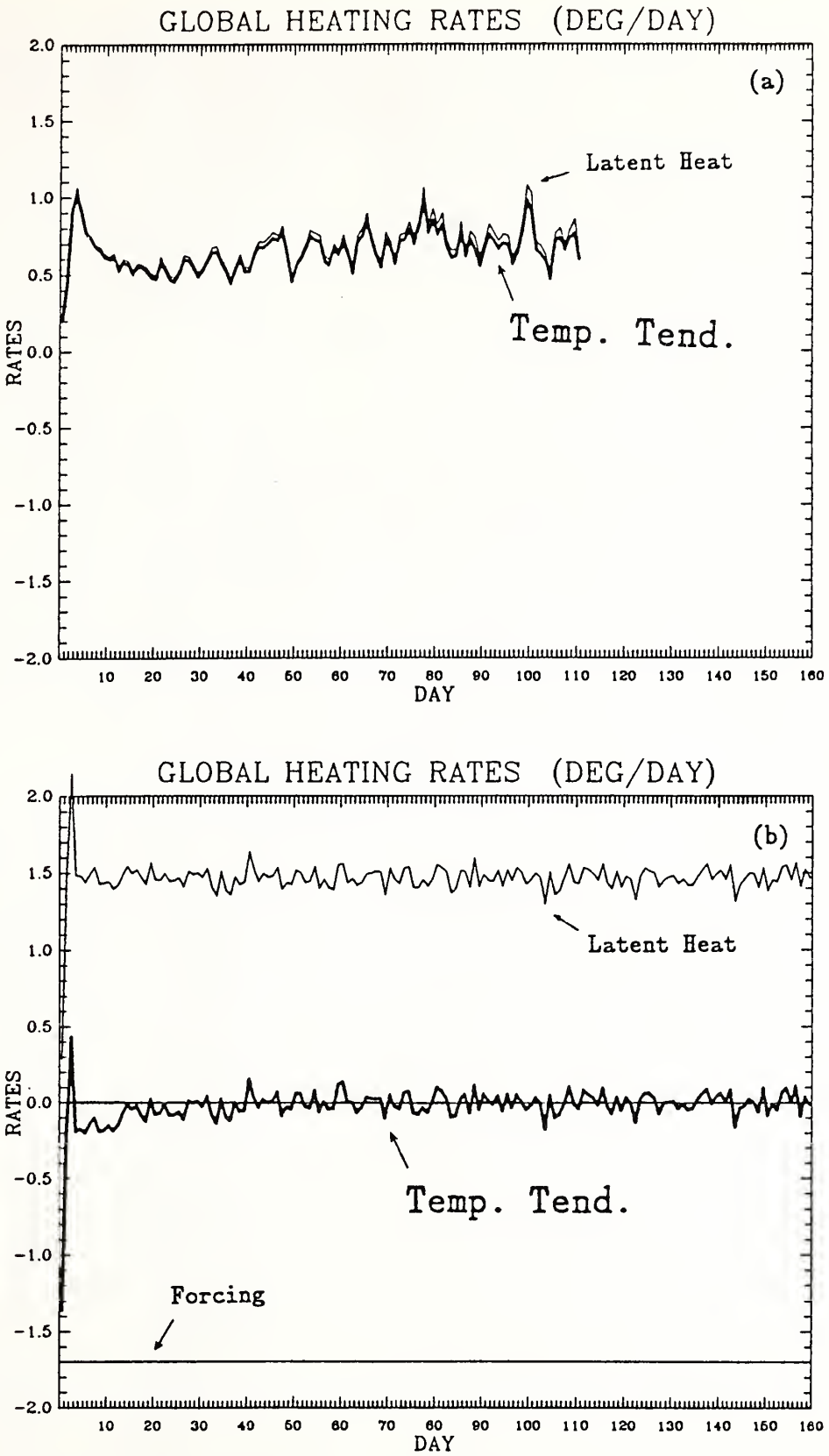

Fig. 1. Global mean temperature tendency (heavy line) and latent heat release (thin line) in °C/day for the (a) model without forcing, and (b) model with forcing. The value of the time independent forcing is also plotted in Fig. 1b.

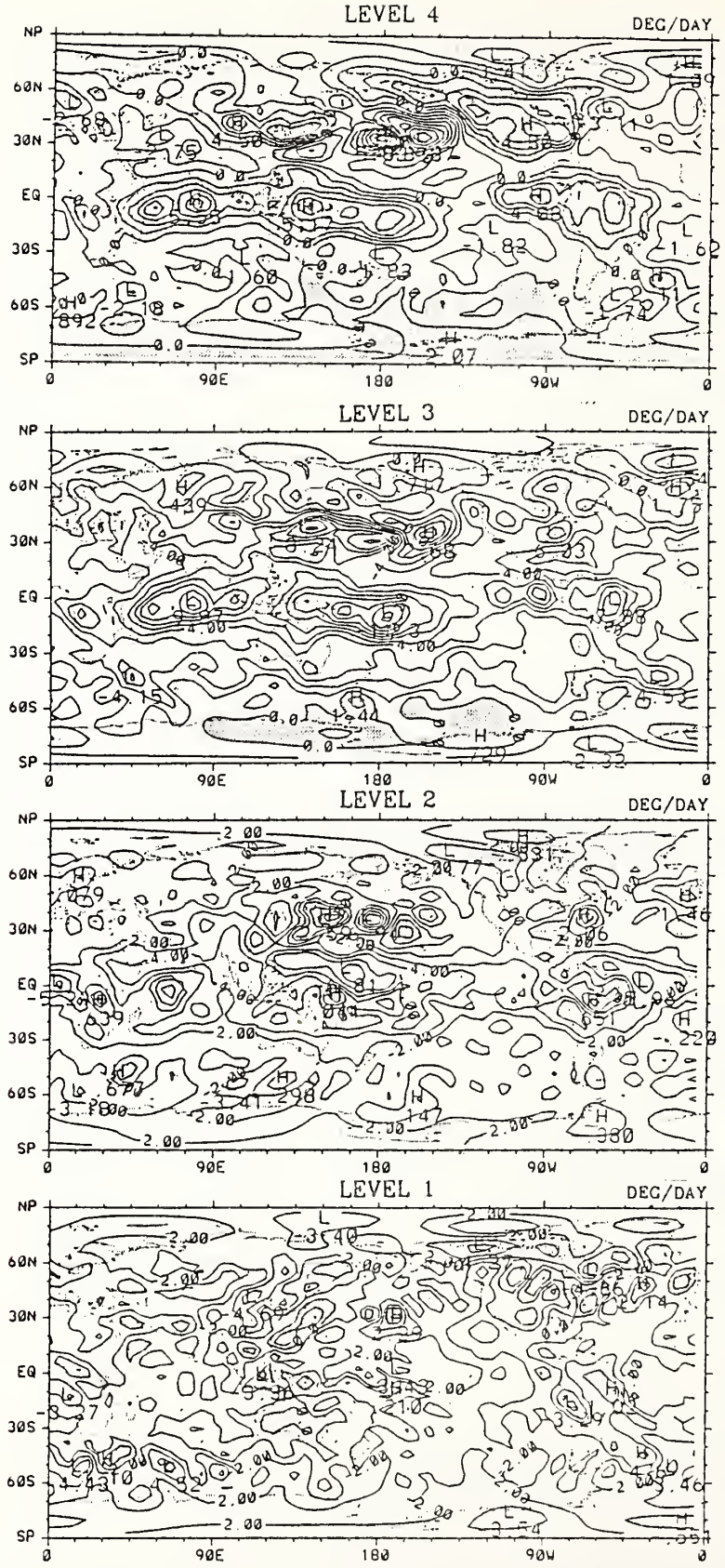

Fig. 2. Temperature forcing at day 2.25 from top (level 4) to the bottom (level 1). The contour interval is 1 °C/day. Heating areas are shaded.

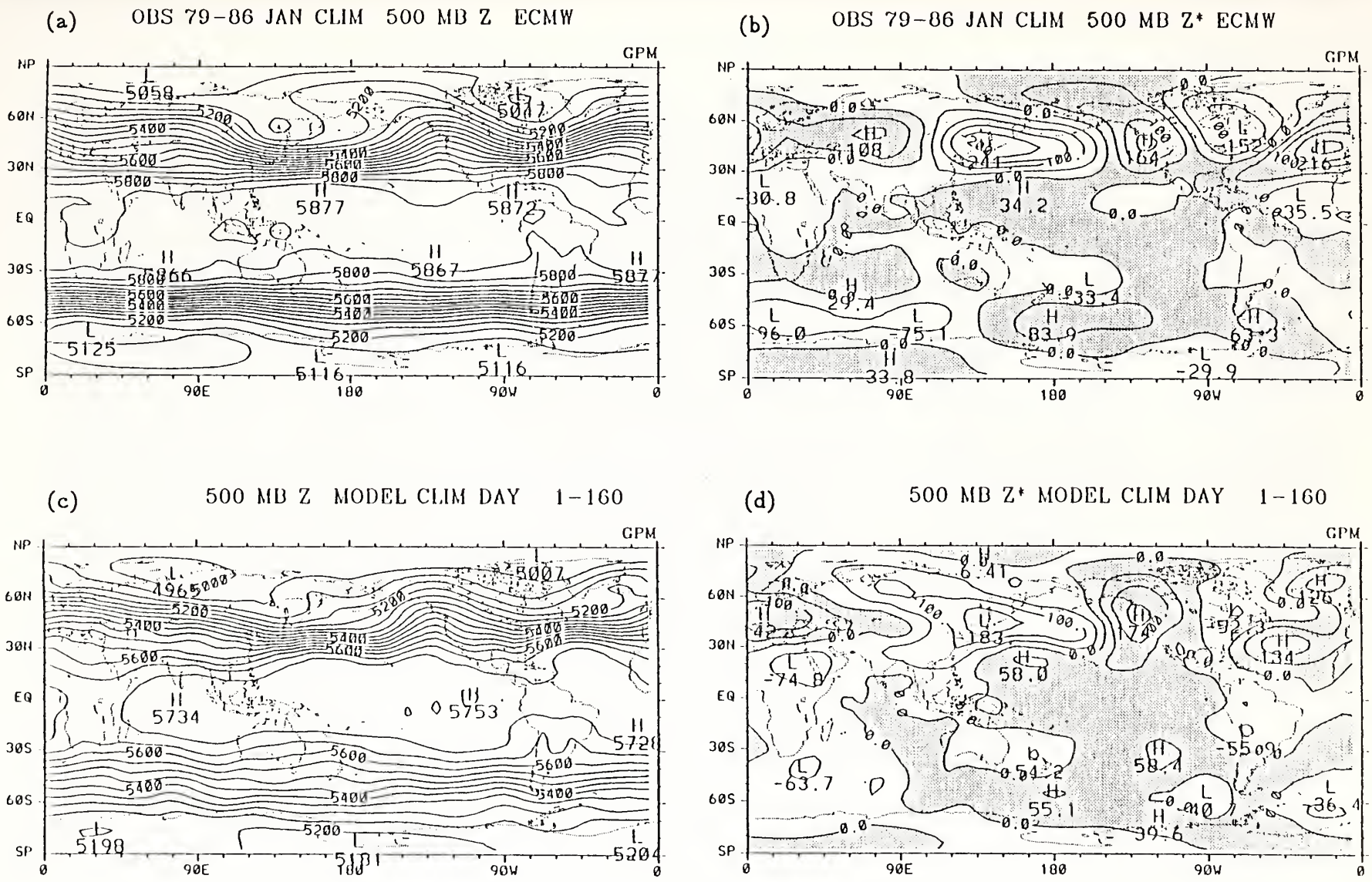

Fig. 3. (a) Observed 500 mb height compiled from January 1979-86 ECMWF analyses, (b) same as (a) except the zonal mean is removed. (c) First 160 days avarage of the forced model run, (d) same as (c) except the zonal mean is removed. The contour interval is 50 m.

A Reduced Version of the NMC DERF II Data Set and A Preliminary Error Growth Analysis

by

Fong-Chiau Chang, Siegfried Schubert, William K.-M. Lau
Experimental Climate Forecast Center
NASA/Goddard Space Flight Center
Greenbelt, MD 20771
and
Robert Kistler
National Meteorological Center, Development Division
Washington D.C., 20233

The National Meteorological Center (NMC) conducted the second phase of the Dynamic Extended Range Forecasting (DERF) experiment During December 1, 1986 - March 31, 1987. For 108 contiguous days (December 14, 1986 through March 31, 1987), 30-day forecasts were performed every day from 00Z analyses using a research model with rhomboidal (R40) horizontal resolution and 18 levels. The purpose of the experiment was to provide a data base from which to establish an optimal configuration for possible operational dynamical monthly forecasts. A major stumbling block for using this dataset has been the sheer volume of data which must be processed in order to perform even the simplest of calculations. As a response to this problem the Experimental Climate Forecast Center at Goddard together with NMC and the University of Maryland (COLA) have produced a reduced version of this data set. In Section 1, we outline the data reduction process and give a brief description of the reduced data set (see Schubert et al., 1988 for details). In Section 2, we describe some initial results of an error growth study based on the reduced data.

1. The DERF Data Reduction

The data processed for this task involved a number of steps which included first obtaining a subset of the original 250 tapes and then reading and processing this subset (54 tapes) consisting of selected pressure level and surface data. The product of the data reduction is a manageable data set which fits comfortably on 5 tapes.

The fields selected from the original data for processing are the global post-processed mandatory pressure level data in spherical harmonic coefficients at a resolution of R30. These fields consist of the surface pressure, geopotential height, $u\cos\phi$, $v\cos\phi$, temperature, vertical velocity and relative humidity. In addition global surface data were provided on a gaussian grid with 102 points in the north-south direction and 128 points in the east-west direction. The surface gridded fields include surface temperature, soil moisture, snow depth, total rainfall, convective rainfall, surface sensible and latent heat flux, surface u-stress and surface v-stress.

The reduction process consisted of reducing the R30 resolution to triangular 20 (T20) and area averaging the gridded surface data to a 5° longitude by 4° latitude grid (72x46). As a test of our reduction programs and to assist the users of this data we have reconstructed selected fields using both the original and final resolutions. Figs. 1 to 3 are three examples.

II. Error Growth in the NMC model

Height fields at 850 mb, 500 mb, 250 mb and temperature at 700 mb have been extracted to study predictability in the NMC model. Our initial experiment focused on the estimation of the rate of the growth of forecst errors by using the "identical twin" technique. This technique measures how fast two model integrations, started from very close initial conditions and computed using the same atmospheric model, depart from each other.

Specifically, the analysis for a given day and the one-day forecast for the same day represent two states which do not differ too greatly. One-day forecasts made from these two states are simply the one-day and two-day prognoses for the following day. Thus, by comparing the average difference between one-day and two-day prognoses for the same day with the average difference between analyses and one-day prognoses the day before, we can obtain an estimate of the average one-day amplification of moderately small errors. To obtain the average two-day amplification we need only compare two-day and three-day prognoses for the same day, and, in fact, we can continue this procedure up to twenty nine day amplifications. Likewise, to obtain amplifications of somewhat larger initial errors we may, for example, compare the average difference between one-day and three-day prognoses with the average difference between analyses and two-day prognoses, or more generally, the difference between j-day and k-day prognoses with the difference between analyses and (k-j)-day prognoses (see Lorenz 1982 for details of this technique).

The error $E^2_{jk} = N^{-1} S^{-1} \Sigma \int_s [Z_{i,j}(\lambda,\phi) - Z_{i,k}(\lambda,\phi)]^2 dS$, where $Z_{i,j}(\lambda,\phi)$ is the j-day forecast for the value of $Z(\lambda,\phi)$ on the ith day of the sample, is defined as the root-mean-square difference between j-day and k-day prognoses for the same day, averaged over the globe and over N days. Fig. 4 shows the global root-mean-square 500 mb height differences E_{jk} for j<k, plotted against k. The heavy curve connects values of E_{0k}, and its upward slope as k increases represents the rate of increase of the model's forecast error. This is the rate at which solutions of two different systems of equations -the true atmospheric equations and those of the model- diverge as time progresses. The thin curves, on the other hand, connect values of E_{jk} having like values of k - j, and their upward slope as k increases represents the rate at which two solutions of the same system of equations - those of the model - diverge. The different values of k-j indicate various magnitudes of initial data difference. The thin curves shows the growth of rms differences between two neighboring series of forecasts, ignoring the model deficiencies and observing an idealized situation of error growth with only the initial uncertainly. Even with a perfect model, a slight initial difference will grow as time goes on due to its instabilitties and nonlinearity.

A substantial portion of the forecast error is due to the model's systematic bias (Miyakoda et al., 1986). It is essential to remove the systematic drift of the prediction model in order to raise the skill of the forecast for the extended range. The differences between the 108-case mean hieght of the 1-day forecast and the corresponding verfiying analyses (see Fig. 5 top panel) shows the systematic cooling of the NMC model. This cooling increases with the forecast range as shown in the 5-day and 10-day forecasts (Fig. 5 middle and lower panels).

Shukla (1983) suggested that the drift may be adjusted by adding the difference between the model climatology and the real climatology so that the prediction and the corresponding predictant have the same mean. Fig. 6 shows the similar results as in Fig. 4, but with the drift removed. In this figure the heavy curve drops, the bottom curve moves upward slightly, hence these two curves approach to each other. The slope of heavy and thin curves are closer to each other in Fig. 6 than in Fig.4. The thin curves level off below the real forecast error curve. This feature indicates that the NMC model underestimates the variance of the atmosphere.

The heavy curve shows the forecast skill of the NMC DERF research model up to 30 days in terms of r.m.s. errors. The r.m.s.error grows rapidly, reaching 80% of the saturation value by the 9th day and then, with rapidly decreasing growth rate, gradually approaching the saturation value, on about the 20th day. From there on the average error is as large as those of the random forecasts as shown in the figure.

Lorenz (1982) showed that the internal r.m.s. forecast error growth can be parameterized reasonably well by $dE/dt = aE(E_\infty - E)$, where a is the growth rate and E_∞ is the asymptotic value of the error at long times. This formula reflects the fact that infintesimal errors grow exponentially in time, and that the average error growth must cease once the system reaches saturation, at which time the two solutions are as different as two random solutions. However, this parametrization is not suitable for real forecast error growth, because by not allowing for errors due to model deficiencies it is valid only for "identical twin" comparisons.

We used the Lorenz' error growth model to estimate the doubling time. In Fig. 7, which present the relevant material of Fig. 6 in an alternative form, shows the tendency of r.m.s. error difference as a function of the r.m.s. error difference. For each of the one-day segments of the thin curves, which have initial error less than 10 days and forecast range shorter than 16 days, we have plotted as dots, the increase in root-mean-square error $E_{j+1,k+1} - E_{j,k}$ against the average root-mean-square error $(E_{j,k} + E_{j+1,k+1})/2$. Thus we have plotted a finite difference estimate of dE/dt against E. Likewise, for each of the 29 one-day segments of the heavy curve we have plotted, as crosses, $E_{j+1,0} - E_{j,0}$ against $(E_{j,0} + E_{j+1,0})/2$. The separation of the dots and crosses indicates that further improvement in forecasting is possible.

If E were really governed by $dE/dt = aE(E_\infty - E)$, the dots would lie on a parabola. The vertical spread of the dots is obvious, they come close to doing so. There is probablly no unequivocal definition of the parabola, $y = ax - bx^2$, which best fits the total 435 dots. We have chosen to use only the lowest 10 thin curves as described above. In this way we give the weight of the individual dots in the left portion of the 435 dots and neglect some of the negative values of y. The resulting parabola, shown in Fig. 7, corresponds to a limiting error of 97.2 m and a doubling time of 2.38 days. The doubling time for 850 mb and 200 mb heights and 700 mb temperatures is close to that of 500 mb heights. The results indicate that these parameters have similar ranges of predictability in global average.

We also applied this twin technique on 850 mb and 200 mb average height and thickness, the results for these two fields are about the same. Meanwhile the data are more plentiful over extratropical regions of the Northern Hemisphere. In order to address the baroclinic versus batroropic and use the better data, regional predictability studies are in progress. The scale dependence will also be included in further studies.

References

Dalcher, A. and E. Kalnay, 1987 : Error growth and predictability in operational ECMWF forecasts. *Tellus, 39,* 474-491.

Lorenz, E. N., 1982 : Atmospheric predictability experiments with a large numerical model. *Tellus, 34,* 505-513.

Miyakoda, K. J. Sirutis and J. Ploshay, 1986 : One-month forecast experiments - - without anomaly boundary forcings. *Mon. Wea. Rev., 114,* 2363-2401.

Schubert, S., F.-C. Chang, K.-M. William Lau and R. Kistler, 1988 : A reduced version of the NMC DERF II Data Set. *NASA Technical Report,* Experimental Climate Forecast Center, NASA/Goddard Laboratory For Atmospheres.

Shukla, J. 1983 : On physical basis and feasibility of monthly and seasonal prediction with a large GCM. *Long-range Forecasting Research Publications Series,* No. 11. WMO, 142-153.

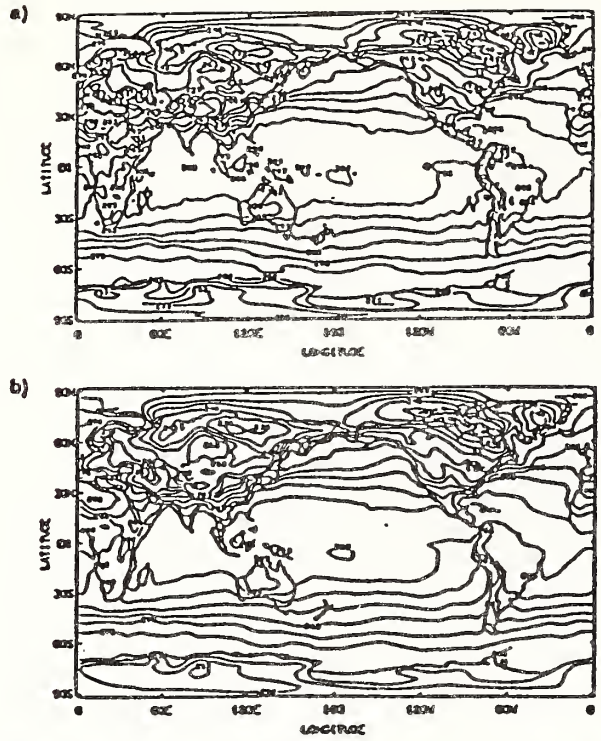

Fig. 1.

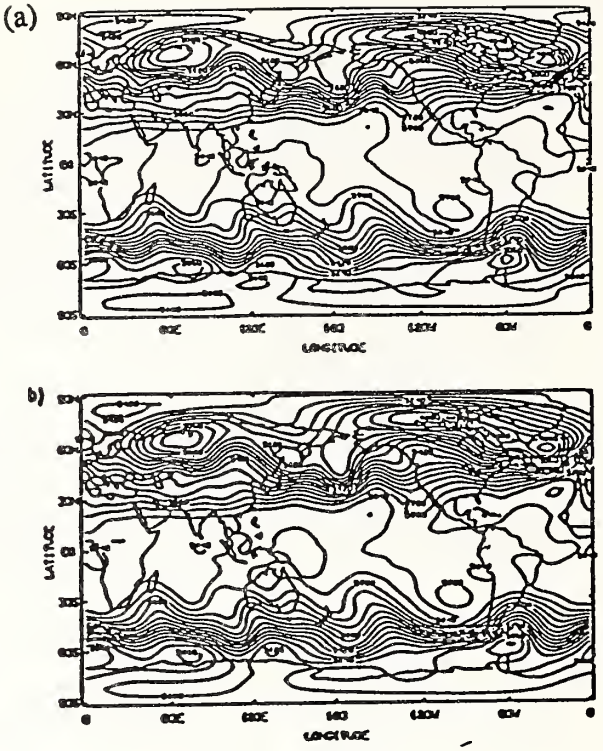

Fig 2.

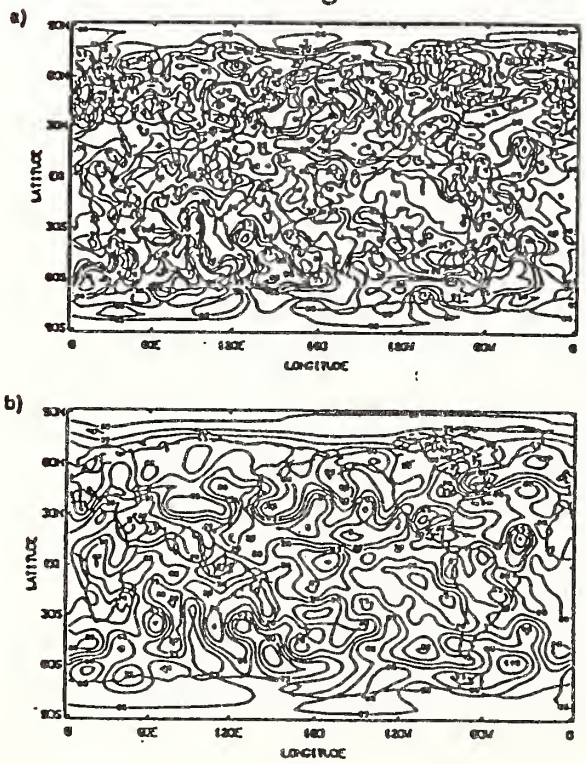

Fig. 3.

Fig. 1. Height at 500 mb for 24 hour Forecast verifying December 15, 1987
(a) R30 truncation (b) T20 truncation
contour interval is 60 m.

Fig 2. Surface temperature for 24 hour forecast verifying December 15, 1987
(a) High resolution grid (128,97)
(b) Loe resolution grid (72x46)

Fig. 3. As in Fig. 1, except for 500 mb relative humidity.

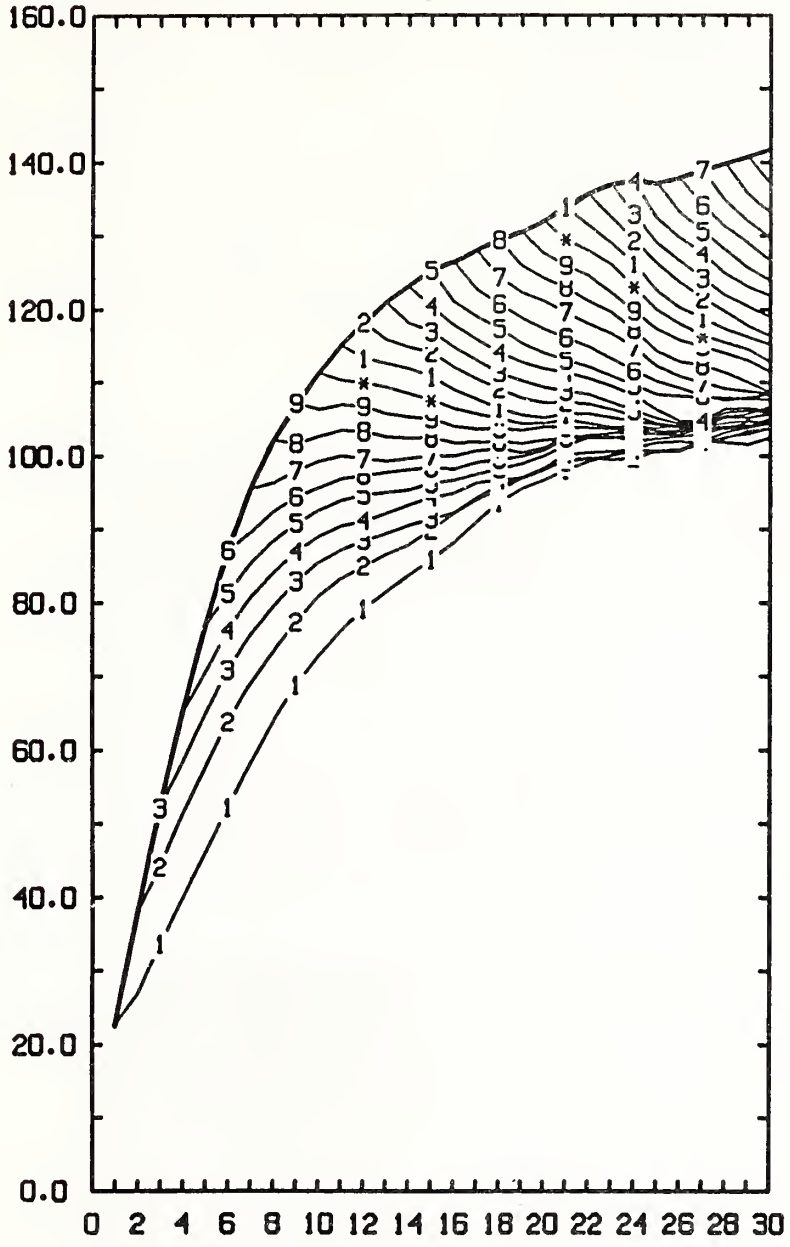

Fig. 4. Global root-mean-square 500 mb height differences E_{jk}, in meters, between j-day and k-day forecasts for the same day, for $j < k$, plotted against k. Heavy curve connects values of E_{0k}. Thin curves connect values of E_{jk} for constant k-j.

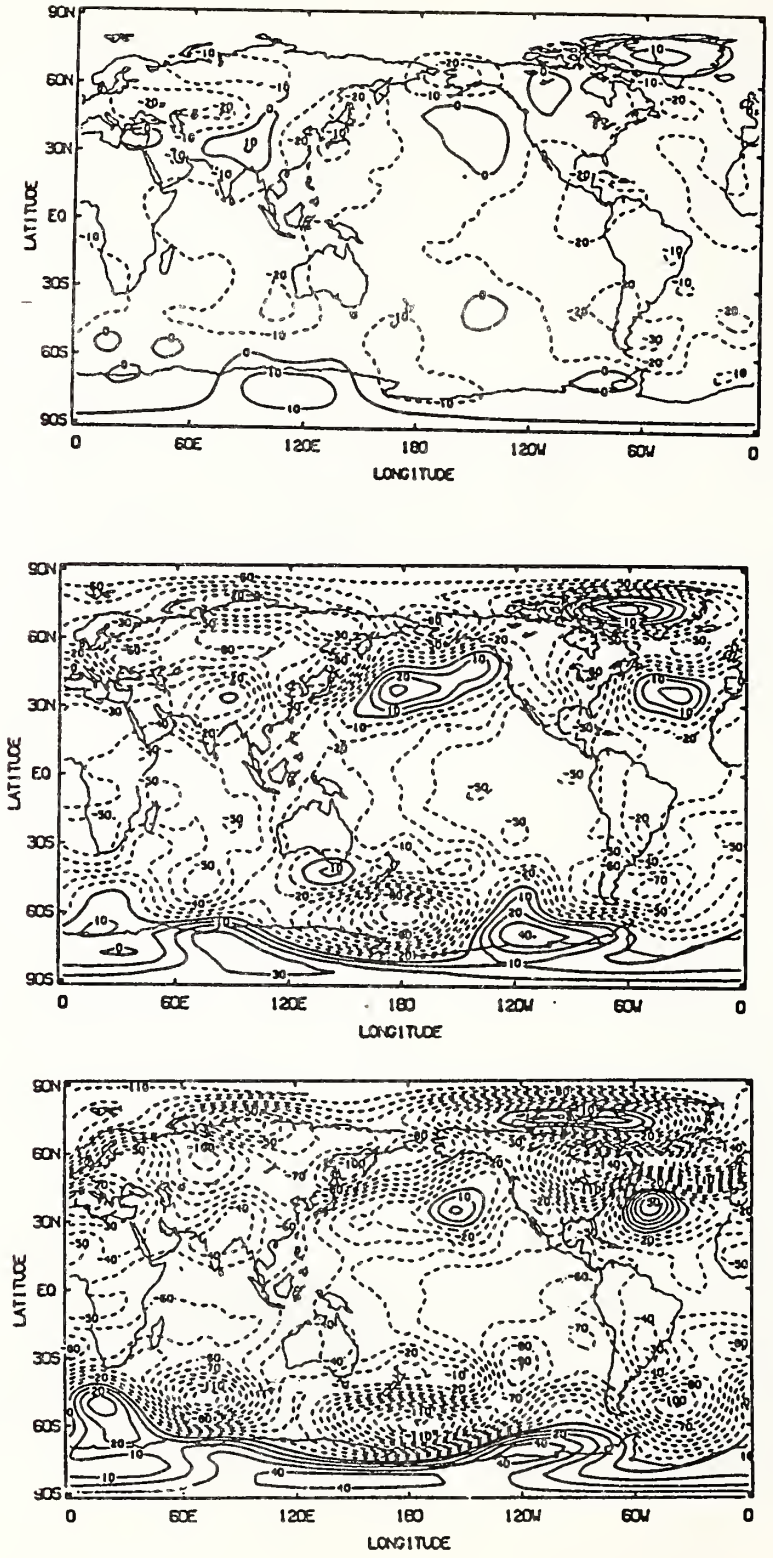

Fi.g. 5. The difference between the mean height for the 1-day (top panel), 5-day (middle panel) and 15-day (lower panel) forecasts and mean of their corresponding verifying analyses.

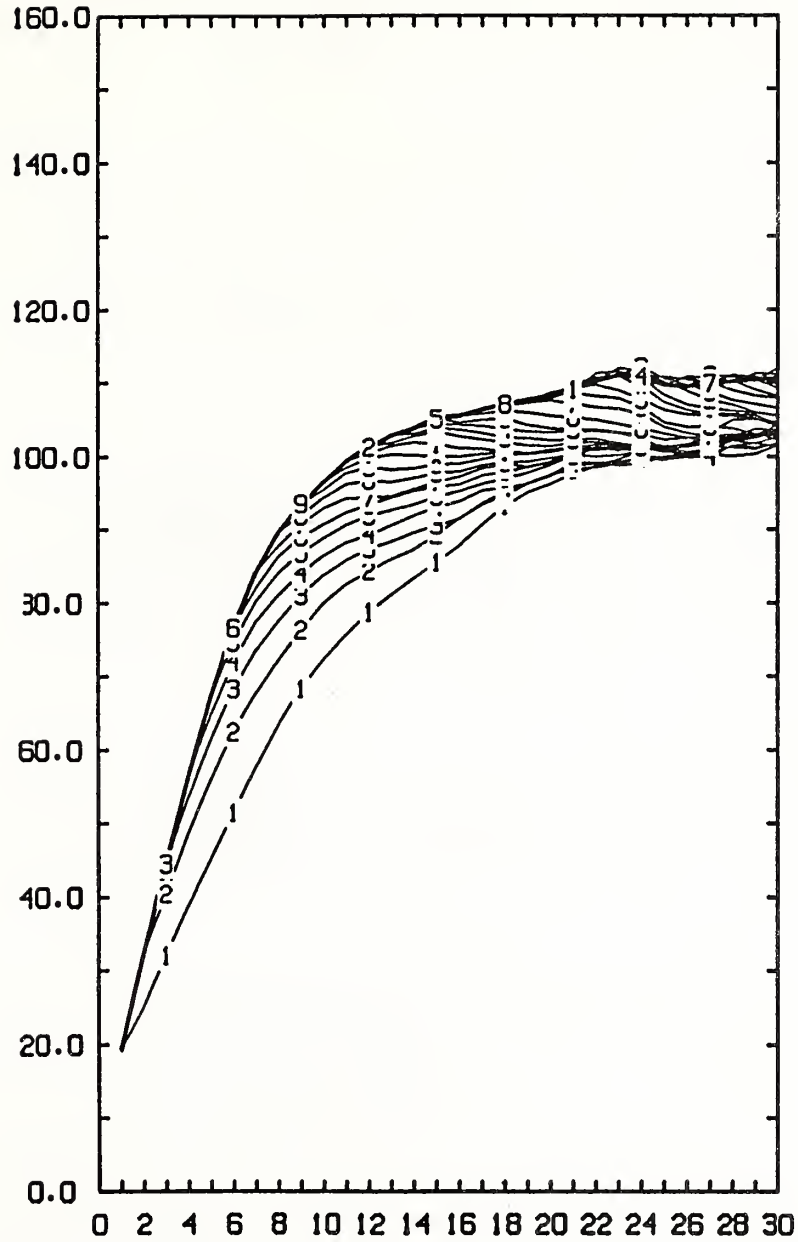

Fig. 6 Same as in Fig. 4, except the climate model drift has been removed.

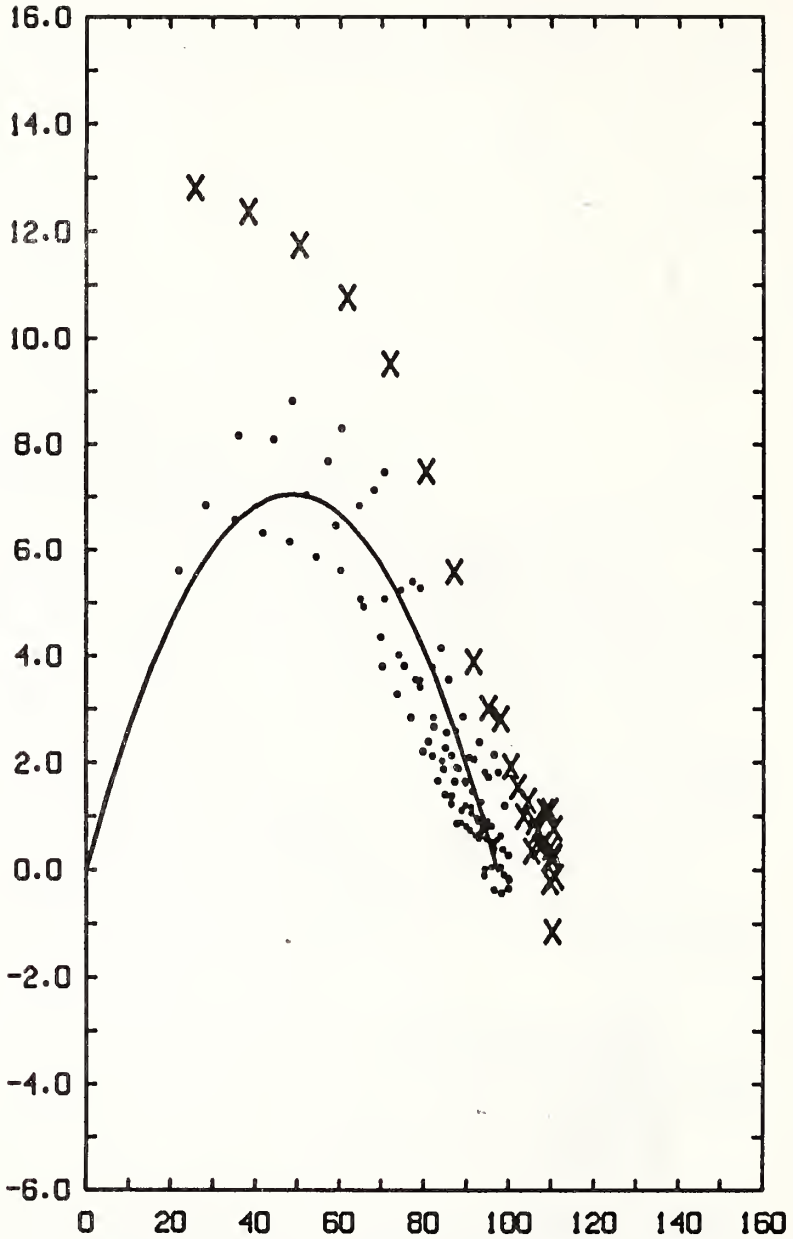

Fig. 7 Increases in global root-mean-square 500 mb height differences, $E_{j+1,k+1} - E_{j,k}$, plotted against average height differences $(E_{j+1,k+1} + E_{j,k})/2$, in meters, for first 15 one-day segment of the lowest 10 thin curves (dots) in Fig. 5, and increases $E_{0,k+1} - E_{0,k}$ plotted against average differences $(E_{0,k+1} + E_{0,k})/2$, for each one-day segment of heavy curve (crosses) in Fig. 5. Parabola of "best fit" to dots is shown.

Slowly Evolving Features in the Winter Northern Hemisphere 500 mb Field and their Influence on Medium Range Forecasts

Nicholas E. Graham

Climate Research Group
Scripps Institution of Oceanography
La Jolla, CA 92093

1. Introduction

Slowly propagating features in the winter Northern Hemisphere 500 mb field have been investigated for more than two decades. Observational studies (e.g., Pratt and Wallace, 1976; Branstator, 1987) suggest that the dominant pattern is characterized by westward propagation of zonal wavenumbers 1-3 with preferential periods between 15 and 30 days. Theoretical studies (e.g., Straus et al. 1987; Tribbia and Madden; 1988), and those combining theory and observations (e.g., Madden, 1978; Daley and Williamson, 1985), suggest that the observed features can be represented as barotropic global rotational normal modes of the linearized primitive equations (i.e., Rossby waves) excited by random atmospheric forcing. Such traveling waves are of interest not only because of their large scale organization and systematic propagation, but also because of their potential impact on medium range numerical forecasts, both via their propagation, and through interactions with smaller scale baroclinic disturbances.

The work described here characterizes low frequency features in the winter Northern Hemisphere 500 mb field and examines their possible impact on numerical forecasts during the six years of the Medium Range Forecast (MRF) experiment (1982-1988). The results show clear evidence of well organized wavenumber 2 and 3 patterns propagating slowly westward with periods between 20 and 30 days. Further, it is suggested that beyond about six days, the behavior of the NMC MRF model diverges from the real atmosphere in that the handling of the low frequency waves is less regular in the model than the observations suggest. A statistical model is described which shows the potential for operational improvement the 10 day 500 mb forecasts on a regional basis. This note is organized into four sections. Following this introduction, the data processing and statistical techniques used are described in Section 2, and the results are presented in Section 3. Section 4 gives a brief discussion and summary.

2. Data and Analysis

The data used in this study came from the MRF experiment, an on-going study in which analyses and numerical forecasts from the NMC are archived for later analysis. These data were painstakingly processed and generously provided by Norm Maisel of the Climatic Analysis Center. For this study, observations for the period November 28 through March 10 (March 9 in leap years) of the following year were used, a total of 104 days for each winter period. The seasonal cycle was approximated and removed separately from each grid point and each year using a quadratic fit. The 2 day through 10 day (at two day intervals) 500 mb forecasts were similarly processed. In addition, the mean model error (or "drift") for each grid point was removed from each forecast set. This was done separately for each year in order to account for changes in the numerical model formulation made over the years. The forecast data covered the period from December 3 (first 2 day forecast) to March 10 (last 10 day forecast) giving a total of 90 sets of forecasts per winter period.

Two statistical methods were used in this analysis, extended empirical orthogonal functions (EEOFs) and canonical correlation analysis (CCA). The first of these is much like ordinary EOF analysis, but differs in that a series of maps, rather than a single map, constitutes a given realization. Thus the EEOF modes represent the evolution of dominant patterns in both time and space allowing propagating features to be depicted. Recent examples applications of this technique can be found in Lau and Chan (1985), Graham et al. (1987a), and Graham and White (1988). Canonical correlation analysis is a linear statistical technique for relating the behavior of one field to another; that is, it is an estimation method. The method involves the decomposition of the between-field covariance structure for the two fields under consideration. Like EOF analysis, CCA gives spatial and temporal expressions for each eigenmode, but in CCA these come in pairs with separate temporal and spatial expressions for each field. The squared correlation between the temporal expressions for each mode, termed the canonical correlation, gives a measure of the degree to which the behaviors of the two fields for that mode are related. Simply put, if the canonical correlation is large, the spatial patterns tend to occur together.

As applied here, both extended and ordinary EOF analysis are used as a preprocessing step to satisfy the dimensional constraints of the prediction problem, to provide a degree of filtering, and to allow valuable visualization of the within-field variability. Thus, the EOF amplitudes serve as input to the CCA procedure. This hybrid technique has proven to be quite valuable in relating the contemporaneous behavior of both observed and modeled fields (e.g., Graham et al., 1988; Graham and White, 1988) and as a tool for constructing prediction models (e.g. Barnett and Preisendorfer, 1987; Graham et al., 1987b; Barnett et al., 1988).

3. Results

Extended EOFs

Extended EOFs of the 500 mb observations were prepared combining all of the data for the six available years (a total of 540 cases) into realizations comprised of days 0, +2, +4, ..., +14, a total of 8 maps per realization. Only data from a single winter period entered into a given realization. The first 5 EEOFs accounted for approximately 21% of the total winter variance in Northern Hemisphere 500 mb height. Such a modest portion is not surprising when consideration is given to the large domain and the high levels of uncorrelated high frequency variability contributed by synoptic disturbances.

Figure 1 shows the spatial expression of the first EEOF mode (5.3% of the total variance) The sequence shows the westward propagation of a zonal wavenumber 2 pattern. On day 0 it can be seen that a strong ridge is present over the Gulf of Alaska, with a weaker ridge over northwestern Europe. A vigorous trough is depicted over the northwest Atlantic with a lobe reaching into the west-central United States; a second weak trough is located over northern Siberia. Following the progression through time, the ridge initially over the Gulf of Alaska moves westward to the Bering Sea by day 6. At the same time, the trough over Siberia also moves west and intensifies over the central Soviet Union, while the ridge over northwestern Europe slides southwest to the extreme western Mediterranean Sea. Meanwhile, the trough complex over the North America and the North Atlantic moves eastward about 15° . Continuing the sequence through day 14, it can be seen that between days 6 and 10 the North American-Atlantic trough system rapidly breaks down as a new trough forms off the coast of western Canada. This system develops quickly and slips northwestward into the Gulf of Alaska. As this occurs, ridging begins over western North America and to the west of Greenland. These features amplify and by day 12 take up the positions over North America and the North Atlantic occupied by troughs on day 0. The ridge over the Bering Sea on day 6 continues to move west and is located over eastern Siberia by day 14. The trough over northwest Europe remains anchored during the period from day 6 to day 14, although it appears to weaken somewhat, while the ridge over the western Mediterranean on day 6 is not apparent by day 14. The progression shown in Fig. 1 is similar in some respects to that shown by Branstator (1987; his Fig. 15) on the basis of a complex EOF analysis of winter 500 mb data from 1976 through 1985. It also is consistent with the wavenumber-frequency spectra of 500 mb data along 50° N presented by Pratt and Wallace (1976) which has the maximum energy associated with westward propagating wavenumber 2 with a period near 20 days.

The second EEOF (5.0% of the variance, not shown) from our analysis is the companion to the first mode in that the two modes are in approximate spatial and temporal quadrature (i.e., they are about 90° out of phase). Figure 2, which shows the amplitudes of EEOF modes 1 and 2 over the six years of data, emphasizes the remarkable regularity and consistent phasing between the two modes. The third and fourth EEOF modes (not shown) have a similar quadrature relationship and depict a westward traveling zonal wavenumber 3 pattern also with a period of 20 to 30 days.

A second, related, set of EEOFs was calculated to investigate how the NMC MRF model behaved with respect to these slowly propagating features. For these calculations, the data set was made up of the same number of realizations, but in this case each realization consisted of three observations (denoted day -4, day -2 and day 0) and numerical forecasts every other day out to day 10. In terms of the EEOFs discussed above, the observed data for days +6 through +14 were replaced by the 2 through 10 day forecasts validating on those days. The spatial and temporal expressions of these EEOFs (not shown) are similar in some respects to those of the purely observational EEOFs, although there is some indication that the model sometimes does not simulate the retrogression of the long wave features, but rather leaves them stationary for some time. Also, the amplitudes of the combined observation-forecast EEOFs are much rougher in character than that seen in Fig. 2. A comparison of the lagged correlations (Fig. 3) between modes 1 and 2 from the purely observational EEOFs and from the mixed observation-forecast EEOFs illustrates this point. In Fig. 3 it can be seen that in each case the the magnitude of the lagged correlations peak at approximately 6 days, indicating a period of approximately 24 days. However, the magnitudes of the correlations are lower for the combined observation-forecasts EOF modes suggesting less systematic low frequency behavior in the numerical model than in the real atmosphere. This is consistent with the results a canonical correlation analysis relating the two sets of EEOFs. These results suggest that behavior of the low frequency waves present in the initial conditions is less systematic in the numerical model than in the real atmosphere after about six days into the integration.

Statistical Forecast Model

There is evidence that the skill of numerical forecasts is better under some initial conditions than others (e.g., Palmer, 1988; O'Lenic and Livezey, 1988). Further, as has been suggested above, the behavior of the low frequency traveling waves is somewhat less consistent in the NMC MRF model than in the real atmosphere. In an effort to take advantage of these systematic errors in the numerical forecasts, statistical models were constructed for the purpose of making adjusted 10 day 500 mb forecasts on the basis of the evolution of a combination of observed and forecast 500 mb fields over a 14 day period. The predictor data for these models were framed as outlined above for the combined observation-numerical forecast EEOFs; that is, Northern Hemisphere observations (0° to 63° N) for day -4, day -2 and day 0 were combined with the forecast 500 mb fields for days +2, +4, +6, +8, and +10. The EEOFs for these data were calculated separately using five of the six years available - in other words, in each of six calculations, one year of the data set was omitted. These EEOFs typically accounted for about 20% of the total variance in 5 modes and about 30% in 10 modes.

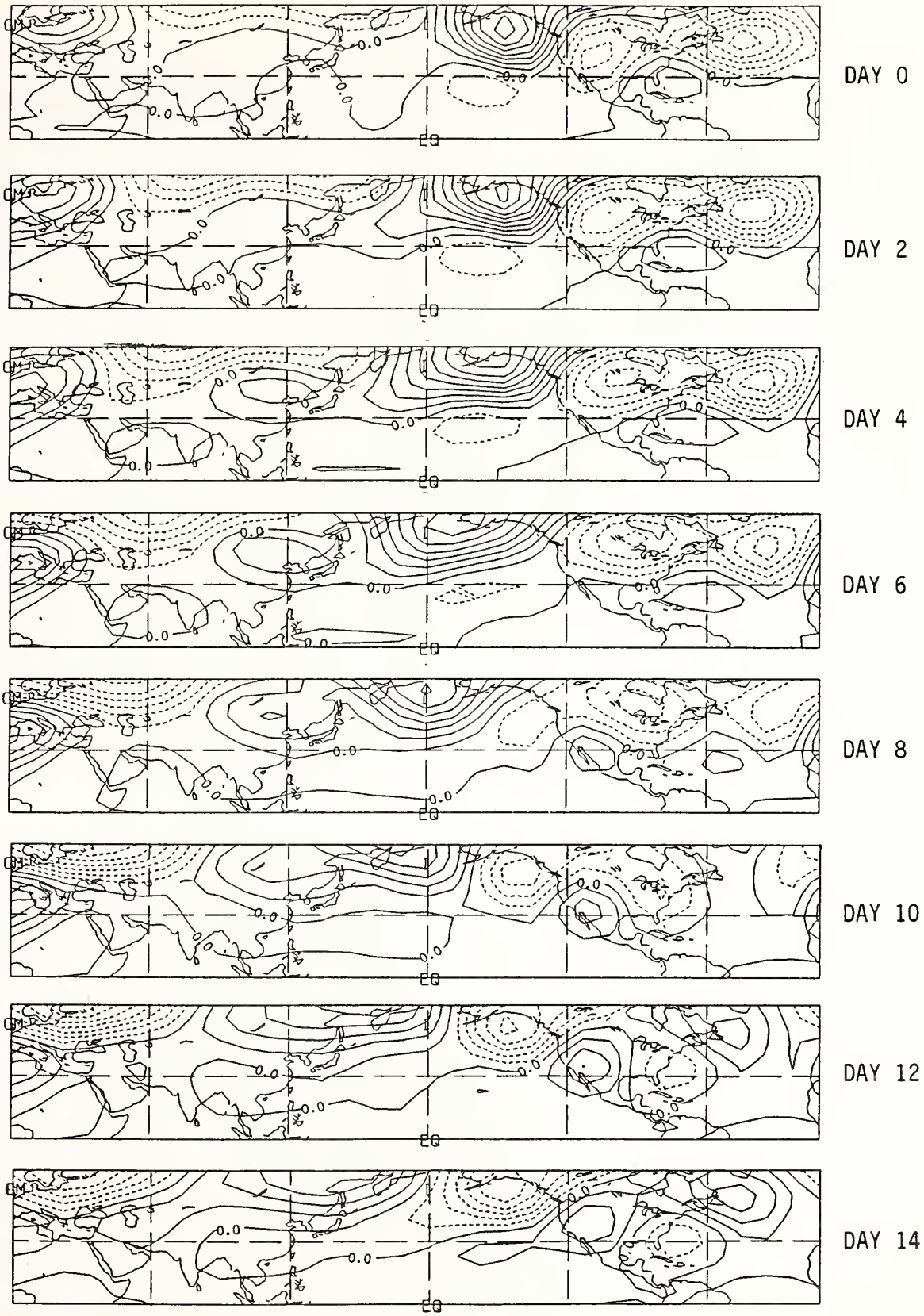

Fig. 1. First EEOF of winter Northern Hemisphere 500 mb heights for 1982-83 through 1987-88. Panels cover two week period from day 0 through day 14. Values are relative; negative contours are dashed.

Observations for day +10 over a region extending from 146° W to 11° W and from 30° N to 63° N. served as predictor data for the models. This region, which covers the North Pacific, North America, and the North Atlantic, was chosen to sharpen the focus of the model on an area of particular interest to weather in the North America. Ordinary EOFs were used to compress and orthogonalize the predictand data Ten EOF modes were retained, which captured between 70% and 75% of the total predictand variance.

Canonical correlation analysis was then used to calculated regression models relating the predictor EEOFs to the predictand EOFs. These models were then used to make cross-validation "predictions" for the year omitted in building the model. Assuming the year to year variability in 500 mb heights is independent, these "predictions" give an estimate of the operational prediction skill statistical models based on five training years would achieve (presumably somewhat better skill would be attainable be having more training years). This procedure is known as cross-validation and has been applied previously to validate statistical forecast models (e.g. Graham et al., 1987b). Separate calculations using five or ten predictor EEOF modes showed a general trend for the ten mode skills to be better, although that was not true at all grid points. Whatever the case, the differences were modest and suggest that the all of the forecast skill could be compressed into between five and ten canonical modes.

The ratios between the cross-validated statistical model skill (in terms of R^2 for the 10 mode models) and the skill of the numerical forecasts for the 540 realizations is shown in Fig. 4a. Also shown (Fig. 4b) are the correlations between the 10 day numerical forecasts and the observations. It can be seen that in two regions where the skill of the numerical model is comparatively high (the Gulf of Alaska and central Canada), the statistical model gives substantial increases in skill. In these regions most of the predictive information comes from the first canonical mode, for which the canonical correlation (i.e., R^2) is 0.34. The canonical predictor pattern for that mode (not shown) is similar to that shown in Fig. 1 for the first EEOF mode, except that the canonical sequence appears to lead the EEOF pattern by a few days. This is as expected because the first and second EEOF modes respectively account for 30% and 44% of the variance of the first canonical mode. Referring to Fig. 2, this combination would produce a pattern leading the first EEOF by three to four days. The first canonical mode predictand pattern (not shown) is similar in many respects to the numerical forecast for day +10 depicted in the canonical predictor pattern for that mode. Both show a trough centered over the Bering Sea and ridging over North America and the western North Atlantic. However, there is some disagreement in the distributions over North America, with the numerical model underestimating the amplitude of the ridge and placing the maximum height anomalies south of the observed position over central Canada. Thus, the skill of the statistical model is due to adjustments for systematic errors in the numerical model's propagation and positioning of features associated with low frequency waves at long forecast times. This is consistent with the fact that the canonical modes place the largest weights on the observations from day 0 and the forecasts from days 2 through 6 and the smallest weights on the forecast for day 10.

Summary and Remarks

This note has described some statistical analyses of observations and numerical forecasts of winter 500 mb heights over the Northern Hemisphere. These studies have produced the following conclusions:

1) The slow westward propagation of zonal wavenumber 2 and 3 patterns with a period of 20 to 30 days was a dominant feature of the Northern Hemisphere winter 500 mb climatology during the winters from 1982-83 through 1987-88.

2) The behavior of these low frequency waves is less systematic in the NMC MRF model than in the real atmosphere, especially after about six days of integration.

3) A hybrid statistical model, combining both observations and numerical forecast data, produced substantial increases in real forecast skill over the numerical model in the Gulf of Alaska and over central Canada. In the first of these regions, the increase in skill is due to the fact that the statistical model distinguishes between the numerical model's relatively good handling of propagating features for the first six days of the integration and the less systematic simulation of those features after that.

A number of issues need to be addressed before such statistical models could be used operationally. These include the questions of how the model "drift" should be removed from forecasts produced by a model undergoing frequent modification, and the impact of interannual variability in the stability of the statistical model. With respect to the latter, it would be of interest to recalculate the models described here using the climatology of the entire data set to remove the annual cycle rather than the year-to-year quadratic fit applied here. Other topics of interest include whether similar procedures could substantially improve shorter range forecasts, the potential impact of tropical data on such models (which would require normalizing the data), and the application of similar modeling techniques to the Southern Hemisphere.

Acknowledgements This work was carried out under NOAA Grant NA86AA-D-CP104 for the Experimental Climate Forecast Center at Scripps Institution of Oceanography.

References

Barnett, T., N. Graham, M. Cane, S. Zebiak, S. Dolan, J. O'Brien, D. Legler, 1988: On the prediction of the El Niño of 1986-87, *Science*, **241**, 192-196.

Barnett, T. P., and R. W. Preisendorfer, 1987: Origins and levels of monthly and seasonal forecast skill for North American surface air temperatures determined by canonical correlation analysis, *Mon. Weather Rev.*, **115**, 1825-1850.

Branstator, G.: 1987: A striking example of the atmosphere's leading traveling pattern, *J. Atmos. Sci*, **44**, 2310-2323.

Daley, R. and D. L. Williamson, 1985: The existence of free Rossby waves during January 1979, *J. Atmos. Sci.*, **42**, 2121-2141.

Graham, N. E., J. Michaelsen, and T. P. Barnett, 1987a: Investigations of the El Niño/Southern Oscillation with statistical models. 1: Predictor field characteristics, *J. Geophys. Res*, **92**, 14251-14270.

Graham, N. E., J. Michaelsen, and T. P. Barnett, 1987b: Investigations of the El Niño/Southern Oscillation with statistical models. 2: Model results, *J. Geophys. Res*, **92**, 14271-14290.

Graham, N. E. and W. B. White, 1988: The El Niño Cycle: A natural oscillation of the Pacific ocean-atmosphere system, *Science*, **240**, 1293-1302.

Graham, N. E., T. P. Barnett, R. M. Chervin, M. E. Schlesinger, and U. Schlese, 1988: Comparisons of GCM and observed surface wind fields over the tropical Indian and Pacific Oceans, *J. Atmos. Sci.*, in press.

Lau, K-M, and P. H. Chan, 1985: Aspects of the 40-50 day oscillation during the northern winter as inferred from outgoing radiation, *Mon. Weather Rev.*, **113**, 1889-1909.

Madden, R. A., 1978: Further evidence of traveling planetary waves, *J. Atmos. Sci*, **35**, 1605-1618.

O'Lenic, E. A., and R. E. Livezey, 1988: Relationships between errors in medium range numerical forecasts and some of the principal model of low-frequency variability of the northern hemisphere 700 mb circulation, *Mon. Weather Rev.*, submitted.

Palmer, T., 1988: Medium and extended range predictability and stability of the Pacific/North American mode, *Quart. J. Roy. Met. Soc.*, **114**, 691-713.

Pratt, R. W. and J. M. Wallace, 1976: Zonal propagation characteristics of large-scale fluctuations in the mid-latitude troposphere, *J. Atmos. Sci.*, **33**, 1184-1194.

Straus, D. M., R. S. Lindzen and A. M. DaSilva, 1987: The characteristic Rossby frequency, *J. Atmos. Sci.*, **44**, 1100-1105.

Tribbia, J. J., and R. A. Madden, 1988: Projection of Time-Mean Geopotential Heights onto normal, Hough modes, *Met. Atmos. Phys.*, **38**, 9-21.

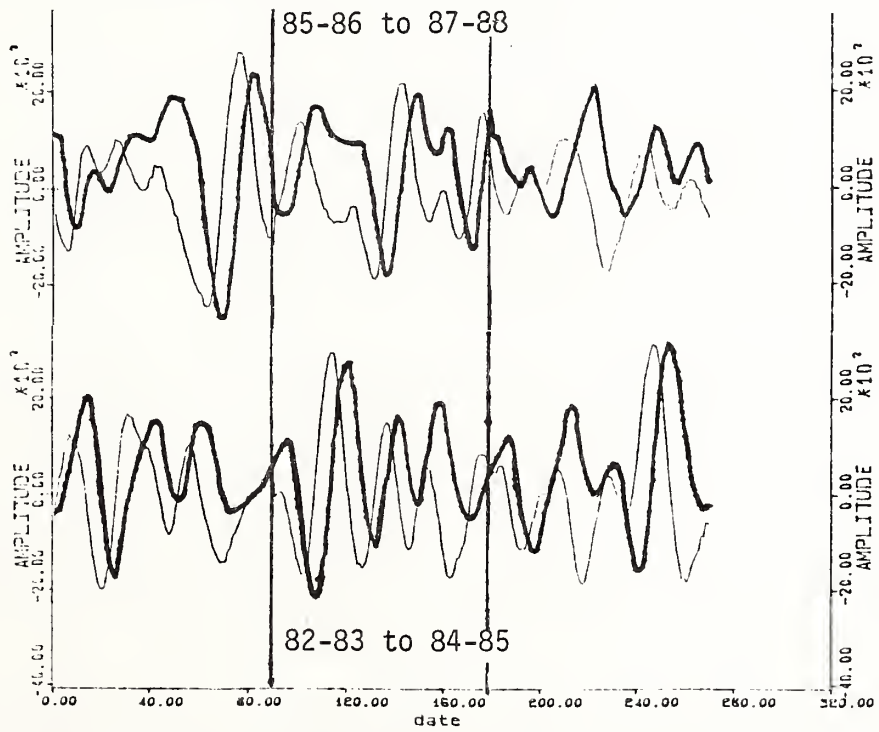

Fig. 2. Temporal amplitudes of first (light) and second (heavy) EEOFs of winter Northern Hemisphere 500 mb heights. Values are relative; vertical lines mark changes from one winter period to the next; each winter period is composed of 90 days.

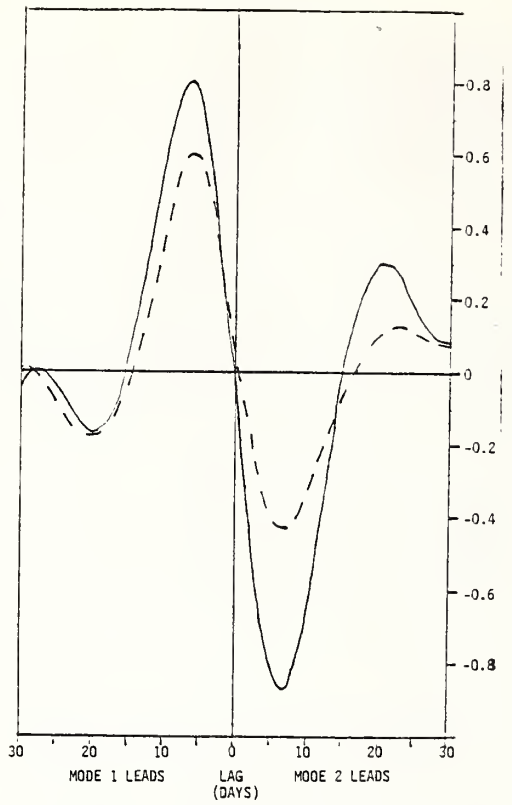

Fig. 3. Lagged correlations between EEOF modes 1 and 2 for observations only (solid) and combined observations and numerical forecasts (dashed).

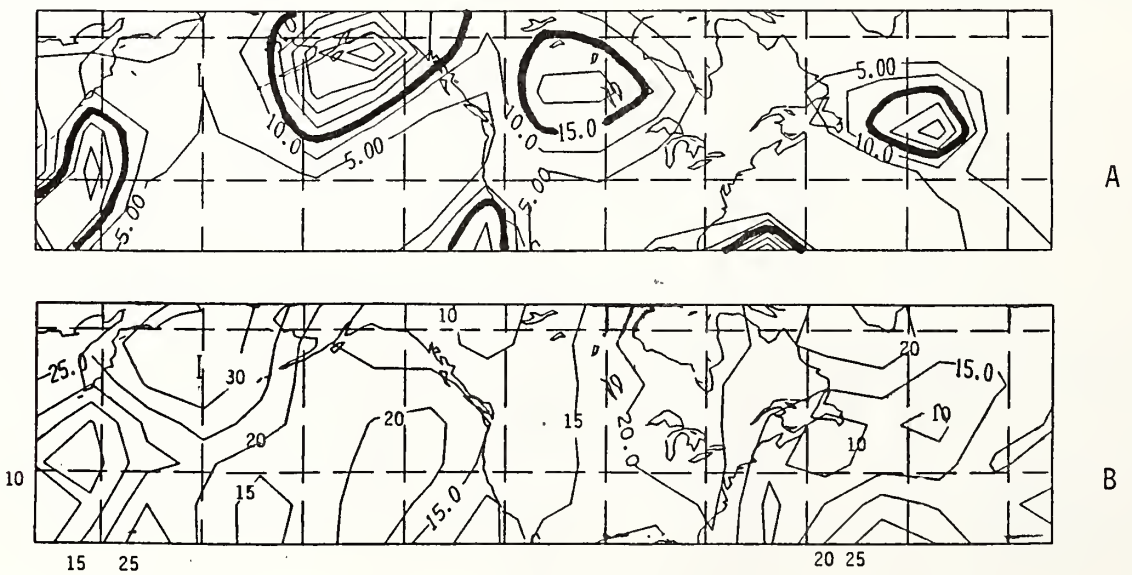

Fig. 4. a) Ratios (x 10) of skill in winter 10 day 500 mb height forecasts; cross-validatated statistical model estimates vs. NMC MRF model; contour interval is 0.5, 1.5 contour is heavy. b) Correlations (x 100) between NMC MRF model 10 day forecasts and observations. Each panel shows results for 540 cases.

Forecasts of zonal wind and global momentum from the NMC MRF model

Richard D. Rosen and David A. Salstein
Atmospheric and Environmental Research, Inc., 840 Memorial Drive
Cambridge, MA 02139

Forecasts of changes in the earth's rate of rotation (or, equivalently, in the length-of-day, Δl.o.d.) are important to those involved in precise navigation, both for terrestrial activities and for deep space missions. Conventional techniques for forecasting Δl.o.d. utilize statistical extrapolation algorithms, such as the Kalman filter used by the Jet Propulsion Laboratory or the autoregressive integrated moving average (ARIMA) approach used by the U.S. Naval Observatory. Recently, Rosen et al. (1987) demonstrated that dynamical forecasts of the atmosphere's angular momentum (M) derived from NMC's medium-range forecasts (MRF) of zonal wind contain positive skill out to 10 days. Given that a close link between changes in M and Δl.o.d. on seasonal and shorter time scales is now well established, skillful forecasts of M may, therefore, represent alternative means for predicting Δl.o.d. In this report, we extend the period of study considered by Rosen et al. for the M forecasts and also examine the source of the errors in these forecasts.

In Fig. 1, we display time series of daily values of MRF forecasted minus observed M for forecast lead times of 2, 5 and 10 days from near the beginning of our archive in December 1985 through the present. Also plotted for comparison are the forecast errors made by a simple persistence model. Although persistence may be regarded as too simple a statistical competitor, the spectrum of M fluctuations is such as to cause the Kalman filter mentioned above to yield Δl.o.d. forecasts that, indeed, closely resemble ones based on persistence alone. Modified versions of persistence forecasts are being considered by us, but for the moment it is worth noting that according to Fig. 1, MRF forecast errors tend in general to be smaller than those for persistence at all three lead times. It is also worth noting that MRF and persistence errors are significantly correlated, reflecting perhaps the tendency of the MRF model to perform better during regimes of persistent atmospheric behavior than otherwise.

The errors in the MRF forecasts of M are considered further in Fig. 2, in which monthly values of the mean square error are plotted along with its components due to a bias and to apparently random errors about the bias. Note that as the forecast lead time lengthens, the bias error tends to become more important. This behavior was already evident in Fig. 1, in which a negative bias indicated that by 10 days the MRF model tends to "lose" momentum. This fact suggests that forecast skill could be improved by empirically accounting for this bias. On the other hand, Fig. 2 indicates that the relative importance of bias and random errors in the 10-day forecasts fluctuates considerably from month to month, complicating an empirical solution.

Noting that M is given by the expression

$$2\pi a^3 g^{-1} \int_{1000}^{100} \int_{\pi/2}^{-\pi/2} [u] \cos^2\phi \, d\phi \, dp$$

where [u] is zonally averaged zonal wind, ϕ latitude, p pressure (in mb), g gravitational acceleration (9.81 m s^{-2}), and a radius of earth (6.37×10^6 m), then examining errors in the forecasts of [u] provides information regarding

regional contributions to the errors in the global M forecasts. In Fig. 3, we plot the annual mean bias in 10-day forecasts of [u] for MRF86 and for MRF87. Note that the bias is not of uniform sign and that, indeed, the tendency is for the MRF to overpredict the strength of the upper tropospheric westerlies in the middle latitudes. With the introduction of a gravity wave drag parameterization in MRF87, the forecast bias associated with the NH subtropical jet has been reduced somewhat and shifted equatorward, rather than poleward, of the jet. Although the bias is somewhat smaller also in the equatorial and SH upper troposphere in MRF87 than in MRF86, a geographical shift of the bias is much less evident in these regions compared to the NH. Finally with regard to the bias, it is worth noting that the spatial pattern of the biases present at 10 days has already begun to emerge, albeit in reduced form, in the 2-day forecasts (not shown).

Figure 4a provides a measure of the nonsystematic component of the forecast errors by illustrating the standard deviation about the mean bias of the 10-day [u] forecast errors made by MRF87. (The comparable field for MRF86 looks quite similar.) To place these values in perspective, Fig. 4b contains the standard deviation of the observed [u] field for the same 12-month period. Note that although the error standard deviations in Fig. 4a exhibit tropical minima and high latitude maxima, in fact the random errors everywhere (outside the jet regions, where the seasonal cycle contributes large values to Fig. 4b) are comparable to the fluctuations observed in [u]. This result implies that further improvements in forecasting [u] are desirable. Fig. 4c demonstrates that it is the nonsystematic forecast error in the tropics that contributes most to the nonsystematic errors in the global M forecasts, so that improvements there will be most important for forecasting M and Δl.o.d. Given that the random errors in 10-day forecasts of [u] in the tropics are on the order of only 2 m s^{-1}, this poses a considerable challenge for the future.

Acknowledgments. The work reported here has been performed under contract 957545 from the Jet Propulsion Laboratory, California Institute of Technology, sponsored by the National Aeronautics and Space Administration. Our study would not have been possible without the efforts of A.J. Miller, Climate Analysis Center/NMC, in making the data available to us.

REFERENCE

Rosen, R.D., D.A. Salstein, T. Nehrkorn, M.R.P. McCalla, A.J. Miller, J.O. Dickey, T.M. Eubanks and J.A. Steppe, 1987: Medium-range numerical forecasts of atmospheric angular momentum. Mon. Wea. Rev., 115, 2170-2175.

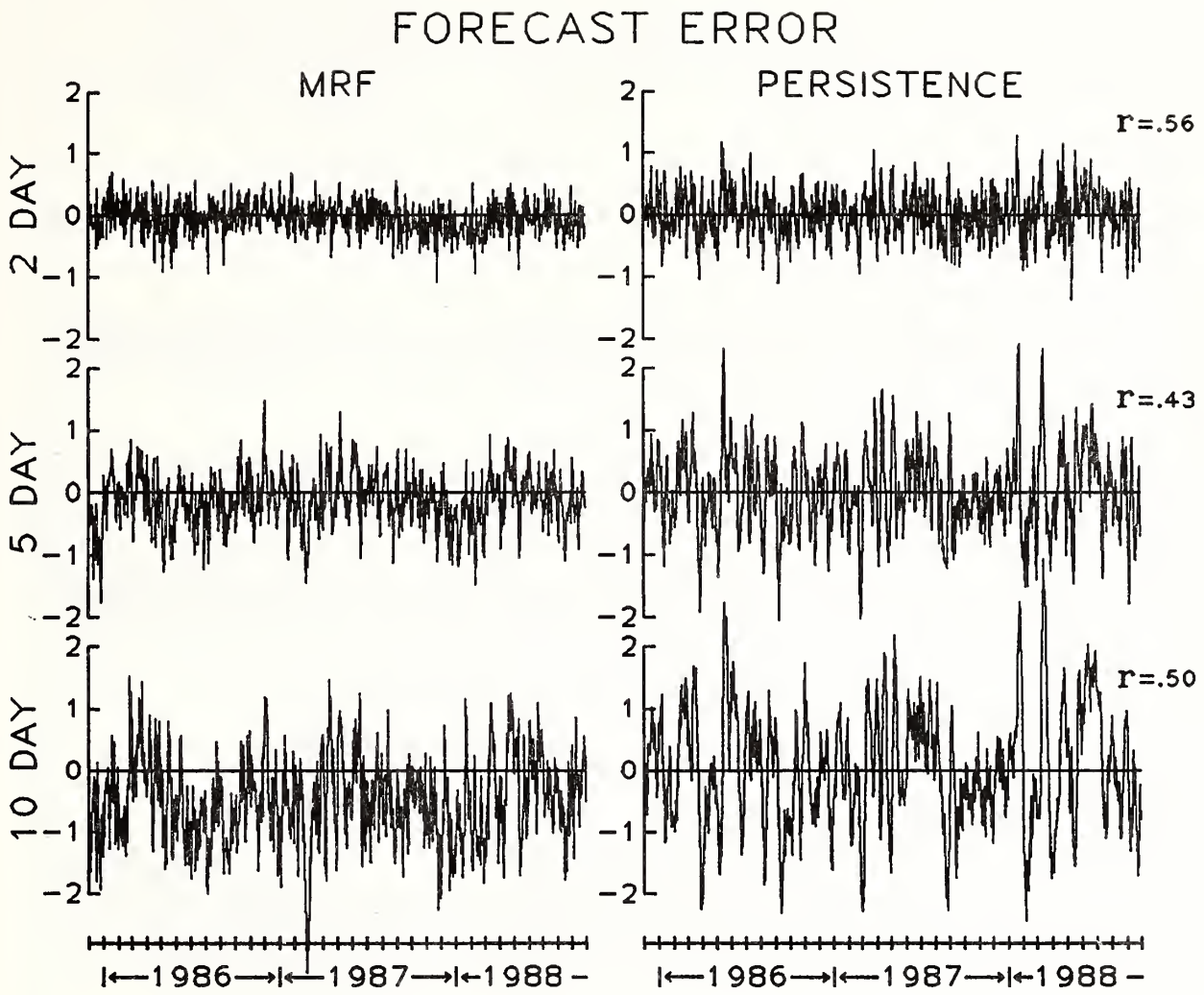

Fig. 1. Daily time series during 1 December 1985 - 30 September 1988 of the difference, MRF forecasted values minus observed values for M, for forecast lead times of 2, 5 and 10 days (left); and the difference, persistence-based M forecast values minus observed values of M for the same forecast lead times (right). Units are 10^{25} kg m^2 s^{-1}. Also shown is r, the correlation between the MRF and persistence errors, for each forecast lead time.

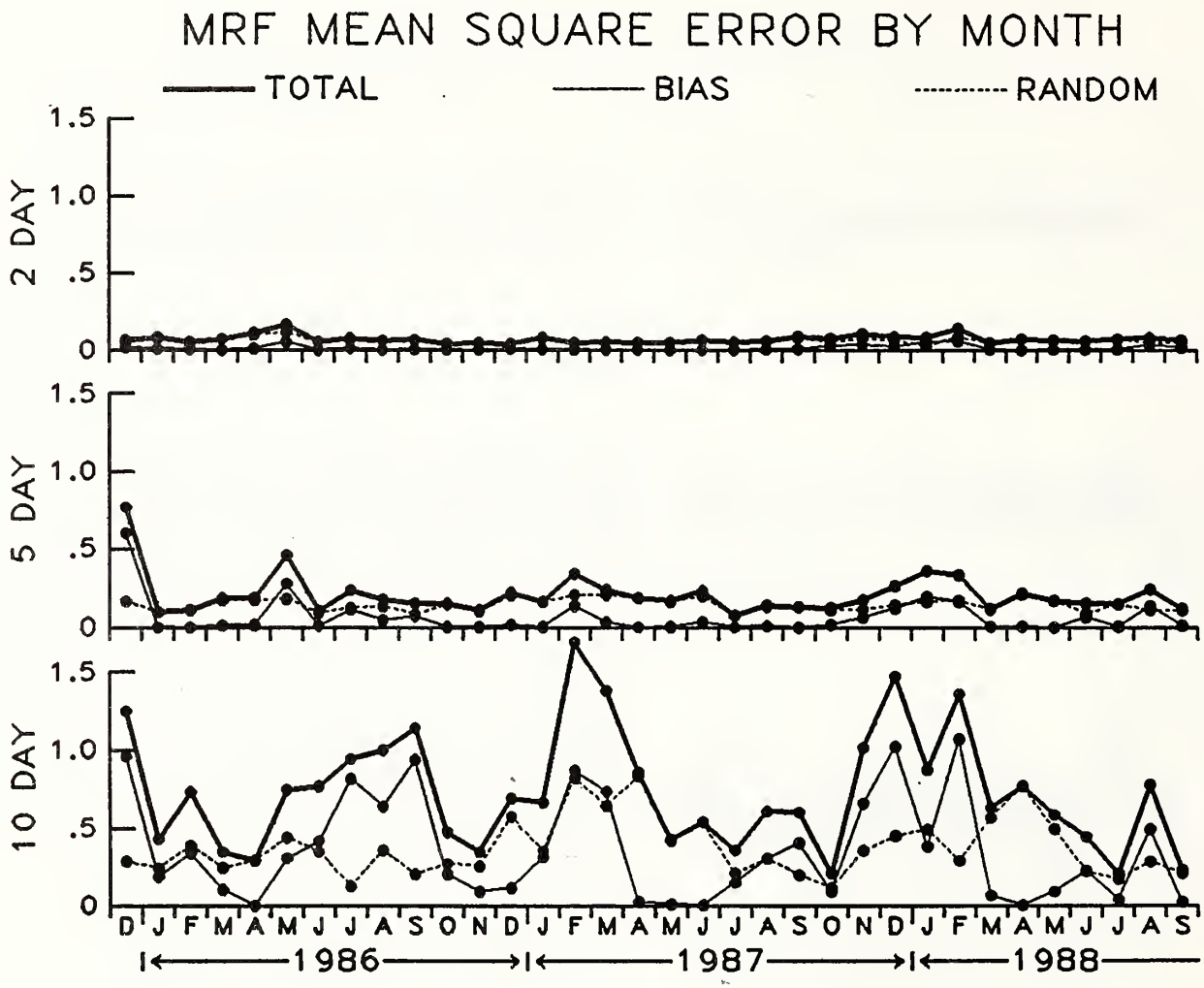

Fig. 2. Total monthly mean square differences between values of M forecasted by the MRF and those observed (heavy solid line), and the portion of that difference due to both monthly biases (light solid line) and nonsystematic variations about those biases (light dashed line) for 2, 5, and 10 day lead times during the period December 1985 - September 1988. Units are $(10^{25}$ kg $m^2 s^{-1})^2$.

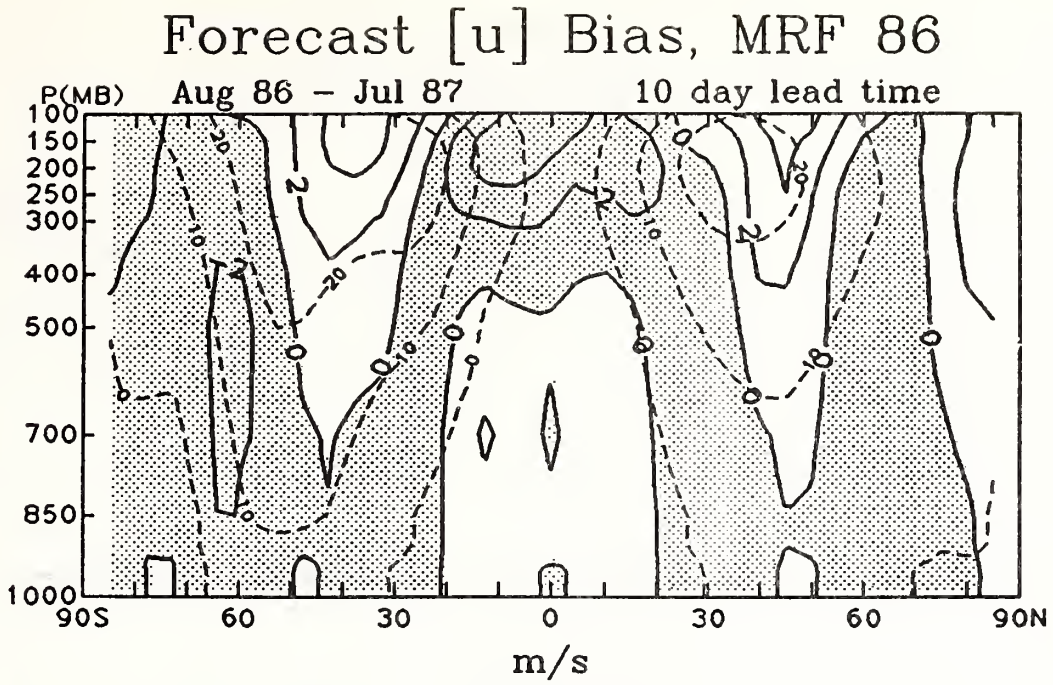

Fig. 3(a). Mean difference between zonally averaged zonal winds, [u], forecasted by MRF86 at a 10-day lead time and those observed (solid lines, with negative values shaded) for the annual period August 1986 - July 1987. Superimposed on this difference are the mean values of [u] for the same period (dashed lines). Units are m s^{-1}.

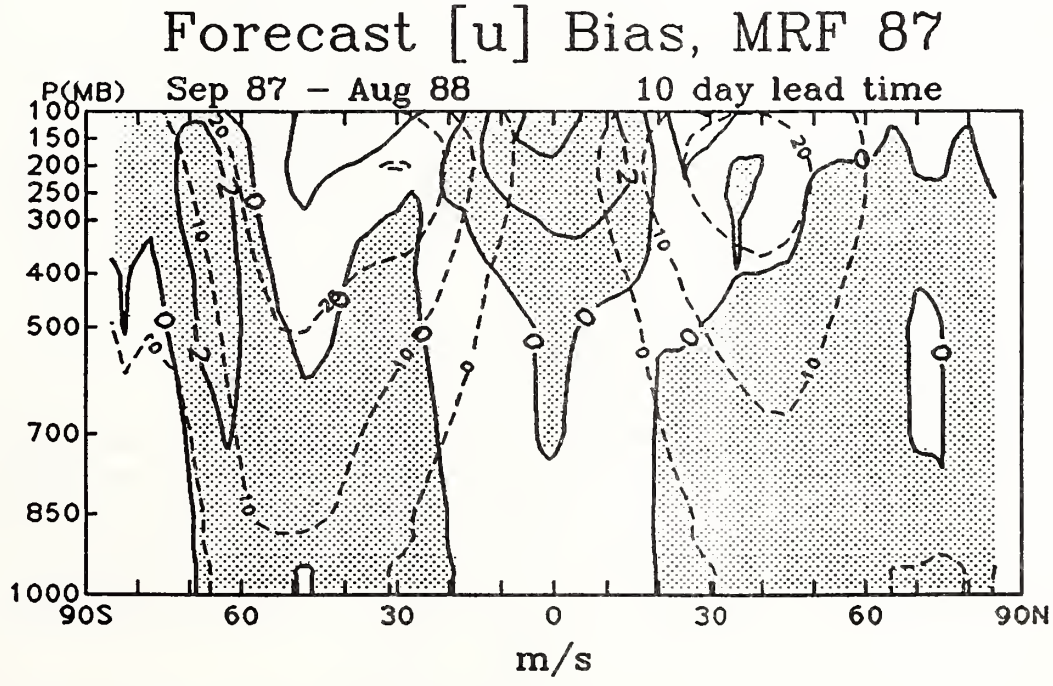

Fig. 3(b). Same as (a) but for MRF87 during the annual period September 1987-August 1988.

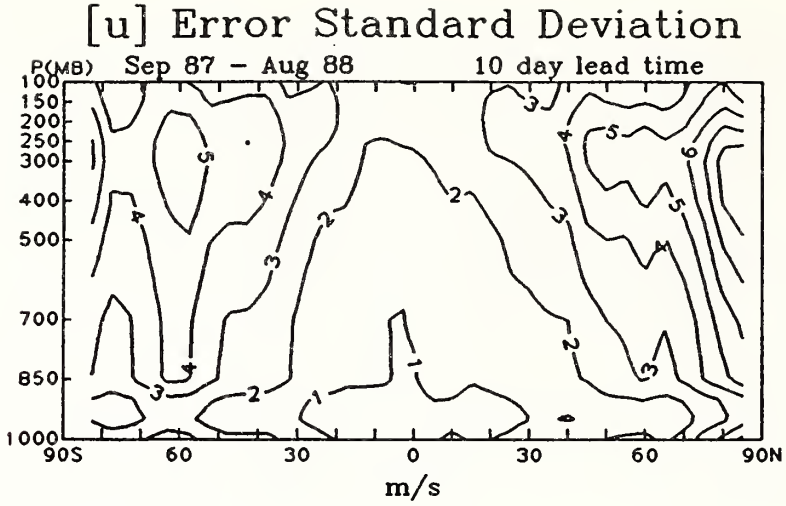

Fig. 4(a). Standard deviation of the departure from the annual bias in Fig. 3b of the difference between MRF-forecasted [u] and those observed, for the period September 1987-August 1988.

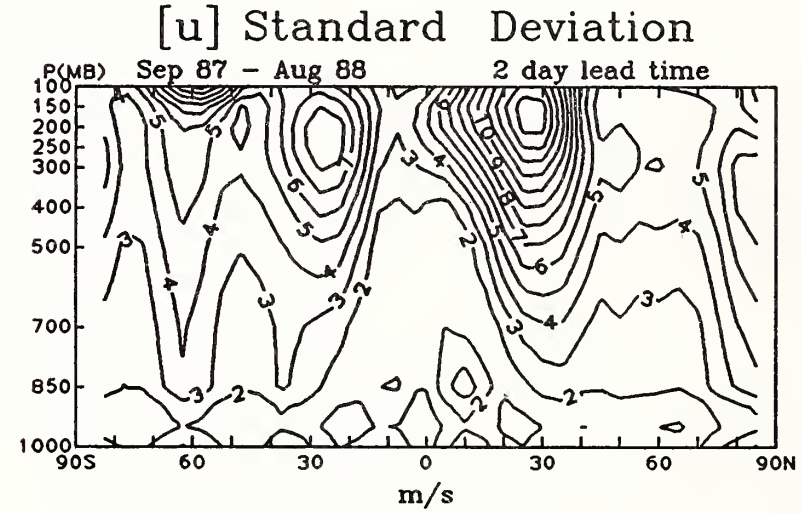

Fig. 4(b). Standard deviation of [u] for the same period.

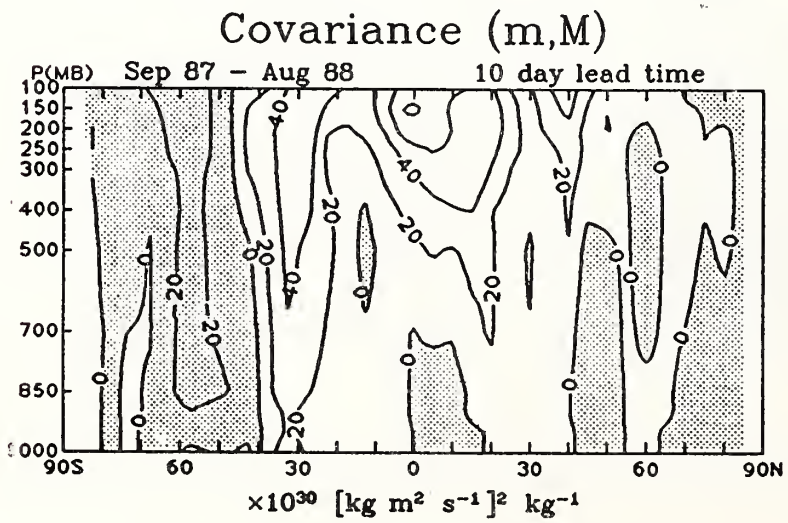

Fig. 4(c). Covariance between errors in the angular momentum per unit mass, m, forecasted at a 10-day lag, and those in forecasted global angular momentum, M, for the same period.

PREDICTABILITY AND ITS RELATIONSHIP TO CYCLONE/PLANETARY SCALE INTERACTIONS

by

M. Steven Tracton

Climate Analysis Center, NMC, NWS, NOAA

Washington, DC 20233

Investigations are underway at the National Meteorological Center (NMC) Washington, D.C., to determine the reasons for the substantial variability in skill of numerical weather predictions, especially at the medium and extended ranges (3-30 days). That variability is characterized by alternating periods, ranging from days to months in length, of relatively good and poor forecasts (Fig. 1). The problem is scientifically intriguing as well as vitally important for developing a capability to provide a priori guidance on the expected accuracy of forecasts. The basic approach in this study is diagnosis and evaluation of circulation regimes and regime transitions as related to variations in forecast skill.

The dominant relationship found thus far is that between forecast skill and the evolution of blocking events.* To illustrate, Fig. 2 displays the sequence of hemispheric AC scores of Fig. 1 oriented to permit direct comparison with a time longitude plot of blocking activity. The blocking index is the difference between the analyzed 500 mb heights at 40^{o} and 60^{o} N (Lejenas and Okland, 1983). Positive values indicate an anticyclone at northerly latitudes and provide a generally reliable measure of the blocking events discerned from subjective appraisal of charts. Certainly not all the variability in skill is related directly to blocking, but a large component clearly is. In particular, the inability of NMC's Medium Range Forecast (MRF) model to capture the blocking events** results in marked declines in skill, and pronounced recoveries in scores occur as the blocks begin to wane. Qualitatively, inspection of synoptic charts clearly reveals that each of the blocking events is recurrent, rather than persistent in nature and reflects smaller-scale baroclinically and barotropically active systems propagating through and interacting with the larger-scale flow in which they are embedded. The model apparently is unable to simulate adequately the strong interplay of circulation systems of differing scales.

Based on the above, research has focused upon that aspect of predictability related to interaction of scale processes in blocking situations. To more fully describe these relationships and gain understanding of the operative physical mechanisms individual case studies are being

---

*Results here from NMC's DERF Phase II experiment (Tracton, et al., 1988)

**This result is similar to that of Tibaldi and Molteni (1987) with regard to the ECMWF model.

diagnosed from the perspective of quasi-geostrophic dynamics. The relevant equations and concepts are shown schematically in Fig. 3. Quantitatively, the evolution of the observed and forecast 500 mb height fields are calculated as functions of the baroclinic versus barotropic interactive and non-interactive scale processes. The role of latent heat release is also considered. Explicit in these calculations are insights on the relative and absolute importance of such factors as vertical stability and the phase and amplitude relationships between circulation systems of differing scales.

Early results suggest that the interaction of planetary and sub-planetary (medium and small) scale processes associated with the motion and development of cyclones is crucial in the development of at least some blocks. By way of example, Fig. 4 displays the 500 mb height and diagnosed total height tendency fields derived from the analysis valid at 0000 GMT 5 January 1987. The height-rise center located southwest of Iceland, between up and downstream major cyclogeneses, is a key feature in the amplification and progression of the sub-planetary scale ridge south of Greenland. This ridge subsequently becomes superimposed upon the quasi-stationary, planetary-scale ridge in the northeastern Atlantic (not shown), which results in establishing there the early phase of the blocking event seen in Fig. 2 and apparent on synoptic charts.

Table 1 lists the contributions of each mechanism identified in Fig. 3 to the total tendency averaged over the height-rise center referred to above. Clearly dominant are barotropic processes, which involve the horizontal advection of (anticyclonic) vorticity of both small and medium-scale waves by the planetary-scale component of the flow. In effect, the evolving vorticity fields of mobile, sub-planetary scale weather systems are advected by the much more slowly evolving planetary-scale circulation. As the associated height rises approach the planetary-scale ridge position, simple superposition results in a high-latitude anticyclone, i.e., a block, in the total height field. The planetary-scale provides both the favorable background for appearance of the block and, through interaction with smaller-scale systems, is a key element in its development. Finally, although barotropic processes are the principal direct contributors to the height rises associated with the blocking, baroclinic mechanisms play an indirect role through their influence on the evolving sub-planetary scale height (i.e., vorticity) fields. In this regard, the latent heat release associated with the cyclogeneses appears as important as thermal advection or differential vorticity advection.

In conclusion it appears that at least some blocking situations are characterized by a complex interplay of baroclinic and barotropic processes associated with circulation systems of differing scales interacting with one another. Further, the inability of the MRF to simulate this complexity is apparently a major source of forecast error and, therefore, a key factor in the observed correspondence between variability in forecast skill and the occurrence of blocking. A primary objective of the research described herein is to identify and understand events and processes relevant to the evolution of blocks - their growth, maturation, and decay - so we can provide <u>a priori</u> estimates of the confidence in forecasts and, possibly, provide feedback for model improvements.

References

Lejenas, H., and H. Okland, 1983: Characteristics of Northern Hemisphere blocking as determined from a long time series of observational data. Tellus, 35A, 350-362.

Tibaldi, S. and F. Molteni, 1987: On the operational predictability of blocking. ECMWF Seminar on the Nature and Prediction of Extratropical Weather Systems, Vol. II, 7-11 Sept. 1987, Reading, U.K., 329-371.

Tracton, M.S., Mo, K., Chen, W., Kalnay, E., Kistler, R., and White, G., 1988: Dynamical Extended Range Forecasting (DERF) at the National Meteorolgical Center. ECMWF Workshop on Predictability in the Medium and Extended Range, 16-18 May, 1988, Reading, U.K. (In press). (Also, submitted to MWR)

TABLE 1

Contributions of baroclinic and barotropic processes to height tendency of rise center (m/hr)

Scales	Barotropic	Baroclinic	Total
P by P	-0.5	-0.1	-0.6
P by M	-2.3	-0.4	-2.5
P by S	-1.0	-0.2	-1.2
M by P	7.2	-1.3	5.8
M by M	0.8	-0.2	0.6
M by S	-2.6	0.4	-2.4
S by P	7.2	-1.1	6.2
S by M	3.5	0.0	3.8
S by S	-0.8	0.2	-0.6
Sum	11.5	-2.7	9.1

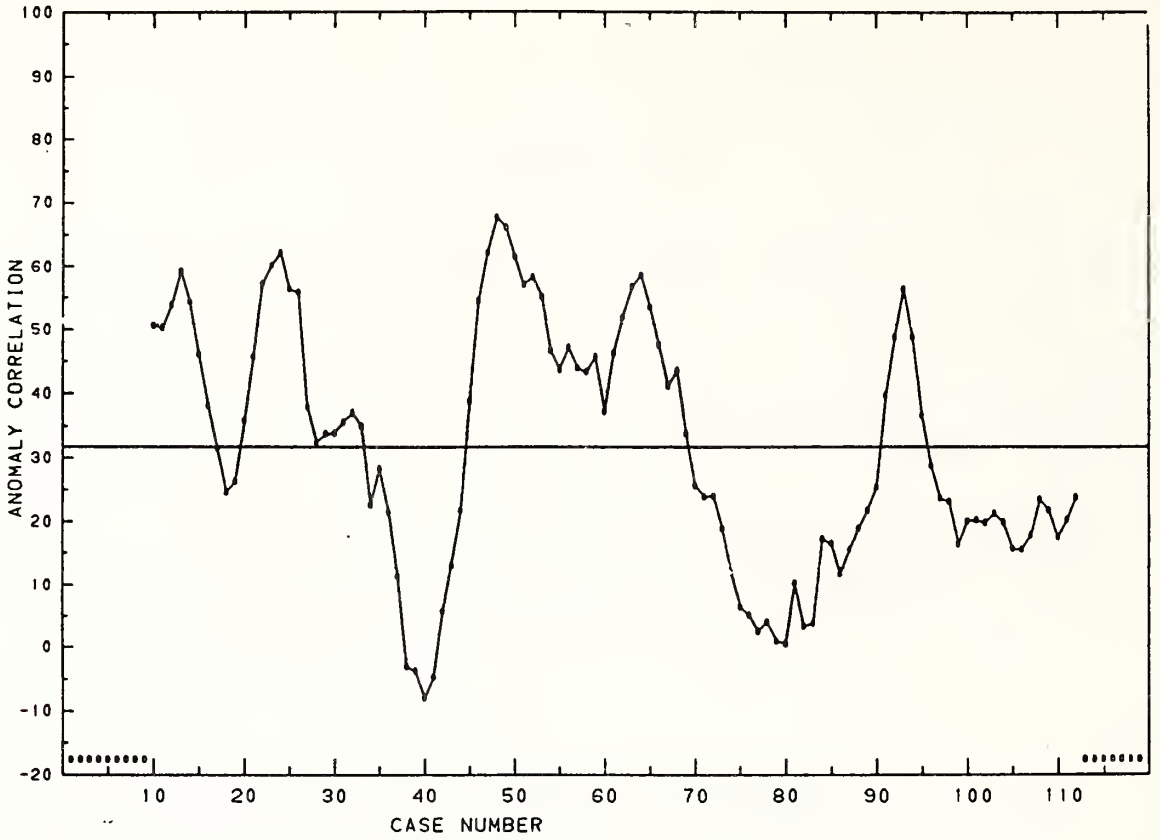

Fig. 1 Anomaly correlation (AC) of NH 6-15 day mean 500 mb height for the contiguous series of 108 DERF II cases plotted at center of verifying period (case 1 = 19 December 1986)

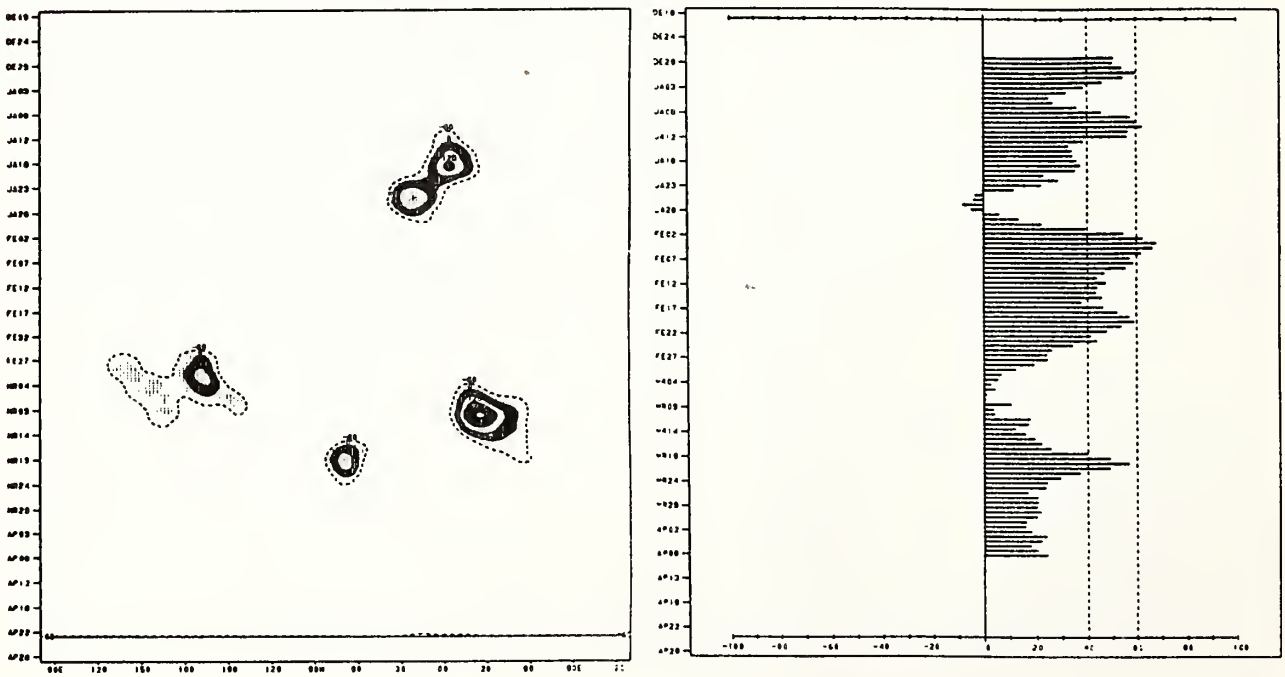

Fig. 2. a) Contiguous series of 500 mb height AC for 6-15 day means
b) time-logitude plot of blocking index derived from 10-day mean 500 mb height analyses (contour interval 60 m)

QG Vorticity Eq.

$$\text{TEND} = \underset{(1)}{\text{VORT ADV}} + \underset{(2)}{\text{DIV}}$$

(1) => barotropic
(2) => baroclinic

QG Omega Eq.

OMEGA (DIV) = DIFFERENTIAL VORT ADV
+ THERMAL ADVEC
+ LATENT HEAT

Scale Decomposition

	2-dimen. waves
Planetary	0-6
Medium	7-12
Small	13-30

Components of Advection Terms

Advec of	by
P	P
* P	M
* P	S
* M	P
M	M
* M	S
* S	P
* S	M
S	S

* => Non Like Terms = Scale Interaction Processes

Fig. 3 Schematic of concepts and equations for calculation of height tendencies.

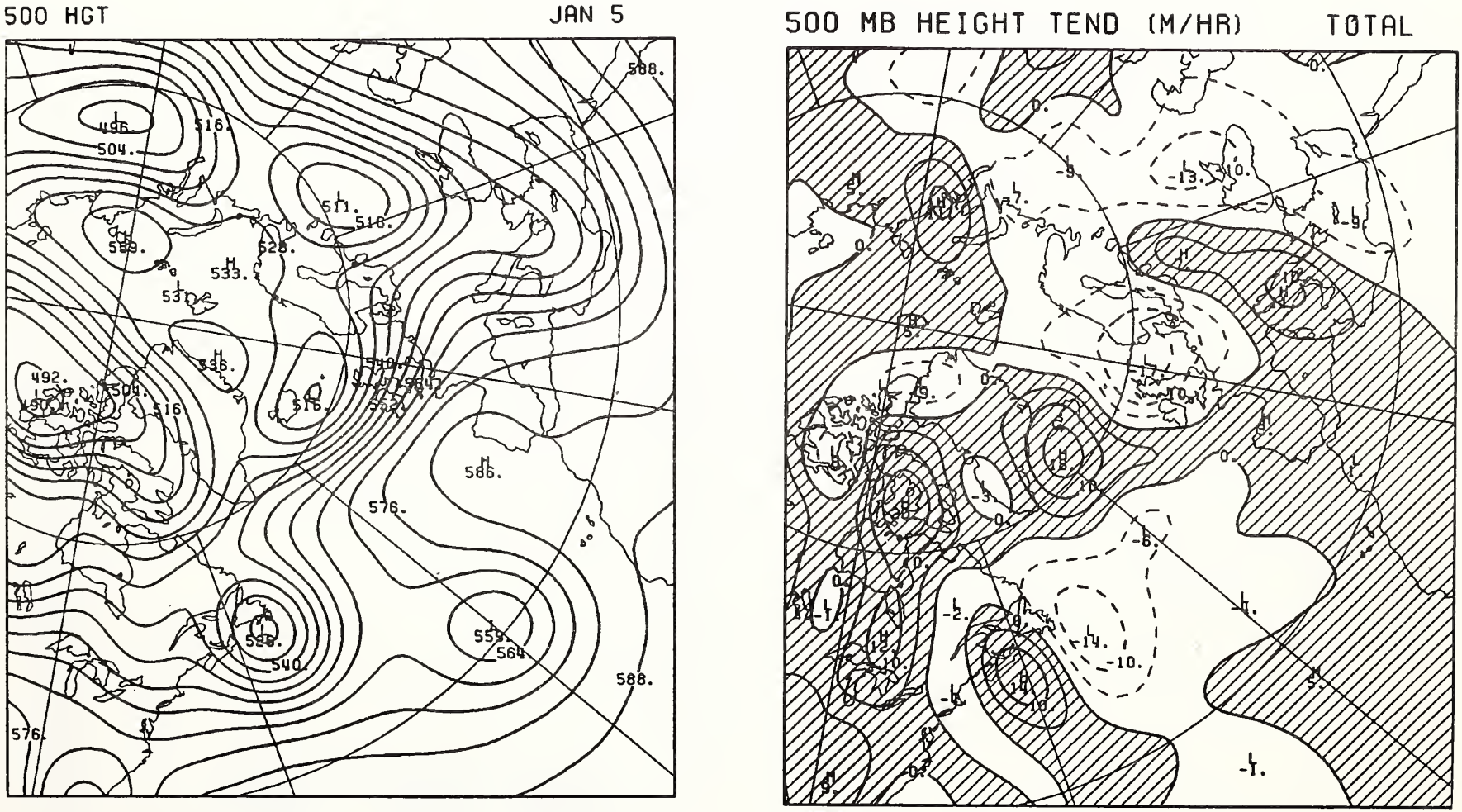

Fig. 4. a) 500 mb height, 0000 5 Jan 1987
b) diagnosed total 500 mb height tendency (m/hr)

COMPARISON OF SURFACE STRESSES AND LATENT HEAT FLUXES OVER OCEANS IN SHORT RANGE FORECASTS BY ECMWF, UKMO AND NMC

K. Arpe and D. Burridge
European Centre for Medium Range Weather Forecasts
Reading, U.K.

A. Gilchrist
U.K. Meteorological Office
Bracknell, U.K.

1. Introduction

The extension of numerical forecasts into the medium and extended range requires a realistic parametrization of diabatic forcing. Verification of such diabatic forcing is often handicapped by a lack of our knowledge of the truth. Comparison between values generated by different models may highlight possible problem areas in one or the other scheme. However agreements between different models need not be a proof of correctness as shown by Reynolds et al. (1988).

Another interest in the comparison of surface fluxes comes from the ocean modelling community (TOGA) who would like to use fluxes from operational forecast models both to drive ocean models, and to gain some knowledge about the uncertainties of such fluxes.

After describing in Section 2 the data which have been used in this study, we will discuss the comparison of surface stresses in Section 3 and of latent heat fluxes in Section 4. Other diabatic forcings are also under investigation but will be reported separately.

2. Data

At ECMWF a complete archive of surface fluxes obtained from operational forecasts is available since 1979. For this project a main problem was the collection of corresponding data from other operational weather centres. Only for the period June and July 1988, data from the United States weather service (NMC) and from the United Kingdom Meteorological Office (UKMO) were available though with some differences in the averaging procedure: the data used from ECMWF are averages over a 24 hour forecast from initial data at 12 GMT, data from NMC are averages of the two forecasts at 00 and 12 GMT for the forecast range 6 to 12 hours and data from UKMO are averages of 12 hour forecasts at 00 and 12 GMT.

Comparisons of 00 with 12 GMT forecasts from the UKMO have shown that differences due to initial times, are of little importance for this study. Comparisons of different forecast ranges, i.e. 6 hour, 12 hour or 24 hour averages in the ECMWF forecasts show some spin-up for the surface stress and the latent heat flux but they were small compared to the differences between different models shown here.

For June and July 1988 NMC provided only data between 60°N and 40°S and therefore we restrict our calculation to this area even when a global comparison could have been done in some cases. For some other months data from either NMC or UKMO were available and have been compared with ECMWF data.

For further calculations the NMC and UKMO data were linearily interpolated to the ECMWF T106 gaussian grid.

3. Surface stresses

Fig. 1 shows surface stresses of the three operational forecast models averaged for June and July 1988. There is not only qualitative but also, for most areas, quantitative agreement between the three data sets. The UKMO fields have the most small-scale structure. Stresses in the trade wind areas are strongest in the NMC fields, particularly in the Southern Hemisphere, and weakest in the ECMWF fields, particularly in the Northern Hemisphere Atlantic. The relatively weak trade winds in the ECMWF scheme are probably due to a tendency of the ECMWF model to generate even weaker trade winds in the medium and extended range forecasts which might have influenced the analyses through the first guess in the analysis scheme.

The Indian Monsoon shows a double structure in the UKMO field with much larger stresses near the Indian continent compared to both other schemes. The simpler structure by ECMWF and NMC agrees better with climatological estimates.

For some selected areas the daily variability of the stresses are shown in Fig. 2. For all investigated areas (not only those shown) one fields a high correlation between all three data sets. Some indications of a time shift between ECMWF data and the others may be due to a different averaging period by 12 hours.

Best agreements between the data sets can be found when the values are low while there are larger differences during extreme events. For the Northern Hemisphere trade winds the ECMWF scheme gives generally less stress than the others especially during extreme events, while NMC provides largest values for the u-component and UKMO for the v-component. In mid-latitudes the ECMWF scheme tends to higher values than the others while UKMO tends to lowest values but less pronounced than the differences in the trades.

The large bias in the UKMO data set in the Somali Basin is clearly present also in the daily data, but despite this one finds a high correlation between all three data sets.

The area south of Greenland has been selected because in the two month means in Fig. 1 this was an area of largest discrepancies compared to its mean values. This finding is less pronounced in the daily data because the relatively small mean values resulted from large northerly stresses in June and large southerly stresses in July.

We have seen that despite some biases the models are able to generate similar daily variabilities which we expect to reflect the variability of the real atmosphere. Because of this we hope further that the models may be able to generate reasonable interannual variabilities. In Fig. 3 the deviations of the stresses by the three models from a climatological mean (Han-Lee, 1981) are presented. Some features are common to all three data sets i.e. anomalous weak trade wind and Indian monsoon circulations. They may reflect genuine anomalies or deficiencies in the climatological means or common deficiencies of all three models.

To investigate this further we studied the anomalies of other months and concluded that at least part of the anomalies are real but further work is needed to substantiate this statement.

Investigations of stresses during Northern Hemisphere winter months also showed good similarities between different models though a tendency to somewhat larger differences than in summer months was found.

4. Latent heat fluxes

The comparison of latent heat fluxes in different models (Fig. 4) reveal larger differences than with the surface stresses. Again the UKMO values are 'noisier' than others. The ECMWF latent heat fluxes are generally lowest especially in the Northern Hemisphere about 10° to 20°N, e.g. in the Pacific off central America and at the date line, in the western subtropical Atlantic and in the Arabian Sea. The UKMO latent heat fluxes are generally lowest in the Southern Hemisphere about 10° to 20°S in all three oceans. The NMC values are higher than those of both other models nearly everywhere with only few exceptions in the northern deep tropics where the UKMO provides some slightly larger values, e.g. north of New Guinea, around Sri Lanka and in the Pacific off central America.

Some of the differences between the three models arise probably from a lack of observational data while others are due to differences in the formulation in the models. E.g. the fluxes in the ECMWF scheme will be enhanced with the introduction of a new radiation scheme (Morcrette, pers. comm.) and a fixed cloud distribution in the UKMO model must have a detrimental effect on the parametrization of latent heat fluxes through the radiation scheme. One often finds lower heat fluxes in the ECMWF scheme where there is convective precipitation. In these areas the air is moistened by falling water drops in the ECMWF model but not in the other two models. We also find mostly lower values in the ECMWF scheme where there are only weak surface winds e.g. in the Pacific off central America.

Daily fluctuations of latent heat fluxes at selected areas are shown in Fig. 5 which reveal for all areas high correlations between the three model outputs. The correlations are especially high in the extra tropics represented here by the northern Pacific area. The ECMWF scheme shows less variance than the others which may be due to a more conservative analysis scheme. Despite the large biases in the Pacific off central America there is a high correlation in the daily variability. Lowest correlations can be found for the fluxes over the Somali Basin.

We also investigated differences in latent heat fluxes during northern hemisphere winter months and found generally slightly larger differences for the tropics than during summer, with too low fluxes in the ECMWF model compared to the other models. We also compared mean latent heat fluxes from the models with climatological estimates by Oberhuber (1988) and found too low ECMWF values in summer and too high UKMO or NMC values in winter.

5. Conclusions

Comparisons of surface stresses in short range forecasts by different models show generally good agreement, not only in monthly means but also in daily variability. The agreement is particularly good in mid-latitudes while

there are areas of poorer agreement in the tropics. The ECMWF stresses are relatively weak in the trade wind region probably due to a model deficiency which leads to too weak trade winds in the medium and extended range forecasts. The UKMO stresses are 'noisiest' of all and deviate from the others considerably over the Indian monsoon area. The NMC scheme provides the strongest stresses in the trade wind areas. Differences are somewhat larger in Northern Hemisphere winter than summer.

Comparison of latent heat fluxes reveal larger differences than surface stresses particularly in the tropics. ECMWF values are generally lower than those by the others and NMC provides highest values. Climatological values by Oberhuber (1988) agree best with NMC in summer and best with ECMWF in winter. Again the UK fields give the noisiest appearance. Despite differences there is generally good agreement to be found in both the mean fields and the daily variability, particularly in mid-latitudes.

References

Han, Y.-J. and S.-W. Lee, 1981: A new analysis of monthly mean wind stresses over the global ocean. Climate Research Institute Report No. 26, Oregon State University, Corvallis, Oregon 97331, 148 p.

Oberhuber, J.M., 1988: An Atlas based on the 'COADS' data set: the budget of heat, buoyancy and turbulent kinetic energy at the surface of the global ocean. Max-Planck-Institute for Meteorology Report No. 15. Max-Planck-Institut für Meteorologie, Hamburg 13, Germany.

Reynolds, R.W., K. Arpe, C. Gordon, S.P. Hayes, A. Leetma and M.J. McPhaden, 1988: A comparison of tropical Pacific surface wind analyses. Accepted by Journal of Climate.

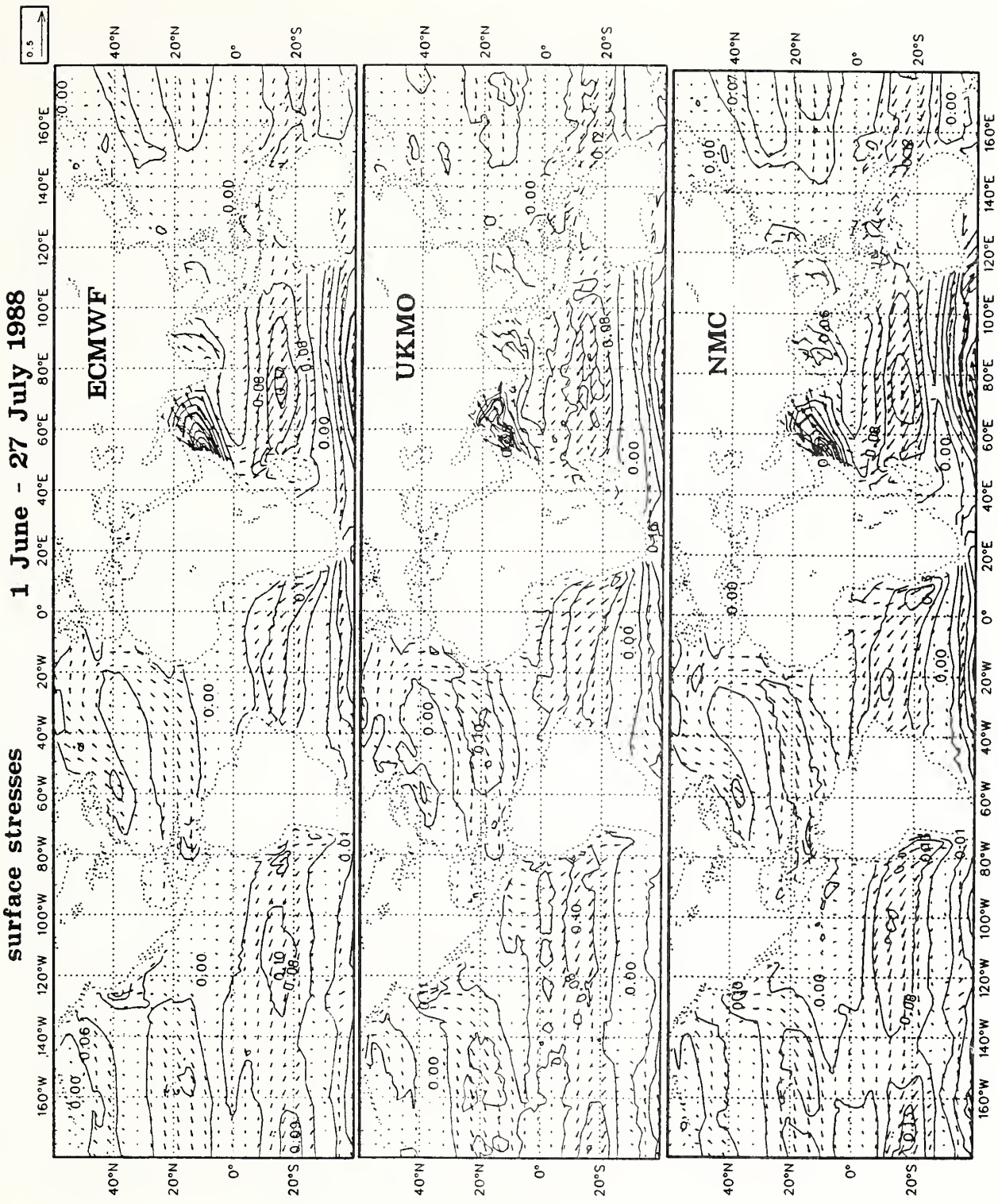

Fig. 1 Mean surface stress in the ECMWF, UKMO, and NMC short range forecasts during June and July 1988. Contour interval: 0.04 N/m^2. The arrow in the small box represents 0.5 N/m^2. Stresses over land have been blanked out.

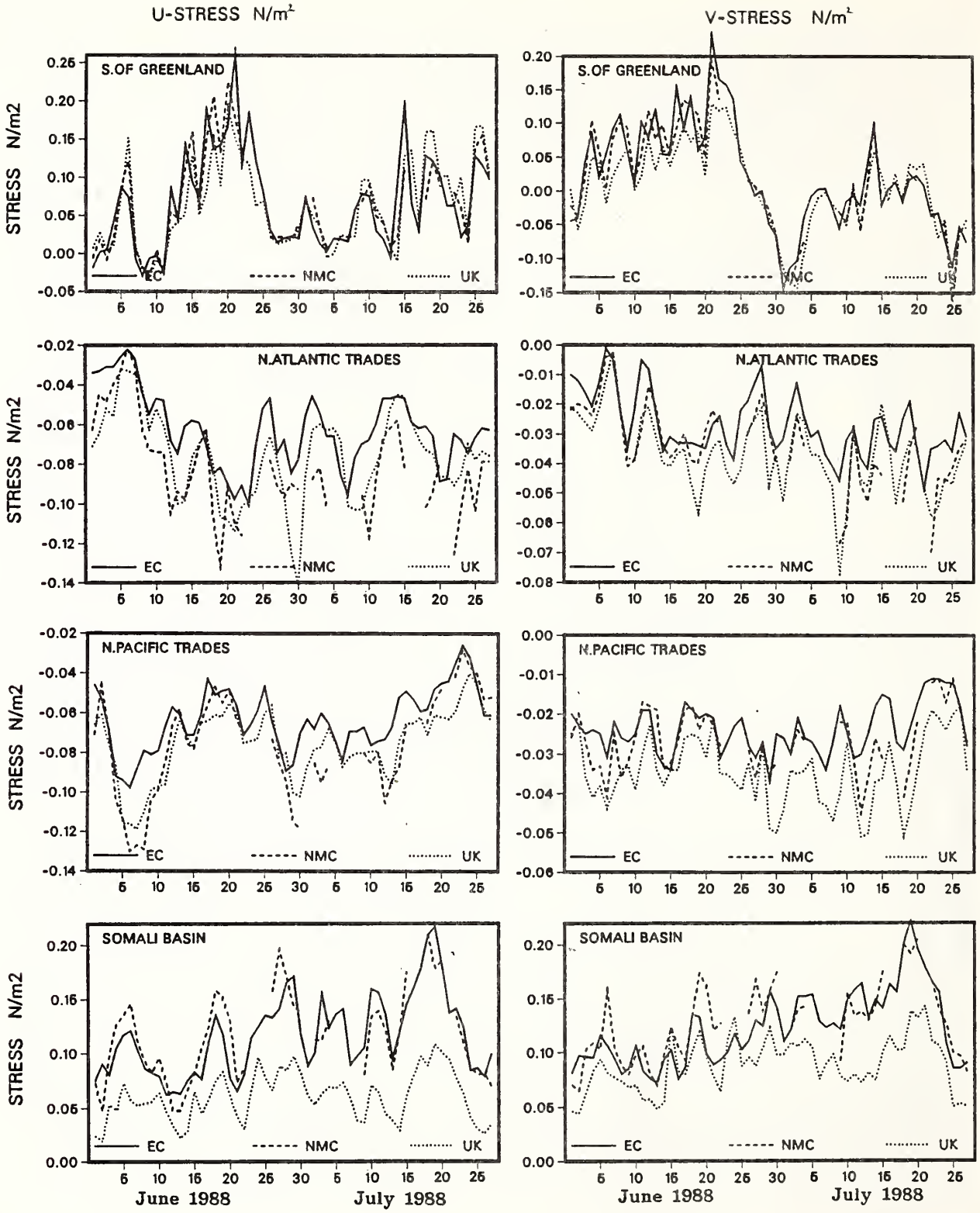

Fig. 2 Daily surface stress components for selected areas in operational short range forecasts by ECMWF, UKMO, and NMC.
S. of Greenland: 53° - 60°N, 20° - 42°W
N. Atlantic Trades: 15° - 25°N, 33° - 50°W
N. Pacific Trades: 13° - 25°N, 140° - 163°W
Somali Basin: 2° - 10°N, 50° - 61°E.

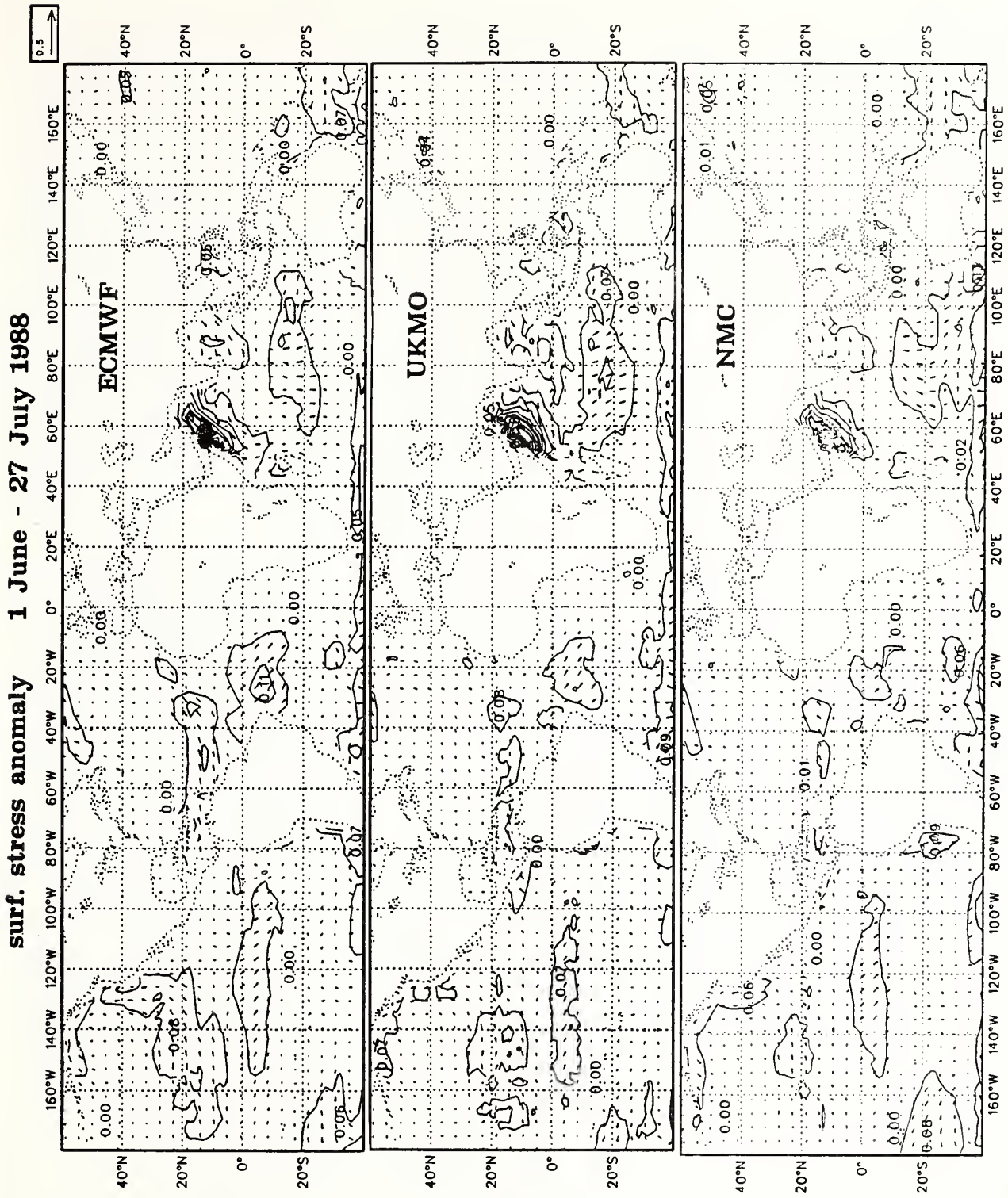

Fig. 3 Surface stress anomalies (deviation from Han-Lee climatology) in the ECMWF, UKMO and NMC model during June and July 1988. Contour interval: 0.04 N/m^2. The arrow in the small box represents 0.5 N/m^2. Stress anomalies over land have been blanked out.

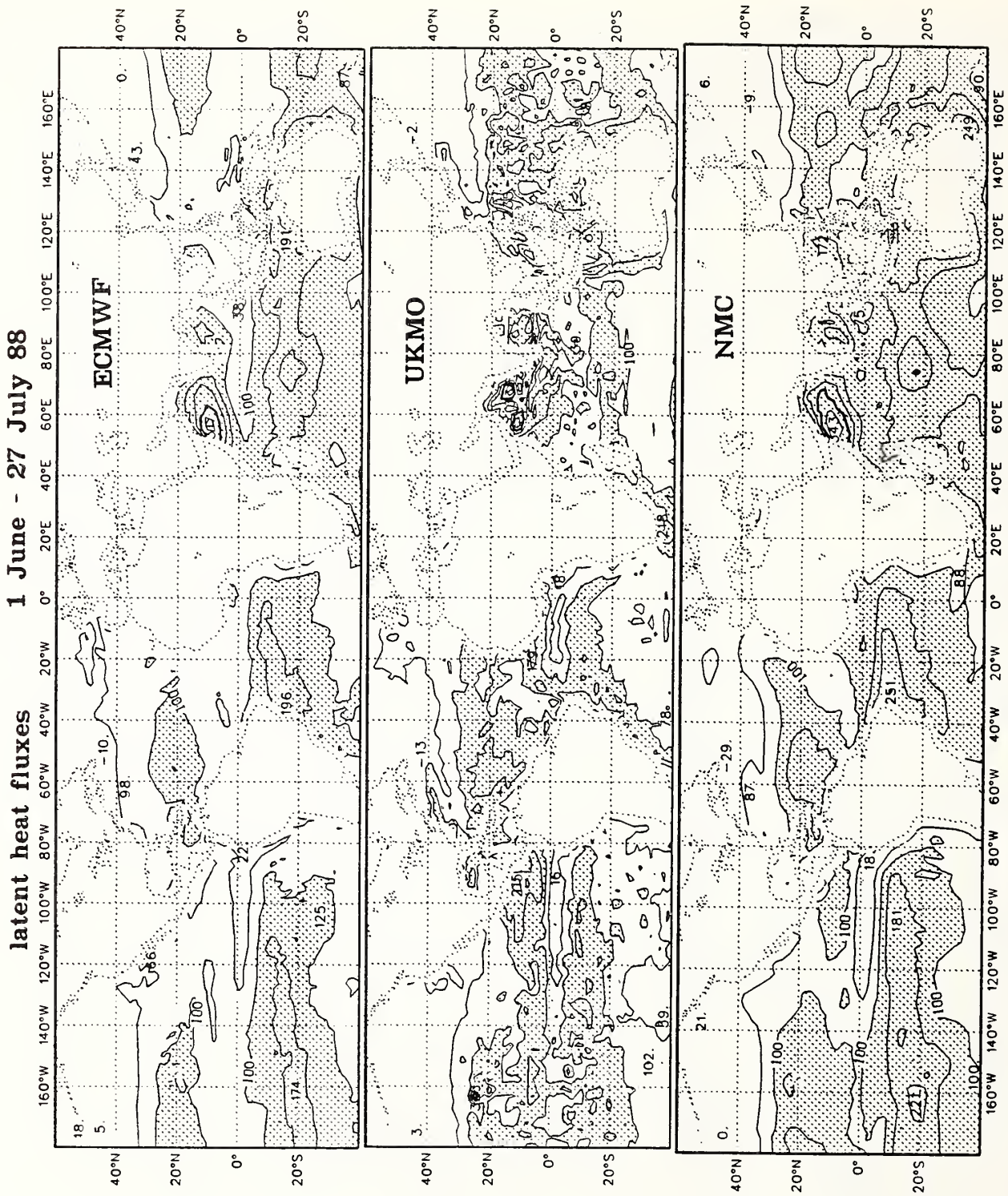

Fig. 4 Mean latent heat fluxes in the ECMWF, UKMO and NMC short range forecasts during June and July 1988. Contour interval: 50 W/m^2. Areas with more than 100 W/m^2 are shaded. Fluxes over land have been blanked out.

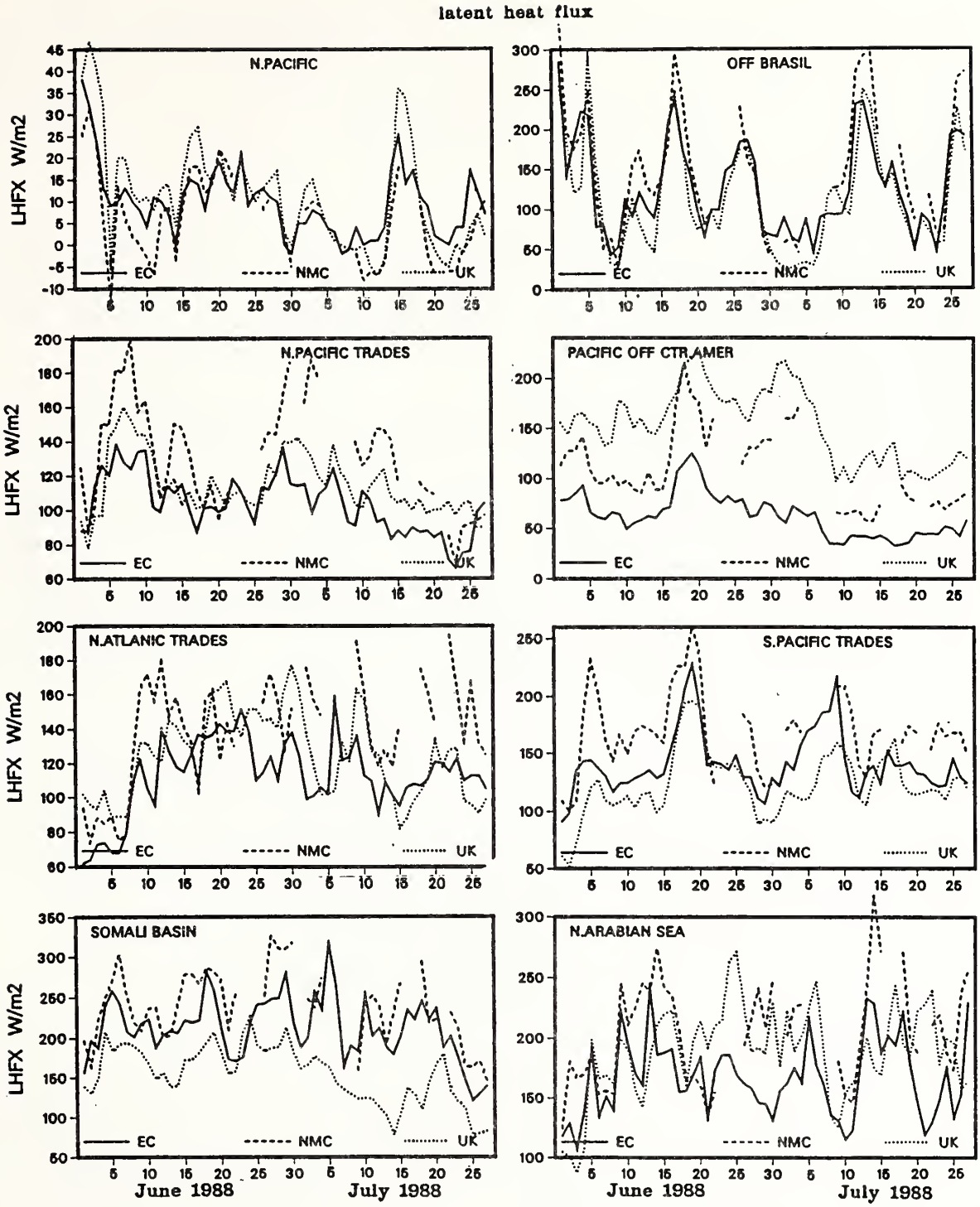

Fig. 5 Daily latent heat fluxes for selected areas in operational short range forecasts by ECMWF, UKMO, and NMC.

N. Pacific:	37° - 46°N, 158°E-174°W
N. Atlantic Trades:	15° - 25°N, 33° - 50°W
N. Pacific Trades:	13° - 25°N, 140° -163°W
Somali Basin:	2° - 10°N, 50° - 61°E
Off Brazil:	23° - 30°S, 30° - 48°
Pacific off Ctr. America:	5° - 15°N, 90° -110°W
S. Pacific Trades:	10° - 20°S, 95° -130°W
N. Arabian Sea:	11° - 22°N, 62° - 71°E

A Dynamical Extended Range Forecasting Experiment with the CCC GCM

G.J. Boer
Canadian Climate Centre
Downsview, Ontario.

1. Introduction

The model used is the Canadian Climate Centre General Circulation model (Boer et al. 1984a, b) at T20L10 resolution, with both annual and diurnal cycles of radiative forcing. The model includes relatively complete parameterizations of the usual physical processes including a parameterization of gravity-wave drag. Sea surface temperatures and zonally averaged cloudiness are prescribed.

Forecasts for December, January and February and for July have been produced for each of the eight years from 1979 to 1986. For each month, up to six individual forecasts are made. The 6 observing periods (3 days) prior to the first day of the month provide initial conditions. All forecasts are terminated at the end of the calendar month. NMC global analyses are used both for initial conditions and as verifying data. No initialization is performed. The boundary conditions are fixed in an "operational" way using only data available prior to the beginning of the forecast for sea surface temperature and snow line information.

2. Systematic Error

Attention is focussed primarily on the traditional forecast variable, Northern Hemisphere 500mb height. In particular, the anomalies of this quantity from the climatic mean must be forecast if skill is to be displayed. The inability of the forecast model to reproduce the mean January climate will reveal itself as model "systematic error". The mean January systematic error is shown in Figure 1. It is comparatively modest, with largest values of something in excess of 8 dm occurring over the Atlantic region. The systematic January forecast error for this model is perhaps distinctive in being both small and non-zonal.

3. January mean forecast skill

The skill of individual forecasts of the January mean together with the "ensemble mean forecast" is obtained by averaging together of all the forecasts (up to 6) made for a particular year is judged in terms of the spatial anomaly correlation coefficients. In Figure (2) dots indicate individual forecasts and crosses the ensemble mean forecast for both the extratropical Northern Hemisphere region from 30-90N and the North American region 30-90N, 50-140W. The results obtained after the removal of an estimate of the systematic error (termed the corrected case) are also given.

Rather than remove the mean January systematic error at all scales as obtained by simple averaging (and as displayed in Figure 1), a procedure to estimate a time dependent version of the systematic error is used in order that it might be applied at any forecast time rather than just to the mean January forecast discussed here. This procedure consists in representing the systematic error as a function of time by fitting fourth order polynomials in time to the real and imaginary parts of the spherical harmonic expansion coefficients for wavenumbers up to a T10 truncation. The time dependent systematic error thus obtained is removed before averaging for the mean January case discussed here. While this is an a posteriori correction for these January cases, the same correction will be applied in an a priori fashion to the December and February set of forecasts.

For the Northern Hemisphere sector the January mean anomaly correlation for the ensemble forecast is below 0.5 in 6 of the 8 years with 1984 and 1986 clearly the worst. After correction, half of the years show values greater than 0.5. For the North American area the correlation coefficients are generally larger than for the Northern Hemispheric sector. In this case, 5 of 8 of the years have ensemble mean forecast anomaly correlations which are greater than 0.5 while after correction this increases to 6 (almost 7) of the 8.

Figure (3) gives the mean January anomaly forecast skill at each geographical point. This correlation coefficient differs from those above which involve the correlation over a geographical region under spatial averaging. This calculation asks to what extent, at each geographical point, mean January forecast anomalies of 500mb height are accompanied by similar observed anomalies. Values greater than 0.4 are shaded in the diagram. Because of the way these correlations are calculated, the systematic error does not enter. The results are, at least, generally positive but values are not high. No attempt is made here to "explain" the result in terms of "natural patterns of variability" such as the PNA pattern or the general pattern of low frequency variability.

4. Forecast behaviour as a function of time

An understanding of error generation and propagation through the spectrum will be a prerequisite for efforts to predict forecast skill. It is intended to evaluate the various terms in the forecast error budget at long times as in Boer (1984). Here, the anomaly correlation as a function of scale is displayed in Figure (4). This gives an indication of the average behaviour in terms of both forecast time and scale. As expected, skill is lost quickly in the smaller scales and more slowly at larger scales. By day 20 the spectral correlation coefficient is virtually zero at all scales.

5. Concluding comments

Monthly forecasts for the 8 Januarys from 1979 to 1986, made with the low-resolution Canadian Climate Centre general circulation model, are considered. Attention is confined to the "traditional" extended range variable, namely the Northern Hemisphere 500mb height field.

The systematic error of this model is comparatively small for January. The zonal component is well forecast so the largest contribution is not from this component. The skill of the mean January anomaly forecast as measured by the anomaly correlation coefficient for the Northern Hemispheric region from 30-90N is in the vicinity of 0.5. Correction for the systematic error makes only a modest improvement in the scores.

The skill of the mean January anomaly forecast for the North American region is surprisingly high, especially after correction for the systematic error. In this case the ensemble mean forecast correlation coefficient is near or greater than 0.5 for 7 of 8 years. The local nature of skill is also seen in the geographical distribution of the local anomaly correlation coefficient for the January means.

Finally, the propagation of the error through the spectrum with time displays the expected behaviour with error dominating the small scales early in the forecast but requiring more time to penetrate the larger scales. Clearly the possibility of skillful extended range forecasting resides in the behaviour of these large scales. The sources of error at these scales, methods of correcting for this error and the prior knowledge of atmospheric states for which these scales are shielded from error are all areas of further analysis of this forecast experiment.

Figure 1. Mean January systematic model error for 500mb height. Units dm.

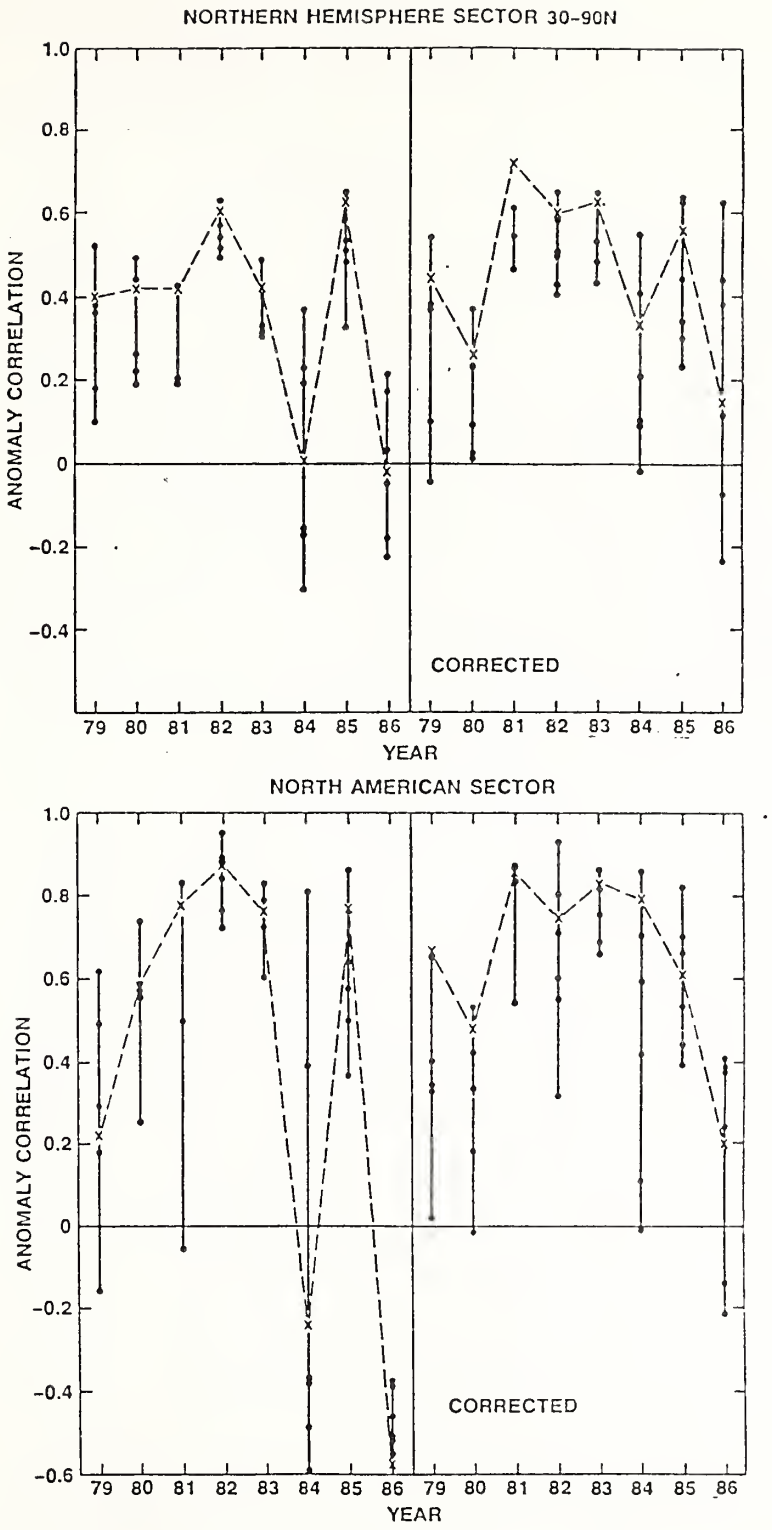

Figure 2. Anomaly correlation coefficients for (top) the Northern Hemispheric sector from 30-90N and (bottom) the North American sector 30-70N 50-150W. Values for individual forecasts are indicated by dots while the values for the ensemble means are indicated by crosses which are also joined by dashed lines. The rightmost panel in each case gives the result after removing systematic error.

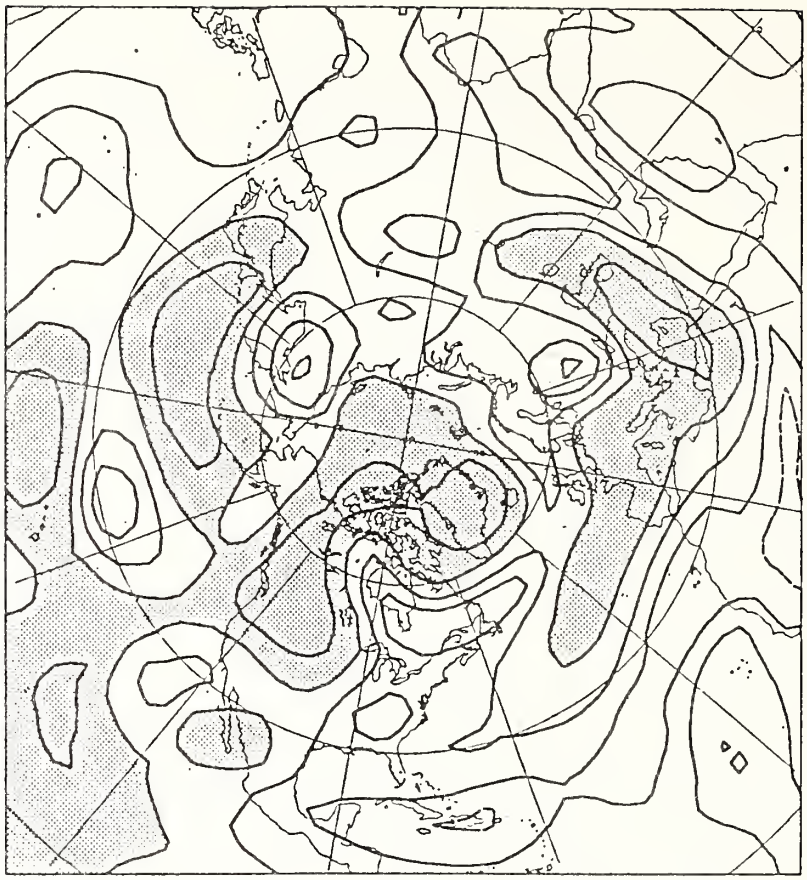

Figure 3. The geographical distribution of the pointwise temporal anomaly correlation coefficient for mean January 500mb height.

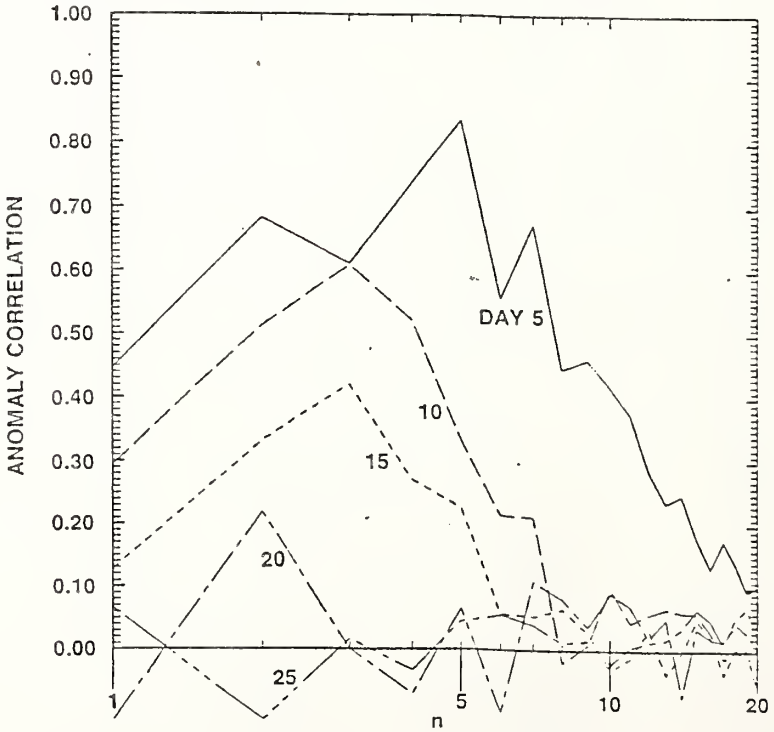

Figure 4. The spectral anomaly correlation coefficient as a function of forecast time averaged over all forecasts.

EXTENDED-RANGE PREDICTABILITY ESTIMATES FROM A SIMPLE COUPLED MODEL OF THE MID-LATITUDE CIRCULATION

Arthur J. Miller and John O. Roads
Climate Research Group
Scripps Institution of Oceanogrphy
University of California, San Diego
La Jolla, CA 92093

A simplified coupled atmosphere-ocean model of the Northern-Hemispheric January circulation has been developed to gain understanding of the influence of evolving mid-latitude sea-surface temperature (SST) anomalies on the extended-range predictability of the atmosphere. The two-layer atmosphere (Roads, 1987a,b) is quasi-geostrophic, with orography and steady forcing. The North-Pacific Ocean (Miller, 1988) includes a two-layer, quasi-geostrophic, deep-ocean component which influences a simple sea-surface temperature model.

Results from the ocean model, forced by the atmospheric model, show that the effects of model geostrophic-current and Ekman-current advection are comparable to the effects of surface heat flux in generating and modifying SST anomalies. Furthermore, compared to cases when only heat fluxes drive the SST anomalies in the coupled system, the cases which include both heat flux and ocean-current advection in SST anomaly evolution exhibit fields of rms monthly-averaged heat flux which are much more comparable to observations (Figure 1).

After generating a base run of the coupled system which represents "observed" flows, various prediction models are implemented to determine their relative success at dynamical prediction. These prediction models, initialized with small-scale error, use the same atmospheric model with different ocean models, categorized as

(a) SST fixed at climatic values (climatic SST),
(b) SST fixed at anomalous intitial values (persistent SST),
(c) SST predicted according to coupled dynamics (predicted SST),
(d) SST specified from base run (true SST).

The results suggest that the success of predictions of *instantaneous* model fields will differ insignificantly among the four atmospheric prediction models. The success of predictions of *time-averaged* model fields, however, will often significantly depend on the prediction model. The results are summarized as follows:

1. With 68% confidence, SST anomalies significantly impact the overlying atmospheric flow fields after approximately 3-4 weeks, as evidenced by comparing time-averaged atmospheric predictions with climatic *vis-a-vis* true SST models.
2. If mid-latitude SST *could* be predicted accurately, or if SST is specified from observations for hindcasting purposes, (at least marginally) significant improvement in forecasts (or hindcasts) of both instantaneous and time-averaged atmospheric flow fields is to be expected. Roughly 20% - 30% of the anomaly variance of 1-month through 3-month time-averages of baroclinic Pacific flow fields can be expected to be dynamically predicted given the observed mid-latitude SST and an excellent atmospheric forecasting model.
3. Coupled atmosphere-ocean models have little chance of outperforming an atmospheric model with SST specified by persistence of day zero (Figure 2). This applies to forecasting either instantaneous or time-averaged atmospheric fields for local or hemispheric regions. This result is a consequence of the following result:

4. Dynamical predictions of mid-latitude SST are expected to be only slightly better than predictions using SST persistence. This result is due to the purely wind-forced nature of the model ocean. After O(2 weeks), the atmospheric flows provide erroneous forcing functions for the ocean flows (*cf.* the stochastic forcing models of Frankignoul and Hasselmann, 1977).

Although the improvements in dynamical prediction are claimed to be significant, they are rather small. For time-averaged predictions using the coupled model *vis-a-vis* the 'climatic SST' model (Figure 3), the enchancement to the anomaly correlation is O(0.10) for Pacific fields, and half that for global fields, for time averages between 30 and 60 days. Longer-term time averages differ insignificantly from atmospheric persistence. For 30-day and 60-day time averages of the atmospheric thermal field over the Pacific, the predicted fraction of anomaly variance increases, respectively, from roughly 25% and 5% for the 'climatic SST' model, to 30% and 15% when implementing either the coupled or 'persistent SST' models. These predictions could be further enhanced by invoking atmospheric persistence at the point where the correlation of the dynamical prediction begins to drop more rapidly than persistence of day zero. Use of the 'true SST' model, which is evidently impractical for forecasting, increases the predicted variance of 60-day averages to roughly 20% and allows predictions of long-term time averages which exhibit skill similar to the 60-day averages (Figure 4). For more details of the results see Miller and Roads, 1988.

Several effects which we have excluded may alter our results:

(i) The heat exchange between the ocean and atmosphere may be strongly influenced by the assumed atmospheric boundary-layer and condensation parameterizations.
(ii) The seasonal cycle of SST response may have considerable import in forcing the overlying atmosphere and, consequently, influencing time-averaged predictions.
(iii) The inclusion of the mechanism of turbulent entrainment of thermal anomalies, which can exist beneath the mixed layer, can couple the slow evolution of oceanic baroclinic waves (upper-ocean heat content) to the mixed-layer temperature, thus imposing longer natural time scales on SST variability. However, the (unpredictable) atmospheric variables will, nonetheless, probably dominate that process (see Miller, 1988).
(iv) The inclusion of ocean topography and non-linearity can support energetic, surface-trapped, geostrophic currents in the 50-100 day period band. In the present model, this band is dominated by (unpredictable) Ekman currents. In the real ocean, advection by such surface-trapped geostrophic currents may be more predictable than was found here, since unstable ocean currents bear intrinsic predictability time scales which are potentially longer than 2 weeks (*e.g.*, Carton, 1987; Rizzoli and Holland, 1988).
(v) Equatorial SST anomalies may significantly impact the predictability of the mid-latitude atmospheric circulation through teleconnections.

These effects will be investigated by us with more sophisticated models.

Acknowledgments. AJM was supported by a Mellon Foundation postdoctoral fellowship through the Climate Research Group and California Space Institute at Scripps. Additional support was provided by CalSpace Grant 47-87, the Climate Analysis Center, NSF grant ATM85-20540 and NOAA Grant NA86-AA-D-CP104. San Diego Supercomputer Center resources were provided by an SDSC grant, the SIO Block Grant and the aforementioned NSF grant.

References

Carton, J. A., 1987: How predictable are the geostrophic currents in the recirculation zone of the North Atlantic? *J. Phys. Oceanogr.*, **17**, 751-762.

Cayan, D., 1988: Large-scale surface heat flux variations over the North Pacific and North Atlantic during winter. *13th Annual Climate Diagnostics Workshop*, this volume.

Frankignoul, C. and K. Hasselmann, 1977: Stochastic climate models: Part 2. Application to sea-surface temperature anomalies and thermocline variability. *Tellus*, **29**, 289-305.

Malanotte-Rizzoli, P. and W. R. Holland, 1988: Data constraints applied to models of the ocean general circulation. Part II. The transient, eddy-resolving case. *J. Phys. Oceanogr.*, **18**, 1093-1107.

Miller, A. J., 1988: A simplified coupled model of extended-range predictability. Part I. Response of the model ocean. Submitted to *Journal of Climate*.

Miller, A. J. and J. O. Roads, 1988: A simplified coupled model of extended-range predictability. Part II. Predictability of the coupled system. Submitted to *Journal of Climate*.

Roads, J. O., 1987a: Predictability in the extended range, *J. Atmos. Sci.*, **44**, 3495-3527.

Roads, J. O., 1987b: Lagged-average predictions in a predictability experiment, *J. Atmos. Sci.*, **45**, 147-162.

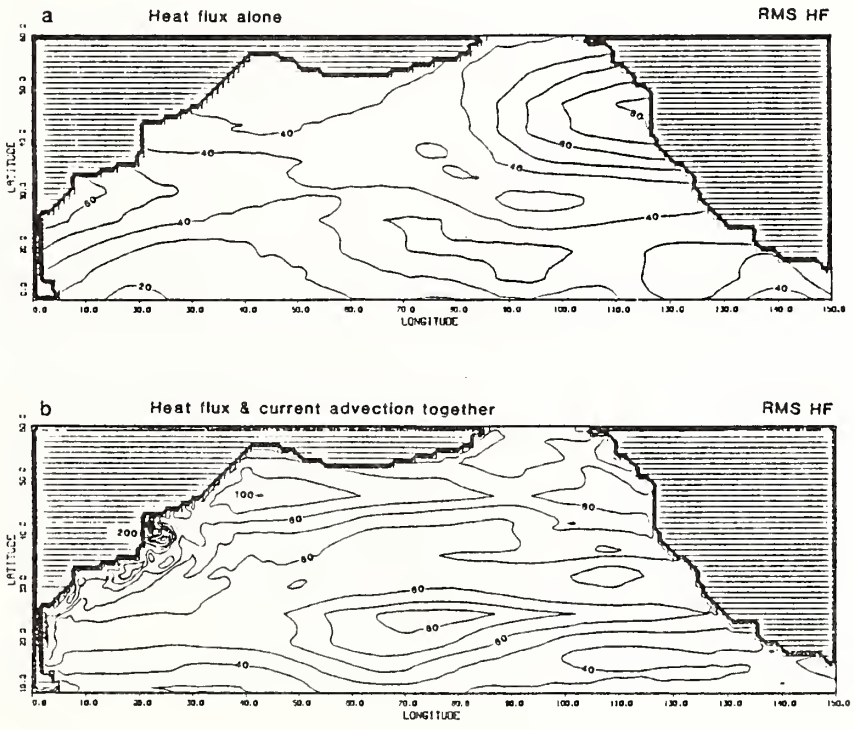

Figure 1. Standard deviations of monthly-averages of model heat flux (CI=10 W/m^2) for coupled model simulations in perpetual January mode for (a) case of heat-flux forcing of SST (b) case of combined forcing of SST by heat flux and ocean-current advection. The structure and amplitude of the heat fluxes in the Northwest Pacific for case (b) is much more realistic based on the January observations discussed by Cayan (1988, this volume).

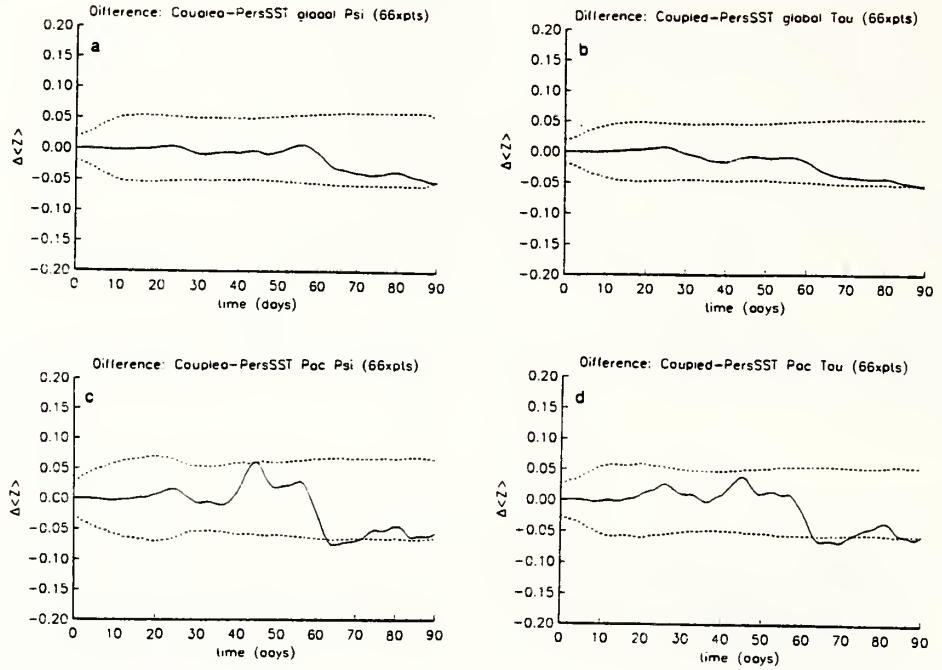

Figure 2. Solid lines are the differences between $\langle Z \rangle$, the ensemble-average of the Fisher-Z transformed correlation values, for time-averaged predictions based on the coupled model and the 'persistent SST' prediction model for (a) hemispheric barotropic streamfunction (b) hemispheric baroclinic streamfunction (c) Pacific barotropic streamfunction and (d) Pacific baroclinic streamfunction for case D. The ordinate represents the time-averaging interval averaged from day zero to day T, with $T = 1, ..., 90$. The distance between the two short-dashed lines equals $2\Delta Z$, where ΔZ is the standard deviation of the distribution of Z values for one case; thus if $\Delta\langle Z \rangle$ equals the distance between the two short dashed lines, the two mean values of Z indeed differ, with 84% confidence. The two prediction models differ insignificantly in performance. Longer than 60-day averages are differ insignificantly in skill from predictions based on atmospheric persistence of day zero.

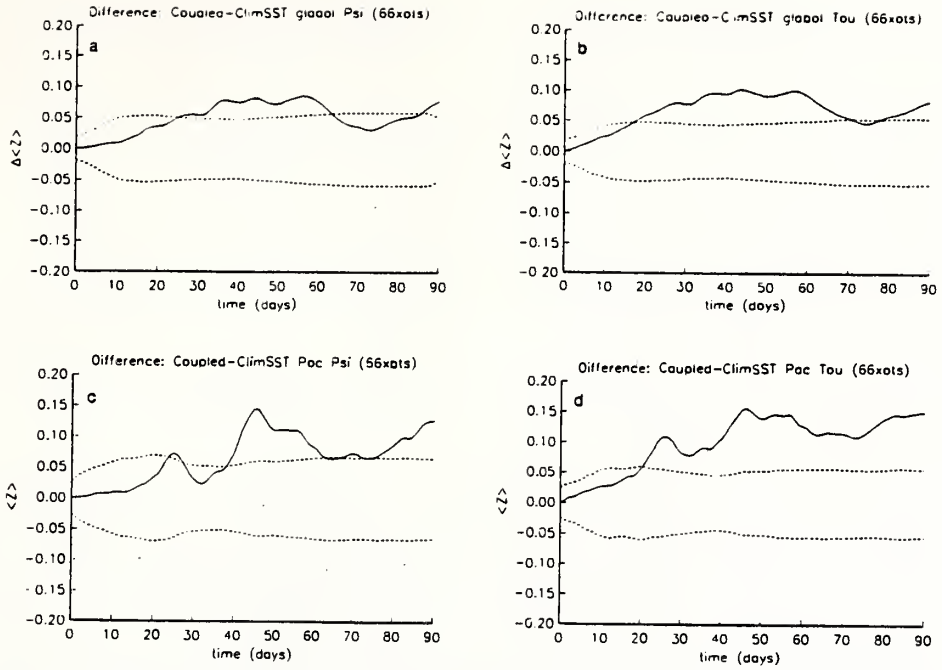

Figure 3. Same as Figure 2 but for difference between the coupled model and the 'climatic SST' prediction model. The coupled model predictions are at least marginally significantly better than the 'climatic SST' predictions for time averages between 30 and 60 days. Longer than 60-day averages differ insignificantly in skill from predictions based on atmospheric persistence of day zero.

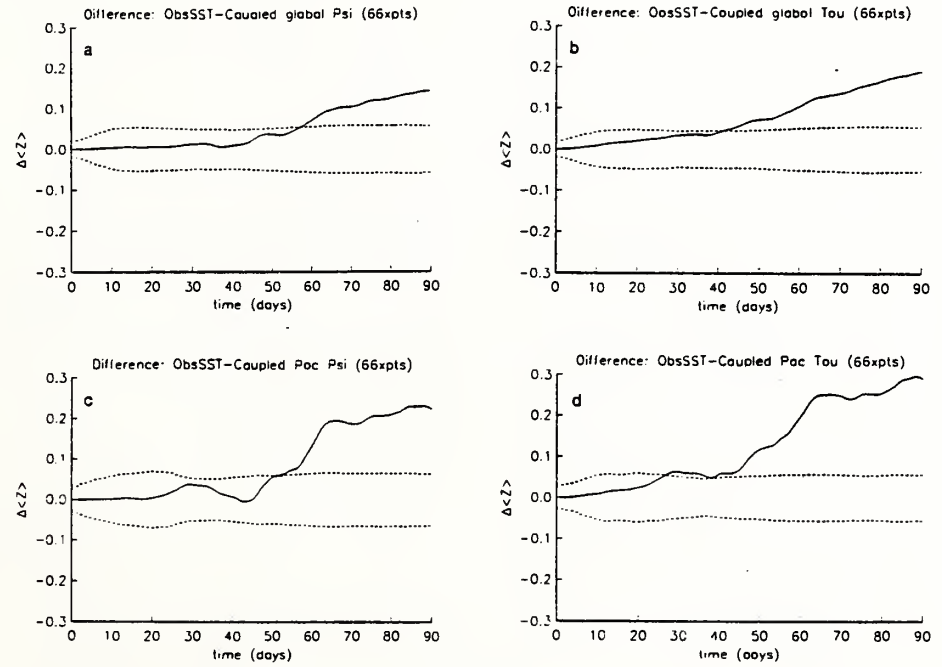

Figure 4. Same as Figure 2 but for difference between the 'true SST' prediction model and the coupled model. For 60-day averages and longer, predictions of atmospheric variables based on the 'true SST' model are significantly better than predictions using the coupled model.

The Effect of Tropical Atlantic Heating Anomalies Upon GCM Rain Forecasts Over the Americas

Julio Buchmann
Dept. de Meteorologia-Inst. Geociencias
Universidade Federal do Rio de Janeiro

Jan Paegle and Lawrence E. Buja
Department of Meteorology
University of Utah

Robert E. Dickinson
National Center for Atmospheric Research

Severe droughts occurred over eastern sections of North America and Central sections of South America in 1986 and 1988. We summarize data suggesting that both periods were characterized by above-normal tropical Atlantic sea surface temperatures and convection, and investigate the response of a general circulation model to positive heating anomalies in the tropical Atlantic sector. An eight case control ensemble of 30 day global predictions is made starting from the atmospheric state observed on 1 January of each year from 1977 through 1984. The same eight cases are integrated in a second experimental ensemble which is identical to the first control ensemble, except that a heating term is added to the thermodynamic equation in a region centered at 30°W, 6.6°N. This is intended to simulate the latent heating of enhanced tropical Atlantic convection. The third ensemble is identical to the second, except the heating is centered at 6.6°S.

Both heated ensembles produced reductions of forecast precipitation over most of North and South America, but these appear to have greater statistical significance over North America (Figs. 1 and 2). Here the greatest precipitation reductions are forecast over the Southern and Eastern United States, and this response does not change substantially between the two experiments. The South American response is more sensitive to the placement of the heating anomaly. When the anomaly is located north of the equator, drying occurs over northeast Brazil, while this region receives increased rainfall when the anomaly is located south of the equator. Both experiment ensembles display a region of reduced rainfall over the Andes mountains, and over southern portions of Brazil. However, only the former region is statistically significant above the 95% confidence level. The present usage of real initial data and an ensemble of cases permit us to draw quantitatively meaningful estimates of the time scale of response and case-to-case variability. For presently tested cases, the South American response is evident by day 5, but exhibits substantial inter-sample variability, and the North American response is fully established by day 10, and exhibits less inter-sample variability (Fig. 3). The model drying effects can be explained only partly by enhanced local subsidence; much of the rainfall reduction appears to be related to a re-orientation of the synoptic-scale wave pattern in which the lower tropospheric circulation is unfavorable for water vapor inflow from source regions over the tropical Atlantic and Amazon Basin (Fig. 4).

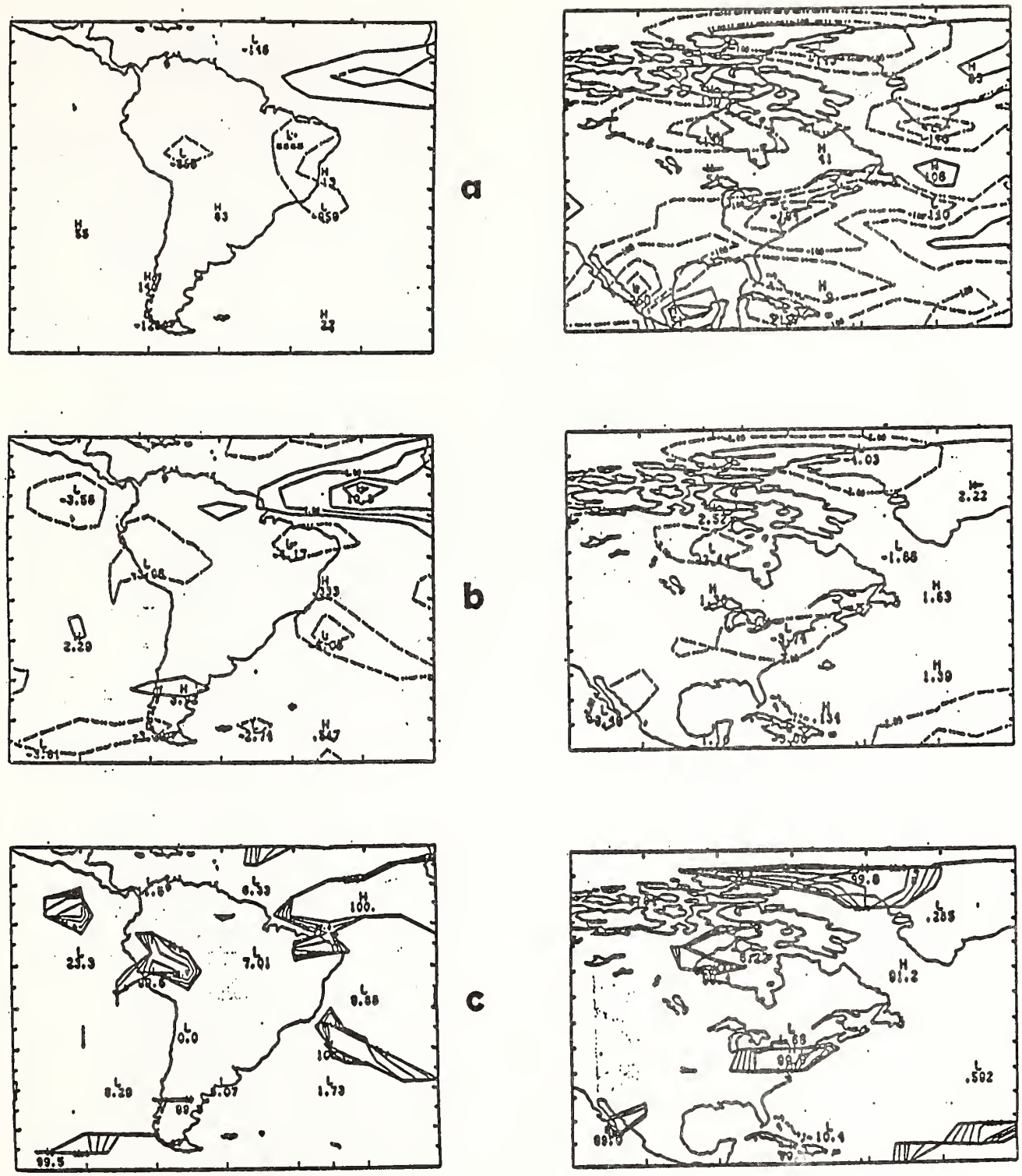

Figure 1a. Ensemble and time averaged precipitation response for ensemble 2. Contour interval is 5 x 10^{-8} m/s (left), 5 x 10^{-9} (right).

1b. T-statistic for response depicted in Fig. 1a. Contour interval is 2.

1c. Probability that the response depicted in Fig. 1a is statistically significant. Contour interval is 1%, and only values of 95% and higher are analyzed. Other plotted values give local maxima and minima.

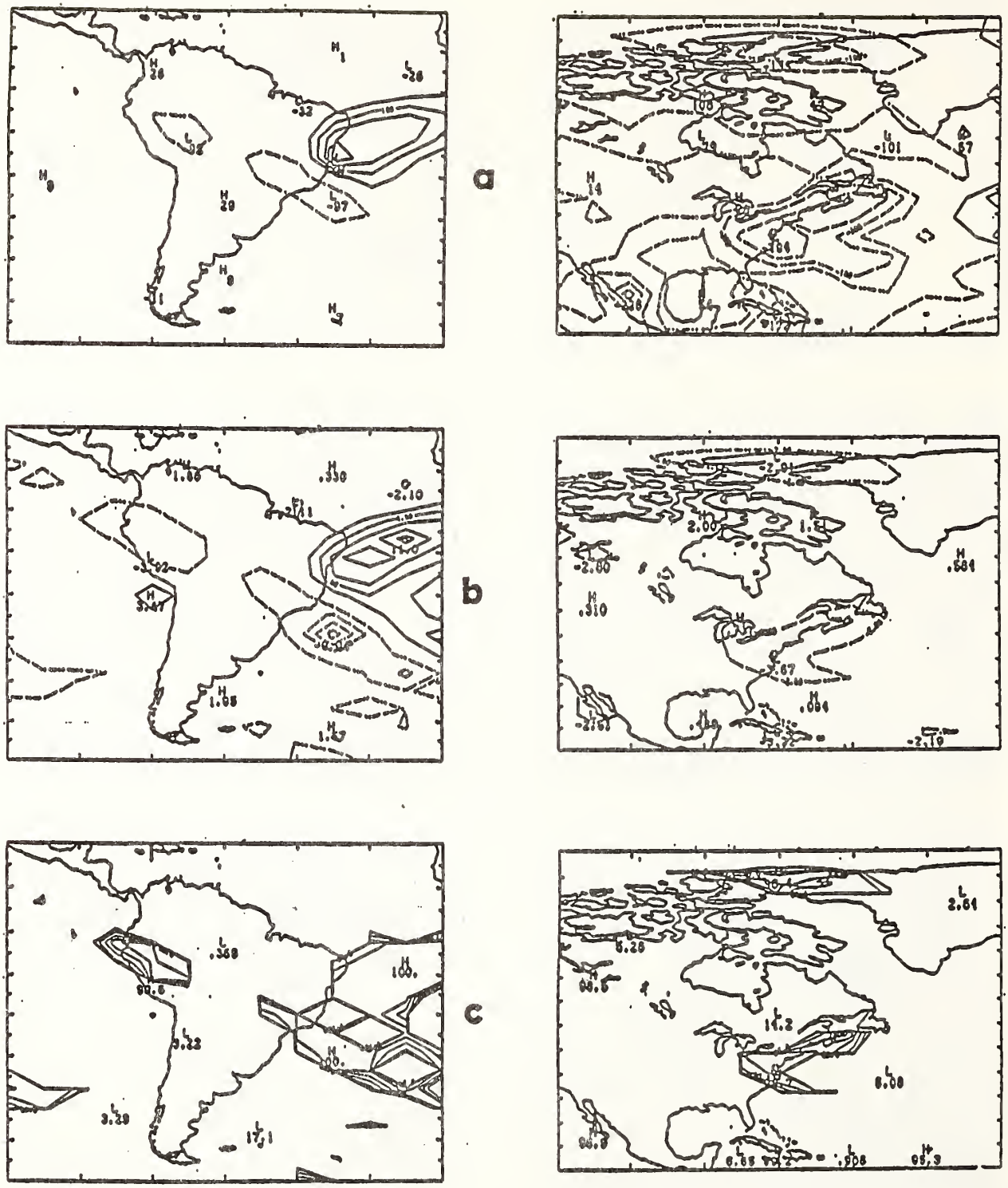

Figure 2. As in Figure 1 for ensemble 3.

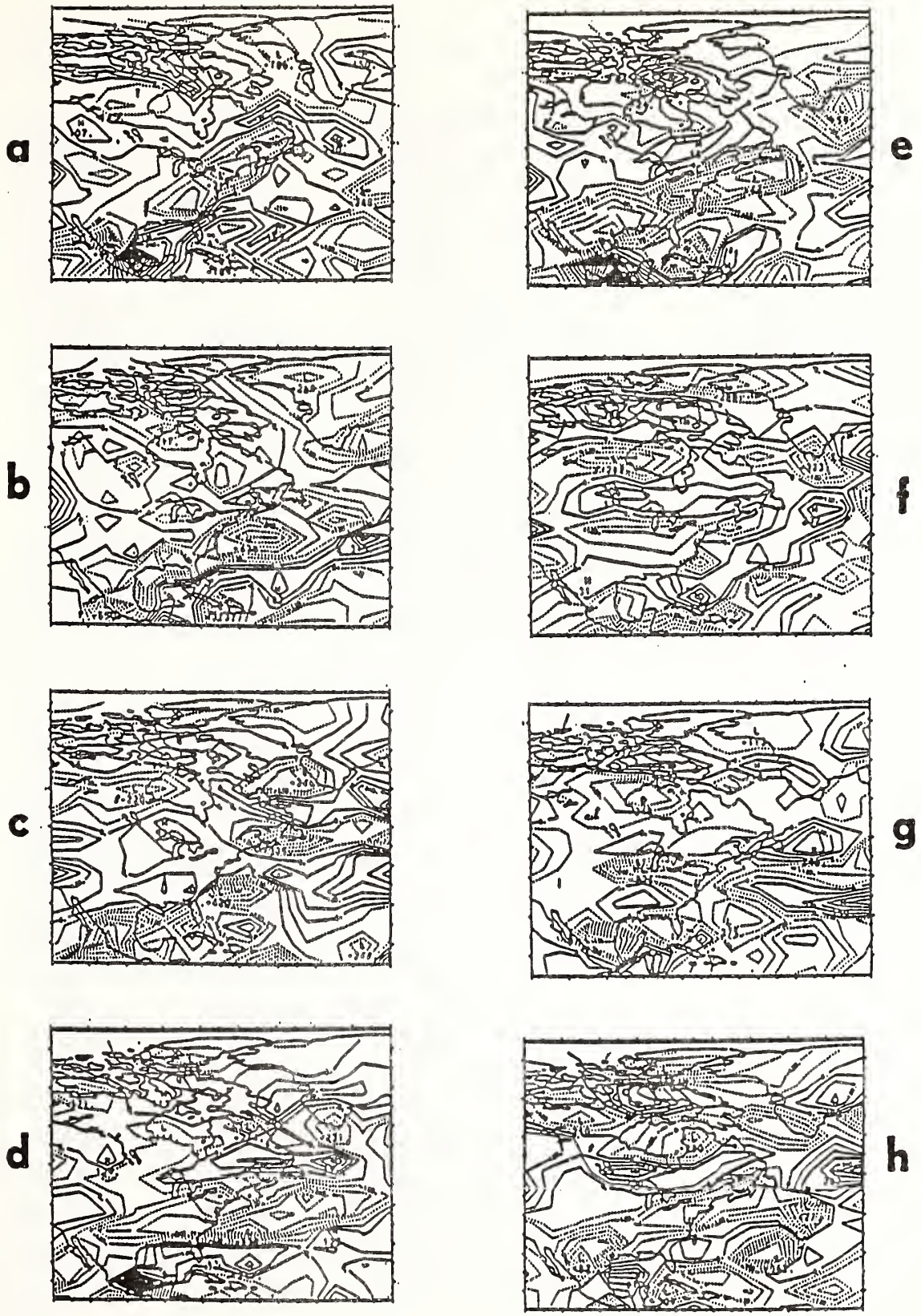

Figure 3. Time averaged precipitation response in ensemble 2 (experiment-control for (a) 1977, (b) 1978, (c) 1979, (d) 1980, (e) 1981, (f) 1982, (g) 1983, (h) 1984. Contour interval equals 1.5×10^{-7} m/s. Dashed contours are negative.

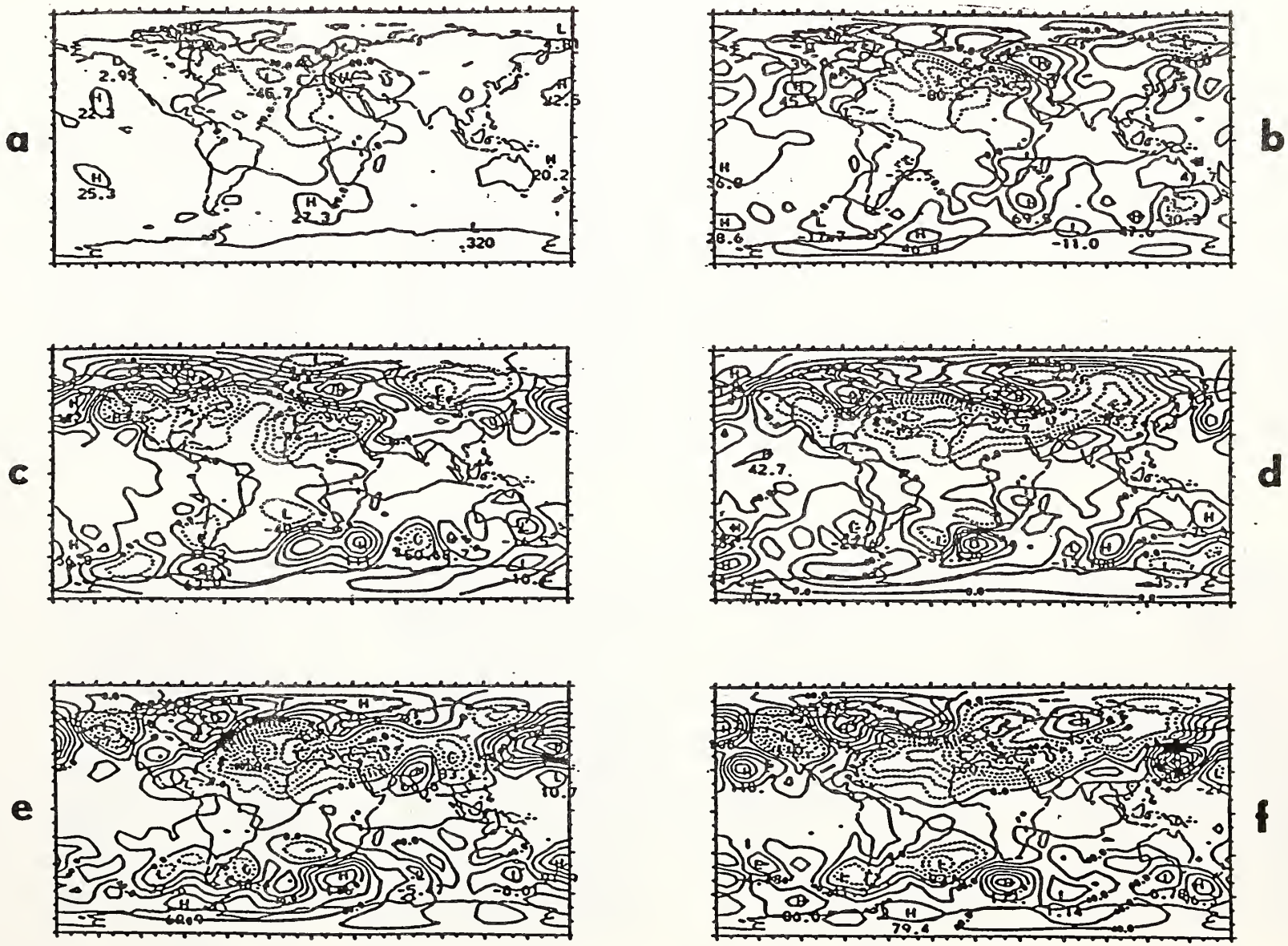

Figure 4. Time evolution of geopotential height response averaged over ensemble 2 for (a) day 5, (b) day 10, (c) day 15, (d) day 20, (e) day 25, (f) day 30. Contour interval equals 20m.

Predictability of Time Averages in a Simple GCM

Siegfried Schubert and Max Suarez
NASA/GSFC Code 611

and

Jae Schemm
Centel Federal Services

Dynamically-based extended range (beyond 1 week) weather forecasts have, in general, shown marginally useful skill. Recently, work has focused on trying to understand and take advantage of periods of enhanced predictability, as well as, determining some type of optimal time (ensemble) and/or spatial averaging to isolate the more predictable signal. A somewhat disconcerting observation is that the dynamical models appear to perform best in the extended range during periods when the atmosphere is highly persistent. The following is a progress report of our attempt at quantifying the connection between predictability and persistence in a simple GCM. The ultimate aim of this work is to provide an assessment of the cost/benefit ratio of extended range forecasts with general circulation models (GCMs) and to provide a better understanding of the impact of time-averaging

We examine predictability in a simple 2-level GCM for perpetual winter conditions. The GCM's error growth behavior (described in Schubert and Suarez, 1989) is determined from a large number of 45-day Monte Carlo forecasts starting from very small initial errors. Dynamical time scales are determined for the dominant modes of variation by projecting the error fields onto the model's climatological empirical orthogonal functions (EOFs) and using the simple Lorenz (1982) quadratic error growth model to determine the doubling time for realistic error amplitudes. These time scales are compared with the statistical time scales for the EOFs using the

definition of the time between independent samples (T_0) introduced into the meteorological literature by Leith (1973).

Figure 1a shows the dynamical and statistical time scales for the first 25 EOFs in groups of five. Not surprisingly, the first few EOFs have the longest time scales. Also, long statistical time scales are associated with long dynamical time scales. We should note that the definition of the dynamical time scales is somewhat arbitrary so that a direct comparison is probably not very meaningful. However, the behavior of the ratio of time scales shown in Figure 1b is perhaps more meaningful. This shows a tendency for the decay of information due to persistence to become more comparable to that of predictability as one goes to the lower order EOFs. For the higher order EOFs the dynamical model will clearly give better forecasts than simple persistence models. On the other hand, for the lowest EOFs it may be more difficult for dynamical models to beat persistence.

Current work involves developing time series models for the dominant EOFs in order to provide a more direct comparison with the GCM. It is found that the dominant eddy (non-zonal) modes are described well by first-order autoregressive (AR) moving average (correlated noise term) models. These models will be used to determine at what point in a forecast we should stop integrating the GCM

REFERENCES

Leith,C.E., 1973: The standard errror of time-average estimates of climatic means. J. Appl. Meteor., 12, 1066-1069.

Lorenz, E.N., 1982: Atmospheric predictability experiments with a large numerical model. Tellus, 34, 505-513.

Schubert, S.D. and M. Suarez, 1989: Dynamical predictability in a simple general circulation model: Average error growth. To appear in J. Atmos. Sci. (January).

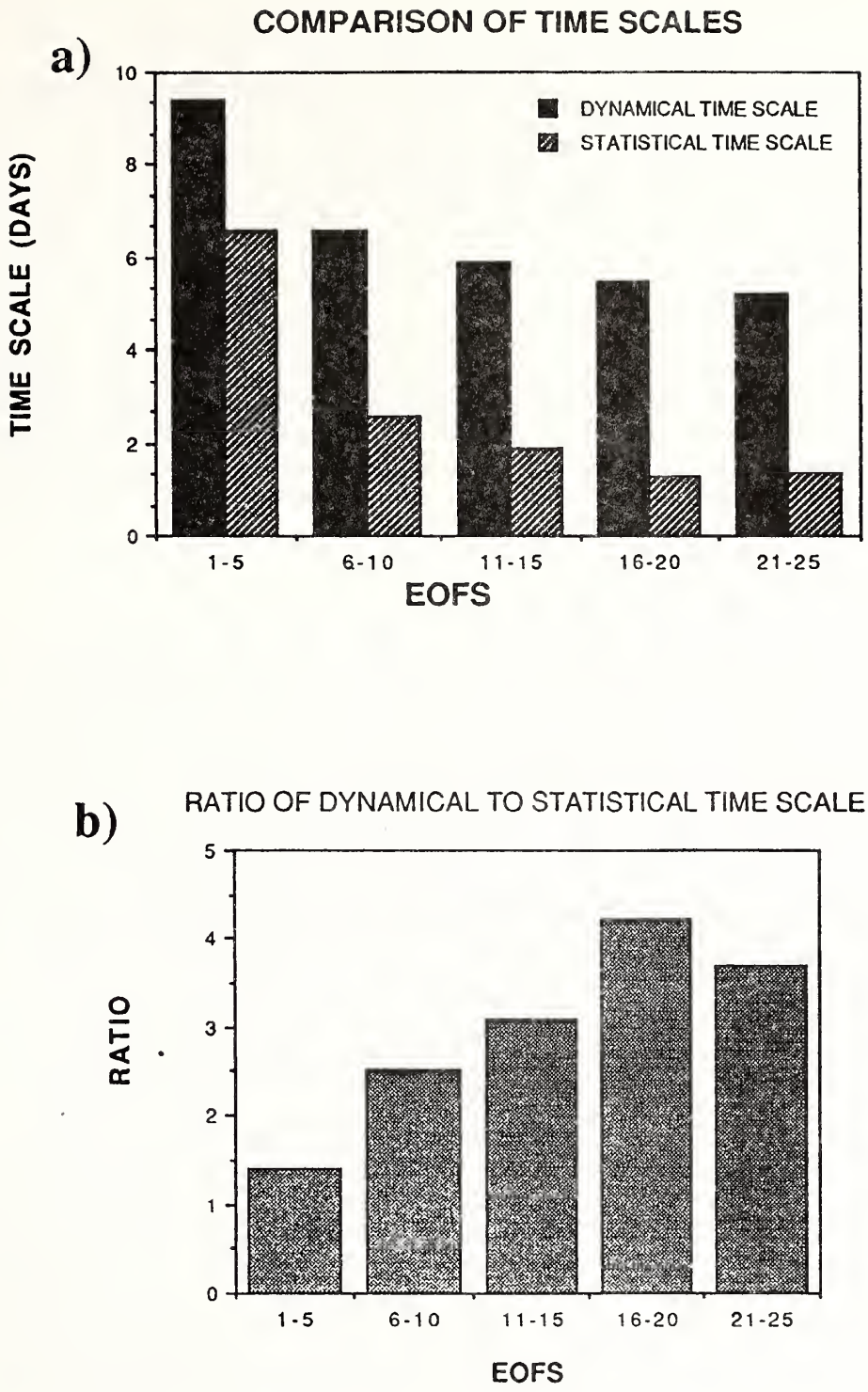

Figure 1. A comparison of the statistical and dynamical time scales ($2/\gamma$, where $1/\gamma$ is the e-folding time) for the first 25 climatological EOFs. a) The times scales for groups of five EOFs ordered by variance explained. b) Same as in a), except for the ratio of dynamical to statistical time scales. See text for details.

Effects of Recent Changes in NMC Models upon Global Analyses and Medium-Range Forecasts

Pete Caplan, Glenn White, and Bradley A. Ballish
Development Division
National Meteorological Center
National Weather Service
Washington, D.C., 20233

1. Introduction

The changes to be described here were implemented since the last Climate Diagnostics Workshop in October, 1987. They affect both NMC's Global Data Assimilation System which produces its global analysis, and the Medium Range Forecast System, which is run from the global analysis and which provides its first-guess fields.

2. Surface Evaporation

A persistent problem in the forecast model has been an overly fast evaporation from land surfaces early in the forecast, resulting in rapidly-increasing relative humidities. This was largely corrected by a pair of changes implemented on May 18, 1988 - first, the downward adjustment of the effective land-surface skin temperature for the calculation of saturation vapor pressures; second, the parameterization of a constant stomatal resistance to simulate the effect of retention of moisture by vegetation. The effect of these changes upon a pair of one-day forecasts is shown in Figs. 1a and 1b.

3. Physical Retrieval of Satellite Data and Other Analysis Changes

In the past at NMC, temperature soundings from satellites were obtained by the comparison of radiance data statistically to large numbers of collocated radiosonde reports. This tended to underestimate departures of the temperature soundings from mean conditions. The newly-implemented method - physical retrievals - uses temperature-radiance relations from inversion of the radiative transfer equation. Extensive tests with analyses incorporating this retrieval method showed that they led to slightly better five-day forecasts.

Other changes in the analysis include adjustments in the relative weights assigned to the first guess and the observations; also a correction was made to the code that recovers geopotential heights from thicknesses.

The combined effects of all of these changes upon the analyses themselves was significant only in the upper troposphere and lower stratosphere, as can be seen from the difference cross-sections in Fig. 2.

4. Horizontal Diffusion

Because of last year's increase in model resolution from R40 to T80, it was decided to test a significant reduction in horizontal diffusion. Another motive for this kind of change is provided by the excessive damping of transient eddy kinetic energy that is consistently noted in the troposphere, a typical example of which is shown in Fig. 3. To address these needs, the new global model contains a strong reduction in most horizontal diffusion coefficients, i.e., by a factor of 3/8 for divergence, vorticity, and specific humidity, and by a factor of 1/6 for heat. This is done for most wavelengths at most model levels; however for very short wavelengths in the upper quarter of the atmosphere, the diffusion was not decreased but increased substantially. In addition, in all regions of very high windspeed, the amplitude of the shortest waves was directly reduced. The predominant effect of these changes is to reduce the horizontal dissipation of energy, as can be seen in the transient eddy kinetic energy cross sections in Fig. 4. The decreased diffusion also had a small side effect - a slight warming of most of the troposphere and an increase in geopotential (Fig. 5).

5. Interactive Clouds

The cloud amounts and heights in both the new and old models are computed only to modify the radiative fluxes; they contain no actual water or ice. In the old model, they were climatologically determined, zonally averaged, and fixed through the forecast. The new clouds are to a certain extent interactive, in that they are diagnosed as a function of model-forecasted variables (relative humidity, vertical velocity, and convection depth and rainfall rate) each time the radiation is calculated. Thus, the new clouds are able to evolve through the forecast.

For five-day forecasts, the strongest effect of the interactive clouds is a tendency to warm the middle troposphere in regions where the old model was too cold and to cool a portion of the upper tropical troposphere. The temperature errors of the old model are shown in the top half of Fig. 6, the changes (new minus old) in the bottom half. Fig. 7 gives the same information for geopotential. These two diagrams depict a set of thirteen 5-day October forecasts in which <u>all</u> of the changes described in this and preceeding sections were included in a single package, but independent tests showed that the clouds were responsible for the bulk of the differences in the forecasts (cf. Fig.5). Other effects of the package of changes include a tendency for synoptic-scale features to be somewhat more intense and faster moving. The skill scores obtained so far indicate a consistent improvement at 1000 mb and 100 mb, especially around day 3 or 4, and a slight improvement at 500 mb.

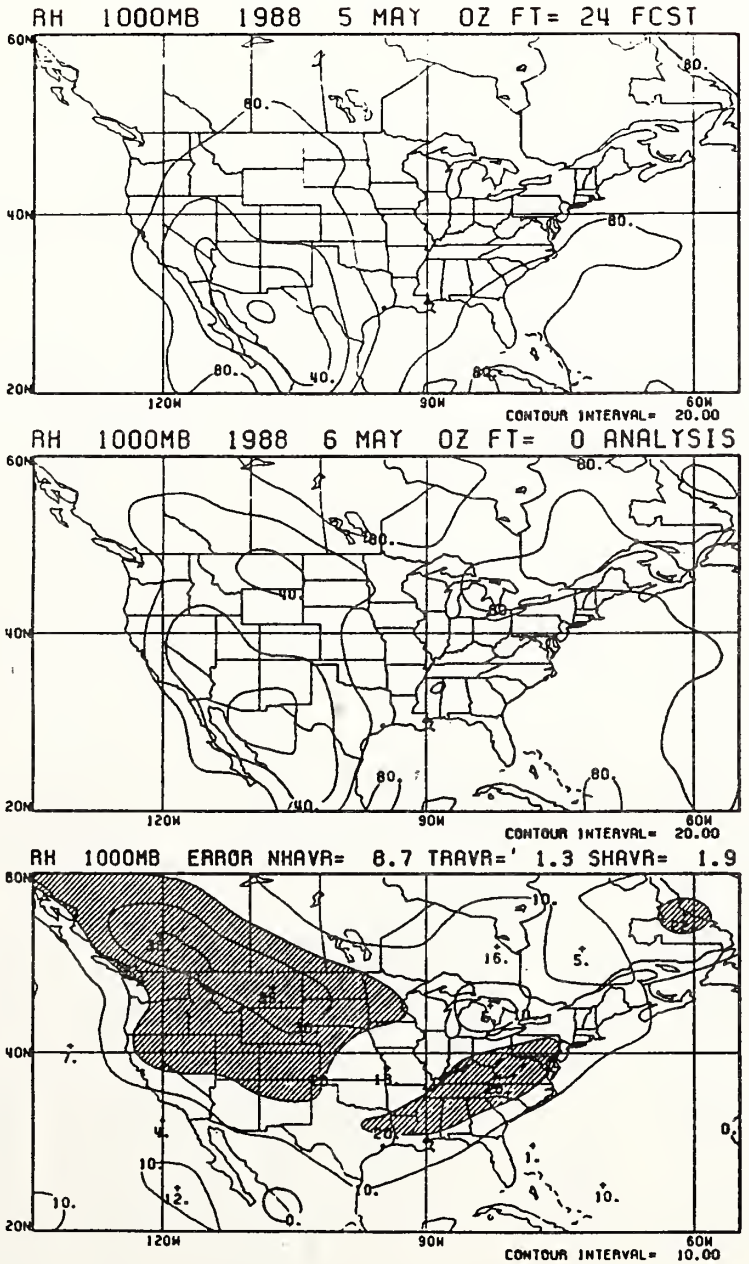
RH 1000MB 1988 5 MAY 0Z FT= 24 FCST
CONTOUR INTERVAL= 20.00
RH 1000MB 1988 6 MAY 0Z FT= 0 ANALYSIS
CONTOUR INTERVAL= 20.00
RH 1000MB ERROR NHAVR= 8.7 TRAVR= 1.3 SHAVR= 1.9
CONTOUR INTERVAL= 10.00

Fig. 1a. Relative humidity at 1000 mb: top - 24-hour operational forecast; middle - verifying analysis; bottom - error(forecast-analysis), values over 20% are shaded (Case of May 5, 1988).

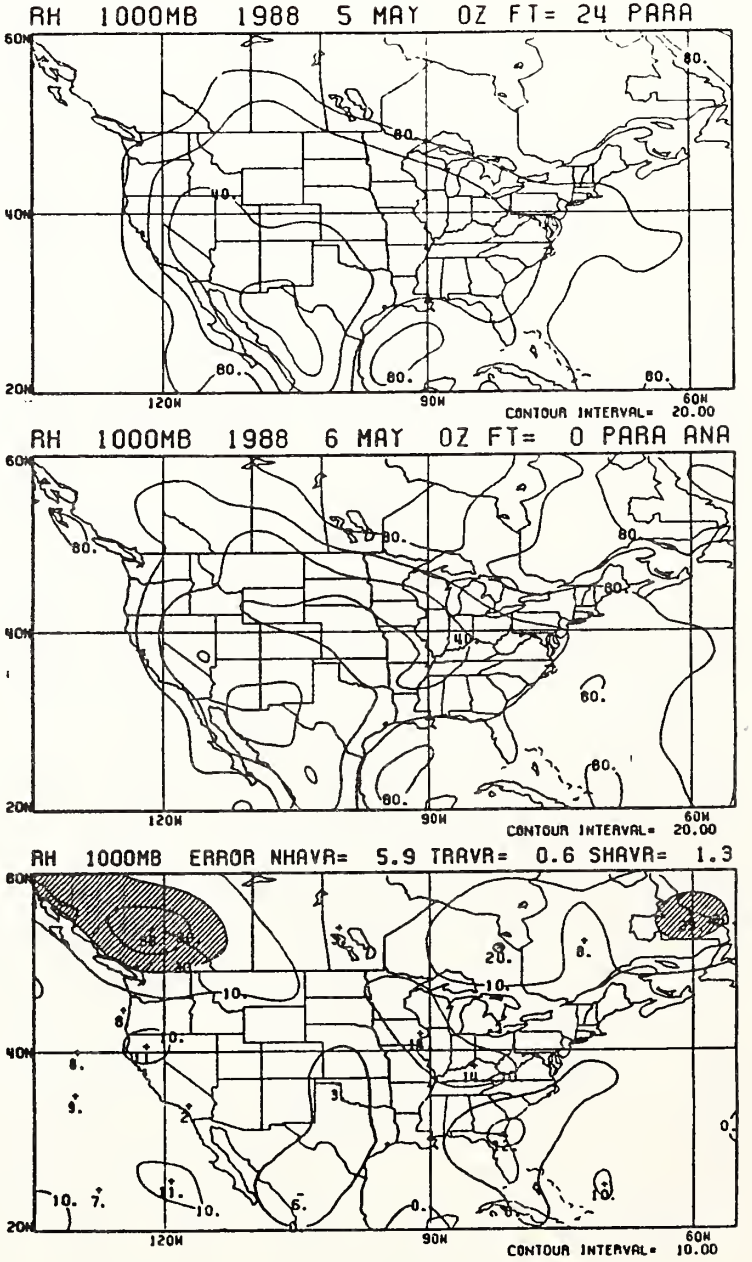
RH 1000MB 1988 5 MAY 0Z FT= 24 PARA
CONTOUR INTERVAL= 20.00
RH 1000MB 1988 6 MAY 0Z FT= 0 PARA ANA
CONTOUR INTERVAL= 20.00
RH 1000MB ERROR NHAVR= 5.9 TRAVR= 0.6 SHAVR= 1.3
CONTOUR INTERVAL= 10.00

Fig. 1b. As in Fig. 1a, but for new surface evaporation formulation.

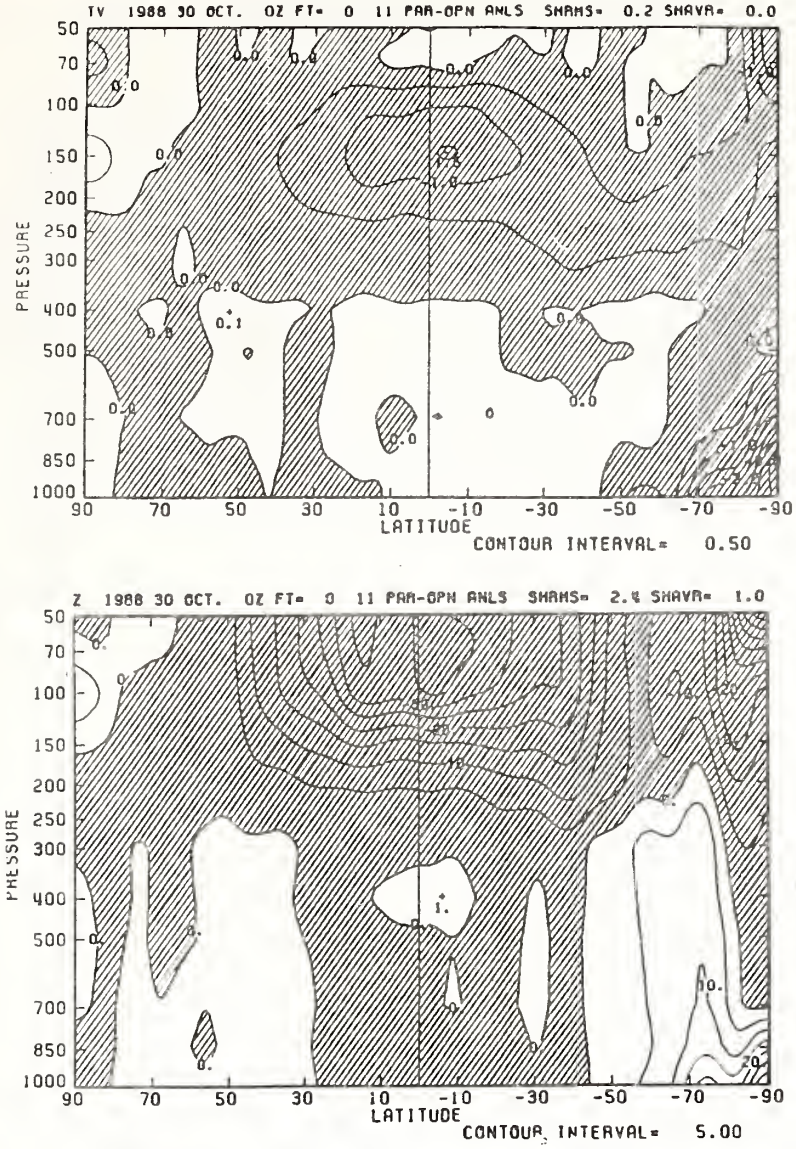
TV 1988 30 OCT. OZ FT= 0 11 PAR-OPN ANLS SHRMS= 0.2 SHAVR= 0.0
PRESSURE
LATITUDE
CONTOUR INTERVAL= 0.50
Z 1988 30 OCT. OZ FT= 0 11 PAR-OPN ANLS SHRMS= 2.4 SHAVR= 1.0
PRESSURE
LATITUDE
CONTOUR INTERVAL= 5.00

Fig. 2 Zonally-averaged cross sections for eleven cases in October, 1988, showing differences between analyses (new - old) for virtual temperature (top, contour interval 0.5C) and geopotential height (bottom, contour interval 5m). Negative values are shaded.

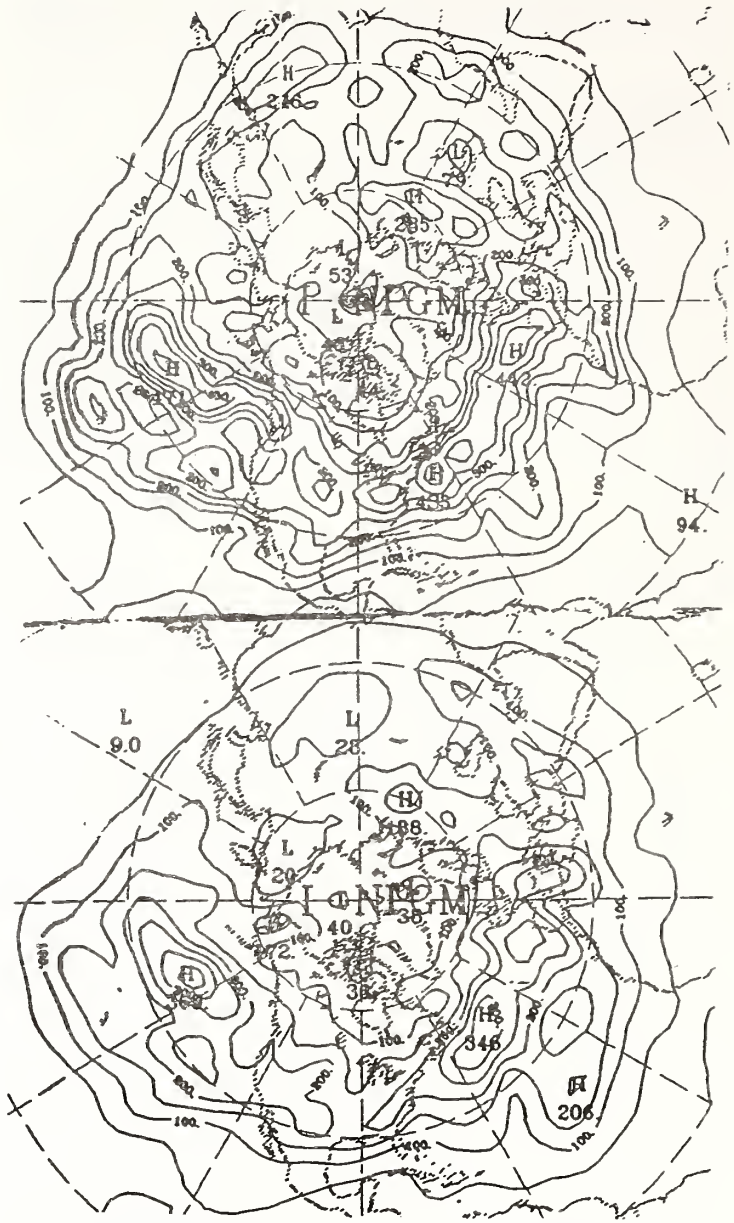

Fig. 3 Transient eddy kinetic energy for initial conditions (top) and for five-day forecasts (bottom) verifying in January, 1988 (contour interval 50m^2/sec^2).

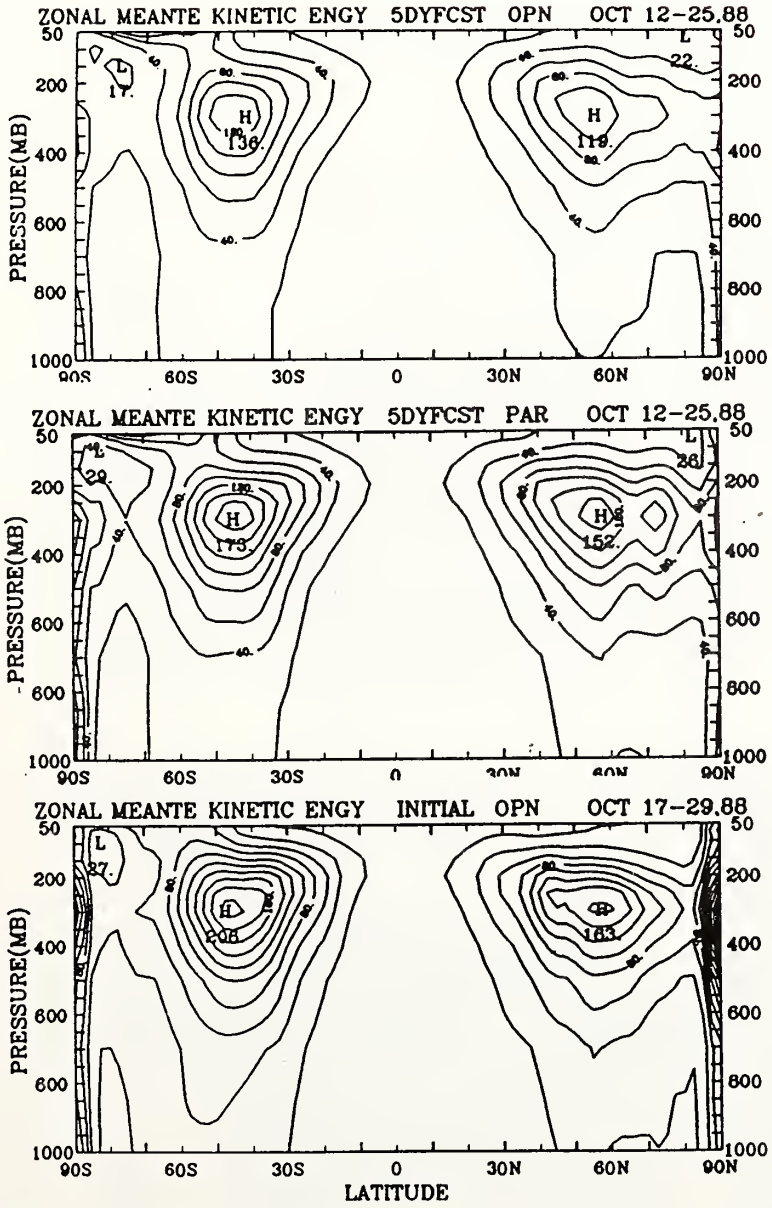

Fig. 4 Zonally averaged transient eddy kinetic energy for 13 five-day forecasts produced by the old model (top) and the new model (middle), to be compared with the verifying initialized analyses (bottom). Contour intevals are $20m^2/sec^2$.

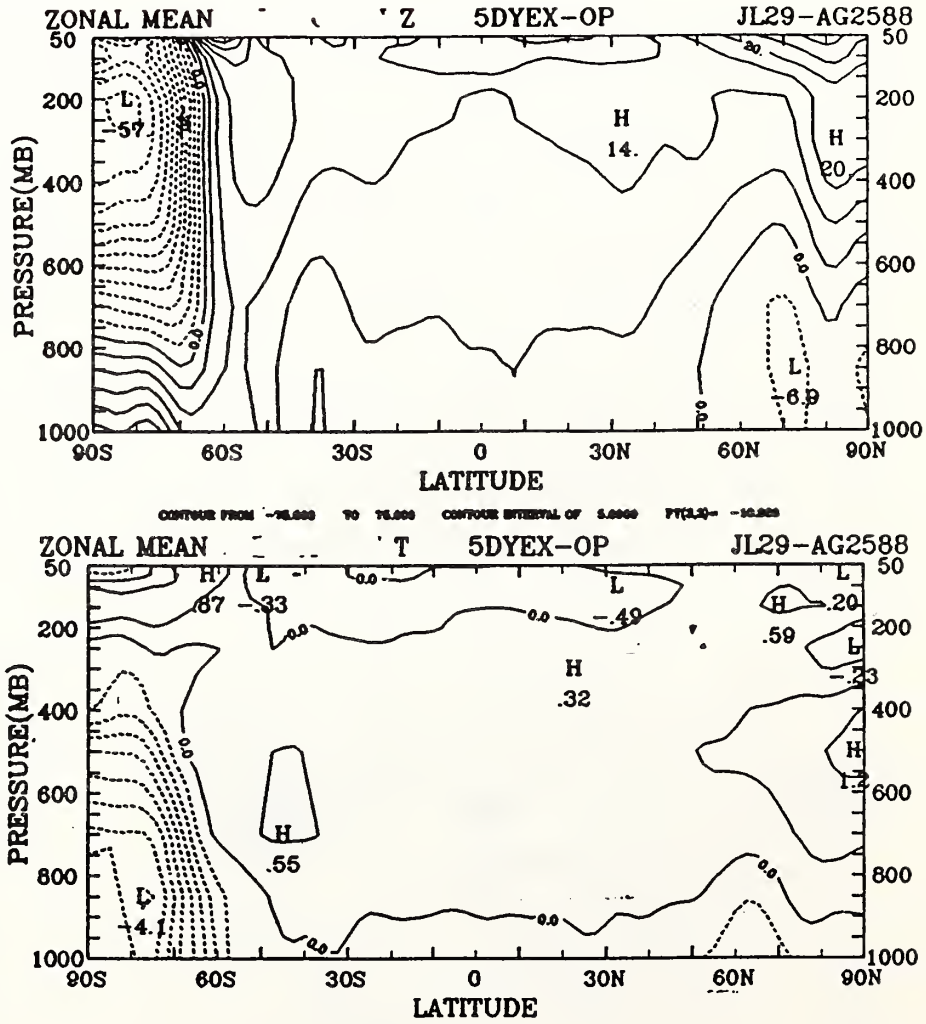

Fig. 5 Zonally-averaged vertical cross sections showing differences in geopotential height (top, contour interval=5m) and temperature (bottom, contour interval=0.5C) for 27 five-day forecasts, new diffusion - old diffusion.

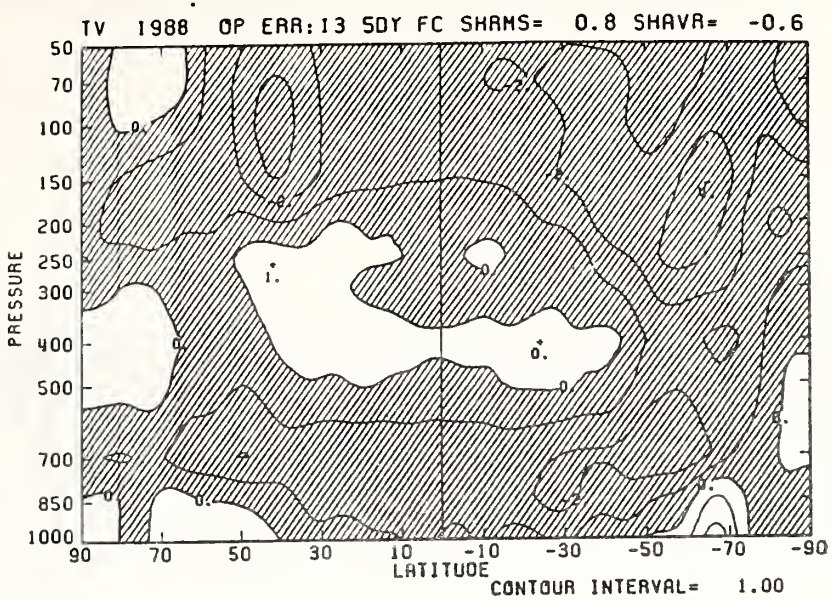
TV 1988 OP ERR:13 SDY FC SRMS= 0.8 SRVR= -0.6
PRESSURE
LATITUDE
CONTOUR INTERVAL= 1.00

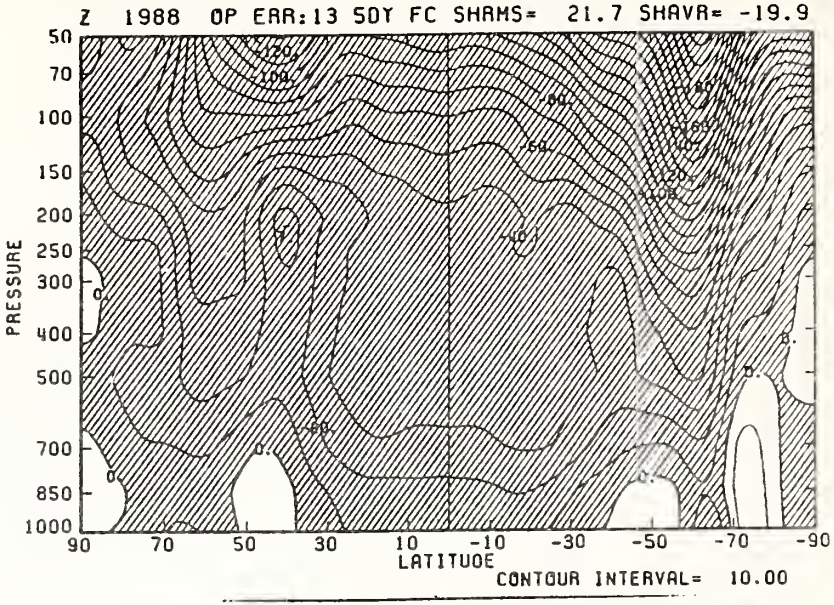
Z 1988 OP ERR:13 SDY FC SRMS= 21.7 SRVR= -19.9
PRESSURE
LATITUDE
CONTOUR INTERVAL= 10.00

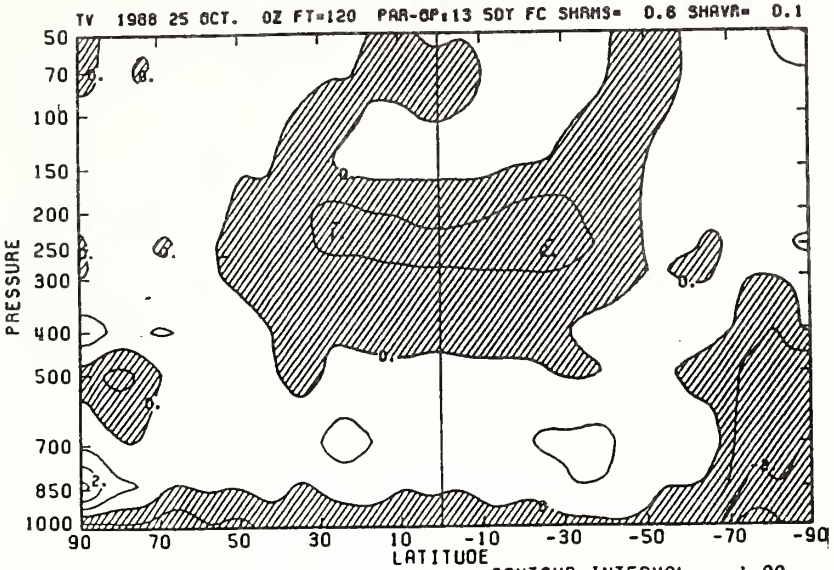
TV 1988 25 OCT. OZ FT=120 PRR-OP:13 SDY FC SRMS= 0.6 SRVR= 0.1
PRESSURE
LATITUDE

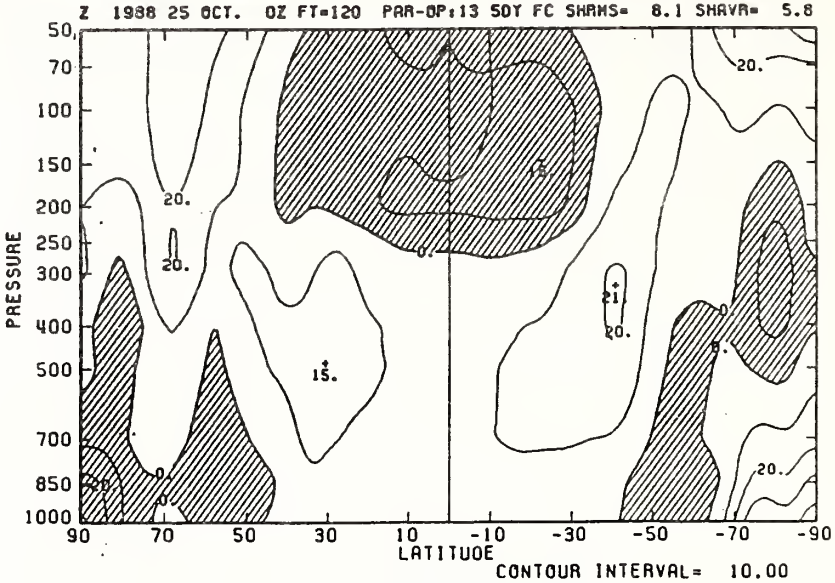
Z 1988 25 OCT. OZ FT=120 PRR-OP:13 SDY FC SRMS= 8.1 SRVR= 5.8
PRESSURE
LATITUDE
CONTOUR INTERVAL= 10.00

Predictability of low frequency modes

T.N. Krishnamurti

Department of Meteorology
Florida State University
Tallahassee, Florida 32306

Observations during the FGGE year and subsequent to that for the recent 8 year period have clearly shown the presence of low frequency motions on the time scale of roughly 30 to 50 days. There are several regional and global aspects of these oscillations that have been emphasized in recent literature. Among these we shall be addressing the following four observational aspects of low frequency motions.

a) Meridionally propagating 30 to 50 day waves in the lower troposphere of the monsoon region. This is a family of trough-ridge systems that can be seen as the streamline-isotach charts of the time filtered motion field. The passage of a trough or a ridge line over central India generally coincides with the occurance of a wet or a dry spell respectively. The meridional scale of this system is roughly 2000 to 3000kms. The speed of meridional motion is roughly 1° latitude/day. During certain years, the meridional motion and passage of these systems during the summer monsoon season is quite regular while over other years the motion is somewhat irregular. The reasons for this type of interannual behavior are not quite clear at the present time.

b) Zonally propagating planetary scale divergent circulations on this time scale. These seem to have a dominant scale of wave numbers 1 and 2. They traverse the globe, from west to east, in roughly 30 to 50 days. The largest amplitude is in the equatorial latitudes. The divergent circulations have a large meridional extent, the east-west circulations can be seen even as far as 35°N and 30°S. These broad divergent circulations appear to be related to equatorial and monsoonal heat sources and sinks. The interannual variation of these eastward propagating waves has also been studied and one finds that the propagations have been somewhat irregular during several recent years.

c) An important aspect on this time scale is the air-sea interactions. We have recently examined the oceanic fluxes of sensible and latent heat on this time scale. When fluxes are calculated using the so-called 'surface similarity theory', the basic variables are the SST, the surface wind, the temperature and humidity at the top of a constant flux layer. The similarity fluxes are defined from expressions that invoke the Monin-Obukhov length and a non-linear coupling of the momentum, heat and moisture. Because of this non-linear coupling, one can diagnose the relative importance of the low frequency variations of SST, surface wind, air temperature and humidity and assess their role in the contribution to fluxes on this time scale. A detailed diagnostic study was recently completed by Krishnamurti et al (1988). It was found that the latent heat flux on the time scale of 30 to 50 days can be as large as 10 to 20 watts/m^2, which was about 5 to 10% of the total flux over the Indian and Pacific oceans. It was also noted that wind variations on this time scale were very important contributors; next in line were the contributions from SST variations on this time scale. The variations in air temperature and humidity were relatively less important. Although the amplitude of SST variation was only of the order of 0.8 to 1°C on the time scale, that coupled with wind variations of the order 3 to 5 ms^{-1} contributed to significant latent heat fluxes, i.e., $\approx$ 10 to 20 watts/m^2. The sign of these low frequency fluxes are preserved for a couple of weeks, thus their role can become significant.

d) The maintenance of low frequency modes has been addressed via detailed computations of energetics in the frequency domain using daily globally analysed data sets over many years. These studies are somewhat analogous to the estimates on energetics in the zonal wave number domain. In the latter approach, one speaks of kinetic energy exchanges from zonal flows to eddies of certain scales, and of waves to waves via nonlinear interactions. The other important interactions in the wave number domain are those from potential to kinetic energy for fixed zonal wave numbers. In the frequency domain, analogous selection rules govern the exchanges of energy. Here, one can visualize a breakdown among long term mean, low frequency and high frequency motions. In a frequency domain, the kinetic to kinetic energy

exchanges can occur among long term time mean flows and other frequencies, or among triads of frequencies (analogous to the wave number domain). The potential to kinetic energy exchanges are restricted to occur the same frequencies.

The results of these energetics calculations performed by Sheng (1987), show that the kinetic energy of low frequency modes on the time scale of 30 to 50 days are maintained by the following processes:

i) They receive a substantial amount of kinetic energy from high frequency modes,
ii) They lose kinetic energy to the long term time mean flow
and iii) they receive a smaller amount of energy from the potential energy on the same frequencies.

The above observational findings were important for our design of experiments to increase the predictability of low frequency modes.

In this context, we should mention some results on the predictability of low frequency modes from long term integration of a global model. Dr. William Heckley, of the ECMWF, examined the presence (or absence) of the monsoonal low frequency modes from several ensembles of predicted data for the FGGE period. The zero day ensemble of 365 days is a string of the initialized FGGE data. This string, as to be expected, contained the meridionally propagating low frequency modes. However, as the strings of the ensemble of 1, 2, 3, 4 and 5 day forecasts were examined, in this context, it was noted that the low frequency modes were lost by about day 5. The conclusion was drawn that the global model has a predictability, for the low frequency modes, of about 4 days.

We feel strongly that this loss of predictability for the low frequeny modes is largely due to the errors the model makes in the prediction of the higher frequency motions. These, in turn, contaminate the low frequency modes by the transfer of errors in these energy exchanges.

The aforementioned observations and ideas were useful in the design of a class of long term integration experiments in order to extend the predictability of low frequency modes.

Specifically, we designed the following experiments:

a) A control experiment with a comprehensive global spectral model (Krishnamurti et al 1989). The model was initialized using nonlinear normal mode initialization using global data for July 31 1979 (1200 UTC). This experiment included an annual cycle of SST. A 270 day integration was carried out starting from that day.

b) A low frequency mode experiment where the initial state was obtained as follows.

i) A time mean state was obtained for all variables at all vertical levels using the data sets for a 120 day period preceding the initial date (i.e., July 31 1979 12UTC).

ii) A low frequency mode for the initial date, this was based on the data sets for the same preceding 120 day period.

iii) SST anamolies on the time scale of 30 to 50 days. These were updated during the course of integration. This data is described in Krishnamurti et al (1988). In order to enhance the response for the model resolution, the anamolies were multiplied by a factor of two.

iv) A long term averaged annual cycle of SST that varies from month to month. (The same fields were also used in the control experiment).

The premise here being that if the high frequency modes are filtered out from the initial state, the contamination for the energy transfers as errors grow could be reduced, thus we might extend the predictability of low frequency modes. The retention of the time mean state and the SST anamolies was to provide some of the other important energy sources for these low frequency modes.

The results of these experiments were quite successful to about 30 days, after which the energy exchanges grew quite large as high frequency motions evolved. The main results of these experiments were as follows:

a) The control experiment failed to predict meridional motion of low frequency modes. The anomaly experiment was quite successful. The meridionally propagating low frequency modes of the lower troposphere over the Asian monsoon region were very accurately predicted for the first 30 days. The occurance of a dry spell over central India in the middle of August was well predicted. The amplitude of the low frequency mode was somewhat underpredicted, however, the phase errors were very small.

b) The eastward propagating planetary scale divergent wave at 200 mb was very reasonably predicted to almost 25 days in the anomaly experiment. The phase speed was very close to that based on obsevations. The control experiment failed to show an eastward motion of the divergent wave.

c) The energetics of the control revealed a large transfer of kinetic energy from the low frequency modes to the higher frequencies. That must be an important factor for the rapid collapse of predictability in the control experiment. In the anamoly experiment (where we had included a time mean state, a low frequency mode and the SST anamolies on the time scale of 30-50 days), the kinetic energy exchange was consistent with the observational results. This experiment was extended to 270 days. The energetics in the frequency domain were calculated for the 270 days of data and also from day 31 to day 270. As stated earlier, the predictability of the low frequency modes was good to about 30 days in this experiment. For the entire 270 day period, the kinetic energy exchange from the high to the low frequencies was positive, but greater than that for the period day 31 to day 270. This implies that the contributions from the first 30 days, for which the predictability was large, was consistent with the observational estimates. As the errors grow, the contribution to the energy exchange slowly reversed signs and the low frequency modes were contaminated.

In conclusion, the present approach simply delays the rate of contamination of low frequency modes, thus extending their predictability to almost one month. Eventually, higher frequency motions do form and the rate of contamination increases rapidly.

Further work is needed to assess the relative importance of the details of the time mean, the definition of the low frequency mode and the details of the SST anamolies in the increase of predictability of low frequency modes. Further experimentation is needed to predict the irregular behavior of low frequency modes, as was noted from the observations from some recent years. If such experimentation is successful in predicting the irregular behavior, then there is a need to diagnose the importance of the aforementioned input parameters.

This approach may hold much promise for predicting the dry and wet spells that are related to the passage of low frequency modes on the intraseasonal time scales.

Normal Mode Structure of the Transient Response of a General Circulation Model to Tropical Heating

Julia Nogues-Paegle and Weili Zhong
Department of Meteorology
University of Utah
Salt Lake City, Utah 84112

The general circulation model of the National Center for Atmospheric Research has been integrated for 10 winter cases to study the adjustment of the global atmosphere to an impulsively initiated tropical thermal forcing (Paegle et al, 1987, Monthly Weather Review, 115, 2975-2995). The integrations are carried out for 10 days and model output is saved in sigma coordinates for the initial .5, 1, 2, 3, 5, 7 and 10 day integration time. The experiments consist in adding a heating term to the thermodynamic energy equation in the region west of of Central America centered at 6.6°N and 105°W decaying with a Guassian profile with half width of about 15° in latitude and 30° in longitude, and a peak around 400 mb of 8°C/day. The ensemble average for day 10 shows a precipitation maximum over the heating region of 3.2 cm/day. The ensemble average response for the zonal wind at 200 mb exhibit maximum equatorial easterlies over the heating area, with westerlies to the east. Extratropical westerly response is found in both hemispheres, colocated in longitude with the regions of maximum heating.

This response is studied here by projecting model output onto the three dimensional eigenfunctions of a linearized primitive equation model. These functions are obtained by separating the unforced primitive equations linearized about a basic state at rest into vertical and horizontal structure equations. The vertical structure equation is solved by finite difference approximations while the Hough functions which are solutions of the horizontal structure equation are approximated as a series of associated Legendre polynomials (Kasahara and Puri, 1981, Monthly Weather Review, 109 37-51). The vertically varying basic state temperature is determined from the global average of temperature obtained from the ensemble average of the initial conditions. These basis functions are similar to those used in normal mode initialization.

The analysis is motivated by results which suggest that tropical heating tends to generate gravity waves, which may exhibit non-negligible energy for the case when the frequency of the forcing is of similar magnitude to that of the frequency of the free gravity waves (Errico and Rasch, 1988, Tellus, 40A, 1-25). Current data assimilating models used to interpolate atmospheric observations to regularly spaced grids make use of normal mode initializations which adjust the amplitude of these modes. This step is advantageous to remove meteorological noise resulting from observational limitations, but at the same time alters the observed characteristics of motions which result from

localized tropical heating. Therefore, meteorological archives of gridded data sets may not be suitable to study atmospheric motions resulting from tropical heating in areas with low data density where the first guess prevails. This first guess is usually obtained from short-term integrations and still exhibit the suppressed gravity wave energy of the initial state. In this instance, GCM integrations may be useful to quantify the level of gravity wave energy that may be excited by tropical heating.

The wind vector response averaged for all cases is shown in Figures 1 and 2. Its root mean square is plotted versus latitude for the original data before projection, and for contribution from different modes to the 200 mb wind response. Figure 1 shows the response to be confined mostly to tropical latitudes during the first 5 days integration time, while the extratropical response becomes apparent after 5 days. The extratropical response at day 10 is about 50% stronger than that of the internal Rossby response in the Northern (winter) hemisphere while it is closer to that of the internal Rossby response in the Southern (summer) hemisphere (Fig. 1 b and c). The Rossby modes appear to propagate meridionally at a speed of about 20° latitude per week. The internal gravity modes remain more confined to tropical latitudes than the Rossby modes, with peak values found about 20° north and south of the heating maximum. These peak values are about half the magnitude of the internal Rossby modes at similar latitudes. At the equator itself, the largest contributions are due to the Kelvin and mixed gravity-Rossby modes, with peak values at day 10 about half the value of the internal Rossby modes there. The mixed mode also exhibit non-negligible amplitudes in the external component, which, due to its larger meridional scale, impacts also in subtropical latitudes.

We have shown that latent heat release of magnitude and extent similar to those observed in single events of organized tropical convection excite structures like those of internal gravity-inertia modes in a general circulation model. The magnitude of these gravity modes are about 50% of those observed in the internal Rossby modes. To the extent that this GCM reflects atmospheric processes, these results indicate the necessity of adequately observing tropical circulations and of developing data assimilation schemes capable of incorporating this information in gridded data sets. This is particularly important for climate studies of tropical-extratropical interactions that rely on accurate global analysis. We have shown that for this GCM, the effect of a localized heating tropical source is felt in the extratropics in 5 days.

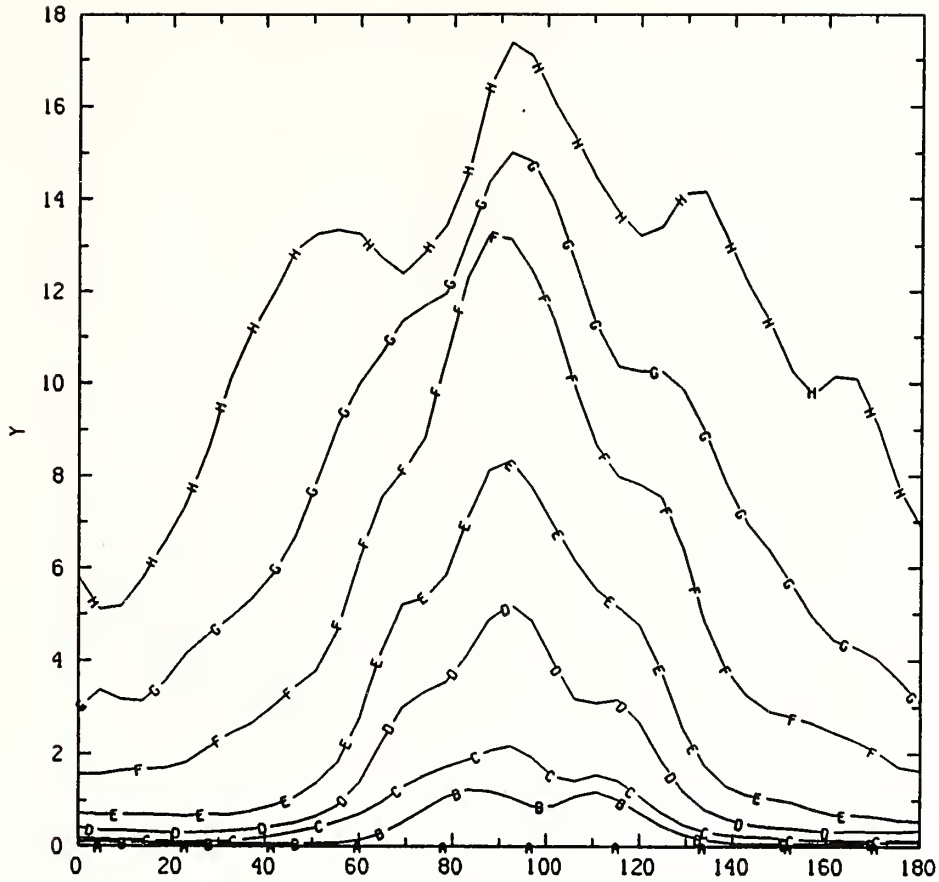

(a)

Figure 1. The square root of the square of the wind response at 200 mb averaged for each latitude

$$R^{1/2}(\psi) = \left(\frac{1}{10} \sum_{c=1}^{10} \frac{1}{2\pi} \int_{0}^{2\pi} \left| W^{c}_{exp} - W^{c}_{control} \right|^{2} d\lambda \right)^{1/2}$$

in m/s as a function of latitude +90°. Total values are shown in (a), contributions from external and internal Rossby modes are shown in (b) and (c) respectively. Lines labeled A through H indicate integration times of 12 hours, 1, 2, 3, 5, 7, and 10 days respectively.

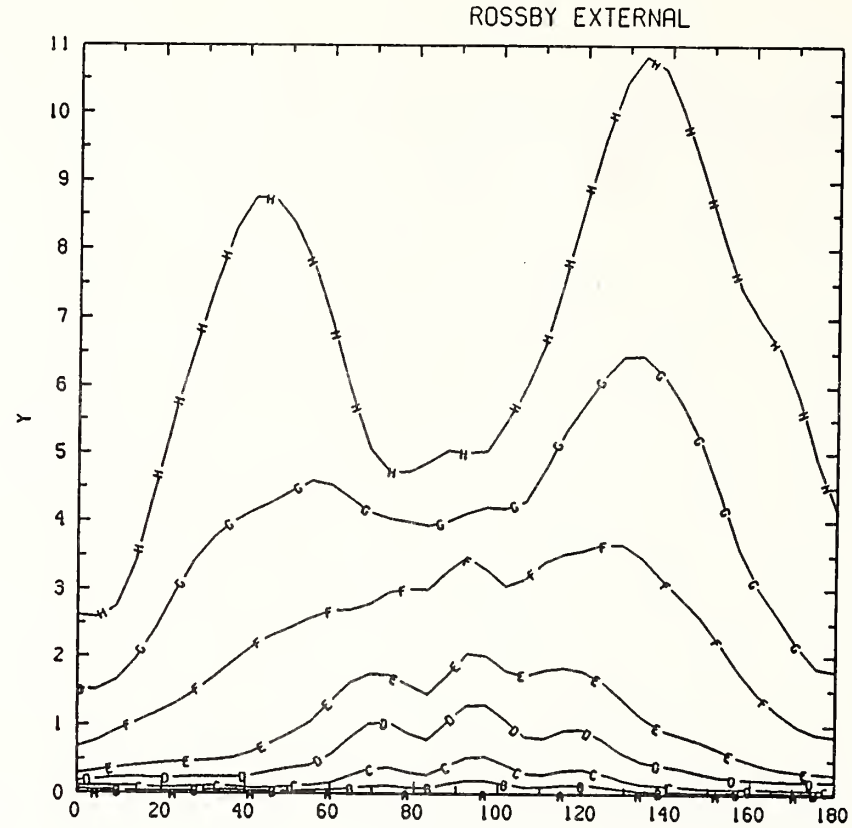

(b)

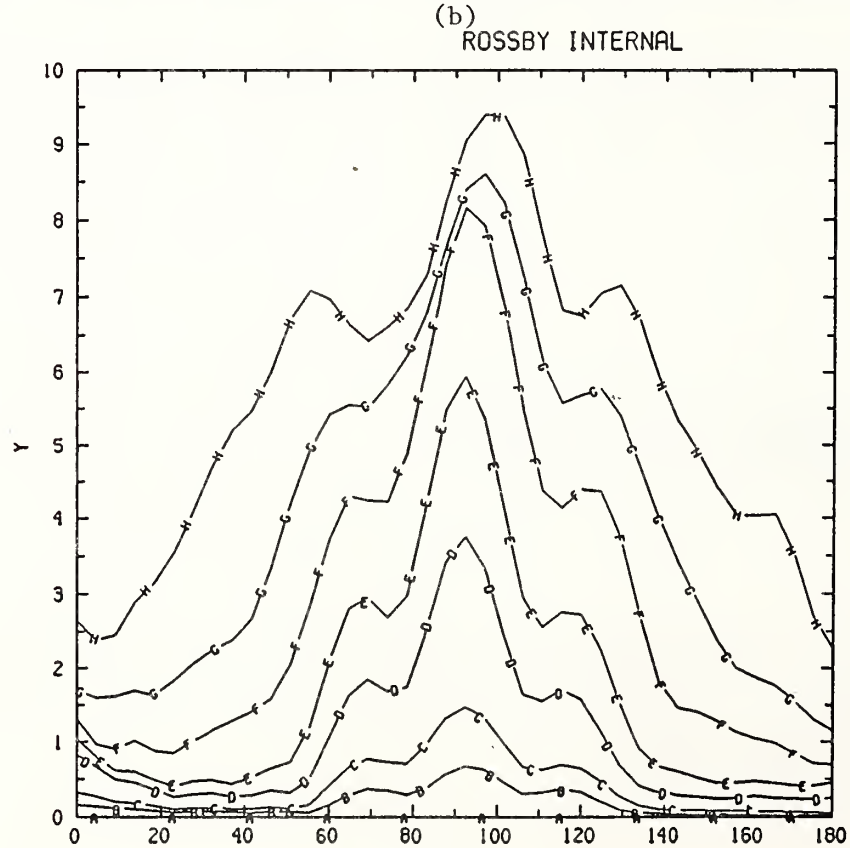

(c)

Figure 1. (continuation).

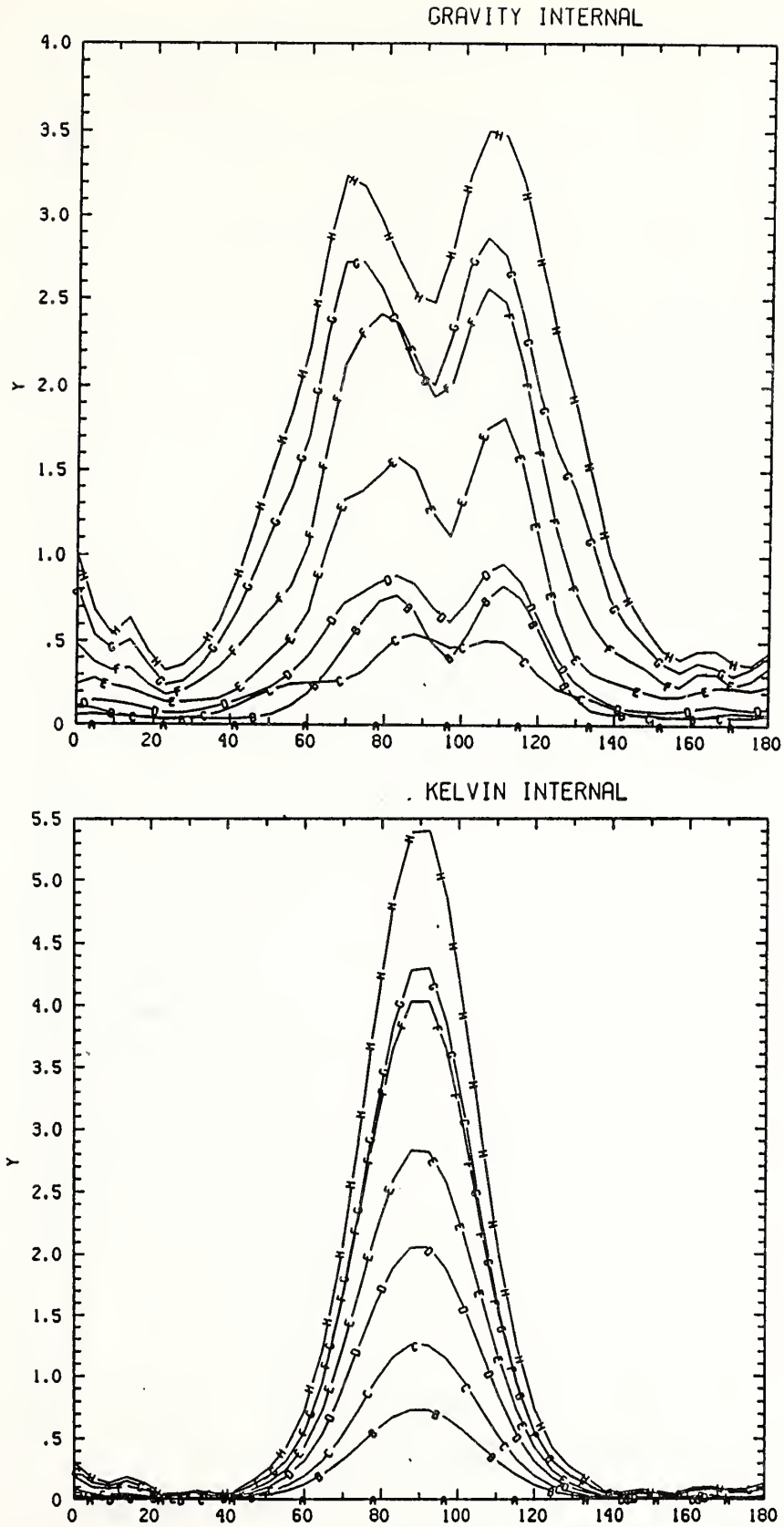

Figure 2. Same as Figure 1 but for contributions from gravity internal (a), Kelvin internal (b), and mixed gravity-Rossby modes external (c) and internal (d).

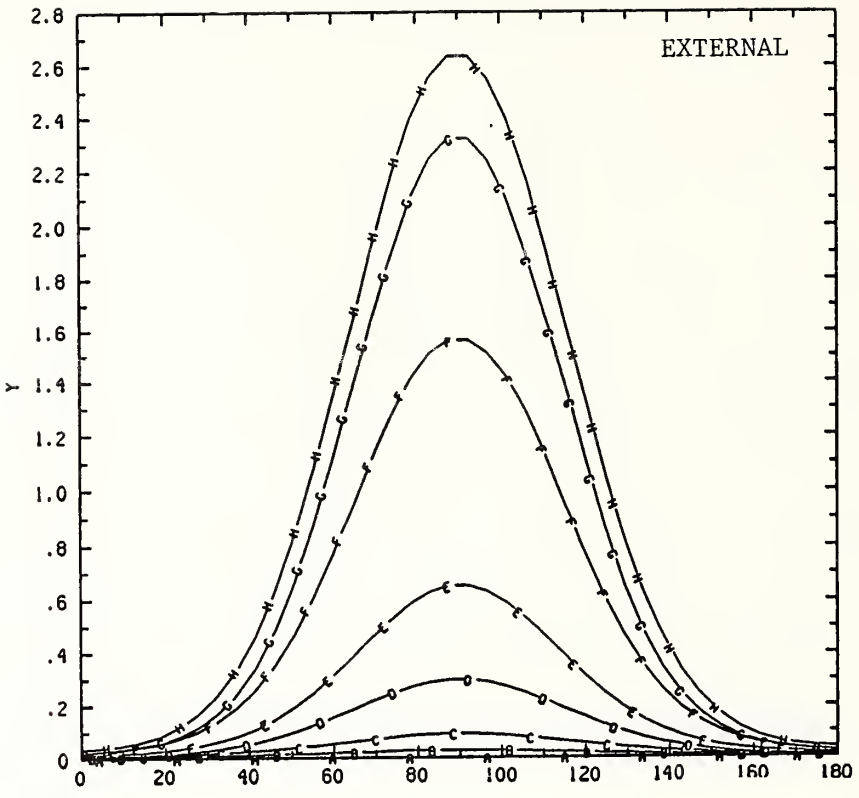

(c)

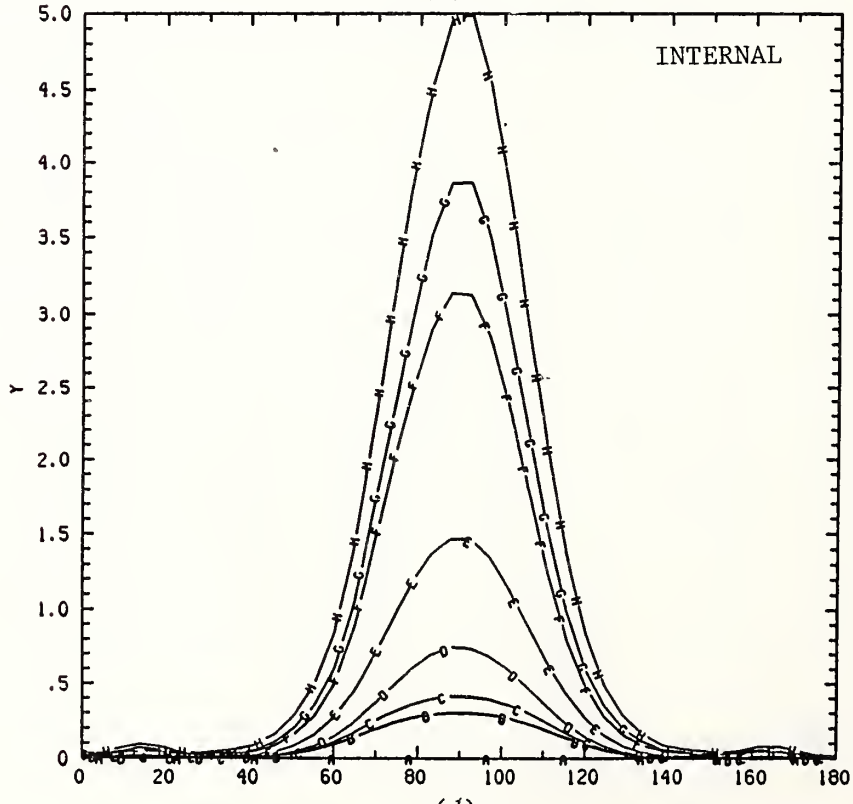

(d)

Figure 2. (continuation).

Estimate of Dynamical Predictability from NMC DERF Experiments

W. Y. Chen
NOAA/NWS/NMC/Climate Analysis Center
Washington, D. C. 20233

In this paper we have obtained the upper and low bounds of dynamical predictability for the NMC operational medium-range forecasting system. The data used are the NMC DERF Phase II experiments. Only the 500 mb height forecasts and their corresponding verifying analyses are used. Owing to the extended range integration, the upper bound of predictability can be estimated without resorting to any empirical model of error growth.

Following Lorenz' approach (1982), we first evaluate the error growth between pairs of prognoses with their initial states one day apart. The subsequent rms differences grow steadily for about a week before slowing down on about the 8th day and gradually approach saturation on about the 20th day. The rms differences for the small-scale eddies show growth with essentially the same rate to reach saturation. Therefore, the later stage slow growth rate appears to result mainly from the large-scale eddies. We divide the DERF Phase II period into 3 equal time segments and repeat the error growth calculations. All three show essentially the same feature as shown in Fig. 1, suggesting that the statistics obtained are rather stable intraseasonally.

The limits of dynamical predictability (defined here as the time the rms difference reaches 98 percent of its saturation level) for various magnitudes of initial data error are then determined. Their relationship appears to be linear, as shown in Fig. 2. Based on this feature, we obtain the upper bound of predictability for an infinitesimal initial resolvable data error, as shown in Fig. 3. The lower bound of predictability is then obtained, with proper adjustment for the systematic drift of the model atmosphere. The skill level obtained is much below its potential, leaving considerable room for further improvements. An attempt is made to estimate the possible contribution to extending the predictability by reducing the initial data uncertainty and improving the model. At the rms error level that equals the climatological standard deviation (about 100 m), the results indicate that, if we keep improving the model until it is perfect, we might be able to obtain 10-day forecasts as skillful as the current 6-day forecasts. On top of that, if we were able to reduce the initial resolvable data error to infinitesimally small, we could stretch another 4 days to about 14 days. These estimates appear to be in excellent agreement with the recent assessment of Lorenz (1984) using the ECMWF model data. The useful forecast intervals for time averages (not investigated in this article) are reported to be longer than those of instantaneous events (Roads, 1986). The predictability is also known to depend on flow regimes (e.g., Palmer, 1988) and long-lived anomalous forcings (e.g., Shukla, 1983). Due to the limitation in scope with this DERF experiment, these issues have not received their deserved attention in this article.

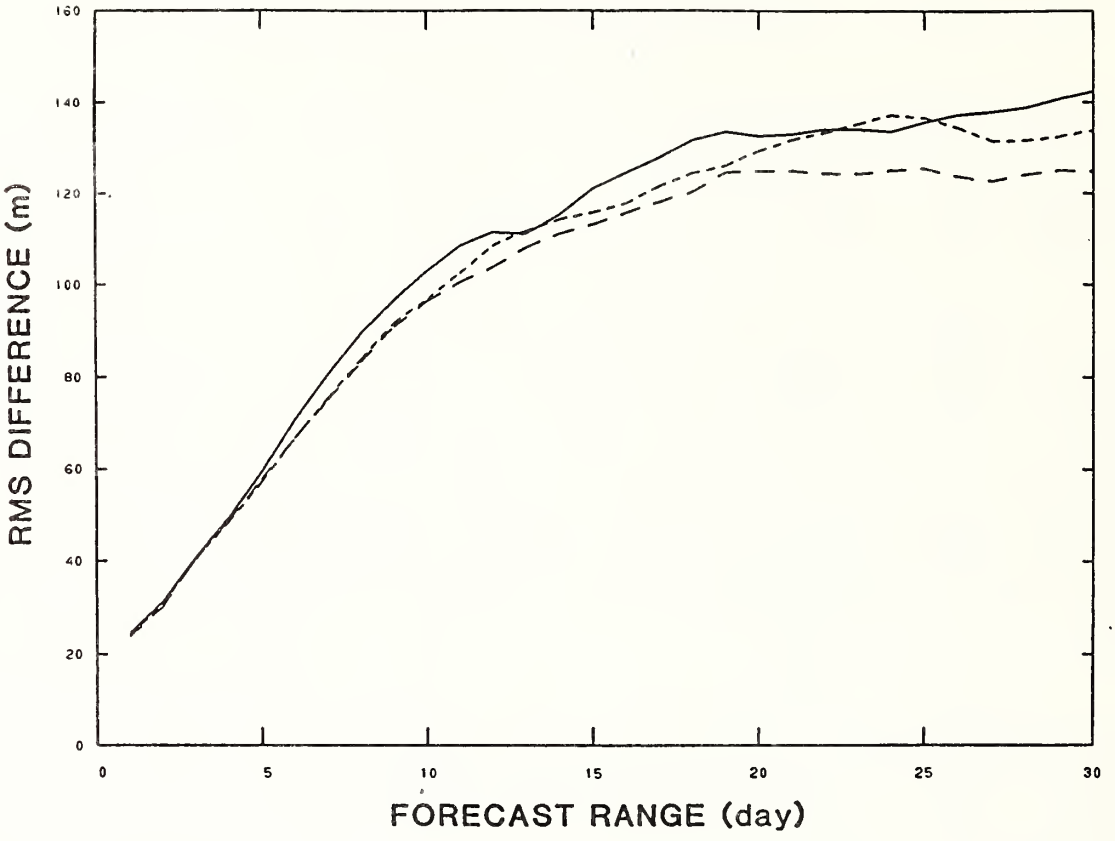

1. Growth of difference between two series of forecasts with their initial states one day apart. The DERF experiments are divided into three equal time segments for the purpose of seeing how stable intraseasonally the statistics are. The solid curve is obtained from the first time segment and the long dashed curve the last segment.

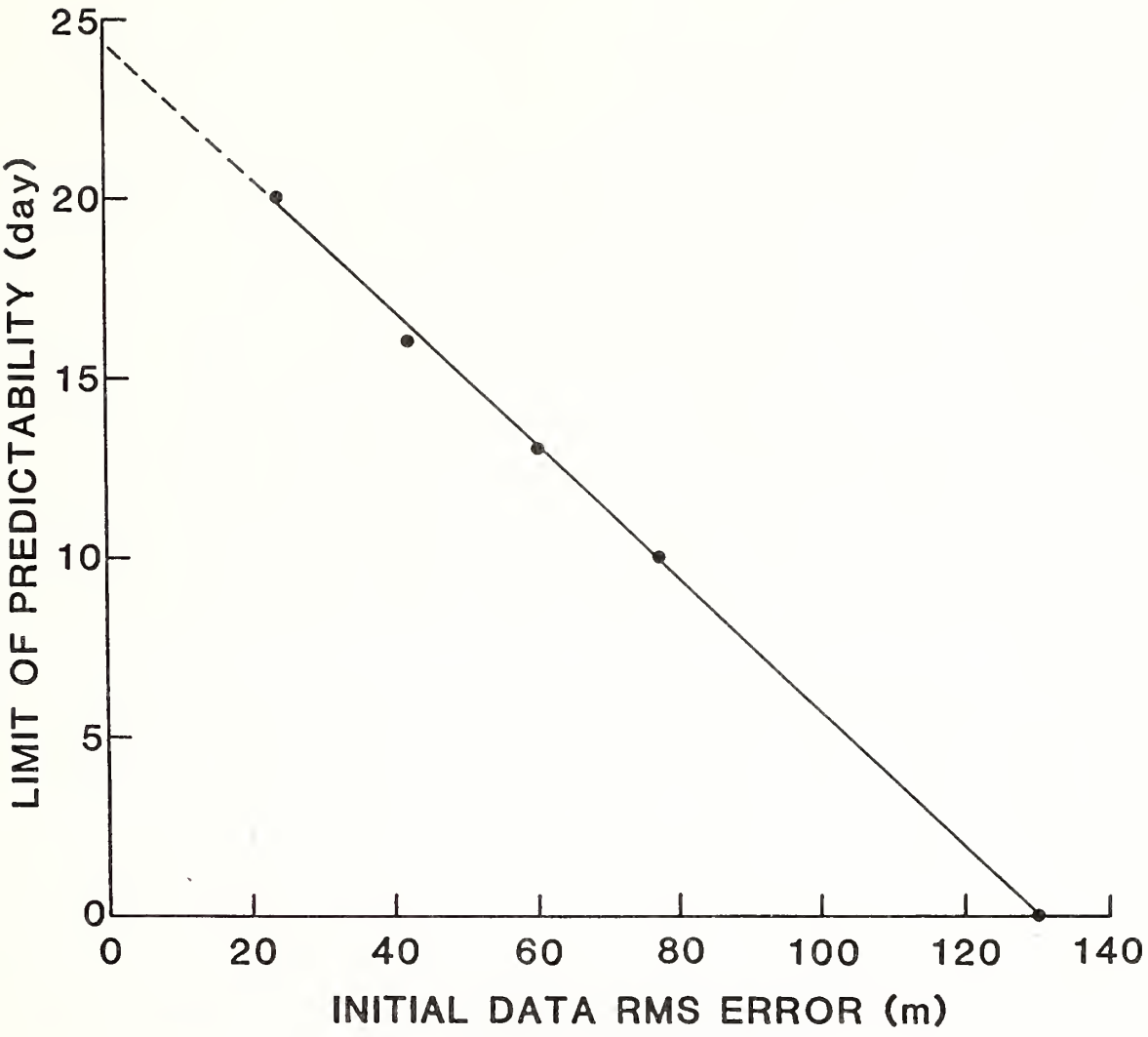

2. Initial data error versus limit of predictability. The dashed line is the extrapolation of the solid line which is a linear fitting of those solid circles. The intersept at infinitesimal initial data error represents the estimate of the ultimate limit of predictability.

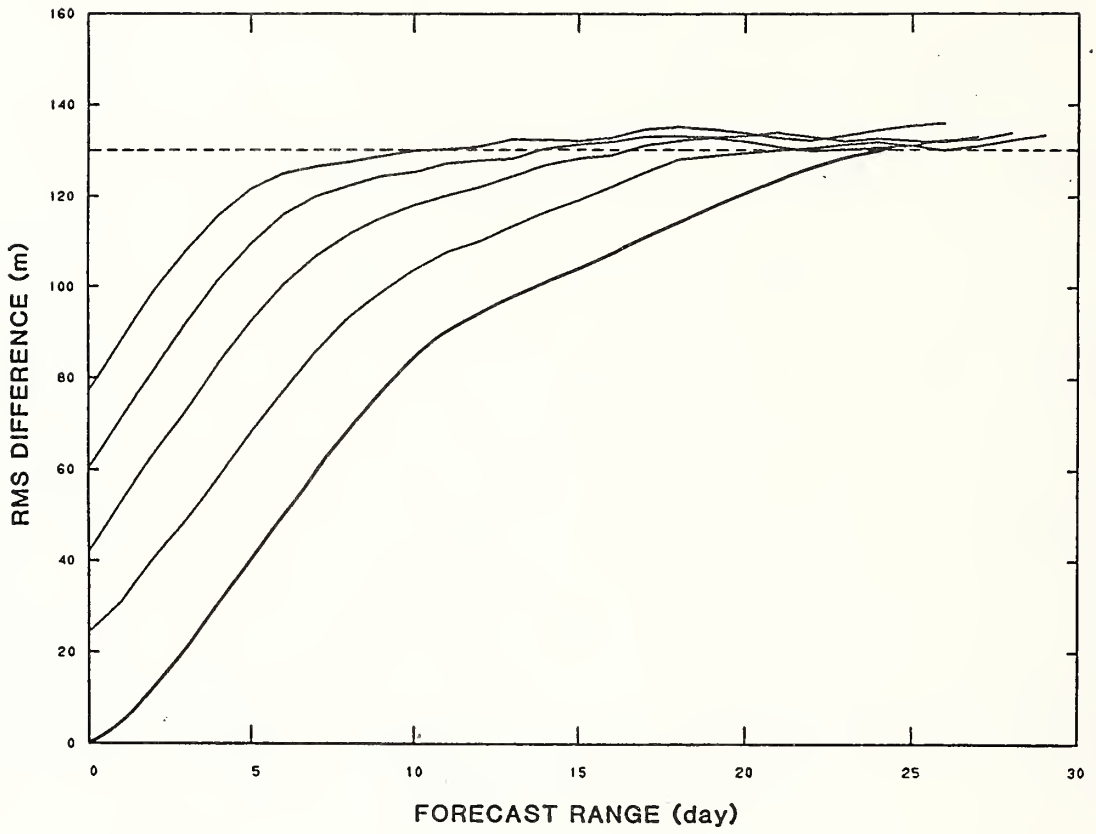

3. The estimate of upper bound of predictability for an infinitesimal initial data error, shown here as the bold faced curve.

Anomalous Climatological Background for some Explosive Storms (BOMBS)

by Jerome Namias
Climate Research Group
Scripps Institution of Oceanography
La Jolla, CA 92093

It is generally believed that abnormal mean circulation patterns on a monthly or seasonal time scale are merely the cumulative result of the component cyclones and anticyclones. Indeed the classical work of Starr showed that the required fluxes of momentum, heat and water vapor are provided by the ensemble of synoptic scale vortices. While this concept is undoubtedly true, it does not explain the abnormal sources, tracks, frequencies and intensities of these systems. While the latter topic has not yet been satisfactorily answered, it is probable that particular ensembles of cyclones and anticyclones are generated and maintained in complex ways by external anomalous boundary influences as well as by internal atmospheric anomalies. Based upon numerous empirical studies, it appears that mean monthly or seasonal patterns (low frequency events) underpin these variations, and it is the anomalous mean patterns which bring about the peculiar distribution of storms- not the other way 'round. Of course, cyclones and anticyclones then operate to manufacture the general circulation.

Thus explosive cyclonic storms, called BOMBS, are frequently preceded by mean circulation patterns which are stable for periods of a month or more and provide a set-up for the extreme events. These quasi-stationary circulation patterns make possible the deployment of air masses with large anomalies of temperature and humidity into specific areas and thereby encourage cyclone intensification. This is accomplished by generating intense baroclinic zones and in altering sea surface temperatures in such a way as to increase the atmospheric contrasts in the potentially vulnerable area.

Three cases of well-documented explosive storms are described to illustrate the above points:

1. the record-breaking North Atlantic cyclone of December, 1986 analysed by Burt (1987, WEATHER)

2. the October 15-16, 1987 severe wind storm over Southern England described in WEATHER, March 1988.

3. The January 17-18, 1988 east Pacific and West Coast storm analysed by Cayan et al (Cal, Shore & Beach Preservation Association, 1988).

Figs. 1 to 4 pertain to the climatological background for the month preceding the first case, Figs. 5 to 10 to the second case, and Figs. 11 to 13 pertain to the 3rd case. It is important to note that in each case atmospheric teleconnections from remote areas reinforced the negative anomalies in the storm-prone areas. It is also noteworthy that prevailing air-sea interactions provided an SST anomaly field in the vulnerable area which enhanced the overlying atmospheric baroclinicity.

This material provides the basis for a theory that short period climatological fluctuations are not merely the result of ensembles of anomalous cyclone and air-mass occurrences, but are in fact the instigators of these synoptic scale developments. Aside from its scientific importance, this concept makes possible an early alert as to the probability of BOMBS though not their exact positions or timing. Perhaps more exact solutions will follow from further empirical research and numerical modelling.

LEGENDS

Fig. 1 Atlantic surface analysis at 00 GMT on 15 December 1986, showing depression track (Low W) and central pressure (mbar) during the preceding 30 hours. The track and central pressure of Low V until incorporation with Low W is also shown. The isobars are drawn every 4mbar.

Fig. 2 700mbar height anomalies (in meters) for the period 11 November to 11 December 1986, preceding the explosive storm. Note the general pattern, that when amplified, could easily produce the storm indicated in Fig. 1.

Fig. 3 Teleconnections (cross-correlations) between 700mbar height anomalies at selected points (solid circles) and all other points in a 5° x 5° grid over the Northern Hemisphere, from winter seasonal means, 1947-72. Note that teleconnections of anomalies remote from the area of the great storm shown in Fig. 1 enhance the probability of abnormally low mid- tropospheric heights in the vulnerable area.

Fig. 4 Sea surface temperature anomalies (° C) for the period 5 to 20 December 1986, essentially preceding the explosive storm (earlier mean charts for preceding two-week periods are very similar). Note the strong SST anomaly gradient in an area which would contribute to the atmosphere's baroclinicity and help develop the strong cyclone.

Fig. 5 Mean 700mbar contours (meters) for the period 12 September to 12 October 1987, preceding the great storm of 15-16 October.

Fig. 6 700mbar height anomalies (meters) for the period mid- September to mid-October, 1987 (from Long Range Prediction Group, National Meteorological Center, U.S. National Weather Service). Note the large scale negative anomaly in the vicinity of Great Britain which when amplified could imply the probability of a big storm.

Fig. 7 Teleconnections (cross-correlations) between 700mbar height anomalies at the key point 45° N, 85° W (solid circle) and all other points in a 5 x 5 grid over the Northern Hemisphere, from months of autumns of the period 1947-72. Note remote teleconnections to other anomalies which would help enhance the low height anomalies over England.

Fig. 8 Composite 700mbar height anomalies (meters) for the autumn maps which had anomalies similar to Fig. 2 in the areas of the eastern Pacific, North America, the Western Atlantic, central Atlantic, and Northern Russia. The domain in the vicinity of England and the Mediterranean has been purposely omitted.

Fig. 9 Sea surface temperature anomalies (° C) for September, 1987 (upper) and for the period 5-20 October, 1987 (lower). Note the pronounced temperature gradient in the eastern North Atlantic which could enhance the atmospheric baroclinicity and assist in the development of one or more big storms.

Fig. 10 Teleconnections from the key point 60° N, 10° W shown as a major anomaly center on the mean chart for mid-September to mid-October shown in Fig. 2. Note that an anomalous trough does not usually extend southward from England, thus implying that the SST gradient shown in Fig. 9 was probably important for the trough and the strong cyclone development.

Fig. 11 Weather maps showing the track and devlopment of the BOMB of 17-18 January, 1988 described by D. Cayan, et. al.

Fig. 12 700mbar height anomalies for the monthly period preceding the BOMB shown in Fig. 11. Note extensive areas of indicated anomalously low heights in the area where the storm would develop.

Fig. 13 Teleconnections from the strong anomalies remote from the vulnerable storm area (see Fig. 12). Note that these imply a probability of strong storm development in the afflicted area.

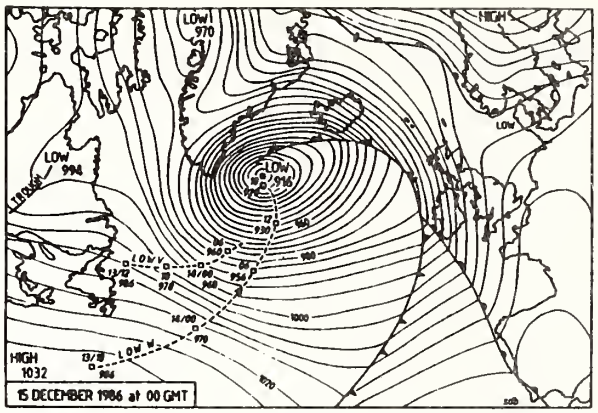

Fig. 1

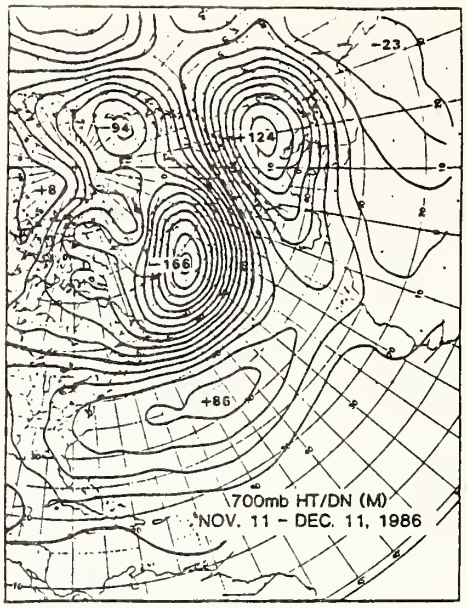

Fig. 2

WINTER TELECONNECTIONS

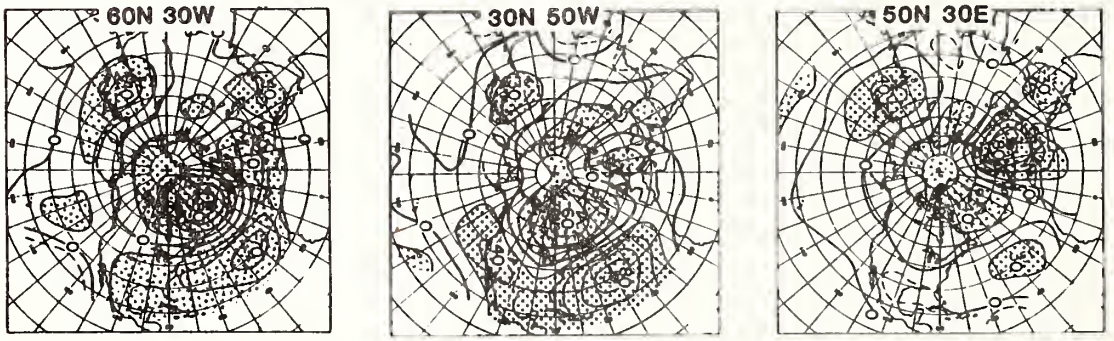

Fig. 3

SST ANOMALIES (°C) DEC. 5 - 20, 1986

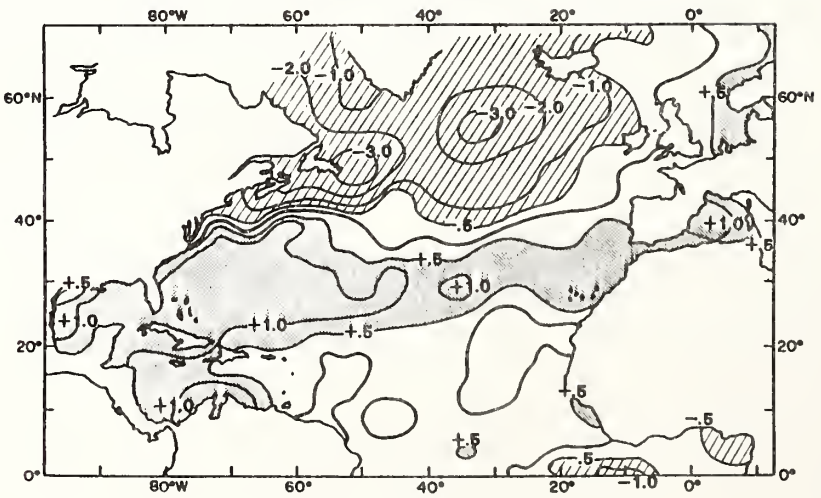

Fig. 4

Fig. 5

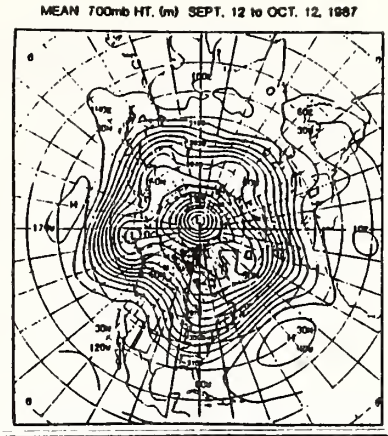

Fig. 6

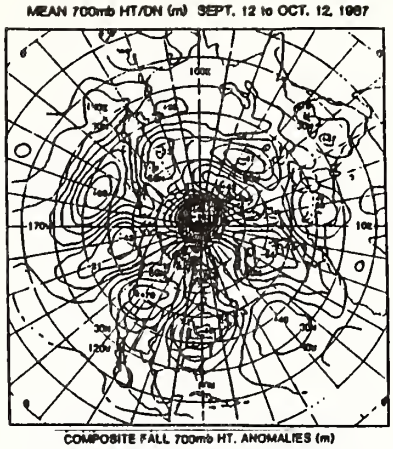

Fig. 7

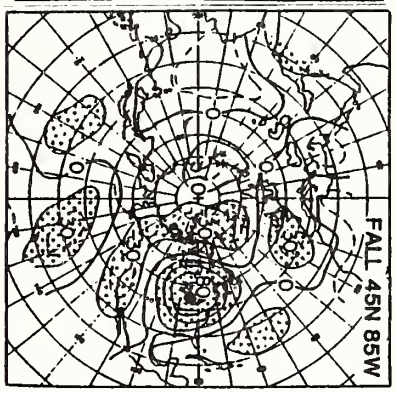

Fig. 8

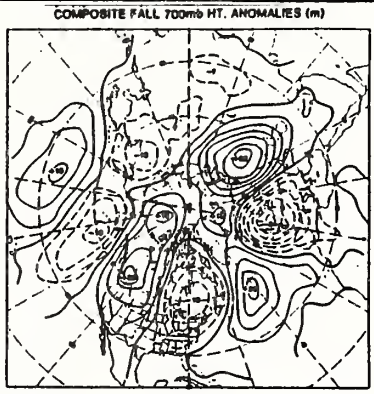

Fig. 9

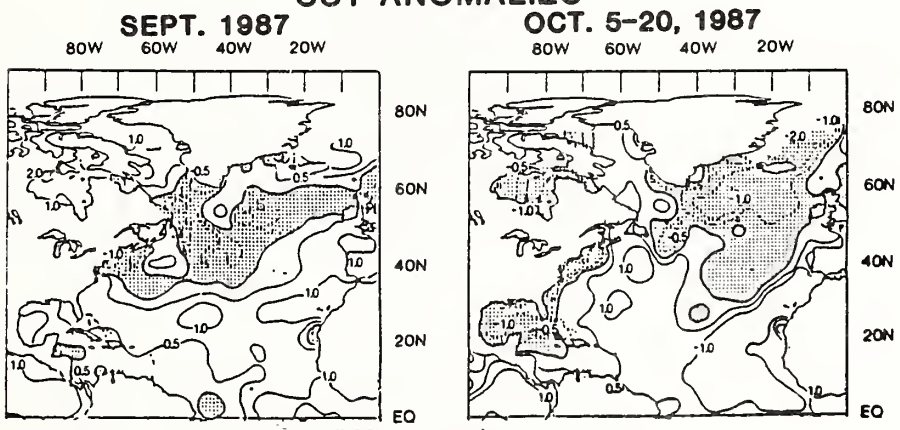

Fig. 10

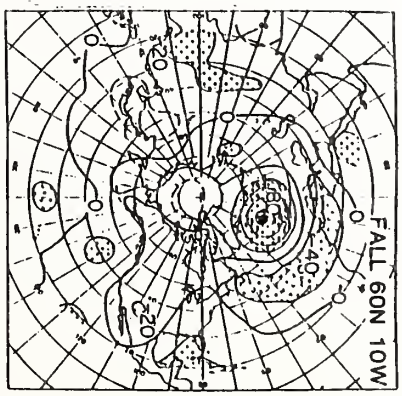

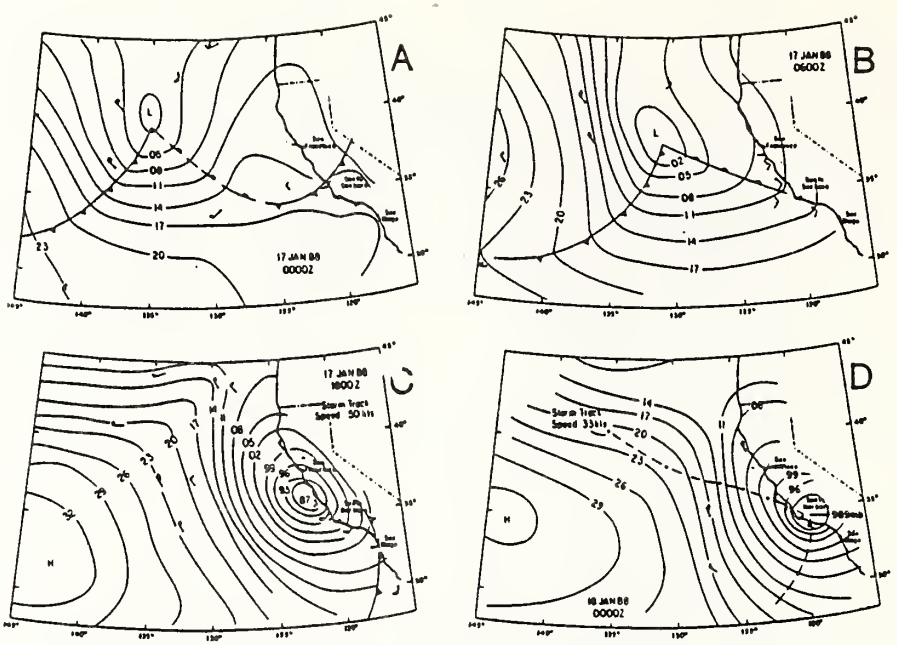

Fig. 11

700mb HT/DN (m) DEC. 13, 1987 - JAN. 12, 1988

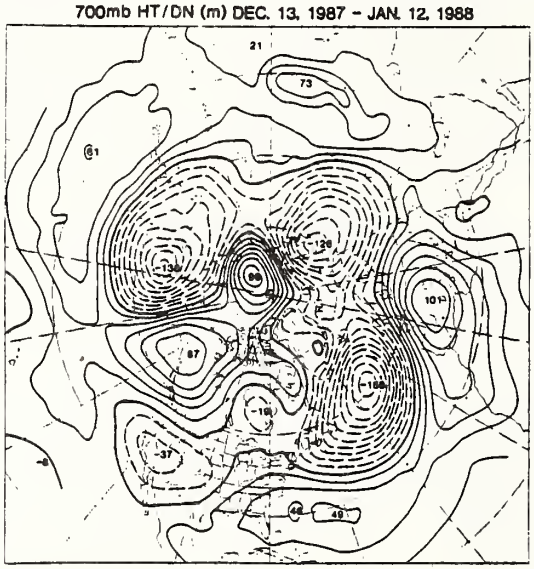

Fig. 12

WINTER TELECONNECTIONS

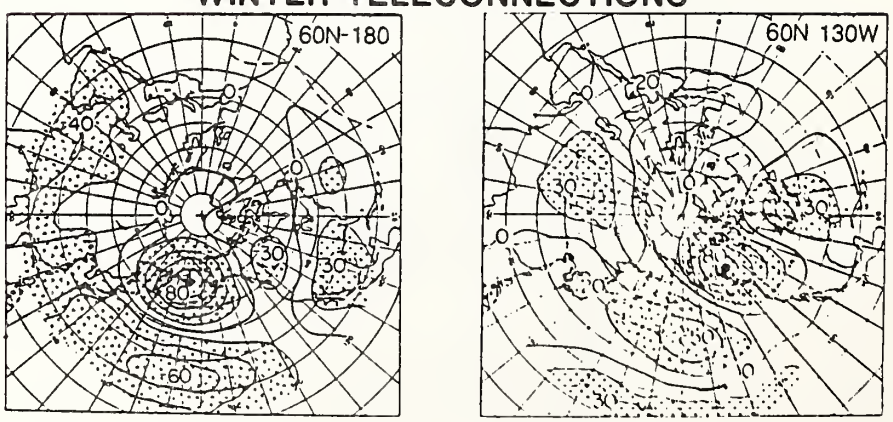

Fig. 13

On tropical climate prediction: a progress report 1985-88.

Stefan Hastenrath
Department of Meteorology
University of Wisconsin, Madison
Madison, Wisconsin 53706

This paper sketches the developments of tropical climate prediction over the past three years, so as to update an earlier review to 1985 on the subject (Hastenrath, 1986; 1988a, pp. 330-352). In that summary, five approaches were recognized, labelled in short (i) periodicities, (ii) statistical, (iii) persistence, (iv) general circulation and statistics, and (v) numerical modelling. As anticipated, the latter two approaches proved particularly promising. Approach (iv) draws on extensive general circulation diagnostics to identify atmospheric and oceanic elements related to the regional climate anomaly. These serve as input to a regression model. The resulting formula is then used in a predictive mode to calculate regional climate anomalies from antecedent departures in the large-scale circulation setting (Fig. 1). Seasonal rainfall anomalies are of particular interest. The first promising results have now also been obtained from numerical modelling (v). Prediction research is considered for the following targets (Fig. 2): seasonal rainfall anomalies in Java, India, Subsaharan Africa (Sahel), and Northeast Brazil (Nordeste); North Atlantic tropical storms; and El Niño.

For Java, about half of the interannual variability of August-November rainfall can be predicted from antecedent pressure anomalies (Hastenrath, 1987a). However, the precipitation at the December- January rainy season peak is less predictable.

For Indian summer monsoon rainfall predictors can be grouped into three families (Hastenrath, 1987,1988b): (a) upper-air flow over India; (b) heat low development over Southern Asia and establishment of meridional pressure gradient and cross-equatorial flow over the Indian Ocean, and (c) the Southern Oscillation (SO). In family (a) Banerjee et al. (1978) introduced the April latitude position of the 500 mb ridge along 75 °E. This has remained the most powerful predictor by far. In family (b) fall May temperature at Indian stations and May meridional wind component over the Western Indian Ocean (Hastenrath, 1988b). In family (c) Shukla and Mooley (1987) found the pressure tendency (April minus January) at Darwin, North Australia, to be more effective than other indices of the SO. Of great benefit for climate prediction research was Mooley and Parthasarathy's (1984) compilation of an all-India rainfall index, which provides a "cleaned-up" predictand series. As reviewed by Parthasarathy et al. (1988), numerous elements from nearby and distant locations are correlated with Indian summer monsoon rainfall but only few are effective as predictors. Eurasian winter snow cover is correlated with the April ridge position (Bhanu Kumar, 1988), but the latter is even more strongly correlated with the summer monsoon rainfall. The effective predictors stem from a limited interval during the monsoon transition, and allow prediction of 60-80 percent of the interannual variability of Indian summer monsoon rainfall.

Diagnostic investigations using observations to 1972 (review in Hastenrath, 1988a, p. 303-309) have elucidated the general circulation mechanisms of interannual rainfall variability in Subsaharan West Africa. It was found that deficient boreal summer

rainy seasons are characterized by an anomalously far southerly position of the Atlantic near-equatorial trough and a band of anomalously cold surface waters across the tropical North Atlantic. More recent studies (Palmer, 1986, Bhatt, 1988) focussed on the diversity of climate anomalies across the African - South Asian monsoon belt and associations with sea temperature departures in the Indian Ocean. A group at the British Meteorological Office (Folland et al., 1986; Meteorological Office, U.K., 1988) is attempting to forecast Sahel seasonal rainfall using eigenvector and discriminant analysis of global sea surface temperature patterns. In this context it seems essential to separate year-to-year and trend-like developments, a challenge both in terms of the general circulation mechanisms and the proper statistical treatment.

The rainy season in Brazil's Nordeste is narrowly concentrated around March-April, when the Atlantic near-equatorial trough reaches its southernmost position in the course of the year. We demonstrated on an independent data set that about half of the interannual rainfall variability can be predicted from antecedent departures in the large-scale circulation setting (Hastenrath et al., 1984). In collaboration with Brazilian colleagues we are identifying a set of consistently reporting rainfall stations in the Nordeste and searching for effective predictors that would also be available on an operational basis.

For several years Gray (1987, 1988); has been issuing seasonal forecasts of North Atlantic hurricane activity, based on stratospheric zonal wind component, El Niño developments in the Pacific, and pre-season pressure in the greater Caribbean basin. Characteristics predicted include the number of hurricanes, number of hurricanes and tropical storms, number of hurricane days, and number of hurricane and tropical storm days. Fig. 3 presents scatter plots of forecast versus observed values of the number of "named" tropical storms and the number of days with hurricanes and tropical storms, for the forecast years from 1984 onward. Although this sample is still limited, the plots show an encouraging agreement in terms of categories "above" and "below" the long-term average.

Applications of numerical modelling to seasonal prediction have been limited to the Pacific El Niño phenomenon. Expanding on Inoue and O'Brien's (1984) landmark paper, O'Brien (1986) uses a numerical ocean model driven by observed surface winds to predict the onset of El Niño. To the same end, Cane et al. (1986) use a coupled ocean-atmospheric model. While this may offer a greater diagnostic insight, the prognostic performance of the two models remains to be compared as a larger sample of verifications accumulates.

On the whole, work over the past three years has shown considerable potential for empirical methods of seasonal climate prediction based on general circulation diagnostics. A sound empirical understanding also appears crucial for the development of numerical modelling applications to seasonal forecasting. For certain target regions - all experiencing their rainy season peak around an extremum in the planetary-scale annual cycle - about half or more of the interannual rainfall variability can be predicted from antecedent departures in the large-scale circulation setting. For extensive other areas of the tropics the prospects for seasonal climate prediction may be more remote.

Acknowledgements:
Supported by NSF Grant ATM-8722410 and NOAA Grant NA86AA-D-AC064.

References

Banerjee, A.K., Sen, P.N., Raman, C.V.R., 1978: On foreshadowing Southwest monsoon rainfall over India with mid-tropospheric circulation anomaly of April.
Indian J. Meteor. Hydrol. Geophys., 29, 425-431.

Bhanu Kumar. O.S.R.U., 1988: Interaction between Eurasian winter snow cover and location of the ridge at the hpa level along 75 °E.
J. Meteor. Soc. Japan, 66 .

Bhatt, U., 1988: Circulation regimes of drought in the eastern versus the western parts of Subsaharan Africa.
pp. in Proceedings of the Thirteenth Annual Climate Diagnostics Workshop, Cambridge, Mass., NOAA, Washington, D.C.

Cane, M.A., Zebiak, S.E., Dolan, S.C., 1986: Experimental forecasts of El Niño.
Nature, 321, 827-832.

Folland, C.K., Parker, D.E., Ward, M.W., Coleman, A.W., 1986: Sahel rainfall, Northern hemisphere circulation anomalies and worldwide sea temperature changes.
Meteorological Office, Met 0.13, LRFC 7, Bracknell, 48 pp.

Gray, W.M., 1987: Summary of 1987 Atlantic tropical cyclone activity and verification of author's seasonal forecast.
Dept. Atm. Sci., CSU, Fort Collins, Colo., 23 pp.

Gray, W.M., 1988: Forecast of Atlantic seasonal hurricane activity.
Dept. Atm. Sci., CSU, Fort Collins, Colo., 39 pp.

Hastenrath, S., 1986: On climate prediction in the tropics.
Bull. Amer. Meteor. Soc., 67, 692-702.

Hastenrath, S., 1987a: Predictability of Java monsoon rainfall anomalies: a case study.
J. Climate Appl. Meteor., 26, 133-141.

Hastenrath, S., 1987b: On the prediction of India monsoon rainfall anomalies.
J. Climate Appl. Meteor., 26, 847-857.

Hastenrath, S., 1988a: Climate and circulation of the tropics.
Reidel, Dordrecht, Boston, Lancaster, Tokyo, second printing, 455 pp.

Hastenrath, S., 1988b: Prediction of Indian monsoon rainfall: further exploration.
J. Climate, 1, 298-304.

Hastenrath, S., Wu, M.C., Chu, P.S., 1984: Towards the monitoring and prediction of Northeast Brazil droughts.
Quart. J. Roy. Meteor. Soc., 110, 411-425.

Inoue, M., O'Brien, J.J., 1984: A forecasting model for the onset of a major El Niño.
Mon. Wea. Rev., 112, 2326-2337.

Meteorological Office, U.K., 1988: Forecast of 1988 seasonal rainfall in the Sahel area of Africa.
Bracknell, U.K.

Mooley, D. A., Parthasarathy B., 1984: Fluctuations in all-India summer monsoon rainfall during 1871-1978.
Climatic Change, 6, 287-301.

O'Brien, J.J., 1986: The El Niño forecasts for 1986.
Paper presented at Eleventh Annual Climate Diagnostics Workshop, 14-17 October 1986, Champaign, Illinois.

Palmer, T.W. 1986: Influence of the Atlantic, Pacific and Indian Oceans on Sahel rainfall.
Nature, 322, 251-253.

Parthasarathy, B., Diaz, H.F., Eischeid, J.K., 1988: Prediction of all-India summer monsoon rainfall with regional and large-scale parameters.
J. Geophys. Res., 93, D5, 5341-5350.

Shukla, J., Mooley, D.A., 1987: Empirical prediction of the summer monsoon rainfall over India.
Mon. Wea. Rev., 115, 695-703.

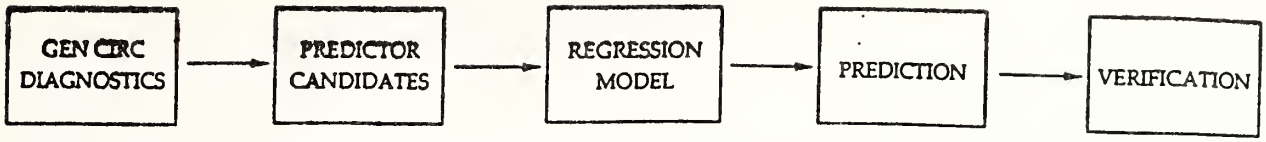

Fig. 1. Scheme of climate prediction based on general circulation diagnostics and statistics.

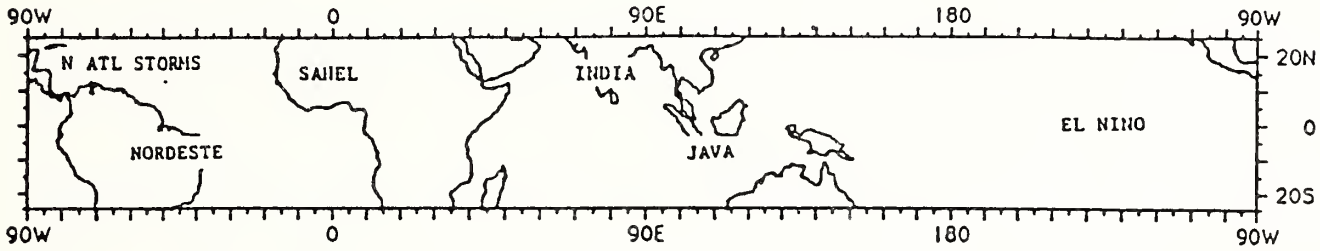

Fig. 2. Orientation map showing location of areas referred to in this review. Rainfall: Java, India, Sahel, Nordeste; North Atlantic tropical storms; El Niño.

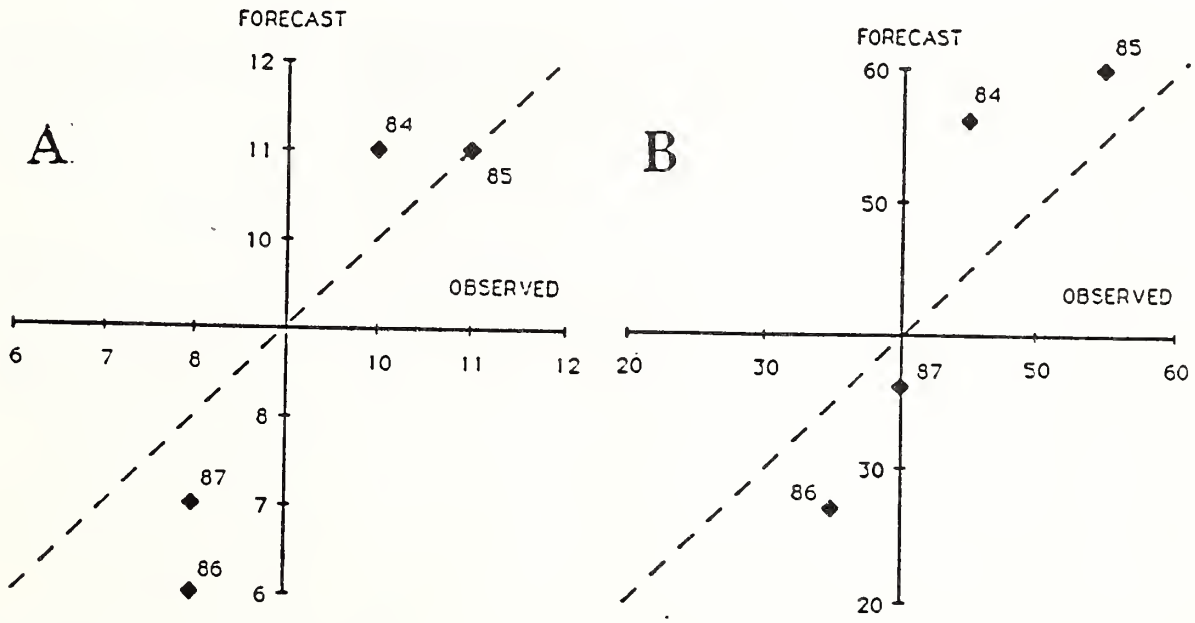

Fig. 3. Scatter plots illustrating performance of Gray's (1987, 1988) seasonal predictions of North Atlantic hurricane activity. (a) number of "named" storms, (b) number of days with hurricanes or tropical storms. Numbers indicate the years.

Amplitude-Persistence-Transitions of Low-Frequency Modes

Edward O'Lenic, Robert Livezey and Laura M. Hinkelman*
NOAA/NWS/NMC/CAC
Washington, D. C. 20233

There is a growing body of evidence that low frequency regimes play an important role in the dynamics of the atmosphere. In lieu of a comprehensive theory of low frequency variability, statistical techniques, e.g., rotated principal component (or rotated empirical orthogonal function analysis) (RPCA and REOFA, respectively) has come to be a widely used, productive tool for studying low frequency variability (LFV) in the atmosphere. If the modes represented by this technique are a pretty good approximation to the structures of LFV, then two key questions arise immediately:

(1) What are the persistence characteristics of these LF structures?

(2) Are there any significant predictive relationships between the existence and transitions of a given mode(s) and any other mode(s), and, if so, what are they?

This paper deals with question 1. Question 2 will be pursued in later work. Obviously, the answers to these questions are likely to find application to long range prediction. They may also bring us a step closer to understanding the dynamics of LFV.

The procedure is to define low frequency regimes (LFR) by performing a (varimax) rotated principal component analysis (RPCA) on a 38-year set of daily 700 mb height anomaly analyses for seasons two months long. The data are given on an equal-area 358 point grid in the Northern Hemisphere, and are subjected to a low pass filter (Blackmon, 1976) prior to the analysis in order to remove oscillations with periods of less than 10 days.

The result of the RPCA is a set of a dozen or so spatial patterns which together explain about 70 percent of the variance of the filtered data. A time series of the amplitudes of the various modes are found by doing a least-squares fit of the maps in the time series of daily data for the two-month seasons to the modes. We also projected the data from the month before and the month after the original two month period (whose data were used for the RPCA) onto the modes from the RPCA. This allows us to include events which cross the boundaries of the 2 month window to be properly included in the statistics. The result of such a projection is illustrated in Figure 1 which shows a portion of the amplitude time series (ATS) for mode 1 from the April-May RPCA.

One standard deviation (+ or -) of the entire ATS was chosen as the threshold criterion for persistent events corresponding to relatively large amplitudes of the modes. The time that the amplitude of a mode spends being either greater than +1 or less than -1 standard deviation corresponds to the lifetime of that persistent event.

* Current affiliation: Eastman Kodak Corporation, Rochester, N.Y.

Lag autocorrelations were computed on the ATS in order to examine their average persistence characteristics. These were not stratified according to the sign (phase + or -) of the mode. The 38-year mean was used in this computation to ensure that interannual variability in the data is preserved. Persistent events lasting exactly 1 day, 2 days,... etc., were counted and summarized via histograms of frequency versus persistence. These computations were performed for the ATS from modes for four two-month seasons: January-February (JF), April-May (AM), July-August (JA), and October-November (ON).

Results for mode 1 from JF (Figure 2a) are shown in Figure 2b-d. The lag autocorrelation curve (Figure 2b) indicates that the ATS for this mode contains either a linear trend or a number of persistent events with lifetimes which are long compared to the 2 month window. The histograms of lifetimes (Figure 2c, d) indicate that while there is a marked tendency for a preferred lifetime of about 1 - 1.5 weeks, there is a considerable number of events out to the 3 week range. This supports the notion that episodes of persistence, and not only some unknown trend, contribute significantly to the persistence implied by the lag autocorrelation curve of Figure 2a.

Results for the PNA during JF are shown in Figure 3. Again, a tendency for long-lived episodes of persistence can be seen.

The mode whose time series exhibits the most marked persistence characteristics of any mode in any season in the subtropical zonal mode (mode 1) for July August (Figure 4a). The lag autocorrelation coefficient for this mode (Figure 4b) is about 0.45 at 10 days, and falls only very slowly to about 0.30 at 25 days. The lifetime histograms reveal many events which persist well beyond 20 days.

Conclusions

Information about the persistence of LRF will clearly have applications to long range prediction. In particular, it can be used to improve forecasts in which the model fails to persist modes which we know do tend to persist. Information about transitions (if any are found) can be used similarly. While those modes that persist tend to live for 1-2 weeks, there is a considerable number of events in the 3-6 week range. Some modes exhibiting marked persistence are:

Summer: SZ(1), mode 12

Fall: NAO(1), PNA(2), WP(10)

Winter: NAO(1), PNA(2), WP(6)

Spring: PNA(2), EP(2)

Future work will include use of obliquely rotated principal component analysis and an examination of the details of the distributions of the amplitudes of the modes.

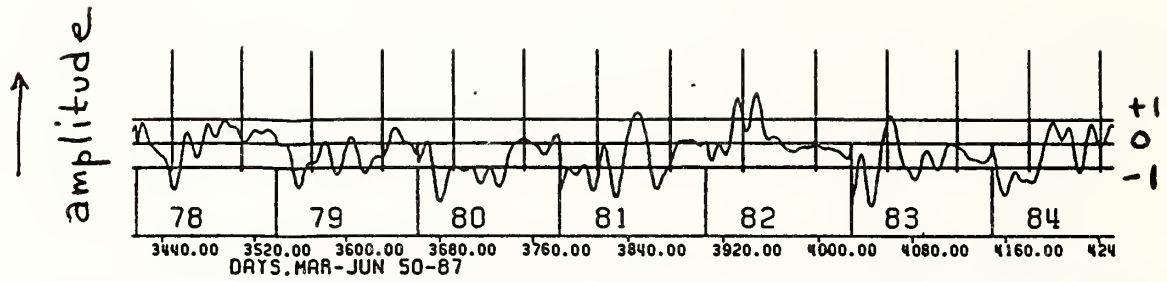

Figure 1. Time series of amplitude of mode 1 derived from April-May 1950-87 data. Shown is projection of observed data from March-June 1978-1984. Horizontal line labeled 0 is mean of the time series. Lines parallel and to either side of mean are the +1 and -1 standard deviations of the 1950-1984 time series. Episodes of mode amplitude greater than +1 or less than -1 standard deviation were included in census of lifetimes of persistent events.

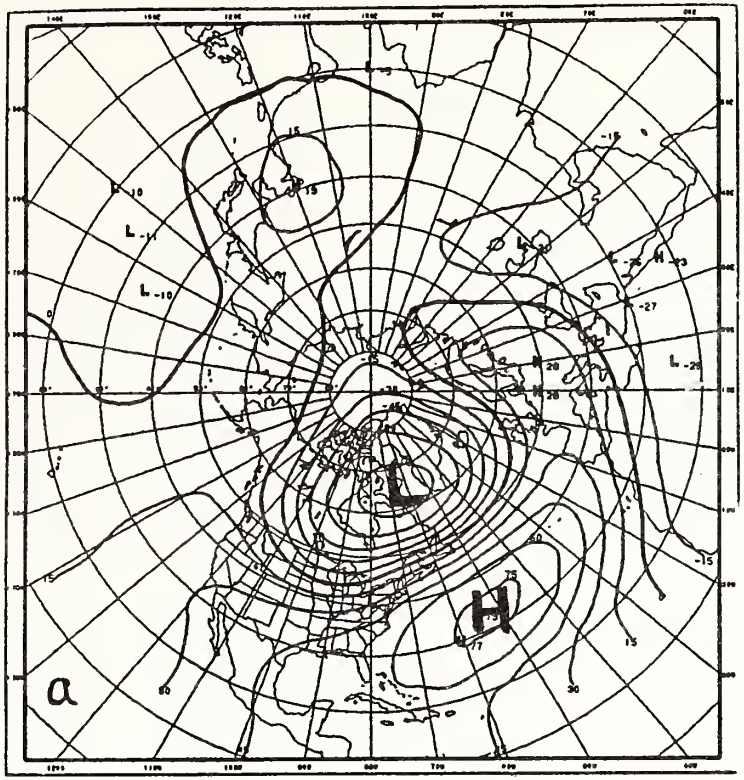

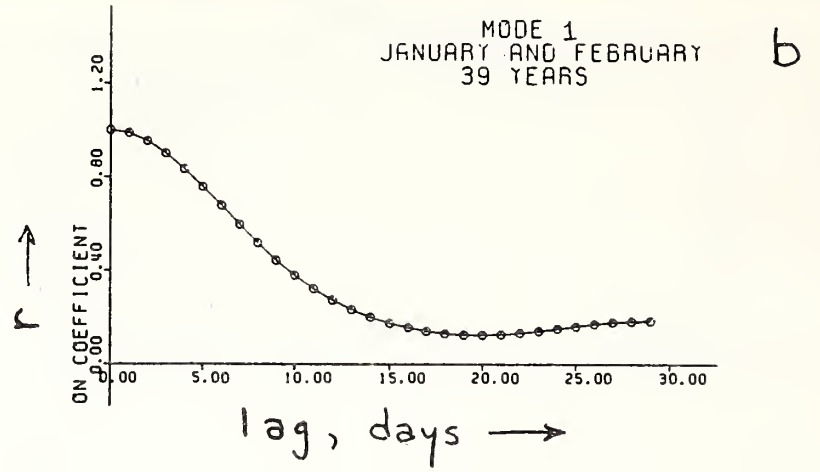

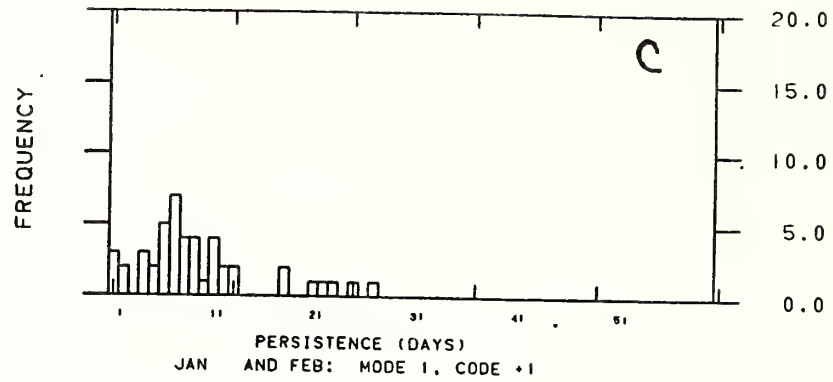

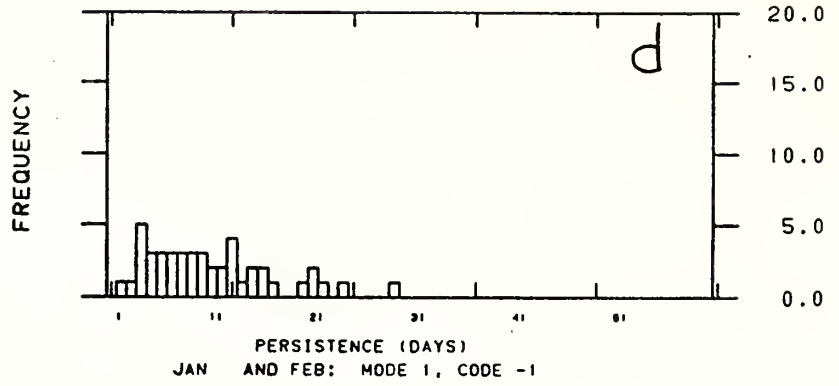

Figure 2. Results for mode 1, January-February.
a) 700 mb height anomaly eigenvector pattern. Contours are correlation coefficients x 100.
b) Lag autocorrelation curve for mode 1.
c) Lifetime histogram for + phase of mode 1.
d) Same as c but for - phase.

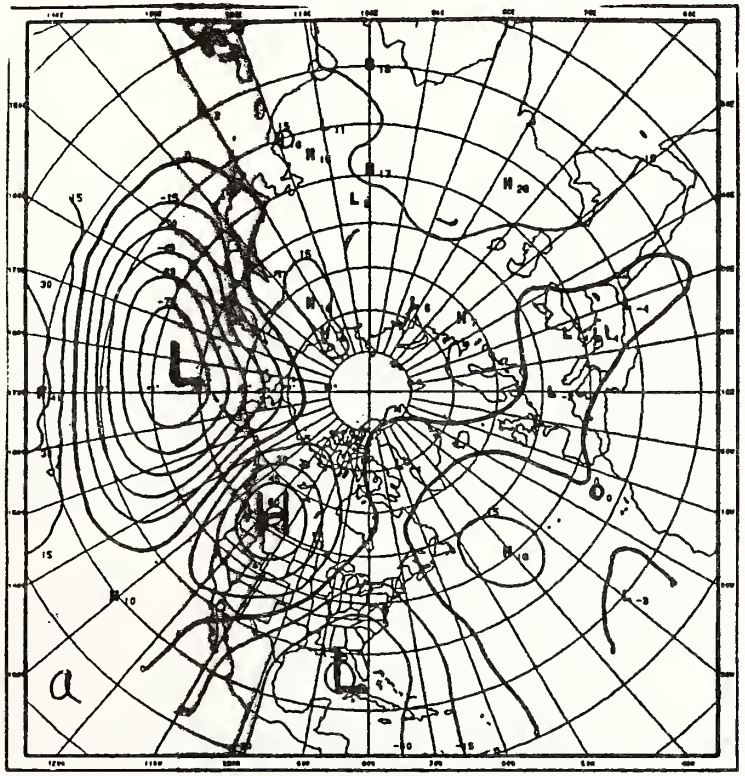

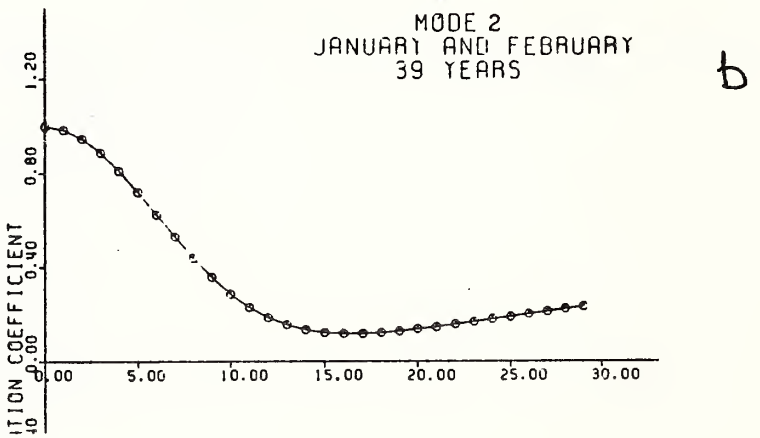

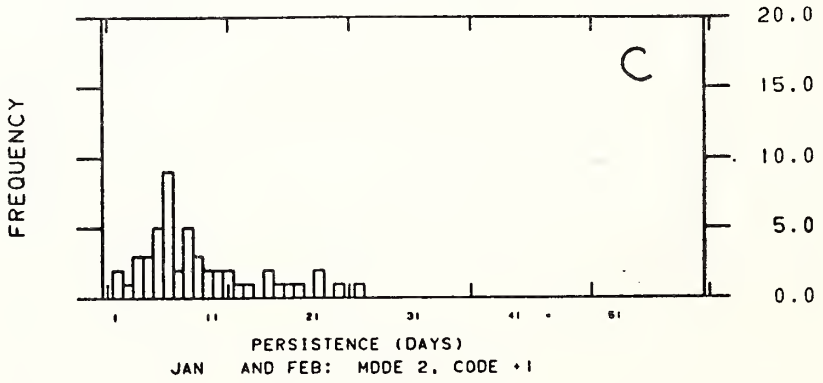

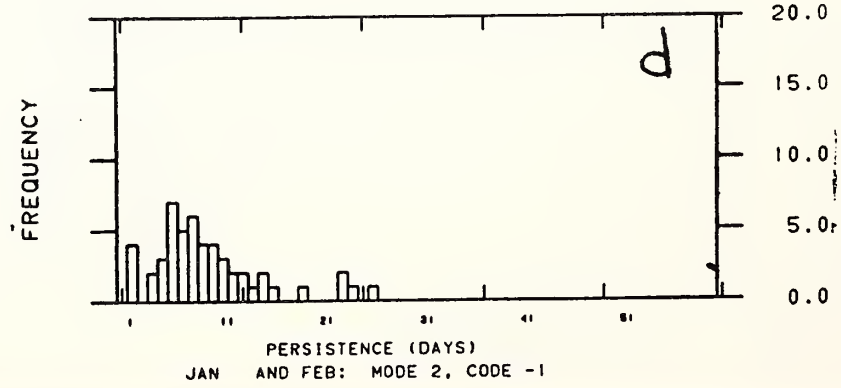

Figure 3. Results for mode 2, January-February.
a) 700 mb height anomaly eigenvector pattern. Contours are correlation coefficients x 100.
b) Lag autocorrelation curve for mode 2.
c) Lifetime histogram for + phase of mode 2.
d) Same as c but for - phase.

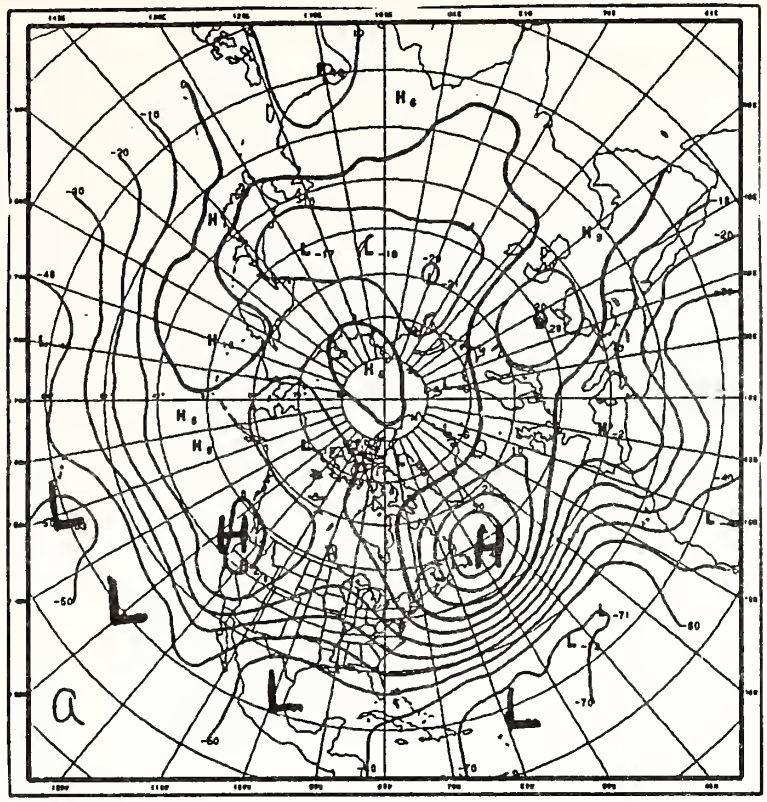

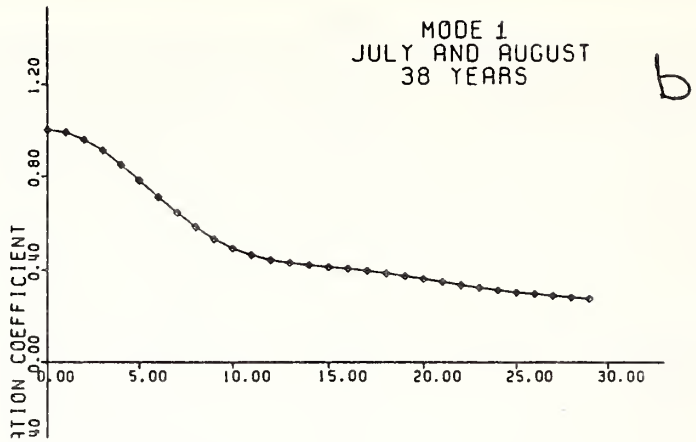

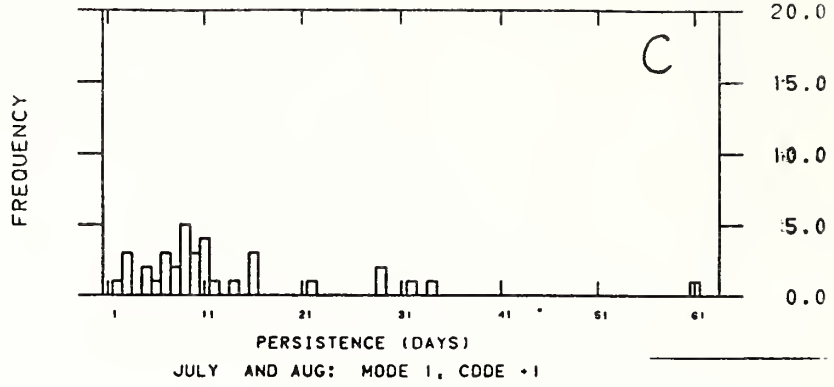

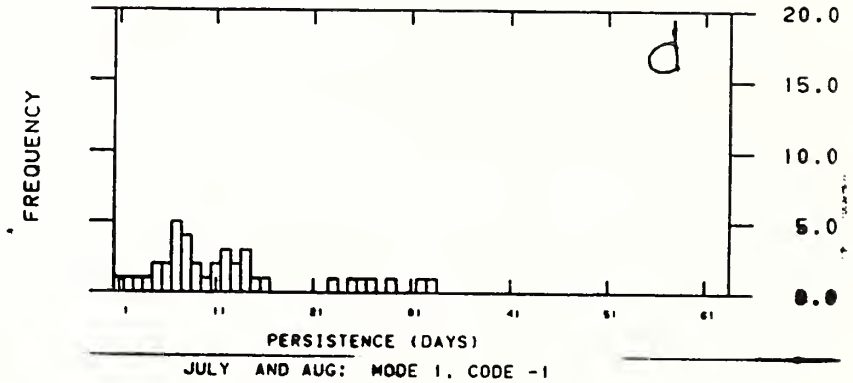

Figure 4. Results for mode 1, July-August.
a) 700 mb height anomaly, eigenvector pattern. Contours are correlation coefficients x 100.
b) Lag autocorrelation curve for mode 1.
c) Lifetime histogram for + phase of mode 1.
d) Same as c but for - phase.

FURTHER CASE STUDIES OF TROPICAL ATLANTIC SURFACE CIRCULATION PATTERNS ASSOCIATED WITH SUBSAHARAN DROUGHT

Peter J. Lamb[1] and Randy A. Peppler
Climate and Meteorology Section
Illinois State Water Survey
Champaign, Illinois 61820

This paper summarizes the results of an investigation that was designed as a follow-up to Lamb's earlier inquiry (Tellus, 1978; Mon. Wea. Rev., 1978) into the tropical Atlantic surface circulation patterns associated with Subsaharan rainfall extremes.

The previous effort suggested that, during particularly deficient Subsaharan rainy seasons (July-September), several near-equatorial surface atmospheric-oceanic features of zonal orientation (pressure trough; kinematic axis between Northern and Southern Hemisphere trades; zone of maximum sea surface temperature [SST]; maxima of precipitation frequency and total cloudiness) were located 200-350 km south of their 60-year mean positions. These near-equatorial displacements were associated with a distinctive tropical Atlantic SST anomaly pattern (positive departures to the south of approximately 10°N; negative departures between 10°-25°N) and a tendency for the North (South) Atlantic subtropical high to extend further (less) equatorward than normal. These findings were the first of their type obtained for a subject (causes of Subsaharan drought) that is now considered to be of substantial importance.

However, the observational basis of the earlier drought-focused work was limited by data availability to the analysis of two data sets of similar size -- one for 1968 (case study) and another that was composited for five additional deficient rainy seasons (1942, 1949, 1970, 1971, 1972). Clearly, there existed a need for further empirical investigation of the above subject. We here capitalize on two factors -- the persistence of Subsaharan drought conditions into the late 1970s-early 1980s and improved data availability for the drought years since 1970 -- to continue contributing to that line of inquiry. Specifically, we present detailed case study analyses of the tropical Atlantic surface atmospheric-oceanic conditions for the four driest Subsaharan rainy seasons (July-September) since 1940 (1972, 1977, 1983, 1984; see Fig. 1) and the wettest rainy season since 1969 (1975; Fig. 1). The source of the surface marine meteorological data used for all years except 1984 (NCDC's TDF-11 file), and the analytical procedures employed to process them, are the same as in the earlier work referenced above. See those papers for details. We compare the patterns for individual years with the same 1911-70 mean fields as used previously. Our limited and preliminary results for 1984 were computed using data kindly supplied by Jacques Servain (ORSTOM, Brest); final results derived from NCDC data will be available soon.

---

[1] Also affiliated with Department of Atmospheric Sciences, The University of Illinois.

The results obtained here for the extremely deficient Subsaharan rainy seasons of 1972, 1977, and 1984 essentially duplicate those yielded by the earlier drought-focused work. Their SST anomaly fields (Fig. 2) strongly feature the distinctive pattern described above and its associated southward displacement of the zone of maximum SST. Those changes were accompanied by southward displacements (250-350 km relative to 1911-70 mean) of the near-equatorial pressure trough (Fig. 3), kinematic axis separating Northern and Southern Hemisphere trades (Fig. 4), and maxima of precipitation frequency and total cloudiness (Fig. 5). In addition, the North (South) Atlantic subtropical high again showed evidence of extending further (less) equatorward than normal (Fig. 3).

The foregoing common set of departure patterns is not nearly so characteristic of the other extremely deficient rainy season investigated (1983). The SST anomaly patterns for that year (Fig. 2) tend to be positive over most of the study domain, and the zone of maximum SST is expanded both northward and southward. Furthermore, while there is some evidence of a southward displacement of the 1983 near-equatorial pressure trough (Fig. 3), this receives little support from the wind field anomalies (Fig. 4) or precipitation frequency/total cloud amount results (Fig. 5) obtained. Clearly, the tropical Atlantic surface atmospheric-oceanic conditions that prevailed during the very deficient 1983 Subsaharan rainy season were somewhat different to those that accompanied both the other recent years of near-comparable rainfall deficiency (1972, 1977, 1984; Fig. 1) and some years of more moderate drought (1968; years contained in earlier drought composite - 1942, 1949, 1970, 1971; see Fig. 1). This finding provides a challenging situation with respect to our understanding of Subsaharan drought, particularly since 1983 was the year of a major ENSO event.

The non-drought Subsaharan rainy season investigated for comparative purposes (1975) received rainfall that was close to the 1941-82 average, and the most abundant since 1969 (Fig. 1). Its tropical Atlantic surface atmospheric-oceanic conditions were also different (but not opposite) to those of the very poor 1972, 1977, and 1984 rainy seasons. The 1975 SST anomaly pattern was rather fragmented and the zone of maximum SST was close to its average position (Fig. 2). The near-equatorial pressure trough (Fig. 3), kinematic axis (Fig. 4), and precipitation frequency/total cloud maxima (Fig. 5) for 1975 were also located in close to their 1911-70 mean latitudinal positions. These 1975 results thus do not duplicate those obtained earlier for the slightly wetter (Fig. 1) 1967 rainy season (Mon. Wea. Rev., 1978), which tended to be the opposite of the patterns identified here and previously as characteristic of most strongly deficient Subsaharan rainy seasons. The 1975 anomaly fields, particularly for SST and wind speeds, are also somewhat different to those obtained for the above non-conforming drought year of 1983 (Figs. 2, 4).

A more complete discussion of the above results will be contained in a paper to be submitted to a refereed journal in early 1989. The paper will also document the evolution of the above rainy season patterns during the preceding six months, and outline the implications of those results for the extended-range prediction of the rainfall. While the potential for such prediction exists, it will need to be capitalized on in a judicious manner.

The research reported here was supported by NOAA Grants NA86AA-D-AC065 and NA87AA-D-AC084. We wish to thank Linda Riggin, Rebecca Runge, and Phyllis Stone for their technical assistance.

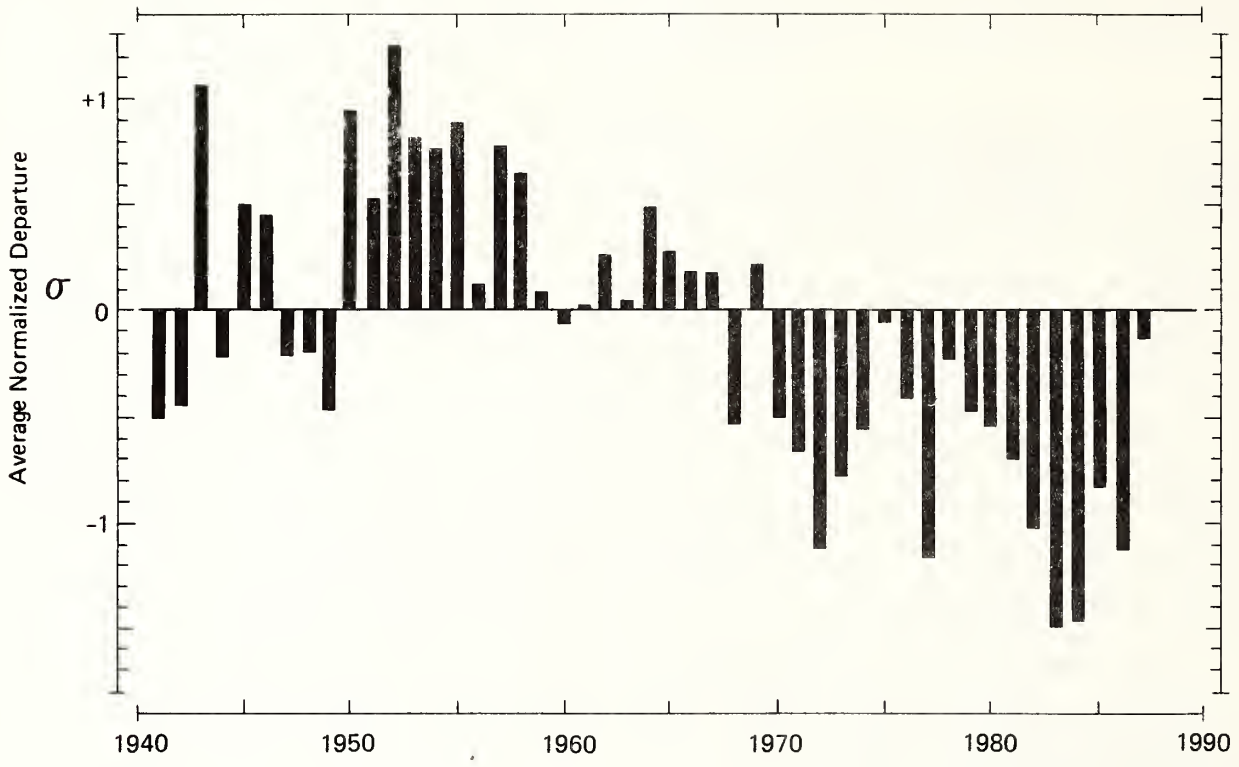

Fig. 1. Time series (1941-88) of the yearly average of normalized April-October rainfall departures for 20 locations in Subsaharan West Africa (11°-18°N; west of 10°E).

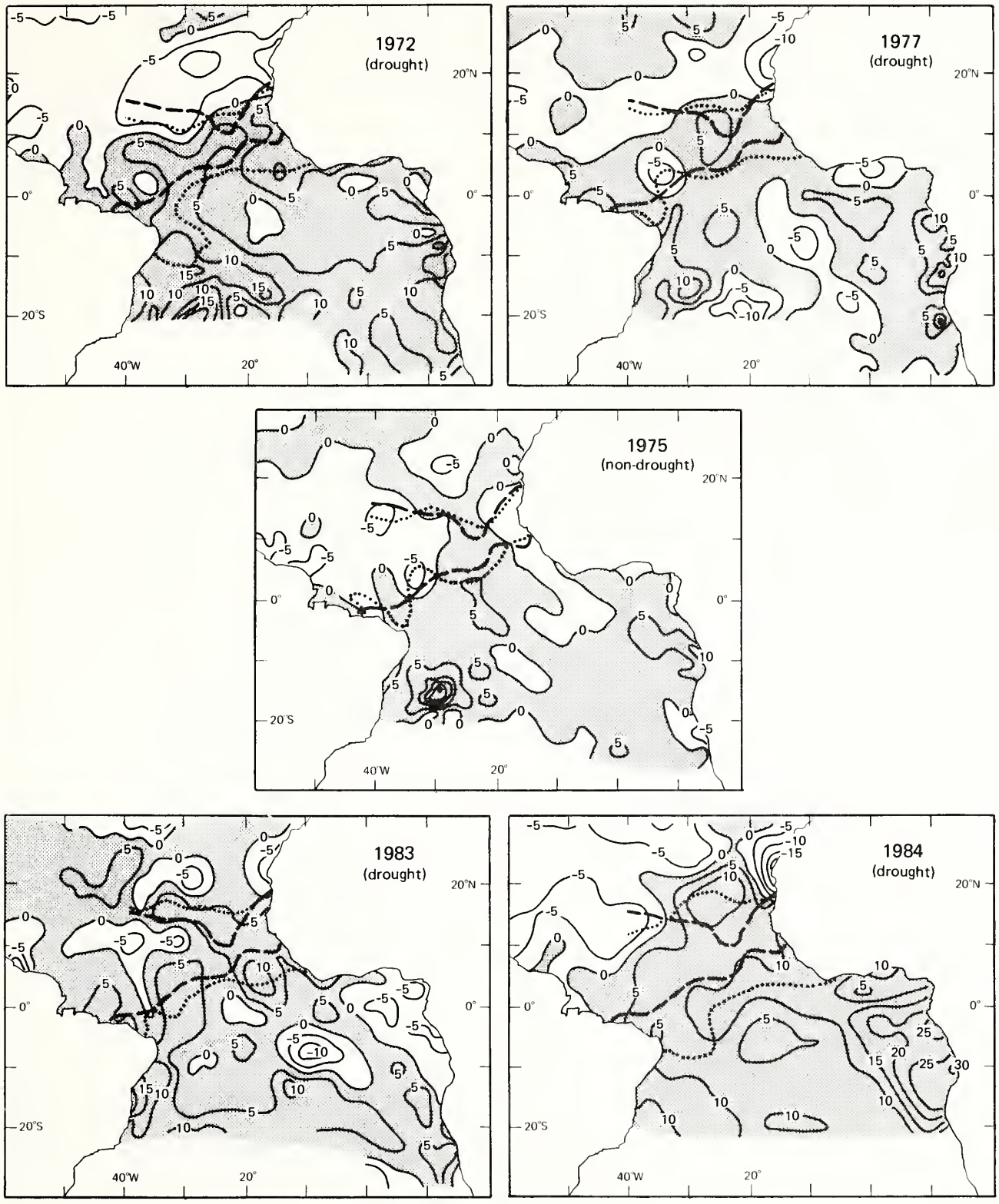

Fig. 2. July-September SST fields for indicated years expressed as departures from the 1911-70 average pattern. Solid lines are departure isotherms (tenths of 1°C), positive values shaded; dotted lines enclose area of maximum SST east of 40°W for indicated year (> 26.7°C), with dashed lines doing likewise for 1911-70 mean.

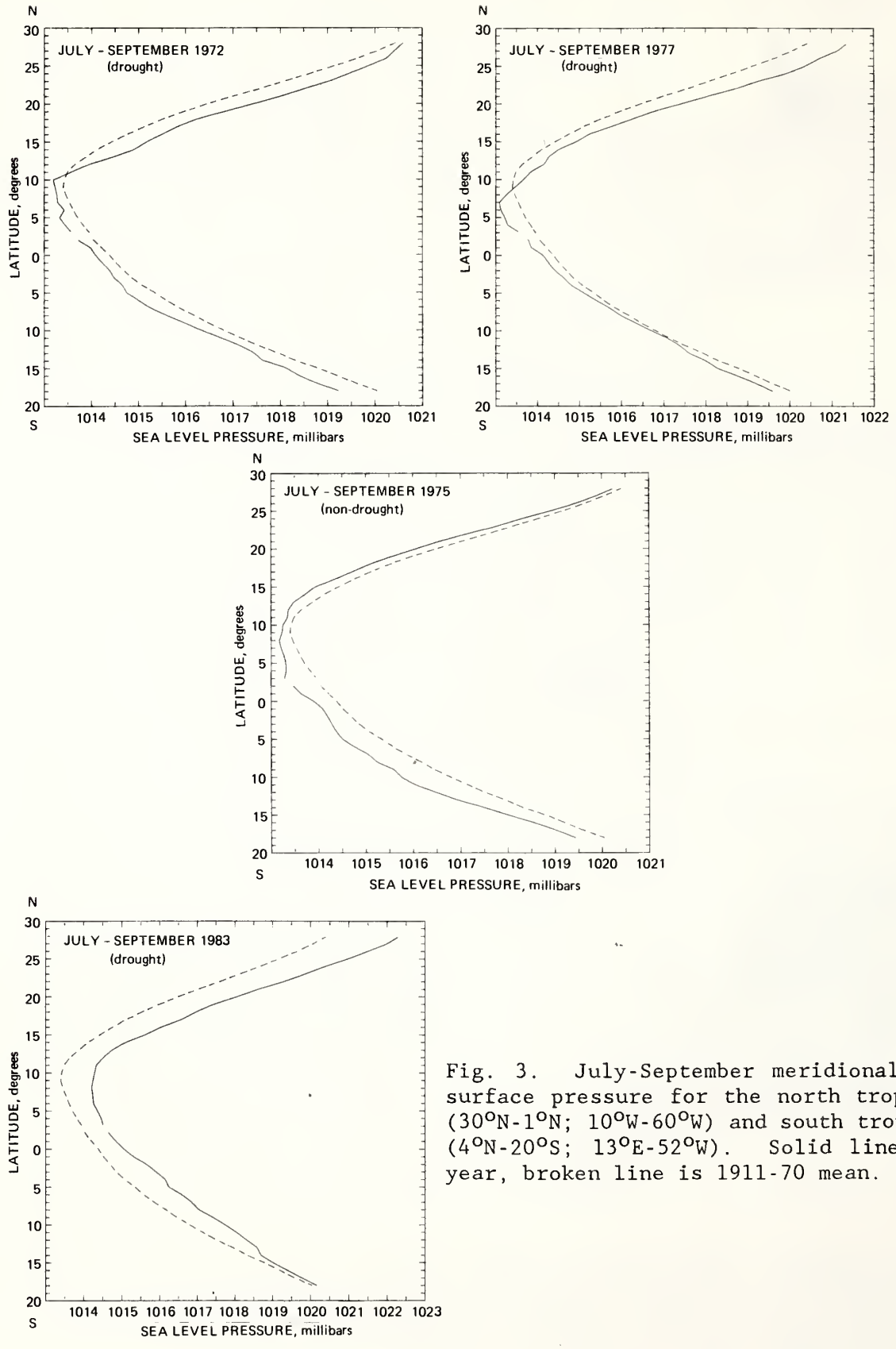

Fig. 3. July-September meridional transects of surface pressure for the north tropical Atlantic (30°N-1°N; 10°W-60°W) and south tropical Atlantic (4°N-20°S; 13°E-52°W). Solid line is indicated year, broken line is 1911-70 mean.

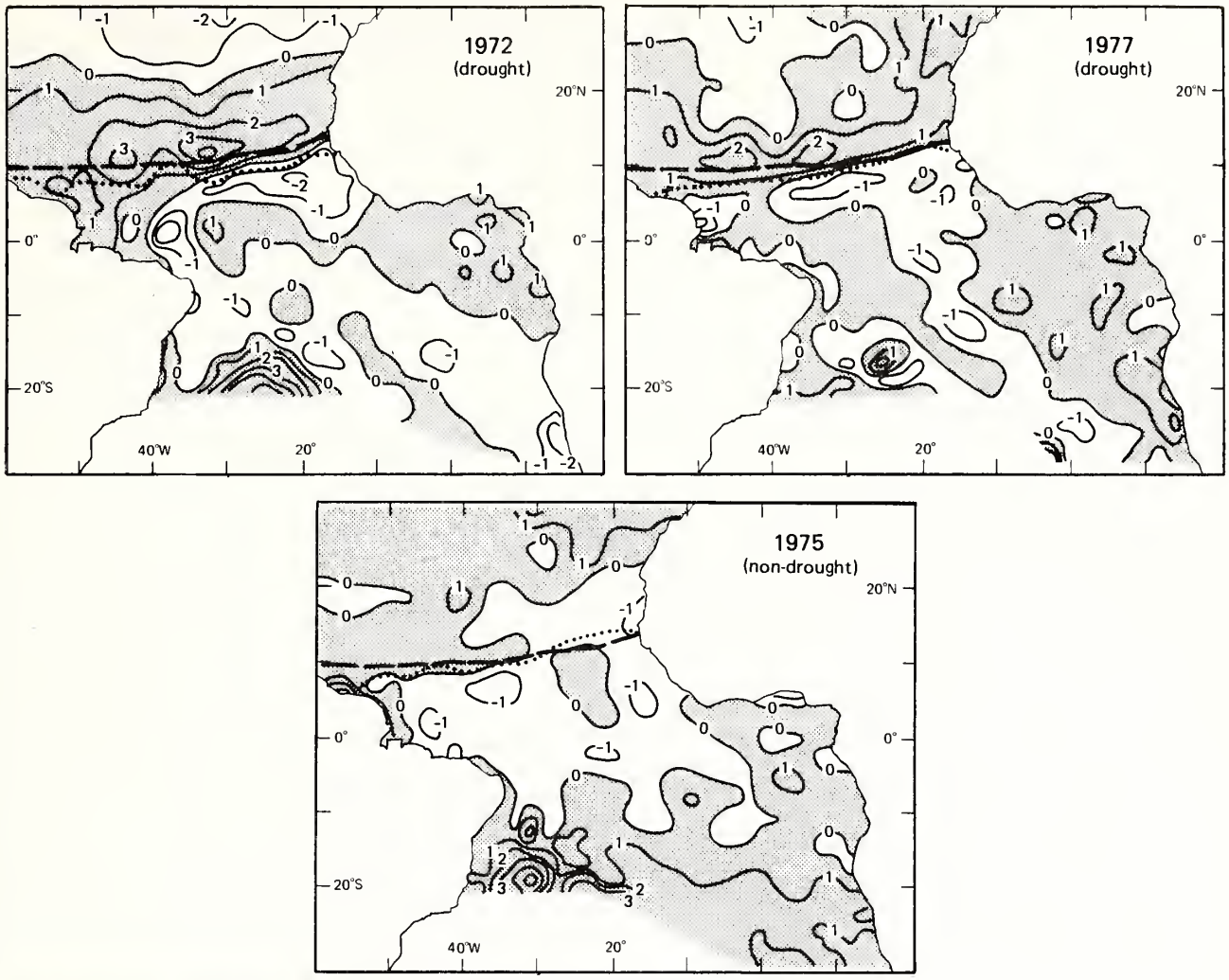

Fig. 4. July-September resultant wind fields for indicated years expressed as departures from the 1911-70 average pattern. Solid lines are departure isotachs (m s^{-1}), positive values shaded; dotted lines locate discontinuity between northerly and southerly resultant wind directions for indicated years, with broken lines doing likewise for the 60-year mean.

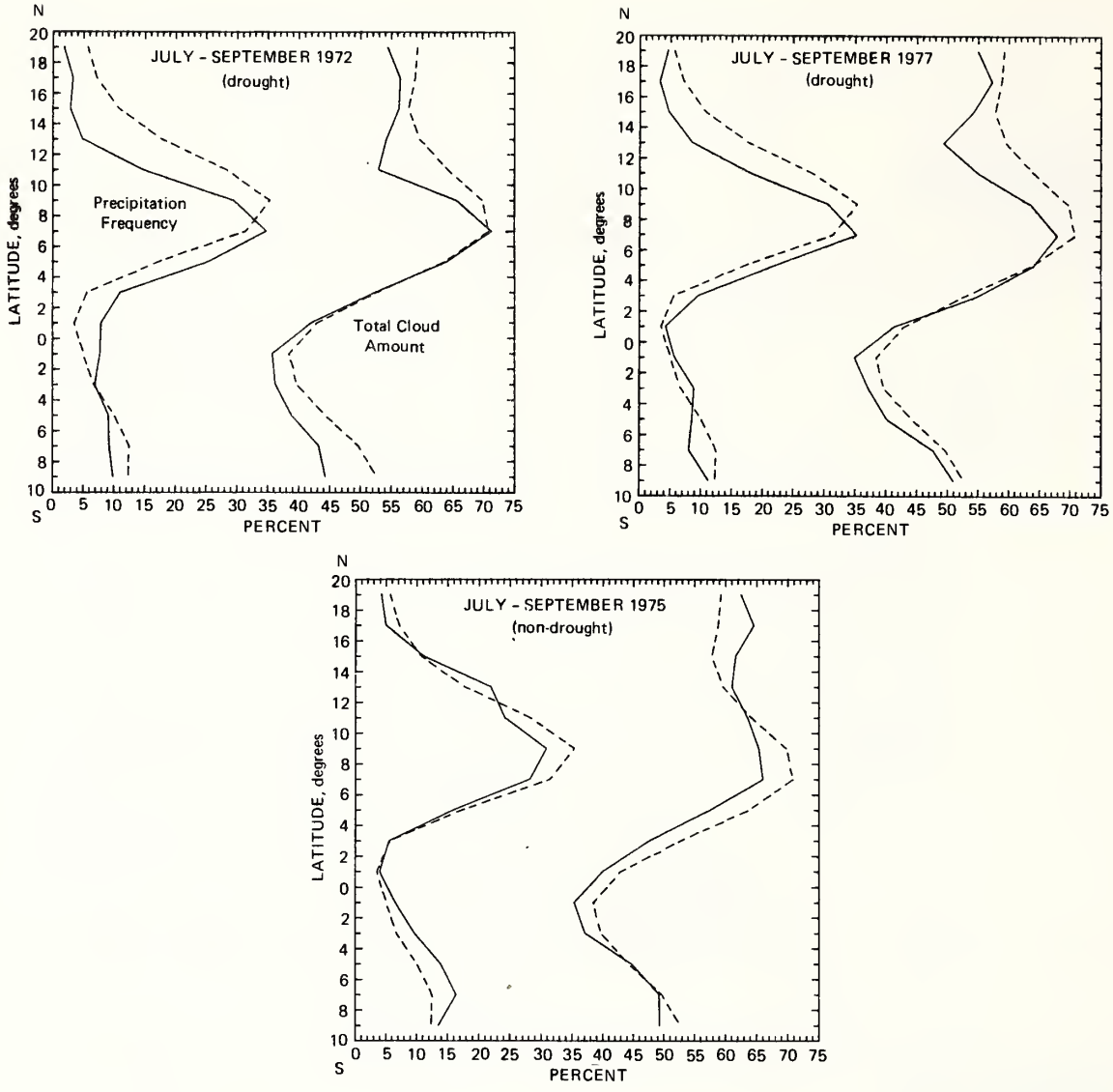

Fig. 5. July-September meridional transects of precipitation frequency (left-hand profiles) and total cloudiness (right-hand profiles) for 10°-40°W. Solid line is indicated year; broken line is 1911-70 mean.

Mixed Analog/Persistence Prediction of U.S. Seasonal Temperatures

Robert E. Livezey, Anthony G. Barnston, and Brian K. Neumeister
Climate Analysis Center, NOAA/NWS/NMC, Washington, D. C. 20233

At the National Weather Service's Climate Analysis Center, official United States seasonal temperature forecasts are currently a synthesis of two different classes of predictions. One of these consists of direct objective forecasts of seasonal mean temperatures and includes (1) simple persistence from one season to the next of standardized temperature departures from normal, and (2) a complex analog/antianalog (hereafter referred to as analog) prediction system (cf. Livezey and Barnston, 1988, and Barnston and Livezey, 1989, hereafter referred to as LB and BL respectively). Our focus here will be on these direct methods and whether they (persistence and analog forecasts) can be combined objectively. The idea is to take advantage of the relative strengths (by season and location) of each to produce forecasts more skillful in an overall sense than either.

This is illustrated in Fig. 1. Note that while overall skills are comparable, persistence has least skill in late winter/early spring but for the analog method this occurs in the fall. We would like to explore whether the forecasts can be combined in a mixed system whose skill curve would be more level from season to season than those shown in Fig. 1 and be above both. Whether this is possible depends on the extent to which the skills of both forecasts making up the mixed system are independent of each other and the extent to which their skill variations are sample dependent. The fact that LB and BL present evidence that persistence and analog forecasts are independent provides the necessary prerequisite for this work.

Two methods were used to blend the forecasts with the most emphasis placed on simple bivariate linear regression. Its use required some modification to the method employed to produce analog forecasts.

The operational analog prediction system currently produces forecast probabilities of three equally distributed station temperature classes (above, near, and below normal). These "conditional" probabilities of class i at station j are given by

$$P^i_j = w_1 P^i_{1j} + w_2 P^i_{2j} + \ldots + w_L P^i_{Lj} \qquad i = 1,\ldots,3 \tag{1}$$

$$j = 1,\ldots,92 \qquad L = 1,\ldots,N$$

where the P^i_{kj} are binary -- one if class i was observed at station j in analog year k (or the opposite class if year k is an antianalog year) and zero if not -- and the w_ℓ are weights given by

$$w_\ell = b/d^2_\ell \qquad b = (1/d^2_1 + \ldots + 1/d^2_L)^{-1} \tag{2}$$

The d^2_ℓ quantify the degree of analogy or antianalogy for the ten antecedent seasons (for example, falls if the forecast is for winter) that are most similar (analogs) or opposite (antianalogs) to the current antecedent season. The smaller a d^2_ℓ is the more alike or opposite a candidate season is to the current one. The determination of these "metrics" is based on a compact description of several elements of the global climate system and is

described at length in LB and BL. Categorical forecasts are currently made from (1) by a simple assignment of forecast class to the class with the largest P^1_j.

To produce anomaly temperature forecasts instead of class probability forecasts in the context of the framework just described is straightforward. These are given by

$$T'_j = w_1 T^*_{1j} + w_2 T^*_{2j} + \ldots + w_L T^*_{Lj} \tag{3}$$

where

$$T^*_{kj} = \begin{cases} T'_{kj} & \text{if k is an analog year,} \\ -T'_{kj} & \text{if k is an antianalog year,} \end{cases} \tag{4}$$

with the prime denoting departures from climatology and w_ℓ's given by (2). Climatological normals for analog prediction are based throughout this work only on the case library of candidate years which will never include forecast years. This prevents introduction of a skill bias pointed out by Van den Dool (1987). A categorical forecast then follows by noting where T'_j falls in the distribution of T^*_j. These forecasts are liable to be more conservative, i.e. an excess of near normal forecasts, than those inferred from (1) using the most probable class, because opposite signed T^*_{kj} will tend to cancel each other.

Two approaches for combining persistence and analog forecasts were examined, but only one will be detailed here, bivariate linear regression. The linear combination of persistence and analog forecasts at a station can be written as

$$T'_M = a\, T'_P + b\, T'_A \tag{5}$$

where the primes now denote standardized anomalies (based on normals of the dependent data set) and M, P, and A denote mixed, persistence, and analog forecasts respectively. If a history of forecasts and observations are available then the weights a and b can be determined for a given station and season by bivariate linear regression to minimize the squared error of T'_M over the dependent data set. Equation (5) can subsequently be used to make independent predictions. Because regression is inherently conservative, (5) is first divided by the square of its dependent data multiple correlation coefficient (the explained variance) before the temperature anomaly is converted to a categorical forecast. This avoids over prediction of the near normal class. The category assignment then is done using dependent data set observations.

If sampling errors are small compared to expected signals then (5) can be applied indiscriminately. This is because either or both the coefficients will be small when little or no signal is present in the dependent data and will lead appropriately to conservative forecasts, even with the inflation factor. This is decidedly not the case here; signal levels will generally be low but dependent sample size cannot exceed 37 if independent testing is performed. Consequently, sampling errors will be large and strategies have to be developed to avoid inappropriate use of (5)

whenever possible. Three such a priori schemes have been devised here, but only two will be presented.

The first is simple and straightforward to implement. It is based on the argument that b<0 implies that the analog term is contributing no independent skill for the particular station and season. A similar argument cannot be invoked for coefficient a because physical bases exist for antipersistence. Thus, for the Regression/Persistence Scheme, categorical forecasts are made from inflated regression forecasts except when b<0, in which case the forecast category is persisted from the preceding season.

In the second and third schemes, advantage is taken of the fact that the IMSL routine RSTAT (IMSL, Inc., 1987) produces as output the p value for a F-test on the multiple correlation coefficent and p values for two-sided t-tests for both of the regression coefficients. These p values are the probabilities that the test statistics could be exceeded by chance. These can be used as guides in the choice of categorical forecast for a station/season from regression, persistence, analog, and default near normal forecasts.

A flow diagram showing how the choice is made is shown in Fig. 2. The regression equation is first checked (through its multiple correlation coefficient) to see whether its p value implies statistical significance at some critical level. If it is and b<0 then the inflated regression categorical forecast is made. If the former is not true, b is checked for the right sign and for significance. If both conditions are met the analog categorical forecast is selected. If instead b<0 for any of the steps above, a is then examined for statistical significance. If it is, then the antecedent season's temperature category is persisted, but if it is not, then near normal is made as the default forecast.

The only difference between Mixed Regression Scheme A and Mixed Regression Scheme B is the way significance tests are conducted. For Mixed Regression Scheme A the p values for the multiple correlation coefficient and coefficients a and b must not exceed a preselected critical value p_0. It turns out that p_0 must be very high, in other words the tests must be very liberal, in order to avoid debilitating Type II errors. These last result when signal is discarded with noise. This is particularly a problem in the applications here, because both weak signal and noise are being amplified through the inflation factor to make categorical forecasts.

Thus, in order to make more discriminating choices in the decision chain in Fig. 2, an expensive alternative approach that reduces the chance of not being able to distinguish real signal from noise was tried. In Mixed Regression Scheme B a complete cross-validation test is conducted on the dependent data set for every forecast. In a cross-validation test, each year is withheld in turn, and a forecast model derived on the remaining years. This model is then checked on the year held in reserve. This process is repeated for every year in the data set. Because the forecasts themselves are made in a cross-validation mode this amounts to nested cross-validations, thus the expense. For each station/season 38 cross-validated forecasts can be made with our data set. Thus, each regression equation is derived on a dependent sample of 37 cases and tested on the 38th. But for each of these forecasts, 37 regression equations derived from only 36 cases apiece can also be formed. (For these equations the appropriate 36-year

normals are used.) It is the collective significance characteristics of these 37 auxiliary equations that form the basis for the choice of categorical forecast, one of which is from the single regression equation based on all 37 years. For this scheme a coefficient's p value must not exceed a critical value p_0 more than M_0 times out of 37 to pass a selection test. For the Mixed Regression Schemes a range of criteria p_0 and M_0 were tried.

All forecast methods and variations thereof were tested for each overlapping 3-month period at 92 stations over 38 years using cross-validation. Information from all years but one were used to construct forecasts for the year withheld, and each year was treated in turn in this way. Thus, because a season in 1 year is effectively independent in a statistical sense from the same season in an adjacent year (Madden, 1977) 38 independent predictions are possible for every station/season.

In formulating the forecasts, particularly the analog and regression forecasts, scrupulous care was taken to ensure no leakage of information from the independent case to the dependent data. For example, note that each time regression coefficients are derived with (5) 37 analog forecasts are needed. These were produced with forward-backward analog/antianalog searches through each 37-year dependent data set. In other words, an analog forecast was made for each year in a dependent data set (which already excludes the year for which the final forecast will be made) from candidates selected from the other 36 years in the set. The final analog forecast, however, that is used as a default in the Mixed Regression Schemes was based on the full 37-year dependent data set.

Skill of categorical analog forecasts made from anomaly forecasts (the modified system) are compared to those for forecasts based on the most probable class (the operational system) in Fig. 3 (by season and overall) and in Table 1 (by class and overall). The modified system is less skillful overall, but this difference is mainly a consequence of late spring/early summer (seasons 4 and 5) and late summer/early fall forecasts (season 8). The modified system tends to forecast near normal twice as often as observed and above and below normal half as often. But, from Table 1, its skill in forecasting the extreme classes is considerably greater than that for the operational system. Consequently, even though its forecasts of above and below are more conservative, they are also more reliable.

Mixed model results are summarized in Table 2. Several things are apparent overall from the table. First, all of the mixed schemes have significantly higher skill than the unmixed forecasts, especially compared to the components of the mixed systems, the modified analog and persistence forecasts. The three scores for the regression schemes reflect our a priori expectations, namely that the Regression/Persistence Scheme performed well and was improved upon only by Mixed Regression Scheme B with very liberal significance criteria. Results for Mixed Scheme B with $p_0 = 0.25$ and $M_0 = 36$ (i.e., one regression equation out of 37 needs to have $p \leq 0.25$) are shown to illustrate that even moderately stringent criteria lowered skill for this approach from those for the straightforward Regression/Persistence Scheme. However, a noticeable improvement in skill is possible with sufficiently lenient criteria--in this case one equation out of 37 needs to have $p \leq 0.55$. Improvement was apparent over a broad range of p_0 for $M_0 = 36$.

Season by season skill variability for Mixed Regression Scheme B (p_o =0.55, M_o=36) is compared to that for its input forecast schemes in Fig. 4. Mixed scheme skill exceeded that for both persistence and analog approaches in 8 three-month periods and effectively matched the better of the two in 3 other periods. Gains were particularly impressive for seasons 1 (January-February-March), 8 (August-September-October), and 12 (December-January-February). It is only in season 3 (March-April-May) that the mixed forecast skill was no better than a compromise between the two other skills.

Our main conclusions from the work herein can now be summarized. First, categorical analog seasonal temperature forecasts made from anomaly predictions tend to be more conservative than those made from most probable class predictions. However, above and below-normal forecasts made from the former are more reliable than those made from the latter. Next, persistence and analog seasonal temperature forecasts can be combined objectively to exploit the strengths of both to produce superior forecasts. However, regression forecasts cannot be indiscriminately used. Highest overall skill is obtained when equations with negative analog coefficients or which unanimously fail liberal statistical significance tests in a cross-validation check are eliminated.

Based on the results presented here mixed analog/persistence prediction will be added to the list of tools available to the seasonal forecaster at CAC. It will be implemented in such a way that it will automatically take advantage of new data available each year as well as any improvements to the operational analog system.

Table 1. Analog Prediction Skill

Type	Total	Near Normal	Above/Below Normal
Operational	9.7	-0.2	14.9
Modified	8.4	1.8	21.7

Table 2. Overall Skill

Scheme	Skill
Operational Analog	9.7
Modified Analog	8.4
Persistence	9.4
Regression/Persistence	11.3
Mixed Regression B (p_o = 0.25, M_o = 36)	11.0
Mixed Regression B (p_o = 0.55, M_o = 36)	11.6

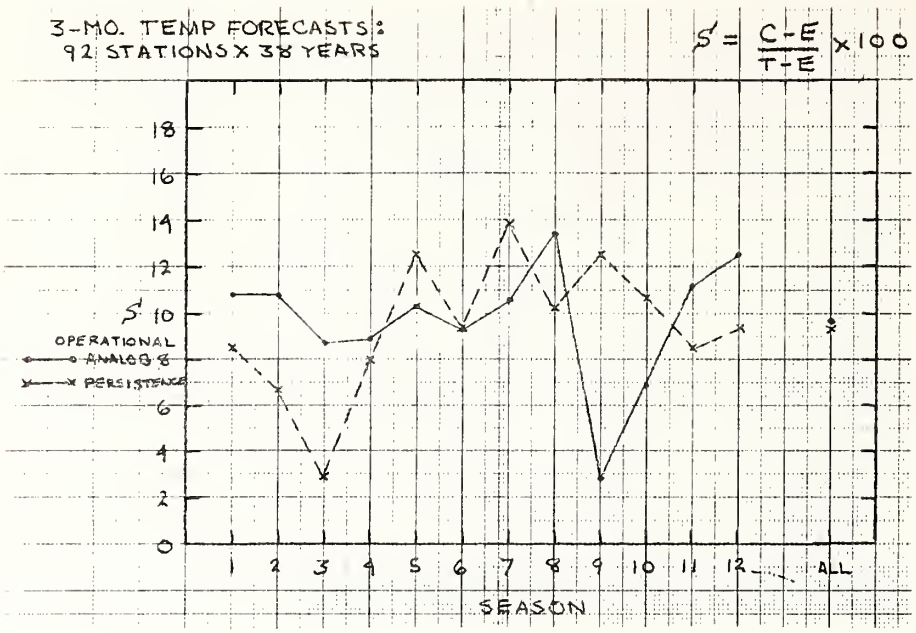

Fig. 1 Skill (S) by 3-month forecast period (number denotes first month of period) and for all periods combined of predictions of three equally-distributed temperature categories made by the operational analog prediction system and by persistence. The letters T, C, E denote the total number of forecasts, the number correct, and the number expected to be correct by chance respectively.

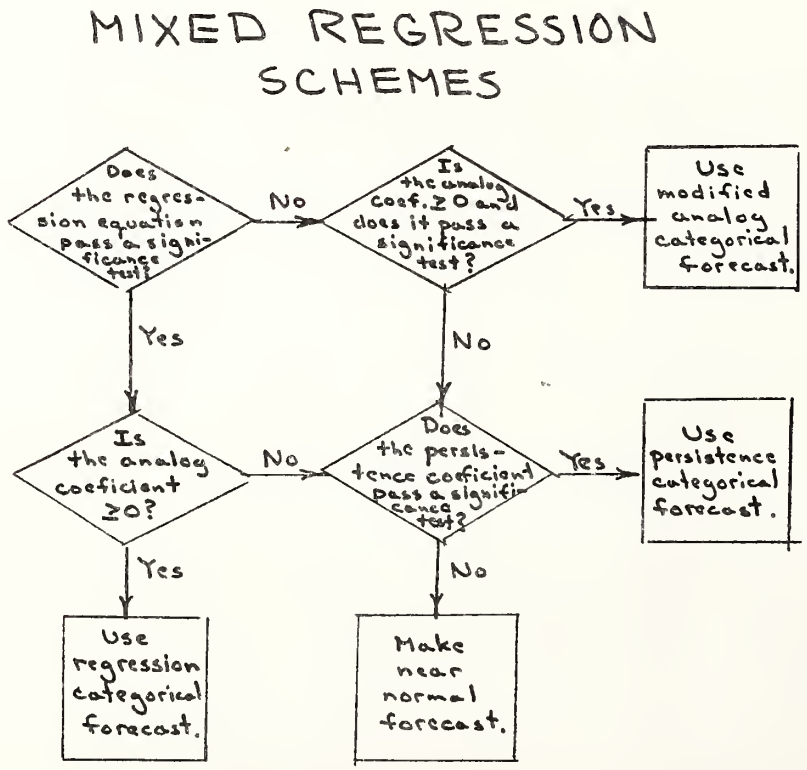

Fig. 2 Flow diagram to choose among persistence, modified analog, regression, or near normal default forecasts in Mixed Regression Schemes. Start at upper left corner.

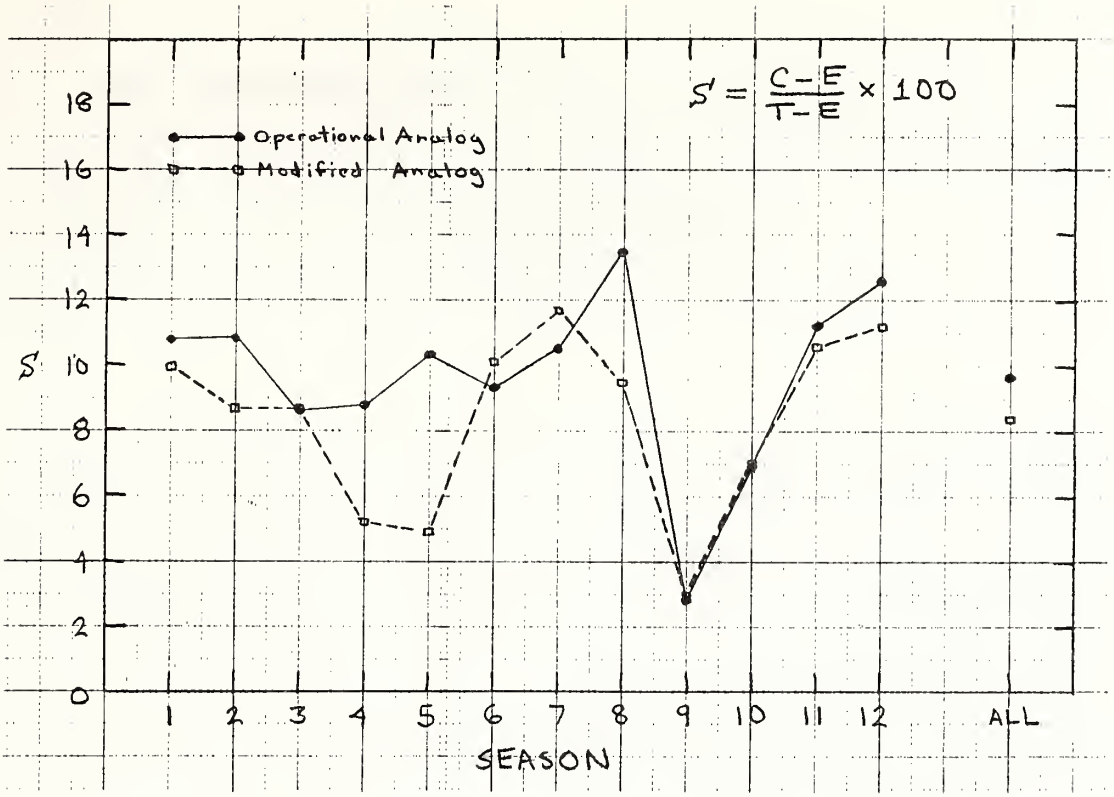

Fig. 3 Same as in Fig. 1 except for forecasts made by the operational and modified analog prediction systems.

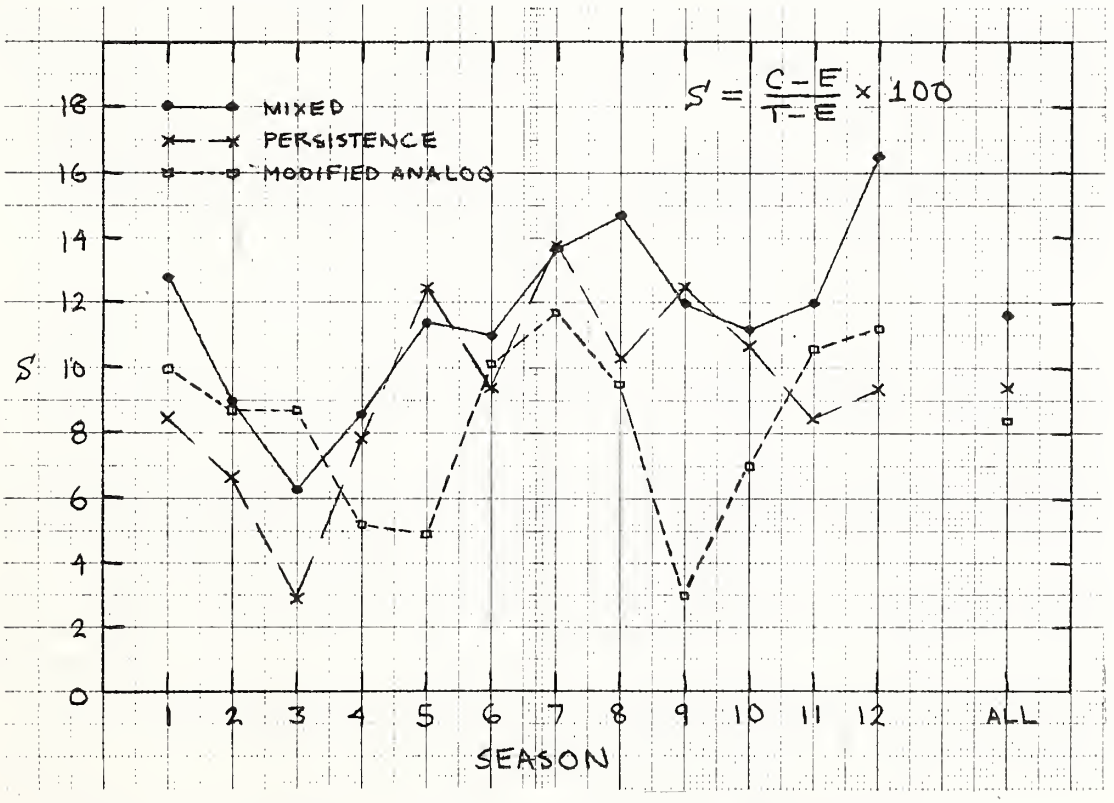

Fig. 4 Same as in Fig. 1 except for forecasts made by persistence, the modified analog prediction scheme, and Mixed Regression Scheme B(p_0 = 0.55, M_0 = 36).

Verification of Canadian Monthly Temperature Forecasts

Amir Shabbar
Canadian Climate Centre
4905 Dufferin Street
Downsview, Ontario, Canada

Introduction

In the Atmospheric Environment Service (AES) long-range forecast, time-lagged correlations of the 50-kPa height anomalies and the forecasts from numerical weather prediction models, such as CMC, NMC and ECMWF up to 10 days, are the main input. The first five unrotated empirical orthogonal functions of the 50-kPa height anomalies are then used to specify forecast hemispheric maps from a set of input anomalies at 50 kPa. The eof filter is useful in two ways. First, it fills the hemispheric map with spatially consistent features, and second it adjusts or introduces height anomalies that are climatologically consistent. In this study, a number of verification statistics have been compiled for the forecasts from January 1986 to August 1988. These statistics include per cent correct sign, Heidke skill score and scatterplots of surface temperatures, and pattern correlations of 50-kPa height anomalies. At present, surface temperatures are verified for the signs of the anomalies only. The purpose of this study is twofold. First, to present verification results that have been seasonally stratified, and second to investigate if we have skill in forecasting the magnitude of the surface temperatures. More generally, this study attempts to investigate the skill of 3-class surface temperatures forecasts.

Results

Verification statistics are compiled for monthly forecasts from January 1986 to August 1988. Surface temperatures from 35 Canadian locations are verified by the signs of the anomalies and in a 3-class category (30:40:30 to BELOW:NORMAL:ABOVE). Heidke scores using chance as a standard are calculated. In order to investigate bias in the forecast, histograms of the mean error are plotted. Finally, a pattern correlation is calculated between the forecast and observed 50-kPa height anomalies. In all cases, persistence is used as a standard for comparison. Figure 1a and b show the network of surface stations and the 50-kpa grid points, respectively, on which the verification is carried out. For comparison, NOAA monthly temperature forecast from January 1986 to August 1988 are also verified for the sign of the anomaly.

i) Per cent Correct Sign

Figure 2a shows monthly stratified scores for per cent correct sign for 35 Canadian stations. Generally, the scores are high in winter and low in summer. Persistence straddles

the AES forecast in most cases, but in some months AES forecasts depart drastically from persistence, e.g., in March and April when the forecast outperforms persistence and NOAA forecasts by a wide margin. In Figure 2b, the results are stratified by climatological season. The AES forecast does better than persistence in winter and spring, but falls behind persistence in fall. Summer scores are about the same for the AES forecast and persistence. AES forecast scores are better than that of NOAA's in winter , spring and summer but worse in fall.

ii) Scatterplot and skill score

In order in investigate the skill in forecasting the magnitude of the temperature anomalies, seasonally stratified AES forecast temperature anomalies are plotted against observed temperature anomalies on scatterplots in Figures 3a-d. These plots are then compared with persistence (not shown). The Heidke skill scores, SS given by

$$SS = \frac{\text{No. correct} - \text{No. correct by chance}}{\text{Total number} - \text{No. correct by chance}}$$

are calculated in Tables 1a-d for the AES forecast, and those for persistence are shown in Tables 2a-d. Once again, the forecast skill is higher than that of persistence in winter and Spring, but lower in summer and fall. The Seasonal skill score plotted in Figure 4 indicates significant skill over persistence in winter and spring.

iii) Pattern correlation at 50 kPa

Since our primary forecast is at 50 kPa, we wanted to investigate skill for the network of 50-kPa grid points shown in Figure 1b. Operationally, Canadian surface temperature anomalies are specified from these 110 points. Although we recognize that any given forecast will not use all 110 points, we still verified the entire sample on the complete network of 110 points. In Figure 5, we plotted the pattern correlations between the following pairs: (forecast, observed); (persistence, observed); and (forecast, persistence). Generally, skilful forecasts at 50 kPa are reflected as skilful forecasts in surface temperatures, for example, the January and November 1986 forecasts. Even though the main input in our monthly forecast is the persistence of 50-kPa height anomalies, the forecast, persistence pair is not well correlated with the forecast, observed pair.

Summary

Based on a sample of 63 forecast from January 1986 to August 1988, we investigated 2- and 3-class skill of Canadian surface temperatures. Our major findings are as follows:

a) We have skill over persistence in winter and spring in both 2- and 3-category forecasts. In summer and fall, persistence outperforms forecast. Note our

forecasts have skill over chance in all four seasons.

b) We tend to underforecast winter temperatures, but error bias is not endemic to a particular month.

c) Skilful forecasts at 50 kPa are reflected in the surface temperatures, and strong reliance of forecast on persistence doesn't necessarily show in pattern correlations at 50 kPa.

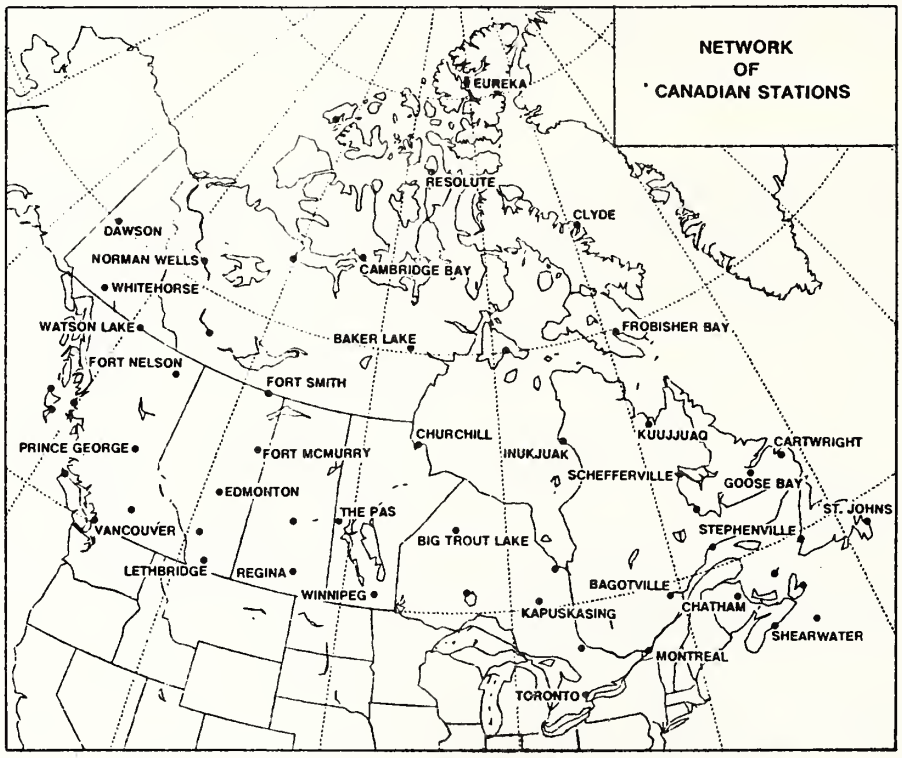

Fig. 1a Forecast verification network of 35 Canadian stations.

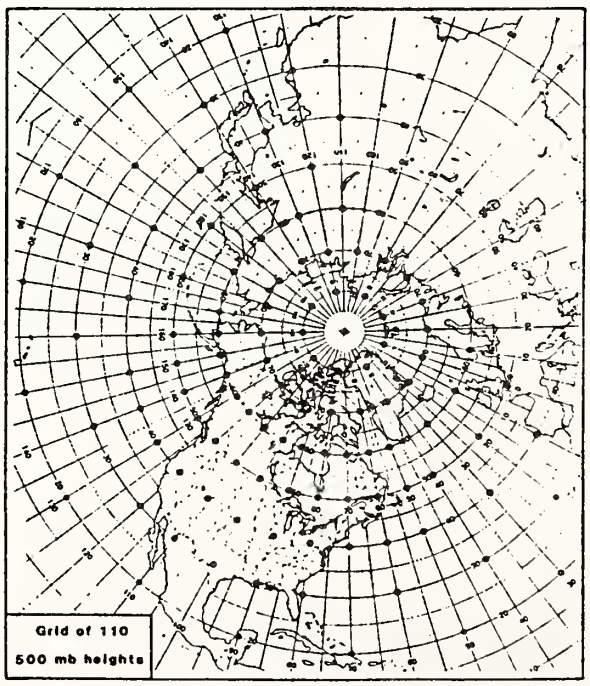

Fig. 1b Network of 110 lat.-long. points used in the specification of Canadian surface temperatures.

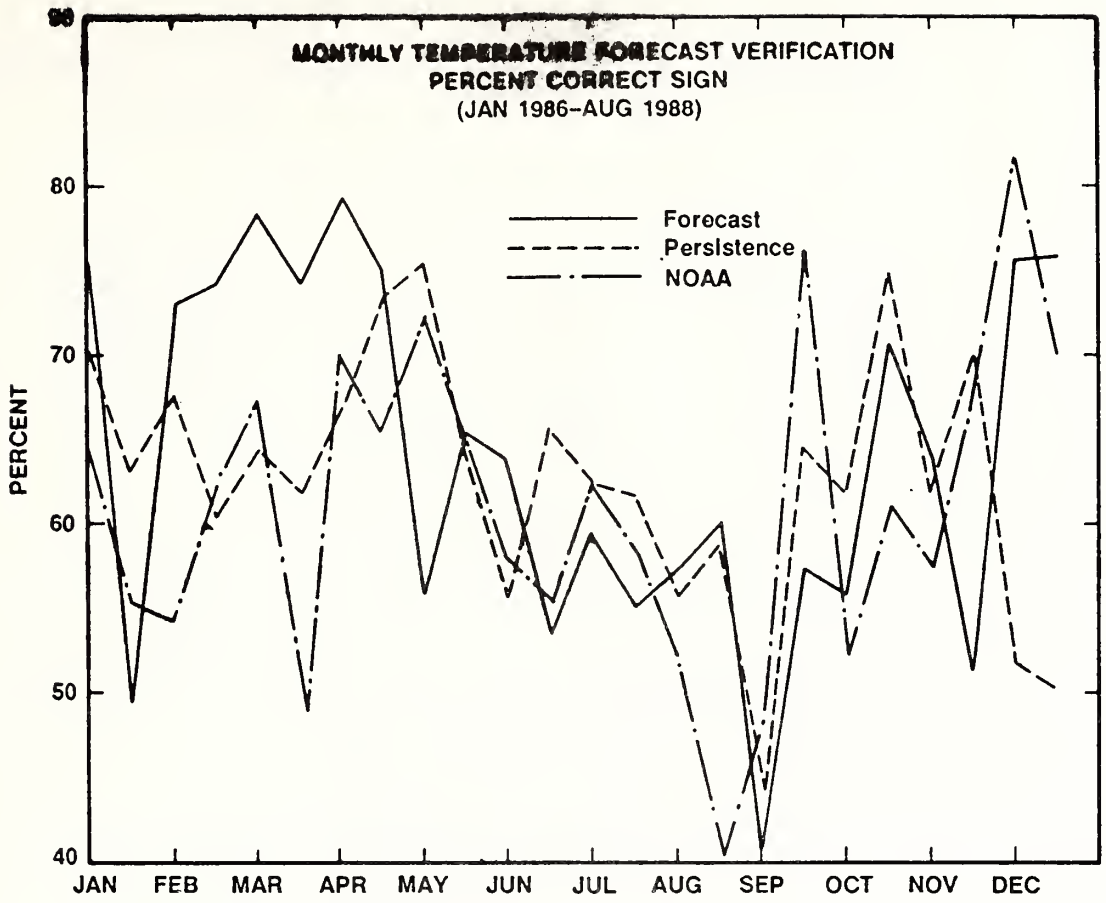

Fig. 2a Mean percent correct sign of surface temperatures from January 1986 to August 1988.

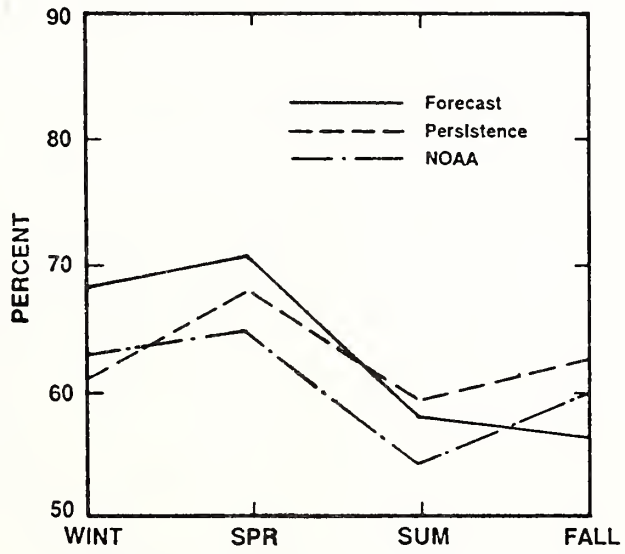

Fig. 2b Percent correct sign of monthly temperature forecasts by season from January 1986 to August 1988.

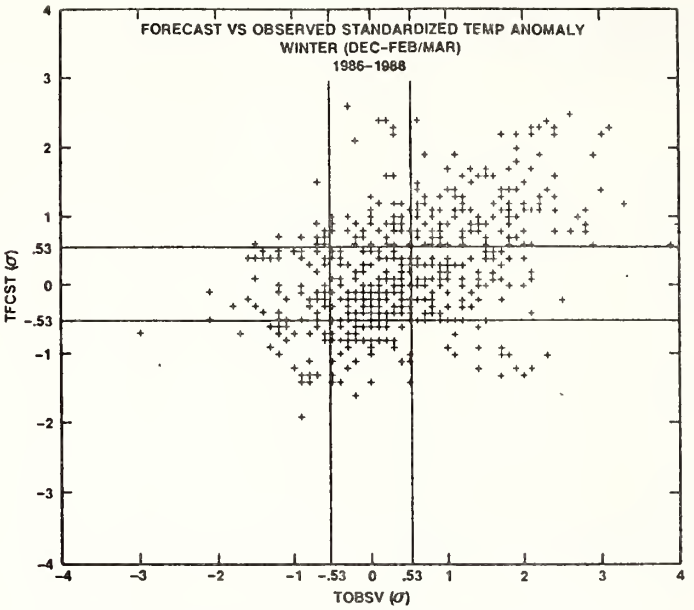

Fig. 3a Scatterplot of the AES forecast vs observed standardized temperature anomaly for winter from 1986 to 1988.

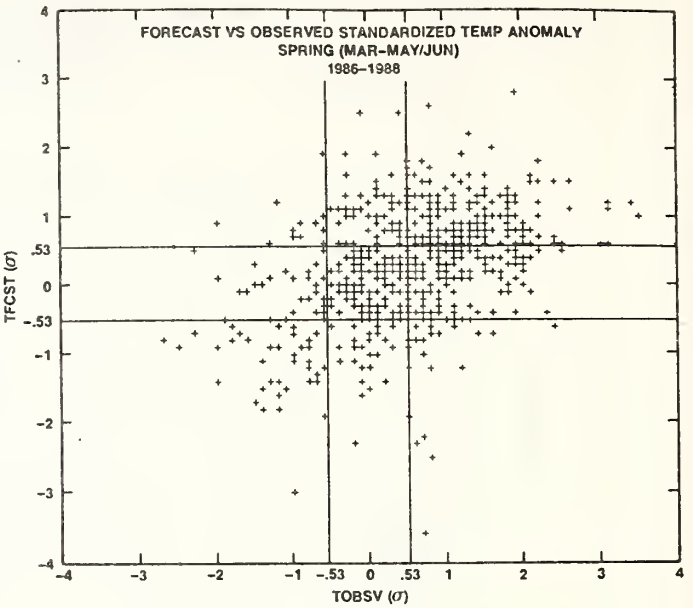

Fig. 3b Same as 3a except for Spring.

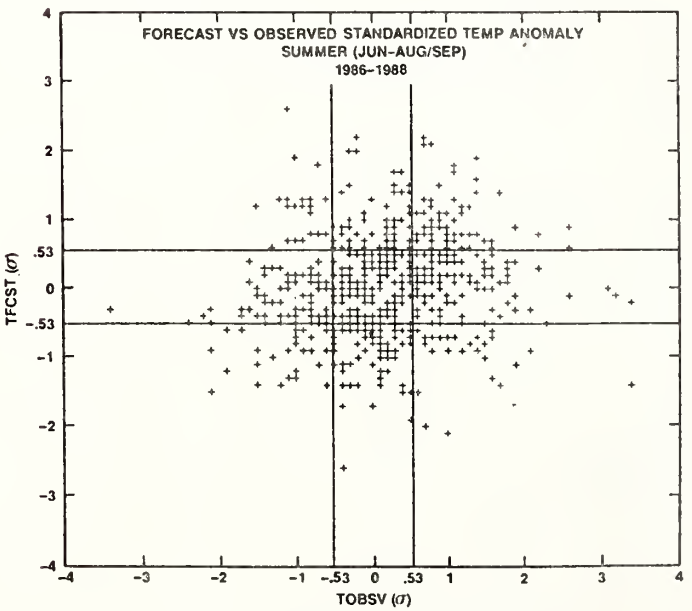

Fig. 3c Same as 3a except for Summer.

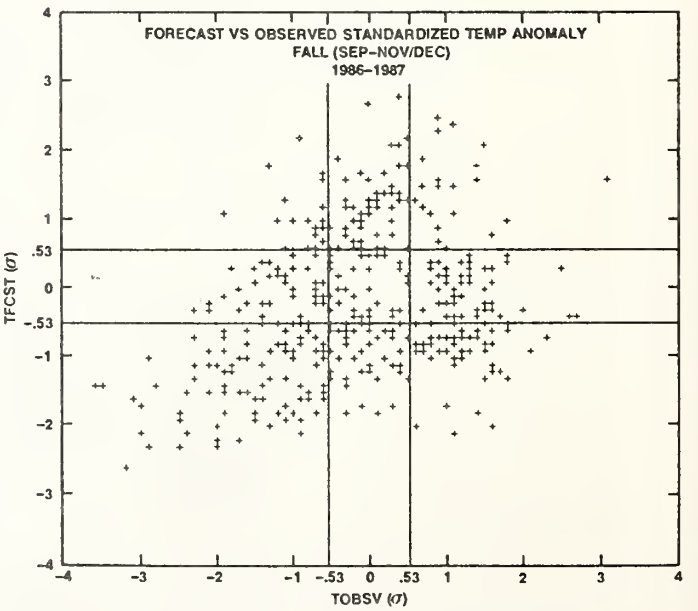

Figure 3d Same as 3a except for Fall.

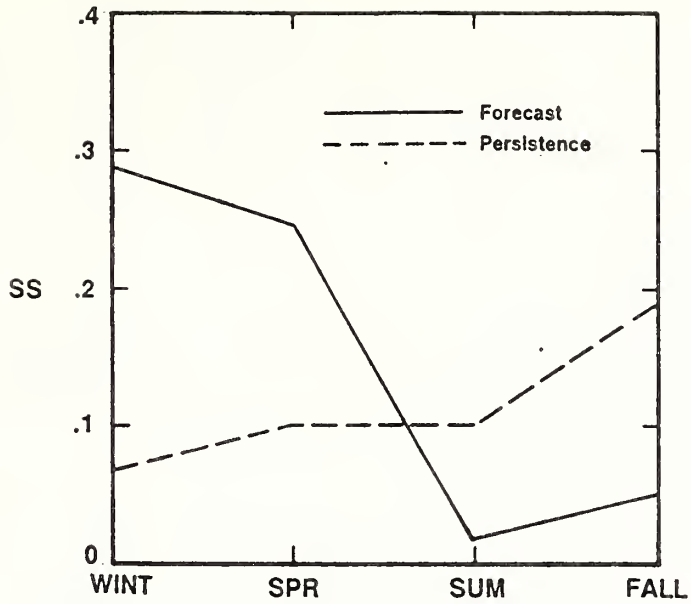

Fig. 4 Heidke skill score between forecast and observed surface temperatures by season from January 1986 to August 1988.

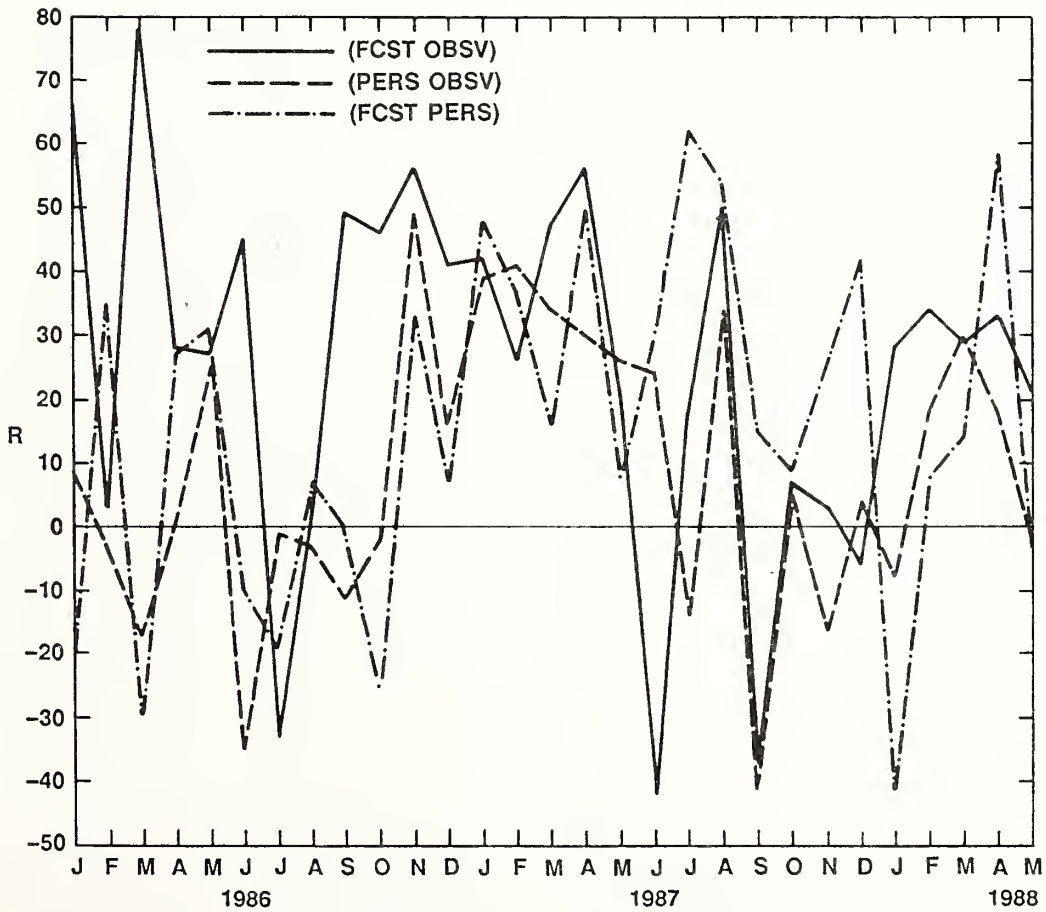

Fig. 5 Pattern of correlation between various pairs of forecast at 50 kPa.

	B	N	A	
A	1.96	8.93	24.29	35.18
N	8.39	25.89	15.36	49.64
B	4.64	7.86	2.68	15.18
	15.00	42.68	42.32	100.00

Heidke skill score SS = 0.27

Table 1a Normalized contigency table for AES forecast - winter (Dec-Feb/Mar) 1986-1988.

	B	N	A	
A	1.90	10.63	28.10	40.63
N	5.08	19.37	20.48	44.92
B	6.19	4.76	3.49	14.44
	13.17	34.76	52.06	100.00

Heidke skill score SS = 0.24

Table 1b Same as a except for spring (Mar-May/Jun) 1986-1988.

	B	N	A	
A	3.70	9.92	9.75	23.36
N	12.61	23.70	18.32	54.62
B	5.38	11.93	4.71	22.02
	21.68	45.55	32.77	100.00

Heidke skill score SS = 0.02

Table 1c Same as a except for summer (Jun-Aug/Sep) 1986-1988.

	B	N	A	
A	4.76	12.14	5.24	22.14
N	11.43	11.90	13.33	36.67
B	20.00	10.00	11.19	41.19
	36.19	34.05	29.76	100.00

Heidke skill score SS = 0.05

Table 1d Same as a except for fall (Sep-Nov/Dec) 1986-1987.

	B	N	A	
A	3.04	17.86	20.71	41.61
N	6.61	14.64	13.75	35.00
B	5.36	10.18	7.86	23.39
	15.00	42.68	42.32	100.00

Heidke skill score SS = 0.07

Table 2a Normalized contigency table for persistence forecast - winter (Dec-Feb/Mar) 1986-1988.

	B	N	A	
A	4.13	15.71	28.89	48.73
N	5.87	14.60	18.41	38.89
B	3.17	4.44	4.76	12.38
	13.17	34.76	52.06	100.00

Heidke skill score SS = 0.10

Table 2b Same as a except for spring (Mar-May/Jun) 1986-1988.

	B	N	A	
A	5 71	15.29	16.30	37.31
N	10.08	20.17	11.76	42.02
B	5.88	10.08	4.71	20.67
	21.68	45.55	32.77	100.00

Heidke skill score SS = 0.10

Table 2c Same as a except for summer (Jun-Aug/Sep) 1986-1988.

	B	N	A	
A	4.52	10.95	11.90	27.38
N	13.57	15.48	11.43	40.48
B	18.10	7.62	6.43	32.14
	36.19	34.05	29.76	100.00

Heidke skill score SS = 0.18

Table 2d Same as a except for fall (Sep-Nov/Dec) 1986-1987.

Specification of Monthly and Seasonal Precipitation in California and Arizona River Basins

William H. Klein and Hal J. Bloom
Department of Meteorology
University of Maryland
College Park, MD 20742

This paper discusses multiple regression equations for specifying monthly and seasonal precipitation amounts (PA) in selected river basins of California and Arizona from concurrent fields of 700 mb height anomaly (HA) in the 6-month wet season (Oct.-March) during the 30 years: 1950-1980. PA was averaged over 16 stations in the North Sierra-Nevada Mountains, 16 stations in the Central Sierra, 11 stations in the South Sierra, and 7 stations in Central Arizona (Fig. 1). It was then expressed as one of 21 percentiles of the gamma distribution, separately for each basin, month and season. Our HA predictors were taken at 79 grid points over North America and the eastern Pacific from 20°N to 60°N (Fig. 2). In order to increase our sample size, we pooled the data for each target month or season with its adjacent period on either side. We applied a stepwise forward selection method to screen PA in each basin during each month and season as a function of HA at each grid point. A Monte Carlo simulation provided an objective criterion for adding terms to the multiple regression equations. Additional cut-off criteria included synoptic reasoning, additional variance explained, probability level, total number of terms, and continuity of regression coefficients.

A sample specification equation for the three-month season of Nov.-Dec.-Jan. is illustrated in Table 1 for central Arizona (35°N, 112°W). The first predictor selected is the HA at 30°N, 120°W, which explains almost 61% of the precipitation variance (RV). The location of this variable and its negative regression coefficient indicate that heavy (light) precipitation in central Arizona during fall and winter is usually accompanied by below (above) normal heights about 600 miles to the southwest. The second HA adds 4.2% to the RV and reinforces the effect of the first. Its location (30°N, 140°W) and negative coefficient suggest that a broad band of below normal heights to the west-southwest enhances incursions of cyclones, fronts and moisture from the Pacific into Arizona. The selection process was terminated with 65% of the variance explained by just two heights because no other variable could increase the RV by more than 2% or exceed the critical F-value. Similar equations were derived for each basin in six overlapping seasons centered on each month from Oct. through March. On an overall basis, the equations explain 63% of the PA variance by means of just 2.2 heights, but temporal and spatial variations are striking.

Figures 3-6 compare the properties of the three-month seasonal equations with their one-month counterparts. Fig. 3 shows that the RV for both sets rises rapidly from minima in Oct. to maxima in Dec. and then declines slowly for the next three months. During all months, the seasonal curve is slightly higher than the monthly, with overall RV's of 63% for the former and 61.2% for the latter. Fig. 4 depicts the annual cycle in terms of average number of heights in monthly and seasonal equations. Here the differences between the two sets is greater than for RV, with maxima in Dec. for monthly and March for seasonal. Overall, the monthly equations contain 2.6 heights, compared to only 2.2 for the seasonal equations.

Figure 5 compares the monthly and seasonal equations on a regional basis, averaged over all six months. The RV's decrease steadily from northwest (No. Cal.) to southeast (Cen. Ariz.) for both sets. They have about the same RV in the three California basins, but in central Arizona the RV is 9% higher for the latter. As a result, the RV for all basins is about 2% greater for the seasonal equations. Fig. 6 is similar but for the average number of heights

in the specification equations. The monthly equations contain more HA's than the seasonal in central and southern California; elsewhere the differences are negligible. Overall, the average number of heights is 0.4 smaller in the seasonal than the monthly equations. This should make the former more stable in the future.

Two additional sets of specification equations were derived for each of the four basins: one for PA and HA during the two-month period of December and January; the other for the four-month period from December through March. Since 2- and 4-month equations were available for one period only, we computed mean values of RV and number of heights from the monthly and seasonal equations for the Dec.-Jan. period and the Dec.-March period, with results summarized in Table 2. The first line shows that, for the Dec.-Jan. period, the 2-month equations are clearly superior to the 1-month equations and slightly better than the 3-month equations. For the Dec.-Mar. period, the 3-month equations are superior to both the 1- and 4-month equations. Thus, the optimum period appears to be about 2 to 3 months.

Finally, the composition of the specification equations was analyzed by tabulating the location and sign for the first and second heights selected in each monthly and seasonal equation. Table 3 shows that the first variable was remarkably similar for both types of equation and from month to month in any one basin. For all six months and all four basins, the first height was usually located a few hundred miles west of the reference basin and its correlation with precipitation was invariably negative. Furthermore, the same grid point was selected first in both the monthly and seasonal equations in 19 out of 24 possible cases. In the remainder, the first height selected by the seasonal equations was at a grid point immediately adjacent to that picked by the monthly equations. Likewise, on a month-to-month basis, the first grid point was nearly always identical or immediately adjacent. The second variable selected in the specification process was also similar in both monthly and seasonal equations, but to a lesser extent than the first. Taken in conjunction with the first variable selected, the second usually indicated a large-scale height gradient and anomalous flow of moist (dry) air favorable for heavy (light) precipitation.

Principal findings for the six months and four basins studied here may be summarized as follows:

1. Approximately 60% of the monthly precipitation variance can be explained by specification equations containing just 2.6 concurrent 700 mb heights.
2. Large geographical and month-to-month variations in the RV suggest that specification is more effective in wetter climates and less effective with dryer conditions.
3. Seasonal specification equations explain about 2% more of the precipitation variance than monthly equations by means of 0.4 less heights.
4. The optimum averaging period for precipitation specification appear to be on the order of 2-3 months.
5. The composition of the specification equations is generally similar from month to month and for different averaging periods.
6. Only a few grid points contain most of the height information required to specify monthly and seasonal precipitation.

Acknowledgment

This research was sponsored jointly by the California Department of Water Resources, the Salt River Project of Arizona, and the Southern California Edison Company. We are grateful to Maurice Roos of the first agency and Dan Phillips of the second for supplying their precipitation data.

Table 1. Summary of the stepwise regression statistics obtained by screening percentiles of total precipitation in the Central Arizona watershed (35°N, 112°W) during the 3-month Nov.-Dec.-Jan. season as a function of the concurrent field of 700 mb height anomalies. The critical F-values were determined by a Monte Carlo procedure. The final equation selected for use in specification is starred.

Step	Grid. point for height	Reg. coeff. on entry	Added RV(%)	Total RV(%)	Computed F-value	Prob. level(%)	Critical F-value	SE (percentiles)
1	30°N,120°W	-2.0503	60.6	60.6	135.6	100.0	10.7	18.6
2*	30°N,140°W	-0.364	4.2	64.8	10.3	99.8	7.4	17.6
3	35°N,75°W	+0.194	1.8	66.6	4.5	96.4	5.8	17.1
4	25°N,125°W	-0.423	1.1	67.6	2.8	90.5	5.0	16.8
5	60°N,80°W	+0.116	1.2	68.8	3.1	91.8	4.6	16.5
6	25°N,135°W	+0.990	1.4	70.2	4.1	95.3	3.9	16.2

Table 2. Reduction of variance (RV in %) and number of heights selected (Terms) in specification equations obtained by screening precipitation amounts (in percentiles) in three Sierra Nevada Basins and Central Arizona during various periods from 1 to 4 months in duration as a function of concurrent 700 mb height anomalies at 79 grid points from 1950 to 1980.

Period	One Month		Two Months		Three Months		Four Months	
	RV	Terms	RV	Terms	RV	Terms	RV	Terms
Dec.-Jan.	67.4	3.3	69.3	2.5	68.8	2.4	-	-
D-J-F-M	64.0	2.7	-	-	66.2	2.4	65.1	3.5

Table 3. Location (latitude in °N and longitude in °W) of first grid point selected in specification equations obtained by screening monthly (M) and seasonal (S) precipitation amounts (in percentiles) in three Sierra Nevada Basins and Central Arizona as a function of concurrent 700 mb height anomalies at 79 grid points from 1950 to 1980.

Month	North		Central		South		Arizona	
	M	S	M	S	M	S	M	S
October	40/130	40/130	45/125	45/125	35/125	40/130	30/120	30/120
November	40/130	40/130	45/125	40/130	40/120	40/130	30/120	30/120
December	40/130	40/130	45/125	45/125	40/120	45/125	30/120	30/120
January	40/130	40/130	40/130	40/130	40/130	40/130	35/125	35/125
February	40/130	40/130	40/130	40/130	35/125	35/125	35/125	35/125
March	40/130	40/130	40/130	40/130	35/125	35/125	30/120	35/125

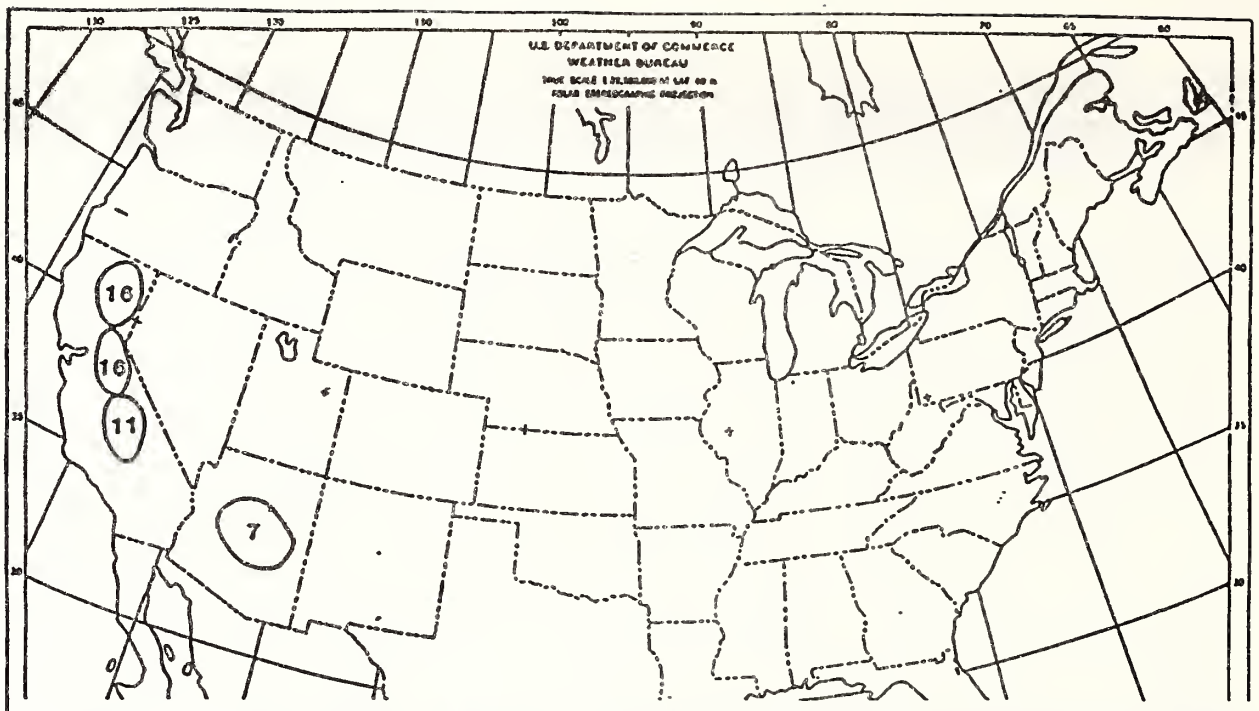

Figure 1. Approximate locations of three drainage basins in the Sierra Nevada mountains of California and one in the Salt and Verde rivers of central Arizona. Monthly and seasonal precipitation amounts were averaged over the number of observing stations indicated inside each basin.

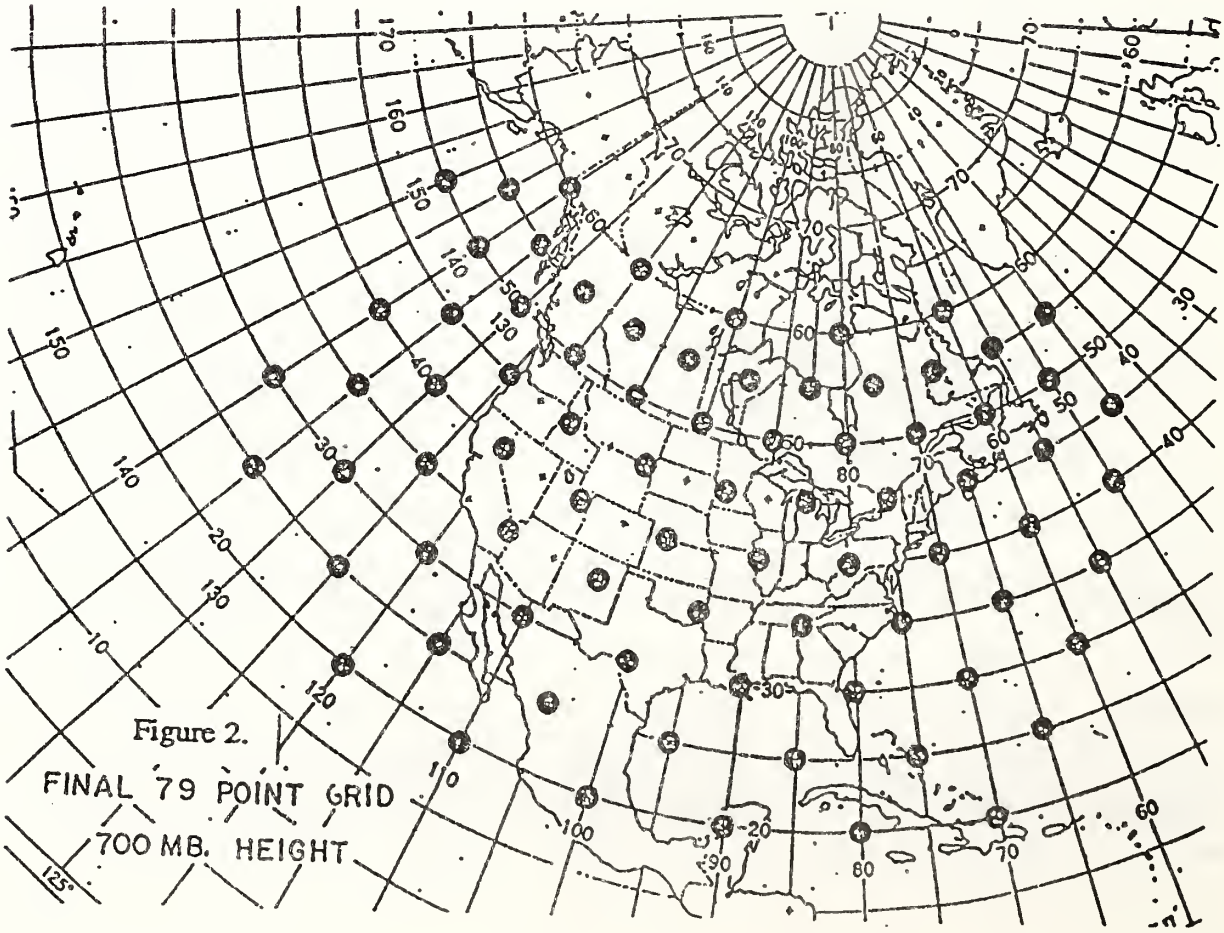

Figure 2. FINAL 79 POINT GRID 700 MB. HEIGHT

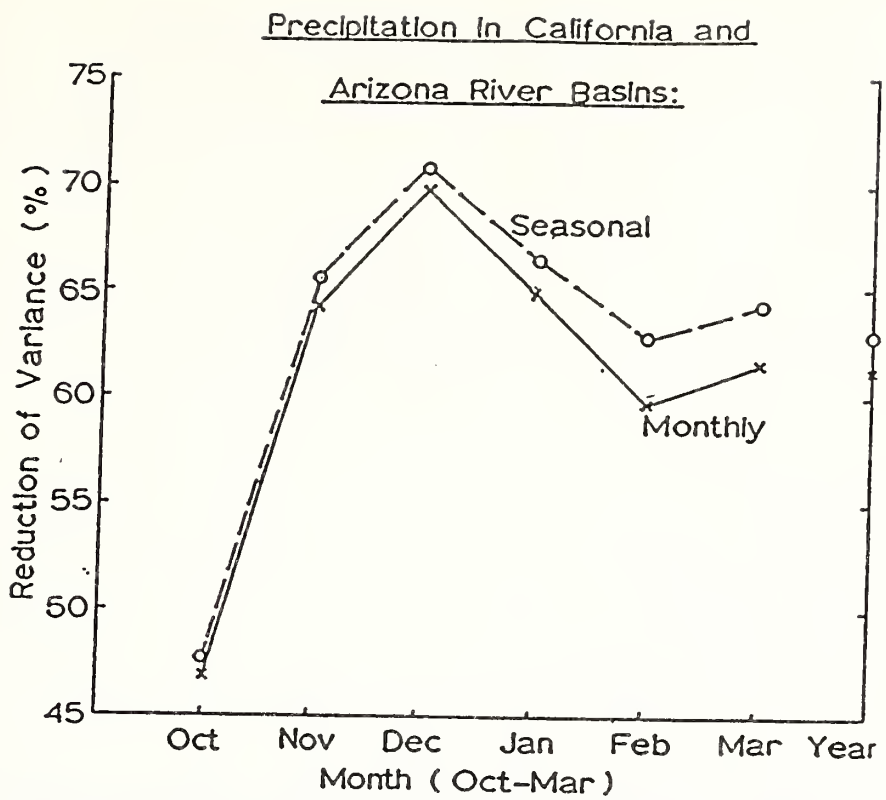

Figure 3. Average percent of precipitation variance explained by specification equations for four basins of Fig. 1 as a function of concurrent 700 mb height anomalies of Fig. 2 for monthly (solid) and seasonal (dashed) periods centered on month given along abscissa. The average values for all six months are plotted on the right ordinate for monthly (cross) and seasonal (circle) equations.

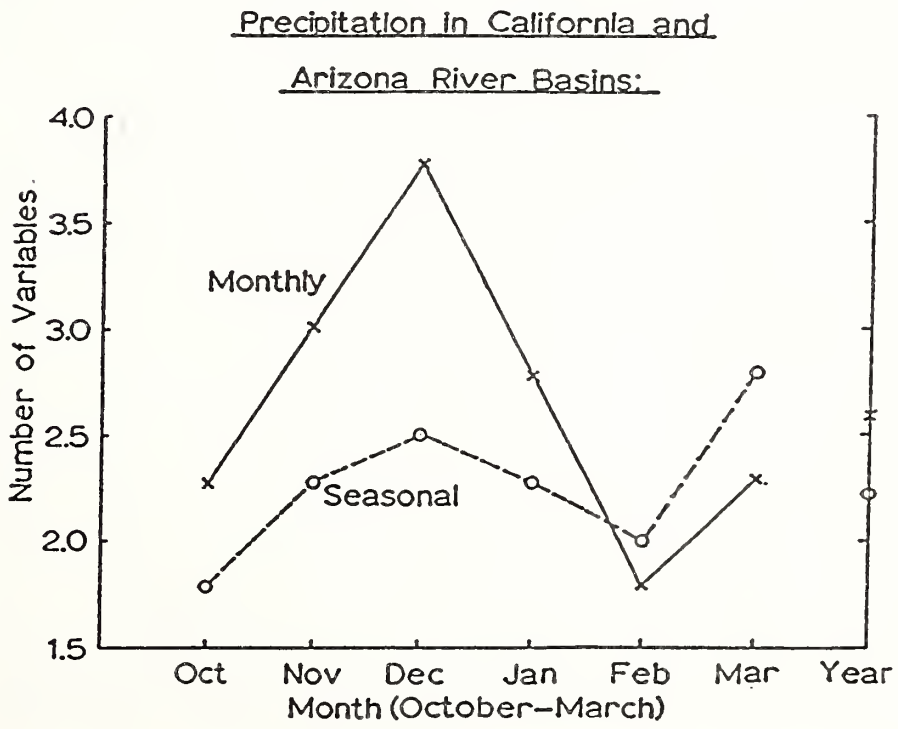

Figure 4. Same as Fig. 3 but for average number of heights in specification equations.

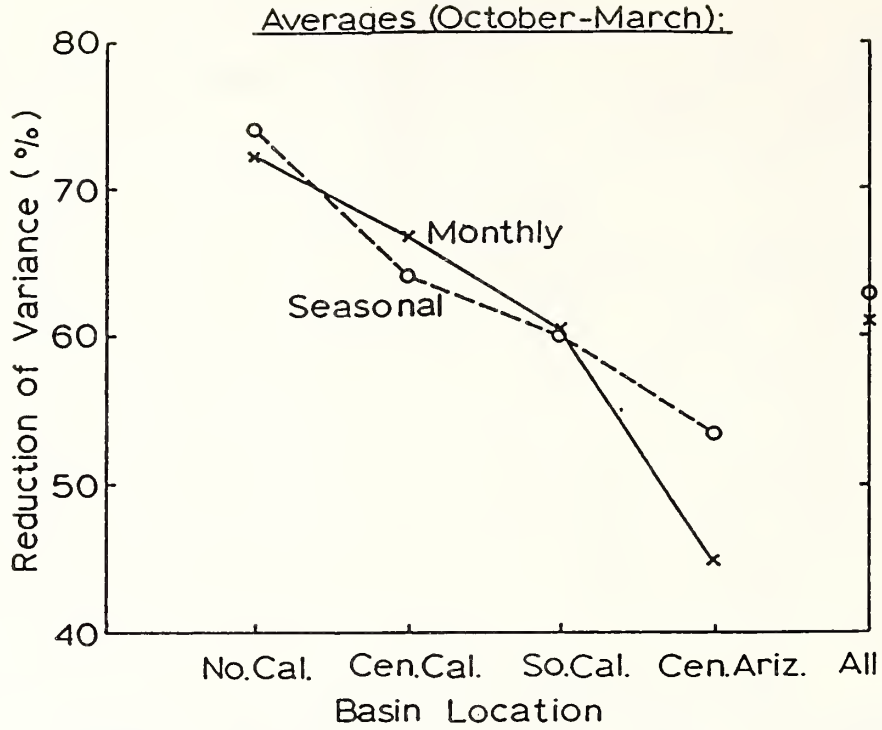

Figure 5. Average percent of precipitation variance explained by specification equations for six months of wet season for monthly (solid) and seasonal (dashed) periods in four basins of Fig. 1 plotted along abscissa. Mean values for all basins are plotted on the right ordinate for monthly (cross) and seasonal (circle) equations.

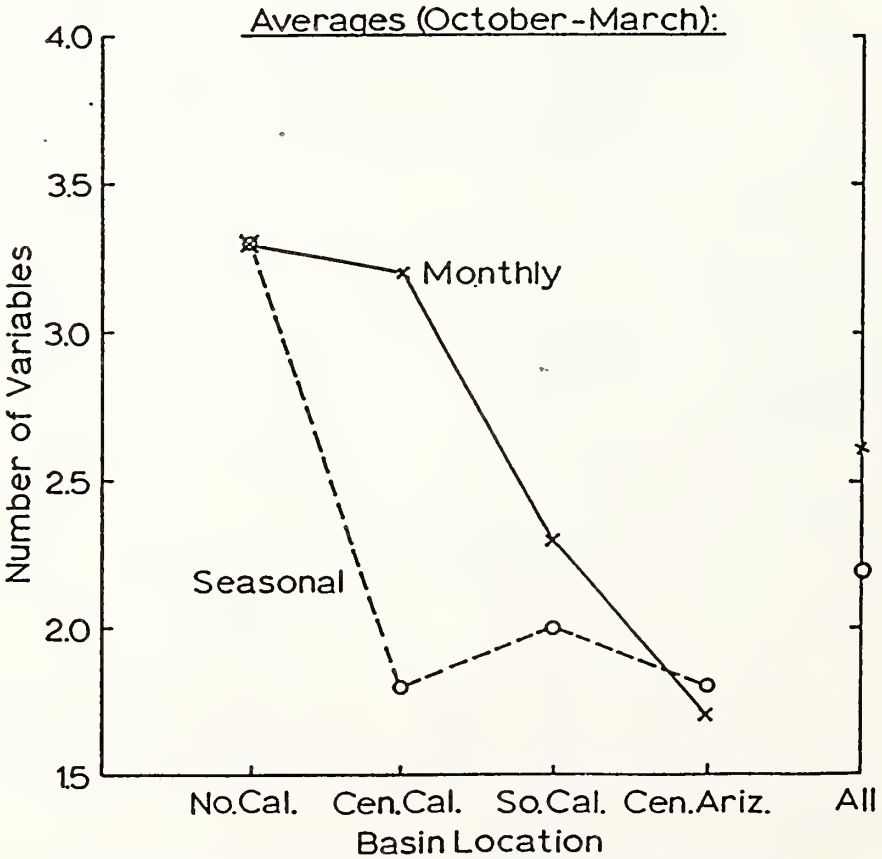

Figure 6. Same as Fig. 5 but for average number of heights in specification equations.

Specification of Winter Precipitation over Canada from the Surrounding 50-kPa Height Field

Amir Shabbar
Canadian Climate Centre
4905 Dufferin Street
Downsview, Ontario, Canada

Introduction

In this paper, we derive relationships between monthly precipitation over Canada and the simultaneous field of monthly mean 50-kPa heights in winter-time. A set of multiple regression equations is obtained between the departures of monthly precipitation from the median and the concurrent field of 50-kPa height anomalies over North America and adjacent oceans.

Data and Methodology

In the development sample monthly anomalies of precipitation and 50-kPa heights from 1946 to 1983 (38 years) were pooled for December, January and February to give 114 observations for regression. The 50-kPa grid for specifying precipitation was chosen at 86 points from 30 to 170W and from 20 to 80N (Fig. 1).

In order to lessen the small-scale and discontinuous effects of precipitation, we delineated climatologically coherent areas of precipitation by correlating precipitation at a given station with that at neighbouring stations. A threshold of 0.5 was chosen to group those stations having similar precipitation regimes (Fig. 2). In southern Canada many of the coherent areas overlapped, whereas large part of Canada north of 60N did not have areas that could be identified as having similar precipitation regimes. Stations within a coherent area were areally averaged by the Theissen polygon technique, which gives more weight to the station by itself and less to those relatively close to each other in the same enclosed area.

In order to test the robustness of the derived equations, we scuffled the predictand precipitation time series 100 times by the Monte Carlo method. Multiple regression equations were then derived for the original and the 100 random predictand time series. The regression procedure used was the modified version of the Forward Stepwise Selection technique. Variables were added one by one to the model, and the F-statistics for a variable to be included had to be significant at the 97.5% level. After a variable was added, however, the stepwise method looked at all the variables already included in the model and deleted any variable that did not produce an F-statistics significant at the 97.5% level. Only after this check was made and the necessary deletions accomplished was another variable added to the model. This process ended when none of the variables

outside the model had an F-statistic significant at the 97.5% level and every variable in the model was significant at the 97.5% level.

Results

So far we have developed regression equations for a few areally averaged areas along the southern border of Canada. Here we present results for three areas: southern Alberta, the southeastern Prairies and southern Ontario. Tables 1 to 3 show the selection of predictors and various statistics for these areas. To test the robustness of the equations and to determine how many predictors to keep in the equations, we draw attention to Figs. 3-5 for the 3 areas mentioned above. In these figures, we plot the added reduction of variance as a function of predictor number for the actual precipitation time series as well as for the average of the 100 random time series. Note the maximum and minimum of the 100 random time series are also plotted. For southern Alberta (Fig. 3), the first predictor, which explains over 23% of the total variance, is much larger than the average of the first predictor of the random time series (6.5%). Predictor number 2 is also significantly higher than the ensemble average of second predictor of the random series; however, predictor number 3 could not be distinguished from the corresponding predictor of random series. For this case, the cut-off number for the predictors would be 2. Both of these predictors are from an upstream ridge over the north Pacific. For the southeastern Prairies, only one predictor (an upstream trough of low pressure over British Columbia), which explains about 16% of the variance, was accepted into the equation. This predictor is significantly different from the average of the predictor of the random precipitation time series. And for southern Ontario, a downstream ridge over the eastern seaboard explains about 26% of the total variance. Predictor number 2 is not significantly different from the average of the random series predictor.

In order to check the linearity assumption and to identify the anomalous nature of the 50-kPa flow that accompanies precipitation over a given area, we plot Figs. 6-8 for southern Alberta, the southeastern Prairies and southern Ontario, respectively. The statistical significance of these maps validates the linearity assumption. Note also, the first 2 predictors in Tables 1-3 are chosen for the 50-kPa grid that has the highest correlation with the averaged precipitation. In all three cases, an anomalous southwesterly flow at 50-kPa is needed to produce precipitation.

Future Plans

1. So that more stations are included in a coherent area, relax the present criterion which rejects stations with any missing obervation.
2. Identify homogenous precipitation areas by empiricial orthogonal functions rather than by the correlation field.
3. Develop similar equations for frequency of precipitation.

4. Perform cube root or logarithmic transformations of precipitation amounts in order to avoid extremes in precipitation.
5. Explore other predictor fields, such as, sea-level pressure or thickness between the various pressure levels, although no objective monthly forecast is available for other levels at present.
6. Validate multiple regression equations by testing their performance on an independent sample (1984-1988).

****

Table 1. Summary of stepwise statistics obtained for southern Alberta.

Step No.	Predictor location	Reg. coeff. upon entry	Prob. F-test	Added RV (%)	Cummulative RV (%)
1	50N,150W	.081	99.9	23.3	23.3
2	60N,170W	.051	99.9	6.7	30.0
3	30N,130W	.087	99.9	3.9	33.9
4	20N,110W	-.149	99.9	3.5	39.4

Table 2. Summary of Stepwise statistics obtained for southeastern prairies.

Step No.	Predictor location	Reg. coeff. upon entry	Prob. F-test	Added RV (%)	Cummulative RV (%)
1	60N,120W	-.060	99.9	15.8	15.8

Table 3. Summary of Stepwise statistics obtained for southern Ontario.

Step No.	Predictor location	Reg. coeff. upon entry	Prob. F-test	Added RV (%)	Cummulative RV (%)
1.	40N,70W	.185	99.9	26.3	26.3
2.	40N,90W	-.141	99.9	3.9	30.2
3.	20N,60W	-.277	99.9	4.5	34.7
4.	20N,110W	-.361	99.9	3.7	38.4

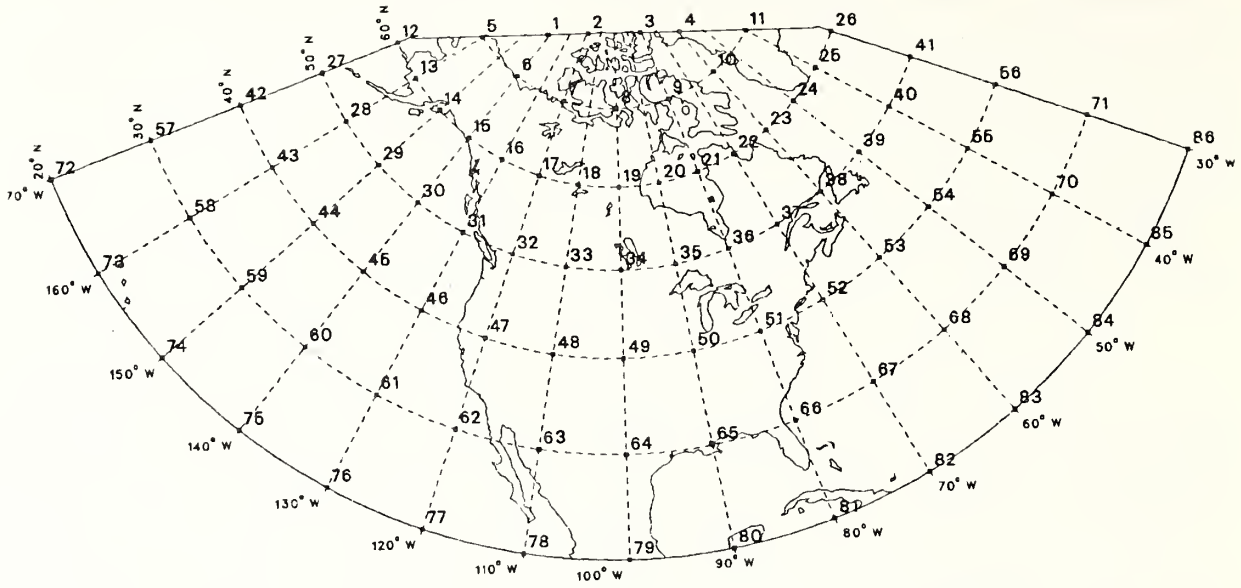

Fig. 1 Network of 86 lat.-long. grid points used, to delineate 50-kPa height anomaly.

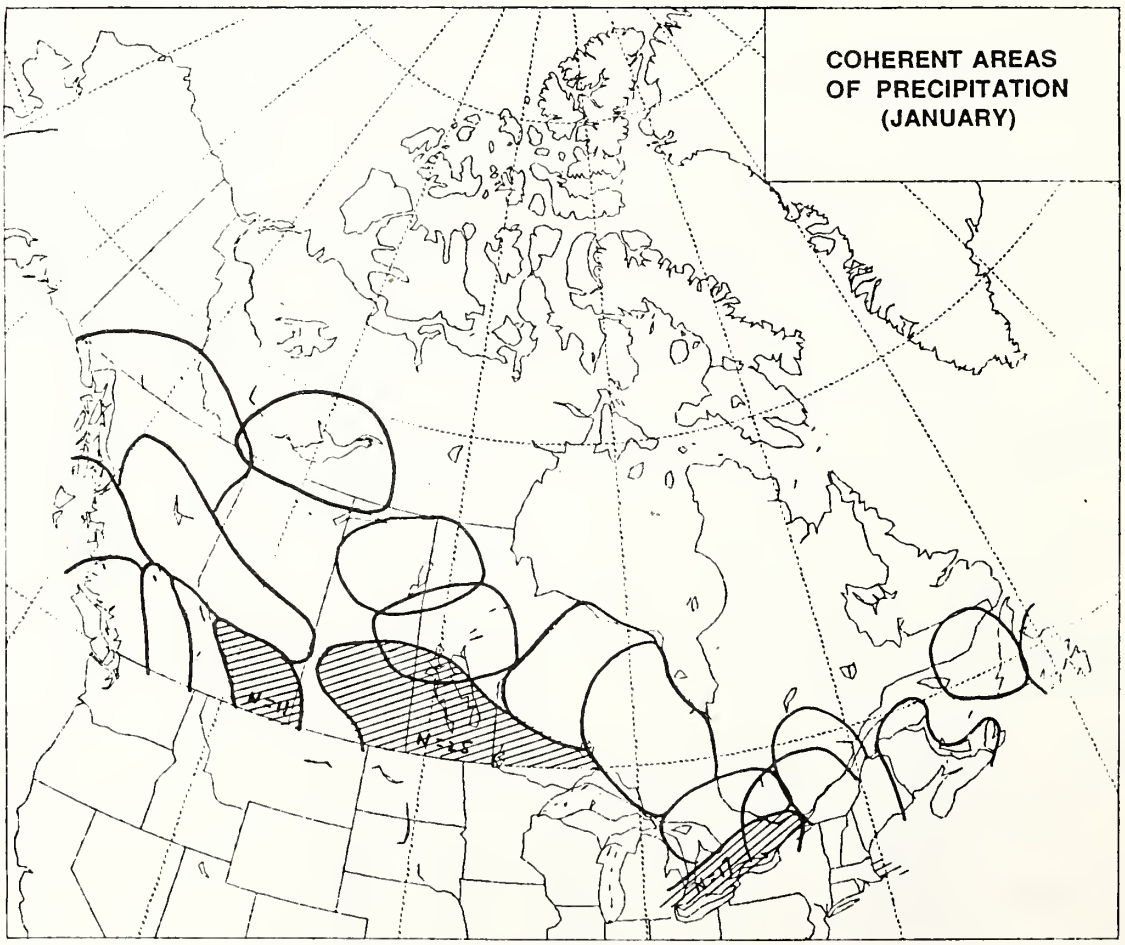

Fig. 2 Coherent areas of monthly precipitation for January as derived by correlation analysis.

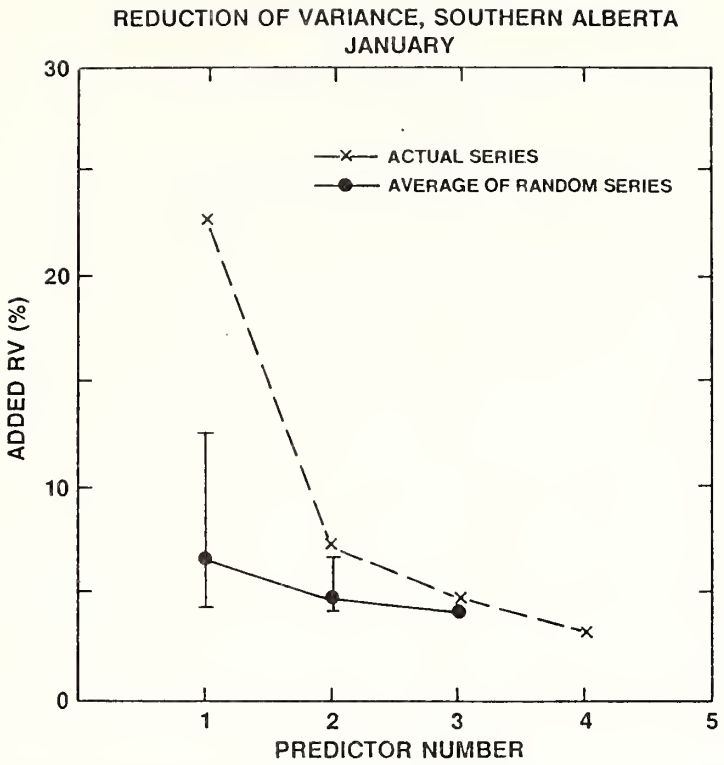

Fig. 3 Added reduction of variance versus predictor number for the actual and the average of 100 random monthly precipitation time series for southern Alberta. Bar represents the range of values in the random series.

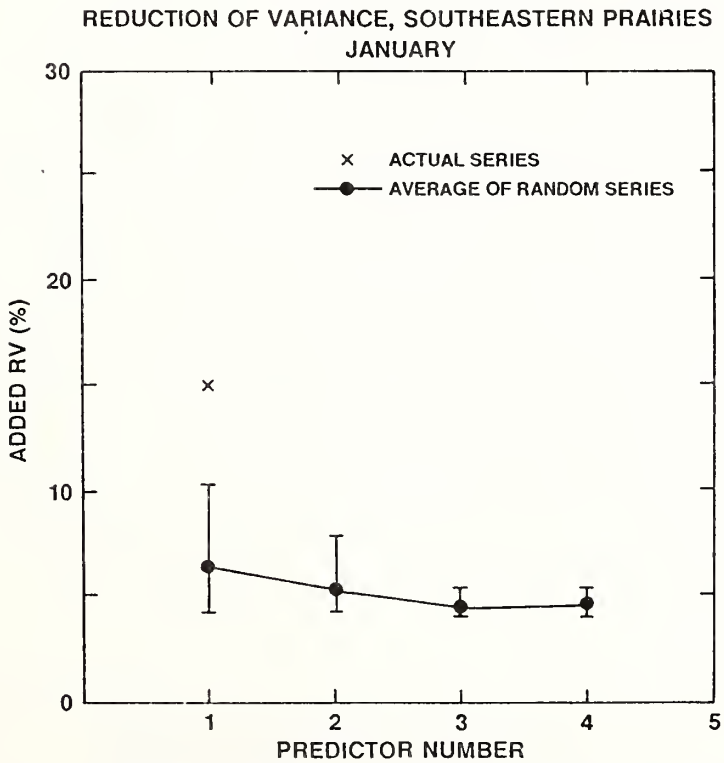

Fig. 4 Same as Fig. 3 except for southeastern prairies.

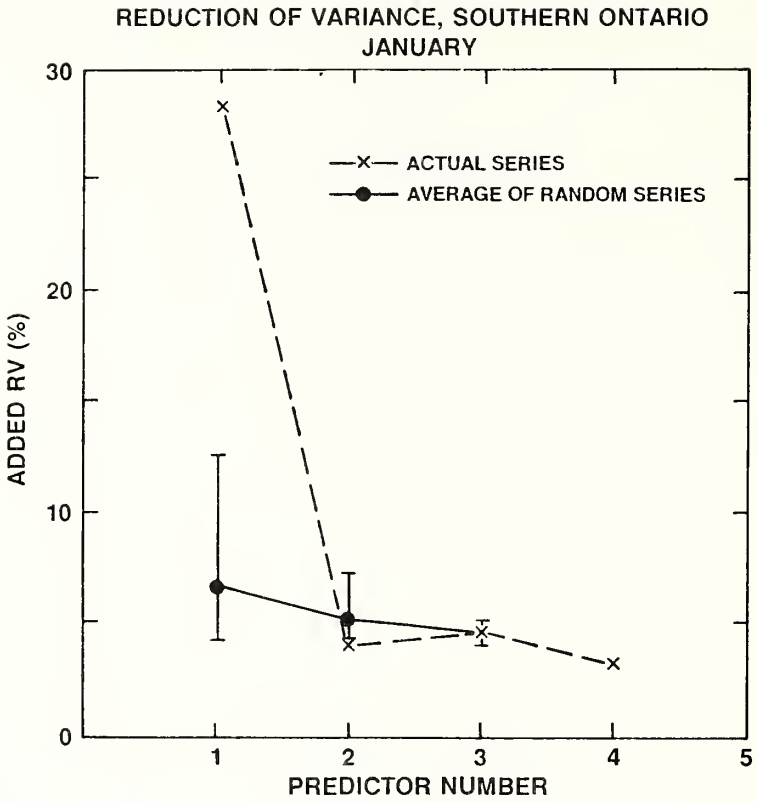

Fig. 5 Same as Fig. 3 except for southern Ontario.

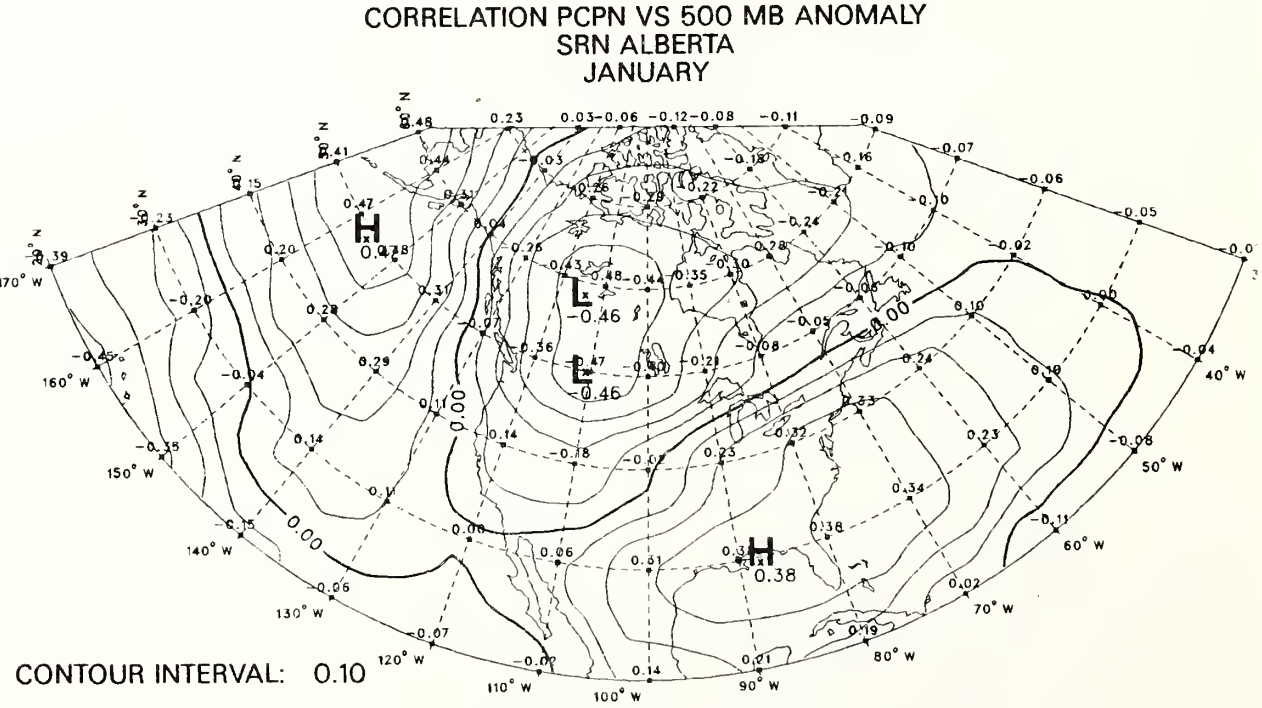

Fig. 6 Correlation field pattern of mean monthly 50-kPa height versus monthly precipitation averaged over southern Alberta. Winter months with 114 cases.

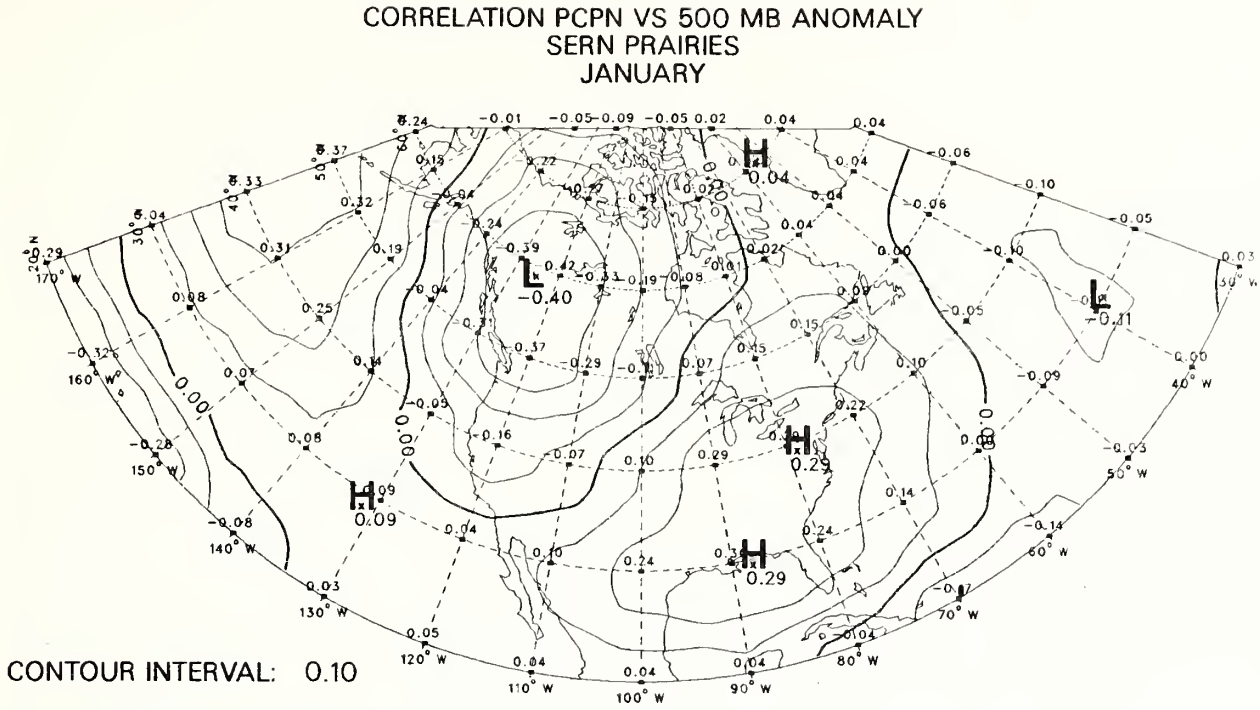

Fig. 7 Same as Fig. 6 except for southeastern prairies.

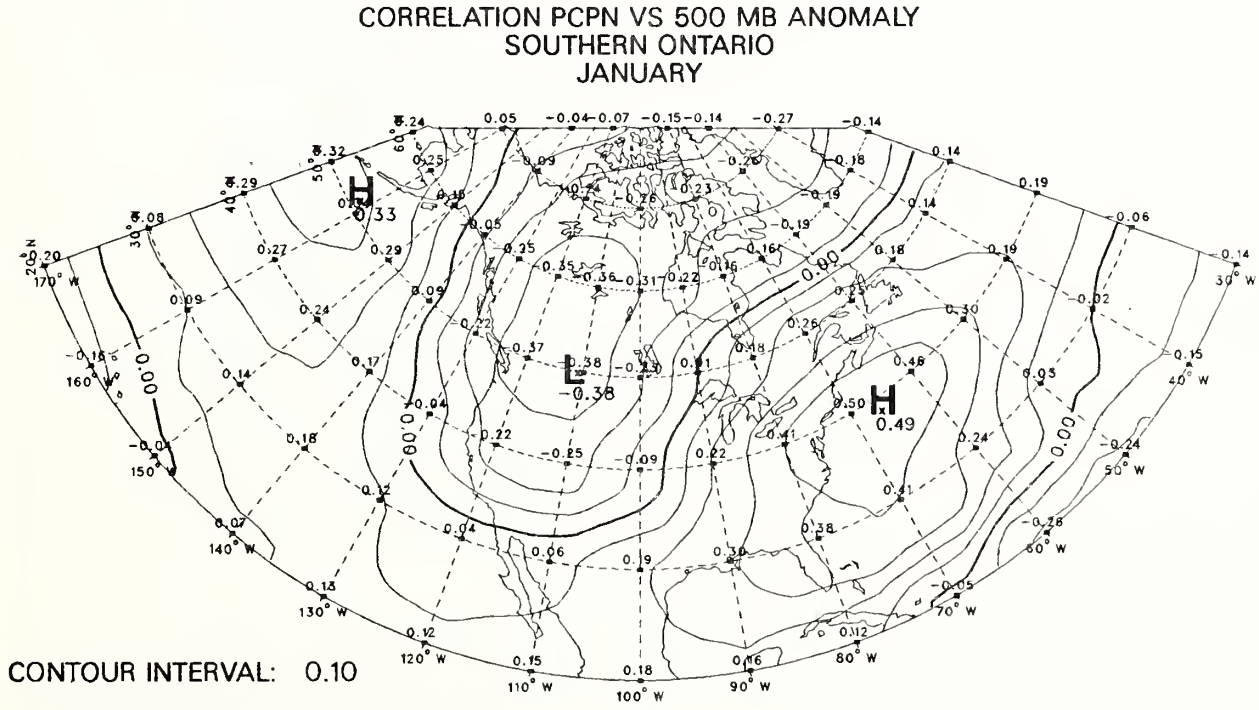

Fig. 8 Same as Fig. 6 except for southern Ontario.

THE RELATIONSHIP BETWEEN CANADIAN PRAIRIE DRY AND WET MONTHS, AND CIRCULATION ANOMALIES IN THE MID-TROPOSPHERE

by

J. L. KNOX and R. G. LAWFORD

Canadian Climate Centre,
Atmospheric Environment Service,
4905 Dufferin St., Downsview, Ont.
Canada, M3H 5T4.

1. Introduction

Canadian prairie dry spells have long been a matter of concern, and this year was no exception. Scholefield et al., 1988, have described in the Workshop Proceedings the evolution during the past winter, spring, and early summer, of the severe drought over southern Saskatchewan and Alberta.

Although such dry spells have been much investigated in a regional sense, we were unable to find studies relating the Canadian Prairie occurrences to anomalous features of the Northern Hemisphere circulation. This presentation is a brief summary of an attempt to do so. The complete report, to be referred to as K-L, will be published by the Canadian Climate Centre (Knox and Lawford,1988).

The Canadian Prairies constitute a vast 1800 km reach of territory extending from the Peace River watershed in the northwest, to southern Manitoba in the east. Earlier studies, e.g. Longley (1972) demonstrated how prairie regions had significantly different features in their synoptic climatology particularly with regard to precipitation. This was confirmed by Richman and Lamb (1987) in their principal component analysis of growing season precipitation patterns in southern Canada. Their results applied strictly to 3- and 7-day mean precipitation, but, in a presentation to this Workshop, Richman and Lamb (1988) they have indicated similar results for 30-day means.

2. Methodology

We used the Richman and Lamb results as a basis for dividing the prairies into the five zones displayed in Figure 1, and selected 4 representative first-order stations per zone, to determine the respective monthly normalized anomalies of precipitation.

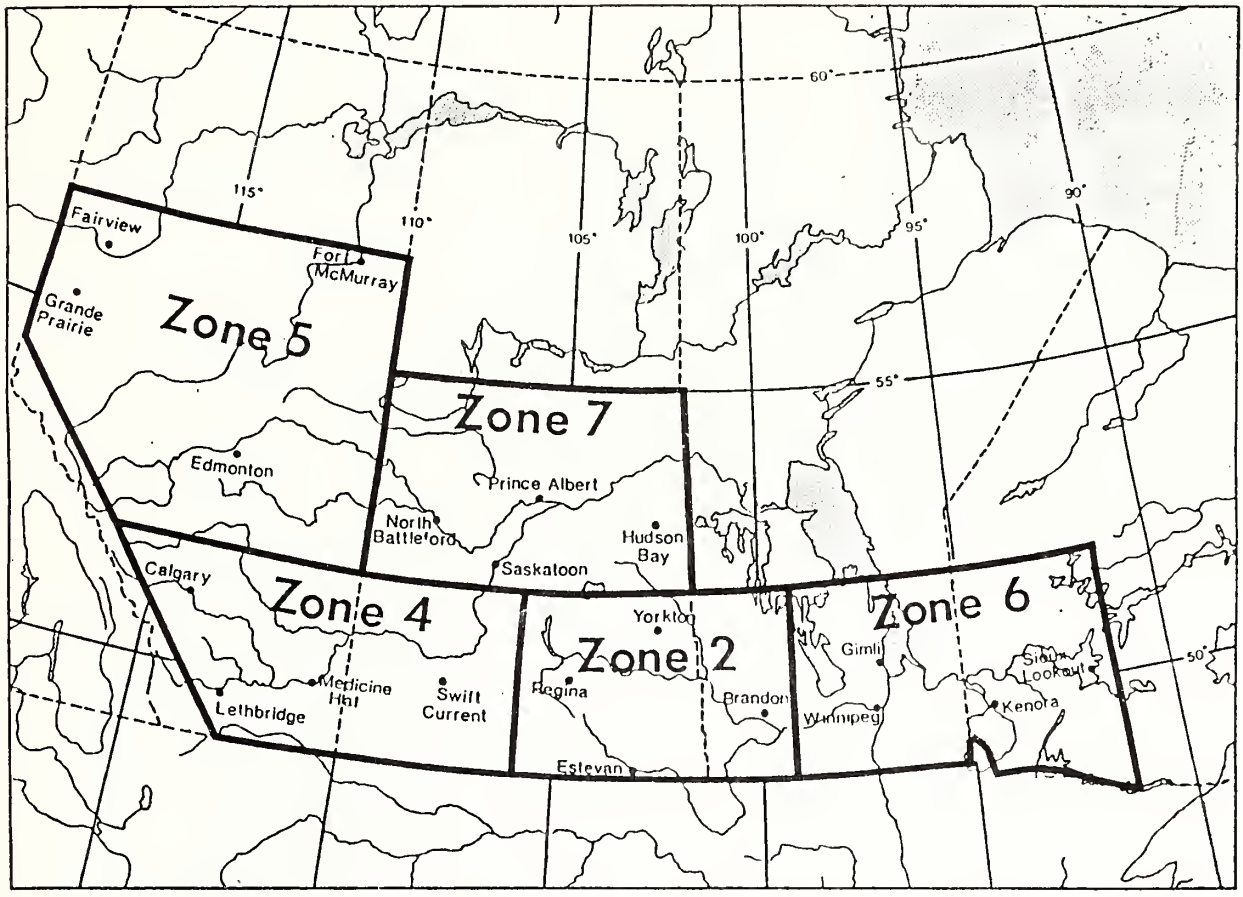

FIGURE 1. The five climate zones and the stations used to define the monthly precipitation.

Our main focus will be on the months of April, May, June and July when crops are planted and undergo their maximum growth. We define two seasons as follows:

SPRING.....April, May

EARLY SUMMER....June, July

and identify anomalously DRY and WET months within those seasons

All data are for the 40-year period 1946-1985 incl, both at the surface (precipitation) and at the 50 kPa and 100 kPa levels (geopotential height). The heights were extracted from Northern Hemisphere 455 lat.-long. grid-point data sets (15N to the pole) for the respective levels.

Details concerning the normalization of monthly mean precipitation amounts will be found in K-L. The selection criteria were as follows:

(i) For a WET case, the normalized anomaly must be > 0.5

(ii) For a DRY case, " " " " " < -0.5

The results are displayed in Table 1, which shows the dates, by Zone and Regime (DRY /WET) of the ranked qualifying cases for (a) Spring and (b) Early Summer.

The next step was to composite the 50 kPa (and 100 kPa) height analyses for those months common to a specified SEASON/ZONE/Monthly Regime (DRY/WET). Subtracting the normal 50kPa field from the composite yielded the anomaly field, examples of which, for Zone 2 Spring, are shown in Figures 2(b), (DRY) and 2(d), (WET). The entire set of these charts, for each of the five zones, both seasons, and the two levels, is available in K-L.

3. Analysis.

In Spring, DRY and WET months are distinguished by distinctly different anomaly fields, not only over the North American continent, but also both flanking oceans. To differentiate more specifically between the salient features of these fields, we used the schematic of N. H. 50 kPa height anomaly teleconnection modes characteristic of the growing seasons shown in Figure 3. The double arrows for the east and west North Pacific (NPO) and North Atlantic (NAO) oscillations terminate at 40N and 60N. In using the schematic to characterize these structures, the following convention was adopted: For both oscillations, negative/positive sign indicates a lower/higher anomaly value at 60N than at 40N.

The attributes for the 10 Spring and 10 Early Summer

TABLE 1. Dates by Zone and Regime (WET/DRY) of the ranked qualifying cases for (a) spring and (b) early summer.

(a) SPRING

ZONE #2		ZONE #4		ZONE #5		ZONE #6		ZONE #7	
WET	DRY	WET	DRY	WET	DRY	WET	DRY	WET	DRY
75 4	49 4	78 4	49 4	48 4	80 4	63 4	80 4	55 4	52 4
70 4	52 4	67 4	77 4	55 4	60 4	74 4	77 4	85 4	80 4
55 4	77 4	53 4	52 4	69 4	70 4	54 4	72 4	73 4	69 4
48 4	83 4	74 4	46 4	62 4	52 4	60 4	49 4	48 4	77 4
79 4	46 4	55 4	62 4	66 4	56 4	67 4	83 4	78 4	74 4
54 4	68 4	54 4	81 4	77 5	56 5	71 4	69 4	75 4	67 4
73 4	82 4	75 4	63 4	84 5	71 5	79 4	52 4	58 4	59 4
65 5	58 5	55 5	82 4	51 5	67 5	57 4	76 5	54 4	56 4
78 5	67 5	81 5	57 5	60 5	58 5	70 4	80 5	77 5	65 4
77 5	80 5	77 5	73 5	64 5	72 5	64 4	52 5	74 5	66 5
74 5	52 5	75 5	58 5	00 0	00 0	65 4	61 5	68 5	71 5
53 5	47 5	82 5	50 5	00 0	00 0	77 5	58 5	84 5	81 5
49 5	71 5	74 5	63 5	00 0	00 0	59 5	00 0	85 5	62 5
62 5	76 5	78 5	00 0	00 0	00 0	62 5	00 0	52 5	56 5
55 5	48 5	00 0	00 0	00 0	00 0	74 5	00 0	00 0	70 5
60 5	00 0	00 0	00 0	00 0	00 0	50 5	00 0	00 0	67 5
00 0	00 0	00 0	00 0	00 0	00 0	53 5	00 0	00 0	57 5
00 0	00 0	00 0	00 0	00 0	00 0	78 5	00 0	00 0	59 5
00 0	00 0	00 0	00 0	00 0	00 0	68 5	00 0	00 0	47 5
00 0	00 0	00 0	00 0	00 0	00 0	70 5	00 0	00 0	00 0
00 0	00 0	00 0	00 0	00 0	00 0	79 5	00 0	00 0	00 0
00 0	00 0	00 0	00 0	00 0	00 0	65 5	00 0	00 0	00 0

(b) EARLY SUMMER

ZONE #2		ZONE #4		ZONE #5		ZONE #6		ZONE #7	
WET	DRY	WET	DRY	WET	DRY	WET	DRY	WET	DRY
53 6	61 6	70 6	85 6	56 6	82 6	84 6	61 6	70 6	64 6
76 6	67 6	63 6	77 6	83 6	63 6	76 6	72 6	65 6	58 6
71 6	74 6	53 6	74 6	71 6	66 6	83 6	62 6	66 6	69 6
47 6	58 6	51 6	61 6	73 6	55 6	81 6	59 6	83 6	77 6
75 6	79 6	65 6	83 6	65 6	67 6	77 6	79 6	76 6	67 6
54 6	82 6	83 7	55 6	61 6	77 6	62 7	76 7	73 6	59 7
63 6	68 6	55 7	49 6	55 7	58 7	58 7	74 7	63 6	84 7
82 7	85 7	50 7	67 7	82 7	85 7	82 7	85 7	71 7	47 7
46 7	51 7	82 7	47 7	83 7	65 7	53 7	60 7	50 7	60 7
70 7	67 7	66 7	73 7	77 7	59 7	48 7	54 7	68 7	75 7
63 7	79 7	00 0	84 7	64 7	84 7	00 0	00 0	82 7	00 0
48 7	60 7	00 0	85 7	57 7	00 0	00 0	00 0	76 7	00 0
83 7	59 7	00 0	00 0	00 0	00 0	00 0	00 0	00 0	00 0
50 7	84 7	00 0	00 0	00 0	00 0	00 0	00 0	00 0	00 0
00 0	47 7	00 0	00 0	00 0	00 0	00 0	00 0	00 0	00 0

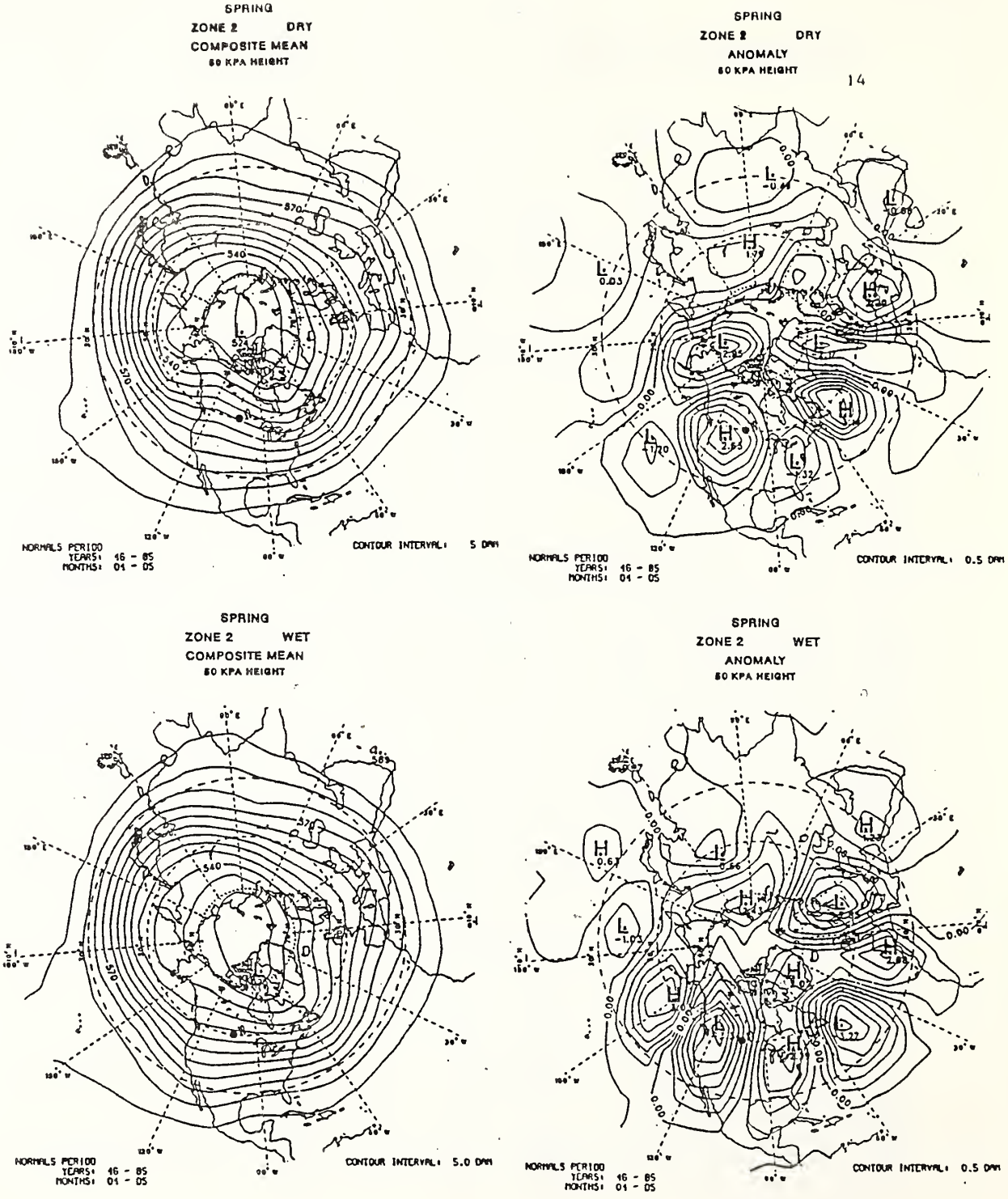

FIGURE 2 (a) Composite mean 50kPa height for ZONE 2 DRY cases in Spring.
(b) Anomalous 50kPa height field for ZONE 2 DRY cases in Spring.
(c) As in (a) except for WET cases.
(d) As in (b) except for WET cases.

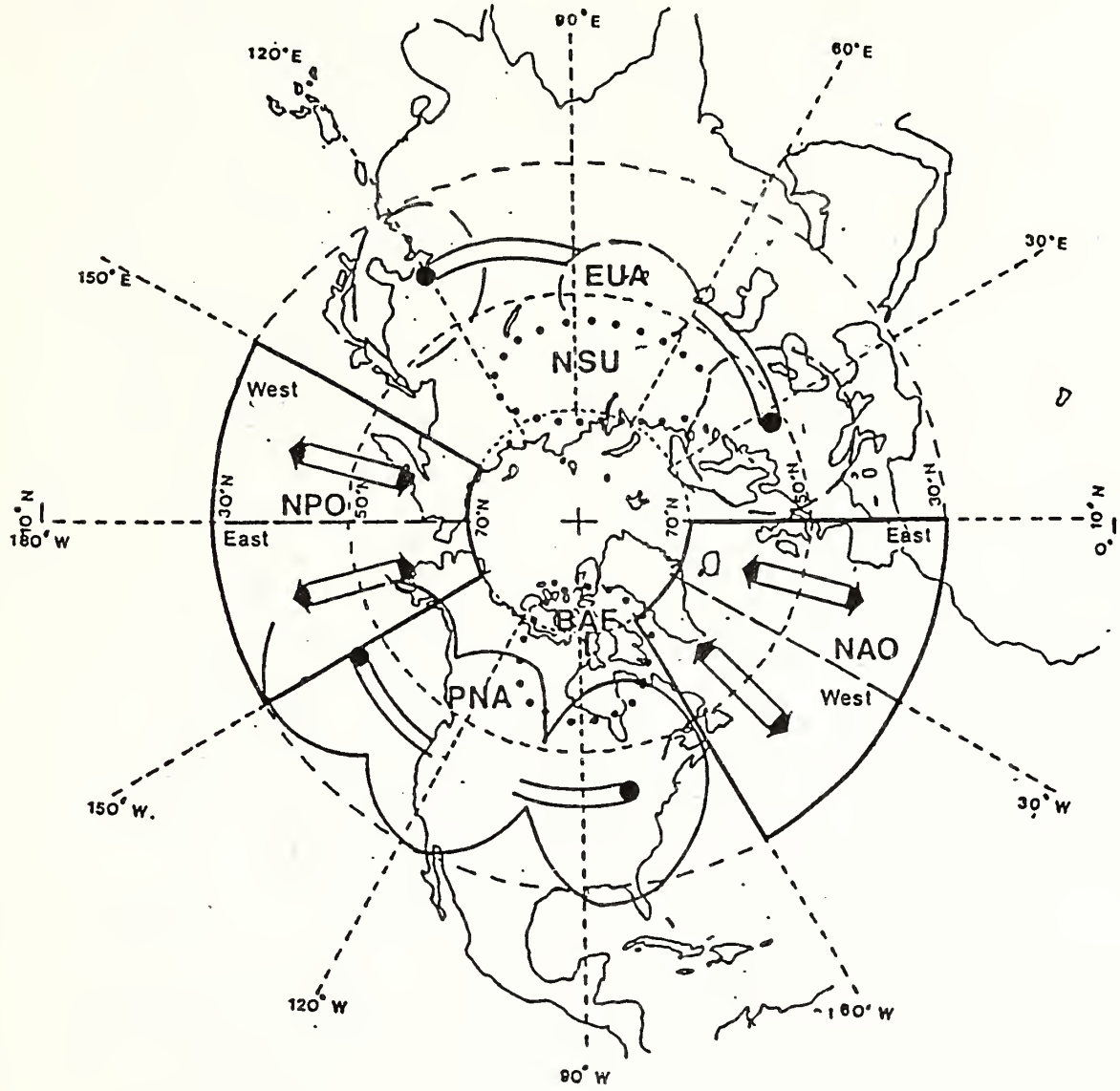

FIGURE 3. Highly idealized representation of characteristic Northern Hemisphere 50kPa height anomaly teleconnection modes adapted to Spring and early Summer. For definitions and phase sign conventions, see text.

composites are listed in Tables 2 and 3 respectively. The sign of the central lobe of the PNA anomaly is not surprising, although there are zone-dependent differences in the centre location. All Spring DRY months are associated with an amplified positive anomaly centred on average about 10 degrees longitude to the west, and 5 degrees latitude to the south of the geographic centre of the Zone. Moreover the PNO and NAO, both west and east, are consistently negative in Spring, indicating an anomalously stronger west to east flow across both the N. Pacific and N. Atlantic. In practically all cases, diametrically opposite attributes are noted for the Spring WET months. In Early Summer, the results relative to the PNA structure, are similar to Spring over North America, but those relative to the NPO and NAO differ from Zone to Zone.

Tables 2. and 3. also contain information concerning the anomalous wind shear between the 100kPa and 50 kPa levels, for each zone and by season. The K-L Report rationalizes these findings. The "Remarks" column lists other associated synoptic structures (e.g. blocking) and also the dates of prototypes.

4. Concluding comments.

We have completed an analysis of the relationship between WET and DRY months over the Canadian prairies and contemporaneous anomalies in the Northern Hemisphere mid- and lower troposphere circulation during Spring and Early Summer. The anomaly fields arising from the composited charts clearly distinguish the circulations associated with the DRY and WET regimes, and also indicate significant differences from zone to zone. The fields are well defined not only over western North America, but also over the North Pacific and North Atlantic Oceans.

In some respects our investigation is similar to that of Stidd (1954) who used correlation fields (monthly mean precipitation for a state vs 70 kPa height over the USA) to geographically discriminate between precipitation producing flow patterns. The amplitudes of his Winter correlation centres were strong, and his fields for the states contiguous to Canada were consistent with our composite anomalies. However, his patterns for Summer were weak and inconclusive, which could be attributed to his very limited data set combined with the greater local variability of warm season precipitation. We had the advantage of a much longer data set, and because candidates for the composites were based on the more extreme cases, it was possible to obtain coherent anomaly fields for all seasons.

We suggest that our results may well provide a useful diagnostic tool in connection with evaluating the likelihood of extreme precipitation events (DRY or WET months) over specific zones of the Canadian prairie, given the corresponding 50 kPa and 100 Kpa predicted height fields.

TABLE 2. Composite Anomaly Field Attributes, SPRING.

TELECONNECTION PATTERNS AT 50 KPA FOR SPRING

ZONE	REGIME	ANOMALOUS WIND		NPO		PNA		NAO		REMARKS: significantly amplified anomalies, blocking, prototype dates, etc.
		100KPA	50KPA	WEST	EAST	Centre of nearest anomaly		WEST	EAST	
6	DRY	260	360	- -	- -	+	50N 105W	-	-	Persistent blocking over Wrn Canada occ'n blkg NSU. (Prototypes: Apr., May 1980).
50N 97W	WET	130	200	+	+	-	45N 115W	+	+	Spring-time blocking anomaly pattern over North Atlantic.
2	DRY	280	300	-	- -	+	45N 110W	-	-	Strong mid-latitude westerlies.
50N 102W	WET	090	180	+	-	-	50W 120W	+ +	-	Blocking North Hudson Bay and Baffin Isl.; also over NSU.
4	DRY	270	280	-	-	+	40N 110W	- -	-	Strong mid-latitude westerlies amplified (+)ve Mid Pacific anomaly 47N 180W.
50N 110W	WET	090	160	+	+	-	40N 120W	+	+	Strong blocking NE Atlantic (Prototype: April 1978).
5	DRY	270	280	- -	- -	+	50N 120W	-	-	Above normal westerlies 50-55N (see May 1956 for a prototype).
55N 115W	WET	090	130	+ +	+ +	-	48N 130W	-	+	Very strong Mid-Pacific blocking (+)ve anomaly 55N 180W. (Prototype: Apr., 1948).
7	DRY	250	320	I	I	+	50N 115W	- -	-	Anomalies much attenuated except Baffin Isl.
52N 102W	WET	090	160	+	+	-	50N 120W	+ +	+	Blocking N. Pac., Baff. I., N. Atl (+) Anom 55N 180W. (Prototype Apr, May '55)

TABLE 3. Composite Anomaly Field Attributes, EARLY SUMMER.

TELECONNECTION PATTERNS AT 50 KPA FOR EARLY SUMMER

ZONE	REGIME	ANOMALOUS WIND		NPO		PNA		NAO		REMARKS: significantly amplified anomalies, blocking, prototype dates, etc.
		100KPA	50KPA	WEST	EAST	Centre of nearest anomaly		WEST	EAST	
6	DRY	260	330	-	-	+	45N 105W	-	- -	Strong westerlies 50N. Prototype: June 1961 Amplified positive anomaly 45N 170W.
50N 97W	WET	160	140	+	+	-	45N 105W	+	+	Blocking over Baffin Isl. and W. Atlantic. (Prototype: June 1983).
2	DRY	270	340	-	+	+	45N 120W	-	-	Amplified positive anomaly 45N 170W. (compared with zone 6 DRY; see June 1961).
50N 102W	WET	090	150	-	-	-	47W 130W	+	+	High arctic blocking. (Prototype: July 1982).
4	DRY	I	270	+	-	+	46N 120W	I	I	Amplified positive anomaly 45N 170W. (c.f. zones 6 & 2 dry; see June 1985)
55N 110W	WET	120	140	+	I	-	34N 120W	-	+ +	Amplified negative anomaly 45N 180W. (Prototype July 1983).
5	DRY	270	280	I	I	+	50N 135W	I	+	Amplified (-)ve NSU anomaly 65N 40E. (for prototype see July 1984).
55N 115W	WET	130	150	+	-	-	50N 140W	-	I	For prototype see July 1983.
7	DRY	310	340	I	+	+	51N 122W	-	+	For prototype see July 1984.
52N 102W	WET	090	120	+	I	I	-- --	-	+	Strong blocking NW Europe centred 58N 10E; amplified (-)ve anomaly 45N 180W.

REFERENCES

Knox, J. L., and Lawford, R. G., 1988. The Relationship between Canadian Prairie Dry and Wet Months and Circulation Anomalies in the Mid-troposphere. Canadian Climate Centre, Report No.xx-x, (in press).

Longley, R. W. 1972. Precipitation on the Canadian Prairies. CLI 2-72. Canadian Climate Centre, Downsview, Ont., Canada.

Richman, M. B. and Lamb, P. J., 1987. Principal component analysis of growing season precipitation patteerns in southern Canada. Atmosphere-Ocean, Vol 25, No 2, 137-158

Richman, M. B. and Lamb, P. J., 1988. The interannual variability of growing season precipitation over central North America. Proceedings of the Thirteenth Annual Climate Diagnostics Workshop, Oct 31- Nov 4, 1988. NOAA, Washington, D.C. USA.

Schofield, P. J., Guezen, T., and Raddatz, R., 1988. Extended dry spell in Western Canada. Proceedings of the Thirteenth Annual Climate Diagnostics Workshop, Oct 31-Nov 4,1988. NOAA, Washington, D. C. USA.

Stidd, C. K. 1954. The use of correlation fields in relating precipitation to circulation. J. of Meteorology. Vol. 11: 202-213.

DEPENDENCY OF LONG-RANGE TEMPERATURE PREDICTABILITY IN HUNGARY ON CIRCULATION WEATHER TYPE AND FORECAST CATEGORY

ZOLTAN TOTH[1]

Central Institute for Weather Forecasting, Budapest,1675 P.O.Box 32, Hungary

INTRODUCTION. In the present literature there are reports about different kind of long-range forecasting methods used in the United States (Gilman, 1986; Livezey and Barnston, 1988), in the United Kingdom (Folland and Varah, 1987) and in Hungary (Toth, 1986) that all fail to show any skill for categorical forecasts for the near normal temperature category. At least two approaches to explain this lack of skill exist. The first, held among others by Gilman and Folland (1988, personal communication), is thought to be due to the limited time resolution of our techniques. For example, if we forecast monthly means, a near normal temperature resulting from the averaging of a cold and a warm subperiod usually will not be predictable. The other argument, expressed most clearly by van den Dool (1988), uses simple statistical reasoning. Assuming that the root mean square error of point-estimate forecasts is independent of the forecast value itself, the skill of forecasts expressed in terms of e.g. three categories resides mainly in the extreme classes. This is because it is easier to escape from a closed interval (near normal), than from a class with an open end (extreme categories).

DATA AND PROCEDURE. In this study we propose another possible explanation using series of two weather types determined independently by Peczely(1983; for Hungary) and Bartholy et al. (1984; for the Atlantic-European region) for the period 1951-1980. First we determined the daily minimum and maximum temperature anomaly class limits for the five climatologically equally probable categories for the same period. Then we derived the distribution of minimum and maximum temperature anomalies respectively observed in different weather types in various months (13 Peczely weather types x 12 months = 156 subsamples on the one hand and 177 subsamples on the other, for Bartholy circulation types.)

RESULTS. The distribution of the "most likely" category of those subsamples whose distribution is significantly different from the whole sample's distribution are shown in Fig. 1 and Fig. 2 respectively. The main findings of this study follow:

1) The distribution of the most likely categories presented in Fig. 1 and Fig. 2 is not uniform (the difference is significant at a much higher probability level (P) than 0.001).

2) The frequency of most likely extreme categories is significantly different from that of near normal category ($P << 0.001$).

3) The number of those subsamples whose most likely category is the near normal cannot be differentiated from chance expectation at the 0.05 probability level.

DISCUSSION. We conclude that even with perfect knowledge of future weather type series, there is no hope for successful near normal forecasts, at least in Hungary. A possible extension of this implication to other geographical areas depends on the

---

[1] Currently at the Department of Meteorology, University of Maryland, College Park, Maryland 20742 USA

underlying mechanism causing these results. In Fig. 3 we present two possible contributing factors that may work at other midlatitude areas as well. If, among others, the ratio between the characteristic distance of advection and the characteristic north- and southward shifts of temperature field is in a certain range and hence the explanation is valid, the first argument mentioned in the Introduction seems to be unnecessary. Although the reasoning about the effect of time-averaging may be true it is redundant if predictability does not exist even on a daily basis. Note that the other, simple statistical argument uses a very similar topological structure (scaled temperature field with three categories on the one hand and "measuring points" - forecast values and origin of advection, respectively - on the other, having relative uncertainty to each other) employed in the explanation presented in Fig. 3.

CONCLUSION. The main conclusion is that without a reliable and somehow independent forecast of large-scale thickness or tropospheric temperature pattern, our long-range forecasting methods based mainly on the prediction of pressure field on one level are probably doomed to failure in the near normal temperature range.

REFERENCES

Bartholy, J., P. Ambrozy and O. Gulyas, 1984: A system of seasonal macrocirculation patterns for the Atlantic-European region. *Idojaras*, **88**, 121-133.

Folland, C. K. and L. D. Varah, 1987: Assessment of probability forecasts of temperature and rainfall for the United Kingdom. Proceedings of the *Second WMO Workshop on the Diagnosis and Prediction of Monthly and Seasonal Variations over the Globe*, June 15-19, 1987, Toulouse, France.

Gilman, D. L., 1986: Expressing uncertainty in long-range forecasts. *Namias Symposium*, Oct. 22, 1985, J. O. Roads, Ed., Ref. Series 86-17, Scripps Institute of Oceanography, La Jolla, 174-187.

Livezey, R. E. and A. G. Barnston, 1988: Objective seasonal temperature predictions by combination of analog and persistence predictors. Proceedings of the *13th Annual Climate Diagnostics Workshop*, Oct. 31-Nov. 4, 1988, Cambridge, Massachusetts, in press.

Peczely, Gy., 1983: Catalogue of the macrosynoptic types for Hungary (1881-1983) (in Hungarian). *Meteorological Reports No.53*, Hungarian Meteorological Service, Budapest, 116 pp.

Toth, Z., 1986: Improvement of analog predictability due to extension of data series. Proceedings of the *1st WMO Conference on Long-Range Forecasting: The Practical Problems and Future Prospects*, Sept. 29 - Oct. 3, 1986, Sofia, Bulgaria, in press.

van den Dool, H., 1988: Prediction of (near) normal class. *Manuscript*, available from the author at Department of Meteorology, University of Maryland, College Park, MD 20742, U.S.A., 4 pp.

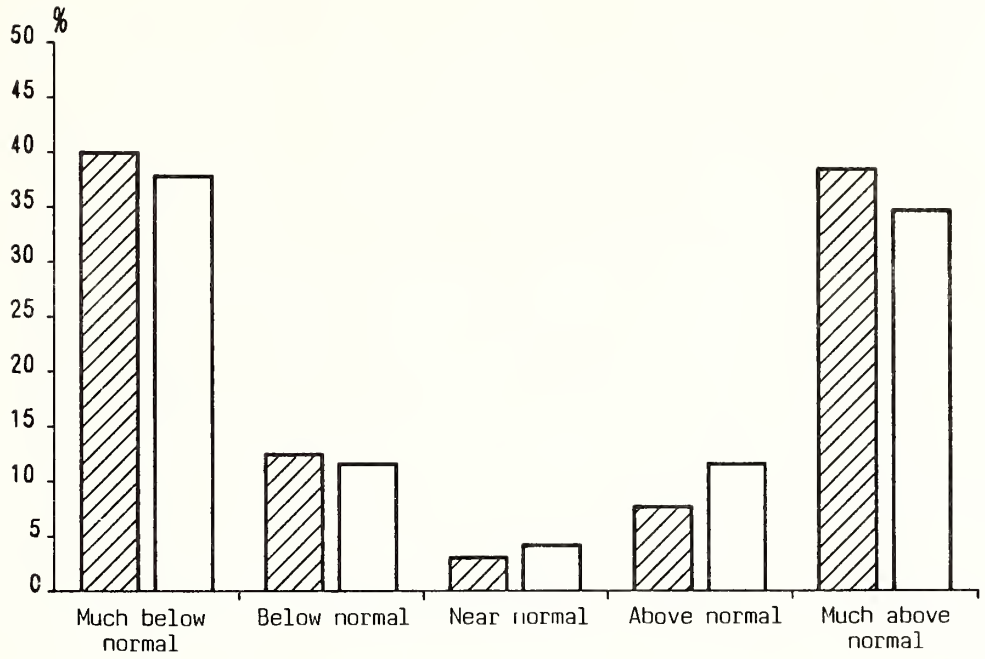

Fig. 1. Frequency distribution of most likely categories of daily minimum (65 subsamples, shaded) and maximum (95 subsamples) temperature anomaly distributions from various Peczely weather types (significantly different from the whole climatological distribution) in different months (chance expectation is 20%).

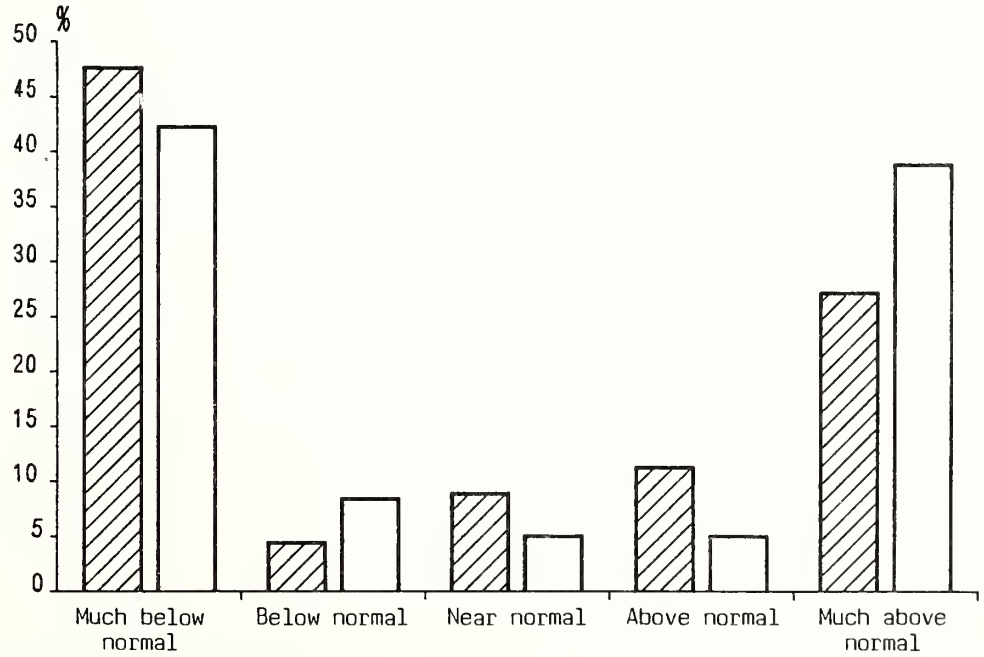

Fig. 2. Same as Fig. 1 except for Bartholy circulation types (44 and 59 subsamples for daily minimum and maximum temperature anomalies respectively.

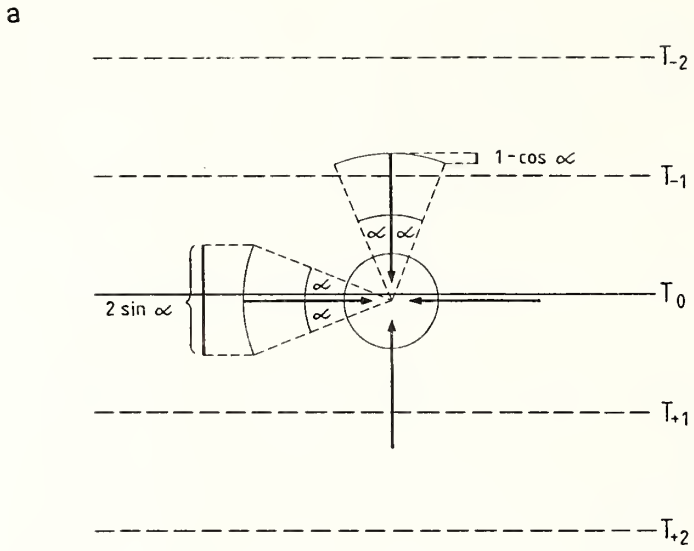

Fig. 3. Advective scheme for explaining the results illustrated in Fig. 1 and 2.

(a) Difference in the uncertainty of air temperature advected from different (parallel and perpendicular to temperature gradient), *but not exactly determined directions.* T_0: the isotherm of the climatic mean temperature in the investigated region (indicated by a circle); T_{-1}, T_{+1}: isotherms of those temperatures causing, if advected, much below and much above temperature in the investigated region (used as arbitrary units for temperature).

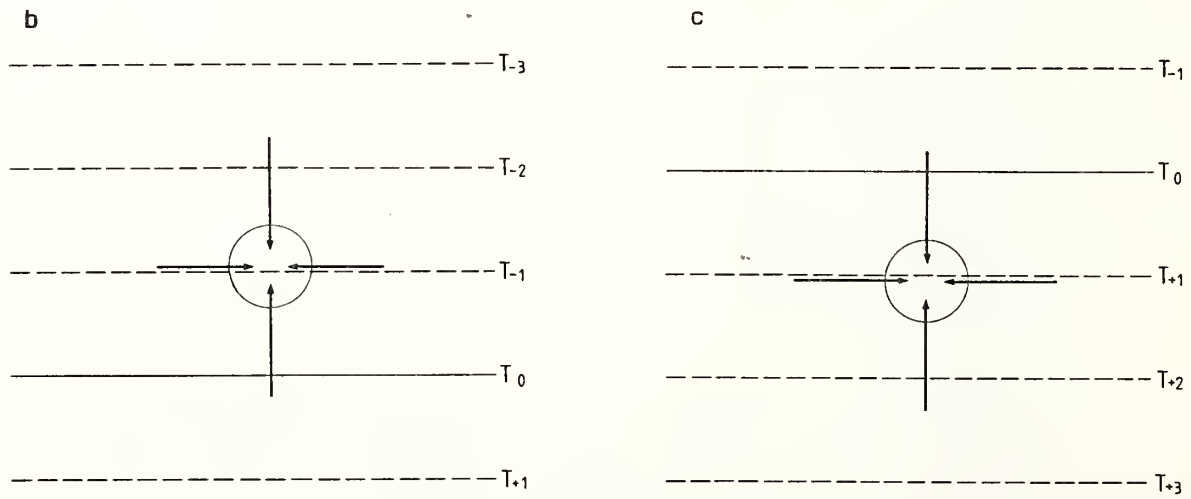

Fig. 3.

(b) and (c) illustrate the greater uncertainty in the category of air temperature advected from zonal direction than that advected by meridional flow as a result of *south- and northward shifts of the temperature field*; the length of the arrows represent the characteristic distance of advection.

Statistical significance of global warming

T.M.L. Wigley, P.D. Jones, P.M. Kelly and S.C.B. Raper
Climatic Research Unit
University of East Anglia
Norwich NR4 7TJ
United Kingdom

Introduction

When the land-plus-marine global temperature record of Jones et al. (1986a, 1988) is updated, 1987 and 1988 are the warmest years on record (Fig. 1). For the land data, three different groups have produced area averages independently. These are compared below. To assess the significance of any warming, one must account for any low-frequency variability that might be inherent in the data. This can be done approximately by using a low-order autoregressive process to define the null background. The results imply a highly significant warming trend. Alternative, energy balance models may be used to estimate the internally-generated low-frequency variability of global-mean temperature.

Data Comparisons

The accuracy of any global-mean temperature estimate depends on the coverage and on the accuracy of the data used. Some authors have claimed that data from the land alone are enough to encapsulate global trends (eg. Hansen and Lebedeff, 1987). This appears to be the case, although the land and marine data do show important differences (Wigley et al., 1987). For the land there are three independent records of hemispheric means; our own work (Jones et al., 1986b,c, Jones 1988; J below), that of Hansen and Lebedeff (1987; HL below), and that of Vinnikov et al. (1987; V below). Do these agree?

Our results differ from those of Hansen and Lebedeff on the regional to continental scale. For example, our data show a twentieth century warming trend over the USA which is about 0.2°C less than that of Hansen and Lebedeff, suggesting some residual warming bias in the latter (see Karl and Jones, 1989, for details). Hemispherically, however, the HL-J difference is not easily attributable to urban warming. Figure 2 shows the difference HL minus J. Although HL gives a greater warming trend for the Northern Hemisphere (and globally) this is mainly due to differences prior to 1930.

When our data are compared with those of Vinnikov et al. (Figure 3) there are no trends in the differences. When Hansen and Lebedeff's data are compared with Vinnikov et al. (Figure 4), trends are obvious in the differences. The HL data seem to be the odd one out in this comparison, giving warming trends which are possibly too high in the Northern Hemisphere and too low in the Southern Hemisphere.

Significance of warming

In Figure 5 we show our land-plus-marine data normalized by the interannual standard deviation. This allows one to readily assess the significance of changes in individual years. Globally, 1987 and 1988 are near the 3-sigma level relative to the 1951-80 reference period. If one chose a nineteenth century reference level, these years would be close to

the 6-sigma level. This clearly implies that these individual years are unusually warm. Note, however, that the years around 1940 are all at the 3-sigma level relative to the nineteenth century data. Can one claim that the warmth of 1987 and 1988 relative to 1951-80 is due to the greenhouse effect? If so, then it would be equally valid to claim that the warmth of individual years around 1940 represented a greenhouse effect relative to the nineteenth century.

Greenhouse warming is a low frequency phenomenon. Thus, it is not appropriate to consider changes on the inter-annual time scale. It would be more appropriate to examine the 50- to 100-year time scale. Before considering this, however, we look at decadal means. In Figure 6, we show running decadal means, normalized by the standard deviation of these means. This presents a problem - what is the appropriate standard deviation?

Because the data are autocorrelated, one must account for this in calculating the standard deviation. The simplest way to do this is to assume the data are well represented by a first-order autoregressive (AR1) process (see, e.g., Wigley and Jones, 1981). In this case, the variance of an n-year mean is given by

$$\mathrm{Var}(\bar{X}) = \frac{\sigma^2}{n} \frac{1+r_1}{1-r_1}$$

where σ^2 is the inter-annual variance and r_1 is the lag-1 autocorrelation. (In Figure 6, σ^2 is based on 1951-80 and r_1 is based on the whole record.) Figure 6 shows that the changes on the decadal time scale are less significant than on the inter-annual time scale. The most recent decadal means are significantly warmer than 1941-70 in the Southern Hemisphere, but not in the Northern Hemisphere. All recent values are significantly warmer than the late nineteenth century level.

What about longer time scales? The difficulty here is in estimating the natural variability of, say, 50-year means. Proxy data are of limited value in answering questions about variability because of uncertainities in their quantitative interpretation, the limited coverage of most data types, their seasonal specificity, dating problems, etc. If one is restricted to using instrumental data, then low-frequency variance could be estimated using an AR1 model. But is such a model appropriate? Alternatively, one could estimate the low-frequency variance using a spectral approach (as in Madden and Ramanathan, 1980). But, is a 100^+ year record long enough to give information about 50-year time scale variability?

The AR1 model's relevance can be assessed using a simple energy balance model approach (c.f. Hasselmann, 1976). For a mixed layer ocean, such a model may be written

$$C \frac{d\Delta T}{dt} + \lambda \Delta T = \Delta Q$$

From this, it is clear that, if the forcing (ΔQ) were white noise, the output (global-mean temperature change, ΔT) would be red noise (i.e. AR1) with r_1 determined by the heat capacity C and the feedback parameter λ:

$$r_1 = \frac{\tau - 1}{\tau}$$

where $\tau = C/\lambda$ is a mixed layer time scale (4-13 yr). The implied r_1 ranges between 0.77 and 0.92, which is considerably higher than the observed value of around 0.7. This might imply that we have underestimated the variance of the decadal means above, and thus overestimated the significance of the changes. Alternatively, it may simply mean that a mixed-layer energy-balance model is not suitable for estimating r_1 reliably.

To gain further insights it is necessary to use a more sophisticated climate model. In this way, via stochastic simulations, it is possible to estimate the ocean-induced natural variability of global-mean temperature on any time scale. The procedure we have used is to force an upwelling-diffusion climate model (we have used the model of Wigley and Raper, 1987) with white noise whose amplitude was tuned to reproduce the observed high-frequency variance of global-mean temperature (which is about $(0.063^{o}C)^2$ after removal of ENSO-related variations). One such simulation is shown in Fig. 7. Similar simulations of low-frequency climate variability have been made by Robock (1979) and Hansen et al. (1988). In these works, the atmospheric forcing was generated by the model (the GISS AGCM in Hansen et al.'s case) rather than imposed, as here. The ocean models used were simple mixed layer oceans with no transport below the mixed layer. Hansen et al.'s results look very similar to those given in Fig. 7.

Figure 7 shows that low-frequency variations quite similar to those observed may occur with no external forcing (compare Figs. 1 and 7). In particular, note the prolonged warming of around $0.4^{o}C$ between the nominal years of 1850 and 1920. It is clear that the spectral character of the simulated variability differs from that of the observed variability at intermediate time scales. These spectral details are sensitive to the choice of values of climate sensitivity, diffusivity and mixed-layer depth. More extensive results will be published elsewhere.

Summary and Conclusions

1. In the global-mean, land-plus-marine temperature record, 1987 and 1988 are the two warmest years.

2. Differences exist between the three available land-only records of hemispheric- and global-mean temperature, with Hansen and Lebedeff's data apparently showing a spuriously inflated global-mean warming.

3. Recent decadal-mean temperatures appear to be significantly warmer than those of last century when the changes are assessed using an AR1 null model.

4. Energy-balance models suggest that an AR1 model, if r_1 is based on observations, may noticeably underestimate natural low-frequency variability.

5. With regard to the detection of greenhouse-gas-induced warming, however, whether or not the warming is statistically significant is a relatively minor issue. The most pressing problem is that of attributing the warming to this particular cause. The possible existence of large low-frequency natural variability, combined with the uncertain influences of other external forcing factors and of ocean circulation changes, makes attribution a difficult task.

References

Hansen, J. and Lebedeff, S., 1987: Global trends of measured surface air temperature. Journal of Geophysical Research 92, 13345-13372.

Hansen, J., Fung, I., Lacis, A., Rind, S., Ruedy, R., Russell, G. and Stone, P., 1988: Global climate chnages as forecast by Goddard Institute for Space Studies Three-Dimensional Model. Journal of Geophysical Reseach 93, 9341-9364.

Hasselman, K., 1976: Stochastic climate models. Part 1. Theory. Tellus 28, 473-485.

Jones, P.D., Wigley, T.M.L. and Wright, P.B., 1986a: Global temperature variations between 1861 and 1984. Nature 322, 430-434.

Jones, P.D., Raper, S.C.B., Bradley, R.S., Diaz, H.F., Kelly, P.M. and Wigley, T.M.L., 1986b: Northern Hemisphere surface air temperature variations: 1851-1984. Journal of Climate and Applied Meteorology 25, 161-179.

Jones, P.D., Raper, S.C.B. and Wigley, T.M.L., 1986c: Southern Hemisphere surface air temperature variations: 1851-1984. Journal of Climate and Applied Meteorology 25, 1213-1230.

Jones, P.D., 1988: Hemispheric surface air temperature variations: Recent trends and an update to 1987. Journal of Climate 1, 654-660.

Karl, T.R. and Jones, P.D., 1989: On the urban biases in global temperature trends. Bulletin of American Meteorological Society (in press).

Madden, R.A. and Ramanathan, V., 1980: Detecting climatic change due to increasing carbon dioxide. Science 209, 763-768.

Robock, A., 1978: Internally and externally caused climatic change. Journal of Atmospheric Sciences 35, 1111-1122.

Vinnikov, K. Ya., Groisman, P. Ya., Lugina, K.M. and Golubev, A.A., 1987: Variations in Northern Hemisphere mean surface air temperature over 1841-1985. Meteorology and Hydrology 1987 (1) 45-53 (In Russian).

Wigley, T.M.L. and Jones, P.D., 1981: Detecting CO_2-induced climatic change. Nature 292, 205-208.

Wigley, T.M.L. and Raper, S.C.B., 1987: Thermal expansion of sea water associated with global warming. Nature 330, 127-131.

Wigley, T.M.L., Jones, P.D. and Kelly, P.M., 1978: Global temperature variations, 1861-1986. Proc. Eleventh Annual Climate Diagnostics Workshop, U.S. Dept. of Commerce, NOAA, 47-53.

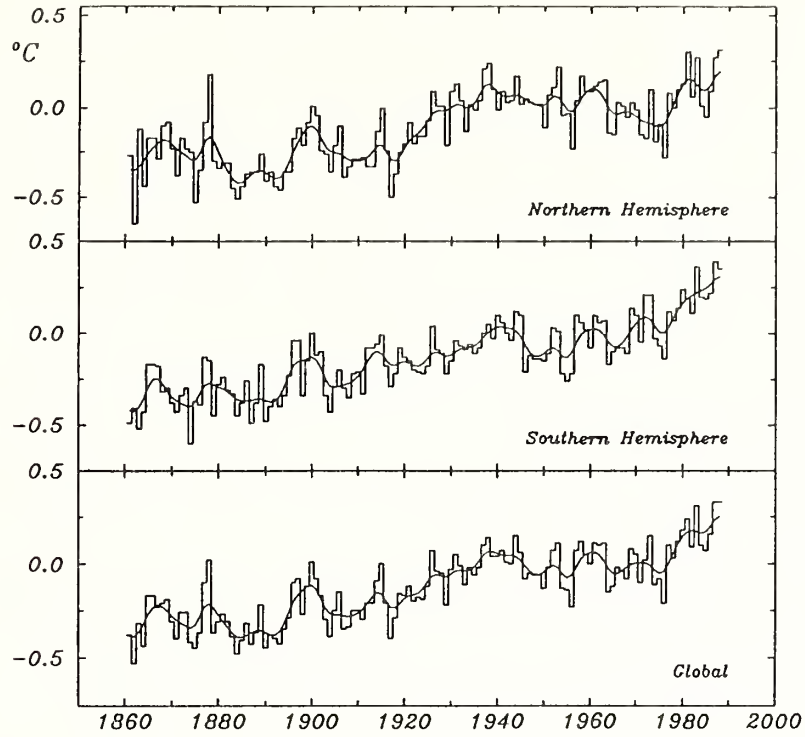

Figure 1: Hemispheric and global-mean temperatures. Data from both land and marine areas are included. The marine data used are sea surface temperatures from COADS through 1986 and using U.K. Meteorological Office data (adjusted to ensure homogeneity with COADS) for 1987 and 1988. The 1988 value is preliminary and includes data only up to and including November.

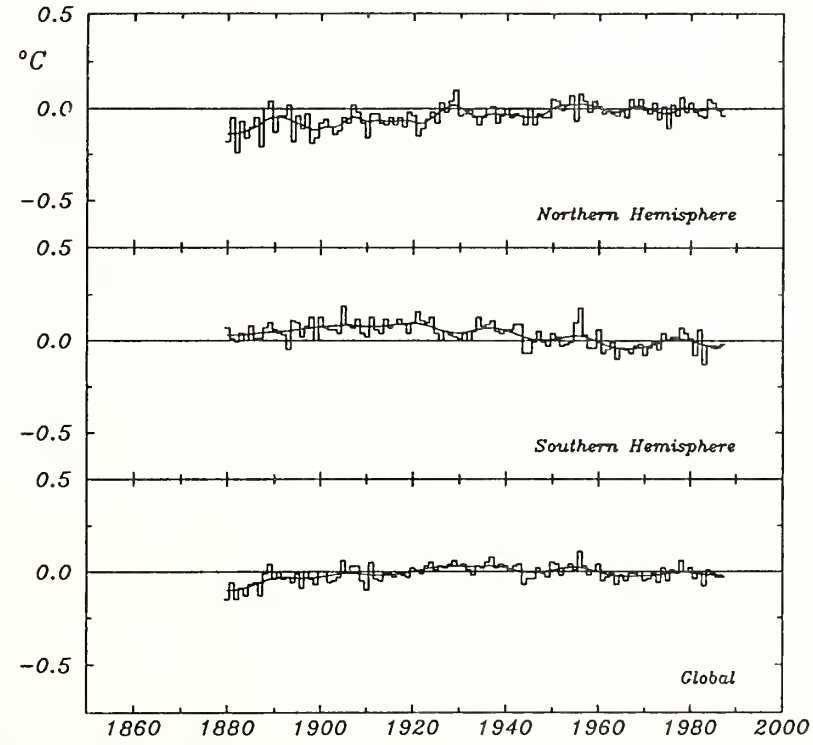

Figure 2: Differences between the land records of Hansen and Lebedeff and Jones et al. (HL minus J).

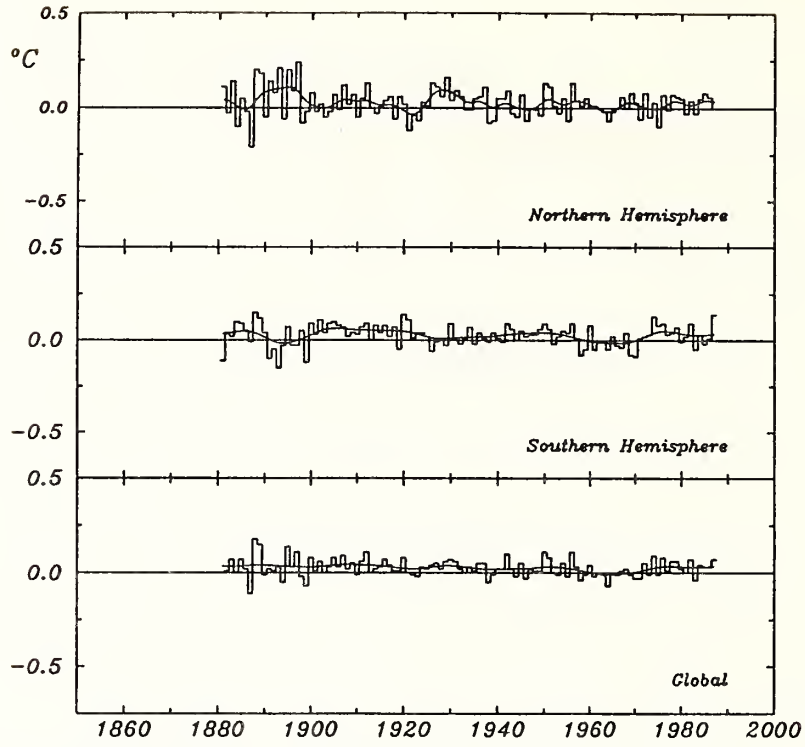

Figure 3: Differences between the land records of Vinnikov et al. and Jones et al. (V minus J).

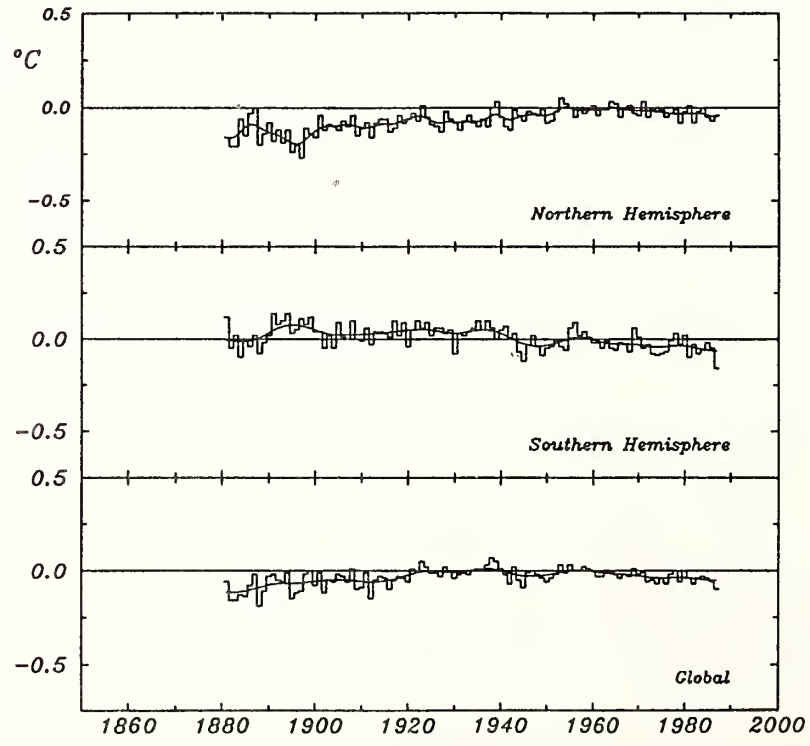

Figure 4: Differences between the land records of Hansen and Lebedeff and Vinnikov et al. (HL minus V).

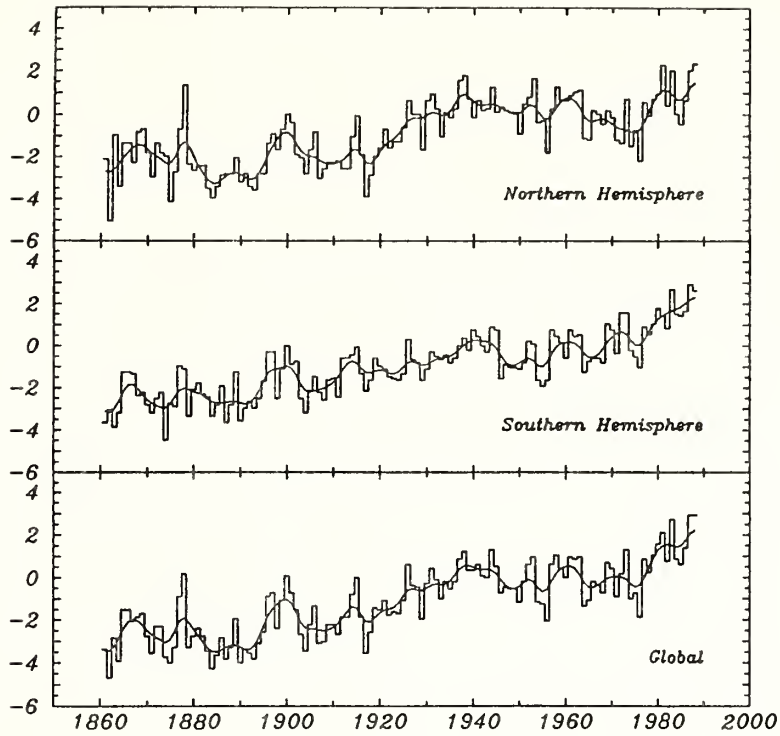

Figure 5: Land-plus-marine temperature variations expressed in σ units where σ^2 is the inter-annual variance (1951-80 data used). This allows one to assess the significance of individual values relative to any given reference level.

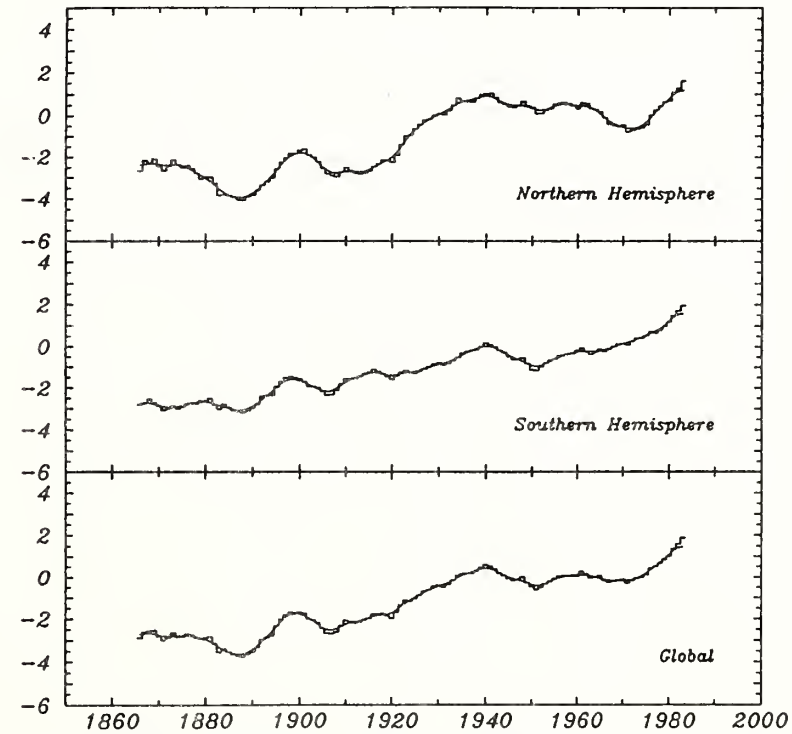

Figure 6: Decadal running means of land-plus-marine temperature normalized by the standard deviation of decadal means, with the latter estimated using an AR1 model.

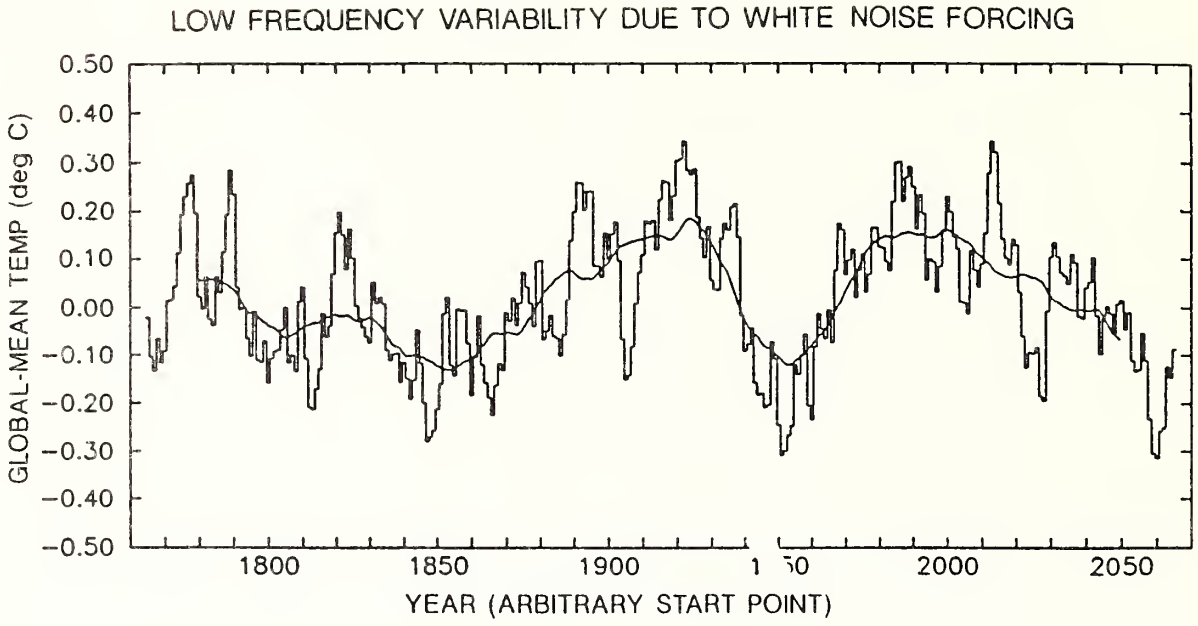

Figure 7: Internally-generated low-frequency variability of global-mean temperature resulting from white noise forcing, as simulated by an upwelling-diffusion, energy-balance climate model.

☆ U.S. GOVERNMENT PRINTING OFFICE: 1989— 2 4 2 - 2 0 2 0 5 0 0 1

PENN STATE UNIVERSITY LIBRARIES
A00007202248L